Handbook of Magnetic Materials

Edited by

K. H. J. Buschow

VOLUME

11

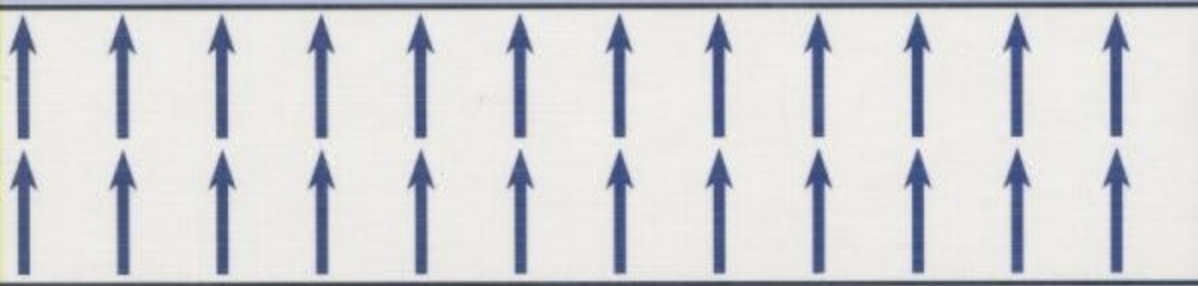

North-Holland

ELSEVIER SCIENCE B.V.
Sara Burgerhartstraat 25
P.O. Box 211, 1000 AE Amsterdam, The Netherlands

Library of Congress Cataloging in Publication Data
A catalog record from the Library of Congress has been applied for.

ISBN: Vol. 1 0 444 85311 1
Vol. 2 0 444 85312 X
Vol. 3 0 444 86378 8
Vol. 4 0 444 87106 3
Vol. 5 0 444 87477 1
Vol. 6 0 444 88952 3
Vol. 7 0 444 89853 0
Vol. 8 0 444 81974 6
Vol. 9 0 444 82232 1
Vol. 10 0 444 82599 1
Vol. 11 0 444 82956 3

ISBN: Set 0 444 85313 8

♾ The paper used in this publication meets the requirements of ANSI/NISO Z39.48-1992 (Permanence of Paper).

Printed in The Netherlands.

PREFACE TO VOLUME 11

The Handbook series Magnetic Materials is a continuation of the Handbook series Ferromagnetic Materials. When Peter Wohlfarth started the latter series, his original aim was to combine new developments in magnetism with the achievements of earlier compilations of monographs, producing a worthy successor to Bozorth's classical and monumental book *Ferromagnetism*. This is the main reason that *Ferromagnetic Materials* was initially chosen as title for the Handbook series, although the latter aimed at giving a more complete cross-section of magnetism than Bozorth's book.

In the last few decades magnetism has seen an enormous expansion into a variety of different areas of research, comprising the magnetism of several classes of novel materials that share with truly ferromagnetic materials only the presence of magnetic moments. For this reason the Editor and Publisher of this Handbook series have carefully reconsidered the title of the Handbook series and changed it into *Magnetic Materials*. It is with much pleasure that I can introduce Volume 11 of this Handbook series to you now.

Over the years there has been a growing interest in intermetallic compounds based on uranium. Initially the interest was focused on binary compounds with a well-defined crystal structure, comprising compounds with a rather broad 5f band as well as compounds belonging to the class of heavy-fermion systems. All these material were reviewed in Volume 4 of this Handbook. Although there still has been some progress in binary uranium compounds most of the experimental effort has been spent on the vast mount of ternary and multinary uranium systems. The reason for this is the possibility to reach a much wider variety in components while preserving the structure type. Simultaneously there has been an increasing amount of work done on well defined single crystals, often with advanced experimental methods such as photoelectron spectroscopy, inelastic neutron scattering and muon spin rotation. All these research activities have finally led to the crystallisation of new concepts in actinide magnetism which, together with the large amount of experimental work, will be reviewed in Chapter 1 of this Volume.

The last few decades have witnessed quite an extraordinary development in magnetic recording technology. This technology continues to evolve at a rapid pace resulting in media in which more data can be stored in ever decreasing volumes. It includes audio, video and data storage applications in the form of tapes, floppy and hard disks in products such as digital video recorders, digital camera recorders, audio equipment, electronic games, video telephones, fax machines and personal organisers. In the near future magnetic recording technology will have an enormous growth potential, it's main aims including further reduction in the peripheral device sizes while maintaining an increase in capacity. Hard disks are the most prominent type of mass storage today thanks to their low cost, high speed, and

relatively high storage capacity. The magnetism and materials aspects of hard disk media will be highlighted in Chapter 2 of this Volume.

Permanent magnetic materials are used as components in a wide range of industrial applications, in measuring and regulating controls and in medical equipment. Permanent magnets are also essential in devices for storing energy in a static magnetic field. Major applications involve the conversion of mechanical to electrical energy and vice versa, or the exertion of a force on soft ferromagnetic objects. The applications of permanent magnet materials in information technology are continuously growing. Important examples are voice coil motors and hard-disc drives. Permanent magnet materials have already been the subject of several chapters in previous volumes of the Handbook. Materials related to $SmCo_5$ and $Nd_2Fe_{14}B$ were extensively discussed in two separate chapters in Volume 4, while interstitially modified materials were reviewed in Volume 9. A more general review including magnetism and processing also of conventional magnet materials was published in Volume 10.

Magnets based on rare earth elements are unequalled with regard to coercivity and maximum energy production. There has been considerable progress in the development of rare earth based permanent magnets and this progress has gone hand in hand with a better understanding of the physical properties and especially the magnetism of the underlying class of materials. Results obtained by modern nuclear magnetic resonance techniques have contributed much to this understanding. Chapter 3 gives a survey of the physical principles involved with this technique and how these can be advantageously applied to the study of strongly ferromagnetic materials.

Inelastic neutron scattering is a powerful technique that is indispensable for in-depth studies of various types of magnetic materials. Prominent examples of how this technique has been helpful in the understanding of the magnetism of valence fluctuations and heavy fermions were already reviewed in a chapter in Volume 7. The last chapter of the present volume is devoted to inelastic neutron scattering when applied to study the crystal field interaction in lanthanide compounds. Included in this review is a description of how this technique is complimentary to various other modern and conventional techniques.

Volume 11 of the Handbook on the Properties of Magnetic Materials, as the preceding volumes, has a dual purpose. As a textbook it is intended to be of assistance to those who wish to be introduced to a given topic in the field of magnetism without the need to read the vast amount of literature published. As a work of reference it is intended for scientists active in magnetism research. To this dual purpose, Volume 11 of the Handbook is composed of topical review articles written by leading authorities. In each of these articles an extensive description is given in graphical as well as in tabular form, much emphasis being placed on the discussion of the experimental material in the framework of physics, chemistry and material science.

The task to provide the readership with novel trends and achievements in magnetism would have been extremely difficult without the professionalism of the North Holland Physics Division of Elsevier Science B.V., and I wish to thank Jonathan Clark and Wim Spaans for their great help and expertise.

K.H.J. Buschow
Van der Waals–Zeeman Institute
University of Amsterdam

CONTENTS

CONTENTS OF VOLUMES 1–10

Volume 1

Volume 2

Volume 3

Volume 4

Volume 5

Volume 6

Volume 7

Volume 8

Volume 9

Volume 10

chapter 1

MAGNETISM OF TERNARY INTERMETALLIC COMPOUNDS OF URANIUM

V. SECHOVSKY and L. HAVELA

Department of Metal Physics
Charles University
121 16 Prague 2
The Czech Republic

Handbook of Magnetic Materials, Vol. 11
Edited by K.H.J. Buschow

CONTENTS

1. Introduction

The electronic structure of lanthanides and actinides is characterized by partially occupied f-electron states (4f and 5f states, respectively). The magnetic and other electronic properties of actinide intermetallic compounds have, however, only little in common with the behaviour of their lanthanide counterparts, and in some characteristic features they resemble more 3d, 4d, or 5d transition metals. This is particularly striking when comparing light lanthanides with light actinides. The 4f states in the former case are usually localized, in contrast to the delocalized 5f states in light-actinide elements. The nature of the 5f states can be strongly affected by external variables like pressure and magnetic field, and also by alloying with other elements. Thus a large diversity of behaviour of compounds based on light-actinides has roots in this variable degree of the 5f-localization and in the dominance of many-body phenomena in the cross-over regime, which give rise to exotic phenomena like heavy fermions. The second vital ingredient of actinide magnetism is the strong spin–orbit interaction, providing significant orbital polarization of 5f-band systems and leading to a strong coupling of the direction of 5f-moments and both crystal and electronic structure. Its most apparent consequence is a huge magnetocrystalline anisotropy observed in U-intermetallics.

Studies of magnetism in U-compounds are dated back to the late forties and fifties, and they were oriented on simple binary systems like UH_3 or binary pnictides and chalcogenides, crystallizing in the simple cubic structure of the NaCl type. Systematic interest in intermetallic compounds in late sixties and seventies was oriented on several few types of compounds like Laves phases, which belong clearly to 5f systems with a rather broad 5f band. The emphasis was shifted to systems with large U–U separation (UPt_3, UBe_{13}, UCd_{11}, U_2Zn_{17}) in eighties with the advent of heavy-fermion systems, and the state of knowledge of that time is reflected in the review written by Sechovsky and Havela (1988). Although still some progress in binaries can be seen since that time, the main experimental effort was concentrated on vast amount of ternary and multinary uranium systems, having much larger variability of components while preserving the same structure type. These broad research activities led finally to the crystallization of new concepts in actinide magnetism. Another tendency is the increasing amount of work done on well defined single crystals. The progress in technology and especially in crystal growth led to inclination to non-cubic materials, for which information about magnetocrystalline anisotropy, anisotropy of exchange coupling, and related anisotropy of other electronic properties provide a clue to fundamentals of magnetism. The development of experimental techniques which most affected the current

level of understanding is the progress in neutron diffraction, a strong contribution being also obtained from μ^+SR. On the other hand, the potentially very promising technique of photoelectron spectroscopy, which obtained a strong impetus by new synchrotron radiation sources, was oriented on solving several controversial issues in interpretation of spectra of strongly-correlated systems, and did not cover larger spectrum of actinide materials. Other emerging techniques based on synchrotron radiation, like magnetic X-ray scattering or magnetic circular dichroism, are expected to contribute in coming years.

Unlike thorium and uranium compounds, studies on transuranium materials are still rare and the knowledge remains quite fragmentary. Probably the strongest limitation is, besides general strengthening of safety and security precautions, the difficulty of low temperature specific heat measurements. It is then often difficult to distinguish without knowledge of the parameters of the electron system around the Fermi level whether a band description is pertinent for a particular neptunium or plutonium system, or whether a more traditional conceptual framework based on local moments and crystal electric field (CEF) should explain the observed magnetic properties. On the other hand, it is interesting to compare the behaviour of U compounds with Np or Pu analogs, and this is respected in the present chapter, too.

The goal of the chapter is to cover the fast growing field of magnetism in uranium ternary compounds in one framework, stressing especially the importance of crystal structure and hybridization of the 5f states with other conduction-electron states.

Crystal structures of ternary compounds can be divided into three principal groups. One group are systems with the crystal structure of a binary compound, which has either three different atom position, or forming a possible superstructure, or having a statistical occupation of a lattice site. In the second group, one or more interstitial positions become occupied. In the third group we can identify the structure as constructed from building blocks of different binary materials. The complexity of crystal structures can become enormous especially in the last group, and one of the goals of solid state chemistry is nowadays the tailoring of materials having fragments of intermetallics intergrown with sub-systems of ionic-bond character containing elements like S and O. The boundary between intermetallic and other compounds is thus not very sharp, and therefore some of the compounds with non-metallic elements have been included in this work without breaking the consistency of the subject. On the other hand, the chapter does not include work done on pseudobinary systems like $U(Cu,T)_5$, although the boundary between the pseudobinaries and ternaries is not sharp, and the number of partly ordered materials is large.

Besides the description of properties of particular materials, the reader can find in this chapter an introductory part reviewing the most important notions of actinide electronic structure and magnetism. The next section dealing with particular experimental techniques and their interpretation is intended as a brief guide for newcomers into the field. For more specialized subjects the reader is referred to specialized monographs, like those written by Holland-Moritz and Lander (1994) on neutron scattering, by Dunlap and Kalvius (1985) on Mössbauer spectroscopy, by Schenck and Gygax (1995) on μ^+SR. More specialized information on heavy-fermion systems can be found in reviews of Grewe and Steglich (1991) and Nieuwenhuys (1995). Transport properties of lanthanides and actinides are compared by Fournier and Gratz (1993). Theoretical aspects are discussed by Johansson and Brooks (1993) and by Norman and Koelling (1993).

2. Electronic structure – magnetic properties

2.1. Uranium 5f states in intermetallics

The idiosyncratic nature of the 5f-electron states is best illustrated by stressing the contrasts between them and the 4f states in lanthanides. Since the majority of 4f electron density is deeply embedded within the core of lanthanide atoms, the interaction of the 4f states with environment is weak. This fact is documented by the results of neutron spectroscopy experiments (Fulde and Loewenhaupt 1986), which have revealed a negligible mixing of the 4f states of regular lanthanides (Pr, Nd, Gd–Tm) with the conduction and other electron states. Consistently, the observed ground state magnetic moments of regular lanthanide ions usually well agree with the R^{3+} free-ion values ($g_J J$) calculated within the LS coupling scheme. Some discrepancies between experimental and calculated moments can be attributed to CEF effects which can lift the orbital degeneracy of the 4f states. These effects originate from the interaction between the aspherical 4f charge cloud and the charge distribution surrounding the 4f electrons, which leads to the *single-ion* magnetocrystalline anisotropy of lanthanide magnetic moments.

The important consequence is that the magnetocrystalline anisotropy arises due to a directional dependence of the energy of a 4f charge cloud in the crystal field, thereby inducing a preferential orientation of the 4f magnetic moments with respect to crystallographic axes. Shape differences of the 4f cloud (which may be shaped like a cigar or a pancake) are reflected in the sign of the second-order Stevens factor, and lead to different easy magnetization directions among analogous materials where the rare-earth ions experience the same CEF (Legvold 1980).

The fundamental difference between the character of the 4f and 5f electron states in metals can be attributed to a much larger spatial extent of the 5f wave functions, and thus a much stronger interaction with the metallic environment, compared to the 4f case. As a consequence, the 5f electrons in actinides are, as a rule, delocalized due to their participation in bonding, and hence a considerable hybridization of the 5f states with the valence states of neighboring atoms (5f-ligand hybridization) in the crystal lattice. The delocalization of the 5f electrons has serious consequences. The most important one is, that the 5f states form a more or less narrow 5f band intersected by the Fermi energy E_F (the bandwidth W_{5f} is of the order of several eV) rather than discrete energy levels. Consequently, the magnetic moments due to the itinerant 5f electrons are much smaller than expected for a free U^{3+} or U^{4+} ion, and magnetic moments can disappear in a broad-band limit leading to weak (Pauli) paramagnetism. This situation resembles to a certain extent the 3d transition metals. The strength of magnetic coupling in cases of existing 5f moments is typically much larger than for the 4f moments interacting via the RKKY interaction. The impact on magnetic excitations is even more dramatic, no crystal-field excitations could be observed by inelastic neutron scattering in the vast majority of uranium intermetallics studied so far, instead of it one observes typically a rather broad quasielastic response reflecting the 5f-moments instability in analogy to, e.g., cerium mixed valence materials. On the other hand, the high density of states at E_F is projected into high γ-values of the low temperature specific heat (which are further renormalized by strong e–e correlations), and into highly anomalous transport properties, resulting from the hybridization of such "heavy" electron states with the non-f states carrying electrical current.

One of important consequences of delocalized nature of 5f states in light actinide intermetallics is an essentially different mechanism of magnetic anisotropy based on a *two ion* (5f–5f) interaction.

2.1.1. Hybridization of the 5f-states with ligands

Generally two one-electron mechanisms can be considered as affecting the ionic character of the 5f states. The first one is the 5f electron hopping due to an overlap of the 5f wave functions centered on neighboring f-sites, which can lead to a formation of the 5f band. Clearly the most important parameter is the U–U (or actinide–actinide) spacing. It was recognized long time ago (Hill 1970), that in U-compounds with a small U–U spacing d_{U-U} one often finds a superconducting, non-magnetic ground state, whereas for large d_{U-U} the ground state is non-superconducting, often magnetic. The critical parameter called the Hill limit was considered to be between 340 and 360 pm. Naturally, the occurrence of magnetic ordering is determined by a Stoner-type criterion (the product of $N(E_F)$ and an effective Coulomb interactions parameter must be larger than 1). Since the number of the 5f electrons is always between 2 and 3 in U-intermetallics (no sizeable charge transfer can take place in the absence of polar bonding) and the Coulomb interaction varies only a little in different types of materials, it is finally the width of the 5f band given by the 5f–5f overlap which affects the occurrence of magnetism. The strong sensitivity of the 5f-band width W_f on the interatomic distance R is seen from the expression (Johansson and Skriver 1982): $W_f \approx W_f^0 (R_0/R)^6$, in which W_f^0 is the band width for the spacing R_0. Besides individual overlap integrals also the number of the nearest U neighbors is important, but the former factor clearly dominates. Naturally, this primitive rule, which does not take into account individual details of the density of states, has several exceptions, from which probably the most apparent case is UNi_2, which despite having $d_{U-U} \leq 310$ pm orders magnetically (Sechovsky and Hilscher 1985).

Even more exceptions may be found on the large-d_{U-U} side of the Hill plot, where other delocalizing mechanism, namely the 5f-ligand hybridization, can dominate, making several compounds with negligible direct 5f–5f overlap non-magnetic. Naturally, besides the importance of overlap integrals also the energy degeneracy of the two types of states is an important pre-requisite. Qualitative rules concerning the strength of the hybridization were discussed by (Koelling et al. 1985) using simple arguments concerning the overlap integrals. In the case of a direct contact of U and a p-metal, like in UX_3 compounds, it is the size of the p-atom which is the most important parameter. The faster decay of the p-wave function on the U-site in case of smaller X ion makes the overlap integrals large, which leads to non-magnetic ground state in, e.g., USi_3 and UGe_3, whereas in compounds with large X ions (UIn_3, UPb_3) the hybridization is weaker and the ground state is magnetic. The prominent parameter in U-compounds with transition metals is the energy degeneracy of the 5f and d states. The 5f states of strongly electropositive uranium (or transuranium elements) remain pinned at E_F, whereas the increasing electronegativity of the d-elements closer to the right end of the transition metal series leads to a narrowing of the d-band (compared to the situation in the pure d-element), and its shifting down towards higher binding energies. This causes a reduction of the 5f–d overlap and consequently a weakening of the 5f–d hybridization. Therefore, the 5f magnetism typically arises in compounds with transition metals from the right end of a particular series. The d-magnetic moments, if observed,

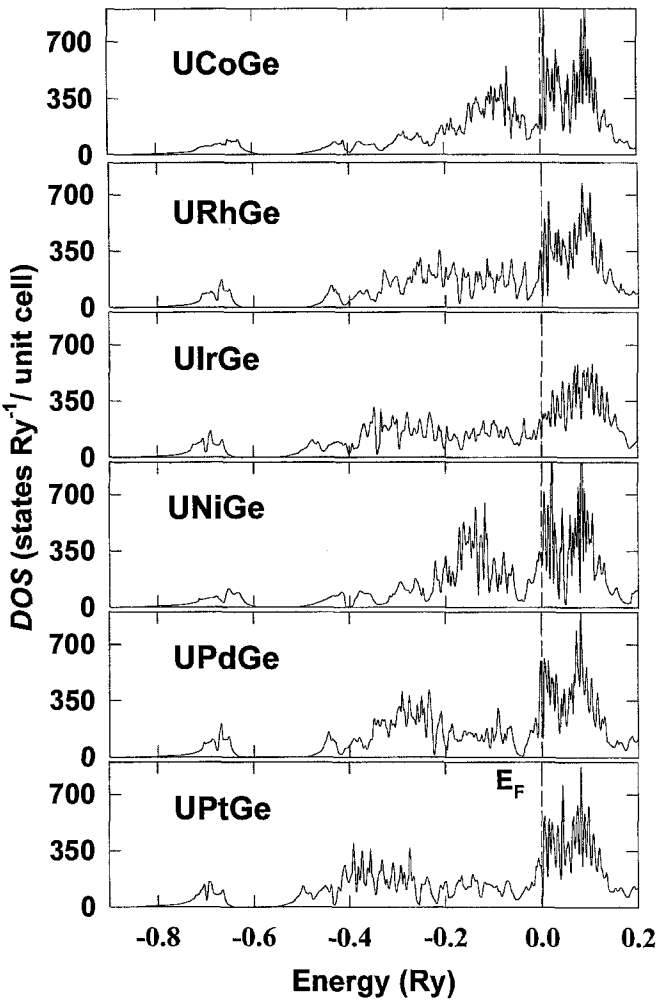

Fig. 2.1. Total densities of states (DOS) for various UTGe compounds, calculated using a Fully Relativistic Optimized LCAO Method (Divis et al. 1996). From this series, all compounds except for UCoGe and UFeGe (fig. 2.2) display a magnetic ground state.

are due to delocalization of the d-electron states greatly suppressed, and not only Ni or Co, but also Fe can behave in many cases as a "non-magnetic" element. The development of the electronic structure in the system of UTGe compounds is seen in fig. 2.1 showing total densities of states (DOS). The features spread from E_F to higher energies belong to the 5f band with two spin–orbit split sub-bands. The maxima below E_F are predominantly of d-origin. They are especially noticeable for the 3d series, whereas the gradually increasing spin–orbit splitting for 4d and 5d states makes this feature more smeared out. The example of a non-magnetic state due to strong 5f hybridization with Fe-3d states is depicted in

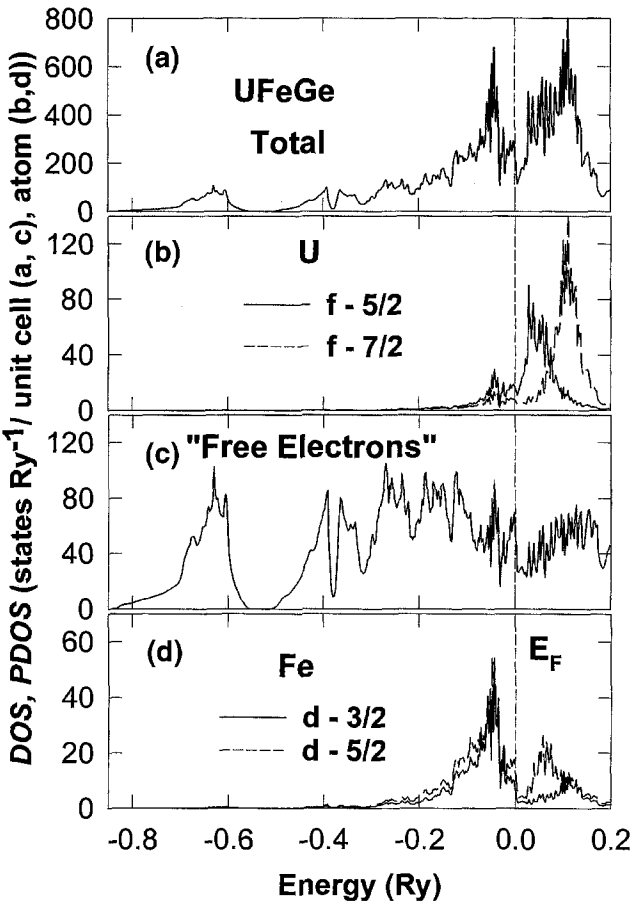

Fig. 2.2. Calculated total DOS (a), projected DOS (b), (d), and the sum of s-, p-, and U-6d-projected DOS (c) of UFeGe. The DOS values are given per unit cell (a), (c), or per atom (b), (d). After Havela et al. (1998a).

more detail in fig. 2.2, where partial densities of states are displayed. One can distinguish a pronounced secondary maximum in the 3d partial DOS above E_F, at energies where the 5f DOS is peaking. This feature is a clear fingerprint of the strong 5f–3d hybridization.

This situation can be somewhat modified by stoichiometry variations, and Fe-rich (U-poor) systems (like $UFe_{10}X_2$) have naturally the tendency to behave like d-magnets. On the other hand, minor magnetic moments on transition metal sites can be induced, mediated by the 5f–d hybridization, by the magnetic ordering of the 5f sublattice even on late transition metal atoms (e.g., Rh in URhAl (Paixao et al. 1992)).

2.2. Uranium magnetic moments

As it has been mentioned already above, a vast majority of U-intermetallics form a 5f band present at E_F. Therefore the band picture is an appropriate starting point for describing the

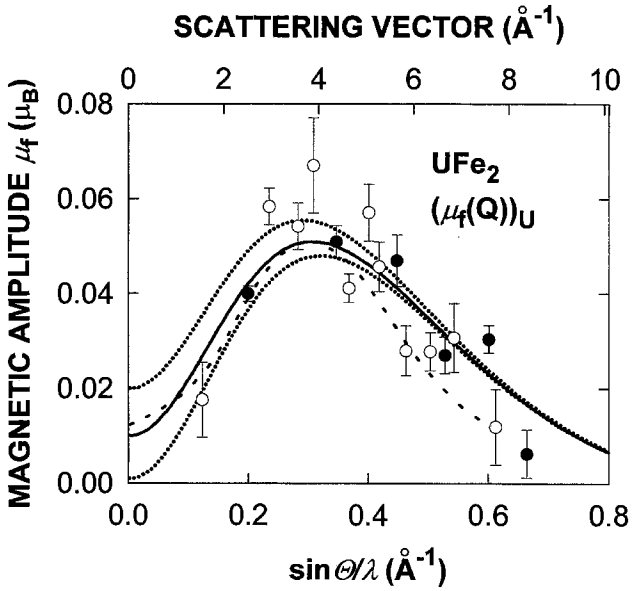

Fig. 2.3. The U-magnetic form factor, $\mu_U f(Q)_U$, as function of $\sin\Theta/\lambda$ in UFe_2 (after Lebech et al. (1989)). The solid circles are deduced from Bragg reflections coming from the U-sublattice only. The solid curve represents the magnetic amplitude given by $\mu_L = 0.23\,\mu_B$ and $\mu_S = -0.22\,\mu_B$, $C_2 = 23$. The precision of the determination of μ_U is demonstrated by the dotted lines; the upper corresponds to $\mu_U = 0.02$ and $C_2 = 12$, the lower to $\mu_U = 0.001\,\mu_B$ and $C_2 = 225$. The dot-dashed curve is the magnetic amplitude calculated using the results of spin-polarized energy band calculations (Eriksson et al. 1990b) re-scaled to match the experimental data.

electronic structure, and also the magnetic moments and their ordering can be understood as due to a spontaneous splitting of spin-up and spin-down sub-bands forming a net spin magnetic moment μ_S. An important difference between, e.g., the 3d transition metals and the light actinides is the relation between the energy of the spin–orbit coupling Δ_{S-O} and the energy width of the 3d (5f) band W_{3d} (W_{5f}). Whereas $\Delta_{S-O} \ll W_{3d}$, the respective values in light actinides become comparable because Δ_{S-O} is of the order of eV. Due to the strong spin–orbit interaction, typically a large orbital magnetic moment μ_L is induced, which is antiparallel to the spin moment for U, in analogy with Nd and the third Hund's rule stating that the total angular momentum is given by $\boldsymbol{J} = \boldsymbol{L} - \boldsymbol{S}$. The existence of such orbital moments for the 5f-band systems has been first revealed from band structure calculations involving a spin–orbit interaction term coupling the spin and orbital moment densities (Brooks and Kelly 1983). They also predicted an impact on the magnetic form factor $f(\boldsymbol{Q})$, where $Q = 4\pi\sin\theta/\lambda$, θ is the Bragg angle, λ – the wavelength, in neutron scattering. $f(\boldsymbol{Q})$ can be expanded in terms of Bessel function transforms of the single electron wave-function density. In the dipole approximation, the spin form factor $f_S(Q) = \langle j_0\rangle$ and the orbital form factor $f_L(Q) = \langle j_0\rangle + \langle j_2\rangle$. The magnetic amplitude, the quantity determined by experiment, is given by:

$$\mu f(Q) = \mu_S f_S(Q) + \mu_L f_L(Q) = \mu\big[\langle j_0\rangle + C_2\langle j_2\rangle\big], \tag{2.1}$$

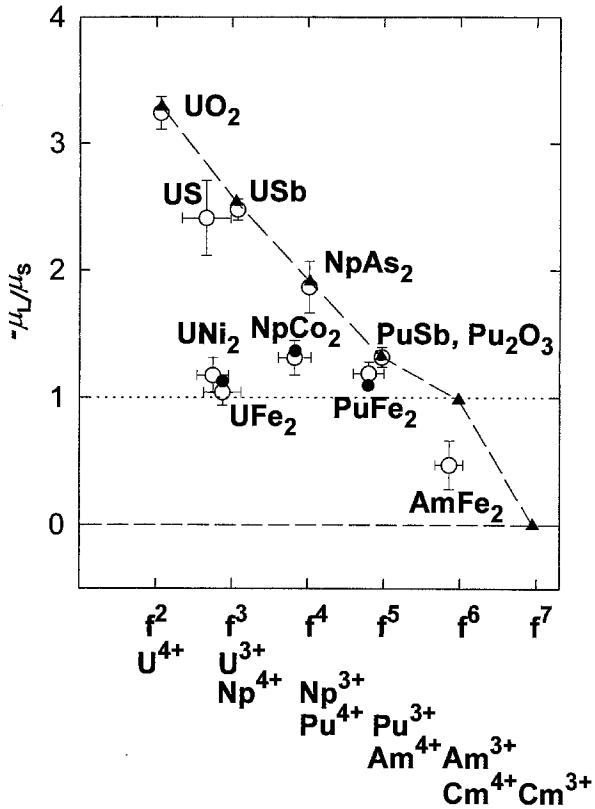

Fig. 2.4. Ratio of the orbital μ_L and spin μ_S moments in a number of magnetically ordered materials (after Lebech et al. (1991)) plotted as a function of the number of the 5f-electrons. The triangles, which are connected by a dashed line, are the values derived from single-ion theory including intermediate coupling. Experimental results are shown by open circles. Results of band structure calculations are shown as solid circles.

where $C_2 = \mu_L/\mu$, μ being the total magnetic moment (Lebech et al. 1991). If the orbital moment is relatively small, C_2 is negligible and the total form factor resembles that of transition metals. But in the case $\mu_L \approx -\mu_S$ a highly anomalous form factor is obtained, which looks simply like $\langle j_2 \rangle$, tending to zero both for high Q and $Q = 0$. Such situation has been indeed identified in experimental form factors in compounds like UFe_2 (Lebech et al. 1991), which has practically zero U moment consisting of $\mu_L = 0.23\,\mu_B$ and $\mu_S = 0.22\,\mu_B$ (see fig. 2.3).

A different sensitivity of spin or orbital moments to external variables like pressure, deduced in the original work already (Brooks and Kelly 1983), led to the assumption that the ratio of orbital and spin moment should reflect the degree of the 5f-delocalization. Indeed, as seen from fig. 2.4, the compounds showing the least delocalized nature of the 5f states (UO_2, USb, $NpAs_2$, PuSb) are located on the line representing values of $-\mu_L/\mu_S$ of a free $5f^n$ ion. On the other hand, magnetically ordered materials with presumably the most itinerant 5f states (UFe_2, UNi_2, $NpCo_2$, $PuFe_2$) have this ratio close to 1 (Lebech et

al. 1991). However, the general validity of this scheme remains still questionable, because a reliable ratio of 1.81 for ferromagnetic URhAl was reported by Paixao et al. (1992), whereas for the more localized antiferromagnet UNiGa one gets 1.98 (Olsovec et al. 1998). On the other hand, the study of the field-induced form factor on UNiAl (antiferromagnet) in the paramagnetic state yields 1.79 (Olsovec et al. 1998), and in the case of UCoAl with a non-magnetic ground state the value is close to the free-ion value 2.6 (Wulff et al. 1990).

A large field-induced orbital moment was predicted even for U metal. Surprisingly, for in an external magnetic field spin and orbital magnetic moments orient parallel, as shown by a simple balance of the Zeeman and spin–orbit energy in the case of weak susceptibility (Hjelm et al. 1993, 1994). Such magnetic form factor in which the orbital and spin parts are not subtracted but added well explains the original experimental data on α-U metal (Maglic et al. 1978).

The electronic structure calculations giving realistic predictions of values of spin and orbital magnetic moments take into account, as a rule, also the orbital polarization besides the standard spin polarization, which is the background of the Hund's second rule (maximization of the orbital momentum). It was first introduced by Eriksson et al. (1990a) and was used in references in the above paragraph. The importance of spin–orbit interaction and orbital polarization is evident from the work of Sandratskii and Kübler (1997a). They showed that, if one takes into account both spin and orbital moments as independent 3-dimensional vectors, one can obtain from the calculations realistic non-collinear magnetic structures, as in U_3X_4 compounds (Sandratskii and Kübler 1997a). Naturally, the strong spin–orbit coupling and the 5f-ligand hybridization make the whole electronic structure strongly dependent on the mutual coupling of magnetic moments and their orientation with respect to crystal axes. Performing calculations with magnetic moments forced into different directions can yield estimates of the type and strength of magnetic anisotropy (Sandratskii and Kübler 1995a). The anisotropy energy is typically found to be of the order of mRy per unit cell, i.e., hundreds Kelvin, which is often found in experiment, too. The example of U_2Pd_2Sn is shown in section 5.3. On the other hand, if moments are not predetermined into special directions by symmetry, i.e., if they can rotate without reducing the symmetry of the problem, they will in reality reach a minimum-energy state in a general orientation not coinciding with any special crystallographic direction (Sandratskii and Kübler 1997a, 1997b). Another important consequence is that in cases in which directions of spin and orbital moments are not imposed by symmetry, the interatomic interactions can disturb their mutual collinearity, existing for free ion due to the axial symmetry of the problem. On the other hand, if the symmetry of the crystal is high and the direction of the spin moment is parallel to a crystal symmetry axis passing through the atom, the two atomic moments will be collinear as a consequence of symmetry properties, as in the case of U_2Pd_2Sn (Sandratskii and Kübler 1996).

2.3. Exchange interactions

The comparison of the respective temperatures of magnetic phase transitions between U-compounds and their rare earth analogs demonstrates clearly a different nature of magnetic coupling in these two classes of materials. If we select materials without any active participation of transition-metal components, we find that a number of U-compounds order

magnetically at temperatures that are an order of magnitude higher than those with Gd, despite the fact that the magnetic moments of the former are nearly 10 times smaller than the latter. A typical example in this sense is UGa_2, which is ferromagnetic below $T_C = 126$ K (Ansorge and Menovsky 1968), whereas for the isostructural $GdGa_2$ one has $T_N = 12$ K (Tsai et al. 1978). For the 4f intermetallic compounds, the standard interaction is the indirect interaction of the RKKY type, mediated by the polarization of weakly interacting conduction electrons. The fact, that the 4f and conduction-electron sub-systems are coupled together by the on-site polarization of the 5d states, does not make much difference. The interaction is oscillatory, leading thus potentially to complicated magnetic structures, with the envelope falling out as $1/R^3$.

The variable degree of delocalization in the 5f systems means that we can encounter several different regimes. For compounds with high U-content, i.e., those with d_{U-U} below or around the Hill limit, the direct 5f–5f overlap leads to a direct exchange coupling within the 5f band. Certain attributes of such systems resemble transition metals. For example, both magnetic moments and ordering temperatures of compounds like UNi_2 or UFe_2 are strongly depressed under external pressure (for an overview see the chapter of Sechovsky and Havela (1988) in Vol. 4). Moreover, ferromagnetism appears as the only type of ordering in this region. U-moments are typically much smaller than 1 μ_B, and although a partial cancellation of spin and orbital moments plays a role, they are distinctly smaller than U-moments outside this region. The ordering temperatures are relatively high. The reason can be found in the Stoner–Edwards–Wohlfarth theory for itinerant magnets, in which the ordering temperatures are proportional to the ordered moment, and not to its square as in other interactions including the RKKY one.

With increasing d_{U-U} more antiferromagnets appear, and above $d_{U-U} = 401$ pm (UGa_2) probably no ferromagnet occurs any more. This development can be seen also in individual materials with two different values of the characteristic U–U spacing. For example, in the UTX compounds with the ZrNiAl structure type (see section 5.1.1), the geometry of the structure leads to the formation of planar systems with d_{U-U} close to the Hill limit, whereas in the third dimension perpendicular to such planes the spacing is larger. Consequently, magnetic structures consist of strongly coupled ferromagnetic sheets with weaker inter-plane coupling, which is frequently of an antiferromagnetic type. For $d_{U-U} > 400$ pm the direct 5f–5f overlap is negligible, and therefore the hybridization starts to play an important role. Thus the hybridization has actually a dual role. In the first approximation it is a primary mechanism of the destabilization of 5f moments, in the second approximation, because the spin information can be conserved in the course of the hybridization process, it leads to an indirect exchange coupling. The maximum ordering temperatures can be consequently expected for a moderate strength of hybridization, because a strong hybridization completely suppresses magnetic moments, whereas a weak one leaves moments intact, but their coupling is weak.

A relatively simple model which leads to qualitatively realistic results has been worked out by Cooper and co-workers (Cooper et al. 1985), on the basis of Coqblin–Schrieffer approach to the mixing of ionic f-states and conduction-electron states (Coqblin and Schrieffer 1969), in which the mixing term of the Hamiltonian of Anderson type is treated as a perturbation, and the hybridization interaction is replaced by an effective f-electron–band-electron resonant exchange scattering. Considering an ion–ion interaction as mediated by

different covalent-bonding channels, each for particular magnetic quantum number m_l, the strongest interaction is for those orbitals, which point along the ion–ion bonding axis, which represents the quantization axis of the system. The two 5f ions maximize their interaction by compression of the 5f charge towards the direction to the nearest 5f ion. This has serious impacts on magnetic anisotropy, because it means a population of the 5f states with orbital moments perpendicular to the bonding axis. This interaction prefers a strong ferromagnetic coupling of actinide atoms along the bonding direction, whereas there is no special general tendency to ferro- or antiferromagnetism perpendicular to it, where the interaction is much weaker, and can be comparable to the "background" isotropic exchange interaction of the standard RKKY type.

An alternative approach explaining the tendency to a ferromagnetic coupling in a certain regime can be seen in the description of variations of the RKKY interaction when considering more realistic properties of the conduction-electron sub-system (Schwartz 1976). For example, a moderate exchange enhancement of that sub-system leads to a lifting up and distorting of the oscillatory function describing the spin polarization at a distance, causing net ferromagnetic polarization. Naturally, a directionality of the 5f bonds and 5f–d hybridization can play a similar role in both mechanisms.

The anisotropy of the two-ion interaction in uranium intermetallics is also responsible for specific magnetic structures in antiferromagnets. We also discuss relations between the symmetry of magnetic structures and the symmetry of the arrangement of U atoms in the crystal lattice.

2.4. Magnetocrystalline anisotropy

Since the spin–spin exchange interaction is essentially isotropic, it is the magnetocrystalline anisotropy which orients magnetic moments relatively to crystallographic axes. The mechanism usually responsible for this phenomena in lanthanide intermetallics with well localized 4f states is the single-ion crystalline electric field (CEF) interaction. We will show that the involvement of delocalized 5f states in light actinide intermetallics (being involved in anisotropic covalent bonding) implies an essentially different, two-ion (5f–5f) interaction, which plays a major role in the anisotropy. The strong spin–orbit interaction is a necessary pre-requisite in both cases.

The fact, that the 5f intermetallic compounds display much stronger magnetic anisotropy than their lanthanide counterparts has been known for a long time. The anisotropy field, estimated as the intercept field of the easy and hard magnetization curves extrapolated to high magnetic fields, frequently reaches values of the order of 10^2–10^3 T (Sechovsky and Havela 1988; Sechovsky et al. 1992a, 1994a). These values represent anisotropy energies of the same order (0.2 eV) as observed for US and obtained by Brooks et al. (1986) in the calculations done within the local density approximation, and the calculations on U_2Pd_2Sn mentioned in the section 2.2 yield values not much lower (Sandratskii and Kübler 1996). We have seen already that depending on the environment of actinide atoms in different intermetallics, we can encounter variable strengths of the 5f-bonding and the 5f-ligand hybridization. Resulting variations of the 5f delocalization lead to a wide spectrum of magnetic properties, ranging from Pauli paramagnetism to ferromagnetic or antiferromagnetic ordering of local 5f moments. The strong magnetocrystalline anisotropy is, however, observed in all uranium compounds exhibiting a 5f contribution to the magnetic moments, and is not thus restricted to magnetically ordered materials.

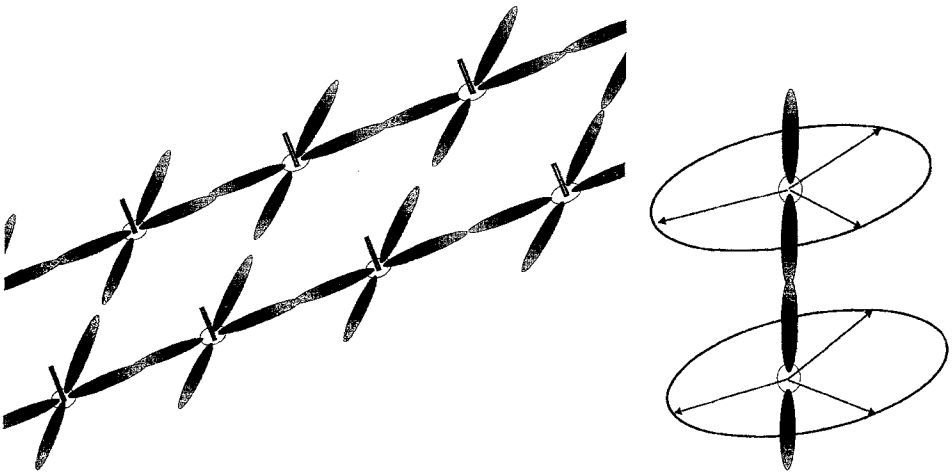

Fig. 2.5. Schematic illustration of the planar bonding geometry, which forces the magnetic moments represented by the bars perpendicular to the plane (a), which contrasts with the columnar bonding leading essentially to an easy-plane anisotropy type (b).

Magnetic anisotropy studies are usually limited only to rarely available single crystals of uranium compounds. Therefore, more systematic information on actinide materials is still lacking. Materials with a uniaxial crystal structure (hexagonal and tetragonal) are of particular interest for offering the possibility of unambiguous interpretation of experimental results from magnetization measurements in external magnetic fields. The easy magnetization direction in these structures is usually either parallel ($\parallel$) or perpendicular ($\perp$) to the c-axis. The systematic occurrence of particular types of anisotropy over diverse groups of U-intermetallics leads to the conclusion that on the vast majority of materials, in which the U–U co-ordination is clearly defined in the crystal structure, the easy-magnetization direction is perpendicular to the nearest U–U links. As follows from simple geometrical considerations, if the links are found in different directions in a plane, moments have to orient themselves perpendicular to the plane yielding the easy-axis anisotropy type (see fig. 2.5(a)). In an opposite case, if U-atoms form linear chains (the intra-chain U–U separation is significantly smaller that the inter-chain one), an easy-plane anisotropy appears (fig. 2.5(b)).

The latter case is represented, e.g., by **UGa_2**, which is a ferromagnet with large local U magnetic moments (Sechovsky and Havela 1988). It crystallizes in the hexagonal structure of the AlB_2 type, in which the U atoms form linear chains along the c-axis. The nearest neighbor U–U spacing d_{U-U} along the c-axis (401 pm) is smaller than the inter-chain spacing (421 pm). Magnetic moments of about $2.7\,\mu_B$/U are oriented perpendicular to the c-axis. The hard magnetization direction [0 0 1] is observed both in the ordered and paramagnetic states. An estimated anisotropy field is about 100 T in both states.

UPt_3 is a heavy fermion spin fluctuator with antiferromagnetic correlations (Franse et al. 1984). It forms in the hexagonal structure of the $MgCd_3$ type. The nearest inter-U distance

$d_{U-U} = 413$ pm is found between atoms in adjacent basal-plane layers. Magnetic data show that the c-axis is the hard-magnetization direction. A metamagnetic transition was found in fields around 20 T applied within the basal plane.

UPd_2Al_3, a heavy-fermion antiferromagnet (see section 5.8). It adopts the hexagonal $PrNi_2Al_3$ structure, and the U-atoms form a triangular network within the basal plane. The distance d_{U-U} is much shorter along the c-axis (418.6 pm) than in the basal plane (536.5 pm). The c-axis is the hard magnetization direction.

Further examples of this behaviour are, e.g., **UPdSn**, an antiferromagnet with localized 5f moments (see section 5.1.3), with non-collinear magnetic structure and non-zero component of the U-moments in the c-axis direction. But still this direction is a hard magnetization direction, and even the weak 5f-band ferromagnet **UNi_2** (Sechovsky and Havela 1988) also shows a strong anisotropy of the easy-plane type, although the U–U co-ordination cannot be so simply specified in its hexagonal Laves phase structure.

Even more apparent is the uniaxial anisotropy, observed for example generally in UTX compounds with the hexagonal ZrNiAl structure type and in UT_2X_2 compounds crystallizing in the tetragonal structures $CeCr_2Si_2$ or $CaBe_2Ge_2$. The broad validity of the rule relating the structure, the U–U co-ordination in particular, with the type of anisotropy, can be well illustrated especially on the first group spanning a large variety of ground state types. **UNiAl** is itinerant antiferromagnet (Brück et al. 1994). The hexagonal structure of the ZrNiAl type (see fig. 5.1) exhibits a relatively close packing of uranium and transition-metal atoms within the U–T layers leading to a highly correlated electron gas within the U–T basal-plane layers. Magnetic moments in UNiAl are oriented along the c-axis, and a magnetic field applied along the c-axis can induce a moment reorientation manifest as a spin-flip transition in the magnetization curve. Magnetic response for fields applied within the basal plane is much weaker (see fig. 5.10), which is also true for the paramagnetic range. **URuAl** (Veenhuizen et al. 1988a; Sechovsky et al. 1992b) is a spin-fluctuator with paramagnetic ground state. Figures 5.19 and 5.21 demonstrate the same type of anisotropy as in UNiAl. An interesting is comparison with **URhAl**, a ferromagnetic isotype (Veenhuizen et al. 1988a, 1988b; Sechovsky et al. 1992b), having U spontaneous moments oriented along c, but magnetic susceptibility for field along the basal plane χ^a is practically identical as in paramagnet URuAl. The inspection of other UTX compounds with this structure type shows that typically a magnetization of 0.10–0.14 μ_B/U (except for UPdIn (fig. 5.27), where it reaches 0.5 μ_B/f.u. (Fujii et al. 1990a)) can be induced by field along the basal plane of 35 T, which is the standard highest field available at the Amsterdam High-Field Installation, where most of the studies were performed. From these findings we can conclude that the basal plane magnetization in all compounds of this group reflects paramagnetic behaviour essentially independent of the magnitude and type of ordering of uranium magnetic moments, which are strongly coupled to the c-axis. This means that no moment rotations are observable in available magnetic fields of tens of Tesla. The common way of estimating anisotropy fields H_a by extrapolation magnetization curves taken at $T = 4.2$ K for field along the easy- and hard-magnetization direction thus fails, because the hard-magnetization curve reflects more the conduction-electron susceptibility than the response of the 5f moments. The values thus obtained can be therefore taken as a sort of lower estimate of the anisotropy field. This method cannot be used then in all in cases in which the 5f moments still develops and is assisted by an external field, ant thus the high

field susceptibility for the easy axis therefore being higher that for the hard axis. A typical example is the 5f-band metamagnet UCoAl (see fig. 5.3). As the bonding anisotropy is not related to magnetic ordering, the same type of anisotropy persists for magnetically ordered materials into a paramagnetic range. The temperature dependencies $\chi^{a}(T)$ and $\chi^{c}(T)$ of most of compounds of the ZrNiAl-structure group can be reasonably approximated by the Curie–Weiss law (although the basal plane susceptibility is only weakly temperature dependent)

$$\chi^{a,c} = C^{a,c}/\left(T - \Theta_{p}^{a,c}\right) \tag{2.2}$$

with Curie constant values $C^{a} \approx C^{c}$. The anisotropy of the paramagnetic susceptibility is expressed by the difference $\Delta\Theta_{p} = |\Theta_{p}^{c} - \Theta_{p}^{a}|$. The values of $\Delta\Theta_{p}$ obtained for available single crystals are all in the range 350–450 K, only the value for UPdIn (see fig. 5.26) is much lower (108 K). Nevertheless, this value is still an order of magnitude larger than found in the rare-earth analog, NdPdIn, for which $\Delta\Theta_{p} = 16$ K (Fujii et al. 1990a). A closer inspection of $\Delta\Theta_{p}$ values reveals that they correlate quite well with the $\mu_{0}H_{A}$ values (Sechovsky et al. 1992a, 1994a).

Unfortunately, also this method of determining the anisotropy has limits. If the "intrinsic" value of $\chi^{a}(T)$ is very small, experimentally the contribution associated with the projection from the easy-axis direction due to crystal mosaicity or imperfect crystal adjustment starts to dominate.

It is interesting to note that polarized neutron experiments on URhAl (Paixao et al. 1992) and URuAl (Paixao et al. 1993) have revealed an order of magnitude higher magnetization density induced on the transition metal atoms in the U–T layers, compared to those in the T–X layers. This result reflects a much stronger hybridization of the uranium 5f states with the d-electron states of the transition metal within the U–T layers.

Although we deal with representatives of several very different classes of uranium magnetism, we can deduce some common features connected with magnetic anisotropy:

(a) Anisotropy fields are much higher than the maximum fields applied in relevant experiments (typically 35 T), and simple extrapolation of magnetization curves to higher fields yields an estimate of $\mu_{0}H_{A}$ being usually of the order of several hundreds of Tesla.
(b) Strong anisotropy extends into the paramagnetic range; the anisotropy energy can be characterized by the difference between paramagnetic Curie temperatures measured in fields applied along the "easy" and "hard" magnetic axes, which amounts typically to several hundred Kelvin.
(c) The same type (symmetry) of anisotropy is observed in the paramagnetic and magnetically ordered states.

A similar situation, in which the easy and hard magnetization directions are, as a rule, orthogonal, is also present in orthorhombic structures. A higher symmetry leading to a higher multiplicity of easy directions makes anisotropy studies more difficult. In particular, the anisotropy within the basal plane is difficult to determine in tetragonal, and especially in hexagonal, structures. Reliable magnetic anisotropy studies in high symmetry systems can be performed only by means of microscopic experiments, as has been demonstrated by

Lander et al. (1990), who were able to determine the anisotropy constant K_1 of cubic US ($K_1 \approx 10^{10}$ erg/cm^3 at 0 K) from neutron diffraction experiments on a US single crystal in external magnetic fields.

In the case of some non-cubic materials, especially those with the uniaxial magnetocrystalline anisotropy, single crystal studies can be, to a certain extent, successfully simulated by means of high-field magnetization experiments on powder samples. Comparisons of data obtained on randomly oriented and field aligned powders can provide valuable information (Sechovsky et al. 1992b).

2.5. *Magnetic structures*

Both specific mechanisms of magnetocrystalline anisotropy and exchange interactions are factors naturally predetermining types of magnetic structures in U-intermetallics. A noticeable difference with respect to rare-earth systems is the inclination to ferromagnetism for moderate U–U spacing, as in the already mentioned case of UGa_2 vs. $REGa_2$, the latter ordering antiferromagnetically (Tsai et al. 1978). A convenient illustration of how particular magnetic structures are constituted is again provided by the UTX compounds with the ZrNiAl structure. The strong bonding within the U–T planes leads to a ferromagnetic coupling of U-moments (kept perpendicular to the plane by the anisotropy) within the plane, and the only exception is UNiAl with a long wavelength periodicity AF structure described by $\boldsymbol{q} = (0.1, 0.1, 0.5)$ (Prokes et al. 1998a). The ferro- or antiferromagnetic coupling in the perpendicular direction is weaker, as expected, e.g., by the two-ion hybridization induced exchange interaction model (Cooper et al. 1985). In UNiGa, the weak AF coupling can be broken by a magnetic field of about 1 T along c. The magnitude of $T_N = 40$ K means that the effective coupling parameters to 4 U neighbors within the basal plane have to be several orders of magnitude larger than for the 2 neighbors along c, the former leading also to the positive value of Θ_p, found in a system with AF ground state. Under the condition of a somewhat stronger 5f–d hybridization (e.g., by replacing Ni in UNiGa by Rh) also the ferro-coupling starts to dominate the coupling along the c-axis. The ferromagnetic coupling within the basal plane is contrasting with the AF coupling found in analogous RENiAl and RECuAl compounds (Tuan et al. 1993; Ehlers and Maletta 1996; Javorsky et al. 1997).

It is interesting at this stage to inquire whether other available data documenting the anisotropy of magnetic coupling of various uranium based materials are also consistent with these common features. If we turn again to the compounds mentioned above, which span a very broad range of the 5f-localizations, we can conclude that in most of the cases in which we can easily determine the strong bonding directions, the easy-magnetization direction is perpendicular to them and ferromagnetic coupling is found along these bonding directions. This is the case, for instance in the strong ferromagnet UGa_2 (Andreev et al. 1979), in heavy-fermion compounds as UPt_3 (Franse et al. 1984) or UPd_2Al_3 (Grauel et al. 1992; de Visser et al. 1992), or in the itinerant ferromagnet UNi_2 (Frings et al. 1986)). However, the case of UPd_2Al_3 shows that there can be exceptions to the rule of ferromagnetic coupling along the strong-bonding direction. In this compound, antiferromagnetic coupling occurs along the c-axis, and the reason may be related to the rather large spacing along the c-axis (albeit shorter than along the a-axis). The vast majority of compounds

in which the rules are obeyed brings us to a situation in which the exceptions are more interesting.

Another noticeable tendency is the preference of collinear structures with moment modulations (spin density waves) over equal-moment non-collinear structures. The reason is that the anisotropy energy is typically stronger than the exchange coupling energies. Non-collinear magnetic structures are stable if the easy-magnetization directions on different sites are not collinear, as in U_2Pd_2Sn, where they are orthogonal. Only in cases in which the lattice symmetry imposes no special requirements on the U-moments directions one can observe cycloidal structures which is observed in the case of UPtGe (Kawamata et al. 1993).

Equal moment structures are normally found in the ground state due to minimum magnetic entropy, but UNiAl is an example of a modulated structure surviving to lowest temperatures as a heavy-fermion antiferromagnet (Brück et al. 1994). However, one or more different magnetic structures are stable at elevated temperatures, often with moment modulations or as incommensurate structures. Whereas magnetic phase transitions between paramagnetic and ordered state are normally of the second order type (exceptions can occur if accompanied by strong magnetoelastic phenomena, or, e.g., if magnetic ordering leads to a re-arrangement of CEF levels or of the whole electronic structure) magnetic phase transition of the order–order type are typically of first order, because no new order parameter appears at the transition. If a new order parameter appears, like ordering of moments in the remaining third dimension as in UPdSn, the transition is again of the second order type.

3. Electronic properties – experimental methods

3.1. Bulk methods

3.1.1. Magnetic susceptibility and magnetization

In the paramagnetic state, the temperature dependence of the magnetic susceptibility provides important information both on the character and magnitude of the individual magnetic moments and on the interactions between them. One can imagine two limit cases:

(a) No local moments, the 5f states contribute to the temperature-independent susceptibility χ_0 by contributing to the density of states at E_F, $N(E_F)$. In such cases (Pauli paramagnetism) one obtains χ-values of the order of 1×10^{-8} m^3/mol U, which is enhanced by at least one order of magnitude compared to the analogous Th-, Y-, or Lu-based metallic compounds.

(b) On the other hand, the susceptibility of a set of interacting local moments follows a Curie–Weiss law:

$$\chi(T) = \frac{n\mu_0\mu_{\mathrm{eff}}^2}{3k_B(T - \Theta_p)}, \tag{3.1}$$

where Θ_p is the paramagnetic Curie temperature, μ_0 is the Bohr magneton, μ_{eff} the effective moment and n the molar concentration of magnetic moments.

In U-intermetallics, two ionic configurations, namely $5f^2$ and $5f^3$, could be considered as reasonable. The effective moments are similar, 3.58 and $3.62\,\mu_B$, respectively. However, the observed μ_{eff} values are frequently smaller. Although we could think of them as affected by CEF, the general band character of the 5f states makes plausible an explanation based on theories of band magnetism. In this respect, the proximity of the experimental μ_{eff} value to the ionic ones is a certain indicator of the proximity to the local-moment regime.

Some caution has to be paid when evaluating of $\chi(T)$ data of polycrystalline samples due to the large anisotropy existing even in the paramagnetic state, as mentioned in section 2.4. First, some texture met in most of the cases prevents the attainment of representative data from bulk polycrystalline pieces of non-cubic materials, and one has to deal with powder samples with randomly oriented grains fixed by glue to prevent orientation by external magnetic fields. In such case, the measured susceptibility χ is the average of the susceptibilities that one would have obtained for fields along the three principal directions. In tetragonal or hexagonal materials we get $\chi = (1/3)\chi_c + (2/3)\chi_a$. Then, assuming (2.2), $1/\chi(T)$ is no more a linear function even for $C^a = C^c$. Instead, we obtain a positive curvature of $1/\chi(T)$ reflecting the increasing dominance of the easy-direction susceptibility when T approaches the higher Θ_p value. In fact, polycrystalline data distorted in this way by averaging of anisotropic susceptibilities can be reasonably well fitted by the so called modified Curie–Weiss law including a temperature-independent term χ_0 (which is typically of the order of 1×10^{-8} m^3/mol U), although this type of fit has no physical meaning. It yields the right estimate of the upper Θ_p value, but the values of the effective moments are far too low. This distortion is naturally stronger in the easy-axis case than in an easy plane case. A real χ_0 term was detected in some cases in single crystalline $\chi(T)$ data, but its values are normally smaller and of the order of 1×10^{-9} m^3/mol U (Brück et al. 1994).

The often observed negative Θ_p-values can reflect both the antiferromagnetic intersite coupling and the presence of an intrinsic instability of magnetic moments (spin fluctuations). The intrinsic fluctuations are clearly manifest below a characteristic temperature, where they become dominant over thermal fluctuations and a departure of the susceptibility from the Curie–Weiss law appears consequently. At low temperatures various types of anomalies related to spin fluctuations appear. For their classification the reader is referred to the report of Ikeda et al. (1991). In particular, one can observe a broad maximum in $\chi(T)$ with saturation at low T. These are of the YCo_2 type, seen, e.g., in URuAl – fig. 5.19 (Veenhuizen 1988; Veenhuizen et al. 1988a). There may also be an upturn developing in addition *in* low T ($CeSn_3$ type). When the upturn starts to dominate, an inflection with the final upturn at low T develops. An example of this UAl_2 type behaviour if found in URuGa – fig. 5.20 (Havela et al. 1983).

In order to study the magnetic anisotropy and its consequences, single crystals are indispensable. However, in some cases, single crystals are not available. In order to account for anisotropy effects, magnetization measurements are usually done on two kinds of samples:

(i) fine powder with single-crystalline grains free to be oriented by the applied external magnetic field, which may provide magnetization data for fields along the easy-magnetization direction,

(ii) powder with its orientation fixed by glue or frozen alcohol, which represents an ideal polycrystal.

The type of magnetic anisotropy can be determined by comparing the values of the saturation magnetization for free (M_{free}) and fixed (M_{fix}) powder obtained from magnetization experiments. In the case of spontaneous magnetization, the ratio M_{fix}/M_{free} close to 0.8 suggests an easy-plane type anisotropy. If the ratio amounts to 0.5, a uniaxial type of anisotropy can be concluded to be present. Useful information about the anisotropy can, however, be deduced from the high-field susceptibility even in paramagnetic systems like URuAl and URuGa (Sechovsky et al. 1992b).

3.1.2. Specific heat

The most prominent feature projected into the temperature dependence of the specific heat C of uranium intermetallics is the strong renormalization of the electron effective mass m^* leading to an enhanced γ-coefficient of the low temperature specific heat. This feature is most pronounced in heavy fermion compounds, which are found typically among Ce and U compounds. In free electron systems the γ-value is proportional to density of electron states at the Fermi level $N(E_F)$, which holds also for magnetic susceptibility χ_0. In HF systems the γ and χ_0 values (the χ-values in the low temperature limit) become enhanced by roughly the same amount, which justifies a description based on the Landau–Fermi liquid theory. The system behaves phenomenologically as consisting of quasiparticles (excitations), and both χ_0 and γ are proportional to the quasiparticle density of states at E_F.

In normal metallic systems, the specific heat at low temperatures can be approximated by:

$$C = \gamma T + \beta T^3, \tag{3.2}$$

where the cubic term accounts for the phonon specific heat. This yields a typical linear C/T vs. T^2 plot, where γ-values are extracted by extrapolation to $T \to 0$. However, in HF systems C/T strongly increases at low temperatures, and the data can be often approximated by:

$$C = \gamma T + \beta^* T^3 + \delta T^3 \ln T \tag{3.3}$$

with $\beta^* = \delta \ln T^*$, where δ is the pre-factor to the characteristic spin fluctuation contribution and T^* a characteristic spin fluctuation temperature. Also here γ is the $T \to 0$ limit of C/T. One should note that the logarithmic term leads to a negative contribution of spin fluctuations to C below T^*. This expression was first derived to describe the effect of nearly ferromagnetic (long wavelength) spin fluctuations in the context of ^{3}He, but can be obtained more generally in the Fermi liquid formalism (Pethick and Carneiro 1977).

The Fermi liquid description does not, of course, account for anisotropic magnetic properties apparent in lower symmetry compounds. Particularly striking cases can be found among actinide HF compounds, as UPt_3 or URu_2Si_2.

A qualitatively different specific heat behaviour is encountered in compounds undergoing magnetic ordering. In this case, the γ-value obtained from the analysis of C/T in the paramagnetic range (denoted as γ_p) is very often much higher than that found in the

0 K limit, i.e., in the magnetic state (γ_0). This is interpreted as due to superzone boundary formation due to an additional periodicity in the AF state, which can remove a substantial portion of electron states from E_F. Although the specific heat anomaly connected with a magnetic phase transition is often very sharp, the integrated (over T) magnetic contribution to C/T yields, as a rule, only a small fraction of $R \ln 2$. This points to a strongly itinerant character of magnetism. For the itinerant limit case, in which local moments disappear at T_C, the magnetic entropy is equal to zero, because the entropy above T_C (no moments) and in the low-T limit (moments ordered, no fluctuations) is equal.

In magnetically ordered compounds with higher ordering temperatures one cannot determine reliable values of γ_p because of the uncertainty in the determination of the phonon part. Nevertheless, the experimental γ-value (i.e., γ_0) is an important indicator of the situation in the vicinity of E_F. A vast majority of compounds display γ-value appearing roughly between two limit cases. The lower limit, 10 mJ/(mol K^2), is approximately a characteristic value of regular rare earths (5d participation at E_F). The upper limit, 400 mJ/(mol K^2), is the generally acknowledged threshold behind which true heavy fermion materials occur. Within this broad range, lower values are mostly found for broad 5f-band materials or, on the other hand, materials with appreciable local moments, having equal-moment magnetic structures. The first group involves typically Pauli paramagnets. Examples are the elemental light actinides, for which the highest γ was found for α-Pu (22 mJ/(mol K^2)) by Gordon et al. (1997), although α-U has only 10 mJ/(mol K^2) (Ho et al. 1966). Materials from the second group belong to narrow 5f-band systems, but the potentially high $N(E_F)$ is strongly reduced due to splitting of the spin-up and spin-down sub-bands. The regimes existing in between, i.e., spin fluctuators or magnetically ordered materials with small magnetic moments can have much higher γ-values. In such case, however, they less and less reflect the bare single particle density of states, but a renormalization due to many body correlations plays a dominant role. The real γ can then be expressed as:

$$\gamma = \gamma_0(1 + \lambda_{e\text{–phonon}} + \lambda_{e\text{–}e}), \tag{3.4}$$

where $\lambda_{e\text{–phonon}}$ and $\lambda_{e\text{–}e}$ are the mass-enhancement coefficients due to electron–phonon and electron–electron interactions, respectively, and γ_0 is the non-renormalized γ-value corresponding to the bare single-particle density of states. In U-compounds the last term $\lambda_{e\text{–}e}$ is very important. Few attempts to calculate the influence of $\lambda_{e\text{–}e}$ going beyond LDA and determining the quasiparticle self-energy have not yet led to fully satisfactory results (Steiner et al. 1994; Olsovec and Divis 1996).

The effect of mass renormalization can be well illustrated by results of de Haas–van Alphen (dHvA) experiments, which can determine both the Fermi surface geometry and the effective masses belonging to different sheets of the Fermi surface. In cases like UPt_3, the branches observed can be well identified with extreme cross-sectional areas of the Fermi surface obtained from LDA calculations, testifying the itinerant character of the 5f states (Taillefer et al. 1987; Kimura et al. 1996a, 1996b; Onuki et al. 1996; Taillefer and Lonzarich 1997). On the other hand, high effective masses of some branches account for experimental $\gamma = 452$ mJ/(mol K^2) (Stewart 1984), although the bare non-renormalized γ_0 obtained from the same calculations as the Fermi surface mentioned above is only 19.8 mJ/(mol K^2) (Oguchi et al. 1987).

Similar conclusions were obtained from Shubnikov–de Hass effect measurements (oscillatory magnetoresistance), which indicated quasiparticle masses m^* as large as $170m_e$, where m_e is the free-electron mass (Julian et al. 1992a, 1992b). Unfortunately, these techniques are restricted to materials for which high quality single-crystal specimens can be grown, and does not thus belong to common diagnostic tools. For ternary U-compounds, it was so far successfully applied to UPd_2Al_3 (Inada et al. 1994). The results show five branches, effective cyclotron masses are found to range approximately from $10m_e$ to $32m_e$.

The deviations from the simple dependence (3.3.) can in some cases be ascribed to magnons with a moderate gap in their dispersion relations, which lead to an exponential term $\exp(-\Delta/T)$, where Δ is the width of the gap, in analogy to the resistivity, but the pre-factor is proportional to $T^{1/2}$ (Andersen and Smith 1979). As the Δ-value is equal to the anisotropy energy, such term cannot be observed in materials with a strong anisotropy of the uniaxial type, because no excitations over the gap can be seen at low temperatures. At higher temperatures a quantitative analysis is impossible due to the dominating phonon contribution which goes beyond the simple cubic power law, or beyond the Debye approximation in general. On the other hand, the exponential terms occur in cases of one hard-magnetization axis and a moderate anisotropy within the plane perpendicular to this direction. In such a case one can detect magnons with a gap attributed to the in-plane anisotropy. The analysis of bulk properties of UNiGe (see section 5.1.2) leads to such exponential terms (both in resistivity and specific heat) with $\Delta \approx 40$ K, which corresponds to the difference of the Θ_p values for measured susceptibilities with $H \| b$ and $H \| c$. In ferromagnets, magnons are expected to be suppressed by the magnetic field due to the increase in Zeeman energy, which is projected into the increase of Δ. In UNiGe this tendency was found in fields above the upper metamagnetic transition, which brings the compound to a state with field-aligned moments (Havela et al. 1996a, 1996b).

3.1.3. Electrical resistivity

Although the effective masses in U-systems can be strongly renormalized, in the relaxation time approximation the ratio m^*/τ, which determines electrical resistivity ρ, is not renormalized. The relaxation time $\tau = l v_F^{-1}$, where the mean free path l cannot decrease below the interatomic spacing. Thus m^* and τ are renormalized in the same way. On the other hand, comparison of resistivity of uranium intermetallics with analogous rare-earth compounds, or with transition metals, shows that in actinide materials we often encounter values an order of magnitude higher at room temperature (resistivity values exceeding 200 $\mu\Omega$ cm are not exceptional). Because similar high values are found in spin-fluctuators and magnetically ordered materials in the paramagnetic state, one may find its origin, e.g., in the strong coupling of electrons to spin fluctuations as a consequence of the strong 5f hybridization. Unlike standard metallic systems, in which the dominating resistance mechanism is the electron–phonon scattering, which leads to monotonously increasing $\rho(T)$, U-systems often show a clear fingerprint of a strong scattering on magnetic fluctuations, which are incoherent at high temperatures. In periodic systems the condensation from the high-temperature local-moment state to a Fermi liquid state manifests itself in a pronounced decrease of ρ below a characteristic temperature marking the onset of such coherent regime, T_{coh}.

One of the specific features of most of U-compounds is a strong non-additivity of partial contributions to ρ (the Matthiessen's rule does not hold) showing a fast suppression of the

low-T decrease with practically any substitution destroying the coherence. At high temperatures, a more or less pronounced tendency to saturation of $\rho(T)$ appears due to a suppressed contribution of electron–phonon scattering, which, when unchanged, yields an increasing slope of $\rho(T)$ in conventional materials. In U-intermetallics this behaviour is different due to the strong electron spin-fluctuation scattering. The mentioned non-additivity means that the standard procedure of subtraction of the phonon contribution in the form of $\rho(T)$ of a non-magnetic analog can yield misleading results.

It is interesting to compare the high-temperature resistivity behaviour of U-intermetallics with that of Ce-compounds, for which a classification scheme based on the characteristic energy of the moment instabilities related to the quasielastic linewidth of neutron spectra Γ_{QE} has been developed (Freimuth 1987). It was noticed that, at least for Ce and Yb systems, whenever the characteristic energy of the moment instabilities Γ_{QE} increases with T (Kondo regime) there is tendency to form a maximum in $\rho(T)$. This was observed for instance in $CeIn_3$, CeB_6, $CePd_3$, $CeCu_6$, $CeAl_3$. The temperature of the maximum scales approximately with the residual Γ_{QE}-value Γ_0. On the other hand, in the case of strongly mixed-valence compounds (Γ_{QE} large and T-independent) one often finds a dull $\rho(T)$ dependence with a knee at generally higher temperature and overall positive $\mathrm{d}\rho/\mathrm{d}T$ ($CeSn_3$, $YbAl_3$, $YbCu_2Si_2$). In this approach a vast majority of U-compounds including HF materials like UPt_3 are analogous to 4f-mixed-valence materials, and are clearly distinguished from Ce HF materials, which are labeled as Kondo (or Kondo lattice) materials.

On the other hand, the resistivity in cases of negative $\mathrm{d}\rho/\mathrm{d}T$ needs not always associated with a Kondo effect. The variations of $\rho(T)$ can be explained, for example, by assuming a temperature induced de-hybridization leading to a decoupling of the f- and conduction electron systems due to thermal fluctuations, which reduce the lifetime of heavy quasiparticles (Weger 1985; Weger and Mott 1985).

In the spirit of the analogy between electron gas and Fermi liquid systems, a simple $\rho \propto aT^2$ behaviour due to electron–electron scattering is observed in the low-T limit in most of U-systems, too. The values of a are many orders of magnitude higher than in simple metals, and an approximate scaling with γ^2 was observed experimentally (yielding the universal ratio $a/\gamma^2 \approx 10^{-5}\ \mu\Omega\,\mathrm{cm\,mJ^{-2}\,K^2\,mol^2}$ (Kadowaki and Woods 1986; Kadowaki 1993)). The validity of this universal behaviour, which supposes that a is determined by Fermionic excitations, can break down in magnetically ordered materials with different types of excitations, or generally in materials where the anisotropy of moment ordering and magnetic excitations leads to anisotropic a-parameters. The value of a involves in more complex cases not only the Fermi liquid interaction parameters, but also an electron scattering in magnetic excitations (e.g., spin waves). Finally, such a magnetic scattering can be affected by the existence of a gap in the electron energy or magnetic excitation spectra. The former affects qualitatively the $\rho(T)$ dependencies mainly in the vicinity of T_{N}. The latter leads generally to exponential terms affecting $\rho(T)$ already from the low temperature limit. The contribution of scattering of electrons on magnon-like excitations can be derived in a simple model mentioned in the context of the contribution to specific heat (Andersen and Smith 1979). It leads to the expression

$$\rho(T) = \rho_0 + aT^2 + bT(1 + 2T/\Delta)\exp(-\Delta/T), \tag{3.5}$$

the last term accounting for electron scattering on magnetic excitations with a gap Δ. Such term was identified, e.g., in UNiGe, where it yields $\Delta \approx 40$ K (Prokes et al. 1994) similar to the value obtained from the specific heat data (see sections 3.1.2 and 5.1.2).

In several cases a power law with an exponent lower than 2 has been observed. Exponents of 3/2 or 5/3 are expected in the spin fluctuation theories to replace the value of 2 for the situation very close to the onset of magnetic order (Mathon 1968; Ueda 1977; Moriya 1991; Moriya and Takimoto 1995). Such behaviour was found for UNiAl (see fig. 5.8(b)), in which inter-site antiferromagnetic spin fluctuations along the c-axis apparently survive into the low temperature limit (Brück et al. 1994). The lower $\rho(T)$ curve for current along the c-axis is rapidly increasing with temperature, and can be described up to $T = 3.5$ K by a power law $\rho \sim T^{5/3}$. This behaviour is attributed to spin fluctuations close to the onset of magnetic ordering and is observed in weak itinerant magnets, and contrasts with the simple aT^2 type of behaviour for current along the basal plane.

A strong anisotropy of the electrical resistivity in actinide intermetallics is not at all exceptional, and is mostly related to the strong anisotropy of the exchange coupling of 5f-moments. It is easily observed in single crystal samples of tetragonal, hexagonal or orthorhombic materials. There can be, in particular, a very striking difference in *type* of the temperature dependence of ρ for different directions of the electrical current. In certain materials, antiferromagnetic correlations can be suppressed by an external magnetic field, and we observe a metamagnetic transition at a critical field which is generally accompanied by a giant magnetoresistance effect. Thus measurements of the $\rho(T)$ dependencies with current along various crystal directions and in different magnetic fields are usually very helpful for understanding the magnetic contribution to the resistivity. What is much less clear, is how the anisotropy in the underlying electronic structure (mainly the anisotropy of hybridization, which must strongly affect conduction-electron states) is reflected in various types of $\rho(T)$ behaviour.

The residual resistivity ρ_0 reaches typically smaller values in ferromagnets. The much larger ρ_0 values observed in antiferromagnets can be explained by several models, which are based either on the notion of gapping due to additional periodicity in the antiferromagnetic state, or, more generally, on spin dependent scattering and k-space restrictions (Havela et al. 1996a). The mechanism of the related "giant magnetoresistance effect" will be discussed later.

A strong anisotropy of the resistivity has been observed for numerous single crystal of low symmetry structures (for example in UT_2X_2 and UTX compounds).

The essential features can be illustrated on the case of UNiGa (see also section 5.1). As seen in fig. 3.1, for the electrical current in the basal plane ($\boldsymbol{i} \perp c$) containing ferromagnetically coupled U magnetic moments, the temperature dependence of the resistivity mimics a ferromagnet with a dramatic drop below the ordering temperature and a gradual saturation in the low temperature limit. The flat part of the $\rho(T)$ curve above T_N demonstrates that the contribution of the electron–phonon scattering, which is normally linearly increasing in this temperature range, plays only a minor role compared to the spin-disorder scattering (which is of the order of 100 $\mu\Omega$ cm). Qualitatively a different resistance behaviour is observed for the current along the c-axis ($\boldsymbol{i} \| c$), which senses the antiferromagnetic coupling of uranium moments. Below 80 K, the resistivity increases with decreasing temperature, becoming more pronounced approaching T_N. In the range 35–40 K, several anomalies emerge due to

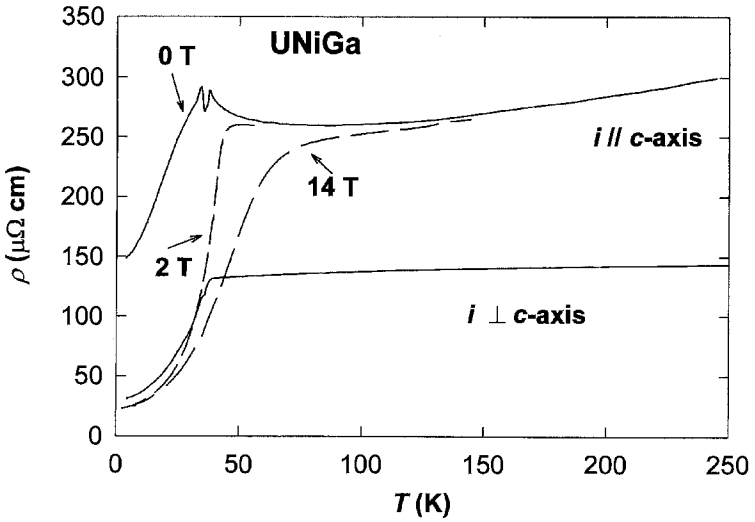

Fig. 3.1. Electrical resistivity ρ vs. temperature T for single-crystalline UNiGa with current i along the c-axis in various magnetic fields applied along the c-axis. The zero field state is antiferromagnetic with several magnetic phase transitions between $T = 35$ and 40 K. In fields higher than 1 T, a ferromagnetic state is induced. The comparison with the resistivity behavior for current within the basal plane ($i \perp c$, in $H = 0$) illustrates the effect of ferromagnetic coupling of the uranium moments within the basal plane UNiGa. Overtaken from Havela et al. (1996a).

magnetic phase transitions, and finally the resistivity decreases at low temperatures. However, the residual resistivity ρ_0 is much higher (140 $\mu\Omega$ cm) for $i \| c$ than for $i \perp c$. The high resistivity is removed in the ferromagnetic state. The negative derivative $d\rho/dT$, which develops gradually below 80 K for $i \| c$, is unambiguously due to incipient antiferromagnetic correlations (Havela et al. 1994a; Prokes et al. 1996a) and can be suppressed in 14 T as shown in fig. 3.1.

A ferromagnetic state is achieved via a spin-flip metamagnetic transition at a magnetic field strength of 1 T (at 4.2 K) applied along the c-axis (Sechovsky et al. 1991). The magnitude of the U magnetic moment is not affected by this transition, but a large drop of the resistivity (for $i \| c$) is apparent amounting to 87% (see fig. 3.1), and the $\rho(T)$ curve measured in the metamagnetic state mimics the behaviour of a ferromagnet.

In most of the materials mentioned, a simple aT^2 law characterizes the low temperature behaviour both in the antiferromagnetic and metamagnetic states. UNiGa can be taken as an example, in which the coefficient a decreases by a factor of 5 (from 0.24 $\mu\Omega\,\mathrm{cm\,K^{-2}}$ to 0.051 $\mu\Omega\,\mathrm{cm\,K^{-2}}$) at the metamagnetic transition, but the basic form of $\rho(T)$ does not change with temperature up to 20 K, as seen in detail in fig. 3.1. Therefore, since the field dependence of the specific-heat γ-value is weak, the coefficient a does not scale with γ^2.

3.1.4. Giant magnetoresistance

Magnetic fields when applied along the basal plane, do not lead to any moment reorientation and have practically no influence on the resistivity. This demonstrates that standard

magnetoresistance effects connected with the evolution of electron trajectories in a magnetic field have only little influence compared to "giant" effects due to spin reorientation. The magnitude of the resistivity changes due to magnetic structure variations in actinides is often larger than so called Giant MagnetoResistance (GMR) effects in magnetic multilayers. For review of the perpendicular magnetoresistance in magnetic multilayers, see the report of Gijs and Bauer (1997). Therefore the notion of the GMR effect is commonly used in actinides, too.

The case of UNiGe (see section 5.2) demonstrates that the giant magnetoresistance effects in U-intermetallics may not always occur in simple layered magnetic structures (as in UNiGa). Two mechanisms can generally be considered as origins of the GMR effect. One is based upon variations of the Fermi surface realized in the metamagnetic transition (for example, due to the disappearance of the superzone gap resulting from antiferromagnetic ordering). Another possible mechanism could be a spin-dependent scattering leading to a reduction of the relaxation time in the AF state. The latter is commonly considered in magnetic multilayer systems, in which, however, the disorder at inter-layer boundaries is thought to be a dominant mechanism of the GMR.

The case of UNiGa provides clues to the mechanism for the GMR effects in this class of compounds. The change of the γ-coefficient, reflecting the total density of electronic states at the Fermi level, at the transition from the AF to F state (from 43 mJ/(mol K^2) to 48 mJ/(mol K^2)) goes in the right direction (Aoki et al. 1996a), but is too small to give an unambiguous proof of substantial Fermi surface reconstruction. However, a complementary information pointing to the reconstruction can be obtained from additional experiments (Hall effect and thermoelectric power (Kobayashi et al. 1996)). The Hall resistivity in magnetic materials is described as a sum of two terms:

$$\rho_{\mathrm{H}}(H) = R_{\mathrm{H}} H = R_0 H + 4\pi R_{\mathrm{s}} M, \tag{3.6}$$

where R_0 and R_{s} are the normal and the extraordinary Hall coefficient, respectively, and M is the volume magnetization.

The normal Hall effect contains information on the Fermi surface, such as carrier concentration and/or the $\boldsymbol{k}$-dependence of the conduction-electron scattering. The extraordinary Hall effect provides information on the left–right asymmetry of the scattering (Hurd 1972). In UNiGa the magnetization at $T = 4.2$ K is practically field-independent both below and above the metamagnetic transition (see section 5.1.1). The same holds for normal resistivity (see fig. 3.1), which means that the anomalous Hall effect contribution can be taken as field independent in both AF and F phase. As can be seen from fig. 3.2, the field dependence of the Hall resistivity at $T = 4.2$ K is indeed linear in both phases, and therefore the change of the normal Hall coefficient R_0 at the transition can be evaluated from the slope of $\rho_{\mathrm{H}}(H)$. We have thus obtained $R_0 = (-2.9 \pm 0.1) \times 10^{-9}$ m^3/C) for the AF state and $(-1.7 \pm 0.1) \times 10^{-9}$ m^3/C for the F state. The difference in R_0 in the two phases reflects a considerable change of the Fermi surface resulting from the spin-reorientation, suggesting that an electronic structure variation is responsible for the GMR effect.

Another complementary information is provided by the field dependence of thermoelectric power. The change of the sign of S at the metamagnetic transition (fig. 3.3) may reflect the sign change of the energy derivative of the density of state (DOS) at the Fermi

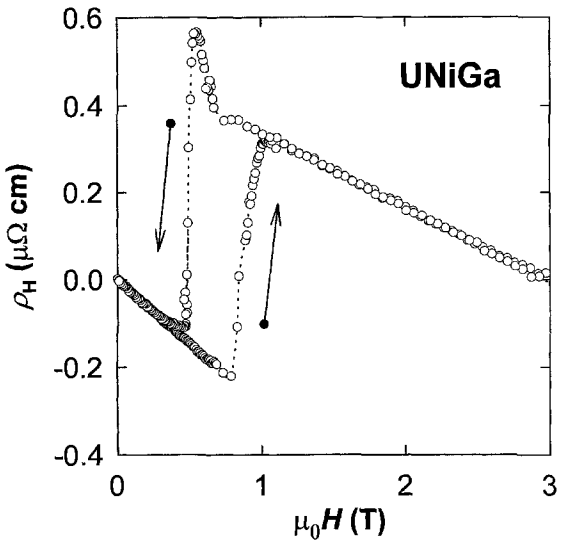

Fig. 3.2. Hall resistivity ρ_H vs. magnetic field $H \| c$ for single crystal UNiGa measured at $T = 4.2$ K. The current i was perpendicular to the c-axis. Dotted line is guide to the eye. Arrows indicate the directions of the field sweep. After Kobayashi et al. (1996).

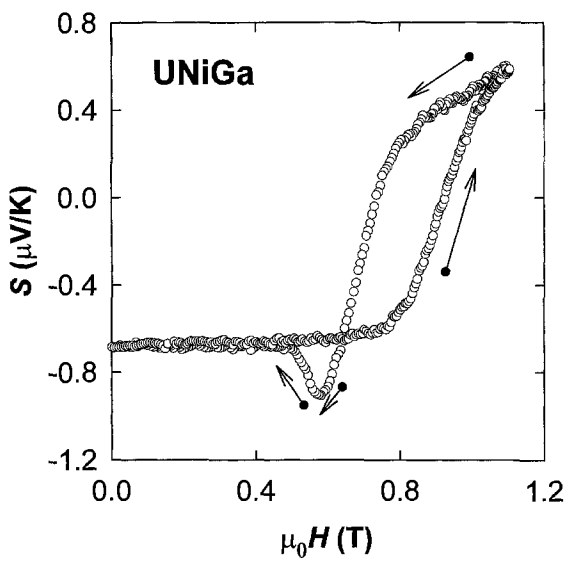

Fig. 3.3. Thermoelectric power coefficient S vs. magnetic field H for single crystal UNiGa measured at $T = 4.2$ K. The temperature gradient ΔT was perpendicular to the c-axis. Arrows indicate the directions of the field sweep. After Kobayashi et al. (1996).

level, which is again due to the Fermi surface reconstruction resulting from the moments reorientation.

The phenomena described here illustrate the fact that in actinide intermetallics the type of magnetic structure, especially the type of magnetic coupling along a particular direction, plays a dominant role both in size and temperature dependence of the electrical resistivity. The impact is much stronger than in analogous lanthanide-based materials (see Fournier and Gratz 1993). The reason can be found in the presence of a narrow f-band at the Fermi surface, and in the stronger hybridization of the 5f-states with other electronic states, which leads to an extreme sensitivity of electronic structure to the orientation of the 5f magnetic moments. The question remains whether it is predominantly a gapping effect which leads to the high resistivity in the AF state due to the enlargement of magnetic unit cell with respect to the crystallographic one. The large bulk of experimental data on various compounds show that there is a reduction of resistivity accompanying ferromagnetic coupling in the majority of cases, consistent with the action of a general superzone boundary effect.

The fact that the GMR effect can be understood on the basis of variations of the electronic structure only (i.e., without any spin-dependent scattering) is corroborated by electronic structure calculations for UNiGa performed using the fully relativistic, spin-polarized LDA approximations in both ferromagnetic and simple antiferromagnetic (+ −) states (Antonov et al. 1996). It is especially interesting that the calculations reproduce the magnitude of the GMR effect without any spin dependent scattering, because notion of spin diffusion length (used widely in the context of magnetic multilayers) cannot be simply applied to actinides with a strong spin–orbit coupling, where S cannot be taken as a good quantum number. Thus, the entire GMR effect in UNiGa can be explained by variations of topology of the Fermi surface. It would be interesting to test additional theoretical predictions of GMR effects for actinide materials with identical magnetic and crystallographic unit cells in the AF state. One example is the calculation of magnetoresistance effects in U_2Pd_2In and U_2Pd_2Sn (Richter et al. 1996). The latter material is expected to exhibit a large positive magnetoresistance at the metamagnetic transition. This would mean that the magnetic superzone effect is not a necessary ingredient for the occurrence of a GMR effect.

3.2. Local-probe methods

From large variety of microscopic (local-probe) methods we briefly comment two, which are currently bringing a qualitatively new view of U intermetallic compounds. For information on other methods reader is advised to see the reviews mentioned in the Introduction.

3.2.1. Inelastic neutron scattering

The dynamics related to magnetic moments is directly revealed by the neutron scattering. For assessing results obtained on U-compounds, the systematics built for Ce compounds can be an important reference. The on-site spin fluctuations are manifest in a relaxation behaviour of the dynamic susceptibility:

$$\chi(q,\omega) = \frac{\chi(q,0)\Gamma}{\Gamma - \mathrm{i}\omega}, \tag{3.7}$$

which yields a Lorentzian spectrum centred at $\hbar\omega = 0$. For stable rare earth moments the half width of the so-called quasielastic response $\Gamma_{QE}/2$,

$$\Gamma_{QE}/2 = \alpha k_B T, \tag{3.8}$$

but for unstable moments, there is a residual half width $\Gamma_0/2$ remaining in the low temperature limit, which corresponds to the intrinsic instability energy. A large portion of the spectral intensity is contained in the q-independent feature of such a shape, but there can be also another contribution peaking at non-zero q indicative of inter-site correlations of an antiferromagnetic type, which become noticeable at low temperatures even for paramagnetic systems. The two types of magnetic fluctuations able to absorb the energy were observed for example in $CeCu_6$ (Rossat Mignod et al. 1988).The first one, q-independent, yields a half width of 0.42 meV, which can be associated with the Kondo temperature $T_K = 5.0$ K, if expressed in Kelvins. The contribution due to inter-site correlations, which is strongly anisotropic, can be described by a Lorentzian centered at a finite energy $\hbar\omega_0 = 0.20$ meV and $\Gamma = 0.21$ meV. The latter contribution begins to disappear above $T = 3$ K.

Another example, with much a larger portion of inter-site fluctuations, is $CeRu_2Si_2$ (Rossat Mignod et al. 1988) having $\gamma = 350$ mJ/(mol K^2). Although no long-range magnetic order was indicated down to the lowest available temperatures by neutron diffraction, intersite fluctuations with a limited coherence length contain a considerable portion of the inelastic response. These inelastic features peaking around $\boldsymbol{k}_1 = (0.3, 0.3, 0)$ and $\boldsymbol{k}_2 = (0.3, 0, 0)$ are centered at $\hbar\omega_0 = 1.2$ meV, $\Gamma/2 = 0.9$ meV. These correlations develop gradually below $T = 70$ K and become temperature independent below $T = 6$ K. The q-independent fraction is well accounted by a quasi-elastic Lorentzian contribution with $\Gamma_0/2 = 2.0$ eV, corresponding to $T_K = 23$ K. The larger value of $\hbar\omega_0$ can be interpreted as being due to much stronger magnetic inter-site coupling than in $CeCu_6$. The tendency to magnetic instability can be supported, e.g., by a substitution of La for Ce. The $Ce_{1-x}La_xRu_2Si_2$ compounds display a modulated antiferromagnetic order for $x \geqslant 0.08$. A high-magnetization state can be induced by a moderate magnetic field of 7.7 T for $x = 0$. Classical metamagnetic transitions are observed in the AF state, with the critical field slightly and continuously decreasing with increasing x. Such a situation makes the impression that it is a coherent interplay of on-site and inter-site fluctuations, which suppresses the long range magnetic order in pure $CeRu_2Si_2$ at low fields, whereas the nature of the metamagnetic state is essentially x-independent. The extreme sensitivity to doping is symptomatic, and similar effects were observed practically in all periodic 4f or 5f HF systems. The breakdown of the antiferromagnetic intersite correlations in magnetic field in $CeRu_2Si_2$ can be followed by neutron scattering, too. The intensity of the inelastic k-dependent features simply disappears at the critical field.

The two examples show that the quasi-elastic response, which can be well approximated by a Lorentzian, accounts for the on-site moment fluctuations. Ce materials of the Kondo type show $\Gamma_0/2 \lesssim 1$ meV (the case of $CeCu_6$ and $CeRu_2Si_2$ mentioned above). A stronger coupling between the 4f moments and the conduction-electron states in mixed-valence materials, leading to faster relaxations, makes the values of $\Gamma_0/2$ typically an order of magnitude larger (Loewenhaupt and Fischer 1993; Holland-Moritz and Lander 1994). A vast majority of U-compounds irrespective of the type of the ground state display, besides other features, a broad quasielastic response with $\Gamma_0/2$ exceeding 5 meV

(Holland-Moritz and Lander 1994). The clear conclusion about strong coupling of the 5f- and conduction-electron states puts doubts on attempts to employ the Kondo model for explaining the properties of a certain class of U-compounds. Even those materials labeled as heavy fermions (UPt_3, UBe_{13}) are more the counterparts of the Ce mixed valence systems than of the Kondo compounds, although the higher specific heat γ-values resemble more the latter group. On the other hand, there are few singular U-materials, in which the quasielastic response is absent, known as the 5f-localized systems. The best known example is UPd_3, which shows sharp CEF excitations consistent with a $5f^2$ ($J = 4$, $^3H_4$) configuration (Buyers and Holden 1985). From ternaries it is, e.g., $U_3Ni_3Sb_4$ (see section 5.4, fig. 5.106), in which the non-metallic character explains the lack of the 5f hybridization, which situation allows for localization of 5f-electron states. One should notice that only in such cases crystal-field excitations were undoubtedly identified. Their apparent suppression in all other cases is clearly related to the essentially band character of the 5f states. Other cases as UPt_2Si_2 (Steeman et al. 1988) can probably not be solved without experiment on a single crystal, which would allow a more reliable subtraction of the phonon scattering.

Unlike such CEF excitations within one multiplet, intermultiplet transitions at higher energies became observable with the advent of neutron spallation sources. (For review of intermultiplet-transition spectroscopy see the report of Osborn et al. (1991).) For UPd_3 the lowest transition is observed at 395 meV, confirming the $5f^2$ state. Surprisingly, a weaker transition supposedly of this type was found in heavy fermion UPt_3, too (Bull et al. 1996), and recently it was found even in the itinerant ferromagnet URhAl (Hiess et al. 1997a). Unfortunately, more systematic information on existence and position of this transition over different classes of U intermetallics is still lacking.

3.2.2. Photoelectron spectroscopy

Photoelectron spectroscopy techniques are traditionally a powerful tool for direct observations of large-scale features of the electronic structure. The progress in instrumentation leading to a substantial improvement in electron-energy resolution has led to ambiguities in interpretation of photoelectron spectra especially for strongly correlated systems. The related issues like observability of Kondo resonance became subject of serious controversies, which leads at present to a crystallization of deeper understanding of electronic structure of U-compounds.

The standard resonance angle-integrated photoelectron spectroscopy using synchrotron radiation can effectively separate the 5f emission from the emission from the d-states of the transition metal in intermetallics. Information on the mutual position and overlap of the 5f and the d-states can be obtained from such experiments. Examples can be found in the report of Ejima et al. (1994) for spectra on UPd_2Al_3, UPt_2Si_2, and U_2PtSi_3. In an earlier report Ejima et al. (1993) showed examples of spectra on $U_3T_3X_4$ compounds. The poor resolution, not much exceeding 0.5 eV in most of cases, cannot distinguish possible details, which yields normally the 5f emission with a characteristic broad (1–2 eV) triangular shape pinned at E_F. It is interesting that no variations in the valence band related to the 5f emission appeared in the course of dilution the UAl_2–YAl_2 system down to low-U concentrations (Kang et al. 1987), which led to the false conjecture that single-site effects dominate the spectrum even in concentrated U systems.

Even high-resolution UPS (HRUPS) providing about one order of magnitude better resolution still show not much of details in the angle-integrated experiment, and the 5f emission is more difficult to distinguish, as found by Grassman (1990) for UT_2Si_2 compounds, or by Havela et al. (1992a) for UNiAl and UPdSn.

The contribution of both such types of studies can be regarded useful mainly for testing different band structure calculations, assuming different alternatives for the situation of 5f-states ($5f^2$, $5f^3$ localized, 5f band). One can naturally obtain qualitatively different valence-band spectra for 5f-localized systems like Am, in which the high-energy nature of the photoemission process leads to the observation of a final-state multiplet, seen as several more or less distinguished emission lines separated from E_F (Naegele et al. 1985). From U-intermetallics, the only material found to display this type of spectrum is UPd_3, which has also qualitatively different 4f-core level spectrum, pointing again to 5f-localization (Grassman 1990).

A step forward are experiments with angle-resolved photoemission (ARPES) with improved resolution, in which the necessity to use single crystals leads to using high-quality samples. Dispersive 5f bands have been observed long time ago in UIr_3, a strongly hybridized broad-band system (Arko et al. 1983). Nevertheless, the wide application of the Gunnarson and Schünhammer single-ion approach (Gunarson and Schonhammer 1987) for interpreting photoelectron spectra of Ce-compounds led to the belief that such type of approach should be pertinent for the interpretation of spectra in the case of narrow 5f-band systems, too. Such analysis was applied, e.g., on the UPd_3–YPd_3 system (Liu et al. 1992; Allen et al. 1993). This approach leads to distinct spectral features related to the Kondo (Abrikosov–Suhl) resonance in the vicinity of E_F. One of characteristics of these features is an anomalously strong temperature dependence. However, it was shown for cerium heavy-fermion compounds, that such temperature dependence is most probably absent and does not show the development expected from variation of the Kondo temperature (Joyce et al. 1992; Arko et al. 1997a). Moreover, ARPES data show a distinct dispersion of the states at E_F, which proves that they must be band states and cannot be treated as isolated impurities (Arko et al. 1997a; 1997b). Similar studies on U-compounds (the effort was concentrated mainly on the heavy fermions UPt_3, UBe_{13}, USb_2, UPd_2Al_3, and URu_2Si_2) show that the 5f emission extends farther below E_F compared to Ce-compounds and shows a greater dispersion due to higher f-occupancy. But in each case a very flat band at E_F showing no temperature dependence besides the Fermi–Dirac statistics was seen (Arko et al. 1997a,b,c). The narrowest feature has until now been found in USb_2. The width 30 meV is limited by experimental resolution (Arko et al. 1997c).

Thus qualitatively a similar picture for Ce and U heavy fermion intermetallics, different from the single ion model, emerged. The nature and proper description of the band states, clearly going beyond simple one electron (LDA) theory, remains to be solved. The necessity of further experiments oriented also on non-heavy fermion materials is obvious. The present effort gives clear hints as to experimental conditions. The observation of narrow dispersive features at E_F is impossible if the surface is anyhow damaged or contaminated, and relevant data could be obtained only on cleaved surfaces of high-quality single crystals.

4. Non-Fermi-liquid behaviour

The so-called non-Fermi liquid (NFL) behaviour represents nowadays one of highlights of the U (as well as Ce) research. The boom triggered by the discovery of certain universal types of scaling of bulk quantities in the vicinity of the onset of magnetic ordering led to investigations of possible cases of deviations from the standard Fermi liquid scaling. This effort is in reality oriented on very diverse phenomena, related in most cases to atomic disorder obtained by tuning the system to the proper regime by different substitutions. Generally, one could speak about non-Fermi liquid in all cases, in which the low-T Fermi liquid characteristics of specific heat (C/T constant), resistivity ($\rho = \rho_0 + aT^2$), and susceptibility (χ = const) are disobeyed. When inspecting the manifold of U compounds, we meet the strict Fermi liquid requirements only for few of them. Thus, to be more restrictive, one has defined the NFL behaviour in positive sense as that showing a distinguishable logarithmic scaling $C/T \sim -\ln(T/T_0)$, a strong T-dependence of the magnetic susceptibility for $T \to 0$ (often approximated by $\chi \sim -c(T/T_0)^{1/2}$), as well as $\rho(T) \sim AT^n$, with $n < 2$. Even with such restrictive characteristics one probably will find that most candidates show fingerprints of different types of magnetic disorder, induced by statistical occupation of certain lattice sites. This includes spin glass phenomena, and Kondo disorder with a statistical distribution of T_K effects (Bernal et al. 1996; MacLaughlin et al. 1996). The relevance of more exotic models based on new concepts like multi-channel Kondo effect (Cox 1987, 1993) remains unclear. Thus among the few well settled NFL cases are those compounds with crystallographic order, which are close to the onset of magnetism and are now traditionally described in the Moriya spin fluctuation theory (Moriya 1991; Moriya and Takimoto 1995), but an explanation of the resistivity exponent $n = 3/2$ or $5/3$ at the boundary of antiferro- or ferromagnetism, respectively, is dated back to the sixties and seventies (Mathon 1968; Ueda 1977). Thus materials like, e.g., UCoAl (see section 5.1.1) fall within the same class as weak itinerant ferromagnet $ZrZn_2$ (Ogawa 1976) or Ni_3Al (Sato 1975).

The importance of crystallographic disorder was recently demonstrated by comparison of $CeRh_2Si_2$, which can be tuned across the magnetic–nonmagnetic boundary by external pressure showing no evidence of the non-Fermi-liquid behaviour, with a system tuned by a substitution of Ru and studied at ambient pressure (Graf et al. 1997). In the latter case it is clearly the Kondo disorder leading to the NFL scaling.

For further discussion of NFL behaviour and its possible sources see, e.g., Löhneysen et al. (1997).

5. Overview of U ternary compounds

5.1. UTX compounds

UTX compounds (stoichiometry 1:1:1) form the most extended family comprising nearly 50 isostoichiometric ternary uranium compounds. Besides that, several dozens of other AnTX compounds (An = Th, Np, Pu, Am) have been discovered and studied so far. The transition metal (T) component is selected from the second half of the 3d-, 4d- and 5d-series, respectively. The X component represents a p-element from the groups IIIA, IVA

TABLE 5.1
Systematics of occurrence of crystal structures in UTX compounds with respect to the transition metal (T) component.

Mn	Fe	Co	Ni	Cu
Tc	Ru	Rh	Pd	Ag
Re	Os	Ir	Pt	Au
hexagonal $MgZn_2$	hexagonal ZrNiAl (Fe_2P) orthorhombic TiNiSi ($CeCu_2$)		hexagonal GaGeLi ($CaIn_2$) cubic MgAgAs	

and VA of the periodic table. When reviewing the occurrence of certain crystal structures in the compounds of the UTX family we observe a systematic behaviour with regard to the transition-metal component which is schematically shown in table 5.1. On the left side (compounds with Mn, Tc, Re and sometimes Fe, Ru, Os) we observe materials which crystallize in the hexagonal $MgZn_2$-type structure (space group $P6_3/mmc$) in which the two Zn sites are occupied by the T and X atoms at random. This means that such UTX structure is not the ordered ternary crystal structure. The majority of UTX compounds crystallizes either in the hexagonal ZrNiAl-type ($P\bar{6}m2$), which is the ordered ternary variant of the Fe_2P-type, or in the orthorhombic ordered ternary TiNiSi-type, which is derived from the $CeCu_2$-type. Many compounds contain transition elements characterized by nearly (Ni, Pd, Pt) or fully (Cu, Ag, Au) occupied 3d-, 4d- or 5d-electron states, respectively. These adopt the hexagonal $CaIn_2$-type or its ordered ternary modification, the GaGeLi-type. Compounds of the cubic structure type are also known. This systematics can be related to the gradually reduced delocalization of uranium 5f-electron states due to reducing the 5f–d hybridization with increasing population of transition metal d-electron states. Larger U–U spacings can be found especially in the last group.

5.1.1. Compounds with the ZrNiAl (Fe_2P) type structure

The hexagonal ZrNiAl-type structure adopted by 24 UTX compounds with X = Al, Ga, In, Sn, Sb discussed (see table 5.2) in this section is schematically shown in fig. 5.1. This structure has a distinct layered character. It is built up of U–T and T–X basal-plane layers alternating along the c-axis. Each uranium atom has four nearest U neighbors within the U–T layer. The U–T layers are separated by the lattice parameter c. The distance between the nearest U neighbors within the basal plane can be found using the relation:

$$d_{U-U} = a\sqrt{1 - 3x + 3x^2}, \tag{5.1}$$

where x is a position parameter of the U atoms. However, without knowing detail value of x, an approximate U–U spacing can be obtained using the expression $d_{U-U} = a\sqrt{2}/(1 + \sqrt{3})$ (Kergadallan 1993).

UFeAl and *UFeGa* may exist in two crystallographic modifications depending on the heat treatment. At high temperatures above 700°C, both compounds crystallize in the hexagonal C14 Laves phase $MgZn_2$ (Steeb et al. 1964) in which also *UMnAl* can be formed. After long-time annealing at 600°C, the former two compounds adopt the ZrNiAl-type structure (Steeb and Petzow 1966; Lam et al. 1967; Kimball et al. 1971). The $MgZn_2$-type structure is much more close packed than the ZrNiAl-type as can be seen in fig. 5.1.

TABLE 5.2

Some basic characteristics of UTX, ThTX and PuTX compounds with the hexagonal ZrNiAl (Fe_2P) type structure: γ – coefficient of the electronic specific heat, type of ground state (F – ferromagnetic, AF – antiferromagnetic, UAF – uncompensated antiferromagnetic, PP – Pauli paramagnetic), μ_U – the uranium ordered magnetic moment (determined by neutron diffraction at $T = 4.2$ K), $T_{C,N}$ – magnetic ordering temperature, T_{tr} – temperatures of other magnetic phase transitions (in the ordered state), Anis. – easy magnetization direction (determined by neutron diffraction and/or magnetization measurements of single crystals), a, c – lattice parameters at room temperature.

Compound	γ (mJ/(mol K^2))	Ground state	μ_U (μ_B)	$T_{C,N}$ (K)	T_{tr} (K)	Ref.	a (pm)	c (pm)	Ref.
$UFeAl^{HT}$	24	PP[a]				[1]	525.5	818.5	[1]
$UFeAl^{LT}$	21	PP[b]				[1,2]	666.87	398.27	[1]
							667.2	398.1	[3]
UCoAl	65	P(SF)		17[c]		[4]	668.6	396.6	[3]
							666.7	396.5	[4,5]
*UCoAl**							596.1	984.6	[6]
UNiAl	164	AF		19.3		[7]	673.3	403.5	[8]
							675.1	404.8	[4]
							669.2[d]	401.0[d]	[9]
URuAl	45	P(SF)				[10,11]	689.5	402.9	[8]
							692.0	402.0	[4]
URhAl	60	F	0.94	27		[11,12]	696.5	401.9	[8]
							697.0	402.1	[4]
UIrAl		F	0.93	64		[4,13]	696.8	403.0	[3]
							695.0	401.0	[4]
UPtAl		F	1.2	46		[14,13]	701.2	412.7	[8]
							701.7	412.4	[4]
$UFeGa^{HT}$	32	PP[e]				[1]	527.0	813.0	[1]
$UFeGa^{LT}$	67	F	0.05	45		[1]	671.0	390.9	[1]
							673.1	390.3	[8]
							672.5	390.1	[4]
UCoGa		F	0.56–0.6[f]	51		[15]	669.3	393.3	[8]
	40	F	0.74[g]	48		[4]	669.1	393.7	[4]
	48	F		47		[16]	666.46[h]	392.65[h]	[16]
UNiGa	41–44	AF	1.4	39	37,36,35[i]	[17–19]	673.3	402.2	[8]
							672.5	401.6	[4]
							669.53[j]	400.2[j]	[9]
URuGa	52	P(SF)				[10]	707.6	381.8	[8,4]
URhGa	40	F	1.2[f]	40		[13,20–22]	700.6	394.5	[8]
							700.2	395.0	[4]
UPdGa		AF	1.37	61.5	41.5	[23]	702.9	411.3	[24]
UIrGa	41	F	0.93	60		[13,20,25]	703.3	394.4	[8]
							703.0	393.5	[4]

TABLE 5.2 (Continued)

Compound	γ (mJ/(mol K^2))	Ground state	μ_U (μ_B)	$T_{C,N}$ (K)	T_{tr} (K)	Ref.	a (pm)	c (pm)	Ref.
UPtGa	72	F	1.33	68		[13,20,25]	706.3	406.5	[8]
							705.7	406.8	[4]
URhIn	250[k]	AF?[l]	[l]	6.5	[m]	[26]	747.0	388.8	[27]
UPdIn	280	UAF	1.5	20.4	8.5	[28,29]	741.4	409.6	[8]
							742.1	409.3	[4]
UPtIn	150[n]	AF°	1.39	15[p]		[27,30,31]	741.3	405.8	[8]
							740.5	405.5	[4]
UCoSn	61	F	1.2–1.3[f]	80–88		[4,32–34]	714.8	399	[8]
							715.3	400.1	[4]
URuSn	50	F	1.1[f]	51–55		[10,13,35,36]	736.9	396.1	[4]
URhSn		F	1.3[f]	17		[13,35–37]	737.5	399.6	[8]
							737.5	403.8	[4]
UIrSn		F	1.24[f]	21–23		[13,35,36]	734.6	401.2	[4]
UPtSn		F	0.6[f]	30		[4]	735.8	412.5	[4]
URuSb		F	0.6[f]	35		[38]	738.5	391.5	[8]
ThCoAl							704.7	403.6	[8]
ThNiAl							708.0	405.5	[8]
ThRhAl							718.3	412.0	[8]
ThPdAl							726.5	418.1	[8]
ThIrAl							717.6	414.2	[8]
ThPtAl							727.1	415.4	[8]
ThCoGa							704.8	398.7	[8]
ThNiGa		PP				[38]	705.7	401.9	[8]
ThRhGa							721.4	404.4	[8]
ThIrGa							721.8	407.4	[8]
ThPtGa							729.7	409.5	[8]
ThNiIn							736.7	411.7	[8]
ThPdIn							754.1	419.0	[8]
ThPtIn							753.5	416.6	[8]
ThCoSn	3.7	PP[r]				[38,39]	737.6	405.9	[40]
ThRhSn							751.5	408.8	[40]
NpCoAl		AF		7			672.2	391.9	[41]
NpNiAl		AF		21			680.0	398.8	[41]
NpRhAl							697.55	402.27	[41]
NpIrAl		AF		17			697.40	403.40	[41]
NpPtAl		AF		12			705.2	409.4	[41]
NpNiGa		AF		16			673.4	392.0	[41]
NpIrSn							685.0	399.2	[41]
PuCoAl							684.4	392.2	[40]
							678.5	392.1	[41]
PuNiAl							686	398	[40]
							686.7	397.5	[41]

TABLE 5.2 (Continued)

Compound	γ (mJ/(mol K^2))	Ground state	μ_U (μ_B)	$T_{C,N}$ (K)	T_{tr} (K)	Ref.	a (pm)	c (pm)	Ref.
PuCoGa							681	390	[40]
PuNiGa							684.8	394.9	[40]
							685.0	394.5	[41]
PuRhGa							707.2	392.9	[40]

[HT] High temperature phase ($MGZn_2$-type)
[LT] Low temperature phase
[a] $\chi_{300\,K} = 2.4 \times 10^{-8}$ m^3/mol, $\chi_{5\,K} = 3.2 \times 10^{-8}$ m^3/mol.
[b] $\chi_{300\,K} = 3.4 \times 10^{-8}$ m^3/mol, $\chi_{5\,K} = 5.3 \times 10^{-8}$ m^3/mol.
[c] Maximum on the χ vs. T curve in low field ($\leqslant 0.5$ T) applied along the c-axis.
[d] Derived from neutron data at $T = 40$ K.
[e] $\chi_{300\,K} = 3.3 \times 10^{-8}$ m^3/mol, $\chi_{5\,K} = 4.2 \times 10^{-8}$ m^3/mol.
[f] Derived from magnetization data at $T = 4.2$ K.
[g] Determined at $T = 10$ K.
[h] Lattice parameters determined by neutron powder diffraction at 60 K (Purwanto et al. 1994a).
[i] Successive magnetic phase transitions (see text).
[j] Derived from neutron data at $T = 60$ K.
[k] A C_p/T value at 1.4 K. Strongly reduced (to approximately 160 mJ/(mol K^2)) in $\mu_0 H = 5$ T (Sechovsky et al. 1995a).
[l] No magnetic scattering has been detected down to 1.5 K by neutron powder-diffraction (Tran et al. 1995a). A complex magnetic structure of small U moments may be expected.
[m] Additional magnetic phase transition below 1.5 K cannot be excluded (Sechovsky et al. 1995a).
[n] A low temperature value; above 19 K, $\gamma = 375$ mJ/(mol K^2) has been derived (Havela et al. 1993a).
[o] A collinear structure (moments along the c-axis), $\boldsymbol{q} = (0, 0, 0.25)$, ferromagnetic U basal planes $+ + - -$ coupled along the c-axis (Tran et al. 1995a).
[p] Maximum on the $\chi(T)$ curve reported at 22 K (Tran and Troc 1990a), 18 K (Havela et al. 1993a), maximum of the $\partial(\chi T)/\partial T$ and C_p observed at 15 K (Havela et al. 1993a).
[r] The susceptibility of ThCoSn is slowly varying with temperature between 3×10^{-9} m^3/mol at $T = 300$ K and 4.5×10^{-9} m^3/mol at $T = 4.2$ K (Sechovsky et al. 1988a).
[*] Compound synthesized by melting under a pressure of 7.7 GPa ($MgZn_2$-type).

References:

[1] Brück (1991)
[2] Troc et al. (1993a)
[3] Lam et al. (1967)
[4] Andreev and Bartashevich (1986)
[5] Havela et al. (1986)
[6] Tsvyashchenko and Fomicheva (1991)
[7] Brück et al. (1994)
[8] Dwight (1969)
[9] Prokes (1997)
[10] Sechovsky et al. (1986a)
[11] Veenhuizen et al. (1988b)
[12] Paixao et al. (1992)
[13] Sechovsky et al. (1990)
[14] Richter et al. (1997)
[15] Andreev et al. (1984c)
[16] Purwanto et al. (1994a)
[17] Sechovsky et al. (1993a)
[18] Aoki et al. (1996a)
[19] Prokes et al. (1996a)
[20] Sechovsky et al. (1987)
[21] Sechovsky et al. (1986b)
[22] Sechovsky et al. (1992b)
[23] Tran et al. (1998a)
[24] Tran and Troc (1991a)
[25] Prokes et al. (1997a)
[26] Sechovsky et al. (1995a)
[27] Tran and Troc (1990a)
[28] Brück et al. (1988)
[29] Fujii et al. (1990a)
[30] Havela et al. (1993a)
[31] Tran et al. (1995a)
[32] Andreev (1985a)
[33] Sechovsky et al. (1988a)
[34] Tran and Troc (1991b)
[35] Kruk et al. (1997)
[36] Tran et al. (1995b)
[37] Mirambet et al. (1995a)
[38] Palstra et al. (1987)
[39] Buschow et al. (1985a)
[40] Dwight (1974)
[41] Kergadallan (1993)

The U atoms occupy the Mg sites whereas transition metal and p-element atoms are randomly distributed over the two Zn sites. The U atoms are arranged within the basal plane in slightly buckled layers separated by TX layers. The buckling is determined by the struc-

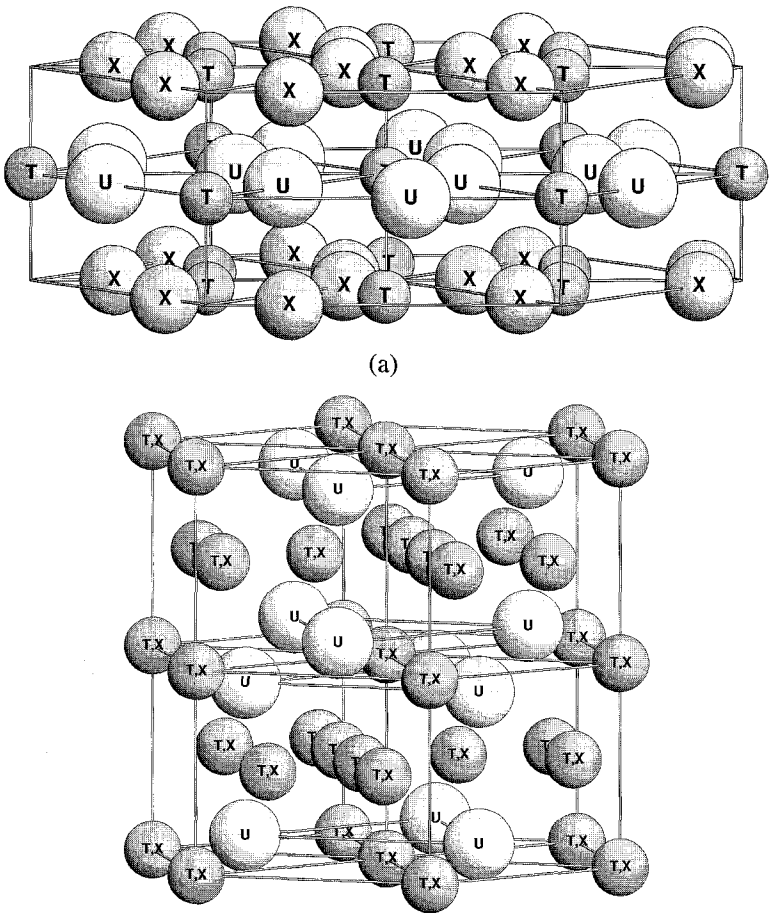

Fig. 5.1. Schematic picture (a) of the hexagonal ZrNiAl-type structure in which crystallize numerous AnTX compounds and (b) of the $MgZn_2$-type characteristic for UMnAl and the high-temperature phase of UFeAl and UFeGa.

ture parameter z. The inter-uranium distance in the Laves-phase structure is only 306.3 and 304.2 pm in UFeAl and UFeGa, respectively. The nearest uranium neighbors are considerably more separated in the ZrNiAl-type structure, namely $d_{U-U} = 345.7$ and 347.8 pm, respectively. This change is clearly reflected in differences between the magnetism in the high- and low-temperature phases of both compounds. The high temperature phases of UFeAl and UFeGa are paramagnetic down to the lowest temperatures with a nearly temperature independent susceptibility (Brück 1991; Troc et al. 1993a). UFeAl remains paramagnetic also in the ZrNiAl-structure phase. However, its susceptibility is enhanced by approximately 40%. The magnetization increases linearly with magnetic field up to 35 T, where it amounts to only 0.11 μ_B. The isostructural UFeGa exhibits weak itinerant ferro-

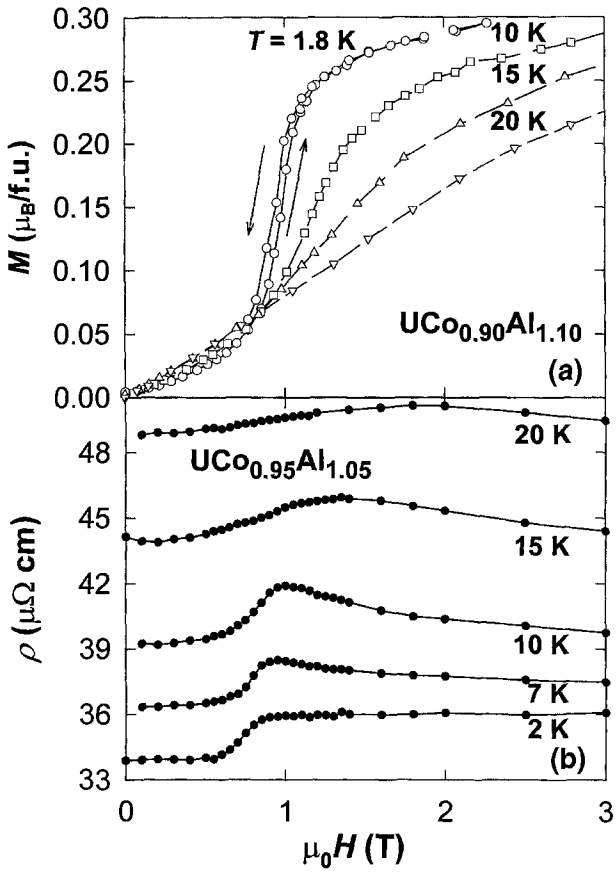

Fig. 5.2. Magnetization (a) and magnetoresistance (b) curves measured at different temperatures T on $UCo_{0.9}Al_{1.1}$ and $UCo_{0.95}Al_{1.05}$ single crystals, respectively, in fields H along the c-axis (Havela et al. 1997a; Kolomiets et al. 1998).

magnetism with a spontaneous moment of 0.05 μ_B/f.u., whereas 0.18 μ_B/f.u. is observed in 35 T. Negligible differences between the free- and fixed-powder magnetization point to absence of strong magnetocrystalline anisotropy in both compounds also in the ZrNiAl-structure (Brück 1991), which indicates strongly delocalized uranium 5f-electrons. Another source of weak ferromagnetism in the low-temperature phase of UFeGa may be ferromagnetism in the Fe sublattice. The lack of anisotropy may than be quite a natural feature of Fe magnetism. A ^{57}Fe Mössbauer effect study on this material is desirable.

UCoAl became one of the most intensively studied UTX compounds. This material shows no spontaneous magnetization down to lowest temperatures, but when a magnetic field of 1 T is applied along the c-axis of a UCoAl single-crystal at temperatures below 16 K, a metamagnetic transition is observed (Andreev 1985b; Havela et al. 1986; Sechovsky et al. 1986b). Results are shown in fig. 5.2. This transition is accompanied by a

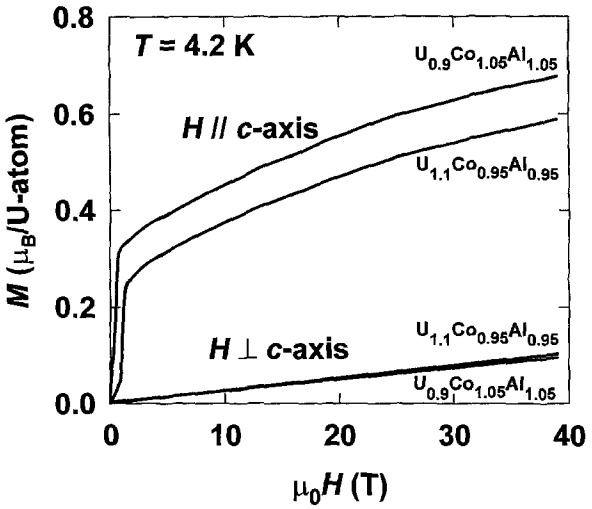

Fig. 5.3. High-field magnetization curves of UCoAl-based single crystals in a magnetic field H up to 35 T applied along and perpendicular to the c-axis (Sechovsky et al. 1986b). Actually, results obtained for $U_{1.1}Co_{0.95}Al_{0.95}$ and $U_{0.9}Co_{1.05}Al_{1.05}$ are shown. Note the anisotropic spontaneous magnetization for the latter composition (Andreev et al. 1997a).

magnetostriction effect of the order of 1×10^{-4}, negative along the c-axis and positive in the basal plane (Andreev 1985b), and a positive magnetoresistance of $\approx 6\%$ (Kolomiets et al. 1998; Andreev 1986). The susceptibility measured in fields ($H \| c$) sufficiently lower than 1 T exhibits a broad maximum around 17 K (Havela et al. 1997a). This is similar to broad maximum in the χ vs. T curves measured for the 3d-band metamagnets YCo_2 or $LuCo_2$ (Goto et al. 1994), although in the 3d systems the maximum is observed at temperatures more than an order of magnitude higher. The unusual magnetization behaviour below $T = 16$ K has motivated several controversial interpretations which can be found in literature. First, antiferromagnetic ordering below 16 K was claimed (Andreev 1985b) in analogy to the antiferromagnet UNiAl, although the critical field H_c in UCoAl is an order of magnitude lower. Absence of any anomaly both in the temperature dependence of the specific heat and the electrical resistivity around 16 K which would indicate a magnetic phase transition, led to the conclusion of a paramagnetic ground state. The metamagnetic transition to the state with a magnetic moment $\mu_U \approx 0.3\,\mu_B$ oriented along the c-axis was in this context attributed to band metamagnetism (Sechovsky et al. 1986b). This conclusion has been corroborated by results of *ab initio* electronic structure calculations (Eriksson et al. 1989) and polarized-neutron diffraction experiment on a single-crystal (Wulff et al. 1990; Papoular and Delapalme 1994). Later on, the occurrence of a ferromagnetic ground state with relatively large canted uranium moments of $0.8\,\mu_B$ was claimed after fitting powder neutron diffraction data (Tran et al. 1995a), ignoring completely the previous single-crystal results (Sechovsky et al. 1986b; Wulff et al. 1990). Finally, the absence of magnetic order in the low-field state was corroborated by a μ^+SR experiment (Havela et al. 1995a). In spite of the anomalous behaviour of UCoAl we observe a huge uniaxial anisotropy simi-

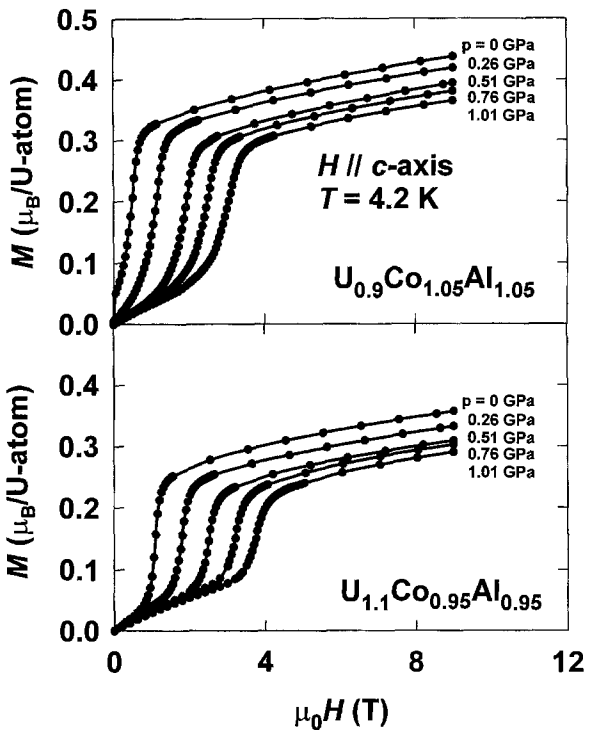

Fig. 5.4. Magnetization curves of the $U_{1.1}Co_{0.95}Al_{0.95}$ and $U_{0.9}Co_{1.05}Al_{1.05}$ single crystals at $T = 4.2$ K in a magnetic field H applied along the c-axis and hydrostatic pressures p up to 1.01 GPa (Andreev et al. 1997a).

lar to that in the magnetically ordered UTX counterparts of the ZrNiAl-structure family. From fig. 5.3 one may infer that the magnetism in UCoAl is concentrated in the c-axis with a metamagnetic transition to $\approx 0.3\ \mu_B$ around 1 T and a further pronounced increase of magnetization up to $0.6\ \mu_B$ in high magnetic field up to 39 T (Sechovsky et al. 1986b; Andreev et al. 1997a). In the basal plane we observe a simple linear paramagnetic response yielding only $0.1\ \mu_B$ at the maximum field. The strong anisotropy is observed also in the high-temperature susceptibility up to at least 300 K (Sechovsky et al. 1986b) showing always much stronger magnetic response in the c-axis direction.

A closer study of single crystals with controlled stoichiometry deviations from 1:1:1 revealed that the crystal structure of UCoAl allows some off-stoichiometry and that Co excess apparently affects the magnetic properties at low temperatures (Andreev 1990). In particular, the value of H_c is enhanced (reduced) in U-rich (-poor) samples. Consequently, a small spontaneous ferromagnetic moment appears in the sample with a deficit of uranium. A small spontaneous magnetization is observed only along the c-axis and should therefore be of 5f-electron origin. Results received on slightly off-stoichiometric crystals showing zero spontaneous moment are shown in figs 5.2 and 5.3. The critical parameters of the metamagnetism in UCoAl were discussed by Andreev et al. (1997a, 1997b, 1997c) and Havela et al. (1997a) and compared with the well-known band metamagnets YCo_2

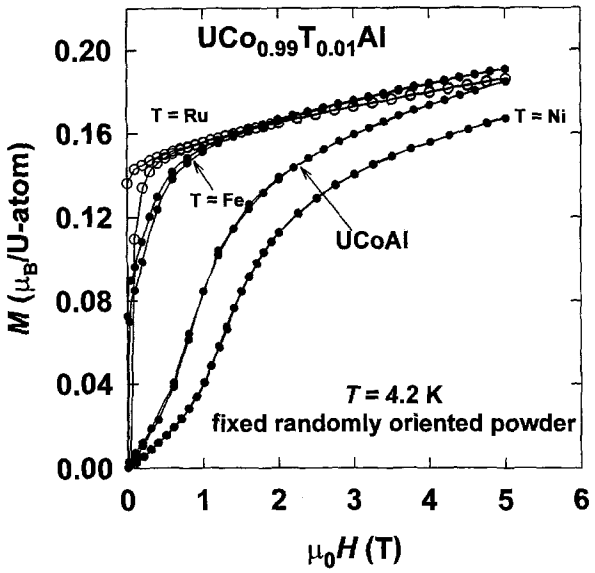

Fig. 5.5. Magnetization curves measured on polycrystalline fixed-powder samples of the $UCo_{0.99}T_{0.01}Al$ solid solutions at $T = 4.2$ K (Andreev et al. 1997c).

and $LuCo_2$ (Goto et al. 1994) in which the 3d electrons of Co are responsible for the extraordinary magnetic behaviour. In UCoAl, however, the 5f electrons of U determine the magnetism while Co does not contribute substantially to the magnetic moment (Wulff et al. 1990). Whereas no anisotropy of metamagnetic phenomena is observed in the 3d-electron metamagnets YCo_2 and $LuCo_2$ (Goto et al. 1994) metamagnetism of the 5f band electrons is observed only along the c-axis. In the both systems, however, the critical parameters are very sensitive to external pressure and also to small specific substitutions (Goto et al. 1994). Pressure effects on the two UCoAl-based single crystals are well demonstrated in fig. 5.4. The critical field H_c of the metamagnetism in UCoAl is linearly increasing with applied pressure:

$$H_c(p) = H(0) + kp \tag{5.2}$$

with $k = 2.7$ T/GPa. The magnetization step ΔM across the transition also decreases linearly with increasing pressure pointing to values of the critical pressure in the interval 2.2–2.4 GPa (Andreev et al. 1997a).

A pilot study of effects of substitutions of 10% Fe, Ni, Ru, Pd for Co in UCoAl which was presented by Andreev et al. (1995a) indicated that substitutions on a much finer scale should be studied. In fig. 5.5 we can see that the substitution of already 1% of other d metals for Co leads to strong changes in magnetic properties. The presence of Ni shifts the metamagnetic transition to higher fields. The substitution of Ru and Fe leads to qualitative changes of the magnetization curves although the lattice parameters do practically not change (Andreev et al. 1997b, 1997c). The Ru doped compound becomes a ferromagnet.

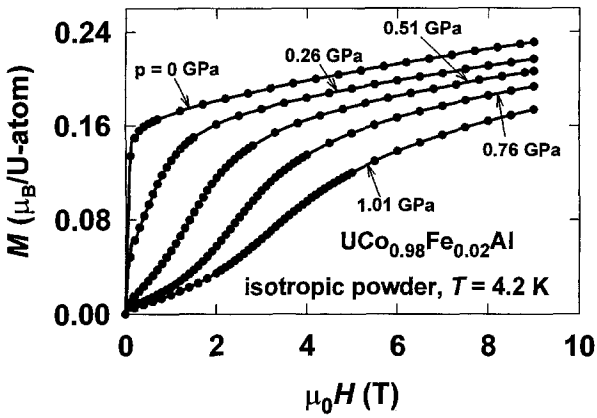

Fig. 5.6. Magnetization curves measured on polycrystalline fixed-powder sample of the $UCo_{0.98}Fe_{0.02}Al$ at $T = 4.2$ K in various external pressures p (Andreev et al. 1997c).

A large spontaneous moment exhibits also the Fe doped compound, but a visible metamagnetic behaviour still remains. At $T = 4.2$ K, the magnetization jump at the transition is roughly equal to the spontaneous moment. The superposition of ferromagnetic and metamagnetic behaviour exists in a wide temperature interval up to T_C (= 20 K). The ratio between the "spontaneous" and "metamagnetic" parts of the magnetic moment increases with decreasing temperature and an almost completely ferromagnetic state is obtained when extrapolating to 0 K. Further Fe doping stabilizes ferromagnetism. As can be seen in fig. 5.6 the magnetization curve of $UCo_{0.98}Fe_{0.02}Al$ shows no traces of metamagnetism. Application of pressure on this sample, however, induces gradual suppression of ferromagnetism via a state with reduced spontaneous magnetization and an additional metamagnetic transition towards the standard metamagnetism of UCoAl-type (Andreev et al. 1997b, 1997c). More extended substitutions of Fe for Co were studied by Tran et al. (1996a) and Troc et al. (1994a) who have shown that the ferromagnetism in $UCo_{1-x}Fe_xAl$ persists up to an Fe content of $x = 0.5$ with a maximum of T_C and a spontaneous magnetization for $x = 0.2$.

Electrical resistivity and AC magnetic susceptibility studies (Kolomiets et al. 1998) have revealed for UCoAl the presence of strong spin fluctuation effects for temperatures below 30 K and magnetic fields below H_c, where a non-Fermi liquid term $\sim T^{3/2}$ is prominent in the ρ vs. T dependence. The standard T^2 Fermi liquid resistivity term and a step-wise drop of the residual resistivity was observed upon increasing a the applied field through the metamagnetic transition.

Owing to the richness of phenomena described above, UCoAl proved an important object to study origin of magnetism in 5f-electron intermetallics. Further results obtained on various $U(Co_{1-x}T_x)Al$ and $UCo(Al_{1-x}X_x)$ solid solutions will be discussed in relevant parts elsewhere in this chapter.

UCoAl has been prepared also by melting under a pressure of 7.7 Pa (Tsvyashchenko and Fomicheva 1991). The resulting sample has been found to crystallize in the hexagonal Laves phase C14 ($MgZn_2$-type). The authors claim that the mean volume per atom in this

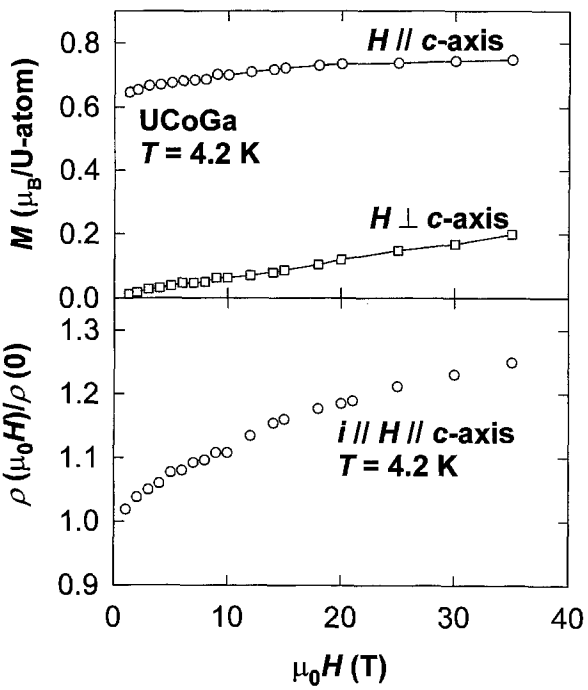

Fig. 5.7. Field dependence of the magnetization M along and perpendicular to the c-axis and of the longitudinal magnetoresistance in UCoGa at $T = 4.2$ in field H applied along the c-axis (Prokes 1997).

phase is by 48% larger that the corresponding volume in UCoAl prepared under ambient pressure (ZrNiAl-type structure). Since the Laves phase structure is rather close packed, this result does not seem probable in the present stage of knowledge. Further experimental effort in this direction is highly desirable.

In the light of previous compounds, *UCoGa* seems to be a much simpler case. The magnetic phase transition from paramagnetism to ferromagnetic ordering at 47 K is clearly reflected in magnetization, specific-heat and resistivity anomalies at this temperature (Sechovsky et al. 1987; Nakotte et al. 1993a; Purwanto et al. 1994a). A neutron powder diffraction study led to a uranium ordered magnetic moment of $0.74\,\mu_B$ at 10 K which is close to the value of $0.78\,\mu_B$/f.u. measured on a single crystal at 4.2 K in a field of 35 T along the c-axis (Nakotte et al. 1993a). In fig. 5.7 we can see that the slow, but non-negligible, increase of the c-axis magnetization in fields up to 35 T is accompanied by an approximately 25% magnetoresistance (Purwanto et al. 1994a). The huge uniaxial anisotropy is manifest by the small linear magnetization response of UCoGa in the basal plane reaching $0.2\,\mu_B$/f.u. at 35 K (see fig. 5.7). The strong uniaxial magnetocrystalline anisotropy is observed also in paramagnetic range. Both the χ^c vs. T and χ^a vs. T dependencies can be characterized by Curie–Weiss law. However, the paramagnetic Curie temperature θ_p, which is positive and very close to T_C in the former case, is large and negative in the latter case (Nakotte et al. 1993a; Prokes 1997). The difference

$\theta_p^c - \theta_p^a \approx$ 300–400 K serves as an estimate of the magnetic anisotropy energy in the paramagnetic state. Also the electrical resistivity is strongly anisotropic, being practically constant above T_C. It decreases by only 10% from T_C down to the low-temperature limit for a current within the basal plane and shows little temperature dependence. For current along the c-axis the resistivity between 300 K and T_C decreases by approximately 45%. Ferromagnetic ordering is clearly marked by a discontinuity of $\partial\rho/\partial T$ at T_C and below T_C the ρ vs. T dependence is typical for a ferromagnet (Purwanto et al. 1994a). UCoGa exhibits an interesting evolution of magnetization curves below T_C, soft-magnet behaviour above 30 K and a sudden onset of rectangular hysteresis loops at lower temperatures (Nakotte et al. 1993a).

Evolution of magnetic properties from paramagnetic UCoAl and ferromagnetic UCoGa can be traced across the series of solid solutions $UCoAl_{1-x}Ga_x$ (Andreev et al. 1998a). Already 5% Ga in the X sublattice gives rise to a spontaneous moment at $T = 4.2$ K although there remains visible metamagnetic behaviour. Further increase of Ga content yields gradual stabilization of ferromagnetism on account of the metamagnetic contribution. For x increasing beyond 0.15, pure ferromagnetism is observed with nearly linear increase both of T_C and μ_s. This all occurs without varying lattice parameter a and with a linear decrease of c amounting to only about 3% reduction across the whole series. Preliminary specific-heat data taken on these solid solutions, which show broad anomalies spread over large temperature intervals (of 10–20 K) around T_C, indicate that the coexistence of ferromagnetism and metamagnetism in these compounds may be connected with a sort of clustering effects connected with statistical distribution of Al and Ga atoms over the X-sublattice sites.

UCoSn is a stable U-moment ferromagnet below T_C = 80–88 K exhibiting strong uniaxial anisotropy with the magnetic moments oriented along the c-axis. The uniaxial anisotropy has been clearly determined from the ratio (≈ 0.5) of the spontaneous moments from fixed-powder and free-powder magnetization measurements (Sechovsky et al. 1988a, 1990). This conclusion is corroborated by results of ^{119}Sn Mössbauer-spectroscopy investigations (Kruk et al. 1997). The free-powder magnetization measured in fields up to 35 T increases from $\mu(0\text{ T}) = 1.2\,\mu_B$/f.u. to $\mu(35\text{ T}) = 1.3\,\mu_B$/f.u. (Sechovsky et al. 1988a, 1990). The lowest value of T_C has been determined from experiments in zero magnetic fields, namely from the location of a specific heat anomaly at 80 K and a clear resistivity anomaly at 81 K (Havela et al. 1986; Sechovsky et al. 1986a; Tran et al. 1995b).

When the U sublattice is diluted by non-magnetic Th atoms in the solid solution $U_{1-x}Th_xCoSn$, the ordering temperature decreases linearly with decreasing uranium concentration and ferromagnetism disappears around $x = 0.6$. The magnetic moment related to one U atom is nearly constant for $0 \leqslant x \leqslant 0.4$ and then rapidly collapses with decreasing U concentration. The compounds in the concentration region critical for ferromagnetism exhibit a strong enhancement of the electronic term of the specific heat amounting to $\gamma = 250$ mJ/(mol U K^2) for $x = 0.6$. The strong uniaxial magnetic anisotropy persists in all ferromagnetic compounds irrespective to dilution of the uranium sublattice (Sechovsky et al. 1988a).

Changes of the magnetic properties of UCoSn due to substitutions of 10% Fe, Ni, Ru and Pd for Co have been studied by Andreev et al. (1995b). The magnetic moment of the solid solutions $UCo_{0.9}T_{0.1}Sn$ increases (decreases) with respect to UCoSn for T =

Fe, Ru (Ni, Pd). The Curie temperature changes in a similar way. Such a behaviour was not expected within the current understanding of magnetism in UTX intermetallics and will be discussed later in context with results of other studies of solid-solution series. A more detailed study was performed on compounds resulting by Fe doping on Co sites (Andreev et al. 1995c). It revealed that $UCo_{1-x}Fe_xSn$ compounds can be formed with Fe concentration up to $x = 0.15$ where the Curie temperature, which increases linearly with increasing x, reaches 98 K and the spontaneous moment is enhanced to $1.29\,\mu_B$.

The ^{119}Sn Mössbauer effect and magnetic studies of $UCoAl_{1-x}Sn_x$ (Sechovsky et al. 1989; Krylov et al. 1990) revealed that already initial substitution of 1% Sn for Al leads to ferromagnetic ordering which, however, may be confined to clusters with higher Sn content. Further increase of Sn content yields monotonous increase both of μ_s and T_C.

UNiAl represents an itinerant 5f-electron antiferromagnet characterized by a reduced U magnetic moment and a strongly enhanced γ-value. The degree of 5f-electron delocalization was the subject of a photoemission study of UNiAl in comparison with UPdSn representing a system on the verge of 5f-electron localization (Havela et al. 1992a, 1992b). Numerous intriguing phenomena observed in this material motivated intensive experimental effort, which was enabled by the relative easiness of single-crystal production (Brück 1991). The temperature dependence of the magnetic susceptibility of UNiAl measured with the magnetic field parallel and perpendicular to the c-axis shown in fig. 5.8 reveals the strong uniaxial magnetocrystalline anisotropy characteristic for the majority of UTX compounds of this isostructural family. The Curie–Weiss like signal above $T = 40$ K, reflecting the behaviour of 5f magnetic moments, is confined to the c-axis whereas the susceptibility in the basal plane is nearly temperature independent. The $\chi^c(T)$ curve exhibits a pronounced maximum around $T = 25$ K, which indicates antiferromagnetic ordering at lower temperatures. This temperature, however, does not coincide with the transition temperature $T_N = 19$ K determined from the specific heat (see fig. 5.9). Also here, the magnetic phase transition is associated with the maximum in $\partial(\chi T)/\partial T$ in agreement with theory (Fisher 1962; Fedders and Martin 1966). Above 35 K, $\chi^c(T)$ can be well fitted with the Curie–Weiss law with the parameters $\mu_{eff} = 2.92\,\mu_B$ and $\theta_p = -16.5$ K (Prokes 1997). Similar results $\mu_{eff} = 2.85\,\mu_B$ and $\theta_p = -13$ K have been reported by Brück et al. (1994). The χ^{ab} vs. T curve is very flat, slightly increasing with decreasing temperature. Attempts to fit this dependence with a Curie–Weiss law or a modified Curie–Weiss law yield large negative values of $\theta_p \approx -400 \div -700$ K and values of the effective moment comparable with the c-axis values (Brück 1991; Brück et al. 1994; Prokes 1997).

The magnetization curves measured at $T = 4.2$ K in magnetic field up to 35 T applied parallel and perpendicular to the c-axis, which are displayed in fig. 5.10, demonstrate the huge uniaxial anisotropy of UNiAl. When the field is applied along the c-axis, a sharp metamagnetic transition is observed around 11.25 T. In fields above the transition, the magnetization slowly saturates, yielding a value of $1.22\,\mu_B$/f.u. in 35 T. Full saturation has been observed around 50 T on an oriented powder sample. The transition becomes more abrupt at $T = 1.5$ K but the hysteresis of approximately 0.1 T remains unchanged. At elevated temperatures the transition is progressively smeared out, while its mid-point is somewhat shifted towards lower fields. A remnant of the S-shape of magnetization curve is still observable at 24 K, i.e., in the range of the susceptibility maximum. The basal-plane magnetization is very small and increases linearly with the field, yielding only $0.14\,\mu_B$/f.u.

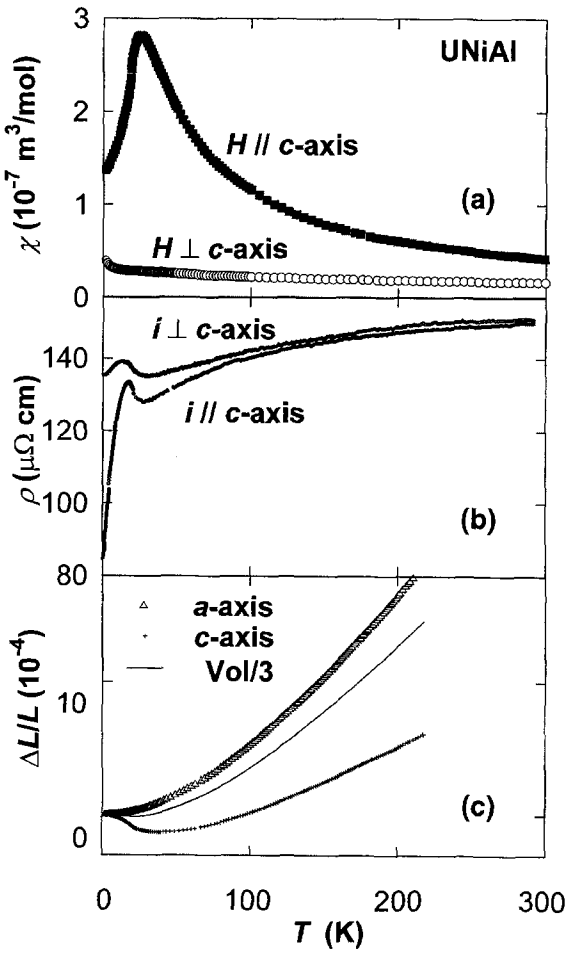

Fig. 5.8. Temperature dependence of the following properties of UNiAl measured on single crystals: (a) Magnetic susceptibility χ in magnetic fields H applied along and perpendicular to the c-axis: data taken from Prokes (1997); (b) Electrical resistivity ρ with current i along and perpendicular to the c-axis; data taken from Brück et al. (1994); (c) Linear ($\Delta L/L$ – along the a- and c-axis) and volume ($\Delta V/V = 2\Delta L_a/L_a + \Delta L_c/L_c$ – full line) thermal expansion (Prokes et al. 1996b; Prokes 1997).

in 35 T. An anisotropy field of several hundred Tesla can be estimated from magnetization curves.

Neutron powder diffraction experiments on UNiAl indicated a complex antiferromagnetic structure at low temperatures (Maletta et al. 1992). Preliminary single-crystal investigations (Paixao 1992) revealed a rather unusual propagation vector $\boldsymbol{q} = (0.1, 0.1, 0.5)$. Prokes et al. (1998a) have shown that this propagation vector is temperature independent from the lowest temperatures up to T_N. The propagation vector suggests antiferromagnetic coupling of the U moments along the c-axis and a modulation of these moments within

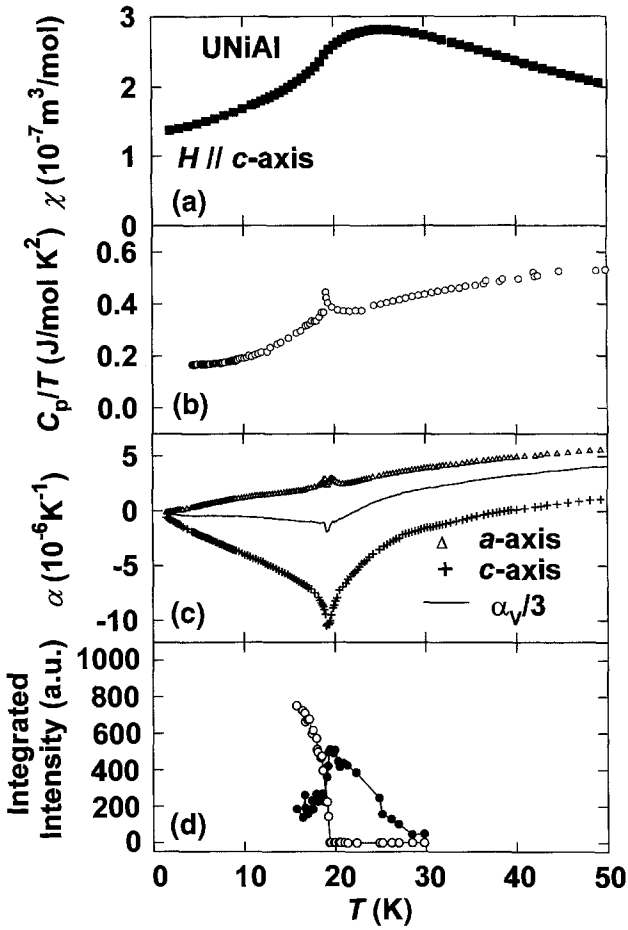

Fig. 5.9. Low-temperature part of the temperature dependence of the following properties of UNiAl measured on single crystals: (a) Magnetic susceptibility χ in low magnetic fields applied along the c-axis; data taken from (Prokes 1997); (b) Specific heat – C_p/T vs. T plot (Prokes 1997); (c) Linear ($\alpha = (1/L)(\partial L/\partial T)$ along the a- and c-axis) and volume ($\alpha_V = 2\alpha_a + \alpha_c$) thermal expansion coefficient (Prokes et al. 1996b; Prokes 1997); (d) Temperature dependence of the integrated intensities of the coherent Bragg reflection (○) and diffuse scattering (●) in the vicinity of the (0.9, 0.9, 0.5) magnetic reflection (Prokes et al. 1998a).

the basal plane. Since no additional intensity is recorded at nuclear Bragg peaks the net magnetic moment in each basal plane is zero. No sign of even partial squaring-up of the in-plane modulation has been observed down to 1.7 K, i.e., the modulation of the U magnetic moments in the basal plane has a sine-wave profile. The Bragg reflections vanish at T_N. However broad diffuse maxima around their original positions may be detected at least up to $T = 25$ K, indicating strong short range antiferromagnetic correlations at least up to temperatures where the susceptibility reaches a maximum (see fig. 5.9). This is consistent with the above mentioned S-shape of $M(T)$ curves vanishing only above this temperature

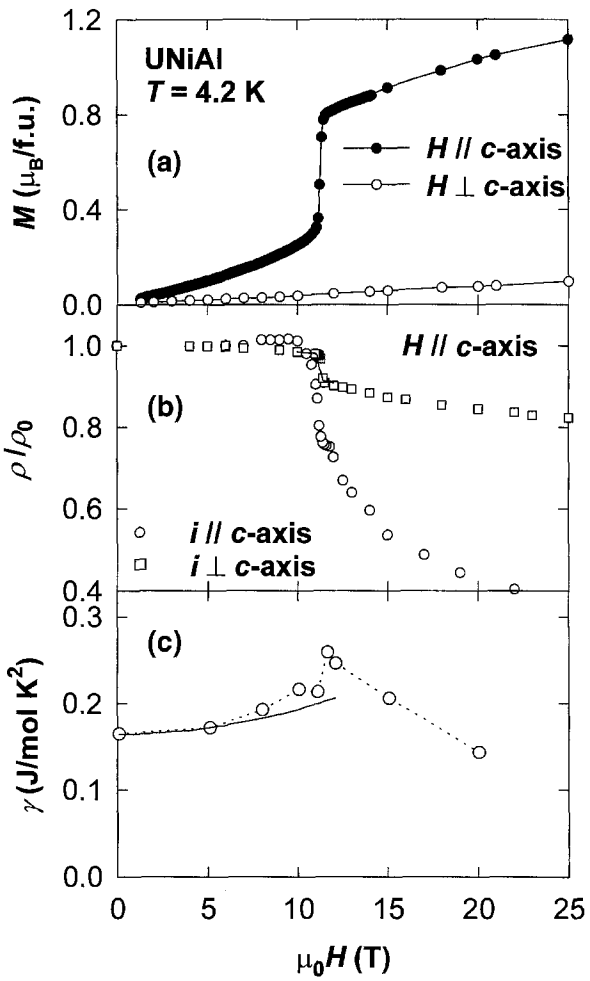

Fig. 5.10. Magnetic-field dependence of the following properties of UNiAl measured on single crystals: (a) Magnetization M at $T = 4.2$ K in a magnetic field H parallel and perpendicular to the c-axis (Brück et al. 1994); (b) Longitudinal and transversal magnetoresistance in a field H applied along the c-axis (Brück et al. 1994); (c) γ-coefficient of the specific heat in a field H applied along the c-axis (Brück et al. 1994). The solid line represents the quadratic fit of the low-T part, the dotted line is guide to the eye.

and with resistivity behaviour (Prokes 1997). In the experiment magnetic fields up to 5.7 T parallel to the c-axis no change of $\boldsymbol{q}$ has been found (Prokes et al. 1998a). The observed negative shift of T_N is in agreement with bulk magnetic measurements. Antiferromagnetic correlations are visible up to 30 K and except that the maximum scattered intensity shifts to lower temperatures, these correlations are only marginally affected. A magnetic field of 4.8 T perpendicular to the c-axis has no effect, neither on $\boldsymbol{q}$, T_N, nor on the temperature evolution of the diffuse integrated intensity (Prokes et al. 1998a). These results are in good

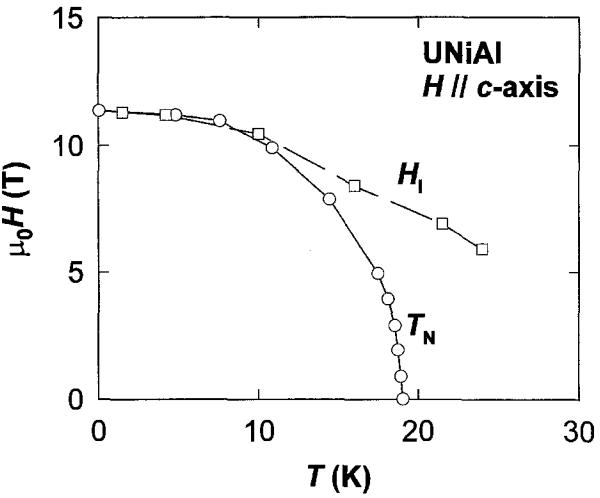

Fig. 5.11. Magnetic phase diagram of UNiAl in fields parallel to the c-axis. T_N marks the field dependence of the Néel temperature determined from the temperature dependence of specific heat, H_I corresponds to inflection points on magnetization curves at various T. After Andreev et al. (1997e).

agreement with the bulk properties and can be explained by magnetic anisotropy, which is present also in the paramagnetic regime (Prokes 1997; Prokes et al. 1998a).

The resistivity of UNiAl (fig. 5.8) shows little anisotropy above 100 K and is nearly temperature independent up to 300 K. Below 30 K, a negative $\partial\rho/\partial T$ gradually evolves and a maximum is found at 19 K for current along the c-axis (Sechovsky et al. 1992c). At low temperatures the resistivity decreases with decreasing temperature following a $\rho \sim aT^2$ dependence for current in the basal plane and $\rho \sim bT^{5/3}$ for the c-axis resistivity (Brück et al. 1994). The magnetoresistance data in fig. 5.10 confirm that the high residual resistivity observed in zero field is due to antiferromagnetic structure of UNiAl (Sechovsky et al. 1992c; Sebek et al. 1994).

Schoenes et al. (1992a) showed that the Hall resistivity follows qualitatively almost the same temperature dependence as the magnetic susceptibility, pointing to dominating magnetic contribution to Hall effect in UNiAl. A normalization of the anomalous part of the Hall effect with the magnetic susceptibility shows that the Fermi surface is reconstructed below T_N although the effect is much less pronounced than in URu_2Si_2 (Schoenes et al. 1987).

The specific heat of UNiAl exhibits a pronounced peak at $T_N = 19.3$ K (see fig. 5.8). With applying a magnetic field along the c-axis, the peak is progressively shifted to lower temperatures. In fields of 11–11.25 T, the peak becomes apparently narrower and sharper, indicating a first-order transition. For fields increasing above 11.5 T the peak disappears due to suppression of antiferromagnetism (Brück et al. 1992, 1994). No effect on the specific heat anomaly and therefore on T_N is observed in fields applied perpendicular to c (Havela et al. 1990; Brück et al. 1994). The magnetic phase diagram in fig. 5.11 (Brück et al. 1992, 1994) displays in one plot the temperature dependence of the metamagnetic

transition field B_I, represented by the inflexion point of the magnetic isotherms (Havela et al. 1990) and the field dependence of T_N taken as the temperature of the maximum of the C_p/T vs. T curve in various magnetic fields. T_N exhibits the usual quadratic dependence on the applied field. The two curves in fig. 5.11 coincide at low temperatures, where the sharp peaks in the specific heat occur. At higher temperatures, the field of the metamagnetic transition, which is gradually smeared out but still visible at 24 K (i.e., above T_N), decreases monotonously to a value of 6 T. This points to antiferromagnetic correlations dominating the system in a limited temperature range above T_N. The γ-coefficient of the specific heat increases from the zero-field value 164 mJ/(mol K^2) up to 260 mJ/(mol K^2) at 11.35 T and then decreases with further increasing field yielding 143 mJ/(mol K^2) in 20 T (Brück et al. 1992, 1994).

The temperature dependencies of the relative length changes, $(\Delta L/L)_a$ and $(\Delta L/L)_b$ with respect to the length of the sample along a particular direction at $T = 1.5$ K are displayed in fig. 5.8, together with the relative change in volume

$$(\Delta V/V) = 2(\Delta L/L)_a + (\Delta L/L)_c. \tag{5.3}$$

In fig. 5.9 one can see how the coefficients of linear thermal expansion

$$\alpha_{a,c} = \frac{1}{L_{a,c}} \frac{dL_{a,c}}{dT}, \tag{5.4}$$

and of volume expansion

$$\alpha_V(T) = 2\alpha_a(T) + \alpha_c(T) \tag{5.5}$$

in UNiAl depend on temperature. It is evident that the thermal expansion of UNiAl is highly anisotropic, similar to most of other bulk properties (Prokes et al. 1996b). Along the a-axis the lattice monotonously expands with increasing temperature (α_a is always positive) whereas the c-axis shrinks considerably with increasing temperature up to $T \approx 35$ K. Around 35 K, $\alpha_c(T)$ changes sign and the lattice expands at higher temperatures. The sharp anomaly observed near 19.3 K in both $\alpha_a(T)$ and $\alpha_c(T)$ clearly marks the magnetic phase transition at T_N. Note that the relatively small value of α_V, especially at low temperatures, is a consequence of mutual cancellation of significantly large coefficients α_a and α_c, one positive and the other negative. This is the main reason why the electronic term of the effective Grüneissen parameter in the case of UNiAl is only $\Gamma_e = 6.8$, which is about one order of magnitude smaller than that of typical heavy-fermion compounds, e.g., UPt_3 (de Visser et al. 1989), although it is considerably enhanced with respect to normal metals ($\Gamma_e \approx 2$).

The thermal expansion data may be better understood in conjunction with results of elastic and inelastic neutron scattering experiments on single crystals (Prokes 1997; Prokes et al. 1998a), which reveal the presence of strong antiferromagnetic fluctuations in UNiAl. The temperature development of fluctuations can be followed from low temperatures up to at least 1.5 T_N. However, no particular dispersion can be assigned to magnetic fluctuations. Instead of that, a wide spread in energy transfer of scattering intensity in the inelastic

spectrum is present in both spectra, below and above T_N. The magnetic fluctuations have entirely different behaviour along and perpendicular to the c-axis. The onset of magnetic fluctuations is visible around 35–40 K, where a deviation from the high-temperature behaviour of the thermal-expansion coefficient α_c can be observed, accompanied by a contraction along the hexagonal axis with lowering temperature. Magnetic fluctuations along the c-axis are clearly of antiferromagnetic type. The behaviour along the a-axis is rather regular, except for the critical region around T_N.

Dilution of the U sublattice by Y leads to a very fast breakdown of the long-range magnetic order in $U_{1-x}Y_xNiAl$ (Havela et al. 1988; Brück et al. 1990). For $x \geqslant 0.05$, the specific-heat anomaly connected with T_N vanishes, although a broad maximum on the $\chi(T)$ curve and a rather smeared out metamagnetic transition on the 4.2 K magnetization curve can still be recorded for $x \leqslant 0.1$. Simultaneously, a low-temperature upturn in the C/T vs. T dependence gradually develops, indicating increasing involvement of magnetic fluctuations and yielding a maximum value of $\gamma = 240$ mJ/(mol K^2) for the 20% Y content. A crystal-structure analysis showed a noticeable lattice expansion (Brück et al. 1990).

The antiferromagnetic state can be also dramatically destabilized by substitutions of Co or Fe for Ni, although here a gradual depression of T_N can be traced on weak, but still detectable anomalies in the specific heat. T_N becomes reduced by a factor of two due to 10% Co doping and the antiferromagnetism disappears for $x \approx 0.2$, which is again associated with a dramatic enhancement of the γ-value up to $\gamma = 250$ mJ/(mol K^2) (Brück et al. 1990) and accompanied by a suppression of the metamagnetic transition. Despite the dramatic changes of the magnetic ground state, the strong uniaxial anisotropy persists in these materials, as was confirmed by comparative measurements of high-field magnetization on oriented and fixed powder samples (Brück et al. 1990). Fe substitutions for Ni yield qualitatively comparable effects to the Co doping. The suppression of antiferromagnetism is approximately twice faster, i.e., antiferromagnetism disappears between 5 and 10% of Fe (Brück et al. 1990, 1994). The solid solutions $UNi_{1-x}Fe_xAl$ were studied over the whole concentration range by Troc et al. (1994a, 1995) and Reznik et al. (1995). They have confirmed the loss of antiferromagnetism for $x > 0.1$ and revealed the existence of a wide concentration range $0.2 > x > 0.65$ (Troc et al. 1994a). The maximum value of $T_C = 55$ K has been observed in $UNi_{0.5}Fe_{0.5}Al$.

Numerous unusual phenomena observed in *UNiGa* make it the most thoroughly studied UTX compound. In early days a number of controversial interpretations could be found in literature. UNiGa has been first claimed to order ferromagnetically (Andreev et al. 1984a, 1984b) or antiferromagnetically (Palstra et al. 1987). Because of magnetic after-effects, UNiGa was also classified as a spin-glass system (Zeleny et al. 1985; Zeleny and Zounova 1989). As soon as the first single crystals became available, the antiferromagnetic ground state of UNiGa has been confirmed (Havela et al. 1991). Systematic studies of off-stoichiometric samples (Andreev et al. 1995d) revealed that some of the above mentioned controversial observations may be due to deviations from the exact 1:1:1 stoichiometry, which can induce a ferromagnetic ground state.

The temperature dependence of the magnetic susceptibility in fields applied along the c-axis (χ_c) and perpendicular to it (χ_a) shown in fig. 5.12, clearly demonstrates the strong uniaxial anisotropy in paramagnetic state. Whereas for χ_c a value of $\theta_p = 40$ K can be derived applying the Curie–Weiss law, the perpendicular susceptibility shows much weaker

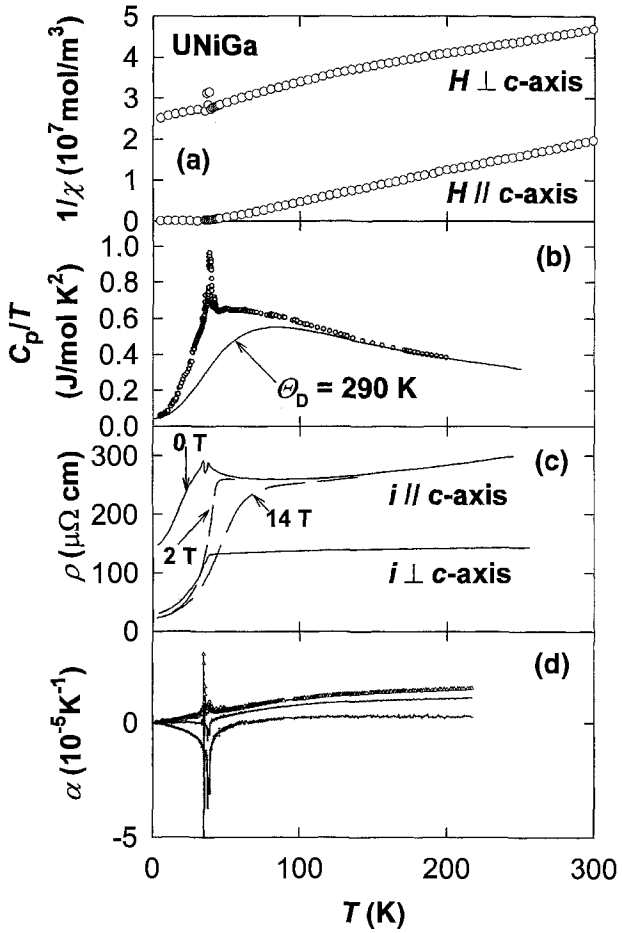

Fig. 5.12. Temperature dependence of the following properties of UNiGa measured on single crystals: (a) Inverse susceptibility χ in magnetic fields H applied along and perpendicular to the c-axis; data taken from Prokes (1997); (b) Specific heat – C_p/T vs. T plot. The Debye function with $\theta_D = 290$ K is shown by the solid line (Prokes 1997); (c) Electrical resistivity ρ with current i along and perpendicular to the c-axis, in the former case also data measured in various fields H applied parallel to the c-axis are shown, after Havela et al. (1996a); (d) Linear ($\Delta L/L$ – along the a- and c-axis – upper and lower curve, respectively) and volume ($\Delta V/V = 2\Delta L_a/L_a + \Delta L_c/L_c$ – full line) thermal expansion (Prokes 1997).

temperature dependence and above 120 K the CW fit yields a paramagnetic Curie temperature $\theta_p = -485$ K. Detailed measurements of the susceptibility of UNiGa in very low magnetic fields applied along the c-axis reveal a very complex behaviour with several anomalies (see fig. 5.13) below 40 K indicating the onset of magnetic ordering with three additional consecutive magnetic phase transitions at lower temperatures. In fig. 5.13 we can see that these transitions are clearly reflected also in related specific-heat, electrical-resistivity and thermal-expansion anomalies. Neutron diffraction studies performed on UNiGa single

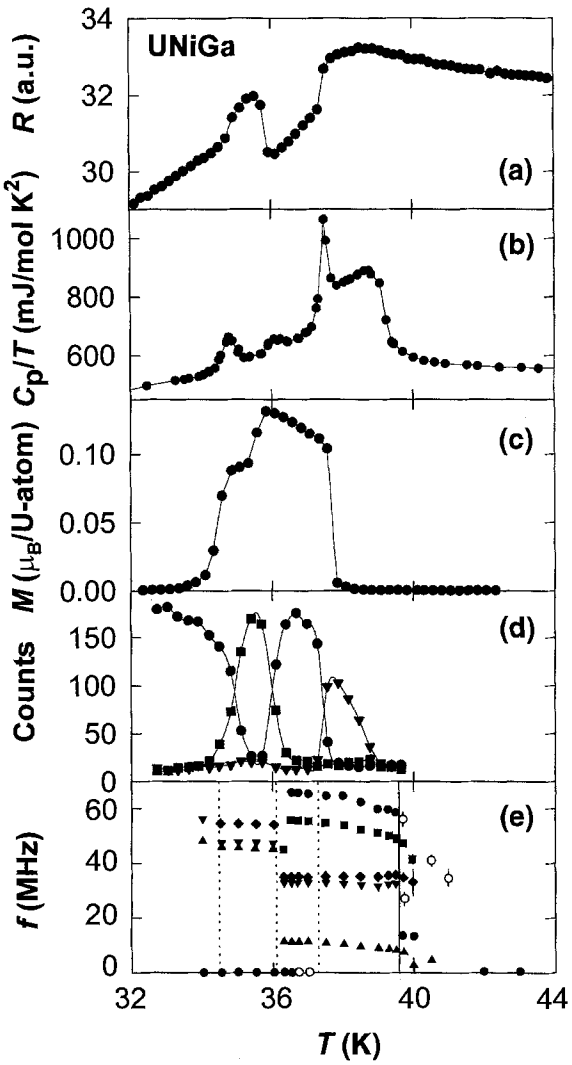

Fig. 5.13. Detailed temperature dependencies of: (a) the reduced electrical resistivity R (Havela et al. 1996a); (b) the specific heat C_p/T (Sechovsky et al. 1993a); (c) the magnetization M in a field of 1.2 mT ($H \| c$) (Prokes et al. 1996a); (d) the peak intensity of magnetic reflections (1, 1, 4/3) (•), (1, 1, 11/8) (■) and (1, 1, 0.36) (▼) measured on a UNiGa single crystal (Prokes et al. 1996a; Prokes 1997); and (e) the characteristic zero-field muon rotation frequencies f in transversal geometry (Prokes et al. 1995; Prokes 1997).

crystals at various temperatures clearly distinguished 4 magnetic phases with transitions observed within a narrow temperature interval, as can be seen in the magnetic phase diagram in fig. 5.14. Magnetic ordering in UNiGa appears through a second-order phase transition around 39 K, where the resistivity, specific-heat and low-field magnetization display

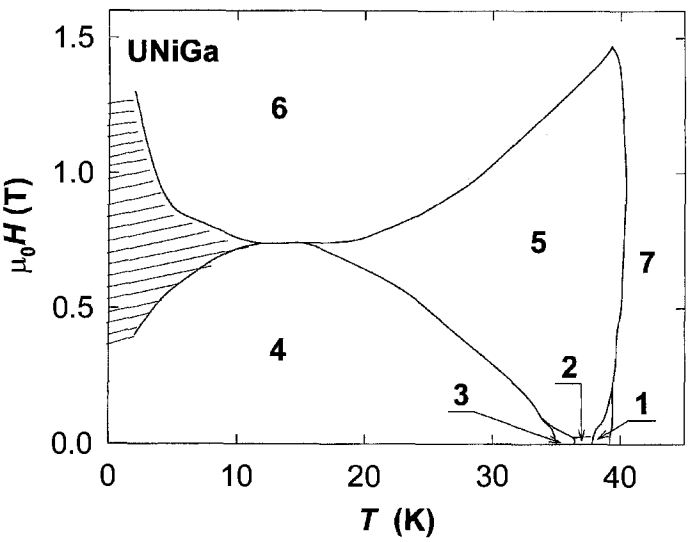

Fig. 5.14. Magnetic phase diagram of UNiGa for magnetic fields H applied along the c-axis. 1 – Incommensurate AF structure, $\boldsymbol{q} = \pm(0, 0, \delta)$, $\delta \approx 0.36$; 2 – AF phase with $\boldsymbol{q} = \pm(0, 0, 1/3)$, frustrated "paramagnetic" moments in each third U–T plane, i.e., $(+\,0\,-)$, 3 – AF phase with the $(+\,+\,-\,+\,-\,-\,+\,-)$ stacking, $\boldsymbol{q} = \pm(0, 0, 1/8)$, $\pm(0, 0, 3/8)$; 4 – AF phase with the $(+\,+\,-\,+\,-\,-)$ stacking, $\boldsymbol{q} = \pm(0, 0, 1/2)$, $\pm(0, 0, 1/3)$, $\pm(0, 0, 1/6)$; 5 – Uncompensated AF phase with the stacking $(+\,+\,-)$, $\boldsymbol{q} = \pm(0, 0, 1/3)$; 6 – Ferromagnetic phase, $\boldsymbol{q} = \pm(0, 0, 0)$; 7 – Paramagnetic phase.

only faint anomalies (see fig. 5.13). More pronounced features are seen in the temperature derivative of these quantities. The appearance of satellites for the reflection $(h, k, l\pm\delta)$ with $\delta = 0.36$–0.37 in the neutron data gives a clear evidence of an incommensurate antiferromagnetic (IAF) structure with $\boldsymbol{q} = (0, 0, \delta)$. The transition temperature can be best defined from the maximum of the critical scattering anomaly measured for $\boldsymbol{Q} = (1, 1, 0.378)$. The IAF phase is stable down to 37.3 K (the δ value is varying between 0.37 at T_N to 0.36 at 37.5 K), where it transforms to the phase 2 through a first order transition. Phase 2 has a periodicity $3c$, but zero spontaneous magnetization. This may be conceived as a stacking sequence $+\,0\,-$, where 0 means basal-plane layer of uranium atoms with the zero ordered magnetic moment. Such a situation can appear in the case of a balanced antiferromagnetic interaction between nearest neighbor and next-nearest neighbor uranium planes. The resistivity drops by several per cent at this transition. With further decreasing temperature, a gradual transformation of the magnetic structure to the ground-state antiferromagnetic phase 4 with the stacking $(+\,+\,-\,+\,-\,-)$ via the "intermediate" phase 3 $(+\,+\,-\,+\,-\,-\,+\,-)$ occurs. While the $2 \rightarrow 3$ transformation is associated with a substantial increase of the resistivity, the transformation $3 \rightarrow 4$ yields a somewhat smaller decrease. As evidenced by the neutron diffraction results, both transitions are characterized by a coexistence of neighboring phases over a certain critical region which can be more than 1 K wide (the transition $3 \leftrightarrow 4$).

The individual antiferromagnetic phases UNiGa have been identified also by the muon spin rotation spectroscopy. In fig. 5.13 we can see temperature evolution of muon rota-

tion frequencies. Detailed analysis of several dozens of magnetic reflections in the UNiGa ground state revealed a U magnetic moment of $1.4\,\mu_B$ at $T = 2$ K. It does not decrease substantially with increasing temperature almost up to 35 K, where it retains more than 90% of the low-temperature value. This feature is more general for the UTX compounds which exhibit high anisotropy yielding an Ising-like behaviour.

The coefficient of the linear electronic contribution γ to the specific heat amounts to 41–44 mJ/(mol K^2) (Sechovsky et al. 1993a; Aoki et al. 1996a; Prokes 1997). Specific-heat data in the low- and the high-temperature limit can be approximated by a Debye function with $\theta_D = 290$ K when considering $\gamma = 44$ mJ/(mol K^2). Closer inspection of fig. 5.12 also shows that the C_p/T vs. T dependence gradually deviates from a Debye function with decreasing temperature below 180 K which may be correlated with the anomalous behaviour of the thermal expansion along the c-axis (Honda et al. 1997a, 1997b, 1998a; Prokes 1997). The electrical resistivity with current along the c-axis shows the onset of an upturn below 150 K. These anomalies are attributed to the short range antiferromagnetic correlations propagating along the c-axis. A neutron diffuse-scattering experiment surprisingly revealed that the diffuse scattering can be followed only to a few K above T_N, even with extremely long counting times (Prokes 1997).

When a field of approximately 1 T is applied along the c-axis of UNiGa at $T = 4.2$ K (see fig. 5.15), it undergoes a single metamagnetic transition which shows hysteresis of ≈ 0.2 T yielding a saturation magnetization of $M_s = 1.4\,\mu_B$/U. Note that lattice defects can play a substantial role both in the type of metamagnetic transition (two stage transitions can be observed on non-annealed crystals) and the strength of the hysteresis (Havela et al. 1991; Prokes 1997). The hysteresis is reduced with increasing temperature. Above 15 K, the metamagnetic transition splits into two transitions (by $(1/3)M_s$ and $(2/3)M_s$ steps, respectively) irrespective of the thermal history of the crystal, as can be seen on the example in fig. 5.16. While the low-field branch shifts rather rapidly towards lower fields as the temperature increases, the upper branch shifts towards higher fields. At 34.5 K, the critical field of the lower transition reaches zero. Above 34.5 K, a metamagnetic transition to a magnetic phase with magnetization equal to $M_s/3$ takes place at very low fields. This situation remains unchanged up to 38 K. Above this temperature, the lower metamagnetic transition shifts again to higher fields, yielding above this transition a magnetization value slightly smaller than $(1/3)M_s$. Simultaneously, the magnetization curve looses its rectangular character seen at lower temperatures. The huge magnetocrystalline anisotropy in UNiGa is clearly manifest by the magnetization measured at $T = 4.2$ K in fields parallel to the c-axis which reaches a saturation value already above 1 T. Only a small magnetization is found in the perpendicular direction, which varies linearly with applied field, and reaches $0.1\,\mu_B$/f.u. at 38 T (Brück 1991). Neutron-diffraction experiments on UNiGa crystals in magnetic fields parallel to the c-axis concerted with relevant data of the magnetization (Havela et al. 1991; Prokes 1997), resistivity (Sechovsky et al. 1991; Jirman et al. 1992) and the specific heat (Sechovsky et al. 1993a) obtained in relevant magnetic fields. This facilitated the determination of magnetic phases above the metamagnetic transitions and the construction of the complex magnetic phase diagram shown in fig. 5.14 (Sechovsky et al. 1995b; Prokes et al. 1996a). In fig. 5.15, we can see that relations exist between the field evolution of the intensity of the (1, 1, 4/3) magnetic reflection measured at 4.2 K, together with the magnetization and the reduced electrical resistivity ($i \| c$) in magnetic fields along the c-axis (Prokes et al. 1996a).

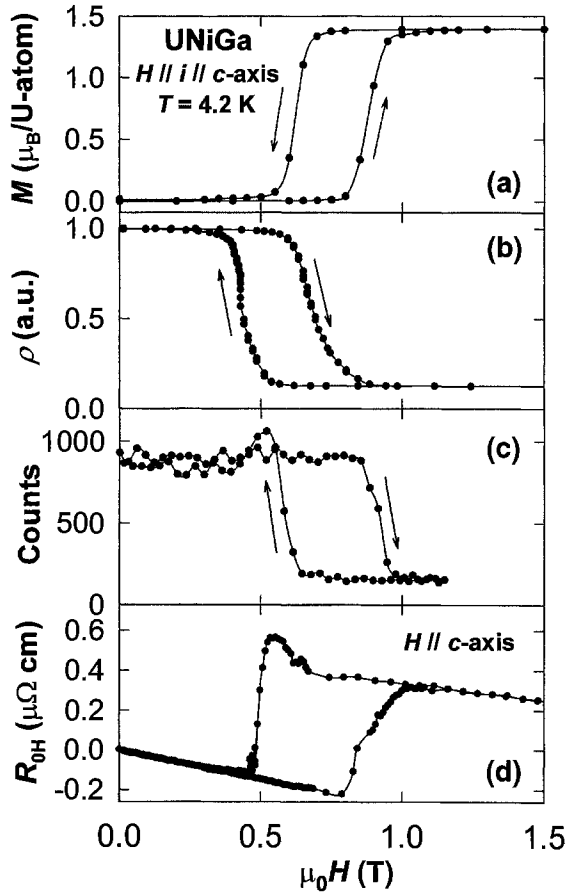

Fig. 5.15. Field dependence of: (a) the magnetization M; (b) reduced electrical resistivity ρ for current i along the c-axis (Jirman et al. 1992); (c) the peak intensity of the neutron diffraction reflection (1, 1, 4/3) (Prokes et al. 1996a); and (d) Hall resistivity R_{0H} measured on UNiGa single crystal at $T = 4.2$ K in magnetic field H applied along the c-axis (Kobayashi et al. 1996). The off-sets in critical fields are due to different demagnetization fields (different sample shapes) in particular experiments.

The temperature dependence of the electrical resistivity seen in fig. 5.12 (Jirman et al. 1992; Prokes et al. 1996a) with current parallel and perpendicular to the c-axis point to a pronounced anisotropy of transport properties in UNiGa. At high-temperatures both $\rho^{\parallel}(T)$ and $\rho^{\perp}(T)$ are large and decrease slowly with decreasing temperature (although it is nearly constant in the latter case). The $\rho^{\perp}(T)$ curve then resembles the behaviour of a ferromagnetic material. It exhibits a dramatic drop below 39 K, showing a quadratic temperature dependence at low temperatures. On the other hand, the $\rho^{\parallel}(T)$ curve exhibits change of sign of $\partial\rho/\partial T$ from positive to negative below 150 K leading to a gradually increasing upturn with decreasing temperature below 80 K. We mentioned already that the magnetic phase transitions below 40 K are accompanied by pronounced anomalies (fig. 5.13). Below

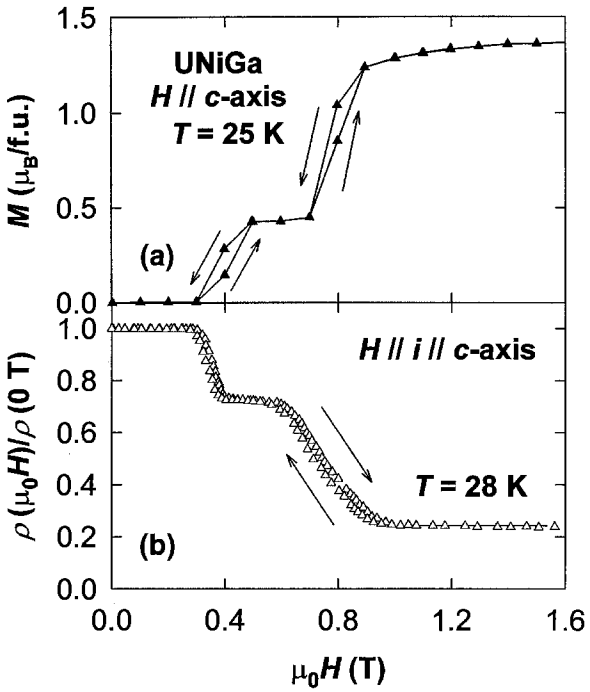

Fig. 5.16. (a) Magnetization M and (b) relative electrical resistivity for $i \| c$ vs. magnetic field H applied along the c-axis measured on a UNiGa single crystal at $T = 25$ and 28 K, respectively. After Jirman et al. (1992).

32 K, $\rho^{\|}(T)$ decreases monotonously and at low temperatures exhibit a quadratic temperature dependence with a very high residual resistivity.

The large resistivity values at low temperatures are drastically reduced by the metamagnetic transition (Sechovsky et al. 1991; Jirman et al. 1992; Prokes et al. 1996a) as can be seen in fig. 5.16. In fields perpendicular to the c-axis, negligible changes are found. Also, as can be seen in fig. 5.12, the upturn in $\rho^{\|}(T)$ above T_N is suppressed upon application of a magnetic field of 14 T along the c-axis. The anomalies in the electrical resistivity correlate well with the magnetic phase transitions determined from the magnetization and the specific heat measurements. Evolution of the temperature dependencies of the resistivity measured in several fields shown in fig. 5.17 document the effect of magnetic state in UNiGa on electrical resistivity. The giant-magnetoresistance phenomena in UNiGa were discussed together with some other UTX antiferromagnets and other intermetallics systems by Sechovsky et al. (1991, 1992c, 1993b, 1996), Havela et al. (1994b, 1996a, 1997b) and Nakotte et al. (1994a, 1994b).

The step-like change of the electrical resistivity, which clearly correlates with the change in magnetic order of UNiGa was interpreted by Aoki et al. (1996a), in terms of Fermi surface gapping (Elliot and Wedgwood 1963) in the antiferromagnetic state. As evidence for a gap the 10% lower γ-value in the ground state with respect to the field-induced ferromagnetic state has been proposed. An idea of a Fermi surface reconstruction by the

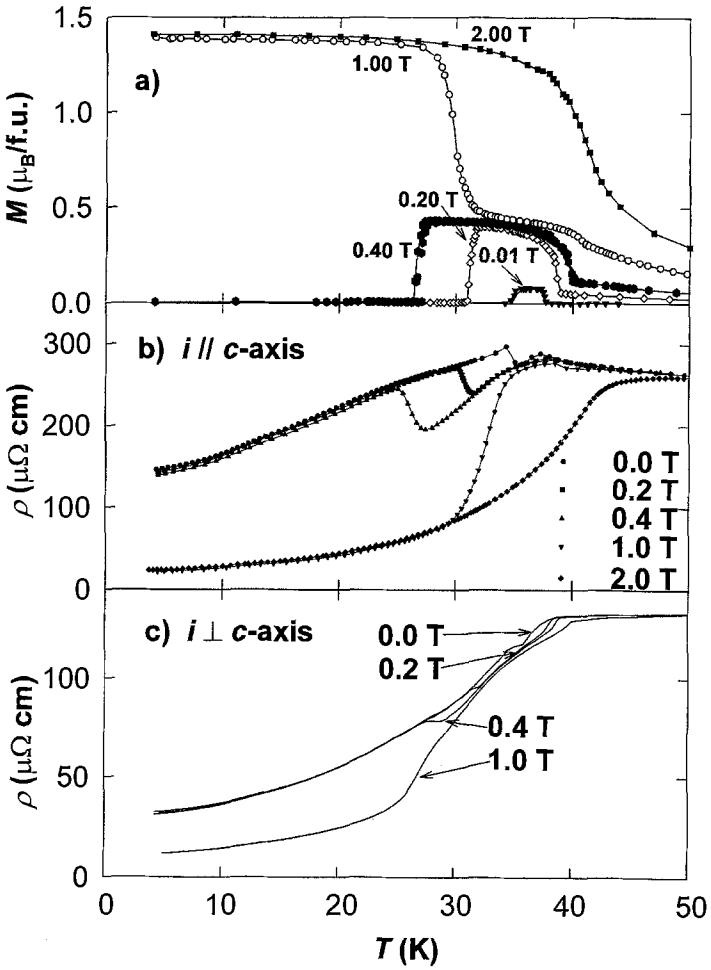

Fig. 5.17. Temperature dependence of (a) the magnetization M, and electrical resistivity ρ of the UNiGa single crystal (b) for $i \| c$ and (c) for $i \perp c$ in various fields H parallel to the c-axis – data taken from Jirman et al. (1992).

metamagnetic transition has been confirmed by *ab initio* local-density approximation calculations, using the fully relativistic LMTO method (Antonov et al. 1996; Perlov et al. 1998). A reduction of the electrical resistivity by 57% was found for the transition from the antiferromagnetic to ferromagnetic state in UNiGa. In the context of the low-temperature specific-heat studies also the magnetocaloric effect connected with the metamagnetic transition was investigated by Aoki et al. (1996b).

In order to provide further information for the discussion of mechanism of the giant magnetoresistance in UNiGa, the Hall effect in this material was studied by Kobayashi et al. (1996). From fig. 5.15 we can see that the normal Hall effect dominates at low temperatures. From the slope of the linear dependence of $\rho_H(H)$ in both regions we ob-

tain the normal Hall coefficient for the antiferromagnetic and ferromagnetic phases as -2.9×10^{-9} m^3/C and -1.7×10^{-9} m^3/C, respectively. The change of the normal Hall coefficients clearly indicates a substantial change of the Fermi surface topology. The descending branch exhibits an additional anomaly, which is due to the formation of a phase with magnetization $M_s/3$, mentioned above for some UNiGa samples. The extraordinary Hall coefficient (Kobayashi et al. 1996) scales in the paramagnetic regime linearly with the electrical resistivity and in the forced ferromagnetic state quadratically (with a large quadratic coefficient). This can be conceived when the 5f-states are strongly hybridized with the conduction states. The sign change of the Seebeck coefficient across the metamagnetic transition observed by Kobayashi et al. (1996) reflects the change of sign of the energy derivatives of the density of states at the Fermi level due to the Fermi surface reconstruction connected with the moment reorientation.

The thermal expansion of UNiGa (see fig. 5.12) is large and highly anisotropic, similar to other electronic properties. Along the a-axis the lattice monotonously expands with increasing temperature (α_a is always positive), whereas the c-parameter considerably shrinks yielding a very sharp and deep minimum in $\alpha_c(T)$ at 35 K. Around 60 K, $\alpha_c(T)$ changes sign and at higher temperatures the lattice expands in the c direction. The sharp anomalies, observed between $T = 34$ and 39 K in both $\alpha_a(T)$ and $\alpha_c(T)$, reflect magnetic phase transitions. Due to mutual compensation of the expansion in the a- and c-axis, the coefficient of the volume expansion α_V is negligible at low temperatures (Honda et al. 1997a, 1997b, 1998a; Prokes 1997). The very anomalous thermal expansion along the c-axis at temperatures far above T_N is attributed to the antiferromagnetic correlations propagating along the c-axis. Note that the a- (c-) parameter expands (shrinks) considerably when the compound becomes antiferromagnetically ordered (Prokes 1997; Honda et al. 1997a, 1997b, 1998a), whereas opposite magnetostriction effects are induced across the metamagnetic transition (Andreev et al. 1995e; Honda et al. 1997b).

The influence of hydrostatic pressure on magnetic phase transitions in UNiGa has been studied by measurements of resistivity anomalies (Sechovsky et al. 1993c; Uwatoko et al. 1994), thermal expansion (Honda et al. 1997a, 1997b, 1998a) and neutron magnetic diffraction (Prokes 1997; Prokes et al. 1998b). The main results seen also in fig. 5.18 may be summarized as:

(i) No change of U magnetic moment could be indicated by neutron diffraction up to 0.9 GPa (Prokes 1997);
(ii) T_N shifts towards lower temperatures, indicating that the ferromagnetic interaction within the basal plane is weakening with increasing pressure;
(iii) The transition towards the field-induced ferromagnetic phase occurs at higher critical fields, suggesting that, unlike the ferromagnetic interaction, antiferromagnetic interactions are enhanced by hydrostatic pressure;
(iv) Some magnetic phases (1, 2) are suppressed in relatively low pressures, the remaining phases have pressure-invariant magnetic structures up to 0.9 GPa, which was the maximum pressure in the neutron-diffraction experiment (Prokes 1997);
(v) A new antiferromagnetic phase is induced in zero field in pressures above 1.8 GPa (Honda et al. 1997b, 1998a).

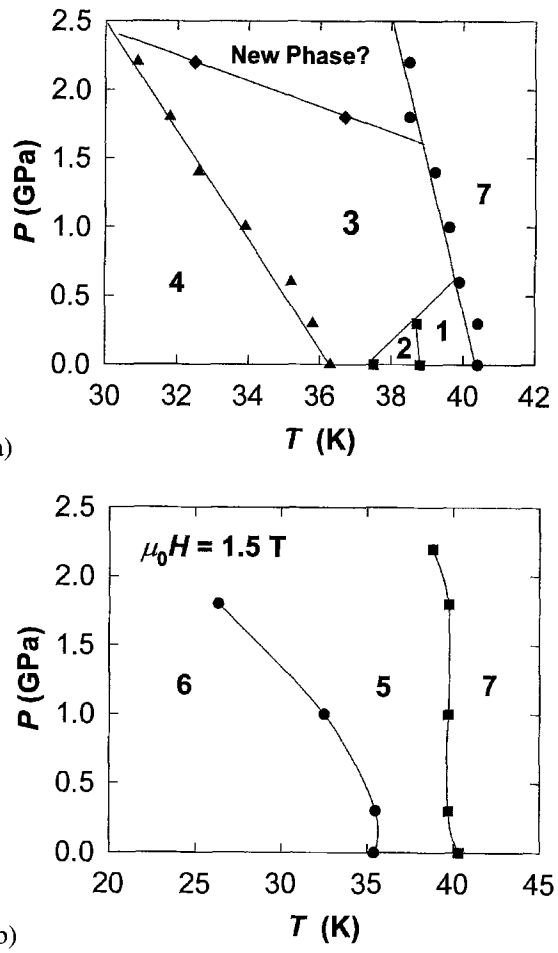

Fig. 5.18. Schematic p–T diagrams of UNiGa (a) in zero magnetic field and (b) in a field of 1.5 T applied along the c-axis (Honda et al. 1997b).

Polar Kerr rotation and ellipticity in the spectral region from 0.6 to 5.2 eV was studied on a UNiGa single crystal by Kucera et al. (1996).

The solid solutions $UNiAl_{1-x}Ga_x$ were studied by Sechovsky et al. (1988b) and Maletta et al. (1988). Substitution of Al by Ga in UNiAl leads to rapid suppression of the heavy-fermion behaviour which is evidenced by a drop of the γ-value by 60% in $UNiAl_{0.6}Ga_{0.4}$. This chemically more complex compound has evidently a much simpler ground state magnetic structure, a simple antiferromagnetic structure with $\boldsymbol{q} = (0, 0, 0.5)$, than the parent compounds as documented by a simple neutron powder-diffraction pattern (Maletta et al. 1992). Compounds with $x > 0.4$ exhibit almost the same γ-value as UNiGa and show also the tendency of this parent compound to the local U magnetic moment behaviour, in

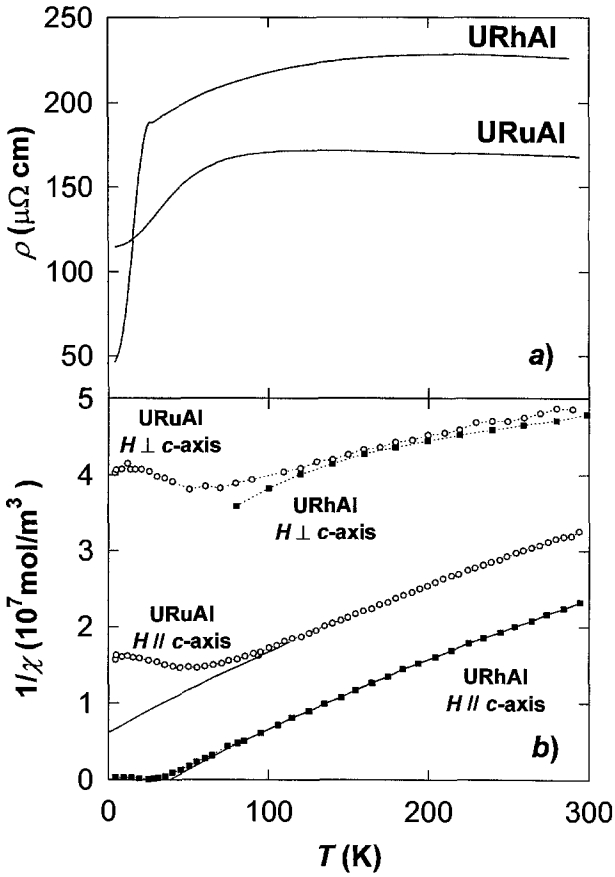

Fig. 5.19. Temperature dependence of the following quantities measured on URuAl and URhAl: (a) Electrical resistivity ρ measured on a polycrystal (Nakotte 1992); (b) Inverse magnetic susceptibility $1/\chi$ in magnetic fields H applied along and perpendicular to the c-axis of a single crystal – from Veenhuizen et al. (1988a).

contrast to more itinerant 5f moment properties of the Al rich compounds (Maletta et al. 1988; Sechovsky et al. 1988b).

URuAl and *URuGa* are paramagnetic down to 20 mK (Sechovsky et al. 1986b), however, both show features resembling spin-fluctuation systems. The possibility to study the former compound in single-crystal form allowed to confirm the huge uniaxial magnetocrystalline anisotropy also in the paramagnetic case (Veenhuizen et al. 1988a; de Boer et al. 1989; Sechovsky et al. 1994a). The susceptibility of URuAl in a field along the c-axis is much larger than in a perpendicular field (see fig. 5.19). Above 100 K, the $\chi_c(T)$ curve can be fitted with a modified Curie–Weiss law with $\mu_{\rm eff} = 2.24\ \mu_B$/f.u. and $\Theta_p = -53$ K, whereas $\mu_{\rm eff} = 2.3\ \mu_B$/f.u. and $\Theta_p = -410$ K has been derived for χ_a. The same value of $\chi_0 = 8 \times 10^{-9}$ m^3/mol has been observed for both directions. The low temperature susceptibility is characterized by a broad maximum around 50 K on the $\chi_c(T)$ curve, which is

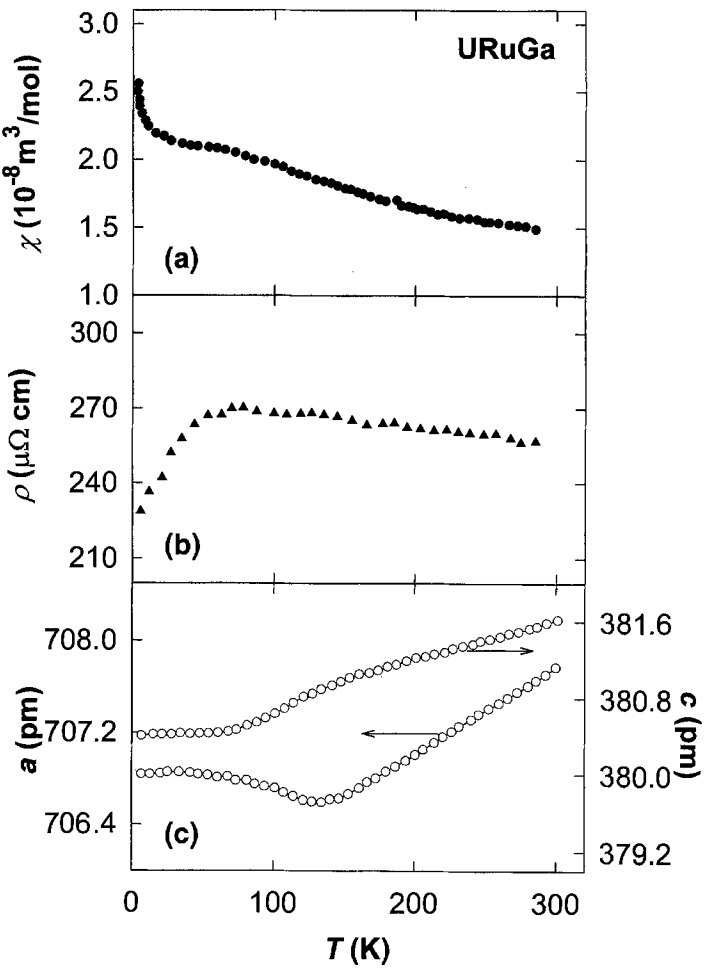

Fig. 5.20. Temperature dependence of the following quantities measured on polycrystalline URuGa: (a) Magnetic susceptibility χ; (b) Electrical resistivity ρ; (c) Lattice parameters a and c (Havela et al. 1983).

seen in much weaker form also in the perpendicular direction. This maximum is reminiscent of behaviour of Pd or UPt_3. The temperature dependence of the resistivity (fig. 5.19) measured only on polycrystals is very weak at high temperatures and exhibits a pronounced knee around 50 K. Also in the case of URuGa (see fig. 5.20) the susceptibility follows a modified Curie–Weiss behaviour above 100 K. With decreasing temperature below 100 K, the susceptibility is leveling off and forms a plateau below 50 K, followed by an upturn with further lowering temperature (Havela et al. 1983, Andreev et al. 1997d; Tran and Troc 1997). Also in this case the ρ vs. T dependence shows a knee. As can be seen from the temperature dependence of lattice parameters in fig. 5.20, the thermal expansion is anisotropic with α_c considerably larger than α_a. Below approximately 150 K, a positive

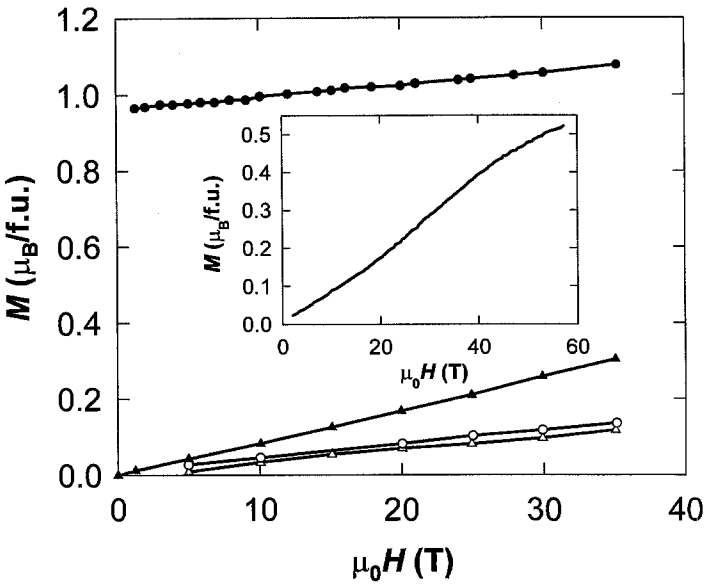

Fig. 5.21. Magnetization M vs. field H measured at $T = 4.2$ K on single crystals of URhAl (circles) and URuAl (triangles) in magnetic fields along (full symbols) and perpendicular (open symbols) to the c-axis. An extension to higher fields for URuAl (solid line) has been measured on an free-powder sample (Veenhuizen et al. 1988a; Sechovsky et al. 1992b).

(negative) anomaly in the c- (a-) axis evolves with lowering temperature (Tran and Troc 1997), which may be tentatively attributed to magnetic correlations. In this context we recall the above discussed thermoexpansion anomalies accompanying antiferromagnetic correlations propagating along c.

Beside the anomalous temperature dependence of the susceptibility, we can also observe an anomaly in the 4.2 K magnetization behaviour of URuAl in high magnetic fields. In fig. 5.21 we can see that the magnetization curve in fields along the c-axis shows an upturn above 15 T which is followed by gradual saturation above 35 T (Sechovsky et al. 1992b; 1994a). The susceptibility $\partial M/\partial H$ has a maximum around 30 T. The characteristic energy of this anomaly can be related to the characteristic energy of the $\chi_c(T)$ maximum at 50 K.

Paixao et al. (1993) have studied magnetization density in a URuAl single crystal by polarized-neutron experiments and observed a considerable magnetization density induced at the Ru site in the U–Ru basal plane by hybridization between the 5f and 4d electrons. These results clearly confirmed the existence of the anisotropic 5f-ligand hybridization.

A very surprising result has been obtained by (Andreev et al. 1996a, 1996b, 1997f) by observation of ferromagnetism in a wide concentration range of solid solutions of the type $UCo_{1-x}Ru_xAl$ although both the parent compounds, UCoAl and URuAl have a non-magnetic ground state. As can be seen in fig. 5.22, ferromagnetism is observed already for very small substitutions of Ru for Co. Both the spontaneous moment μ_s and the ordering temperature T_C grow rapidly with increasing x, reach their maximum values for $x = 0.3$

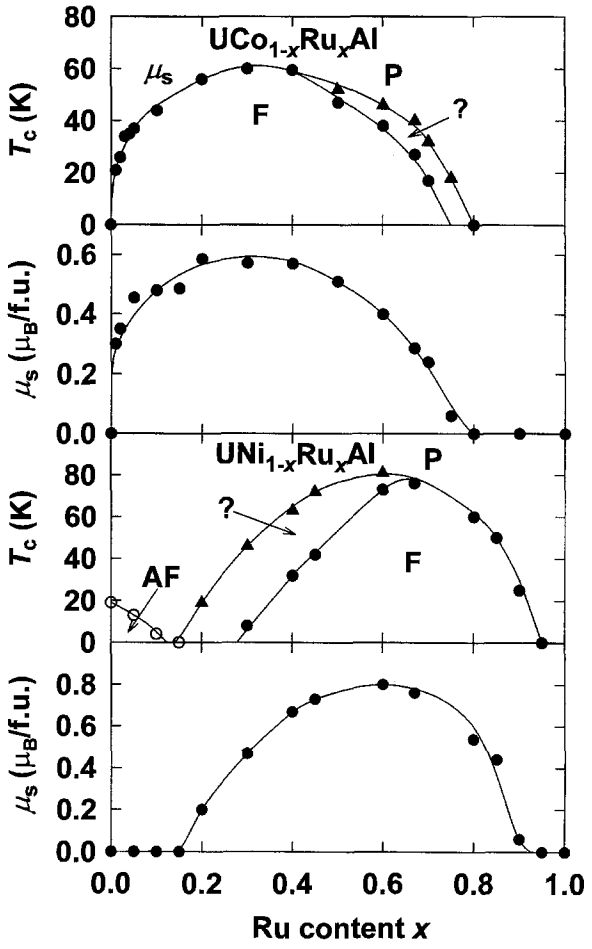

Fig. 5.22. Concentration dependence of the ordering temperature T_C and spontaneous magnetic moment μ_S in $UCo_{1-x}Ru_xAl$ and $UNi_{1-x}Ru_xAl$ solid solutions – after Andreev et al. (1997e, 1997f).

and then decrease with increasing Ru content up to $x = 0.8$, where ferromagnetism in this systems disappears.

A complex evolution of magnetism has been observed in the pseudoternary system *$UNi_{1-x}Ru_xAl$* (Andreev et al. 1997e) mainly due to the fact that one of the parent compounds, UNiAl, is an antiferromagnet. As can be seen in fig. 5.22, antiferromagnetism is rapidly suppressed and the compounds with $x = 0.15$ has a paramagnetic ground state. Ferromagnetic compounds are observed in a wide concentration region $0.15 < x < 0.95$ with concentration dependencies of T_C and μ_S as in $UCo_{1-x}Ru_xAl$, although the maximum values are approximately 30% larger in $UNi_{1-x}Ru_xAl$.

URuSn orders ferromagnetically below 51–55 K (Sechovsky et al. 1986a, 1990; Tran et al. 1995b; Kruk et al. 1997) with a spontaneous magnetic moment of 1.1 μ_B/f.u. de-

rived from free-powder magnetization data at $T = 4.2$ K extrapolated to 0 T. As seen in fig. 5.24, in 35 T nearly $1.2\,\mu_B$/f.u. is recorded. The ratio of the fixed-powder (μ^{fixed}) and the free-powder (μ^{free}) spontaneous magnetization is ≈ 0.5 which confirms uniaxial anisotropy with the c-axis as the easy-magnetization direction (Sechovsky et al. 1990). Since μ^{fixed} cannot reach μ^{free} even in 35 T, a huge anisotropy field $\mu_0 H_a \gg 35$ T can be concluded from the high-field magnetization data. Measurements of the pressure dependence of the AC susceptibility anomaly around T_C revealed a negative effect of $\partial \ln T_C/\partial p = -6.2\ \text{Mbar}^{-1}$.

Ferromagnetism is observed over all compositions in the $UCo_{1-x}Ru_xSn$ solid solutions with T_C nearly constant (≈ 80 K) for $x < 0.6$ and gradually falling with further increasing x. The spontaneous magnetic moment is increasing up to $1.5\,\mu_B$/f.u. at $x = 0.5$ which is followed by a decrease with increasing Ru content. This variation seems to correlate with a pronounced non-linearity in concentration dependence of the lattice constants around $x = 0.6$ (Andreev et al. 1995f).

When Sn is substituted for Al in URuAl, ferromagnetism is rapidly achieved in $URuAl_{1-x}Sn_x$ for $x = 0.2$ and both T_C and μ_s increase almost linearly with x (Andreev et al. 1996b). A pronounced non-linearity in the a vs. x and c vs. x is observed also in these solid solutions, in this case around $x \approx 0.4$.

URuSb is ferromagnetic below $T = 35$ K with a spontaneous magnetic moment of $0.6\,\mu_B$/f.u. derived from magnetization data taken at $T = 4.2$ K (Palstra et al. 1987). Also here we observe uniaxial anisotropy with magnetic moments pointing along the c-axis.

URhAl becomes ferromagnetic at $T_C = 27$ K with a spontaneous magnetic moment of $0.94\,\mu_B$/f.u. at 4.2 K, observed exclusively along the c-axis (Veenhuizen et al. 1988a), whereas in the a-axis only a linear paramagnetic response is observed which, as can be seen in fig. 5.21, is nearly identical with the a-axis magnetization in the paramagnetic URuAl (de Boer et al. 1989). Qualitatively the same anisotropy is observed in the paramagnetic range (see fig. 5.19). The a-axis susceptibilities of URuAl and URhAl do not differ substantially at high temperatures (and are much lower than the χ_c values), although the $\chi_c(T)$ curve for URhAl in fields along the c-axis is declines dramatically from the appropriate curve for URuAl (Veenhuizen et al. 1988a). This comparison provides strong arguments for understanding the mechanisms that may be responsible for the uniaxial anisotropy in the UTX compounds in the ZrNiAl-family.

Paixao et al. (1992) performed experiments with polarized neutrons in order to measure the magnetization density in URhAl. The magnetization density analysis shows that the total moment, as measured by magnetization, has four contributions, $\mu_U = 0.94\,\mu_B$, $\mu_{Rh(I)} = 0.28\,\mu_B$, $\mu_{Rh(II)} = 0.03$ and $-0.11\,\mu_B$ as a conduction electron contribution. The Rh(I) and Rh(II) sites are located within the U–Rh and Rh–Al planes, respectively. The observation of a large moment at the Rh(I) site provides a clear evidence of an anisotropic 5f(U)–4d(Rh) hybridization, which is strong within the U–Rh basal plane. This effect, in conjunction with the observed large orbital-moment contribution, is supposed to be the source of the huge uniaxial anisotropy. The ratio between the observed spin and orbital moments $\mu_L/\mu_S = 1.81$ is substantially reduced with respect to the theoretical value for a free $5f^3$ ion ($= 2.6$). The reduction is proposed as a quantitative measure of hybridization in URhAl. Inelastic neutron scattering experiment on URhAl has been performed by Hiess et al. (1997a) in order to characterize the magnetic response function with respect to energy. The three prominent features of the observed spectra were attributed to hybridization

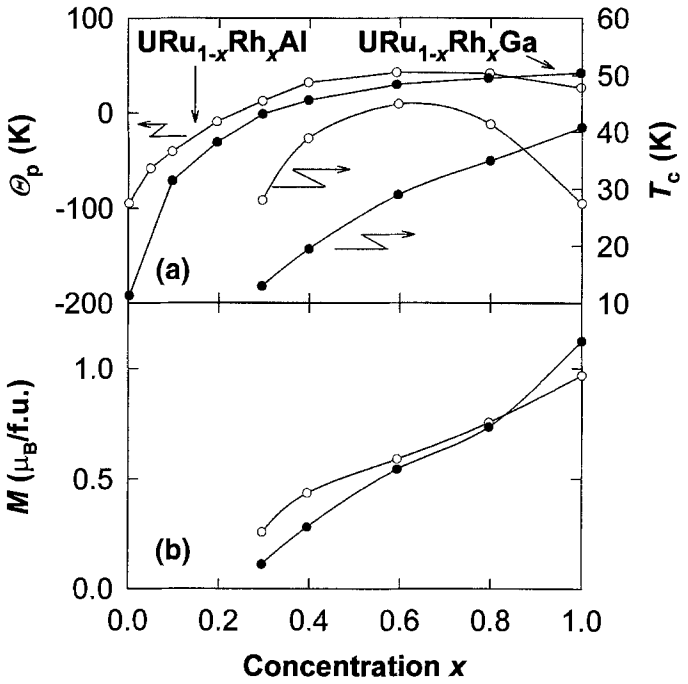

Fig. 5.23. Concentration dependence (a) of the ordering temperature T_C and paramagnetic Curie temperature θ_p, and (b) the spontaneous magnetic moment in $URu_{1-x}Rh_xAl$ (○) and $URu_{1-x}Rh_xGa$ (●) solid solutions – from Sechovsky et al. (1992b).

of 5f electrons with conduction electrons (broad quasielastic response, $\Gamma_{QE}/2 \approx 6$ meV, the presence of a spin-wave gap (around $\Delta E = 90$ meV) and the occurrence of an inter-multiplet transition ($\Delta E \approx 380$ meV).

URhGa alike *URhAl* is a uniaxial ferromagnet but the former has a considerably higher T_C (40 K) and spontaneous magnetic moment μ_s ($1.2\,\mu_B$) than the latter (Sechovsky et al. 1986b, 1990, 1992b).

When Rh is substituted for Ru in URuAl and URuGa, the susceptibility anomalies below $T = 100$ K are gradually pushed to lower temperatures and suppressed, due to the growing upturn of the $\chi(T)$ curves at low temperatures, and ferromagnetism is reached around $x = 0.3$ both for the $URu_{1-x}Rh_xAl$ and the $URu_{1-x}Rh_xGa$ compounds (Sechovsky et al. 1988c, 1992b; Veenhuizen et al. 1988b). The evolution of the high-field magnetization anomalies in Rh doped URuAl towards ferromagnetism has also been studied for concentrations up to 35% Rh (Sechovsky et al. 1993d, 1993e). As can be seen in fig. 5.23, the spontaneous moment is growing monotonously with increasing x beyond 0.3 to reach the maximum values in the terminal URhX compounds. Whereas also T_C increases monotonously in the $URu_{1-x}Rh_xGa$ system, the Al containing counterparts exhibit a maximum of $T_C = 45$ K for $x = 0.6$ and then the ordering temperature gradually falls off to 27 K in URhAl. Rh substitutions for Co in $UCo_{1-x}Rh_xAl$ (Andreev 1998) yield first the

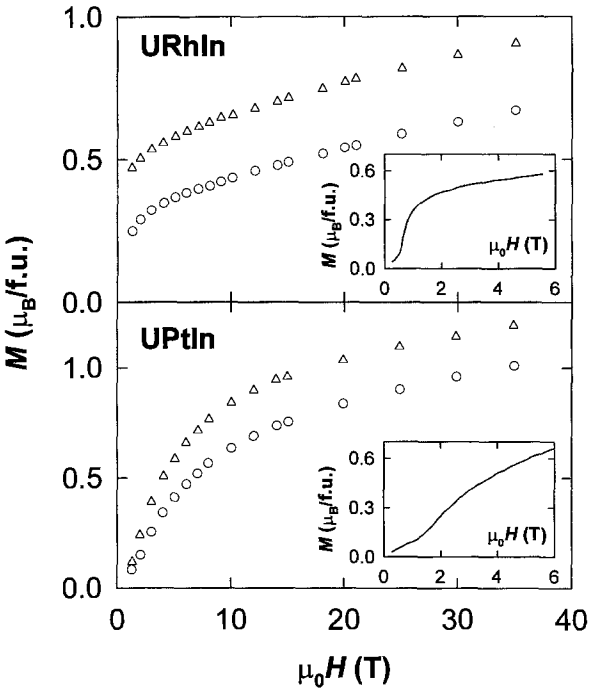

Fig. 5.24. Magnetization curves measured on free-powder and fixed-powder samples of URhIn and UPtIn at $T = 4.2$ K. The insets show the low-field parts of $M(H)$ curves obtained on oriented-powder samples (after Havela et al. 1993a; Sechovsky et al. (1995a)).

appearance of a mixed ferromagnetic-metamagnetic behaviour. Whereas the spontaneous magnetization is increasing, a gradual lowering of the critical field of the metamagnetic transition is observed with increasing Rh concentration. At $x = 0.1$, a pure ferromagnetic behaviour is observed and when x is further increased also the spontaneous magnetization increases, first very slowly (for $x \leqslant 0.4$) and then rapidly ($\mu_s \approx 0.35$, for $x = 0.4$).

Pressure studies of the AC susceptibility on $URu_{0.7}Rh_{0.3}Al$, $URu_{0.4}Rh_{0.6}Al$ and URhAl provided values of $\partial \ln T_C/\partial p = +5.9$, $+5.6$ and -1.0 Mbar^{-1}, respectively (Cuong et al. 1996). Closer analysis of these results would require knowledge of the linear compressibility in these materials.

URhIn was first studied by Tran and Troc (1990a) who assigned the susceptibility maximum and a sudden change of slope of the $\rho(T)$ curve at $T = 7$ K to a transition to antiferromagnetic ordering at lower temperatures. Sechovsky et al. (1995a) observed a clear peak in the temperature dependence of the specific heat at 6.5 K and an upturn below 3 K, which might indicate another magnetic phase transition below 1.4 K (minimum temperature of the specific-heat experiment). The latter suggestion may be corroborated by the gradual shift of the magnetic entropy towards higher temperatures when a magnetic field is applied. No magnetic contribution to neutron powder-diffraction down to $T = 1.5$ K has been detected (Tran et al. 1995a), however, which may be due to low U moments or to a

complex magnetic structure. Magnetization curves measured at $T = 4.2$ K, displayed in fig. 5.24, show a metamagnetic transition already below 1 T. About 0.5 μ_B/f.u. is observed at 2 T on an oriented-powder sample. The magnetization grows to 0.9 at 35 T, still far from saturation. A saturated magnetization value of 1.2 μ_B/f.u. can be extrapolated (Sechovsky et al. 1995a). The ratio of magnetization values of the fixed-powder and free-powder in fields just above the metamagnetic transition is close to 0.5, which points to the c-axis as the easy-magnetization axis. The metamagnetic transition is by far not as sharp as in other UTX antiferromagnets of the ZrNiAl-type family, which might be attributed to the fact that the temperature of the experiment is close to the proposed T_N. A giant magnetoresistance effect of about −20% (at 4 T), associated with the metamagnetic transition, has been reported by Tran and Troc (1990a), which is strongly supporting the idea of an antiferromagnetic ground state in URhIn.

Ferromagnetism in *URhSn* appears below $T = 17$ K as evidenced by ^{119}Sn Mössbauer spectroscopy (Kruk et al. 1997), specific heat (Mirambet et al. 1995a) and resistivity measurements (Mirambet et al. 1995a; Tran et al. 1995b). Mirambet et al. (1995a) have observed an additional phase transition, apparently without any connection to magnetism, at 58 K in the ρ vs. T and C_p/T vs. T dependencies. Matar et al. (1995) studied the magnetic properties of URhSn by using of scalar relativistic calculations within LDA and including spin–orbit coupling effects. An orbital moment with a large magnitude (3.1 μ_B) and a spin component (1.84 μ_B) of opposite sign were obtained for uranium (yielding $\mu_L/\mu_S = 1.68$) whereas very small moments have been calculated on the Rh atoms (0.08 and 0.05 μ_B on Rh(I) and Rh(II), respectively). The resulting calculated moment of 1.24 μ_B is in very good agreement with the experimental value of the spontaneous moment of 1.3 μ_B determined from free-powder magnetization data obtained at $T = 4.2$ K (Sechovsky et al. 1990).

Besides the orthorhombic TiNiSi-type structure (Kergadallan 1993) *UPdGa* has been reported to appear also in the hexagonal ZrNiAl-type version (Tran and Troc 1991a). Possible antiferromagnetism below 62 K with an additional magnetic phase transition at 30 K has been derived from susceptibility anomalies at these temperatures. Neutron-powder diffraction study (Tran et al. 1998a) allowed to determine at 7 K an antiferromagnetic structure with incommensurate longitudinal modulation, characterized by a propagation vector $\boldsymbol{q} = (0, 0, 0.3)$ and an ordered uranium magnetic moment of 1.37 μ_B oriented along the c-axis.

Ferromagnetism is observed in the *URu$_{1-x}$Pd$_x$Ga* solid solutions (Tran et al. 1997, 1998a) in a wide concentration range (x from 0.1 to 0.7) showing a maximum in $T_C \approx 79$ K for x around 0.4–0.5 (see fig. 5.25). For concentrations above $x = 0.7$ a gradual transition of the system towards the antiferromagnetic structure of UPdGa is observed with an admixture of a ferromagnetic and antiferromagnetic phase for x around 0.8. In this context it might be worth to consider the depression of the magnetic transition temperature in higher Rh concentrations in URu$_{1-x}$Rh$_x$Al, in terms of possible involvement of antiferromagnetic interactions as a consequence of increasing population of 4d states. Further studies are needed, however, to confirm this *ad hoc* suggestion.

UPdIn was originally quoted to be a ferromagnet below $T = 6$ K (Troc 1986). Andreev and Bartashevich (1986) reported a much higher value of T_C (22 K) and a spontaneous moment of 0.15 μ_B. Brück et al. (1988) studied the specific-heat, AC and DC magnetic susceptibility, magnetization on free- and fixed-powder samples in fields up to 35 T, and electrical resistivity on polycrystals. Besides, $\rho(T)$ has been measured on a single-crystalline

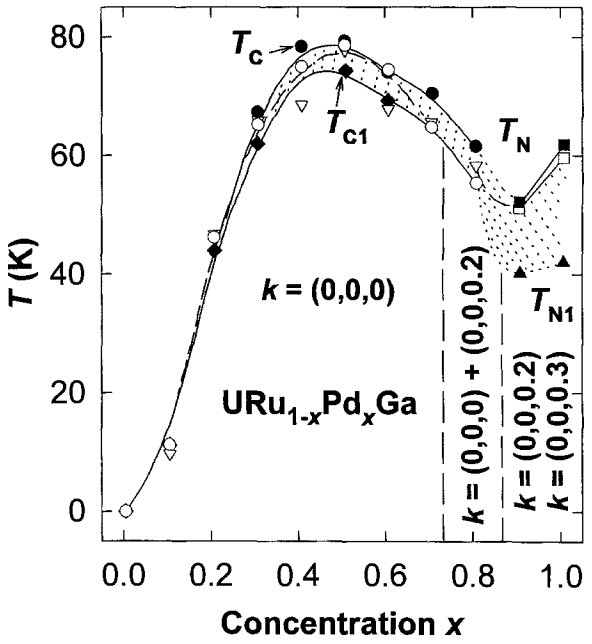

Fig. 5.25. Magnetic phase diagram of the $URu_{1-x}Pd_xGa$ pseudoternary system (Tran et al. 1998a).

whisker grown along the c-axis. The data pointed to a transition to an antiferromagnetic state below $T_N = 20.4$ K and an additional transition at 8.5 K (which can be well seen in the specific-heat data shown in fig. 5.26), to a state with a small spontaneous magnetization of about $0.15\,\mu_B$ observed on an oriented-powder sample. The latter transition is shifted to higher temperatures when a magnetic field is applied. The low temperature specific heat revealed a heavy-fermion-like behaviour with $\gamma = 280$ mJ/(mol K^2). The temperature dependence of the resistivity measured on the whisker sample shows a minimum at 50 K which is followed by a steep decrease with further increasing temperature and tends to saturate in the low-temperature limit. Similar data (see fig. 5.26) has been reported by Fujii et al. (1990a) who succeeded to grow a single crystals of UPdIn. Kurisu et al. (1991) performed measurements of $\rho(T)$ curves of UPdIn under external hydrostatic pressures. They associated the inflection point on these curves with T_N (at 22 K in ambient pressure) and determined the pressure dependence of the Néel temperature, revealing $\partial \ln T_N/\partial p = 11$ Mbar^{-1}.

The χ vs. T dependencies for magnetic field along the a- and c-axis (shown in fig. 5.26) follow a Curie–Weiss law above 100 K with an effective magnetic moment of $2.87\,\mu_B$ identical for both field directions, whereas $\theta_p = -74$ and 34 K for the a- and c-axis, respectively. This points again to a strong magnetocrystalline anisotropy, however considerable weaker than observed in majority of other UTX compounds of the ZrNiAl-family. The electrical resistivity along the a-axis is reminiscent of a ferromagnet, although the upturn above T_N is quite unusual.

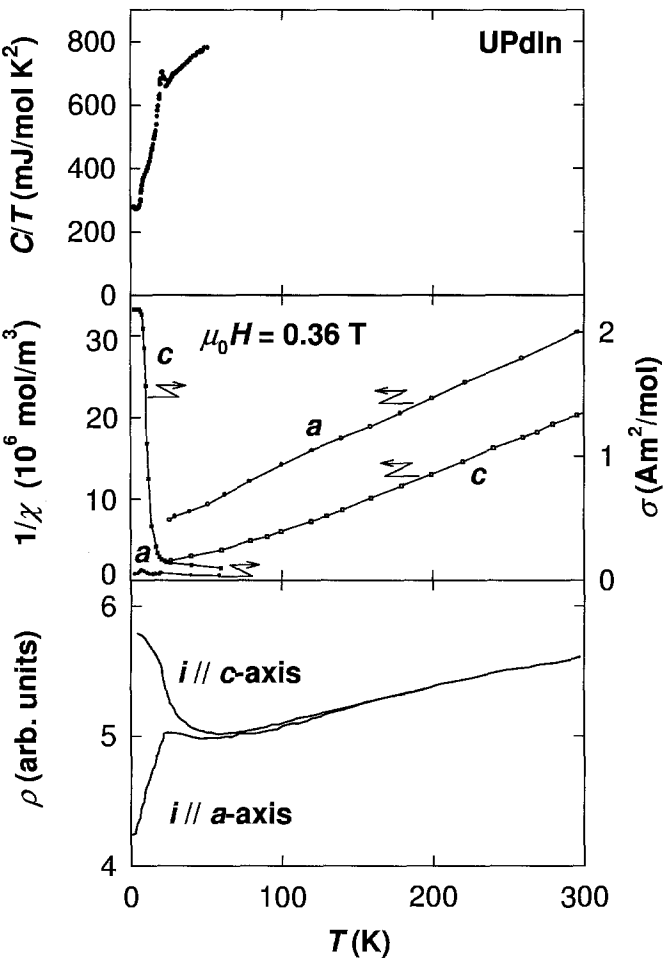

Fig. 5.26. Temperature dependence (a) of the specific heat C/T measured on the polycrystalline sample of UPdIn (Fujii et al. 1990a), and single-crystal data: (b) inverse magnetic susceptibility $1/\chi$ and magnetization σ in 0.36 T (Fujii et al. 1990a) in fields applied along the a- and c-axis, and (c) electrical resistivity ρ for current i along the a- and c-axis.

The magnetization below T_N is strongly anisotropic showing again the c-axis as the easy-magnetization direction (see fig. 5.27). Paramagnetic linear response of the magnetization to a field applied within the basal plane yields about $0.5\,\mu_B$/f.u. at 35 T. The c-axis magnetization at $T = 4.2$ K shows two metamagnetic transitions at 3 T and 16 T, yielding a step-like increase of the magnetization from 0.3 to $0.5\,\mu_B$ and from $0.5\,\mu_B$ to $1.5\,\mu_B$, respectively. The evolution of these transitions with respect to temperature has been studied by Sugiura et al. (1990). The results in conjunction with the neutron diffraction results (Fujii et al. 1990a) have been used to construct the magnetic phase diagram shown in fig. 5.28. UPdIn orders antiferromagnetically below $T = 20.4$ K. The magnetic structure

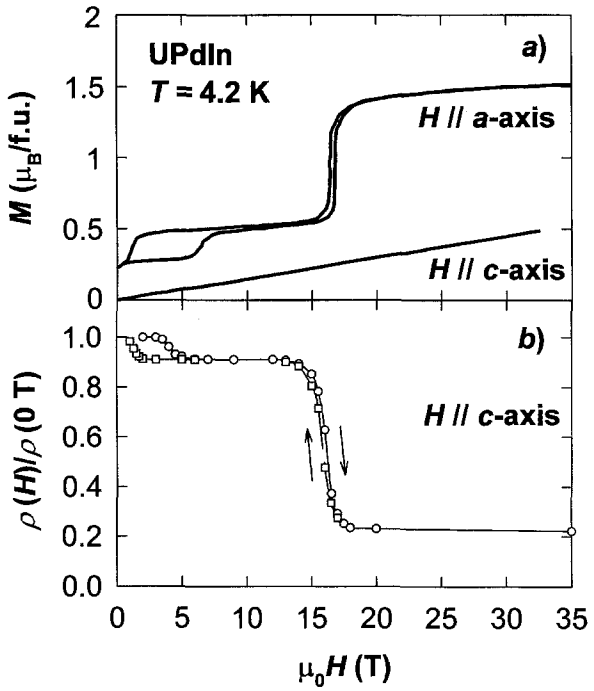

Fig. 5.27. Field dependence (a) of the magnetization M for field H along the a- and c-axis, and (b) of the reduced electrical resistivity ρ for current along the c-axis of a UPdIn single crystals at $T = 4.2$. The arrows indicate directions of the field sweep. After Fujii et al. (1990a); Nakotte et al. (1992).

consists of ferromagnetic basal planes of U moments which are sinusoidally modulated along the c-axis with $\boldsymbol{q} = (0, 0, 0.4)$. Below 8.5 K this structure squares up and as a result the ground-state phase with an uncompensated antiferromagnetic structure (UAF) with the stacking $(+ - + + -)$ along the c-axis appears. Above the first metamagnetic transition, UAF with the stacking $(+ + -)$ along the c-axis with $\boldsymbol{q} = (0, 0, 1/3)$ is formed and finally above 16 T, ferromagnetically aligned U moments are observed. A theoretical explanation of the metamagnetic transitions was given by Sugiura et al. (1990) using the model of Date (1968). Also Iwata et al. (1992) applied a molecular field model with a long-range oscillatory interaction involved. Similar to other UTX antiferromagnets, the metamagnetic transitions are connected with the changes in periodicity of the magnetic structure and are accompanied by giant magnetoresistance effects (Sechovsky et al. 1993b, 1995c; Nakotte et al. 1992) which can be seen in fig. 5.27. These effects will generally be discussed in section 2.6.

UIrAl and *UPtAl* were investigated by Andreev and Bartashevich (1986) and Sechovsky et al. (1990). These compounds order ferromagnetically below $T = 64$ and 46 K, respectively. There is a spontaneous magnetic moment along the c-axis of 0.93 and 1.2 μ_B/f.u., respectively. A fast onset of ferromagnetism with small substitutions of Ir for Co in UCoAl and a linear evolution of the magnetic moment is observed in the solid solutions

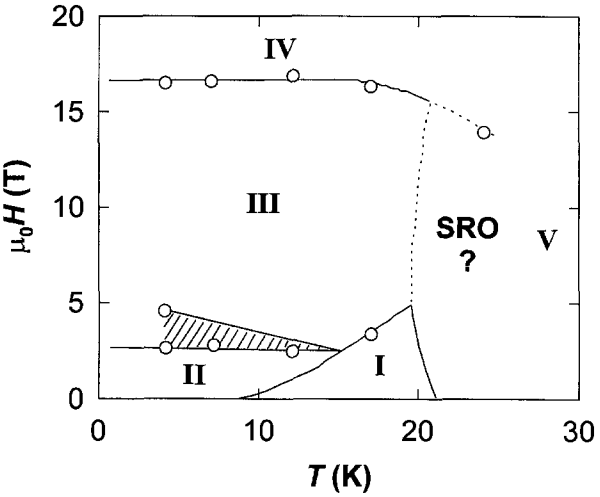

Fig. 5.28. Magnetic phase diagram of UPdIn in a magnetic applied along the c-axis. 1 – AF phase sinusoidally modulated along the c-axis, $\boldsymbol{q} = (0, 0, 0.4)$; 2 – Uncompensated AF phase (UAF) with the stacking $(+ - + + -)$ along the c-axis, $\boldsymbol{q} = (0, 0, 0.4)$; 3 – Uncompensated AF phase (UAF) with the stacking $(+ + -)$ along the c-axis, $\boldsymbol{q} = (0, 0, 1/3)$; 4 – Ferromagnetic phase, $\boldsymbol{q} = (0, 0, 0)$; 5 – Paramagnetic phase.

$UCo_{1-x}Ir_xAl$ (Andreev 1998), whereas Pt doping initially resembles the effects of Ni substitutions in UCoAl, and 10% Pt in the T sublattice is enough to whip off the last features of metamagnetism (Andreev et al. 1998b). $UCo_{0.8}Pt_{0.2}Al$ is a simple paramagnet, but further increase of the Pt concentration induces ferromagnetism ($T_C \approx 8$ K for $x = 0.3$) and a rapidly increasing both T_C and μ_s for x up to 0.6, followed by gradual saturation of both values for $x \geqslant 0.6$.

UIrGa and *UPtGa* are also uniaxial ferromagnets (Sechovsky et al. 1987, 1990; Prokes et al. 1997a) below $T_C = 60$ K and 68 K, respectively. The corresponding spontaneous moments at 4.2 K are 0.93 and 1.33 μ_B/f.u. A very high value of the coercivity of 2.4 T has been observed, when measuring a hysteresis loop on UPtGa polycrystals and similar value was found for powder, which indicates that the coercivity is of intrinsic character for a large part.

Also *UIrSn* has a ferromagnetic ground state with $T_C = 21$–23 K determined from ^{119}Sn Mössbauer spectroscopy (Kruk et al. 1997) and resistivity data (Tran et al. 1995b). The spontaneous magnetic moment appearing again along the c-axis amounts to 1.24 μ_B at $T = 4.2$ K (Sechovsky et al. 1990).

UPtIn can be classified as an antiferromagnet below $T_N = 15$ K (Havela et al. 1993a), where a maximum in $\partial(\chi T)/\partial T$ and the specific heat is observed. A susceptibility maximum has been reported at 18 K (Havela et al. 1993a) or 22 K (Tran and Troc 1990a). The value $\gamma = 150$ mJ/(mol K^2) has been determined from specific-heat data below T_N, whereas 375 mJ/(mol K^2) has been extrapolated from data above 19 K (Havela et al. 1993a). Analyzing the neutron powder diffraction data, Tran et al. (1995a) determined the magnetic structure consisting of U magnetic moments of 1.39 μ_B (at $T = 1.5$ K), ferromagnetically coupled within the basal plane and $+ + - -$ coupled along the c-axis, i.e.,

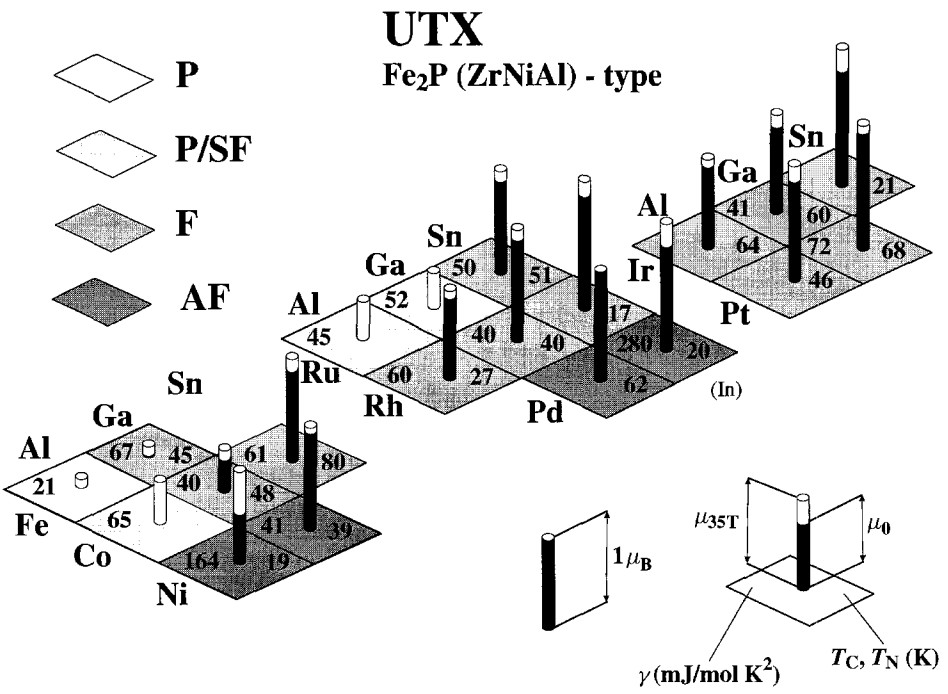

Fig. 5.29. Schematic plot illustrating evolution of some electronic properties (type of magnetic ground state, magnetic ordering temperature, γ-value (linear coefficient of the specific heat), spontaneous magnetic moment (black part of the columns – extrapolated from high magnetic field data to zero field), induced magnetic moment in field of 35 T (white top parts of the columns) of UTX compounds with the hexagonal ZrNiAl-type structure. Data are compiled from the information given in table 5.2.

$\boldsymbol{q} = (0, 0, 0.25)$. Magnetization curves measured on free-powder and fixed-powder samples (fig. 5.24) display a broad metamagnetic transition (onset around 1 T), which is not typical for the UTX antiferromagnets of the ZrNiAl-type family (sharp first order transitions are observed in UNiAl, UNiGa, UPdIn). When considering also the rather high ratio $M_{\text{fixed}}/M_{\text{free}} \approx 0.7$ in 4 T (above the transition) we may conclude that the clear "uniaxial anisotropy" situation may not be present in UPtIn. Single-crystal data are strongly desired. A saturation magnetization of $1.3\,\mu_B$ has been derived from extrapolating the high-field free-powder magnetization to infinite field (Havela et al. 1993a). This value is in a good agreement with $1.39\,\mu_B$ determined from the neutron diffraction experiment (Tran et al. 1995a). A giant magnetoresistance value of about -20% at 4 T has been observed by Tran and Troc (1990a).

Two crystallographic modifications have been reported in literature, namely the hexagonal ZrNiAl-type (Andreev and Bartashevich 1986) and the cubic MgAgAs-type, which shall be discussed in section 5.1.4. The hexagonal modification was found to order ferromagnetically with a spontaneous moment of $0.6\,\mu_B$/f.u.

Some basic parameters are summarized in a graphical form in fig. 5.29 in order to visualize the systematic changes in electronic properties. For the UTAl series, electronic

TABLE 5.3

Parameters of ^{237}Np Mössbauer spectra collected for the known NpTX compounds at T = 30 K – paramagnetic state and T = 4.2 K – antiferromagnetic state (Kergadallan 1993). Isomer shift δ, quadrupole splitting e^2qQ, magnetic hyperfine splitting B_{hf} and the related magnetic moment of Np – μ_{Np}.

Compound	$\delta_{30\,K}$ (mm/s)	$\lvert e^2qQ\rvert$ (mm/s)	$\delta_{4.2\,K}$ (mm/s)	$\lvert e^2qQ\rvert$ (mm/s)	B_{hf} (T)	μ_{Np} (μ_B)
NpCoAl	−14.03	49.0				
NpIrAl	−12.78	34	−13.4	36	259	1.20
			−13.4	36	176	0.82
NpRhAl	−10.26	39.2	−11.4	36	229	1.07
			−11.2	36	170	0.79
NpNiAl	−9.27	39.2	−9.6	42	223	1.04
			−9.8	40	156	0.73
NpNiGa	−7.39	38	−7.6	42	228	1.06
			−7.8	38	170	0.79
NpPtAl	−5.37	39.2	−5.7	35	284	1.32
			−5.7	35	178	0.83

structure calculations were performed systematically (Gasche et al. 1992, 1995a, 1995b). Results of these calculations provided a good understanding of the evolution of the U magnetic moments, depending on the changes of electronic structure parameters including the aspect of orbital and spin components. In addition to this extended list of UTX compounds with the ZrNiAl-type structure, a number of ThTX, NpTX and PuTX compounds, which are listed in table 5.3, have been synthesized. Little information, however, is available at present. Using ^{237}Np Mössbauer spectroscopy measurements, hyperfine interactions were studied on several NpTX compounds (Kergadallan 1993) which are reviewed in table 5.3. Two inequivalent magnetic Np sites have been detected with a population 2:1. Considering the Kagome-like network of actinide atoms in the basal plane of the ZrNiAl-type structure (fig. 5.1), one can easily conclude that antiferromagnetic coupling within this plane necessarily yields one frustrated Np moment which should have zero moment or rather a reduced magnetic moment. This conclusion is indeed compatible with the observation of a considerably reduced hyperfine magnetic field on one of the three sites in the basal plane.

One of the big surprises in magnetism research was the observation of ferromagnetism in the solid solutions $UCo_{1-x}Ru_xAl$ (Andreev et al. 1997f), which seemingly is in conflict with the previous understanding of the evolution of magnetism in the UTX compounds of ZrNiAl-type structure family (see fig. 5.29). Figure 5.22 shows the x–T magnetic phase diagram which we have constructed after analysis of the above discussed results. The bell-shaped $T_C(x)$ dependence is rather similar to the concentration dependence of the magnetic moment. In a broad maximum around x = 0.3–0.4, T_C reaches 60 K. In the same figure we can see another puzzle, namely the appearance of ferromagnetism within $UNi_{1-x}Ru_xAl$, whereas the terminal compounds are antiferromagnetic (UNiAl) and paramagnetic (URuAl) (Andreev et al. 1997e). An analogous situation was reported for the $URu_{1-x}Pd_xGa$ (Tran et al. 1998a).

Both parent compounds of this system, UCoAl and URuAl, have a paramagnetic ground state. Therefore, it is surprising that their solid solutions become ferromagnetic for a wide concentration range. An analogy can be found on the Ru rich side in the $URh_{1-x}Ru_xAl$ compounds (Sechovsky et al. 1992b), where substitutions of Rh for Ru lead to the ferromagnetic state for comparable x values. It is interesting to considering that Rh and Co have approximately the same population of 4d and 3d band states, respectively. Nevertheless, the onset of ferromagnetism in the $URh_{1-x}Ru_xAl$ system is natural because URhAl itself is a ferromagnet. But also here we observe a maximum in the concentration dependence of T_C, which indicates a somewhat closer relationship between the $URh_{1-x}Ru_xAl$ and $UCo_{1-x}Ru_xAl$ systems. In the $UNi_{1-x}Ru_xAl$ system ferromagnetism appears for even lower (Ni) doping level in URuAl than in the case of the Co (or Ru) doping. Naturally, T_C vs. x exhibits also a maximum for intermediate concentration and ferromagnetism disappears for high Ni concentrations (in $UNi_{0.85}Ru_{0.15}Al$). UNiAl itself and compounds with $x < 0.15$ are antiferromagnetic (Andreev et al. 1997e).

At this moment we may consider a simple model able to account for all these "striking" results, which seem to be in conflict with the standard picture of the development of magnetism in UTX ternaries of the ZrNiAl-structure, mentioned in section 1. As the prominent mechanisms affecting the size of U magnetic moments and their ordering, one should consider the overlap of neighboring U atom 5f wave functions and the hybridization of the U 5f states with the s, p, d valence states of ligands (T and X atoms). Both mechanisms induce two important effects in the actinide compounds:

- delocalization of the U 5f states leading ultimately to the washout of magnetic moments
- exchange interactions correlating the U 5f magnetic moments via direct 5f–5f and indirect exchange involving non-f states.

It is evident from the structure consideration already, that these effects are strongly anisotropic in the ZrNiAl-structure family. The close packing of U and T atoms in the basal plane probably results both in a non-negligible 5f–5f overlap and a strong 5f–d hybridization involving the transition metal d states, which compresses the 5f charge density towards the basal plane. Since the 5f states with strong spin–orbit interaction promote orbital magnetic moments, which are indeed observed experimentally (Wulff et al. 1990), a strong uniaxial anisotropy with magnetic moments locked along the c-axis is an inevitable element of magnetism leading to Ising like systems. Another consequence of the 5f–5f overlap and the 5f–d hybridization within the basal plane is a strong ferromagnetic coupling of the involved U magnetic moments. This situation leads to magnetic structures build up of ferromagnetic basal-plane layers.

Inspecting the crystal structure, we may deduce that along the c-axis both, the 5f–d (U–T) and 5f–3p (U–Al) hybridization should be considered. The first type should dominate for earlier d-elements (Ru), but it ceases with additional filling of the d-shell leaving the 5f–3p hybridization channel gradually more important. We may speculate that the former type leads preferably to a ferromagnetic type of U–U coupling along c, whereas the latter tends to an antiferromagnetic type of coupling.

Starting from URuAl, the 5f–d hybridization becomes reduced when partly substituting Rh, Co, or Ni for Ru, which allows formation of the U 5f magnetic moments (coupled ferromagnetically within the basal plane) for certain concentration of the substituent,

but the moments are relatively small and the interaction along c is ferromagnetic. When proceeding further with the substitution, the U-moments increase in magnitude, but the coupling along c weakens. Finally, after the decay of the 5f–d exchange polarization the 5f–3p channel overtakes the dominance leading to the relatively weak antiferromagnetic coupling along c. Thus the reduction of the exchange coupling along c leads to the final decay of the ordering temperature, despite of the fact that a strong coupling along the other two dimensions persists.

Not only the strength of the hybridization, but also the U–U exchange interaction as the second order effect, can influence the magnitude of U-moments. This can be deduced from the non-magnetic ground state of UCoAl. In the framework of our simple model this compound represents a delicate balance of ferromagnetic and antiferromagnetic components of the exchange interaction along c. It would be interesting to see if existence of the two non-contiguous regions, one ferro- and the other antiferromagnetic, occur more generally in pseudoternary UTX compounds, at least in those with the ZrNiAl structure type. Generally, the frustration in itinerant system can suppress local moments, as, e.g., in $REMn_2$ compounds (Ballou et al. 1991). Also intersite exchange interactions have been shown to be important for the moment stability in f-systems (Krishnamurthy et al. 1995). It is interesting to compare the case of UCoAl with a less delocalized counterpart, in which weak competing interactions along c lead to a complex stacking of U moments (Prokes et al. 1996a). A possible preferential occupation of T_1 or T_2 sites may substantially influence this picture. Therefore, relevant X-ray and neutron-diffraction studies are desirable to further explore this issue.

A proper theoretical background for the hybridization induced two-ion exchange interaction is being constantly developed (Hu and Cooper 1993). *Ab initio* calculations using this approach are strongly desirable to explain the intriguing magnetic properties of UTX compounds.

5.1.2. Compounds with the TiNiSi ($CeCu_2$) type structure

The first paper devoted to UTSi and UTGe compounds (Troc and Tran 1988) reported 14 materials (with T = Co, Ni, Ru, Rh, Pd, Ir, Pt) all forming in the orthorhombic $CeCu_2$-type crystal structure (space group Imma) in which the uranium atoms occupy the 4e Ce positions and the transition metal and Si or Ge atoms are randomly distributed over the 8h Cu sites (see fig. 5.30). This conclusion was partly supported also by Buschow et al. (1990), Brück (1991), de Boer et al. (1991) and Murasik et al. (1991). Careful analysis of neutron and X-ray diffraction data (Canepa et al. 1996; Prokes et al. 1997b) revealed that, except for UPtSi and the low-temperature phase of URhSi (Lloret 1988) and possibly URuSi, all the UTSi systems crystallize in the orthorhombic TiNiSi type of structure (space group Pnma) which is also shown in fig. 5.30. It is an ordered variant of the $CeCu_2$ type of structure where the transition metal atoms and Si atoms occupy 4c positions with specific x, y and z parameters. The random occupation of the 8h positions by transition metal and Si atoms in the $CeCu_2$ type of structure introduces a new symmetry element and the lattice is body centred, in contrast to the primitive lattice of the TiNiSi type of structure. Consequently, new extinction rules apply, namely reflections h, k, l with $h + k + l =$ odd number are extinct for diffraction on the $CeCu_2$-type lattice. Observation of this type of reflections, although very weak, can then be taken as clear evidence for the ordered ternary

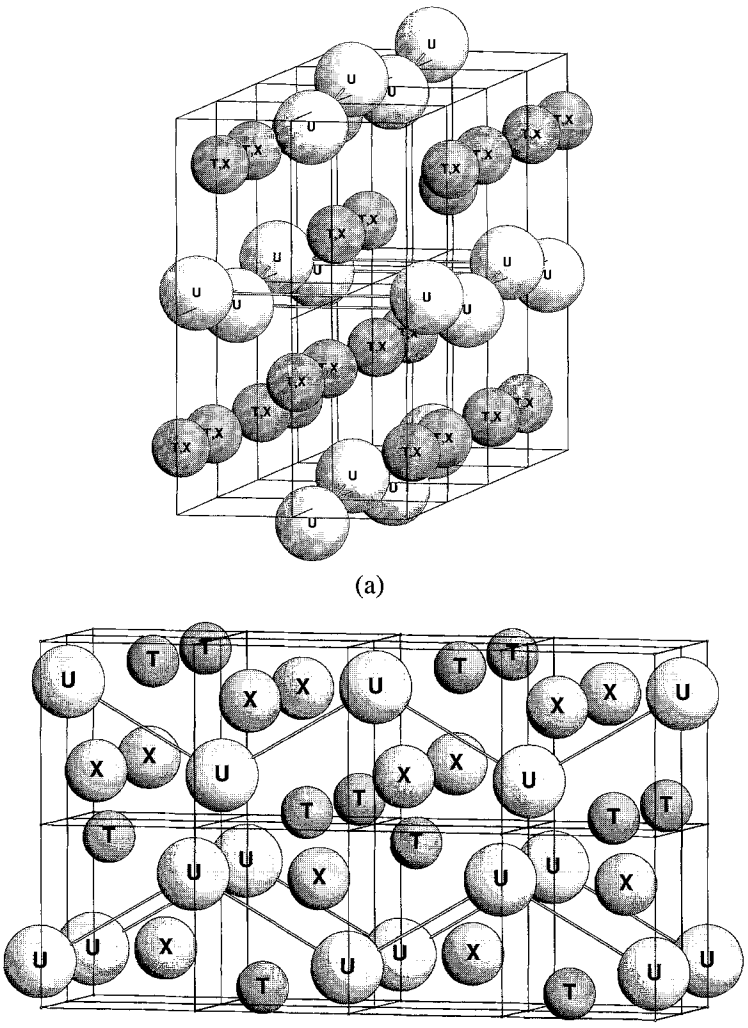

Fig. 5.30. Schematic picture of the (a) orthorhombic $CeCu_2$-type structure and (b) TiNiSi-type structure in which crystallize UTX silicides, germanides and some other AnTX compounds.

TiNiSi-type (Prokes et al. 1997b). To enable a straightforward comparison of lattice constants measured by different authors the TiNiSi-type structure notation will always be used, i.e., a and b are interchanged with respect to the notation for the $CeCu_2$-type structure. The TiNiSi-type structure has been finally confirmed also in a majority of germanides (Chevalier et al. 1988; Lloret 1988; Kawamata et al. 1992a; Canepa et al. 1996). In addition, Canepa et al. (1996) succeeded in synthesizing the Fe containing UFeSi and UFeGe, both crystallizing in the ordered ternary structure as well. The majority of silicides and germanides were prepared only in polycrystalline form. The available single crystals of the three germanides UPdGe, UPtGe and especially of UNiGe have naturally attracted much

interest. The important activity of theorists who performed *ab initio* electronic-structure calculations focused on magnetism (Prokes et al. 1997a; Havela et al. 1998a) has been particularly welcome and has helped to explain the exotic properties of this family of materials. (See figs 2.1 and 2.2.) Relevant basic structural and magnetic characteristics and electronic specific heat coefficient γ of the orthorhombic UTX compounds can be found in tables 5.4 (silicides) and 5.5 (germanides).

In order to keep the advantage of comparing properties of isostructural compounds we include in this chapter also some aluminides and gallides adopting the orthorhombic $CeCu_2$- or TiNiSi-type structure.

UFeSi has been prepared only in polycrystalline form (Canepa et al. 1996). The resistivity reported in this work has anomalous large values (11.6 mΩ cm at room temperature) but the temperature dependence of ρ is rather of the metallic type, decreasing with decreasing temperature and saturating at 2 mΩ cm at the low temperature limit. These extraordinary large values are most probably not intrinsic but caused by the bad quality (internal cracks) of the measured sample. From arguments that follows from the electron structure calculations performed for UFeGe (Havela et al. 1998a), no magnetic ordering can be expected in this material.

UCoSi is also paramagnetic, at least down to $T = 1.4$ K, as evidenced by the anomaly in the temperature dependencies of the susceptibility (Troc and Tran 1988) and specific heat (Brück 1991; de Boer et al. 1991). The high-field magnetization at $T = 4.2$ K (fig. 5.31) is practically linear up to 35 T yielding only $0.12\,\mu_B$/f.u. at this field with no anisotropy between the fixed-powder and free-powder data (de Boer et al. 1990), which indicates lack of magnetism connected with the uranium 5f-electrons. The electrical resistivity shows no anomaly between $T = 4.2$ K and 300 K (Canepa et al. 1996) and the ρ vs. T curve, which is qualitatively resembling that of materials like YCo_2, strongly saturates with increasing temperature, reflecting a broad 5f band intersected by E_F. The moderate value of $\gamma = 18$ mJ/(mol K^2) corroborates this picture.

Several contradictory structure reports appeared on *UNiSi*. Troc and Tran (1988) claim the occurrence of the $CeCu_2$ type. The hexagonal structure of the AlB_2 type, which has the same co-ordination as the $CeCu_2$ type, was suggested by Brück (1991) and de Boer et al. (1991). Finally, the TiNiSi-type has been unambiguously determined by X-ray and neutron diffraction experiments made by several groups (Lloret 1988; Canepa et al. 1996; Prokes 1997; Prokes et al. 1997b). Material properties could be so far measured only on polycrystalline samples. The first information on the magnetism in UNiSi was provided by Troc and Tran (1988) who suggested two magnetic phase transitions at $T = 80$ K and 7.5 K, respectively, as inferred from two anomalies at these temperatures in the χ vs. T curve. Specific-heat and magnetization measurements made by Brück (1991) and de Boer et al. (1991) pointed out another magnetic phase transition around $T = 18$ K. Below this transition a spontaneous magnetization is observed, which means a ferromagnetic phase or a phase with some ferromagnetic component. The other two magnetic phase transitions appear clearly as specific-heat anomalies at 87 K and 10 K in C vs. T measurements made over an extended temperature range (Prokes 1997). The temperature evolution of magnetization curves shown in fig. 5.32 (Prokes 1997) allows certain conclusions to be drawn as to the magnetic phases in this material. The lack of spontaneous magnetization and the occurrence of S-shaped M vs. T curves measured above 18 K point to antiferromagnetic

TABLE 5.4

Some basic characteristics of UTSi and other AnTSi compounds:

γ – coefficient of the electronic specific heat, type of ground state (F – ferromagnetic, AF – antiferromagnetic, UAF – uncompensated antiferromagnetic, PP – Pauli paramagnetic), μ_U - the uranium ordered magnetic moment (determined by neutron diffraction at 4.2 K), $T_{C,N}$ – magnetic ordering temperature, T_{tr} – temperatures of other magnetic phase transitions (in the ordered state), Anis. – easy magnetization direction (determined by neutron diffraction and/or magnetization measurements of single crystals), *a*, *b*, *c* – lattice parameters at room temperature (for the orthorhombic structures TiNiSi-type structure notation used, i.e., *a* and *b* are interchanged with respect to the notation in the $CeCu_2$-type structure).

Compound	γ mJ/(mol K^2)	Ground state	μ_U (μ_B)	$T_{C,N}$ (K)	T_{tr} (K)	Anis.	Ref.	*a* (pm)	*b* (pm)	*c* (pm)	Str. type	Ref.
UFeSi		P[v]					[1]	699.7	406.3	686.7	TiNiSi	[1]
UCoSi		P					[2]	685.2	410.4	714.3	$CeCu_2$	[2]
		P					[3]	683.9	411.9	705.8	TiNiSi	[3]
	18–20	P	(0.12)[l]				[4,5,6]	684.8	411.0	705.7	$CeCu_2$	[5]
								684.2	411.6	705.6	TiNiSi	[1]
								684.59	410.16	704.88	TiNiSi	[7]
UNiSi		AF[B]		80	7.5		[2]	696.5	410.7	739.7	$CeCu_2$	[2]
	134		≈0.2[d]				[6,5]	404.6		373.0	AlB_2[a]	[4,5]
	133.4	F[c]	≈0.14[e]	87	10;18		[8]	695.9	414.2	705.3	TiNiSi	[1]
								683.9[m]	408.5[m]	750.85[m]	TiNiSi	[7,8]
URuSi		P(SF)					[2]	705.5	416.5	709.1	$CeCu_2$	[2]
	58	P	(0.15)[l]				[5,6,9]	708.43	417.35	710.88	$CeCu_2$	[10]
URhSi		F		9.5			[2]	700.2	412.1	745.1	$CeCu_2$	[2]
		F					[3]	700.3	411.6	745.1	TiNiSi[f]	[3]
		P					[3]	693.1	419.3	741.4	$CeCu_2$[g]	[3]
	133	F	0.31[k]	9.5			[6,5]	698.61	411.25	742.71	$CeCu_2$	[10]
	147[j]	F	0.11	9.5		$\|c$	[8,11,12]	702.42[n]	412.10[n]	745.84[n]	TiNiSi[h]	[7]

TABLE 5.4 (Continued)

Compound	γ mJ/(mol K^2)	Ground state	μ_U (μ_B)	$T_{C,N}$ (K)	T_{tr} (K)	Anis.	Ref.	a (pm)	b (pm)	c (pm)	Str. type	Ref.
UPdSi		AF		29	10		[2]	700.9	420.9	766.5	$CeCu_2$	[2]
	27	AF		26			[6,5]	700.76	419.80	765.42	$CeCu_2$	[10]
	27	AF	1.4[r]	33	27[p]		[8,13]	702.61°	420.46°	767.01°	TiNiSi	[7]
UIrSi		P					[2]	690.9	421.6	743.5	$CeCu_2$	[2]
		P(SF)					[14]	689.5	422.1	742.0	TiNiSi	[14]
	17	P	(0.22)[l]				[5,6]	688.4	421.85	742.48	$CeCu_2$	[15]
								696.04	424.80	748.24	TiNiSi	[7]
UPtSi		AF		50	24		[2]	697.9	422.4	734.4	$CeCu_2$	[2]
	92	AF	0.94	45			[4,5]	724.99	423.84	734.80	$CeCu_2$	[10]
		AF[t]	0.96[t]	50		$\perp a$[t]	[16]	722.5	435.8	734.2	$CeCu_2$	[16]
	44	AF[u]	1.3[u]	51		$\perp a$[u]	[7,8,17]	723.33	424.80	734.72	$CeCu_2$	[7]
ThIrSi		S		6.5			[18,19]				AlB_2	[18,19]
NpRhSi								702.6	414.4	731.6		[20]
NpPtSi								720.4	424.8	730.9		[20]
AmRuSi								623	384	723		[20]

[a] Hexagonal structure.

[b] Another antiferromagnetic structure reported between 7.5 and 80 K.

[c] Above 18 K, a magnetic phase without spontaneous magnetization (probably antiferromagnetic) seems to exist.

[d] Estimated spontaneous moment μ_s/f.u. extrapolated from high-field magnetization data obtained on free powder ($M_{35\,T}^{free} = 0.25\ \mu_B$); roughly half of that value has been obtained on a "fixed-powder" sample (de Boer et al. 1990).

[e] Estimated from low-field magnetization measurements (Prokes 1997) taking anisotropy into account.

[f] High-temperature phase (as cast).

[g] Low-temperature phase (annealed).

[h] Neutron-diffraction data at $T = 80$ K (Prokes et al. 1997b).

TABLE 5.4 (Continued)

[j] Linear extrapolation of C_p/T vs. T^2 curve to $T = 0$ K provides $\gamma = 185.6$ mJ/(mol K^2). This value is reduced to 142.7 mJ/(mol K^2) in 5 T (Prokes 1997; Prokes et al. 1997a).

[k] Derived from the zero-field extrapolation of magnetization data on a free powder sample at $T = 4.2$ K consistently with the low-field magnetization measured on a fixed powder (Prokes 1997; Prokes et al. 1997a) and corrected for anisotropy.

[l] Magnetization/f.u. measured in 35 T on a free-powder sample (de Boer et al. 1990).

[m] Derived from neutron data at 100 K (Prokes et al. 1997b).

[n] Derived from neutron data at 80 K (Prokes et al. 1997b).

[o] Derived from neutron data at 62 K (Prokes et al. 1997b).

[p] Between 27 K and 33 K an antiferromagnetic incommensurate phase with $\boldsymbol{q} = (0.217, 0, 0.217)$ is formed.

[r] Measured at $T = 3.5$ K (Prokes et al. 1997c).

[s] Magnetic moment per f.u. measured on a free powder in 50 T where the magnetization seems to be near to saturation.

[t] Sinusoidal modulation of U magnetic moment, $\boldsymbol{q} = (0, 0.535, 0)$, U magnetic moments collinear with components $\mu_y = 0.87\ \mu_B$, $\mu_z = 0.40\ \mu_B$.

[u] Sinusoidal modulation of U magnetic moment with an amplitude of $1.3\ \mu_B$ at 1.3 K; $\boldsymbol{q} = (0, 0.533, 0)$, U magnetic moments collinear in the a–c plane making an angle of 40° with the a-axis.

[v] No sign of any magnetic transition observed in the temperature dependence of resistivity, χ weakly temperature dependent (Havela et al. 1998a).

References:

[1] Canepa et al. (1996)
[2] Troc and Tran (1988)
[3] Lloret (1988)
[4] de Boer et al. (1991)
[5] Brück (1991)
[6] de Boer et al. (1990)
[7] Prokes et al. (1997b)
[8] Prokes (1997)
[9] Sechovsky et al. (1990)
[10] Buschow (1987)
[11] Prokes et al. (1997a)
[12] Prokes et al. (1996c)
[13] Prokes et al. (1997d)
[14] Chevalier et al. (1988)
[15] Ramirez et al. (1987)
[16] Tran et al. (1995a)
[17] Prokes et al. (1996d)
[18] Chevalier et al. (1986)
[19] Solanki-Moser et al. (1987)
[20] Kergadallan (1993)

TABLE 5.5

Some basic characteristics of UTGe, other AnTGe compounds and structure-related UTAl and UTGa materials:
γ – coefficient of the electronic specific heat, type of ground state (F – ferromagnetic, AF – antiferromagnetic, P – paramagnetic, PP – Pauli paramagnetic, SG – spin-glass or cluster-glass state), μ_U – the uranium ordered magnetic moment (determined by neutron diffraction at 4.2 K), $T_{C,N}$ - magnetic ordering temperature, T_{tr} – temperatures of other magnetic phase transitions (in the ordered state), Anis. – easy magnetization direction (determined by neutron diffraction and/or magnetization measurements of single crystals), a, b, c – lattice parameters at room temperature (TiNiSi-type structure notation used, i.e., a and b are interchanged with respect to the notation in the $CeCu_2$-type structure).

Compound	γ mJ/(mol K^2)	Ground state	μ_U (μ_B)	$T_{C,N}$ (K)	T_{tr} (K)	Anis.	Ref.	a (pm)	b (pm)	c (pm)	Str. type	Ref.
$UFeGe^{LT}$		P					[1]	698.6	430.8	699.2	UFeGe[a]	[2]
$UFeGe^{HT}$								682.8	425.9	728.6	TiNiSi	[2]
UCoGe		P					[3]	684.3	420.5	722.7	$CeCu_2$	[3]
		P					[4]	687.6	420.6	722.8	TiNiSi	[4]
	65	P	(0.58)[b]				[5,6,7]	684.66	420.65	722.74	$CeCu_2$	[8]
								685.2	420.8	722.6	TiNiSi	[2]
UNiGe		AF		44			[3]	700.2	423.8	720.6	$CeCu_2$	[3]
	27	AF					[5,9]	700.7	423.7	720.7	TiNiSi	[15]
	23–24	AF	0.8[c]	42			[10,11]	699.9	423.6	720.0	TiNiSi	[2]
	27.3	AF	1.4	51	41.5		[12,13,14]	696.5[d]	424.5[d]	719.2[d]	TiNiSi	[14]
URuGe	35	P	(0.17)[b]				[5,6,7]	667.8	435.9	753.9	$CeCu_2$	[3]
								668.71	434.27	755.88	$CeCu_2$	[8]
URhGe		F					[3]	689.7	434.8	752.9	$CeCu_2$	[3]
	100	F	0.33[e]	9			[16,5]	689.79	434.03	753.58	$CeCu_2$	[8]
								687.6	433.3	751.3	TiNiSi	[4]
UPdGe		F		50	30		[3]	705.4	435.7	761.7	$CeCu_2$	[3]
	17	F[f]	1.4[c]	50	28–33	gen.[f]	[10,17,11]	705.62	435.96	761.28	$CeCu_2$	[8]

TABLE 5.5 (Continued)

Compound	γ mJ/(mol K^2)	Ground state	μ_U (μ_B)	$T_{C,N}$ (K)	T_{tr} (K)	Anis.	Ref.	a (pm)	b (pm)	c (pm)	Str. type	Ref.
	22	F		50	32		[5]	705.0	435.8	759.6	TiNiSi	[18,11]
						gen.[f]	[18]					
		F[g]	1.70									
UIrGe	18[h]	AF		16			[19]	687.5	431.8	757.62	$CeCu_2$	[3]
		AF		17			[3]	686.40	430.50	757.9	$CeCu_2$	[8]
	14	AF		16			[5]	683.7	429.2	756.4	TiNiSi	[20]
								683.6[i]	429.1[i]	756.2[i]	TiNiSi	[18]
UPtGe		AF		52			[3]	720.11	433.6	751.8	$CeCu_2$	[3]
	26	AF		52			[16,5]	720.88	435.27	762.68	$CeCu_2$	[8]
	25	AF	1.0	50		b–c	[10,11,17]	714.5[j]	430.5[j]	747.2[j]	TiNiSi	[21]
								714.7[k]	440.6[k]	745.9[k]	TiNiSi	[21]
								717.12[l]	431.98[l]	749.93[l]	TiNiSi	[22]
UPdAl		P[m]					[23]	682.5	418.3	749.7	TiNiSi	[23]
UPdGa		AF		48			[24]	681.2	464.4	773.4	TiNiSi	[24]
UAuAl		SG or P		12[n]			[25]	767.1	391.3	805.5	$CeCu_2$	[25]
UAuGa		AF	0.68	60	18	$\|c$	[18,26]	799.6	388.1	764.1	$CeCu_2$	[25]
		AF[o]	1.35	60		$\|c$	[20]	703.3	449.7	778.2	TiNiSi	[18]
UAuSi		SG		12[n]			[25]	798.2	418.1	724.1	$CeCu_2$	[25]
								419.5[p]	436.7	397.2[p]	$LiBaSi$[p]	[27]
UAuGe		SG		40[n]			[25]	763.8	436.7	752.3	$CeCu_2$	[25]

TABLE 5.5 (Continued)

Compound	γ mJ/(mol K^2)	Ground state	μ_U (μ_B)	$T_{C,N}$ (K)	T_{tr} (K)	Anis.	Ref.	a (pm)	b (pm)	c (pm)	Str. type	Ref.
UCuSi		SG		48			[28]	403.0	–	395.0	$CeCd_2$	[28]
								402.0	–	393.8	$CeCd_2$	[29]
UCuGe		AF		58			[30]	419.4	–	377.6	$CeCd_2$	[28]
		AF		51			[29,31]	419.9	–	375.0	$CeCd_2$	[29]
ThNiGe	5						[10]					
ThPdGe	3						[10]					
ThPtGe	3						[10]					
NpNiGe								697.0	423.3	717.9	TiNiSi	[24]
PuPtGe								711.5	439.21	758.30	TiNiSi	[24]
PuPtAl								695.4	434.71	771.6	TiNiSi	[24]
PuRhAl								697.1	414.5	1575.6	PuRhAl	[24]
PuIrAl								629.3	414.17	1572.45	PuRhAl	[24]

[a] Low temperature phase below 500 K is a monoclinically distorted TiNiSi-type structure with $\beta = 93.71°$.

[b] Magnetization/f.u. measured in 35 T on a free-powder sample (de Boer et al. 1990).

[c] Determined at $T = 10$ K (Kawamata et al. 1992a).

[d] Derived from neutron data at $T = 60$ K (Prokes 1997).

[e] Determined by extrapolation of the free-powder magnetization to zero magnetic field (de Boer et al. 1990).

[f] Collinear ferromagnetic structure with U magnetic moment in a general orientation making non-zero angles with all the three main crystallographic axes (Kawamata et al. 1992a).

[g] Conical ferromagnetic structure with the total moment along the c-axis, $\boldsymbol{q}_c = (0, 0, 0)$, $\boldsymbol{q}_{ab} = (0.537, 0, 0)$, $\mu_{ab} = 0.28\,\mu_B$ (Tran et al. 1995a).

[h] A very high $\gamma = 145$ mJ/(mol K^2) can be deduced from specific-hat data above the temperature of the phase transition proposed as T_N (Ramirez et al. 1987).

TABLE 5.5 (Continued)

[i] At $T = 1.5$ K.
[j] At $T = 60$ K.
[k] At $T = 2$ K.
[l] At $T = 75$ K.
[m] $\chi_{300\,K} \approx 1.3 \times 10^{-8}$ m^3/mol constant down to 200 K, then roughly linearly increasing with decreasing temperature up to $\chi_{4.2\,K} = 1.9 \times 10^{-8}$ m^3/mol.
[n] Spin freezing temperature T_{sf}.
[o] Collinear, $\boldsymbol{q} = (0, 0, 0)$, $\mu_{ord} \| c$ (Tran et al. 1995a).
[p] Hexagonal, derived from the AlB_2-type when the boron sites are occupied by Au and Si atoms in a way to get the ordered ternary structure (Pöttgen et al. 1996).

References:

[1] Havela et al. (1998a)
[2] Canepa et al. (1996)
[3] Troc and Tran (1988)
[4] Lloret (1988)
[5] Buschow et al. (1990)
[6] Brück (1991)
[7] de Boer et al. (1990)
[8] Buschow (1987)
[9] Dmitriev et al. (1991)
[10] Kawamata et al. (1992b)
[11] Kawamata et al. (1992a)
[12] Nakotte et al. (1996a)
[13] Sechovsky et al. (1994b)
[14] Prokes (1997)
[15] Prokes et al. (1994)
[16] Sechovsky et al. (1990)
[17] Kawamata et al. (1990)
[18] Tran et al. (1995a)
[19] Ramirez et al. (1987)
[20] Tran et al. (1996b)
[21] Szytula et al. (1992)
[22] Robinson et al. (1993a)
[23] Tran and Troc (1993a)
[24] Kergadallan (1993)
[25] Tran and Troc (1993b)
[26] Tran et al. (1993)
[27] Pöttgen et al. (1996)
[28] Tran and Troc (1990b)
[29] Leciejewicz et al. (1991)
[30] Murasik et al. (1976)
[31] Zeleny et al. (1988)

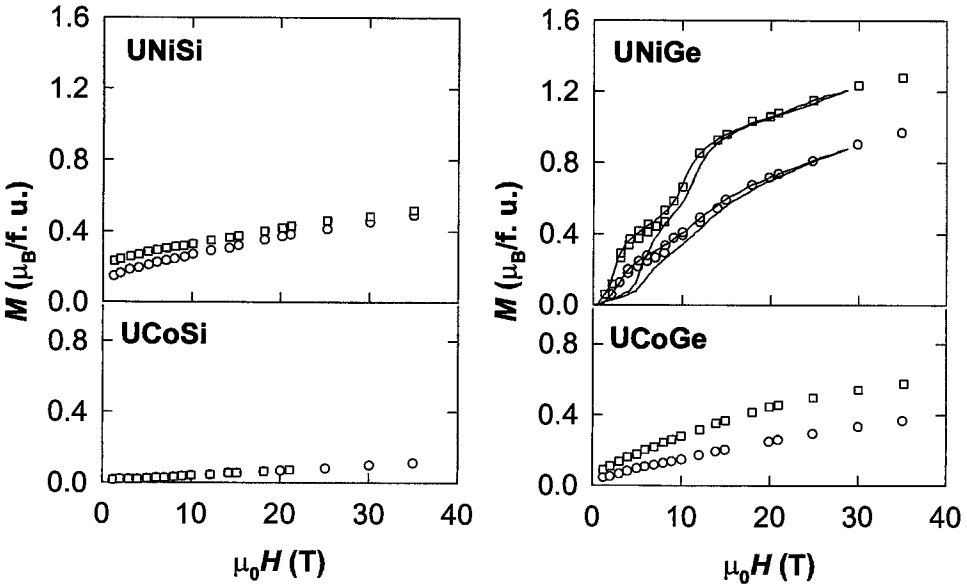
UNiSi
UCoSi
UNiGe
UCoGe
M (μB/f. u.)
μ0H (T)

(a)

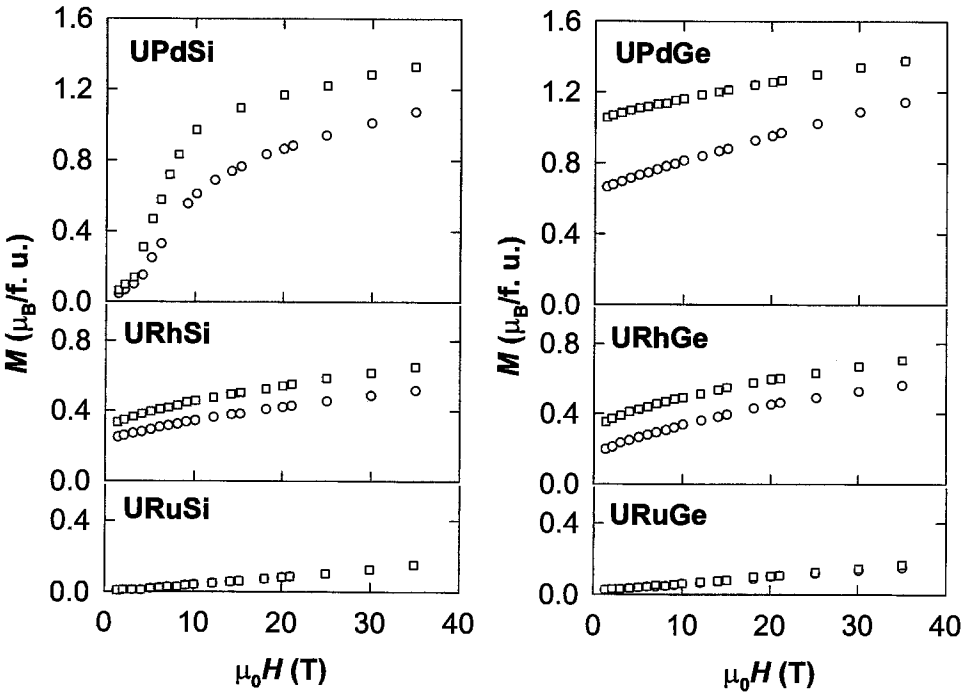
UPdSi
URhSi
URuSi
UPdGe
URhGe
URuGe
M (μB/f. u.)
μ0H (T)

(b)

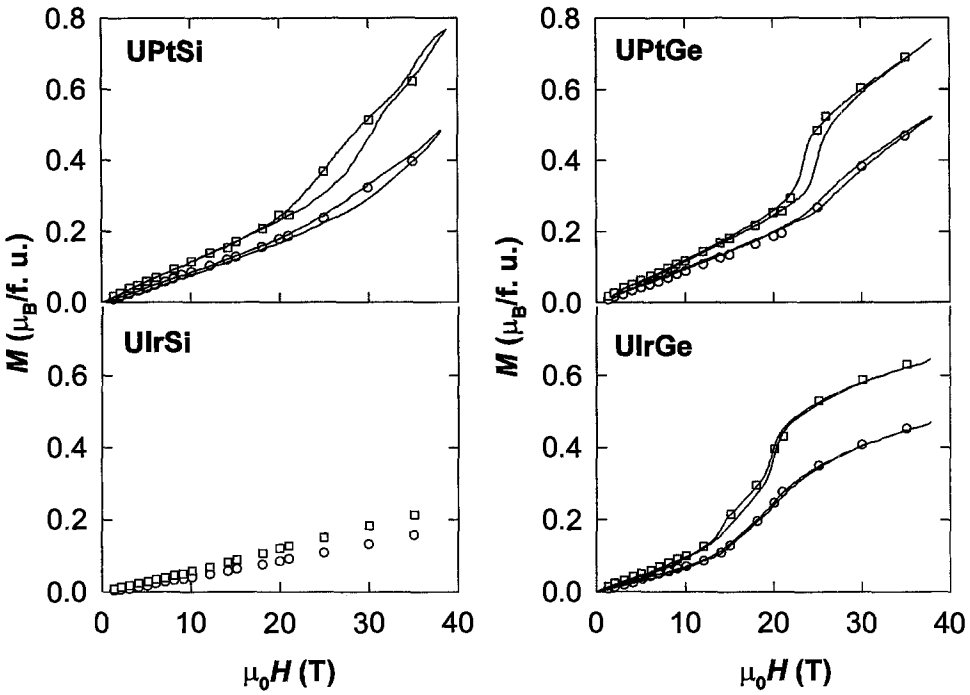

(c)

Fig. 5.31. Magnetization curves of UTSi and UTGe compounds at $T = 4.2$ K measured on free (□) and fixed (○) powder (de Boer et al. 1990; Brück 1991). The solid lines correspond to data taken with pulses in which the magnetic field increases (lower curves) and subsequently decreases (upper curves), both linearly with time at rate of 40 T/s. On the solid curves with maximum field of 38 T, the data with decreasing field have been collected with magnetic field decreasing at a rate of 55 T/s. The data with increasing field were measured during much faster uncontrolled field sweep. Note that magnetization of UPtSi and UPtGe should be considerably higher than observed in 38 T because the cascades of metamagnetic transitions are not yet completed. This supposition has been proven as right by measurements in pulsed fields up to 60 T performed at the High Magnetic Field Facility at Osaka University. Magnetic moment over $1.2\,\mu_B$/f.u. has been observed on a free powder sample at 60 T in UPtSi and the magnetization was already almost saturated (de Boer et al. 1991). In UPtGe, however, the lack of saturation even at 60 T, where about $1\,\mu_B$/f.u. was recorded on a free powder sample (Buschow et al. 1990), points to necessity to use still higher fields to discover the intrinsic saturated magnetic moment in this material.

ordering at temperatures between 18 K and 87 K. In the temperature interval from 10 to 18 K a narrow ferromagnetic-like hysteresis loop can be observed. In the lowest temperature range (below 10 K) wide hysteresis loops of a complex S-shape were observed. This indicates that the ground state phase should be a sort of uncompensated antiferromagnetic structure or a canted ferromagnetic structure which yields approximately half of spontaneous magnetization compared to the phase existing between 10 and 18 K. The difference between the "free-powder" and "fixed-powder" high-field magnetization curves measured at $T = 4.2$ K (see fig. 5.31) provide a clear evidence of strong magnetocrystalline anisotropy, although the anisotropy field of the order of 50 T, which can be estimated from these data, can be considered as exceptionally low within the family of 5f electron mag-

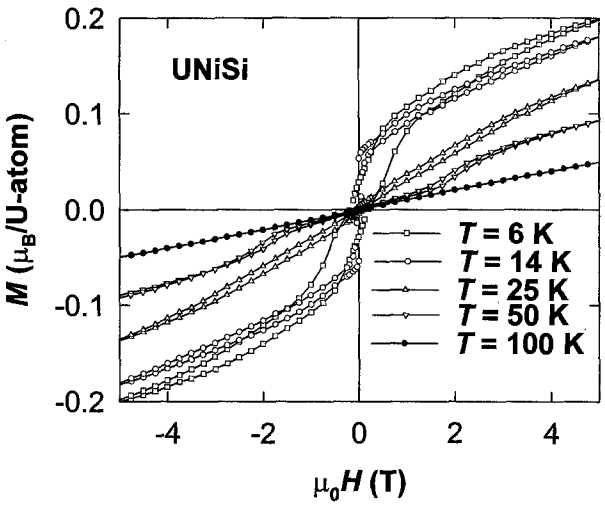

Fig. 5.32. Magnetization curves of UNiSi in magnetic fields sweeping between −5 and 5 T measured on fixed-powder samples at $T = 6$ K (□), 14 K (○), 25 K (△), 50 K (▽) and 100 K (•) (Prokes 1997).

nets. The ratio $M_s^{fix}/M_s^{free} \approx 0.5$ points to uniaxial magnetocrystalline anisotropy in this compound. Single-crystal data, however, are desirable to be more conclusive regarding this point. In view of the results on other UNiX compounds, the estimated value of spontaneous moment (about $0.14\,\mu_B$/f.u.) can be attributed predominantly to the moment residing on uranium sites. This very low moment manifests strongly delocalized 5f-electron states. This judgement is corroborated also by the poor saturation of the "free-powder" magnetization curve even in 35 T, where $M = 0.52\,\mu_B$/f.u. is recorded. It is also corroborated by undetectable magnetic scattering intensity within the sensitivity of the neutron powder diffraction experiment (Prokes 1997).

The electrical resistivity of polycrystalline UNiSi is nearly temperature independent at high temperatures. Below $T = 80$ K, the ρ vs. T curve is falling down with gradually increasing slope with decreasing temperature. Closer inspection reveals a sharp maximum of $\partial\rho/\partial T$ at 17 K, which is apparently connected with the 18 K magnetic phase transition, and a much less pronounced anomaly around 10 K (Prokes 1997).

URuSi is a weakly temperature dependent paramagnet with $\chi_{300\,K} \approx 1.9 \times 10^{-8}$ m^3/mol and $\chi_{4.2\,K} \approx 2.7 \times 10^{-8}$ m^3/mol. The very broad bump in the χ vs. T curve above 50 K (Troc and Tran 1988) may be an attribute of spin-fluctuations, which can be also associated with the quadratic behaviour of the low-temperature resistivity (Tran et al. 1990). High-field magnetization measurements did not reveal any anisotropy between "free-powder" and "fixed powder" data (de Boer et al. 1990). A moderately enhanced coefficient $\gamma = 58$ mJ/(mol K^2) has been derived from low-temperature specific-heat data (de Boer et al. 1991; Prokes 1997).

Ferromagnetism in *URhSi* below 9.5 K has been reported in several papers (Troc and Tran 1988; Brück 1991; de Boer et al. 1991; Prokes 1997; Prokes et al. 1997a). All results, unfortunately, were achieved only on polycrystals. The high-field magnetization

data (de Boer et al. 1990) provide an estimated ratio $M_s^{fix}/M_s^{free} \approx 0.76$ indicating an easy-plane magnetocrystalline anisotropy. The most profound study was focused on magnetization, specific-heat and resistivity measurements together with crystal and magnetic structure investigations made by X-ray and neutron powder diffraction (Prokes et al. 1996c; Prokes 1997). Also combination with *ab initio* electronic structure calculations is available (Prokes et al. 1997a). The magnetic ordering transition at $T = 9.5$ K is reflected in the diverging susceptibility and the appearance of a spontaneous magnetization at lower temperatures, a relatively broad but well pronounced peak in the temperature dependence of the specific heat and a maximum of $\partial\rho/\partial T$ at this temperature. The observation of magnetic contribution to the neutron diffraction on top of the nuclear reflections below 9.5 K confirms the conclusion about ferromagnetism in URhSi. A very reduced uranium ordered moment of only $0.11\,\mu_B$ has been derived from the magnetic structure refinement of the powder diffraction data. The electronic-structure calculations were performed using the optimized LCAO method. They offer an even lower uranium moment $\mu_U = 0.09\,\mu_B$ (Prokes et al. 1997a), which corroborates the conclusion that URhSi is an itinerant 5f-electron ferromagnet. Note, that URhSi serves as one of the few outstanding examples of itinerant 5f magnets with tiny magnetic moments exhibiting extremely strong magnetic anisotropy. High-field magnetization data up to 35 T (de Boer et al. 1990) indicate the anisotropy field which may exceed the maximum field of experiment by more than order of magnitude. Fully relativistic spin-polarized calculations including orbital polarization enhancement provide a magnetocrystalline anisotropy energy of 59 meV (Prokes et al. 1997a). These results manifest the existence of a considerable orbital 5f-moment which is compensated by the opposite oriented spin component leaving the resultant uranium moment as low as one tenth of μ_B. Indeed, a spin moment $\mu_s = 0.15\,\mu_B$ and an orbital moment of $0.24\,\mu_B$ oriented antiparallel has been obtained from calculations (Prokes et al. 1997a). Later neutron powder-diffraction study made by Tran et al. (1998a, 1998b) was concluded in terms of ferromagnetism below 9.5 K with collinear U magnetic moments ($\|c$) of $0.5\,\mu_B$ at $T = 1.4$ K. The latter value is considerably higher that that reported by Prokes et al. (1997a). Polarized neutron diffraction and/or X-ray magnetic scattering experiments on single crystals of this material are strongly desirable to confirm this prediction of the orbital magnetism, which came out as a result of electronic structure calculations (Prokes et al. 1997a). Another interesting aspect of URhSi is that it can appear also in a low-temperature phase, which is characterized by a disordered ternary crystal structure of the $CeCu_2$-type, smaller unit cell volume (see table 5.4) and paramagnetic ground-state (Lloret 1988), probably due to more delocalized 5f states of uranium assisted by the Rh–Si sublattice disorder.

Inspection of the specific heat data plotted for a URhSi polycrystals in fig. 5.33 shows that when a field of 5 T is applied, a substantial portion of magnetic entropy is shifted to far above T_C and the anomaly connected with the magnetic ordering is removed. In the same figure we can see that application of a magnetic field leads also to a dramatic reduction of the electrical resistivity far above T_C which yields a giant negative magnetoresistance around T_C in this material (Tran and Troc 1998). The negative magnetoresistance in the vicinity of T_C is usually explained by the variations of the spin-disorder scattering (Yamada and Takada 1973a, 1973b; Ueda 1976), but the magnetoresistance effect in URhSi is exceptionally large. Field-induced variations of short range ordering in a wide interval above T_C were discussed by Tran and Troc (1998) as a possible source. Single-crystals are

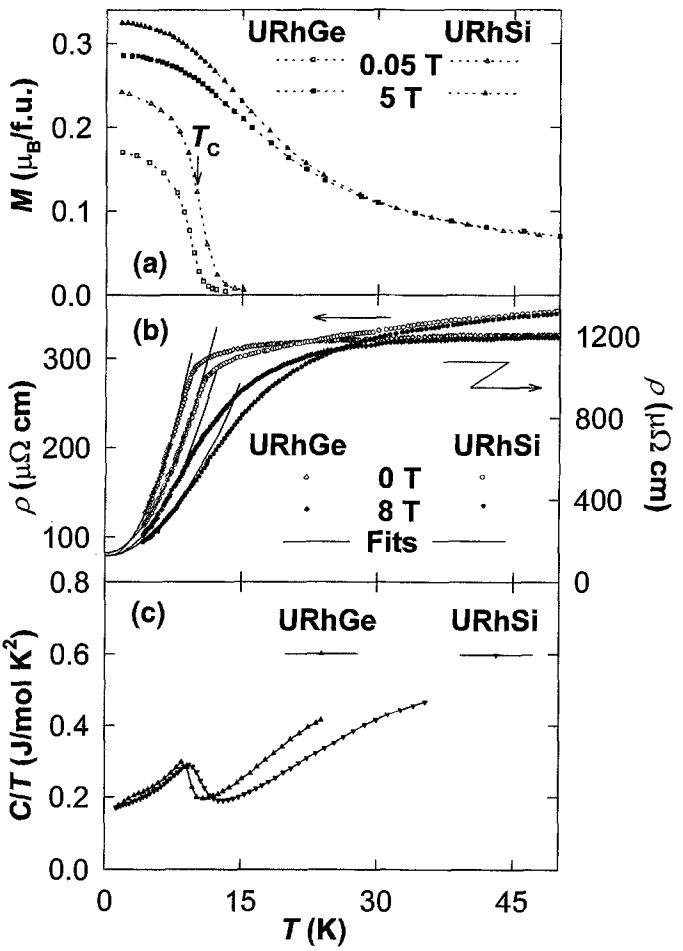

Fig. 5.33. Temperature dependence of: (a) Magnetization M in fields 0.05 T and 5 T (Tran and Troc 1998); (b) Electrical resistivity ρ in 0 T and 8 T (Tran and Troc 1998); (c) Specific heat (C_p/T vs. T plot) in zero magnetic field. External field leads to a smearing of the anomaly and shift of magnetic entropy to higher temperatures (Buschow et al. 1990; de Boer et al. 1991), as measured on polycrystalline samples of URhSi and URhGe.

highly desirable to study intrinsic effects with magnetic field and electrical current applied along various crystallographic directions.

In the original work of Troc and Tran (1988), *UPdSi* has been reported as an antiferromagnet below $T_N = 29$ K, undergoing an order-to-order magnetic phase transition at $T = 10$ K, as inferred from two anomalies observed in the temperature dependence of the susceptibility at these temperatures. Following magnetic and specific-heat studies by other authors failed to confirm the latter transition although a shoulder can be observed around this temperature on the ρ vs. T curve (Tran et al. 1990; Prokes 1997; Prokes et al. 1997d). A complete study of polycrystalline samples, involving magnetic, specific-heat,

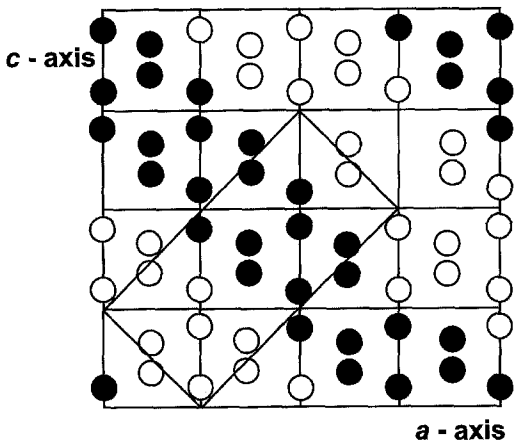

Fig. 5.34. Schematic picture of the ground-state antiferromagnetic structure of UPdSi. For clarity only uranium atoms are shown. U magnetic moments are parallel to the b-axis oriented up (o) and down (•).

electrical resistivity measurements and X-ray and neutron powder diffraction experiments was performed by Tran et al. (1990), Prokes (1997) and Prokes et al. (1997b, 1997c). Results of this complex of experiments allow the formulation of a quite realistic picture of magnetism in UPdSi. The intrinsic Néel temperature is 33 K, below which an incommensurate antiferromagnetic phase with the uranium magnetic moment propagating sinusoidally with $\boldsymbol{q} = (\delta, 0, \delta)$ is formed. At 31 K, the values $q = 0.217$ and $\mu_U = 0.65\,\mu_B$ have been determined. At 27 K, a first-order magnetic phase transition is observed where the high-temperature incommensurate phase locks-in into a commensurate sinusoidally modulated phase with $\boldsymbol{q} = (0.25, 0, 0.25)$. This structure becomes completely squared up at low temperatures as confirmed by detailed measurement at 3.5 K. The originally reported susceptibility and resistivity anomalies around 10 K may then be connected with the squaring up of the magnetic-moment wave. The magnetic structures in UPdSi are collinear with magnetic moments oriented along the b-axis. The ground-state structure (see fig. 5.34) consists of ferromagnetic (1 0 1) planes of uranium moments stacked in the sequence $(+++\,+---)$ along the [1 0 1] direction. The incommensurate phase propagates in the same direction. The uranium magnetic moment at 3.5 K amounts to $1.4\,\mu_B$. Evolution of magnetic ordering with temperature, including the temperature dependence of the incommensurate moment propagation in UPdSi can be understood from fig. 5.35. The magnetization curve measured on a free powder at $T = 4.2$ K (fig. 5.31) reveals two metamagnetic transitions (at 4 T and 7 T, respectively) in which the antiferromagnetic coupling in UPdSi is gradually destroyed, transforming towards the high-field ferromagnetic alignment of U moments. The magnetization of $1.31\,\mu_B$/f.u. observed at 35 T is close to the value of U moment determined at $T = 3.5$ K by neutron diffraction.

UIrSi has been classified as a weakly temperature dependent paramagnet (Troc and Tran 1988) with $\chi_{300\,K} \approx 2.2 \times 10^{-8}$ m^3/mol and $\chi_{4.2\,K} \approx 3.7 \times 10^{-8}$ m^3/mol. Nevertheless, the susceptibility above 100 K can be approximated by a Curie–Weiss law with $\Theta_p = -126$ K and $\mu_{eff} = 2.74\,\mu_B$ (Chevalier et al. 1988). This result, together with the

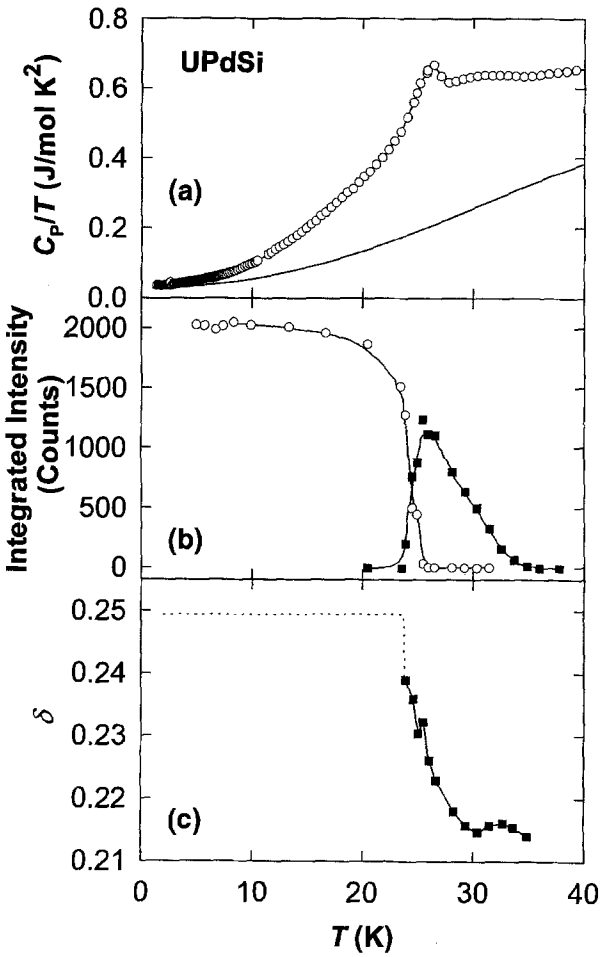

Fig. 5.35. Temperature dependence of the: (a) Specific heat C_p/T; (b) Integrated intensity of the strongest $(0\,0\,0)^{+/-}$ commensurate reflection (o) and of the reflection observed for the incommensurate phase (■); (c) Of δ component of the propagation vector $\boldsymbol{q} = (\delta, 0, \delta)$ in UPdSi below 50 K; data taken from Prokes et al. (1997c, 1997d).

susceptibility minimum around $T = 11.5$ K, led Chevalier et al. (1988) to the conclusion of Kondo-fluctuation behaviour at low temperatures. The rather broad shoulder in the χ vs. T curve around 40 K may be taken as an indication of spin-fluctuation involvement (Troc and Tran 1988). Further studies, especially on single-crystals, are strongly desirable to learn more about this materials. The need of single crystals is stressed by the strong magnetic anisotropy, which can be seen in fig. 5.31 when comparing the "free-powder" and "fixed-powder" linear magnetization data measured up to 35 T (de Boer et al. 1990).

UPtSi is the only silicide crystallizing in the disordered $CeCu_2$-type structure, on which agreed all involved authors (Troc and Tran 1988; Brück 1991; Prokes et al. 1997b). Troc

and Tran (1988) reported two diffuse maxima at 24 K and 50 K in the χ vs. T curve indicating two magnetic phase transitions in an antiferromagnet. Prokes (1997) has clearly shown that the lower-temperature transition cannot be intrinsic. A neutron powder diffraction study (Tran et al. 1995a) revealed a collinear structure of uranium moments confined in the b–c plane and sinusoidally modulated along the b-axis with a propagation vector $\boldsymbol{q} = (0, 0.535, 0)$. Prokes et al. (1996d, 1997b) and Prokes (1997) have confirmed the sinusoidal modulation of uranium moments, which is not squaring up down to $T = 1.3$ K, where the amplitude of the sine wave amounts to $1.3\,\mu_B$. The complex magnetic structure and the relatively high Néel temperature may explain the complex staircase of metamagnetic transitions, observed on a "free powder" sample in magnetic fields up to 50 T (see fig. 5.31), where the magnetization amounts to $0.94\,\mu_B$ (de Boer et al. 1991). Two rather different the γ-values have been reported in literature, in particular 92 mJ/(mol K^2) (Brück 1991; de Boer et al. 1991) and 44 mJ/(mol K^2) (Prokes et al. 1996d, 1997b; Prokes 1997) the lower one being more likely intrinsic. The temperature dependence of the resistivity is rather flat down to 70 K with a slight negative derivative above 150 K. With lowering temperature below 70 K, the ρ vs. T curve turns gradually up and reaches a maximum at 38 K, which is followed by a sharp, nearly linear drop down to lowest temperatures. The inflection point of the ρ vs. T curve, found at 51 K fits perfectly with the Néel temperature (Prokes 1997).

ThIrSi crystallizes in the hexagonal AlB_2 type structure and becomes superconducting below 6.5 K (Chevalier et al. 1986). Using point-contact spectroscopy measurements Solanki-Moser et al. (1987) suggested that the width of the superconducting gap extrapolated to 0 K in this material is 1.6 eV.

UFeGe has been prepared only in polycrystalline form only by Canepa et al. (1996). However, tiny single-crystalline grains were used for part of a crystal structure study on a four-circle diffractometer. At room temperature, a monoclinically distorted TiNiSi-type structure has been observed. The monoclinic distortion is removed above 500 K, which is accompanied by an about 10% reduction of the electrical resistivity. This crystallographic transition exhibits hysteresis of more than 50 K (Canepa et al. 1996).

Also *UCoGe* does not show any sign of magnetic order down to $T = 1.3$ K, although some attributes of a nearness of ferromagnetic ordering may be traced in the high-field magnetization data (Buschow et al. 1990). The high-field magnetization curve measured on a free-powder sample exhibits a positive curvature and certain tendency to saturation in the whole field range up to 35 T, where it reaches nearly $0.6\,\mu_B$/f.u. Also the γ-value of 65 mJ/(mol K^2) may be taken as an additional argument corroborating this conclusion. The electrical resistivity is almost linearly growing with decreasing temperature between 300 K and 50 K (Canepa et al. 1996), showing a final increase of about 10%. This behaviour is terminated at 46 K where the resistivity starts to decrease with decreasing temperature. The associated maximum on the ρ vs. T curve has been speculated by Canepa et al. (1996) as being a sign of a magnetic phase transition. Although UCoGe is paramagnetic, a strong magnetocrystalline anisotropy is clearly documented by the pronounced difference between the free-powder and fixed-powder magnetization curves (de Boer et al. 1990) which is increasing in the whole field range up to 35 T.

UNiGe is certainly the by far most thoroughly studied germanide at present and the results, which have been observed on very good quality single crystals, allow the demonstration of several prominent features of uranium intermetallics. The first papers on this

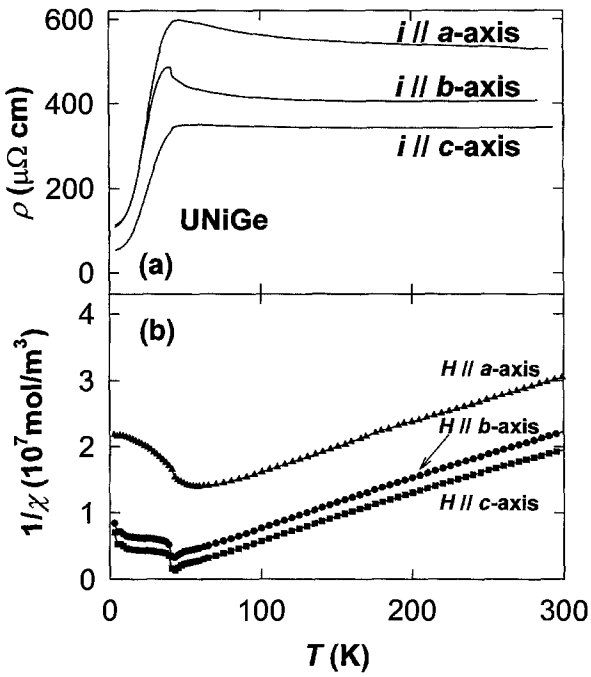

Fig. 5.36. Temperature dependence of the following properties of UNiGe measured on single crystals: (a) Electrical resistivity ρ with current i along the a-, b- and c-axis; data taken from Prokes et al. (1994); (b) The inverse susceptibility in magnetic fields applied along the a-, b- and c-axis; data taken from Prokes (1997).

material reported the orthorhombic $CeCu_2$-type structure (Troc and Tran 1988). By observing some prominent $h + k + l = 2n + 1$ reflections several authors proved, however, that the TiNiSi-type is the proper structure of this material (Kawamata et al. 1992a; Prokes et al. 1994; Canepa et al. 1996). The temperature dependence of the inverse susceptibility (see fig. 5.36) above 60 K follows very well the Curie–Weiss law with $\mu_{\text{eff}} = 3.01$, 2.97 and 2.93 μ_B/f.u. for the susceptibility along the a-, b- and c-axis, respectively. This means that the effective magnetic moment is isotropic within the experimental error. The values of the paramagnetic Curie temperature $\Theta_p = -126$, -4, and 34 K (Havela et al. 1992c, Prokes 1997) are strikingly different, pointing to the fact that UNiGe exhibits a strong magnetic anisotropy in the paramagnetic state. The anisotropy energy can be estimated considering the difference of the respective Θ_p values, e.g., the anisotropy within the b–c plane is about 40 K, whereas the anisotropy energy in the a–c and a–b planes is larger than 100 K (Havela et al. 1992c). In fig. 5.36 one can see that also the electrical resistivity is rather anisotropic, which is, especially in the lower temperature range, closely connected with the evolution of magnetism. The magnetocrystalline anisotropy may affect also the temperature dependence of specific heat, namely due to the anisotropy induced gap Δ in the magnon spectrum, which yields a term which in its simplest form can be expressed as:

$$C_m = fT^{1/2}e^{-\Delta/T}, \tag{5.6}$$

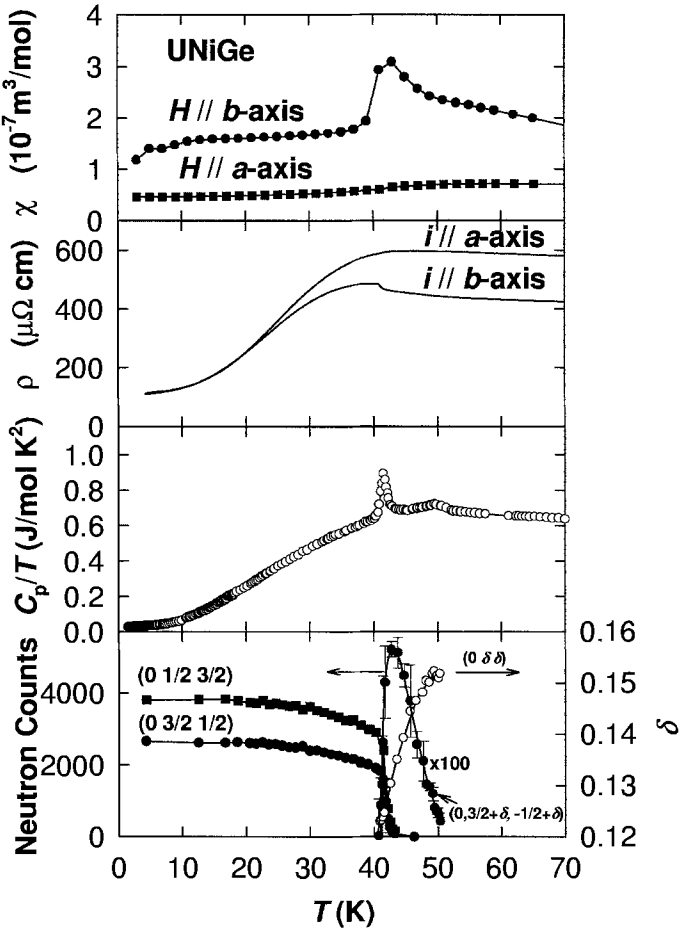

Fig. 5.37. Temperature dependence of the following properties of UNiGe measured on single crystals below 70 K: (a) Susceptibility χ in magnetic fields H applied along the a- and b-axis; data taken from Prokes (1997); (b) Electrical resistivity ρ with current i along a- and b-axis; data taken from Prokes et al. (1994); (c) Specific heat (C/T vs. T plot) – data taken from Prokes et al. (1994); (d) Magnetic neutron diffraction reflections (0, 1/2, 3/2), (0, 3/2, 1/2) and (0, 1/2, −3/2) + (0, δ, δ) – the intensity scale of the latter reflection is expanded by a factor of 50; data taken from Sechovsky et al. (1994b, 1994c).

where the factor f depends on details of the magnon spectrum such as the slope of magnon dispersion relation (Andersen and Smith 1979). The low-temperature part of the specific heat of UNiGe shown in fig. 5.37 allows to determine $\Delta = 48$ K and $f = 5.5$ mJ/(mol K$^{3/2}$) (Prokes 1997). The value of Δ compares well with the anisotropy within the b–c plane estimated from susceptibility data. Several authors have agreed on the value of $\gamma = 27$ mJ/(mol K^2) (Buschow et al. 1990; Brück 1991; Dmitriev et al. 1991; Prokes 1997). A somewhat lower value, $\gamma = 23$ mJ/(mol K^2) has been reported by Kawamata et al. (1992b).

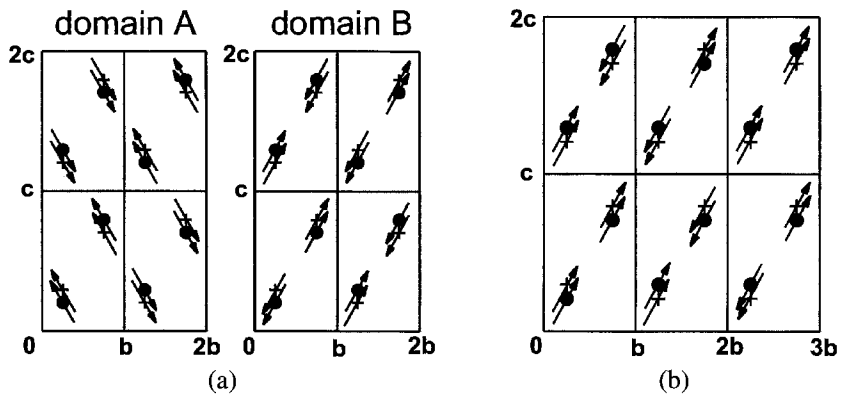

Fig. 5.38. (a) The ground-state magnetic structure of UNiGe consisting of two magnetic domains. (b) The incommensurate magnetic structure in UNiGe consisting of two domains (only one domain is shown). The arrows represent the magnetic moment components in the b–c plane. The dots and crosses represent the mutually antiparallel a-axis moment components.

UNiGe has been reported to become antiferromagnetic below 42–44 K as inferred from the susceptibility (Troc and Tran 1988) and specific-heat (Kawamata et al. 1992b) anomalies and from emerging new reflections in the neutron powder diffraction pattern at lower temperatures (Murasik et al. 1991). Two rather contradictory reports on the type of magnetic structure, however, have appeared (Murasik et al. 1991; Kawamata et al. 1992a), the former authors claiming a propagation vector $\boldsymbol{q} = (0, 1/2, 1/2)$ whereas the latter authors presented $\boldsymbol{q} = (0, 1, 1)$. Neutron diffraction investigations of the ground-state antiferromagnetic phase on single crystals (Sechovsky et al. 1994b; Purwanto et al. 1996a) confirmed the former result. The sharp anomaly in the C/T vs. T curve, which can be seen in fig. 5.37, allowed the determination of the upper temperature limit of this magnetic ordering as 41.5 K. The related magnetic-phase transition is of the first order type as first proposed by Murasik et al. (1991) and besides the sharp specific-heat peak, it is documented by the sharp drop of the magnetic-reflection intensity at this temperature. From this plot it is clear, that the uranium magnetic moment at $T = 40$ K retains more than 80% of its ground-state value. Final refinement of the neutron diffraction data, collected on a UNiGe single-crystal, led to the determination of the magnetic structure which is schematically shown in fig. 5.38(a) (Purwanto et al. 1996a). This structure can be imagined when we consider a collinear structure with magnetic moments within the b–c plane and modify it by attributing to the a-axis component a constant non-zero value with alternating sign, as shown in the figure. Within the b–c plane the uranium magnetic moment makes an angle of approximately 17° with the c-axis and the canting angle out of the plane has been determined as 21° (Purwanto et al. 1996a). This complex magnetic structure has been unambiguously confirmed by Nakotte et al. (1996a), who performed an elaborate neutron diffraction experiment using polarized neutrons and special configurations of the single-crystal and the applied magnetic field.

Close inspection of the specific heat, magnetic susceptibility and electrical resistivity above $T = 41.5$ K (see fig. 5.37) reveals anomalies around $T = 51$ K indicating that

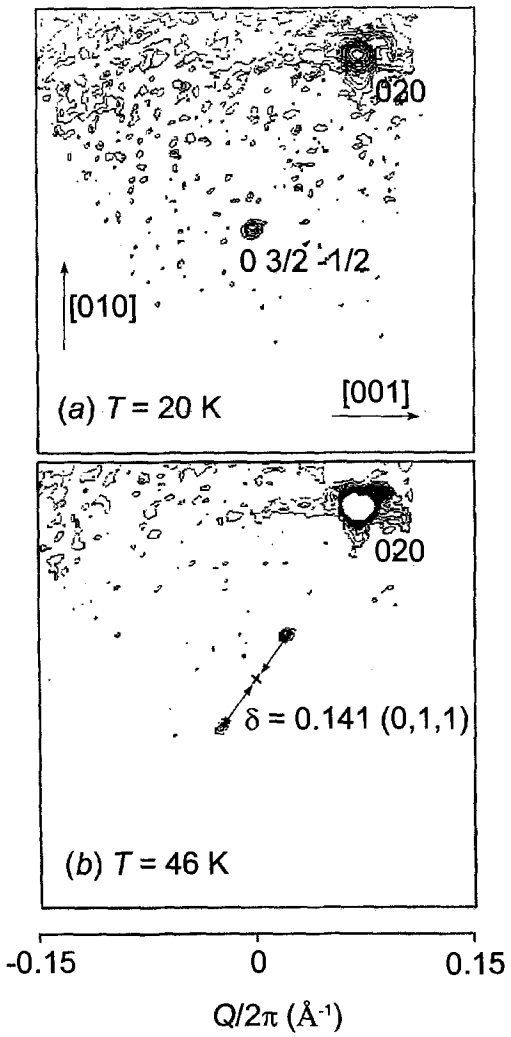

Fig. 5.39. Representative contour plots in reciprocal space in the vicinity of the $(0, 3/2, -1/2)$ reflection in UNiGe obtained: (a) At $T = 20$ K (commensurate antiferromagnetic phase); (b) At $T = 46$ K (incommensurate satellites); data taken from Sechovsky et al. (1994b).

the onset of magnetic ordering may be located near this temperature (Prokes et al. 1994; Sechovsky et al. 1994b, 1994c). This point has been confirmed by the extended neutron diffraction investigation in the suspected temperature region. The essential result of the crucial experiment performed on the Single Crystal Diffractometer (SCD) at LANSCE, which has unambiguously proved the existence of an incommensurate phase above 41.5 K is shown in fig. 5.39. For the ground-state phase at temperatures below 41.5 K (fig. 5.39(a)) the $(0, 3/2, -1/2)$ reflection is a characteristic attribute of the commensurate antiferromag-

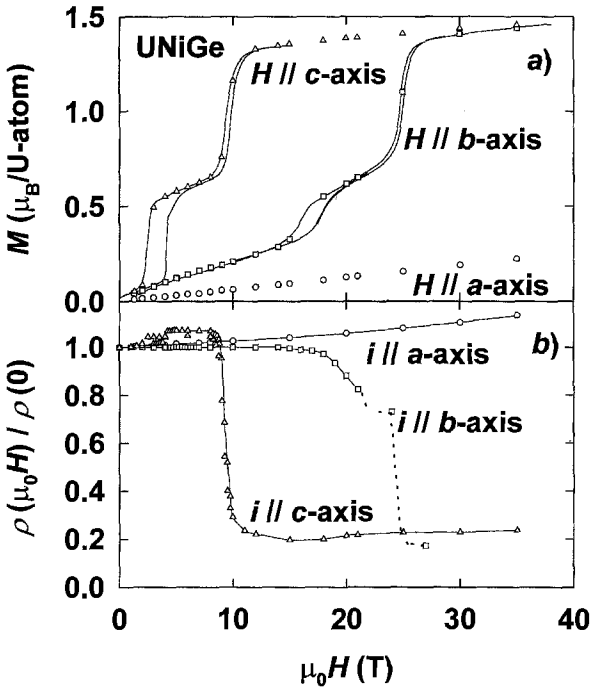

Fig. 5.40. (a) Magnetization curves, and (b) longitudinal magnetoresistance curves for UNiGe at $T = 4.2$ K with the magnetic field H applied along the a-, b- and c-axis; data taken from Prokes et al. (1994). For the magnetization curves, the lines show data obtained with continuously swept magnetic field up and down.

netic phase. But this reflection is absent in the 46 K pattern and the two satellites shifted by $\pm(0, 0.141, 0.141)$ are the fingerprints of an incommensurate phase with the propagation vector $\boldsymbol{q} = (0, 1/2, -1/2) \pm (0, \delta, \delta)$. These reflections reach their maximum intensity around 43 K and then decay nearly linearly with increasing temperature to vanish around $T = 50$ K, although a somewhat enhanced background can be traced at least up to 53 K (Sechovsky et al. 1994c). The value of δ varies between 0.123 (at 41.5 K) and 0.15 (50 K). This incommensurate structure can be schematically visualized as shown in fig. 5.38(b). In fact, this structure consists of a $+ + -$ stacking of adjacent (0 1 1) planes of U moments. However there occurs a phase shift of π every 20 planes or so. Also in this phase the alternating canting of U moments towards the a-axis has been unambiguously determined by using polarized neutrons (Nakotte et al. 1996a).

The magnetization curves shown in fig. 5.40(a) (Havela et al. 1992c; Prokes et al. 1994) clearly demonstrate that the magnetocrystalline anisotropy in UNiGe is of an easy-plane type (b–c plane), leaving the a-axis as hard magnetization direction. The magnetization in a field applied along c responds linearly with very small slope up to 35 T yielding $0.23\,\mu_B$/f.u. In contrast, when the field is oriented along the c-axis, two metamagnetic transitions are induced at 3 and 10 T, respectively. Approximately $1.3\,\mu_B$/f.u. is reached at 11 T. With further increasing field the magnetization increases linearly up to the value

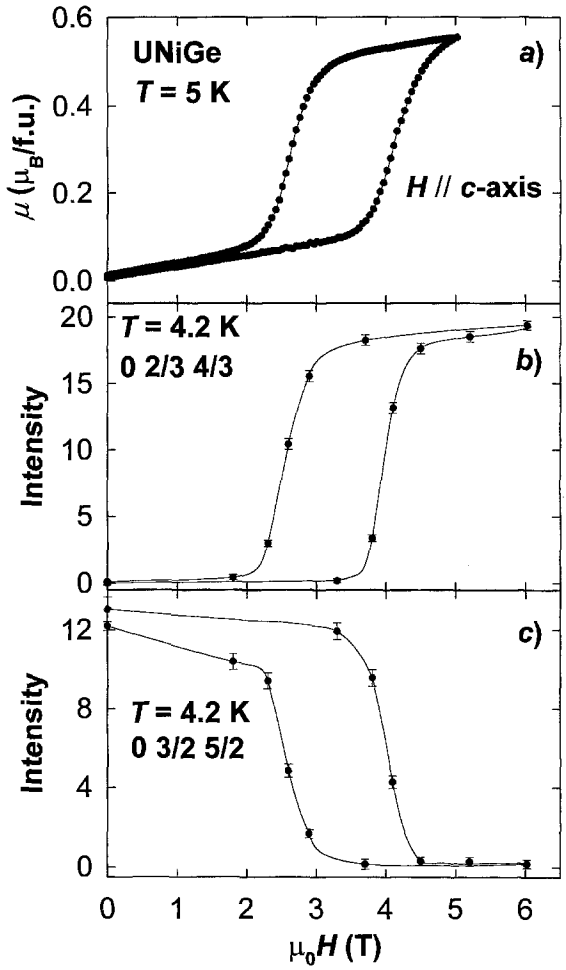

Fig. 5.41. Magnetic-field dependence of the (a) magnetization μ, (b) intensity of the $(0, 2/3, 4/3)$ reflection and (c) intensity of the $(0, 3/2, 5/2)$ reflection in UNiGe at $T = 4.2$ K in fields up to 6 T applied along the c-axis data; taken from Sechovsky et al. (1994b).

of $1.47\,\mu_B$/f.u. at 35 T. Figure 5.41 demonstrates the fact that the first metamagnetic transition involves a substantial transformation of the magnetic structure from the antiferromagnetic structure with $\boldsymbol{q} = (0, 1/2, 1/2)$, i.e., $+-+-+-$ stacking of adjacent (0 1 1) planes of uranium moments to an uncompensated antiferromagnetic structure with $\boldsymbol{q} = (0, 1/3, 1/3)$, i.e., $++-++-$ stacking. Two metamagnetic transitions, but at considerably higher fields as 17 and 25 T, are observed when a field is applied along the b-axis. Also in this case the high field magnetization does not saturate and grows to reach $1.45\,\mu_B$/f.u. at 35 T. Especially this feature has been used by de Châtel et al. (1998) to show the anisotropic nature of the exchange interactions in UNiGe. In fig. 5.40(b) one can

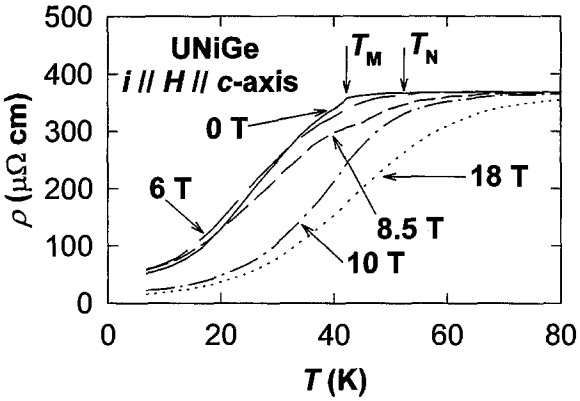

Fig. 5.42. Temperature dependence of the electrical resistivity ρ of a single crystal UNiGe for current i along the c-axis and in magnetic fields 0, 6, 8.5, 10 and 18 T applied along the c-axis. T_N and T_M show the two magnetic phase transitions (after Nakotte et al. (1995)).

see that the metamagnetic transitions in UNiGe are accompanied by giant magnetoresistance effects (Havela et al. 1994c; Prokes et al. 1994; Sechovsky et al. 1994d). Except for the first metamagnetic transition in the c-axis field where the c-axis resistivity shows an approximately 4% increase, all the other transitions produce huge negative changes of resistivity. The evolution of the temperature dependence of the c-axis resistivity in magnetic fields up to 18 T applied along the c-axis shown in fig. 5.42 demonstrates that a large negative magnetoresistance can be observed also in the paramagnetic range at temperatures up to 80 K. This indicates the importance of antiferromagnetic correlations, which enhance the resistivity far above T_N but can be suppressed by strong enough magnetic field. A more general discussion of GMR effects in UNiGe may be found in several papers devoted to giant magnetoresistance in bulk intermetallic materials with a special emphasis on uranium systems (Nakotte et al. 1994a, 1994b; Havela et al. 1994b, 1994c, 1996a; Sechovsky et al. 1994d, 1996).

In order to determine the complex magnetic phase diagrams, magnetization curves in magnetic fields up to 35 T applied along the b- and c-axis, respectively, were measured also at elevated temperatures up to 60 K (de Boer et al. 1994). This effort was supported by detailed studies of neutron diffraction in magnetic fields up to 6 T (Sechovsky et al. 1994b, 1994c; Nakotte et al. 1996a) and in the final stage, by specific-heat measurements in magnetic fields up to 18 T (Nakotte et al. 1998). As a result, two magnetic phase diagrams for fields applied along the b- and c-axis have been constructed as shown in fig. 5.43. Besides the extended short range ordering determined by neutron scattering up to high temperature, it is worth to mention the close similarity between the phases 1 a 3, which is discussed by Nakotte et al. (1996a).

The magnetic phase diagrams were studied also by specific-heat measurements in magnetic fields up to 18 T (Hagmusa et al. 1997; Nakotte et al. 1998). For a magnetic field $H \| c$, the γ-value seems to be nearly constant up to 4 T, where the first metamagnetic state appears. Further increase of the magnetic field yields a roughly quadratic γ enhancement up to 37.5 mJ/(mol K^2) in 11 T, where the second metamagnetic transition appears at

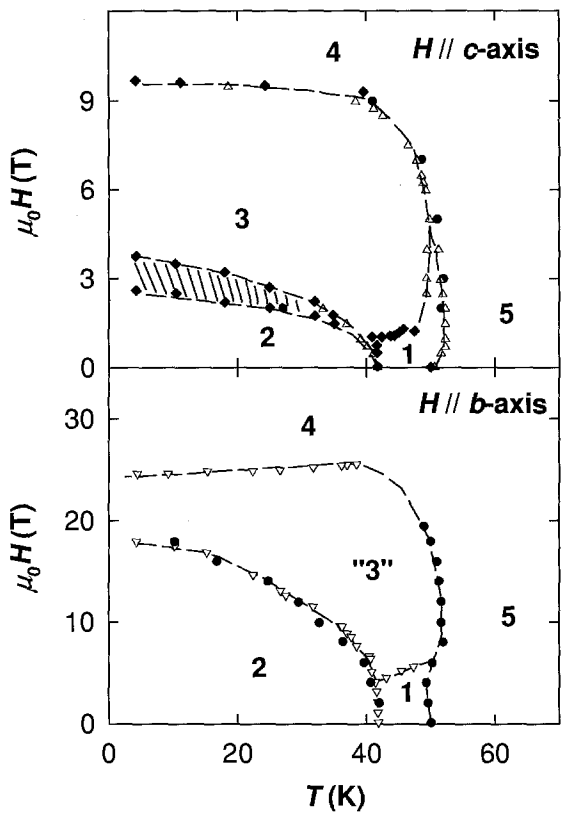

Fig. 5.43. Magnetic phase diagrams of UNiGe with the field oriented along the c-axis (a) and along the b-axis (b): 1 – Incommensurate antiferromagnetic phase, $\boldsymbol{q} = (0, 1/2, -1/2) \pm (0, \delta, \delta)$; 2 – Ground state antiferromagnetic phase, $\boldsymbol{q} = (0, 1/2, 1/2)$; 3 – Uncompensated antiferromagnetic phase, $\boldsymbol{q} = (0, 1/3, 1/3)$; "3" – Yet unknown phase (probably an analogue to the phase 3); 4 – "Ferromagnetically" aligned phase; 5 – Paramagnetic phase.

850 mK. A slow nearly linear decrease is observed with a further field increase amounting to 35 mJ/(mol K^2) in 17.5 T (Nakotte et al. 1998).

URuGe is a weakly temperature dependent paramagnet which, however, shows certain URuGa-like features of the χ vs. T curve below 100 K, that might indicate involvement of spin fluctuations (Troc and Tran 1988). The susceptibility increases from its room-temperature value of 1.8×10^{-8} m^3/mol to 3.0×10^{-8} m^3/mol at 4.2 K (de Boer et al. 1990). The magnetization increases linearly with magnetic field up to 35 T (see fig. 5.31) amounting to 0.17 μ_B/f.u. at the maximum field (de Boer et al. 1990). Lack of any visible difference between the free-powder and fixed-powder data (fig. 5.31) suggests a rather isotropic magnetization in this material.

URhGe behaves, similar to URhSi, as an itinerant 5f electron ferromagnet with spontaneous moment around 0.3 μ_B/f.u. as inferred from free-powder magnetization data (de Boer et al. 1990). The high field susceptibility is also large and the magnetization reaches 0.71 μ_B/f.u. at 35 T. URhGe is another weak 5f ferromagnet exhibiting huge magnetocrys-

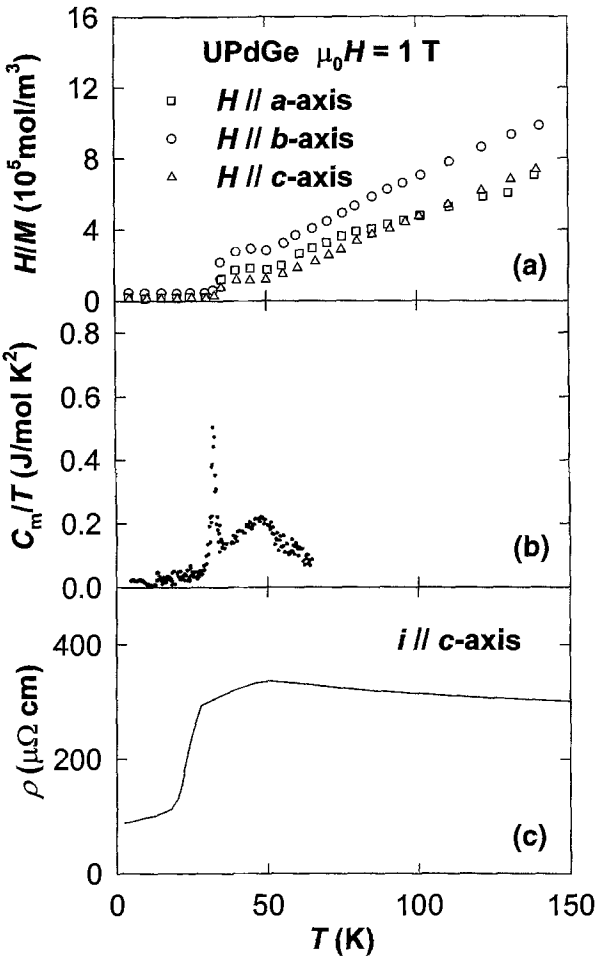

Fig. 5.44. Temperature dependence of the following quantities measured on UPdGe: (a) Inverse susceptibility H/M measured on a single crystal with magnetic field applied along the a-, b- and c-axis (Kawamata et al. 1990); (b) Magnetic contribution to the specific heat C_m/T (Kawamata et al. 1992b); (c) Electrical resistivity ρ with current i applied along the c-axis (Kawamata et al. 1992c).

talline anisotropy which is documented by a clear difference between the free-powder and fixed-powder magnetization curves shown in fig. 5.31. The reported high value for γ (see table 5.4) may be, similar to URhSi, affected by non-negligible magnetic contribution due to the low Curie temperature. Clear analogies between URhGe and URhSi can be found also in the magnetic-field induced variations of the specific heat (Buschow et al. 1990; Brück 1991) and in the electrical resistivity (Tran and Troc 1998) in a wide temperature interval around T_C as can be seen in fig. 5.33. The neutron powder diffraction data obtained at low temperatures were interpreted in terms of a non-collinear magnetic structure, which can be described by two magnetic components (Tran et al. 1998a, 1998b). The predom-

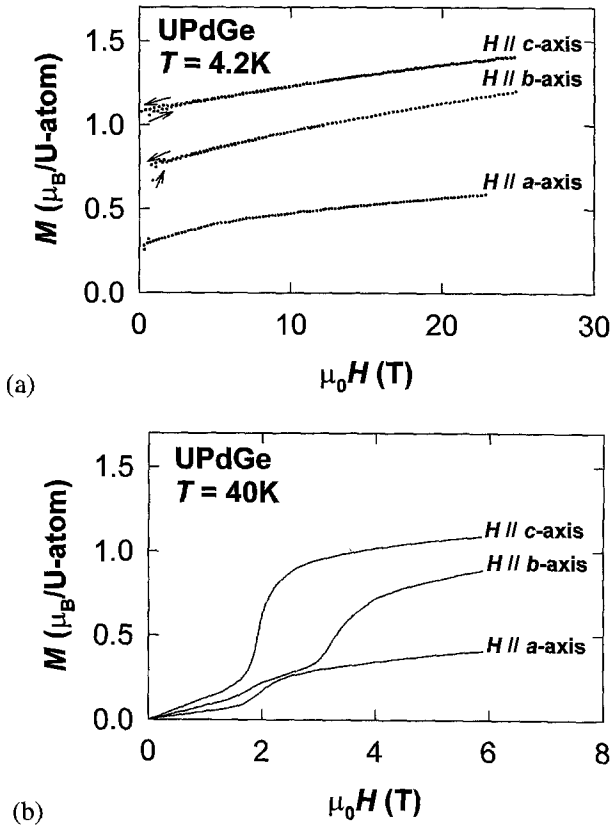

Fig. 5.45. Magnetization curves measured on an UPdGe single crystal at (a) $T = 4.2$ K, (b) $T = 40$ K, with magnetic field H applied along the a-, b- and c-axis (Kawamata et al. 1990).

inant ferromagnetic component ($\mu_F = 0.43\,\mu_B$) is oriented along the c-axis. The other component is antiferromagnetic ($\mu_{AF} = 0.26\,\mu_B$) is found along the a-axis. The latter aspect resembles the non-collinear magnetic structure in UNiGe.

UPdGe becomes ferromagnetic below 28–33 K (Troc and Tran 1988; Buschow et al. 1990; Kawamata et al. 1990). At higher temperatures antiferromagnetic ordering persisting up to 50 K has been reported in the same papers. A first order type of magnetic phase transition between the ferromagnetic and antiferromagnetic phase in UPdGe has been suggested by Kawamata et al. (1992b) who reported a sharp peak in the C/T vs. T curve at $T = 33$ K, which can be seen in fig. 5.44. In contrast, Buschow et al. (1990) observed only a rounded maximum near this temperature. This transition is accompanied also by a pronounced step in the temperature dependence of the elastic constant c_{33} measured by sound velocity measurements (Ishiyama et al. 1993). The magnetic phase transitions are well seen also in the temperature dependence of the susceptibility in all the three principal crystallographic directions (Kawamata et al. 1990) shown in fig. 5.44. Note the anisotropy, which, however, is less pronounced than in UNiGe. Also the low-temperature magnetiza-

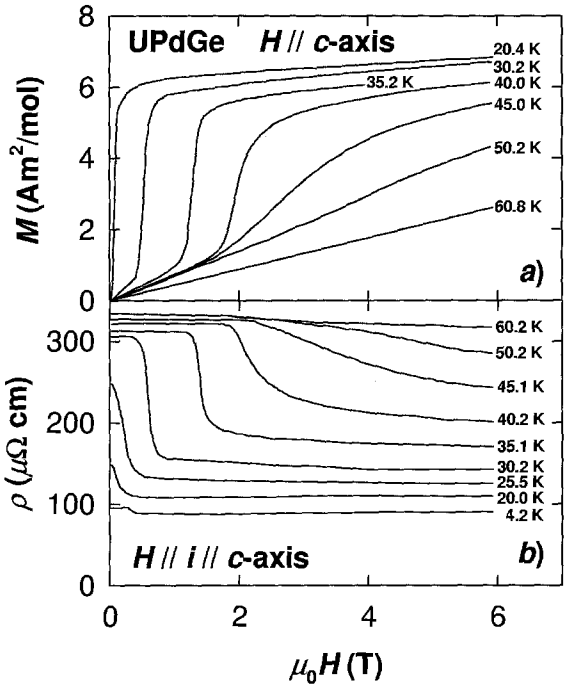

Fig. 5.46. (a) Magnetization curves, and (b) longitudinal magnetoresistance curves for UPdGe single crystals at selected temperatures with the magnetic field applied along the c-axis; data taken from Kawamata et al. (1992c).

tion data, obtained on a single crystals (see fig. 5.45), point to quite a generally oriented easy magnetization direction which is reflected by non-zero moment projections of the remanent magnetization in all the three crystallographic axes ($\mu_a = 0.35$, $\mu_b = 0.85$ and $\mu_c = 1.11\,\mu_B$), yielding a total uranium moment of $1.37\,\mu_B$ at $T = 4.2$ K (Kawamata et al. 1992d). A neutron diffraction investigation (Kawamata et al. 1992a) of the single crystal has confirmed this result and allowed to determine a collinear ferromagnetic structure at low temperatures. Tran et al. (1995a), however, claimed that the ferromagnetic structure is conical with $\mu_z \| c$ and with the projection of U moments on the a–b plane equal to $0.28\,\mu_B$.

The high-temperature phase has been determined as being an antiferromagnetic longitudinal spin-density wave with $\boldsymbol{q} = (0, 0, \delta)$, where $\delta = 0.33$ at $T = 35$ K with a magnetic moment amplitude of $1.0\,\mu_B$ (Kawamata et al. 1992a; Tran et al. 1995a). The application of magnetic fields leads again to a rather anisotropic magnetization response as can be deduced from fig. 5.44 (Kawamata et al. 1992d). The a- and c-axis magnetization exhibits a metamagnetic transition at the same field (around 20 T at 40 K) whereas the metamagnetic transition in the b-axis magnetization curve occurs at an approximately 50% higher field. The magnetizations along the b- and c-axes reach at high fields considerable values and seem to saturate. However, the c-axis magnetization presumably should show another metamagnetic transition at higher fields. The critical-field values decrease with temperature approaching the AF $\rightarrow$ F magnetic phase transition, as can be seen in fig. 5.46. The

metamagnetic transitions are accompanied by giant magnetoresistance effects as can be clearly seen in fig. 5.46 (Kawamata et al. 1992c). These are intimately connected with the dramatic reduction of the resistivity the AF $\rightarrow$ F in zero magnetic field (Kawamata et al. 1992c), shown in fig. 5.43.

The evolution of magnetization behaviour in the pseudoternary system $UNi_{1-x}Pd_xGe$ was studied by Kawamata et al. (1993). All three lattice constants increase linearly with increasing x. The most pronounced increase across the series is found in the c-axis, more than 5%, whereas the change in the a-axis is only marginal. When we consider also the corrected results for UNiGe (Kawamata et al. 1992a, 1992b; Sechovsky et al. 1994b; Nakotte et al. 1996a; Prokes 1997), it may be concluded that the Néel temperature is composition invariable and that the high-temperature phase is always incommensurate although the propagation is varying considerably with Pd substitution for Ni. Major changes are observed with respect to the ground state which is non-collinear antiferromagnetic in UNiGe (Nakotte et al. 1996a) and changes probably gradually to a collinear ferromagnet (Kawamata et al. 1992a) or to a conical structure (Tran et al. 1995a).

UIrGe is one of the most puzzling cases despite considerable effort of several groups. All bulk properties which have been studied so far point to antiferromagnetism in this compound below 16–18 K. This concerns the maximum in the temperature dependence of susceptibility (Ramirez et al. 1987; Troc and Tran 1988; Buschow et al. 1990), a sharp peak in the C/T vs. T curve (Ramirez et al. 1987; Buschow et al. 1990) accompanied by a dramatic reduction of the γ-value from 145 to 18 mJ/(mol K^2) across the transition from the high to the low-temperature phase and a dramatic resistivity drop below 17 K (Chevalier et al. 1988; Buschow et al. 1990; Tran et al. 1990). The specific-heat anomaly shifts by 0.5 K to lower temperatures when a field of 5 T is applied (Buschow et al. 1990; Brück 1991). Note that the onset of the resistivity drop around 30 K (Chevalier et al. 1988) might indicate the onset of a sort of magnetic order already around this temperature. Moreover, the magnetization curves measured on free-powder samples (no single crystals available so far) at $T = 4.2$ K exhibit two clear metamagnetic transitions at 13 and 19 T. As a big surprise no indication of magnetic order down to 1.5 K has been observed by neutron powder diffraction experiments (Robinson 1993; Tran et al. 1996b). Certain signs of magnetic ordering in UIrGe may be concluded from μ^+SR measurements (Havela et al. 1995a).

A gradual transition between weak itinerant ferromagnetism of URhGe and the presumed antiferromagnetism of UIrGe was studied by magnetization measurements (Chevalier et al. 1990) of selected U($Rh_{1-x}Ir_x$)Ge solid solutions. Ferromagnetism is clearly present in compounds with $x \leqslant 0.45$. Whereas T_C decreases with increasing x only slowly, the spontaneous magnetization seems to decrease much faster. The $URh_{0.5}Ir_{0.5}Ge$ compound is characterized by a round maximum at $T_{max} = 4$ K in the temperature dependence of the magnetization which has been taken to be a clear attribute of the onset of antiferromagnetism. The value of T_{max} increases linearly while the maximum magnetization is drastically suppressed.

UPtGe shows all attributes of an antiferromagnet with $T_N = 50$–52 K. The temperature dependence of the susceptibility measured on polycrystals exhibits a maximum in this temperature range (Troc and Tran 1988; Buschow et al. 1990). Measurements of a single crystal (Kawamata et al. 1990) revealed such a maximum only in the b- and c-axis susceptibility, whereas the a-axis signal is practically temperature independent, as can be seen in

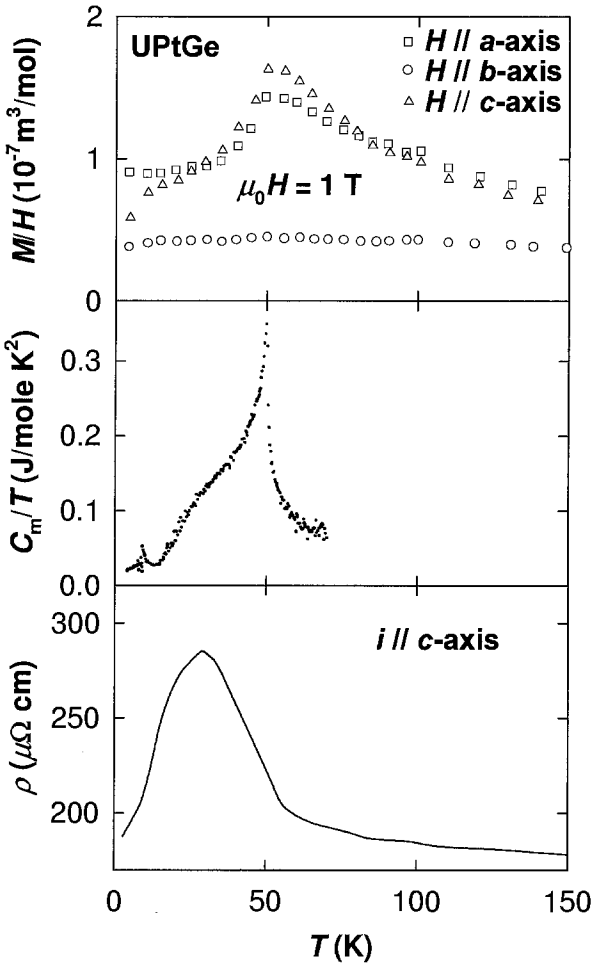

Fig. 5.47. Temperature dependence of the following properties of UPtGe measured on single crystals: (a) Magnetic susceptibility M/H in magnetic fields 1 T applied along the a-, b- and c-axis; data taken from Kawamata et al. (1990); (b) Magnetic contribution to the specific heat C_m/T (Kawamata et al. 1992b); (c) Electrical resistivity ρ with current i applied along the c-axis (Kawamata et al. 1992c).

fig. 5.47. A pronounced peak is observed also in the temperature dependence of specific heat shown in the same figure. The ρ vs. T curve with current along the c-axis (see also fig. 5.47) has a very anomalous shape with a pronounced maximum at 30 K (Kawamata et al. 1992c), which reflects a complex temperature evolution of conduction-electron scattering. A similar resistivity behaviour has been observed also on a polycrystal (Tran et al. 1990). As can be seen in fig. 5.31, the high field magnetization data collected in fields up to 50 T on an oriented powder sample at $T = 4.2$ K (Buschow et al. 1990) exhibit two broad metamagnetic transitions centred at 23 and 42 T, but no sign of saturation in the maximum fields which indicates that another transition might be expected above 50 T. The transition

below 30 T has been measured on a single crystal (Kawamata et al. 1992d) in fields along the *b*- and *c*-axis, whereas a considerably weaker linear response can be observed along the *a*-axis, yielding less than 0.3 μ_B/f.u. in a field of 30 T. This result seems to be consistent with neutron diffraction data (Kawamata et al. 1992d; Szytula et al. 1992; Robinson et al. 1993a), pointing to a magnetic structure with magnetic moments confined to the *b*–*c* plane. UPtGe exhibits incommensurate magnetic order with a temperature invariant propagation vector $\boldsymbol{q} = (0, 0.5543, 0)$. The only order parameter of the system is then the uranium moment. The values of 0.98 μ_B at 15 K (Robinson et al. 1993a) and 1.0 μ_B at 10 K (Kawamata et al. 1992a) have been reported. The moment rotates by 99.8° between adjacent planes of U atoms along the *b*-axis (cycloidal structure).

A rather complex development of magnetism may be concluded for the series of solid solutions $UPd_{1-x}Pt_xGe$ (Kawamata et al. 1993), although also here (similar to $UNi_{1-x}Pd_xGe$) the magnetic ordering temperature does not show much variation across the series. This is indicated already by the non-linear changes of the lattice constants *a* and *b* and by the change of sign of Θ_p ($\approx$ 21 K for $x = 0.5$ and ≈ -29 K for $x = 0.75$) as measured an polycrystals for $x > 0.5$.

In fig. 5.48 we can find the essential information on all known isostructural UTSi and UTGe compounds available so far.

In a contrast to other UPdX counterparts, *UPdAl* exhibits sound attributes of an itinerant electron paramagnet. This compound was found to be a weakly temperature-dependent paramagnet with the susceptibility keeping an almost constant value of approximately 1.3×10^{-8} m^3/mol between 300 and 200 K. Below 200 K, the susceptibility increases roughly linearly by 50% when cooling down to $T = 4.2$ K. The almost linear temperature dependence of the resistivity, resembling the behaviour of a simple metal (Tran and Troc 1993a), may be understood in terms of a rather low density of the 5f states at E_F in conjunction with a rather broad 5f band. This conjecture is corroborated by a considerably shrunk unit-cell volume of UPdAl in comparison with the isostructural UPdGe, UPdSi and UPdGa.

UPdGa was studied also by Kergadallan (1993) on a tiny single crystal extracted from polycrystalline ingot. By means of a four-circle X-ray diffractometer he unambiguously determined that this compound has the TiNiSi-type structure. The compound UPdGa shows a clear maximum in the χ vs. T curve at $T = 48$ K, which indicates antiferromagnetic ordering below this temperature.

UAuSi has been originally reported to crystallize in the TiNiSi-type structure (Tran and Troc 1993b; Pöttgen et al. 1996). The latter authors re-investigated this material and have shown that this materials adopts the hexagonal LiBaSi-type structure ($P\bar{6}m2$ space group) with the lattice parameters $a = 419.5$ pm, $c = 397.2$ pm at room temperature. This structure is derived from the AlB_2-type by an ordered arrangement of the gold and silicon atoms on the boron sites. Magnetic susceptibility measured on a polycrystal above 50 K follows roughly a modified Curie–Weiss law. Complex magnetic history phenomena occur at low temperatures, characterized by a susceptibility cusp in the ZFC curve at $\approx$ 12 K which disappears of FC curve (measured in 0.6 T), which was interpreted in terms of spin-glass or cluster glass behaviour (Tran and Troc 1993b; Pöttgen et al. 1996). This is rather surprising in case of an ordered ternary crystallographic structure. The $\rho(T)$ curves were found to depend strongly on the heat treatment of the samples, varying from a negative ρ–T slope

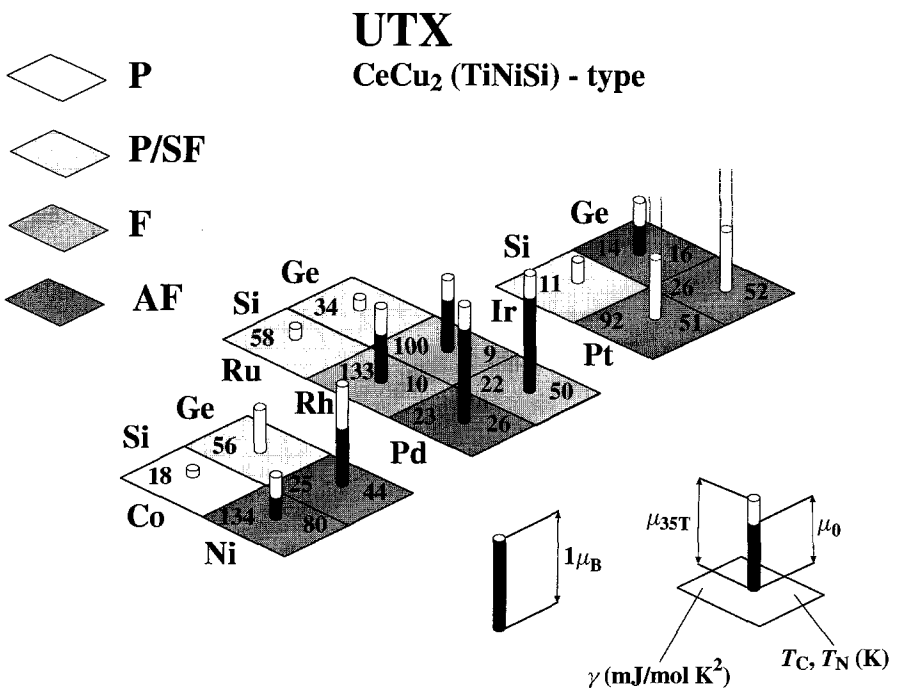

Fig. 5.48. Schematic plot illustrating evolution of some electronic properties (type of magnetic ground state, magnetic ordering temperature, γ-value (linear coefficient of the specific heat), spontaneous magnetic moment (black part of a column – extrapolated from high magnetic field data to zero field), induced magnetic moment in field of 35 T (white top parts of a column) of UTSi and UTGe compounds with the orthorhombic TiNiSi- and $CeCu_2$-type structure. Data are compiled from the information given in table 5.4.

in annealed sample to more metallic-like behaviour after annealing at 800°C. In all cases, clear resistivity anomalies have been observed around 16 K. An analogously complex behaviour has been reported by Tran and Troc (1993b) also for *UAuAl* and *UAuGe* with somewhat different characteristic temperatures, although the authors admitted the possibility of a paramagnetic ground state in the former case.

UAuGa orders antiferromagnetically below 60 K with another transition at 18 K, as inferred from anomalies in the temperature dependencies of the susceptibility and resistivity measured on polycrystals (Tran et al. 1993; Tran and Troc 1993b). The crystal and magnetic structures of UAuGa was investigated by means of X-ray and neutron powder diffraction measurements by Tran et al. (1996b). The crystal structure of UAuGa is orthorhombic, but no decision has been reached between the ordered TiNiSi-type or the disordered $CeCu_2$-type structure. The magnetic structure in UAuGa is collinear antiferromagnetic with uranium magnetic moments parallel to the orthorhombic c-axis. The uranium magnetic moment at $T = 7$ K equals 1.35 μ_B as has been reported by Tran et al. (1996b). This contradicts very much the value 0.68 μ_B claimed somewhat earlier (Tran et al. 1995a).

5.1.3. *Compounds with the GaGeLi ($CaIn_2$) type structure*

Another structure of UTX compounds for which reliable experimental data exist (UPdSn, UAuSn, UCuSn, UCuGa, and UPdSb) is the hexagonal structure of the $CaIn_2$ type (GaGeLi type for the ordered ternary version, as shown in fig. 5.49). The nearest uranium atoms, with a spacing $d_{U-U} = c/2$ (typically around 360 pm), form linear chains along the c-axis in this structure. The inter-uranium distance in the basal plane is significantly larger. Essential structural and magnetic data can be found in table 5.6.

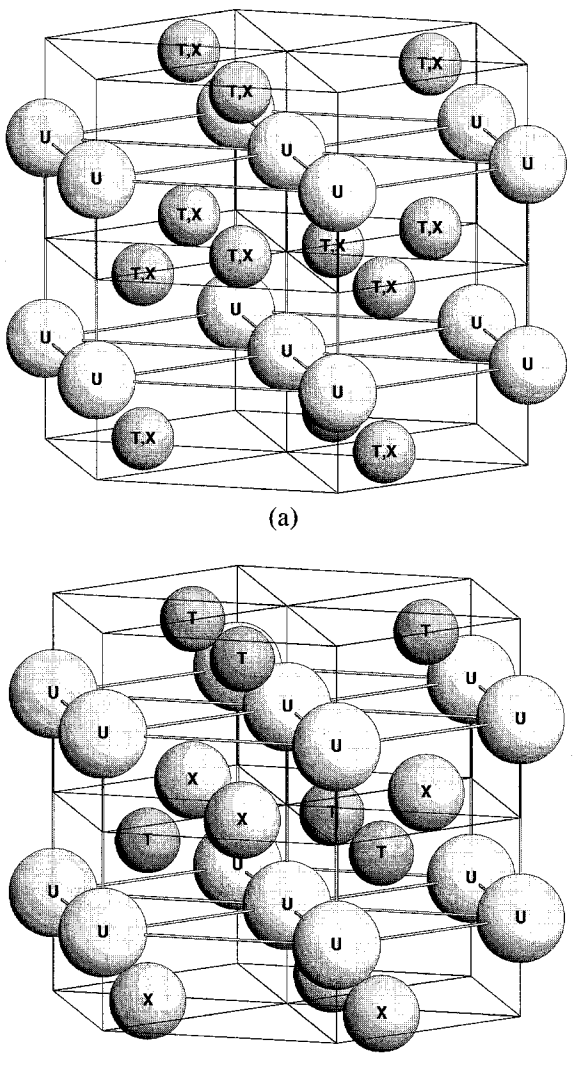

Fig. 5.49. Schematic picture of the hexagonal $CaIn_2$-type structure and its ordered ternary variant GaGeLi, in which crystallize several UTX compounds.

TABLE 5.6

Basic characteristics of UTX compounds with the $CaIn_2$ (GaGeLi) structure type:

Lattice parameters at room temperature a, b, c – type of ground state (F – ferromagnetic, AF – antiferromagnetic), T_C, T_N – magnetic ordering temperature, γ–coefficient of the electronic specific heat, fitting parameters of the temperature dependence of susceptibility in the paramagnetic state (μ_{eff} – effective moment, Θ_p – paramagnetic Curie temperature, χ_0 – temperature independent term), μ_U – the uranium ordered magnetic moment, d_{U-U} – interuranium spacing.

Compound	Structure variant	a (pm)	b (pm)	c (pm)	Type	T_C, T_N (K)	γ (mJ/(mol K^2))	μ_{eff} (μ_B/U)	Θ_p (K)	χ_0 (10^{-8}m^3/mol)	μ_U (μ_B)	d_{U-U} (pm)	Ref.
UPdSn	GaGeLi	460.8	657.9	731.0	AF	40 (27)	5	3.31[a]	−2.5 −113		2.05	365	[1–4]
UAuSn	$CaIn_2$	471.7		720.8	AF	35–36		3.06	−4		1.10	360	[1]
							80	2.7	12	0.45			[2,5]
UCuSn	distorted GaGeLi	453.91	783.9	722.03	AF	62	64	3.2	25		1.9	361	[6–9]
UCuGa	$CaIn_2$ (?)	434.1		699.4	AF	29–30	115	2.36	0	2		350	[10]
		436.6		700.3				2.58	13	0.13	...		[11,12]
		434.9		702.9							1.27		
UPdSb	?	458.7		721.5	F	65	62	2.92	70		1.3[b]	361	[1,13]

[a] Single-crystal data for fields along the basal plane and c-axis, respectively. $\chi(T)$ of a polycrystal can be approximated using parameters $\Theta_p = -8$ K, $\mu_{eff} = 3.1\,\mu_B$/U, and $\chi_0 = 2.1 \times 10^{-9}$ m^3/mol.

[b] Value per formula unit from spontaneous magnetization data.

References:

[1] Palstra et al. (1987)
[2] de Boer et al. (1992)
[3] Kaczorowski et al. (1997)
[4] Robinson et al. (1991)
[5] Robinson et al. (1993b)
[6] Nakotte et al. (1996b)
[7] Fujii et al. (1990b)
[8] Szytula et al. (1996)
[9] Kawanaka et al. (1997)
[10] Sechovsky and Havela (1988)
[11] Pöttgen and Kaczorowski (1993)
[12] Tran et al. (1995a)
[13] Sechovsky (1988)

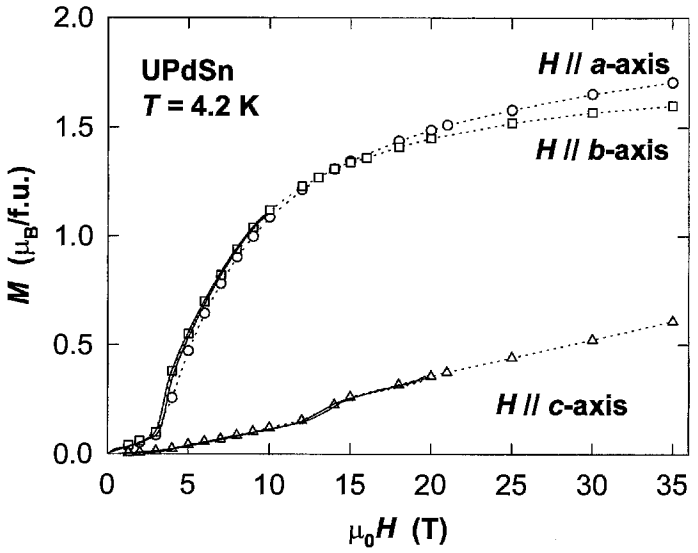

Fig. 5.50. Magnetization M for a single-crystal of UPdSn at $T = 4.2$ K in a magnetic field H applied along the a-, b- and c-axis. The full lines show behaviour for field swept continuously up and down. The dotted lines are guides to the eye. After de Boer et al. (1992).

The first four compounds are antiferromagnetic at low temperatures, whereas UPdSb is a ferromagnet. *UPdSn* crystallizes in the ordered ternary GaGeLi structure, in which Pd and Sn atoms occupy different positions (Robinson et al. 1991; de Boer et al. 1992). An AF transition was first reported at $T = 29$ K (Palstra et al. 1987), but a more detailed study (de Boer et al. 1992) revealed two transitions at $T = 40$ K and 27 K. Results of magnetization and susceptibility measurements performed on a single-crystal (see figs 5.50 and 5.51) show an easy-plane type of magnetism, with c-axis as a hard-magnetization axis. $\chi(T)$ for fields applied along the a- or b-axis follows the Curie–Weiss law with $\mu_{\rm eff} = 3.31\ \mu_{\rm B}$/U and $\Theta_{\rm p} = -2.5$ K. The same type of fit for $H \| c$ leads to the same $\mu_{\rm eff}$ value but to $\Theta_{\rm p} = -113$ K. It is interesting to see how is the susceptibility affected in a polycrystal even for the case of two easy and one hard magnetic direction. The averaging of the three susceptibilities leads to $\Theta_{\rm p} = -8$ K, $\mu_{\rm eff} = 3.1\ \mu_{\rm B}$/U, and we obtain in addition a small temperature independent term $\chi_0 = 4.5 \times 10^{-9}$ m^3/mol, accounting for the curvature of $1/\chi$ vs. T. A prominent feature in the $M(H)$ at $T = 4.2$ K is the metamagnetic transition of the spin-flop type, starting at $\mu_0 H = 3$ T for $H \| ab$. The magnetization curve tends gradually to saturation. The asymptotic value can be estimated as $\approx 1.9\ \mu_{\rm B}$. Extrapolating the weak linear response for $H \| c$ to high fields, we obtain the intercept of the two branches at $\mu_0 H \approx 110$ T, which is the measure of the anisotropy energy consistent with the difference of the respective $\Theta_{\rm p}$-values. Basic features of the development of magnetic structures were revealed using neutron diffraction by Robinson et al. (1991). Both the low temperature structure and the structure stable between 40 K and 27 K are non-collinear, with reduced symmetry due to a orthorhombic unit cell ($P_C mc2_1$). In the latter type the

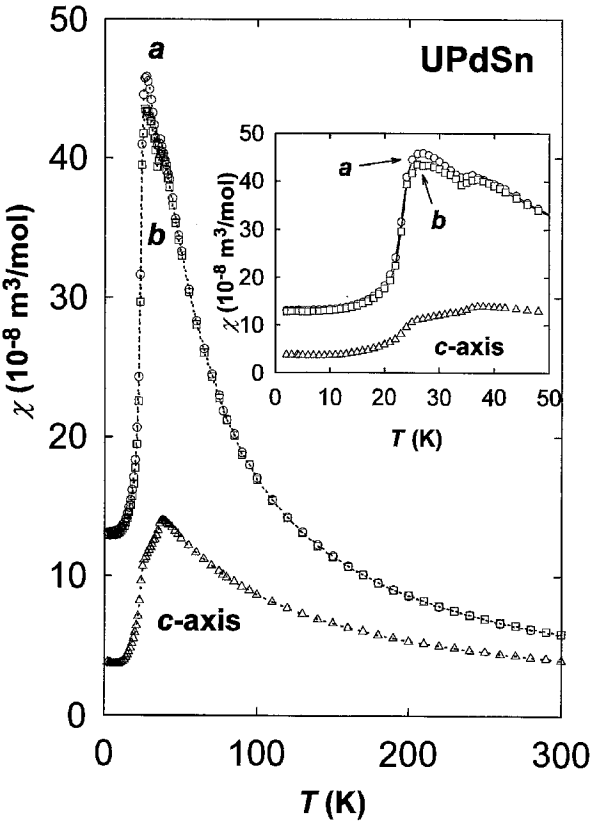

Fig. 5.51. Magnetic susceptibility χ vs. temperature T for a single-crystal of UPdSn in magnetic field $\mu_0 H = 1.6$ T applied along the a-, b- and c-axis. The curves for the former two configurations are almost identical except near the two magnetic phase transitions, which take place at $T = 40$ K and 27 K. The lines are guides to the eye. After de Boer et al. (1992). The inset shows the low-T details.

U-moments are lying in the bc-plane, with alternating sign of the inclination with respect to the b-axis, and a ferromagnetic coupling long the a-axis (see fig. 5.52). This coupling remains ferromagnetic even in the low-T structure, but the moments deviate out of the bc-plane leading to non-zero x-component. Thus the symmetry is further reduced to the space group P_C2_1. The size of the U-moments was estimated as $(2.05 \pm 0.13)\,\mu_B$ at $T = 13$ K (Robinson et al. 1991).

A more detailed study of the temperature dependence of the scattered intensities (Robinson et al. 1992) shows that the x-component of the U-moments starts to stabilize gradually around the lower magnetic phase transition, which probably means that we deal with a gradual slowing down of a fluctuating component of the moments, which becomes static below $T \approx 27$ K. The appearance of this component as a new order parameter is consistent with the second-order type of this magnetic phase transition, displayed by the specific-heat experiment. The onset of the lower symmetry magnetic structure is associated with an

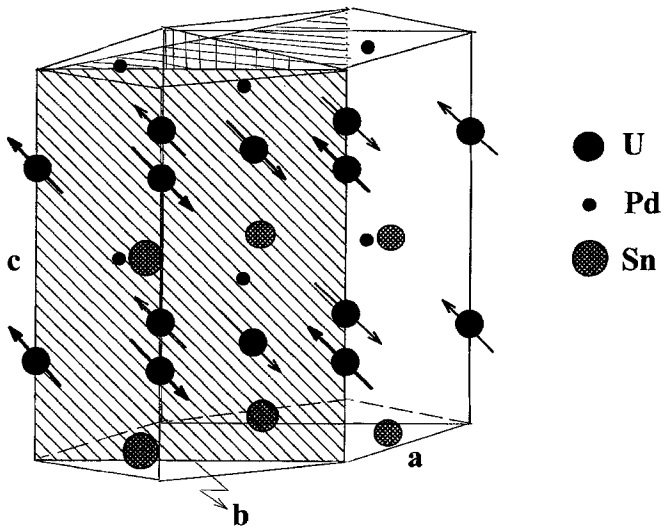

Fig. 5.52. The magnetic structure of UPdSn at temperatures between $T = 27$ and 40 K. The moments are aligned in the orthorhombic bc-plane indicated by the diagonally hatched rectangle. The canting angle from the c-axis is about 54°. In reality there are other two equivalent domains characterized by the planes indicated by horizontal and vertical hatching. Below 25–27 K, the moments turn out of the bc-plane by another canting angle of about 45°. Note that for the sake of clarity, the c-axis is expanded with respect to the b-axis. After Nakotte et al. (1993b).

appreciable monoclinic distortion, which reaches about 0.35° at $T = 10$ K (Robinson et al. 1993c). However, the alternative understanding of the order–order phase transition as a gradual rotation could not be excluded even after neutron single crystal experiments (Nakotte et al. 1993d), because the situation is severely complicated by presence of three equivalent domains arising due to the orthorhombic symmetry of the magnetic unit cell (6 domains are actually present in the monoclinic state). Thus the magnetic state is strongly history dependent, and it is also difficult to discriminate any possible moment rotations from re-population of such domains (Nakotte et al. 1993b, 1993d). A clear point is that the low symmetry structure is restricted by limit values $\mu_0 H = 3.5$ T, $T = 25$ K. On the other hand, no phase boundary exists between the high-field phase at low temperatures and the phase stable at 27 K $< T <$ 40 K, in which applied fields can induce domain re-populations as well as a certain degree of rotation (Nakotte 1998). A remarkable feature of UPdSn is the low value $\gamma = 5$ mJ/(mol K^2) (Palstra et al. 1987; de Boer et al. 1992; Kawanaka et al. 1997), which together with a rather high magnetic entropy $\Delta S \approx 1.1\, R \ln 2$ (see fig. 5.53) can point to localized 5f states, because such a low γ-value was found in UPd_3, in which the 5f states do not participate in the Fermi surface states (Andres et al. 1978; Baer et al. 1980). This was not, however, confirmed by high-resolution UPS and XPS spectroscopy results, which indicate the presence of the 5f states in UPdSn at E_F (Havela et al. 1992a, 1992b). The situation was further complicated by electron structure calculations (Trygg et al. 1994), which led to the conclusion that none of the situations considered (5f itinerant, localized 5f^2, localized 5f^3) is able to account

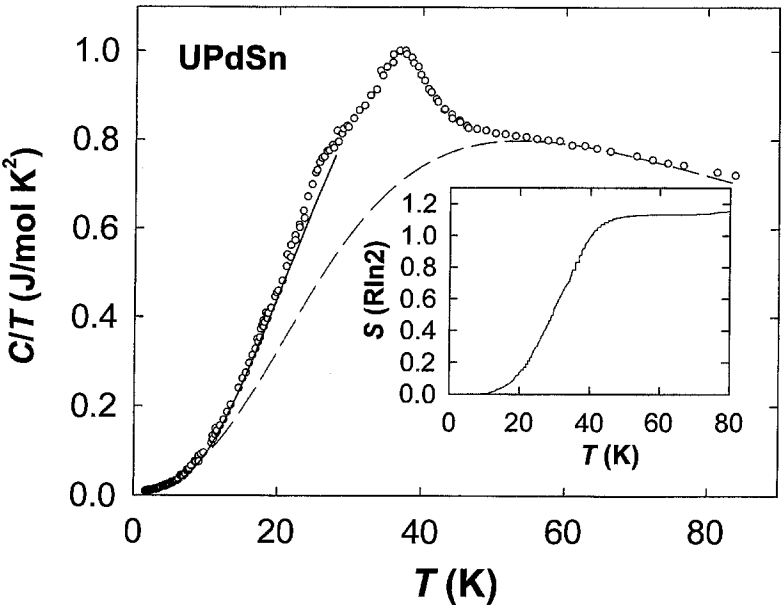

Fig. 5.53. Specific heat in the C/T representation vs. temperature for UPdSn. The dashed line represents the non-magnetic background approximated by a Debye function. The full line is the contribution of the exponential term mentioned in the text, which accounts for collective spin excitations. The inset shows the temperature development of the magnetic entropy. After Havela et al. (1993b).

for all important features of the photoelectron spectra. Finally this turned out to be due to the insufficiency of the calculations themselves. New calculations performed for a realistic magnetic structure (Sandratskii and Kübler 1997b) gave an overall agreement with the spectra and also revealed that the Fermi energy resides in a deep minimum of the density of states, which is a plausible explanation for the low γ-value. Interesting results are provided by the dilution experiment with Lu, substituting for U up to 25%. Magnetic properties develop in a smooth way with weakly decreasing T_N, but the γ-value jumps to 78 mJ/(mol K^2) in $U_{0.85}Lu_{0.15}PdSn$ (Havela et al. 1998b). The $\rho(T)$ dependence studied on pure UPdSn does not reflect clearly the magnetic phase transitions. It is dominated by a broad knee at around 50 K, which is followed by a gradual saturation on the high temperature side. For $T > 150$ K another weak upturn appears (see fig. 5.54). The absolute values were found as high as 2000 μΩ cm at room temperature for a polycrystal, whereas somewhat lower values ($\approx$ 700 μΩ cm) were found for a single crystal bar measured with the current i nearly perpendicular to the c-axis. Even higher absolute values were detected by Kurisu et al. (1991) where they reach nearly 3 mΩ cm, although the same metallic type of behaviour is preserved. Remarkably high values were found also in the temperature dependence of the thermopower, which reaches nearly $S = 50$ μV/K in a broad maximum around $T = 150$ K. At lower T they decrease progressively below $S = 0$ and form a minimum at $T \approx 20$ K.

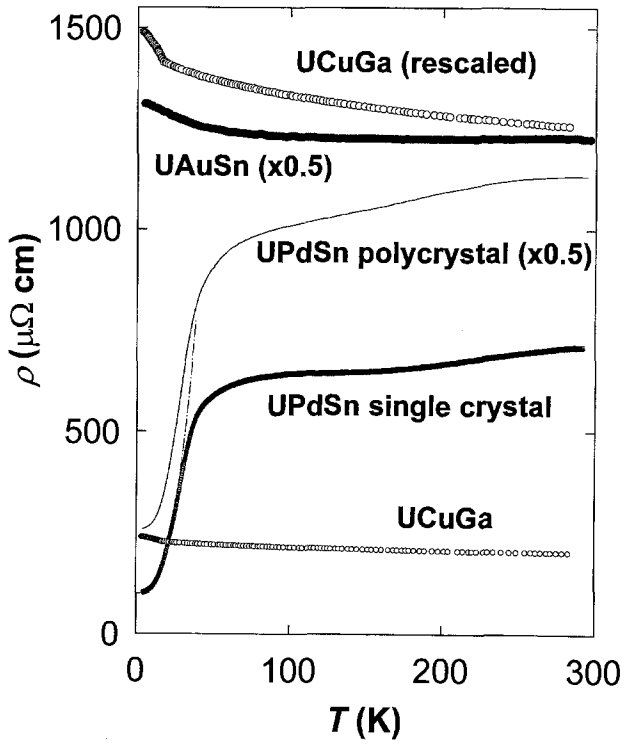

Fig. 5.54. Temperature dependence of the electrical resistivity for various UTSn compounds. The dash-dotted line represents the fit including the exponential term mentioned in the text. For UCuGa, resistivity is displayed twice, showing details with approximately 6 times expanded values (on the top). Compiled from references mentioned in the text.

The saturation of the resistivity at the low-T side can be well described by using an additional exponential term (fig. 5.55) derived for electron-magnon scattering (Andersen and Smith 1979). The total resistivity is described by the expression

$$\rho = \rho_0 + aT^2 + bT(1 + 2T/\Delta)\exp(-\Delta/T),$$

where besides a pre-factor b one may recognize also Δ, the width of the gap in magnon dispersion relations. The latter was found to be equal to about 44 K for UPdSn (Havela et al. 1993b). This value is consistent with $\Delta = 48$ K, the value extracted from the specific heat $C(T)$ assuming an analogous term describing the magnon heat capacity $C_m = fT^{1/2}\exp(-\Delta/T)$ (see fig. 5.53). Provided that we indeed deal with magnons, the Δ value is thus the energy of the lowest magnon mode, and should be smaller than the anisotropy energy of the hard- and easy-axis, which is indeed the case. Such anisotropy can be estimated, e.g., as the difference of the respective paramagnetic Curie temperatures, amounting to ≈ 100 K.

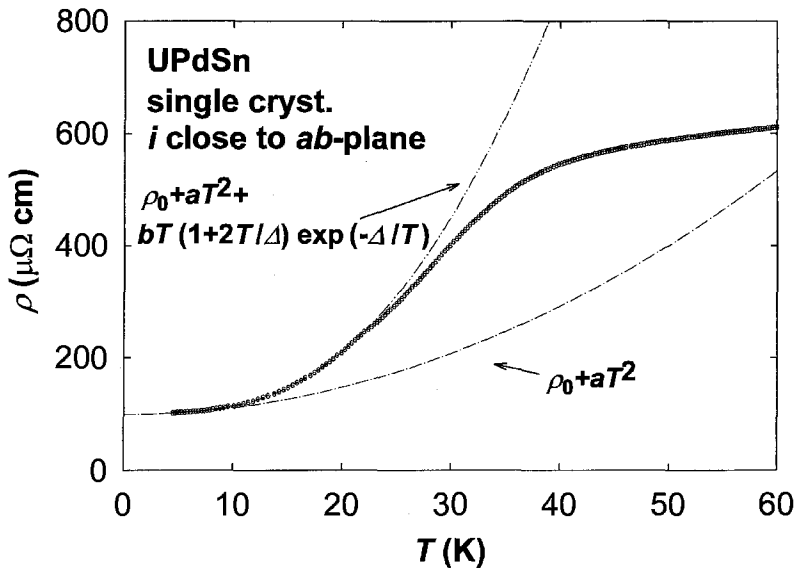

Fig. 5.55. Temperature dependence of the electrical resistivity for a single crystal UPdSn. The direction of electrical current i was close to the ab-plane. The lines represent the fits mentioned in the text. After Havela et al. (1993b).

Figure 5.56 shows how the canting of magnetic moments in the high-field phase affects the resistivity in the low-T limit. The magnetic phase diagram for the field along the a- and b-axis was determined by detailed magnetization measurements complementing neutron diffraction studies (Nakotte et al. 1993b). It was shown that the high-temperature magnetic phase vanishes in fields of about 1 T (see fig. 5.57).

The maximum slope of $\rho(T)$ shifts to higher temperatures with increasing hydrostatic pressure. The estimated shift of T_N reaches 0.14 K/kbar (Kurisu et al. 1991). The field dependence of resistivity was studied at $T = 4.2$ K on a single crystal with $H \| b$-axis (Sechovsky et al. 1995c). It is constant up to $\mu_0 H = 3$ T, but starts to decrease due to a metamagnetic transition, providing practically a mirror image to the increase of the magnetization. In $\mu_0 H = 35$ T it is reduced by about 35% compared to the zero-field value.

Interesting information has been provided by ^{119}Sn (de Boer et al. 1992; Kruk et al. 1996b) and ^{57}Fe (Vagizov et al. 1997) Mössbauer effect experiments, which show that a certain fraction of Sn atoms or Fe atoms in Pd sites experience zero magnetic hyperfine field. This fraction decreases with decreasing T and disappears at 25–30 K with the appearance of the low temperature structure. This phenomenon can be associated with the above-mentioned fluctuations of the x-component of the U-moments at 25 K $< T <$ 40 K.

The Au and Sn atoms in *UAuSn* are randomly distributed over the In positions in the $CaIn_2$ structure type (de Boer et al. 1992; Robinson et al. 1993b). This compound has been studied in polycrystalline form only. A cusp in $\chi(T)$ at $T = 36$ K (fig. 5.58) points to AF ordering, but there is only a very broad anomaly in $C(T)$ around this temperature. At higher temperatures (above 80 K) a modified Curie–Weiss law was observed with the

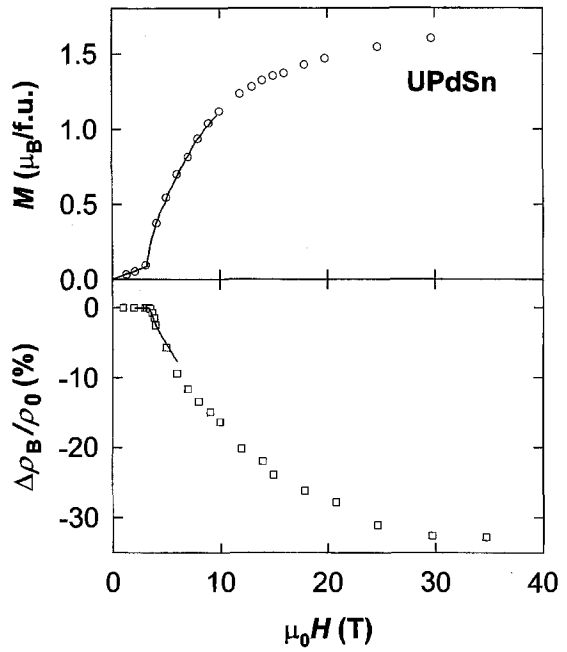

Fig. 5.56. Magnetization curve and the relative electrical resistivity for $i \| b$-axis in UPdSn at $T = 4.2$ K in the magnetic field H applied along the b-axis. The lines represent data taken with field swept continuously. After Sechovsky et al. (1995c).

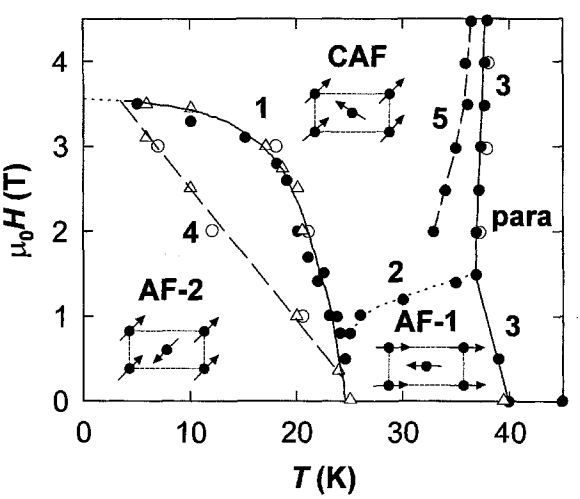

Fig. 5.57. Schematic magnetic phase diagram UPdSn. For details see the text.

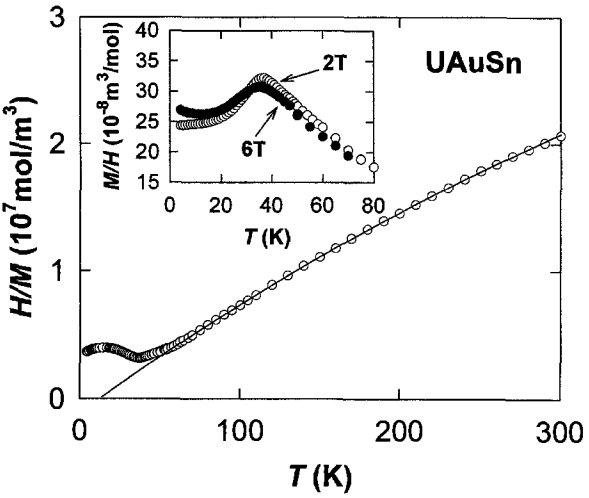

Fig. 5.58. Temperature dependence of the inverse susceptibility H/M measured on a UAuSn polycrystal. The inset shows low temperature details of M/H in various magnetic fields. After de Boer et al. (1992).

parameters $\Theta_p = 12$ K, $\mu_{eff} = 2.7\,\mu_B$/U, and $\chi_0 = 4.5 \times 10^{-9}$ m^3/mol. A γ-value of about 80 mJ/(mol K^2) can be estimated form the linear C/T vs. T^2 part between 5 and 14 K, but an upturn below $T = 5$ K leads to $\gamma \approx 110$ mJ/(mol K^2). This value can be gradually suppressed by a magnetic field, and could thus be attributed to magnetic excitations in a presumably frustrated system. Magnetization measurements at $T = 4.2$ K performed on field-oriented powder show no noticeable metamagnetic transition, only a weak tendency to saturation, and a magnetization corresponding to $1.2\,\mu_B$/U is achieved in $\mu_0 H = 35$ T. Powder neutron diffraction experiments showed long-range order with a collinear antiferromagnetic structure and an orthorhombic magnetic unit cell similar to UPdSn. The U-magnetic moments are parallel to the orthorhombic b-axis (Robinson et al. 1993b). The ferromagnetic coupling along the c-axis conforms to the strongest bonding along this direction. The U-moments $(1.10 \pm 0.02)\,\mu_B$ determined from the neutron diffraction experiment are smaller than those found in the high field magnetization. A signature of a strong disorder was derived from a broad distribution of transferred magnetic hyperfine fields observed by ^{119}Sn Mössbauer spectroscopy (de Boer et al. 1992; Kruk et al. 1996a). It has been deduced that such distribution implies a large randomness in the degree of hybridization of Sn ad U states, leading to certain magnetic inhomogeneity (Kruk et al. 1996a). Then the effect of strong magnetic fields can be seen in forcing the misaligned moments into the field direction.

The atomic disorder is a clear reason for the practically flat $\rho(T)$ dependence shown in fig. 5.54 that increases only slightly with decreasing T. The ρ-value was estimated as 300 μΩ cm (de Boer et al. 1992). Values around 400 μΩ cm were obtained later by Tran and Troc (1993b), who observed also a more pronounced increase of the resistivity below T_N.

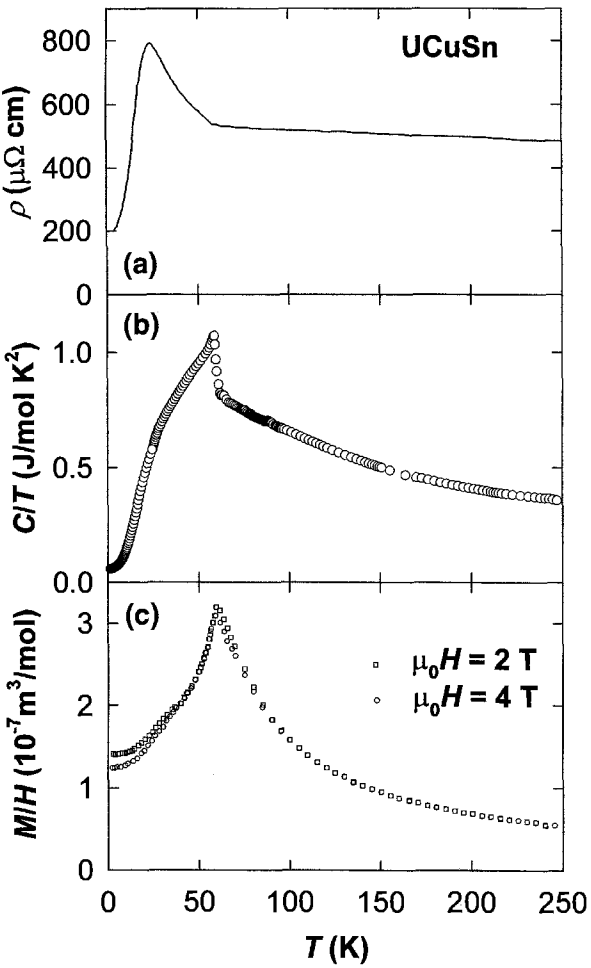

Fig. 5.59. Temperature dependence of the resistivity ρ (a), specific heat C/T (b) and susceptibility M/H of UCuSn. After Nakotte et al. (1996b).

UCuSn has an ordered ternary structure similar to UPdSn, but small displacements of atoms from the lines along the c-axis reduce the symmetry to an orthorhombic one corresponding to space group $P2_1cn$ (Nakotte et al. 1996b). Bulk properties were studied by Fujii et al. (1990b). The most complete work (Nakotte et al. 1996b) shows that UCuSn is antiferromagnetic below $T_N = 62$ K. This temperature is indicated by a sharp cusp in $\chi(T)$. At higher temperatures Curie–Weiss behaviour yields $\mu_{eff} = 3.20\,\mu_B$/U. The positive $\Theta_p = 25$ K can indicate a strong ferromagnetic coupling, presumably along the c-axis (Fujii et al. 1990b). The $\rho(T)$ dependence is flat above T_N ($\rho_{300\,K} = 450$ μΩ cm), and starts to increase abruptly below T_N reaching the maximum value 800 μΩ cm at $T = 25$ K (fig. 5.59). A strong minimum at this temperature was found in the temperature depen-

dence of thermopower (Kawanaka et al. 1997). Weaker anomalies around $T = 25$ K could be found in the specific heat and susceptibility, as well, but neutron diffraction does not show any change of the magnetic structure around this temperature (Nakotte et al. 1996b), the experimental data demonstrated that the magnetic unit cell coincides with the crystallographic one. Interesting results are provided by magnetization measurements at $T = 4.2$ K on free- and fixed-powder samples (fig. 5.60). Both data sets show a two-step metamagnetic behaviour with critical fields of 13 T and 25 T. $M(H)$ tends to saturation in the high field state, and a magnetization corresponding to $1.8\,\mu_B$/U was reached in $\mu_0 H = 38$ T. The fixed-powder branch of the magnetization joins the free-powder one above $\mu_0 H = 30$ T, which means that there is as anomalously low magnetic anisotropy in this compound. Specific-heat measurement yielded $\gamma = 53$ mJ/(mol K^2), as reported by Fujii et al. (1990b). Latter experiments led to $\gamma = 64$ mJ/(mol K^2) and a magnetic entropy estimate of $R \ln 2$ (Kawanaka et al. 1997). Finally, details of the non-collinear magnetic structure have been specified by neutron diffraction and ^{119}Sn Mössbauer spectroscopy (Kruk et al. 1995; Szytula et al. 1996). The coupling along c was found (unlike UPdSn and UAuSn) to be essentially ferromagnetic. The U-moments of $1.9\,\mu_B$ lie in the bc-plane and form an angle of 25° with the b-axis.

For *UCuGa* it was not possible to specify by neutron diffraction if the structure is ordered (GaGeLi-type) or disordered ($CaIn_2$-type) (Tran et al. 1995c). On the other hand, the fact that the magnetic structure is identical with that of UAuSn, with U-moments of $(1.27 \pm 0.06)\mu_B$ oriented along the b-axis, points more to the second possibility. The $\chi(T)$ curve shows a sharp cusp in the vicinity of $T = 30$ K, which marks the transition to an AF state (Sechovsky et al. 1988d; Tran and Troc 1993a). The behaviour in the paramagnetic range is described by the Curie–Weiss law with $\mu_{eff} = 2.54\,\mu_B$/U and $\Theta_p = -7$ K (Tran and Troc 1993a). Specific heat measurements show only a weak anomaly at T_N and lead to a value $\gamma = 115$ mJ/(mol K^2) (Sechovsky and Havela 1988; Sechovsky et al. 1988d). The electrical resistivity equals about 200 μΩ cm at room temperature, and increases progressively with decreasing T (fig. 5.54). Another weak anomaly in the magnetic susceptibility

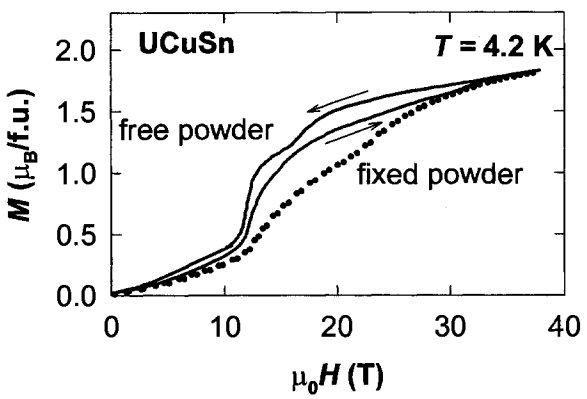

Fig. 5.60. Magnetization curves measured on free-powder and fixed-powder samples of UCuSn at $T = 4.2$ K. Arrows indicate directions of the field sweeps. After Nakotte et al. (1996b).

and the specific heat around $T = 15$ K could be suggestive of a second magnetic phase transition (Sechovsky et al. 1988d). The situation is somewhat unclear, because no such feature was found in latter $\chi(T)$ measurement, although the a noticeable upturn in $\rho(T)$ was seen on the same sample around this temperature but not at T_N (Tran et al. 1993).

The only compound with Sb and the only ferromagnet of this group is *UPdSb*. It is ordered below $T_C = 65$ K. Originally a magnetic moment of $0.7\,\mu_B$/f.u. was reported on the basis of bulk polycrystalline data (Palstra et al. 1987), which also display a remarkably (more than 7 T) wide rectangular hysteresis loop. However, high-field magnetization measurements at $T = 4.2$ K show a spontaneous moment of $1.3\,\mu_B$/f.u. (Sechovsky 1988). The value $\gamma = 52$ mJ/(mol K^2) was deduced from specific heat data. The electrical resistivity has metallic character with a pronounced decrease below T_C. The enormous absolute values (> 5000 μΩ cm) were attributed to cracks in the sample (Palstra et al. 1987).

5.1.4. Compounds with the MgAgAs type structure

Three UTX compounds, *UNiSn, URhSb* and *UPtSn*, and their ThTX counterparts have been reported to crystallize in the cubic MgAgAs-type structure schematically shown in fig. 5.61 (Dwight 1974; Buschow et al. 1985a). This f.c.c. type crystal structure (space group $F\bar{4}3m$), which is closely related ordinary Heusler alloys, is considered as a source of exceptional electronic properties of these UTX and ThTX materials, high-temperature semiconducting behaviour in particular (de Groot et al. 1983; Albers et al. 1987; Ögüt and Rabe 1995). For the ordinary Heusler alloys X_2YZ, the f.c.c. lattices are characterized by the positions: X_1 (1/4, 1/4, 1/4), X_2 (3/4, 3/4, 3/4), Y (0, 0, 0) and Z (1/2, 1/2, 1/2). The X_1 positions are empty in the 1:1:1 transition metal ternaries, as, e.g., NiMnSb (de Groot et al. 1983) and also in UTX and ThTX compounds.

High-temperature susceptibility behaviour of *UNiSn, URhSb* and *UPtSn* can be well approximated by a Curie–Weiss law with $\mu_{eff} = 3.08$, 3.25 and $3.55\,\mu_B$ and $\Theta_p = -75$,

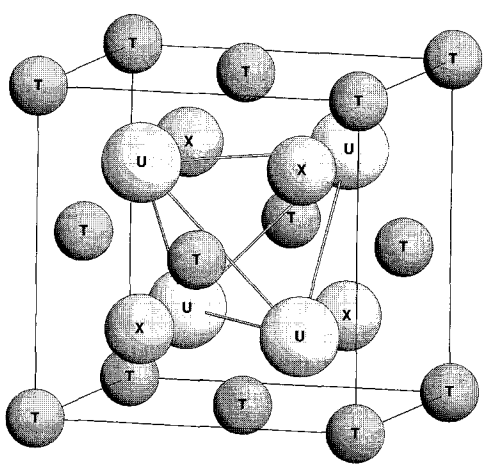

Fig. 5.61. Schematic picture of the cubic MgAgAs-type structure in which crystallize several UTX compounds.

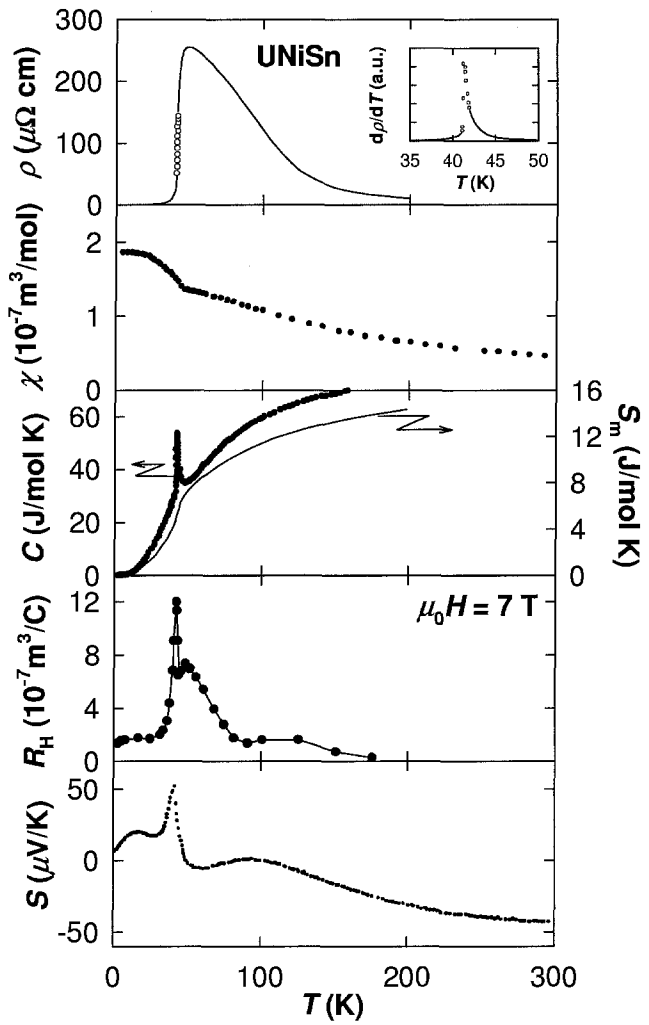

Fig. 5.62. Temperature dependence of the following properties of UNiSn: (a) Electrical resistivity ρ and $\partial\rho/\partial T$, after Kawamata et al. (1992c); (b) Magnetic susceptibility χ, after Aoki et al. (1993a); (c) Specific heat – C, and magnetic entropy S_m, after Aoki et al. (1993a); (d) Hall coefficient, after Diehl et al. (1993); (e) Thermoelectric power S, after Fujii et al. (1989).

-111 and -100 K, respectively. These results indicate local moment character of the U-5f electrons at high temperatures (Palstra et al. 1988). For UNiSn, slightly modified values of $\mu_{\text{eff}} = 3.15\,\mu_B$ and $\Theta_p = -58$ K have been obtained on a high-quality well-annealed sample (Fujii et al. 1989). The Th containing analogues are nearly temperature independent paramagnets (Palstra et al. 1988).

The $\chi(T)$ curve for UNiSn (see fig. 5.62) exhibits a sudden change of slope at 47 K increasing steeper with decreasing temperature and saturating at $\approx 18.5 \times 10^{-8}$ m^3/mol

in the low-temperature limit. This behaviour is strongly suggestive of ferromagnetism below 47 K (Palstra et al. 1986a, 1988; Bykovetz et al. 1988). The magnetic phase transition is reflected in a drastic change of the electrical resistivity. The $\rho(T)$ curve shows a sharp maximum at $T_{max} \approx 52$ K. At temperatures above this maximum, semiconducting behaviour is observed (Palstra et al. 1986a; Fujii et al. 1989), which can be described by a formula $\rho(T) \sim \exp(E_g/(2k_BT))$ with a semiconducting gap of 67 meV (Bykovetz et al. 1988; Fujii et al. 1989). Below T_{max}, the resistivity falls sharply with decreasing temperature with a maximum $\partial\rho/\partial T$ at 41.4 K. As can bee seen in fig. 5.62, an extremely sharp peak at 42 K is observed in the temperature dependence of the thermoelectric power (Fujii et al. 1989, 1993). The temperature dependence of the specific heat (fig. 5.62) yields a sharp λ-type anomaly and abrupt increase of magnetic entropy at 43 K (Bykovetz et al. 1988; Aoki et al. 1990, 1993a; Yuen et al. 1991) clearly demonstrating a first-order magnetic phase transition at this temperature. The magnetic entropy at 43 K is nearly $R \ln 2$. The γ-value is relatively low, 18.2 mJ/(mol K^2). From the analysis of specific heat and susceptibility data, Aoki et al. (1993a) proposed for UNiSn an energy level scheme for the $5f^2$ configuration of the U^{4+} ion in the cubic crystalline-electric-field. It consists of a non-magnetic ground-state doublet Γ_3 a magnetic triplet Γ_4 at 180 K above Γ_3, a non-magnetic singlet at 430 K above Γ_3 and a magnetic triplet Γ_5 at $\approx$ 3000 K above Γ_3. The first order magnetic phase transition to low-temperature antiferromagnetic state was shown to originate from Γ_4. The degeneracy of a quadrupolar moment in the ground state Γ_3 implies the possibility of a Jahn–Teller lattice distortion (Cox 1987), which has indeed been observed experimentally (Akazawa et al. 1996a; Suzuki et al. 1997). From fig. 5.63, one may deduce that at $T = 43$ K a first-order crystallographic transition from the high-temperature cubic symmetry to the low-temperature tetragonal lattice. Both, the longitudinal and transverse elastic moduli decrease rapidly below 100 K. The lattice softening is terminated at T_N, below which a substantial hardening follows (Akazawa et al. 1996a). In contrast to the sharp specific-heat anomaly and the discontinuous change of the lattice parameters at T_N, which are suggestive of a first-order transition, the temperature variation of elastic moduli implies a second-order transition.

Sharp anomalies in the vicinity of 43 K are observed also in the temperature dependence of Hall effect (a sharp peak, see fig. 5.62) and the magnetoresistance (deep sharp minimum). Analysis of Hall data points to at least three types of carriers in the semiconducting state and a complex behaviour at the transition from paramagnetic semiconductor to antiferromagnetic metal (Diehl et al. 1993). The transition is accompanied by only small changes of the carrier density but a large increase of the carrier mobility.

Neutron powder diffraction experiments allowed to determine the type of magnetic ordering at temperatures below the above discussed phase transition. As a result, an AF I magnetic structure of U-moments of 1.42 μ_B (Yethiraj et al. 1989) and 1.55 μ_B (Kawanaka et al. 1989) has been observed. In fact, the magnetic structure consists of ferromagnetic (0 0 1) sheets of moments oriented in the [0 0 1] direction and coupled $+ - + -$ along the same axis. The temperature dependence of the intensity of neutron diffraction peak revealed the onset of a coherent magnetic signal below 47 K (see fig. 5.63). The ^{119}Sn Mössbauer effect investigations (Bykovetz et al. 1988; Yuen et al. 1991), clearly indicated sites with non-zero hyperfine field up to temperatures above 50 K (fig. 5.63), which can be attributed to considerable antiferromagnetic correlations well above the magnetic ordering

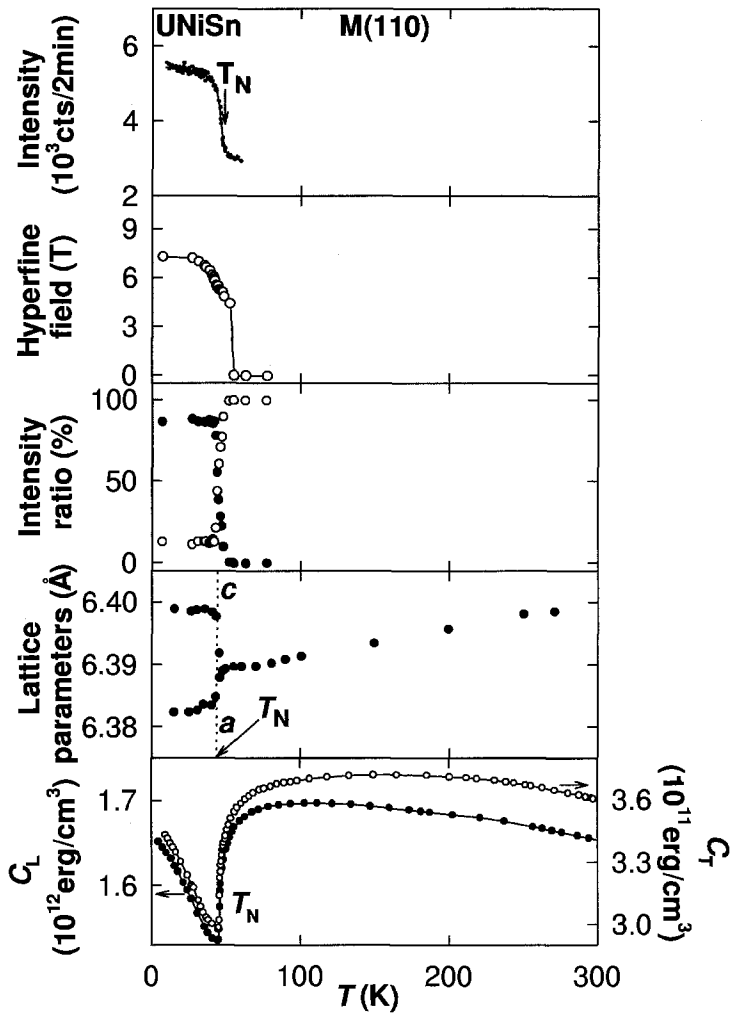

Fig. 5.63. Temperature dependence of the following properties of UNiSn: (a) Neutron diffraction (1 1 0) magnetic peak intensity, after Kawanaka et al. (1989); (b) ^{119}Sn hyperfine field, after Akazawa et al. (1996a); (c) Intensity ratios of the sub-spectrum due to Sn nuclei feeling the internal magnetic field (•) and feeling zero internal magnetic field (○), after Akazawa et al. (1996a); (d) Lattice parameters (Suzuki et al. 1997); (e) Longitudinal and transverse elastic constants, C_L and C_T, respectively, after Akazawa et al. (1996a).

temperature defined by the specific heat anomaly. In fig. 5.63 one can see that in a temperature interval from T_N to 52 K the hyperfine field does not vanish but the number of Sn sites feeling it becomes rapidly reduced.

Kilibarda-Dalafave et al. (1993a, 1993b) studied UNiSn and UThSn by means of far-infrared spectroscopy. In the antiferromagnetic state of UNiSn, they have observed a conductivity mode at 18 cm^{-1}. This mode, which disappears at temperatures above 43 K was

ascribed to a pinned spin density wave. Two phonon lines at 157 and 175 cm^{-1}, detected above T_N, split into four lines below the magnetic phase transition, which is consistent with the tetragonal distortion of the UNiSn lattice at low temperatures.

Within the period of intensive research of UNiSn, it has been found that all the above discussed properties, especially the concomitant appearance of the antiferromagnetic-paramagnetic, metal-semiconductor and tetragonal-cubic crystallographic transitions at $T = 43$ K, are critically dependent on the thermal treatment after melting the compound. The related metallurgical and magnetic phenomena were thoroughly studied by Bykovetz et al. (1988) who have shown that annealing around 800°C for 200 days leads to the formation of mainly that phase exhibiting the low temperature magnetic ordering.

The effects of pressure up to 25 kbar on the resistivity anomaly at T_N (= 43 K) was investigated by Fujii et al. (1989) and Kurisu et al. (1991), who have observed a gradual suppression of the semiconducting behaviour ($\partial \ln E_g/\partial T = -0.60$ meV/kbar) and an increase of T_N ($\partial \ln T_N/\partial T = 11$ $Mbar^{-1}$) with increasing pressure. The positive pressure effect on the Néel temperature is very large and similar to UPdIn (Kurisu et al. 1991) or UCd_{11} (Thompson et al. 1986). In UNiSn it is ascribed to the increase of the carrier density with applied pressure. The rate of the pressure induced suppression of the semiconducting gap is comparable with that observed for CeNiSn (Kurisu et al. 1988). The parameter a of quadratic low-temperature resistivity behaviour $\rho = \rho_0 + aT^2$ and also the value of the residual resistivity ρ_0 are gradually reduced with increasing pressure, which has been attributed to suppression of spin fluctuations (Kurisu et al. 1991). In contrast to pronounced pressure effects, application of a magnetic field up to 13.5 T does not influence the resistivity behaviour substantial. It induces only a slight positive effect on T_N and a negligible change of E_g (Fujii et al. 1989).

Basic features of the valence band in the all three U-compounds were studied by means of resonant photoemission using synchrotron radiation (Höchst et al. 1986). ^{119}Sn NMR investigations of UNiSn were made by Kojima et al. (1990). The observed temperature dependence of the relaxation rate $1/T_1$ was attributed to a local character of 5f-electron fluctuations. Electron spin resonance in UNiSn was studied in comparison its Hf, Zr and Ti counterparts (El-Sayed et al. 1988).

The first theoretical approach to the UNiSn problem has been motivated mainly by the crystal-structure analogy of the MgAgAs structure with the Heusler alloys and with the transition-metal based half-metallic ferromagnets. Albers et al. (1987) have calculated the electronic structure of UNiSn using a spin-polarized scalar relativistic LMTO method. Similar to transition-metal analogues, e.g., NiMnSb, also UNiSn has been found to be a half-metallic magnet with a semiconducting gap minority-spin band structure and metallic behaviour for the majority-spin bands. A U magnetic moment of $1.99\,\mu_B$ has been calculated. In this context, Daalderop et al. (1988) calculated the optical conductivity and magneto-optic Kerr effect. The double polar Kerr angle, 2ϕ, equals 10° in the infra-red and 4° in the visible spectrum. The Kerr rotation originates from interband transitions.

Oppeneer et al. (1996) and Yaresko et al. (1997) have explained the concomitant magnetic phase transition and the metal-insulator transition in UNiSn on the basis of electronic-structure calculations. The energy band approach in which the local density Hamiltonian is generalized with an additional on-site Coulomb interaction U provides a fully satisfactory

TABLE 5.7

Some basic characteristics of UTX and ThTX compounds with the MgAgAs structure: γ–coefficient of the electronic specific heat, type of ground state (AF – antiferromagnet, P – paramagnet, WP – weak paramagnet), μ_U – the uranium ordered magnetic moment (determined by neutron diffraction at 4.2 K), $T_{C,N}$ – magnetic ordering temperature, a, c – lattice parameters at room temperature.

Compound	γ (mJ/(mol K^2))	Ground state	μ_U (μ_B)	$T_{C,N}$ (K)	Ref.	a (pm)	c (pm)	Ref.
UNiSn	28	AF	1.55	46–47	[1–5]	638.5		[1]
	81–20	AF		43	[6]	638.2[1]	639.9[1]	[6]
URhSb	2	P			[1,2]	653.1		[7]
UPtSn	11	?			[1,2]	661.7		[7]
ThNiSn	1.5	WP			[1,2]	654.4		[1]
ThRhSb		WP			[1,2]	666.3		[7]
ThPtSn	2	WP			[1,2]	674.8		[7]

[1] At $T = 5$ K.

References:

[1] Buschow et al. (1985a)
[2] Palstra et al. (1986a)
[3] Kawanaka et al. (1989)
[4] Aoki et al. (1993a)
[5] Aoki et al. (1990)
[6] Suzuki et al. (1997)
[7] Dwight (1974)

picture of both the metallic antiferromagnetic ground state and the paramagnetic semiconducting state. For the semiconducting state a band gap of 120 meV has been obtained. Antiferromagnetic ordering was found to close the gap due to strong interaction between the Ni 3d-states, Sn 4p-states, and completely spin- and orbit-polarized U 5f-states through polarization dependent hybridization and exchange interaction.

The stability of the antiferromagnetism in UNiSn was theoretically investigated by (Isoda 1992), and Isoda and Takahashi (1997). The magnetic-metal and paramagnetic-insulator transition was studied within the extended periodic Anderson model modified by adding the c–f exchange. Isoda and Takahashi analyzed the effect of the crystalline electric field on the magnetic properties of UNiSn.

Attempts to study effects of dilution of the uranium sublattice by non-magnetic Th in solid solutions $U_{1-x}Th_xNiSn$ (Aoki et al. 1990; 1993a) and (Akazawa et al. 1996b) were not successful because of the two phase character of all the prepared samples, except for the terminal compounds (Akazawa et al. 1996b). Both phases crystallize in the MgAgAs-type structure and have generally the $U_{1-x}Th_xNiSn$ stoichiometry, but belong to two different values of χ_r and have different magnetic-transition temperature. For instance the sample with a nominal content of 10% Th shows two peaks in the temperature dependence of the specific heat, namely at $T_1 \approx 39$ and $T_1 \approx 29$ K.

The $\chi(T)$ curve for URhSb shows a broad maximum around $T = 45$ K (Palstra et al. 1988). This result together with the upturn of the magnetization curve above 25 T (Sechovsky and Havela 1988) may be signs of spin-fluctuation effects reminiscent of, e.g., URuAl (see section 5.1.1).

Tran et al. (1995a) reported for the cubic modification of UPtSn the possibility to have an analogous magnetic structure as UNiSn.

5.1.5. Compounds of other structure types

UCuSi and *UCuGe* crystallize in the hexagonal $CeCd_2$-type crystal structure with the space group $P\bar{3}ml$ (Lam et al. 1974). Tran and Troc (1990b) discussed magnetic behaviour of the former compound in terms of simple spin-glass behaviour and the latter material have been described as a re-entrant spin glass system. The conclusion made for UCuSi is corroborated by a neutron diffraction experiment which failed to indicate any magnetic diffraction peaks at low temperatures (Leciejewicz et al. 1991). In the case of UCuGe, the two neutron-diffraction studies (Tran and Troc 1990b; Leciejewicz et al. 1991) revealed antiferromagnetic order. The latter work reported a canted antiferromagnetic structure of uranium magnetic moments of $2.0\,\mu_B$ (at 4.2 K). The magnetic moments are aligned perpendicular to the trigonal axis. In the basal plane they make an angle of 60° with the a-axis, whereas the moments in the plane with $z = 1/2$ are turned by 90° with respect to the direction of moments in the plane with $z = 0$. An explanation why some reports claimed the re-entrant spin-glass behaviour in UCuGe can be found in the work of Tran et al. (1996c). Such effects can be observed in Cu deficient samples, whereas the stoichiometric UCuGe has an antiferromagnetic ground state.

Also two silver containing UTX compounds, UAgAl and UAgGa, have been synthesized (Sechovsky and Havela 1988). High-field magnetization measurements at 4.2 K revealed ferromagnetism in UAgGa with $\mu_s = 0.5\,\mu_B$/f.u. and $\mu_{21T} = 0.78\,\mu_B$/f.u., whereas the Al containing counterpart shows paramagnetic response (Sechovsky and Havela 1988).

5.2. UT_2X_2 compounds

Traditionally, two large families of UT_2X_2 compounds are known and studied intensively, namely the silicides UT_2Si_2 and the germanides UT_2Ge_2, both with various late transition metals T. The two crystal structures characteristic for these materials are ordered ternary variants of the $BaAl_4$-type tetragonal structure. A more frequently occurring structure, in which more than 700 intermetallic compounds are known to crystallize, is the body-centred $ThCr_2Si_2$-type associated with the space group I4/mmm (Parthé and Chabot 1984; Villars and Calvert 1991). The other is the $CaBe_2Ge_2$-type structure which has a similar tetragonal cell dimensions. Its Bravais lattice, however, is primitive (space group: P4/nmm) because of an interchange of one half of the Be and Ge position with respect to the Cr and Si positions in $ThCr_2Si_2$ (see fig. 5.64). An extended review on the co-ordination in the former type compounds can be found in the report of Just and Paufler (1996). Single crystal refined structure parameters of various RET_2Ge_2 compounds including UMn_2Ge_2 can be found in (Venturini and Malaman 1996). Both types of structure adopted by the UT_2X_2 compounds are built up of U, T and X basal-plane atomic layers pilled up along the c-axis. The main difference between the two types is the stacking along c, which is U–X–T–X–U–X–T–X–U... for the $ThCr_2Si_2$-type and U–T–X–T–U–X–T–X–U... for the $CaBe_2Ge_2$-type. Thus in the former structure type the uranium and transition metal atoms are separated by the X-atom layers, whereas the T- and X-atom layers are interchanged in one half of the unit cell in the latter one. This difference should definitely have important consequences for the electronic structure of the involved UT_2X_2 compounds, especially with respect to the 5f-ligand hybridization and electronic properties in which the hybridization plays a considerable role. These structures, in defected form, are observed also in some non-stoichiometric compounds (with respect to the 1:2:2 stoichiometry) U–T–Ga and U–T–Sn

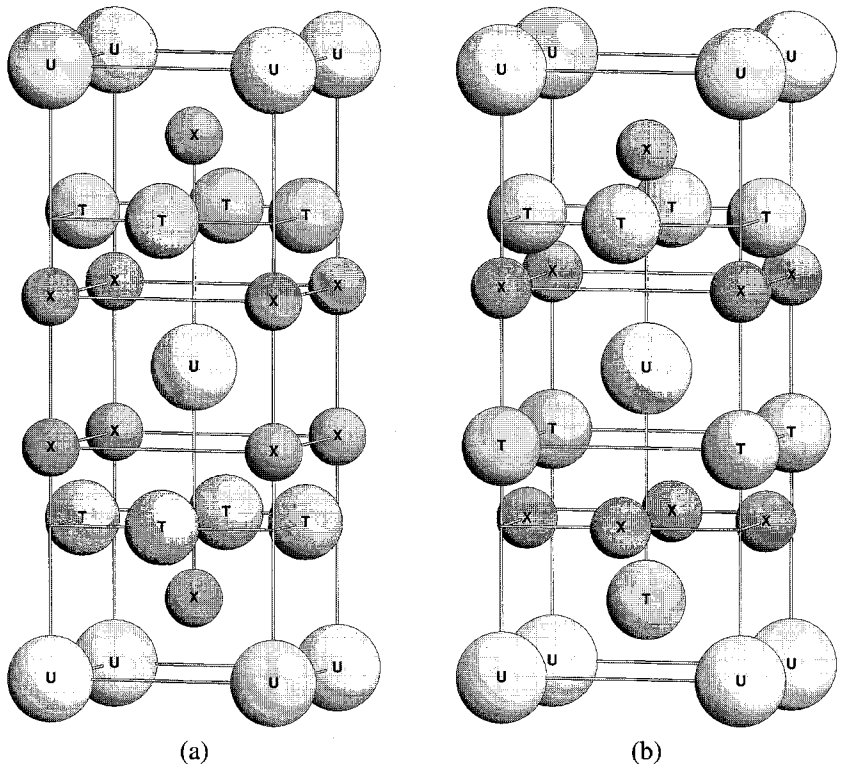

Fig. 5.64. Schematic drawing of crystal structure types adopted by the UT_2X_2 (X = Si, Ge, Sn, Ga) compounds: (a) $ThCr_2Si_2$ type, (b) $CaBe_2Ge_2$ type.

which are included in this sub-chapter, as well. Whereas the gallides crystallize by rule in the $ThCr_2Si_2$-type structure the stannides adopt the $CaBe_2Ge_2$-type. Finally, we should also consider the UT_2X_2 pnictides with X = P, As.

Despite severe metallurgical difficulties in some cases, newly available single crystals of a good number of 1:2:2 compounds facilitated physicists to realize important macroscopic and microscopic experiments revealing outstanding anisotropic features of these materials. This was especially effective in the case the most attractive member of the 1:2:2 class – URu_2Si_2 owing to its unconventional behaviour with heavy-fermion features and the coexistence of antiferromagnetic order of very low U magnetic moments and superconductivity.

Besides uranium based materials the research has progressed also in the direction of NpT_2X_2 and PuT_2X_2 compounds which are reviewed at the end of this chapter.

For practical reasons we include also information on Th analogues, which are frequently considered as reference compounds with a nonmagnetic element on the actinide sites.

5.2.1. Silicides – UT_2Si_2

Review of some structure, magnetic and electronic parameters of UT_2Si_2 compounds can be found in table 5.8.

TABLE 5.8

Some basic characteristics of UT_2Si_2 compounds:
γ – coefficient of the electronic specific heat, type of ground state (F – ferromagnetic, AF – antiferromagnetic, UAF – uncompensated antiferromagnetic, PP – Pauli paramagnetic), μ_U – the uranium ordered magnetic moment (determined by neutron diffraction at 4.2 K), $T_{C,N}$ – magnetic ordering temperature, T_{tr} – temperatures of other magnetic phase transitions (in the ordered state), Anis. – easy magnetization direction (determined by neutron diffraction and/or magnetization measurements of single crystals), a, c – lattice parameters at room temperature, str. type (I – tetragonal body-centered $ThCr_2Si_2$-type structure, P – tetragonal primitive $CaBe_2Ge_2$-type structure).

Compound	γ (mJ/(mol K^2))	Ground state	μ_U (μ_B)	$T_{C,N}$ (K)	T_{tr} (K)	Anis.	Ref.	a (pm)	c (pm)	Str. type	Ref.
UCr_2Si_2	–	AF	–	27	–	–	[1]	391.09	1050.38	I	[1]
		AF		30			[2]	391.06	1050.28	I	[2]
UMn_2Si_2	–	F[a]	1.14	375	80[b]	$\|c$	[1,3]	391.76	1028.85	I	[1]
UFe_2Si_2	17.5	PP	–	–	–	–	[4,3]	394.47	954.41	I	[1]
UCo_2Si_2	–	AF	1.42	85	–	$\|c$	[5]	390.78	963.71	I	[1]
UNi_2Si_2	22	UAF	2.2	124	103, 53	$\|c$	[6,7]	396.97	952.25	I	[1]
UCu_2Si_2	–	F	2.0	103	–	$\|c$	[8,5]	398.53	994.63	I	[1]
URu_2Si_2	180	AF/(S)	0.04	17.5	(0.8)[c]	$\|c$	[9,10]	412.79	959.18	I	[8]
URh_2Si_2	10	AF	1.96	137	137	$\|c$	[11,12,13]	400.78	1002.23	I	[1]
UPd_2Si_2	–	AF	2.3	136	108	$\|c$	[14]	423.0	987.3	I	[15]
URe_2Si_2	–	PP[d]	–	–	–	–	[15]	–	–	–	–
UOs_2Si_2	–	PP[d]	–	–	–	–	[15,16]	412.14	964.84	I	[16]
UIr_2Si_2	105	AF	0.1	6	–	$\|c$	[17,18]	408.71	981.62	P	[1]
UPt_2Si_2	32	AF	1.67	35	–	$\|c$	[19]	419.72	969.06	P	[19]
UAu_2Si_2	92	?[e]	1.16	55	48, 21.5	?	[20,21]	421.14	1027.41	I	[1]

[a] Ferromagnetic alignment of both the U and Mn (2.36 μ_B) magnetic moments.
[b] Magnetic phase transition between the ground state magnetic structure and the high-temperature phase in which Mn moments only are ferromagnetically ordered whereas no ordering is observed in the U sublattice.
[c] Critical temperature of transition to superconducting state.
[d] $\chi = 1.8 \times 10^{-8}$ m^3/mol.
[e] Magnetic ordering with a considerable spontaneous magnetization, complex magnetic structure may be inferred from resistivity data (Lin et al. 1997).

References:

[1] Buschow and de Mooij (1986)
[2] Hiebl et al. (1990)
[3] Szytula et al. (1988a)
[4] Szytula et al. (1988b)
[5] Chelmicki et al. (1985)
[6] Ning et al. (1991)
[7] Lin et al. (1991a??)
[8] Giorgi et al. (1988)
[9] Palstra et al. (1985)
[10] Broholm et al. (1991)
[11] Miyako et al. (1992)
[12] Ptasiewicz-Bak et al. (1981)
[13] Burlet et al. (1992)
[14] Shemirani et al. (1993)
[15] Palstra et al. (1986b)
[16] Hiebl et al. (1983a)
[17] Dirkmaat et al. (1990a)
[18] Verniere et al. (1996a)
[19] Steeman et al. (1990)
[20] Lin et al. (1997)
[21] Rebelsky et al. (1991a)

Only basic crystal-structure data and susceptibility results obtained on polycrystals are available for *UCr_2Si_2* (Buschow and de Mooij 1986; Hiebl et al. 1990) suggesting antiferromagnetic ordering below 27–30 K, where the temperature dependence of susceptibility shows a sharp maximum. Dilution of the uranium sublattice by non-magnetic yttrium in $(U_{1-x}Y_x)Cr_2Si_2$ does not only lead to a rapid suppression of magnetic ordering but also

to loss of the high-temperature Curie–Weiss behaviour. The compounds with $x \geqslant 0.5$ then behave as temperature independent paramagnets with $\chi_{300\,K} < 2 \times 10^{-8}$ m^3/mol whereas the room-temperature susceptibility of YCr_2Si_2 amounts less than half of that value (Hiebl et al. 1990).

In *UMn_2Si_2*, a typical situation of the UMn_2T_2 compounds is observed. Both U and Mn atoms are carrying magnetic moments. The spontaneous magnetization observed below 377 K indicates ferromagnetic ordering (Buschow and de Mooij 1986). A powder neutron scattering study (Szytula et al. 1988a) provided a detailed explanation of the peculiar magnetization behaviour above and below 80 K (Dirkmaat et al. 1990b). In particular, it has been shown that the ground state magnetic structure consists of both the U and Mn magnetic moments ferromagnetically ordered and parallel to the *c*-axis. Above 80 K, however, magnetic ordering of moments in the uranium sublattice disappears whereas the ferromagnetism in the Mn sublattice persists up to T_C. This result points to the fact that the U–Mn inter-sublattice exchange interaction is apparently much weaker than the exchange interaction within the individual U and Mn sublattices and above 80 K virtually no coupling between the two sublattices exists. The pulsed NMR study of the hyperfine magnetic field at the ^{55}Mn site (Chaghule et al. 1991) brought a contradictory result claiming that the NMR data can only be explained if the uranium sub-lattice orders antiferromagnetically or if the uranium atoms carry a small or no magnetic moment. An analogous result was obtained from this study also for the germanide counterpart.

The fact that the exchange interactions within the Mn sublattice are responsible for determining the magnetic ordering temperature of UMn_2Si_2 is well documented by little effect on T_C produced by the substitution of uranium atoms in by thorium in solid solutions $U_{1-x}Th_xMn_2Si_2$ (Bazela and Szytula 1989) for $x < 0.5$. When further increasing the Th concentration the magnetic ordering temperature even increases but the character of the susceptibility anomaly points to a change of magnetic order from ferromagnetic to antiferromagnetic.

UFe_2Si_2 exhibits Pauli paramagnetism down to lowest temperatures with the susceptibility of the order of (1–2) $\times 10^{-8}$ m^3 mol^{-1} (Szytula et al. 1988a). The rather low value of $\gamma = 17.5$ mJ mol^{-1} K^{-1} is points to a low density of 5f states at E_F, which is consistent with lack of magnetism in this compound.

An interesting case is represented by the development of magnetism across the *$U(Fe_xMn_{1-x})_2Si_2$* quasiternary series (Bazela and Szytula 1989; Bara et al. 1991). The strong ferromagnetism in UMn_2Si_2 is rapidly suppressed with substitutions of Mn by Fe and T_C is approaching zero already around $x = 0.4$. Analysis of the effective paramagnetic moments suggests the loss of U magnetic moment already for $x = 0.1$.

UCo_2Si_2 orders antiferromagnetically with ferromagnetic basal-plane layers of U magnetic moments parallel to the *c*-axis which are coupled in a simple sequence $+ - + -$ (AF type-I structure) in the same direction (Chelmicki et al. 1985). This magnetic ordering appears below $T = 85$ K where the temperature dependence of the susceptibility exhibits a clear maximum. No data on single crystals are available.

Compared to previous materials, *UNi_2Si_2* has attracted considerably much more attention mainly owing to its rich magnetic phase diagram (see fig. 5.65). Several magnetic phase transitions which appear in a zero magnetic field have been first indicated by magnetization measurements on polycrystals (McElfresh et al. 1990) and powder neutron diffraction experiment (Chelmicki and Leciejewicz 1983; Chelmicki et al. 1985). They were later

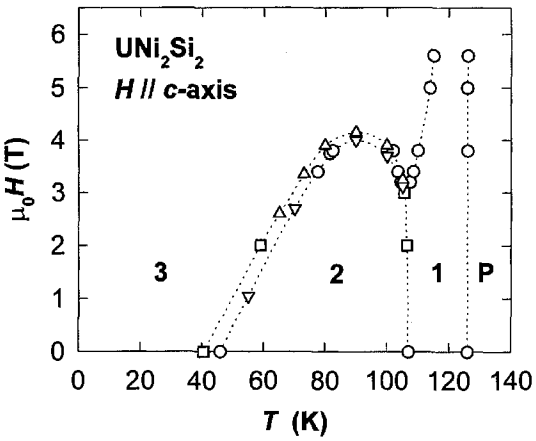

Fig. 5.65. Schematic magnetic phase diagram of UNi_2Si_2 in a magnetic field parallel to the c-axis. The data are taken from neutron diffraction study of a single crystal (Svoboda et al. 1997) made in regimes of isofield heating (○) and cooling (□) and isothermal increase (△) and decrease (▽) of a magnetic field. The pronounced hysteresis of the transition between the ground-state phase and antiferromagnetic phase.

confirmed and specified in detail by single-crystal investigations using neutron scattering (Lin et al. 1991a; Rebelsky et al. 1991b) and by measurements of the magnetization, resistivity and Hall effect (Ning et al. 1990), thermoelectric power (Ning et al. 1991) and thermal expansion (Zochovski et al. 1995; Honda et al. 1998b). We shall devote here some more space to this compound in order demonstrate the specific features of 1:2:2 compounds in some detail.

Below the magnetic ordering temperature (124 K), UNi_2Si_2 exhibits in zero external magnetic field three ordered phases, all with the uranium magnetic moments oriented along the c-axis and coupled ferromagnetically within the basal plane sheets, but with various coupling along the c-axis. Such magnetic structures can be described by a general propagation vector $\boldsymbol{q} = (0, 0, q)$ and appear with decreasing temperature in the following sequence:

1. Phase 1 – an incommensurate longitudinal spin-density wave (ILSDW) in the high-temperature range 103 K $< T <$ 124 K. The propagation vector of this structure varies with temperature ($q = 0.745$ at $T = 110$ K).
2. Phase 2 – a simple body-centred antiferromagnet AFI with a uranium moment of $(1.6 \pm 0.3)\mu_B$ in the intermediate temperature interval between 53 and 103 K. This phase has $q = 1$, which means a uranium moment coupling along the c-axis of the sequence $+ - + - + -$.
3. Phase 3 – the low-temperature phase ($T <$ 53 K) shows a similar scattering pattern as that of the high-temperature phase, with $q = 2/3$ producing additional magnetic scattering at the nuclear Bragg peaks corresponding to a ferromagnetic moment of $(1.0 \pm 0.3)\mu_B$/U atom. This can be attributed either to a longitudinal spin-density wave with a maximum moment of $2.7\,\mu_B$ superimposed on a constant ferromagnetic background component or as a squared-up wave with equal uranium moment

of 2.22 μ_B coupled along the c-axis in the sequence $++-++-$. The former one is claimed by Rebelsky et al. (1992) to be the more probable option.

The phase transitions at 53 K and 103 K are both first order (the former one is connected with a considerable hysteresis as seen in fig. 5.65 indicating that the spin flips at the transition cost the system a lot of energy), whereas magnetic ordering appears by a second order transition and with a conventional critical scattering above 124 K centred on the wave vector $\boldsymbol{q}$. The effect of biquadratic exchange of the axial Heisenberg model has been analyzed (Mailhot et al. 1992) as an alternative to the ANNNI (Anisotropic Next Nearest Neighbor Ising) model (Selke 1988) to reproduce properly the transition between the $q = 1/2$ and $q = 2/3$ phases in materials of the UNi_2Si_2 type.

In fig. 5.65 showing the magnetic phase diagram, we can see that when applying an external magnetic field along the c-axis the stability range of the low-temperature phase (3) moves to higher temperatures. The disappearance of the ferromagnetic component in fields above 2 T reported by (Rebelsky et al. 1992) has not been confirmed by measurements of Svoboda et al. (1997). Results of magnetization measurements (Rebelsky et al. 1992; Takeuchi et al. 1994; Svoboda et al. 1997) in conjunction with thermal expansion and magnetostriction data (Zochovski et al. 1995) point to the disappearance of phase 2 in fields above 3.8 T. Neutron data shown in fig. 5.67 reveal that in 2.95 T the LSDW phase appears in between phases 1 and 2 in the temperature region around $T = 103$ K. This phase actually emerges above 2 T. Refinement of data taken for phase 3 show that q varies with magnetic fields ($q = 0.72$ in 2.9 T) approaching the value of the high-field phase ($q = 2/3$). Above 6 T only the LSDW is suggested to exist in the whole temperature range up to T_N (Zochovski et al. 1995). This phase exists at $T = 4.2$ K, at least up to 40 T, as follows from the lack of any metamagnetic transition on the c-axis magnetization curve (Honda et al. 1998b). Magnetization data at $T = 77$ K (Takeuchi et al. 1994) confirm the stability of this phase at least up to 25 T, which was the maximum field of the reported measurement.

The magnetic phase transitions in UNi_2Si_2 are well identified by anomalies in the temperature dependence of the magnetization (Takeuchi et al. 1994), ac susceptibility (Torikachvili et al. 1992), electrical resistivity (Ning et al. 1990; Honda et al. 1998b), thermoelectric power (Ning et al. 1991), thermal expansion (Zochovski et al. 1995; Honda et al. 1998b) and magnetostriction (Zochovski et al. 1995) measured in various magnetic fields. Zero-field data are shown in fig. 5.66. Some results measured in 3 T can be seen in fig. 5.67. The transitions $1 \leftrightarrow 2$ and $2 \leftrightarrow 3$ in zero magnetic field are as a rule accompanied by pronounced anomalies, the onset of magnetic ordering (ILSDW) around 123 K is not very well visible. The anomalies are particularly well seen for the measurements in a magnetic field or the temperature gradient along the c-axis which are strongly sensing a sudden change of the propagation vector of the magnetic structure at the transition. In this respect the sudden increase of the resistivity at the $2 \rightarrow 3$ transition, which is associated with the increase of the size of the magnetic unit cell along the c-axis (from $2c$ to $3c$), should be pointed out. The onset of magnetic ordering at T_N can be recognized very well in the temperature dependence of thermoelectric power where a clear anomaly characterized by a sudden change of slope of the $S(T)$ curve is seen. Optical reflectance study on UNi_2Si_2 (Cao et al. 1993) suggests the formation of a pseudo-gap over a portion of Fermi surface, opening in the ILSDW phase between 103 and 124 K.

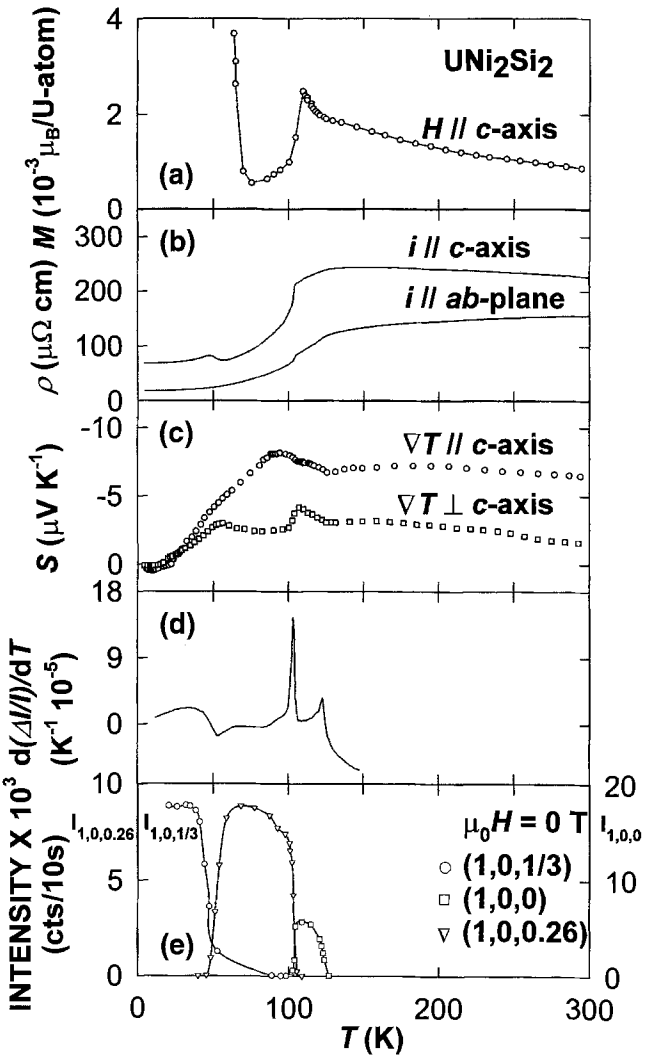

Fig. 5.66. Temperature dependence of the following properties of UNi_2Si_2 measured on single crystals (in the temperature region involving all the magnetic phase transitions): (a) Magnetization M in the magnetic field $\mu_0 H = 0.01$ T applied along the c-axis (authors' own data); (b) Electrical resistivity ρ for different directions of the current i – data taken from Ning et al. (1990) or Honda et al. (1998b); (c) Thermoelectric power S along and perpendicular to the c-axis – data taken from Ning et al. (1991); (d) Thermal expansion coefficient along the c- (α_c) axis – data taken from Zochovski et al. (1995); (e) Intensity of the magnetic neutron reflections (1, 0, 1/3), (1, 0, 0) and (1, 0, 0.26) – data taken from Rebelsky et al. (1992).

The high-field magnetization data obtained on a single crystal at 4.2 K in fields up to 40 T (Honda et al. 1998b) and at 77 K in fields up to 25 K (Takeuchi et al. 1994) confirm the huge magnetocrystalline anisotropy with the easy-magnetization direction along the c-axis

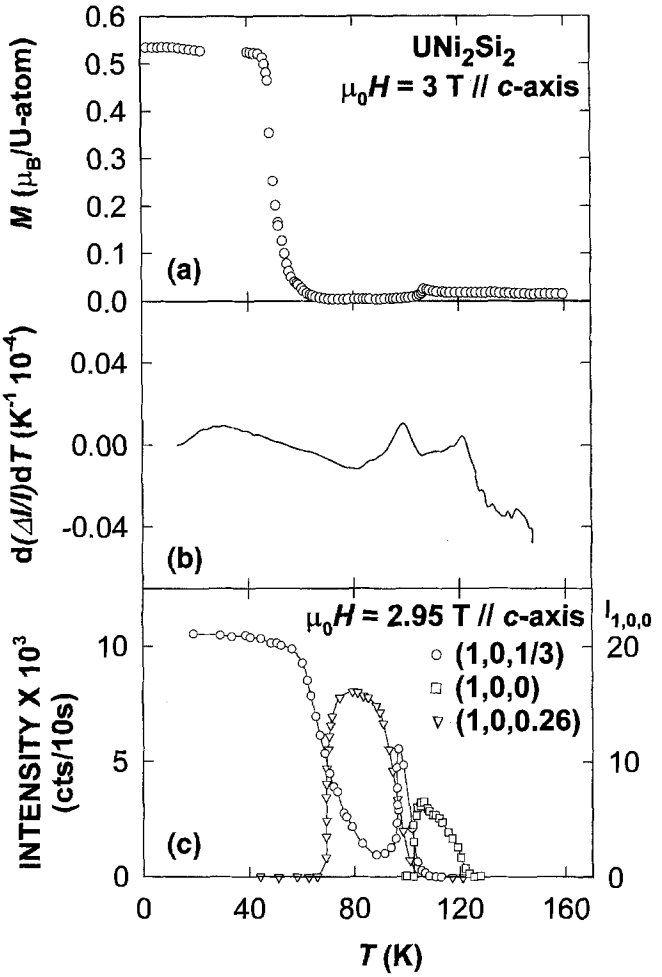

Fig. 5.67. Temperature dependence of the following properties of UNi_2Si_2 measured on single crystals in the magnetic field along the c-axis (in the temperature region involving all the magnetic phase transitions): (a) the c-axis magnetization in 3 T – data taken from Takeuchi et al. (1994); (b) thermal expansion coefficient along the c- (α_c) axis in 3 T – data taken from Zochovski et al. (1995); (c) intensity of the magnetic neutron reflections (1, 0, 1/3), (1, 0, 0) and (1, 0, 0.26) in 2.95 T applied along the c-axis – data taken from Rebelsky et al. (1992).

also in this material. Also here the anisotropy field by far exceeds the maximum fields of the experiments. The c-axis magnetization at $T = 4.2$ K yields a spontaneous moment of $\approx 0.53\,\mu_B$/f.u. The perpendicular component is paramagnetic yielding only $0.16\,\mu_B$/f.u. in 40 T, whereas $0.6\,\mu_B$/f.u. is measured in the easy magnetization direction in the same field. The uniaxial anisotropy is observed also in the high temperature susceptibility data (Takeuchi et al. 1994; Ning et al. 1991). From the room temperature down to 124 K the susceptibility along the c-axis follows the Curie–Weiss law with $\mu_{eff} = 3.34\,\mu_B$/f.u. and

$\Theta_p = -4.3$ K (Takeuchi et al. 1994). In the perpendicular direction the value of the effective moment compares well with the c-axis value. However, the Θ_p value is large and negative, more negative than 400 K (Ning et al. 1991), which is a situation similar to that in the hexagonal UTX compounds of the ZrNiAl-type (see section 5.1). We observe a pronounced anisotropy also in other electronic properties like the electrical resistivity and thermoelectric power, as displayed in fig. 5.66 (Ning et al. 1991), and the thermal expansion and compressibility ($\kappa_a = 2.4 \times 10^{-3}$ GPa^{-1}, $\kappa_c = 1.6 \times 10^{-3}$ GPa^{-1}) reported by Honda et al. (1998b). Measurements of the electrical resistivity of UNi_2Si_2 under external pressure up to 2.2 GPa (Honda et al. 1998b) revealed that T_N is nearly pressure independent, whereas the "103 K" transition shifts to lower temperatures with a rate $dT_2/dp = -2.5$ K/GPa. On the other hand, the temperature T_1 of the low-temperature transition rapidly grows with pressure ($dT_1/dp = +10$ K/GPa above 0.6 GPa). Thus, external pressure suppresses the intermediate magnetic phase as a consequence of pressure induced changes of the exchange interaction along the c-axis.

When inspecting the magnetization curves, one can see that the value of the spontaneous magnetization measured along the c-axis, ranging from 0.53 μ_B/f.u. (Honda et al. 1998b) to 0.56 μ_B/f.u. (Takeuchi et al. 1994), in the case of the above suggested $++-$ coupling along the c-axis yields a magnetic moment 1.59–1.68 μ_B/f.u. which is considerably lower than 2.22 μ_B/U atom. This discrepancy may be partly explained when admitting the possibility of a nonzero moment induced on the Ni sites oriented antiparallel to the U moment.

UCu_2Si_2, in contrast to the previous complex case, exhibits only simple collinear ferromagnetic ordering below $T = 104$ K with uranium magnetic moments oriented along the c-axis, which was inferred from several powder neutron diffraction studies (Chelmicki et al. 1985; Giorgi et al. 1988). The low-field magnetization shows a peak at 107 K (McElfresh et al. 1990) indicating that the ferromagnetic ordering may have an antiferromagnetic precursor. This is probably sort of an incommensurate spin density wave similar to UNi_2Si_2, although no magnetic ordering between 104 K and 107 K has been confirmed by neutron diffraction. The fact that the magnetic behaviour of different samples of this material may suffer of metallurgical difficulties (antistructure atoms, stacking faults, stoichiometry deviations) is probably the main source of occasional antiferromagnetic behaviour reported and discussed by Kuznietz et al. (1995a). The pronounced thermomagnetic irreversibility observed in polycrystalline samples in low magnetic fields below T_C is discussed by Roy et al. (1995a) in terms of a metastable magnetic response due to the effect of strong temperature dependent magnetic anisotropy in co-operation with randomness introduced by lattice defects.

Dilution of the uranium sublattice by yttrium atoms leads to a linear decrease of the ordering temperature. For concentrations $0.4 < x \leqslant 0.875$ susceptibility anomalies and metamagnetism are observed as evidences of antiferromagnetism (Hiebl et al. 1990). In $U_{0.5}Y_{0.5}Cu_2Si_2$, a modulated antiferromagnetic collinear structure of U magnetic moments (parallel to the c-axis) with $\boldsymbol{q} = (0, 0, 0.866)$ is observed (Leciejewicz et al. 1993) suggesting that the RKKY-type exchange interactions are dominating in this system. Effects of dilution of the uranium sublattice by Th were studied on samples of the *$Th_{1-x}U_xCu_2Si_2$* system by means of specific heat, susceptibility, magnetization and electrical resistivity measurements (Giorgi 1987; Lenkewitz et al. 1997). Materials with $x \geqslant 0.15$ are ferromagnetic and the samples in the critical concentration region show enhanced values of

C/T (= 460 mJ mol^{-1} K^{-1}). The compounds showing no magnetic ordering down to lowest temperatures exhibit the specific heat behaviour following the relation $C/T \sim -\ln T$, while the susceptibility follows in a large temperature range (up to 200 K) a power law $\chi \sim T^{\eta}$ and the temperature dependence of the resistivity is linear close to the low temperatures limit. These results are used to discuss these materials in terms of a non-Fermi-liquid (NFL) system. Hiebl et al. (1990) reported that the substitution of Cr for Cu does not alter the magnetic ordering temperature, which remains above 100 K for $x \leqslant 0.84$ although magnetization curves show rather non-monotonous development, which may reflect the evolution of random anisotropy induced by substitutions.

The variety of couplings of ferromagnetic uranium basal-plane layers along the c-axis observed in UCo_2Si_2, UNi_2Si_2 and UCu_2Si_2 and considerations of responsible exchange interactions motivated Kuznietz and his collaborators to perform systematic AC susceptibility studies (Kuznietz et al. 1994a, 1994b) and powder neutron diffraction studies (Kuznietz et al. 1992a, 1993a, 1993b, 1994c) in order to determine the evolution of magnetic phase transitions and magnetic structures in the solid solutions *U(Co,Ni)$_2$Si$_2$*, *U(Ni,Cu)$_2$Si$_2$* and *U(Co,Cu)$_2$Si$_2$*. A further aim was the construction of relevant magnetic phase diagrams (Kuznietz et al. 1995b, 1996; Melamud et al. 1998). Typical magnetically ordered phases existing in these compounds are:

(i) AF-I structure, $+-+-+-+-$ stacking, $\boldsymbol{q} = (0, 0, 1)$;
(ii) AF-IA structure, $++--++--$ stacking, $\boldsymbol{q} = (0, 0, 1/2)$;
(iii) uncompensated AF $++-++-++-$ stacking, $\boldsymbol{q} = (0, 0, 1/3)$;
(iv) ferromagnetic $++++++++++$ stacking, $\boldsymbol{q} = (0, 0, 0)$.

It is worth to note that in principle all these phases can be observed already in UNi_2Si_2, which represents an intermediate case between UCo_2Si_2 and UCu_2Si_2. The complex development of magnetic phases (see the magnetic phase diagrams in fig. 5.68) is discussed in terms of varying strength and sign of the RKKY-type exchange interactions.

Substitutions of Mn for Cu in *U(Cu$_{1-x}$Mn$_x$)$_2$Si$_2$* yields an initial rapid increase of T_C and the coercive force whereas the spontaneous magnetization is increasing much slower (Smith et al. 1987; Giorgi et al. 1988). When the Mn content increases beyond this value, ferromagnetism is lost very fast (for $x > 0.35$).

URu$_2$Si$_2$ is the most prominent member of the UT_2X_2 class owing to the co-existence of antiferromagnetic ordering (T_N = 17.5 K) of weak uranium moments with superconductivity (T_c = 0.8 K) at low temperatures. Enormous amount of publications on this compound has appeared. We shall concentrate mainly on aspects of magnetism studied on single crystals. We will more or less omit problems of superconductivity and heavy-fermion behaviour which are treated in detail in several specialized reviews (Rauchschwalbe 1987; Grewe and Steglich 1991; Nieuwenhuys 1995). The first susceptibility and magnetization data obtained by measurements on single-crystals and specific-heat results on polycrystals have been reported by Palstra et al. (1985). These results confirmed that magnetism in URu_2Si_2 is strongly anisotropic, in a similar manner as in the majority of UT_2Si_2 compounds. In fig. 5.69 one can see that the susceptibility measured with a magnetic field applied along the c-axis direction is strongly temperature dependent. At high temperatures (above 150 K) the c-axis susceptibility follows the Curie–Weiss law

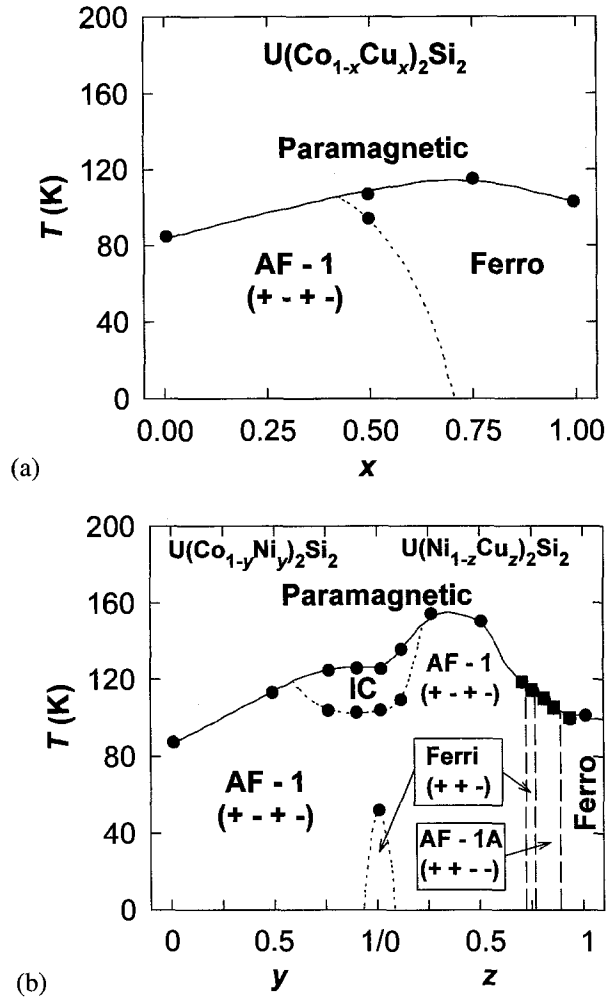

Fig. 5.68. Magnetic phase diagrams (T vs. concentration plots) of the solid solutions $U(Co_{1-x}Cu_x)_2Si_2$ (a) and $U(Co_{1-y}Ni_y)_2Si_2 + U(Ni_{1-z}Cu_z)_2Si_2$ (b).

with $\Theta_p = -65$ K and the effective moment $\mu_{eff} = 3.51\,\mu_B$/f.u. When lowering temperature below 150 K the susceptibility progressively deviates from the Curie–Weiss dependence forming a broad maximum at approximately 50 K which is followed by a fast decrease with further temperature lowering. The Néel temperature of 17.5 K has been determined from the location of a maximum in $d\chi(T)/dT$. In the low-temperature limit the c-axis susceptibility saturates at approximately 6×10^{-8} m^3/mol. The susceptibility with the field applied along the a-axis is nearly temperature independent at the level of 1.2×10^{-8} m^3/mol. Even this low value is about six times larger than the susceptibility of $ThRu_2Si_2$ (Hiebl et al. 1983b) which indicates that the Ru magnetism in these compounds is negligible.

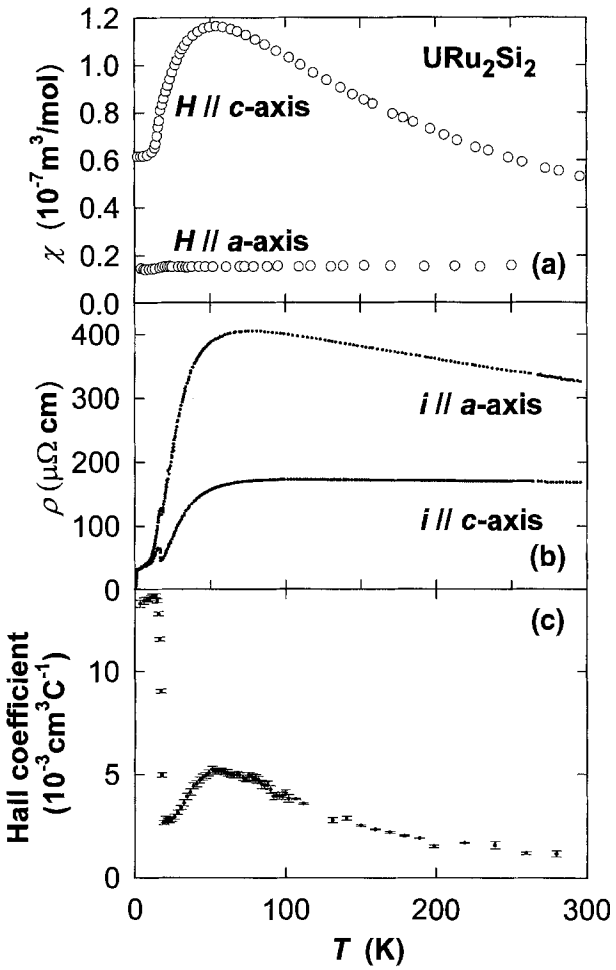

Fig. 5.69. Temperature dependence of the following properties of URu_2Si_2 measured on single crystals: (a) the magnetic susceptibility χ with magnetic field H along the a- and c-axis, respectively, data taken from Palstra et al. (1985); (b) the electrical resistivity ρ with current along the a- and c-axis, respectively, data taken from Palstra et al. (1986c); (c) the Hall effect coefficient with magnetic field parallel and current perpendicular to the c-axis, data taken from Dawson et al. (1989).

The magnetic phase transition at 17.5 K is clearly discerned by a λ-type anomaly in the temperature dependence of the specific heat seen in fig. 5.70 (Palstra et al. 1985), whereas the transition to superconducting state is expressed by a peak at $T = 1.1$ K. Extrapolation of the specific-heat data from the paramagnetic regime yields a value of $\gamma = 180$ mJ/(mol K^2). Between 2 and 17 K, the specific heat can be well fitted by the formula:

$$C = \gamma T + \beta T^3 + \delta e^{-\Delta/T} \tag{5.7}$$

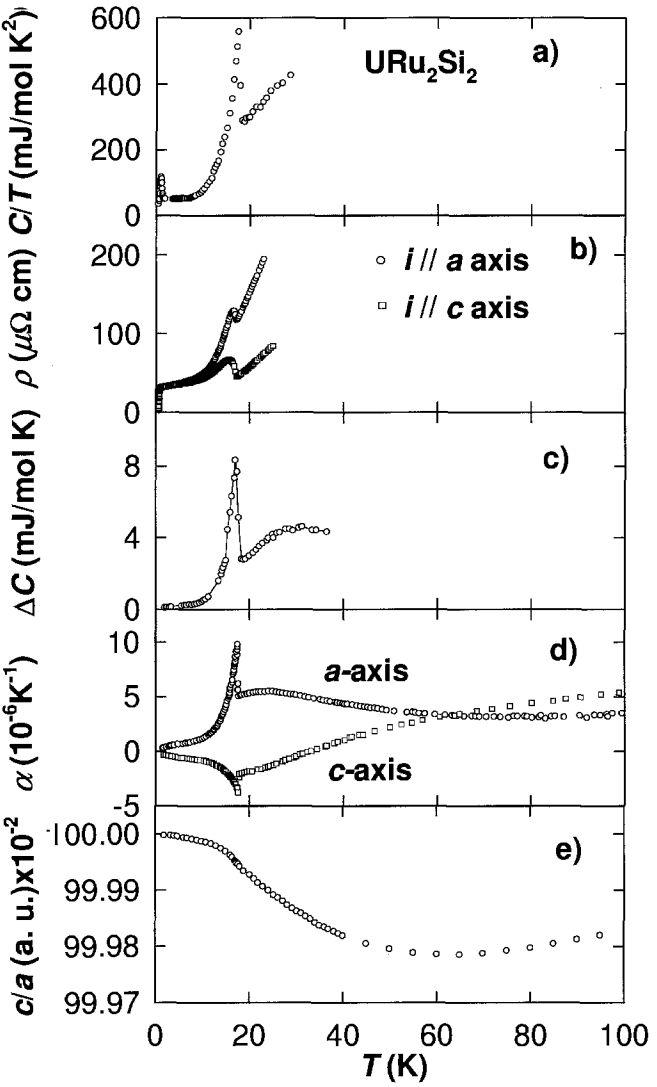

Fig. 5.70. Temperature dependence of the following properties of URu_2Si_2: (a) Specific heat – data taken from de Visser et al. (1986); (b) Electrical resistivity ρ with current i along the a- and c-axis – data taken from Palstra et al. (1986c); (c) Difference ΔC between the specific heat of URu_2Si_2 and $ThRu_2Si_2$ – data taken from Schlabitz et al. (1986), Franse et al. (1987), Santini and Amoretti (1994); (d) Coefficient of thermal expansion α along the a- and c-axis – data taken from de Visser et al. (1986); (e) c/a ratio normalized to 1 at $T = 1.4$ K – data taken from de Visser et al. (1986).

providing the values of $\gamma = 50$ mJ/(mol K^2) and $\Delta = 115$ K (Palstra et al. 1985), which has been attributed to opening of an energy gap over at least a part of the Fermi surface. Similar magnetic and specific-heat data have been reported by Schlabitz et al. (1986) and Maple et al. (1986) who performed their experiments only on polycrystals. Evidence for

TABLE 5.9
Fitting parameters of (5 2 2) to the resistivity in URu_2Si_2 for current i along the a- and c-axis (Palstra et al. 1986c).

	ρ_0 ($\mu\Omega$ cm)	A ($\mu\Omega$ cm/K^2)	B ($\mu\Omega$ cm/K)	Δ (K)	C ($\mu\Omega$ cm/K^2)
$i \| c$	33	0.1	52	68	0.126
$i \| a$	33	0.17	800	90	0.35

a comparable energy gap in the antiferromagnetic state has also been provided by nuclear magnetic resonance and relaxation studies on ^{29}Si nuclei by Kohara et al. (1986) and Benakki et al. (1988), and by the far-infrared reflectance measurements of Bonn et al. (1988). An attempt to study point-contact spectra has been made by Nowack et al. (1992). EPR studies of URu_2Si_2 were performed by Spitzfaden et al. (1996).

Also other electronic properties of URu_2Si_2 are highly anisotropic. In particular, the room-temperature resistivity (see fig. 5.69) along the a-axis (ρ_a) is almost twice of that along the c-axis (ρ_c). Moreover it shows a large nearly-constant negative slope in the temperature range above 80 K whereas the resistivity in the c-axis is rather flat. Below 80 K a knee is seen both in ρ_a vs. T and ρ_c vs. T followed by a precipitous decrease below 50 K and distinct anomalies around the phase transition, which are reminiscent of the behaviour of Cr (SDW antiferromagnet) around T_N (Miwa 1963; Suezaki and Mori 1969; Rapp et al. 1978). The maximum negative derivative of $\rho(T)$ curve is observed at 17 K. Between 1 and 17 K the resistivity can be fitted very well to formula:

$$\rho = \rho_0 + AT^2 + BT(1 + 2T/\Delta)e^{-\Delta/T}, \tag{5.8}$$

describing the resistivity of an energy gap antiferromagnet (Andersen 1980) with the AT^2 term due to Fermi-liquid behaviour. The fitting parameters are displayed in table 5.9. We can see that the residual resistivity is isotropic having the same value of 33 $\mu\Omega$ cm both in the a- and c-axis.

The shape of the temperature dependence of the Hall coefficient (displayed also in fig. 5.69) above T_N including a maximum around 50 K (Schoenes et al. 1987; Dawson et al. 1989) resembles the susceptibility behaviour. The Hall coefficient increases abruptly to a more than four times higher value in the vicinity of T_N and then decreases slowly with decreasing temperature down to $T = 2$ K. Besides the Hall effect, Dawson et al. (1989) measured and analyzed in detail also resistivity and susceptibility of URu_2Si_2. Magnetic phase transition at T_N is reflected also by a sharp dip in the temperature dependence of the thermoelectric power (Hundley et al. 1987).

The magnetoresistance measured at temperatures between 4 K and 40 K in fields up to 6 T (parallel to the c-axis) follows a parabolic dependence.

$$\Delta\rho/\rho = aH^2. \tag{5.9}$$

For both current directions (a- and c-axis), the coefficient a decreases with increasing temperature and vanishes above 20 K.

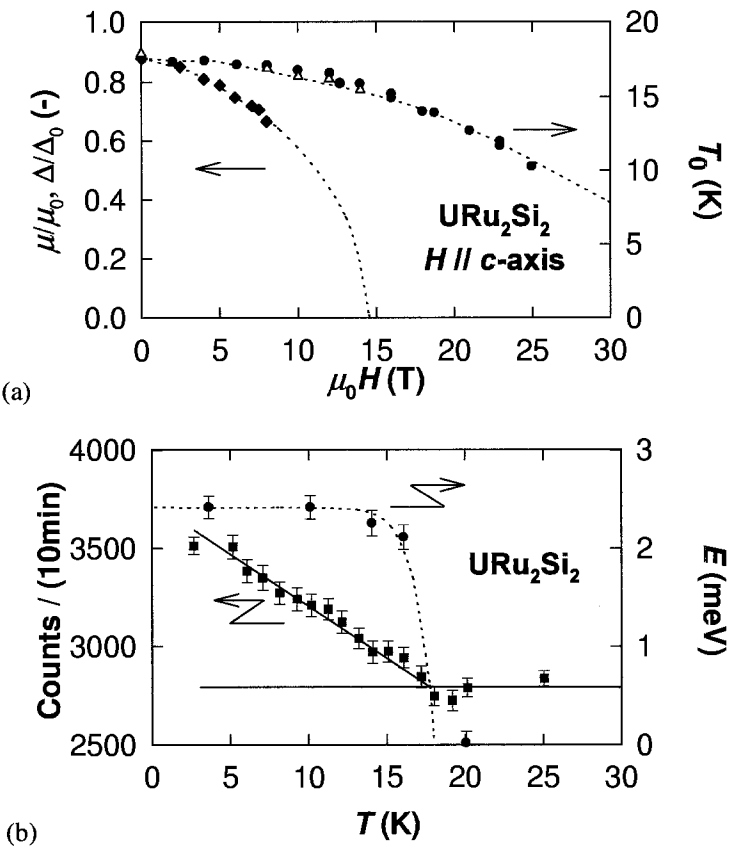

Fig. 5.71. (a) Magnetic-field (parallel to the c-axis) dependence of the reduced staggered magnetic moment μ/μ_0 (♦), the ordering temperature (•), and the reduced energy gap Δ/Δ_0 (△) in URu_2Si_2 determined from a polarized neutron experiment at 4.3 K (Mason et al. 1995), and derived from temperature dependence of the resistance behaviour below T_N (Mentink et al. 1996a); (b) Temperature dependence of the energy gap in the magnetic excitation spectrum (•) and intensity of the magnetic Bragg peak (■) at $Q = (1, 0, 0)$ for URu_2Si_2 single crystal in a magnetic field of 12 T applied parallel to the c-axis. The background level for the Bragg peak is about 2800 counts/10 min, as determined in the paramagnetic range. The dashed and solid lines are guides to the eye. Data are taken from van Dijk et al. (1997).

Measurements of the resistivity in magnetic fields up to 25 T have been done by Mentink et al. (1996a) in order to examine the phase diagram (T_N vs. H, Δ vs. H). They concluded that the magnetic field dependence of the uranium magnetic moment, determined by neutron-scattering experiments (Mason et al. 1995), strongly differs from the field dependence of T_N and Δ, with estimated critical fields of 14.5 T for the magnetic moment and 40 T for T_N and Δ (see fig. 5.71). This would point to two energy scales relevant to the magnetic phase transition of URu_2Si_2, opening a possibility of two order parameters, which shall be discussed lower.

Also the thermal expansion of URu_2Si_2 is highly anisotropic (de Visser et al. 1986, 1990) which can be seen in fig. 5.70. The thermal expansion coefficient along the c-axis

(α_c) is negative up to 30 K, where it changes sign. Above 60 K, it exceeds α_a, which shows always positive values. The magnetic phase transition at T_N is reflected by a sharp anomaly both in α_a and α_c. Moreover, the $\alpha_a(T)$ curve shows a maximum around 30 K, where also a broad bump is observed in the C vs. T dependence (which can be well demonstrated in the temperature dependence of the difference between the specific heat of URu_2Si_2 and $ThRu_2Si_2$ seen in also in fig. 5.70). These features have been attributed to crystal-field effects (de Visser et al. 1986; Franse et al. 1987; Renker et al. 1987). The anisotropy of the thermal expansion is projected in the temperature dependence of c/a (fig. 5.70), which decreases with increasing temperature up to approximately 60 K, where it passes a minimum. The magnetic phase transition at 17.5 K is reflected in the maximum negative derivative of c/a vs. T.

The low-temperature specific-heat and thermal-expansion data measured by de Visser et al. (1986) allowed the determination of the value of the electronic Grüneissen parameter $\Gamma_e = 25$ according to the expression:

$$\Gamma_e = 3aV_m/\kappa\gamma, \tag{5.10}$$

where $a = \alpha_V/T$, $\alpha_V = (2\alpha_a + \alpha_c)/3$, κ = compressibility, V_m = molar volume and γ is the coefficient of electronic specific heat. This value is about an order of magnitude larger than for normal metals. However, it is considerably smaller when compared to that in heavy-fermion materials. Applying the Ehrenfest relation:

$$\frac{\partial \ln T_N}{\partial p} = \frac{3\Delta\alpha_V}{\Delta C} \tag{5.11}$$

the value of the reduced pressure derivative of ordering temperature equals $\partial \ln T_N/\partial p = 8.0\ \text{Mbar}^{-1}$ which is in reasonable agreement with $6.8\ \text{Mbar}^{-1}$ reported from pressure measurements of de Boer et al. (1986).

The neutron scattering experiments performed on single crystals and focused on the magnetic ordering below T_N revealed antiferromagnetism with propagation vector $\boldsymbol{q} = (0, 0, 1)$ and a very reduced uranium magnetic moment of 0.02–$0.04\,\mu_B$ parallel to the c-axis of the tetragonal structure (Broholm et al. 1987, 1991; Mason et al. 1990a, 1990b; Wei et al. 1992). The latter authors presented clear evidence that this antiferromagnetic order survives at least down to $T = 0.2$ K, i.e., the antiferromagnetism coexists with superconductivity below T_c (between 0.2 and 3 K, the magnetic intensity remains constant within 7%). The extraordinary small size of the ordered moment and the observed finite correlation length have thrown doubts on the intrinsic character of magnetic order. Employing combined neutron scattering, specific-heat, magnetic susceptibility and electrical resistivity measurements, Fak et al. (1996, 1997) studied the influence of sample quality on the parameters of the magnetic order in URu_2Si_2 and proved that the long range magnetic ordering in URu_2Si_2 with a uranium moment of $0.0023\,\mu_B$ is indeed intrinsic, although the temperature dependence of the integrated intensity of several magnetic peaks may vary considerably from sample to sample. The finite size of the correlated length of ≈ 50 nm is related to lattice defects.

Inelastic neutron-scattering experiments on single crystals revealed sharp dispersive excitations with a magnetic-zone-centre gap of 1.8 meV at low temperatures. The magnetic

excitations are longitudinally polarized with a large transition matrix element of the order of 1–2 μ_B which does not split or broaden when a magnetic field is applied along the c-axis (Broholm et al. 1991). The gap in the magnetic excitation spectrum at the magnetic zone center $\boldsymbol{Q} = (1, 0, 0)$ softens with increasing temperature. Above T_N, the magnetic zone-center scattering becomes quasielastic and finally vanishes (Bourdarot 1994). Strong inelastic magnetic scattering is also observed also at another points of the nuclear zone boundary like $\boldsymbol{Q} = (1.4, 0, 0)$ and $\boldsymbol{Q} = (1.3, 1.3, 1)$. In these cases, however, the excitations remain inelastic although strongly overdamped above T_N. These magnetic correlations persist up to about 150 K (Bourdarot 1994). These single-crystal results provided a relevant explanation of previous data obtained on polycrystals by Walter et al. (1986) and Holland-Moritz et al. (1987, 1989).

Critical behaviour of URu_2Si_2 in the vicinity of T_N has been studied by high-resolution neutron scattering experiment by Buyers et al. (1994) and Mason et al. (1995). They have observed that for the ordering wave vector the spin-wave energy collapses and the susceptibility diverges at T_N. This confirms that the magnetic dipole is the order parameter, as suggested from a polarized neutron scattering experiment by Walker et al. (1993, 1994). The conclusion of a possible quadrupolar instability at T_N drawn by Ramirez et al. (1992), Miyako et al. (1993) and Kuwahara et al. (1997), is based on the temperature dependence of the elastic constants c_{11}, c_{66} and $(c_{11}-c_{12})/2$ and on non-linear susceptibility behaviour, respectively. On the other hand, Park et al. (1997) studied the magnetization anomaly at T_N in magnetic fields up to 20 T applied along the c-axis and concluded that the field dependence of the anomaly is different from the dependence of the magnetic moment of dipole origin which would imply that a new order parameter other than the dipole moment is responsible for most of anomalies around 17.5 K. Similar conclusions have been proposed by Mentink et al. (1996a, 1997a) on the basis of an analysis of the resistivity, thermal expansion and specific heat measurements near T_N in magnetic fields up to 25 T. A theoretical approach to this problem has been presented by Santini and Amoretti (1994) who proposed a crystal-field model based on quadrupolar ordering of localized 5f-electrons at 17.5 K. This model can account for the observed linear (Palstra et al. 1985) and non-linear (Onuki et al. 1989) susceptibility through the transition. Further and especially theoretical effort is desirable to clarify the problem of order parameters in URu_2Si_2 in the critical temperature region. From the experimental point of view a crucial test has been done by van Dijk et al. (1997) who have performed elastic and inelastic neutron scattering experiments on a URu_2Si_2 single crystal in an external magnetic field of 12 T. They measured both the ordered magnetic moment and the magnetic gap at $\boldsymbol{Q} = (1, 0, 0)$. The observed temperature dependence of these two parameters is displayed in fig. 5.71. This result clearly shows that the reported decoupling of the magnetic moment from the gap (Mentink et al. 1996a) derived from the high-field extrapolations seen in fig. 5.71 does not occur and that the critical temperatures of the magnetic gap and the ordered moment are comparable. Nevertheless, the strikingly different temperature dependencies of the gap in the magnetic excitation spectrum and the reduced ordered magnetic moment in URu_2Si_2 impose the question whether the dipole ordered moment is the main order parameter which controls the magnetic phase transition.

Application of strong magnetic fields on single crystalline samples in various experiments played a substantial role in the investigation of the magnetism in URu_2Si_2. Results of magnetization measurements (Dirkmaat 1989; Sugiyama et al. 1997) are shown

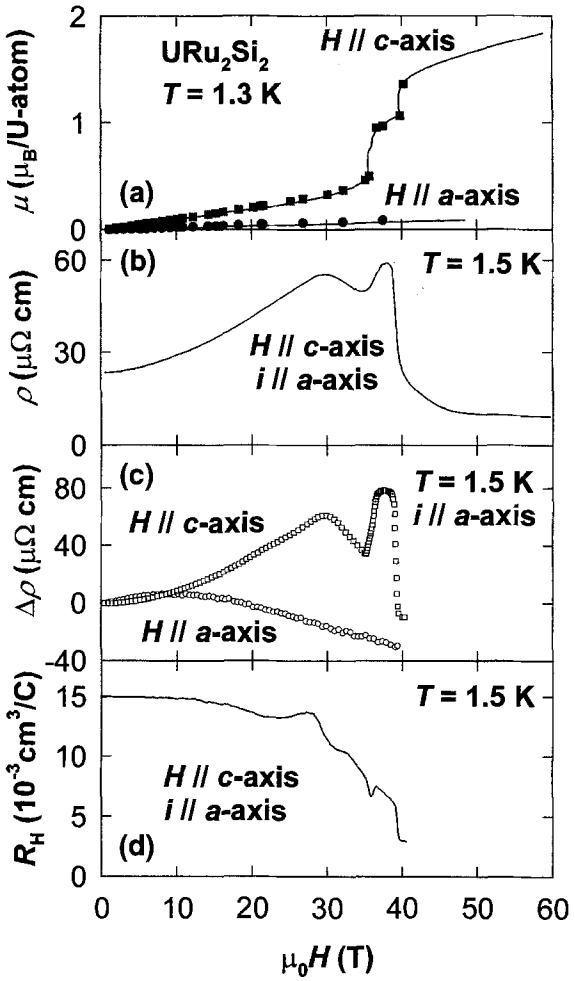

Fig. 5.72. (a) Magnetization curves measured on URu_2Si_2 single crystals at $T = 1.4$ K in fields up to 40 T in the Amsterdam magnet (points) and at $T = 1.3$ K in fields up to 60 T (solid lines) in the Osaka magnet along the a-axis and along the c-axis – data taken from de Boer et al. (1986) and Sugiyama et al. (1997), respectively. (b) Transverse magnetoresistance curve measured on URu_2Si_2 single crystal at $T = 1.3$ K in fields up to 60 T in the Osaka magnet (solid lines) with current along the a-axis and magnetic field along the c-axis – data taken from Sugiyama et al. (1997). (c) Transverse ($H \| c$, $i \| a$) and longitudinal ($H \| a$, $i \| a$) magnetoresistance curves measured on URu_2Si_2 single crystal at $T = 1.5$ K in fields up to 40 T in the Amsterdam magnet – data taken from Bakker et al. (1993a). (d) Magnetic-field dependence of the Hall coefficient R_H in measured on URu_2Si_2 single crystal at $T = 1.5$ K in fields up to 40 T in the Amsterdam magnet ($H \| c$, $i \| a$) – data taken from Bakker et al. (1993a).

in fig. 5.72. First, we should stress again the huge uniaxial magnetocrystalline anisotropy which is reflected in the weak paramagnetic response of URu_2Si_2 in magnetic fields (parallel to the a-axis) up to 48 T which was the maximum field in this experimental configu-

ration (Sugiyama et al. 1997). In fields up to 30 T also the c-axis magnetization is rather low and varies linearly with applied magnetic field. Above 30 T, it shows a progressively increasing upturn which is then converted to three successive metamagnetic transitions at 35.8, 36.5 and 39.6 T, where the c-axis magnetization exhibits step-like increases yielding approximately $1.4\,\mu_B$/f.u. in 40 T followed by a continuous increase with further increasing field without much saturation even in fields up to 58 T, here reaching $1.9\,\mu_B$/f.u. Some differences between the data collected in the 40 T magnet in Amsterdam and in the 60 T magnet in Osaka may be attributed to the difference in the time scale of the experimental facilities, which is much shorter in the latter case. The magnet in Osaka works in a typical pulsed field regime with a pulse width of 0.4 ms (i.e., 300 T/ms) field sweep rate whereas most of data points in the Amsterdam magnet were collected within a quasistatic regime with a 100 ms long constant field level or within linearly sweeping field at rate lower than 0.1 T/ms. This causes a certain smearing out of the sharp intrinsic transitions appearing as artifacts in the fast experiment in Osaka. The results indicate that the SDW weak moment antiferromagnetism in URu_2Si_2 with attributes of a heavy-fermion ground state can be destroyed by applying magnetic filed larger than 40 T along the c-axis. Sugiyama et al. (1997) have proposed a mean-field model explaining the complex cascade of metamagnetic transitions in this material. These authors attributed the three field-induced magnetization states successively to two phases with antiferromagnetically coupled uranium magnetic moments with a propagation vector $\boldsymbol{q} = (0, 0, 1/3)$, $\boldsymbol{q} = (0, 0, 3/5)$, leading finally to a phase with ferromagnetic coupling.

The three metamagnetic transitions in URu_2Si_2 are accompanied by abrupt changes of the magnetoresistance (de Visser et al. 1987; Bakker et al. 1993a) which can be seen in fig. 5.72. The first two transitions yield step increases of the transversal magnetoresistance which may be attributed to the increasing size of the magnetic unit cell along the c-axis. The final transition to the ferromagnetically coupled lattice leads to a huge drop of the resistance to a level lower than the zero-field resistivity. Although the magnetization curve in fields along the c-axis increases monotonously up to the field of the first metamagnetic transition the (positive) magnetoresistance increases only up to 30 T, where it reaches its maximum value and starts to decrease strongly with further increasing magnetic field. On the other hand, the magnetoresistance in magnetic fields applied along the a-axis is more than one order of magnitude weaker and shows no anomalies because of a negligible effect of the magnetic field applied in a direction perpendicular to the easy magnetization axis.

Figure 5.72 shows also the field dependence of the Hall coefficient ($H \| c$, $i \| a$) measured for URu_2Si_2 at 1.5 K by Bakker et al. (1993a). In low fields it is equal to 15×10^{-3} cm^3/C. Similar values were reported also by Schoenes et al. (1987), Onuki et al. (1989) and Dawson et al. (1989). Below 22 T, R_H is slowly decreasing with increasing magnetic field followed by a bump around 28 T and a faster decrease up to 35 T. Anomalies at higher fields (steps down, up and down) are associated with the three metamagnetic transitions. Analysis of the Hall coefficient in a simple one band model in a zero field yields a carrier concentration of 0.03 holes/f.u. (Schoenes et al. 1987), whereas at 40 T more than 1 electron/f.u. or hole/f.u. was estimated by Bakker et al. (1993a). The clear anomalies both in $R_H(H)$ and $\Delta\rho(H)$ observed around 30 T, although the magnetization varies monotonously up to 35 T, indicate the onset of an electronic structure change in URu_2Si_2 associated with the destruction of the heavy fermion state.

URu_2Si_2 has been studied in high magnetic fields up to 40 T also by means of ESR (Kindo and Date 1994). Results of first measurements of de Haas–van Alphen oscillations can be found in the report of Ohkuni et al. (1997).

An X-ray diffraction structural study at room temperature in pressures up to 50 GPa has been made by Luo et al. (1988) revealing a stable crystal structure, a nearly constant compressibility of 2.8×10^{-3} GPa^{-1} and an invariable c/a value in the whole pressure range. The low compressibility value compares well with that in UPt_3. A positive effect of the external hydrostatic pressure both on the temperature of the resistivity maximum T_{max} in the paramagnetic range and on the value of the gap energy Δ has been reported by Maple et al. (1986), de Boer et al. (1986), McElfresh et al. (1987) and Ido et al. (1993). Analogous results for T_N and Δ have been obtained from specific heat measurements under external pressure (Fisher et al. 1990). The external pressure is also gradually smearing out the magnetic phase transition. Iki et al. (1992) and Kagayama et al. (1994) demonstrated that the value of $\partial T_N/\partial p$ becomes gradually reduced above 5 GPa and these authors proposed that the value of Néel temperature may reach its maximum value (which is approximately doubled with respect to the ambient-pressure value) around 8 GPa and may decrease with further increasing pressure. They have also estimated the value $\Gamma = 23$ of the magnetic Grüneissen parameter from the formula:

$$\Gamma = -\frac{\partial \ln T_V}{\partial \ln V} = \frac{1}{\kappa}\frac{\partial \ln T_N}{\partial P}, \tag{5.12}$$

as which result is in a good agreement with the value $\Gamma = 25$ derived by de Visser et al. (1986, 1990). The value $\kappa = 4.9 \times 10^{-3}$ GPa^{-1} was taken from (Iki et al. 1990). Oomi et al. (1994) and Kagayama et al. (1994) analyzed the low temperature resistivity data which can be well approximated by the simplified formula:

$$\rho = \rho_0 + AT^2. \tag{5.13}$$

The ambient-pressure data satisfy this formula in the temperature range 1–8 K. This interval is gradually expanding with increasing pressure up to 1–20 K in 5 GPa and the value of the quadratic coefficient decreases rapidly with applied pressure (by two orders of magnitude between ambient pressure and 8 GPa). A complex magnetoresistance behaviour in magnetic fields up to 5 T in pressures up to 2 GPa has been reported by Uwatoko et al. (1992).

Bakker et al. (1992) demonstrated by measurements of the electrical resistivity of URu_2Si_2 that the pressure effects both on the Néel temperature T_N and the superconducting temperature T_c is highly anisotropic. Uniaxial stress applied along and perpendicular to the c-axis induces qualitatively opposite effects. In the former (latter) case T_N is increased (decreased) and T_c is decreased (increased). Whereas the effect of stress on T_c in the two perpendicular directions is comparable in absolute value, the basal plane stress leads to an enhancement of T_N that is three times larger than is the rate of the decrease induced by the c-axis stress.

Ab initio calculations of electronic structure in URu_2Si_2 have been performed by Monachesi and Continenza (1995) using the FLAPW method within the local density approximation including the spin–orbit interaction, which provided also spin-polarization density maps.

Numerous experimental studies have been devoted to solid solutions $U_{1-x}A_xRu_2Si_2$ in which the uranium sublattice is modified by introducing various alloying elements. The majority of experiments, unfortunately, has been done only on polycrystalline samples. Effects of small doping by various rare-earth elements on the resistivity anomaly around T_N were studied by Park and Coles (1993, 1995). Variations of spin dynamics with La and Th doping were investigated by means of μ^+SR (Cywinski et al. 1995; Park et al. 1996). Thermopower measurements of $U_{1-x}La_xRu_2Si_2$ and $U_{1-x}Ce_xRu_2Si_2$ compounds over a wide range of concentrations have been performed by Ocko and Park (1997). Resistivity and magnetization data on some selected compositions are presented by Roy and Coles (1992). The resistivity measurements of quasiternary compounds $(U_{1-x}Y_x)Ru_2Si_2$ performed by Dalichaouch et al. (1989) and Radha et al. (1996) indicate that, although the value of T_N is initially not very much changed by Y substitutions, the Cr-like anomaly of the resistivity in the critical temperature region gradually smears out and for $x > 0.5$ any sign of antiferromagnetism is lost. Specific-heat measurements made by Amitsuka et al. (1992a) and Patrikios et al. (1992) of $U_{1-x}La_xRu_2Si_2$ revealed an initial (for $x \leqslant 0.07$) rapid depression of T_N and a broadening of the related specific-heat anomaly. The anomaly broadens further with increasing x beyond 0.07 but its center becomes gradually pushed to higher temperatures, reaching 20 K in $U_{0.7}La_{0.3}Ru_2Si_2$. This surprising development is confirmed by the evolution of a sharp feature in the temperature dependence of susceptibility in the interval $0.07 \leqslant x \leqslant 0.3$ (Amitsuka et al. 1992a). Neutron-scattering experiments on single crystals are desirable for clarifying the ground state of these compositions.

Mauramoto et al. (1996) claim that they have found Kondo screening in dilute $(U_xLa_{1-x})Ru_2Si_2$ compounds for $x \leqslant 0.15$. They explain the anisotropic high-temperature susceptibility by a crystal field model with a non-Kramers doublet ground state. They propose that the low-temperature susceptibility, specific heat and high-field magnetization is well described by the Kondo model, which suggests that a single-site Kondo screening should be considered to explain the Fermi liquid state in URu_2Si_2.

Quasiternary compounds $U_{1-x}Th_xRu_2Si_2$ with a strongly diluted uranium sublattice have been investigated mainly in the single crystal form by Amitsuka et al. (1993, 1997), and Amitsuka and Sakakibara (1994). Results partly obtained on polycrystals have been reported by Kim et al. (1997). Not only the magnetization curves at low temperatures but also the temperature dependence of susceptibility measured in fields along the principal crystallographic directions clearly demonstrate a strong uniaxial magnetic anisotropy. The U-concentration controlled evolution of unusual temperature dependencies of the specific heat ($C/T \sim -\ln T$), electrical resistivity ($\rho \sim \ln T$ for $1 \leqslant T \leqslant 10$ K, $\rho \sim T^{1/2}$ for $1 \leqslant T \leqslant 10$ K) and susceptibility measured along the c-axis ($\chi \sim -\ln T$) and observed at low temperatures has been interpreted in terms non-Fermi-liquid behaviour. The non-Fermi-liquid behaviour is attributed to properties of a single U ion embedded in the Th site of the $ThRu_2Si_2$ compound (Amitsuka and Sakakibara 1994). A two-channel Kondo model (Nozieres and Blandin 1980; Cox 1987) has been proposed as a possible explanation tool for these phenomena in context with thermal expansion data (Amitsuka et al. 1997). Note that also the temperature dependence of thermal expansion is highly anisotropic. The thermal expansion coefficient along the c-axis (α_c) increases with increasing temperature whereas α_a is extremely small and almost temperature independent.

Also the quasiternary compounds $U_{1-x}Ce_xRu_2Si_2$ (for $x \leqslant 0.05$ and for $x \geqslant 0.85$) have been prepared in the form of single crystals and were investigated by magnetization, susceptibility, electrical-resistivity and specific-heat measurements by Mihalik et al. (1993a, 1993b, 1993c, 1993d). The high uniaxial magnetocrystalline anisotropy of the parent compound persists also in the solid solutions. In the uranium rich compounds, Ce substitutions induce effects analogous to those in La substituted compounds. A rapidly reduced value of the linear specific-heat $\gamma = 33$ mJ/(mol K^2) for initial substitution ($x = 0.99$) indicates suppression of the heavy-fermion behaviour by alloying of URu_2Si_2 with Ce.

Similar to UCo_2Si_2, also *URh_2Si_2* exhibits antiferromagnetic ordering of type-I, in this case below $T_N = 137$ K as inferred from powder neutron diffraction and basic magnetic studies (Ptasiewicz-Bak et al. 1981; Buschow and de Mooij 1986). The simple behaviour of this material has not attracted any further experimental interest.

The magnetic properties of the isostructural compounds URu_2Si_2 and URh_2Si_2 attracted the attention of Continenza and Monachesi (1994) who performed electronic structure calculations for these materials and compared the calculated and experimentally determined magnetic properties to ascertain the different role played by Ru vs. Rh. The total magnetic moment, obtained by spin-polarized electronic calculations with the full potential augmented plane-wave method within local spin-density approximation, agrees quite satisfactorily with the measured one in URh_2Si_2, whereas it is orders of magnitude too large in URu_2Si_2. The important differences calculated for the two materials are connected with the substantial contribution to the total magnetic moment of negative d spin polarization and with the larger radial extension and asphericity of the magnetization density (in two crystal planes) in the Ru compound compared to URh_2Si_2. Also, the f positive spin-polarization density on U differs in the two compounds, which should be reflected in different magnetic form factors in diffraction experiments.

In spite of little experimental effort on URh_2Si_2 itself, an appreciable amount of research was focused on the evolution of the electronic properties in the solid solutions between URh_2Si_2 and URu_2Si_2 in order to trace the way from the large U moment system to the very reduced magnetic moment in the heavy fermion state (Miyako 1993). The combined results of studies of the high-field magnetization (Amitsuka et al. 1990b), susceptibility and specific-heat (Amitsuka et al. 1988, 1990a; Miyako et al. 1991, 1992) and neutron diffraction (Burlet et al. 1992, 1994a; Kawarazaki et al. 1994) made on *$U(Ru_{1-x}Rh_x)_2Si_2$* compounds makes it possible to construct the schematic magnetic phase diagram T_N vs. x. The latter is shown in fig. 5.73 together with μ_U vs. x and T_N vs. x plots. When substituting Ru for Rh we observe an initial increase of T_N reaching a maximum value of 174 K for $x = 0.625$ and then decreases down to 101 K with further increasing Rh content to $x = 0.4$. Between $x = 0.4$ and 0.35 T_N drops down to 44 K although no dramatic change of the U magnetic moment is observed in this interval, but the simple AFI magnetic structure is transformed to the commensurate antiferromagnetic ordering with $\boldsymbol{q} = (1/2, 1/2, 1/2)$ which consists of $++--++--$ stacking of antiferromagnetic (0 0 1) planes. Nearness of this transformation is seen in the γ-value for $x = 0.4$, which is almost doubled with respect to the values observed in samples with $x = 0.5$ and 0.3. For x decreasing beyond 0.35, T_N decreases continuously and magnetic order collapses for x below 0.1 to reappear again in URu_2Si_2 in the form of an AFI structure of tiny U magnetic moments which is formed below the relatively high Néel temperature of 17.5 K.

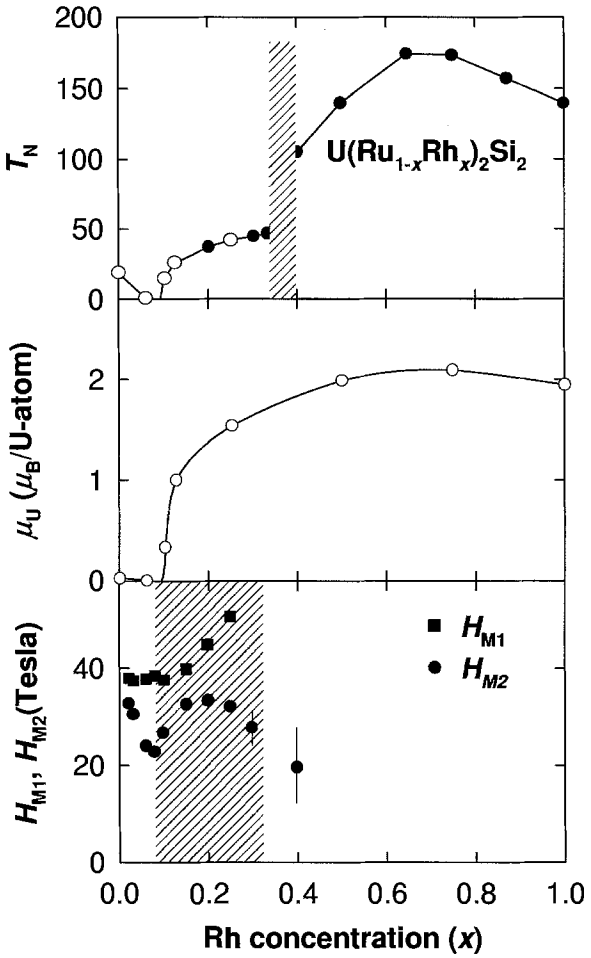

Fig. 5.73. (a) Magnetic phase diagram (T_N vs. Rh concentration x) of $U(Ru_{1-x}Rh_x)_2Si_2$ together with the μ_U vs. x and T_N vs. x plots – data taken from Amitsuka et al. (1990b), Burlet et al. (1992), Miyako et al. (1992); (b) Magnetic phase diagram H vs. x of the $U(Ru_{1-x}Rh_x)_2Si_2$ – data taken from Amitsuka et al. (1990a, 1990b), and Sakakibara et al. (1992). H_{M1} and H_{M2} are the critical field of the first and the second metamagnetic transition, respectively.

A special attention has been paid to the neutron scattering investigation of a single crystal of $U(Rh_{0.06}Ru_{0.94})_2Si_2$ (Burlet et al. 1992) which, according to the proposed magnetic phase diagram, should be nonmagnetic. Indeed, despite strong efforts no magnetic Bragg reflection has been observed down to 1.5 K. On the other hand, significant short-range correlations were detected around the reciprocal vector (1/2, 1/2, 1/2). The experimental width of the scattering maximum points to a correlation length of several interatomic distances. The low Rh ($x < 0.05$) part of the magnetic phase diagram has been investigated by magnetization measurements made on single crystals in high magnetic fields, up

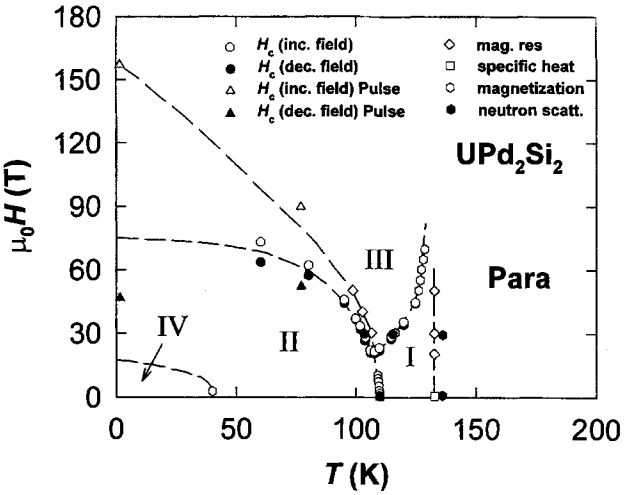

Fig. 5.74. Schematic magnetic phase diagram of UPd_2Si_2 in a magnetic field H parallel to the c-axis, which has been constructed by using data of magnetization, resistivity and specific heat (Honma et al. 1993), and neutron scattering (Collins et al. 1993; Shemirani et al. 1993) data.

to 55 T. Three-step metamagnetic transitions were observed similar to pure URu_2Si_2. Free energy considerations of the transition fields indicate that the partially gaped heavy fermion state with weak antiferromagnetic moment (SDW) is destroyed at the first transition field (Sakakibara et al. 1992). The low-field susceptibility studies in this concentration region show that the magnetic ordering temperature T_N and the temperature of the susceptibility maximum correlate very well (Amitsuka et al. 1990a). The ^{29}Si NMR studies made by Kohori et al. (1992) on the $U(Rh_{1-x}Ru_x)_2Si_2$ system point to an antiferromagnetic ordering of fairly large U magnetic moments for $x \leqslant 0.7$. For low Rh concentrations Kohori et al. (1992) show that the nuclear spin lattice relaxation time T_1 points to a Fermi liquid state below 60 K. Muon spin relaxation experiments performed in the paramagnetic and magnetically ordered states of URh_2Si_2 and $U(Rh_{0.35}Ru_{0.65})_2Si_2$ indicated that the uniaxial magneto-crystalline anisotropy of the parent compound probably persists also in the solid solutions $U(Rh_{1-x}Ru_x)_2Si_2$. High-field magnetization measurements performed with field along the c-axis made it possible to construct a H vs. x magnetic phase diagram which is also shown in fig. 5.73.

Besides Rh doping, also effects of replacement of Ru in URu_2Si_2 by some other transition metals on the weak antiferromagnetism was studied. Substitutions of Re, Tc and Os for Ru yield initially smearing out of the magnetic phase transition (Dalichaouch et al. 1990a). However, when increasing the substituent content by more than 10%, weak ferromagnetism is observed in $U(Ru_{1-x}T_x)_2Si_2$ for T = Re, Tc and Mn (Dalichaouch et al. 1990b; Thieme et al. 1996). Clear long-range ferromagnetic order has been confirmed in $URu_{1.2}Ru_{0.8}Si_2$ below 30 K by neutron diffraction (Torikachvili et al. 1990). Ferromagnetic ordering in $U(Ru_{1-x}Re_x)_2Si_2$ compounds with $x \geqslant 0.2$ has been detected also by the broadening of the ^{29}Si NMR line measured by Kohori et al. (1993). Similar conclusions

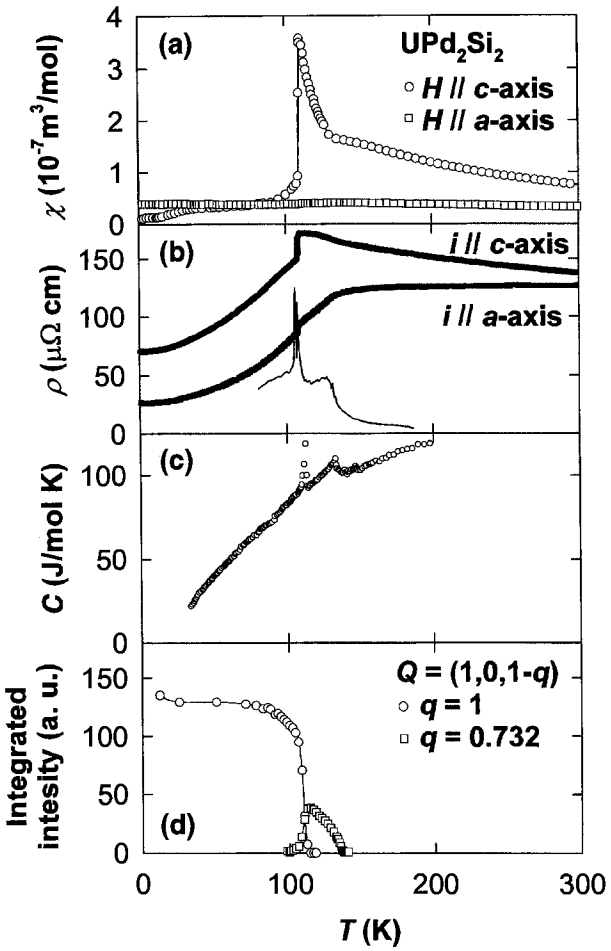

Fig. 5.75. Temperature dependence of the following properties of UPd_2Si_2 measured on single crystals: (a) Magnetic susceptibility χ in low magnetic fields H along and perpendicular to the c-axis – data taken from Honma et al. (1993); (b) Electrical resistivity ρ (the narrow dashed lines represents the $\partial\rho/\partial T$ vs. T dependency for $i \| a$) with current i along and perpendicular to the c-axis – data taken from Honma et al. (1993); (c) Specific heat C – data taken from Honma et al. (1993); (d) Intensity of the magnetic neutron reflections (1, 0, 0) and (1, 0, 0.268) – data taken from Shemirani et al. (1993).

about the effect of substitutions of Re were reached from studies of the optical properties of various $U(Ru_{1-x}Re_x)_2Si_2$ compounds with $0 < x < 0.8$.

Substitutions of Ge for Si lead to gradual expansion of the lattice volume and the reduction of T_N in the $URu_2Si_{2-x}Ge_x$ compounds. This is consistent with results of studies of the above discussed positive effect of external pressure on the Néel temperature and the opposite influence of substitutions of La for U, yielding a "negative pressure". These solid solutions crystallize with ThC_2Si_2-type structure at least up to $x = 0.6$. Beyond this limit no single phase samples could be prepared (Dhar et al. 1992).

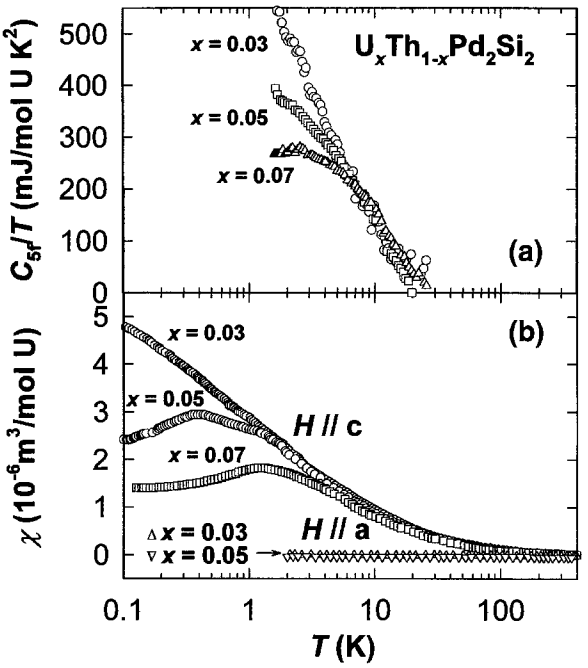

Fig. 5.76. Temperature dependence of: (a) 5f electronic specific heat (C_{5f}/T vs. $\ln T$ plot) measure on polycrystalline samples; (b) Magnetic susceptibility along the a- and c-axis measured on single crystals of $U_xTh_{1-x}Pd_2Si_2$ for $x = 0.03, 0.05, 0.07$ – data taken from Amitsuka et al. (1990b).

UPd_2Si_2 is an antiferromagnet with many features of the magnetic phase diagram (see fig. 5.74) found also for UNi_2Si_2. Magnetic ordering is observed in UPd_2Si_2 below 133 K (Shemirani et al. 1993) where an incommensurate spin density wave with $\boldsymbol{q} = (0, 0, 0.732)$ develops. At $T_1 = 108$ K a clear first order magnetic phase transition takes place to a simple AFI magnetic phase, which is stable to lowest temperatures. Nevertheless, the low-temperature phase contains less than 1% of a $\boldsymbol{q} = (0, 0, 2/3)$ phase, which is similar to the ground-state phase in UNi_2Si_2. When a magnetic field larger than 1.9 T along the c-axis is applied at T_1, a new phase which corresponds to a commensurate spin density wave with $\boldsymbol{q} = (0, 0, 2/3)$ emerges (Collins et al. 1993; Honma et al. 1993). The wave amplitude of this phase is 3.0 μ_B, while magnetization measurements show a net ferromagnetic moment of 0.30 μ_B in 3 T (Collins et al. 1993).

As seen in fig. 5.75, the magnetic phase transitions are well marked by accompanying anomalies in the susceptibility, specific heat and electrical resistivity (Honma et al. 1993) and in the temperature dependence of the intensity of relevant magnetic reflections (Shemirani et al. 1993). The first order magnetic phase transition at T_1 is accompanied also by a pronounced lattice distortion $|\Delta L/L| \approx 10^{-4}$ and clear step anomalies in the electrical resistivity (Honma et al. 1993). The susceptibility and resistivity data confirm the outstanding anisotropic features of the UT_2Si_2 compound. In particular, the uniaxial anisotropy with an easy magnetization direction along the c-axis of the tetragonal structure

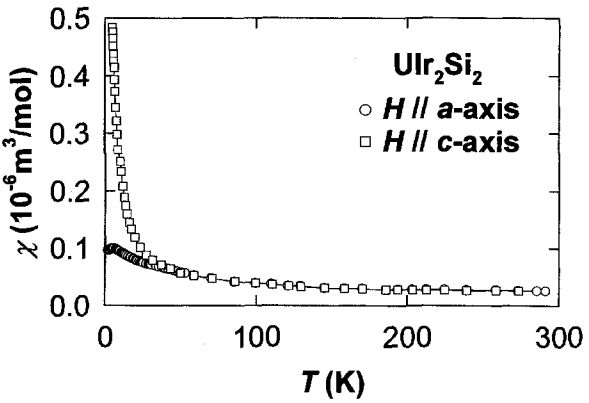

Fig. 5.77. Temperature dependence of the magnetic susceptibility χ of UIr_2Si_2 measured on a single crystal with the magnetic field H along the a- and c-axis – data taken from Dirkmaat et al. (1990a).

is observed not only in the magnetically ordered state where the basal plane response to an applied magnetic field is paramagnetic and where all the aspects of the antiferromagnetic system are detected only along c. The c-axis is also the exclusive direction of orientation of the individual moments in the magnetic structure, which may be complex but always collinear. Also the strikingly different temperature dependence of the electrical resistivity measured with electrical current along and perpendicular to the c-axis is well representing the distinct anisotropy of the electric charge transport in this materials. The electric transport anisotropy reflects not only the anisotropy of the Fermi surface in this antiferromagnet but also the interaction of the conduction electrons with the 5f electron subsystem contributes substantially. The resistivity anomalies are much more pronounced for the current along the c-axis, which is the propagation direction of the antiferromagnetic structure. In this context we should also consider that the negative derivative of the resistivity for current along the c-axis is gradually more enhanced when approaching T_N in the paramagnetic region which is due to progressively enhancing antiferromagnetic correlations propagating along the c-axis.

Plumer (1994) calculated magnetic field vs. temperature magnetic phase diagrams by the axial next-nearest-neighbor Ising model within the framework of a Landau-type expansion of the free energy derived from molecular field theory and obtained a good qualitative agreement with the experimentally observed behaviour of UPd_2Si_2. The question about the possibility to extend this approach to the related UT_2X_2 antiferromagnets is a challenge to theorists.

The properties of a strongly diluted U sublattice in $U_xTh_{1-x}Pd_2Si_2$ ($x \leqslant 0.07$) were investigated by means of magnetic susceptibility, electrical resistivity and specific heat measurements down to $T = 100$ mK (Amitsuka et al. 1995b). With decreasing x, an unusual $-\ln T$ behaviour of the susceptibility and specific heat develops below 6 K, as can be seen in fig. 5.76, which is argued to be a sign of non-Fermi liquid behaviour. Note that the susceptibility data measured along the two principal crystallographic directions confirm that the strong uniaxial magnetocrystalline anisotropy persists even in the diluted

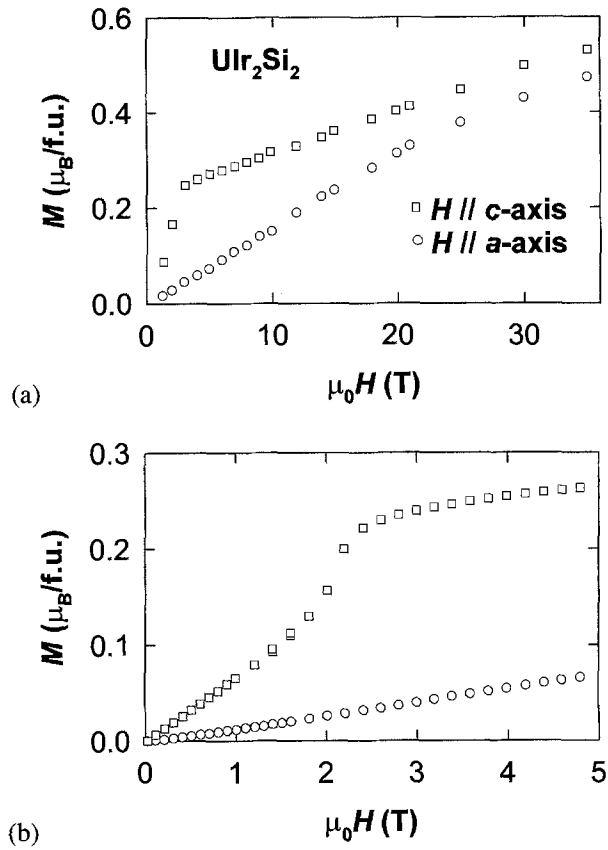

Fig. 5.78. Magnetization curves measured at $T = 1.66$ K on an annealed UIr_2Si_2 single crystal with magnetic field along the a- and c-axis – data taken from Dirkmaat et al. (1990a). The lower panel shows the low-field part in more detail.

limit. This clearly proofs that the exotic non-Fermi-liquid like behaviour is indeed due to 5f electrons of uranium.

The compounds URe_2Si_2 and UOs_2Si_2 are reported as temperature independent paramagnets with low susceptibility $\chi = 1.8 \times 10^{-8}$ m^3/mol (Palstra et al. 1986b). Structural data only can be found, however, for the latter compound, which was studied also by Hiebl et al. (1983a).

UIr_2Si_2 and UPt_2Si_2 are the only silicides which adopt the primitive-cell $CaBe_2Ge_2$-type structure (space group P4/nmm). For the majority of the UT_2X_2 materials with this crystal structure we sometimes observe rather contradictory results on samples (even single crystalline) of somewhat different thermal history. Possible metallurgical difficulties connected with lattice defects in the case of UIr_2Si_2 are indicated by the very high residual resistivity values at low temperatures (Dirkmaat et al. 1990a; Verniere et al. 1996a). This assumption has been confirmed experimentally (Verniere et al. 1996b) by careful struc-

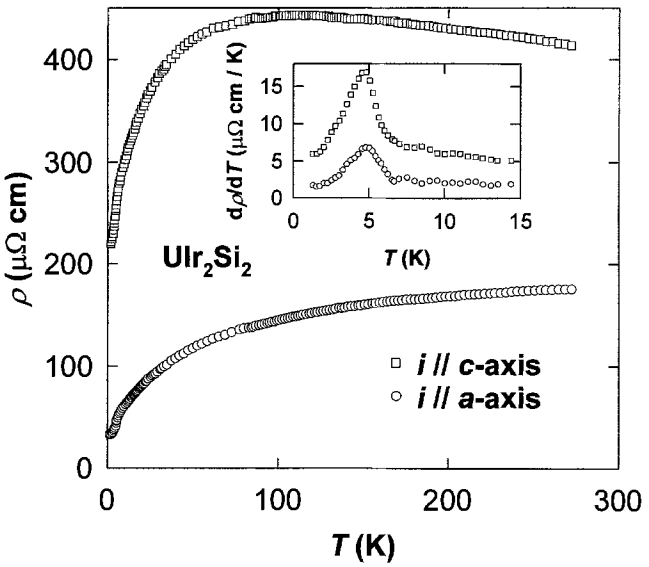

Fig. 5.79. Temperature dependence of the electrical resistivity of UIr_2Si_2 measured on a single crystals with current i along and perpendicular to the c-axis – data taken from Dirkmaat et al. (1990a). The inset shows the respective derivatives.

ture studies of single crystals with varying stoichiometry and heat treatment following the crystal growth procedure. The temperature dependence of magnetic susceptibility and the low temperature magnetization curves (Dirkmaat et al. 1990a), which are shown in figs 5.77 and 5.78, respectively, indicate antiferromagnetic ordering in this material. This has been confirmed by neutron scattering (Verniere et al. 1996a). This study revealed antiferromagnetic ordering of the type-I and a very reduced uranium magnetic moment of $0.1\,\mu_B$ pointing to itinerant character of the uranium 5f states. There are also some other features which may suggest that UIr_2Si_2 is in a situation not very far from that in URu_2Si_2: (a) the magnetic moment obtained from the magnetization curve above the metamagnetic transition is much larger than the moment determined by neutron scattering in zero field, (b) $\gamma > 100\ \mathrm{mJ\,mol^{-1}\,K^{-1}}$, (c) the resistivity (see fig. 5.79) shows a broad bump far above T_N. In spite of the different crystal structure, also UIr_2Si_2 exhibits a distinct uniaxial magnetocrystalline anisotropy although only in the magnetically ordered state.

UPt_2Si_2 exhibits quite simple behaviour. Below $T = 35$ K, it orders antiferromagnetically (type-I) with uranium magnetic moments ($1.67\,\mu_U$) parallel to the c-axis. This ordering is again accompanied by a strong uniaxial magnetocrystalline anisotropy (Steeman et al. 1990; Amitsuka et al. 1992b) which can be well seen both in the high-field magnetization curves (fig. 5.80) and in the temperature dependence of magnetic susceptibility (fig. 5.81) measured on single crystals in magnetic fields applied along the two main crystallographic axes. In contrast to susceptibility behaviour of other silicides we can see that the basal-plane χ_a vs. T curve is not at all featureless and strongly depends on temperature. Moreover, the two curves, χ_a vs. T and χ_c vs. T cross at two temperatures, and although

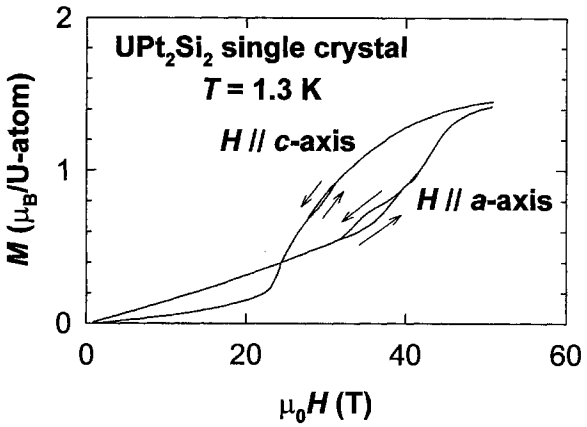

Fig. 5.80. High-field magnetization curves of a UPt_2Si_2 single crystal in magnetic fields H applied along the a- and c-axis, respectively – data taken from Amitsuka et al. (1992b).

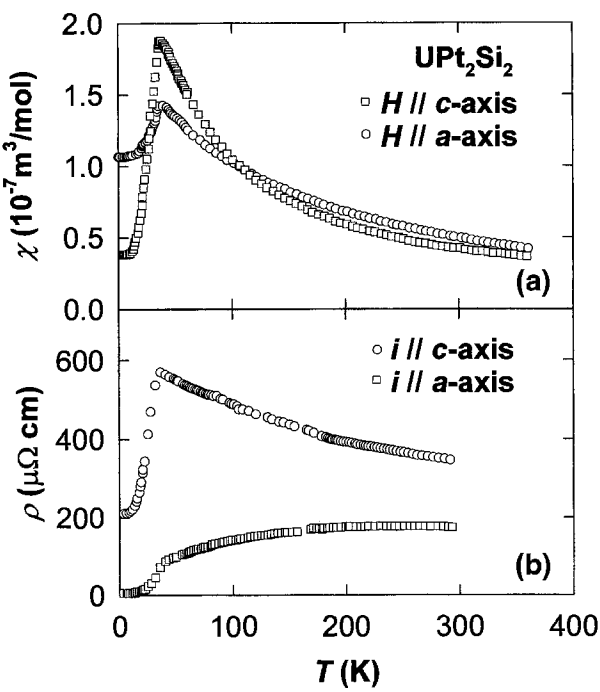

Fig. 5.81. Temperature dependence of: (a) Magnetic susceptibility χ with magnetic field H along the a- and c-axis, respectively – data taken from Amitsuka et al. (1992b); (b) Electrical resistivity ρ of UPt_2Si_2 measured on a single crystals with current i along the a- and c-axis respectively – data taken from Steeman et al. (1990).

the peak value of χ_c at T_N is considerably higher than that of χ_a, at the low temperature-limit one has $\chi_a > 2\chi_c$. An interesting type of crossing one can also see in the two related magnetization curves. Another unique feature of UPt_2Si_2 is a relatively low anisotropy field. Both magnetization curves are joining above the metamagnetic transitions (in fields > 50 T) and tend to saturate to a value which is close to the ordered magnetic moment determined by neutron diffraction experiment. Note that the anisotropy fields estimated in the other magnetic silicides are far above this value. The unusual susceptibility and magnetization behaviour has been successfully described within a crystal-field model, which is consistent with the appearance of crystal-field excitations in the neutron inelastic scattering spectra discussed below. Also the electrical resistivity (Steeman et al. 1990), which is also shown in fig. 5.80, exhibits a distinct anisotropy and a strongly anomalous temperature dependence. Similar to some other 5f electron antiferromagnets, the resistivity of UPt_2Si_2 with current along the propagation vector of the AF structure is increasing with decreasing temperature when approaching T_N. In this case, however, the negative slope of the $\rho(T)$ curve is observed already at room temperature. The resistivity in the c-axis direction reaches a maximum just at T_N and then sharply decreases with further decreasing temperature. The residual resistivity is, however, anomalously large and since the very low residual resistivity in the perpendicular direction excludes extensive lattice defects we may expect giant magnetoresistance effects at a metamagnetic transition in this compound. We note that no change of the resistivity due to Fermi surface gapping can be expected at the metamagnetic transition because the AF phase is of type-I in tetragonal 1:2:2 materials and this implies the same size of the magnetic and crystallographic unit cell. The a-axis resistivity displays a "d-electron intermetallics" behaviour with saturation at high temperatures. Several attempts have been made to interpret the magnetic properties of uranium intermetallic compounds, in terms of crystalline electric field model (Nieuwenhuys 1987, 1995). The UT_2X_2 compounds, and especially UPt_2Si_2, were also targeted by such efforts (Nieuwenhuys 1987; Santini et al. 1993). Only few cases, however, exist where crystal-field excitations have been observed experimentally. UPt_2Si_2 seems to be one of such rare cases where the inelastic neutron scattering experiment revealed crystal field excitations which has led Steeman et al. (1988) to propose a CEF level scheme. UPt_2Si_2 together with UPd_2Al_3 and U_2PtSi_3 were also subjects of resonant and X-ray photoemission studies (Ejima et al. 1994) and NMR studies (Benakki et al. 1988).

Similar to the Pd counterpart discussed above also in the UPt_2Si_2 case investigations of a strongly diluted U sublattice of $U_xTh_{1-x}Pt_2Si_2$ ($x \leqslant 0.07$) were performed by means of magnetic susceptibility, electrical resistivity and specific heat measurements (Amitsuka et al. 1995a). Also here a conclusion about a non-Fermi liquid scaling has been reached.

Only polycrystals were studied in case of UAu_2Si_2 with somewhat contradictory results reported in different papers. Palstra et al. (1986b) attributed the sharp increase of the magnetization (measured in 1 T) below 78 K to magnetic ordering with a canted ferromagnetic structure. Saran and McAlister (1988) suggested the onset of a spiral structure below $T = 80$ K, where they observed a sudden change of slope of the temperature dependence of the resistivity. Finally, Rebelsky et al. (1991a) reported a rise of magnetization (measured in 27 mT) below 48 K and Torikachvili et al. (1992) revealed a sharp peak in the ac susceptibility at $T = 44.3$ K, which can easily be removed by a field of 0.21 T. The resistivity curve shown in the latter report has nothing in common with that presented by Saran

and McAlister (1988), which indicates that the corresponding samples were rather incomparable. All authors, at least, agree in reporting an order–order magnetic phase transition at $T = 18$ K to the ground-state ferromagnetic ordering. A powder neutron diffraction experiment performed at several temperatures (11, 30, 45, 65, 150 and 300 K) clearly reveals that the magnetic phase transitions at 48 K and 18 K are associated with pronounced crystal structure changes, whereas no magnetic phase transition has been identified around 80 K (Rebelsky et al. 1991a). The comparative investigation of annealed and as-cast samples (Lin et al. 1997) has clearly shown that the magnetic transition at 80 K should be related to a spurious phase (most probably a ferromagnetic one with $T_C \approx 80$ K) present in the as cast sample. The annealed material exhibits clear anomalies around 21 K in the temperature dependencies of the specific heat, magnetization and electrical resistivity all indicating a magnetic phase transition at this temperature. A possible appearance of magnetic ordering already around 55 K may be inferred from the magnetization behaviour in this temperature range. No anomalies, however, are seen in this temperature range neither in the specific heat nor in the resistivity. Below this temperature, magnetic ordering with a considerable spontaneous magnetization can be deduced. The high residual resistivity does not suggest any a simple ferromagnetic ordering of uranium moments in the ground state. Further serious experimental efforts are desirable for improving the unsatisfactory state of knowledge about UAu_2Si_2.

5.2.2. *Germanides – UT_2Ge_2*

A compilation of the most important structural, magnetic and electronic parameters of UT_2Ge_2 compounds can be found in table 5.10. The magnetic behaviour of *UMn_2Ge_2* is analogous to that of UMn_2Si_2. Both U and Mn atoms are carrying magnetic moments. Also here the magnetic ordering in the U and Mn sublattice appear separately due to the weak U–Mn inter-sublattice exchange interaction. First the Mn magnetic moments order ferromagnetically at 390 K (Buschow and de Mooij 1986) whereas ferromagnetism in the uranium sublattice appears below 100–150 K, the latter temperatures being much higher than in the corresponding silicides. Whereas the magnetic phase transition connected with the ordering of the Mn moments is reflected in a clear λ-type anomaly of the specific heat (Slaski et al. 1992) and in a kink in the temperature dependence of the resistivity (Dirkmaat 1989), no irregularity on the C/T vs. T curve is seen in a wide temperature interval around 150 K. The ferromagnetic ordering of the Mn moments has been indicated also by high-temperature magnetization measurements (Szytula et al. 1988a). The measured size of the polar Kerr rotation in UMn_2Ge_2 (Kirby et al. 1991) increases from 0.05° at room temperature to 0.15° below 150 K when the U moments are ordered.

UFe_2Ge_2 similar to UFe_2Si_2 is a weakly temperature dependent paramagnet with susceptibility values of the order of (4–5) $\times 10^{-8}$ and 3×10^{-8} $m^3\,mol^{-1}$ along and perpendicular to the c-axis, respectively, as obtained on a single crystal (Dirkmaat 1989). The broad maximum around 200 K may indicate a characteristic spin-fluctuation temperature in this material.

UCo_2Ge_2 can appear in two different phases depending on heat treatment. Endstra et al. (1991) have studied the effect of annealing on the structural and magnetic properties of UCo_2Ge_2 and confirmed the existence of two different crystallographic structures. The

TABLE 5.10

Some basic characteristics of UT_2Ge_2 compounds:

γ – coefficient of the electronic specific heat, type of ground state (F – ferromagnetic, AF – antiferromagnetic, UAF – uncompensated antiferromagnetic, PP – Pauli paramagnetic), μ_U – the uranium ordered magnetic moment (determined by neutron diffraction at 4.2 K), $T_{C,N}$ – magnetic ordering temperature, T_{tr} – temperatures of other magnetic phase transitions (in the ordered state), Anis. – easy magnetization direction (determined by neutron diffraction and/or magnetization measurements of single crystals), a, c – lattice parameters at room temperature, Str. type (I – tetragonal body-centered $ThCr_2Si_2$-type structure, P – tetragonal primitive $CaBe_2Ge_2$-type structure).

Compound	γ (mJ/(mol K^2))	Ground state	μ_U (μ_B)	$T_{C,N}$ (K)	T_{tr} (K)	Anis.	Ref.	a (pm)	c (pm)	Str. type	Ref.
UMn_2Ge_2	30.3	F[a]	1.99	390	100–150[b]	$\|c$	[1,2,3]	399.3	1080.9	I	[3]
								398.77	1074.2		[4]
UFe_2Ge_2	24.4	PP[c]	–		–	[c]	[1,2]	402.43	996.36	I	[3]
UCo_2Ge_2[d]	34	AF	1.5	174	–	$\|c$	[5,6]	401.0	987.8	I	[5]
				160	–	–	[7]				
UCo_2Ge_2[e]	62	P	–	–	–	–	[5]	404.3	929.5	P?	[5]
UNi_2Ge_2	39.5	AF	2.35	77	–	$\|c$	[1,8]	408.9	947.2	I	[8]
UCu_2Ge_2	26.4	AF[f]	1.61	100[f]	43[f]	$\|c$	[1,8]	405.8	1020.7	I	[8]
URh_2Ge_2	130	SG	–	9[g]	–	$\|c$	[9,10]	414.64	975.10	I–P[h]	[9]
UPd_2Ge_2	–	UAF	1.97[i]	140	(87, < 80)[j]	$\|c$	[11,12]	420.0	1023.0	I	[11]
UIr_2Ge_2[e]	–	AF	–	19	–	–	[13]	416.5	983.3	P	[14]
UIr_2Ge_2[d]	–	AF	–	33	–	–	[13]	[k]	1025	P[k]	[13]
UPt_2Ge_2	14	AF	?	72	–	–	[15]	433.0	975.2	P	[15]

[a] Ferromagnetic alignment of both the U and Mn (2.36 μ_B) magnetic moments.

[b] Magnetic phase transition between the ground state magnetic structure and the high-temperature phase in which Mn moments only are ferromagnetically ordered whereas no ordering is observed in the U sublattice.

[c] Weakly temperature dependent, showing a shallow maximum around 200 K. Susceptibility values of the order of 4–5 $\times 10^{-8}$ and 3×10^{-8} m^3 mol^{-1} along and perpendicular to the c- and a-axis.

[d] Low-temperature phase.

[e] High-temperature phase.

[f] Ferromagnetic ordering from $T_C = 100$ K down to 43 K, below 43 K antiferromagnetic ordering.

[g] Freezing temperature T_f for $\omega \to 0$.

[h] Either $ThCr_2Si_2$ with random occupation of Cr and Si sites by Rh and Ge atoms (P4/mmm) or $CaBe_2Ge_2$ (P4/nmm).

[i] Root-mean square of the U magnetic moment.

[j] Derived from magnetization anomalies measured on polycrystals [10].

[k] Orthorhombic (space group Pmmm) with lattice parameters $a = 405.4$ pm, $b = 419.5$ pm.

[l] Tentatively deduced from an anomaly in the temperature dependence of electrical resistivity.

References:

[1] Endstra et al. (1990a)
[2] Szytula et al. (1988a)
[3] Dirkmaat (1989)
[4] Venturini and Malaman (1996)
[5] Endstra et al. (1991)
[6] Kuznietz et al. (1989)
[7] Hickey et al. (1992)
[8] Chelmicki et al. (1985)
[9] Süllow et al. (1997a)
[10] Süllow et al. (1997b)
[11] Ptasiewicz-Bak et al. (1981)
[12] Tien et al. (1994)
[13] Lloret et al. (1987)
[14] Shelton et al. (1984)
[15] Endstra et al. (1992a)

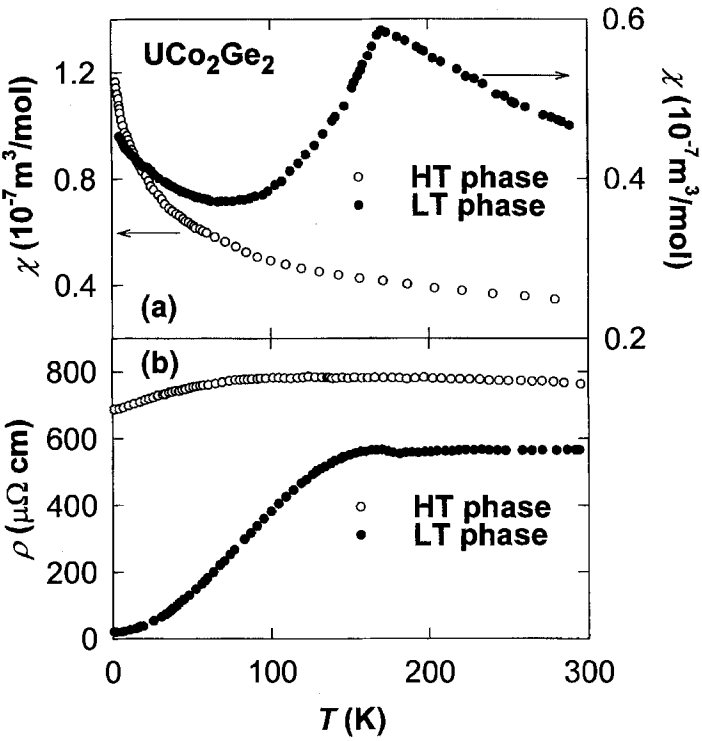

Fig. 5.82. Temperature dependence (a) of the susceptibility χ (in 3 T) and (b) electrical resistivity ρ of the high-temperature phase (o) and of the low-temperature (•) phase of UCo_2Ge_2, respectively – data taken from Endstra et al. (1991).

as-cast samples form a high-temperature phase, which adopts a yet unknown crystal structure, which has a symmetry lower than I4/mmm. After annealing at 750°C for 5 days a low-temperature phase with the $ThCr_2Si_2$ (I4/mmm) structure is formed. Besides the symmetry change, the c-axis in the high-temperature phase is approximately 6% shorter than in the low-temperature phase. This expansion of the unit cell greatly influences the magnetic properties of this compound. The low-temperature crystallographic phase orders antiferromagnetically at $T = 174$ K whereas the as cast sample does not order magnetically down to 350 mK. These results agree well with conclusions of Kuznietz et al. (1991) and Hickey et al. (1992) and can explain the discrepancies between lattice constants reported by Marazza et al. (1977) and Kuznietz et al. (1989) on the one side and by Chelmicki et al. (1985), Buschow and de Mooij (1986), and Endstra et al. (1990a) on the other side. The antiferromagnetic order in the low-temperature phase is of the type-I with ferromagnetic basal-plane sheets of uranium moments (1.5 μ_B at 4.2 K) and displays the $+-+-+-$ stacking along the c-axis (Kuznietz et al. 1989). The susceptibility (fig. 5.81) of the high temperature phase (polycrystalline data) follows a modified Curie–Weiss law down to 100 K and with further lowering it deflects upward from the

high-temperature MCW dependence reaching $\approx 7 \times 10^{-8}$ m^3/mol in the low temperature limit. From fig. 5.82 we can see that the change of structure in UCo_2Ge_2 is clearly reflected in the electrical resistivity. The resistivity of the as-cast sample (only polycrystalline data are available), which has a large room-temperature value of about 770 $\mu\Omega$ cm, increases slightly with decreasing temperature down to 100 K and then it slowly decreases, reaching about 700 $\mu\Omega$ cm in the low-temperature limit. The annealed sample exhibits an almost temperature independent resistivity (of about 580 $\mu\Omega$ cm) down to T_N. The latter is marked by a small dip in the ρ vs. T curve and is followed by a small bump around 160 K. The resistivity then decreases to rather low values (< 20 $\mu\Omega$ cm) in the low-temperature limit. The Néel temperature is well determined also by a peak in the C/T vs. T curve. It is worth to mention that the appearance of two tetragonal structure variants in UCo_2Ge_2 is not exceptional within the 1:2:2 class of intermetallics. Similarly, $LaIr_2Si_2$ is characterized by a low-temperature phase with the $ThCr_2Si_2$ structure and a high-temperature phase adopting the $CaBe_2Ge_2$ type, the latter one showing superconductivity whereas the former does not (Braun et al. 1983, 1985). Hickey et al. (1992) who investigated the $UCo_{2-x}Ge_{2+x}$ alloys for $-0.2 \leqslant x \leqslant 0.5$ revealed that there is a narrow range of homogeneity on the cobalt-rich side and established that the stoichiometric compound orders antiferromagnetically near 160 K. The lattice parameters and the magnetic ordering parameters of the compounds containing an excess of cobalt depend on their thermal treatment which may serve as a tool for explaining numerous discrepancies between literature sources on this material. Hickey et al. (1992) have discovered a new ternary germanide $U_2Co_3Ge_5$ which orders ferromagnetically below $T_C = 21$ K. Details will be discussed in section 5.9.9.

By means of neutron diffraction experiments, Kuznietz et al. (1995c, 1995d, 1997) studied the relative orientation of magnetic moments of uranium and a lanthanide (Ln = Nd, Tb) atoms which occupy the same site statistically in the quasi-ternary series of compounds $(U_{1-x}Ln_x)Co_2Ge_2$ crystallizing in the $ThCr_2Si_2$-type structure. Most of these compounds exhibit antiferromagnetic structures of type I consisting of basal planes of (U, Ln) magnetic moments oriented along the c-axis and coupled $+ - + - + -$ along the same direction. U and Nd magnetic moments in $(U_{1-x}Nd_x)Co_2Ge_2$ are coupled parallel and U and Tb moments in $(U_{1-x}Tb_x)Co_2Ge_2$ are coupled antiparallel, which means that U acts in this sense as a light rare earth.

Type-I antiferromagnetic ordering has been observed by means of powder neutron diffraction experiments in *UNi_2Ge_2* below 80 K by Chelmicki et al. (1985) and was confirmed in a similar way somewhat later by Kuznietz et al. (1993c). The magnetic phase transition at 77 K is very well determined by studies of the specific heat (Endstra et al. 1990a), magnetic susceptibility (Ning et al. 1992; Endstra et al. 1993a), electrical resistivity and Hall effect (Ning et al. 1992). Some of these properties are displayed in fig. 5.83, which demonstrates again the strong uniaxial anisotropy of magnetism and electrical transport. The spectacularly huge and narrow bump in the ρ vs. T curve just below T_N is discussed by Ning et al. (1992) in the framework of theoretical models originally developed by Miwa (1963) and Suezaki and Mori (1969) to explain the Cr-type resistivity anomaly below T_N. The temperature dependence of the Hall coefficient was explained in terms of a theoretical model of skew-scattering processes (Fert and Levy 1987). Perlov et al. (1998) investigated theoretically the zero-temperature electrical resistivity in UNi_2Ge_2 by applying the density functional theory and linear response approach to calculate the resistivity

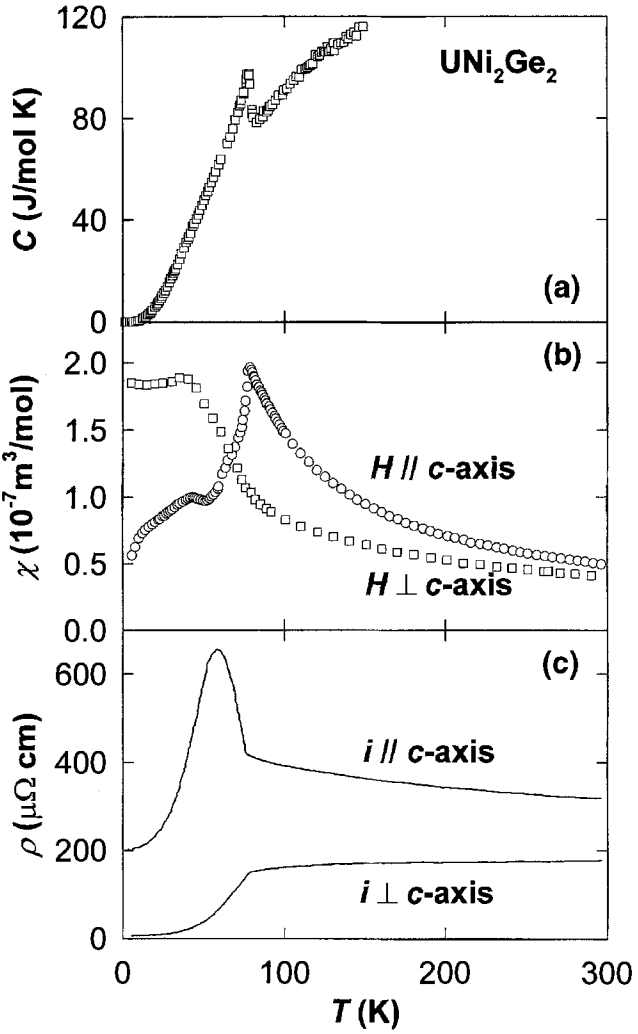

Fig. 5.83. Temperature dependence of following properties of UNi_2Ge_2: (a) Specific heat C – data taken from Endstra et al. (1990a); (b) Magnetic susceptibility χ with magnetic field H along and perpendicular to the c-axis, respectively – data taken from Ning et al. (1992); (c) Electrical resistivity ρ with current i along and perpendicular to the c-axis, respectively – data taken from Ning et al. (1992).

for the ground-state antiferromagnetic phase and the expected field induced ferromagnetic phase. The calculated ground-state resistivity is quite anisotropic ($\rho_\parallel/\rho_\perp \approx 2.1$, $\rho_\parallel$ and $\rho_\perp$ represent the resistivity for current parallel and perpendicular to the c-axis, respectively). For some Fermi surface sheets, however, a much larger anisotropy of ($\rho_\parallel/\rho_\perp \approx$ 10–40) has been calculated. In case of the metamagnetic AF $\rightarrow$ F transition a giant magnetoresistance has been predicted being much larger for current parallel to the c-axis $(\Delta\rho/\rho)_\parallel = -61\%$,

whereas for the perpendicular case $(\Delta\rho/\rho)_\perp = -14\%$. Roy et al. (1994) reported a distinct irreversibility and a metastable magnetization behaviour of polycrystalline samples below T_N in applied fields below 1 T. With small Ce doping, T_N is slightly suppressed but the irreversibility becomes more pronounced. Specific macroscopic magnetic characteristics which, can be used to distinguish an antiferromagnet unequivocally from a spin glass, were discussed.

Metallurgical problems and related inconsistencies reported for results on UCu_2Ge_2 led to intensive studies by several groups. Several investigators reported ferromagnetic ordering below 100–110 K (Leciejewicz et al. 1982; McAlister et al. 1989; Kuznietz et al. 1990a; Yusuf et al. 1996a, 1996b) as a result of combined powder neutron diffraction and ac-susceptibility or magnetization experiments. These results were supported also by neutron-depolarization (Yusuf et al. 1996a) and specific-heat data (Endstra et al. 1990a). Three different conclusions about the ground state phase can be sorted out from various mutually contradicting investigations all dealing with studies of polycrystals of various origins:

(a) Chelmicki et al. (1985), McAlister et al. (1989) and Dirkmaat et al. (1990b), based on powder neutron-diffraction data, propose that the ferromagnetic phase transforms below a certain temperature (25–40, 43 and 65 K, respectively), to an antiferromagnetic structure consisting of ferromagnetic basal-plane layers of uranium moments coupled along the c-axis in a $++--++--$ sequence. Although discussing "spin-glass features" of the low temperature magnetic behaviour, the existence of antiferromagnetism at low temperatures is admitted by Chakravarti et al. (1992) and Roy et al. (1995b) after a critical analysis of magnetization measurements including time dependencies. The conclusion about antiferromagnetism at low temperatures is corroborated also by a magnetoresistance study (Nigam et al. 1994).
(b) Yusuf et al. (1996a, 1996b) interpret their combined ac-susceptibility, magnetization and powder neutron diffraction results in terms of a sperromagnetism (Hurd 1983) below 45 K, which consists in a "randomly canted ferromagnetic phase".
(c) Kuznietz et al. (1990a) claim that they observed no transition to any low-temperature phase and therefore the homogeneous ferromagnetic ordering persists down to the lowest temperatures.

Note that $U_3Cu_3Ge_4$, which becomes ferromagnetic below 71 K, has been observed as an impurity phase when preparing UCu_2Ge_2 (Pechev et al. 1996). This may help to explain some of results in other reports mentioned above. These contradictory results on the magnetism of UCu_2Ge_2 are discussed by Kuznietz et al. (1993d). The absence or appearance of a low-temperature antiferromagnetic phase in UCu_2Ge_2 is ascribed to different annealing conditions that may lead to variations in stoichiometry, a view supported by neutron studies of the magnetic phase diagram of the $U(Ni_{1-x}Cu_x)_2Ge_2$ solid solutions (Melamud et al. 1998).

A study of $U_{1-x}Ce_xCu_2Ge_2$ compounds with higher Ce contents ($x \leqslant 0.5$) was made by Roy and Coles (1991) who showed that T_C is depressed fairly rapidly with increasing x, whereas the temperature of the F $\leftrightarrow$ AF transition becomes progressively enhanced. In $U_{0.5}Ce_{0.5}Cu_2Ge_2$ only the antiferromagnetic ordering is observed.

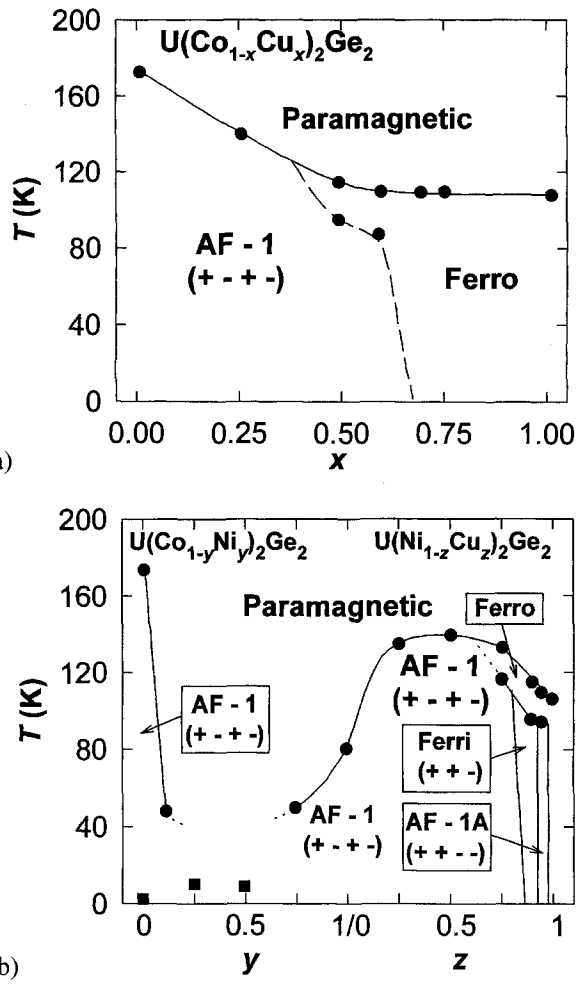

Fig. 5.84. Magnetic phase diagrams (T vs. concentration plots) of the solid solutions $U(Co_{1-x}Cu_x)_2Ge_2$ (a) and $U(Co_{1-y}Ni_y)_2Ge_2$ + $U(Ni_{1-z}Cu_z)_2Ge_2$ (b).

Similar to efforts on $U(T',T'')_2Si_2$ compounds, Kuznietz with his colleagues performed extended studies of the evolution of magnetic phase transitions and magnetic structures in the solid solutions *U(Co,Ni)$_2$Ge$_2$* (Kuznietz et al. 1990b, 1992b, 1994d, 1996), *U(Ni,Cu)$_2$Ge$_2$* (Kuznietz et al. 1990b, 1992c) and *U(Co,Cu)$_2$Ge$_2$* (Kuznietz et al. 1990a, 1990b). No pressure effect on the crystal and magnetic structures of UCu_2Ge_2 and $U(Ni_{0.05}Cu_{0.95})_2Ge_2$ together with an isotropic compressibility has been observed by neutron diffraction studies on samples in pressures up to 0.65 GPa. The magnetic results were explained in terms of the RKKY model (Caspi et al. 1998).

The main difference between the magnetic phase diagrams (Kuznietz et al. 1996) of these germanides (see fig. 5.84) and the analogous silicides (see fig. 5.68 and the related

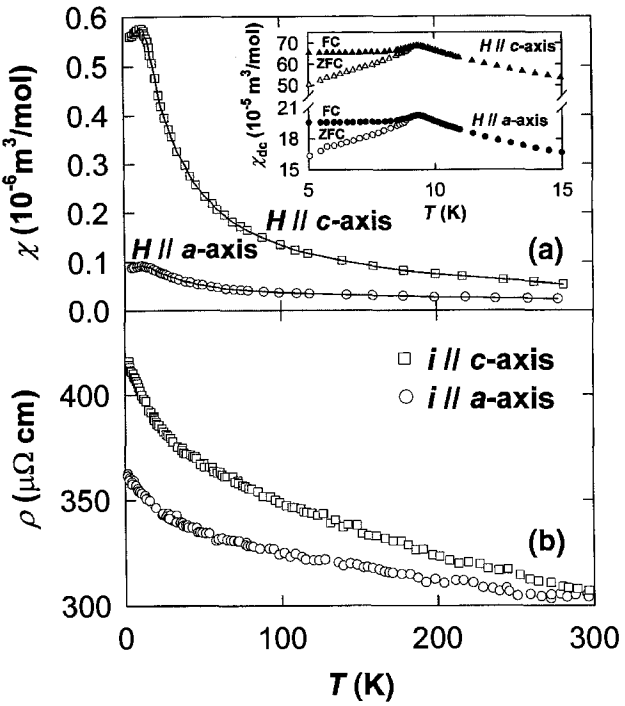

Fig. 5.85. Temperature dependence of: (a) Magnetic susceptibility with the magnetic field along the *a*- and *c*-axis, respectively – data taken from Dirkmaat et al. (1990c); (b) Electrical resistivity ρ with current *i* along and perpendicular to the *a*- and *c*-axis, respectively – data taken from Dirkmaat et al. (1990c); measured on a URh_2Ge_2 single crystal. The inset shows the field-cooled (FC – full symbols) and zero-field-cooled (ZFC – open symbols) data reported by Süllow et al. (1997b).

text) consists in the loss of magnetism in the *U(Co,Ni)$_2$Ge$_2$* series. Although UCo_2Ge_2 as well as UNi_2Ge_2, crystallize in the body-centred tetragonal $ThCr_2Si_2$-type structure and order with the AF-I antiferromagnetic structure, the intermediate solid solution of these compounds ($UCoNiGe_2$) crystallize in the lower-symmetric primitive tetragonal $CaBe_2Ge_2$-type structure (Kuznietz et al. 1994d). The Co/Ni distribution in the (Co,Ni) planes in both samples is not statistical. In planes close to the U planes Co:Ni ratios of about 1:2 are found whereas this ration is and 2:1 in the doubly dense and distant planes. The absence of magnetic order in this compound is attributed to the lower symmetry of the structure. Endstra et al. (1993a), however, report indications of magnetic ordering (below 21 K) even in $UCoNiGe_2$.

A maximum in the temperature dependence of the magnetic susceptibility of *URh_2Ge_2* polycrystals observed at 8 K (Ptasiewicz-Bak et al. 1981, 1985) or at 12 K (Lloret et al. 1987) was interpreted in terms of the onset of antiferromagnetic ordering although no magnetic contribution to the neutron diffraction spectrum has been observed at $T = 4.2$ K by the former authors. As shown by Lloret et al. (1987), the temperature of the susceptibility maximum strongly depends on stoichiometry deviations. Thompson et al. (1985)

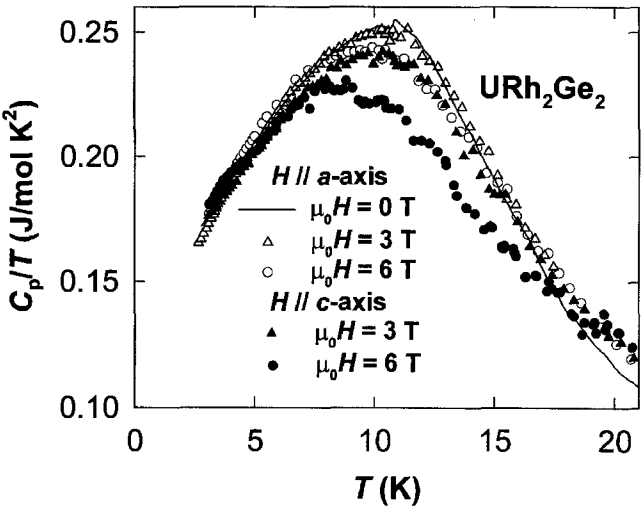

Fig. 5.86. Temperature dependence of the specific heat (C_p/T vs. T plot, data corrected for the lattice contribution by subtracting specific heat values of the non-magnetic analogue UFe_2Ge_2) of a URh_2Ge_2 single crystal in various magnetic fields H applied along the a- or c-axis – data taken from Süllow et al. (1997b).

claimed antiferromagnetism in this compound below 2 K because of a precipitous decrease of the electrical resistivity. The lack of pressure influence on the magnetic ordering temperature has been attributed to the high stability of the uranium magnetic moment in this compound. These contradictory reports required further experimental efforts to shed more light on the low temperature behaviour of this materials. Substantial progress has been made after single crystals of this material were grown and careful experimental work was performed.

Dirkmaat et al. (1990c) reported results of magnetic susceptibility, magnetization, resistivity and specific heat measurements made on such a high-quality single crystal. The temperature dependence of the susceptibility and resistivity measured along the two principal crystallographic directions is shown in fig. 5.85. The susceptibility displays strong uniaxial anisotropy which is a common feature of the whole class of UT_2X_2 compounds where the c-axis response is distinctly larger than the perpendicular signal. In both directions a broad maximum is observed at about 10 K, which confirms the previous polycrystalline data (Ptasiewicz-Bak et al. 1981, 1985). Above the maximum, the susceptibility follows a modified Curie–Weiss law with anisotropy in all three parameters: $\theta_p = -10$ K and -19 K, $\mu_{eff} = 2.98\,\mu_B$ and $1.25\,\mu_B$, $\chi_0 = 0.6 \times 10^{-8}$ and 1.1×10^{-8} m^3/mol for fields applied along the c- and a-axis, respectively. Below the susceptibility maximum the progressive splitting of FC and ZFC branches with lowering temperature indicates magnetic irreversibility. The ac-susceptibility (Süllow et al. 1997a, 1997b) exhibits a clear frequency dependence pushing the susceptibility maximum towards higher temperatures with increasing ω.

Also the resistivity shows some anisotropy, being somewhat larger for current along the c-axis. For both current directions one finds a very similar temperature dependence, ρ in-

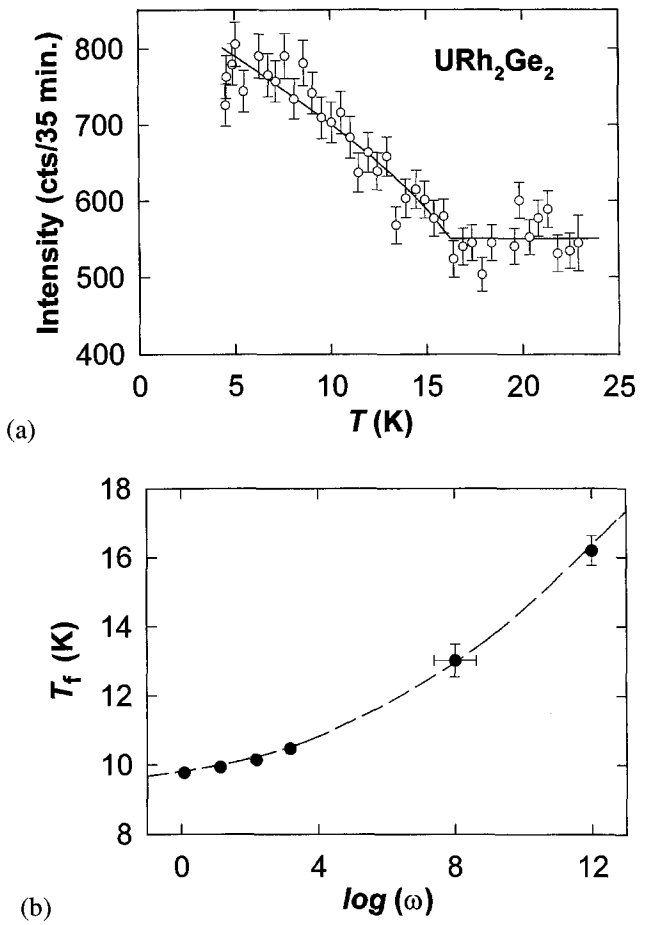

Fig. 5.87. (a) Temperature dependence of the elastic neutron scattering intensity in URh_2Ge_2 at $Q = (1, 0, 0)$, demonstrating the onset of magnetic correlations slower than 10^{-12} s below $T_f = 16.2$ K. The line is a guide to the eye. (b) Frequency dependence of the freezing temperature T_f derived from the *ac* susceptibility, neutron-scattering and μ^+SR data for URh_2Ge_2. Data taken from Süllow et al. (1997b).

creasing monotonously with decreasing temperature. Below 20 K the ρ vs. T dependence is linear down to 35 mK. This indicates that the resistivity decrease reported by Thompson et al. (1985) and Lloret et al. (1987) on polycrystals below 2 K is probably due to a secondary phase. The specific heat corrected for the lattice contribution is displayed in fig. 5.86. It shows a broad bump above 10 K which can be smeared out (by pushing the magnetic entropy to higher temperatures) by applying magnetic fields, which process is much more effective for magnetic fields applied along the c-axis. Structure analysis using nuclear reflections from neutron diffraction (Ptasiewicz-Bak et al. 1981, 1985; Süllow et al. 1997a) indicates that the symmetry of the crystal is tetragonal. However it is not possible to distinguish between the P4/nmm and P4/mmm space groups.

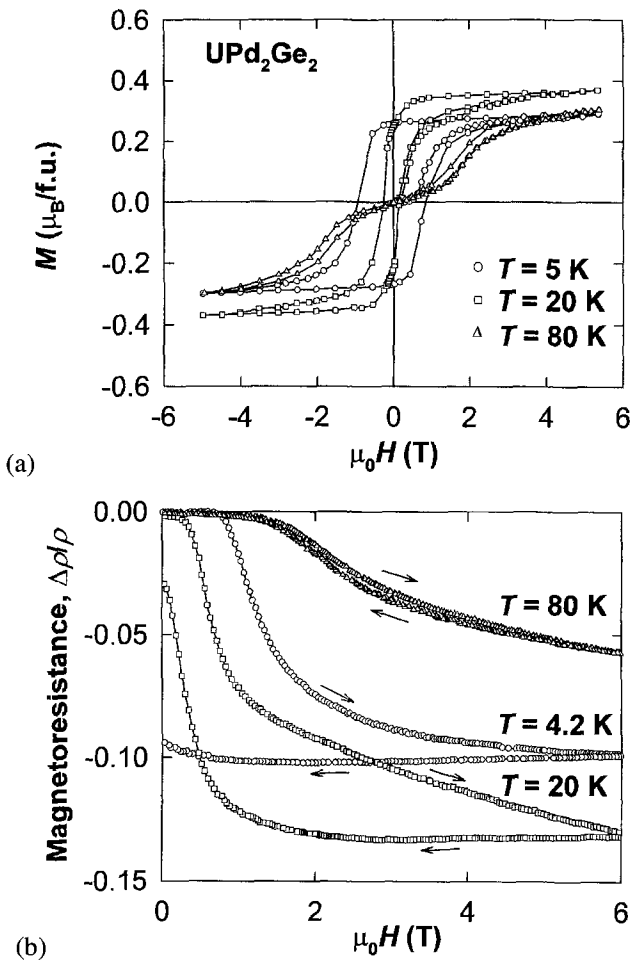

Fig. 5.88. Magnetic-field dependence of the magnetization M at $T = 5$, 20 and 80 K (upper panel), and magnetoresistance at $T = 4.2$, 20 and 80 K (lower panel) measured on UPd_2Ge_2 polycrystals – data taken from Tien et al. (1994) and Duh et al. (1996a), respectively.

All the above findings on single crystals point to the possibility that the low-temperature properties of URh_2Ge_2 are determined by a spin glass state (Mydosh 1993). This assumption has been finally confirmed by neutron scattering (Süllow et al. 1997b). The neutron scattering data in fig. 5.87 point to the onset of magnetic correlation slower than 10^{-12} s at 16.2 K. The frequency dependence of the freezing temperature T_f derived from all the available data points to the onset of static correlations on a time scale of 10^{-3} s below 10 K.

All the available experimental evidences manifest that URh_2Ge_2 has an extraordinary position in the class of UT_2Ge_2 owing to its spin-glass ground state. Strong anisotropy of the susceptibility clearly shows that we deal with an Ising-like spin-glass system.

UPd_2Ge_2 have been studied so far only in polycrystalline form. Ptasiewicz-Bak et al. (1981) reported an anomaly in the magnetic susceptibility at 138 K, indicating a phase transition between paramagnetism and antiferromagnetic ordering. They also have performed powder neutron diffraction experiments at 4.2 K, 80 K, and 300 K and made a temperature scan of characteristic magnetic reflections. The latter data point to $T_N = 140$ K. The magnetic reflections observed at low temperatures can be attributed to an incommensurate spin density wave (ISDW) with a propagation vector $\boldsymbol{q} = (0, 0, 0.748)$ and an amplitude of the U magnetic moment of 2.79 and 2.68 μ_B at 4.2 K and 80 K, respectively. More detailed measurements of the temperature dependence of the magnetization point to the possibility of more magnetic phase (order–order) transitions below T_N (Tien et al. 1994; Duh et al. 1995a) which show up in the magnetization measured in 0.05 T as a maximum at 87 K, a steep increase below 80 K, and a broad maximum around 50 K followed by a precipitous decrease with further decreasing temperature. The low-temperature magnetization behaviour was interpreted by Duh et al. (1995a, 1995b) in terms of spin glass state. Magnetization curves at various temperatures (Tien et al. 1994; Duh et al. 1995a) and related magnetoresistance curves (Duh et al. 1996a) are displayed in fig. 5.88. The latter curves show a GMR effect when magnetizing from zero-field-cooled state. This leads to a conclusion that the ground-state phase in UPd_2Ge_2 is antiferromagnetic, as originally proposed by Ptasiewicz-Bak et al. (1981). The ferromagnetic phase is then induced by a metamagnetic transition seen on the virgin magnetization curve and finally remains frozen in the material when decreasing the field to 0 T and even when applying a magnetic field of opposite direction. In many aspects this situation strongly resembles the case of UNiGa (see section 5.1.1). Single crystals of well defined composition and a detailed concerted magnetization, magnetoresistance, and neutron scattering study in the whole temperature range of the magnetic ordering are strongly desirable if one wishes to resolve open questions about the magnetism in UPd_2Ge_2. The importance of well defined composition in these studies is demonstrated by the fact that tiny substitutions (1–3%) of Fe for Pd drastically change the low-temperature magnetization behaviour (Duh et al. 1995c). The overall evolution of magnetic properties in the series $U(Pd_{1-x}Fe_x)_2Ge_2$ has been described by Duh et al. (1996b).

UIr_2Ge_2 can be observed in two allotropic phases. The high-temperature phase obtained by quenching from the melting point crystallizes in the $CaBe_2Ge_2$-type structure similar to the corresponding silicide. The low-temperature phase is obtained after annealing at 800°C. It forms in an orthorhombic phase, which has been observed also in $GdIr_2Ge_2$ (François et al. 1985). These two phases exhibit different low-temperature magnetic properties. The maximum in the temperature dependence of susceptibility can be attributed to the onset of antiferromagnetic ordering. For the low-temperature phase the maximum is observed at 33 K, whereas it appears at 19 K in the other phase. Principal differences between the two phases are observed also in the low temperature resistivity behaviour. The resistivity in the low-temperature phase precipitously decreases below 33 K while the high-temperature phase exhibits an increase with decreasing temperature below 19 K. Both allotropic phases, however, show rather similar susceptibility behaviour above 40 K, following Curie–Weiss behaviour. Similar to URh_2Ge_2, also UIr_2Ge_2 has a narrow homogeneity range (Lloret et al. 1987) similar to YIr_2Si_2 (Hirjak et al. 1985). This is probably the main source of the large scatter of magnetic parameters reported for such systems in different literature sources.

As can be inferred from the magnetic susceptibility, specific-heat and electrical resistivity data observed on polycrystalline samples, UPt_2Ge_2 exhibits simple antiferromagnetic ordering below $T_N = 72$ K (Endstra et al. 1992a). This is corroborated by the paramagnetic susceptibility behaviour of the polycrystal, which very well satisfies the Curie–Weiss law with $\Theta_p = -52$ K and $\mu_{eff} = 2.98\,\mu_B$/f.u.

5.2.3. Non-stoichiometric gallides and stannides U–T–Ga and U–T–Sn

A compilation of the available structure and magnetic information on the compounds treated in this section can be found in table 5.11. Zolnierek and Zaleski (1992), and Zolnierek and Szulc (1992) have shown that within the ternary *U–Cu–Ga* system several non-stoichiometric phases (see table 5.11) exist and all these phases crystallize in the I4/mmm space group. Magnetization and resistivity measurements performed at finite magnetic fields revealed in some of these materials unusual antiferromagnetism below 55 K with a strong ferromagnetic component vanishing at temperatures fairly higher than T_N. The more Ge-rich U–T–Ga compounds form, however, the simple collinear AFI-type antiferromagnetic structure. The ground state phase in the former materials has a new type of canted magnetic structure which has been proposed from the analysis of neutron powder diffraction data (Stüsser et al. 1998). This structure has been denoted by Zolnierek as AFIV and it is illustrated in fig. 5.89. Values of the basal-plane and c-axis components of the U moment can be found in table 5.12. The formation of this structure has been attributed to a special distribution of the Ga- and Cu-atoms over the crystallographic (4e) and (4d) sites (Stüsser et al. 1998). Due to the close structure similarity (I4/mmm space group) we include also $UAu_{1.3}Ga_{2.5}$ which orders antiferromagnetically in the AFI-type structure below 49 K (Zolnierek and Mulak 1995).

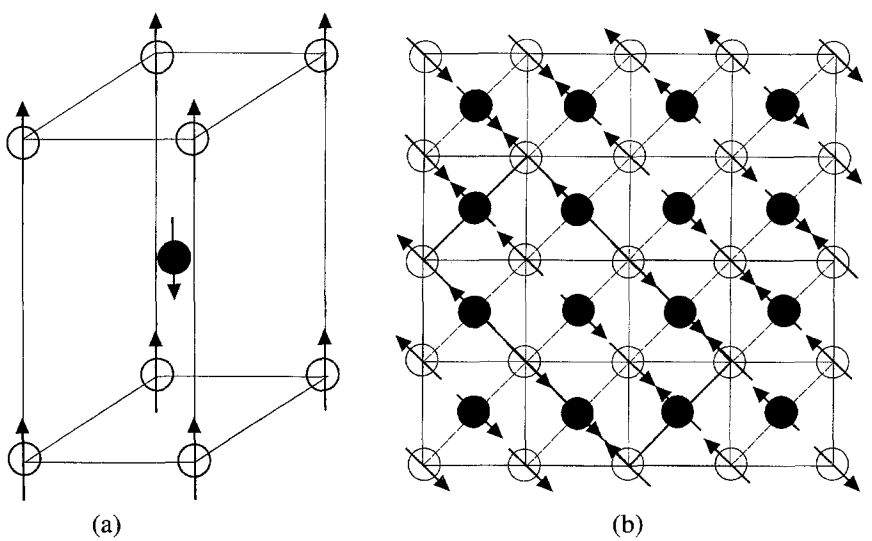

Fig. 5.89. Spin arrangement in the AFI (a) and AFIV (b) magnetic structure appearing in U–Cu–Ga compounds. The latter figure represents a projection in the basal plane. Data taken from Stüsser et al. (1998).

TABLE 5.11

Some basic characteristics of U–T–Ga and U–T–Sn compounds:
Type of ground state (AF – antiferromagnetic, P – paramagnetic), μ_U – the uranium ordered magnetic moment (determined by neutron diffraction at 4.2 K), T_N – magnetic ordering temperature, Anis. – easy magnetization direction (determined by neutron diffraction and/or magnetization measurements of single crystals), space group or structure type (I – tetragonal body-centered $ThCr_2Si_2$-type structure, P – tetragonal primitive $CaBe_2Ge_2$-type structure), a, c – lattice constants at room temperature.

Compound	Magn. order	T_N (K)	μ_U (μ_B)	Anis.	Ref.	Space group	a (pm)	c (pm)	Ref.
$UCu_{1.5}Ga_{2.5}$	AF[a]	49	2.47	$\|c^a$	[1]	I	412.9	1007.8	[2]
$UCu_{1.33}Ga_{2.5}$	AF[a]	49	2.6	$\|c^a$	[2,3]	I	413.4	1007.8	[2]
$UCu_{1.25}Ga_{2.5}$	AF[a]		2.5	$\|c^a$	[3]	I			
$UCu_{1.45}Ga_{2.55}$	AF[a]		2.3	$\|c^a$	[3]				
$UCu_{1.40}Ga_{2.60}$	AF[a]		2.3	$\|c^a$	[3]				
$UCu_{1.16}Ga_{2.66}$	AF[b]	55	2.1	$\|c$	[2,3]	I	415.2	991.1	[2]
$UCu_{1.33}Ga_{2.66}$	AF[b]	53	2.1	$\|c$	[2,3]	I	415.2	996.6	[2]
$UAu_{1.3}Ga_{2.5}$	AF[b]	45/49	1.87	$\|c$	[1]	I			
$UCo_{1.5}Sn_2$[c]	AF[d]	110	0.68[d]	$\|c$	[4,5]	P	437.8[e]	905.4[e]	[5]
$UNi_{1.4}Sn_2$[f]	AF[b]	35	1.89	$\|c$	[7]	P	439.01	925.73	[6]
$UCu_{1.3}Sn_2$[g]	AF[b]	108	2.32	$\|c$	[7]	P	438.3	960.2	[6]
$UCu_{1.5}Sn_2$[g]	AF[b]	107	2.01	$\|c$	[8]	P	439.20	964.80	[8]
$ThCo_{1.50}Sn_{1.96}$						P	443.5	974.9	[6]
$ThCo_2Sn_2$	AF	65			[9]				
$ThNi_{1.50}Sn_{1.91}$						P	442.1	993.9	[5]
$ThCu_{1.50}Sn_{1.77}$						P	441.3	1022.7	[6]

[a] Canted antiferromagnetic structure AFIV (Zolnierek and Mulak 1995; Stüsser et al. 1998), see fig. 5.89.
[b] (AFI) Antiferromagnetic structure type I.
[c] Composition of $UCo_{1.45}Sn_2$ reported in (Mirambet et al. 1992) and $UCo_{1.41}Sn_{1.85}$ (Kim and Stewart 1995).
[d] $\boldsymbol{q} = (0, 0, 1/2)$, Co moment of 0.63 μ_B at the 2*b* position and 0 at the 2*c* position, at 1.4 K.
[e] At 160 K.
[f] Composition of $UNi_{1.42}Sn_{1.88}$ reported in Kim and Stewart (1995).
[g] Composition of $UCu_{1.30}Sn_{1.91}$ reported in (Kim and Stewart 1995) and $UCu_{1.5}Sn_2$ (Purwanto et al. 1996b).

References:

[1] Zolnierek and Mulak (1995)
[2] Zolnierek and Szulc (1992), Zolnierek and Zaleski (1992)
[3] Stüsser et al. (1998)
[4] Thuery and Zolnierek (1993)
[5] Mirambet et al. (1992)
[6] Pöttgen et al. (1993)
[7] Kaczorowski and Stüsser (1996)
[8] Purwanto et al. (1996b)
[9] Kaczorowski et al. (1993a)

Kaczorowski et al. (1993a) have studied structure, magnetization (susceptibility) and electrical resistivity of the ternary stannides UT_2Sn_2 and ThT_2Sn_2 (T = Co, Ni, Cu) which all crystallize with the $CaBe_2Ge_2$-type crystal structure. *UCu_2Sn_2* and *UNi_2Sn_2* are reported as antiferromagnets with Néel temperature of 108 K and 35 K, respectively as inferred both from magnetic susceptibility and electrical resistivity anomalies. The occurrence of complex magnetic behaviour of *UCo_2Sn_2* is claimed due to two subsequent maxima in the temperature dependence of the magnetic susceptibility and a strong field depen-

TABLE 5.12
Basal-plane ($\mu_{U-x,y}$) and c-axis (μ_{U-z}) projections of uranium moment in U–Cu–Ga compounds with the canted antiferromagnetic structure AFIV (Stüsser et al. 1998).

Compound	μ_U (μ_B)	$\mu_{U-x,y}$ (μ_B)	μ_{U-z} (μ_B)
$UCu_{1.5}Ga_{2.5}$	2.5	1.8	1.6
$UCu_{1.33}Ga_{2.5}$	2.6	1.6	2.0
$UCu_{1.25}Ga_{2.5}$	2.5	1.4	2.1
$UCu_{1.45}Ga_{2.55}$	2.3	1.5	1.8
$UCu_{1.40}Ga_{2.60}$	2.3	1.0	2.1

dence of the magnetization. *$ThCo_2Sn_2$* orders antiferromagnetically below 65 K whereas *$ThCu_2Sn_2$* and *$ThNi_2Sn_2$* remain paramagnetic down to 4.2 K. Resistivity data reported by Baran and du Plessis (1993) for three *UCu_2Sn_2* samples annealed in various ways exhibit a common anomaly at 110 K, which is close to above mentioned value of T_N. Subsequent work of Pöttgen et al. (1993) focused on crystal structure refinement confirmed that these stannides crystallize with the $CaBe_2Ge_2$-type structure, however with extensive defects in occupation of lattice sites. At least one of the transition metal sites in each compound is not fully occupied. Partial occupancies were also found for most of the Sn sites. The compositions of these phases have been determined as $ThCo_{1.50}Sn_{1.96}$, $ThNi_{1.80}Sn_{1.91}$, $ThCu_{1.50}Sn_{1.77}$, $UCo_{1.41}Sn_{1.85}$, $UNi_{1.42}Sn_{1.88}$ and $UCu_{1.30}Sn_{1.91}$. Mirambet et al. (1992) claim that the optimal composition of the U–Co–Sn compound is $UCo_{1.45}Sn_2$ and report the latter to be antiferromagnetic below $T_N = 110$ K. Thuery and Zolnierek (1993) studied the U–Co–Sn phase (nominally $UCo_{1.5}Sn_2$) by neutron diffraction. They propose that a collinear antiferromagnetic structure with $\boldsymbol{q} = (0, 0, 1/2)$ forms below 130 K and consists of both uranium moments (0.68 μ_B) and cobalt moments (0.63 μ_B at the $2b$ position and 0 at the $2c$ position). A powder neutron-diffraction investigation of the crystal and magnetic structures of the U–Ni–Sn ($UNi_{1.4}Sn_2$) and U–Cu–Sn ($UCu_{1.3}Sn_2$) phases made by Kaczorowski and Stüsser (1996) has revealed AFI ordering of uranium moments (1.89 and 2.32 μ_B) in both cases. Somewhat different values, $T_N = 107$ K and $\mu_U = 2.01$ μ_B, have been reported by Purwanto et al. (1996b). These authors found larger lattice parameters in a sample with the composition $UCo_{1.5}Sn_2$ without indicating any Cu deficiency, in contrast to work of Pöttgen et al. (1993).

5.2.4. Pnictides UT_2X_2 (X = P, As)

In table 5.13 a survey of the basic properties of 1:2:2 pnictides is given. One can see that besides the $CaBe_2Ge_2$ and $ThCr_2Si_2$ structure types we can find examples of the hexagonal $CaAl_2Si_2$-type, including UCu_2X_2 compounds (Zolnierek et al. 1986) and their thorium analogues (Klüfers et al. 1979). The ruthenium compounds URu_2P_2 and $ThRu_2P_2$ crystallize in a prototype orthorhombic structure which is rather close to the $BaZn_2As_2$ structure (Klüfers and Mewis 1978) and the $BaCu_2S_2$ structure (Iglesias et al. 1974). These are characterized by the same space group and similar atomic positions) but the co-ordination polyhedra are different (Glaum et al. 1992). Refinement of X-ray and/or neutron diffraction

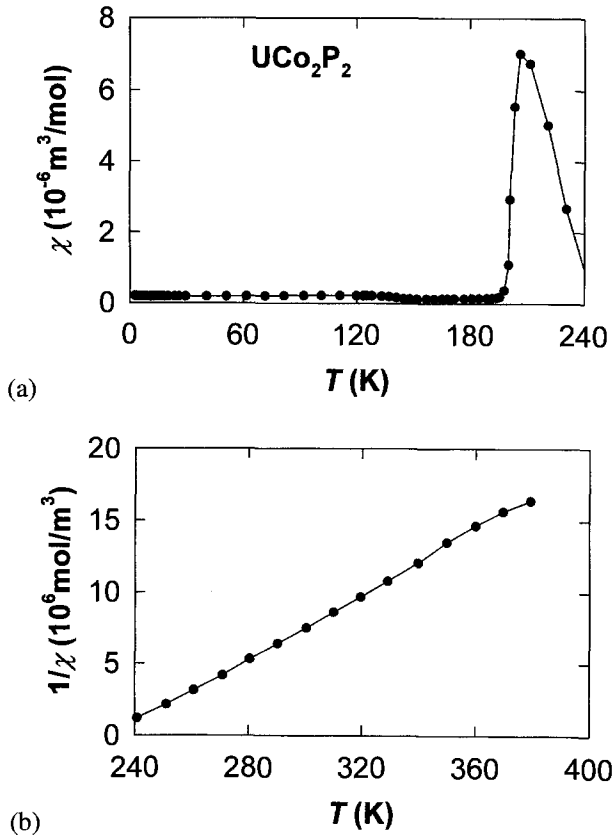

Fig. 5.90. (a) Temperature dependence of the magnetic susceptibility χ in a UCo_2P_2 polycrystal in a magnetic field of 0.15 T. (b) Temperature dependence of the inverse susceptibility of a UCo_2P_2 polycrystal above 240 K. Data taken from Reehuis et al. (1991).

data of Ni and Rh containing compounds revealed that they form in a defective structure due to a deficiency of Ni atoms in the former case, and a deficiency of Rh and As in the U–Rh–As system (see table 5.13 and attached comments). The defect ordering in $URh_{1.6}As_{1.9}$ causes formation of a superstructure (Zemni et al. 1988).

The temperature dependence of the magnetization (susceptibility) of UCo_2P_2 is rather complex as it can be seen in fig. 5.90. The susceptibility tends to diverge when cooling below 230 K. This trend, however, is terminated around 225 K (which was considered as the temperature of magnetic ordering), the increase of the magnetization is gradually reduced and below 180 K the magnetization falls to very low values and does not vary substantially down to lowest temperatures. Reehuis et al. (1991) have demonstrated that the temperature (T_1) of the latter transition is strongly suppressed by an applied magnetic field although the width of the transition is not affected. Extrapolation of these results to zero field yields $T_1 = 199$ K, whereas a field of 5 T reduces T_1 to below 140 K (Reehuis et al. 1991). A neutron-diffraction experiment, which was performed on a UCo_2P_2 powder sample at 2,

TABLE 5.13

Some basic characteristics of various UT_2X_2 and ThT_2X_2 pnictides:

Type of magnetic ordering (F – ferromagnetic, AF – antiferromagnetic), μ_{An} – the actinide ordered magnetic moment (determined by neutron diffraction at 4.2 K, $T_{C,N}$ – magnetic ordering temperature, T_{tr} – temperatures of other magnetic phase transitions (in the ordered state), Anis. – easy magnetization direction (determined by neutron diffraction and/or magnetization measurements of single crystals), space group, structure type, a, b, c – lattice parameters at room temperature.

Compound	Ground state	μ_{An} (μ_B)	$T_{C,N}$ (K)	T_{tr} (K)	Anis.	Ref.	Space group	Str. type	a (pm)	b (pm)	c (pm)	Ref.
UFe_2P_2							I4/mmm	$ThCr_2Si_2$				[1]
UCo_2P_2	AF		225	199, (145)		[2]	P4/nmm	$CaBe_2Ge_2$	392.1		894.3	[4]
	AF	1.78 [a]	225	175	$\|c$	[3]	P4/nmm	$CaBe_2Ge_2$	381.2		929.3	[5]
UNi_2P_2 [b]	AF		111			[6,7]	I4/mmm	$ThCr_2Si_2$	382.3		944.0	[6]
	AF [c]	1.59 [d]	101		$\|c$							[8]
UCu_2P_2	F	1.78 [e]	216		$\|c$	[9]	$P\bar{3}m1$	$CaAl_2Si_2$	392.5		635.0	[6,10]
		1.72–1.85 [f]				[11]			394.1		636.6	[11]
URu_2P_2 [f]							Pnma	[g]	753.15	406.7	1029.4	[12]
UCo_2As_2							P4/nmm	$CaBe_2Ge_2$	399.2		927.0	[4]
UNi_2As_2							P4/nmm	$CaBe_2Ge_2$	403.06		934.6	[13]
$UNi_{1.6}As_2$	AF [c]	1.4	145	95 [h]	$\|c$	[14]	P4/nmm	$CaBe_2Ge_2$	399.4		928.1	[15]
UCu_2As_2	F		140			[6]	$P\bar{3}m1$	$CaAl_2Si_2$	410.3		654.4	[6]
URh_2As_2 [I]							P4/nmm	$CaBe_2Ge_2$ [j]	408.2		967.5	[4]
$ThCo_2P_2$							P4/nmm	$CaBe_2Ge_2$				[1]
$ThCu_2P_2$							$P\bar{3}m1$	$CaAl_2Si_2$				[16]
$ThRu_2P_2$							Pnma	[g]	737.9	413.95	1047.8	[12]

TABLE 5.13 (Continued)

[a] Observed at $T = 2$ K. A moment of $0.18\ \mu_B$ has been found at Co sites (Troc et al. 1993b).
[b] Structure refinement from neutron data revealed a Ni deficiency, actual composition was $UNi_{1.56}P_2$ (Fischer et al. 1989).
[c] AFI – antiferromagnetic type I structure (Fischer et al. 1989).
[d] Magnetic moment at 7.5 K (Fischer et al. 1989).
[e] Derived from magnetization data (Zolnierek et al. 1986).
[f] Actual composition was $URu_2P_{1.894}$ (Glaum et al. 1992).
[g] Close similarity to $BaZn_2As_2$ (Klüfers and Mewis 1978) and $BaCu_2S_2$ (Iglesias et al. 1974) structures. They have the same space group and similar atomic positions. However, the coordination polyhedra are different (Glaum et al. 1992).
[h] Between $T = 95$ and 145 K two sets of magnetic peaks corresponding to $\boldsymbol{q}_1 = (0, 0, 0)$ and $\boldsymbol{q}_2 = (0, 0, 1/2)$ and two magnetic Fourier components of about the same amplitude along the c-axis, respectively, coexist (Troc et al. 1994b).
[i] The actual composition was $URh_{1.6}As_{1.9}$ (Zemni et al. 1988).
[j] Superstructure derived from the $CaBe_2Ge_2$-type structure with some of Rh and As atom position partially or completely empty. The basal-plane atomic plane stacking with ordered and disordered vacancies U-As-Rh-(As, □)-U-(Rh, □)-As-(Rh, □), where □ represents a vacancy (Zemni et al. 1988).

References:

[1] Jeitschko et al. (1985)
[2] Reehuis et al. (1991)
[3] Troc et al. (1993b)
[4] Zemni et al. (1988)
[5] Kaczorowski (1992)
[6] Zolnierek et al. (1986)
[7] Fischer et al. (1989)
[8] Hofmann and Jeitschko (1984)
[9] Kaczorowski and Troc (1990)
[10] Zolnierek et al. (1987)
[11] Delapalme et al. (1994)
[12] Glaum et al. (1992)
[13] Jeitschko et al. (1988)
[14] Troc et al. (1994b)
[15] Troc et al. (1990)
[16] Klüfers et al. (1979)

180, 210, and 240 K (the latter temperature was chosen to collect the reference paramagnetic data), allowed to determine the ground-state magnetic structure (2 K data), but failed to discover any fingerprints of magnetism around 200 K (Reehuis et al. 1991). One may speculate about an incommensurate antiferromagnetic phase which can be hardly traced in the poor-statistics powder diffractograms. Further effort to determine the high-temperature phase in UCo_2P_2 by neutron scattering investigations is strongly desirable. The ground-state antiferromagnetism consists of antiparallel coupled sublattices of the U ($1.78\,\mu_B$) and Co ($0.18\,\mu_B$) magnetic moments, and has a propagation vector $\boldsymbol{q} = (0, 0, 1/2)$. The magnetic structure is collinear with magnetic moment parallel to the c-axis.

Above 240 K, the susceptibility measured on a UCo_2P_2 polycrystal up to 380 K mimics Curie–Weiss law behaviour with $\Theta_p = 239$ K and $\mu_{eff} = 2.28\,\mu_B$ (Reehuis et al. 1991). Extension of such a measurement up to 1000 K reveals that the $1/\chi$ vs. T plot becomes really linear only above 600 K and than it can be approximated by a Curie–Weiss law with $\mu_{eff} = 3.6\,\mu_B$ and $\Theta_p = -300$ K. After a simple simulation calculus we can find that this behaviour may be obtained by averaging the signals of a single crystal with anisotropic Curie–Weiss susceptibility with $\Theta_p^a = -300$ K, $\Theta_p^c = 239$ K and $\mu_{eff}^{a,c} = 3.6\,\mu_B$. The value derived for the effective moment conforms with theoretical values for free U^{3+} or U^{4+} ions which may point to localized 5f states in this materials. The strikingly different values of the paramagnetic Curie–Weiss temperatures reflect a uniaxial anisotropy with the main paramagnetic response concentrated in the c-axis, which is also the easy magnetization axis of the ground state.

UNi_2P_2 orders antiferromagnetically with the AFI structure (Fischer et al. 1989) with uranium moments ($1.59\,\mu_B$) collinear and parallel to the c-axis, which is frequently observed in 1:2:2 compounds. The value of Néel temperature $T_N = 101$ K derived on the base of vanishing of the intensity of magnetic reflections is considerably lower than 111 K proposed by Zolnierek et al. (1986) from the temperature of the susceptibility maximum. However, the former value coincides well with the temperature of the maximum of $\partial(\chi T)/\partial T$ derived from the temperature dependence of the genuine thermodynamic variable χT (Fisher 1962; Fedders and Martin 1966), which can be revealed by closer inspection of the susceptibility data presented by Zolnierek et al. (1986). The temperature dependence of the intensity of the magnetic reflections also reveals that the uranium magnetic moment remains almost constant up to approximately 70 K ($\approx 0.7\,T_N$).

UCu_2P_2 becomes ferromagnetic below 216 K, which is the highest ordering temperature of a 5f-electron ferromagnet. The ordered moment equals about $1.8\,\mu_B$/f.u. and points along the c-axis (Zolnierek et al. 1986; Kaczorowski and Troc 1990; Delapalme et al. 1994). These attributes of a localized uranium moment system have been completed by the result of AC susceptibility measurements under hydrostatic pressure up to 1 GPa (Kaczorowski et al. 1989) revealing a positive linear response of the Curie temperature at a normalized rate $\partial \ln T_C/\partial p = 4.7 \times 10^{-3}$. Also the results of optical and magnetooptical studies corroborate the conclusion about the localized character of uranium moments in UCu_2P_2. Optical reflectivity measurements performed on a UCu_2P_2 single crystal (Fumagalli et al. 1988a; Schoenes et al. 1989) pointed to the fact that this material is a "bad" metal with a rather low free carrier contribution (< 0.2 carriers/f.u.) to the optical conductivity. The magnetooptic study revealed a maximum Kerr rotation of 3.5° at 0.75 eV. The high-temperature susceptibility which exhibits strong anisotropy was interpreted by

Kaczorowski (1988) using a phenomenological crystal-field model and molecular field approximation. The clear anomaly of the resistivity at 212 K can be associated with magnetic ordering (Kaczorowski and Troc 1990). When comparing the temperature dependence of the spontaneous magnetic moment with theoretical predictions for Ising systems (Yang 1952; Guttman et al. 1970) we find a very good agreement.

"UNi_2As_2" forms with a large concentration of vacant Ni positions. By an X-ray single crystal structure refinement the composition of $UNi_{1.6}As_2$ has been determined. A combined magnetization, resistivity and neutron diffraction study made on single crystals of this materials revealed antiferromagnetic ordering below 145 K. The ground state phase shows simple AFI ordering of uranium magnetic moments ($= 1.6\,\mu_B$) oriented along the c-axis. Above 95 K an additional propagation vector emerges and then two sets of magnetic peaks corresponding to $\boldsymbol{q}_1 = (0, 0, 0)$ and $\boldsymbol{q}_2 = (0, 0, 1/2)$ and two magnetic Fourier components of about the same amplitude along the c-axis coexist in the whole temperature range up to T_N (Troc et al. 1994b).

Ferromagnetism in UCu_2As_2 has been observed below 140 K by magnetization measurements on polycrystalline samples. For the rest of compounds only structure information is available.

5.2.5. *Thorium and transuranium AnT_2Si_2 and AnT_2Ge_2 compounds*

Most of thorium and transuranium 1:2:2 intermetallics (see tables 5.14 and 5.15) crystallize with the $ThCr_2Si_2$-type structure. Exceptions form only some Ir and Pt containing materials. Although numerous compounds, especially germanides, probably can be formed, no information is available because of the limited possibilities of laboratories specialized on the work with transuranium elements. In number of investigated cases crystallographic information is the only one available. In case of neptunium compounds we have frequently important microscopic data from Mössbauer experiments as can be seen in the report of Kalvius et al. (1992) and references therein. From the magnetic hyperfine fields measured at ^{237}Np nuclei a value of the Np magnetic moment was derived (Dunlap and Lander 1974).

The onset of magnetic ordering in $NpCr_2Si_2$ is accompanied by a considerable change of the electric quadrupole interaction. This can be attributed to a situation when the main principal axis of the electric gradient (which is identical with the tetragonal c-axis) is deflected from the magnetic quantization axis. In this case an angle of 46° between the direction of the Np magnetic moment and the c-axis has been estimated. This result indicates that we may deal with a complex magnetic structure. From the observed magnetic hyperfine field on the ^{237}Np nuclei, a Np magnetic moment of $1.7\,\mu_B$ has been determined. The temperature dependence of magnetization shows a maximum well below the magnetic ordering temperature (73 K) determined by Mössbauer spectroscopy (Gal et al. 1976a, 1977).

$NpMn_2Si_2$ becomes ferromagnetic above room temperature. Magnetization measurements made at $T = 4.2$ K provide a magnetic moment value of $2.87\,\mu_B$/f.u., whereas a neptunium moment of $1.1\,\mu_B$ has been determined from the Mössbauer data at the same temperature. This suggests that Mn magnetic moments should be involved in the magnetic ordering in this compound (Gal et al. 1976a, 1977).

The occurrence of antiferromagnetic ordering of the Np magnetic moments ($1.5\,\mu_B$ at $T = 4.2$ K) in $NpFe_2Si_2$ has been concluded from combined magnetization and Mössbauer experiments (Gal et al. 1976a, 1977). Although experimental results are reminiscent

TABLE 5.14

Some basic characteristics of ThT_2Si_2, NpT_2Si_2 and PuT_2Si_2 compounds:
Type of ground state (F – ferromagnetic, AF – antiferromagnetic (without specification), AFI – antiferromagnetic type I, P – paramagnetic), μ_{An} – the actinide ordered magnetic moment at 4.2 K, $T_{C,N}$ – magnetic ordering temperature, Anis. – easy magnetization direction, a, c – lattice parameters at room temperature, structure type (I – tetragonal body-centred $ThCr_2Si_2$-type structure, P – tetragonal primitive $CaBe_2Ge_2$-type structure).

Compound	Ground state	μ_{An} (μ_B)	$T_{C,N}$ (K)	Anis.	Ref.	a (pm)	c (pm)	Str. type	Ref.
$ThTc_2Si_2$						410.92	1006.8	I	[1]
$NpCr_2Si_2$	AF	1.7[a]	73	canted[b]	[2]	386.33	936.70	I	[2]
$NpMn_2Si_2$	F	1.1[a]	> 300		[2]	389.50	953.80	I	[2]
$NpFe_2Si_2$	AF	1.5[a]	87	$\|c$	[2]	386.97	996.21	I	[2]
$NpCo_2Si_2$	AFI	1.5[b]	42–46	canted[c]	[2–4]	387.70	973.20	I	[2]
$NpNi_2Si_2$	AF	1.0[a]	33	$\|c$	[2]	393.50	946.60	I	[2]
$NpCu_2Si_2$	F	1.5	34–41	$\| c$	[2,4]	392.21	941.06	I	[2]
$NpRu_2Si_2$	AF	1.5	27.5	$\|c$	[5]	412.9	958.6	I	[1]
$NpRh_2Si_2$						401.0	1002.2	I	[1]
$NpPd_2Si_2$						411.26	1004.5	I	[1]
$NpOs_2Si_2$						411.7	969.9	I	[1]
$NpIr_2Si_2$						409.24	984.0	P	[1]
$NpPt_2Si_2$						419.49	975.5	P	[1]
$NpAu_2Si_2$						424.22	1027.5	I	[1]
$PuCr_2Si_2$	F		81		[6]	391.33	1065.8	I	[1]
$PuMn_2Si_2$	F		215		[6]	393.13	1044.4	I	[1]
$PuFe_2Si_2$	F		38		[6]	393.37	988.1	I	[1]
$PuCo_2Si_2$	P					390.50	981.3	I	[1]
$PuNi_2Si_2$	F		42			397.04	964.8	I	[1]
$PuCu_2Si_2$						400.30	994.0	I	[1]
$PuRu_2Si_2$						415.14	966.2	I	[1]
$PuRh_2Si_2$						403.96	1006.2	I	[1]
$PuPd_2Si_2$						414.77	996.4	I	[1]
$PuOs_2Si_2$	P					412.45	978.5	I	[1]
$PuIr_2Si_2$	P					411.15	984.9	P	[1]
$PuPt_2Si_2$						420.11	978.5	P	[1]
$PuAu_2Si_2$						425.0	1021.3	I	[1]

[a] Derived from the hyperfine magnetic field H_{hf} measured by Mössbauer spectroscopy on ^{237}Np using the empirical relationship between the empirical relationship between H_{hf} and μ_{Np} (Dunlap and Lander 1974; Dunlap and Kalvius 1985).

[b] Np magnetic moment makes an angle of 46° with the c-axis.

[c] Np magnetic moment is $1.5 \pm 0.2\,\mu_B$ (at 6 K) makes an angle of $52° \pm 15°$ with the c-axis (a possibility of the Np moment in the basal plane is, however, not excluded) (de Novion et al. 1980).

References:

[1] Wastin et al. (1993b)
[2] Gal et al. (1976a)
[3] Potzel et al. (1981)
[4] de Novion et al. (1980)
[5] Bogé et al. (1989)
[6] Wastin et al. (1993a)

TABLE 5.15

Some basic characteristics of NpT_2Ge_2 compounds:
Type of ground state (AF – antiferromagnetic), μ_{An} – the actinide ordered magnetic moment at 4.2 K, T_N – magnetic ordering temperature, Anis. – easy magnetization direction, a, c – lattice parameters at room temperature, structure type (I – tetragonal body-centred $ThCr_2Si_2$-type).

Compound	Ground state	μ_{An} (μ_B)	T_N (K)	Anis.	Ref.	a (pm)	c (pm)	Str. type	Ref.
$NpCr_2Ge_2$	AF	1.4[a]	62		[1]	390.9	947.0	I	[1]
$NpMn_2Ge_2$						400.94	1082.3	I	[2]
$NpFe_2Ge_2$	AF	0.9[a]	28	$\parallel c$	[1]	391.8	940.3	I	[1]
$NpCo_2Ge_2$	AF	1.5[a]	36		[1]	380.0	955.6	I	[1]
$NpNi_2Ge_2$	AF	1.3[a]	27	$\parallel c$	[1]	390.3	955.6	I	[1]
$NpCu_2Ge_2$	AF	1.2[a]	34		[1]	388.8	941.8	I	[1]
$NpRh_2Ge_2$						412.65	1010.3	I	[2]
$NpPd_2Ge_2$						425.23	1011.0	I	[2]

[a] Derived from the hyperfine magnetic field H_{hf} measured by Mössbauer spectroscopy on ^{237}Np using the empirical relationship between the empirical relationship between H_{hf} and μ_{Np} (Dunlap and Lander 1974; Dunlap and Kalvius 1985).

References:

[1] Gal et al. (1976b)
[2] Wastin et al. (1993b)

of $NpCr_2Si_2$, no change of the electric-quadrupole interaction across the magnetic phase transition (at 87 K) takes place. Absence of hyperfine field in ^{57}Fe Mössbauer spectra at 4.2 K proofs that Fe atoms carry no magnetic moments in this material.

Besides results of Mössbauer spectroscopy and magnetization measurements (Gal et al. 1976a, 1977) we have also neutron diffraction data available for *$NpCo_2Si_2$* (de Novion et al. 1980). The Np magnetic moments (1.5 μ_B at $T = 4.2$ K) order antiferromagnetically in the type-I structure. The considerable difference in the electric-quadrupole splittings above and below T_N as well as the non-zero intensity of the magnetic (0, 0, 1) reflection manifest the fact that the Np moments are not oriented along the c-axis. Analysis of the neutron-diffraction data provided a value of $52° \pm 15°$ for the angle between the direction of the Np moment and the c-axis. However, the possibility of confinement of the Np moments to the basal plane cannot be fully excluded within the experimental uncertainty. Mössbauer spectroscopy was applied also to study $NpCo_2Si_2$ under influence of high pressure (Potzel et al. 1981). The observed values of $\partial \ln T_N/\partial p = 2.2\ \mathrm{Mbar}^{-1}$ and $\partial \ln \mu_{Np}/\partial p = 0.05\ \mathrm{Mbar}^{-1}$ can be interpreted as an evidence of rather localized 5f electron magnetic moment on the Np atoms.

Although the values of the magnetic ^{237}Np hyperfine fields in $NpFe_2Si_2$ and $NpCo_2Si_2$ at 4.2 K are nearly identical, the solid solutions *$NpFeCoSi_2$* and *$NpFe_{0.5}Co_{1.5}Si_2$* exhibit considerably smaller values and, moreover, also the magnetic ordering temperature of these materials is also suppressed. A correlation between T_N and H_{eff} has been observed.

$NpNi_2Si_2$ exhibits also a maximum in the temperature dependence of the low-field magnetization below the proposed magnetic-ordering temperature. This maximum is removed by fields of the order of Teslas (Gal et al. 1977). The quadrupole splitting in the Mössbauer spectra is negligible (or zero) both in the paramagnetic and in the antiferromagnetic state.

$NpCu_2Si_2$ has been reported to order magnetically by a first-order magnetic phase transition (Gal et al. 1976a) and shows wide hysteresis of 6 K (AF→P at 37 K, P→AF at 31 K as observed by Mössbauer spectroscopy) although no sharp transition can be observed in the temperature dependence of the magnetization (Gal et al. 1977). A neutron scattering experiment performed by de Novion et al. (1980) brought a clear evidence of ferromagnetic ordering of the Np magnetic moments (1.5 μ_B at 4.2 K) which is in contrast with the originally reported antiferromagnetism (Gal et al. 1976a, 1977). The considerable difference between the lattice constants $a = 399.0$ pm, $c = 992.0$ pm of a sample studied by de Novion et al. (1980) and the values $a = 392.21$ pm, $c = 941.06$ pm measured by Gal et al. (1976a) can be tentatively attributed to a different composition of the two samples. Kalvius et al. (1985) re-examined the ^{237}Np Mössbauer spectra and explained the effect of the simultaneous appearance of both the nonmagnetic single line and the magnetic spectra within the critical temperature range between 30 and 39 K, originally interpreted in terms of a first order magnetic phase transition, by peculiarities of the crystalline electric field. Specific-heat measurements reveal a pronounced increase of the C/T below 4 K, amounting to 800 mJ/(mol K^2). This effect is insensitive to magnetic fields up to 11 T, which points to a possible heavy-fermion behaviour of $NpCu_2Si_2$, as suggested also by Stewart and Elliott (1986).

$NpRu_2Si_2$ orders antiferromagnetically below 27.5 K with a Np ordered moment of 1.5 μ_B as inferred from results on neutron-diffraction experiments (Bogé et al. 1989). The magnetic structure is collinear ($\mu_{Np} \| c$) consisting of ferromagnetically coupled basal-plane sheets. The incomplete square modulation along the c-axis is incommensurate, with q varying continuously between T_N and 1.3 K. Consistently with the incommensurate propagation, the Mössbauer spectra reflect a distribution of the magnetic hyperfine field values, with a maximum value relevant to the Np magnetic moment.

As inferred from Mössbauer effect data obtained at low temperatures, the Np magnetic moment in the solid solutions *$U_{1-x}Np_xRu_2Si_2$* remains parallel to the c-axis and remains nearly constant over the whole concentration range. Also T_N varies monotonously between the values of the ordering temperature of the parent compounds. It stays nearly constant for $x > 0.5$ and decreases nearly linearly with decreasing x in the low Np concentration range (Zwirner et al. 1997; Wastin et al. 1996a). Resistivity measurements of $U_{1-x}Np_xRu_2Si_2$ compounds indicate that a pronounced variation of the transport properties accompanies the substitutions of Np for uranium (Wastin et al. 1997). For low Np doping ($x \leqslant 0.1$) a considerable enhancement of the Cr-like anomaly with respect to pure URu_2Si_2 is observed. To understand the overall complex evolution of $\rho(T)$ curves across the series, further experiments, if possible on single crystals, would be desirable.

$PuCr_2Si_2$ orders ferromagnetically below 81 K but does not follow the Curie–Weiss law in the paramagnetic range (Wastin et al. 1993a).

$PuMn_2Si_2$ become ferromagnetic at much higher temperature (215 K) which is, however, considerably lower that the ordering temperatures the isostructural counterparts with Th, U and Np (Wastin et al. 1993a). Nevertheless, Mn magnetism can be expected also in the Pu materials.

The other two ferromagnets $PuFe_2Si_2$ and $PuNi_2Si_2$ order at much lower temperatures (38 and 42 K, respectively) which points to an inferior (if not negligible) role of the transition metals in the magnetization of these materials. The paramagnetic susceptibility of these compounds can be well described by a modified Curie–Weiss law (Wastin et al. 1993a).

The electrical resistivity behaviour of $PuRh_2Si_2$ (on which magnetic measurements have not been done) suggests magnetic ordering below 95–150 K (Wastin et al. 1993a).

The remaining Pu compounds studied by Wastin et al. (1993a) $PuCo_2Si_2$, $PuOs_2Si_2$ and $PuPt_2Si_2$, remain paramagnetic down to the lowest temperatures.

Only Np germanides with 3d transition metals (Cr, Fe, Mn, Ni and Cu) have been prepared and studied by Gal et al. (1976b). All of them exhibit antiferromagnetic ordering at low temperatures ($\leqslant$ 62 K). Crystal structure and magnetic parameters can be found in table 5.15.

Combined Mössbauer effect studies of the hyperfine interactions on ^{57}Fe and ^{237}Np isotopes have shown that the Fe atoms in $NpFe_2Ge_2$ carry no magnetic moment. The observation of only small changes of the quadrupole splitting across the magnetic ordering transition points to Np moment oriented along the c-axis.

The ^{237}Np spectra measured on $NpCu_2Ge_2$ below 30 K and above 40 K show a well-defined hyperfine structure. It becomes considerably broadened in the critical temperature range probably due to a modulated probably incommensurate magnetic structure. An orientation of the Np moments along the c-axis follows from the quadrupole splitting, which is invariant with the onset of magnetic ordering in $NpCu_2Ge_2$. The ^{237}Np Mössbauer spectra of $NpCu_2Ge_2$ are broadened due to a distribution of the magnetic hyperfine field values, which can be taken as an indication of a modulated and possibly incommensurate magnetic structure.

5.2.6. General comments on 122-compounds

Zolnierek and Mulak (1995) analyzed systematically the occurrence of magnetic structures in U-intermetallics with the $ThCr_2Si_2$-type crystal structure and argued that the magnetic phases in the compounds of this large isostructural family can be reasonably reproduced within a crystal-field model. This model includes hybridization effects on the crystal field potential and considers lattice imperfections. Hybridization matrix elements were calculated within a tight binding approach (Straub and Harrison 1985; Harrison and Straub 1987). To test this approach a detailed analysis of inelastic neutron scattering spectra with respect to the presence of crystal-field excitations is desirable. However, the only more or less clear case in which the inelastic neutron scattering data may show visible crystal-field excitations is represented by UPt_2Si_2 (Steeman et al. 1988).

Endstra (1992), Endstra et al. (1993b) and Mydosh et al. (1993) analyzed how the occurrence of magnetic ordering in UT_2X_2 and CeT_2X_2 intermetallic compounds and the magnetic-ordering temperatures are related to the strength of the f–d hybridization. Values of relevant hybridization matrix elements were calculated using a semiquantitative band-structure approach (Harrison 1969, 1983; Harrison and Froyen 1980; Straub and Harrison 1985; Harrison and Straub 1987) and used to reproduce features of a Kondo-lattice phase diagram (Doniach 1977a, 1977b).

An important advance in understanding the trends in evolution of magnetism in the UT_2Si_2 family was made by Sandratskii and Kübler (1994a, 1994b, 1995b), who per-

formed self-consistent calculations of the electronic structure of UT_2Si_2, where T = Cr, Mn, Fe, Co, Ni, Cu, Ru, Rh, Pd, Os within the density-functional theory in the local density approximation treating the U 5f states as band states. The calculated densities of states compare well with results of photoemission experiments (Grassman 1990). These results confirmed that the development of magnetic behaviour within the UT_2Si_2 family observed experimentally is indeed controlled by the 5f(U)–d(T) hybridization. In this scheme also the non-monotonous behaviour in the series from UMn_2Si_2 through UCu_2Si_2 can be well reproduced, including the Pauli paramagnet UFe_2Si_2 between the two magnetic compounds UMn_2Si_2 and UCo_2Si_2. They also found that the strong hybridization of the 5f(U)–4d(Ru) states is responsible for the fact that URu_2Si_2 is very close to a nonmagnetic-magnetic instability.

5.3. U_2T_2X compounds

Several interesting phenomena can be observed in materials forming part of the large group of U_2T_2X compounds, which crystallize in the tetragonal structure of the U_3Si_2 type (space group P4/mbm), and which provide also a number of transuranium analogues. First, there is the decay of 5f magnetism for earlier transition metals T, which is, as in other intermetallics, driven by the 5f–d hybridization. Second, there is the occurrence of heavy fermion compounds at the verge of magnetism. And third, it is a variable type of U-moment direction and magnetocrystalline anisotropy, apparently associated with changes in the type of the nearest U–U co-ordination.

U_3Si_2 itself is a non-magnetic spin fluctuator (Nowak et al. 1993) due to the proximity of the nearest U-atoms, but one of the two U-positions in U_3Si_2 can be occupied by a non-transition metal like In or Sn, if the Si positions are occupied by a transition metal T. The occurrence of a ternary compound crystallizing in such a structure was first noticed in 1968 (Sampaio et al. 1968), but systematic investigations of the magnetic properties of the large group of U- and Np-compounds were started only much later (Peron et al. 1993).

Schematically, the structure (fig. 5.91) consists of two alternating types of basal plane sheets separated by $c/2$, one containing exclusively all U-atoms, the other T and X atoms.

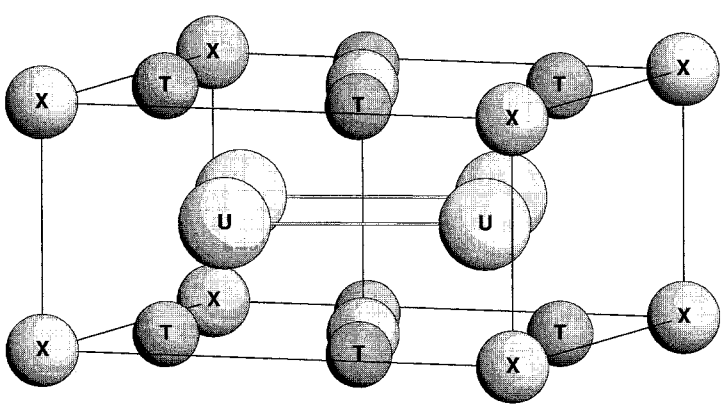

Fig. 5.91. Schematic picture of the tetragonal structure of the U_3Si_2 type in which crystallize An_2T_2X compounds including the U_2T_2X materials.

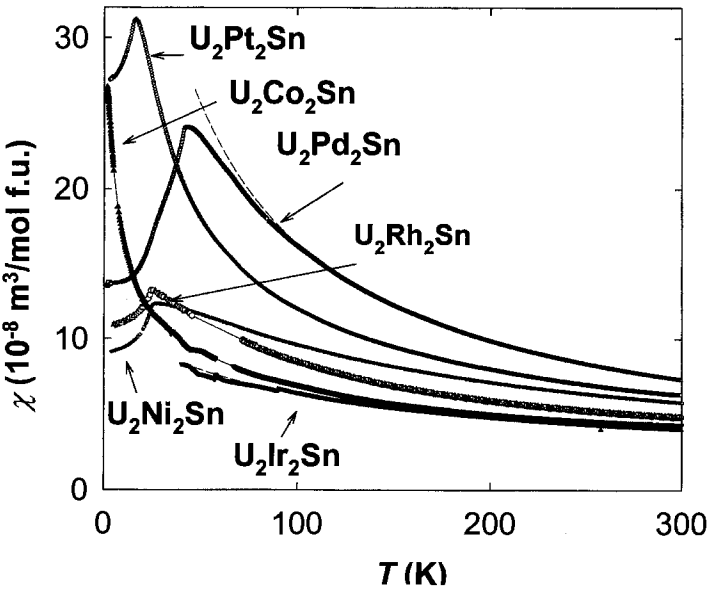

Fig. 5.92. Temperature dependence of the magnetic susceptibility of selected U_2T_2Sn compounds. After Havela et al. (1994d, 1995b).

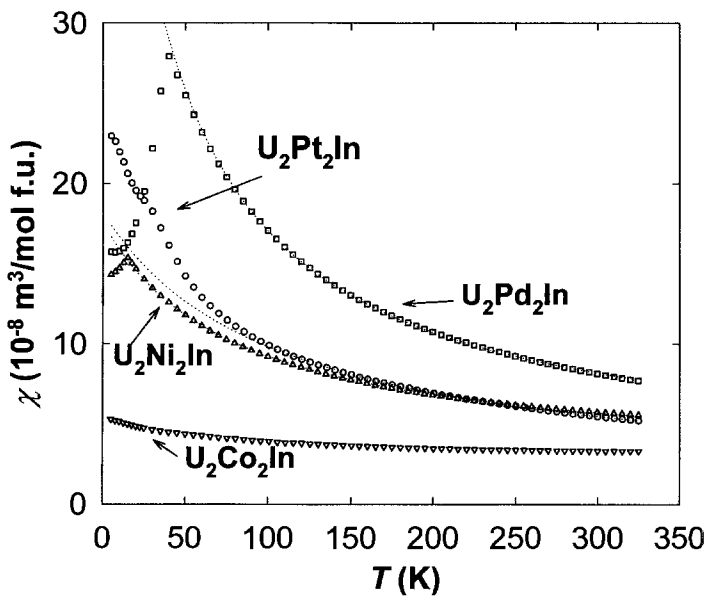

Fig. 5.93. Temperature dependence of the magnetic susceptibility of selected U_2T_2In compounds. After Havela et al. (1994d, 1995b).

TABLE 5.16

Some basic characteristics of An_2T_2X compounds:
a, c- lattice constants at room temperature, type of ground state (AF – antiferromagnetic, SF – spin fluctuator, WP – weak paramagnet), γ – coefficient of the electronic specific heat, $d_{\|}$ – inter-actinide distance within the basal plane, T_N – magnetic ordering temperature. The inter-actinide spacing along the c-axis is equal to the lattice parameter c.

Compound	a (pm)	c (pm)	Type	T_N (K)	γ (mJ/(mol K^2))	$d_{\|}$ (pm)	Ref.
U_2Fe_2Sn	729.6	344.6	WP	–		350.0	[1]
U_2Co_2In	736.6	343.2	WP	–	32	353.0	[2,5]
U_2Co_2Sn	728.9	350.5	SF	–	250	353.1	[3,4,5]
Np_2Co_2In	732.2	351.5	AF	≈ 20		351.1	[2,4,9]
Np_2Co_2Sn	726.2	356.5	SF	–		353.9	[3,4]
U_2Ni_2In	737.4	357.2	AF	14	206 (350)	360.2	[2,4,5,6,7]
U_2Ni_2Sn	726.3	369.1	AF	26	172	358.1	[3,5,8]
Np_2Ni_2In	736.5	359.0	AF	45		358.6	[2,12]
Np_2Ni_2Sn	729.3	366.1	AF	55		358.9	[3,4,13]
Pu_2Ni_2In	733.6	369.0	AF	8		358.9	[10]
Pu_2Ni_2Sn	727.2	374.5	AF	≈ 5		360.9	[10]
Am_2Ni_2Sn	731.5	367.5	[a]			360.5	[10]
U_2Ru_2In	750.5	354.5	WP			?	[3,11]
U_2Ru_2Sn	748.9	355.6	WP	–	20	356.2	[4,5,6]
Np_2Ru_2Sn	742.4	362.6		–		354.5	[4]
U_2Rh_2In	755.3	360.5	SF	–	280	364.7	[2]
U_2Rh_2Sn	752.4	363.0	AF	24	131	370.3	[7]
Np_2Rh_2In	752.4	364.9	AF	49		359.4	[4,16]
Np_2Rh_2Sn	750.2	366.8	SF	–		364.3	[4]
Pu_2Rh_2In	745.1	374.1	[a]			354.5	[10]
U_2Pd_2In	763.7	375.2	AF	36	393	376.7	[2,14]
U_2Pd_2Sn	760.3	378.5	AF	41	203	377.4	[14]
$U_2Pd_{2.44}Sn_{0.56}$	749.0	393.8	AF	13		365.4	[15]
Np_2Pd_2In	764.4	379.9	AF	18		374.9	[4,16]
Np_2Pd_2Sn	762.2	381.6	AF	18		377.9	[4,17]
Pu_2Pd_2In	765.7	381.8	?			375.6	[10]
Pu_2Pd_2Sn	760.7	386.7	?			373.7	[10]
Am_2Pd_2Sn	760.3	385.1	[a]			375.4	[10]
U_2Ir_2In	759.6	358.2	WP			?	[3]
U_2Ir_2Sn	755.7	719.5 [b]	SF		130		[11,5]
Np_2Ir_2In	756.9	362.4	?			361.3	[3,4]
U_2Pt_2In	765.4	372.5	SF		850	373.9	[3,4,5]
U_2Pt_2Sn	768.1	739.1 [b]	AF	15.5	334	346.1	[18,5]
Np_2Pt_2In	767.5	371.6	AF	40		372.8	[3,4,16,12]
Np_2Pt_2Sn	365.6	373.0	AF	32(39)		375.8	[3,4,13,16]
Pu_2Pt_2In	766.3	379.5				371.6	[10]
Pu_2Pt_2Sn	762.9	380.6				373.7	[10]
U_2Co_2Al	713.6	346.3				342	[19]
U_2Co_2Ga	707.2	347.6	WP			347.1	[11,4]
U_2Ni_2Zn	725.2	368.8				?	[3]

[a] Melts incongruently, single phase samples has not been obtained and no magnetic data are available.
[b] Unit cell doubling.

TABLE 5.16 (Continued)

References:

[1] Mirambet et al. (1993a)
[2] Peron et al. (1993)
[3] Wastin et al. (1995)
[4] Rebizant (1994)
[5] Havela et al. (1995b)
[6] Havela et al. (1994d)
[7] Nakotte et al. (1996c)
[8] Kindo et al. (1995)
[9] Pereira and Wastin (1996)
[10] Pereira et al. (1997)
[11] Pereira et al. (1994)
[12] Pereira et al. (1996a)
[13] Pereira et al. (1995)
[14] Purwanto et al. (1994b)
[15] Mirambet et al. (1994)
[16] Colineau (1996)
[17] Sanchez et al. (1995)
[18] Gravereau et al. (1994a)
[19] Sampaio et al. (1968)

Each U-atom has thus two nearest U-neighbors perpendicular to the ab-plane separated by $d_\perp = c$. One U neighbor within the basal plane (belonging to the adjacent unit cell) is at roughly the same distance ($d_\parallel \approx d_\perp$), and the other four are somewhat more apart. These typical distances cannot be much smaller than 350 pm, which allows for formation of U-magnetic moments, provided the hybridization of the 5f-states with the d-states of the transition metal is relatively weak. The observed tendencies in the occurrence of the magnetic order are well understood in the framework of local density fully relativistic electron structure calculations performed for U_2T_2In (Divis et al. 1994; Havela et al. 1994d), U_2T_2Sn (Divis et al. 1995; Matar 1995), and for Np_2T_2X compounds (Divis et al. 1997). These calculations show a traditional picture of 5f states more or less hybridized with the d-states of the transition metal located at somewhat lower energies. The occurrence of magnetic ordering is well correlated with fulfillment of the Stoner criterion for those compounds.

Inspecting systematically the type of magnetic anisotropy, it is very interesting to establish in detail how far the phenomenological rule is followed where U-moments occur perpendicular to the nearest U–U link. Therefore we give both types of the nearest U–U spacings in the table 5.16.

Susceptibility behaviour of selected U_2T_2In and U_2T_2Sn compounds can be seen in figs 5.92 and 5.93. *U_2Fe_2Sn* is a Pauli paramagnet (Mirambet 1993). The electrical resistivity shows only a weak saturation tendency at high temperatures (du Plessis et al. 1995). The resistivity drop at $T = 3.7$ K is probably due to Sn precipitates (Strydom et al. 1996). Very similar behaviour was found for *U_2Co_2In*, which is also weakly paramagnetic with a susceptibility of about 6×10^{-8} m^3/mol f.u. in the low-T limit and $\gamma = 32$ mJ/(mol f.u. K^2) (Havela et al. 1994d, 1995b). *U_2Co_2Sn* is also non-magnetic, but with strong spin-fluctuation features. $\chi(T)$, which can be described by a modified Curie–Weiss law with $\mu_{\rm eff} = 1.5\,\mu_{\rm B}$/U, $\Theta_{\rm p} = -51$ K, and a relatively large $\chi_0 = 2.3 \times 10^{-8}$ m^3/mol f.u., becomes strongly field-dependent below $T = 10$ K. The field $\mu_0 H = 4$ T lowers $\chi(T = 1.8\,{\rm K})$ from 26×10^{-8} m^3/mol f.u. to 18×10^{-8} m^3/mol f.u. Preliminary results of single-crystal studies (Pereira 1996) show that the c-axis response is predominant and field dependent. The magnetization at $T = 5$ K corresponds to $\chi = 55 \times 10^{-8}$ m^3/mol f.u., whereas it is by a factor of 4 smaller for fields applied along the a-axis. Spin fluctuations are a plausible source of the upturn of the low-temperature specific heat, which leads to an enhanced value of $\gamma = 250$ mJ/(mol f.u. K^2) (Havela et al. 1995b). They are also responsible for the high slope of the $\rho(T)$ curve at low temperatures and for its approach to saturation in the high temperature range (Nakotte 1994; Pinto et al. 1995).

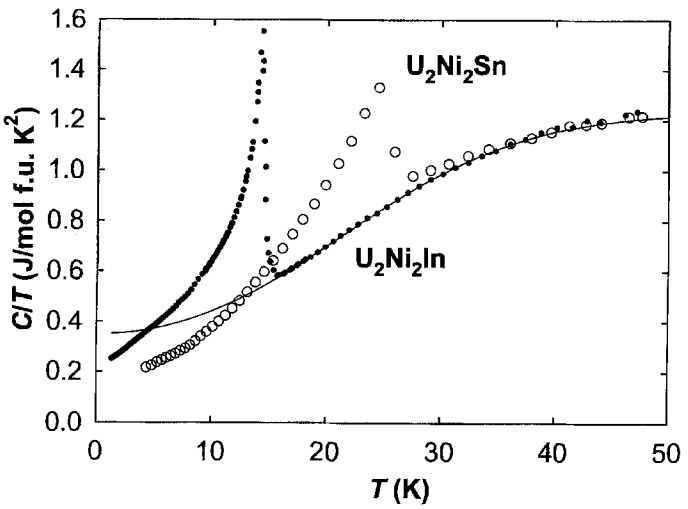

Fig. 5.94. Temperature dependence of the specific heat (C/T vs. T plot) of U_2Ni_2Sn and U_2Ni_2In. The full line represents the non-magnetic contribution with γ adjusted to account for the specific heat in the paramagnetic state. Data from Kindo et al. (1995) and Nakotte et al. (1996c).

Magnetic order in *Np_2Co_2In* is documented by magnetic hyperfine splitting seen in the ^{237}Np Mössbauer spectra at $T = 4.2$ K, which yield Np-moments of 0.7 μ_B. Spectra taken at $T = 80$ K correspond to a paramagnetic state already (Peron et al. 1993). The onset of magnetic ordering can be connected with an antiferromagnetic-type anomaly in the $\rho(T)$ dependence at T about 20 K (Pereira et al. 1996a). The onset of magnetic ordering was recently indicated by the appearance of magnetic hyperfine splitting at $T = 21$ K (Colineau 1996).

Np_2Co_2Sn was found to be non-magnetic at $T = 4.2$ K by ^{237}Np Mössbauer spectroscopy (Sanchez et al. 1995). The $\rho(T)$ curve can be characterized as a belonging to a spin fluctuator, with a knee between 50 and 70 K, and a saturated resistivity above 100 K. A large quadratic coefficient $a = 0.124$ μΩ cm K^{-2} may suggest heavy fermion behaviour.

For *U_2Ni_2In*, a sharp anomaly in the specific heat and a maximum in the $\chi(T)$ curve mark the antiferromagnetic transition at $T = 14.3$ K. The enhanced value $\gamma = 206$ mJ/(mol f.u. K^2), and the even higher value obtained by extrapolation from the paramagnetic range (350 mJ/(mol f.u. K^2)) point to a strongly itinerant character of magnetism, which is underlined by the low magnetic entropy of only $0.4\,R\ln 2$ (Havela et al. 1994d; Nakotte et al. 1996c). Specific heat data are reproduced in fig. 5.94. In the paramagnetic state, the $\chi(T)$ dependence is well accounted for by the Curie–Weiss law with $\mu_{eff} = 2.0\,\mu_B$/U and $\Theta_p = -80$ K (Havela et al. 1994d). A neutron diffraction experiment shows a non-collinear structure with U-moments of 0.60 μ_B (at $T = 10$ K) oriented along (1, 1, 0) and coupled antiferromagnetically between adjacent basal plane layers (fig. 5.95). This corresponds thus to a doubling of the magnetic unit cell, compared to the crystallographic one (Nakotte et al. 1996c; Tran et al. 1996d).

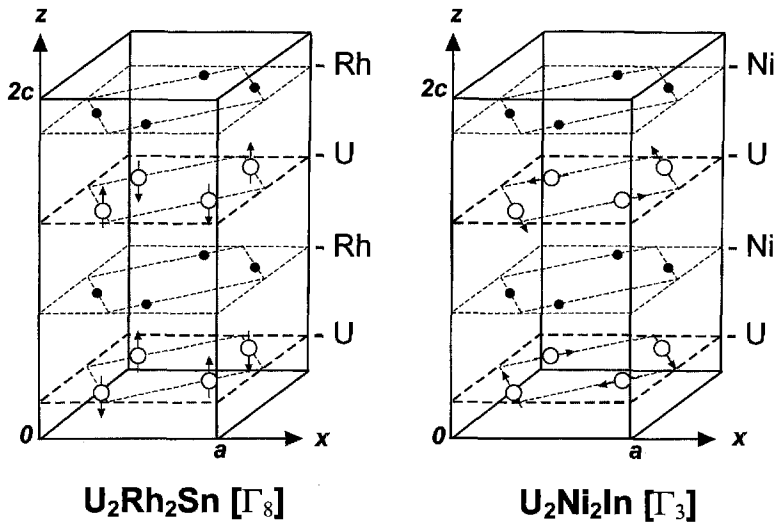

Fig. 5.95. Magnetic structures of U_2Rh_2Sn and U_2Ni_2In – after Nakotte et al. (1996c).

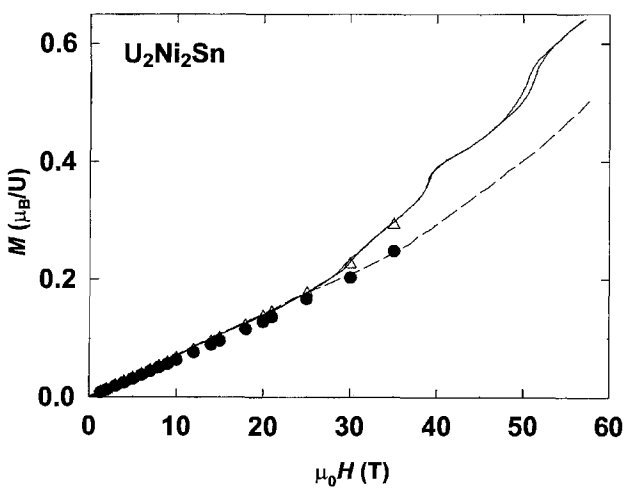

Fig. 5.96. Magnetic field dependence of the magnetic moment M of U_2Ni_2Sn at $T = 4.2$ K measured on powder free to rotate (△) and on randomly oriented fixed powder (•). The full lines represent short-pulse field sweeps. After Kindo et al. (1995).

U_2Ni_2Sn is an antiferromagnet below $T_N = 25$–26 K (Havela et al. 1995b; Kindo et al. 1995). In the paramagnetic range, the susceptibility can be described by a modified Curie–Weiss law with the parameters $\mu_{eff} = 2.3\,\mu_B$/U, $\Theta_p = -110$ K, and $\chi_0 = 1.8 \times 10^{-8}$ m^3/mol (Havela et al. 1994d, 1995b). The high field magnetization measured on free powder at $T = 4.2$ K shows three metamagnetic transitions at 30, 39, and 51 T

reaching magnetization 1.3 μ_B/f.u. at 57 T (Kindo et al. 1995). Results are reproduced in fig. 5.96. The $\rho(T)$ curve measured on a polycrystal has a slightly decreasing tendency with increasing temperature above approx. 70 K. The Néel temperature manifests itself as a kink due to superzone gapping. It is followed by a strongly decreasing part and finally by a T^2 dependence is found below about 20 K. This is suggestive of absence of low-lying magnon-like excitations and thus of a strong uniaxial anisotropy (Kindo et al. 1995; Strydom et al. 1995). The γ-value is moderate and reaches 172 mJ/(mol f.u. K^2) (Havela et al. 1995b). In the fig. 5.94 one can see that γ in the paramagnetic state is significantly higher, corroborating thus the Fermi surface gapping in the AF state. The thermopower coefficient S is close to 0 in the paramagnetic range, but starts to decrease abruptly to a minimum value -12μV/K at $T \approx 10$ K in the antiferromagnetic state (Strydom et al. 1995; Pinto et al. 1996). A powder neutron diffraction experiment revealed an antiferromagnetic structure with a propagation vector $\boldsymbol{q} = (0, 0, 1/2)$ and AF coupling also within the basal plane (Bourée et al. 1994). Although the interpretation in terms of a collinear structure with basal-plane orientation of the U-moments ($\mu_U = 1.05\,\mu_B$) was somewhat preferred in this powder experiment, a later single-crystal neutron diffraction study seems to point to c-axis orientation (Laffargue 1996). The fact that U_2Ni_2Sn is close to the onset of magnetic ordering is documented by the fast decay of the ordering temperature when Co is substituted for Ni. Long range order was found to disappear at about 30% Co. But also Pd substitution leads to a decrease of T_N (down to about 10 K for 40% Pd), which can be understood as the result of frustration induced by the interplay of different types of magnetic interactions (Laffargue et al. 1996).

A Np-ordered moment of 1.6 μ_B was detected at $T = 4.2$ K in *Np_2Ni_2In* by ^{237}Np Mössbauer spectroscopy (Peron et al. 1993), whereas the experiment at $T = 45$ K points to the paramagnetic state already. The $\rho(T)$ curve shows a strong anomaly, which can be associated with a magnetic phase transition, just at $T = 45$ K, where resistivity drops precipitously, whereas above this temperature a weak negative slope develops into a saturated behaviour above $T = 200$ K (Pereira et al. 1996a). The onset of magnetic ordering was indicated by the appearance of magnetic hyperfine splitting at $T = 44$ K (Colineau 1996). The same value of Np ordered moment, 1.6 μ_B, was found also in Np_2Ni_2Sn, which orders at $T = 55$ K (Sanchez et al. 1995). Based on the maximum in the $\chi(T)$ dependence at this temperature an antiferromagnetic state can be deduced (Pereira et al. 1995). The character of the $\rho(T)$ curve is similar to that of Np_2Ni_2In (Pereira et al. 1995).

Pu_2Ni_2In and *Pu_2Ni_2Sn* display a maximum on the $\chi(T)$ dependence at 8 K and at approx. 5 K, respectively. At higher temperatures, a modified Curie–Weiss behaviour was observed on polycrystalline samples with parameters given in table 5.17. The electrical resistivity of the former compound has a character of spin fluctuators, with a broad knee at approx. 100 K and a weak negative slope at high temperatures (Pereira et al. 1994). Of the other Pu compounds, antiferromagnetic order (below $T_N \approx 8$ K) can be deduced for *Pu_2Pt_2Sn*.

U_2Ru_2Sn is a weak itinerant paramagnet with low $\gamma = 20$ mJ/(mol f.u. K^2) (Havela et al. 1995b; Nakotte et al. 1996c). The $\chi(T)$ curve reaches only 2.5×10^{-8} m^3/mol f.u. at $T = 300$ K, and this value is further gradually reduced below about 200 K to 2.0×10^{-8} m^3/mol f.u. in the low temperature limit (Pereira 1996).

TABLE 5.17

Curie–Weiss law parameters of some Pu_2T_2X compounds (μ_{eff} – effective magnetic moment per Pu atom, Θ_p – paramagnetic Curie temperature, χ_0 – temperature independent contribution to susceptibility). Data from Pereira et al. (1997).

Compound	μ_{eff} (μ_B/Pu)	Θ_p (K)	χ_0 (10^{-8} m^3/mol)
Pu_2Ni_2In	0.35	−19	1.7
Pu_2Ni_2Sn	0.37	−6	1.6
Pu_2Pd_2In	0.64	−56	1.4
Pu_2Pd_2Sn	0.56	−30	1.5
Pu_2Pt_2In	0.67	−72	1.1
Pu_2Pt_2Sn	0.50	−16	1.4

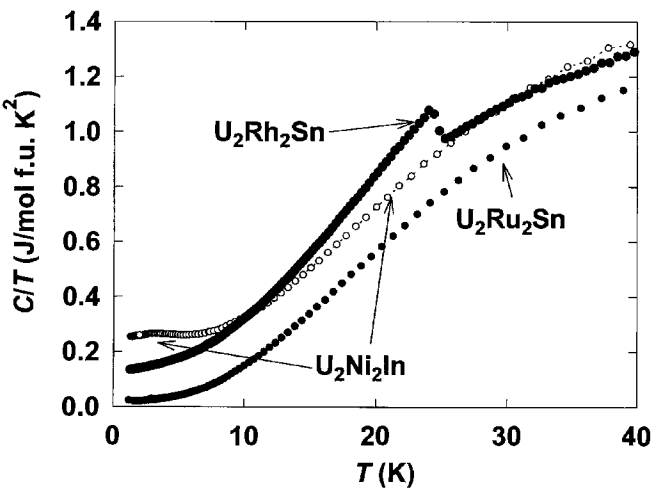

Fig. 5.97. Temperature dependence of the specific heat (C/T vs. T plot) of U_2Ru_2Sn, U_2Rh_2Sn, U_2Rh_2In – data from Nakotte et al. (1996c).

Np_2Ru_2Sn was studied by ^{237}Np Mössbauer spectroscopy at $T = 4.2$ K. The absence of magnetic hyperfine splitting in zero field points to a non-magnetic ground state (Sanchez et al. 1995).

U_2Rh_2In is non-magnetic, but a strong influence of spin fluctuations can be seen in the specific heat. C/T vs. T shows a weak upturn at low temperatures reaching $\gamma = 280$ mJ/(mol f.u. K^2), as seen fig. 5.97 (Havela et al. 1994d). The $\rho(T)$ curve saturates above $T = 200$ K, while it decreases progressively for decreasing T and does not saturate at $T = 5$ K, which was the lowest temperature of the experiment (Nakotte 1994). No susceptibility data are available, but high-field magnetization measurements at $T = 4.2$ K show a rather high induced magnetization (nearly $0.5\,\mu_B$/U in $\mu_0 H = 35$ T on a free-powder sample). Comparison with randomly oriented fixed-powder sample points to a large anisotropy (Nakotte et al. 1994c).

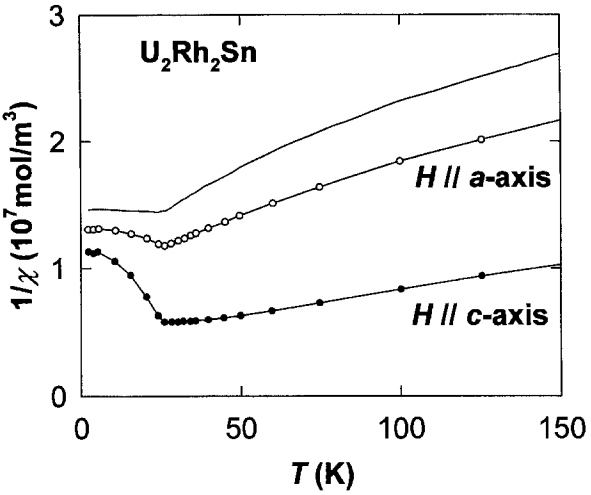

Fig. 5.98. Temperature dependence of the inverse susceptibility $1/\chi$ of U_2Rh_2Sn measured on a single crystal with magnetic fields H applied along the principal crystallographic directions. The upper line represents the corrected susceptibility for $H \| a$ assuming tentatively a misalignment of 5° between the a-axis and the field direction. After Pereira et al. (1996b).

U_2Rh_2Sn is antiferromagnetic below $T_N = 24$ K. The temperature dependence of the susceptibility was studied on a polycrystal and can be described by a modified Curie–Weiss law with parameters $\mu_{eff} = 2.41\,\mu_B$/U, $\Theta_p = -106$ K, and $\chi_0 = 1.0 \times 10^{-8}$ m^3/mol (Havela et al. 1995b). Investigations of a single crystal (having a somewhat higher $T_N = 28$ K) made by Pereira et al. (1996b) shows that the susceptibility is higher for a field applied along the c-axis. In the paramagnetic range it can in this direction be described in the limited temperature range (up to 150 K) by the Curie–Weiss law with $\mu_{eff} = 2.80\,\mu_B$/U, $\Theta_p = -105$ K (fig. 5.98). Specific heat shows an enhanced γ-value of 131 mJ/(mol f.u. K^2). Estimated magnetic entropy values range from 0.45 to 0.8 $R \ln 2$ depending on the estimate of the lattice contribution to the data shown in fig. 5.97 (Nakotte et al. 1996c). Neutron diffraction studies of the magnetic structure point to a collinear arrangement of the U-moments ($\mu_U = 0.38\,\mu_B$) along the c-axis. There is a ferromagnetic coupling to a U basal plane nearest neighbor across the unit cell boundary, whereas the coupling to other U neighbors is antiferromagnetic. This leads to a doubling of the magnetic unit cell compared to the crystallographic one (fig. 5.95). This structure was confirmed by a single crystal study, yielding somewhat higher value of the U-moment, $0.53\,\mu_B$ (Pereira et al. 1996b). The antiferromagnetic coupling can be broken by a magnetic field of about 21 T, where a metamagnetic transition was found (Nakotte et al. 1994c; Fukushima et al. 1995). The ratio of the magnetization recorded on fixed and free powders confirms the uniaxial anisotropy of magnetism in U_2Rh_2Sn. The absence of low energy spin excitations is corroborated by the quadratic $\rho(T)$ dependence with the coefficient $A = 0.16$ μΩ cm K^{-2} and $\rho_0 = 60$ μΩ cm (Nakotte et al. 1996c). The prominent feature of the $\rho(T)$ dependence is the broad knee between 50 and 100 K, followed by saturated high temperature part. On

the low temperature side, with high slope, an anomaly related to AF ordering is observed, pointing to a gapping of the Fermi surface (du Plessis et al. 1995; Nakotte et al. 1996c). This phenomenon can be responsible also for the dramatic change of the thermoelectric power S, decreasing steeply from about 0 to $-5\ \mu V\,K^{-1}$ between 25 and 15 K (Strydom et al. 1996).

The Np atoms in *Np_2Rh_2In* carry ordered moments estimated as $1.3\,\mu_B$ at $T = 4.2$ K (Peron et al. 1993). The $\rho(T)$ curve has a weakly decreasing tendency above $T = 150$ K. At lower temperatures it displays a weak bump at $T \approx 50$ K, and another one at $T \approx 12$ K. The upper bump was associated with the onset on magnetic ordering (Pereira et al. 1996a). The onset of magnetic ordering was also indicated by the appearance of magnetic hyperfine splitting at $T = 49$ K (Colineau 1996).

Unlike Np_2Rh_2In and U_2Rh_2Sn, *Np_2Rh_2Sn* is paramagnetic down to 4.2 K, as shown by the lack of the magnetic hyperfine splitting in ^{237}Np Mössbauer spectroscopy (Sanchez et al. 1995). The $\rho(T)$ curve is saturated above $T = 40$ K, below $T = 9$ K it shows a quadratic dependence with very high coefficient $A = 1.1\ \mu\Omega\,cm\,K^{-2}$ (Pereira and Wastin 1996). This points to the proximity of magnetic order and to possible heavy fermion behaviour.

In *U_2Pd_2In*, which orders antiferromagnetically at $T_N = 37$ K, the U-moments of $1.6\,\mu_B$ are oriented along equivalent [1 1 0] directions and form a non-collinear, square-like magnetic structure within the basal plane (Purwanto et al. 1994b; Tran et al. 1996d). The magnetic and crystallographic unit cells are identical, which implies ferromagnetic interplane coupling. Studies on a single crystal (Prokes et al. 1996e) reveal that the paramagnetic susceptibility χ^c for magnetic fields H applied along the c-axis is much smaller than for fields applied within the basal plane (χ^{ab} for $H \perp c$). For both field orientations the susceptibility above 70 K (fig. 5.99), can be described by a modified Curie–Weiss law with the parameters $\mu_{eff} = 3.0\,\mu_B$/U, $\Theta_p = -125$ K and $\chi_0 = 0.9 \times 10^{-8}$ m^3/mol f.u. for $H \| c$, and $\mu_{eff} = 2.5\,\mu_B$/U, $\Theta_p = -23$ K and $\chi_0 = 2.0 \times 10^{-8}$ m^3/mol f.u. for $H \perp c$. The anisotropy energy in the paramagnetic state, which can be estimated from the difference between the Θ_p-values for the two directions, is about 100 K. Below T_N, the $\chi^{ab}(T)$ curve drops significantly, as is usual in antiferromagnets. On the other hand, χ^c increases even faster than would be expected from the high temperature modified CW behavior. Thus, in the low temperature limit, the response for a field perpendicular to the moment directions is about three times larger than for a field applied within the basal plane. For the latter orientation, however, a spin-flip transition can be achieved in $\mu_0 H = 25$ T and the magnetization finally reaches higher values in this configuration (fig. 5.100). Finally, experiments of Prokes (1997) show that there is a certain anisotropy even within the basal plane, and the U-moments can be flipped only if the field is applied along [1 1 0]. The specific heat of U_2Pd_2In, displayed in fig. 5.101. It is dominated by a pronounced magnetic anomaly at 36 K. In the range above 55 K, the specific heat can be well described by a Debye model for the lattice specific heat with a Debye temperature of $\Theta_D = 185$ K assuming that the linear coefficient of the electron specific heat equals $\gamma_0 = 65$ mJ/(mol f.u. K^2). The effect of a magnetic field of 5 T on the temperature dependence of the specific heat is almost negligible. This applies also to the low temperature upturn, indicating that its origin is intrinsic. It can be fitted using the additional spin fluctuations term $C_{sf} = \delta T^3 \ln T$, which leads to $\gamma = 393$ mJ/(mol f.u. K^2). The magnetic entropy normalized to 1 mol U equals

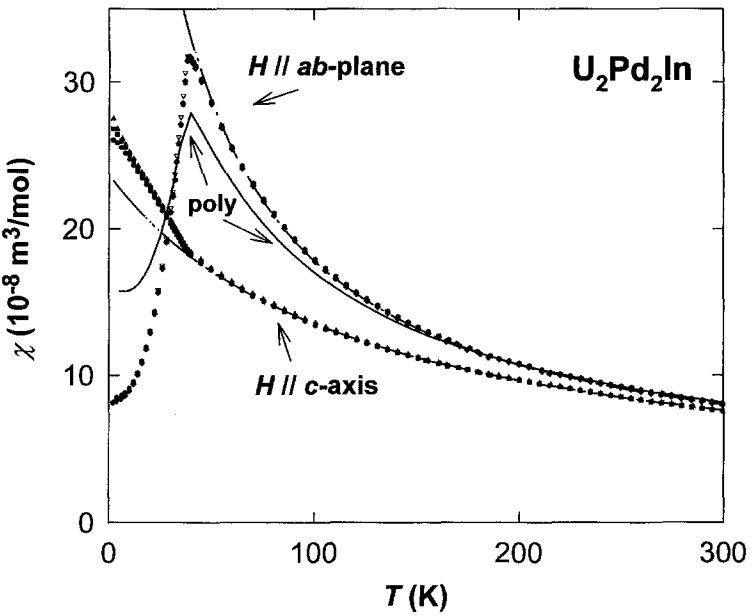

Fig. 5.99. Temperature dependence of the susceptibility of U_2Pd_2In measured on a single crystal with magnetic fields H applied along the principal crystallographic directions. The dash-dotted lines are fits to the Curie–Weiss law mentioned in the text, the full line shows the data obtained on a polycrystal. For $H \| c$, χ weakly decreases with increasing field in the low-T limit, as demonstrated by the spread of data in $\mu_0 H = 1$, 3, and 5 T (from above). After Prokes et al. (1996e).

1.1 $R \ln 2$. The $\rho(T)$ curve shows a distinct maximum at T_N, followed by a negative slope at higher temperatures. On the low temperature side, the resistivity decreases steeply, and no T^2 type dependence could be detected down to $T = 150$ mK (on the polycrystalline sample). Instead we observed a dependence of the type $\rho(T) = \rho_0 + aT^n$, where $n = 1.36$.

U_2Pd_2Sn is an antiferromagnet with $T_N = 41$ K, and displays the highest ordering temperature of all U_2T_2X compounds. Above 60 K, the $\chi(T)$ data can be approximated by the Curie–Weiss law with the parameters $\mu_{eff} = 2.83\,\mu_B$/U and $\Theta_p = -50$ K. Its magnetic structure was identified by neutron diffraction to be the same as in U_2Pd_2In, but the ordered moment is higher ($2.0\,\mu_B$/U). The γ-coefficient of the specific heat is smaller, 203 mJ/(mol f.u. K^2), and no low-T upturn as in U_2Pd_2In was found. The field necessary to induce a moment reorientation is higher comparing to U_2Pd_2In, and the metamagnetic transition was observed between 40–50 T (Fukushima et al. 1995). Unlike U_2Pd_2In, the $\rho(T)$ dependence of its Sn analogue is flat above T_N (Purwanto et al. 1994b). U_2Pd_2Sn, unlike all other U_2T_2X compounds (but similar to numerous analogues of rare earths compounds) can give rise to a substantial off-stoichiometry with excess of Pd and a corresponding defficiency of Sn. It was found that the excess Pd atoms occupy a split position around the replaced Sn position, which leads to a new structure type (Mirambet et al. 1994; Chevalier et al. 1997). At room temperature, the U–U spacing within the basal plane is slightly smaller than that along the c-axis. Therefore this compound seems to contra-

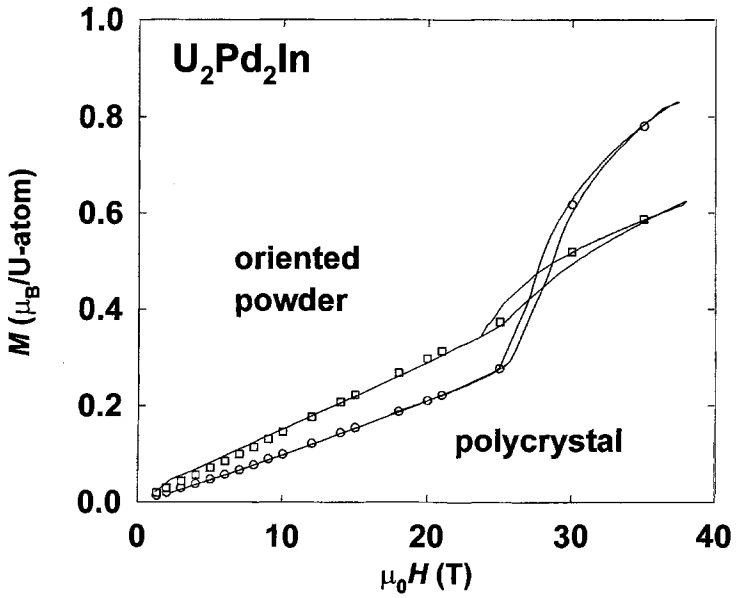

Fig. 5.100. Magnetization curves of U_2Pd_2In measured at $T = 4.2$ K on a fixed powder (polycrystal) and oriented powder. The lines represent data taken with continuous field sweeps. After Prokes et al. (1996e).

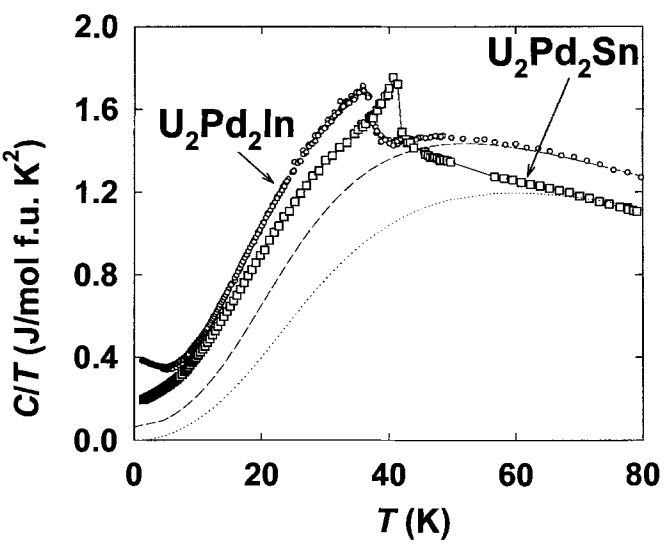

Fig. 5.101. Temperature dependence of the specific heat (C/T vs. T plot) of U_2Pd_2In and U_2Pd_2Sn. The lines represent the non-magnetic background approximated by Debye curves. After Purwanto et al. (1994b).

dict the rule about U-moment directions mentioned above. But due to anisotropic thermal expansion, the two spacings cross over at $T \approx 225$ K, and at low T one already has $d_\perp/d_\parallel < 1$. This is the situation, at which moments in the basal plane should be preferred ($d_\perp/d_\parallel = 1.002$, at $T = 300$ K, and below T_N we obtain $d_\perp/d_\parallel = 0.993$). Furthermore, the value of $d_\perp/d_\parallel$ can be tuned across the critical value 1 by substitution of Pd for Sn in this system, because the lattice parameter a decreases whereas c increases with increasing Pd content. Thus for the limiting case we obtain $d_\perp/d_\parallel = 1.078$. Although the behaviour in the paramagnetic range does not change significantly, T_N decreases to about 13 K for the limit concentration $U_2Pd_{2.44}Sn_{0.56}$ (Mirambet et al. 1994). Neutron diffraction showed that not only the U-moments decrease, but also that the type of order changes and the direction of the U-moments develops into c-axis orientation (Laffargue et al. 1997). $U_2Pd_{2.35}Sn_{0.65}$ forms a collinear structure with a propagation vector $\boldsymbol{q} = (0, 0, 1/2)$. U-moments of $0.90\,\mu_B$ oriented parallel to c are ferromagnetically coupled within a basal plane, whereas the coupling between neighbor planes is antiferromagnetic. The same magnetic structure is preferred by $U_2Pd_{2.25}Sn_{0.75}$ ($d_\perp/d_\parallel = 1.045$ at $T = 300$ K, 1.052 at $T = 1.5$ K), but the non-collinear structure of U_2Pd_2Sn is preserved locally. Its amount is, however, reduced by annealing (Laffargue et al. 1997). *Ab initio* calculations were performed for U_2Pd_2In and U_2Pd_2Sn in order to estimate the changes of resistivity due to Fermi surface reconstruction between the ferromagnetic and antiferromagnetic state. The latter was taken as collinear for simplicity (Richter et al. 1996). As a consequence of strong spin–orbit interaction, the reconstruction can be very dramatic even in cases, in which crystallographic and magnetic unit cells remain identical, i.e., without a traditional superzone gapping effect. In particular, a large drop of the resistivity was predicted (experimental data do not exist) for the latter compound with the current along the basal plane. In U_2Pd_2In a weaker negative effect is expected to arise for current along the c-axis. A further step is the remarkably successful employment of the Local Spin Density Functional Theory allowing for non-collinear arrangements of U-moments (Sandratskii and Kübler 1995a, 1996), which lends full credibility to the 5f-band description, accounting both for the magnitude of U-moments ($\mu_L = -4.21\,\mu_B$, $\mu_S = 2.17\,\mu_B$, total $\mu = -2.04\,\mu_B$) and for the type of ordering, because the real magnetic structure yields indeed the lowest total energy from all possible configurations. Furthermore, one can learn from these calculations that for a realistic description both the spin–orbit interaction and the orbital polarization (corresponding to the second Hund's rule) must be taken into account. Interestingly, the second lowest-energy configuration is the one with a collinear ferromagnetic alignment of the U-moments along c, which is only 0.50 mRy/U atom higher than the ground state one, whereas the energies necessary to rotate the moments within the basal plane are an order of magnitude larger. These energies can be associated with magnetic anisotropy energies (originating from exchange interactions), and are much smaller than those deduced for many other U compounds. However, calculations of this type are not yet systematic enough to be able to judge whether such situation is related to the nearly equal U–U spacings in different orthogonal directions.

Np_2Pd_2In was found to be ordered with a Np moment of $1.4\,\mu_B$ at $T = 4.2$ K by ^{237}Np Mössbauer spectroscopy (Peron et al. 1993), whereas the spectra taken at $T = 45$ K show no magnetic hyperfine splitting. The onset of magnetic ordering was detected by the appearance of magnetic hyperfine splitting at $T = 18$ K (Colineau 1996). *Np_2Pd_2Sn* shows

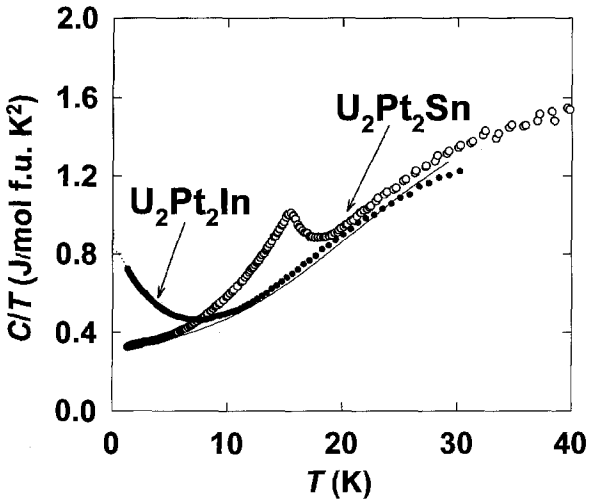

Fig. 5.102. Temperature dependence of the specific heat (C/T vs. T plot) of U_2Pt_2In and U_2Pt_2Sn. After Havela et al. (1994d).

a weakly T-dependent electrical resistivity. The upturn at low T can be associated with AF ordering below $T_N = 18$ K (Pereira et al. 1995), which is manifest also as a maximum in $\chi(T)$ (Pereira et al. 1995), and as the onset of magnetic hyperfine splitting in the ^{237}Np Mössbauer spectra. In the low T limit, the magnetic hyperfine splitting corresponds to $\mu_{Np} = 1.2\,\mu_B$ (Sanchez et al. 1995).

U_2Ir_2In is probably weak paramagnet. Reliable susceptibility data could not be obtained because of considerable contamination by ferromagnetic UIr (Havela et al. 1995b). *U_2Ir_2Sn*, similar to U_2Pt_2Sn, shows a deformation of the U_3Si_2 structure type, which can be described as its superstructure with doubling of the c-axis (Gravereau et al. 1994a; Pereira et al. 1994). The U atoms do not form linear chains, but form zig-zag chains along the c-axis. This leads to a reduction of the shortest U–U spacing within the basal plane, which becomes therefore significantly smaller that the U–U spacing along the zig-zag chain. Moreover, the T-atoms show an alternating displacement out of the original T–X planes. The susceptibility is relatively weakly temperature dependent, but above $T = 100$ K it can be well described by a modified Curie–Weiss law with a relatively small effective moment $\mu_{eff} = 1.73\,\mu_B$/U, $\Theta_p = -100$ K, and $\chi_0 = 1.6 \times 10^{-8}$ m^3/mol f.u. (Havela et al. 1995b). Preliminary data on a single crystal (Pereira 1996) point to a weak maximum in $\chi(T)$ for $H \| c$ around $T = 40$ K ($\chi = 8.8 \times 10^{-8}$ m^3/mol f.u. in the maximum, 8.5×10^{-8} m^3/mol f.u. at $T = 5$ K). The susceptibility is smaller for $H \| a$ (4.4×10^{-8} m^3/mol f.u. at $T = 5$ K) which is consistent with the shortest U–U link within the basal plane. The existence of the susceptibility maximum, as well as the enhanced value $\gamma = 130$ mJ/(mol f.u. K^2) (Havela et al. 1995b; Kindo et al. 1995), point to an important contribution of spin fluctuations, which is corroborated by a typical $\rho(T)$ dependence with saturation above $T = 200$ K (Nakotte 1994).

One of the most prominent features of *U_2Pt_2In* is the low temperature upturn in C/T vs. T (fig. 5.102). When approximated by $T^2 \ln T$ term it leads to $\gamma = 830$ mJ/(mol f.u. K^2)

(Havela et al. 1994d). The absence of any sharp anomaly in the specific heat (down to $T = 1.2$ K) or in other bulk data lead to a classification of this compound as spin fluctuator. The $\chi(T)$ data obtained on a polycrystal are described by a modified Curie–Weiss law above $T = 100$ K with the parameters $\mu_{\text{eff}} = 2.4\,\mu_B$/U, $\Theta_p = -106$ K, and $\chi_0 = 1.0 \times 10^{-8}$ m^3/mol f.u. In the low-T range the data deviate towards higher values and χ reaches 23×10^{-8} m^3/mol f.u. in the 0 K limit. This upturn is not dependent on magnetic field in the Tesla range, the high field experiment at $T = 4.2$ K showing a certain tendency to saturation in fields above 20 T, while reaching a relatively large magnetization ($0.72\,\mu_B$/U in $\mu_0 H = 55$ T). A comparison of the free- and fixed powder magnetization data shows surprisingly no difference (Fukushima et al. 1995). Preliminary data from susceptibility studies of a single crystal suggest indeed a relatively weak anisotropy, with higher values found for field along the c-axis, where $\chi(T)$ forms a weak maximum at about 2 K. The upturn below $T = 100$ K seen in the polycrystalline data is found in susceptibility for both field directions (Pereira 1996). The $\rho(T)$ dependence has a broad maximum at $T \approx 80$ K and a weak negative slope at higher temperatures (Nakotte 1994; Strydom and du Plessis 1996, 1997). For low T (down to 1.4 K) one observes a linear decrease of ρ with decreasing T, which led to the conjecture of non-Fermi liquid behaviour in U_2Pt_2In. The standard aT^2 behaviour is recovered by applying a magnetic field of $\mu_0 H = 7.7$ T, or by a small substitution of Th for U (Strydom and du Plessis 1997).

U_2Pt_2Sn is antiferromagnetic below $T_N = 15.5$ K. In the paramagnetic state, the $\chi(T)$ dependence measured on a polycrystal is described by a modified Curie–Weiss law with the parameters $\mu_{\text{eff}} = 2.03\,\mu_B$/U, $\Theta_p = -34$ K, and $\chi_0 = 2.5 \times 10^{-8}$ m^3/mol f.u. (Havela et al. 1995b). The high value $\gamma = 334$ mJ/(mol f.u. K^2) (390 mJ/(mol f.u. K^2) obtained when extrapolating from the paramagnetic range) and the low value of the magnetic entropy $\Delta S = 0.2\,R \ln 2$ are suggestive of strongly itinerant magnetism (Havela et al. 1994d). The magnetization at $T = 4.2$ K shows a metamagnetic transition between 20 and 30 T, but even in the highest field applied (35 T) a magnetization corresponding to only $0.5\,\mu_B$/U atom is reached (Nakotte et al. 1994c). The $\rho(T)$ curve, is remarkably flat. It displays a broad maximum at 30–40 K, followed by a negative slope at the high-temperature side. Below T_N a weak feature related to gapping is observed (Nakotte 1994).

Np_2Pt_2In was found to display ordered Np moments of $1.5\,\mu_B$ at $T = 4.2$ K (Peron et al. 1993). The onset of magnetic ordering can be associated with a sharp anomaly at $T = 39$ K, below which the resistivity increases and saturates without any sign of a decrease (Pereira et al. 1996a). This anomaly can undoubtedly be connected with a Fermi surface reconstruction due to AF ordering. *Np_2Pt_2Sn* was reported to order antiferromagnetically at $T_N = 32$ K, but the $\chi(T)$ data show another possible magnetic phase transition at $T = 15$ K. The upper transition coincides with a marked anomaly in the $\rho(T)$ curve, which is flat above this point, but decreases below this temperature (Pereira et al. 1995). ^{237}Np Mössbauer spectroscopy yields Np-moments of $1.5\,\mu_B$ at $T = 4.2$ K (Sanchez et al. 1995). The magnetic hyperfine splitting disappears at $T = 39$ K, which is somewhat higher than the ordering temperature indicated by bulk data (Colineau 1996).

Of the other compounds, the susceptibility was studied for *U_2Co_2Ga*. The susceptibility increases weakly with decreasing T from 3.3×10^{-8} m^3/mol at $T = 300$ K. Details of the low temperature behaviour could not be studied because of contamination by ferromagnetic UCoGa (Havela 1994).

5.4. $U_3T_3X_4$ compounds

The compounds $U_3T_3Sb_4$ and $U_3T_3Sn_4$ crystallize in the $Y_3Au_3Sb_4$ structure type (space group $I\bar{4}3d$), with 4 f.u./cell. This structure type can be derived from the Th_3P_4 structure by filling (in some cases uncomplete) interstitials by transition metal T atoms (Dwight 1977). A schematic picture of the structure in shown in fig. 5.103. Because the U–U spacing for U_3Sb_4 is larger than 400 pm ($d_{U-U} = 0.468\,a$, a is the lattice parameter given for all compounds in the table 5.18), additional expansion of the lattice due to the presence of the T atoms in $U_3T_3Sb_4$ does not affect the electronic structure by increasing the 5f–5f overlap. The influence of the hybridization of the 5f states with the transition metal d-states dominates, and can partly or completely suppress the magnetic order observed in U_3Sb_4 (ordered below $T_c = 146$ K). For $U_3T_3Sn_4$ such comparison is not possible, as the reference binary compound U_3Sn_4 in not formed. Whereas the stannides are metallic with either a non-magnetic or an antiferromagnetic ground state, the antimonides are either ferromagnetic metals ($U_3Co_3Sb_4$, $U_3Cu_3Sb_4$) or non-magnetic semiconductors (as, e.g., $U_3Ni_3Sb_4$ or $U_3Pt_3Sb_4$) with gaps of the order of 0.2 eV. A general picture of the band formation can be obtained from band structure calculations of $Th_3Ni_3Sb_4$, which show a gap formation with a width of 0.36 eV (Takegahara et al. 1990). The valence band consists of the Ni-3d states and Sb-5p states. Due to the hybridization of the Ni-3d states and Th-6d states, the 6d states are shifted above E_F. An analogous situation was found in $La_3Au_3Sb_4$ (Takegahara and Kaneta 1992).

In some cases the filling of the lattice by the transition metal atoms is not complete and the equilibrium T-metal concentration can be much lower as discussed by Endstra (1992),

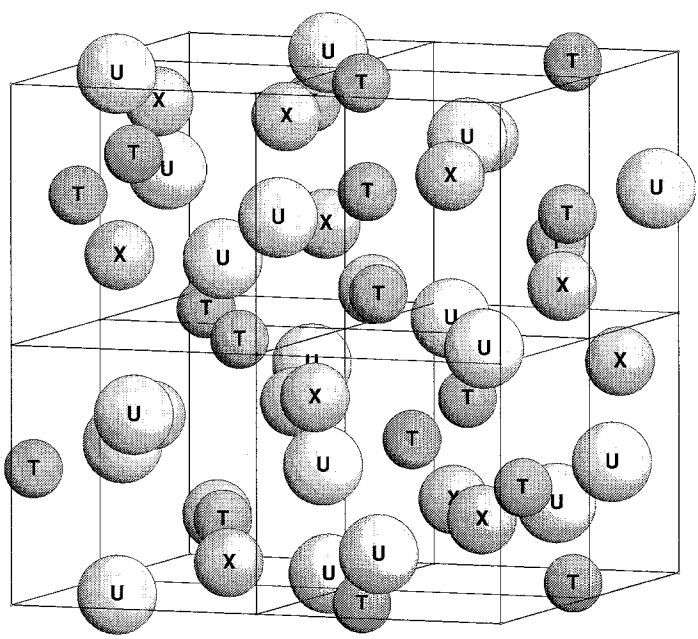

Fig. 5.103. Schematic picture of the cubic structure of the $Y_3Au_3Sb_4$-type structure in which crystallize $U_3T_3X_4$ compounds.

TABLE 5.18

Some basic characteristics of $U_3T_3X_4$ compounds:
a – lattice parameter at room temperature, type of ground state (met. – metallic, semi. – semiconducting, AF – antiferromagnetic, F – ferromagnetic, SF – spin fluctuator, supercon. – superconducting), $T_{C,N}$ – magnetic ordering temperature, T_c – temperature of transition to superconducting state, γ – coefficient of the electronic specific heat related to 1 mol U, and parameters of the Curie–Weiss law describing $\chi(T)$ in the paramagnetic state (μ_{eff} – effective magnetic moment per U atom, Θ_p – paramagnetic Curie temperature, χ_0 – temperature independent contribution).

Compound	a (pm)	Type	T_C, T_N, T_c (K)	γ (mJ/(mol U K^2))	μ_{eff} (μ_B/U)	Θ_p (K)	χ_0 (10^{-8} m^3/mol)	Ref.
U_3Sb_4	911.2	met.	146		3.0	150	0	[1]
$U_3Fe_1Sb_4$	920.7	?, F	120		2.7	111		[2]
$U_3Co_3Sb_4$	928.4	met., F	10	69	2.1	12	2.5	[3,2]
$U_3Ni_3Sb_4$	937.7	semi., SF		2	3.0	−61		[3,4]
$Th_3Ni_3Sn_4$	936.3	supercon.	1.4	10.4[a]			0.6	[5]
$U_3Ni_3Sn_4$	936.4	met., SF		92	1.8	−58	3.1	[3,4]
$U_3Cu_3Sb_4$	944.5	met., F	88		3.0	98		[3]
	945.1		91		3.39	110		[4]
$U_3Cu_3Sn_4$	952.2	met., AF	12	380 375	3.34	−13		[4]
	950.5				3.3	−50		[6]
$U_3Rh_3Sb_4$	953.1	?, F	105		2.4	7.6		[2]
$U_3Au_3Sn_4$	982.4	met., SF		280 850	3.58	−87		[4]
	981.8				3.2	−90		[6]
$U_3Pd_3Sb_4$	968.4	semi.			3.58	−98		[4]
$U_3Ir_3Sb_4$	957.2							[7]
$U_3Pt_3Sb_4$	968.3	semi			3.68	−184		[4]
$U_3Pt_3Sn_4$	967.5	met.		94	1.84	−38	5.1	[4]

[a] γ value per mol Th.

References:

[1] Trzebiatowski (1980)
[2] Endstra (1992)
[3] Endstra et al. (1990b)
[4] Takabatake et al. (1990a)
[5] Aoki et al. (1992)
[6] Corsepius et al. (1996)
[7] Dwight (1979)

and as demonstrated in the ultimate case of *$U_3Fe_1Sb_4$*. This material orders ferromagnetically at $T_C = 120$ K (Endstra 1992), which is not much different from U_3Sb_4. An appreciable magnetic moment (about 1.1 μ_B/U) and a strong coercive field of 1.45 T were observed at $T = 4.2$ K.

$U_3Co_3Sb_4$ undergoes a transition to the ferromagnetic state at $T_C = 10$ K. Its magnetization does not saturate in fields up to 10 T (Endstra et al. 1990b; Endstra 1992). The linear slope in higher fields corresponds to an appreciable susceptibility, 34×10^{-8} m^3/mol f.u. It was interpreted as being due to a high magnetocrystalline anisotropy. But taking into account the small spontaneous magnetization, obtained by extrapolating the linear part to $H = 0$ and pointing to 0.2 μ_B/U atom, an interpretation in terms of weak itinerant ferromagnetism seems more plausible. The parameters obtained by fitting the $\chi(T)$ data in the paramagnetic range with a modified Curie–Weiss law are given in table 5.18. Surprisingly, no anomaly related to the magnetic order has been found in electrical resistivity. The

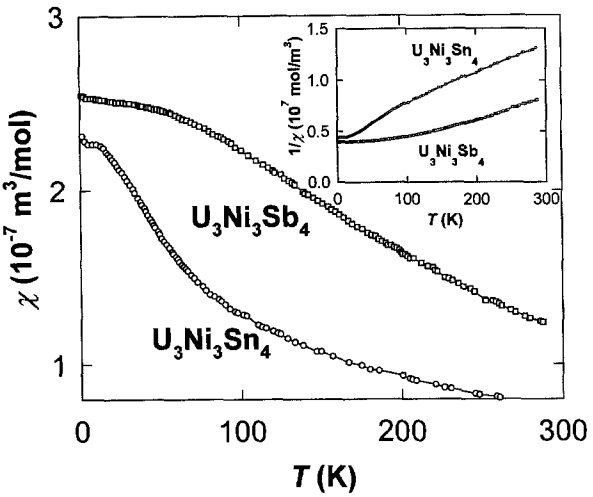

Fig. 5.104. Temperature dependence of the susceptibility χ of $U_3Ni_3Sn_4$ and $U_3Ni_3Sb_4$ (after Endstra et al. (1990b)). The inset shows the inverse susceptibility.

$\rho(T)$ curve increases from $\rho_0 = 180$ μΩ cm through a broad knee and a high-temperature linear part with positive lope to $\rho(300\ \text{K}) = 450$ μΩ cm. Similarly, no trace of a transition was found in the specific heat data, yielding $\gamma = 69$ mJ/(mol U K^2). The results of NQR experiments at Sb sites correspond to a nearly ferromagnetic material (Ohama et al. 1993a).

$U_3Ni_3Sb_4$ and *$U_3Ni_3Sn_4$* do not order magnetically (Endstra et al. 1990b). The temperature dependence of the susceptibility for both compounds can be found in fig. 5.104. At high temperatures the $\chi(T)$ dependence of $U_3Ni_3Sb_4$ can be described by the Curie–Weiss law with an effective moment $\mu_{\text{eff}} = 3.0\,\mu_B$/U and $\Theta_p = -61$ K. Below $T \approx 150$ K it tends gradually to saturation at $\chi_0 = 25 \times 10^{-8}$ m^3/mol. (Note that 1 f.u. contains 3 U atoms). $\chi(T)$ of $U_3Ni_3Sn_4$ can be described by the modified Curie–Weiss law with $\mu_{\text{eff}} = 1.8\,\mu_B$/U, $\Theta_p = -58$ K, and $\chi_0 = 3.1 \times 10^{-8}$ m^3/mol f.u. down to about 30 K. Below that temperature the susceptibility saturates to $\chi(0\ \text{K}) = 21.6 \times 10^{-8}$ m^3/mol f.u. (Endstra et al. 1990b). A very dramatic difference between these two compounds is observed in the electrical resistivity. $U_3Ni_3Sb_4$ has a large resistivity and displays semiconducting behaviour (similar to $Th_3Ni_3Sb_4$) with an estimated energy gap of 175 meV. The large positive Hall coefficient R_H points to a p-type semiconductor (Takabatake et al. 1990a). On the other hand, $U_3Ni_3Sn_4$ is metallic and has a very low residual resistivity (0.88 μΩ cm). At low temperatures (up to 16 K) the resistivity increases as aT^2 with $a = 0.234$ μΩ cm K^2, and saturates at $T > 200$ K to $\rho = 400$ μΩ cm. As expected from the appreciable a value, the low temperature specific heat coefficient γ is also enhanced (92 mJ/(mol U K^2)), which contrasts with the low value $\gamma = 2$ mJ/(mol U K^2) in $U_3Ni_3Sb_4$ (Takabatake et al. 1990a). Sb NMR and NQR experiments on $U_3Ni_3Sb_4$ (Ohama et al. 1992) show an activation type of behaviour of the inverse spin-lattice relaxation time $1/T_1$. This is attributed to varying concentration of the Sb-5p hole concentration

under the conditions of strong U-5f to Sb-5p hybridization. Similar experiments on ^{119}Sn nuclei in $U_3Ni_3Sn_4$ show a crossover from the high temperature local moment Korringa regime to the low-temperature Fermi liquid regime, in which $(1/T_1T)_f$ is constant (Kojima et al. 1992a). The symbol f denotes the part of the spin-lattice relaxation time due to f-moments fluctuations. The relaxation rate of the f-moments derived in the high T regime (above 120 K) is of the Korringa type $\hbar/(k_B\tau_f) = 0.82\,T + 86$ K pointing to a local f-moment behaviour. Below $T = 100$ K it tends to a saturation, and the observation that $\hbar/(k_B\tau_f) =$ const at low T demonstrates the Fermi liquid behaviour.

That we deal exclusively with the 5f magnetism in the $U_3T_3X_4$ compounds is demonstrated by the fact that *$Th_3Ni_3Sn_4$* is a weak paramagnet with $\chi \approx 6 \times 10^{-9}$ m^3/mol f.u. and undergoes a superconducting transition at $T_c = 1.38$ K (Aoki et al. 1992).

$U_3Cu_3Sb_4$ is a metallic ferromagnet below $T_C = 88$ K. The spontaneous magnetization corresponds to U moments of 1.5 μ_B (Endstra et al. 1990b). Above the transition $\chi(T)$ behaves according to the Curie–Weiss law with $\mu_{eff} = 3.0\,\mu_B$/U and $\Theta_p = 98$ K. The $\rho(T)$ curve shows a smooth increase without any anomaly reaching $\rho(300\text{ K}) = 150$ μΩ cm. The relatively large value $\rho_0 = 70$ K can be explained by vacancies on Cu sites, corresponding to a stoichiometry $U_3Cu_{\approx 2}Sb_4$, revealed by electron-probe microanalysis.

$U_3Cu_3Sn_4$ displays a very pronounced maximum in $\chi(T)$ at $T = 12$ K, which marks the transition to the AF state. At this temperature also a λ-type anomaly appears in C/T vs. T. On its low temperature side, C/T decreases to a minimum at about 6 K and then increases again yielding the γ-value 380 mJ/(mol U K^2) (Takabatake et al. 1990a). A detailed study of the low temperature specific heat (Corsepius et al. 1996) showed that C/T reaches a maximum at $T = 1.25$ K (410 mJ/(mol U K^2)) and that C/T is constant below 0.7 K, corresponding to $\gamma = 375$ mJ/(mol U K^2). $\rho(T)$ is high and practically temperature independent except for a weak increase below 40 K, which becomes steeper below T_N. No sign of saturation was found down to 4.2 K, where $\rho = 820$ μΩ cm. From NMR experiments the ^{63}Cu nuclear relaxation rate was obtained, reflecting the relaxation rate of the 5f moments. A linear relation of the type $\hbar/(k_B\tau_f) = 0.086\,T + 26$ K was observed above $T = 110$ K, which is consistent with local moment behaviour (Kojima et al. 1992b).

$U_3Rh_3Sb_4$ could not be obtained free of spurious URhSb (Endstra 1992). Therefore the relatively high reported value $T_C = 105$ K should be taken with caution. The spontaneous magnetization at $T = 4.2$ K corresponds only to about 0.6 μ_B/f.u. (similar to the Co-counterpart).

The susceptibility of *$U_3Au_3Sn_4$* shows spin fluctuation features (see fig. 5.105), namely a deviation from the Curie–Weiss behaviour below $T \approx 70$ K with a sign of saturation, and a subsequent low temperature upturn (Takabatake et al. 1990a). The C/T vs. T plot shows lower C/T values at $T > 1$ K (280 mJ/(mol U K^2)) than in $U_3Cu_3Sn_4$, but it shows a stronger low-T upturn. The value $\gamma = 850$ mJ/(mol K^2) was obtained by extrapolation from the mK range (Corsepius et al. 1996). Therefore the value of 280 mJ/(mol K^2) (Takabatake et al. 1990a), deduced from the behaviour at higher temperatures, is severely underestimated. In the $\rho(T)$ curve, the knee around $T = 35$ K is followed by an almost flat high-T part. The resistivity decreases to only ≈ 550 μΩ cm in the low-T limit, while about 650 μΩ cm was found at the room temperature (Takabatake et al. 1990a). The value $\rho_0 = 495$ μΩ cm was obtained by extrapolation to $T \to 0$ K (Takagi et al. 1993). ^{119}Sn NMR measurements proved that the low-T upturn in $C(T)$ is followed by a similar behaviour of the Knight shift and thus is intrinsic. The spin-lattice relaxation rate $1/T_1$ is

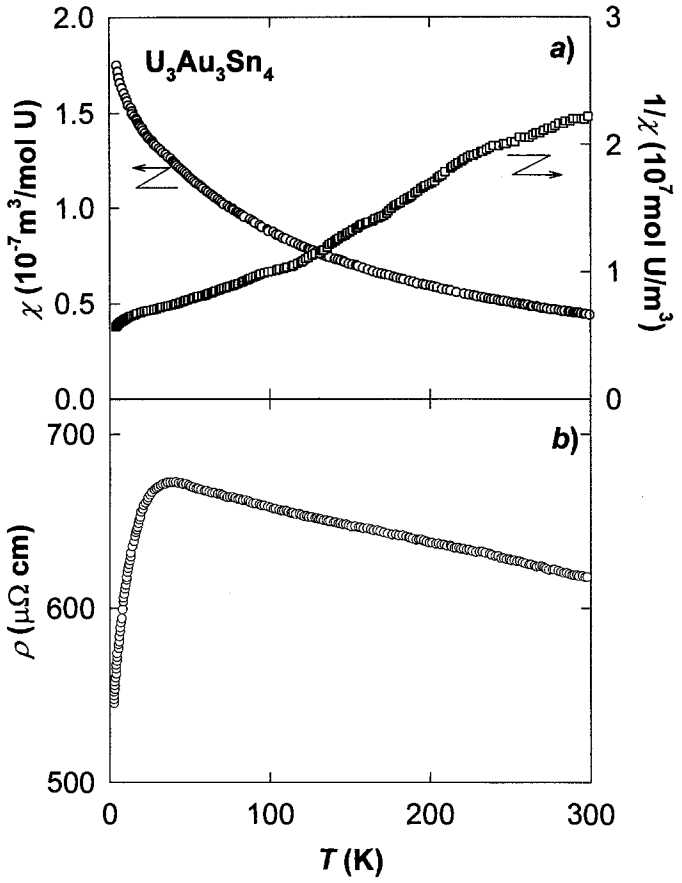

Fig. 5.105. Temperature dependence of the susceptibility χ and inverse susceptibility $1/\chi$ (a) and resistivity ρ (b) of $U_3Au_3Sn_4$ (after Takagi et al. (1993)).

practically constant at low T showing thus a deviation from the standard Korringa-type of behaviour (Takagi et al. 1993). An interesting substitution study of the $U_3(Cu_xAu_{1-x})_3Sn_4$ system shows that the maximum in $\chi(T)$ shifts down to lower temperatures with decreasing x and survives down to 5% Cu, but probably it marks only a short-range order. This is demonstrated by the substantial broadening of the sharp peak in C/T vs. T found for the Cu-compound at 2% Au already (Corsepius et al. 1996). The γ-value is depressed to 180 mJ/(mol U K^2) in the middle of the concentration range.

$U_3Pd_3Sb_4$ and $U_3Pt_3Sb_4$ are non-magnetic and show semiconducting behaviour with the low-temperature resistivity reaching an order of magnitude of several Ω m. The magnetic susceptibility is Curie–Weiss like at high T (parameters are given in table 5.18). At low temperatures it bends to a saturation and reaches $\chi(4.2\ \mathrm{K}) = 9.9 \times 10^{-8}$ m^3/mol and 8.9×10^{-8} m^3/mol U for the Pd and Pt compound, respectively (Takabatake et al. 1990a). The fact that the analogous compound $Th_3Ni_3Sb_4$ is semiconducting, too, means that the

gap formation is not related to the 5f states excluding any interpretation in terms of a Kondo gap. This is in agreement with the insensitivity of the gap width ($k_B\Delta \approx 200$ K between 50 and 150 K) to external pressure, studied for the latter system by (Canfield et al. 1992).

$U_3Pt_3Sn_4$ is a metallic spin fluctuator with specific heat ($\gamma = 94$ mJ/(mol U K^2)) and susceptibility parameters (see table 5.18) similar to those of $U_3Ni_3Sn_4$. The susceptibility reaches 30.5×10^{-8} m^3/mol f.u. in the low-T limit.

The large diversity of properties in the $U_3T_3X_4$ compounds makes it very intriguing to pursue further local probe experiments. Photoelectron spectroscopy results (Takabatake et al. 1992a) in $U_3Ni_3Sn_4$ and $U_3Ni_3Sb_4$ show a standard picture of the Ni-3d states situated at about -2 eV, whereas a broad triangular 5f emission is pinned to E_F. The latter is true also for the analogous Cu-compounds, in which the maximum of the Cu-3d emission is seen around -4 eV. A large difference was found, however, between the shape of the 3d emission. It is broader and asymmetric in $U_3Cu_3Sb_4$ extending significantly to -3 eV where the Sb-5p emission is expected. This fact points to a stronger Cu-3d and Sb-5p hybridization. On the other hand, it is symmetric and much narrower in $U_3Cu_3Sn_4$, which can be interpreted as being due to 3d localization. This fact was associated also with the anomalous shrinking of the lattice parameter in $U_3Cu_3Sb_4$ compared to $U_3Cu_3Sn_4$. The experimental resolution of these experiments, which is not better that 0.22 eV, did not allow to observe the gap in the electron energy spectrum in $U_3Ni_3Sb_4$. The 4f core level spectra of the four compounds (Ejima et al. 1993) display maxima at binding energies corresponding to "well-screened" 4f holes in all cases. Except for $U_3Cu_3Sb_4$, which can be thus characterized as the one with the most itinerant 5f states, the spectra of all compounds show satellite maxima at higher binding energies. The standard energy difference of about 7 eV is by 0.5 eV higher in the case of $U_3Ni_3Sb_4$. As this difference reflects the higher energy of the 4f hole screened by the non-f states of ligands, this shift can be, e.g., ascribed to the existence of a gap in this material. Practically no difference was found between the BIS spectra of these compounds (Ejima et al. 1993).

The intensity of the emission corresponding to the final state with a well screened 4f hole is dominating even in $U_3Ni_3Sb_4$, which means that some itinerancy of the 5f states is preserved. However, inelastic neutron scattering experiment revealed clear crystal-field excitations and lack of any quasielastic response, which is more typical for localized 5f systems (Rainford et al. 1996). The absence of magnetic ordering can be then understood as due to a singlet $5f^2$ ground state. Qualitatively, a similar situation was found in $U_3Pt_3Sb_4$ (Rainford et al. 1995). On the other hand, the broad quasielastic response extending to about 70 meV and the lack of well resolved crystal-field excitations in $U_3Cu_3Sn_4$ (Rainford et al. 1996) is well compatible with the moderate heavy-fermion nature of this metallic antiferromagnet. Intermultiplet transitions were observed at 370 meV in $U_3Ni_3Sb_4$ (Rainford et al. 1996) and at 400 meV in $U_3Pt_3Sb_4$ (Rainford et al. 1995). For the inelastic neutron scattering spectra observed for $U_3Ni_3Sb_4$ and $U_3Cu_3Sn_4$, see fig. 5.106.

The systematics shows that the occurrence of semiconducting behaviour is restricted to the antimonides with Ni, Pd, or Pt only, whereas any increase or decrease of the d-occupation produces metallic ferromagnetic state. This evokes the idea that the absence of ordering for compounds with T element of that particular transition metal column is related to a lack of conduction electrons, i.e., to absence of exchange interaction of the

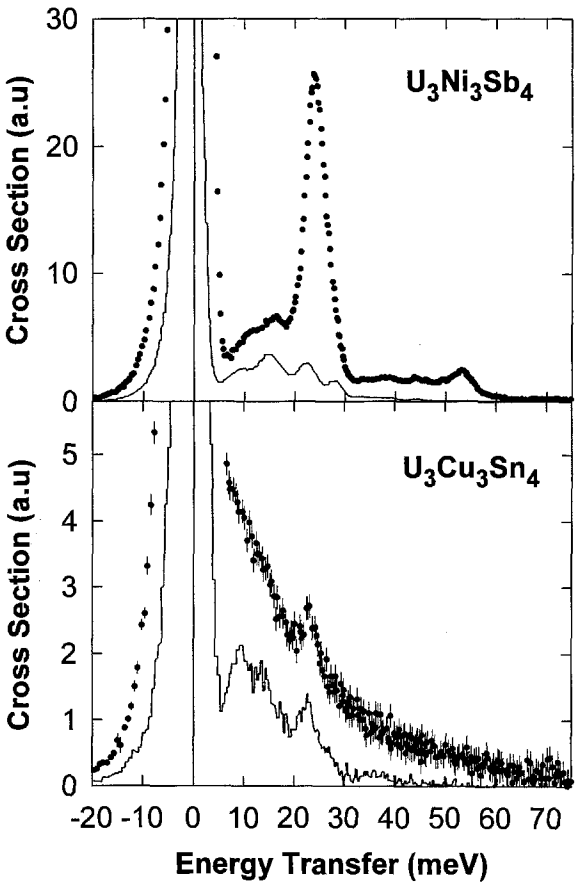

Fig. 5.106. Inelastic neutron scattering spectra of $U_3Ni_3Sb_4$ and $U_3Cu_3Sn_4$, taken at $T = 15$ K and 20 K, respectively, at a time-of-flight spectrometer with 80 meV incident energy. The dots represent the spectra from low-angle detectors, the lines are an estimate of the phonon scattering extrapolated from high-angle detectors. After Rainford et al. (1996).

RKKY type. As shown by a substitution study in the system $U_3(Ni_{1-x}Cu_x)_3Sb_4$ (Fujii et al. 1992), gap formation is not a very robust effect, as the typical semiconducting behaviour disappears gradually but fast, leaving nearly metallic behaviour already for 10% Cu. Ferromagnetism appears at about 30% Cu, which demonstrates that a certain minimum strength of magnetic (RKKY) interactions is needed to overcome the crystal-field splitting that forces the system into a singlet $5f^2$ state in pure $U_3Ni_3Sb_4$. The spontaneous moment increases monotonously with increasing Cu content reaching $\mu_s = 1.5\,\mu_B$/U in $U_3Cu_3Sb_4$. Supposing the same type of anisotropy as in U_3Sb_4 with an [1 0 0] easy magnetization direction, we obtain moments of $1.80\,\mu_B$/U, which is compatible with $2.0\,\mu_B$/U found in U_3Sb_4. One should notice the similarities in values of the paramagnetic Curie temperatures and effective moments in the table 5.18.

Another possibility to trace out the metal-semimetal transition is the study on the pseudoternary $U_3Ni_3(Sb_{1-x}Sn_x)_4$ system, in which the semimetallic behaviour of $U_3Ni_3Sb_4$ is gradually suppressed by Sn substitution (Endstra et al. 1992b), while the spin-fluctuation character of magnetism remains. The development of the γ-coefficient is non-monotonous. At low temperatures an upturn develops in the C/T vs. T^2 dependence around the 50–50 concentration, giving rise to $\gamma = 255$ mJ/(mol U K^2) in $U_3Ni_3(Sb_{0.5}Sn_{0.5})_4$.

5.5. *Compounds with the $ThMn_{12}$ structure*

The tetragonal body centred structure of the $ThMn_{12}$-type (space group I4/mmm), a ternary derivative of the $BaAl_4$-type (Andress and Alberti 1935), is a common representative of an extended family of actinide and lanthanide intermetallic compounds. Since some rare-earth compounds with the $ThMn_{12}$-type structure exhibited promising magnetic parameters for permanent-magnet applications, strong interest has been shown in actinide analogues as well. Detailed information on these materials can be found in reviews by Li and Coey (1991), Fujii and Sun (1995) and Suski (1996). A schematic drawing of the structure is shown in fig. 5.107. The actinide compounds of this structural family can be characterized by general formulas AnT_xX_{12-x} and AnT_xM_{12-x}, respectively (X = Al, Ga, Si, M = another transition metal). In all cases the An atoms occupy the "Th" 2*a* sites. The distribution of the atoms of the remaining components over the other three inequivalent "Mn" sites (8f, 8i, 8j) depends on the actual composition.

Despite the enormous experimental effort of researchers of several laboratories performing experiments on these materials most of the data have suffered for a long time of rather poor quality of samples, which was caused by severe metallurgical difficulties, and this has introduced much "information noise". Studies performed on single crystals, which

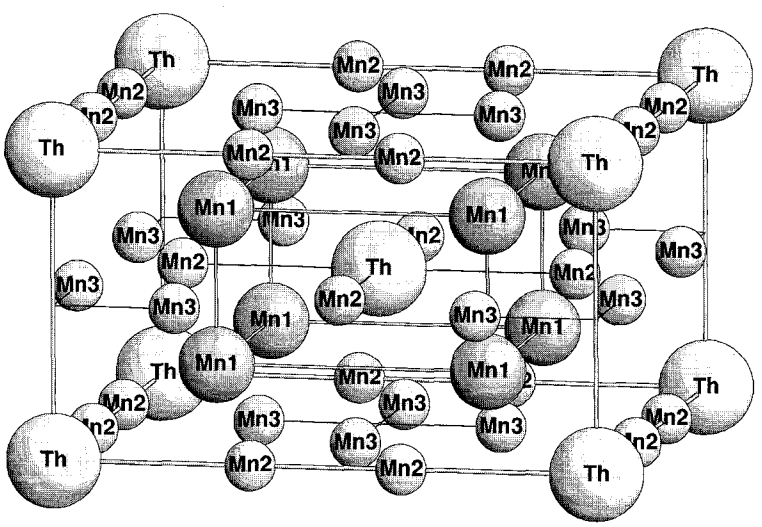

Fig. 5.107. Schematic picture of the $ThMn_{12}$-type structure.

are indispensable to carry out reliable experiments addressing the theoretically predicted phenomena, have appeared only in late nineties (Gonçalves et al. 1994, 1995a). In numerous cases, however, polycrystals are still the only available samples. In such cases, e.g., comparative magnetization measurements on oriented and random powder samples are frequently very helpful in determining the type of anisotropy and estimate the magnetization in the principal crystallographic directions (Andreev and Suski 1992; Andreev et al. 1992a). Essential magnetic and structure information is given in table 5.19.

An important effort has finally also been made in the field of theory. Lorenz et al. (1995) after the theoretical investigation of the high-Fe content compounds of the $ThMn_{12}$ family proposed non-collinear magnetic structures and spin-glass behaviour. This is the first real theoretical excursion into the class of materials for which so many contradictory experimental results exist.

5.5.1. AnT_xAl_{12-x} compounds

Structural aspects of materials in this group were discussed by Melamud et al. (1987) who have shown that in the $REFe_xAl_{12-x}$ compounds the Fe atoms occupying the 8i positions carry a substantial magnetic moment in contrast to atoms in the other two, i.e., 8f and 8j sites where the moments are usually rather small. Investigation of UFe_xAl_{12-x} compounds (for $x = 4, 5, 6$) by means of ^{57}Fe Mössbauer spectroscopy (Vagizov et al. 1995) allowed to determine that in UFe_4Al_8 the Fe atoms reside only on the 8f sites, whereas in UFe_5Al_7 (UFe_6Al_6) the Fe atoms occupy 54, 43 and 3% (58, 35, 7) of 8f, 8i and 8j, respectively. Generally, $AnFe_xAl_{12-x}$ compounds with $x \geqslant 3$ can be synthesized. However, UFe_{12} does not exist.

Both *$ThCr_4Al_8$* and *UCr_4Al_8* are paramagnets with weakly temperature dependent susceptibility. Polycrystalline samples of *$NpCr_4Al_8$* studied by Gal et al. (1987) suffered of Al evaporation during preparation to such an extent that the actual stoichiometry was $NpCr_4Al_6$. ^{137}Np Mössbauer spectroscopy investigation evidenced ordering of Np magnetic moments below $T = 55$ K whereas the susceptibility data pointed to $T_N = 46$ K. An effective hyperfine field on the ^{137}Np nucleus of 290 T has been determined at 4.2 K which points to a Np magnetic moment of 1.3 μ_B applying the Dunlap–Lander formula (Dunlap and Lander 1974).

The χ vs. T of *$ThMn_4Al_8$* is roughly hyperbolic. However, no magnetic ordering appears down to 4.2 K. The room-temperature susceptibility ($\chi_{300\,K} = 14.1 \times 10^{-8}$ m^3/mol) is more than an order of magnitude larger than in the Cr analogue and down to 4.2 K it becomes enhanced about 3-times (Baran et al. 1987).

In *UMn_4Al_8* the room-temperature susceptibility is only about 10% higher than in the Th counterpart and down to liquid-helium temperature it increases less than twice reaching only about 70% of the susceptibility value observed in $ThMn_4Al_8$ (Baran et al. 1987). This may be attributed to the antiferromagnetic polarization of Mn and U magnetic moments. Down to 1.45 K, however, no sign of magnetic order has been observed by means of neutron powder diffraction. *UMn_xAl_{12-x}* alloys exist for various Mn contents in the range $3 \leqslant x \leqslant 7$ (Suski et al. 1995). The lattice volume (including both lattice constants) exhibits a linear increase with decreasing x. All compounds are paramagnetic down to the lowest temperatures except for *UMn_3Al_9*. Here anomalies in the ac and dc susceptibility around 30 K indicate ferromagnetic ordering at lower temperatures with a very reduced spontaneous moment of approximately 0.08 μ_B/f.u., which can be estimated from

TABLE 5.19

Some basic characteristics of AnT_xX_{12-x} and AnT_xM_{12-x} compounds with the $ThMn_{12}$-type structure: Type of ground state (F – ferromagnetic, AF – antiferromagnetic, P – paramagnetic, PP – Pauli paramagnetic), μ_{An}, μ_{Fe} – the actinide and iron ordered magnetic moment (determined by neutron diffraction at 4.2 K), $T_{C,N}$ – magnetic ordering temperature, a, c – lattice parameters at room temperature.

Compound	Ground state	μ_{An} (μ_B)	μ_{Fe} (μ_B)	$T_{C,N}$ (K)	Ref.	a (pm)	c (pm)	Ref.
$ThCr_4Al_8$	P				[1]	901.1	515.1	[1]
UCr_4Al_8	P[a]				[2]	890.7	512.2	[1]
						891.32	510.91	[2]
$NpCr_4Al_8$[b]	AF	1.3[c]		55	[3]	893	515	[3]
$ThMn_4Al_8$	P					896.3	515.0	[1]
UMn_4Al_8						884.9	510.4	[1]
	P[a]				[2]	884.74	509.93	[2]
$ThFe_4Al_8$	AF	–	0.7[d]	147	[4]	884.2	507.6	[5]
						882.7	509.5	[6]
UFe_4Al_8						873.6	504.6	[6]
	F[e]	0.47	1.08	148	[7,8]	874.0	503.6	[8]
$NpFe_4Al_8$	F[f]	0.7[c]	1.05[d]	130	[3]	875.9	505.5	[3]
		0.6	1.1	130	[6]			
UCu_4Al_8	AF			30	[9]	876	510	[10]
$NpCu_4Al_8$								
$ThMn_3Al_9$	P				[11]			
UMn_3Al_9	F	0.08[e]	–	~ 30	[11]	888	511	[11]
UMn_6Al_6	P				[11]			
UFe_5Al_7	F			268	[12]	869.2	501.8	[12]
			0.814	261				
UFe_6Al_6	F[g]	3.2		355	[13]	863.8	498.7	[12]
			0.917	334	[14]			
UFe_6Ga_6	F			515	[15]	h	h	[15]
$UCu_{4.25}Al_{7.75}$	AF	1.6	–	37	[16,17]	874.6	509.6	[16,17]
$UCu_{4.5}Al_{7.5}$	AF		–	30[i]	[9]			
	AF[j]	1.3	–	37[k]	[13]			
	AF[j]	1.65	–	35	[16,17]	872.5	509.0	[16,17]
$UCu_{4.75}Al_{7.25}$	AF[j]	1.6	–	27	[16,17]	870.7	508.3	[16,17]
UCu_5Al_7	AF[j]	1.2	–	18	[16,17]	869.8	508.1	[16,17]
$UCu_{5.25}Al_{6.75}$	AF[j]	< 0.25	–	10	[9,16,17]	868.2	507.1	[16,17]
$UCu_{5.5}Al_{6.5}$	P	–	–		[16,17]	868.0	506.2	[16,17]
$UCu_{5.9}Al_{6.1}$	P	–	–		[16,17]	868.0	505.8	[16,17]
$UCu_2Ni_2Al_8$	AF[j]	1.04[k]		24	[18]	872.2[l]	5.116[l]	[18]
						872.1[k]	5.114[k]	
UCu_3NiAl_8	AF[j]	1.13[k]		26	[18]	874.9[l]	5.117[l]	[18]
						874.9[k]	5.118[k]	

TABLE 5.19 (Continued)

Compound	Ground state	μ_{An} (μ_B)	μ_{Fe} (μ_B)	$T_{C,N}$ (K)	Ref.	a (pm)	c (pm)	Ref.
$UFe_{10}Si_2$	F	0.5			[19–21]	837.29	472.69	[23]
	F	1.4	1.85	650	[22–24]	837.00	472.08	[25]
$UCo_{10}Si_2$	F			510	[25]	823.61	462.90	[25]
$UCo_5Fe_5Si_2$	F			750	[25]	833.8	464.8	[25]
$UNi_{10}Si_2$	P				[26]	818.5	468.6	[26]
$UFe_{10}Mo_2$	F	1.8	0.6[m]	198	[27,28]	848.59	475.08	[23]
$UFe_{10}Re_2$	F			340	[29]	854.1	471.4	[29]

[a] No magnetic order indicated down to $T = 1.45$ K within the accuracy of the neutron powder diffraction experiment.

[b] Due to high Al weight loses, the actual composition was approximately $NpCr_4Al_8$ (Gal et al. 1987).

[c] Determined from hyperfine field measured on the ^{237}Np isotope.

[d] Determined from hyperfine field measured on the ^{57}Fe isotope.

[e] Ferromagnetic collinear ordering in the U sublattice, antiferromagnetic coupling in the Fe sublattice (perpendicular to U moments), Fe moments canted yielding a ferromagnetic component (Paixao et al. 1997).

[f] Ferromagnetic collinear ordering in the Np sublattice (ordering below 115 K), antiferromagnetic coupling in the Fe sublattice (Gal et al. 1987).

[g] Ferromagnetic ordering of Fe moments perpendicular to the c-axis (Ptasiewicz-Bak et al. 1988).

[h] Orthorhombic $ScFe_6Ga_6$ structure, $a = 854.84$, $b = 869.14$, $c = 505.60$ (Gonçalves et al. 1996).

[i] Temperature above which magnetic reflections in a neutron powder diffraction vanish (Ptasiewicz-Bak et al. 1988).

[j] Antiferromagnetic ordering of the AFI type.

[k] At $T = 1.4$ K.

[l] At $T = 42$ K.

[m] Derived from the saturation magnetization measured on a single crystal along the c-axis.

References:

[1] Baran et al. (1987)
[2] Bourée-Vigneron et al. (1990)
[3] Gal et al. (1987)
[4] Buschow and van der Kraan (1978)
[5] Buschow et al. (1985b)
[6] Schäfer et al. (1989)
[7] Godinho et al. (1995)
[8] Paixao et al. (1997)
[9] Baran et al. (1986)
[10] Rauchschwalbe et al. (1985)
[11] Suski et al. (1995)
[12] Baran et al. (1985)
[13] Ptasiewicz-Bak et al. (1988)
[14] Vagizov et al. (1995)
[15] Gonçalves et al. (1996)
[16] Krimmel et al. (1992b)
[17] Krimmel et al. (1992a)
[18] André et al. (1997)
[19] Andreev et al. (1992b)
[20] Sechovsky et al. (1993c)
[21] Andreev et al. (1993b)
[22] Estrela et al. (1995)
[23] Gonçalves et al. (1995a)
[24] Berlureau et al. (1989)
[25] Berlureau et al. (1991)
[26] Suski et al. (1993)
[27] Gonçalves et al. (1995b)
[28] Gonçalves et al. (1995a)
[29] Gueramian et al. (1991)

the magnetization curve presented by Suski et al. (1995). No sign of saturation is observed up to 14 T where the magnetic moment reaches 0.25 μ_B/f.u. Suski et al. suggest that this behaviour reflects a complex non-collinear structure although a weak itinerant ferromagnet would behave in a similar manner. Since *$ThMn_3Al_9$* shows no indication of magnetic ordering down to the lowest temperatures, it was concluded that ordered magnetic moments reside exclusively on the uranium sites in UMn_3Al_9 (Suski et al. 1995).

The thorium compound *$ThFe_4Al_8$* orders magnetically below 147 K (Buschow and van der Kraan 1978) with Fe magnetic moments of approximately 0.7 μ_B as determined from

Mössbauer data. This compares well with values of Fe magnetic moments in $REFe_4Al_8$ compounds. Below T_C $ThFe_4Al_8$ exhibits noticeable magnetic history effects (only polycrystalline data are available). A broad maximum is observed on the ZFC curve whereas the FC curve shows a standard monotonous increase with decreasing temperature and saturation when approaching the low-temperature limit (Baran et al. 1985).

The most prominent representative of this family of compounds, *UFe_4Al_8*, has attracted a special interest. In this material, at least ideally, the Fe atoms form the 8f sublattice whereas the other two eight-fold sites 8i and 8j host the Al atoms. In this configuration the U atom is surrounded by a parallelepiped of eight Fe atoms (see fig. 5.107) which implies zero molecular field acting on the U atom in case of antiferromagnetic arrangement of the Fe moments (Buschow and van der Kraan 1978). Preparation of this material and structure and basic magnetic data have been first reported by Baran et al. (1984) and Stepien-Damm et al. (1984). The first reports on neutron powder diffraction experiments (Ptasiewicz-Bak et al. 1988) claimed magnetic ordering at 150 K only in the Fe sublattice with moments of 1.6 μ_B parallel to the c-axis, in agreement with results of ^{57}Fe Mössbauer experiments. Later on Schäfer et al. (1989) proposed an analogous magnetic structure of the Fe sublattice with Fe magnetic moment of $\approx 1.0\,\mu_B$ but in addition ferromagnetically ordered moments of 0.8 μ_B in the uranium sublattice have been proposed. Gal et al. (1990) analyzed an extended set of ac- and dc-susceptibility, neutron diffraction (in zero field and in 3 T) and Mössbauer effects data collected on polycrystals of UFe_4Al_8, $NpFe_4Al_8$ and $ThFe_4Al_8$. These authors proposed a spin-glass state in these materials below $T_{SG} \approx 130$ K, 120 K, and 110 K, respectively. Note, that the same authors arrived in a similar way to the same unusual conclusion on a spin glass state also in another isostructural crystallographically ordered ternary compound $HoFe_4Al_8$ (Gal et al. 1989). Results of the high-field magnetization study on oriented and random powders (Andreev et al. 1992c) were interpreted in terms of strong magnetocrystalline anisotropy with the easy-magnetization axis lying within the basal plane. The latter conclusion was in strong contradiction with the above mentioned results of neutron diffraction experiment. Clear cut experiments have been made after the first high-quality single crystals of UFe_4Al_8 became available. The first "puzzle" about anisotropy has been solved by magnetization measurements in magnetic fields applied along the principal crystallographic directions (Godinho et al. 1995, 1996; Bonfait et al. 1996). Results confirmed previous conclusions of Andreev et al. (1992c) that UFe_4Al_8 is an easy plane (a–b plane) system, i.e., that the hard magnetization axis in this material is the c-axis. Magnetization curves measured in magnetic fields along the a-axis show ferromagnetic behaviour below 148 K (yielding 1.9 μ_B/f.u. in 2 T measured at 4.2 K) and the differences between the ZFC and FC curves can be explained by the temperature variation of the coercive force (Godinho et al. 1995) which is connected with pinning of narrow domain walls. The M vs. T curves (FC and ZFC) are seen in fig. 5.108. Above 200 K, the inverse susceptibility vs. temperature increases linearly (Curie–Weiss law) yielding a paramagnetic Curie temperature Θ_p of 120 and 80 K for $\boldsymbol{H} \| a$ and $\boldsymbol{H} \| c$, respectively. The common effective moment is 13 μ_B/f.u.

Results of neutron diffraction experiments (combined measurements with unpolarized and polarized neutrons) on a UFe_4Al_8 single crystal (Paixao et al. 1997) in combination with magnetization data provided microscopic information on aspects of magnetism in this material, namely:

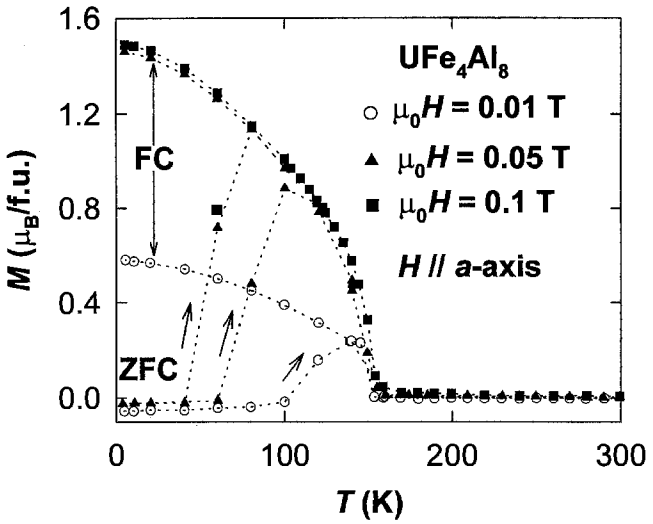

Fig. 5.108. ZFC and FC magnetization for UFe_4Al_8 in magnetic fields H parallel to the a-axis (Godinho et al. 1995).

- Commensurate antiferromagnetic ordering occurs in the Fe sublattice with an Fe magnetic moment of $1.08\,\mu_B$ at 4.2 K in the basal plane. Symmetry arguments suggest weak ferromagnetic component of the Fe sublattice in the c-axis of about $0.3\,\mu_B$ which is compatible with a canting angle of 16° in zero magnetic field. An applied magnetic field causes further canting from the a-axis towards the field direction ($\approx 25°$ in 4.6 T at $T = 4.2$ K).
- Ferromagnetic uranium magnetic moment of $0.47\,\mu_B$ per U atom are present. These are oriented along the b- (or a-) axis.

These results are schematically expressed in fig. 5.109. The size of the Fe magnetic moment is compatible with the value derived from hyperfine field data (Gal et al. 1990). Application of magnetic field on this spin arrangement leads to anomalous magnetization curves (see fig. 5.110).

Additional polarized neutron experiment performed in the paramagnetic state revealed that the Fe magnetic response is almost isotropic in contrast to the uranium susceptibility which is much larger in the basal plane than along the c-axis (Paixao et al. 1997).

The perpendicular configuration between the magnetic moments in the uranium and iron sublattice may provide a reasonable basis for explaining the rather exotic magnetization processes and related magnetoresistance phenomena (fig. 5.110) reported by Bonfait et al. (1996) and Godinho et al. (1996) and measured on the same single crystal. Also the magnetoresistance measurements performed on a single crystal in magnetic fields up to 16 T (Bonfait et al. 1995) revealed strong anisotropy of the magneto-transport phenomena.

Only polycrystalline samples of *$NpFe_4Al_8$* were studied. The samples were probably deficient in Al due to evaporation during the preparation procedure, similar to $NpCr_4Al_8$

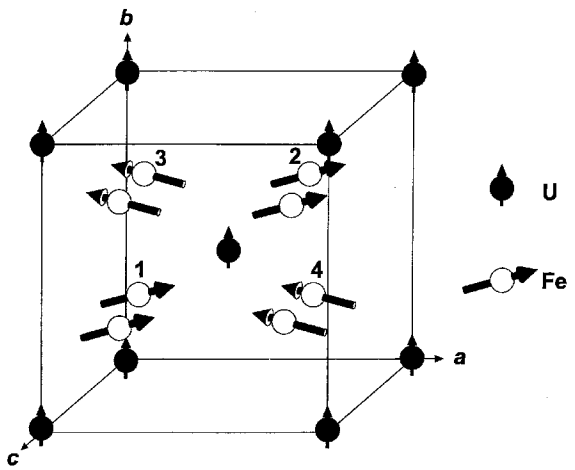

Fig. 5.109. Magnetic structure of UFe_4Al_8 in $\mu_0 H = 4.6$ T. Data from Paixao et al. (1997).

(Gal et al. 1987) mentioned above. Since not only ^{57}Fe but also ^{237}Np is a suitable Mössbauer isotope, Mössbauer spectroscopy provided very important information on this material (Gal et al. 1987). Besides, also neutron powder diffraction experiments have been performed in zero field (Gal et al. 1987; Schäfer et al. 1989) and in non-zero magnetic field (Schäfer et al. 1991). Based on results of these experiments and considering the clear results obtained on UFe_4Al_8 single crystals (Godinho et al. 1995, 1996; Bonfait et al. 1996) and the very similar ordering temperature of the Fe moments, one may tentatively suppose that the antiferromagnetic ordering of the Fe sublattice is also similar in all three compounds $ThFe_4Al_8$, UFe_4Al_8 and $NpFe_4Al_8$ (and assume an analogous ferromagnetic ordering of the moments in the An sublattice in the latter two compounds). The interpretation of these three crystallographically ordered ternary materials in terms of spin-glass systems as suggested by Gal et al. (1990) is most probably incorrect. It should be noted that pronounced magnetic history effects cause frequently a strong temptation to use such exotic approaches to interpret ordinary phenomena caused by a strong domain-wall pinning in highly anisotropic materials as the uranium intermetallics.

All the UFe_xAl_{12-x} compounds, which were reported to form in the composition range $3.2 \leqslant x \leqslant 4.8$, are ferromagnetic. The concentration dependence of the saturation magnetization is non-monotonous showing a minimum for $x = 4$ (Baran et al. 1986; Andreev et al. 1992c). In case of UFe_6Al_6 neutron powder experiments (Ptasiewicz-Bak et al. 1988) suggest ferromagnetic ordering only of the Fe magnetic moments ($3.2\,\mu_B$ at 4.2 K) perpendicular to the c-axis.

$UCu_{4+x}Al_{8-x}$ alloys attracted extraordinary interest due to their heavy-fermion features. UCu_4Al_8 was originally reported to order antiferromagnetically below 30 K (Baran et al. 1986) and to show an enhanced γ-value of about 100 mJ/(mol K^2) (Drulis et al. 1989). A detailed metallurgical investigation performed by (Geibel et al. 1990a) showed that $UCu_{4+x}Al_{8-x}$ has a wide homogeneity range for $0.1 \leqslant x \leqslant 1.95$. The unit cell becomes

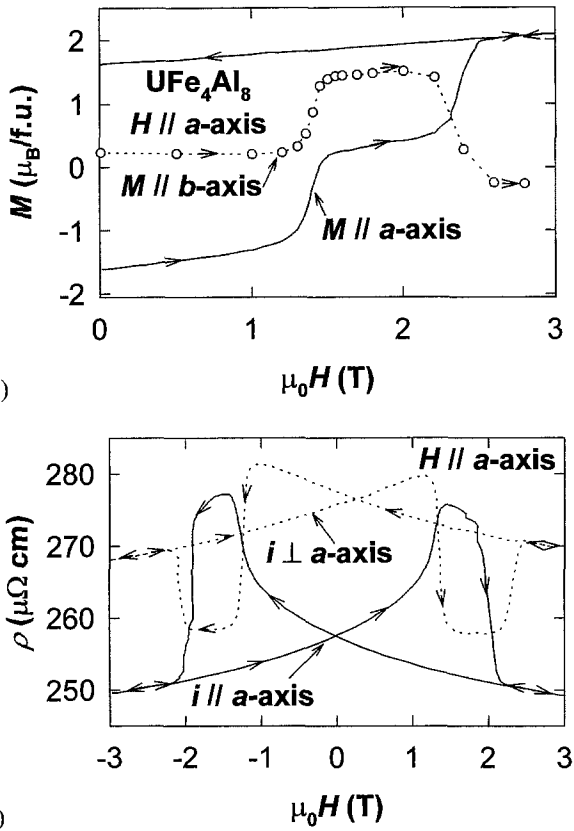

Fig. 5.110. (a) Longitudinal ($H \| a$, $M \| a$) and transversal ($H \| a$, $M \| b$) magnetization of UFe_4Al_8 at $T = 2$ K. (b) Longitudinal ($H \| a$, $i \| a$) and transversal ($H \| a$, $i \perp a$) magnetoresistance of UFe_4Al_8 at $T = 2$ K. Data from Bonfait et al. (1996).

gradually compressed (both in the a- and the c-direction) with increasing Cu content. Susceptibility and resistivity measurements pointed to gradually decreasing Néel temperatures from 42 K for $x = 0$ (Geibel et al. 1990a) to 10 K for $x = 1.5$ (Krimmel et al. 1992a) whereas the samples with $x \geqslant 1.5$ showed no indication of magnetic order. The uranium magnetic moment collapses in this region as can be seen in table 5.19. This collapse is accompanied by a progressive evolution of the heavy-fermion state as documented by the increasing γ-value from 100 mJ/(mol K^2) for $x = 0.1$ through 400 mJ/(mol K^2) for $x = 0.125$ to 800 mJ/(mol K^2) for $x = 0.195$ (Steglich et al. 1990a, 1990b). The development of a pronounced negative slope of the ρ vs. T curve in the vicinity of the critical composition for magnetism has been interpreted in terms of a Kondo lattice (Geibel et al. 1990a). A similar approach to the understanding of results of magnetization, specific-heat, resistivity, and NMR and NQR studies has been presented by Nishioka et al. (1996) and Kontani et al. (1997). Inelastic neutron scattering experiments (Krimmel et al. 1997) show that in contrast to Ce heavy-fermion systems the line width of the quasielastic re-

sponse does not scale with the Kondo temperature derived from bulk measurements. On the other hand, the line width becomes reduced with the expected increasing hybridization. This result creates doubts about the interpretation of the system as a Kondo lattice.

Suski et al. (1992a) have shown that $UFe_xCu_{4-x}Al_8$ solid solutions of the $ThMn_{12}$-type structure form in the whole concentration range. Measurements of the magnetization performed on polycrystals do not allow to reach a straightforward conclusion on the evolution of behaviour of these materials. Indications of the existence of solid solutions of the $UNi_xCu_{4-x}Al_8$-type and some resistivity data on these materials can be found in reports of Suski et al. (1985), Drulis et al. (1989), and Suski et al. (1997). For two such compounds, UCu_2Ni_2Al and UCu_3NiAl, a neutron powder diffraction study revealed a type I antiferromagnetic structure of the U magnetic moments (1.04 and 1.13 μ_B, respectively) below T_N (= 24, 26 K, respectively). The structure consists of ferromagnetic (0 0 1) planes with U moments oriented along the c-axis (André et al. 1997).

The results of studies of $NpCu_4Al_8$ reported by Gal et al. (1987) are rather controversial. Whereas ^{237}Np Mössbauer spectroscopy points to an ordered Np magnetic moment of 1.5 μ_B, the neutron powder diffraction experiment suggests only 0.5 μ_B. This discrepancy was explained in terms of only slow paramagnetic moment relaxation rather than magnetic ordering (Gal et al. 1987).

Due to a similar stoichiometry, we include here also UFe_6Ga_6 although it is crystallizing in another structure (orthorhombic $ScFe_6Ga_6$-type). This compound is ferromagnetic below 515 K and exhibits a spontaneous magnetization (free-powder) of 10.5 μ_B/f.u. (Gonçalves et al. 1996).

5.5.2. $UT_{10}Si_2$ and $UT_{10}T'_2$ compounds

$UFe_{10}Si_2$ exhibits ferromagnetic ordering below 650 K as indicated by ac susceptibility measurement on a single crystal (Gonçalves et al. 1995a) which is in agreement with previous results on polycrystals (Berlureau et al. 1989; Suski et al. 1989). Results of a magnetic anisotropy study made on aligned powders (Andreev et al. 1995g) have been later confirmed by single-crystal measurements (see below). Using X-ray diffraction experiments, Andreev et al. (1995g) have also determined the magnetostriction constants as: $\lambda_1^{\alpha,0} = 2.14 \times 10^{-3}$, $\lambda_2^{\alpha,0} = 6.07 \times 10^{-3}$, $\lambda_1^{\alpha,2} = -0.4 \times 10^{-4}$, $\lambda_2^{\alpha,2} = -0.9 \times 10^{-4}$ and $\lambda^{\gamma,2} = -0.9 \times 10^{-4}$. Also the sublattice magnetizations were studied by Andreev et al. (1993b) by magnetization measurements made on aligned powders of $UFe_{10-x}Al_xSi_2$ solid solutions, from which the existence of U magnetic moments of approximately 0.5 μ_B has been determined. By magnetization measurements made on $UFe_{10}Si_2$ single crystals Estrela et al. (1995) confirmed the uniaxial anisotropy in this material and determined a saturation magnetization of 19.5 μ_B/f.u. along the c-axis, which is the easy magnetization direction. This value is considerably larger than 16.4 μ_B/f.u. derived from magnetization studies of oriented powders (Andreev et al. 1992a, 1995g). When the field is applied along the magnetically hard a-axis, a first order transition is induced around 3 T above which the a-axis magnetization curve rapidly joins the c-axis magnetization curve and saturates, as can be seen in fig. 5.111. The anisotropy constants $K_1 = 38.5 \times 10^6$, $K_2 = -16.1 \times 10^6$ and $K_3 = 3.9 \times 10^6$ erg/cm^3 were determined from the magnetization curves using the formula (Asti 1990):

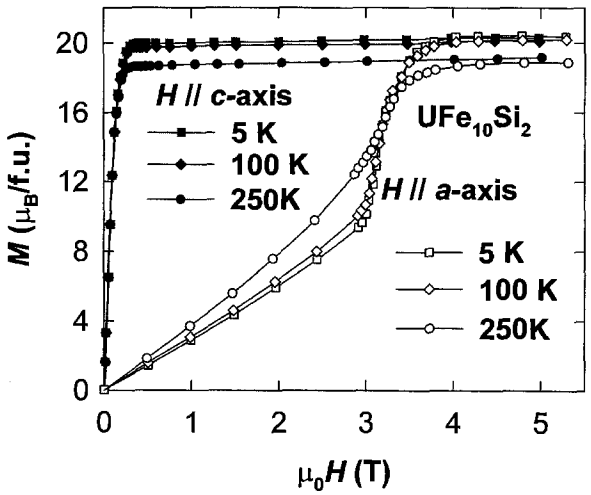

Fig. 5.111. Magnetization curves for $UFe_{10}Si_2$ in magnetic fields applied along the c- and a-axis at $T = 5$, 100, and 250 K.

$$HM_S = 2K_1\frac{M_\perp}{M_S} + 4K_2\left(\frac{M_\perp}{M_S}\right)^3 + 6K_3\left(\frac{M_\perp}{M_S}\right)^5, \tag{5.14}$$

suitable for uniaxial systems, where H is the applied magnetic field, M_S the spontaneous magnetization, and $M_\perp$ the magnetization perpendicular to the c-axis. The critical field is hardly dependent on temperature up to 250 K in agreement with previous studies of oriented powders (Andreev et al. 1995g), from which the following values were obtained $\mu_0 H_c = 2.7$ T at 4.2 K, $K_1 = 30 \times 10^6$, $K_2 = -9 \times 10^6$ erg/cm^3. The values of the anisotropy constants indicate an important role of the U magnetic moments in the magnetism of this material. Comparison of the saturation magnetization of $UFe_{10}Si_2$ with the values of the non-magnetic rare-earth analogues $YFe_{10}Si_2$ (Li et al. 1991; Andreev et al. 1992a) and $LuFe_{10}Si_2$ (Li et al. 1991; Suski et al. 1992b) allowed Estrela et al. (1995) to reach conclusions about the occurrence of ferromagnetic interactions between the uranium and the iron sublattices and to estimate the U moment to be equal to $1.4\,\mu_B$. This value is, however, considerably larger than $0.5\,\mu_B$ previously reported by Andreev et al. (1992b, 1993b). The presence of a magnetic moment on the uranium sites in $UFe_{10}Si_2$ has been indicated already by van Engelen and Buschow (1990) who reported an enhanced polar Kerr effect in this material in comparison with the rare-earth counterparts.

Berlureau et al. (1991) have found that $UFe_{10}Si_2$ and $UCo_{10}Si_2$ are characterized by different occupation of the crystallographic sites by transition-metal and silicon atoms. In both compounds silicon is distributed between the 8f and 8j sites in different proportions: (i) for $UFe_{10}Si_2$, 75% of the silicon atoms are in 8f site and 25% in the 8j site; (ii) for $UCo_{10}Si_2$, nearly all the silicon atoms (> 90%) are in the 8f site. *$UCo_{10}Si_2$* becomes ferromagnetic below 510 K (Berlureau et al. 1991). By a study of aligned powders of $UCo_{10}Si_2$ Andreev et al. (1995h) observed a strong uniaxial magnetic anisotropy in this

material with $K_1 = 3.3$ MJ/m^3 at 4.2 K. Waerenborgh et al. (1997) studied $UFe_{10}Si_2$ by ^{57}Fe Mössbauer spectroscopy in the temperature range 5–643 K ($T_C = 640$ K). These authors confirmed a preferential occupation of the 8f site by Si atoms and shown that the hyperfine field B_{hf} follows for $T < T_C$ a relation:

$$\frac{B_{hf}(T)}{B_{hf}(0)} \approx 1 - D_s\left(\frac{T}{T_C}\right)^3. \tag{5.15}$$

The Curie temperature of the $U(Fe_{10-x}Co_x)Si_2$ solid solutions increases with increasing x up to a maximum $T_C = 750$ K for $x \approx 5$–6 (Berlureau et al. 1991; Suski et al. 1991) and then it slowly decreases. The ^{57}Fe Mössbauer spectroscopy study indicates that the Co and Fe atoms are not randomly distributed over the 8f, 8i and 8j sites (Berlureau et al. 1991). Magnetic domain structures in polycrystalline $UFe_{10}Si_2$ and $UCo_{10}Si_2$ and their changes throughout the whole hysteresis cycle were studied by (Wyslocki et al. 1990). A similar study has been made also on UFe_9AlSi_2 and UFe_6Al_6 (Wyslocki et al. 1995, 1996). The spontaneous magnetostriction in $UFe_{10}Si_2$ and $UCo_{10}Si_2$ (Andreev et al. 1991; Andreev and Zadvorkin 1997) was studied by X-ray diffraction. It was proposed to have two contributions, one attributed to the exchange interaction within the transition-metal (Fe or Co) sublattice and the other ascribed to an inter-sublattice (Fe/Co $\Leftrightarrow$ U) interaction. When Ni is substituted for Fe in the $UFe_{10-x}Ni_xSi_2$ system the ordering temperature decreases. The results of a combination of magnetization and ^{57}Fe Mössbauer effect measurements led to the conclusion that only iron contributes to the magnetic ordering observed at lower temperatures. It was shown that the substitution of Ni for Fe results in a strong preferential occupation of the 8f site by Ni. The effects of substitutions of Cr for Fe and Sn for Si were studied by Suski et al. (1996) and no visible effect on T_C has been observed for a 10% substitution. A change of the anisotropy has been revealed in $UFe_{10-x}Al_xSi_2$ around $x = 2$ as inferred from magnetization and ^{57}Fe Mössbauer studies (Andreev and Suski 1992; Andreev et al. 1993a; Vagizov et al. 1993c). The conclusion that the anisotropy in these compounds is determined by two components, in particular by a large uniaxial contribution from the uranium and Fe 8i sites and by a basal-plane contribution of the Fe 8f sublattice, was principally right, as was later confirmed by single-crystal investigations (Paixao et al. 1997).

$UNi_{10}Si_2$ does not show long-range magnetic order down to the lowest temperatures and exhibits an enhanced γ-value of approximately 100 mJ/(mol K^2) (Suski et al. 1993).

The temperature dependence of the magnetization of $UFe_{10}Mo_2$ indicates ferromagnetic ordering in this material below 198 K (Suski et al. 1989; Gonçalves et al. 1995a, 1995b). X-ray diffraction analysis (Gonçalves et al. 1995b) confirmed that the Mo atoms are randomly distributed in the 8i positions. ^{57}Fe Mössbauer spectra collected below T_C show a distribution of hyperfine fields from 0 to 20 T which can be attributed to different local surroundings of Fe atom which is compatible with X-ray data. Magnetization measurements performed on a single crystal clearly indicated strong magnetocrystalline anisotropy which, in contrast to $UFe_{10}Si_2$, is not uniaxial. Estrela et al. (1997) propose "basal plane anisotropy" but the considerable spontaneous moment measured also along the c-axis (the main signal is measured along a) points to a multi-axial anisotropy and indicates the possibility of a canted magnetic structure. Estrela et al. (1997) analyzed the magnetization data

in comparison with data obtained for $YFe_{10}Mo_2$ (Christides et al. 1993), and estimated the size of the ferromagnetically coupled moments on uranium sites ($\approx 1.8\,\mu_B$) and iron sites ($0.6\,\mu_B$).

Ferromagnetism below 340 K is reported for *$UFe_{10}Re_2$* by Gueramian et al. (1991).

5.6. *UT_2X_3 compounds*

The prominent representatives of this group are UNi_2Al_3 and UPd_2Al_3, discovered in 1991 as heavy fermion superconductors with antiferromagnetic order of the U-moments at low temperatures (Geibel et al. 1991a, 1991b). Further members are heavy fermion UPd_2Ga_3, and similar compounds with heavier actinides. They crystallize in the hexagonal structure of the $PrNi_2Al_3$ type (space group P6/mmm), which is a structure derived from the $CaCu_5$ structure by replacing 3 of the Cu atoms by Al (see fig. 5.112). It consists of U–T basal plane sheets with Al(Ga) interlayers, but the U–U spacing within the sheet is always larger than that along the c-axis. This crystal structure is typical also for numerous compounds with rare-earth elements, and their investigation (Higashi et al. 1993; Mulder et al. 1995) showed an imperfect occupation of the T sublattice or other possible types of a small atomic disorder. This can account for a strong sensitivity of the electronic properties to off-stoichiometry and to details of the heat treatment. Basic crystallographic and magnetic information on 1:2:3 compounds can be found in table 5.20.

Both UPd_2Al_3 and UNi_2Al_3 are antiferromagnetic, *UPd_2Al_3* has higher ordered moment and higher ordering temperature of 14.4 K (Geibel et al. 1993). Powder neutron diffraction experiments showed the ordered moment to be equal to $(0.85 \pm 0.03)\,\mu_B$/U (Krimmel et al. 1993a). The magnetic structure corresponds to a wave vector $\boldsymbol{q} = (0, 0, 1/2)$ with U-moments perpendicular to the c-axis. Although a second, incommensurate, magnetic phase was reported in (Krimmel et al. 1993a), its existence has not been confirmed in latter neutron experiments on a single crystal (Krimmel et al. 1993b). Unlike the Néel temperature, the critical temperature of superconductivity is strongly sample dependent,

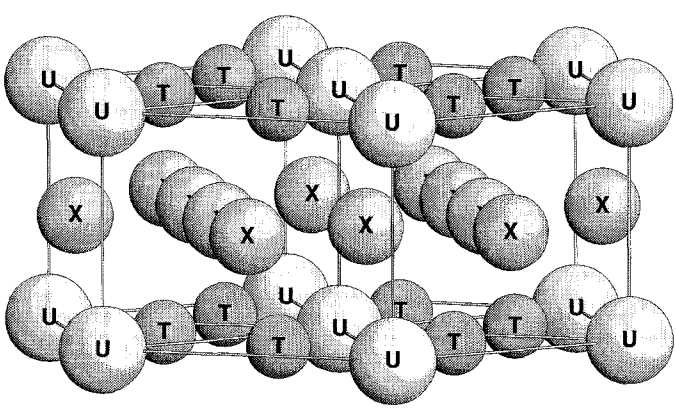

Fig. 5.112. Schematic picture of the hexagonal structure of the $PrNi_2Al_3$ type in which crystallize AnT_2X_3 compounds including the UT_2X_3 materials.

TABLE 5.20

Some basic characteristics of $U_1T_2X_3$ compounds: a, c – lattice parameters at room temperature, T_N – magnetic ordering temperature, T_c – temperature of transition to superconducting state.

Compound	a (pm)	c (pm)	T_N (K)	T_c (K)	Ref.
UPd_2Al_3	536.5	418.6	14.4	2.0	[1]
$NpPd_2Al_3$	539.1	419.6	38(42)		[2,3,4]
$PuPd_2Al_3$	540.2	419.4			[2]
UNi_2Al_3	520.7	401.8	4.4	1.1	[1]
$NpNi_2Al_3$	522.2	399.5	23		[2]
UPd_2Ga_3	530.15	851.12[a]	13		[5]
UNi_2Ga_3	516.61	403.63			[6]
UNi_3Ga_2	500.40	410.55			[6]
UCu_3Al_2	514.02	414.72			[7]
$UCu_{3.5}Al_{1.5}$	509.0	415.9			[8]

[a] Unit cell doubled.

References:

[1] Geibel et al. (1993)
[2] Seret et al. (1995)
[3] Zwirner et al. (1993)
[4] Hiess et al. (1997b)
[5] Süllow et al. (1995)
[6] Zelinsky et al. (1995)
[7] Nakotte et al. (1994e)
[8] Nakotte et al. (1996d)

varying with a slight off-stoichiometry and/or heat treatment of single crystalline samples between 1.5 K and 2.0 K (Sato et al. 1994). The best results can be obtained with about 1% excess of Al, accounting probably for losses due to evaporation in the melting process. The study of polycrystals (Schank et al. 1994) showed that superconductivity is lost completely, e.g., for $UPd_2Al_{2.97}$. Although magnetic properties are strongly anisotropic, the upper critical field $\mu_0 H_{c2} = 2.5$ T is only weakly dependent on the direction of the applied magnetic field (Sato et al. 1992a). A later detailed study made with another sample showed that $\mu_0 H_{c2} = 3.9$ T for $H \| c$ is reduced to 3.1 T for $H \| a$ (Sato et al. 1997). The intimate connection of the superconductivity and the heavy fermion character of the electronic structure is manifest in the huge jump of the specific heat C, scaling with γT_c, $\gamma = 140$ mJ/(mol K^2) (Geibel et al. 1991b) at T_c. The unconventional superconductivity has been deduced from NMR experiments, pointing to an anisotropic energy gap with line nodes and d-wave pairing (Kitaoka et al. 1995).

The magnetic susceptibility (see fig. 5.113) is strongly anisotropic. For $H \perp c$, a broad maximum between 30 and 40 K is followed by a Curie–Weiss behaviour on the high temperature side. Its analysis yields the values $\mu_{eff} = 3.2\,\mu_B$/U and $\Theta_p = -55$ K. The response for $H \| c$ is weaker both in magnitude and in the temperature dependence, although it can also be tentatively fitted to the CW law with parameters $\mu_{eff} = 3.0\,\mu_B$/U and $\Theta_p = -300$ K (Grauel et al. 1993). A similar character but somewhat different values ($\mu_{eff} = 3.6\,\mu_B$/U in both geometries, and $\Theta_p = -33$ K for $H \perp c$ and -215 K for $H \| c$ were reported by de Visser et al. (1992). The Néel temperature is reflected only as a weak anomaly, similar to, e.g., URu_2Si_2. Although the field dependence of the susceptibility, resistivity, and other bulk properties with $H \perp c$ show a sequence of anomalies in the low

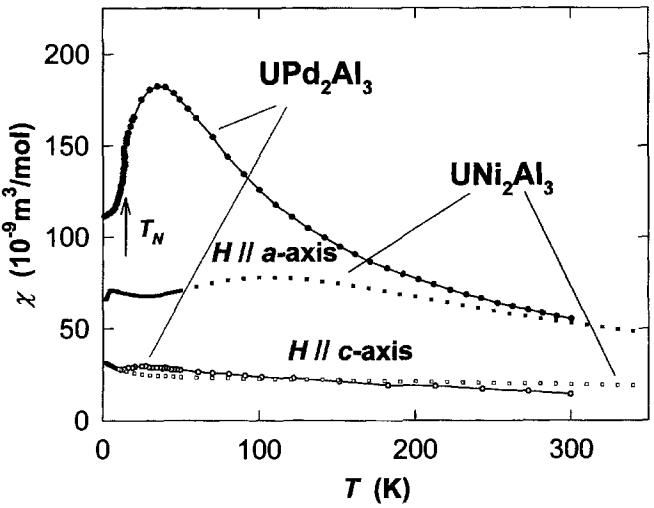

Fig. 5.113. Temperature dependence of the susceptibility of UPd_2Al_3 and UNi_2Al_3 measured on single crystals with magnetic field applied along the principal crystallographic directions.

field range (below 5 T), single crystal neutron diffraction reveals in this area only effects of re-population of those equivalent antiferromagnetic domains of the ⟨1 0 0⟩ type that have moments perpendicular to the field direction. But rotation of moments within the basal plane could not be excluded (Kita et al. 1994; Paolasini et al. 1994).

The field definitely causes the magnetic moments to turn towards the field direction – it can be associated with the metamagnetic transition at 18 T for $H \perp c$ (de Visser et al. 1992; Oda et al. 1994). The response for $H \| c$ is linear up to 35 T (fig. 5.114). The fact that the magnetization in high fields corresponds to about 1.7 μ_B/U, which is the value twice as large as the low-field moment obtained from the neutron diffraction experiment, points to a significant increase of the U-moments at the transition. The metamagnetic transition involves also as a large drop of the electrical resistivity. It is more pronounced for current along c sensing the AF coupling in the ground state, as shown in fig. 5.115 (de Visser et al. 1993). The temperature dependencies of the electrical resistivity for both $i \| c$ and $i \perp c$ are characterized by broad maxima between 50 and 100 K, usually taken as a fingerprint of spin fluctuations, and show a negative slope at higher temperatures (fig. 5.116). The magnetic ordering temperature correlates with a weak anomaly on the low-T side in both cases (Sato et al. 1992a). The Néel temperature decreases weakly with external pressure, while T_c is practically unaffected (Bakker et al. 1993b; Wassilew et al. 1994; Link et al. 1995).

The coexistence of magnetic ordering (with sizeable U magnetic moments) and superconductivity opened a discussion on how much the heavy quasiparticles form Cooper pairs related to the electrons giving rise to magnetic moments. The fact that magnetism is not affected by the onset of superconductivity while they coexist on a microscopic scale was shown primarily by the invariable internal-field distribution in zero external magnetic field (Amato et al. 1992a; Uemura and Luke 1993). On the other hand, the nearly isotropic

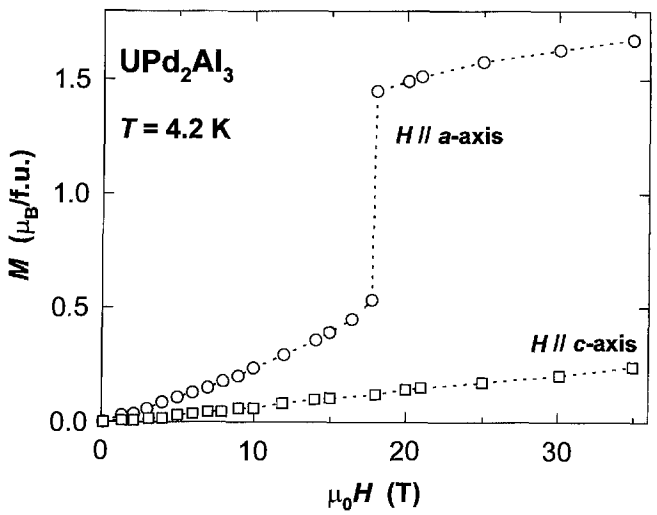

Fig. 5.114. Magnetization curves of UPd_2Al_3 measured at $T = 4.2$ K on a single crystal with magnetic field applied along the principal crystallographic directions. Data compiled from references mentioned in the text.

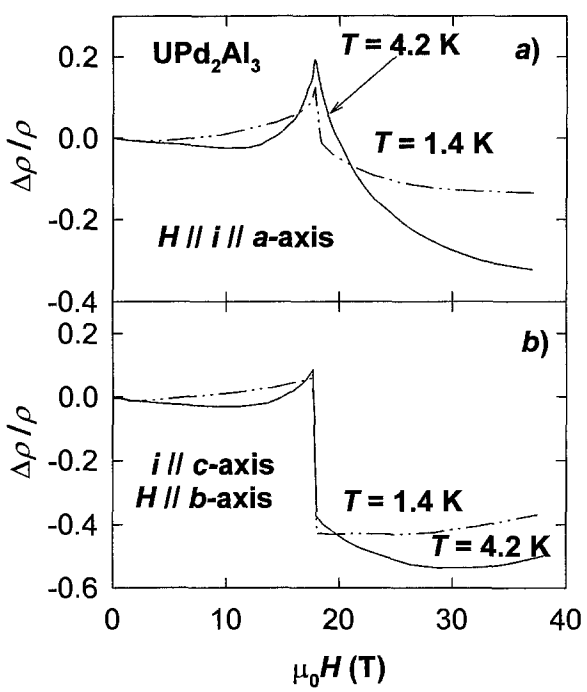

Fig. 5.115. Electrical resistivity of UPd_2Al_3 as a function of magnetic field (a) in the longitudinal ($H \| i \| a$) and (b) transversal ($H \| b$, $i \| c$) geometry measured on a single crystal at $T = 4.2$ K directions (after de Visser et al. (1993)).

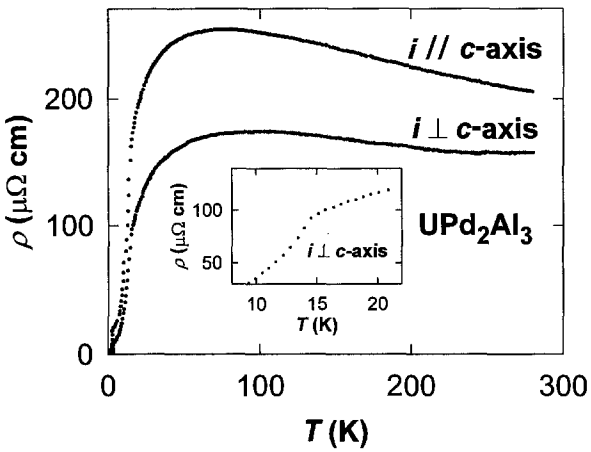

Fig. 5.116. Temperature dependence of the resistivity of UPd_2Al_3 measured on a single crystal with current i along the principal crystallographic directions. The inset shows in more detail the behaviour around the magnetic phase transition After Sato et al. (1992a).

changes of the μ^+-Knight shift below T_c, which were attributed to dipolar fields originating from magnetically polarized U-ions (while the bulk magnetism is anisotropic) seem to point to the existence of two sub-systems. One 5f local-moment sub-system is responsible for most of the magnetic features. The other is a heavy-quasiparticle sub-system, roughly isotropic, responsible for the enhanced γ-value, and for superconductivity (Feyerherm et al. 1994).

^{105}Pd NMR and NQR experiments (Matsuda et al. 1997) show only weak coupling of the Pd 4d states to the 5f states, which is in good agreement with magnetization density study using polarized neutron diffraction (Paolasini et al. 1993). The lack of induced Pd moments can be understood as a consequence of the directionality of U–U bonds and/or as a consequence of reduced overlap of the respective states in electron energy spectrum. The first explanation is corroborated by the strong anisotropy of the U-moments within the basal plane, which suggests that the charge density is mainly concentrated along the c-axis, where nearest U–U links are found.

Another information coming from ^{105}Pd and ^{27}Al NMR and NQR is that the spin-lattice relaxation rate $1/T_1$ decreases in the superconducting state as T^3, which indicates the occurrence of an anisotropic superconducting gap. A consensus about the type of pairing has not been reached yet, speculations appear about the d- or s-wave pairing type (Kyogaku et al. 1992, 1993; Kitaoka et al. 1995; Kohori et al. 1995).

The dual nature of the 5f states led to an explanation of bulk magnetic properties on the basis of crystal field effects assuming a tetravalent U-state (Grauel et al. 1992, 1993). A fingerprint of 5f localized states was found also in neutron scattering experiment, in which some of the features were tentatively identified as crystal-field excitations, occurring in parallel with a quasielastic response, which is a standard type response in 5f-band systems (Krimmel et al. 1996).

On the other hand, electronic structure calculations assumed itinerant character of the 5f states (Sticht and Kübler 1992; Sandratskii et al. 1994; Knöpfle et al. 1996). These calculations are in good agreement both with results of photoelectron spectroscopy experiments showing undoubtedly the 5f emission at E_F (Ejima et al. 1996; Takahashi et al. 1996) and dHvA experiments (Inada et al. 1994), which make the existence of crystal field phenomena questionable. The latter show clearly the presence of heavy-mass states at E_F. Also elastic properties miss any anomaly related to crystal-field effects (Matsui et al. 1994).

UNi_2Al_3 with a somewhat smaller unit cell volume than UPd_2Al_3 orders antiferromagnetically below $T_N = 4.5$ K and the magnetic order coexists again with superconductivity below $T_c \approx 1$ K (Geibel et al. 1991a; Amato et al. 1992b). Metallurgical difficulties exist due to peritectic formation from the melt and UAl_2 (Schank et al. 1994). Therefore the information is not so complete as for the Pd-case. Its magnetic structure has been identified as a longitudinal spin-density wave with propagation vector $(1/2 \pm \tau, 0, 1/2)$, $\tau = 0.110$, with small U-moments $(0.24 \pm 0.10)\ \mu_B$ polarized in the basal plane (Lussier et al. 1994). Neutron studies in magnetic field (Lussier et al. 1997) show that anomalies seen in fields of several Tesla (Modler et al. 1994) have to be attributed to re-population of equivalent magnetic domains. Unlike the previous compound, a strong depression of both T_c and T_N has been found with increasing pressure, but the value $\gamma = 120$ mJ/(mol K^2) remains invariable (Wassilew et al. 1994; Steglich et al. 1996). In the paramagnetic state, the magnetic susceptibility with the field along the basal plane is higher and shows a broad maximum around $T = 120$ K, whereas T_N is seen as a sharp kink (fig. 5.113). For the field along c, a weakly temperature dependent response similar to UPd_2Al_3 was observed (Mihalik et al. 1997; Sato et al. 1997). No metamagnetic transition has been observed on a powder sample in fields up to 35 T (Nakotte et al. 1994d).

Electronic structure calculations show that the 5f–d hybridization is stronger with Ni 3d states than with Pd-4d states, making the 5f states more delocalized in UNi_2Al_3 than in UPd_2Al_3.

Studies of the quasiternary system $U(Pd_{1-x}Ni_x)_2Al_3$ show that T_N first increases with increasing Ni concentration reaching a maximum $T_N = 17$ K at $x = 0.4$, and then decreases steeply towards the Ni end. The superconducting transition decreases fast with increasing doping concentration from both sides and superconductivity is suppressed at less than 5% Pd in UNi_2Al_3 or 12% Ni in UPd_2Al_3 (Schank et al. 1993). As shown by Ghosh et al. (1993), Pd can be substituted by Pt up to 50%, which leads to the decrease of both lattice parameters, whereas T_N stays approximately constant. The absence of superconductivity was proved for 10% Pt down to $T = 0.5$ K. Dilution of the U-sublattice in UPd_2Al_3 by Y, Pr, Gd, Th, or La leads to a depression of T_N (Geibel et al. 1994). 1% of Gd doping in UNi_2Al_3 leads to a complete suppression of T_N (Schank et al. 1994). For higher dopant concentration a weak ferromagnetism is established around $U_{0.5}La_{0.5}Pd_2Al_3$ (Sakon et al. 1995). On the contrary, Th-doping in UPd_2Al_3 and UPd_2Ga_3 (du Plessis et al. 1997; Dalichaouch and Maple 1994) seems to lead to the development of non-Fermi liquid features.

UPd_2Ga_3 melts also incongruently, and crystallizes in a hexagonal superstructure of the $PrNi_2Al_3$ type, denoted as BaB_2Pt_3 type, with a doubled c-parameter (Süllow et al. 1995). It orders antiferromagnetically at $T_N = 13$ K, no superconductivity has

been observed down to 50 mK. It is a moderately heavy-fermion materials with $\gamma = 230$ mJ/(mol K^2). Powder neutron diffraction experiment revealed a magnetic structure equivalent to UPd_2Al_3, i.e. with AF coupled moments in adjacent ferromagnetic U basal plane sheets. The U-moments of $0.50\,\mu_B$ are parallel to the basal plane (Mentink et al. 1996b). A metamagnetic transition was detected in 16 T (Mentink et al. 1996b). The dilution study between UPd_2Al_3 and UPd_2Ga_3 (Süllow et al. 1997d) shows that the $PrNi_2Al_3$ structure is preserved to 80–90% Ga. The superconductivity is lost for low Ga content already (< 25%), whereas the ordering temperature varies only weakly.

In contrast to the U-counterpart, *$NpPd_2Al_3$* (Zwirner et al. 1993) is not superconducting, but magnetic order was detected by ^{237}Np Mössbauer spectroscopy below 38 K. In the ordered region three different magnetic Np sites with different occupation were detected pointing to a modulated magnetic structure. The maximum hyperfine field $\mu_0 H_{hf} = 360$ T points to a Np moment of $1.67\,\mu_B$. The isomer shift value +10 mm/s relative to $NpAl_2$ locates $NpPd_2Al_3$ in the vicinity of the Np^{3+} charge state, and this assumption is consistent with the effective moment $\mu_{eff} = 2.65\,\mu_B$/Np observed in the $\chi(T)$ measurement (Hiess et al. 1997b), $\mu_{eff} = 2.75\,\mu_B$ corresponding to the free-ion $5f^4$ configuration. The same value of the electric field gradient below and above the magnetic phase transition points to Np moments oriented along the c-axis. This fact was confirmed by neutron diffraction experiment (Hiess et al. 1997b), that revealed another phase transition at $T = 25$ K, which can be associated with a drop in resistivity (Seret et al. 1995). An incommensurate structure with a propagation vector $\boldsymbol{q} = (1/3, 1/3, 1/2 - \tau)$, where $\tau = 0.14$, is stable above this temperature, and converts suddenly, but not entirely, to the commensurate structure with $\boldsymbol{q} = (1/3, 1/3, 1/2)$. Thus the two magnetic structures are apparently coexisting at low T (Hiess et al. 1997b). It could not be specified yet whether these different q values belong to different parts of the sample, or if they account for two Fourier components of a single complicated structure. In the latter case an interesting analogy could be found between the twofold character of electronic states in UPd_2Al_3. In $NpPd_2Al_3$ the incommensurate structure persists probably to the lowest temperatures due to the Kondo effect or similar f-moment instability, because a tendency to form an equal-moment structure prevails in regular cases. Thus the occurrence of the commensurate structure with squaring-up features can be felt as due to the more localized part of the 5f spectral density (Hiess et al. 1997b).

An anomaly of the electrical resistivity at $T = 23$ K was interpreted as a magnetic phase transition in *$NpNi_2Al_3$*. *$PuPd_2Al_3$* is probably non-magnetic (Seret et al. 1995).

Similar to other substitutions in the U-sublattice, also Np doping reduces T_N to about 4 K in $U_{0.7}Np_{0.3}Pd_2Al_3$ (Seret et al. 1995). The Np moment deduced from ^{237}Np Mössbauer spectroscopy is for lower Np concentrations smaller than the U-moment (0.2–0.4 μ_B/Np), and not aligned along the c-axis as in $NpPd_2Al_3$. For x larger than 0.3 it increases in magnitude and rotates towards the c-axis.

Other types of UT_2X_3 ternaries preserve smaller or larger randomness in site occupation keeping the isotypism with the $CaCu_5$ structure. A thorough structure analysis of the $U(Ni_{1-x}Ga_x)_5$ system (Zelinsky et al. 1995) shows that the single-phase region of the $CaCu_5$ structure is very broad extending from *UNi_4Ga* to *UNi_2Ga_3*. For the Ni-rich side up to UNi_3Ga_2 no Ga atoms enter the Ni-sites (in the U–Ni basal planes). The remaining sites in Ni–Ga inter-layers are statistically occupied by Ni and Ga atoms. When

decreasing the Ni concentration one does not reach the isotypism with the $PrNi_2Al_3$ structure, but the occupation of both types of sites becomes almost random. Furthermore, the large flexibility of this structure allows a large U deficiency (up to 17%) leading to vacancies in the U-sublattice and to an orthorhombic distortion of the crystal structure. Magnetic characteristics of all compounds show spin-fluctuation features with a typical broad maximum in $\chi(T)$ at 50–60 K and Curie–Weiss law, with an appreciable effective moment (3.3–4.0 μ_B/U) and a large negative Θ_p (typically (−100)–(−200) K), at high temperatures. A cusp in $\chi(T)$ at lower temperatures was found only for $U_{15}Ni_{40}Ga_{45}$ and $U_{16.5}Ni_{40}Ga_{43.5}$ (at $T = 23$ and 26 K, respectively). Because of suppression of these features in field of 0.2 T it is not clear whether they point to an antiferromagnetism, or whether they are a spurious effect. For the latter compound, a weak feature at $T = 30.5$ K was found in specific heat. At low T, the value $\gamma = 110$ mJ/(mol U K^2) can be deduced, and this value is only very weakly dependent on magnetic field.

An analogous structure (and probably also analogous magnetic properties) was found by neutron diffraction for UCu_3Al_2, studied in single-crystal form (Rauchschwalbe et al. 1985). As expected for U-atoms co-ordinated in chains along the c-axis ($d_{U-U} = c$, the values given in table 5.20), the c-axis direction is the hard magnetization direction. In the $C(T)$ curve for $H \| a$ one observes a broad rounded maximum at about 10 K. The high-temperature Curie–Weiss behaviour yields the parameters $\mu_{eff} = 3.35\,\mu_B$, $\Theta_p = -101$ K. The magnetic response in the c-axis direction is much weaker. Although it can be again approximated by Curie–Weiss law with $\mu_{eff} = 3.55\,\mu_B$/U, its asymptotic temperature is −314 K. The suppression of spin fluctuations in magnetic fields (oriented along c) is demonstrated in a magnetization experiment at $T = 4.2$ K, which shows a weak S-shape of $M(H)$ starting below $\mu_0 H = 15$ T. In a field of 35 T, a magnetization corresponding to $\mu = 1.0\,\mu_B$/U is achieved, whereas for $H \| c$ it is only $0.3\,\mu_B$/U. Another single phase sample that can be prepared in the $U(Cu_{1-x}Al_x)_5$ system was $UCu_{3.5}Al_{1.5}$ (Nakotte et al. 1996d). Its susceptibility is similar to UCu_3Al_2, but at low-T a dominating upturn overwhelms the maximum, which develops into a weak shoulder. Both compounds display an increase of C/T with decreasing T below about 6 K, yielding the extrapolated value $\gamma \approx 400$ mJ/(mol K^2) for $T \to 0$. A weak maximum in C/T vs. T appearing at $T = 8$ K brings back the idea about possible magnetic ordering. In $UCu_{3.5}Al_{1.5}$, the increase of C/T is logarithmic below $T = 6$ K. This, together with the resistivity scaling as $\rho \sim T^{2/3}$, led to a discussion in terms of non-Fermi liquid theories (Nakotte et al. 1996d).

5.7. UTX_n compounds

5.7.1. Pnictides UTX_2 (X = P, As, Sb, Bi)

The UTX_2 pnictides with X = P, As, Sb and Bi listed in table 5.21 have been synthesized so far. These compounds crystallize in structure types, which are closely related to structures of their UX_2 counterparts (see fig. 5.117). The majority of members of this group adopts the ZrCuSiAs-type structure with space group P/nmm (Johnson and Jeitschko 1974) which can be considered as a filled ZrSiS structure (Stepien-Damm et al. 1987). An exception is represented by $UCuP_2$ which is isotypic to $SrZnBi_2$ (Gordier et al. 1974). The latter can be described as a filled UGeTe-type (space group I4/mmm). As one can see, similar to the $CaBe_2Ge_2$ and $ThCr_2Si_2$ structures typical for UT_2X_2 compounds also the ZrCuSiAs and $SrZnBi_2$ structure types in which the UTX_2 pnictides are formed consist of

TABLE 5.21

Some basic characteristics of various UTX_2 compounds:

Type of ground state (F – ferromagnetic, AF – antiferromagnetic, P – paramagnetic with temperature dependent susceptibility, SF – spin fluctuator), WTP – paramagnet with weak temperature dependence of susceptibility, μ_U – the U ordered magnetic moment (determined by neutron diffraction at $T = 4.2$ K), $T_{C,N}$ – magnetic ordering temperature, T_{tr} – temperatures of other magnetic phase transitions (in the ordered state), Anis. – easy magnetization direction (determined by neutron diffraction and/or magnetization measurements on single crystals), space group, structure type, a, c – lattice parameters at room temperature.

Compound	Ground state	μ_U (μ_B)	$T_{C,N}$ (K)	T_{tr} (K)	Anis.	Ref.	Space group	Str. type	a (pm)	c (pm)	Ref.
$UCoP_2$							P4/nmm	ZrCuSiAs[a]	381.2	929.3	[1]
$UCuP_2$	F	0.98[b]	75		$\|c$	[2]	I4/mmm	$SrZnBi_2$[c]	380.3	1852.3	[3]
$UFeAs_2$							P4/nmm	ZrCuSiAs	395.8	917.6	[1]
$UCoAs_2$	F		144			[1]	P4/nmm	ZrCuSiAs	395.3	903.7	[1]
$UNiAs_2$	AF		228			[3]	P4/nmm	ZrCuSiAs	395.3	915.0	[3]
	AF[d]	1.85[e]	195			[4]			395.1	913.8	[4]
$UCuAs_2$	F	1.27[b]	133		$\|c$	[2]	P4/nmm	ZrCuSiAs	394.8	953.3	[3]
$UPdAs_2$	AF[f]	1.69[g]	235		$\|c$	[5]	P4/nmm	ZrCuSiAs	398.7	949.3	[5]
$UNiSb_2$	AF		174			[1]	P4/nmm	ZrCuSiAs	431.6	910.4	[1]
$UCuSb_2$	F		102			[1]	P4/nmm	ZrCuSiAs	431.2	964.0	[1]
$UNiBi_2$	AF		166			[1]	P4/nmm	ZrCuSiAs	447.0	907.3	[1]
$UCuBi_2$	AF		51	15		[1]	P4/nmm	ZrCuSiAs	452.6	937.6	[1]
$U_4Cu_4P_7$	AF	1.1, 2.2[h]	146		$\|c$	[6]	I4/mmm	unique	380.3	3495.4	[7]
$UFeSi_2$[i]	WTP					[8]		$CeNiSi_2$			[8]
$UCoSi_2$	SF					[8]		$CeNiSi_2$			[8]
$UNiSi_2$	F	1.16[j]	95–100			[8,9]		$CeNiSi_2$			[8]
$UPtSi_2$	F		85–86			[9,10]		$CeNiSi_2$			[9]
$UCrC_2$	P					[11]					[12]

[a] The tetragonal ZrCuSiAs-type structure (Johnson and Jeitschko 1974) can be also described as a filled ZrSiS type (Stepien-Damm et al. 1987). The term "filled" refers to the intercalation of planes of transition metal atoms into the unit cell of UP_2 (generally UX_2) (Kaczorowski 1992).

[b] Derived from magnetization data in magnetic field along the c-axis (easy magnetization direction).

[c] The tetragonal $SrZnBi_2$-type structure (Gordier et al. 1974) can be described also as a filled UGeTe type.

[d] AFI (antiferromagnetic type I structure) (Fischer et al. 1989).

[e] Magnetic moment at $T = 7.5$ K.

[f] Antiferromagnetic IA type $(++--++--\cdots)$ stacking of ferromagnetic U-moment basal-plane layers).

[g] Magnetic moment at $T = 8.7$ K.

[h] Antiferromagnetic structure consisting of two inequivalent magnetic uranium sites $\mu_{U1} = 1.1\,\mu_B$ and $\mu_{U2} = 2.2\,\mu_B$ with a complex coupling: $+\mu_{U1}, +\mu_{U2}, -\mu_{U2}, -\mu_{U1}, -\mu_{U1}, -\mu_{U2}, +\mu_{U2}, +\mu_{U1}$ within one unit cell of $U_4Cu_4P_7$ (Burlet et al. 1994b).

[i] Defected structure, actual composition was $UFe_{0.8}Si_2$ (Kaczorowski 1996).

[j] Determined from magnetization data obtained on a polycrystal (Kaczorowski 1996).

References:

[1] Kaczorowski (1992)
[2] Kaczorowski et al. (1991a)
[3] Zolnierek et al. (1986)
[4] Fischer et al. (1989)
[5] Murasik et al. (1990)
[6] Kaczorowski et al. (1990)
[7] Noël et al. (1987)
[8] Kaczorowski (1996)
[9] Geibel et al. (1990b)
[10] Sato et al. (1992b)
[11] Vomhof et al. (1993)
[12] Jeitschko and Behrens (1986)

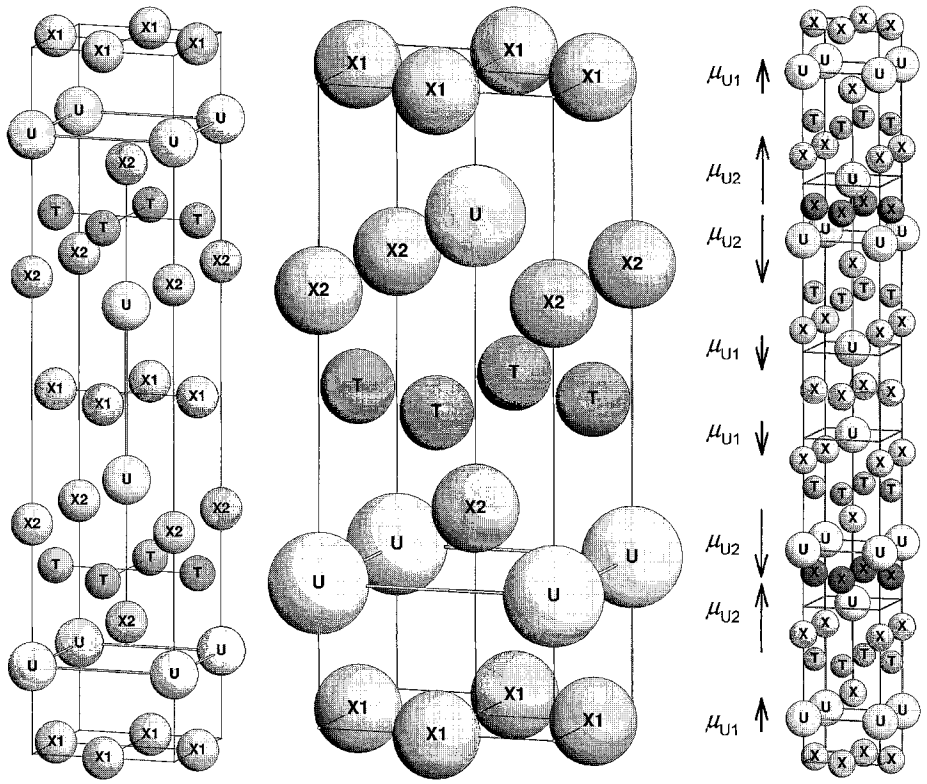

Fig. 5.117. Schematic drawing of crystal structure types adopted by the UTX_2 (X = P, As, Sb, Bi) compounds: (a) $SrZnBi_2$-type, (b) ZrCuSiAs-type, (c) $U_4Cu_4P_7$-type In the latter case also the magnetic structure is visualized.

stacking of (0 0 1) uniatomic layers of U, T and X atoms. Due to intimate structure relation we also include here the compound $U_4Cu_2P_7$ (Noël et al. 1987), which can be considered as a partly defect UTX_2 compound with the composition $UCuP_{1.75}$. The crystal structure of this compound is build up of one $UCuP_2$ unit cell, which has one of the phosphorus sites only half filled, sandwiched between two $UCuAs_2$-type cells mutually inverted to maintain the body centred symmetry. The unit cell of this structure accommodates two formula units and it is considerably elongated along the *c*-axis.

Two 1:1:2 phosphides are known. Only the structural information given in table 5.21 is known for *$UCoP_2$* so far (Kaczorowski 1992). *$UCuP_2$*, the second example is, on the other hand, the most thoroughly studied member of the UTX_2 pnictide family.

$UCuP_2$ orders ferromagnetically below 75 K (Kaczorowski et al. 1991a). Strong lattice softening ($\approx$ 7%) in the vicinity of the magnetic phase transition has been revealed by acoustic measurements of the c_{33} and c_{44} elastic constants (Kaczorowski et al. 1993b). The ordering temperature is not affected by external hydrostatic pressures up to 1 GPa

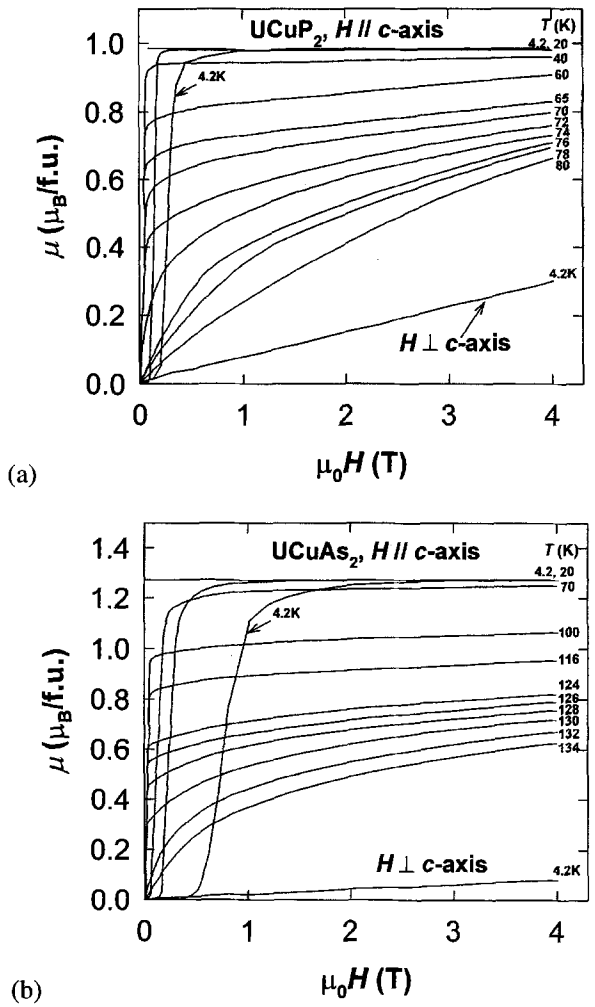

Fig. 5.118. Magnetization curves measured on $UCuP_2$ (a) and $UCuAs_2$ (b) single crystals with field H along the c-axis at different temperatures (at $T = 4.2$ K the relevant first-quadrant hysteresis loop is shown) and perpendicular to the c-axis at $T = 4.2$ K. Data taken from Kaczorowski et al. (1991a).

which points to rather localized uranium moments in this compound (Kaczorowski et al. 1989). This picture is, however, not corroborated by the low value of magnetic entropy of 1.2 J/(mol K), which is much lower than $R \ln 2$ (Böhm et al. 1993). The magnetization in the ordered state is anisotropic with the easy-magnetization direction along the c-axis (see fig. 5.118(a)). By applying the formula (valid for case of uniaxial anisotropy with the easy-magnetization direction along the c-axis):

$$\frac{H}{M_\perp} = \frac{2K_1}{M_s^2} + \frac{2K_2 M_\perp}{M_s^4} \tag{5.16}$$

on the magnetization data at $T = 4.2$ K (H is applied magnetic field, M_s the spontaneous magnetization, $M_\perp$ the magnetization perpendicular to the c-axis), the value of $K_1 = 9 \times 10^5$ J/m^3 has been determined. The second anisotropy constant turned out to be negligible. An anisotropy field of 13 T has been derived (Kaczorowski et al. 1991a). As can be seen from the evolution of magnetization curves in fig. 5.118(a), the character of magnetization process changes substantially around 40 K. Below this temperature considerable hysteresis emerges and the magnetization curves become rectangular which can be attributed to the onset of pinning of narrow domain walls at low temperatures. When considering $UCuP_2$ in terms of localized magnetism one can be surprised by the value of magnetic moment of 0.98 μ_B which can be ascribed to uranium atoms. The fact that this value is so much reduced with respect to the U^{3+} (3.20 μ_B) or U^{4+} (3.27 μ_B) free-ion moments has been attributed by Kaczorowski et al. (1991a) to the effect of splitting of the uranium ground state multiplet due to a crystal field potential. This explanation applies also for the reduced values of the effective moment derived from the anisotropic susceptibility presented in the same work.

The electrical resistivity shows a small negative slope in the paramagnetic range (up to ≈ 600 K) and a precipitous decrease below T_c. The ordering temperature is clearly marked by a Fisher–Langer-type anomaly in the temperature derivative of the resistivity (Kaczorowski et al. 1991a). The high temperature (up to 1000 K) resistivity behaviour has been discussed in terms of the Kondo formula by Korner et al. (1989), and Kaczorowski and Schoenes (1990). Results of optical reflectivity studies of $UCuP_2$ single crystals Fumagalli et al. (1988a, 1988b) classify this material as a semimetal with only a low free carrier contribution (< 0.2 carriers/f.u.) to the optical conductivity. The maximum Kerr rotation of 1.6 degrees at 0.8 eV, has been found by magnetooptic measurements (Fumagalli et al. 1988b). Thermal conductivity studies were performed by Mucha et al. (1992). Also Hall-effect measurements point to a low concentration of carriers (Korner et al. 1989).

Rather scarce information is available in case of *$UFeAs_2$* and *$UCoAs_2$* (Kaczorowski 1992). Both compounds crystallize in the primitive tetragonal ZrCuSiAs-type structure. No magnetic studies were done on the former material, whereas ferromagnetism below 144 K without further specification has been reported in the same source.

Antiferromagnetism in *$UNiAs_2$* below 228 K has been reported by Zolnierek et al. (1986). The position of the susceptibility maximum was considered as the transition temperature whereas the maximum of $\partial(\chi T)/\partial T$ may be located around 220 K by closer inspection of the susceptibility data. Antiferromagnetism of type I (AFI) at low temperatures has been confirmed by means of neutron powder diffraction. The uranium magnetic moment of 1.85 μ_B is parallel to the c-axis and remains almost constant up to 150 K. The magnetic intensity of the (1 0 0) reflection falls abruptly at 195 K which has been claimed to be the Néel temperature of $UNiAs_2$ (Fischer et al. 1989). Nevertheless, the magnetic (1 0 0) intensity presented by Fischer et al. (1989) does not vanish at this temperature, but about 20% of the low-temperature value persists up to about 220 K where it disappears. Further neutron-scattering effort is desirable to confirm the type of magnetic ordering in the temperature interval 195–220 K.

$UCuAs_2$ is a ferromagnet which is in many aspects analogous to $UCuP_2$ (see above). This applies for the magnetization shown in fig. 5.118, the magnetic anisotropy (Kaczorowski et al. 1991a), the negligible response of the ordering temperature to external pressure (Kaczorowski et al. 1989), the specific heat (Böhm et al. 1993), the electrical resistivity (Korner

et al. 1989; Kaczorowski and Schoenes 1990), the optical and magnetooptical properties (Fumagalli et al. 1988a; Schoenes et al. 1989), the thermal conductivity behaviour (Mucha et al. 1992), and finally also to the elastic properties in the critical temperature region for magnetic ordering (Kaczorowski et al. 1993b). Nevertheless, it should be noted that $UCuAs_2$ exhibits a much higher Curie temperature (133 K), spontaneous U magnetic moment (1.27 μ_B), magnetic anisotropy field (70 T in contrast to 13 T in $UCuP_2$) and coercive force at $T = 4.2$ K (≈ 0.9 T) than $UCuAs_2$ and it also has a nearly 3-times larger magnetic entropy (3.1 J/(mol K)).

$UPdAs_2$ orders antiferromagnetically with the IA-type of magnetic structure. It involves the $++--++--\cdots$ type stacking of ferromagnetic basal plane layers consisting of U moments ($\mu_U = 1.69\,\mu_B$ at 8.7 K) oriented parallel to the c-axis. $T_N = 235$ K, above which the intensity of relevant magnetic reflections vanishes. This value coincides well with the temperature of the maximum of $\partial(\chi T)/\partial T$, whereas the susceptibility maximum appears at 240 K (Murasik et al. 1990).

Only very basic information derived from magnetization behaviour of polycrystalline samples is available on antimonides and bismuthides. *$UNiSb_2$*, *$UNiBi_2$* and *$UCuBi_2$* exhibit a maximum in the temperature dependence of the susceptibility at 174, 166 and 51 K, respectively. These temperatures were considered by Kaczorowski (1992) as Néel temperatures. A side susceptibility maximum in case of $UCuBi_2$ observed at 15 K may point to an additional magnetic phase transition between two antiferromagnetic phases.

$UCuSb_2$ similar to pnictide and arsenide analogues orders ferromagnetically below 106 K (Kaczorowski 1992). The type of hysteresis loop at 34 K, although measured on a polycrystal, provides further arguments for the close similarity with $UCuAs_2$.

$U_4Cu_4P_7$ forms in a special crystal structure build up of one $UCuP_2$ unit cell, which has one of its phosphorus sites only half filled, sandwiched between two $UCuAs_2$-type cells mutually inverted to maintain the body centred symmetry. The unit cell of this structure accommodates two formula units and it is considerably elongated in the c-axis (Noël et al. 1987). This compound orders antiferromagnetically below 146 K where the susceptibility along the c-axis shows a maximum (Kaczorowski et al. 1990) and above which the magnetic reflections of neutron diffraction vanish (Burlet et al. 1994b). The magnetic structure consists of ferromagnetic basal-plane layers with magnetic moments oriented along the c-axis. Two types of ferromagnetic sheets, one with uranium magnetic moments $\mu_{U1} = 1.1\,\mu_B$ and the other with $\mu_{U2} = 2.2\,\mu_B$ (at $T = 4.2$ K) are coupled along the c-axis in the scheme $+\mu_{U1}, +\boldsymbol{\mu_{U2}}, -\boldsymbol{\mu_{U2}}, -\mu_{U1}, -\mu_{U1}, -\boldsymbol{\mu_{U2}}, +\boldsymbol{\mu_{U2}}, +\mu_{U1}$ within one unit cell of $U_4Cu_4P_7$ (Burlet et al. 1994b), i.e., magnetic and chemical unit cells are equivalent. The size of uranium magnetic moments reflects two different ionic states of uranium, U^{3+} (2.2 μ_B) and U^{4+} (1.1 μ_B) (Burlet et al. 1994b). The latter moment is considered to be induced, as in the case of UP_2 (Amoretti et al. 1984), and it diminishes with increasing temperature much faster than the Brillouin type temperature variation of the moment on the U^{3+} sites, as can be seen in fig. 5.119 (Burlet et al. 1994b). The susceptibility is strongly anisotropic above 80 K. The c-axis response shows a pronounced maximum located at T_N whereas the basal plane signal mimics the Curie–Weiss behaviour with a negative paramagnetic Curie temperature. Below 80 K, the susceptibility in both direction follows the same temperature dependence which is roughly an extension of the high-temperature basal plane dependence. The anisotropic magnetism in $U_4Cu_4P_7$, especially

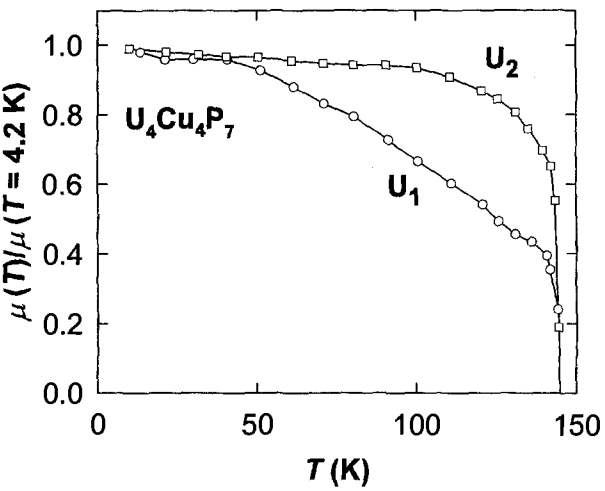

Fig. 5.119. Temperature dependence of the normalized magnetic moments $\mu(T)/\mu(4.2\ \mathrm{K})$ on the two uranium sites U_1 and U_2 in $U_4Cu_4P_7$ (Burlet et al. 1994b).

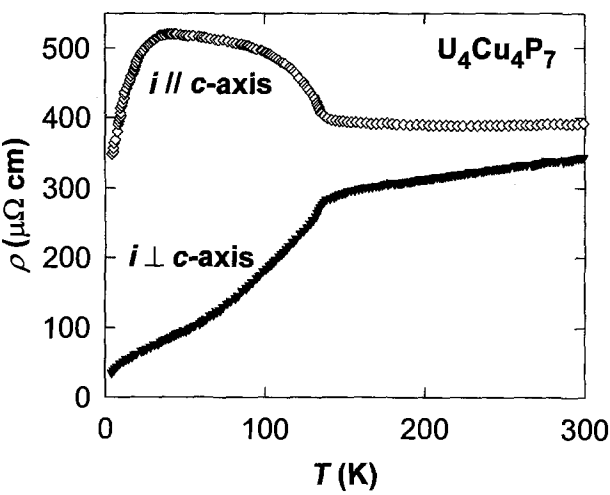

Fig. 5.120. Temperature dependence of the electrical resistivity ρ measured on a $U_4Cu_4P_7$ single crystal with current i parallel and perpendicular to the c-axis. Data from Schoenes et al. (1992b).

the anisotropy in coupling of magnetic moments, is clearly reflected in the electrical resistivity behaviour (Kaczorowski et al. 1990; Schoenes et al. 1992b), which is shown in fig. 5.120. The c-axis resistivity is nearly constant in the temperature interval between 160 and 300 K. It starts to increase with cooling below 160 K. This upturn becomes pronounced especially below T_N, yielding a sharp minimum of the temperature derivative $\partial\rho/\partial T$ at 134 K. The resistivity reaches a maximum ($\approx 550\ \mu\Omega\,\mathrm{cm}$) around 50 K and than it falls

rapidly to 340 μΩ cm at $T = 4.2$ K (Burlet et al. 1994b). On the contrary, for current in the basal plane, an increasing resistivity with increasing temperature over the whole temperature range up to 1000 K has been observed (Schoenes et al. 1992b). The anomaly at 136 K (which is somewhat lower than T_N) in the form of a knee, where the temperature derivative $\partial\rho/\partial T$ shows a sharp maximum, mimics the behaviour of a ferromagnet. Such anisotropic resistivity is characteristic for a certain class of uranium antiferromagnets which consist of ferromagnetic layers coupled antiferromagnetically in the direction perpendicular to these layers.

5.7.2. *Other UTX_2 compounds*

Several $UTSi_2$ compounds have been synthesized so far, all adopting the orthorhombic $CeNiSi_2$-type crystal structure (for lattice parameters see table 5.21). Incongruent melting prevents easy crystal growth. Therefore only polycrystalline compounds $UTSi_2$ (T = Fe, Co and Ni) were studied by magnetization, magnetic susceptibility electrical resistivity and magnetoresistivity measurements (Kaczorowski 1996). *$UFe_{0.8}Si_2$* is a paramagnet down to lowest temperatures with weakly temperature dependent susceptibility, especially at higher temperatures, *$UCoSi_2$* resembles spin fluctuation systems, whereas *$UNiSi_2$* orders ferromagnetically below 95–100 K, which has been observed also by Geibel et al. (1990b), with an ordered magnetic moment of $1.16\,\mu_B$/f.u. However, we should note that the negative derivative of the resistivity above T_C used as an argument for interpretation of this material in terms of the Kondo lattice model is a rather common feature of numerous uranium intermetallics. This evolution of magnetic properties throughout the series reflects the weakening of the 5f–3d hybridization in this respect.

Geibel et al. (1990b) and Sato et al. (1992b) have shown that *$UPtSi_2$* orders ferromagnetically. The electrical resistivity has quite a typical temperature dependence for ferromagnets with narrow 5f-band at E_F. It is almost flat above T_C followed by a dramatic decrease with decreasing temperature below T_C. The magnetization curve measured at 4.2 K reveals a rather small spontaneous moment of about 0.6 μ_B/f.u. and no saturation in fields up to 8 T. Further research of $UTSi_2$ and a possible extension to the germanides is desirable when compared with their rare-earth analogs (Pelizzone et al. 1982; François et al. 1987; Malaman et al. 1990).

5.7.3. *$UTGa_5$ compounds*

These compounds crystallize in the tetragonal $HoCoGa_5$-type structure (P4/mmm – D^1_{4h}). As seen in fig. 5.121, this structure is build by combining structural units of the $AuCu_3$ and $PtHg_2$ types. Structural parameters are given by Grin et al. (1986), and Noguchi and Okuda (1992). Magnetic properties of the whole series were first studied by Hiebl et al. (1987) followed by more specific studies of some individual compounds (Noguchi and Okuda 1992, 1993; Sechovsky et al. 1992d). Due to metallurgical difficulties, all measurements were performed only on polycrystals. The available data are concentrated in table 5.22.

Only *$UNiGa_5$*, *$UPdGa_5$* and *$UPtGa_5$*, the compounds with the end members of each transition-metal series, show anomalies in the temperature dependence of susceptibility. These may be considered as marking the onset of antiferromagnetism below 85.5, 50 and

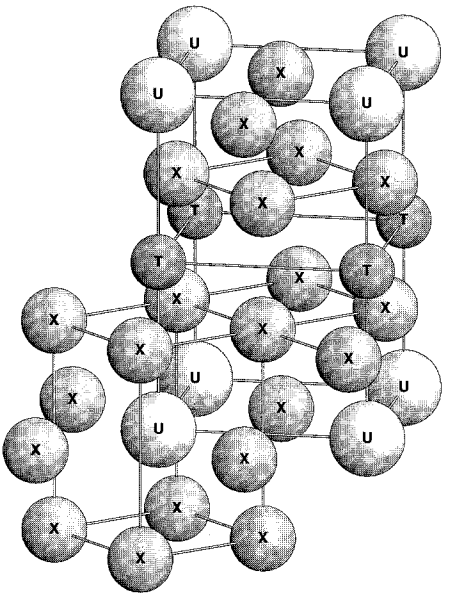

Fig. 5.121. Schematic drawing of the tetragonal crystal structure of $UTGa_5$ compounds (from Kojima et al. (1992b)).

26 K, respectively. This picture is corroborated for the former two compounds by observed anomalies in the temperature dependence of the specific heat around the proposed T_N (Sechovsky et al. 1992d; Noguchi and Okuda 1992, 1993). For $UNiGa_5$, an additional argument is provided by an anomaly in the ρ vs. T curve characteristic for an antiferromagnetic transition (Noguchi and Okuda 1992, 1993). The susceptibility above T_N may be roughly approximated by a modified Curie–Weiss law with very large negative values of $\Theta_p = -677$ K, -316 K, and -236 K, respectively. Although these values seem to be physically unreasonable, one may tentatively argue that the decreasing tendency of the sequence reflects the expected reduced 5f-ligand hybridization, which nevertheless remains very strong. Neutron powder diffraction studies of $UPdGa_5$ at 9 K failed to detect any considerable magnetic intensity, which has led to the conclusion of uranium magnetic moments being smaller than 0.5 μ_B (Sechovsky et al. 1992d). Note that the inter-uranium spacing in these compounds ranges from 423 to 434 pm, which practically excludes the role of direct 5f–5f overlap in the delocalization of 5f magnetic moments. This means that we probably deal with antiferromagnetic ordering of strongly reduced magnetic moments as a consequence of the strong hybridization of the uranium 5f electrons states with valence states of the ligands. Close similarity of the crystal structure and magnetic properties of these antiferromagnets with the behaviour of UGa_3 (Buschow and van Daal 1972) points to the important role of the hybridization with the Ga 4p states. The considerable effect of the 5f–d (transition metal) hybridization is, on the other hand, manifest by the property development with respect to the nature of the transition metal component in the frame of Koelling's picture (Koelling et al. 1985).

TABLE 5.22

Some basic characteristics of $UTGa_5$ compounds:
γ – coefficient of the electronic specific heat, type of ground state (AF – antiferromagnetic, PP – Pauli paramagnetic, SF – spin fluctuator), $T_{C,N}$ – magnetic ordering temperature, T_{tr} – temperatures of other magnetic phase transitions (in the ordered state), a, c – lattice parameters at room temperature.

Compound	γ (mJ/(mol K^2))	Ground state	$T_{C,N}$ (K)	T_{tr} (K)	Ref.	a (pm)	c (pm)	Ref.
$UFeGa_5$					[1]	426.1	673.4	[2]
$UCoGa_5$		PP			[1]	423.57	672.78	[2]
	10	PP			[3,4]	423.3	672.3	[3]
$UNiGa_5$		AF	87		[1]	423.7	678.5	[2]
	30	AF	85.5	40	[3,4]	423.1	677.4	[3]
$URuGa_5$	37	PP			[5,1]	431.2	680.0	[2]
U_2RuGa_8	57	SF			[5]	428.8	1106.2	[5]
$URhGa_5$					[1]	429.9	680.0	[2]
$UPdGa_5$		AF	33		[1]	432.1	686.2	[2]
	42–49.6	AF	50	30	[6]			
$UOsGa_5$					[1]	431.8	681.3	[2]
$UIrGa_5$		PP			[1]	431.7	674.5	[2]
	6.8	PP			[6]			
$UPtGa_5$		AF	26		[1]	434.1	681.3	[2]

References:

[1] Hiebl et al. (1987)
[2] Grin et al. (1986)
[3] Kojima et al. (1992b)
[4] Noguchi and Okuda (1993)
[5] Schonert et al. (1995)
[6] Sechovsky et al. (1992d)

The remaining $UTGa_5$ compounds are weak paramagnets with an only slightly temperature dependent susceptibility in a wide temperature region between 2 and 100 K (Hiebl et al. 1987). The very broad bump on the $\chi(T)$ curve around 600 K observed for the compounds with Co, Rh and Ir is reminiscent of spin fluctuators with a characteristic temperature of several hundred K. No feature is observed in the temperature dependence of susceptibility of the Fe, Ru and Os containing counterparts although they exhibit approximately twice as high χ values (around 2×10^{-8} m^3/mol) with respect to the previous triad of compounds. From table 5.22 one can see that the antiferromagnets exhibit somewhat enhanced γ-values ($\geqslant$ 30 mJ/(mol K^2)), in contrast to the values measured for the paramagnets ($\leqslant$ 10 mJ/(mol K^2)). These values are for uranium intermetallics unexpectedly reduced, which is most probably due to the fact that a substantial portion of the 5f states has been removed from E_F as a result of an extended 5f-ligand hybridization.

Using measurements of the susceptibility, specific heat and resistivity, Noguchi and Okuda (1993) studied the evolution of magnetism between the antiferromagnet $UNiGa_5$ and the paramagnet $UCoGa_5$. The Néel temperature becomes rapidly reduced when Co is substituted for Ni in $U(Ni_{1-x}Co_x)Ga_5$ and any sign of antiferromagnetism is practically lost for $x > 0.3$. The critical concentration of $x \approx 0.3$ is confirmed by the observed maximum in the concentration dependencies of the low-temperature susceptibility and the Sommerfeld coefficient (Noguchi and Okuda 1993).

Due to their structural similarity with $UTGa_5$ compounds, we include here also a note on U_2TGa_8 compounds. Structural information on these materials has been given by Grin et al. (1988) and Daams et al. (1991). In the former paper also some basic magnetic data can be found. Susceptibility and specific-heat measurements both on $URuGa_5$ and U_2RuGa_8 were presented by Schonert et al. (1995). Both compounds are weak paramagnets, however the latter one exhibits a clear but broad maximum around 40 K, which may be signs of spin-fluctuation phenomena. Consistently, the γ-value of U_2RuGa_8 is considerably enhanced (57 mJ/(mol K^2)) with respect to the 1-1-5 analogue (37 mJ/(mol K^2)).

5.7.4. Other UTX_x compounds

$UNiGa_3$ (table 5.23) crystallizes in the $BaNiSn_3$-type type structure of the space group I4mm (Zolnierek and Mulak 1995). This material exhibits a sharp peak in the χ vs. T curve at 34 K. This peak and a resistivity maximum at 37 K were attributed to the onset of antiferromagnetic ordering (Zolnierek and Szulc 1992; Zolnierek and Zaleski 1992). Takabatake et al. (1993) determined the Néel temperature as 39 K. A neutron diffraction investigation (Zolnierek and Mulak 1995) revealed a simple antiferromagnetic structure of type I. Free-powder magnetization data collected up to 35 T show the onset of a metamagnetic transition above 5 T, but poor saturation even in the highest applied fields. The magnetization at 35 T amounts to 1.06 μ_B/f.u. The law of approach to saturation would yield a saturation magnetization of roughly 1.3 μ_B/f.u., a value comparable to that of UNiGa (see section 5.1.1). The high field magnetization behaviour resembles materials with a non-collinear magnetic structure.

$UNiGa_4$ (table 5.23) has been synthesized and studied in polycrystalline form by Takabatake et al. (1993). The crystal structure, however, has not been resolved so far. The susceptibility shows a huge and quite narrow peak around 42 K, which seems to be a

TABLE 5.23

Some basic characteristics of some UTX_n compounds:

Type of ground state (AF – antiferromagnetic, μ_U – the U ordered magnetic moment (determined by neutron diffraction at 4.2 K, T_N – magnetic ordering temperature, Anis. – easy magnetization direction (determined by neutron diffraction and/or magnetization measurements of single crystals), space group, structure type, a, c – lattice parameters at room temperature.

Compound	Magn. order	T_N (K)	μ_U (μ_B)	Anis.	Ref.	Structure type	Space group	a (pm)	c (pm)	Ref.
$UNiGa_3$	AF[a]	37	1.66	$\|c$	[1]	$BaAl_4$	I/4mm	414.3	979.1	[2]
	AF	39	(1.06)[b]		[3]	$BaAl_4$	I/4mm	415.3	978.6	[3]
$UNiGa_4$	AF	42	(0.73)[b]		[3]	unknown				[3]

[a] (AFI) Antiferromagnetic structure type I.

[b] Measured in $\mu_0 H = 30$ T on a free powder sample (Takabatake et al. 1993).

References:

[1] Zolnierek and Mulak (1995)
[2] Zolnierek and Szulc (1992); Zolnierek and Zaleski (1992)
[3] Takabatake et al. (1993)

clear indication of antiferromagnetism. Also the metamagnetic transition measured on a free-powder sample around about 3 K corroborates the conclusion on antiferromagnetism. The hysteresis of this transition is very large (amounting approximately 5 T). The linear dependence of the magnetization, with a considerable slope above the transition up to 35 T, and the relatively low magnetization value at the ultimate field ($0.73\,\mu_B$/f.u.) strongly suggest that the antiferromagnetic coupling is not destroyed even at 35 T and an additional metamagnetic transition yielding the final alignment of U moments can be expected at even higher fields.

5.8. UT_2X compounds

The large number of compounds of the UT_2X stoichiometry, X = In, Si, Ge, Sn, Pb, and Sb, comprises several structure types offering a large variety of structural characteristics. Those with X = In and some with X = Sn and X = Pb are formed in the cubic Heusler type structure, which shows, though, a proclivity to an orthorhombic distortion or to a structural disorder (to the CsCl structure type). In several cubic compounds a tendency to form a deficient structure $UT_{2-d}X$ has been described.

Heusler 1–2–1 compounds are related to the 1–1–1 compounds of the Heusler type. Their crystal structure of the $MnCu_2Al$ type (space group $Fm\bar{3}m$) is characterized by filling the vacancies in the Heusler 1–1–1 compounds by extra transition metal atoms (fig. 5.122). This affects strongly the electronic properties because of better conditions for 5f–d hybridization, and although the U–U spacing becomes larger than 450 pm, the majority of the compounds are paramagnets. An important role is definitely played by the number of transition-metal ligands of U atoms, which is eight in this structure. Essential information

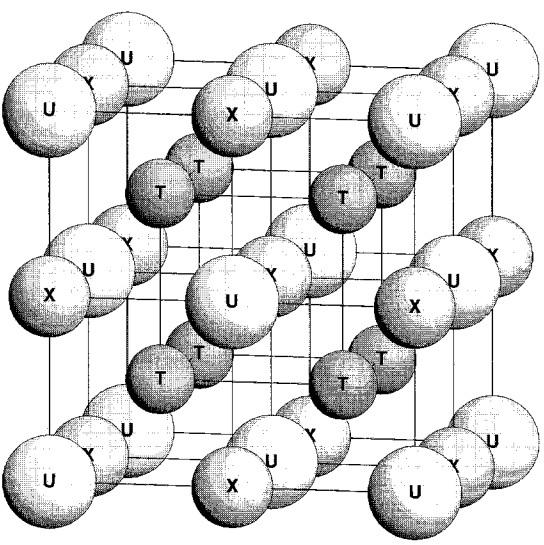

Fig. 5.122. Schematic drawing of the $MnCu_2Al$-type crystal structure.

TABLE 5.24

Some basic characteristics of UT_2X compounds:
a, b, c – lattice parameters at room temperature, type of ground state (AF – antiferromagnetic, SF – spin fluctuator, WP – weak paramagnet), T_N – magnetic ordering temperature, γ – coefficient of the electronic specific heat.

Compound	a (pm)	b (pm)	c (pm)	Type	T_N (K)	γ (mJ/mol K^2))	Ref.
UNi_2Sn	645.9			WP	–	50	[1–3]
UNi_2In	650.1			WP	–	45	[3]
UPd_2In	680.4			AF	22	200	[4]
UAu_2In	696.9			AF	61	60	[5,6]
$ThAu_2In$	707.0					2	[5]
UPd_2Pb	685			AF	35	98	[7]
$ThPd_2Pb$	688						[7]
$UPd_{1.85}Sn$	677.1			AF(SG)	28	55	[8]
UPd_2Sn	997.9	458.8	689.2	SF	–	80	[9,10]
UCo_2Sn	940.3	432.4	661.1	WP			[11,12]
URh_2Sn	979.2	437.5	696.4	SF			[11,12]
UAu_2Sn[a]	696.3			SF		220	[6]
	700.2						[13]
UAu_2Sn[b]	470.4		920.8	AF	13.8	290	[13]
UCu_2Sn	445.9		871.2	AF	16.6	60	[14]
UPt_2Sn	455.0		902.1	AF	60	17	[14,6]
	455.5		899				
UNi_2Ga	420.6		838.5	WP		62	[15]
UAu_2Al	768.3	723.9	537.0	AF	25	102	[14]
UPd_2Ga	731.5	704.1	541.2	AF	39	172	[15]

[a] Cubic modification.
[b] Hexagonal modification.

References:

[1] Endstra et al. (1990c)
[2] Drost et al. (1993)
[3] Takabatake et al. (1990b)
[4] Takabatake et al. (1989)
[5] Besnus et al. (1988)
[6] Zolnierek (1988)
[7] Seaman et al. (1996)
[8] Süllow et al. (1997c)
[9] Marezio et al. (1988)
[10] Rossel et al. (1986)
[11] Gravereau et al. (1994b)
[12] Mirambet et al. (1995b)
[13] Maeda et al. (1996)
[14] Takabatake et al. (1992b)
[15] Takabatake et al. (1993)

regarding structural and magnetic characteristics, and the electronic-specific-heat coefficient γ is cumulated in table 5.24.

One of the examples documenting this tendency is *UNi_2Sn*, which is non-magnetic, although the compounds UNiSn and U_2Ni_2Sn are magnetically ordered. The detailed comparison (Bourée et al. 1994) shows that although the minimum U–Ni distance is not much different with respect to UNi_2Sn, they have only four and six nearest Ni ligands, respectively. UNi_2Sn can be characterized as a weak paramagnet with $\chi_{300\,K} = 1.6 \times 10^{-8}$ m^3/mol (Endstra et al. 1990c). Between 210 and 240 K a structural phase transition into an orthorhombic structure (Drost et al. 1993) occurs, which is accompanied by an increase of χ to about 3×10^{-8} m^3/mol (fig. 5.123). The transition leads also to an

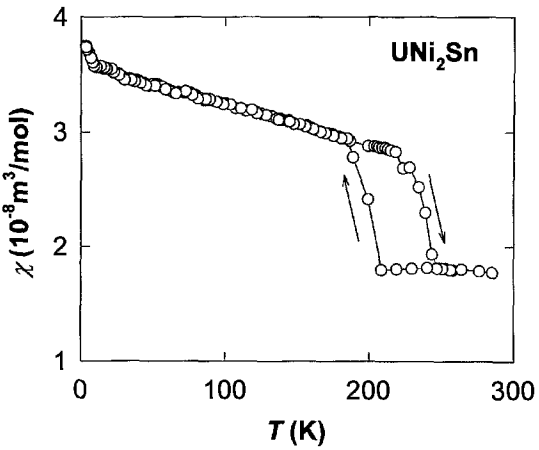

Fig. 5.123. Temperature dependence of the magnetic susceptibility χ of UNi_2Sn. After Endstra et al. (1990c).

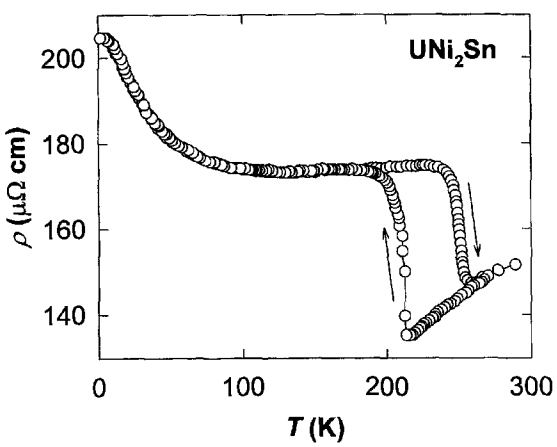

Fig. 5.124. Temperature dependence of the electrical resistivity ρ of UNi_2Sn. After Endstra et al. (1990c).

increase of the resistivity, which shows a rather flat behaviour both above and below the transition and has even an increasing tendency below $T = 100$ K (fig. 5.124). As seen later, this type of resistivity behaviour is very common in this group of compounds, and could be attributed, e.g., to atomic disorder. However, the conclusions of neutron diffraction (Drost et al. 1993) point more to a Ni deficiency (5–10%) as the origin of the disorder, being compensated by UNi_4Sn formation, leaving vacancies on the Ni sites. A single crystal study yields the stoichiometry $UNi_{1.87}Sn$ (Waerenborgh et al. 1996). An interesting information on the dynamics of the structural phase transition is provided by ^{119}Sn Mössbauer spectroscopy (Mulder et al. 1996). An extraordinary broadening of the spectral line width in the transition region suggests a thermally excited domain walls motion on the characteristic Mössbauer time scale.

UNi_2In is reported to exist in the cubic Heusler structure only in as cast form, whereas annealing at 980°C leads to decomposition. It is a weak paramagnet with temperature independent $\chi \approx 1.3 \times 10^{-8}$ m^3/mol and moderate $\gamma = 45$ mJ/(mol K^2) (Takabatake et al. 1990b).

UPd_2In exhibits heavy fermion behaviour ($\gamma = 200$ mJ/(mol K^2)) and antiferromagnetic ordering below $T_N = 22$ K (Takabatake et al. 1989). Similar to UNi_2Sn, it undergoes a structural phase transition of the first order type near $T = 180$ K. The $\rho(T)$ dependence is rather flat, increasing from $\rho_{300\,K} \approx 140$ μΩ cm to 165 μΩ cm in the maximum corresponding to T_N. On the dominating negative slope one can distinguish a small step at the structural transition. Compared to the weak resistance effect, the impact on the thermoelectric power is much more dramatic, pointing to a Fermi surface reconstruction. A noticeable step occurs also in $\chi(T)$ with decreasing T at the transition. The $\chi(T)$ data, which follow the Curie–Weiss law for both crystal structures. The effective moments and paramagnetic Curie temperatures are estimated as $3.78\,\mu_B$/U, −307 K, and $3.16\,\mu_B$/U and −111 K above and below the structural transition, respectively. The maximum in $\chi(T)$ at about 20 K confirms the AF ground state, which can be affected by a field. For $\mu_0 H = 26$ T a spin-flop transition was observed (Takabatake et al. 1989).

The maximum in the $\rho(T)$ curve disappears at a hydrostatic pressure 3 kbar, which was interpreted as a loss of magnetic ordering (Kurisu et al. 1992). Furthermore, the pressure leads apparently to a decrease of the critical temperature of the structural phase transition. At the beginning up to 3 kbar the pressure derivative is −4 K/kbar, but it is much smaller in higher pressures, −0.7 K/kbar. The coincidence of the disappearance of the magnetic ordering with the abrupt change of the pressure derivative of the structural phase transition can be taken as indication of close relation of the 5f magnetism and the structural properties.

No structural transition appears in *UAu_2In*. It orders antiferromagnetically below $T_N = 61$ K. $\chi(T)$ follows CW law with parameters $\mu_{eff} = 3.52\,\mu_B$/U and $\Theta_p = -270$ K. Specific heat experiments yield the moderate value of $\gamma = 60$ mJ/(mol K^2) (Besnus et al. 1988; Zolnierek 1988). $\rho(T)$ shows a maximum at T_N and a negative slope at higher temperatures (Besnus et al. 1988; Zolnierek 1988). When the U-sublattice is diluted by Th or Y, the values of C/T per U atom increase monotonously up to the lowest U concentration examined. Thus, the value $C/T = 720$ mJ/(mol U K^2) is reported for $U_{0.1}Y_{0.9}Au_2In$ (Besnus et al. 1988). The maximum in $\chi(T)$ shifts rapidly to lower temperatures with U-lattice dilution and in the 30–40% Y range one obtains only a plateau instead of maximum, and no anomaly related to a magnetic phase transition is seen in the specific heat. X-ray diffraction displays no additional reflections belonging to the Heusler structure (claimed to be weak even for the pure UAu_2In) in this concentration range. This means that the system develops into a disordered structure (CsCl) with increasing substitutional disorder. In the dilution limit (10% U) the system still behaves in a Curie–Weiss way, preserving the value of the U effective moment and reducing markedly only the absolute value of Θ_p to −84 K. No magnetic ordering has been detected down to 0.15 K (Besnus et al. 1988).

UPd_2Pb is antiferromagnetic as deduced from the sharp cusp in $\chi(T)$ at $T_N = 35$ K (Seaman et al. 1996). In the paramagnetic range, $\chi(T)$ follows a modified Curie–Weiss law with parameters $\mu_{eff} = 2.77\,\mu_B$/U, $\Theta_p = -50$ K, and $\chi_0 \approx 8 \times 10^{-9}$ m^3/mol. Low-T specific heat data yield $\gamma = 98$ mJ/(mol K^2). The electrical resistivity is nearly constant

at high temperatures but decreases below $T = 100$ K. T_N is manifest as a small kink at 35 K.

UPd_2Sn has probably the orthorhombically distorted Heusler structure (space group Pnma), similarly to UNi_2Sn. But other *b.c.c.*-related structures could not entirely be excluded, because the X-ray powder diffraction experiment was not able to determine the occurrence of a possible disorder in occupation of the Pd and Sn lattice sites (Marezio et al. 1988). The $\chi(T)$ data follow the Curie–Weiss law with the parameters $\mu_{eff} = 3.18\,\mu_B$/U and $\Theta_p = -77$ K. Below $T = 10$ K, the $\chi(T)$ curve tends to saturate to $\chi_0 \approx 18 \times 10^{-8}$ m^3/mol. The $\rho(T)$ curve nearly saturates above $T = 100$ K. At low temperatures, it follows approximately a quadratic temperature dependence, all pointing to the influence of spin fluctuations. The specific heat in the C/T vs. T^2 representation is linear below $T = 5$ K only, where it yields $\gamma = 80$ mJ/(mol K^2). Subtraction of the specific heat data of isostructural $ThPd_2Sn$ showed that the non-linearity can be interpreted as being due to an extra contribution of approximately Schottky type with maximum at $T \approx 10$ K (Rossel et al. 1986). The cubic Heusler structure is, however, preserved for the Pd deficient $UPd_{1.85}Sn$, which undergoes magnetic ordering at $T = 28$ K (Süllow et al. 1997c). Below a maximum in $\chi(T)$ found at this temperature a pronounced difference between data obtained in the field-cooled and zero-field-cooled regime develops, which points to an influence of atomic disorder producing a strong spin disorder. This is reflected in an anomalous C/T vs. T dependence (yielding $\gamma = 41$ mJ/(mol K^2)) and in the μ^+SR data, showing only an increase of the relaxation rate without any spontaneous precession in the ordered state.

The effect of spin fluctuations can be traced out also in *UCo_2Sn* and *URh_2Sn*, which show the same type of orthorhombic distortion as, e.g., UPd_2Sn (Gravereau et al. 1994b). Although the distortion leads to a shortening of certain U–U links, they are still well above the Hill limit (the smallest value is d_{U-U} in UCo_2Sn, 378.1 pm), and it seems obvious that the situation of the 5f band is predominantly determined by the 5f–d hybridization. As noticed by Mirambet et al. (1995b), d_{U-Co} in UCo_2Sn is even smaller than in the very compact cubic Laves phase UCo_2. This compound was classified as a weak paramagnet with $\chi \approx 3 \times 10^{-8}$ m^3/mol. On the other hand, URh_2Sn shows a Curie–Weiss behaviour above $T \approx 100$ K, with $\mu_{eff} = 3.12\,\mu_B$ and $\Theta_p = -200$ K. At low T it saturates to $\chi_0 \approx 13 \times 10^{-8}$ m^3/mol. Also the $\rho(T)$ dependence shows spin fluctuation features, saturation above $T = 100$ K, and a T^2 dependence with a large slope at low temperatures.

UAu_2Sn has two allotropic modifications. It was originally reported as a cubic Heusler phase (Zolnierek 1988), but annealing at $T = 800$°C led to the hexagonal structure of the $ZrPt_2Al$ type (fig. 5.125). In this structure, the U atoms form a triangular lattice with an U–U spacing equal to the lattice parameter a given in table 5.24. The structural phase transition was found at $T = 820$°C (Maeda et al. 1996). The hexagonal modification is antiferromagnetic. The Néel temperature shows up as a sharp peak in $\chi(T)$ at $T = 13.8$ K (fig. 5.126). The Curie–Weiss law is obeyed in the paramagnetic range down to $T = 30$ K, with $\mu_{eff} = 3.15\,\mu_B$/f.u. and $\Theta_p = -101$ K. The cubic phase has practically identical μ_{eff}, but Θ_p is much more negative (-224 K). At low temperatures, it exhibits a weak broad maximum at $T = 17$ K and finally a weak upturn reaching $\chi \approx 6 \times 10^{-8}$ m^3/mol. Thus it can be classified as spin fluctuator. The similarly flat $\rho(T)$ curves for both modifications (fig. 5.127) were attributed to a crystallographic disorder of the Sn and Au atoms, which

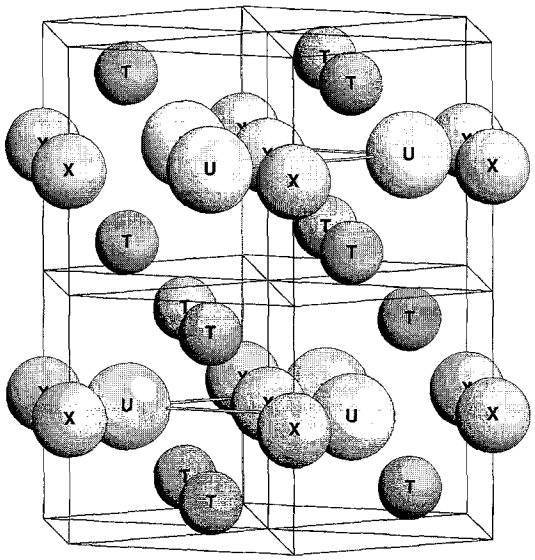

Fig. 5.125. Schematic drawing of the $ZrPt_2Al$-type crystal structure.

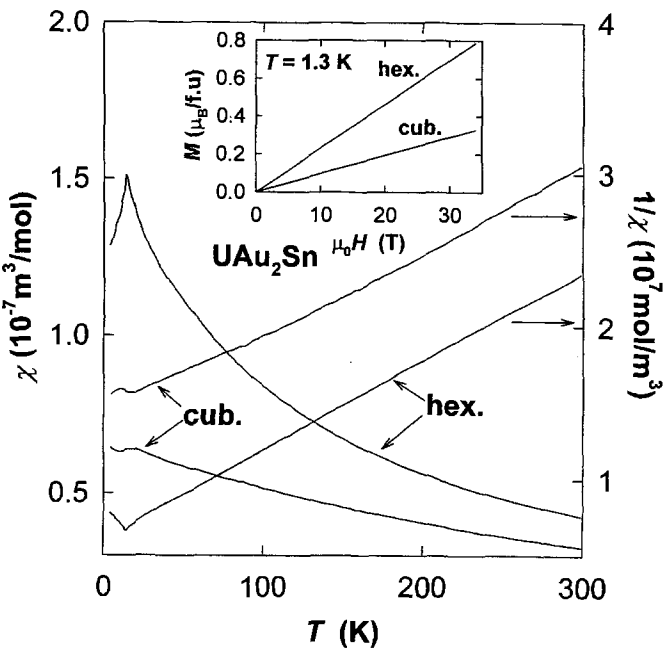

Fig. 5.126. Temperature dependence of the susceptibility χ and inverse susceptibility $1/\chi$ of both modifications of UAu_2Sn. The inset shows the field dependence of the magnetization M at low temperatures. After Maeda et al. (1995).

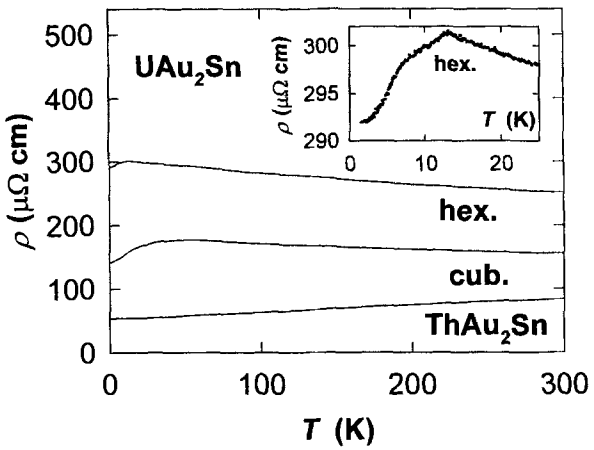

Fig. 5.127. Temperature dependence of the electrical resistivity ρ of both modifications of UAu_2Sn together with that of $ThAu_2Sn$. The inset shows the detail for the hexagonal modification (after Maeda et al. (1995)).

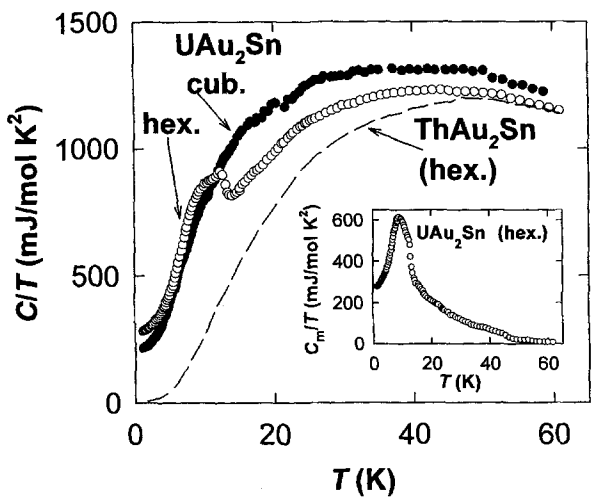

Fig. 5.128. Temperature dependence of the specific heat (C/T vs. T plot) of both modifications of UAu_2Sn together with that of $ThAu_2Sn$ (after Maeda et al. (1995)). The inset shows in an expanded scale the estimated magnetic contribution C_m/T for the hexagonal modification.

is supported by a similar feature in $ThAu_2Sn$. For both modifications, the $\rho(T)$ dependence in UAu_2Sn has a weak negative slope at high temperatures. The cubic modification has generally lower ρ and its highest value (180 $\mu\Omega$ cm) is reached in a broad maximum centred around $T \approx 40$ K. The hexagonal one has a sharper maximum at temperature corresponding to T_N, and another anomaly appears at $T = 7$ K. A counterpart of this feature is seen also in the low temperature specific heat (fig. 5.128). It marks definitely another phase

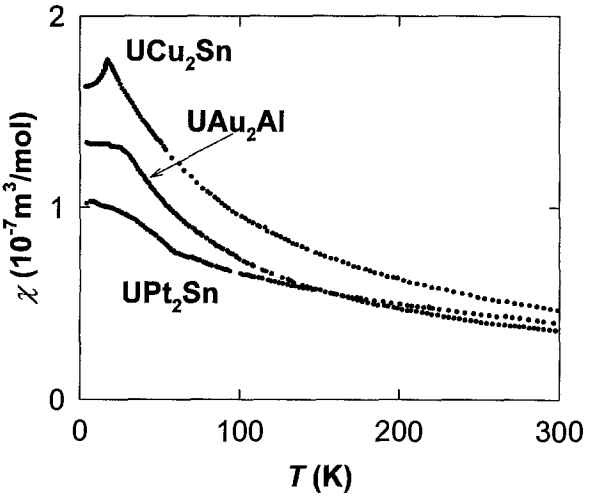

Fig. 5.129. Temperature dependence of the magnetic susceptibility χ of UCu_2Sn, UAu_2Al, UPt_2Sn (after Takabatake et al. (1992b)).

transition, related perhaps to a change of the magnetic structure. A noteworthy feature of the specific heat is also the high C/T value 290 mJ/(mol K^2) seen still at $T = 1.3$ K, but a possible magnetic contribution due to frustration of the U magnetic moments (which may be induced by the crystallographic disorder) or due to short range order cannot be excluded. The cubic modification has a somewhat lower value $C/T = 220$ mJ/(mol K^2). Structural considerations, especially the reduction of the number of nearest Au ligands and the larger U–Au distance in the hexagonal modification, can explain that the cubic modification is less magnetic due to the stronger 5f–d hybridization (Izawa et al. 1996).

The hexagonal structure of the $ZrPt_2Al$ type is adopted also by several other UT_2X intermetallics. *UCu_2Sn* is antiferromagnet with T_N showing up as a pronounced cusp at $T = 16.6$ K (fig. 5.129). The Curie–Weiss behaviour of the susceptibility in the paramagnetic range yields $\mu_{eff} = 3.36\,\mu_B$/U and $\Theta_p = -89$ K (Takabatake et al. 1992b). The high-field magnetization experiment displays a spin flop transition at 23.5 T. The $\rho(T)$ curve shown in fig. 5.130 is nearly constant between 100 and 300 K, reaching 300 μΩ cm. The increasing tendency at lower temperatures leads to a very pronounced sharp peak related to T_N ($\rho_{max} \approx 400$ μΩ cm), which can be attributed to a substantial Fermi surface gapping, and finally $\rho(T)$ decreases with a high slope. The specific heat (fig. 5.131) displays a sharp λ-type anomaly at T_N. The magnetic entropy was estimated as $R \ln 2$ (Takabatake et al. 1992b). $\gamma = 60$ mJ/(mol K^2) was deduced from the low-temperature behaviour. A high-pressure resistivity study showed that the gap properties do not change with pressure, whereas T_N is slightly depressed by −0.096 K/kbar (Kurisu et al. 1993, 1995).

UPt_2Sn (figs 5.129–5.131) shows a Curie–Weiss behaviour at high temperatures with $\mu_{eff} = 3.61\,\mu_B$ and $\Theta_p = -220$ K (Zolnierek 1988; Takabatake et al. 1992b). At $T = 60$ K, the $\chi(T)$ curve turns up abruptly and finally saturates at a low-temperature value $\chi_0 = 10.2 \times 10^{-8}$ m^3/mol. The transition at 60 K is manifest also in the specific heat

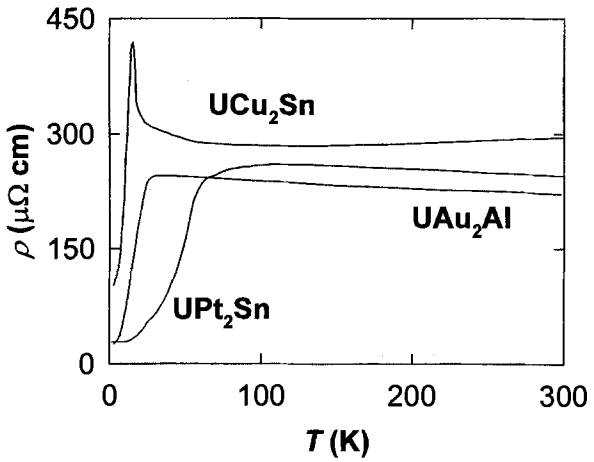

Fig. 5.130. Temperature dependence of the electrical resistivity ρ of UCu_2Sn, UAu_2Al, UPt_2Sn (after Takabatake et al. (1992b)).

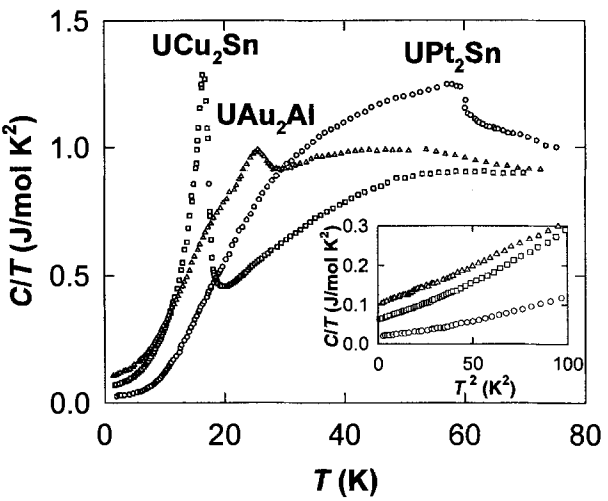

Fig. 5.131. Temperature dependence of the specific heat (C/T vs. T plot) of UCu_2Sn, UAu_2Al, UPt_2Sn (after Takabatake et al. (1992b)). The inset shows the low temperature behaviour of C/T vs. T^2.

(Takabatake et al. 1992b), and as a broad knee also in the $\rho(T)$ curve, which saturates gradually to $\rho \approx 250$ μΩ cm at high temperatures (Zolnierek 1988; Takabatake et al. 1992b). The low value $\gamma = 17$ mJ/(mol K^2) (Takabatake et al. 1992b) is exceptional among UT_2X compounds. The pressure sensitivity of T_N has a similar magnitude as in UCu_2Sn, but is of opposite sign (dT_N/dp) = 0.090 K/kbar (Kurisu et al. 1995). A ^{119}Sn NMR study points to an antiferromagnetic structure leading to a cancellation of the transferred magnetic hy-

perfine field on the Sn atoms, which are located in atomic layers between two U layers. This means that the adjacent U layers are coupled antiferromagnetically to each other. From the anisotropy of the Knight shift one can deduce that the c-axis susceptibility is higher in the overall temperature range, and that the upturn in the $\chi(T)$ curve below $T = 60$ K is mainly due to variations of the susceptibility with field along this direction. The ^{195}Pt NMR signal disappears in the ordered state (Kojima et al. 1993). Takabatake et al. (1992b) attributed the difference in properties of UPt_2Sn comparing to UCu_2Sn mainly to much stronger 5f–d hybridization, because the nearest neighbour distance between U and T atoms is 3.5% smaller in UPt_2Sn. This fact is in agreement with ^{119}Sn Mössbauer spectroscopy results (Wiese et al. 1997), which display rather large quadrupole splitting (compared with UCu_2Sn), which cannot be explained by crystal lattice variations only. Similarly, the additional anomalous increase of the quadrupole splitting below T_N cannot be accounted for by a weak reduction of the volume observed at T_N, but should be a fingerprint of stronger hybridization of the 5f and Pt electronic states. The type of the magnetovolume anomaly corresponds to a positive pressure dependence of T_N.

UNi_2Ga is a weak paramagnet with a broad maximum in $\chi(T)$ data at $T = 32$ K ($\chi_{max} = 3.4 \times 10^{-8}$ m^3/mol, $\chi_{300\,K} = 2.1 \times 10^{-8}$ m^3/mol) and a moderate γ-value of 62 mJ/(mol K^2) (Takabatake et al. 1993). Ga NMR and NQR studies seem to show that the moderate susceptibility enhancement is localized at the centre of the Brillouin zone (Ohama et al. 1993b).

UAu_2Al (figs 5.129–5.131) forms an orthorhombic structure (Takabatake et al. 1992b), different from that of, e.g., UPd_2Sn. It is the structure of the YPd_2Si type, which is the superstructure of the Fe_3C structure (Jorda et al. 1983). U atoms form a zig-zag chain along the a-axis with a U–U spacing of 403 pm. It is an antiferromagnet with the susceptibility following the Curie–Weiss law with parameters $\mu_{eff} = 2.96\,\mu_B$/U and $\Theta_p = -97$ K above $T_N = 25$ K. Below this temperature the $\chi(T)$ curve bends abruptly and tends to saturation at $\chi_0 \approx 13 \times 10^{-8}$ m^3/mol. The resistivity increases weakly with decreasing temperature down to T_N ($\rho_{max} \approx 230$ μΩ cm), and then decreases abruptly without any sign of Fermi surface reconstruction. The specific heat shows an enhanced value $\gamma = 102$ mJ/(mol K^2) (Takabatake et al. 1992b).

UPd_2Ga is known as an antiferromagnet below $T_N = 6.5$ K, with an enhanced γ-value of 172 mJ/(mol K^2) (Takabatake et al. 1993).

5.9. Other ternary compounds

5.9.1. $U_3T_4Si_4$ and $U_3T_4Ge_4$

$U_3Cu_4Ge_4$ and $U_3Cu_4Si_4$ crystallize in the orthorhombic structures of the $Gd_3Cu_4Ge_4$ type (the former) and the $U_3Ni_4Si_4$ type (the latter) with the space group Immm. The U-atoms occupy two different crystallographic sites (Kaczorowski et al. 1997). As shown by Hovestreydt et al. (1982), these structures are closely related to each other and can be considered as inter-grown segments of AlB_2 and $BaAl_4$ types, pointing thus to a close relation of these compounds to UCu(Si,Ge) on one side and UCu_2(Si,Ge)$_2$ on the other side.

Above 150 K, $\chi(T)$ in *$U_3Cu_4Ge_4$* is well described by the Curie–Weiss law with $\mu_{eff} = 3.19\,\mu_B$/U and the positive $\Theta_p = 40$ K. Magnetization in the ferromagnetic state, which sets in at $T_C = 71$ K, corresponds to 0.9 μ_B/U atom (Pechev et al. 1996). Kaczorowski et al. (1997) reported somewhat different data, from which the Curie temperature $T_C = 67$ K

has been deduced. The $\chi(T)$ data were fitted by a modified Curie–Weiss law, which yields $\Theta_p = 74$ K, $\mu_{eff} = 2.72\,\mu_B$/U, and $\chi_0 = 0.63 \times 10^{-8}$ m^3/mol. The electrical resistivity is very high (700 μΩ cm) and practically constant in the paramagnetic range. Below a sharp kink at T_C it decreases down to $\rho_0 = 40$ μΩ cm. Below $T = 25$ K it displays an exponential term, which can be attributed to the existence of magnons with an anisotropy gap (Kaczorowski et al. 1997).

$U_3Cu_4Si_4$ undergoes an AF transition at $T_N = 135$ K (Kaczorowski et al. 1997), but another magnetic phase transition occurs at $T = 70$ K. The presence of spontaneous magnetization at low temperatures could mean that the ground state is ferromagnetic, but pronounced magnetic history phenomena and a very low magnetization together with a high slope of the $M(H)$ dependence point more to a canted magnetic structure with glassy features. This seems plausible in the context of a certain randomness in the occupation of the Cu and the Si sites, as detected by the X-ray analysis. Dominating ferromagnetic interactions are also the reason for the large positive Θ_p value (see table 5.25). A statistical occupation of the lattice sites is demonstrated also in the $\rho(T)$ dependence, which, in comparison with $U_3Cu_4Ge_4$, remarkably flat ($\rho_0 = 130$ μΩ cm, $\rho_{300\,K} = 200$ μΩ cm). The resistivity reflects the upper transition as a typical P–AF transition accompanied by a Cr-like anomaly, but the lower transition is not manifest at all.

5.9.2. $U_3T_4X_{13}$ (X = Ge or Sn)

A large number of compounds of general formula $M_3T_4X_{13}$ (M = Y, Sc, Ca, Sr, Th, and lanthanides, X = Si, Ge, Sn), crystallize in the cubic $Yb_3T_4Ge_{13}$ structure type or its tetragonally distorted derivative. $U_3T_4Ge_{13}$ compounds were described for T = Ru, Os, Rh, and Ir (Lloret et al. 1988). *$U_3Os_4Ge_{13}$* and *$U_3Ru_4Ge_{13}$* were found to be nonmagnetic (Lloret 1988; Lloret et al. 1988). For the Os compound, the $\chi(T)$ dependence follows a modified Curie–Weiss law with parameters given in table 5.25. Above room temperature (data collected up to 500 K) one can use also a simple Curie–Weiss law with $\mu_{eff} = 3.24\,\mu_B$/U. A similar analysis made for the Ru-compound yields $2.86\,\mu_B$/U. The saturation of the $\chi(T)$ dependence below $T = 7$ K, if intrinsic, can be understood as a spin fluctuation effect. The $\rho(T)$ dependence for $U_3Ru_4Ge_{13}$ has a common transition-metal form showing only a weak tendency to saturation in the high-temperature range, but increasing slightly below 10 K (Lloret 1988). Crystal structures of *$U_3Rh_4Ge_{13}$* and *$U_3Ir_4Ge_{13}$* undergo an unspecified distortion of the cubic structure (Lloret 1988; Lloret et al. 1988). The $\chi(T)$ data of both compounds at high temperatures shows a character similar to that at the previous two materials, but the values of Θ_p are positive. Below $T = 15$–17 K, $U_3Ir_4Ge_{13}$ shows ferromagnetic ordering with a small spontaneous magnetization corresponding to about $0.2\,\mu_B$/U. $U_3Rh_4Ge_{13}$ is antiferromagnet with a sharp maximum in $\chi(T)$ at $T_N = 22$ K. As indicated by the positive Θ_P, AF interactions are weak, and a two-step metamagnetic process can be observed in fields 2–4 T. The magnetization of the high-field state corresponds to $0.4\,\mu_B$/U.

From stannides only *$U_3Rh_4Sn_{13}$* has been investigated (Mirambet et al. 1993b). Its crystal structure is cubic, similar to the rhodium stannides with divalent or tetravalent M elements (Eu^{2+}, Yb^{2+}, Ca^{2+}, Sr^{2+}, Th^{4+}), whereas normal trivalent rare earths form the distorted structure type. This compound melts incongruently. For its synthesis an annealing at 800°C was used. The U–U spacing is far above the Hill limit. The fact that U–Rh and

TABLE 5.25

Some basic characteristics of various uranium ternary compounds:

Type of crystal structure, a, b, c – lattice parameters at room temperature, type of ground state (AF – antiferromagnetic, SF – spin fluctuator, WP – weak paramagnet), T_N – magnetic ordering temperature, γ–coefficient of the electronic specific heat evaluated per mol U, parameters of the Curie–Weiss law describing $\chi(T)$ in the paramagnetic state (μ_{eff} – effective magnetic moment per U atom, Θ_p – paramagnetic Curie temperature, χ_0 – temperature independent contribution), and the inter-actinide spacing d_{An-An}.

Compound	Structure	a (pm)	b (pm)	c (pm)	Type	T_N (K)	γ (mJ/(mol U K^2))	μ_{eff} (μ_B/U)	Θ_p (K)	χ_0 (10^{-8} m^3/mol)	d_{An-An} (pm)	Ref.
$U_3Cu_4Ge_4$	orth. $Gd_3Cu_4Ge_4$	1393.2	657.9	427.3	F	71		2.72	74	0.63	375	[1,2]
$U_3Cu_4Si_4$	orth. $U_3Ni_4Si_4$	395.2	401.9	2386.3	AF	135		3.05	71	0.61		[2]
$U_3Ru_4Ge_{13}$	cubic $Yb_3Rh_4Sn_{13}$	893.9			SF			2.07	−25	1.9	447	[3,4]
$U_3Os_4Ge_{13}$	cubic $Yb_3Rh_4Sn_{13}$	894.9			Para			1.83	−30	3.5	447	[3,4]
$U_3Rh_4Ge_{13}$	distorted $Yb_3Rh_4Sn_{13}$	894.3[c]			AF	22		2.32	20	2.1	447	[3,4]
$U_3Ir_4Ge_{13}$	distorted $Yb_3Rh_4Sn_{13}$	895.3[c]			F	15		2.30	20	1.6	447	[3,4]
$U_3Rh_4Sn_{13}$	cubic $Yb_3Rh_4Sn_{13}$	964.16			AF	17.5	225	2.38	1.8	4.2	482	[5]
$UIrSi_3$	tetr. $BaNiSn_3$	416.8		970	AF	42		3.2	−150		416.8	[6]
$U_2Fe_{15}Ge_2$	hex. Th_2Ni_{17}	842.3		835.6	F	505						[7,8]
		841.9		835.5		540						
$U_2Fe_{13.7}Si_{3.3}$	hex. Th_2Ni_{17}	833.0		826.7	F	525						[9]
$U_2Fe_{12.5}Si_{4.5}$	hex. Gd_2Ni_{17}[a]	835.8		813.0	F	430						[9]
$U_2Co_{15}Si_2$	hex. Th_2Ni_{17}	821.62		814.23	F	590						[9,10]
$U_2Co_{15}Ge_2$	hex. Th_2Ni_{17}	830.3		818.0	F	650						[8]
$U_2Co_{15.7}Ge_{1.3}$	hex. Th_2Ni_{17}	830.6		817.6	F	735						[11]
$U_2Co_{14}Ge_3$	hex. Th_2Ni_{17}	832.1		824.0	F	315						[11]
$U_2Ni_{15}Ge_2$	hex. Th_2Ni_{17}	828.2		811.8	?							[8]

TABLE 5.25 (Continued)

Compound	Structure	a (pm)	b (pm)	c (pm)	Type	T_N (K)	γ (mJ/(mol U K^2))	μ_{eff} (μ_B/U)	Θ_p (K)	χ_0 (10^{-8} m^3/mol)	d_{An-An} (pm)	Ref.
$U_4Ir_{13}Ge_9$	orth. $Er_4Ir_{13}Si_9$	1936.1	1119.8	394.7	?	25[b]	23				394.7	[12]
$U_4Ir_{13}Si_9$	orth. $Er_4Ir_{13}Si_9$	1894.0	1092.6	390.2	AF	18	43	2.20	−44	6.4	390.2	[12]
$U_4Ru_7Ge_6$	cubic $U_4Re_7Si_6$	828.7			F	6.8	109	2.54			415	[13,14]
		829.3										
$Np_4Ru_7Ge_6$	cubic $U_4Re_7Si_6$	830.83			SF			1.6	−315		415	[15,16]
$Pu_4Ru_7Ge_6$	cubic $U_4Re_7Si_6$	832.1										[17]
$U_4Os_7Ge_6$	cubic $U_4Re_7Si_6$	830.2									415	[13]
$U_4Re_7Ge_6$	cubic $U_4Re_7Si_6$	822.4									411	[18]
$U_4Tc_7Ge_6$	cubic $U_4Re_7Si_6$	832.08									416	[19,20]
$U_4Tc_7Si_6$	cubic $U_4Re_7Si_6$	820.57			AF	25					410	[19,20]
$U_2Pt_{15}Si_7$	f.c.c.	1681			SF							[21,22]
$U_2Nb_3Ge_4$	orth. Sm_5Ge_4	701.8	1347.3	715.0	F	130		2.27	119	0.27	351	[23]
$U_2Ta_3Ge_4$	orth. Sm_5Ge_4	701.5	1345.4	713.9	F	105		2.42	95	0.16		[23]
$U_2Mo_3Si_4$	monocl.	687.6	688.3	676.0	SF			2.3	−240	0.14	337	[20,24]
	$U_2Mo_3Si_4$	$\beta = 109.79°$										
$U_2Mo_3Ge_4$	monocl.	670.7	699.6	694.8	SF		≈100	2.86	−136	0.08	343	[20,24,25]
	$U_2Mo_3Si_4$	$\beta = 110.09°$										
		701.6	699.5	694.9								
		$\beta = 110.21°$										
$Np_2Mo_3Si_4$	monocl.	686.8	687.7	675.4								[20]
	$U_2Mo_3Si_4$	$\beta = 109.68°$										
$Pu_2Mo_3Si_4$	monocl.	690.3	688.3	672.2								[20]
	$U_2Mo_3Si_4$	$\beta = 109.88°$										
$Np_2Tc_3Si_4$	monocl.	680.8	808.1	556.7							341	[20]
	$Np_2Tc_3Si_4$	$\beta = 103.61°$										
$Np_2Tc_3Ge_4$	monocl.	677.8	810.2	560.5								[20]
	$Np_2Tc_3Si_4$	$\beta = 104.09°$										
$Pu_2Tc_3Si_4$	monocl.	684.3	807.2	558.1								[20]
	$Np_2Tc_3Si_4$	$\beta = 103.47°$										

TABLE 5.25 (Continued)

Compound	Structure	a (pm)	b (pm)	c (pm)	Type	T_N (K)	γ (mJ/(mol U K^2))	μ_{eff} (μ_B/U)	Θ_p (K)	χ_0 (10^{-8} m^3/mol)	d_{An-An} (pm)	Ref.
$U_2W_3Si_4$	monocl.	684.7	685.8	676.7				2.73	−560	0.10	299	[24]
	$U_2Mo_3Si_4$	$\beta = 109.77°$										
$U_2V_3Ge_4$	monocl.	698.6	697.9	692.7	F	60		2.38	41	0.25	?	[24]
	$Np_2Tc_3Si_4$	$\beta = 109.94°$										
$U_2Co_3Si_5$	orth. $U_2Co_3Si_5$	959.1	1112.9	561.7	SF			3.03	−97			[26]
$U_2Fe_3Si_5$	monocl.	1084.8	1147.6	551.8	WP					6.3		[27]
	$Lu_2Co_3Si_5$	$\beta = 119.4°$										
$U_2Ru_3Si_5$	monocl.	1109.2	1176.2	570.7	SF		72	3.21	−208			[26,27]
	$Lu_2Co_3Si_5$	$\beta = 119.3°$										
$U_2Os_3Si_5$	monocl.	1110.3	1172.6	576.0	SF			2.78	−223	1.2		[27]
	$Lu_2Co_3Si_5$	$\beta = 118.9°$										
$Th_2Rh_3Si_5$	monocl.	1152.5	1164.3	592.9								[28]
	$Lu_2Co_3Si_5$	$\beta = 120.94°$										
$U_2Rh_3Si_5$	monocl.	1140.4	1143.5	581.5	AF	25	20	3.14	−62			[26,27,28]
	$Lu_2Co_3Si_5$	$\beta = 120.7°$				26						
$U_2Tc_3Si_5$	tetr. $Lu_2Fe_3Si_5$	1085.6		553.1	AF	11						[19,20]
$Pu_2Tc_3Si_5$	tetr. $Lu_2Fe_3Si_5$	1091.7		553.8								[29]
$Th_2Re_3Si_5$	tetr. $Lu_2Fe_3Si_5$	1098		575.8								[29]
$U_2Re_3Si_5$	tetr. $Lu_2Fe_3Si_5$	1086.7		551.8								[29]
$Np_2Re_3Si_5$	tetr. $Lu_2Fe_3Si_5$	1089		550.9								[19,20]
$Pu_2Re_3Si_5$	tetr. $Lu_2Fe_3Si_5$	1092.9		553.5								[19,20,29]
$U_3Co_4Ge_7$	tetr.	410.85		2748.7	F	21.5	110	2.15	−16	4.3	411	[30]
U_2MnSi_3	hex. U_2RuSi_3	804.5		380.82								[31]
U_2FeSi_3	hex. AlB_2	401		384	SF			2.77	−86	1.8	386	[32,33,
		400.4		386.4				3.35	−132			34,35]
U_2CoSi_3	hex. AlB_2	398.8		388.3	F	10		2.03	≈ 0	2.9	388	[33,34]
U_2NiSi_3	hex. AlB_2	397.9		394.9	F	25–30		2.38	11	1.9	394	[31,33,
		397.20		394.61				2.75[d]	(+6, −70)[d]			34,36]
U_2CuSi_3	tetr. α-$ThSi_2$	397.1		1392.6	F	30		2.56	5	1.1	397	[33,34]

TABLE 5.25 (Continued)

Compound	Structure	a (pm)	b (pm)	c (pm)	Type	T_N (K)	γ (mJ/(mol U K^2))	μ_{eff} (μ_B/U)	Θ_p (K)	χ_0 (10^{-8} m^3/mol)	d_{An-An} (pm)	Ref.
U_2RuSi_3	hex. AlB_2	407.5		383.8	SF			3.02	−130		385	[31,33]
	hex. U_2RuSi_3	814.8		385.5								
U_2RhSi_3	hex. AlB_2	407.6		388.3	F	19.5		2.32	17	2.0	392	[31,33]
	orth.	703.6	406.2	392.9								
U_2PdSi_3	hex. AlB_2	408.5		393.5	F	15.5		2.39	7	3.1	394	[31,33]
	orth.	706.7	408.0	393.9								
U_2OsSi_3	hex. AlB_2	406.66		385.17							384	[31,33]
	hex. U_2RuSi_3	816.0		384.4								
U_2IrSi_3	hex. AlB_2	407.2		389.50	F	11		1.93	3	2.7	390	[31,33]
U_2PtSi_3	hex. AlB_2	408.4		397.3	F	8	200	2.1	(+19, −7)[d]		397	[33,37,38]
		406.7		396.4								
U_2AuSi_3	hex. AlB_2	414.5		398.9	F	11.6		1.65	5	5.0	399	[31,33]
U_2CuGa_3	hex. Lu_2CoGa_3	865.8		725.9	AF	15					363	[39,40]
U_2RuGa_3	orth. $CeCu_2$	465.2	703.7	788.6	F	73		2.12	73	2.5		[41]
U_2RhGa_3	orth. $CeCu_2$	438.5	696.4	701.7	F	60		2.20	61	2.7		[41]
U_2PdGa_3	orth. $CeCu_2$	437.2	701.7	769.1	AF	33		2.58	8	1.5		[41]
U_2IrGa_3	orth. $CeCu_2$	434.3	692.7	769.4	F	72		1.85	72	3.0		[41]
U_2PtGa_3	orth. $CeCu_2$	438.1	703.3	770.3	AF	30						[41]
$U_2Rh_3Al_9$	orth. $Y_2Co_3Ga_9$	1305	761	938	AF	35		3.13				[42]
$U_2Ir_3Al_9$	orth. $Y_2Co_3Ga_9$	1313	758	934	AF	15	30	3.54				[42]
$U_2Rh_3Ga_9$	orth. $Y_2Co_3Ga_9$	1303	768	940	AF	13		2.87				[42]
$U_2Ir_3Ga_9$	orth. $Y_2Co_3Ga_9$	1322	746	936	AF	7.5		2.92				[42]
$ThNi_2B_2C$	tetr. $LuNi_2B_2C$	369.5		1019.7	SC	$T_c = 6.5$					370	[43]
$ThRh_2B_2C$	tetr. $LuNi_2B_2C$	386.3		1017.7							386	[43]
$ThPt_2B_2C$	tetr. $LuNi_2B_2C$	382.8		1085.3	SC	$T_c = 6.7$					383	[43]
UNi_2B_2C	tetr. $LuNi_2B_2C$	351.3		1054.0	AF	218		3.31	−280		351	[43]
URh_2B_2C	tetr. $LuNi_2B_2C$	378.2		1021.4	F	185		2.59	153		378	[43]
UNi_4B	hex. $CeCo_4B$	495.2		695.4	AF	20	470	2.90[e]	−65[e]		348	[44,45]
UCo_4B	hex. $CeCo_4B$	490.2		694.9	SF		62	3.20	−210	3	347.5	[46]
UAl_3C_3	hex. $ScAl_3C_3$	338.9		1739.4	AF	13		1.52	−9	?	339	[47]

TABLE 5.25 (Continued)

Compound	Structure	a (pm)	b (pm)	c (pm)	Type	T_N (K)	γ (mJ/(mol U K^2))	μ_{eff} (μ_B/U)	Θ_p (K)	χ_0 (10^{-8} m^3/mol)	d_{An-An} (pm)	Ref.
U_2PtC_2	b.c.t.	352		1254	SC	$T_c = 1.47$	75				352	[48,49]
U_2OsC_2	b.c.t.	346			WP		20				346	[50]
U_2IrC_2	b.c.t.	348			SF (?)		110				348	[50]
$U_2Cu_4As_5$	b.c.t.	399.0		2430	AF	189		1.95	168	1.2	399	[51]
$U_3Cu_2S_7$	hex.	973.08		570.45	SF			2.50	−33	?	422	[52]
$U_3Cu_2Se_7$	hex.	1013.8		595.25	AF	13		2.64	−28	?	441	[52]
UMn_4P_2	tetr. $ZrFe_4P_2$	720.1		370.1	AF	125 (22)					370	[53]
$U_3Ni_{3.34}P_6$	tetr.	381.8		1350.1	F	139		2.1	107		382	[54]
UCuPO	hex. ZrCuSiAs	379.3		823.3	AF	220		2.68	0		379	[55]
UFe_4P_{12}	b.c.c. $LaFe_4P_{12}$	777.29			F	3.2		2.25	≈ 0		673	[56,57,58]
UCr_2Al_{20}	cub. $CeCr_2Al_{20}$	1439.6			WP		80				623	[59]
UFe_2Zn_{20}	cub. $CeCr_2Al_{20}$	1409.98			SF						610	[60]

[a] For comparison lattice parameters given in the Th_2Ni_{17} structure type.
[b] Anomaly found in AC susceptibility measurement.
[c] Indexed in the cubic symmetry.
[d] Data obtained on a single crystal. Θ_p for $\boldsymbol{H}$ along the basal plane and c-axis, respectively.
[e] Data obtained on a single crystal for field along the basal plane.

TABLE 5.25 (Continued)

References:

[1] Pechev et al. (1996)
[2] Kaczorowski et al. (1997)
[3] Lloret et al. (1988)
[4] Lloret (1988)
[5] Mirambet et al. (1993b)
[6] Buffat et al. (1986)
[7] Berlureau et al. (1989)
[8] Shiokawa et al. (1994)
[9] Berlureau et al. (1993)
[10] Berlureau (1991)
[11] Chevalier et al. (1996b)
[12] Verniere et al. (1995)
[13] Lloret et al. (1987)
[14] Mentink et al. (1991)
[15] Jeandey et al. (1996)
[16] Wastin (1997)
[17] Higgins et al. (1996)
[18] Akselrud et al. (1978)
[19] Wastin et al. (1995)
[20] Wastin (1991)
[21] Geibel et al. (1990b)
[22] Guha et al. (1996)
[23] Le Bihan et al. (1994)
[24] Le Bihan and Noël (1995)
[25] Endstra (1992)
[26] Piraux et al. (1993)
[27] Hickey et al. (1990)
[28] Becker et al. (1997)
[29] Leithe-Jasper et al. (1996)
[30] Pöttgen et al. (1995)
[31] Chevalier et al. (1996a)
[32] de Lourdes Pinto (1966)
[33] Pöttgen and Kaczorowski (1993)
[34] Kaczorowski and Noël (1993)
[35] Nakotte et al. (1996b)
[36] Schröder et al. (1995)
[37] Sato et al. (1991)
[38] Sato et al. (1992c)
[39] Tran et al. (1993)
[40] Tran et al. (1995c)
[41] Tran (1996)
[42] Buschinger et al. (1997)
[43] Takabatake et al. (1994)
[44] Mentink et al. (1993)
[45] Mentink et al. (1997b)
[46] Nakotte et al. (1993c)
[47] Gesing et al. (1992)
[48] Matthias et al. (1969)
[49] Meisner et al. (1984)
[50] Killer et al. (1994)
[51] Kaczorowski et al. (1991b)
[52] Daoudi et al. (1996a)
[53] Jeitschko et al. (1990)
[54] Ebel and Jeitschko (1995)
[55] Kaczorowski et al. (1994)
[56] Jeitschko and Braun (1977)
[57] Torikachvili et al. (1987)
[58] Torikachvili et al. (1986)
[59] Okuda et al. (1989)
[60] Gonçalves et al. (1998)

U–Sn spacings are larger than in URh_3 and USn_3 points to a weak 5f-ligand hybridization. The $\chi(T)$ dependence shows a high temperature modified Curie–Weiss law with parameters given in table 5.25. The kink in $\chi(T)$ at $T = 18$ K points to AF ordering. The $\rho(T)$ curve is flat above about 100 K and progressively decreases at lower temperatures. AF ordering is manifest as a shoulder centred at 18–22 K. The magnetic phase transition is seen also as a small but distinct anomaly at $T = 17.5$ K in the specific heat. The enhanced value $\gamma = 225$ mJ/(mol U K^2) demonstrates heavy fermion character of $U_3Rh_4Sn_{13}$. Further transport properties (Hall effect, thermopower) point to a Fermi surface reconstruction at T_N (Aoki et al. 1993b).

5.9.3. $UTSi_3$

One can obtain the $UTSi_3$ compounds by replacing one of the transition metal layers by a Si layer in the $ThCr_2Si_2$ type compounds, which is though possible only for a limited number of cases. For uranium the only case is *$UIrSi_3$*, which is in agreement with the fact that Ir silicides are the only ones that can accommodate the smaller rare earth atoms (Zhong et al. 1985). In the $\chi(T)$ curve of $UIrSi_3$ studied up to $T = 600$ K (Buffat et al. 1986) one can distinguish two important features. These are a sharp maximum at $T = 42$ K, which marks the AF phase transition, and the onset of a weak spontaneous magnetization below $T = 35$ K. However, the low value of $M_s = 0.03\,\mu_B$/U reached in the low-temperature limit means that it can be due to a ferromagnetic impurity. The $1/\chi$ vs. T dependence is linear above $T = 250$ K yielding the CW parameters given in table 5.25. A metamagnetic behaviour can be traced down to about 30 K. At lower temperatures the critical metamagnetic field exceeds 6 T, the maximum field available in the experiment. $\rho(T)$ shows a tendency to saturation at high temperatures, whereas it drops strongly below $T = 42$ K, forming thus a kink at T_N.

5.9.4. $U_2T_{15}Si_2$ and $U_2T_{15}Ge_2$

Unlike thorium, uranium does not form compounds of the 2–17 stoichiometry with late transition metals. However, similar to the 1–12 compounds, stable U-compounds can be obtained by partial replacement of the transition metal by Si or Ge. Originally two compounds of this type were reported to crystallize in the hexagonal Th_2Ni_{17} structure type (space group $P6_3/mmc$), namely $U_2Fe_{13}Si_4$ and *$U_2Fe_{15}Ge_2$* (Berlureau et al. 1989). The latter compound becomes ferromagnetic below $T_C = (505 \pm 10)$ K, which is lower than the value in, e.g., $UFe_{10}Si_2$. But the saturation magnetization is higher already at room temperature (22.7 μ_B/mol at $T = 300$ K), and this value further increases to 25.5 μ_B/mol at $T = 4.2$ K. Single-crystal magnetization measurements at $T = 4.2$ K (Shiokawa et al. 1994) yield a spontaneous magnetization as high as 27.5 μ_B/f.u. The a-axis is the easy-magnetization direction, but the anisotropy field does not exceed 6 T. A more detailed crystallographic study undertaken later (Berlureau et al. 1993) shows that in the Si case the range of stability is limited by the concentrations *$U_2Fe_{12.5}Si_{4.5}$* and *$U_2Fe_{13.7}Si_{3.3}$*. T_C decreases with increasing Si concentration and reaches 430 K and 525 K, respectively. The study revealed furthermore that the U atoms substitute for "dumbbell" dimers of Fe atoms inducing a progressive disorder with increasing Si content. For $U_2Fe_{13.7}Si_{3.3}$ the substitutions are partially ordered, whereas a statistical distribution of such substitution was found in $U_2Fe_{12.5}Si_{4.5}$, which means a transition to another structure type (Gd_2Fe_{17},

P6/mmm). On the other hand, the variations in composition in the $U_2Fe_{17-x}Ge_x$ system, which are possible within the range $x = 2$–3 (only $x = 2.5$ is found in as-cast samples), lead to modifications in the occupancy of the Fe and the Ge sites, whereas the U-sublattice remains intact (Chevalier et al. 1996b). The highest $T_C = 540$ K was found for $x = 2.5$. The spontaneous magnetization decreases with increasing Ge content. $U_2Co_{15}Ge_2$ has an even higher Curie temperature about 600 K, but the magnetization is lower. The saturated moment corresponds to 14.2 μ_B/f.u. at $T = 4.2$ K (Shiokawa et al. 1994; Chevalier et al. 1996b). T_C could be still enhanced by decreasing the Ge contents up to $T_C = 735$ K in $U_2Co_{15.7}Ge_{1.3}$, which is the stability limit in the $U_2Co_{17-x}Ge_x$ system. The other limit, $U_2Co_{14.0}Ge_{3.0}$ has a T_C of 315 K only (Chevalier et al. 1996b). The spontaneous moment corresponds then to only 5.8 μ_B/f.u., which points to a strong reduction of the Co moments due to shorter mean Co–Co spacing. A further increase of T_C could be obtained by optimization of the Fe/Co ratio within the solid solution $U_2Co_{15-x}Fe_xGe_2$, where a maximum of 750 K can be found around 40% Fe (Shiokawa et al. 1994). $U_2Co_{15}Si_2$ was found to become ferromagnetic below $T_C = 590$ K (Berlureau 1991), $U_2Ni_{15}Ge_2$ was reported as non-magnetic at room temperature (Shiokawa et al. 1994). Magnetic properties in this type of compounds are, similar to 1:12 compounds, clearly dominated by the behaviour of the 3d sublattice. The role of the 5f states is unclear until now. Indirect evidence, as higher T_C in $U_2Fe_{15}Ge_2$ than in rare-earth RE_2Fe_{17}, point to a role of the 5f states in the exchange interactions.

5.9.5. $U_4T_{13}Si_9$ and $U_4T_{13}Ge_9$

Other ternary silicides and germanides with the general formula $U_4T_{13}X_9$ were prepared with T = Rh or Ir and these were studied together with rare-earth analogs (Verniere et al. 1995). The systematics shows that their occurrence excludes mutually the occurrence of RT_3X_2 compounds with a $CaCu_5$-related structure. They crystallize in a complicated orthorhombic structure Pnmm with 3 different crystallographic U-sites. The $\chi(T)$ data in $U_4Ir_{13}Si_9$ show an AF transition at $T_N = 18$ K and possibly another transition at lower temperatures. $U_4Ir_{13}Ge_9$ studied by AC susceptibility only displays anomalies at $T = 25$ K and 7 K. The parameters of the modified Curie–Weiss type behaviour are shown in table 5.25.

An analogous metallurgical situation can be found for the system $U_2Cu_{17-x}Al_x$ crystallize the rhombohedral structure of the Th_2Zn_{17} type. However, the large homogeneity range $5 \leqslant x \leqslant 10$ classifies this system more as a pseudo-binary system (albeit without boundary binaries), and such compounds do not fall into the scope of this chapter. The reader is referred to the report of Pietri et al. (1997) and the references cited therein.

5.9.6. $U_4T_7X_6$

Although the range of stability of the 1–2–2 compounds is very large, in several few cases (as URu_2Ge_2) the compounds of this type could not be synthesized. This led to the discovery of $U_4Ru_7Ge_6$ and other materials (Akselrud et al. 1978; François et al. 1985), which crystallize in the cubic structure of the $U_4Re_7Si_6$ type (space group Im3m). These compounds are stable only if components allow for a fitting of the lattice parameter so these can fall into a rather restricted range (Higgins et al. 1997). The structure

is derived from $AuCu_3$ structure, in which the Si and part of the Re atoms are ordered in Cu positions, while the remaining Re atoms occupy sites which were interstitial in the $AuCu_3$ structure. *$U_4Ru_7Ge_6$* orders ferromagnetically at $T_C = 6.8$ K and has small ordered moment of $0.2\,\mu_B$/U. The $1/\chi$ vs. T dependence is strongly non-linear. The value $\mu_{eff} = 2.54\,\mu_B$/U was derived at high temperatures (Lloret et al. 1987). A specific heat study yields $\gamma = 109$ mJ/(mol U K^2) and small magnetic entropy up to the transition of $0.11\,R\ln 2$ (Mentink et al. 1991). The $\rho(T)$ curve reaches a value of about 330 μΩ cm in the maximum at room temperature. A subsequent weak decrease is followed up to $T = 500$ K. On the low-temperature side, the resistivity decreases progressively and drops at T_C. The large value $d_{U-U} = 586.4$ pm is in conformity with the suggested concentrated Kondo lattice character, but the generally strong 5f–4d hybridization can be an argument why an explanation in terms of weak band ferromagnetism should not be dismissed. *$U_4Os_7Ge_6$* is non-magnetic. $\chi(T)$ increases with decreasing temperature and reaches a value of about 5.2×10^{-8} m^3/mol U in the low-temperature limit. The electrical resistivity behaviour resembles that of a transition metal with a substantial positive slope at high T (Lloret et al. 1987). *$Np_4Ru_7Ge_6$* was found to be non-magnetic at $T = 4.2$ K by ^{237}Np Mössbauer spectroscopy (Jeandey et al. 1996). Experiments made in magnetic fields show magnetic splitting corresponding to a local susceptibility at Np site of 3.0×10^{-8} m^3/mol Np. The $\chi(T)$ data show a Curie–Weiss behaviour with low μ_{eff} and large negative Θ_p (see table 5.25) at high temperatures (Wastin 1997). Below $T = 100$ K one finds that the susceptibility values saturate to 4.2×10^{-8} m^3/(mol Np), which can be taken as being in an agreement with the Mössbauer data. The $\rho(T)$ curve decreases progressively below $T = 60$ K and saturates to 110 μΩ cm in the low-temperature limit. The high-temperature flat part corresponds to 190 μΩ cm. The low temperature resistivity scales as aT^2 with the moderate value $a = 0.06$ μΩ cm K^{-2} (Wastin et al. 1996b). The behaviour of $Np_4Ru_7Ge_6$ can be understood as being due to spin fluctuations. From Tc compounds, *$U_4Tc_7Si_6$* was reported to order antiferromagnetically at $T_N = 25$ K (Wastin 1991).

5.9.7. $U_2Pt_{15}Si_7$ and substitutions

A new group of materials with the 2-15-7 stoichiometry was discovered by Geibel et al. (1990b). It crystallizes in the f.c.c. structure, which is supposedly a ternary ordered derivative of the Th_6Mn_{23} structure type. *$U_2Pt_{15}Si_7$* displays no magnetic phase transition, but the susceptibility reaches about 220×10^{-8} m^3/mol in the low-temperature limit. The resistivity decreases strongly below $T = 40$ K, whereas it the $\rho(T)$ curve tends to a saturation when approaching the room temperature. The specific heat shows the moderate value of $\gamma = 100$ mJ/(mol U K^2). Guha et al. (1996) studied details of the low-temperature behaviour of pure $U_2Pt_{15}Si_7$ and the influence of Ni, Co, Ge, or Th substitutions. The study showed that C/T vs. T displays a shoulder at $T = 7$ K, which shifts to lower temperatures with increasing Ni substitution, forming a rounded maximum below $T = 2$ K for the limit concentration $U_2Pt_{11}Ni_4Si_7$. On the other hand, Co substitution leads to suppression of this anomaly and a regular specific heat behaviour with $\gamma \approx 50$ mJ/(mol U K^2) was found in $U_2Pt_{13}Co_2Si_7$. Ni substitution suppresses monotonically the large susceptibility values, which were, however, found to be field dependent. Magnetization measurements reveal a substantial tendency to saturation.

5.9.8. $U_2T_3X_4$ compounds

$U_2T_3Ge_4$ compounds with T = Nb and Ta have been found to crystallize in an orthorhombic structure, which is an ordered variant of the Sm_5Ge_4 structure type with space group Pnma (Le Bihan et al. 1994). *$U_2Nb_3Ge_4$* is a ferromagnet with the appreciable T_C = 130 K and spontaneous moment corresponding to 0.7 μ_B/U at low temperatures. A similar behaviour was found for *$U_2Ta_3Ge_4$*, which has a lower T_C value (105 K) and a higher moment of 0.95 μ_B/U. The $\chi(T)$ dependence can be described by a modified Curie–Weiss law in both cases, the parameters are given in table 5.25.

For other actinide compounds of the $An_2T_3X_4$ type, two different monoclinic structure types have been identified. All compounds with T = Mo crystallize in the $U_2Mo_3Si_4$ structure type (Le Bihan and Noël 1995, and references given by these authors). The compounds with T = Tc crystallize in the $Np_2Tc_3Si_4$ type (Wastin 1991). They share the same space group $P2_1/c$. The environment of the actinide atoms is similar in both structure types, the Mo variety is somewhat more compact. *$U_2Mo_3Si_4$* and *$U_2Mo_3Ge_4$* were reported to be non-magnetic and to have spin fluctuation features (Le Bihan and Noël 1995). At high temperatures a modified Curie–Weiss law was found for the $\chi(T)$ data with parameters shown in table 5.25. Below T = 50 K, the $\chi(T)$ curve tends to saturation reaching $\chi(0\ \mathrm{K}) \approx 7.4 \times 10^{-8}$ m^3/mol in $U_2Mo_3Si_4$. The characteristic temperature marking the deviation from the modified Curie–Weiss law is lower for $U_2Mo_3Ge_4$ (25 K), and the value of $\chi(0\ \mathrm{K})$ is higher (16.1×10^{-8} m^3/mol). This tendency, together with a higher μ_{eff}/U atom and a less negative Θ_p can be associated with the somewhat higher U–U spacing in the Ge-compound. One should note that this parameter is in the critical range of the Hill limit. Accordingly, a large negative Θ_p, a lower saturated susceptibility value ($\chi(0\ \mathrm{K}) \approx 5.0 \times 10^{-8}$ m^3/mol), and a higher characteristic temperature of the deviation from the modified Curie–Weiss law (80 K) was found for *$U_2W_3Si_4$*, where d_{U-U} is very small as can be seen in table 5.25 (Le Bihan and Noël 1995). The only known magnetically ordered representative of this class of compounds is *$U_2V_3Ge_4$*, which is ferromagnetic below T_C = 60 K. Its magnetization at T = 5 K corresponds to 0.68 μ_B/U, but a participation of V moments can not be excluded (Le Bihan and Noël 1995). However, a comparison with the magnetic properties of rare-earth based $RE_2Mo_3Ge_4$ compounds (formed generally in the Sm_5Ge_4 structure), for which magnetic ordering temperatures do not exceed 10 K and the type of ordering is antiferromagnetic (Le Bihan et al. 1996a) points to a dominant role of the 5f moments and to a strong ferromagnetic 5f–5f exchange interaction in the magnetically ordered U-compounds of this type.

5.9.9. $U_2T_3Si_5$ and $U_2T_3Ge_5$ compounds

$An_2T_3Si_5$ compounds crystallize in several different structures derived from the tetragonal $ThCr_2Si_2$ structure type (Braun 1984; Chabot and Parthé 1985). *$U_2Co_3Si_5$* is orthorhombic (space group Ibam). It was classified as non-magnetic Kondo system (Piraux et al. 1993). To our opinion the anomalies in $\chi(T)$ and especially in $\rho(T)$, which shows a sharp maximum at T = 15 K, could be well understood in terms of an antiferromagnetic transition. $U_2T_3Si_5$ with T = Fe, Ru, Rh, and Os are formed in the $Lu_2Co_3Si_5$ structure type, derived from the $U_2Co_3Si_5$ type and showing a monoclinic distortion (space group C2/c). *$U_2Fe_3Si_5$* is a weak paramagnet with temperature independent $\chi_0 \approx 6.3 \times 10^{-8}$ m^3/mol (Hickey et al. 1990). *$U_2Os_3Si_5$* shows a $\chi(T)$ behaviour following a modified Curie–Weiss law above T = 80 K with parameters given in table 5.25.

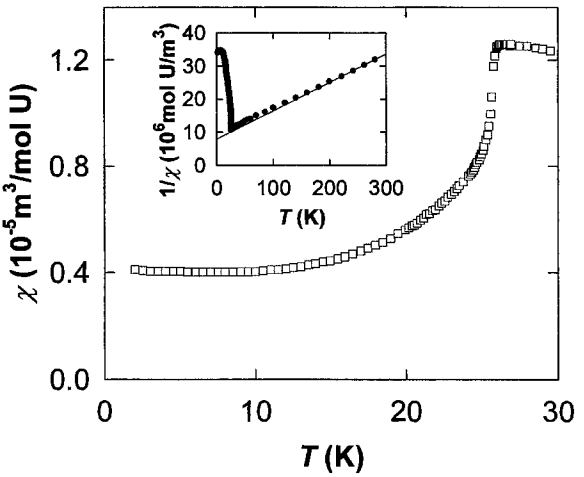

Fig. 5.132. Magnetic susceptibility χ vs. temperature T for $U_2Rh_3Si_5$ (after Becker et al. (1997)). The inset shows the inverse susceptibility.

At lower temperatures a plateau followed by a weak upturn point to the importance of spin fluctuations. The $\rho(T)$ curve displays a broad knee around $T = 50$ K followed by saturation on the high-temperature side (Hickey et al. 1990).

The $\chi(T)$ curve of $U_2Ru_3Si_5$ forms a broad maximum at $T = 15$ K reaching $\chi \approx 12.6 \times 10^{-8}$ m^3/mol f.u., which is followed by the Curie–Weiss type of behaviour on the high-temperature side (Hickey et al. 1990; Piraux et al. 1993). The parameters are given in table 5.25. A maximum in the range 20–30 K was found also in the $\rho(T)$ dependence. A negative $d\rho/dT$ was found both at high temperatures (above the maximum) and in the low-temperature limit (below $T = 5$ K). Low-temperature specific heat measurements yield $\gamma = 72$ mJ/(mol U K^2).

In the case of $U_2Rh_3Si_5$, a sharp cusp in the $\chi(T)$ dependence marks the onset of AF order (fig. 5.132). At high temperatures, the $\chi(T)$ data are accounted by the Curie–Weiss law with parameters given in table 5.25. The $\rho(T)$ dependence is flat at high temperatures and drops abruptly at T_N without any maximum (fig. 5.133). The low-temperature part can be described using an exponential term deduced for the electron–magnon scattering, which yields the width of the gap in the magnon spectrum as $\Delta \approx 67$ K. The thermoelectric power coefficient S changes its sign at T_N from positive at high-temperatures to negative at low-temperatures (Piraux et al. 1993). A more detailed analysis of the low temperature properties (Becker et al. 1997) shows details of the apparently first order magnetic phase transition. The resistivity, which is about 300 $\mu\Omega$ cm above T_N, drops by a factor of 65 below T_N. The pronounced drop in the $\chi(T)$ data and the large peak in the specific heat (fig. 5.134) associated with T_N and corresponding to a magnetic entropy of $S = R \ln 2$ led to the conjecture that $U_2Rh_3Si_5$ is a two-level system with two crystal-field singlets in the ground state and an exchange-induced magnetic ordering. Neutron-diffraction experiment (Feyerherm et al. 1997) revealed an equal-moment non-collinear magnetic structure with

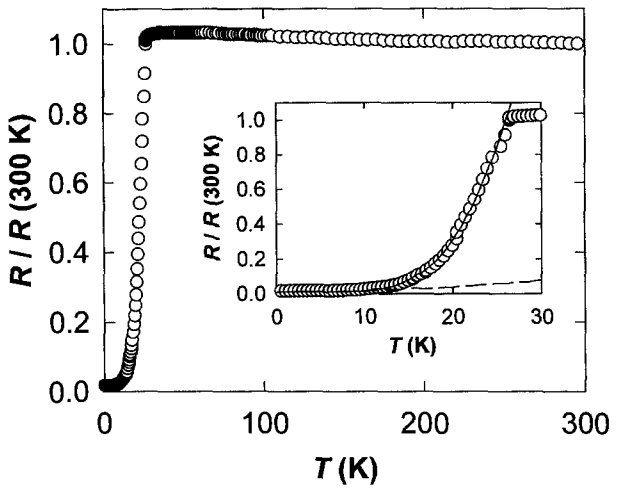

Fig. 5.133. Electrical resistivity related to the resistivity at $T = 300$ K, R/R (300 K) vs. temperature T for $U_2Rh_3Si_5$ (Becker et al. 1997). The inset shows the low temperature detail of the same dependence.

$\mu_U \approx 1.8\,\mu_B$. The temperature dependence of thermal expansion is strongly anisotropic as can be seen in fig. 5.134 (Takeuchi et al. 1997). There are discontinuities in $\Delta l_i(T)/l_i$ at 25.7 K of opposite sign in the a and b directions while the c-axis changes step-like. As a result a large volume change is derived. The magnetization along the b-axis exhibits a sharp temperature dependent metamagnetic transition where the induced U-moments switch from 0.1 to $1.7\,\mu_B$. The huge anisotropy is reflected in the fact that in fields perpendicular to the b-axis no metamagnetism is observed up to 30 T. The magnetization response in the a- and the b-axis is weak and linear yielding only about $0.15\,\mu_B$ in the maximum field (Takeuchi et al. 1997). The thermoexpansion and magnetization anomalies were related by Takeuchi et al. (1997) to first-order transitions of strongly coupled spin and quadrupole orderings.

A dilution study between $U_2Ru_3Si_5$ and $U_2Rh_3Si_5$ shows the onset of magnetic order at about 25% Rh. T_N reaches a maximum of 10 K at 35% Rh and then drops again around 50% Rh, suggesting a change of magnetic structure type. At higher Rh concentrations T_N increases linearly up to $T_N = 25$ K in $U_2Rh_3Si_5$ (Chevalier et al. 1995). Neutron diffraction has shown indeed that the magnetic structure of $U_2(Ru_{0.65}Rh_{0.35})_3Si_5$ is different from that in $U_2Rh_3Si_5$ and that it consists of collinear U-moments ($0.63\,\mu_B$). The type of stacking is similar in both structures, i.e., the moments in the distorted U-planes are ferromagnetically coupled, whereas the inter-plane coupling is antiferromagnetic (Chevalier et al. 1994, 1995).

The last group of the $An_2T_3Si_5$ compounds adopts the primitive tetragonal structure of the $Lu_2Fe_3Si_5$ type (space group P4/mnc). From these compounds $U_2Tc_3Si_5$ was reported to show an AF transition at $T_N = 11$ K. The high temperature modified Curie–Weiss law yields parameters given in table 5.25.

The sample prepared with a nominal composition $U_2Co_3Ge_5$ was indexed as tetragonal without detailed specification of the structure type (Hickey et al. 1992). A subsequent

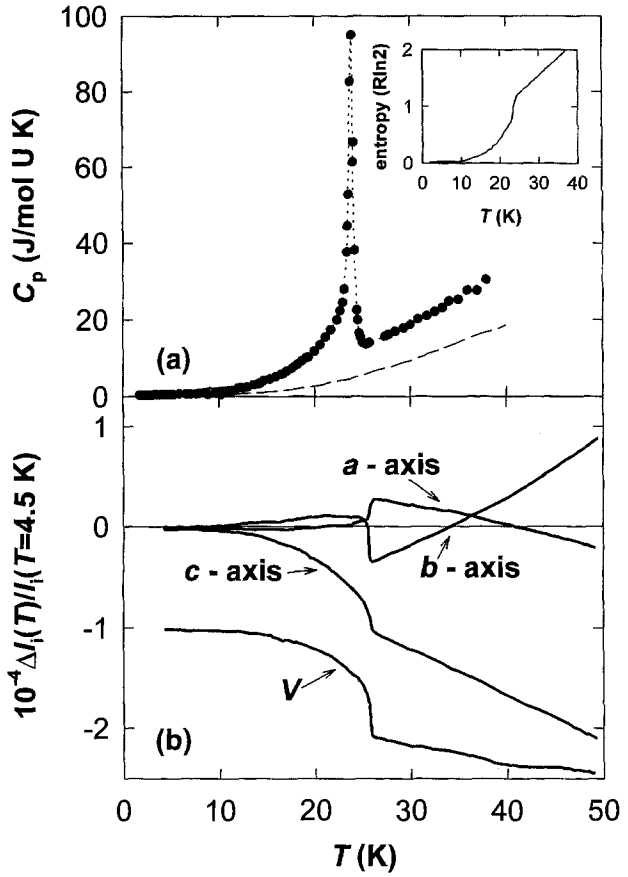

Fig. 5.134. (a) Specific heat C_p vs. temperature T for $U_2Rh_3Si_5$ (full dots) and $Th_2Rh_3Si_5$ (dashed line). After Becker et al. (1997). The inset shows the magnetic entropy in the temperature dependence. (b) Thermal expansion $\Delta l_i/l_i$ vs. temperature T along three orthogonal axes (quasiorthorhombic notation used, $a \perp bc$), and resulting relative volume change (shown with off set -1×10^{-4}). After Takeuchi et al. (1997).

detailed study of the crystal structure showed that in fact one was dealing with a material with the composition $U_3Co_4Ge_7$, which crystallizes in a structure that can be viewed as inter-grown blocks of the $CaBe_2Ge_2$ and $AuCu_3$ structure types. The resulting structure is tetragonal with the space group I4/mmm (Pöttgen et al. 1995). Below $T \approx 20$ K, the $\chi(T)$ data show a spontaneous magnetization corresponding to 0.3–0.4 μ_B/U atom (Hickey et al. 1992). On he other hand, the low temperature decrease of the magnetization in the field-cooled regime points to a non-collinear arrangement of the U-moments. The ordering temperature shows up as a pronounced specific-heat anomaly at $T = 20.5$ K. The specific heat data yield a γ-value of 110 mJ/(molU K^2) (Pöttgen et al. 1995). The $\rho(T)$ curve shows a broad knee around $T \approx 100$ K followed by a gradual saturation at higher temperatures. A shoulder around the magnetic ordering temperature is more typi-

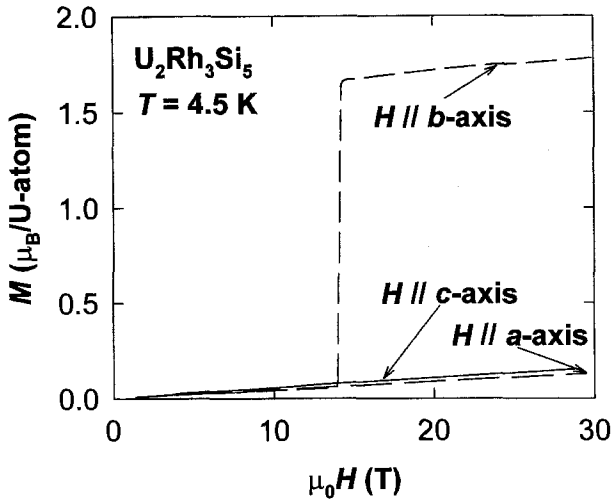

Fig. 5.135. Magnetization curve on a single crystal of $U_2Rh_3Si_5$, measured at T = 4.5 K with field H along orthogonal axes a, b, and c, $a \perp bc$. After Takeuchi et al. (1997).

cal for antiferromagnets, which points to a complicated magnetic structure (Hickey et al. 1992). The ordering temperature was confirmed by AC susceptibility measurements on the sample with the $U_3Co_4Ge_7$ composition (Pöttgen et al. 1995).

5.9.10. U_2TSi_3 and U_2TGa_3 compounds

Numerous ternary uranium transition metal silicides U_2TSi_3 (T = Mn, Fe, Co, Ni, Cu, Ru, Rh, Pd, Os, Ir, Pt, Au) crystallize in structures related to the hexagonal AlB_2-type structure, while U_2CuSi_3 adopts the tetragonal structure of α-$ThSi_2$. Originally the transition metal atoms were supposed to be randomly distributed on the silicon positions (Kaczorowski and Noël 1993; Pöttgen and Kaczorowski 1993). The formation of the AlB_2-structure ternaries can be understood on the basis of $USi_{1.67}$, which leaves some B-sites of the AlB_2 structure vacant. Those can be filled by T atoms, which can substitute ultimately about one ten of Si atoms. Thus, as shown for some ternary lanthanide silicides, the homogeneity range spans $RET_{0.5-0.7}Si_{1.7-1.5}$ (Kaczorowski and Noël 1993; Nakotte et al. 1996b and references given by these authors). However, a detailed X-ray and electron diffraction work showed that for the case of U_2RuSi_3 a new type of ordered ternary derivative appears (Pöttgen et al. 1994) with doubled a-parameter, in which Si and Ru atoms are not located in the same plane. Such superstructure was found also for U_2MnSi_3 and U_2OsSi_3 (Chevalier et al. 1996a). On the other hand, in an other superstructure the periodicity is doubled in [0 0 1] direction only. This leads to orthorhombic symmetry (Pmmm) and results in U-positions, one purely Si-position, and one position occupied randomly by Si atoms and transition metal atoms. Such structural variety was found in the case of U_2RhSi_3, and a weak tendency to such preferential occupation was indicated for U_2PdSi_3, too (Chevalier et al. 1996a).

U_2FeSi_3 has a non-magnetic ground state. $\chi(T)$ follows a modified Curie–Weiss law down to 50 K with parameters given in table 5.25. A weak saturation tendency is followed by a low-T upturn (Kaczorowski and Noël 1993; Chevalier et al. 1996a). Very similar properties magnetic properties were found also in *U_2RuSi_3* and *U_2OsSi_3* (Chevalier et al. 1996a).

Several other U_2TSi_3 materials studied till now show clear ferromagnetic characteristics, although both magnetic-history phenomena (difference in $M(T)$ for the field-cooled and zero-field-cooled regimes) and certain features in AC susceptibility data led to an interpretation in terms of spin glass or re-entrant spin glass behaviour, induced by the crystallographic randomness (Kaczorowski and Noël 1993). However, to our view, such effects are obtained typically in the case of narrow domain wall ferromagnets, and are rather common for a broad class of U magnetics without any randomness. The weakest ferromagnetic properties were found in *U_2CoSi_3* with $T_C = 10$ K. As in the following cases, the magnetization curve at low-T does not saturate. The magnetization in $\mu_0 H = 3$ T reaches $0.28\,\mu_B$/U, whereas the remanence corresponds to $0.05\,\mu_B$/U only.

A somewhat higher T_C value (25 K) and a magnetization reaching $0.67\,\mu_B$/U in $\mu_0 H = 3$ T was found in *U_2NiSi_3* (Kaczorowski and Noël 1993). The transition around 100 K can be most probably attributed to a spurious phase, because the Θ_p value is much lower (see table 5.25). The $\chi(T)$ curves obtained on a single crystal (Schröder et al. 1995) display the same planar anisotropy type as in isostructural UGa_2 (Andreev et al. 1979) and $USi_{1.67}$ (Sato et al. 1992c). The μ_{eff} values determined for $H \| c$ and $H \perp c$ are identical ($2.75\,\mu_B$/U), whereas the difference in Θ_p values (see table 5.25) amounts to 76 K. Neutron diffraction data (Schröder et al. 1995) confirm that this compound is ferromagnet with $\mu_U = (0.6 \pm 0.1)\,\mu_B$. The resolution limited width of Bragg peaks means that the coherence length ξ is larger than 30 nm, which excludes the spin glass conjecture. Moreover, the neutron depolarization in the ordered state points to the existence of ferromagnetic domains. Only bulk magnetic data are known for *U_2RhSi_3* (Chevalier et al. 1996a). The magnetization reaches $0.45\,\mu_B$/U at $T = 4.2$ K, the parameters of the modified Curie–Weiss law are shown in table 5.25. In *U_2PdSi_3*, a rather broad cusp at $T = 15.5$ K was found by AC susceptibility measurements. The $M(H)$ dependence is also uncommon for a ferromagnet. It is almost linear in low fields, then slowly saturates up to $\mu_0 H = 2$ T, showing no remanence and practically no hysteresis (Chevalier et al. 1996a). This behaviour led to a conjecture about glassy state, caused by to the random Si–Pd distribution. A weak ferromagnetism with magnetization of $0.22\,\mu_B$/U in $m_0 H = 2$ T at $T = 4.2$ K was reported for *U_2IrSi_3* (Chevalier et al. 1996a).

The same type of anisotropy as in the Ni-compound exists in *U_2PtSi_3*, which becomes ferromagnetic below $T_C = 8$ K (Sato et al. 1991, 1992c). The effective moment found in a single crystal is much lower than in the Ni-compound (see table 5.25). It is not possible to determine ordered moments of uranium from the low-temperature magnetization curves, as the $M(H)$ dependencies shows strong negative curvature in fields up to 9 T. The remanence in fields along the basal plane corresponds to about $0.25\,\mu_B$/U. The specific heat experiments do not show any sharp transition. This and the high γ-value (200 mJ/(mol U K^2)) led to the conclusion of weak itinerant character of the magnetism in this compound.

U_2CuSi_3 crystallizes in the tetragonal structure of the α-$ThSi_2$ type. Similar to other U_2TSi_3 compounds it undergoes ferromagnetic ordering and reaches a magnetization of

0.52 μ_B/U in $\mu_0 H = 3$ T (Kaczorowski and Noël 1993). Other parameters are shown in table 5.25.

U_2CuGa_3 was originally reported to form also in the AlB_2 structure type (Tran et al. 1993). However, detailed neutron diffraction experiments (Tran et al. 1995c) revealed a superstructure leading probably to the Lu_2CoGa_3 (or alternatively Eu_2RhSi_3) structure type, both having the space group $P6_3/mmc$ (Gladyshevskii et al. 1992). A cusp in the $\chi(T)$ curve at $T = 15$ K is reminiscent of an AF transition, but no sign of magnetic order was seen in the low-temperature neutron diffraction. Based on significant magnetic history phenomena, speculations as to a spin glass origin of the maximum in the $\chi(T)$ data were made. A hexagonal lattice with AF interactions can indeed yield frustration necessary for spin-glass effects, but unlike ternaries with random occupation of the boron sites (all silicides mentioned above), the structure types envisaged for U_2CuGa_3 are true ordered ternaries with lack of randomness. Therefore the interpretation in terms of long-range AF order with frustrated structure and small moments ($\mu_U < 0.3\ \mu_B$) is to our opinion a more plausible one.

U_2TGa_3 compounds with T = Ru, Rh, Ir, Pd, and Pt, were found to form in the orthorhombic $CaCu_2$ structure, as found also for UTGe and UTSi (Tran 1996). A very flat $\rho(T)$ behaviour characteristic for all of them except for U_2RuGa_3 ($\rho_0/\rho_{300\,K} \approx 0.5$) is indeed suggestive of a statistical occupation of the Cu sites. All the compounds are magnetically ordered (Tran 1996). For more details see table 5.25. Ferromagnetism dominates for a T metals with less filled d-shell (Ru, Rh, Ir). From magnetization measurements spontaneous moments of 0.9 μ_B/U, 0.4 μ_B/U, and 0.6 μ_B/U, respectively, were estimated. U_2PdGa_3 is antiferromagnetic, which is probably also the case of U_2PtGa_3, in which the apparent ferromagnetic transition between 70 and 80 K, introducing a weak spontaneous moment, is probably due to a small amount of spurious UPtGa.

5.9.11. $U_2T_3Al_9$ and $U_2T_3Ga_9$

4 compounds with T = Rh and Ir were synthesized in the orthorhombic structure of the $Y_2Co_3Ga_9$ type (space group Cmcm). They order antiferromagnetically between 7.5 K ($U_2Ir_3Ga_9$) and 35 K ($U_2Rh_3Al_9$). For details see table 5.25 and the report of Buschinger et al. (1997).

5.9.12. Borocarbides

A large interest in rare-earth based borocarbides, in which superconductivity coexists with magnetic ordering, led to the synthesis of several isotypic Th and U compounds, summarized in table 5.25. Their tetragonal structure of the $LuNi_2B_2C$-type is considered as a filled version of the body-centered $ThCr_2Si_2$ structure, in which C atoms are inserted into the layer of Lu atoms (Siegrist et al. 1994). Two U-borocarbides have been successfully synthesized (Takabatake et al. 1994). *UNi_2B_2C* is antiferromagnet with a rather high value of T_N (218 K) where a pronounced cusp in the $\chi(T)$ curve is observed. Below T_N, the susceptibility decreases markedly and reaches about 1.5×10^{-8} m^3/mol in the low-temperature limit. The high-temperature part is accounted for by the Curie–Weiss law, with parameters given in table 5.25.

A somewhat lower ordering temperature (185 K) and ferromagnetic order was found in *URh_2B_2C* (Takabatake et al. 1994). The spontaneous magnetization at $T = 4.2$ K corresponds approximately to 0.52 μ_B/U. The two compounds were not found to be

superconducting. Their $\rho(T)$ dependencies are practically identical up to 100 K, showing a pure quadratic increase with the rather small coefficient $a = 0.0033$ $\mu\Omega$ cm K^{-2} and $\rho_0 \approx 3$ $\mu\Omega$ cm. The ordering temperatures are manifest in both cases as a standard kink (more pronounced in case of URh_2B_2C) without any sign of a maximum. The high-temperature parts increase monotonously reaching 180 $\mu\Omega$ cm for URh_2B_2C and 145 $\mu\Omega$ cm for UNi_2B_2C, both at $T = 300$ K. The absence of any exponential term in the low-temperature resistivity behaviour points to an Ising-like magnetism with moments along the c-axis and a high anisotropy disabling collective spin excitations (magnons). Geometrical considerations lead us to assume that the high ordering temperatures (exceeding even those of UT_2X_2 compounds) are due to strong U–U coupling within the basal plane, where the inter-uranium spacing is about the Hill limit (see table 5.25). On the other hand, the spacing along c is much larger ($\approx$ 500 pm) which implies that the c-axis coupling is weaker.

Two ThT_2B_2C compounds were found superconducting, namely $ThPt_2B_2C$ ($T_c = 6.7$ K) and $ThNi_2B_2C$ ($T_c = 6.5$ K), whereas for the Rh-compound no superconductivity was found down to 1.3 K (Takabatake et al. 1994).

5.9.13. UNi_4B

This compound crystallizes in the hexagonal $CeCo_4B$ structure and orders antiferromagnetically below $T_N = 20$ K (Mentink et al. 1993). The crystal structure, derived from the binary $CaCu_5$ type, is characterized by a short U–U-spacing $d_{U-U} = 348$ pm along c, whereas the inter-uranium spacing within the hexagonal basal planes is equal to $a = 495.2$ pm (see table 5.25). The unique magnetic structure (Mentink et al. 1994) consists of two U sub-systems, one forming a true three-dimensional antiferromagnetic structure, the other, involving 1/3 of U atoms, forms linear ferromagnetic chains along c, which remain free down to lowest temperatures due to geometrical frustration (see fig. 5.136). Such unusual situation affects seriously the bulk properties. The magnetic

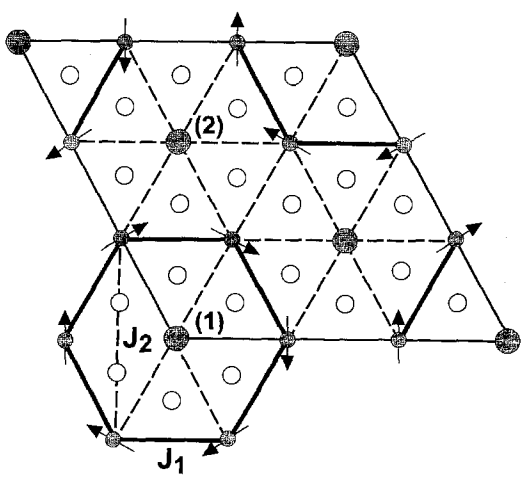

Fig. 5.136. Magnetic structure of hexagonal UNi_4B projected on the basal plane. The magnetic U-layers are ferromagnetically stacked along c. The thin solid lines represent the magnetic unit cell (after Nieuwenhuys et al. (1995)). The U-moments indicated by (1) and (2) located in the centre and in between the magnetic vortices (thick lines) form ferromagnetic linear chains along c.

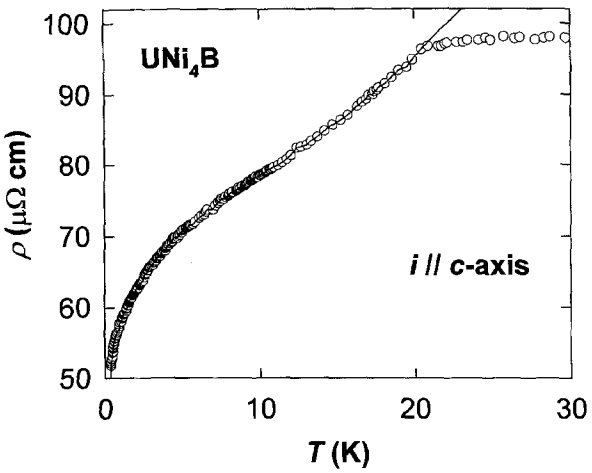

Fig. 5.137. Electrical resistivity ρ vs. temperature T for a single crystal of UNi_4B. The current i was applied along c. The solid line represents the fit mentioned in the text. After Mentink et al. (1995a).

susceptibility (Mentink et al. 1993) follows the Curie–Weiss law at high temperatures for $H \| ab$-plane. Below T_N a broad maximum develops in low fields around $T = 7$ K ($\chi_{max} \approx 32 \times 10^{-8}$ m^3/mol in $\mu_0 H = 0.5$ T), which can be suppressed in higher fields making the cusp at T_N more apparent. The susceptibility for $H \| c$, which is clearly the hard magnetization direction, is weak ($\approx 5 \times 10^{-8}$ m^3/mol) and weakly T-dependent (Mentink et al. 1993). The easy-plane anisotropy is demonstrated also by magnetization measurements at $T = 4.2$ K. While the response to field along c is weak and linear, the field along a or b can induce a sequence of metamagnetic (spin-flop) transitions. The highest transition occurs at 19.8 T, and is followed by a gradual saturation tendency, attributed to the paramagnetic chains, which was traced up to $\mu_0 H = 52$ T (Mentink et al. 1993, 1995b). The estimated saturated magnetization of $1.2\,\mu_B$/U corresponding to U-moments obtained for the ordered sub-system by neutron diffraction (Mentink et al. 1994), suggests that the magnitude of all U-moments is equal in the high-field limit. The electrical resistivity ρ is strongly anisotropic, reflecting the ferromagnetic coupling along c and leading to a simple temperature independent resistivity for current i along c. Below T_N, ρ starts to decrease, as in a ferromagnet. For $i \| ab$-plane, ρ is much higher (about 250 $\mu\Omega$ cm compared to about 100 $\mu\Omega$ cm at room temperature for the previous geometry), and increases weakly with decreasing T (Mentink et al. 1993). In both geometries, the resistivity starts to fall rapidly below $T = 5$ K (figs 5.137 and 5.138). For $i \| c$, it was well described assuming $\rho = AT^{0.11} + BT^2$. The second term was attributed by Mentink et al. (1995a) to spin wave excitations within the AF network, the first term to an increase of the correlation length with decreasing temperature in the one-dimensional chains. The temperature dependence of the specific heat shows a pronounced λ-type anomaly at T_N in zero field (fig. 5.139). The C/T vs. T curve increases with decreasing temperature below 5 K, leading to the large value $\gamma \approx 470$ mJ/(mol K^2). This upturn, attributed to 1D excitations in

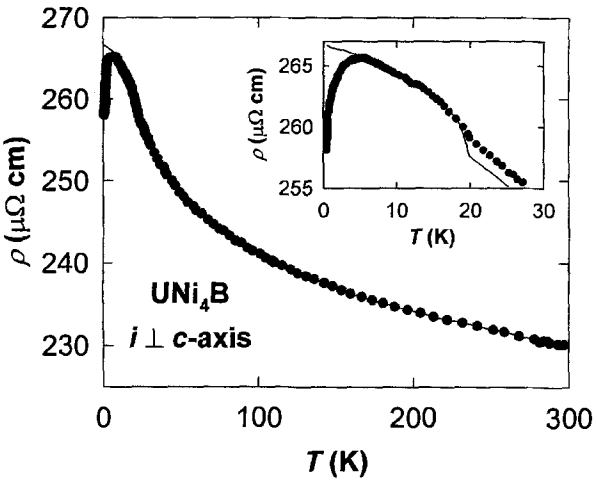

Fig. 5.138. Electrical resistivity ρ with current i perpendicular to c vs. temperature T for a single crystal of UNi_4B. The inset shows a low-temperature detail. After Mentink et al. (1995a).

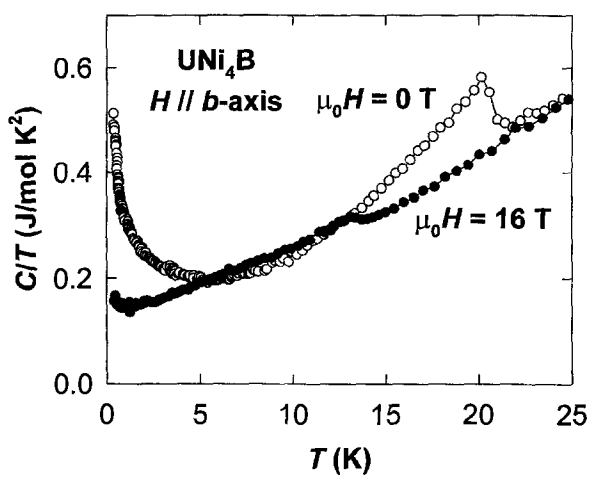

Fig. 5.139. Temperature dependence of the specific heat (in the C/T vs. T representation) for a single crystal of UNi_4B, measured in zero field (open circles) and in $\mu_0 H = 16$ T applied along the b-axis (full circles). After Mentink et al. (1997b).

the chains, is suppressed by a magnetic field ($H \| b$), which also shifts down the Néel transition. A possibility of Kondo compensation of U-moment in the 1D chains by the Kondo effect arising due to the geometrical frustration was suggested by Lacroix et al. (1996).

UCo_4B forms in the same structure type but remains paramagnetic and shows spin fluctuation features. The high-temperature part of the $\chi(T)$ data follows modified Curie–Weiss law (parameters are given in table 5.25) and saturates below about 100 K on level of

8×10^{-8} m^3/mol (Nakotte et al. 1993c). The low temperature upturn seen below $T = 20$ K is probably extrinsic. The magnetization studied at $T = 4.2$ K shows a weak S-shape with an inflection around $\mu_0 H = 30$ T, although no clear tendency to saturation was observed up to 50 T, where magnetization corresponding to 0.65 μ_B/U was found on a free-powder sample (Nakotte et al. 1993c). The C/T vs. T dependence shows a weak upturn below $T = 5$ K, which can be described by the additional logarithmic term (eq. (3.3)) yielding a value of $\gamma = 62$ mJ/(mol K^2). The $\rho(T)$ data follow a quadratic power law below $T = 14$ K, with the coefficient $a = 0.0152$ μΩ cm K^{-2}. A gradual resistivity saturation at $T > 100$ K is consistent with the spin-fluctuation picture.

5.9.14. Other borides

A large variety of ternary actinide borides is described in the excellent review of Rogl (1991), dealing primarily with structures and phase equilibria, but including also information on magnetic properties. For the fundamental research of the electronic structure, the group of monoborides UT_3B_x has been very important. It is based on cubic compounds of the UT_3 type, in which B atoms occupy interstitial positions in the centre of the unit cell. The B concentration can vary between 0 and 1 which enables to tune the 5f-localization probably mainly by expanding the lattice. These systems were reviewed already by Sechovsky and Havela (1988). Of later works, a single-crystal study of the strongly anisotropic spin fluctuator URu_4B_4 (Mentink et al. 1992) deserves a special attention.

5.9.15. Carbides

From the large family of U ternary carbides, only a small fraction has been studied including their magnetic properties. One example is UAl_3C_3, which crystallizes in a complicated hexagonal structure (space group $P6_3/mmc$) determined for $ScAl_3C_3$ (Gesing et al. 1992 and references given by these authors). The modified Curie–Weiss law observed above $T = 30$ K leads to parameters given in table 5.25. A maximum in the susceptibility at $T = 11$ K marks probably the onset of AF ordering. A pronounced hysteretic metamagnetic transition with critical field around 1.5 T leads to a high-field magnetization of 0.27 μ_B/U at $T = 5$ K. As described by Gesing et al. (1992), the Al carbides are characterized by strong Al–C covalent bonding. Despite the short Al–Al spacings, there is little or no Al–Al interaction, which leads to a non-metallic character of materials like Al_4C_3. Similar bonding characteristics can be expected for UAl_3C_3, the structure of which can be deduced from the binary carbide by inserting U basal plane layers. Thus there is a high U–U coordination within each layer, each U-atom has six U neighbors at 339 pm, whereas the inter-layer U–U spacing is about 870 pm. Therefore we can expect a weak AF inter-layer magnetic coupling, which can be broken in moderate magnetic fields. Of the other carbides, a majority belongs to weak paramagnets, e.g., $UCrC_2$, UCr_4C_4, UW_4C_4, and $U_5Re_3C_8$, studied by Vomhof et al. (1993). U_2NiC_3 is antiferromagnetic below $T_N = 52$ K. Further information can be found in the report of Vomhof et al. (1993) and references given therein. One of the most prominent ternary U carbides is U_2PtC_2, known as an exotic superconductor with the enhanced value $\gamma = 75$ mJ/(mol U K^2) (Meisner et al. 1984). Its magnetic susceptibility is weakly temperature dependent, increasing from 1.9×10^{-8} m^3/mol U at $T = 150$ K to 2.8×10^{-8} m^3/mol U at $T = 4$ K (Meisner et al. 1984). Its superconductivity below $T_c = 1.47$ K was discovered already in 1969 (Matthias et al. 1969). The

critical temperature T_c is reduced by pressure ($\partial T_c/\partial p = -53$ mK/kbar). The superconductivity is rapidly suppressed by small substitutions of Os or Ir for Pt (Killer et al. 1994), which leads to a strengthening of the magnetic correlations manifest in the strong low-temperature upturn in the $\chi(T)$ and $C/T(T)$ curves. The terminal phases U_2IrC_2 and U_2OsC_2 are non-magnetic (for basic data see table 5.25).

5.9.16. Phosphides and arsenides

$U_2Cu_4As_5$ crystallizes in the body-centered tetragonal structure (space group I4/mmm). U-atoms form square-lattice layers (intra-layer $d_{U-U} = 399$ pm), whereas individual U layers are separated by as many as five non-magnetic layers. The co-ordination is similar as in $UCuAs_2$ (see section 5.7.1), and similar to that compound a covalent Cu–As bonding and ionic U–As bonding can be considered. The prominent feature in the temperature dependence of the susceptibility is a pronounced cusp at $T = 189$ K, marking the AF transition. At high T, a modified Curie–Weiss law with parameters given in table 5.25 was observed for a powder sample. There is a shallow minimum at $T \approx 150$ K followed by a weak increase and saturation in the low-temperature limit. The electrical resistivity studied on a single crystal has a metallic character. Above T_N, the $\rho(T)$ curve is flat (on a level of 220 $\mu\Omega$ cm) and shows a weak negative slope. T_N is marked as a pronounced decrease, gradually tending to saturation with a very low residual value ($\rho_0 = 4$ $\mu\Omega$ cm). The resistance shows thus features typical of an antiferromagnet, and we thus can speculate about the ferromagnetic nature of intra-plane coupling. This is corroborated by the high positive value $\Theta_p = 168$ K, pointing to a dominance of ferromagnetic coupling.

UMn_4P_2 crystallizes in the tetragonal structure of the $ZrFe_4P_2$ type. It shows two AF transitions, ascribed to the ordering of the Mn (at 125 K) and U (22 K) sublattice (Jeitschko et al. 1990).

The structure of phosphide *$U_3Ni_{3.34}P_6$* (space group P4/mmm) consists of alternating slabs of $AuCu_3$ and $ThCr_2Si_2$ structures (Ebel and Jeitschko 1995), leading to two different U-sites. Neutron diffraction shows that two types of ferromagnetic basal-plane U-layers are coupled antiparallel leading to ferrimagnetic ordering below $T = 139$ K (Reehuis et al. 1996). The U-moments are equal to $(1.4 \pm 0.1)\ \mu_B$ and $(1.6 \pm 0.2)\ \mu_B$, and are aligned along c, as expected for the shorter spacing $d_{U-U} = 382$ pm within each layer. The different temperature variations of the magnetization in each sublattice can explain the complicated non-monotonous $M(T)$ dependence in the ordered state, leading to a compensation point at $T = 130$ K.

The quaternary oxiphosphide *UCuPO* crystallizes in the tetragonal ZrCuSiAs structure type (space group P4nmm). It displays a relatively high AF ordering temperature 220 K. For details see table 5.25 and the report of Kaczorowski et al. (1994).

One of the most thoroughly studied ternary U-phosphides is *UFe_4P_{12}*. It crystallizes in the body-centered cubic structure with space group Im3 (Jeitschko and Braun 1977), leading to a large spacing $d_{U-U} = 673$ pm. Unlike superconducting $LaFe_4P_{12}$ and other rare-earth and Th isotypes displaying a metallic behaviour, only $CeFe_4P_{12}$ and UFe_4P_{12} show a semiconducting character of the electrical resistivity. The value of the resistivity at low temperatures is 6–7 orders of magnitudes larger than the value at room temperature (Meisner et al. 1985; Torikachvili et al. 1987), which points to a hybridization gap. Specific heat and magnetization measurements revealed ferromagnetic ordering at $T_C = 3.15$ K

(Torikachvili et al. 1986), which classifies UFe_4P_{12} as a ferromagnetic superconductor. A magnetization corresponding to a moment of $1.2\,\mu_B$/U was achieved at $T = 1.9$ K in a field of 3 T. High pressure studies (Guertin et al. 1987) show a relatively strong increase of T_C (compared to $NdFe_4P_{12}$) with $\partial T_C/\partial p \approx 0.26$ K/kbar.

5.9.17. Sulfides and selenides

$U_3Cu_2S_7$ and $U_3Cu_2Se_7$ crystallize in a hexagonal structure with space group $P6_3$. For details see the report of Daoudi et al. (1996a). Whereas the sulfide can be classified as spin fluctuator on the basis of susceptibility data, the selenide shows a cusp attributed to AF ordering at $T = 13$ K.

5.9.18. Hexagonal Laves phases with early d-metals

Although U-binaries with close packed structures of the Laves phase type are formed only for late transition metals starting from the Mn column, compounds with Mo and Cr can be stabilized in the hexagonal Laves phase structure $MgZn_2$ if the transition metal is partly replaced by Si. This leads to a statistical distribution of Si and transition-metal atoms. Materials with an extended stability range around $U_4Mo_5Si_3$ and $U_4Cr_6Si_2$ were synthesized by Le Bihan et al. (1996b). The compounds behave as weak paramagnets due to very small d_{U-U}.

5.9.19. Chevrel phases

From ternary molybdenum chalcogenides containing U, $U_{0.82}Mo_6Se_8$ was identified as a weak ferromagnet below $T = 25$ K. For further information see the report of Daoudi et al. (1996b).

Acknowledgements

We are very grateful to Prof. A.V. Andreev, Drs. M. Diviš, H. Nakotte, K. Prokeš and P. Svoboda for stimulating discussions and critical reading of the manuscript, and to Dr. P. Svoboda, S. Syshchenko and T. Khmelevska for assistance in preparation of figures. Most of our results could not be achieved without support received from the Alexander von Humboldt Foundation, the University of Amsterdam, Japan Society for Promotion of Science, the U.S.–Czechoslovak Science and Technology Joint Fund (project # 93039), the Grant Agency of the Charles University (projects # 312, 40/97) and the Grant Agency of the Czech Republic (projects # 202/93/0184, 202/94/0454, 202/96/0207, and 202/95/0008).

References

Akazawa, T., T. Suzuki, F. Nakamura, T. Fujita, T. Takabatake and H. Fujii, 1996a, J. Phys. Soc. Japan **65**, 3661.

Akazawa, T., T. Suzuki, T. Fujita, S. Nishizaki, F. Nakamura, Y. Maeda, T. Takabatake and H. Fujii, 1996b, Physica B **224**, 218.

Akselrud, L.G., Y.P. Yarmolyuk and E.I. Gladishevskii, 1978, Dopov. Akad. Nauk Ukr. RSR **A4**, 359.

Albers, R.C., A.M. Boring, G.H.O. Daalderop, and F.M. Mueller, 1987, Phys. Rev. B **36**, 3661.

Allen, J.W., L.Z. Liu, R.O. Anderson, C.L. Seaman, M.B. Maple, Y. Dalichaouch, J.S. Kang,

M.S. Torikachvili and M.L. de la Torre, 1993, Physica B **186–188**, 307.

Amato, A., R. Feyerherm, F.N. Gygax, A. Schenck, M. Weber, R. Caspary, P. Hellmann, C. Schank, C. Geibel, F. Steglich, D.E. MacLaughlin, E.A. Knetsch and R.H. Heffner, 1992a, Europhys. Lett. **19**, 127.

Amato, A., C. Geibel, F.N. Gygax, R.H. Heffner, E. Knetsch, D.E. MacLaughlin, C. Schank, A. Schenck, F. Steglich and G. Weber, 1992b, Z. Phys. B **86**, 159.

Amitsuka, H. and T. Sakakibara, 1994, J. Phys. Soc. Japan **63**, 736.

Amitsuka, H., K. Hyomi, T. Nishioka, Y. Miyako, and T. Suzuki, 1988, J. Magn. Magn. Mater. **76–77**, 168.

Amitsuka, H., T. Sakakibara and Y. Miyako, 1990a, J. Magn. Magn. Mater. **90–91**, 517.

Amitsuka, H., T. Sakakibara, Y. Miyako, K. Sugiyama, A. Yamagishi and M. Date, 1990b, J. Magn. Magn. Mater. **90–91**, 47.

Amitsuka, H., K. Tateyama, C.C. Paulsen, T. Sakakibara and Y. Miyako, 1992a, J. Magn. Magn. Mater. **104**, 60.

Amitsuka, H., T. Sakakibara, K. Sugiyama, T. Ikeda, Y. Miyako, M. Date and A. Yamagishi, 1992b, Physica B **177**, 173.

Amitsuka, H., T. Hidano, T. Honma, H. Mitamura, and T. Sakakibara, 1993, Physica B **186–188**, 337.

Amitsuka, H., T. Hidano, T. Sakakibara, T. Suzuki, T. Akazawa and T. Fujita, 1995a, J. Magn. Magn. Mater. **140**, 1403.

Amitsuka, H., T. Shimamoto, T. Honma and T. Sakakibara, 1995b, Physica B **206–207**, 461.

Amitsuka, H., T. Sakakibara, A. de Visser, F.E. Kayzel and J.J.M. Franse, 1997, Physica B **230–232**, 613.

Amoretti, G., A. Blaise and J. Mulak, 1984, J. Magn. Magn. Mater. **42**, 65.

Andersen, H.N., 1980, in: Crystalline fields and structural effects in f-electron systems, eds J.E. Crow, R.P. Guertin and T.W. Mihalishin (Plenum, New York) pp. 373–387.

Andersen, N.H. and H. Smith, 1979, Phys. Rev. B **19**, 384.

Andreev, A.V., 1985a, Phys. Met. Metallogr. **60**, 193.

Andreev, A.V., 1985b, Sov. Phys. Solid State **27**, 1145.

Andreev, A.V., 1986, personal communication.

Andreev, A.V., 1990, Phys. Met. Metallogr. **69**(5), 68.

Andreev, A.V., 1997, personal communication.

Andreev, A.V., 1998, personal communication.

Andreev, A.V. and M.I. Bartashevich, 1986, Phys. Met. Metallogr. **62**(2), 50.

Andreev, A.V. and W. Suski, 1992, J. Alloys Comp. **187**, 381.

Andreev, A.V. and S.M. Zadvorkin, 1997, Physica B **237–238**, 512.

Andreev, A.V., K.P. Belov, A.V. Deryagin, R.Z. Levitin and A. Menovsky, 1979, J. Phys. (Paris) **40** (Suppl. 4), 82.

Andreev, A.V., A.V. Deryagin and R.Y. Yumagushin, 1984a, Sov. Phys.–JETP **59**, 1082.

Andreev, A.V., M. Zeleny, L. Havela and J. Hrebik, 1984b, Phys. Status Solidi A: **81**, 307.

Andreev, A.V., L. Havela, M. Zeleny and J. Hrebik, 1984c, Phys. Status Solidi A: **82**, 191.

Andreev, A.V., M.I. Bartashevich, A.V. Deryagin, L. Havela and V. Sechovsky, 1986, Phys. Status Solidi A: **98**, K47.

Andreev, A.V., S.V. Andreev and E.N. Tarasov, 1991, J. Less-Common Metals **167**, 255.

Andreev, A.V., W. Suski and N.V. Baranov, 1992a, J. Alloys Comp. **187**, 293.

Andreev, A.V., F.G. Vagizov, W. Suski and H. Drulis, 1992b, J. Alloys Comp. **187**, 401.

Andreev, A.V., H. Nakotte and F.R. de Boer, 1992c, J. Alloys Comp. **182**, 55.

Andreev, A.V., Y.V. Scherbakova, T. Goto and W. Suski, 1993a, J. Alloys Comp. **198**, 43.

Andreev, A.V., W. Suski, F.G. Vagizov and H. Drulis, 1993b, Physica B **186–188**, 730.

Andreev, A.V., H. Aruga Katori and T. Goto, 1995a, J. Alloys Comp. **224**, 117.

Andreev, A.V., H. Aruga Katori and T. Goto, 1995b, J. Alloys Comp. **224**, 86.

Andreev, A.V., M.I. Bartashevich, H. Nakotte, K. Prokes, F.R. de Boer, V. Sechovsky, L. Havela and T. Goto, 1995c, J. Alloys Comp. **224**, 89.

Andreev, A.V., L. Havela, V. Sechovsky, R. Kuzel, H. Nakotte, K.H.J. Buschow, J.H.V.J. Brabers, F.R. de Boer, E. Brück, M. Blomberg and M. Merisalo, 1995d, J. Alloys Comp. **224**, 244.

Andreev, A.V., M.I. Bartashevich and T. Goto, 1995e, J. Alloys Comp. **219**, 267.

Andreev, A.V., H. Aruga Katori, T. Goto, V. Sechovsky and L. Havela, 1995f, J. Magn. Magn. Mater. **140**, 1383.

Andreev, A.V., M.I. Bartashevich, H. Aruga Katori and T. Goto, 1995g, J. Alloys Comp. **216**, 221.

Andreev, A.V., M.I. Bartashevich, S.S. Sigaev, D.A. Andreev, W. Suski, K. Wochowski and T. Goto, 1995h, J. Alloys Comp. **230**, 30.

Andreev, A.V., V. Sechovsky, L. Havela, J. Sebek, M.I. Bartashevich, T. Goto, K. Kamishima, D.A. Andreev, V.S. Gaviko, R.V. Dremov and I.K. Kozlovskaya, 1996a, Czech. J. Phys. **46**, 3385.

Andreev, A.V., L. Havela, V. Sechovsky, H.A. Katori and T. Goto, 1996b, J. Alloys Comp. **235**, 72.

Andreev, A.V., M.I. Bartashevich, T. Goto, K. Kamishima, L. Havela and V. Sechovsky, 1997a, Phys. Rev. B **55**, 5847.

Andreev, A.V., L. Havela, V. Sechovsky, M.I. Bartashevich, T. Goto and K. Kamishima, 1997b, Physica B **239**, 88.

Andreev, A.V., L. Havela, V. Sechovsky, M.I. Bartashevich, T. Goto and K. Kamishima, 1997c, J. Magn. Magn. Mater. **169**, 229.

Andreev, A.V., R.V. Dremov, M.I. Bartashevich, T. Goto, L. Havela and V. Sechovsky, 1997d, Physica B **230–232**, 68.

Andreev, A.V., V. Sechovsky, L. Havela, M.I. Bartashevich, T. Goto, R.V. Dremov and I.K. Kozlovskaya, 1997e, Physica B **237–238**, 224.

Andreev, A.V., L. Havela, V. Sechovsky, M.I. Bartashevich, R.V. Dremov and I.K. Kozlovskaya, 1997f, Philos. Mag. B **75**, 827.

Andreev, A.V., Y. Homma, Y. Shiokawa and V. Sechovsky, 1998a, J. Alloys Comp., in press.

Andreev, A.V., I.K. Kozlovskaya and V. Sechovsky, 1998b, J. Alloys Comp. **165**, 38.

André, G., F. Bourée, K. Wochowski and W. Suski, 1997, Solid State Commun. **104**, 189.

Andres, K., D. Davidov, P. Dernier, F. Hsu, W.A. Reed and G.J. Nieuwenhuys, 1978, Solid State Commun. **28**, 405.

Andress, K.R. and E. Alberti, 1935, Z. Metallkde **27**, 12.

Ansorge, V. and A. Menovsky, 1968, Phys. Status Solidi **30**, K31.

Antonov, V.N., A.Y. Perlov, P.M. Oppeneer, A.N. Yaresko and S.V. Halilov, 1996, Phys. Rev. Lett. **77**, 5253.

Aoki, Y., T. Suzuki, T. Fujita, H. Kawanaka, T. Takabatake and H. Fujii, 1990, J. Magn. Magn. Mater. **90–91**, 496.

Aoki, Y., T. Suzuki, T. Fujita, T. Takabatake, S. Miyata and H. Fujii, 1992, J. Phys. Soc. Japan **61**, 684.

Aoki, Y., T. Suzuki, T. Fujita, H. Kawanaka, T. Takabatake and H. Fujii, 1993a, Phys. Rev. B **47**, 15060.

Aoki, Y., H. Sato, T. Fukuhara, S. Takayanagi, Y. Onuki and N. Wada, 1993b, Physica B **186–188**, 738.

Aoki, Y., Y. Kobayashi, H. Sato, H. Sugawara, V. Sechovsky, L. Havela, K. Prokes, M. Mihalik and A. Menovsky, 1996a, J. Phys. Soc. Japan **65**, 3312.

Aoki, Y., Y. Kobayashi, H. Sato, H. Sugawara, V. Sechovsky, L. Havela, K. Prokes, M. Mihalik and A.A. Menovsky, 1996b, Czech. J. Phys. **46**, 2015.

Arko, A.J., D.D. Koelling and B. Reihl, 1983, Phys. Rev. B **27**, 3955.

Arko, A.J., J.J. Joyce, A.B. Andrews, J.D. Thompson, J.L. Smith, E. Moshopoulou, Z. Fisk, A.A. Menovsky, P.C. Canfield and C.G. Olson, 1997a, Physica B **230–232**, 16.

Arko, A.J., J.J. Joyce, A.B. Andrews, J.D. Thompson, J.L. Smith, D. Mandrus, M.F. Hundley, A.L. Cornelius, E. Moshopoulou, Z. Fisk, P.C. Canfield, and A. Menovsky, 1997b, Phys. Rev. B **56**, R7041.

Arko, A.J., J.J. Joyce, A.B. Andrews, D. Mandrus, E. Moshopoulou, Z. Fisk and P.C. Canfield, 1997c, Philos. Mag. B **75**, 603.

Asti, G., 1990, in: Ferromagnetic Materials, Vol. 5, eds K.H.J. Buschow and E.P. Wohlfarth (North-Holland, Amsterdam) pp. 398–464.

Baer, Y., H.R. Ott and K. Andres, 1980, Solid State Commun. **36**, 387.

Bakker, K., A. de Visser, E. Brück, A.A. Menovsky and J.J.M. Franse, 1992, J. Magn. Magn. Mater. **108**, 63.

Bakker, K., A. de Visser, A.A. Menovsky and J.J.M. Franse, 1993a, Physica B **188**, 720.

Bakker, K., A. de Visser, L.T. Tai, A.A. Menovsky, and J.J.M. Franse, 1993b, Solid State Commun. **86**, 497.

Ballou, R., C. Lacroix and M.D. Núnez-Regueiro, 1991, Phys. Rev. Lett. **66**, 1910.

Bara, J.J., H.U. Hrynkiewicz and A. Szytula, 1991, J. Less-Common Metals **175**, 259.

Baran, A. and P. de V. du Plessis, 1993, Physica B **186–188**, 781.

Baran, A., W. Suski and T. Mydlarz, 1984, J. Less-Common Metals **96**, 269.

Baran, A., W. Suski and T. Mydlarz, 1985, Physica B **130**, 219.

Baran, A., W. Suski, O.J. Zogal and T. Mydlarz, 1986, J. Less-Common Metals **121**, 175.

Baran, A., W. Suski and T. Mydlarz, 1987, J. Magn. Magn. Mater. **63–64**, 196.

Bazela, W. and A. Szytula, 1989, J. Magn. Magn. Mater. **82**, 151.

Becker, B., S. Ramakrishnan, S. Süllow, C.C. Mattheus, C.E. Snel, G.J. Nieuwenhuys and J.A. Mydosh, 1997, Physica B **230–232**, 83.

Benakki, M., A. Quachau and P. Panissod, 1988, J. Magn. Magn. Mater. **73**, 141.

Benedict, U., 1993, J. Alloys Comp. **193**, 88.

Berlureau, T., 1991, Thesis, University of Bordeaux.

Berlureau, T., B. Chevalier, L. Fournès, and J. Etourneau, 1989, Mater. Lett. **9**, 21.

Berlureau, T., B. Chevalier, P. Gravereau, L. Fournès and J. Etourneau, 1991, J. Magn. Magn. Mater. **102**, 166.

Berlureau, T., P. Gravereau, B. Chevalier, and J. Etourneau, 1993, J. Solid State Chem. **104**, 328.

Bernal, O.O., D.E. MacLaughlin, A. Amato, R. Feyerherm, F.N. Gygax, A. Schenck, R.H. Heffner, L.P. Le, G.J. Nieuwenhuys, B. Andraka, H. von

Löhneysen, O. Stockert and H.R. Ott, 1996, Phys. Rev. B **54**, 13000.

Besnus, M.J., M. Benakki, J.P. Kappler, P. Lehmann, A. Meyer and P. Panissod, 1988, J. Less-Common Metals **141**, 121.

Bogé, M., D. Bonnisseau, P. Burlet, J.M. Fournier, E. Pleska, S. Quezel, J. Rebizant, J. Rossat Mignod, J.C. Spirlet and M. Wulff, 1989, J. Nucl. Mater. **166**, 77.

Bonfait, G., A.P. Gonçalves, J.C. Spirlet, and M. Almeida, 1995, Physica B **211**, 139.

Bonfait, G., M. Godinho, P. Estrela, A.P. Gonçalves, M. Almeida and J.C. Spirlet, 1996, Phys. Rev. B **53**, R480.

Bonn, D.A., J.D. Garrett and T. Timusk, 1988, Phys. Rev. Lett. **61**, 1305.

Bourdarot, F., 1994, Thesis, CENG Grenoble.

Bourée, F., B. Chevalier, L. Fournès, F. Mirambet, T. Roisnel, V.H. Tran and Z. Zolnierek, 1994, J. Magn. Magn. Mater. **138**, 307.

Bourée-Vigneron, F., M. Pinot, A. Oles, A. Baran and W. Suski, 1990, Solid State Commun. **75**, 929.

Böhm, A., D. Kaczorowski, G. Weber and F. Steglich, 1993, J. Alloys Comp. **196**, L11.

Braun, H.F., 1984, J. Less-Common Metals **100**, 105.

Braun, H.F., N. Engel and E. Parthé, 1983, Phys. Rev. B **28**, 1389.

Braun, H.F., T. Jarlborg and A. Junod, 1985, Physica B **135**, 397.

Broholm, C., J.K. Kjems, W.J.L. Buyers, P.T. Matthews, T.T.M. Palstra, A.A. Menovsky and J.A. Mydosh, 1987, Phys. Rev. Lett. **58**, 1467.

Broholm, C., H. Lin, P.T. Matthews, T.E. Mason, W.J.L. Buyers, M.F. Collins, A.A. Menovsky, J.A. Mydosh, and J.K. Kjems, 1991, Phys. Rev. B **43**, 12809.

Brooks, M.S.S. and P.J. Kelly, 1983, Phys. Rev. Lett. **51**, 1709.

Brooks, M.S.S., B. Johansson, O. Eriksson, and H.L. Skriver, 1986, Physica B **144**, 1.

Brück, E., 1991, Hybridization in cerium and uranium intermetallic compounds, Thesis, University of Amsterdam.

Brück, E., F.R. de Boer, V. Sechovsky and L. Havela, 1988, Europhys. Lett. **7**, 177.

Brück, E., F.R. de Boer, P. Nozar, V. Sechovsky, L. Havela, K.H.J. Buschow and A.V. Andreev, 1990, Physica B **163**, 379.

Brück, E., H.P. van der Meulen, A.A. Menovsky, F.R. de Boer, P.F. de Châtel, J.J.M. Franse, J.A.A.J. Perenboom, T.T.J.M. Berendschot, H. van Kempen, L. Havela and V. Sechovsky, 1992, J. Magn. Magn. Mater. **104**, 17.

Brück, E., H. Nakotte, F.R. de Boer, P.F. de Châtel, H.P. van der Meulen, J.J.M. Franse, A.A. Menovsky, N.H. Kim Ngan, L. Havela, V. Sechovsky, J.A.A.J. Perenboom, N.C. Tuan and J. Sebek, 1994, Phys. Rev. B **49**, 8852.

Buffat, B., B. Chevalier, B. Czeska, J. Etourneau, and P. Hagenmuller, 1986, J. Magn. Magn. Mater. **62**, 53.

Bull, M.J., K.A. McEwen, R. Osborn and R.S. Eccleston, 1996, Physica B **223–224**, 175.

Burlet, P., F. Bourdarot, S. Quezel, J. Rossat Mignod, P. Lejay, B. Chevalier and H. Hickey, 1992, J. Magn. Magn. Mater. **108**, 202.

Burlet, P., L.P. Regnault, J. Rossat Mignod, C. Vettier and J. Flouquet, 1994a, J. Magn. Magn. Mater. **129**, 10.

Burlet, P., R. Troc, D. Kaczorowski, H. Noël, and J. Rossat Mignod, 1994b, J. Magn. Magn. Mater. **130**, 237.

Buschinger, B., C. Geibel, M. Weiden, C. Dietrich, G. Cordier, G. Olesch, J. Köhler and F. Steglich, 1997, J. Alloys Comp. **260**, 44.

Buschow, K.H.J., 1987, personal communication.

Buschow, K.H.J. and H.J. van Daal, 1972, in: Proc. AIP, New York, 1971, eds C.D. Graham Jr. and J.J. Rhyne, p. 1464.

Buschow, K.H.J. and A.M. van der Kraan, 1978, J. Phys. F: Metal Phys. **8**, 921.

Buschow, K.H.J. and D.B. de Mooij, 1986, Philips J. Res. **41**, 55.

Buschow, K.H.J., D.B. de Mooij, T.T.M. Palstra, G.J. Nieuwenhuys and J.A. Mydosh, 1985a, Philips J. Res. **40**, 313.

Buschow, K.H.J., J.H.N. van Vucht and W.W. van den Hoogenhof, 1985b, J. Less-Common Metals **50**, 145.

Buschow, K.H.J., E. Brück, R.G. van Wierst, F.R. de Boer, L. Havela, V. Sechovsky, P. Nozar, E. Sugiura, M. Ono, M. Date and A. Yamagishi, 1990, J. Appl. Phys. **67**, 5215.

Buyers, W.J.L. and T.M. Holden, 1985, in: Handbook on the Physics and Chemistry of the Actinides, Vol. 2, eds A.J. Freeman and G.H. Lander (North-Holland, Amsterdam) pp. 239–328.

Buyers, W.J.L., Z. Tun, T. Petersen, T.E. Mason, J.-G. Lussier, B.D. Gaulin and A.A. Menovsky, 1994, Physica B **199**, 95.

Bykovetz, N., W.N. Herman, T. Yuen, C.S. Jee, C.L. Lin and J.E. Crow, 1988, J. Appl. Phys. **63**, 4127.

Canepa, F., P. Manfrinetti, M. Pani and A. Palenzona, 1996, J. Alloys Comp. **234**, 225.

Canfield, P.C., A. Lacerda, J.D. Thompson, G. Sparn, W.P. Beyermann, M.F. Hundley and Z. Fisk, 1992, J. Alloys Comp. **181**, 77.

Cao, N., J.D. Garrett and T. Timusk, 1993, Physica B **191**, 263.

Caspi, E., H. Shaked, H. Pinto, M. Melamud, Z. Hu, O. Chmaissem, S. Short and J.D. Jorgensen, 1998, J. Alloys Comp., in press.

Chabot, B. and E. Parthé, 1985, J. Less-Common Metals **106**, 53.

Chaghule, R.S., R. Nagarjan, L.C. Gupta, R. Vijayaraghavan, A.D. Kylkarni, P. Raj, P. Suryanarayana, A. Sathyamoorthy, K. Shashikala and R.J. Begum, 1991, J. Alloys Comp. **178**, 385.

Chakravarti, A., R. Ranganathan and S.B. Roy, 1992, Phys. Rev. B **46**, 6236.

Chelmicki, L. and J. Leciejewicz, 1983, Solid State Commun. **48**, 177.

Chelmicki, L., J. Leciejewicz and A. Zygmunt, 1985, J. Phys. Chem. Solids **46**, 529.

Chevalier, B., W.X. Zhong, B. Buffat, J. Etourneau, J. Hagenmuller, P. Lejay, L. Porte, T.M. Duc, M.J. Besnus and C. Kappler, 1986, Mater. Res. Bull. **21**, 183.

Chevalier, B., B. Lloret, P. Gravereau, B. Buffat and J. Etourneau, 1988, J. Magn. Magn. Mater. **75**, 13.

Chevalier, B., E. Hickey and J. Etourneau, 1990, J. Magn. Magn. Mater. **90–91**, 499.

Chevalier, B., T. Roisnel and J. Etourneau, 1994, J. Magn. Magn. Mater. **134**, 88.

Chevalier, B., E. Hickey, T. Roisnel, L. Piraux, and J. Etourneau, 1995, J. Magn. Magn. Mater. **140**, 1409.

Chevalier, B., R. Pöttgen, B. Darriet, P. Gravereau and J. Etourneau, 1996a, J. Alloys Comp. **233**, 150.

Chevalier, B., P. Gravereau, T. Berlureau, L. Fournès and J. Etourneau, 1996b, J. Alloys Comp. **233**, 174.

Chevalier, B., F. Fourgeot, D. Laffargue, P. Gravereau, L. Fournès and J. Etourneau, 1997, J. Alloys Comp. **262–263**, 114.

Christides, C., A. Kostikas, G. Zoiuganelis, V. Psycharis, X.C. Koy and R. Grössinger, 1993, Phys. Rev. B **47**, 11230.

Colineau, E., 1996, Thesis, University J. Fourier, Grenoble.

Collins, M.F., B. Shemirani, C.V. Stager, J.D. Garrett, H. Lin, W.J.L. Buyers and Z. Tun, 1993, Phys. Rev. B **48**, 16500.

Continenza, A. and P. Monachesi, 1994, J. Appl. Phys. **75**, 7027.

Cooper, B.R., R. Siemann, D. Yang, P. Thayamballi, and A. Banerjea, 1985, in: Handbook on the Physics and Chemistry of the Actinides, Vol. 2, eds A.J. Freeman and G.H. Lander (North-Holland, Amsterdam) pp. 435–500.

Coqblin, B. and J.R. Schrieffer, 1969, Phys. Rev. **185**, 847.

Corsepius, S., M. Lenkewitz, E.W. Scheidt, and G.R. Stewart, 1996, J. Alloys Comp. **235**, 192.

Cox, D.L., 1987, Phys. Rev. Lett. **59**, 1240.

Cox, D.L., 1993, Physica B **186–188**, 312.

Cuong, T.D., Z. Arnold, J. Kamarad, A.V. Andreev, L. Havela and V. Sechovsky, 1996, J. Magn. Magn. Mater. **158**, 694.

Cywinski, R., B.R. Coles, S.H. Kilcoyne and J.G. Park, 1995, Physica B **206–207**, 412.

Daalderop, G.H.O., F.M. Mueller, R.C. Albers, and A.M. Boring, 1988, J. Magn. Magn. Mater. **74**, 211.

Daams, J.C., P. Villars and J.H.N. van Vucht, 1991, Atlas of Crystal Structure Types for Intermetallic Phases, p. 3654.

Dalichaouch, Y. and M.B. Maple, 1994, Physica B **199–200**, 176.

Dalichaouch, Y., M.B. Maple, M.S. Torikachvili, and A.L. Giorgi, 1989, Phys. Rev. B **39**, 2423.

Dalichaouch, Y., M.B. Maple, J.W. Chen, T. Kohara, C. Rossel, M.S. Torikachvili and A.L. Giorgi, 1990a, Phys. Rev. B **41**, 1829.

Dalichaouch, Y., M.B. Maple, R.P. Guertin, M.V. Kuric, M.S. Torikachvili and A.L. Giorgi, 1990b, Physica B **163**, 113.

Daoudi, A., M. Lamire, J.C. Levet and H. Noël, 1996a, J. Solid State Chem. **123**, 331.

Daoudi, A., M. Potel and H. Noël, 1996b, J. Alloys Comp. **232**, 180.

Date, M., 1968, J. Phys. Soc. Japan **57**, 3682.

Dawson, A.L., W.R. Datars, J.D. Garrett and F.S. Razavi, 1989, J. Phys.: Condens. Matter **1**, 6817.

de Boer, F.R., J.J.M. Franse, E. Louis, A.A. Menovsky, J.A. Mydosh, T.T.M. Palstra, U. Rauchschwalbe, W. Schlabitz, F. Steglich and A. de Visser, 1986, Physica B **138**, 1.

de Boer, F.R., E. Brück, A.A. Menovsky, P.A. Veenhuizen, V. Sechovsky, L. Havela and K.H.J. Buschow, 1989, Physica B **155**, 231.

de Boer, F.R., E. Brück, V. Sechovsky, L. Havela and K.H.J. Buschow, 1990, Physica B **163**, 175.

de Boer, F.R., E. Brück, J.C.P. Klaasse, H. Nakotte, K.H.J. Buschow, L. Havela, V. Sechovsky, P. Nozar, E. Sugiura, M. Ono, M. Date and A. Yamagishi, 1991, J. Appl. Phys. **69**, 4702.

de Boer, F.R., E. Brück, H. Nakotte, A.V. Andreev, V. Sechovsky, L. Havela, P. Nozar, C.J.M. Denissen, K.H.J. Buschow, B. Vaziri, M. Meissner, H. Maletta and P. Rogl, 1992, Physica B **176**, 275.

de Boer, F.R., K. Prokes, H. Nakotte, E. Brück, M. Hilbers, P. Svoboda, V. Sechovsky, L. Havela and H. Maletta, 1994, Physica B **201**, 251.

de Châtel, P.F., K. Prokes, H. Nakotte, A. Purwanto, V. Sechovsky, L. Havela, E. Brück, R.A. Robinson and

F.R. de Boer, 1998, J. Magn. Magn. Mater. **177–181**, 785.

de Groot, R.A., F.M. Mueller, P.G. van Engen, and K.H.J. Buschow, 1983, Phys. Rev. Lett. **50**, 2024.

de Lourdes Pinto, M., 1966, Acta Crystallogr. **21**, 999.

de Novion, C.H., J. Gal and J.L. Buevoz, 1980, J. Magn. Magn. Mater. **21**, 85.

de Visser, A., F.E. Kayzel, A.A. Menovsky, J.J.M. Franse, J. van der Berg and G.J. Nieuwenhuys, 1986, Phys. Rev. B **34**, 8168.

de Visser, A., F.R. de Boer, A.A. Menovsky, and J.J.M. Franse, 1987, Solid State Commun. **64**, 527.

de Visser, A., J.J.M. Franse and J. Flouquet, 1989, Physica B **161**, 324.

de Visser, A., A. Lacerda, J.J.M. Franse and J. Flouquet, 1990, J. Magn. Magn. Mater. **90–91**, 369.

de Visser, A., H. Nakotte, L.T. Tai, A.A. Menovsky, S.A.M. Mentink, G.J. Nieuwenhuys and J.A. Mydosh, 1992, Physica B **179**, 84.

de Visser, A., K. Bakker, L.T. Tai, A.A. Menovsky, S.A.M. Mentink, G.J. Nieuwenhuys and J.A. Mydosh, 1993, Physica B **186–188**, 291.

Delapalme, A., Z. Zolnierek, R. Troc and D. Kaczorowski, 1994, J. Phys. C.: Condens. Matter **6**, 8877.

Dhar, S.K., R.J. Begum, P. Raj, P. Suryanarayana, L.C. Gupta and R. Vijayaraghavan, 1992, Solid State Commun. **83**, 965.

Diehl, J., H. Fischer, R. Kohler, C. Geibel, F. Steglich, Y. Maeda, T. Takabatake and H. Fujii, 1993, Physica B **186–188**, 708.

Dirkmaat, A.J., 1989, Thesis, Rijksuniversiteit Leiden.

Dirkmaat, A.J., T. Endstra, E. Knetsch, J.A. Mydosh, A.A. Menovsky, F.R. de Boer and Z. Tarnawski, 1990a, Phys. Rev. B **41**, 2589.

Dirkmaat, A.J., T. Endstra, E.A. Knetsch, A.A. Menovsky, G.J. Nieuwenhuys and J.A. Mydosh, 1990b, J. Magn. Magn. Mater. **84**, 143.

Dirkmaat, A.J., T. Endstra, A.A. Menovsky, G.J. Nieuwenhuys and J.A. Mydosh, 1990c, Europhys. Lett. **11**, 275.

Divis, M., M. Richter and H. Eschrig, 1994, Solid State Commun. **90**, 99.

Divis, M., M. Olsovec, M. Richter and H. Eschrig, 1995, J. Magn. Magn. Mater. **140–144**, 1365.

Divis, M., M. Richter and M. Olsovec, 1996, unpublished work.

Divis, M., M. Richter and H. Eschrig, 1997, J. Alloys Comp. **255**, 11.

Dmitriev, V.M., V.N. Eropkin, A.M. Gurevich, A.P. Isakina, V.M. Kobelev, A.I. Prokhvatilov, L.V. Shlyk, R. Troc and V.H. Tran, 1991, Fiz. Nizkikh Temp. **17**, 1051.

Doniach, S., 1977a, in: Valence Instabilities and Related Narrow-Band Phenomena, ed. R.D. Parks (Plenum Press, New York) p. 169.

Doniach, S., 1977b, Physica B **91**, 231.

Drost, A., W.G. Haije, E. Frikkee, T. Endstra, G.J. Nieuwenhuys and K.H.J. Buschow, 1993, Solid State Commun. **88**, 327.

Drulis, H., A. Baran, B. Stalinski, W. Suski, R. Felten, F. Steglich and L. Pawlak, 1989, Thermochim. Acta **139**, 219.

du Plessis, P. de V., A.M. Strydom and A. Baran, 1995, Physica B **206–207**, 495.

du Plessis, P. de V., A.M. Strydom and R.P. Gers, 1997, Physica B **230–232**, 610.

Duh, H.M., I.S. Lyubutin, C.S. Wur, K.J. Lin, J.S. Hwang, C. Tien and I.J. Chang, 1995a, J. Magn. Magn. Mater. **145**, 337.

Duh, H.M., I.S. Lyubutin, C.S. Wur, K.J. Lin, J.S. Hwang, I.J. Chang and C. Tien, 1995b, J. Phys.: Condens. Matter **7**, 2165.

Duh, H.M., I.S. Lyubutin and K.D. Lain, 1995c, Phys. Rev. B **52**, 4294.

Duh, H.M., I.S. Lyubutin, C.J. Cheng and M.K. Wu, 1996a, Physica B **217**, 102.

Duh, H.M., I.S. Lyubutin, I.M. Jiang, G.H. Hwang and K.D. Lain, 1996b, J. Magn. Magn. Mater. **153**, 86.

Dunlap, B.D. and G.M. Kalvius, 1985, in: Handbook on the Physics and Chemistry of the Actinides, Vol. 2, eds A.J. Freeman and G.H. Lander (North-Holland, Amsterdam) pp. 329–434.

Dunlap, B.D. and G.H. Lander, 1974, Phys. Rev. Lett. **33**, 1046.

Dwight, A.E., 1969, in: Developments in the Structural Chemistry of Alloy Phases, ed. B.C. Giessen (Plenum, New York) p. 181.

Dwight, A.E., 1974, J. Less-Common Metals **34**, 279.

Dwight, A.E., 1977, Acta Crystallogr. B **33**, 1579.

Dwight, A.E., 1979, J. Nucl. Mater. **79**, 417.

Ebel, T. and W. Jeitschko, 1995, J. Solid State Chem. **116**, 307.

Ehlers, G. and H. Maletta, 1996, Z. Phys. B **99**, 145.

Ejima, T., Y. Kudo, S. Suzuki, T. Takahashi, S. Sato, T. Kasuya, T. Takabatake and T. Ishii, 1993, Physica B **186–188**, 86.

Ejima, T., S. Suzuki, S. Sato, N. Sato, S. Fujimori, M. Yamada, K. Sato, T. Komatsubara, T. Kasuya, Y. Tezuka, S. Shin and T. Ishii, 1994, J. Phys. Soc. Japan **63**, 2428.

Ejima, T., S. Sato, S. Suzuki, S. Fujimori, M. Yamada, N. Sato, Y. Onuki, T. Komatsubara, Y. Tezuka, S. Shin and T. Ishii, 1996, J. Electron Spectrosc. Relat. Phenom. **78**, 147.

El-Sayed, A.H., G.J. Nieuwenhuys, J.A. Mydosh, and K.H.J. Buschow, 1988, J. Phys. F: Metal Phys. **18**, 2265.

Elliot, R.J. and F.A. Wedgwood, 1963, Proc. Phys. Soc. **81**, 846.

Endstra, T., 1992, Electronic properties of some ternary intermetallic uranium compounds, Thesis, Leiden University.

Endstra, T., A.J. Dirkmaat, S.A.M. Mentink, A.A. Menovsky, G.J. Nieuwenhuys and J.A. Mydosh, 1990a, Physica B **163**, 309.

Endstra, T., G.J. Nieuwenhuys, J.A. Mydosh, and K.H.J. Buschow, 1990b, J. Magn. Magn. Mater. **89**, L273.

Endstra, T., S.A.M. Mentink, G.J. Nieuwenhuys, J.A. Mydosh and K.H.J. Buschow, 1990c, J. Phys.: Condens. Matter **2**, 2447.

Endstra, T., G.J. Nieuwenhuys, A.A. Menovsky, and J.A. Mydosh, 1991, J. Appl. Phys. **69**, 4816.

Endstra, T., G.J. Nieuwenhuys, A.A. Menovsky, and J.A. Mydosh, 1992a, J. Magn. Magn. Mater. **108**, 67.

Endstra, T., G.J. Nieuwenhuys, K.H.J. Buschow, and J.A. Mydosh, 1992b, J. Magn. Magn. Mater. **108**, 69.

Endstra, T., B.J. van Rossum, G.J. Nieuwenhuys, and J.A. Mydosh, 1993a, Physica B **186–188**, 778.

Endstra, T., G.J. Nieuwenhuys and J.A. Mydosh, 1993b, Phys. Rev. B. **48**, 9595.

Eriksson, O., B. Johansson and M.S.S. Brooks, 1989, J. Phys.: Condens. Matter **1**, 4005.

Eriksson, O., B. Johansson and M.S.S. Brooks, 1990a, Phys. Rev. B **41**, 7311.

Eriksson, O., M.S.S. Brooks and B. Johansson, 1990b, Phys. Rev. B **41**, 9087.

Estrela, P., M. Godinho, A.P. Gonçalves, M. Almeida and J.C. Spirlet, 1995, J. Alloys Comp. **230**, 35.

Estrela, P., A.P. Gonçalves, M. Godinho, M. Almeida and J.C. Spirlet, 1997, J. Magn. Magn. Mater. **167**, L185.

Fak, B., C. Vettier, J. Flouquet, F. Bourdarot, S. Raymond, A. Verniere, P. Lejay, P. Boutrouille, N.R. Bernhoef, S.T. Bramwell, R.A. Fisher and N.E. Phillips, 1996, J. Magn. Magn. Mater. **154**, 339.

Fak, B., C. Vettier, J. Flouquet, P. Lejay, and J.M. Mignot, 1997, Physica B **230–232**, 415.

Fedders, P.A. and P.C. Martin, 1966, Phys. Rev. **143**, 245.

Fert, A. and P. Levy, 1987, Phys. Rev. B **36**, 1907.

Feyerherm, R., A. Amato, F.N. Gygax, A. Schenck, C. Geibel, F. Steglich, N. Sato and T. Komatsubara, 1994, Phys. Rev. Lett. **73**, 1849.

Feyerherm, R., B. Becker, M.F. Collins, J.A. Mydosh, G.J. Nieuwenhuys and S. Ramakrishnan, 1997, Physica B **234–236**, 891.

Fisher, M.E., 1962, Philos. Mag. **7**, 1731.

Fischer, P., A. Murasik, D. Kaczorowski and R. Troc, 1989, Physica B **156–157**, 829.

Fisher, R.A., S. Kim, Y. Wu, N.E. Phillips, M.W. McElfresh, M.S. Torikachvili and M.B. Maple, 1990, Physica B **163**, 419.

Fournier, J.M. and E. Gratz, 1993, in: Handbook on the Physics and Chemistry of Rare Earths, Vol. 17, eds K.A. Gschneidner Jr., L. Eyring, G.R. Choppin, and G.H. Lander (North-Holland, Amsterdam) pp. 409–537.

François, M., G. Venturini, J.F. Maréché, B. Malaman and B. Roques, 1985, J. Less-Common Metals **113**, 231.

François, M., G. Venturini, E. McRae, B. Malaman, and B. Roques, 1987, J. Less-Common Metals **128**, 249.

Franse, J.J.M., P.H. Frings, A. de Visser, A. Menovsky, T.T.M. Palstra, P.H. Kes and J.A. Mydosh, 1984, Physica B **126**, 116.

Franse, J.J.M., A.A. Menovsky, A. de Visser, J. van der Berg and G.J. Nieuwenhuys, 1987, J. Appl. Phys. **61**, 3383.

Freimuth, A., 1987, J. Magn. Magn. Mater. **68**, 28.

Frings, P.H., J.J.M. Franse, A. Menovsky, S. Zemirli and B. Barbara, 1986, J. Magn. Magn. Mater. **54–57**, 541.

Fujii, H. and H. Sun, 1995, in: Handbook of Magnetic Materials, Vol. 9, ed. K.H.J. Buschow (North-Holland, Amsterdam) pp. 303–404.

Fujii, H., H. Kawanaka, T. Takabatake, M. Kurisu, Y. Yamaguchi, H. Sakurai, H. Fujiwara, T. Fujita, and I. Oguro, 1989, J. Phys. Soc. Japan **58**, 2495.

Fujii, H., H. Kawanaka, M. Nagasawa, T. Takabatake, Y. Aoki, T. Suzuki, T. Fujita, E. Sugiura, K. Sugiyama, and M. Date, 1990a, J. Magn. Magn. Mater. **90–91**, 507.

Fujii, H., H. Kawanaka, T. Takabatake, E. Sugiura, K. Sugiyama and M. Date, 1990b, J. Magn. Magn. Mater. **87**, 235.

Fujii, H., S. Miyata and T. Takabatake, 1992, J. Magn. Magn. Mater. **104**, 45.

Fujii, H., T. Takabatake, T. Suzuki, T. Fujita, J. Sakurai and V. Sechovsky, 1993, Physica B **192**, 219.

Fukushima, T., S. Matsuyama, T. Kumada, K. Kindo, K. Prokes, H. Nakotte, F.R. de Boer, L. Havela, V. Sechovsky, J.M. Winand, J. Rebizant and J.C. Spirlet, 1995, Physica B **211**, 142.

Fulde, P. and M. Loewenhaupt, 1986, Adv. Phys. **34**, 589.

Fumagalli, P., J. Schoenes and D. Kaczorowski, 1988a, Solid State Commun. **65**, 173.

Fumagalli, P., J. Schoenes, H. Rüegsegger, and D. Kaczorowski, 1988b, Phys. Acta **61**, 829.

Gal, J., M. Kroupp, Z. Hadari and I. Nowik, 1976a, Solid State Commun. **20**, 421.

Gal, J., M. Kroupp, Z. Hadari and I. Novik, 1976b, Solid State Commun. **20**, 515.

Gal, J., M. Kroupp, Z. Hadari and I. Novik, 1977, Phys. Rev. B **16**, 3913.

Gal, J., H. Pinto, S. Fredo, H. Shaked, W. Schäfer, G. Will, F.J. Litterst, W. Potzel, L. Asch and G.M. Kalvius, 1987, Hyperfine Interact. **33**, 173.

Gal, J., I. Yaar, E. Arbaboff, D. Etedgi, F.J. Litterst, K. Arggarwal, J. Pereda, G.M. Kalvius, G. Will and W. Schäfer, 1989, Phys. Rev. **40**, 745.

Gal, J., I. Yaar, D. Regev, S. Fredo, G. Shani, E. Arbaboff, W. Potzel, K. Aggarwal, J.A. Pereda, G.M. Kalvius, F.J. Litterst, W. Schäfer and G. Will, 1990, Phys. Rev. B **42**, 8507.

Gasche, T., S. Auluck, M.S.S. Brooks and B. Johansson, 1992, J. Magn. Magn. Mater. **104**, 37.

Gasche, T., M.S.S. Brooks and B. Johansson, 1995a, J. Phys.: Condens. Matter **7**, 9499.

Gasche, T., M.S.S. Brooks and B. Johansson, 1995b, J. Phys.: Condens. Matter **7**, 9511.

Geibel, C., U. Ahlheim, A.L. Giorgi, G. Sparn, H. Spille, F. Steglich and W. Suski, 1990a, Physica B **163**, 194.

Geibel, C., C. Kammerer, E. Goring, R. Moog, G. Sparn, R. Henseleit, G. Cordier, S. Horn and F. Steglich, 1990b, J. Magn. Magn. Mater. **90–91**, 435.

Geibel, C., S. Thies, D. Kaczorowski, A. Mehner, A. Grauel, B. Seidel, U. Ahlheim, R. Helfrich, K. Petersen, C.D. Bredl and F. Steglich, 1991a, Z. Phys. B **83**, 305.

Geibel, C., C. Schank, S. Thies, S. Kitazawa, C.D. Bredl, A. Böhm, M. Rau, A. Grauel, R. Caspary, R. Helfrich, U. Ahlheim, G. Weber and F. Steglich, 1991b, Z. Phys. B **84**, 1.

Geibel, C., A. Böhm, R. Caspary, K. Gloos, A. Grauel, P. Hellmann, R. Modler, C. Schank, G. Weber, and F. Steglich, 1993, Physica B **186–188**, 188.

Geibel, C., C. Schank, F. Jährling, B. Buschinger, A. Grauel, T. Lühmann, P. Gegenwart, R. Helfrich, P.H.P. Reinders and F. Steglich, 1994, Physica B **199–200**, 128.

Gesing, T.-M., R. Pöttgen, W. Jeitschko, and U. Wortmann, 1992, J. Alloys Comp. **186**, 321.

Ghosh, K., S. Ramakrishnan and G. Chandra, 1993, Phys. Rev. B **47**, 8305.

Gijs, M.A.M. and G.E.W. Bauer, 1997, Adv. Phys. **46**, 285.

Giorgi, A.L., 1987, J. Appl. Phys. **61**, 4003.

Giorgi, A.L., A.C. Lawson, J.A. Goldstone, K.J. Volin and J.D. Jorgensen, 1988, J. Appl. Phys. **63**, 3604.

Gladyshevskii, R.E., K. Cenzual and E. Parthé, 1992, J. Alloys Comp. **189**, 221.

Glaum, R., J.H. Albering, W. Jeitschko and L. Boonk, 1992, J. Alloys Comp. **185**, 301.

Godinho, M., G. Bonfait, A.P. Gonçalves, M. Almeida and J.C. Spirlet, 1995, J. Magn. Magn. Mater. **140**, 1417.

Godinho, M., P. Estrela, A.P. Gonçalves, M. Almeida, J.C. Spirlet and G. Bonfait, 1996, J. Magn. Magn. Mater. **158**, 690.

Gonçalves, A.P., M. Almeida, C.T. Walker, J. Ray and J.C. Spirlet, 1994, Mater. Lett. **19**, 13.

Gonçalves, A.P., G. Bonfait, M. Almeida, P. Estrela, M. Godinho and J.C. Spirlet, 1995a, J. Magn. Magn. Mater. **140**, 1419.

Gonçalves, A.P., P. Estrela, J.C. Waerenborgh, M. Godinho, M. Almeida and J.C. Spirlet, 1995b, J. Alloys Comp. **218**, 183.

Gonçalves, A.P., M. Almeida, A. Amaro, M. Godinho, J.A. Paixao and J.C. Spirlet, 1996, J. Magn. Magn. Mater. **158**, 692.

Gonçalves, A.P., J.C. Waerenborgh, A. Amaro, M. Godinho and M. Almeida, 1998, J. Alloys Comp., in press.

Gordier, G., B. Eisenman and H. Schäfer, 1974, Z. Anorg. Allg. Chem. **426**, 205.

Gordon, J.E., R.A.O. Hall, J.A. Lee and M.J. Mortimer, 1997, Proc. R. Soc. London A **351**, 179.

Goto, T., H. Aruga Katori, T. Sakakibara, H. Mitamura, K. Fukamichi and K. Murata, 1994, J. Appl. Phys. **76**, 6682.

Graf, T., J.D. Thompson, M.F. Hundley, R. Movshovich, Z. Fisk, D. Mandrus, R.A. Fisher and N.E. Phillips, 1997, Phys. Rev. Lett. **78**, 3769.

Grassman, A., 1990, Physica B **163**, 547.

Grauel, A., A. Böhm, P. Fischer, C. Geibel, R. Köhler, R. Modler, C. Schank, F. Steglich, G. Weber, T. Komatsubara and N. Sato, 1992, Phys. Rev. B **46**, 5818.

Grauel, A., A. Böhm, C. Geibel, G. Weber, F. Steglich, N. Sato, T. Komatsubara and S. Horn, 1993, J. Appl. Phys. **73**, 5421.

Gravereau, P., F. Mirambet, B. Chevalier, F. Weill, L. Fournès, D. Laffargue, F. Bourée, and J. Etourneau, 1994a, J. Mater. Chem. **4**, 1893.

Gravereau, P., H. Guengard, F. Mirambet, L. Trut, J. Grannec, B. Chevalier, A. Tressaud and J. Etourneau, 1994b, in: Proc. 3rd European Powder Diffraction Conference (EPDIC 3), parts 1 and 2, pp. 671–676.

Grewe, N. and F. Steglich, 1991, in: Handbook on the Physics and Chemistry of Rare Earths, Vol. 14, eds

K.A. Gschneidner Jr. and L. Eyring (North-Holland, Amsterdam) pp. 343–474.

Grin, Y.N., P. Rogl and K. Hiebl, 1986, J. Less-Common Metals **121**, 497.

Grin, Y.N., P. Rogl, L.G. Akselrud, V.K. Pecharskii, and Y.P. Yarmolyuk, 1988, Russ. Metall. **4**, 206.

Gueramian, M., K. Yvon and F. Hulliger, 1991, J. Less-Common Metals **175**, 321.

Guertin, R.P., C. Rossel, M.S. Torikachvili, M.W. McElfresh, M.B. Maple, S.H. Bloom, Y.S. Yao, M.V. Kuric, and G.P. Meisner, 1987, Phys. Rev. B **36**, 8665.

Guha, E., E.W. Scheidt and G.R. Stewart, 1996, Phys. Rev. B **53**, 6477.

Gunarson, O. and K. Schonhammer, 1987, in: Handbook on the Physics and Chemistry of Rare Earths, Vol. 10, eds K.A. Gschneidner Jr., L. Eyring, and S. Hüfner (North-Holland, Amsterdam) pp. 103–163.

Guttman, A.J., C. Domb and P.E. Fox, 1970, J. Phys. (Paris) **32**, C1.

Hagmusa I.H., J.C.P. Klasse, E. Brück, F.R. de Boer and H. Nakotte, 1997, J. Appl. Phys. **81**, 4157.

Harrison, W., 1969, Phys. Rev. **181**, 231.

Harrison, W., 1983, Phys. Rev. B **28**, 550.

Harrison, W. and S. Froyen, 1980, Phys. Rev. B **21**, 3214.

Harrison, W. and G.K. Straub, 1987, Phys. Rev. B **36**, 2695.

Havela, L., 1994, unpublished work.

Havela, L., J. Hrebik, M. Zeleny and A.V. Andreev, 1983, Acta Phys. Polonica A **68**, 493.

Havela, L., L. Neuzil, V. Sechovsky, A.V. Andreev, C. Schmitzer and G. Hilscher, 1986, J. Magn. Magn. Mater. **54–57**, 551.

Havela, L., V. Sechovsky, F.R. de Boer, E. Brück, P.A. Veenhuizen, J.B. Bouwer and K.H.J. Buschow, 1988, J. Magn. Magn. Mater. **76–77**, 89.

Havela, L., V. Sechovsky, P. Nozar, E. Brück, F.R. de Boer, J.C.P. Klaasse, A.A. Menovsky, J.M. Fournier, M. Wulff, E. Sugiura, M. Ono and M. Date, 1990, Physica B **163**, 313.

Havela, L., V. Sechovsky, L. Jirman, F.R. de Boer and E. Brück, 1991, J. Appl. Phys. **69**, 4813.

Havela, L., T. Almeida, J.R. Naegele, V. Sechovsky, and E. Brück, 1992a, J. Alloys Comp. **181**, 205.

Havela, L., V. Sechovsky, J.R. Naegele, T. Almeida, E. Brück, H. Nakotte and F.R. de Boer, 1992b, J. Magn. Magn. Mater. **104**, 23.

Havela, L., V. Sechovsky, F.R. de Boer, E. Brück and H. Nakotte, 1992c, Physica B **177**, 159.

Havela, L., V. Sechovsky, H. Nakotte, E. Brück, P. Svoboda and F.R. de Boer, 1993a, in: Proc. Int. Conf. on the Physics of Transition Metals, Darmstadt, Germany, 1992, eds P. Oppeneer and J. Kübler, p. 842.

Havela, L., V. Sechovsky, H. Nakotte, E. Brück, and K. Prokes, 1993b, in: Proc. 23iémes Journées des Actinides, Schwarzwald, Germany, p. O5.4.

Havela, L., V. Sechovsky, H. Nakotte, E. Brück, and F.R. de Boer, 1994a, IEEE Trans. Magn. **30**, 1130.

Havela, L., V. Sechovsky, K. Prokes, H. Nakotte, F.R. de Boer and E. Brück, 1994b, J. Alloys Comp. **207–208**, 249.

Havela, L., V. Sechovsky, H. Nakotte, E. Brück, and F.R. de Boer, 1994c, J. Alloys Comp. **213–214**, 243.

Havela, L., V. Sechovsky, P. Svoboda, M. Divis, H. Nakotte, K. Prokes, F.R. de Boer, A. Purwanto, R.A. Robinson, A. Seret, J.M. Winand, J. Rebizant, J.C. Spirlet, M. Richter and H. Eschrig, 1994d, J. Appl. Phys. **76**, 6214.

Havela, L., E. Brück and P. Svoboda, 1995a, μ^+-SR on UIrGe and UCoAl, unpublished work.

Havela, L., V. Sechovsky, P. Svoboda, H. Nakotte, K. Prokes, F.R. de Boer, A. Seret, J.M. Winand, J. Rebizant, J.C. Spirlet, A. Purwanto and R.A. Robinson, 1995b, J. Magn. Magn. Mater. **140–144**, 1367.

Havela, L., V. Sechovsky, K. Prokes, H. Nakotte, H. Fujii and A. Lacerda, 1996a, Physica B **223–224**, 245.

Havela, L., V. Sechovsky, H. Nakotte, A. Lacerda, K. Prokes and E. Brück, 1996b, Czech. J. Phys. **46**, 2043.

Havela, L., A.V. Andreev, V. Sechovsky, I.K. Kozlovskaya, K. Prokes, P. Javorsky, M.I. Bartashevich, T. Goto and K. Kamishima, 1997a, Physica B **230–232**, 98.

Havela, L., V. Sechovsky, Y. Aoki, K. Kobayashi, H. Sato, K. Prokes, M. Mihalik and A.A. Menovsky, 1997b, J. Appl. Phys. **81**, 5778.

Havela, L., A.V. Kolomiets, V. Sechovsky, M. Divis, M. Richter and A.V. Andreev, 1998a, J. Magn. Magn. Mater. **177–181**, 47.

Havela, L., R.V. Dremov, A.V. Andreev, V. Sechovsky, J. Sebek and K. Prokes, 1998b, J. Alloys Comp., in press.

Hickey, E., B. Chevalier, P. Gravereau and J. Etourneau, 1990, J. Magn. Magn. Mater. **90–91**, 501.

Hickey, E., B. Chevalier, B. Lepine, J. Etourneau, M.A. Frey Ramos, J.F. Da Silva, M.M. Amando and J.B. Sousa, 1992, J. Alloys Comp. **178**, 413.

Hiebl, K., C. Horvath, P. Rogl and M.J. Sienko, 1983a, Solid State Commun. **48**, 211.

Hiebl, K., C. Horvath, P. Rogl and M.J. Sienko, 1983b, J. Magn. Magn. Mater. **37**, 287.

Hiebl, K., Y.N. Grin, P. Rogl and H. Noël, 1987, in: Proc. 17èmes Journées des Actinides, Signal de Chexbres, p. 47.

Hiebl, K., P. Rogl, C. Horvath, K. Renshnig, and H. Noël, 1990, J. Appl. Phys. **67**, 943.

Hiess, A., L. Havela, K. Prokes, R. Eccleston, and G.H. Lander, 1997a, Physica B **230–232**, 89.

Hiess, A., F. Bourdarot, P. Burlet, E. Ressouche, J.P. Sanchez, F. Wastin, J. Rebizant, G.H. Lander, and E. Suard, 1997b, Phys. Rev. B **55**, 1138.

Higashi, I., H. Kitazawa, K. Kobayashi, M. Yoshida, N. Sato and T. Komatsubara, 1993, J. Alloys Comp. **191**, L21.

Higgins, E.J., J. Rebizant, A.D. Stalios, C.T. Walker, F. Wastin and M.J. Hynes, 1996, in: Proc. 26iémes Journées des Actinides, Sklarska Poreba, Poland, p. 97.

Higgins, E.J., S. Heathman, Y. Meresse, J. Rebizant, F. Wastin and M.J. Hynes, 1997, in: Proc. 27èmes Journées des Actinides, Dijon, p. 145.

Hill, H.H., 1970, in: Plutonium 1970 and Other Actinides, ed. W.N. Miner (AIME) pp. 1–19.

Hirjak, M., P. Lejay, B. Chevalier, J. Etourneau, and J. Hagenmuller, 1985, J. Less-Common Metals **105**, 139.

Hjelm, A., O. Eriksson and B. Johansson, 1993, Phys. Rev. Lett. **71**, 1459.

Hjelm, A., J. Trygg, O. Eriksson, B. Johansson, and J. Wills, 1994, Phys. Rev. B **50**, 4332.

Ho, J.C., N.E. Phillips and T.F. Smith, 1966, Phys. Rev. Lett. **17**, 694.

Hofmann, W.K. and W. Jeitschko, 1984, J. Solid State Chem. **51**, 152.

Holland-Moritz, E. and G.H. Lander, 1994, in: Handbook of the Physics and Chemistry of Rare Earths, Vol. 19, eds K.A. Gschneidner Jr., L. Eyring, G.H. Lander and G.R. Choppin (Elsevier, Amsterdam) pp. 1–121.

Holland-Moritz, E., W. Schlabitz, M. Loewenhaupt, U. Walter and C.-K. Loong, 1987, J. Magn. Magn. Mater. **63–64**, 187.

Holland-Moritz, E., W. Schlabitz, M. Loewenhaupt, and U. Walter, 1989, Phys. Rev. B **39**, 551.

Honda, F., G. Oomi, A.V. Andreev, L. Havela, K. Prokes and V. Sechovsky, 1997a, Physica B **239**, 109.

Honda, F., K. Prokes, G. Oomi, T. Kagayama, A.V. Andreev, V. Sechovsky, L. Havela and E. Brück, 1997b, J. Phys. Soc. Japan **66**, 1904.

Honda, F., K. Prokes, M. Olsovec, F. Bourdarot, P. Burlet, T. Kagayama, G. Oomi, L. Havela, V. Sechovsky, A.V. Andreev, E. Brück, F.R. de Boer, A. Menovsky, and M. Mihalik, 1998a, J. Alloys Comp., in press.

Honda, F., G. Oomi, T. Kagayama, A.V. Andreev, V. Sechovsky, L. Havela, M.I. Bartashevich, T. Goto, and A.A. Menovsky, 1998b, J. Magn. Magn. Mater. **177–181** 49.

Honma, T., H. Amitsuka, T. Sakakibara, K. Sugiyama and M. Date, 1993, Physica B **186–188**, 684.

Hovestreydt, E., K. Klepp and E. Parthé, 1982, Acta Crystallogr. B **38**, 1803.

Höchst, H., K. Tan and K.H.J. Buschow, 1986, J. Magn. Magn. Mater. **54–57**, 545.

Hu, G.J. and B.R. Cooper, 1993, Phys. Rev. B **48**, 12743.

Hundley, M.F., L.C. Bourne, A. Zettl, C. Rossel, and M.B. Maple, 1987, Solid State Commun. **62**, 603.

Hurd, C.M., 1972, The Hall Effect in Metals and Alloys (Plenum Press, New York).

Hurd, M., 1983, Contemp. Phys. **23**, 469.

Ido, M., Y. Segawa, H. Amitsuka and Y. Miyako, 1993, J. Phys. Soc. Japan **62**, 2962.

Iglesias, J.E., K.E. Pachali and H. Steinfink, 1974, J. Solid State Chem. **9**, 6.

Ikeda, K., S.K. Dhar, M. Yoshizawa and K.A. Gschneidner Jr., 1991, J. Magn. Magn. Mater. **100**, 292.

Iki, K., H. Takakura, H. Okita, Y. Uwatoko, G. Oomi, Y. Onuki and T. Komatsubara, 1990, J. Magn. Magn. Mater. **90–91**, 526.

Iki, K., G. Oomi, Y. Uwatoko, H. Takahashi, N. Mori, Y. Onuki and T. Komatsubara, 1992, J. Alloys Comp. **181**, 71.

Inada, Y., H. Aono, A. Ishiguro, J. Kimura, N. Sato, A. Sawada and T. Komatsubara, 1994, Physica B **199–200**, 119.

Ishiyama, H., M. Yoshizawa and S. Kawamata, 1993, Physica B **186–188**, 700.

Isoda, M., 1992, J. Magn. Magn. Mater. **104**, 41.

Isoda, M. and Y. Takahashi, 1997, Physica B **237–238**, 229–230.

Iwata, N., M. Ito, T. Kishino, H. Fujii, T. Shigeoka, K. Sugiyama and M. Date, 1992, J. Magn. Magn. Mater. **104**, 27.

Izawa, K., T. Suzuki, T. Fujita, Y. Maeda, T. Takabatake and H. Fujii, 1996, J. Phys. Soc. Japan **65**, 3260.

Javorsky, P., P. Burlet, V. Sechovsky, R.R. Arons, E. Ressouche and G. Lapertot, 1997, Physica B **232–236**, 665.

Jeandey, C., J.P. Sanchez, J.L. Oddou, J. Rebizant, J.C. Spirlet and F. Wastin, 1996, J. Phys.: Condens. Matter **8**, 4259.

Jeitschko, W. and K. Behrens, 1986, Z. Metallkde **77**, 788.

Jeitschko, W. and D.J. Braun, 1977, Acta Crystallogr. B **33**, 3401.

Jeitschko, W., U. Meisen, M.H. Möller and M. Reehuis, 1985, Z. Anorg. Allg. Chem. **527**, 73.

Jeitschko, W., W.K. Hofmann and L.J. Terbüchte, 1988, J. Less-Common Metals **137**, 133.

Jeitschko, W., L.J. Terbüchte, E.J. Reinbold, P.G. Pollmeier and T. Vomhof, 1990, J. Less-Common Metals **161**, 125.

Jirman, L., V. Sechovsky, L. Havela, W. Ye, T. Takabatake, H. Fujii, T. Suzuki, E. Brück and F.R. de Boer, 1992, J. Magn. Magn. Mater. **104–107**, 19.

Johansson, B. and M.S.S. Brooks, 1993, in: Handbook on the Physics and Chemistry of Rare Earths, Vol. 17, eds K.A. Gschneidner Jr., L. Eyring, G.R. Choppin and G.H. Lander (North-Holland, Amsterdam) pp. 149–244.

Johansson, B. and H.L. Skriver, 1982, J. Magn. Magn. Mater. **29**, 217.

Johnson, V. and W. Jeitschko, 1974, J. Solid State Chem. **11**, 161.

Jorda, J.L., M. Ishikawa and E. Hovestreydt, 1983, J. Less-Common Metals **92**, 155.

Joyce, J.J., A.J. Arko, J.M. Lawrence, P.C. Canfield, Z. Fisk, R.J. Barlett and J.D. Thompson, 1992, Phys. Rev. Lett. **68**, 236.

Julian, S.R., P.A.A. Teunissen and S.A.J. Wiegers, 1992a, Phys. Rev. B **46**, 9821.

Julian, S.R., P.A.A. Teunissen and S.A.J. Wiegers, 1992b, Physica B **177**, 135.

Just, G. and P. Paufler, 1996, J. Alloys Comp. **232**, 1.

Kaczorowski, D., 1988, J. Magn. Magn. Mater. **76–77**, 366.

Kaczorowski, D., 1992, J. Alloys Comp. **186**, 333.

Kaczorowski, D., 1996, Solid State Commun. **99**, 949.

Kaczorowski, D. and H. Noël, 1993, J. Phys.: Condens. Matter **5**, 9185.

Kaczorowski, D. and J. Schoenes, 1990, Solid State Commun. **74**, 143.

Kaczorowski, D. and N. Stüsser, 1996, Solid State Commun. **100**, 43.

Kaczorowski, D. and R. Troc, 1990, J. Phys.: Condens. Matter **2**, 4185.

Kaczorowski, D., R. Duraj and R. Troc, 1989, Solid State Commun. **70**, 619.

Kaczorowski, D., R. Troc and H. Noël, 1990, J. Less-Common Metals **161**, 239.

Kaczorowski, D., R. Troc and H. Noël, 1991a, J. Phys.: Condens. Matter **3**, 4959.

Kaczorowski, D., H. Noël and R. Troc, 1991b, J. Less-Common Metals **170**, 255.

Kaczorowski, D., Z. Zolnierek, C. Geibel and F. Steglich, 1993a, J. Alloys Comp. **200**, 115.

Kaczorowski, D., D. Finsterbusch and B. Lüthi, 1993b, in: Proc. Int. Conf. on the Physics of Transition Metals, Darmstadt, 1992, eds P. Oppeneer and J. Kübler, p. 212.

Kaczorowski, D., J.H. Albering, H. Noël, and W. Jeitschko, 1994, J. Alloys Comp. **216**, 117.

Kaczorowski, D., H. Noël and M. Potel, 1997, Physica B **206–207**, 456.

Kadowaki, K., 1993, Physica B **186–188**, 727.

Kadowaki, K. and S.B. Woods, 1986, Solid State Commun. **58**, 507.

Kagayama, T., G. Oomi, K. Iki, N. Mori, Y. Onuki and T. Komatsubara, 1994, J. Alloys Comp. **213**, 387.

Kalvius, G.M., W. Potzel, J. Moser, F.J. Litterst, L. Asch, J. Zänkert, U. Potzel, A. Kratzer, M. Wunsch, J. Gal, S. Fredo, D. Dayan, M. Bogé, J. Chappert, J.C. Spirlet, U. Benedict and B.D. Dunlap, 1985, Physica B **130**, 393.

Kalvius, G.M., J. Gal, L. Asch and W. Potzel, 1992, Hyperfine Interact. **72**, 77.

Kang, J.S., J.W. Allen, M.B. Maple, M.S. Torikachvili, B. Pate, W. Ellis and I. Lindau, 1987, Phys. Rev. Lett. **59**, 493.

Kawamata, S., K. Ishimoto, H. Iwasaki, N. Kobayashi, Y. Yamaguchi, T. Komatsubara, G. Kido, T. Mitsugashira and Y. Muto, 1990, J. Magn. Magn. Mater. **90–91**, 513.

Kawamata, S., K. Ishimoto, Y. Yamaguchi and T. Komatsubara, 1992a, J. Magn. Magn. Mater. **104**, 51.

Kawamata, S., H. Iwasaki and N. Kobayashi, 1992b, J. Magn. Magn. Mater. **104**, 55.

Kawamata, S., H. Iwasaki, N. Kobayashi, K. Ishimoto, Y. Yamaguchi and T. Komatsubara, 1992c, J. Magn. Magn. Mater. **104**, 53.

Kawamata, S., G. Kido, K. Ishimoto, Y. Yamaguchi, H. Iwasaki, N. Kobayashi and T. Komatsubara, 1992d, Physica B **177**, 169.

Kawamata, S., K. Ishimoto, Y. Yamaguchi, H. Iwasaki and N. Kobayashi, 1993, Physica B **186–188**, 741.

Kawanaka, H., H. Fujii, M. Nishi, T. Takabatake, K. Motoya, Y. Uwatoko and Y. Ito, 1989, J. Phys. Soc. Japan **58**, 3481.

Kawanaka, H., H. Nakotte, E. Brück, K. Prokes, N.H. Kim-Ngan, T. Takabatake, H. Fujii and J. Sakurai, 1997, Physica B **237–238**, 226.

Kawarazaki, S., Y. Kobashi, T. Taniguchi, Y. Miyako and H. Amitsuka, 1994, J. Phys. Soc. Japan, **63**, 716.

Kergadallan, Y., 1993, Synthese, croissance et etudes de composes et d'alliages intermetalliques de stoichiometrie 1.1.1 base d'actinides, Thesis, Université de Paris XI Orsay.

Kilibarda-Dalafave, S., H.K. Ng, J.E. Crow, P. Pernambuco-Wise, T. Yuen and C.L. Lin, 1993a, Physica B **186–188**, 989.

Kilibarda-Dalafave, S., H.K. Ng, T. Yuen, C.L. Lin, J.E. Crow and D.B. Tanner, 1993b, Phys. Rev. B **48**, 297.

Killer, U., W.W. Kim, A. Mielke, G. Fraunberger, J.J. Rieger, E.W. Scheidt and G.R. Stewart, 1994, Phys. Rev. B **49**, 1188.

Kim, J.S. and G.R. Stewart, 1995, Phys. Rev. B **51**, 16190.

Kim, W.W., G.R. Stewart and B. Andraka, 1997, Physica B **199–200**, 384.

Kimball, C.W., R.H. Hannon, C.M. Hummel, A.E. Dwight and G.K. Shenoy, 1971, in: Proc. Institute of Physics, London, p. 105.

Kimura, N., R. Settai, Y. Onuki, K. Maezawa, H. Aoki and H. Harima, 1996a, Physica B **216**, 313.

Kimura, N., R. Settai, Y. Onuki, E. Yamamoto, K. Maezawa, H. Aoki and H. Harima, 1996b, Physica B **224**, 181.

Kindo, K. and M. Date, 1994, Physica B **201**, 239.

Kindo, K., T. Fukushima, T. Kumada, F.R. de Boer, H. Nakotte, K. Prokes, L. Havela, V. Sechovsky, A. Seret, J.M. Winand, J.C. Spirlet and J. Rebizant, 1995, J. Magn. Magn. Mater. **140–144**, 1369.

Kirby, R.D., J.X. Shen, J.A. Woolman and D.J. Sellmyer, 1991, J. Appl. Phys. **69**, 4574.

Kita, H., A. Dönni, Y. Endoh, K. Kakurai, N. Sato and T. Komatsubara, 1994, J. Phys. Soc. Japan **63**, 726.

Kitaoka, Y., H. Tou, G. Zheng, K. Ishida, K. Asayama, T.C. Kobayashi, A. Kohda, N. Takeshita, K. Amaya, Y. Onuki, C. Geibel, C. Schank and F. Steglich, 1995, Physica B **206–207**, 55.

Klüfers, P. and A. Mewis, 1978, Z. Naturforsch. Sect. B **33**, 151.

Klüfers, P., A. Mewis and H.-U. Schuster, 1979, Z. Kristallogr. **149**, 211.

Knöpfle, K., A. Mavromaras, L.M. Sandratskii, and J. Kübler, 1996, J. Phys.: Condens. Matter **8**, 901.

Kobayashi, Y., Y. Aoki, H. Sugawara, H. Sato, V. Sechovsky, L. Havela, K. Prokes, M. Mihalik and A.A. Menovsky, 1996, Phys. Rev. B **54**, 15330.

Koelling, D.D., B.D. Dunlap and G.W. Crabtree, 1985, Phys. Rev. B **31**, 4966.

Kohara, T., Y. Kohori, K. Asayama, Y. Kitaoka, M.B. Maple and M.S. Torikachvili, 1986, Solid State Commun. **59**, 603.

Kohori, Y., Y. Noguchi, T. Kohara, K. Asayama, H. Amitsuka and Y. Miyako, 1992, Solid State Commun. **82**, 479.

Kohori, Y., Y. Noguchi, T. Kohara, Y. Dalichaouch, M.A. Lopez de la Torre and M.B. Maple, 1993, Physica B **188**, 792.

Kohori, Y., K. Matsuda and T. Kohara, 1995, Solid State Commun. **95**, 121.

Kojima, K., Y. Hukuda, H. Kawanaka, T. Takabatake, H. Fujii and T. Hihara, 1990, J. Magn. Magn. Mater. **90–91**, 505.

Kojima, K., Y. Hukuda, S. Miyata, T. Takabatake, H. Fujii and T. Hihara, 1992a, J. Phys. Soc. Japan **60**, 2546.

Kojima, K., Y. Hukuda, S. Miyata, T. Takabatake, H. Fujii and T. Hihara, 1992b, J. Magn. Magn. Mater. **104**, 49.

Kojima, K., H. Iwasaki, T. Takabatake, H. Fujii and T. Hihara, 1993, Physica B **186–188**, 691.

Kolomiets, A.V., L. Havela, V. Sechovsky, L. Delong and D.B. Watkins, 1998, J. Appl. Phys., in press.

Kontani, M., T. Nishioka, H. Makino and K. Hayashi, 1997, Physica B **230–232**, 229.

Korner, N., J. Schoenes and D. Kaczorowski, 1989, Helv. Phys. Acta **62**, 207.

Krimmel, A., A. Loidl, C. Geibel, F. Steglich, and G.J. McIntyre, 1992a, J. Magn. Magn. Mater. **104**, 25.

Krimmel, A., A. Loidl, C. Geibel, F. Steglich, and G.J. McIntyre, 1992b, J. Magn. Magn. Mater. **103**, 73.

Krimmel, A., P. Fischer, B. Roessli, H. Maletta, C. Geibel, C. Schank, A. Grauel, A. Loidl and F. Steglich, 1993a, Z. Phys. B **86**, 161.

Krimmel, A., A. Loidl, P. Fischer, B. Roessli, A. Donni, H. Kita, N. Sato, Y. Endoh, T. Komatsubara, C. Geibel and F. Steglich, 1993b, Solid State Commun. **87**, 829.

Krimmel, A., A. Loidl, R. Eccleston, C. Geibel, and F. Steglich, 1996, J. Phys.: Condens. Matter **8**, 1677.

Krimmel, A., A. Severing, R. Spitzfaden, A. Grauel, B. Buschinger, C. Geibel and A. Loidl, 1997, Z. Phys. B **102**, 9.

Krishnamurthy, V.V., S.N. Mishra, M.R. Press, and S.H. Devare, 1995, Phys. Rev. Lett. **74**, 1661.

Kruk, R., K. Latka, K. Tomala, R. Kmiec, R. Troc and V.H. Tran, 1995, J. Alloys Comp. **219**, 256.

Kruk, R., R. Kmiec, K. Latka, K. Tomala, R. Troc and V.H. Tran, 1996a, J. Alloys Comp. **232**, L8.

Kruk, R., R. Kmiec, K. Latka, K. Tomala, R. Troc and V.H. Tran, 1996b, in: Proc. 26iémes Journées des Actinides, Sklarska Poreba, Poland, p. 73.

Kruk, R., R. Kmiec, K. Latka, K. Tomala, R. Troc and V.H. Tran, 1997, Phys. Rev. B **55**, 5851.

Krylov, V.I., A.V. Andreev, V. Sechovsky and L. Havela, 1990, Hyperfine Interact. **59**, 395.

Kucera, M., P. Berankova, M. Matyas, V. Sechovsky, and L. Havela, 1996, J. Magn. Magn. Mater. **158**, 700.

Kurisu, M., T. Takabatake and H. Fujiwara, 1988, Solid State Commun. **68**, 595.

Kurisu, M., H. Kawanaka, T. Takabatake and H. Fujii, 1991, J. Phys. Soc. Japan **60**, 3792.

Kurisu, M., T. Takabatake and H. Fujii, 1992, J. Magn. Magn. Mater. **104**, 29.

Kurisu, M., T. Takahashi, Y. Maeda, H. Iwasaki, T. Takabatake and H. Fujii, 1993, Physica B **186–188**, 766.

Kurisu, M., T. Takabatake, H. Iwasaki and H. Fujii, 1995, Physica B **206–207**, 505.

Kuwahara, K., H. Amitsuka, K. Tenya, T. Sakakibara, O. Suzuki, S. Nakamura, T. Goto, M. Mihalik, A.A. Menovsky, A. de Visser and J.J.M. Franse, 1997, Physica B **230–232**, 77.

Kuznietz, M., H. Pinto, H. Ettedgui and M. Melamud, 1989, Phys. Rev. B **40**, 7328.

Kuznietz, M., H. Pinto and M. Melamud, 1990a, J. Magn. Magn. Mater. **83**, 321.

Kuznietz, M., H. Pinto and M. Melamud, 1990b, J. Appl. Phys. **67**, 4808.

Kuznietz, M., H. Pinto and M. Melamud, 1991, J. Magn. Magn. Mater. **96**, 245.

Kuznietz, M., H. Pinto, H. Ettedgui and M. Melamud, 1992a, J. Magn. Magn. Mater. **104–107**, 13.

Kuznietz, M., H. Pinto, H. Ettedgui and M. Melamud, 1992b, Phys. Rev. B **45**, 7282.

Kuznietz, M., H. Pinto, H. Ettedgui and M. Melamud, 1992c, Physica B **180–181**, 55.

Kuznietz, M., G. André, F. Bourée, H. Pinto, H. Ettedgui and M. Melamud, 1993a, J. Appl. Phys. **73**, 6075.

Kuznietz, M., G. André, F. Bourée, H. Pinto, H. Ettedgui and M. Melamud, 1993b, Solid State Commun. **87**, 689.

Kuznietz, M., H. Pinto, H. Ettedgui and M. Melamud, 1993c, Phys. Rev. B **48**, 3183.

Kuznietz, M., H. Pinto and M. Melamud, 1993d, Philos. Mag. B **68**, 195.

Kuznietz, M., G. André, F. Bourée, H. Pinto, H. Ettedgui and M. Melamud, 1994a, J. Magn. Magn. Mater. **137**, 322.

Kuznietz, M., H. Pinto and M. Melamud, 1994b, J. Appl. Phys. **75**, 7134.

Kuznietz, M., G. André, F. Bourée, H. Pinto, H. Ettedgui and M. Melamud, 1994c, Phys. Rev. B **50**, 3822.

Kuznietz, M., F. Bourée, H. Pinto and M. Melamud, 1994d, Solid State Commun. **90**, 93.

Kuznietz, M., H. Pinto and M. Melamud, 1995a, Phys. Rev. B **51**, 16410.

Kuznietz, M., G. André, F. Bourée, H. Pinto, H. Ettedgui and M. Melamud, 1995b, J. Alloys Comp. **219**, 244.

Kuznietz, M., H. Pinto and H. Ettedgui, 1995c, J. Magn. Magn. Mater. **140–144**, 1405.

Kuznietz, M., H. Pinto, M. Melamud and K. Tomala, 1995d, Phys. Rev. B **52**, 15975.

Kuznietz, M., H. Pinto and M. Melamud, 1996, Physica B **223–224**, 234.

Kuznietz, M., E. Caspi, H. Pinto, M. Melamud, and H. Shaked, 1997, Physica B **230–232**, 102.

Kyogaku, M., Y. Kitaoka, K. Asayama, C. Geibel, C. Schank and F. Steglich, 1992, J. Phys. Soc. Japan **61**, 2260.

Kyogaku, M., Y. Kitaoka, K. Asayama, N. Sato, T. Sakon, T. Komatsubara, C. Geibel, C. Schank and F. Steglich, 1993, Physica B **186–188**, 285.

Lacroix, C., B. Canals and M.D. Núnez-Regueiro, 1996, Phys. Rev. Lett. **77**, 5126.

Laffargue, D. 1996, private communication.

Laffargue, D., B. Chevalier, S.F. Matar and F. Bourée, 1996, in: Proc. 26iémes Journées des Actinides, Sklarska Poreba, Poland, p. 53.

Laffargue, D., F. Bourée, B. Chevalier, T. Roisnel, P. Gravereau and J. Etourneau, 1997, J. Magn. Magn. Mater. **170**, 155.

Lam, D.J., J.B. Darby Jr., J.W. Downey and L.J. Norton, 1967, J. Nucl. Mater. **22**, 22.

Lam, D.J., J.B. Darby Jr. and M.V. Nevitt, 1974, in: The Actinides: Electronic Structure and Related Properties, Vol. 2, eds A.J. Freeman and J.B. Darby Jr. (Academic Press, New York) p. 175.

Lander, G.H., M.S.S. Brooks, B. Lebech, P.J. Brown, O. Vogt and K. Mattenberger, 1990, J. Appl. Phys. **69**, 4803.

Le Bihan, T. and H. Noël, 1995, J. Alloys Comp. **227**, 44.

Le Bihan, T., H. Noël and P. Rogl, 1994, J. Alloys Comp. **213–214**, 540.

Le Bihan, T., H. Noël, K. Hiebl and P. Rogl, 1996a, J. Alloys Comp. **232**, 142.

Le Bihan, T., J.C. Levet and H. Noël, 1996b, J. Solid State Chem. **121**, 479.

Lebech, B., M. Wulff, G.H. Lander, J. Rebizant, J.C. Spirlet and A. Delapalme, 1989, J. Phys.: Condens. Matter **1**, 10229.

Lebech, B., M. Wulff and G.H. Lander, 1991, J. Appl. Phys. **69**, 5891.

Leciejewicz, J., L. Chelmicki and A. Zygmunt, 1982, Solid State Commun. **41**, 167.

Leciejewicz, J., A. Szytula and A. Zygmunt, 1991, J. Magn. Magn. Mater. **97**, 219.

Leciejewicz, J., A. Szytula and P. Rogl, 1993, J. Magn. Magn. Mater. **119**, 167.

Legvold, S., 1980, in: Ferromagnetic Materials, Vol. 1, ed. E.P. Wohlfarth (North-Holland, Amsterdam) pp. 184–295.

Leithe-Jasper, A., P. Rogl and P.E. Potter, 1996, J. Nucl. Mater. **230**, 302.

Lenkewitz, M., S. Corsepius, G.-F. v. Blankenhagen, and G.R. Stewart, 1997, Phys. Rev. B **55**, 6409.

Li, H.-S. and J.M.D. Coey, 1991, in: Handbook of Magnetic Materials, Vol. 6, ed. K.H.J. Buschow (North-Holland, Amsterdam) pp. 1–83.

Li, Q., Y. Lu, R. Zhao, O. Tegus and F. Yang, 1991, J. Appl. Phys. **70**, 6116.

Lin, H., L. Rebelsky, M.F. Collins, J.D. Garrett, and W.J.L. Buyers, 1991a, Phys. Rev. B **43**, 3232.

Lin, C., G.Z. Li, Z.X. Liu, H.W. Jiang, Z. Wan, J.L. Yang, B.S. Zhang and Y.F. Ding, 1991b, J. Appl. Phys. **70**, 6543.

Lin, K.J., J.S. Hwang, C.S. Wur, R. Hsu and C. Tien, 1997, Solid State Commun. **103**, 185.

Link, P., D. Jaccard, C. Geibel, C. Wassilew, and F. Steglich, 1995, J. Phys. C.: Condens. Matter **7**, 373.

Liu, L.Z., J.W. Allen, C.L. Seaman, M.B. Maple, Y. Dalichaouch, J.S. Kang, M.S. Torikachvili and M.A. Lopez de la Torre, 1992, Phys. Rev. Lett. **68**, 1034.

Lloret, B., 1988, Crystal chemistry and physical properties (Kondo, intermediate or mixed valence, heavy fermions) of new ternary compounds in the systems: Ce, Eu, or U – transition element (3d, 4d, 5d) – silicium or germanium), Thesis, University of Bordeaux I.

Lloret, B., B. Buffat, B. Chevalier and J. Etourneau, 1987, J. Magn. Magn. Mater. **67**, 232.

Lloret, B., B. Chevalier, P. Gravereau, B. Darriet and J. Etourneau, 1988, J. Phys. (Paris) **49**(C8), 487.

Loewenhaupt, M. and K.H. Fischer, 1993, in: Handbook of Magnetic Materials, Vol. 7, ed. K.H.J. Buschow (North-Holland, Amsterdam) pp. 503–608.

Lorenz, R., J. Hafner, S. Jaswal and D.J. Sellmyer, 1995, Phys. Rev. Lett. **74**, 3668.

Löhneysen, H. v., F. Huster, S. Mock, A. Neubert, T. Pietrus, M. Sieck, O. Stockert and M. Waffenschmidt, 1997, Physica B **230–232**, 550.

Luo, H., S. Dabos, U. Benedict and J.C. Spirlet, 1988, J. Less-Common Metals **142**, L23.

Lussier, J.-G., A. Schröder, B.D. Gaulin, J.D. Garrett, W.J.L. Buyers, L. Rebelsky and S.M. Shapiro, 1994, Physica B **199–200**, 137.

Lussier, J.-G., A. Schröder, J.D. Garrett, B.D. Gaulin and W.J.L. Buyers, 1997, Physica B **230–232**, 354.

MacLaughlin, D.E., O.O. Bernal and H.G. Lukefahr, 1996, J. Phys.: Condens. Matter **8**, 9855.

Maeda, Y., T. Takabatake, H. Fujii, K. Izawa, T. Suzuki, T. Fujita, A. Minami, K. Oda, K. Sugiyama, and K. Kindo, 1995, J. Magn. Magn. Mater. **140**, 1363.

Maeda, Y., T. Takabatake, Y. Bando, H. Fujii, K. Oda, K. Sugiyama, K. Kindo, K. Izawa, T. Suzuki, and T. Fujita, 1996, Physica B **224**, 228.

Maglic, R.C., G.H. Lander, M.H. Mueller and R. Kleb, 1978, Phys. Rev. B **17**, 308.

Mailhot, A., M.L. Plumer, A. Caille and P. Azaria, 1992, Phys. Rev. B **45**, 399.

Malaman, B., G. Venturini, L. Pontonnier and D. Fruchart, 1990, J. Magn. Magn. Mater. **86**, 349.

Maletta, H., V. Sechovsky, P.A. Veenhuizen, F.R. de Boer, L. Havela and G. Hilscher, 1988, Z. Phys. B **72**, 455.

Maletta, H., R.A. Robinson, A.C. Lawson, V. Sechovsky, L. Havela, L. Jirman, M. Divis, E. Brück, F.R. de Boer, A.V. Andreev, K.H.J. Buschow and P. Burlet, 1992, J. Magn. Magn. Mater. **104**, 21.

Maple, M.B., J.W. Chen, Y. Dalichaouch, T. Kohara, C. Rossel, M.S. Torikachvili, M.W. McElfresh, and J.D. Thompson, 1986, Phys. Rev. Lett. **56**, 185.

Marazza, R., R. Ferro, G. Rombaldi and G. Zanicchi, 1977, J. Less-Common Metals **53**, 193.

Marezio, M., D.L. Cox, C. Rossel and M.B. Maple, 1988, Solid State Commun. **67**, 831.

Mason, T.E., B.D. Gaulin, J.D. Garrett, Z. Tun, W.J.L. Buyers and E.D. Isaacs, 1990a, Phys. Rev. Lett. **65**, 3189.

Mason, T.E., H. Lin, M.F. Collins, W.J.L. Buyers, A.A. Menovsky and J.A. Mydosh, 1990b, Physica B **163**, 45.

Mason, T.E., W.J.L. Buyers, T. Petersen, A.A. Menovsky and J.D. Garrett, 1995, J. Phys.: Condens. Matter **7**, 5089.

Matar, S.F., 1995, J. Magn. Magn. Mater. **151**, 263.

Matar, S.F., F. Mirambet, B. Chevalier and J. Etourneau, 1995, J. Magn. Magn. Mater. **140**, 1389.

Mathon, J., 1968, Proc. Roy. Soc. A **306**, 355.

Matsuda, K., Y. Kohori and T. Kohara, 1997, Phys. Rev. B **55**, 15223.

Matsui, H., T. Goto, N. Sato and T. Komatsubara, 1994, Physica B **199–200**, 140.

Matthias, B.T., C.W. Chu, E. Corenzwit and D. Wohlleben, 1969, Proc. Nat. Acad. Sci. USA **64**, 459.

Mauramoto, K., T. Takeuchi and Y. Miyako, 1996, Phys. Rev. B **54**, 12194.

McAlister, S.P., M. Olivier and T. Siegrist, 1989, Solid State Commun. **69**, 113.

McElfresh, M.W., J.D. Thompson, J.O. Willis, M.B. Maple, T. Kohara and M.S. Torikachvili, 1987, Phys. Rev. B **35**, 43.

McElfresh, M.W., L. Rebelsky, M.S. Torikachvili, H. Borges, K. Reilly, S. Horn and M.B. Maple, 1990, J. Appl. Phys. **67**, 5218.

Meisner, G.P., A.L. Giorgi, A.C. Lawson, G.R. Stewart, J.O. Willis, M.S. Wire and J.L. Smith, 1984, Phys. Rev. Lett. **53**, 1829.

Meisner, G.P., M.S. Torikachvili, K.N. Yang, M.B. Maple and R.P. Guertin, 1985, J. Appl. Phys. **57**, 3073.

Melamud, M., L.H. Bennett and R.E. Watson, 1987, J. Appl. Phys. **61**, 4246.

Melamud, M., M. Kuznietz, H. Pinto, E. Caspi, and H. Shaked, 1998, J. Magn. Soc. Japan, in press.

Mentink, S.A.M., G.J. Nieuwenhuys, A.A. Menovsky, and J.A. Mydosh, 1991, J. Appl. Phys. **69**, 5484.

Mentink, S.A.M., G.J. Nieuwenhuys, C.E. Snel, A.A. Menovsky and J.A. Mydosh, 1992, J. Magn. Magn. Mater. **104–107**, 15.

Mentink, S.A.M., H. Nakotte, A. de Visser, A.A. Menovsky, G.J. Nieuwenhuys and J.A. Mydosh, 1993, Physica B **186–188**, 270.

Mentink, S.A.M., A. Drost, G.J. Nieuwenhuys, E. Frikkee, A.A. Menovsky and J.A. Mydosh, 1994, Phys. Rev. Lett. **73**, 1031.

Mentink, S.A.M., G.J. Nieuwenhuys, A.A. Menovsky, A. Drost and E. Frikkee, 1995a, Physica B **206–207**, 373.

Mentink, S.A.M., G.J. Nieuwenhuys, A.A. Menovsky, J.A. Mydosh, K. Sugiyama, Y. Bando and T. Takabatake, 1995b, J. Magn. Magn. Mater. **140**, 1415.

Mentink, S.A.M., T.E. Mason, S. Süllow, G.J. Nieuwenhuys, A.A. Menovsky, J.A. Mydosh and J.A.A.J. Perenboom, 1996a, Phys. Rev. B **53**, R6014.

Mentink, S.A.M., T.E. Mason, S. Süllow, G.J. Nieuwenhuys, J.A. Mydosh and R.L. Donaberger, 1996b, Physica B **223–224**, 204.

Mentink, S.A.M., U. Wyder, J.A.A.J. Perenboom, A. de Visser, A.A. Menovsky, G.J. Nieuwenhuys, J.A. Mydosh and T.E. Mason, 1997a, Physica B **230–232**, 74.

Mentink, S.A.M., H. Amitsuka, A. de Visser, Z. Slanic, D.P. Belager, J.J. Neumeier, J.D. Thompson, A.A. Menovsky, J.A. Mydosh and T.E. Mason, 1997b, Physica B **230–232**, 108.

Mihalik, M., N.H. Kim-Ngan, F.E. Kayzel, A.A. Menovsky, R.W.A. Hendrikx and T.J. Gortenmulder, 1993a, J. Cryst. Growth **134**, 342.

Mihalik, M., A. de Visser, A.A. Menovsky, and J.J.M. Franse, 1993b, Physica B **186–188**, 507.

Mihalik, M., S. Matas, M. Hrabcak, N.H. Kim-Ngan, and A.A. Menovsky, 1993c, IEEE Trans. Magn. **30**, 1196.

Mihalik, M., S. Matas, K. Prokes, H. Nakotte, N.H. Kim-Ngan and A.A. Menovsky, 1993d, IEEE Trans. Magn. **30**, 1142.

Mihalik, M., F.E. Kayzel, T. Yoshida, K. Kuwahara, H. Amitsuka, T. Sakakibara, A.A. Menovsky, J.A. Mydosh, and J.J.M. Franse, 1997, Physica B **230–232**, 364.

Mirambet, F., 1993, Thesis, University of Bordeaux.

Mirambet, F., B. Chevalier, P. Gravereau, and J. Etourneau, 1992, Solid State Commun. **82**, 25.

Mirambet, F., P. Gravereau, B. Chevalier, L. Trut and J. Etourneau, 1993a, J. Alloys Comp. **191**, L1.

Mirambet, F., B. Chevalier, L. Fournès, M.J. Besnus, P. Gravereau and J. Etourneau, 1993b, J. Magn. Magn. Mater. **118**, 187.

Mirambet, F., L. Fournès, B. Chevalier, P. Gravereau and J. Etourneau, 1994, J. Magn. Magn. Mater. **138**, 244.

Mirambet, F., B. Chevalier, L. Fournès, J.F. Da Silva, M.A.F. Ramos and T. Roisnel, 1995a, J. Magn. Magn. Mater. **140**, 1387.

Mirambet, F., B. Chevalier, P. Gravereau, L. Fournès and J. Etourneau, 1995b, J. Magn. Magn. Mater. **140**, 1361.

Miwa, H., 1963, Prog. Theor. Phys. **29**, 477.

Miyako, Y., 1993, in: Transport and Thermal Properties of f-Electron Systems, eds G. Oomi, H. Fujii and T. Fujita (Plenum Press, New York) pp. 187–202.

Miyako, Y., S. Kawarazaki, H. Amitsuka, C.C. Paulsen and K. Hasselbach, 1991, J. Appl. Phys. **70**, 5791.

Miyako, Y., T. Kuwai, T. Taniguchi, S. Kawarazaki, H. Amitsuka, C.C. Paulsen and T. Sakakibara, 1992, J. Magn. Magn. Mater. **108**, 190.

Miyako, Y., H. Amitsuka, S. Kunii and T. Kasuya, 1993, Physica B **186–188**, 236.

Modler, R., M. Lang, C. Geibel, C. Schank, and F. Steglich, 1994, Physica B **199–200**, 145.

Monachesi, P. and A. Continenza, 1995, J. Magn. Magn. Mater. **140–144**, 1401.

Moriya, T., 1991, J. Magn. Magn. Mater. **100**, 261.

Moriya, T. and T. Takimoto, 1995, J. Phys. Soc. Japan **64**, 960.

Mucha, J., H. Misiorek, D. Kaczorowski and A. Jezowski, 1992, J. Alloys Comp. **189**, 217.

Mulder, F.M., R.C. Thiel and K.H.J. Buschow, 1995, J. Alloys Comp. **223**, 127.

Mulder, F.M., A. Drost, R.C. Thiel and E. Frikkee, 1996, Phys. Rev. Lett. **77**, 3477.

Murasik, A., J. Leciejewicz, H. Ptasiewicz-Bak, R. Troc, A. Zygmunt and Z. Zolnierek, 1976, in: Proc. 2nd Int. Conf. on the Electronic Structure of the Actinides, Wroclaw, 1976, eds J. Mulak, W. Suski and R. Troc, p. 405.

Murasik, A., P. Fischer and D. Kaczorowski, 1990, J. Phys.: Condens. Matter **2**, 3967.

Murasik, A., P. Fischer, R. Troc and V.H. Tran, 1991, J. Phys.: Condens. Matter **3**, 1841.

Mydosh, J.A., 1993, Spin Glasses: An Experimental Introduction (Taylor and Francis, London).

Mydosh, J.A., T. Endstra and G.J. Nieuwenhuys, 1993, in: Transport and Thermal Properties of f-Electron Systems, eds G. Oomi, H. Fujii and T. Fujita (Plenum Press, New York) pp. 93–102.

Naegele, J.R., J. Ghijsen and L. Manes, 1985, in: Actinides – Chemistry and Physical Properties, ed. L. Manes (Springer, Berlin) pp. 197–262.

Nakotte, H., 1992, unpublished work.

Nakotte, H., 1994, Magnetism in cerium and uranium intermetallics, Thesis, University of Amsterdam.

Nakotte, H., 1998, to be published.

Nakotte, H., E. Brück, F.R. de Boer, A.J. Riemersma, L. Havela and V. Sechovsky, 1992, Physica B **179**, 269.

Nakotte, H., F.R. de Boer, L. Havela, P. Svoboda, V. Sechovsky, Y. Kergadallan, J.C. Spirlet and J. Rebizant, 1993a, J. Appl. Phys. **73**, 6554.

Nakotte, H., E. Brück, F.R. de Boer, P. Svoboda, N.C. Tuan, L. Havela, V. Sechovsky and R.A. Robinson, 1993b, J. Appl. Phys. **73**, 6551.

Nakotte, H., L. Havela, J.P. Kuang, F.R. de Boer, K.H.J. Buschow, J.H.V.J. Brabers, T. Kuroda, K. Sugiyama and M. Date, 1993c, in: Proc. Int. Conf. on the Physics of Transition Metals, Darmstadt, 1992, eds P. Oppeneer and J. Kübler, p. 838.

Nakotte, H., R.A. Robinson, J.W. Lynn, E. Brück and F.R. de Boer, 1993d, Phys. Rev. B **47**, 831.

Nakotte, H., K. Prokes, E. Brück, F.R. de Boer, V. Sechovsky, L. Havela and H. Fujii, 1994a, IEEE Trans. Magn. **30**, 1139.

Nakotte, H., K. Prokes, E. Brück, F.R. de Boer, V. Sechovsky, L. Havela and H. Fujii, 1994b, J. Appl. Phys. **75**, 6522.

Nakotte, H., K. Prokes, E. Brück, N. Tang, F.R. de Boer, P. Svoboda, V. Sechovsky, L. Havela, J.M. Winand, A. Seret, J. Rebizant and J.C. Spirlet, 1994c, Physica B **201**, 247.

Nakotte, H., K. Bakker, Z. Koziol, F.R. de Boer and A.V. Andreev, 1994d, IEEE Trans. Magn. **30**, 1199.

Nakotte, H., E. Brück, J.H.V.J. Brabers, K. Prokes, F.R. de Boer, V. Sechovsky, K.H.J. Buschow, A.V. Andreev, R.A. Robinson, A. Purwanto and J.W. Lynn, 1994e, IEEE Trans. Magn. **30**, 1217.

Nakotte, H., A. Lacerda, A. Purwanto, A.C. Larson, K. Prokes, L. Havela, V. Sechovsky, R.A. Robinson, Z. Tun, E. Brück and F.R. de Boer, 1995, in: Proc. 25ièmes Journées des Actinides, L'Aquila, Italy, p. 140.

Nakotte, H., A. Purwanto, R.A. Robinson, Z. Tun, K. Prokes, A.C. Larson, L. Havela, V. Sechovsky, and H. Maletta, 1996a, Phys. Rev. B **54**, 7201.

Nakotte, H., A. Purwanto, R.A. Robinson, K. Prokes, F.R. de Boer, L. Havela, V. Sechovsky and I.P. Swainson, 1996b, J. Appl. Phys. **79**, 6408.

Nakotte, H., A. Purwanto, R.A. Robinson, K. Prokes, J.C.P. Klaasse, P.F. de Châtel, F.R. de Boer, L. Havela, V. Sechovsky, L.C.J. Pereira, A. Seret, J. Rebizant, J.C. Spirlet and F. Trouw, 1996c, Phys. Rev. B **53**, 3263.

Nakotte, H., K. Prokes, E. Brück, K.H.J. Buschow, F.R. de Boer, A.V. Andreev, M.C. Aronson, A. Lacerda, M.S. Torikachvili, R.A. Robinson, M.A.M. Bourke and A.J. Schultz, 1996d, Phys. Rev. B **54**, 12176.

Nakotte, H., I.H. Hagmusa, J.C.P. Klaasse, M.S. Torikachvili, A. Lacerda, E. Brück, K. Prokes, and F.R. de Boer, 1998, Physica B, in press.

Nieuwenhuys, G.J., 1987, Phys. Rev. B **35**, 5620.

Nieuwenhuys, G.J., 1995, in: Handbook of Magnetic Materials, Vol. 9, ed. K.H.J. Buschow (North-Holland, Amsterdam) pp. 1–55.

Nieuwenhuys, G.J., S.A.M. Mentink, A.A. Menovsky, A. Amato, R. Feyerherm, F.N. Gygax, R.H. Heffner, L.P. Le, D.E. MacLaughlin and A. Schenck, 1995, Physica B **206–207**, 470.

Nigam, A.K., S.B. Roy and G. Chandra, 1994, Phys. Rev. B **49**, 1127.

Ning, Y.B., J.D. Garrett and W.R. Datars, 1990, Phys. Rev. B **42**, 8780.

Ning, Y.B., V.V. Gridin, C.V. Stager, W.R. Datars, A.L. Dawson and D.H. Ryan, 1991, J. Phys.: Condens. Matter **3**, 4399.

Ning, Y.B., J.D. Garrett, C.V. Stager and W.R. Datars, 1992, Phys. Rev. B **46**, 8201.

Nishioka, T., Y. Kurahashi, R. Fukuda and M. Kotani, 1996, Czech. J. Phys. **46**, 2065.

Noël, H., Z. Zolnierek, D. Kaczorowski, R. Troc and J. Stepien-Damm, 1987, J. Less-Common Metals **135**, 61.

Noguchi, S. and K. Okuda, 1992, J. Magn. Magn. Mater. **104**, 57.

Noguchi, S. and K. Okuda, 1993, Physica B **188**, 749.

Norman, M.R. and D.D. Koelling, 1993, in: Handbook on the Physics and Chemistry of Rare Earths, Vol. 17, eds K.A. Gschneidner Jr., L. Eyring, G.R. Choppin and G.H. Lander (North-Holland, Amsterdam) pp. 1–86.

Nowack, A., Y.G. Naidyuk, P.N. Chubov, I.K. Yanson and A.A. Menovsky, 1992, Z. Phys. B **83**, 295.

Nowak, B., O.J. Zogal, K. Niedzwiedz, R. Troc, K. Wochowski and Z. Zolnierek, 1993, Physica B **192**, 213.

Nozieres, P. and A. Blandin, 1980, J. de Physique **41**, 193.

Ocko, M. and J.G. Park, 1997, Physica B **230–232**, 71.

Oda, K., T. Kumada, K. Sugiyama, N. Sato, T. Komatsubara and M. Date, 1994, J. Phys. Soc. Japan **63**, 3115.

Ogawa, S., 1976, J. Phys. Soc. Japan **40**, 1007.

Oguchi, T., A.J. Freeman and G.W. Crabtree, 1987, J. Magn. Magn. Mater. **63–64**, 645.

Ohama, T., H. Yasuoka, T. Takabatake, S. Miyata, and H. Fujii, 1992, J. Phys. Soc. Japan **61**, 437.

Ohama, T., H. Yasuoka, T. Takabatake and H. Fujii, 1993a, Physica B **186–188**, 717.

Ohama, T., H. Yasuoka, Y. Maeda, T. Takabatake, and H. Fujii, 1993b, J. Phys. Soc. Japan **62**, 3023.

Ohkuni, H., T. Ishida, Y. Inada, Y. Haga, E. Yamamoto, Y. Onuki and S. Takahashi, 1997, J. Phys. Soc. Japan **66**, 945.

Okuda, K., S. Noguchi, Y. Nakazawa and M. Ishikawa, 1989, J. Phys. Soc. Japan **58**, 4296.

Olsovec, M. and M. Divis, 1996, Phys. Status Solidi B: **195**, K13.

Olsovec, M., J. Schweizer, L. Paolasini, V. Sechovsky and K. Prokes, 1998, Physica B, in press.

Onuki, Y., T. Yamazaki, I. Ukon, T. Komatsubara, A. Umazawa, W.K. Kwok, G.W. Crabtree and D.G. Hinks, 1989, J. Phys. Soc. Japan **58**, 2119.

Onuki, Y., R. Settai and H. Aoki, 1996, Physica B **224**, 141.

Oomi, G., T. Kagayama, Y. Onuki and T. Komatsubara, 1994, Physica B **199**, 148.

Oppeneer, P.M., A.N. Yaresko, A.Y. Perlov, V.N. Antonov and H. Eschrig, 1996, Phys. Rev. B **54**, R3706.

Osborn, R., S.W. Lovesey, A.D. Taylor and E. Balcar, 1991, in: Handbook on the Physics and Chemistry of Rare Earths, Vol. 14, eds K.A. Gschneidner Jr. and L. Eyring (North-Holland, Amsterdam) pp. 1–61.

Ögüt, S. and K.M. Rabe, 1995, Phys. Rev. B **16**, 10453.

Paixao, J.A., 1992, Polarized neutron experiment on UNiAl single crystal, unpublished work.

Paixao, J.A., G.H. Lander, P.J. Brown, H. Nakotte, F.R. de Boer and E. Brück, 1992, J. Phys.: Condens. Matter **4**, 829.

Paixao, J.A., G.H. Lander, A. Delapalme, H. Nakotte, F.R. de Boer and E. Brück, 1993, Europhys. Lett. **24**, 607.

Paixao, J.A., B. Lebech, A.P. Gonçalves, P.J. Brown, G.H. Lander, P. Burlet, A. Delapalme and J.C. Spirlet, 1997, Phys. Rev. B **55**, 14370.

Palstra, T.T.M., A.A. Menovsky, J. van der Berg, A.J. Dirkmaat, P.H. Kes, G.J. Nieuwenhuys and J.A. Mydosh, 1985, Phys. Rev. Lett. **55**, 2727.

Palstra, T.T.M., G.J. Nieuwenhuys, J.A. Mydosh, and K.H.J. Buschow, 1986a, J. Magn. Magn. Mater. **54–57**, 549.

Palstra, T.T.M., A.A. Menovsky, G.J. Nieuwenhuys, and J.A. Mydosh, 1986b, J. Magn. Magn. Mater. **54–57**, 435.

Palstra, T.T.M., A.A. Menovsky and J.A. Mydosh, 1986c, Phys. Rev. B **33**, 6527.

Palstra, T.T.M., G.J. Nieuwenhuys, R.F.M. Vlastuin, J. van der Berg, J.A. Mydosh and K.H.J. Buschow, 1987, J. Magn. Magn. Mater. **67**, 331.

Palstra, T.T.M., G.J. Nieuwenhuys, R.F.M. Vlastuin, J.A. Mydosh and K.H.J. Buschow, 1988, J. Appl. Phys. **63**, 4279.

Paolasini, L., J.A. Paixao, G.H. Lander, A. Delapalme, N. Sato and T. Komatsubara, 1993, J. Phys.: Condens. Matter **5**, 8905.

Paolasini, L., J.A. Paixao, G.H. Lander, P. Burlet, N. Sato and T. Komatsubara, 1994, Phys. Rev. B **49**, 7072.

Papoular, R.J. and A. Delapalme, 1994, Phys. Rev. Lett. **72**, 1486.

Park, J.G. and B.R. Coles, 1993, Physica B **186–188**, 795.

Park, J.G. and B.R. Coles, 1995, Physica B **206–207**, 418.

Park, J.G., B.R. Coles, C. Scott and R. Cywinski, 1996, Physica B **223–224**, 189.

Park, J.G., K.A. McEwen, S. de Brion, G. Chouteau, H. Amitsuka and T. Sakakibara, 1997, J. Phys.: Condens. Matter **9**, 3065.

Parthé, E. and B. Chabot, 1984, in: Handbook on the Physics and Chemistry of Rare Earths, Vol. 6, eds K.A. Gschneidner Jr. and L. Eyring (North-Holland, Amsterdam) pp. 113–334.

Patrikios, N., M. de Podesta, S.B. Roy and K.A. McEwen, 1992, J. Magn. Magn. Mater. **108**, 95.

Pechev, S., B. Chevalier, B. Darriet, P. Gravereau, and J. Etourneau, 1996, J. Alloys Comp. **243**, 77.

Pelizzone, M., H.F. Braun and J. Muller, 1982, J. Magn. Magn. Mater. **30**, 33.

Pereira, L.C.J., 1996, personal communication.

Pereira, L.C.J. and F. Wastin, 1996, unpublished work.

Pereira, L.C.J., J.M. Winand, F. Wastin, J. Rebizant and J.C. Spirlet, 1994, in: Proc. 24ièmes Journées des Actinides, Obergurgl, Austria, p. 109.

Pereira, L.C.J., A. Seret, F. Wastin, A. Hiess, J.P. Sanchez, J. Rebizant and J.C. Spirlet, 1995, in: Proc. 25ièmes Journées des Actinides, L'Aquila, Italy, p. 136.

Pereira, L.C.J., F. Wastin, B. Kanellakopoulos, J. Rebizant and J.C. Spirlet, 1996a, in: Proc. 26iémes Journées des Actinides, Sklarska Poreba, Poland, p. 51.

Pereira, L.C.J., J.A. Paixao, P. Estrela, M. Godinho, F. Bourdarot, M. Bonnet, J. Rebizant, J.C. Spirlet and

M. Almeida, 1996b, J. Phys.: Condens. Matter **8**, 11167.

Pereira, L.C.J., F. Wastin, J.M. Winand, B. Kanellakopoulos, J. Rebizant, J.C. Spirlet and M. Almeida, 1997, J. Solid State Chem. **134**, 138.

Perlov, A.Y., P.M. Oppeneer, V.N. Antonov, A.N. Yaresko and B.Y. Yavorsky, 1998, J. Alloys Comp., in press.

Peron, M.N., Y. Kergadallan, J. Rebizant, D. Meyer, J.M. Winand, S. Zwirner, L. Havela, H. Nakotte, J.C. Spirlet, G.M. Kalvius, E. Colineau, J.L. Oddou, C. Jeandey and J.P. Sanchez, 1993, J. Alloys Comp. **201**, 203.

Pethick, C.J. and G.M. Carneiro, 1977, Phys. Rev. A **7**, 304.

Pietri, R., B. Andraka, R. Troc and V.H. Tran, 1997, Phys. Rev. B **56**, in press.

Pinto, R.P., M.M. Amado, M.A. Salgueiro, M.E. Braga, J.B. Sousa, B. Chevalier, F. Mirambet and J. Etourneau, 1995, J. Magn. Magn. Mater. **140–144**, 1371.

Pinto, R.P., M.M. Amado, M.E. Braga, M.A. Salgueiro, J.B. Sousa, B. Chevalier, D. Laffargue, and J. Etourneau, 1996, J. Magn. Magn. Mater. **157–158**, 698.

Piraux, L., E. Grivei, B. Chevalier, P. Dordor, E. Marquestaut and J. Etourneau, 1993, J. Magn. Magn. Mater. **128**, 313.

Plumer, M.L., 1994, Phys. Rev. B **50**, 13003.

Potzel, W., J. Moser, G.M. Kalvius, C.H. de Novion, J.C. Spirlet and J. Gal, 1981, Phys. Rev. B **24**, 6762.

Pöttgen, R. and D. Kaczorowski, 1993, J. Alloys Comp. **201**, 157.

Pöttgen, R., J.H. Albering, D. Kaczorowski, and W. Jeitschko, 1993, J. Alloys Comp. **196**, 111.

Pöttgen, R., P. Gravereau, B. Darriet, B. Chevalier, E. Hickey and J. Etourneau, 1994, J. Mater. Chem. **4**, 463.

Pöttgen, R., B. Chevalier, P. Gravereau, B. Darriet, W. Jeitschko and J. Etourneau, 1995, J. Solid State Chem. **115**, 247.

Pöttgen, R., V.H. Tran, R.D. Hoffmann, D. Kaczorowski and R. Troc, 1996, J. Mater. Chem. **6**, 429.

Prokes, K., 1997, Magnetism in uranium intermetallic compounds, Thesis, University of Amsterdam.

Prokes, K., H. Nakotte, E. Brück, F.R. de Boer, L. Havela, V. Sechovsky, P. Svoboda and H. Maletta, 1994, IEEE Trans. Magn. **30**, 1214.

Prokes, K., P. Svoboda, V. Sechovsky, E. Brück, A. Amato, R. Feyerherm, F.N. Gygax, A. Schenck, H. Maletta and F.R. de Boer, 1995, J. Magn. Magn. Mater. **140**, 1381.

Prokes, K., E. Brück, F.R. de Boer, M. Mihalik, A. Menovsky, P. Burlet, J.M. Mignot, L. Havela, and V. Sechovsky, 1996a, J. Appl. Phys. **79**, 6396.

Prokes, K., A. de Visser, A.A. Menovsky, E. Brück, F.R. de Boer, V. Sechovsky and T.J. Gortenmulder, 1996b, J. Appl. Phys. **79**, 6358.

Prokes, K., E. Brück, K.H.J. Buschow, F.R. de Boer, V. Sechovsky, P. Svoboda, X. Hu, H. Maletta, and T.J. Gortenmulder, 1996c, J. Appl. Phys. **79**, 5221.

Prokes, K., V. Sechovsky, E. Brück, F. Bourée, G. André, V.H. Tran, R. Sonntag, F.R. de Boer, K.H.J. Buschow, R. Troc, K. Kindo and H. Maletta, 1996d, Physica B **225**, 166.

Prokes, K., H. Nakotte, L. Havela, V. Sechovsky, L.C.J. Pereira, C. Rijkeboer, A. Seret, J.C. Spirlet, P. Svoboda and F.R. de Boer, 1996e, Physica B **223–224**, 225.

Prokes, K., M. Divis, V. Sechovsky, P. Svoboda, M. Richter, K.H.J. Buschow and F.R. de Boer, 1997a, Solid State Commun. **104**, 597.

Prokes, K., K.H.J. Buschow, E. Brück, F.R. de Boer, P. Svoboda and V. Sechovsky, 1997b, Physica B **230–232**, 39.

Prokes, K., V. Sechovsky, R.A. Robinson, R. Sonntag, P. Svoboda and F.R. de Boer, 1997c, Physica B, in press.

Prokes, K., V. Sechovsky, E. Brück, F.R. de Boer, K.H.J. Buschow, R. Sonntag, R.A. Robinson, and H. Maletta, 1997d, Physica B **229**, 101.

Prokes, K., F. Bourdarot, P. Burlet, P. Javorsky, M. Olsovec, V. Sechovsky, E. Brück, F.R. de Boer, and A.A. Menovsky, 1998a, Phys. Rev. B, in press.

Prokes, K., M. Olsovec, F. Bourdarot, K.E. Pachali, M. Mihalik, A.A. Menovsky, F.R. de Boer and V. Sechovsky, 1998b, Physica B, in press.

Ptasiewicz-Bak, H., J. Leciejewicz and A. Zygmund, 1981, J. Phys. F: Metal Phys. **11**, 1225.

Ptasiewicz-Bak, H., J. Leciejewicz and A. Zygmund, 1985, Solid State Commun. **55**, 601.

Ptasiewicz-Bak, H., A. Baran, W. Suski and J. Leciejewicz, 1988, J. Magn. Magn. Mater. **76–77**, 439.

Purwanto, A., R.A. Robinson, K. Prokes, H. Nakotte, F.R. de Boer, L. Havela, V. Sechovsky, N.C. Tuan, Y. Kergadallan, J.C. Spirlet and J. Rebizant, 1994a, J. Appl. Phys. **76**, 7040.

Purwanto, A., R.A. Robinson, L. Havela, V. Sechovsky, P. Svoboda, H. Nakotte, K. Prokes, F.R. de Boer, A. Seret, J.M. Winand, J. Rebizant and J.C. Spirlet, 1994b, Phys. Rev. B **50**, 6792.

Purwanto, A., V. Sechovsky, L. Havela, R.A. Robinson, H. Nakotte, A.C. Larson, K. Prokes, E. Brück, and F.R. de Boer, 1996a, Phys. Rev. B **53**, 758.

Purwanto, A., R.A. Robinson, H. Nakotte, I.P. Swainson and M.S. Torikachvili, 1996b, J. Appl. Phys. **79**, 6411.

Radha, S., J.G. Park, S.B. Roy, B.R. Coles, A.K. Nigam and K.A. McEwen, 1996, Physica B **224**, 195.

Rainford, B.D., D.T. Adroja, A. Severing, E.A. Goremychkin, J.D. Thompson and Z. Fisk, 1995, Physica B **206**, 464.

Rainford, B.D., D.T. Adroja, G.J. Bowden, I.M. Benson and R.S. Eccleston, 1996, Physica B **224**, 231.

Ramirez, A.P., B. Batlogg and E. Bucher, 1987, J. Appl. Phys. **61**, 3189.

Ramirez, A.P., P. Coleman, P. Chandra, E. Brück, A.A. Menovsky, Z. Fisk and E. Bucher, 1992, Phys. Rev. Lett. **68**, 2680.

Rapp, O., G. Benediktsson, H.U. Aström, S. Arajs and K.V. Rao, 1978, Phys. Rev. B **18**, 3665.

Rauchschwalbe, U., 1987, Physica B **147**, 1.

Rauchschwalbe, U., U. Gottwick, U. Ahlheim, M.H. Meyer and F. Steglich, 1985, J. Less-Common Metals **111**, 265.

Rebelsky, L., M.W. McElfresh, M.S. Torikachvili, B.M. Powell and M.B. Maple, 1991a, J. Appl. Phys. **69**, 4810.

Rebelsky, L., H. Lin, M.F. Collins, J.D. Garrett, W.J.L. Buyers, M.W. McElfresh and M.S. Torikachvili, 1991b, J. Appl. Phys. **69**, 4807.

Rebelsky, L., H. Lin, M.W. McElfresh, M.F. Collins, J.D. Garrett, W.J.L. Buyers and M.S. Torikachvili, 1992, Physica B **180–181**, 43.

Rebizant, J., 1994, personal communication.

Reehuis, M., T. Vomhof and W. Jeitschko, 1991, J. Less-Common Metals **169**, 139.

Reehuis, M., T. Ebel, W. Jeitschko, R. Sonntag, and N. Stüsser, 1996, J. Phys. Chem. Solids **57**, 521.

Renker, B., F. Gompf, E. Gering, P. Frings, H. Reitschel, R. Felten, F. Steglich and G. Weber, 1987, Physica B **148**, 41.

Reznik, I.M., F.G. Vagizov and R. Troc, 1995, Phys. Rev. B **51**, 3013.

Richter, M., P. Zahn, M. Divis and I. Mertig, 1996, Phys. Rev. B **54**, 11985.

Richter, M., L. Steinbeck, M. Divis and H. Eschrig, 1997, Acta Phys. Slovaca **46**, 101.

Robinson, R.A., 1993, personal communication.

Robinson, R.A., A.C. Lawson, K.H.J. Buschow, F.R. de Boer, V. Sechovsky and R.B. von Dreele, 1991, J. Magn. Magn. Mater. **98**, 147.

Robinson, R.A., A.C. Lawson, J.W. Lynn and K.H.J. Buschow, 1992, Phys. Rev. B **45**, 2939.

Robinson, R.A., A.C. Lawson, J.W. Lynn and K.H.J. Buschow, 1993a, Phys. Rev. B **47**, 6138.

Robinson, R.A., J.W. Lynn, V. Nunez, K.H.J. Buschow, H. Nakotte and A.C. Lawson, 1993b, Phys. Rev. B **47**, 5090.

Robinson, R.A., A.C. Lawson, J.A. Goldstone, and K.H.J. Buschow, 1993c, J. Magn. Magn. Mater. **128**, 143.

Rogl, P., 1991, in: Handbook on the Physics and Chemistry of the Actinides, eds A.J. Freeman and C. Keller (North-Holland, Amsterdam) pp. 75–154.

Rossat Mignod, J., L.P. Regnault, J.L. Jacoud, C. Vettier, P. Lejay, J. Flouquet, E. Walker, D. Jaccard, and A. Amato, 1988, J. Magn. Magn. Mater. **76–77**, 376.

Rossel, C., M.S. Torikachvili, J.W. Chen and M.B. Maple, 1986, Solid State Commun. **60**, 563.

Roy, S.B. and B.R. Coles, 1991, Philos. Mag. **64**, 741.

Roy, S.B. and B.R. Coles, 1992, J. Magn. Magn. Mater. **108**, 43.

Roy, S.B., A.K. Pradhan and P. Chaddah, 1994, J. Phys.: Condens. Matter **6**, 5155.

Roy, S.B., A.K. Pradhan and P. Chaddah, 1995a, Philos. Mag. B **71**, 97.

Roy, S.B., A.K. Pradhan, P. Chaddah and B.R. Coles, 1995b, Physica B **206–207**, 498.

Sakakibara, T., H. Amitsuka, T. Goto, K. Sugiyama, Y. Miyako and M. Date, 1992, Physica B **177**, 151.

Sakon, T., K. Imamura, N. Koga, N. Sato and T. Komatsubara, 1995, Physica B **206–207**, 427.

Sampaio, A., E. Santa Marta and G. Petzow, 1968, Z. Metallkde **59**, 118.

Sanchez, J.P., E. Colineau, C. Jeandey, J.L. Oddou, J. Rebizant, A. Seret and J.C. Spirlet, 1995, Physica B **206–207**, 531.

Sandratskii, L.M. and J. Kübler, 1994a, Phys. Rev. B **50**, 9258.

Sandratskii, L.M. and J. Kübler, 1994b, Solid State Commun. **91**, 183.

Sandratskii, L.M. and J. Kübler, 1995a, Phys. Rev. Lett. **75**, 947.

Sandratskii, L.M. and J. Kübler, 1995b, J. Magn. Magn. Mater. **140–144**, 1397–1398.

Sandratskii, L.M. and J. Kübler, 1996, Physica B **217**, 167.

Sandratskii, L.M. and J. Kübler, 1997a, Phys. Rev. B **55**, 11395.

Sandratskii, L.M. and J. Kübler, 1997b, J. Phys.: Condens. Matter **9**, 4897.

Sandratskii, L.M., J. Kübler, P. Zahn and I. Mertig, 1994, Phys. Rev. B **50**, 15834.

Santini, P. and G. Amoretti, 1994, Phys. Rev. Lett. **73**, 1027.

Santini, P., G. Amoretti, A. Blaise and R. Caciuffo, 1993, J. Appl. Phys. **73**, 6560.

Saran, M. and S.P. McAlister, 1988, J. Magn. Magn. Mater. **75**, 345.

Sato, M., 1975, J. Phys. Soc. Japan **39**, 98.

Sato, N., M. Kagawa, K. Tanaka, N. Takeda, T. Satoh, S. Sakatsume and T. Komatsubara, 1991, J. Phys. Soc. Japan **60**, 757.

Sato, N., T. Sakon, N. Takeda, T. Komatsubara, C. Geibel and F. Steglich, 1992a, J. Phys. Soc. Japan **61**, 32.

Sato, N., M. Kagawa, K. Tanaka, N. Takeda, and T. Komatsubara, 1992b, J. Magn. Magn. Mater. **104**, 31.

Sato, N., M. Kagawa, K. Tanaka, N. Takeda, T. Satoh and T. Komatsubara, 1992c, J. Magn. Magn. Mater. **108**, 115.

Sato, N., Y. Inada, T. Sakon, K. Imamura, A. Ishiguro, J. Kimura, A. Sawada, T. Komatsubara, H. Matsui and T. Goto, 1994, IEEE Trans. Magn. **30**, 1145.

Sato, N., N. Aso, N. Tateiwa, N. Koga, T. Komatsubara and N. Metoki, 1997, Physica B **230–232**, 367.

Schank, C., F. Jährling, U. Tegel, C. Geibel, A. Grauel, A. Böhm, R. Borth, R. Helfrich, D. Jaeckel, G. Weber and F. Steglich, 1993, in: Proc. Int. Conf. on the Physics of Transition Metals, Darmstadt, 1992, eds P. Oppeneer and J. Kübler, p. 46.

Schank, C., F. Jährling, A. Grauel, R. Borth, R. Helfrich, T. Lühmann, P.H.P. Reinders, C. Geibel and F. Steglich, 1994, J. Alloys Comp. **213–214**, 509.

Schäfer, W., G. Will, J. Gal and W. Suski, 1989, J. Less-Common Metals **149**, 237.

Schäfer, W., G. Will and J. Gal, 1991, Eur. J. Solid State Inorg. Chem. **28**, 563.

Schenck, A. and F.N. Gygax, 1995, in: Handbook of Magnetic Materials, Vol. 9, ed. K.H.J. Buschow (North-Holland, Amsterdam) pp. 57–302.

Schlabitz, W., J. Baumann, B. Pollit, U. Rauchschwalbe, H.M. Mayer, U. Alheim and C.D. Bredl, 1986, Z. Phys.: Condens. Matter **62**, 171.

Schoenes, J., C. Schönenberger, J.J.M. Franse and A.A. Menovsky, 1987, Phys. Rev. B **35**, 5375.

Schoenes, J., P. Fumagalli, H. Rüegsegger, and D. Kaczorowski, 1989, J. Magn. Magn. Mater. **81**, 112.

Schoenes, J., F. Troisi, E. Brück and A.A. Menovsky, 1992a, J. Magn. Magn. Mater. **108**, 40.

Schoenes, J., D. Kaczorowski and C. Beeli, 1992b, Z. Phys. B **88**, 135.

Schonert, M., S. Corsepius, E.W. Scheidt, and G.R. Stewart, 1995, J. Alloys Comp. **224**, 108.

Schröder, A., M.F. Collins, C.V. Stager, J.D. Garrett, J.E. Greedan and Z. Tun, 1995, J. Magn. Magn. Mater. **140**, 1407.

Schwartz, B.B., 1976, in: Magnetism, Selected Topics, ed. S. Foner (Gordon and Breach, New York) pp. 93–116.

Seaman, C.L., N.R. Dilley, M.C. de Andrade, J. Herrmann, M.B. Maple and Z. Fisk, 1996, Phys. Rev. B **53**, 2651.

Sebek, J., N.C. Tuan, L. Havela, V. Sechovsky, T. Suzuki, T. Fujita, M. Nohara, C. Ikeda and H. Goshima, 1994, Physica B **194–196**, 247.

Sechovsky, V., 1988, unpublished work.

Sechovsky, V. and L. Havela, 1988, in: Handbook of Magnetic Materials, Vol. 4, eds E.P. Wohlfarth and K.H.J. Buschow (Elsevier, Amsterdam) pp. 309–491.

Sechovsky, V. and G. Hilscher, 1985, Physica B **130**, 207.

Sechovsky, V., L. Havela, L. Neuzil, A.V. Andreev, G. Hilscher and C. Schmitzer, 1986a, J. Less-Common Metals **121**, 169.

Sechovsky, V., L. Havela, F.R. de Boer, J.J.M. Franse, P.A. Veenhuizen, J. Sebek, J. Stehno and A.V. Andreev, 1986b, Physica B **142**, 283.

Sechovsky, V., L. Havela, N. Pillmayr, G. Hilscher and A.V. Andreev, 1987, J. Magn. Magn. Mater. **63–64**, 199.

Sechovsky, V., L. Havela, G. Hilscher, N. Pillmayr, A.V. Andreev, P.A. Veenhuizen and F.R. de Boer, 1988a, J. Appl. Phys. **63**, 3070.

Sechovsky, V., H. Maletta, L. Havela, P.A. Veenhuizen and F.R. de Boer, 1988b, J. Appl. Phys. **63**, 3067.

Sechovsky, V., L. Havela, F.R. de Boer, P.A. Veenhuizen and E. Brück, 1988c, J. Physique **49**, 497.

Sechovsky, V., L. Havela, F.R. de Boer, P.A. Veenhuizen, A.V. Andreev and K.H.J. Buschow, 1988d, in: Proc. 18èmes Journées des Actinides, Paris, p. 161.

Sechovsky, V., L. Havela, V.I. Krylov and A.V. Andreev, 1989, Hyperfine Interact. **51**, 943.

Sechovsky, V., L. Havela, P. Nozar, E. Brück, F.R. de Boer, A.A. Menovsky, K.H.J. Buschow and A.V. Andreev, 1990, Physica B **163**, 103.

Sechovsky, V., L. Havela, L. Jirman, W. Ye, T. Takabatake, H. Fujii, E. Brück, F.R. de Boer, and H. Nakotte, 1991, J. Appl. Phys. **70**, 5794.

Sechovsky, V., L. Havela, F.R. de Boer and E. Brück, 1992a, J. Alloys Comp. **181**, 179.

Sechovsky, V., L. Havela, F.R. de Boer, P.A. Veenhuizen, K. Sugiyama, T. Kuroda, E. Sugiura, M. Ono, M. Date and A. Yamagishi, 1992b, Physica B **177**, 164.

Sechovsky, V., L. Havela, L. Jirman, E. Brück, F.R. de Boer, H. Nakotte, W. Ye, T. Takabatake, H. Fujii, T. Suzuki and T. Fujita, 1992c, Physica B **177**, 155.

Sechovsky, V., L. Havela, G. Schaudy, G. Hilscher, N. Pillmayr, P. Rogl and P. Fischer, 1992d, J. Magn. Magn. Mater. **104**, 11.

Sechovsky, V., L. Havela, F.R. de Boer, E. Brück, T. Suzuki, S. Ikeda, S. Nishigori and T. Fujita, 1993a, Physica B **186–188**, 775.

Sechovsky, V., L. Havela, F.R. de Boer, H. Fujii and T. Fujita, 1993b, in: Transport and Thermal Properties of f-Electron Systems, eds G. Oomi, H. Fujii and T. Fujita, pp. 113–122.

Sechovsky, V., L. Havela, F.R. de Boer, E. Brück, Y. Uwatoko and G. Oomi, 1993c, Physica B **186–188**, 697.

Sechovsky, V., L. Havela, H. Nakotte, F.R. de Boer, K. Sugiyama, M. Ono, T. Kuroda and M. Date, 1993d, in: Proc. Int. Conf. on Physics of Transition Metals, Darmstadt, 1992, eds P. Oppeneer and J. Kübler, p. 847.

Sechovsky, V., L. Havela, F.R. de Boer, H. Nakotte, K. Sugiyama, T. Kuroda, M. Ono and M. Date, 1993e, Physica B **186–188**, 752.

Sechovsky, V., L. Havela, H. Nakotte, F.R. de Boer and E. Brück, 1994a, J. Alloys Comp. **207–208**, 221.

Sechovsky, V., L. Havela, A. Purwanto, A.C. Larson, R.A. Robinson, K. Prokes, H. Nakotte, E. Brück, F.R. de Boer, P. Svoboda, H. Maletta and M. Winkelmann, 1994b, J. Alloys Comp. **293–294**, 536.

Sechovsky, V., L. Havela, P. Svoboda, A. Purwanto, A.C. Larson, R.A. Robinson, K. Prokes, H. Nakotte, F.R. de Boer and H. Maletta, 1994c, J. Appl. Phys. **76**, 6217.

Sechovsky, V., L. Havela, H. Nakotte, K. Prokes, F.R. de Boer and E. Brück, 1994d, J. Appl. Phys. **76**, 6913.

Sechovsky, V., L. Havela, H. Nakotte, K. Prokes, E. Brück, F.R. de Boer, K.H.J. Buschow and A.V. Andreev, 1995a, J. Magn. Magn. Mater. **140**, 1391.

Sechovsky, V., L. Havela, P. Svoboda, A.V. Andreev, P. Burlet, K. Prokes, H. Nakotte, F.R. de Boer, E. Brück, R.A. Robinson and H. Maletta, 1995b, J. Magn. Magn. Mater. **140**, 1379.

Sechovsky, V., L. Havela, H. Nakotte, K. Prokes, and E. Brück, 1995c, Physica B **206–207**, 501.

Sechovsky, V., L. Havela, H. Nakotte and E. Brück, 1996, IEEE Trans. Magn. **32**, 4687.

Selke, W., 1988, Phys. Rep. **170**, 213.

Seret, A., F. Wastin, J.C. Waerenborgh, S. Zwirner, J.C. Spirlet and J. Rebizant, 1995, Physica B **206–207**, 525.

Shelton, R.N., H.F. Braun and E. Musick, 1984, Solid State Commun. **52**, 797.

Shemirani, B., H. Lin, M.F. Collins, C.V. Stager, J.D. Garrett and W.J.L. Buyers, 1993, Phys. Rev. B **47**, 8672.

Shiokawa, Y., M. Hara, Y. Haga, R. Amano, and M. Takahashi, 1994, J. Alloys Comp. **213–214**, 513.

Siegrist, T., H.W. Zandbergen, R.J. Cava, J.J. Krajewski and W.F. Peck, 1994, Nature **367**, 254.

Slaski, M., T. Laegrid, K. Fossheim, Z. Tomkowicz, and A. Szytula, 1992, J. Alloys Comp. **178**, 249.

Smith, J.L., S.E. Brown, B.R. Cooper, Z. Fisk, A.L. Giorgi, J.D. Thompson and J.O. Willis, 1987, J. Magn. Magn. Mater. **70**, 347.

Solanki-Moser, M., B. Buffat, P. Wachter, W.X. Zhong, B. Czeska, B. Chevalier and J. Etourneau, 1987, J. Magn. Magn. Mater. **63–64**, 677.

Spitzfaden, R., A. Loidl, J.G. Park and B.R. Coles, 1996, J. Phys.: Condens. Matter **8**, 2857.

Steeb, V.S. and G. Petzow, 1966, Trans. Metall. Soc. AIME **236**, 1756.

Steeb, V.S., G. Petzow and R. Tank, 1964, Acta Crystallogr. **17**, 90.

Steeman, R.A., E. Frikkee, C. van Dijk, G.J. Nieuwenhuys and A.A. Menovsky, 1988, J. Magn. Magn. Mater. **76–77**, 435.

Steeman, R.A., E. Frikkee, S.A.M. Mentink, A.A. Menovsky, G.J. Nieuwenhuys and J.A. Mydosh, 1990, J. Phys.: Condens. Matter **2**, 4059.

Steglich, F., C. Geibel, S. Horn, U. Ahlheim, M. Lang, G. Sparn, A. Loidl, A. Krimmel and W. Assmus, 1990a, J. Magn. Magn. Mater. **90–91**, 383.

Steglich, F., U. Ahlheim, C. Schank, C. Geibel, S. Horn, M. Lang, G. Sparn, A. Loidl and A. Kimmel, 1990b, J. Magn. Magn. Mater. **84**, 271.

Steglich, F., P. Gegenwart, C. Geibel, R. Helfrich, P. Hellmann, M. Lang, P. Link, R. Modler, G. Sparn, N. Büttgen and A. Loidl, 1996, Physica B **223–224**, 1.

Steiner, M.M., R.C. Albers and L.J. Sham, 1994, Phys. Rev. Lett. **72**, 2923.

Stepien-Damm, J., A. Baran and W. Suski, 1984, J. Less-Common Metals **102**, L5.

Stepien-Damm, J., D. Kaczorowski and R. Troc, 1987, J. Less-Common Metals **132**, 15.

Stewart, G.R., 1984, Rev. Mod. Phys. **56**, 755.

Stewart, G.R. and R.O. Elliott, 1986, Bull. Am. Phys. Soc. **31**, 345.

Sticht, J. and J. Kübler, 1992, Z. Phys. B **87**, 299.

Straub, G.K. and W. Harrison, 1985, Phys. Rev. B **31**, 7668.

Strydom, A.M. and P. de V. du Plessis, 1996, Physica B **223–224**, 222.

Strydom, A.M. and P. de V. du Plessis, 1997, Physica B **230–232**, 62.

Strydom, A.M., P. de V. du Plessis and V.V. Gridin, 1995, Solid State Commun. **95**, 867.

Strydom, A.M., P. de V. du Plessis and V.V. Gridin, 1996, Physica B **225**, 89.

Stüsser, N., Z. Zolnierek and X. Hu, 1998, J. Magn. Magn. Mater. **177–181**, 815.

Suezaki, Y. and H. Mori, 1969, Prog. Theor. Phys. **41**, 1177.

Sugiura, E., K. Sugiyama, H. Kawanaka, T. Takabatake, H. Fujii and M. Date, 1990, J. Magn. Magn. Mater. **90–91**, 65.

Sugiyama, K., H. Fuke, K. Kindo, K. Shimohata, A.A. Menovsky, J.A. Mydosh and M. Date, 1997, J. Phys. Soc. Japan **59**, 3331.

Suski, W., 1996, in: Handbook on the Physics and Chemistry of Rare Earths, Vol. 22, eds K.A. Gschneidner Jr. and L. Eyring (North-Holland, Amsterdam) pp. 143–294.

Suski, W., K. Wochowski and D. Badurski, 1985, Bull. Pol. Acad.: Chem. **42**, 285.

Suski, W., A. Baran and T. Mydlarz, 1989, Phys. Lett. A **136**, 89.

Suski, W., A. Baran, K. Wochowski and T. Mydlarz, 1991, J. Magn. Magn. Mater. **95**, L133.

Suski, W., A. Baran, L. Folcik, K. Wochowski, and T. Mydlarz, 1992a, J. Alloys Comp. **181**, 249.

Suski, W., F.G. Vagizov, H. Drulis, J. Janczak, and K. Wochowski, 1992b, J. Magn. Magn. Mater. **117**, 203.

Suski, W., A. Zaleski, D. Badurski, L. Folcik, K. Wochowski, B. Seidel, C. Geibel and F. Steglich, 1993, J. Alloys Comp. **198**, L5.

Suski, W., K. Wochowski, A. Zaleski and T. Mydlarz, 1995, J. Alloys Comp. **219**, 275.

Suski, W., F.G. Vagizov, K. Wochowski, H. Drulis and T. Mydlarz, 1996, J. Magn. Magn. Mater. **154**, 207.

Suski, W., T. Cichorek, K. Wochowski, B. Badurski, B.Y. Kotur and O.I. Bodak, 1997, Physica B **230–232**, 324.

Suzuki, T., T. Akazawa, F. Nakamura, K. Tanaka, H. Fujisaki, S. Aono, T. Fujita, T. Takabatake and H. Fujii, 1997, Physica B **188–200**, 483.

Süllow, S., B. Ludoph, B. Becker, G.J. Nieuwenhuys, A.A. Menovsky, J.A. Mydosh, S.A.M. Mentink, and T.E. Mason, 1995, Phys. Rev. B **52**, 12784.

Süllow, S., S.A.M. Mentink, T.E. Mason, W.J.L. Buyers, G.J. Nieuwenhuys, A.A. Menovsky and J.A. Mydosh, 1997a, Physica B **230–232**, 105.

Süllow, S., G.J. Nieuwenhuys, A.A. Menovsky, J.A. Mydosh, S.A.M. Mentink, T.E. Mason and W.J.L. Buyers, 1997b, Phys. Rev. Lett. **78**, 354.

Süllow, S., C.C. Mattheus, B. Becker, C.E. Snel, A. Schenck, G.J. Nieuwenhuys and J.A. Mydosh, 1997c, Physica B **230–232**, 43.

Süllow, S., B. Ludoph, B. Becker, G.J. Nieuwenhuys, A.A. Menovsky and J.A. Mydosh, 1997d, Phys. Rev. B **56**, 846.

Svoboda, P., P. Javorsky, V. Sechovsky and A.A. Menovsky, 1997, Magnetic phase diagram of UNi_2Si_2, unpublished work.

Szytula, A., S. Siek, J. Leciejewicz, A. Zygmund, and Z. Ban, 1988a, J. Phys. Chem. Solids **49**, 1113.

Szytula, A., M. Slaski, B.D. Dunlap, Z. Sungaila, and A. Umezawa, 1988b, J. Magn. Magn. Mater. **75**, 71.

Szytula, A., M. Kolenda, R. Troc, V.H. Tran, M. Bonet and J. Rossat Mignod, 1992, Solid State Commun. **81**, 481.

Szytula, A., M. Kolenda, V.H. Tran, R. Troc, F. Bourée and T. Roisnel, 1996, J. Magn. Magn. Mater. **153**, L255.

Taillefer, L. and G.G. Lonzarich, 1997, Phys. Rev. Lett. **60**, 1570.

Taillefer, L., R. Newbury, G.G. Lonzarich, Z. Fisk and J.L. Smith, 1987, J. Magn. Magn. Mater. **63–64**, 372.

Takabatake, T., H. Kawanaka, H. Fujii, Y. Yamaguchi, H. Sakurai, Y. Aoki and T. Fujita, 1989, J. Phys. Soc. Japan **58**, 1918.

Takabatake, T., S. Miyata, H. Fujii, Y. Aoki, T. Suzuki, T. Fujita, J. Sakurai and T. Hiraoka, 1990a, J. Phys. Soc. Japan **59**, 4412.

Takabatake, T., H. Fujii, S. Miyata, H. Kawanaka, Y. Aoki, T. Suzuki, T. Fujita, Y. Yamaguchi and J. Sakurai, 1990b, J. Phys. Soc. Japan **59**, L16.

Takabatake, T., S. Miyata, H. Fujii, K. Yokoyama, and M. Taniguchi, 1992a, Solid State Commun. **81**, 433.

Takabatake, T., H. Iwasaki, H. Fujii, S. Ikeda, S. Nishigori, Y. Aoki, T. Suzuki and T. Fujita, 1992b, J. Phys. Soc. Japan **61**, 778.

Takabatake, T., Y. Maeda, H. Fujii, S. Ikeda, S. Nishigori, T. Fujita, A. Minami, I. Oguro, K. Sugiyama, K. Oda and M. Date, 1993, Physica B **186–188**, 734.

Takabatake, T., Y. Maeda, T. Konishi and H. Fujii, 1994, J. Phys. Soc. Japan **63**, 2853.

Takagi, S., H. Suzuki and T. Kusumoto, 1993, J. Phys. Soc. Japan **62**, 1037.

Takahashi, T., N. Sato, T. Yokoya, A. Chainani, T. Morimoto and T. Komatsubara, 1996, J. Phys. Soc. Japan **65**, 156.

Takegahara, K. and Y. Kaneta, 1992, Prog. Theor. Phys. (Suppl. 108), 55.

Takegahara, K., Y. Kaneta and T. Kasuya, 1990, J. Phys. Soc. Japan **59**, 4394.

Takeuchi, T., K. Watanabe, T. Taniguchi, T. Kuwai, A. Yamagishi and Y. Miyako, 1994, Physica B **201**, 243.

Takeuchi, T., T. Yamada, Y. Miyako, K. Oda, K. Kindo, B. Becker, S. Ramakrishnan, A.A. Menovsky, G.J. Nieuwenhuys and J.A. Mydosh, 1997, Phys. Rev. B **56**, 10778.

Thieme, S., L. Degiorgi, P. Wachter, Y. Dalichaouch, and M.B. Maple, 1996, Physica B **223–224**, 192.

Thompson, J.D., Z. Fisk and L.C. Gupta, 1985, Phys. Lett. A **110**, 470.

Thompson, J.D., Z. Fisk and H.R. Ott, 1986, J. Magn. Magn. Mater. **54–57**, 393.

Thuery, P. and Z. Zolnierek, 1993, Solid State Commun. **85**, 485.

Tien, C., C.S. Wur, H.M. Duh, I.J. Jang, J.S. Hwang, K.J. Lin, J.I. Yuh and S.T. Lin, 1994, Solid State Commun. **89**, 171.

Torikachvili, M.S., C. Rossel, M.W. McElfresh, M.B. Maple, R.P. Guertin and G.P. Meisner, 1986, J. Magn. Magn. Mater. **54–57**, 365.

Torikachvili, M.S., J.W. Chen, Y. Dalichaouch, R.P. Guertin, M.W. McElfresh, C. Rossel, M.B. Maple, and G.P. Meisner, 1987, Phys. Rev. B **36**, 8660.

Torikachvili, M.S., L. Rebelsky, K. Motoya, S.M. Shapiro, Y. Dalichaouch and M.B. Maple, 1990, Physica B **163**, 117.

Torikachvili, M.S., R.F. Jardim, C.C. Becerra, C.H. Westphal, A. Paduan, A. Lopez and L. Rebelsky, 1992, J. Magn. Magn. Mater. **104**, 69.

Tran, V.H., 1996, J. Phys.: Condens. Matter **8**, 6267.

Tran, V.H. and R. Troc, 1990a, J. Magn. Magn. Mater. **88**, 287.

Tran, V.H. and R. Troc, 1990b, J. Magn. Magn. Mater. **86**, 231.

Tran, V.H. and R. Troc, 1991a, J. Less-Common Metals **175**, 267.

Tran, V.H. and R. Troc, 1991b, J. Magn. Magn. Mater. **102**, 74.

Tran, V.H. and R. Troc, 1993a, in: Proc. Int. Conf. on Physics of Transition Metals, Darmstadt, 1992, eds P. Oppeneer and J. Kübler, p. 850.

Tran, V.H. and R. Troc, 1993b, Physica B **186–188**, 744.

Tran, V.H. and R. Troc, 1997, Acta Phys. Polonica A **92**, 299.

Tran, V.H. and R. Troc, 1998, Phys. Rev. B, in press.

Tran, V.H., R. Troc and B. Badurski, 1990, J. Magn. Magn. Mater. **291**, 291.

Tran, V.H., R. Troc and D. Badurski, 1993, J. Alloys Comp. **199**, 193.

Tran, V.H., R. Troc, F. Bourée, T. Roisnel, and G. André, 1995a, J. Magn. Magn. Mater. **140–144**, 1377.

Tran, V.H., R. Troc and D. Badurski, 1995b, J. Alloys Comp. **219**, 285.

Tran, V.H., D. Kaczorowski, T. Roisnel, R. Troc, H. Noël, F. Bourée and G. André, 1995c, Physica B **205**, 24.

Tran, V.H., R. Troc, A.J. Zaleski, F.G. Vagizov, and H. Drulis, 1996a, Phys. Rev. B **54**, 15907.

Tran, V.H., F. Bourée, G. André and R. Troc, 1996b, Solid State Commun. **98**, 111.

Tran, V.H., A.J. Zaleski, R. Troc and P. de V. du Plessis, 1996c, J. Magn. Magn. Mater. **162**, 247.

Tran, V.H., Z. Zolnierek, F. Bourée and T. Roisnel, 1996d, J. Magn. Magn. Mater. **161**, 270.

Tran, V.H., R. Troc, P. de V. du Plessis, G. André and F. Bourée, 1997, Phys. Rev. B **56**.

Tran, V.H., G. André, F. Bourée, R. Troc and H. Noël, 1998a, J. Alloys Comp., in press.

Tran, V.H., R. Troc and G. André, 1998b, J. Magn. Magn. Mater., in press.

Troc, R., 1986, in: Proc. 16èmes Journées des Actinides, Eibsee, Germany, p. 39.

Troc, R. and V.H. Tran, 1988, J. Magn. Magn. Mater. **73**, 389.

Troc, R., D. Kaczorowski, H. Noël and R. Guerin, 1990, J. Less-Common Metals **159**, L21.

Troc, R., V.H. Tran, F.G. Vagizov and H. Drulis, 1993a, J. Alloys Comp. **200**, 37.

Troc, R., D. Kaczorowski, M. Kolenda, A. Szytula, M. Bonnet, J. Rossat Mignod and H. Noël, 1993b, Solid State Commun. **87**, 573.

Troc, R., V.H. Tran, F.G. Vagizov, I.M. Reznik, and L. Shlyk, 1994a, Physica B **199–200**, 647.

Troc, R., P. Burlet, H. Noël, D. Kaczorowski, and J. Rossat Mignod, 1994b, Physica B **202**, 167.

Troc, R., V.H. Tran, F.G. Vagizov and H. Drulis, 1995, Phys. Rev. B **51**, 3003.

Trygg, J., B. Johansson and O. Eriksson, 1994, Phys. Rev. B **49**, 7165.

Trzebiatowski, W., 1980, in: Ferromagnetic Materials, Vol. 1, ed. E.P. Wohlfarth (North-Holland, Amsterdam) pp. 415–449.

Tsai, T.H., J.A. Gerber, J.W. Weymout and D.J. Sellmyer, 1978, J. Appl. Phys. **49**, 1507.

Tsvyashchenko, A.V. and L.N. Fomicheva, 1991, J. Less-Common Metals **171**, L5.

Tuan, N.C., V. Sechovsky, M. Divis, P. Svoboda, H. Nakotte, F.R. de Boer and N.H. Kim-Ngan, 1993, J. Appl. Phys. **73**, 5677.

Ueda, K., 1976, Solid State Commun. **19**, 965.

Ueda, K., 1977, J. Phys. Soc. Japan **43**, 1497.

Uemura, Y.J. and G.M. Luke, 1993, Physica B **186–188**, 223.

Uwatoko, Y., K. Iki, G. Oomi, Y. Onuki and T. Komatsubara, 1992, Physica B **177**, 147.

Uwatoko, Y., G. Oomi, V. Sechovsky, L. Havela, E. Brück and F.R. de Boer, 1994, J. Alloys Comp. **213–214**, 281.

Vagizov, F.G., H. Drulis, W. Suski and A.V. Andreev, 1993, J. Alloys Comp. **191**, 213.

Vagizov, F.G., W. Suski, K. Wochowski and H. Drulis, 1995, J. Alloys Comp. **219**, 271.

Vagizov, F.G., R. Troc, V.H. Tran and H. Drulis, 1997, J. Magn. Magn. Mater. **168**, 299.

van Dijk, N.H., F. Bourdarot, B. Fak, F. Lapierre, L.P. Regnault, P. Burlet, J. Bossy, N. Pyka and A.A. Menovsky, 1997, Physica B **234–236**, 692.

van Engelen, P.P.J. and K.H.J. Buschow, 1990, J. Magn. Magn. Mater. **84**, 47.

Veenhuizen, P.A., 1988, Thesis, University of Amsterdam.

Veenhuizen, P.A., F.R. de Boer, A.A. Menovsky, V. Sechovsky and L. Havela, 1988a, J. Phys. (Paris) **49**(C8), 485.

Veenhuizen, P.A., J.C.P. Klaasse, F.R. de Boer, V. Sechovsky and L. Havela, 1988b, J. Appl. Phys. **63**, 3064.

Venturini, G. and B. Malaman, 1996, J. Alloys Comp. **235**, 201.

Verniere, A., P. Lejay, P. Bordet, J. Chenavas, J.L. Tholence, J.X. Boucherle and N. Keller, 1995, J. Alloys Comp. **218**, 197.

Verniere, A., S. Raymond, J.X. Boucherle, P. Lejay, B. Fak, J. Flouquet and J.M. Mignot, 1996a, J. Magn. Magn. Mater. **153**, 55.

Verniere, A., P. Lejay, J.X. Boucherle, J. Muller, S. Raymond, J. Flouquet and A. Sulpice, 1996b, J. Magn. Magn. Mater. **153**, 55.

Villars, P. and L.D. Calvert, 1991, Pearson's Handbook of Crystallographic Data for Intermetallic Phases, 2nd edn (American Society for Metals, Materials Park, OH).

Vomhof, T., R. Pöttgen and W. Jeitschko, 1993, J. Alloys Comp. **196**, 173.

Waerenborgh, J.C., L. Shlyk and M. Almeida, 1996, in: Proc. 26iémes Journées des Actinides, Sklarska Poreba, Poland, p. 84.

Waerenborgh, J.C., M.S. Rogalski, A.P. Gonçalves, J.B. Sousa and M. Almeida, 1997, Solid State Commun. **104**, 271.

Walker, M.B., W.J.L. Buyers, Z. Tun, W. Que, A.A. Menovsky and J.D. Garrett, 1993, Phys. Rev. Lett. **71**, 2630.

Walker, M.B., Z. Tun, W.J.L. Buyers, A.A. Menovsky and W. Que, 1994, Physica B **199**, 165.

Walter, U., C.-K. Loong, M. Loewenhaupt and W. Schlabitz, 1986, Phys. Rev. B **33**, 7875.

Wassilew, C., B. Kirsch, G. Sparn, C. Schank, C. Geibel and F. Steglich, 1994, Physica B **199–200**, 162.

Wastin, F., 1991, Synthesis, characterisation and studies of physico-chemical properties of actinide intermetallic compounds, Thesis, University of Liege.

Wastin, F., 1997, unpublished work.

Wastin, F., J. Rebizant, J.C. Spirlet, J. Fuger, B. Kanellakopulos and V. Sechovsky, 1993a, J. Alloys Comp. **193**, 119.

Wastin, F., J. Rebizant, J.C. Spirlet, C. Sari, C.T. Walker and J. Fuger, 1993b, J. Alloys Comp. **196**, 87.

Wastin, F., J.C. Spirlet and J. Rebizant, 1995, J. Alloys Comp. **219**, 232.

Wastin, F., S. Zwirner, A. Seret, J.C. Waerenborgh, L.C.J. Pereira, E. Bednarczyk and J. Rebizant, 1996a, Physica B **224**, 211.

Wastin, F., E. Bednarczyk, J. Rebizant and J.P. Sanchez, 1996b, in: Proc. 26iémes Journées des Actinides, Sklarska Poreba, Poland, p. 99.

Wastin, F., E. Bednarczyk, J. Rebizant, S. Zwirner and G.H. Lander, 1997, J. Alloys Comp. **262**, 124.

Weger, M., 1985, Philos. Mag. B **52**, 701.

Weger, M. and N.F. Mott, 1985, J. Phys. C **18**, L201.

Wei, W., Z. Tun, W.J.L. Buyers, B.D. Gaulin, T.E. Mason, J.D. Garrett and E.D. Isaacs, 1992, J. Magn. Magn. Mater. **108**, 77.

Wiese, S., E. Gamper, H. Winkelmann, B. Büchner, M.M. Abd-Elmeguid, H. Miklitz and T. Takabatake, 1997, Physica B **230–232**, 95.

Wulff, M., J.M. Fournier, A. Delapalme, B. Gillon, V. Sechovsky, L. Havela and A.V. Andreev, 1990, Physica B **163**, 331.

Wyslocki, J.J., W. Suski and A. Baran, 1990, J. Less-Common Metals **163**, 115.

Wyslocki, J.J., W. Suski, P. Pawlik and K. Wochowski, 1995, J. Magn. Magn. Mater. **140**, 1915.

Wyslocki, J.J., W. Suski, P. Pawlik, K. Wochowski, B. Kotur and O.I. Bodak, 1996, J. Magn. Magn. Mater. **162**, 239.

Yamada, H. and S. Takada, 1973a, Prog. Theor. Phys. **49**, 1401.

Yamada, H. and S. Takada, 1973b, J. Phys. Soc. Japan **34**, 51.

Yang, C.N., 1952, Phys. Rev. **85**, 808.

Yaresko, A.N., P.M. Oppeneer, V.N. Antonov, A.Y. Perlov and H. Eschrig, 1997, Physica B **230–232**, 513.

Yethiraj, M., R.A. Robinson, J.J. Rhyne, J.A. Gotaas and K.H.J. Buschow, 1989, J. Magn. Magn. Mater. **79**, 355.

Yuen, T., C.L. Lin, P. Schlottmann, N. Bykovetz, P. Pernambuco-Wise and J.E. Crow, 1991, Physica B **171**, 362.

Yusuf, S.M., L.M. Rao, P. Raj, T.V.C. Rao and V.C. Sahni, 1996a, Physica B **223–224**, 201.

Yusuf, S.M., L.M. Rao and P. Raj, 1996b, Phys. Rev. B **53**, 28.

Zeleny, M. and F. Zounova, 1989, Czech. J. Phys. B **39**, 466.

Zeleny, M., J. Schreiber and S. Kobe, 1985, J. Magn. Magn. Mater. **50**, 31.

Zeleny, M., F. Zounova and A.V. Andreev, 1988, Phys. Status Solidi A: **109**, K67.

Zelinsky, A., Y.N. Grin, K. Hiebl, P. Rogl, H. Noël, G. Hilscher and G. Schaudy, 1995, J. Magn. Magn. Mater. **139**, 23.

Zemni, S., J. Vicat, B. Lambert, R. Madar, P. Chaudouet and J.P. Senateur, 1988, J. Less-Common Metals **143**, 113.

Zhong, W.-X., B. Lloret, W.L. Ng, B. Chevalier, J. Etourneau and P. Hagenmuller, 1985, Rev. Chim. Miner. **22**, 711.

Zochovski, S.W., S.A. Greeger and M.F. Collins, 1995, J. Magn. Magn. Mater. **140–144**, 1399.

Zolnierek, Z., 1988, J. Magn. Magn. Mater. **76–77**, 231.

Zolnierek, Z. and J. Mulak, 1995, J. Magn. Magn. Mater. **140–144**, 1393.

Zolnierek, Z. and E. Szulc, 1992, J. Alloys Comp. **187**, 255.

Zolnierek, Z. and A.J. Zaleski, 1992, Solid State Commun. **84**, 917.

Zolnierek, Z., D. Kaczorowski, R. Troc and H. Noël, 1986, J. Less-Common Metals **121**, 193.

Zolnierek, Z., H. Noël and D. Kaczorowski, 1987, J. Less-Common Metals **128**, 265.

Zwirner, S., J.C. Spirlet, J. Rebizant, W. Potzel, G.M. Kalvius, C. Geibel and F. Steglich, 1993, Physica B **186–188**, 681.

Zwirner, S., J.C. Waerenborgh, F. Wastin, J. Rebizant, J.C. Spirlet, W. Potzel and G.M. Kalvius, 1997, Physica B **230–232**, 80.

chapter 2

MAGNETIC RECORDING HARD DISK THIN FILM MEDIA

J.C. LODDER

Information Storage Technology Group
MESA Research Institute
University of Twente, P.O. Box 217
7500 AE Enschede, The Netherlands

So, naturalists observe, a flea
Hath smaller fleas that on him prey;
And these have smaller still to bite 'em;
And so proceed *ad infinitum*

Jonathan Swift (1667–1745);
On Poetry, A Rhapsody [1733]

Handbook of Magnetic Materials, Vol. 11
Edited by K.H.J. Buschow

CONTENTS

1. Introduction to magnetic recording

Information has been stored throughout history. It started with cuneiform and cave-paintings a long time ago using primitive technologies. Perhaps the oldest example of a recorded transition of magnetization can be found in the magnetic rock formation situated on the bottom of the Atlantic Ocean (Cox et al. 1967).

Nowadays, information storage plays a major role in our society by using advanced technologies and production methods to produce recording apparatus for audio, video and data applications.

In 1888 an original method for recording sound signals was published by Oberlin Smith (Smith 1888). He described how a thread of cotton or silk covered with small particles (the medium) could record and play. In August 1898 Valdemar Poulsen invented his Telegraphone which he demonstrated at the World Fair in Paris in 1900 (Poulsen 1890). This first working magnetic recording apparatus was honoured with the Grand Prix.

1.1. Introduction to storage technologies

This early invention has been evaluated to the present high quality and very compact magnetic recording products. Magnetic recording technology is continuing to evolve at a rapid pace resulting in longer playing times and more data being stored in ever decreasing volumes. It includes: audio, video and data storage applications in the form of tapes, floppy and hard disks in products such as digital video recorders, digital camera recorders, audio equipment, electronic games, video telephones, fax machines and personal organizers. Magnetic recording technology has an excellent future growth potential. Market requirements include continued reduction in the peripheral device size and power consumption while maintaining an exponential increase in capacity with time. This trend will continue in the future because science and technology still have enough room for increasing densities with high recording performance using smaller volumes. More data in smaller volumes for a lower price is one of the goals of the storage manufacturers. In addition they continue to improve the speed, reliability, and throughput.

Information can be recorded by applying a variety of principles. In fig. 1.1 an overview is given of the various principles such as the human brain, cryoelectric, semiconductor, and the various applications of magnetic and optical storage.

The various types of storage are given in the relation capacity vs. average access time.

Different types of storage technologies are for instance: solid state memories, magnetic hard disk memories, magnetic tape, magnetic floppies, optical disks and tapes (write once or rewritable – WORM). A kind of storage hierarchy can be drawn based on access time and cost per byte (e.g., Hoagland and Monson 1991). In fig. 1.2 such a hierarchy is presented.

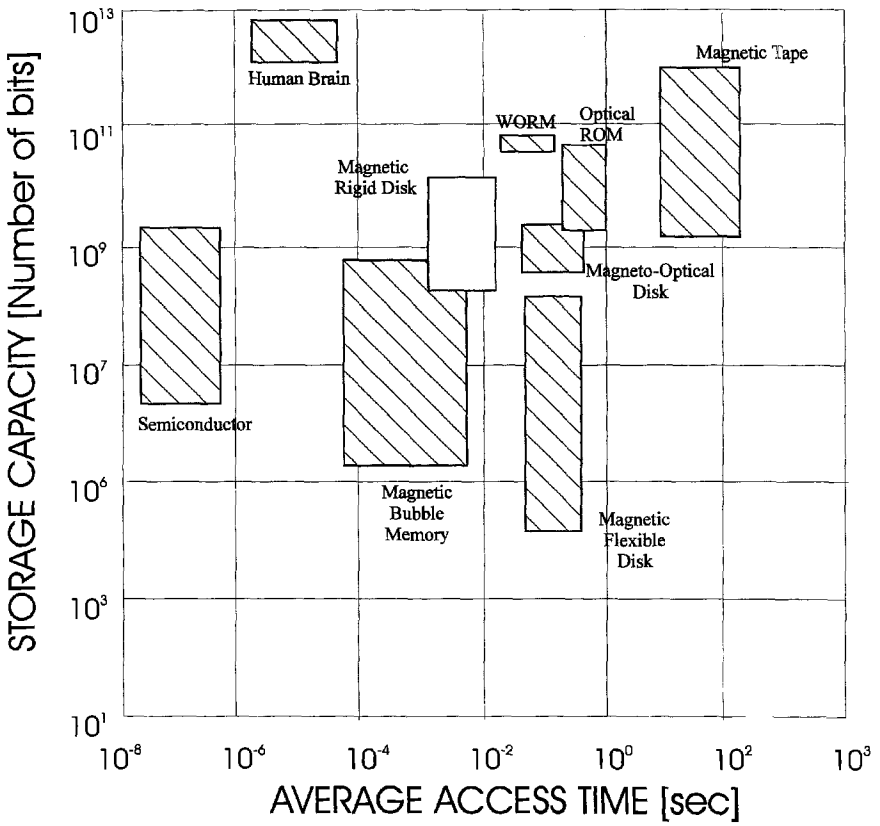

Fig. 1.1. Capacity as a function of access time for various storage principles.

Semiconductor memories are very fast (about 20 times that of most of the disk drives), they are expensive but interact directly with the processor in a mass storage system. This memory is volatile (needs a power supply at all times to maintain its contents) while the magnetic disk and tape are non-volatile. Although the access rate is very fast and the capacity very high this type of memory is still very expensive. Depending on the application one should use a specific type of recording. Although disk drives offer access times of a few milliseconds they are cheaper and standard in PC and laptop applications. The removable storage is the floppy disk but it is envisaged that even removable hard disks can take this over. Magnetic tape recording is used if the application of low-cost off-line storage is allowed.

Optical technology is growing day by day. A compact disk can store 650 Mbytes and has a very low price. For other applications in which fewer copies of the disk are required a number of CD-ROM recorders are on the market at a much higher price. A relatively new type of optical digital video disk (DVD) will be available very soon and can store up to 17 gigabytes.

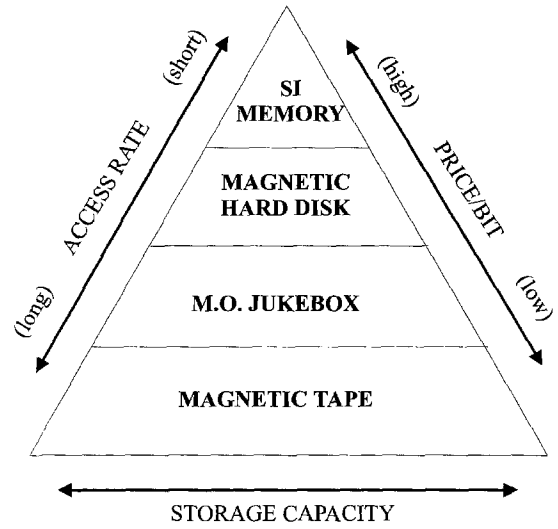

Fig. 1.2. Hierarchy for various storage technologies.

In the future we can expect many new applications in storage technologies. One of the most important ones so far is the holographic storage technology. With this technology a laser is used to etch a hologram in a crystal or other holographic media. The pattern can then be read from the media by beaming a laser at the appropriate angle. By changing the angle different patterns can be read. A capacity of terabytes is expected in a volume compared to a sugar-cube-size crystal.

Because hard disks are the most common type of mass storage today thanks to their low cost, high speed, and relatively high storage capacity we shall discuss this type of magnetic media further.

1.1.1. Magnetic recording

At present, most information (about 95%) is still stored on paper, 3% on microfiche and the remaining 2% by magnetic, optical, magneto-optical and semiconductor storage devices. Nevertheless, magnetic recording nowadays represents a multibillion dollar industry and is still a growing market.

Magnetic recording is the storage of information achieved through changing the magnetization of a recording medium using a magnetic field generated by the recording head. At the end of the 19th century a start was made to use magnetism and magnetic media to store information.

The concept of magnetic recording is given in fig. 1.3. Here the head is positioned above the moving media (magnetized in one direction) and when the (electromagnetic) head is switched on and off, magnetized areas, with opposite magnetizations, are written in the media (fig. 1.3(a)). The cross-section in fig. 1.3(b) shows the magnetic field of the head gap.

This track of information can be read by the inverse process. The head senses the electric current generated by the moving flux originating from the written bits in the medium.

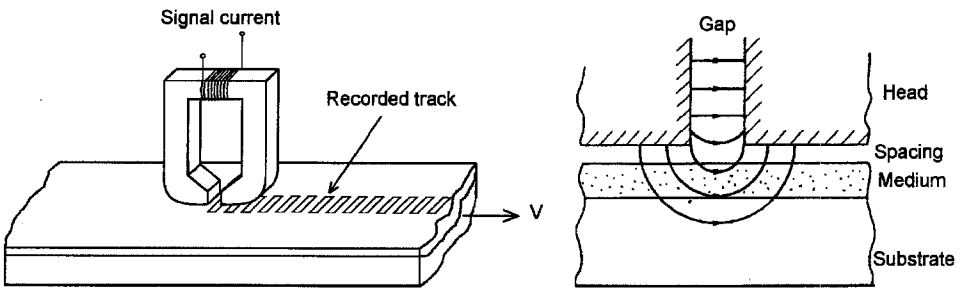

Fig. 1.3. Principle sketch of longitudinal magnetic recording.

The area density is given by the product of the linear bit density and the track density. Higher density means creating narrower tracks and more compact bits. In order to achieve higher densities the head and medium must become closer to each other (smaller spacing in fig. 1.3(b)) and this fundamental requirement has encouraged much of the technological challenge for both components.

From the first demonstration by Poulson (1890) the magnetic recording medium has gone through dramatic improvements. The original steel wire was replaced in the early 1930s by small spherical Fe particles and later by cubic Fe_3O_4. Since then great improvements have been made by changing the material and the shape and size of the particle. In 1949 γ-Fe_2O_3 acicular particles with a length of 0.5 μm and an aspect ratio of 10 were used. Compact cassette tape made from CrO_2 particles was introduced in 1966. From the early 1950s thin magnetic films have been proposed as a magnetic recording medium. Since then extensive research has been carried out and many thin film media have been developed by electroless and electrodeposition, vacuum evaporation and sputtering. At present, many recording media are prepared by vacuum deposition technologies, such as metal evaporated tape and hard disks for magnetic recording as well as for magneto-optic recording. An enormous amount of research is nowadays being carried out on the new hard disk media, mostly produced by sputtering, in order to obtain very high densities. Since 1977 research has been published of media with the magnetic anisotropy perpendicular to the medium surface (PMR). This is in contrast with the longitudinal magnetic recording mode (LMR). The former is not a subject of discussion in this chapter. Here we shall concentrate on the longitudinal mode of magnetic recording as used nowadays. Magnetic recording can be used for professional as well as for consumer applications but until now only the LMR technology is commercially available. A storage medium for the various applications can be made in the form of tape, floppy or hard disk. The trends in magnetic recording technology are continuously increasing recording densities and storage capacity with a decreasing price per bit. The following books (Mee and Daniel 1987–1988; Mee and Daniel 1990, 1996; Hoagland and Monson 1991; Bertram 1994; Buschow 1993; Mallinson 1993; Asher 1997) can be consulted for general references on the subject of recording and related technologies.

1.1.1.1. Magnetic recording modes. As previously mentioned, we can define different modes of magnetic recording dependent on the direction of the magnetization (magnetic

anisotropy), namely LMR and PMR. In the former the magnetic anisotropy lies in the plane of the medium and in the case of PMR the anisotropy is directed parallel to the medium normal. MOR also requires a perpendicular magnetic anisotropy. As said before we shall focus our discussion on hard disk recording with the magnetization parallel to the disk.

1.1.1.2. Digital recording. Modern recording technologies are based on digital signal processing, even for audio and video recording. The reason for moving into the digital technologies is that they accept a much lower signal-to-noise ratio, ease of error detection and correction and integration of LSI circuit technology. The input data may be either analogue (audio, video; using an A/D converter) or digital (computer data). Examples are the Minidisk and DCC (Digital Compact Cassette) for audio application and the not yet commercialized HDTV digital VTR. More information on digital recording technologies can be found in the books mentioned at the end of section 1.1.1.

1.1.1.3. Rigid disk recording. The first commercial disk drive (IBM Ramac, 1956) used fifty, 24 inch diameter disks providing a capacity of 5 Mbytes and access time of almost 1 second. Today, the 2.5 inch form factor is slowly becoming the volume leader at the low end, while 3.5 inch drives are the leaders in performance. Capacity is more than 1 Gbyte with an access time of 6–11 milliseconds.

In this chapter we focus on one of the most important mass storage technologies namely the hard disk or "Winchester" technology (introduced by IBM). In our case the medium consists of a magnetic thin film on a rigid substrate and as rigid disk can be installed as a non-removable stack in a disk drive. The disk rotates at a constant angular speed (V) and consists of recorded concentric data tracks. The recording heads (for fast accessing, usually two) are mounted on a slider, fly above the tracks and are moved by an actuator that positions the head(s) above a selected track for reading or writing. Figure 1.4 gives the principle of the heads moving above the disk.

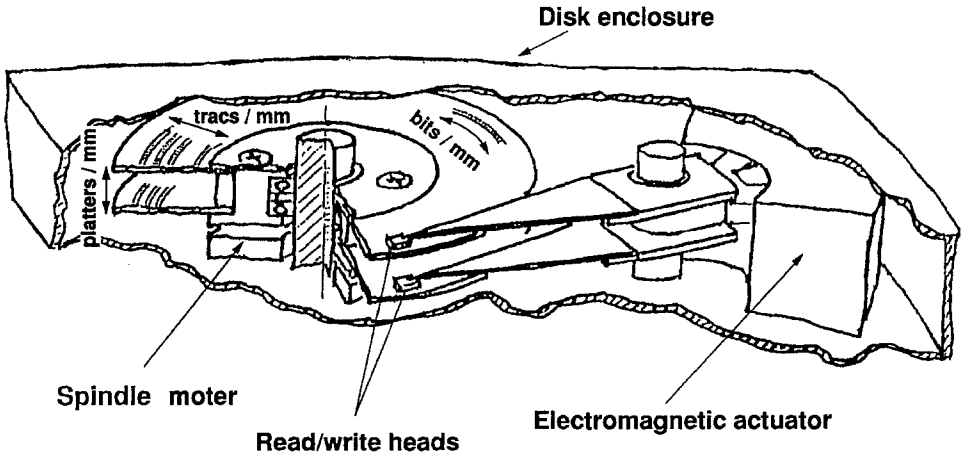

Fig. 1.4. Schematic of magnetic disk drive components (Miura 1991).

The load of the suspension slider on the medium is about 50 mN while the apparent area of contact is about 2 mm^2 and consequently the nominal contact pressure is about 30 kPa. The rotating speed is 3600 rpm with a diameter of 2.5 inch (= 63.5 mm) or 3.5 inch (= 88.9 mm).

In contrast to tape recording the disk drives provide almost instantaneous access to a very large number of data records. The data is stored in the circular tracks that are divided into sectors. The achievable track density depends primary on controlling the head positioning precision. Playback signals and noise strongly depend on the head positioning accuracy. In order to maintain a good signal-to-noise ratio and resolution at higher track densities the spacing between the head and medium is reduced. The limit of such a reduction is contact recording, which will create problems in the area of friction and wear. The linear bit density is, in principle, dependent upon the minimum recordable wavelength (λ) and the latter can be given by:

$$\lambda = v/f \quad [\text{m}], \tag{1.1}$$

here f is the recorded frequency and v the speed of the disk. In principle it is possible to record at high frequency at a slow speed. However to obtain a high data rate the speed of the disk should be fast.

The smallest wavelength of recorded amplitude is governed by the extent to which the transition zone (the area between two opposite magnetization directions) can be made narrow and sharply defined.

The entire assembly of a hard disk drive is housed in a sealed casing, thereby reducing the likelihood of dust and other particles from interfering with the head assembly and causing "head crash". The drive is attached to a host computer through a controller and host interface.

The Winchester disk technology is almost exclusively used to implement the "on-line" storage of most computer systems. Capacities of drive units are increasing continuously and are at present in the range of tens of megabytes to many gigabytes. In the case of conventional drives the data transfer rates are in the order of 10 MByte/s but can be increased by using parallel transfer disks or disk arrays.

The demand for hard disk technology is still increasing due to growing number of applications such as in desktop computers, laptop PCs, multimedia, network data basis, note books etc.

1.1.1.4. Magnetic recording complexity. As with many electronic systems magnetic recording is very complex. It can be divided into different major areas like the *recording performance* (i.e., capacity, noise, error rate, durability), the *mechanics* (i.e., velocity of the media, stability of speed, positioning of the head), *circuit technology* (i.e., peak detection, bandwidth, write current frequency), *head* (i.e., magnetic properties, track width, gap length, profile), *medium* (i.e., magnetic properties, roughness, corrosion resistance) and, last but not least, the *head-medium interface* (i.e., mechanics, tribology and magnetic).

The large increase in areal density during the past decade is not only dependent on improvements in one of the above aspects but without any doubt the recording medium performance is one of the most important factors for increasing the recording density.

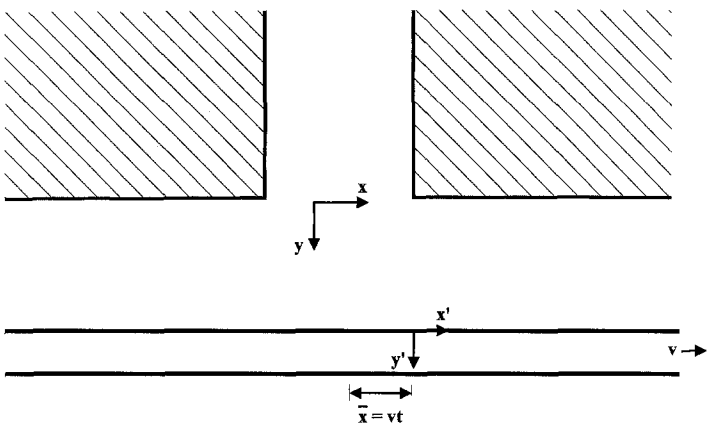

Fig. 1.5. Principle sketch of the spacing between the ring head and the medium for longitudinal recording.

1.1.1.5. Head–medium interaction: flying height. One of the important parameters for increasing of the areal density is the spacing between the head and the medium. The so-called magnetic spacing loss between the recording head and the disk must be reduced.

In fig. 1.5 a principle sketch shows the spacing d between the ring head and the medium having a thickness δ and a speed v. For such a configuration the field distribution is given by Karlqvist (1954) and can be defined as:

$$H_x = \frac{H_g}{\pi}\left[\arctan\left\{\frac{g/2+x}{y}\right\} + \arctan\left\{\frac{g/2-x}{y}\right\}\right] \quad [\mathrm{A\,m^{-1}}]. \tag{1.2}$$

Here H_x is the longitudinal head-field distribution, H_g is the field in the gap of the head, and g is the gap length. In the case of high-density recording it is necessary to know that this equation is not very precise especially at small head to medium separations. In this case peaks in H_x appear near to the gap edges (Middleton 1996). The variation of the head field is then given by:

$$H_x(0, y) = \frac{2H_g}{\pi}\arctan\frac{g}{2y} \quad [\mathrm{A\,m^{-1}}]. \tag{1.3}$$

If the head comes closer to the medium (y/g is small) the reduced field amplitude (H_x/H_g) approaches one. The output (PW_{50}) introduced by a transition is given by a formula in section 2.3.

Three different areas of head to medium spacing can be defined, namely, the conventional air bearing having a flying height of about 50 nm, the so-called proximity recording, which varies between 13–40 nm, while a space of less than 2.5 nm is called contact recording.

It can be estimated that for densities in the (near) future, the head must be in contact with the medium in order to obtain the high densities with a sufficient signal. This immediately

brings us to one of the most important aspects of magnetic recording, i.e., the wear and tribology problems. In order to overcome these problems disk overcoat and lubrication properties are very important. Another very important property is the surface structure of the substrate used. Textured substrates are used to avoid head–medium stiction.

1.2. Basic magnetic properties

In general, to understand the magnetic recording processes (reading, writing and the interaction between head and medium) a knowledge of the relationship between the three quantities $\boldsymbol{B}$ (magnetic flux density or magnetic induction), $\boldsymbol{H}$ (the magnetic field) and $\boldsymbol{M}$ (the magnetization) is essential. At all points in three dimensional space their magnitude and direction of the vector quantity is defined. Magnetism is a phenomenon that results from the motion of charged particles. In the magnetic recording process we have to deal with two types of motion namely electrons in a conductor and orbital and spin motion of electrons in solids.

A *magnetic field* is generated by the motion of an electrical charge and there are two ways to generate such a field, either by an electric current through a conductor or by a permanent magnet. In the latter there are no conventional electrical currents but the source comprises the orbit motion and the spinning electrons. The concept of magnetic dipole moment is perhaps the most basic parameter for the materials discussed for recording applications. Especially the spins of the unpaired electrons which also generate a magnetic moment without a conventional electric current are important.

If an electric current i flows through a coil having an axial length of l and n turns then the axial magnetic field inside the coil will be:

$$H = ni/l \quad [\mathrm{A\,m^{-1}}]. \tag{1.4}$$

The generated magnetic field lines form close patterns around this current through the wire.

The direction of the magnetic field lines inside the coil is from S to N and outside the coil from N to S. Magnetic field lines from a permanent magnet travel from N to S inside as well outside the magnet, which means that the latter has an "open" path at the poles of the magnet.

Magnetization is defined as:

$$M \cong \lim_{v \to 0} (1/V) \sum_i \mu_i \quad [\mathrm{A\,m^{-1}}], \tag{1.5}$$

where V is the volume and μ_i the atomic moment. The magnetization is the net vector moment per unit volume.

When a field is applied to the material each moment experiences a torque that tends to rotate it towards the direction of that field. If the applied field is large enough then all magnetic dipole moments are directed parallel to this field. At this point the material has reached its saturation field. As will be seen later, for a recording medium material this is not sufficient because even in the absence of any external or applied field the medium must be able to sustain its own magnetic flux. In other words for this application the materials must sustain magnetic flux by virtue of its own internal field, which will require spontaneous

alignment of the dipole moments. This is sometimes called spontaneous magnetization or remanent magnetization.

Because the origin of magnetization are the spinning electrons in atoms the magnetization in the free space is zero. The two motions of the electrons (spinning on its own axis and orbits around the nucleus) are governed by the laws of quantum physics. The magnetic moment of a spinning electron is called Bohr magneton μ_B and is determined by:

$$\mu_B = \frac{eh}{4\pi m} = 0.92740154 \times 10^{-24} \quad [\mathrm{A\,m^2}] = [\mathrm{J/T}], \tag{1.6}$$

where e = electron charge = 1.602×10^{-19} C, h = Planck's constant = $6.6260755 \times 10^{-34}$ J s and m = electron mass = $9.1093897 \times 10^{-31}$ kg.

The group of 3d transition metals (Mn, Cr, Fe, Ni and Co) do have an unfilled 3d shell and consequently a non compensated electron spin moment. This shows immediately the potential for applications.

The magnetic moments for the 3d elements Ni, Co, Fe, Mn and Cr given in fig. 1.10. From this figure it can be seen that the most important ferromagnetic materials used in recording media (Fe, Co and Ni) have a positive value of the exchange integral, while the antiferromagnetic 3d elements Cr and Mn has a negative value. The netto magnetic moment μ_B for Fe, Co and Ni are, respectively, 2.2, 1.7 and 0.6.

If a magnetic field is generated by a current in a material than the material reacts with the generation of a magnetic induction $\boldsymbol{B}$ [T].

In the free space $\boldsymbol{B}$ a linear function of $\boldsymbol{H}$ is given by:

$$\boldsymbol{B} = \mu_0 \boldsymbol{H} \quad [\mathrm{T}]. \tag{1.7}$$

Here μ_0 is a universal constant called permeability in vacuum ($\mu_0 = 4\pi \times 10^{-7}$ H/m = 1.256×10^{-6} H/m).

In recording materials (ferromagnets and ferrimagnets), B is no longer a linear function of H (see also fig. 1.8). The relation between B and H is then given by $\boldsymbol{B} = \mu \boldsymbol{H}$. In this case $\mu = \mu_0 \mu_r$ and is no longer constant with μ_0 – permeability in vacuum, μ – the permeability of the medium and μ_r – the relative permeability of the medium.

For magnetic recording media and heads we mostly consider the application of ferromagnetic materials and then the contribution to the flux density $\boldsymbol{B}$ is given by the applied field $\boldsymbol{H}$ and the magnetization $\boldsymbol{M}$ of the materials:

$$\boldsymbol{B} = \mu_0(\boldsymbol{H} + \boldsymbol{M}) \quad [\mathrm{T}]. \tag{1.8}$$

All three are macroscopic parameters of a permanent magnetic material, having a remanent magnetization.

If we consider a permanent magnetic material (producing magnetic field lines even if the applied field is zero) the field lines are pointed in the same direction (from N to S) inside as well as outside the material and this initiates a magnetic charge at the end of the magnet (see fig. 1.6). The field lines are bent inside the material because the shape is not ideal (rectangular instead of ellipsoidal). The direction of the B field lines outside the material is the same as the H field lines ($\boldsymbol{B} = \mu_0 \boldsymbol{H}$). Moreover $\nabla \cdot \boldsymbol{B} = 0$ which means that isolated poles cannot exist.

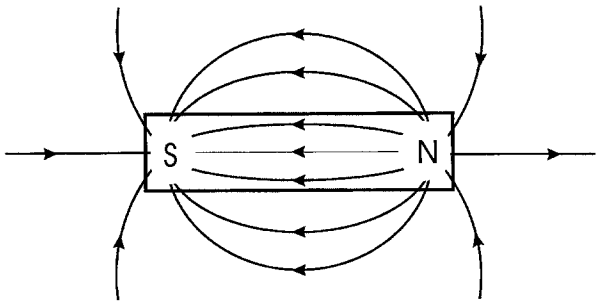

Fig. 1.6. The magnetic field H lines inside and outside a permanent magnet.

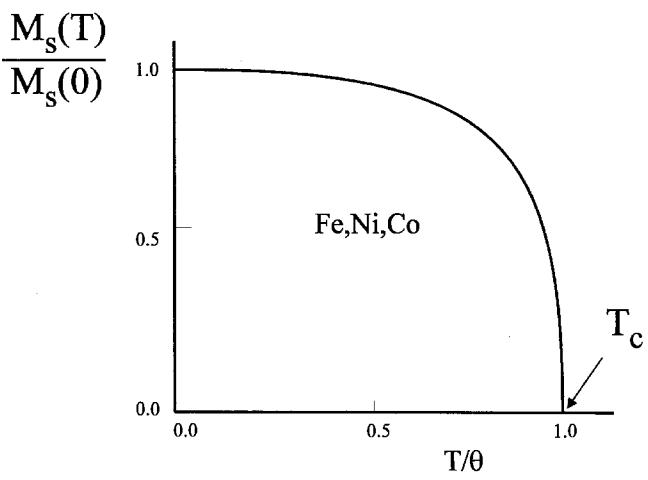

Fig. 1.7. Spontaneous magnetization as a function of the temperature for materials such as Fe, Ni and Co. The parameter θ is a positive constant depending on the material. For a ferromagnet θ equals T_c.

1.2.1. Curie temperature

As we have seen the interactions between the magnetic dipoles can lead to ordering in the materials. On the other hand the temperature motion is directed against ordering. It can be expected that below a certain temperature the material is ordered, but above this temperature this will be not the case. The latter state is called paramagnetic. At this temperature the thermal energy is equal to the exchange energy and the spin moments are randomly directed. The transition temperature from ferromagnetic to paramagnetic is called the Curie temperature (T_c for Co, Fe and Ni is 1130, 770 and 358°C respectively). In fig. 1.7 the spontaneous magnetization vs. the temperature is given. The magnetization is maximal if T becomes zero. At T_c the μ decreases drastically and the H_c and M_r become zero.

1.2.2. Magnetic unit systems

The two most commonly used unit systems in magnetism are the CGS system in which $\boldsymbol{B} = \boldsymbol{H} + 4\pi\boldsymbol{M}$ and the MKS or SI system in which $\boldsymbol{B} = \mu_0(\boldsymbol{H} + \boldsymbol{M})$. In this paper we

TABLE 1.1
The most important quantities of the magnetic unit systems.

Quantity	MKSA/SI	CGS	Equivalents
Induction $\boldsymbol{B}$	Tesla (T)	Gauss (G)	1 T = 10000 G
Field $\boldsymbol{H}$	A/m	Oersted (Oe)	1 A/m = $4\pi \times 10^{-3}$ Oe
Magnetization $\boldsymbol{M}$	A/m	emu/cc	1 kA/m = 1 emu/cc
Magnetic moment (Mv) $\boldsymbol{m}$	A/m^2		
Field equation	$\boldsymbol{B} = \mu_0(\boldsymbol{H} + \boldsymbol{M})^*$	$\boldsymbol{B} = \boldsymbol{H} + 4\pi\boldsymbol{M}$	
Energy of free space moment	$E = -\mu_0 \boldsymbol{m} \cdot \boldsymbol{H}$	$E = -\boldsymbol{m} \cdot \boldsymbol{H}$	
Torque on free space moment	$\tau = \mu_0 \boldsymbol{m} \times \boldsymbol{H}$	$\tau = \boldsymbol{m} \times \boldsymbol{H}$	

* $\mu_0 = 4\pi \times 10^{-7}$ H/m.

will use the SI system as much as possible but we still use inches in the case of recording densities.

For example: The earth's magnetic field $\boldsymbol{H} = 56$ A/m (or 0.7 Oe). The saturation magnetization of a hard disk thin film medium $\boldsymbol{M}_s = 550$ emu/cc (or 550 kA/m). The field generated by an electromagnet used for magnetic measurements is $\boldsymbol{H} = 30$ kOe or 2388 kA/m, $\boldsymbol{B} = 4\pi \times 10^{-7} \times 2388 = 3$ Tesla.

1.3. Magnetic properties of recording materials

The materials Fe, Co and Ni and their alloys and oxides are mostly used for recording application materials. Their magnetic properties are described by intrinsic and extrinsic parameters. The intrinsic properties (saturation magnetization M_s, magneto-crystalline anisotropy K, Curie temperature T_c and the magnetostriction λ_s are determined by the type and number of atoms, their arrangement in the crystal structure and their temperature.

The saturation magnetostriction λ_s can be defined as the fractional change in length if the sample is saturated from the demagnetized state along the field direction. The field-induced magnetostriction is the variation of λ with H or B and is a very important parameter for magnetic head materials.

The extrinsic properties (remanent magnetization M_r, coercivity H_c and permeability μ) can also be influenced by the size and shape of the magnetic material and its (magnetic) history. Consequently, in the case of thin-film media, the microstructure and morphology play a key role in determining the extrinsic properties.

Figure 1.8 shows the two hysteresis loops for a medium (right) and a head material. The coercivity H_c, remanent magnetization M_r or induction B_r and the permeability μ differ for the two materials, although the saturation magnetization M_s or induction B_s are the same.

If a very high field is applied the magnetization can reach its saturated state in which all the magnetic dipoles are aligned in the direction of the field. If the magnetic field is switched off the remanent magnetization M_r is left. If the M (or B) is then reduced to zero, a special field strength, the coercivity H_c, is required.

The hysteresis loop, in general, provides information about the magnetic properties, such as coercivity H_c, saturation magnetization M_s, remanent magnetization M_r, preferred

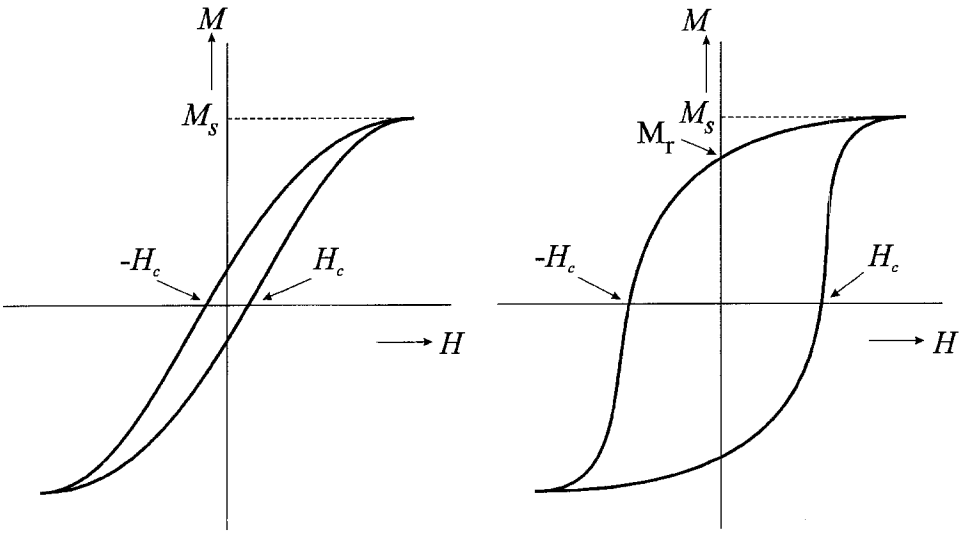

Fig. 1.8. Basic hysteresis properties for a recording head (left) and for a magnetic medium.

direction of the magnetization or anisotropy, and it can even give some idea about the magnetization reversal process involved.

Recording media requirements are usually high coercivity, high remanent magnetization, high squareness ($S = M_r/M_s$) of the hysteresis loop and low noise.

The properties for head materials can be summarized as large saturation magnetization for producing a large gap field, high permeability at all frequencies in order to ensure high efficiency, small coercivity with low hysteresis loss, low magnetostriction for obtaining low medium contact noise and small but not zero magnetic anisotropy to suppress the domain noise. In order to ensure good reliability and a long operating time, the head materials must exhibit a good thermal stability and a high resistance to wear and corrosion. The choice of materials and preparation technologies are the tools for tailoring head and medium properties.

1.3.1. Demagnetization

Inside the material the field lines $\boldsymbol{B}$ and $\boldsymbol{H}$ are in opposite directions. The direction of the magnetization $\boldsymbol{M}$ is from S to N (orientation of the dipoles) and this results in free poles at the end of the material (+ at the N and − at the S side). In fig. 1.9 the magnetic induction B is given inside as well as outside the permanent magnet.

Magnetic poles are very important because they generate magnetic fields always in the direction from + to −. Consequently a demagnetizing field H_d in the magnet (so-called because it decreases the magnetization) occurs. In order to determine H_d, the M should be known at all points so that the magnetic pole density can then be calculated at each point. The magnetic volume charge density can be given by:

$$\rho_m - \nabla \cdot M = -\left(\frac{dM_x}{dx} + \frac{dM_y}{dy} + \frac{dM_z}{dz}\right) \quad [A\,m^{-2}], \tag{1.9}$$

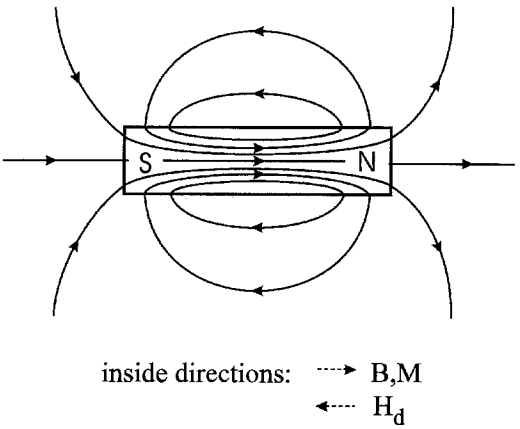

Fig. 1.9. A permanent magnet with magnetic induction B lines inside and outside the bar. Magnetic poles are formed at both ends of the bar (+ at N and − at S side).

in which:
ρ_m – magnetic volume charge density (A/m^2),
∇ – divergency (linear operator),
M_x, M_y, M_z – orthogonal components of the magnetization vector.

It is conventional that if the magnetization becomes smaller the pole is called N or positive. In general the fields generated by a realistic material are very complicated and impose a non-homogeneous magnetization. This is not valid for just one shape (ellipsoid of revolution). In this case the demagnetizing tensor N_d is the same for all points.

1.3.2. Magnetic interactions and moment formation

In ferromagnetic materials the individual atomic dipoles are coupled with each other and form magnetically ordered states. Such a coupling is quantum mechanical in nature and is know as the exchange interaction. The lowest value of energy in a material occurs when the magnetic moment and the magnetic field are aligned. The process of alignment due to their own internal fields is called exchange interaction. A qualitatively representation of the exchange integral J_{ex} as function of the inter-atomic spacing r_{ab}/r_d is given in the Bethe–Slater curve. Here r_{ab} is the inner atomic spacing and r_d is the radius of the unfilled 3d shell. There has been serious criticism on the validity of the Bethe–Slater curve, however, as discussed by Herring (1966).

The situation for the various magnetic materials is indicated on the curve. It clearly shows that the 3d ferromagnetic elements (Fe, Co, Ni) have a positive and the antiferromagnetic materials (Mn and Cr) a negative exchange integral (antiferromagnetic order at small values of r_{ab}/r_d). The nature of the exchange interaction is dependent on the interatomic and interelectronic spacing, which immediately refers to the microstructural and chemical behaviour of the materials used in hard disk media. Exchange interactions are very short distance interactions, consequently by changing the atomic structure they can be reduced or cut off. It can be seen from fig. 1.10a that if the ratio r_{ab}/r_d becomes larger than 1.5, a positive exchange interaction occurs and the material is called ferromagnetic.

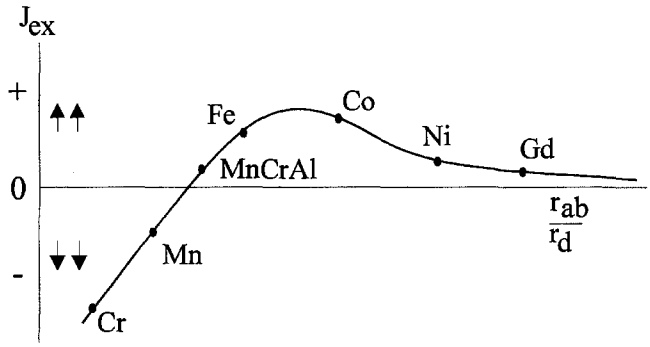

Fig. 1.10a. The Bethe–Slater curve qualitatively represents the exchange coefficient as a function of the interatomic spacing.

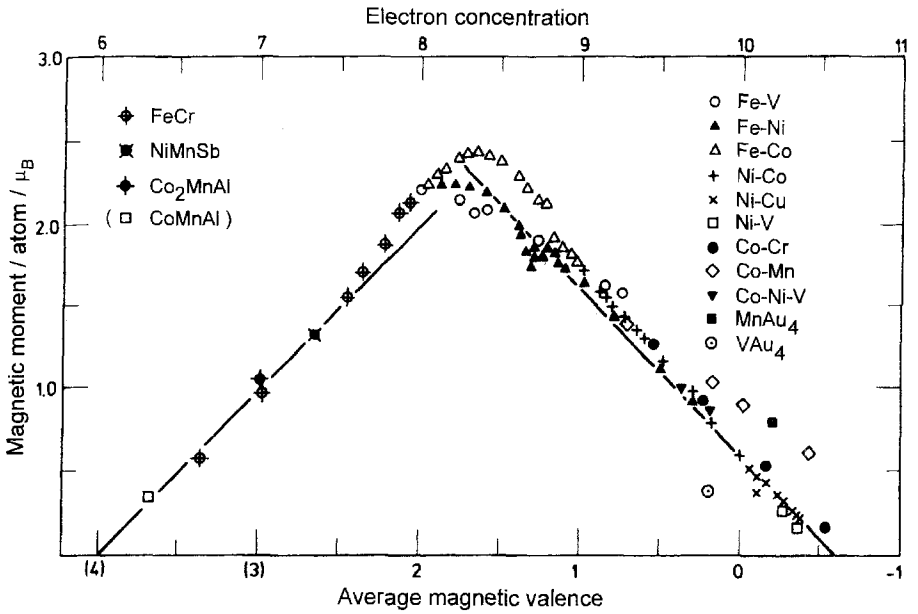

Fig. 1.10b. Slater–Pauling–Friedel curve. The data on the right are plotted versus magnetic valence while the data on the left are plotted versus electron calculation (Kübler and Eyert 1991).

Another type of interaction is the so-called dipole–dipole interaction which finds its origin in the case of a B field of surrounding dipoles influencing a certain dipole. This type of interaction is very small (0.1 Wb/m^2) in relation to the exchange interaction (10^9 A/m) but operates, in principle, over a longer distance.

As a consequence of the exchange interactions there are various types of magnetically ordered materials, because the interactions influence the alignment of the magnetic moments.

The magnitude of the magnetic moment in magnetic alloys of 3d elements can be read from the Slater–Pauling–Friedel curve shown in fig. 1.10b. In contrast to the Bethe–Slater curve the SPF curve is well reproduced by modern band structure calculations (Kübler and Eyert 1991).

In the case of diamagnetic materials the atoms have no permanent dipole moments. However, with paramagnetic materials the atoms have a permanent dipole moment but they do not interact. If the atoms have an permanent dipole moment and the interaction results in an antiparallel direction this material is defined as an antiferromagnet. If the unequal moments are aligned antiparallel than we have a ferrimagnet and if the moments are equal and aligned parallel than we have ferromagnetic material.

1.3.3. Magnetic anisotropy

As we have seen the exchange interactions are essentially isotropic, as they depend primarily on the orientations of the moments relative to each other. Dipole interactions, which depend on the special locations of the atoms relative to their moment directions are anisotropic but are normally too weak to contribute to the material properties in terms of magnetic anisotropy. However, many magnetic materials show preferential directions for the alignment of the magnetization. These directions are energetically favorable and called "easy axes". The energetically unfavorable directions are known as "hard axes" and are rotated through 90° from the easy axes. When a material has only one easy axis the material is said to have uniaxial magnetic anisotropy. (Multiaxial anisotropy occurs in some materials but is less common.) The formation of uniaxial anisotropy not only originates from the crystal symmetry but also from preferential (poly-)crystallite orientation (texture), shape and size of the sample and stresses. Anisotropy can also be induced by applying a strong magnetic field during preparation.

In the case of thin films and especially multilayer structures the so-called interface anisotropy (related to the surface anisotropy and strain) is also of great influence. The magnetic behaviour at surfaces and interfaces is modified by the reduced symmetry, the lower co-ordination number and the presence of localized surface-to-interface states. This type of anisotropy was introduced by Néel and can be large enough to contribute to the total anisotropy of the material.

The strength of the anisotropy determines the difficulty of rotating the magnetization direction away from its stable alignment along the preferred axis and is thus an influencing factor for the magnitude of the coercivity.

The magnetic anisotropy or the magnetic-anisotropy energy can be determined by torque measurements. The definitions of the angles between H, M and film plane are given in fig. 1.12.

Here θ is the angle between the sample surface (= anisotropy plane) and the direction of M, and φ is the angle between the applied field and the sample surface while α is the angle between the M and H.

If an isolated ferromagnetic particle is considered, the magnetization reversal depends on the dimensions of this particle. Mostly, for recording, we have to deal with the so-called Single-Domain Particles (SDP) dispersed in the medium. The single-domain behaviour can be described by the classical nucleation theory (e.g., Aharoni 1986). A so-called Stoner–Wohlfarth particle is characterized by a uniaxial anisotropy K, the applied field H, and the direction of the magnetization due to H is M.

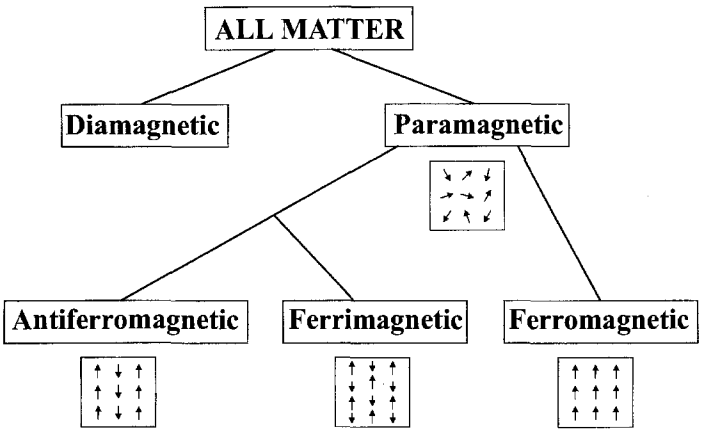

Fig. 1.11. A schematic overview of the various kind of magnetism.

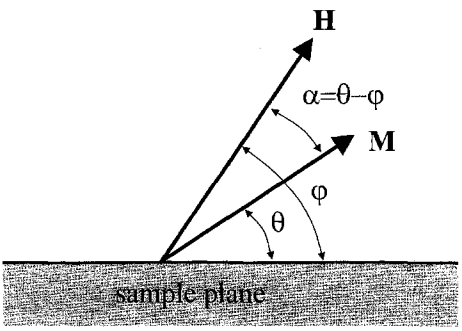

Fig. 1.12. Definitions of the angles between H, M and the film plane.

If an external field H is applied at angle φ with respect to the easy axis, the magnetization M of the particle will have an equilibrium between the external field direction and the easy axis. This equilibrium direction can be found by minimizing the total energy of the system which is composed of the anisotropy energy

$$E_a = -K \sin^2 \theta \quad [\mathrm{J\,m^{-3}}], \tag{1.10}$$

and the external field energy

$$E_H = -\mu_0 H M_s \cos(\varphi - \theta) \quad [\mathrm{J\,m^{-3}}]. \tag{1.11}$$

In equilibrium

$$\frac{dE_{tot}}{dt} = \frac{d(E_a + E_H)}{d\theta} = 0, \tag{1.12}$$

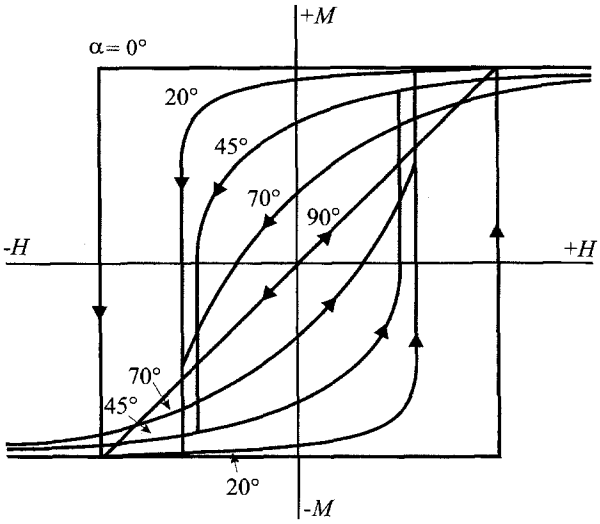

Fig. 1.13. Magnetization in the direction of the applied field for various applied-field angles with the easy axis (Stoner and Wohlfarth 1948).

which results in

$$K \sin 2\theta = \mu_0 H M_s \sin(\varphi - \theta). \tag{1.13}$$

If the external field is applied perpendicular to the easy axis ($\varphi = 90°$), the equation can be solved easily

$$\sin\theta = \frac{\mu_0 H M_s}{2K} \quad \text{for} \quad H < H_k = \frac{2K}{\mu_0 M_s}. \tag{1.14}$$

It can be seen that $\sin\theta = 1$ for $H > H_k$. The field H_k is defined as the anisotropy field. The magnetization in the direction of the field $M_s \sin\theta$ is a linear function of H with saturation at $H = H_s = H_k$.

In this case a completely reversible change of M, by pure rotation, occurs without hysteresis. Inversely, if a field is applied parallel to the anisotropy axis the particle will switch irreversibly (no rotation) only after applying a field greater than H_k. (Equation (1.13) has only two solutions at $\theta = 0$ and 180°.)

This critical field called coercivity (H_c) or switching field (H_s) is also equal to H_k. If a field is applied between 0 and 90° the coercivity will vary from maximum to zero. In the case of this special example the applied field $H_a = H_s = H_c = H_k$.

Based on the classical theory, Stoner–Wohlfarth (Stoner and Wohlfarth 1948) considered the rotation unison for non-interacting, randomly oriented, elongated particles. The anisotropic axis may be due to the shape anisotropy (depending on the size and shape of the particle) or to the crystalline anisotropy. In the prolate ellipsoids "b" is the short axis

and "a" the longest axis. The demagnetizing factors are N_a (in the easy direction) and N_b. The demagnetizing fields can then be calculated by:

$$H_{da} = -N_a M_s \quad \text{and} \quad H_{db} = -N_b M_s. \tag{1.15}$$

The shape anisotropy field is:

$$H_d = (N_a - N_b) M_s. \tag{1.16}$$

Then the switching field can be given as:

$$H_s = H_d = (N_a - N_b) M_s. \tag{1.17}$$

If there is a crystal anisotropy, with the easy axis parallel to the shape-anisotropy axis of the particle, the total anisotropy is:

$$H_a = H_{a,\text{shape}} + H_{a,\text{crystal}}, \tag{1.18}$$

and the total switching field is:

$$H_s = (N_a - N_b) M_s + \frac{2K_1}{\mu_0 M_s}. \tag{1.19}$$

Here K_1 is crystal anisotropy constant. In the case of practical materials it became clear that H_s was much lower than predicted by the Stoner–Wohlfarth theory. Therefore, the incoherent rotation modes (fanning, curling, buckling) have been explored. The aim of the "chain of spheres" reversal mode (Jacobs and Bean 1955) was to give a more realistic picture for an elongated particle used in a particulate recording medium. This reduced the switching field drastically. Furthermore, curling has been introduced as another non-uniform rotation process. In this reversal mode the particle is assumed to be spheroid or an infinite cylinder with its long axis in the field direction. The nucleation field with the applied field parallel and opposite in the long axis is given by:

$$H_n = -\frac{2K_i}{\mu_0} + N_a M_s - \frac{2\pi k A}{\mu_0 M_s} \frac{1}{R^2}. \tag{1.20}$$

Here, K_i is the intrinsic anisotropy constant due to the crystalline anisotropy, k is the shape-dependent constant (infinite cylinder 1.38), A the exchange constant and R the particle radius. An infinite cylinder with only shape anisotropy gives:

$$H_n = -6.8 \frac{A}{\mu_0 M_s} \frac{1}{R^2}. \tag{1.21}$$

Isolated particles, i.e., non-interacting particles, are not realistic in recording media. The magnetostatic interaction of the particles should be taken into account. Although the packing densities are not high there is still cluster forming and particles are at very close distances. These kinds of effects and also, for instance, the particle-size distributions influence

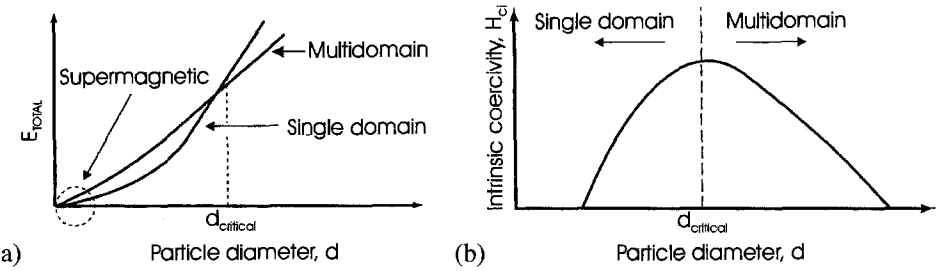

Fig. 1.14. Total energy versus particle diameter for SDP and MDP (a) and (b) the intrinsic coercivity H_{ci} versus the particle diameter d (e.g., Bean 1955).

the switching fields and coercivity behaviour. Below a critical size the particle becomes superparamagnetic; in other words the thermal activation energy kT exceeds the particle anisotropy energy barrier. A typical length of such a particle is less than 10 nm and is, of course, strongly dependent on the material and its shape. The reversal of the magnetization in this type of particle is the result of the thermal motion.

Multidomain particles (MDP) exist beside SDP particles. The distribution in domains lowers the magnetostatic energy but increases the exchange energy caused by the domain walls. The reversal in such particles mainly takes place by domain-wall motion. This kind of reversal mechanism influences the coercivity.

Figure 1.14(a) gives the relation between the total energy and the particle diameter for MDP and SDP. The crossing shows the critical diameter where the particle changes from SD to MD. At very low energies super paramagnetic particles can be found.

In fig. 1.14(b) the relation between the intrinsic coercivity H_{ci} and the particle diameter D is given. The figure is based on a model described in by Bean (1955). The maximum is found around the critical particle diameter D_s. In general, the particle diameter and size are not very well defined. In the case of MDP ($D > D_s$) the H_{ci} is smaller than the intrinsic anisotropy field of the particle. Nucleation effects cause a decrease in H_c as D increases. This behaviour is understood only qualitatively. A full description can be found in the book of Culity (1972). Low-noise media should consist of SDP; reversal by domain walls is slow and introduces noise.

1.3.3.1. Shape anisotropy of a prolate spheroid. Shape anisotropy can be simply defined as the measure of the difference in the energies associated with magnetization in the shortest and longest dimensions of a ferromagnetic material (see also fig. 1.15). For instance a long cylinder has a higher magnetostatic energy in the direction perpendicular to its axis than for the magnetization parallel to this axis (parallel to the axis the magnetic poles are at a longer distance from each other and have a lower magnetostatic energy). In fig. 1.15 $N_a - N_b$ are given as the function of the dimensional ratio a/b. N_a is demagnetizing factor along the shortest axis and N_b – along the longest axis. Moreover, $2N_a + N_b = 1$ and consequently N_a and N_b are given for a magnetic needle ($N_a = 1/2$), a sphere $N_a = N_b = 1/3$ and for a thin film $N_a = 0$ and $N_b = 1$.

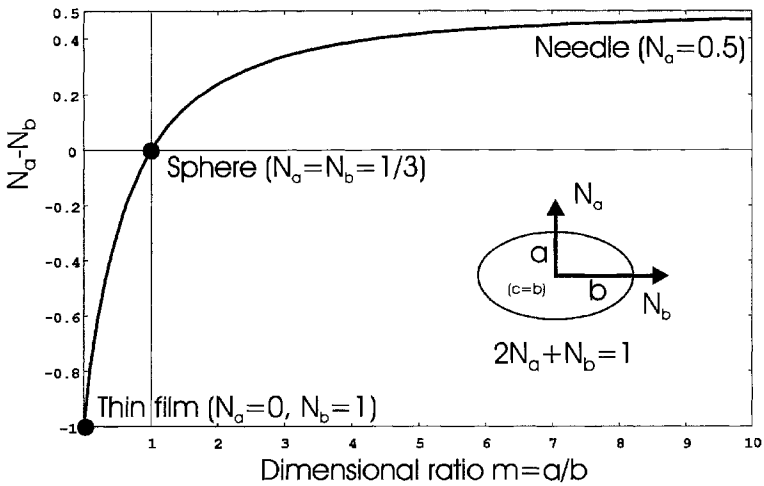

Fig. 1.15. Variation of $N_a - N_b$ as a function of the axial ratio $a : b$ is in principle given for a prolate ellipsoid of revolution. For a needle, sphere and thin film shape the values of N_a and N_b are given.

The anisotropy energy for a shape of a prolate spheroid is given by:

$$E_{\text{shape}} = \frac{1}{2}\mu_0 M_s^2 (N_a - N_b) \sin^2\theta \quad [\text{J m}^{-3}]. \tag{1.22}$$

The shape anisotropy constant can then be written as:

$$K_s = \frac{1}{2}\mu_0 M_s^2 (N_a - N_b) \quad [\text{J/m}^3]. \tag{1.23}$$

Finally the direction of H_d depends on the ratio $N_a : N_b$.

1.3.3.2. Shape anisotropy of a thin film. The shape anisotropy in certain directions depends on the dimensions of the sample and varies with the shape (sphere, elongated particle, thin film). This anisotropy is inherently uniaxial.

The shape of a thin film sample can be associated with demagnetizing energy. In the case of a homogeneously magnetized film the demagnetizing energy as a function of magnetization direction is given by:

$$E_{\text{shape}} = K_d \sin^2\theta = \frac{1}{2}\mu_0 M_s^2 N_d \sin^2\theta. \tag{1.24}$$

Here K_d is the shape anisotropy term and N_d is the demagnetizing factor. The thicknesses of the thin film samples are very small compared to the lateral dimensions and consequently the infinite plate approximation can be made ($N_d = N_z = 1$), which results in:

$$E_{\text{shape}} = \frac{1}{2}\mu_0 M_s^2 \sin^2\theta \quad [\text{J m}^{-3}]. \tag{1.25}$$

Based on this relation the shape anisotropy term for a thin film can be given by:

$$K_d = \frac{1}{2}\mu_0 M_s^2 \quad [J/m^3]. \tag{1.26}$$

The corresponding shape anisotropy field perpendicular on the thin film surface ($H_d = N_d M_s$) is then:

$$H_d = \frac{2K_d}{\mu_0 M_s} \quad [A/m]. \tag{1.27}$$

1.3.3.3. Crystalline anisotropy. Magnetocrystalline anisotropy arises from exchange forces within the crystal lattice and is therefore an intrinsic material parameter in contrast to the shape anisotropy. In general terms magnetocrystalline anisotropy is determined by the spin state of the magnetic ions and by the symmetry of their atomic arrangement in the lattice.

Materials do have crystal anisotropy if the magnetic moments prefer to lie along special crystallographic axes. This preferential direction of the magnetization leads to a lower energy.

The magnetocrystalline energy depends on the relative direction of the magnetization with respect to the crystallographic axes and is given by:

$$E_c = K_1 \sin^2\theta + K_2 \sin^4\theta + \cdots \quad [J]. \tag{1.28}$$

Here θ is defined as the angle between the anisotropy axis and the magnetization and K_1 and K_2 are the first- and second-order anisotropy constants, respectively, the exact form of formula (1.29) depends on the angle definition and on the easy axis of magnetization when following the definition of fig. 1.12 and a thin film with an easy axis perpendicular to the surface all sine functions should be replaced by cosines.

For Co at room temperature $K_1 = 4.1 \times 10^5\ J\,m^{-3}$ and $K_2 = 1.0 \times 10^5\ J\,m^{-3}$.

The magnitude of K_1 at room temperature for Co is the largest (Co $\approx$ 10 $\times$ Fe). The magnetocrystalline anisotropy is sensitive to temperature and stress and in alloys or compounds can undergo irreversible changes if the site occupancy of the ions changes.

The anisotropy direction(s) are different for the various materials used. Easy axes can be found for Fe (b.c.c.) ⟨1 0 0⟩; Ni (f.c.c.) ⟨1 1 1⟩ and h.c.p. Co [1 0 0 0]. The hard axes are ⟨1 1 1⟩, ⟨1 0 0⟩ and [1 0 1 0], respectively. The E_c, for a hexagonal crystal, is minimum with the magnetization parallel to the [0 0 0 1] axis. The magnetocrystalline anisotropy field can be defined as:

$$H_k = \frac{2(K_1 + 2K_2)}{\mu_0 M_s} \quad [A/m]. \tag{1.29}$$

A wide range of H_k values (in kA/m) are available depending on the materials: Fe $\approx$ 45, Co (h.c.p.) $\approx$ 674, BaM $\approx$ 1350 and SmCo $\approx$ 20 000.

1.3.3.4. Strain anisotropy. Last but not least, the strain or stress anisotropy can play a significant role in the total anisotropy. It may be caused by stresses in magnetostrictive materials. Stress anisotropy can make a significant contribution to the total anisotropy especially in magnetic thin films due to the special preparation conditions and by thermal mismatch between substrate and thin film. The stress energy can be given by:

$$E_{\text{stress}} = -\frac{3}{2}\lambda_s \sigma \sin^2\theta \quad [\text{J m}^{-3}]. \tag{1.30}$$

Here λ_s is the saturation magnetostriction coefficient, and σ is the stress in $[\text{N/m}^2]$.

1.3.3.5. Total anisotropy. Finally, the total anisotropy in a material depends strongly on the material properties such as microstructure, chemical composition and preparation methods. The total anisotropy acting in a material is the sum of individual anisotropies. Neglecting the stress anisotropy, in a thin film we have to deal with at least the contribution of crystalline anisotropy and the thin film shape anisotropy. Confining ourselves to only the first- and the second-order anisotropy term we can write:

$$E_t = (K_1 + K_d)\sin^2\theta + K_2 \sin^4\theta \quad [\text{J m}^{-3}]. \tag{1.31}$$

Experimentally the anisotropy easy axis and the individual anisotropy terms K_1 and K_2 can be determined by torque measurements.

Using this method an effective anisotropy constant K_{eff} can be determined. For a thin film medium, having an easy axis in the plane, the effective anisotropy can be written as:

$$\begin{aligned}\frac{dE_t}{d\theta} &= (K_d + K_1)\sin 2\theta + 4K_2 \sin^3\theta \cos\theta \\ &= (K_d + K_1 + K_2)\sin 2\theta - \frac{1}{2}K_2 \sin 4\theta,\end{aligned}$$

and finally,

$$K_{\text{eff}} = K_d + K_1 + K_2, \tag{1.32}$$

because K_d supports the in-plane anisotropy. In the case of perpendicular anisotropy:

$$K_{\text{eff}} = K_d - K_1 - K_2, \tag{1.33}$$

which means that the film-shape anisotropy does not add constructively to the terms for perpendicular anisotropy.

1.3.4. Magnetization rotation

The state in which a ferromagnetic material (except in a reasonably large applied field) is usually found is one of zero magnetization. In the case of a polycrystalline material in which each crystal is uniformly magnetized, the directions of the saturation magnetization

are distributed randomly. In other words the material is subdivided into domains (areas having opposite directions of magnetization) in order to be in a state in which its energy is a minimum. Between the magnetic domains a boundary occurs, the so-called domain wall. If the domains are magnetized in the easy direction then there is no anisotropy energy associated with the domains. However, in the wall some anisotropy energy is also present because the magnetization in the wall is not parallel to an easy axis direction (rotation of the magnetic moments in the wall).

The wall width can be given by:

$$w_{\text{wall}} = \pi(A/K)^{1/2} \quad [\text{m}]. \tag{1.34}$$

The Bloch wall energy per unit area, determined by the exchange and anisotropy energies, can be given by:

$$\gamma \approx 4(AK)^{1/2} \quad [\text{J/m}^2]. \tag{1.35}$$

In a typical ferromagnetic material we may find that $A \approx 10^{-11}$ J/m and K is about 10^3–10^5 J/m^3 which shows that w_{wall} is in the order of 100 nm. Usually the observed size of the domains is much larger than the domain wall width. Given the above values of A and K, the wall energy γ can be estimated to be in the order of 10^{-3} J/m^2

Reversing the magnetization in a ferromagnetic material consisting of domains is based on movement of the walls. Domain walls can move reversibly in very small applied fields which means that after removing the field the wall returns to its original position. The motion becomes irreversible (walls do not return to their original positions after the field is removed) at larger fields. The reason for this behaviour is that the wall energy varies with the position of the wall, due to inhomogeneities (grain boundaries, voids, dislocations etc.) in the sample.

If the dimensions of the ferromagnetic material become smaller, for instance for small recording particles, domains can no longer exist. In these cases the magnetization rotation occurs by coherent or incoherent rotation of the magnetic moments

This type of reversal behaviour will be discussed in chapter 2.5.

2. Considerations for designing recording media

The influence of thin film preparation conditions on the microstructure and finally on the magnetic properties are important for acquiring the optimum design for a recording medium. It is important to understand that, for instance, small changes in deposition technology may have a large influence on the final magnetic properties. In the total research scheme one should discriminate between the various aspects and when dealing with thin film media for high density recording application the following scheme can be used as a guideline for developing an optimum product:

- Recording properties (mode and type of recording, properties, S/N, overwrite);
- Choice of materials;
- Thin film technology and deposition parameters;

- Microstructure and local chemical composition;
- Macromagnetic properties (e.g., hysteresis loop measured with VSM);
- Micromagnetic properties (simulation and calculation);
- Mesoscopic experimental characterization methods.

2.1. *Introduction*

In order to understand the relation between the aspects mentioned above it is necessary to understand that they all operate at a variety of length scales. Starting at the atomic level the interaction phenomena between spins and orbit, magnetic exchange interactions and dipole–dipole interactions must be considered (micromagnetic behaviour). Moreover, practical magnetic materials and also the thin film media discussed here are composed of small crystallites consisting of a 3D periodic arrangement of (magnetic) atoms (mesoscopic behaviour). In the simplest case, each magnetic atom has the same local environment in which the neighboring atoms (magnetic or otherwise) form a spatial configuration of a particular symmetry.

A typical thin film medium for high density recording consists of individual crystals with a diameter of about 40 nm. When a VSM hysteresis loop from a typical sample (5×5 mm^2) is measured, a hysteresis curve of 15 000 interacting ferromagnetic crystals is obtained. If a typical bit size for such media is about 3 μm^2 the recorded information is obtained from 2500 crystals. The micromagnetic calculations are mostly obtained from 20–100 of such crystals because of limited computer capacity and reasonable calculating time. Consequently, there is a large gap between micromagnetic simulations and the macromagnetic properties obtained by experimental methods (e.g., hysteresis loop). Therefore, it is necessary to develop experimental methods from which magnetic and microstructural information from smaller volumes can be obtained. Only then is it possible to find a more definitive relation between the microstructure, local chemical composition and the magnetic behaviour on a length scale more related to high density recording areas.

In the case of bit densities of 1–10 GBits/in^2 discussed nowadays (commercially 10 GBits/in^2 is expected in the year 2000) the fundamental structural dimensions (crystal size and surface topology), intrinsic magnetic structures (domains) and the bit dimensions are approaching similar dimensions. In order to tailor the properties on this scale, development of nano- and atomic engineering is necessary.

2.2. *Towards smaller bits*

High-density recording depends on how to shorten the recording wavelengths λ or in other words how to make the recorded bitlength (bl) as small as possible. In order to increase the areal density the track width (tw) also has to be made smaller. The basic recording principles are described in detail in the standard literature (Mee and Daniel 1987–1988; Bhushan 1990; Mee and Daniel 1990, 1996; Hoagland and Monson 1991; Buschow 1993; Mallinson 1993). In fig. 2.1 the most important parameters for the head and medium are given.

The digital storage of a bit in a moving medium beneath a soft magnetic head can be achieved by a current pulse in the recording head. The magnetic flux associated with the writing current travels through the magnetic circuit of the head. The recording medium is

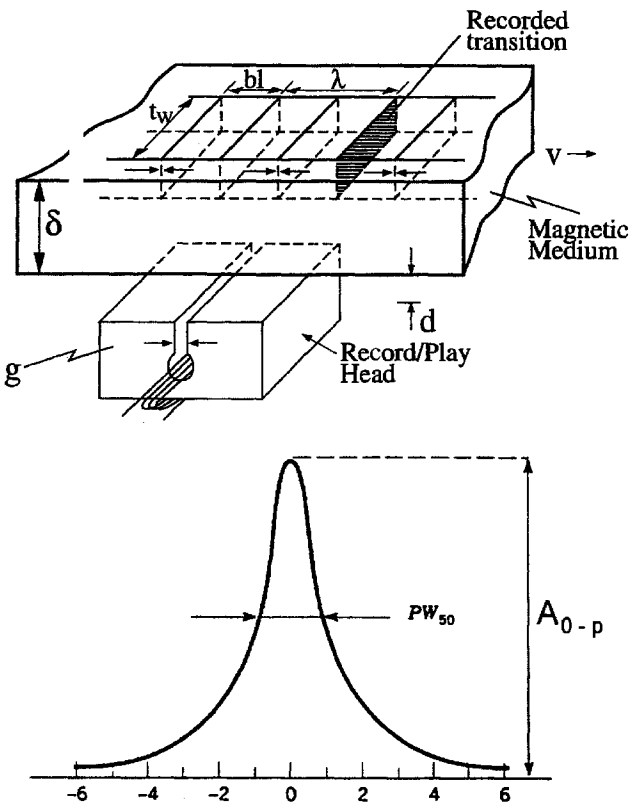

Fig. 2.1. Recording parameters for the head and medium with written track tw, recording wavelength λ, linear bit length bl and the recorded transition (a), and the output pulse from reading a transition (b).

in contact with or at a small distance from the gap of the magnetic head. The gap fringe flux penetrates the medium and magnetizes small volumes of the material. In the case of longitudinal recording the horizontal fringing field component is the most important one. It can be concluded from analytical models and experimental data that this field should be several times the value of the coercive field of the medium (e.g., Mee and Daniel 1987–1988; Hoagland and Monson 1991; Mallinson 1993). The bit size area (bit length × track width) should be small for high density recording and the transition length (magnetization reversal) as sharp as possible. The change of the head current from one polarity to another produces a magnetization that is not spatially sharp but varies over a distance from one direction to the opposite one. The transition length in longitudinal recording is mainly determined by the head field gradient and the demagnetizing fields generated by the magnetostatic fields of the transition itself and the switching field distribution of the magnetic units in the medium.

A principle configuration of the recording geometry is given in fig. 2.1(a). Here a ring head is used which operates on a head medium spacing d from the media in motion. The

gap length of the head is g, the magnetic thickness δ of the recording medium (in the case of thin hard disk media δ is equal to the film thickness; in the case of thick magnetic particle tape δ is smaller than the coating thickness) and the recorded bit length (bl) with a track width (tw). A bit cell is defined as the distance between recorded transitions a and is obtained by bl $= v/T$. Here T is the bit duration in sec., $1/T$ is the bit frequency in Hz and v is the head-to-medium speed in m/s. The bit cell area (ba) as recorded has the dimension tw $\times$ bl. As previously mentioned, the transition length is an important factor for discussing the limitations for the recording density. The transition length/width a is given by Williams and Comstock (1971):

$$a \cong \left[\left\{\frac{4M_r\delta(d+\delta/2)}{QH_c}\right]^{1/2} \quad [\mathrm{m}]. \tag{2.1}$$

Here:
M_r – remanent magnetization,
δ – layer thickness,
d – head-to-medium spacing,
Q – a value related to the field gradient of an inductive head (0.75),
H_c – medium coercivity.

In the case of a small transition width H_c should be large in relation to $M_r\delta$ (remanence thickness product) and d as small as possible (contact). The stored bit (transition) can be read by the head due to the flux changes in the head which give an induced voltage. The isolated output voltage pulse is given in fig. 2.1(b). One of the models for the shape of the magnetization transition which is often used is the arc tangent model of Williams and Comstock (1971) described by:

$$M(x) = \frac{2}{\pi}M_r \arctan(x/a) \quad [\mathrm{A\,m^{-1}}]. \tag{2.2}$$

It describes the recorded magnetization in the x direction (longitudinal) in response to a step function change in the write head current. The arc tangent parameter a is inversely proportional to the maximum slope of the transition.

In fig. 2.2 the characteristics of the arctangent model are given. Figure 2.2(a) shows the x-component of the magnetization at the central plane of the medium. Increasing the density (smaller bit size) yields a larger influence of the self-demagnetizing field. In fig. 2.2(b) this demagnetizing field is given for various medium thickness. For further reading see the report of Middleton (1996).

It would be an ideal case to expect an infinitely sharp transition. The change in magnetization in one bit results in a so-called zigzag transition configuration (see fig. 2.3) which is strongly preferred because the energy associated with it is lower than the straight line transition. Such a transition can show a very irregular shape which is determined by the local variations of the magnetization and anisotropy. Consequently the microstructure and chemical homogeneity of the medium play an important role in the final shape of the transition. Variation in the transition is immediately related to the noise of the medium.

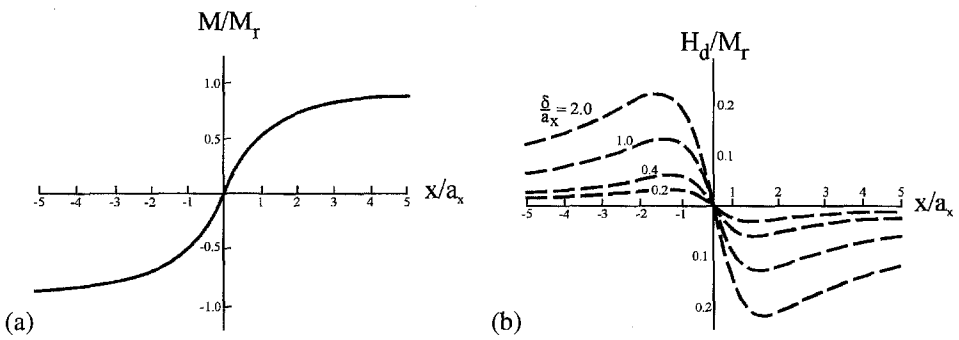

Fig. 2.2. Characteristics of the arc tangent transition (width = a_x): (a) magnetization vs. the x-axis, and (b) demagnetizing field H_d along the centre of the plane of various thicknesses δ of the medium (Middleton 1996).

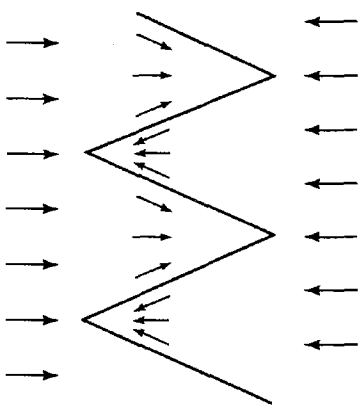

Fig. 2.3. Magnetic zigzag transition in longitudinal magnetic recording.

Narrow transitions (small a) yield large peak voltages (Ao-p) and narrow pulse shapes (PW_{50}). The width at half height is given by Williams and Comstock (1971):

$$PW_{50} \cong \left[g^2 + 4(d+a)(d+a+\delta)\right]^{1/2} \quad [\text{m}]. \tag{2.3}$$

Here g – gap length of the head. A small PW_{50} gives a better resolution without interference from neighboring transitions and a higher read voltage.

The intensity of PW_{50} is proportional to $M_r\delta(1 - e^{-k\delta})$, here k is the wave number and equals $2\pi/\lambda$, where λ is the recording wavelength.

2.3. Medium configuration

The general properties desirable for thin film recording media are a sufficient magnetization M for reading by the head with an appropriate S/N and an acceptable field strength to create a magnetization reversal which is directly related to the coercivity (H_c). The latter

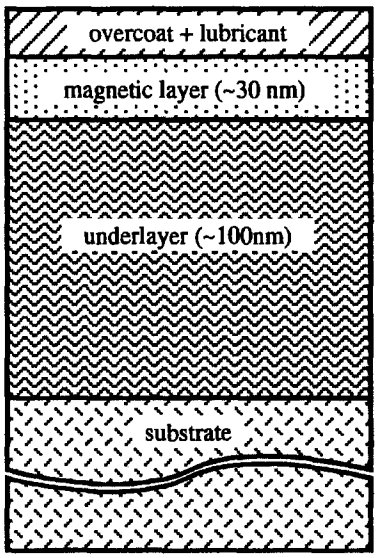

Fig. 2.4. Typical configuration of a commercial thin-film medium.

should not be too high for successful writing by the head field but it must be large enough to protect the medium against an unwelcome reduction in the stored information by demagnetization. A major potential for changing the signal in high density recording during the required storing time is the self-demagnetizing field originating in the material itself and this field is proportional to the medium magnetization. Consequently, the H_c must become higher for a more strongly magnetizable medium and this is also the case if the recording density increases.

Based on the preparation technology used and the medium morphology we can define two different types of recording media, namely: "particulate"-coated media and "thin-film" media. The first one consists of discrete magnetic particles dispersed in organic resins and the second is created on the substrate (tape, floppy, hard disk) by depositing a continuous layer of a magnetic metal, alloy or oxide.

Although many different configurations have to be discussed for the different types of thin-film media used in the various fields of application, the essential design parts of such thin-film media are generally those given in fig. 2.4.

As can be seen in fig. 2.4 the medium consists of a substrate made of glass, aluminum, polyester, PET. A transition layer (called: intermediate, seed or under-layer) between the substrate and the magnetic (recording) layer (s) and a covering layer (protective and/or lubrication layer). All these layers are made of different materials, with a variety of chemical compositions, microstructures and thicknesses.

An example of written bits in a longitudinal recording hard disk medium is given in fig. 2.5. This image was taken with an Magnetic Force Microscope (MFM). In this Co based hard disk the bits are written by a standard ringhead. The stray field emanates from the gap between two head pole pieces which ensures a high in plane component of the

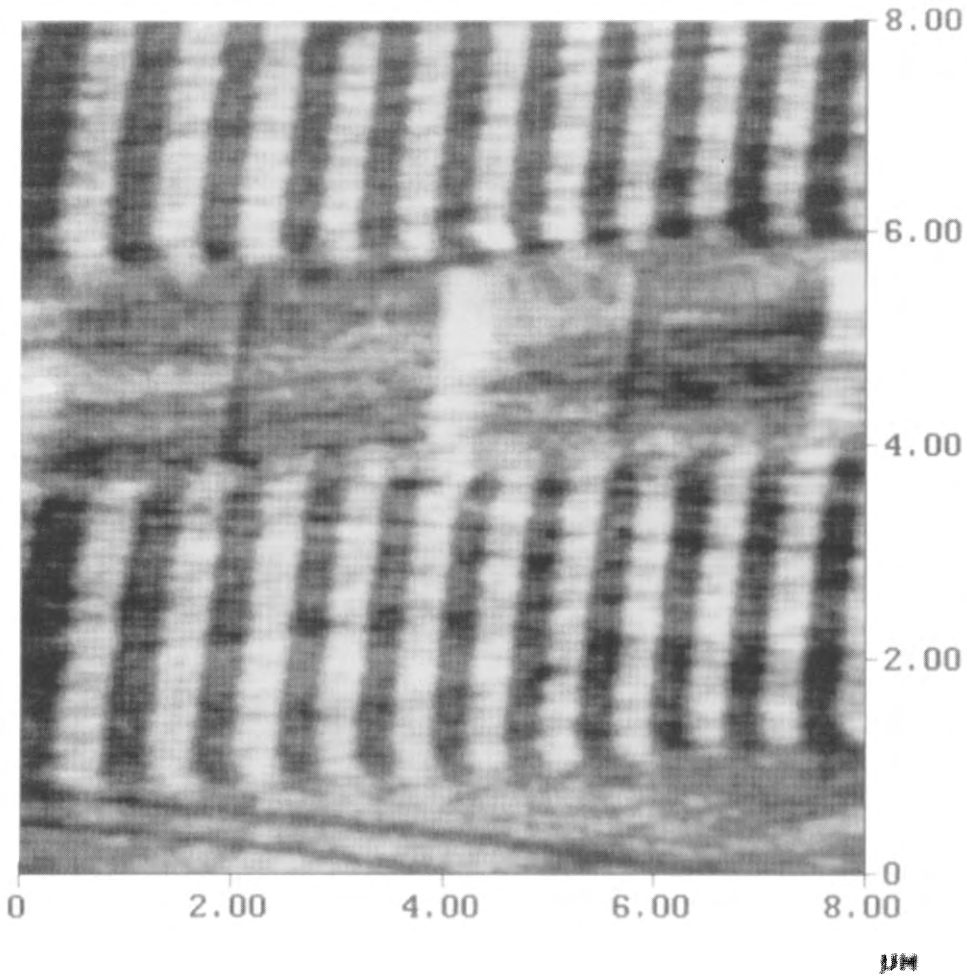

Fig. 2.5. A typical MFM image of written tracks in a longitudinal hard disk medium with a trackwidth of about 3 μm and a linear bit lenght of about 0.35 μm.

field which is large enough to magnetize the medium in one or another direction. In fig. 2.5 the track is written with a recording wavelength λ of about 0.7 μm and a width of about 3 μm.

2.4. Switching-field distribution

Both M_r and H_c have a strong relation with the recording process. M_r determines the maximum output signal of a recording medium and hence the signal-to-noise ratio. H_c ascertains how easily data can be recorded and erased or changed, but it also determines the maximum head field. On the other hand it also controls the ease with which data can

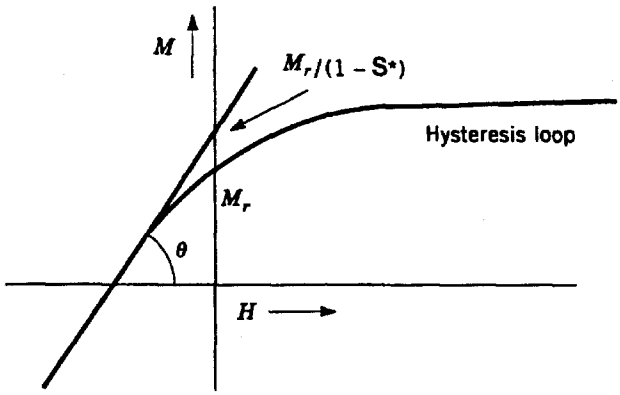

Fig. 2.6. Williams–Comstock construction for defining S^*.

be destroyed, e.g., by stray fields. The lower H_c, the more sensitive the medium is to all kinds of fields. In this way, H_c influences the noise level as well. The squareness ratio:

$$S = M_r/M_s \tag{2.4}$$

can also be derived from the hysteresis loop. A high value means that a large part of the magnetization is preserved, which is essential for recording. The slope of the hysteresis loop in H_c is also an important parameter. The parameter S^* can be derived from this slope. The Williams and Comstock (1971) construction is given in fig. 2.6.

In this figure a part of the hysteresis loop (M as a function of the applied field H) is given. The point at which M is constant as a function of the applied field is defined as saturation magnetization M_s. Taking the slope at H_c we can write:

$$\tan\theta = \frac{M_r}{H_c} = \frac{1}{1 - S^*} \quad \text{or} \quad \frac{dM}{dH} = \frac{M_r}{H_c(1 - S^*)}. \tag{2.5}$$

Thus the S^* is defined in relation to the slope of the loop at H_c. In the case of longitudinal recording experimental data have shown that there is a relation between S^* and recording parameters (Richards and Szczech 1978; Koster et al. 1981). Although S^* is normally used as an Switching Field Distribution (SFD) parameter, it is not always suitable. The SFD may be regarded as a distribution function of the number of units reversing at a certain field. In the case of a particulate medium without collective behaviour, this function is closely related to the particle size distribution, as differently sized and shaped particles reverse at different fields. Of course, the shape, orientation and interaction between particles influence the SFD as well. Media with a high H_c and a small SFD are more suitable for high density recording (Suzuki 1984) because the distribution of the switching fields is very small. An alternative definition is SFD $= \Delta H/H_c$. In this case the ΔH is the full width at half the height of the differentiated loop dM/dH.

2.5. *Magnetization reversal mechanisms*

The reversal of the magnetization is a basic principle of magnetic recording. Magnetization in a material can be reversed by applying a field and finally the whole material will be saturated in a direction parallel to the field. The two different states of + and − magnetization are the basic idea for digital information storage. The mode of magnetization reversal depends on the material and its size and shape. The two principal methods for reversing the magnetization are rotation and domain-wall motion.

Both modes can be examined in terms of energy considerations. The coherent and incoherent rotation of the magnetization only occur in single-domain particles. A particle is single domain below certain dimensions. Above a critical radius a domain wall may exist and the reversal takes place by domain-wall motion (see also chapter 1).

In the coherent rotation mode the atomic spins remain parallel during the reversal process and this may apply only for very small particles. If the particle size increases, incoherent switching mechanisms like curling, buckling and fanning are used.

Magnetic thin films with a polycrystalline structure are strongly exchange coupled and consequently their magnetization reversal will take place by domain-wall motion.

In the case of high density recording low noise is a requirement (particulate reversal behaviour is necessary for a sharp transition) and certain magnetic properties (high H_c and M_r). By tailoring the microstructural properties "continuous" thin films are also very promising candidates for actual and future applications.

In fig. 2.7 a schematic overview is given of the hierarchy of magnetization reversal in relation to the dimensions of the magnetic entities. Depending on the crystal size and the chemical homogeneity, the thin film structures can operate as a continuous layer (reversed by domain-wall motion) or more like a particulate medium (less exchange between the crystallites) which reverses its magnetization by one of the rotation mechanisms. If we first consider the magnetization reversal in isolated (with no interactions) single domain

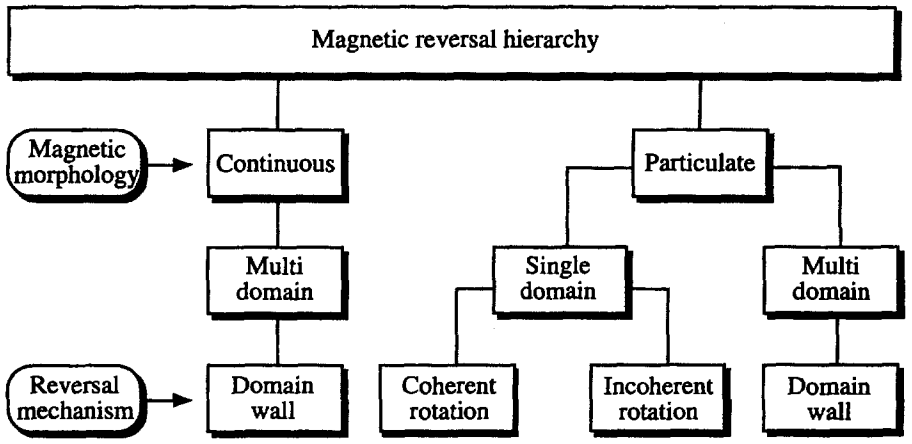

Fig. 2.7. Schematic overview of the possible reversal mechanisms depending on the dimensions of the sample.

particles (which in a thin film is not the case) we first have to look at the so-called Stoner and Wohlfart particles (rotation unison), as discussed in 1.3.3.

In the case of coherent rotation the atomic spins remain parallel, thus minimizing the exchange energy. With respect to larger particles magnetostatic interactions also become significant because the various incoherent modes are active. Consequently, it turned out that the measured switching fields were much lower than those predicted by the Stoner–Wohlfart theory. More realistic reversal mechanism were introduced such as a chain of spheres, curling, buckling and fanning.

2.5.1. Critical dimensions for magnetic particles

It is essential for high density recording to use thin film media with low media noise. Therefore thin films with reduced intergranular exchange coupling and a very small grain size are necessary (Bertram and Arias 1992). Moreover it is suggested (Murdock et al. 1992; Yogi et al. 1991) that for obtaining low particle noise contribution about 1000 grains are needed in one bit cell. Higher densities means smaller grains. Moreover besides the particle diameter the coercivity is also extremely important (see also section 2.2). A qualitative relation between H_c and the particle diameter is given in fig. 2.8.

The shape of the curve is strongly dependent on the chemical homogeneity of the particle and its microstructure (Kronmüller 1991). In this figure d_{th} is the initial diameter at which below the single domain particle (SDP) becomes superparamagnetic. The boundary between coherent and incoherent switching is given by d_{crit}. The diameter at which the particle becomes multi domain (MDP) is given as D_{crit}.

As we have seen in fig. 2.7, the active reversal mechanism can be coherent or incoherent rotation, domain wall motion. In general a few critical diameters can be given for the

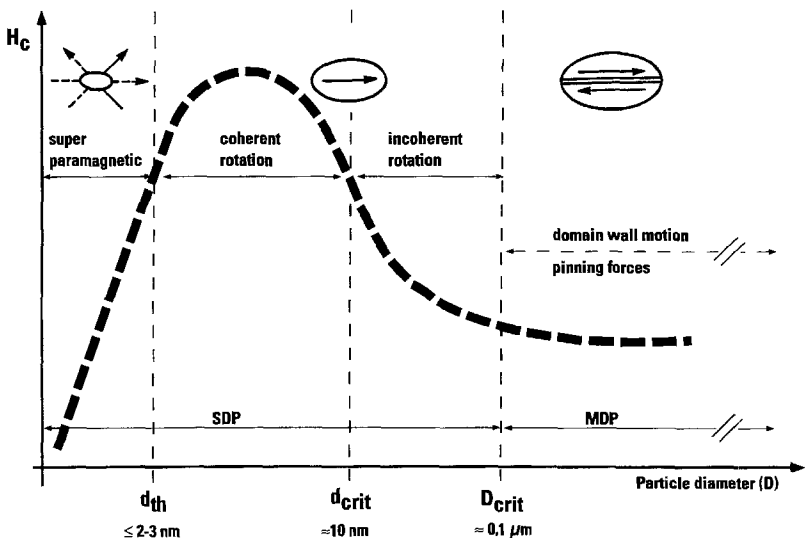

Fig. 2.8. A schematic qualitative relation between the coercivity as a function of the diameter of a magnetic particle.

different areas such as the critical diameter between the coherent and incoherent rotation, between single and multidomain behaviour and last but not least the critical dimension for superparamagnetic behaviour.

2.5.1.1. Coherent vs. incoherent rotation. The critical diameter (d_{crit}) for particles at the boundary between coherent and incoherent rotation (curling mode) is given by:

$$\text{For an infinite cylinder:} \quad d_{crit} = 5.20\sqrt{A/(N_{\perp}\mu_0 M_s^2)}, \tag{2.6}$$

$$\text{For an oblate spheroid:} \quad d_{crit} = 5.97\sqrt{A/(N_{\perp}\mu_0 M_s^2)}. \tag{2.7}$$

Here d_{crit} is the diameter where the nucleation field of both rotation modes becomes equal. Choosing realistic parameters, $d_{crit} \cong 15$–20 nm.

2.5.1.2. Single domain particles vs. multidomain particles. The boundary between single and multidomain particle is given by the critical diameter of the particles D_{crit}. The critical diameter of a spherical particle is given by:

$$D_{crit} = \frac{9\gamma_B}{\mu_0 M_s^2}. \tag{2.8}$$

Here γ_B is the specific wall energy ($\cong 4\sqrt{AK_1}$). For $D < D_{crit}$ the particle is a single domain particle.

For a prolate ellipsoid:

$$D_{crit} = \frac{3\gamma_B}{\mu_0 M_s^2}. \tag{2.9}$$

It can be concluded from the values calculated for $D_{crit\,sphere}$ and $D_{crit\,plate}$ that spherical or polyhedral particles have 3 × larger critical diameters than particles forming a platelet plane.

Finally long needles are characterized by larger D_{crit} therefore needle type particles have been important for a very long time in magnetic recording particle media systems.

TABLE 2.1
Critical SDP diameter (D_{crit}) of spherical particles.

Material	M_S (kA/m)	γ_B (10^3 J/m^2)	D_{crit} (nm)
Co	1400	8	70
Fe	1710	3	14
Ni	480	1	55
γ-Fe_2O_3	417	2	166
CrO_2	400	2	200
Co–Cr	450	1	71

2.5.1.3. Superparamagnetic behaviour. In particles with very small volumes V the reduction of H_c is due to the other incoherent reversal mechanisms. The total anisotropy energy KV corresponds to the energy barrier for reversing the magnetization in the coherent model. When V is very small, then the thermal fluctuation energy kT will determine the reversal of M. The decay of magnetization can be given by the relaxation time τ as:

$$\tau = \tau_0 \exp\left(K_{\text{eff}} V/(kT)\right) \tag{2.10}$$

with:
τ_0 – resonance relaxation time of the spin system, which is about 10^{-8} s,
K_{eff} – effective anisotropy energy, either K_1 or $(1/2)\,(N_\perp - N_\parallel)M_s^2$,
V – particle volume $(\pi/(6D^3))$.

If we use realistic parameters ($K_{\text{eff}} = 10^5$ J/m^3, $T = 300$ K, $\tau_0 = 10^{-8}$ s) we can calculate a relaxation time of $\tau = 0.1$ s for a critical diameter $d_{\text{th}} = 3.4$ nm. (If we choose $d_{\text{th}} = 4.4$ nm we find already $\tau = 10^8$ s). This example shows a very narrow area in which the particle changes from a stable to an unstable state.

In magnetically hard materials with $K_{\text{eff}} = 10^6$ J/m^3 the magnetic lifetime becomes longer than 10 years. This shows that particles with diameters > 4 nm are required for the development of permanent magnets.

The change from a stable SDP to an unstable super paramagnetic behaviour is given in fig. 2.8. The relation between the relaxation time and the particle diameter is given for well-known particulate materials and Co (h.c.p.).

It can be seen from fig. 2.9 that the change from a stable particle to an unstable superparamagnetic particle can take place in a very narrow range via reduction of the particle

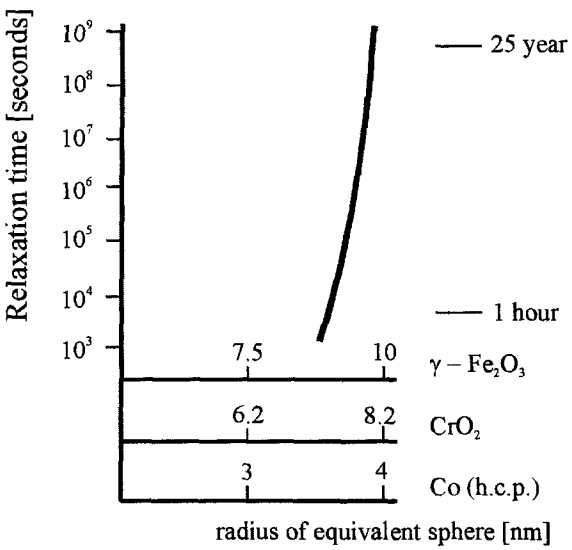

Fig. 2.9. Relaxation time as a function of the particle diameter.

volume. If the particle of a certain material becomes smaller, then the thermal stability ($KV/(kT)$) becomes smaller.

Because the anisotropy constant K can only be enlarged a little (due to the limited head field), the ratio becomes very critical at room temperature. For the materials discussed here the ratio is about 40–60 while for a continuous thin film it will be around 1000. This means that a very small crystal volume (small diameter and film thickness) becomes thermally unstable. In Lu and Charap (1994a) it is shown that for such a small $KV/(kT)$ value the thermal stability of the grain becomes questionable and a signal reduction takes place. The same authors have shown (Lu and Charap 1994b) that thermal effects become more serious with increasing magnetostatic interaction when discussing media properties for 10 Gbit/in^2 and higher. Optimization of the anisotropy and magnetization in relation to the head field and signal-to-noise ratio is one of the important issues for magnetic media of the future. Beside measuring the thermal stability of magnetic particle media nowadays a growing numbers of published results is available on hard disk media. In general it shows that there is a significant time decay brickwall facing storage of longitudinal magnetic recording at densities beyond 10 Gbit/in (Judy 1997).

2.5.1.4. Intrinsic coercivity and single domain particles. Determination of the total coercivity of a particulate medium is very difficult because of particle interactions. The coercivity H_c is the field strength at which the magnetic induction can be reduced to zero. The intrinsic coercivity H_{ci} is defined as the field at which the magnetization becomes zero. In soft magnetic materials $H_c \approx H_{ci}$ and in hard magnetic materials $H_c < H_{ci}$. The coercivity of an SDP is called the intrinsic coercivity h_{ci}. For instance, for a cylinder-shaped particle (aspect ratio 1:10) an indication can be obtained about the coercivity for different materials. Of course the coercivity can be determined by the crystalline-, shape- and stress-anisotropy or a combination of them. The particle shape discussed here for Co, Ni and Fe particles always has a contribution from the shape anisotropy. The main anisotropy source depends on the material. Crystalline anisotropy is the main source for the coercivity of Co particles ($h_{ci} = 2K_1/(\mu_0 M_s)$). The coercivity for a SDP of Fe is mainly determined by the shape of the particle ($h_{ci} = (N_b - N_a)M_s$) while strain mainly determines the Ni particles ($h_{ci} = (3/2)\lambda_s\sigma/(\mu_0 M_s)$). We can conclude from this global approach that in the case of shape anisotropy the coercivity is proportional to the magnetization, while in the case of strain and crystalline anisotropy the coercivity is inversely proportional to M_s. The final coercivity in a medium depends strongly on the interactions and the related interaction field H_i from the neighbor particles. It has been shown that the medium coercivity can be given by:

$$H_c = (h_{ci} - H_i)^2/h_{ci}. \tag{2.11}$$

When h_{ci} is determined by the shape anisotropy then the H_c of the medium is also determined by the packing fraction p, namely $H_c = h_{ci}(1 - p)$. When $p = 1$ all particles have interaction (contact), the particle shape anisotropy is lost and H_c becomes zero if only the shape anisotropy determines the anisotropy.

2.5.2. Reversal mechanism in thin films

The ideal magnetic structure for a magnetic recording medium consisting of a polycrystalline microstructure is a crystallite that reverses its magnetization by rotation and not by domain-wall motion. In other words, for high density recording the crystallites should act as independent single-domain particles without exchange coupling.

Of course in this type of medium magneto static interaction will play an important role and depends on the type of material and the intercrystalline distances.

In practice thin films possess a wide distribution of grain size and not all crystallites are completely separated from each other. This mixture of exchange and magneto static coupling will influence the reversal behaviour.

There are two main models from the microstructural point of view, namely the particulate and the continuous microstructural models. In the first one the crystals that are formed during film deposition are believed to interact only through magnetostatic interaction. No exchange force acts over the column boundaries due to physical separation. In the continuous model the reversal mechanism is thought to take place by Bloch walls as in stripe domains, hindered by the column boundaries which may increase the coercivity of the medium.

2.6. Hysteresis loop and reversal processes

Materials used as storage media should have a non-equilibrium behaviour which may be designated as a "memory". In the case of a magnetic recording medium this behaviour is represented by hysteresis loops. The transition between two states of $+M_r$ and $-M_r$ represents the presence of information. Due to the Weiss domain theory the atomic moments in a ferromagnetic material are ordered. The difference between the demagnetized and the magnetized state is due to the dimensions and the number of domains having opposite directions of magnetization.

In the transition from the demagnetized state ($H = 0$; $M = 0$) to saturation ($H =$ large; $M = M_s$) small domains (aligned favorably with the field) grow in the direction of the field (wall motion). If the field is increased, another reversal mechanism is relevant, namely the rotation of the magnetization into the easy axis. At very high fields the moments lying in the direction of the easy axis, which is close to the applied field, are coherently rotated in the direction of the field. The final state of the material is a single domain (if the applied field is sufficiently high). In this description the magnetization is reversed mainly by domain-wall motion which means movement and bowing of the wall. Bowing of the wall at low fields is a reversible process, but irreversible bowing may occur if the wall is sufficiently deformed. It can be stacked by pinning sites. Many microstructural properties can influence the domain wall motion such as grain boundaries, defects, chemical inhomogeneities and magnetostriction. Magnetization reversal by domain-wall motion may also be the origin of (very) high coercivities.

The question is, can such materials be used for low-noise recording? The answer is "no", because for sharp transitions (no zigzag configuration) it is necessary to avoid exchange coupling between the "magnetic units" (grains, columns, particles) and to lower the magnetostatic interactions. Furthermore, reversal by domain-wall motion, even in a real particulate medium, acts as a noise source. Consequently, we have to design small non exchange coupled single-domain grains.

2.7. *Aspects of medium noise*

In magnetic recording systems three types of noise must be considered: medium, head and electronic noise (Bertram and Arias 1992). Electronic or amplifier noise depends on current or voltage noise. Head noise arises from the loss impedance due to the complex part of the permeability of the head. Since the head impedance is matched to the amplifier, inductive head noise results as Johnson noise with the loss impedance as the effective noise resistor (Daveport Jr. and Root 1958). Medium noise is the most important factor influencing the performance of the recording system. This type of noise is the random component of the magnetization pattern produced when a signal is recorded, or any spatial random property of the medium (such as surface roughness), which gives rise to noise in the electrical output of the read head and electronics. The noise can be separated into three somewhat distinct sources: amplitude modulation, particle or granularity noise, and phase or transition noise. The latter refers to fluctuations that are concentrated near the recording transition and increases with the recording density. It was mentioned already in connection with fig. 2.3 that the transitions in a thin film media are not straight but have a zigzag structure caused by the magnetic interactions that make such a "domain wall" structure energetically favorable. Transition noise is strongly dependent on the type of medium used. Local structural and chemical variations in the medium can cause distortions in the direction and magnitude of the magnetization and anisotropy. The general opinion is that to reduce the transition noise finer grains and weaker magnetic interactions are required. This demand can be more or less realized by choosing the right materials and deposition parameters to create the proper microstructure and morphology of the thin film media. The main aim for thin film media is to create small uniform high packed crystallites magnetically separated at the crystal boundary. These crystallites act as single domain particles. In fig. 2.10 a schematic illustration is given of such particles in written bits.

Although the transition is given as a straight line this is not true for the practical case (see fig. 2.3). Consequently the magnetization direction of the particles around the transition is uncertain. Therefore the magnetization direction is given with a small arrows.

For this type of media, at high densities, the particle noise also plays an important role. The magnitude of noise in particulate medium is determined by the properties of the individual particles and the relatively weak magnetostatic interactions between the particles. As each single domain grain passes the read head, a voltage di-pulse is produced. The random dispersions of grain orientations, sizes and locations creates a background noise to the recorded signals (Thurlings 1983).

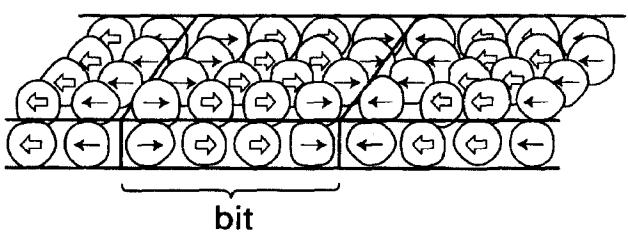

Fig. 2.10. A schematic illustration of the individual particles in one bit.

In the case of a thin film medium the signal-to-noise ratio can be written (Bertram 1994) as:

$$\mathrm{SNR} = n\,\mathrm{tw}\,\delta\lambda/2 = n\,\mathrm{tw}\,\mathrm{bl}\,\delta. \tag{2.12}$$

It can be seen from this expression that the SNR is directly proportional to the packing density n (the ratio between a magnetic and a non-magnetic material). For a particulate medium one has SNR $\propto n^{1/2}$.

In general, smaller particles have a statistical reduction of noise given the same bit area. This rule is valid if the medium does not have exchange coupling and if there are only small effects of magnetostatic interaction. However, very small particles give a continuous decrease in coercivity until the particles become superparamagnetic. New materials having higher switching energies either with higher coercivities or higher magnetization have been developed in the area of typical particulate recording materials such γ-Fe_2O_3 particles used for video applications. In the case of tapes consisting of this type of particles the density for a particle with a length of 1 μm is about 10^{11} per cubic millimeter. Co-modified γ-Fe_2O_3 (length 0.5 μm) increases its density by a factor of 10. The later developed metallic Fe particles (length 0.25 μm) have a density of 10^{13}. Smaller particles having higher switching fields (higher H_c and/or M_s) are continuously under development.

In the metal thin-film media consisting of very small grains a 10 times larger grain-packing density has been achieved but individual grains are not single acting magnetic particles. Depending on microstructural aspects we must take into account the contribution of the exchange coupling and the magnetostatic interaction (the intergranular distance is only very small compared with that of the particulate medium). Switching of clusters of grains is more obvious. This results in irregular magnetization patterns in the written transition and, therefore, to noise in the output signal.

Higher densities and lower noise consequently result from smaller bits containing crystallites with smaller sizes. For example, a bit cell in the Co-based medium used for the IBM 1.19 Gbit/in^2 demonstration disk (Yogi et al. 1990) consists of about 1900 grains with a grain size of about 20 nm. Consequently, for a 10 Gbit/in^2 thin-film medium a grain size of about 10 nm is necessary (smaller grain size is not possible due to the superparamagnetic limit). In this case there will be about 600 grains in a 1-bit area. Another source of noise is the so-called transition noise. Here due to the strong demagnetizing fields at higher linear densities, the transition of magnetization does not appear as a sharp wall but as a zigzag type (see also fig. 2.3). This makes a significant contribution to the noise of the system during reading.

It has been seen that H_c plays an important role in the formula used for the determination of the transition width (see section 2.2) but the question arises if this macroscopically measured H_c is the right parameter. At least it does describe the average behaviour of a large volume of the material (see also the introduction of section 2) while the transition is very small. Essential microscopical knowledge of the switching of the local grains is necessary. The relations between microstructural parameters, magnetic measurements and micromagnetic calculations are extremely important for understanding the noise behaviour of thin film hard disk media.

3. Preparation technologies of hard disk media

In general a thin film can be defined as an area (volume) on top of a carrier (substrate) with properties differing from it. The interface between the substrate and the thin film has a large influence on the properties of the layer. The interface is determined by the properties of the substrate, deposition parameters, thin film material(s), method of deposition and the deposition parameters used.

In the case of thin film media for magnetic recording four deposition methods have been used: electroless deposition, electro-deposition, vacuum evaporation and sputtering. Electro-deposition and autocatalytic plating (electroless deposition) were initially investigated in the early 1950s. The first magnetic disk for digital magnetic recording was introduced in 1960 and made by electro-deposition. Nowadays most of the hard disk media are prepared by sputtering.

It will be obvious that a close relationship exists between deposition conditions, nucleation and growth of the layer and its physical properties. Thin layers have properties that differ greatly from those of the bulk materials. These unique properties may be due to:

- The small thickness of a few of their atomic layers up to micron values. As a consequence, the surface/volume ratio of the layer is different from that of the bulk;
- Because of their typical growth processes they are found in certain microstructures which are, in many cases, directly related to the physical properties;
- Layer and substrate form a composite system resulting in a combination of properties based partly on the substrate properties and partly on the layer itself.

By changing the deposition method and/or varying the different deposition parameters various layer structures and morphologies can be created over a wide range. The interaction between the layer and substrate, i.e., the interface, plays an important role in defining the structure and properties. In contrast to other fabrication methods it is possible to deposit solid materials which may have equilibrium as well as non-equilibrium properties. More information about deposition technologies in general, sputter technologies and thin film properties can be found in for example (Chopra 1969; Maisel and Glang 1970; Chapman 1980; Ohring 1992; Bunshah 1994). With deposition technologies, multilayers consisting of a few monolayers of ferromagnetic material alternating with a non-ferromagnetic material can also be prepared. Multilayers are used for preparing media for magneto-optic recording and thin-film heads based on the magnetoresistance principle.

Because hard disk media are mainly prepared by sputtering we only want to focus on this method.

3.1. Sputtering

From the physical point of view sputtering is a process totally different from evaporation. Generally, the sputter deposition process concerns the ejection of atoms from the target by energetic particles. The ejected atoms then condense on the substrate to form a thin film. The accepted theory of sputtering is based on Wehner's research (Wehner 1957) which showed that it is a momentum-transfer process. When ions bombard the target surface, interactions between ions and target atoms is in the form of binary collisions involving a

basic momentum exchange. The collisions can be produced as deep as 5–10 nm but most of the momentum exchange occurs within about 1 nm below the target surface.

In the case of the systems discussed here, the sputtered atoms leave the target at an appreciable kinetic energy (3–10 eV). Part of this energy will be dissipated by the collision process with atoms of the sputtering gas. Upon arrival at the substrate the energy is still 1–2 eV (evaporation 0.03 eV). Typical deposition rates are 5–50 nm/min.

As a result the sputtered atoms arriving at the substrate surface will possess substantial energies compared to vacuum evaporated atoms. This can lead to higher surface temperatures and better adhesion of the films. The flux of recoil atoms from the target is assumed to be isotropic. Experimentally an angular distribution depending on $\cos^2\theta$ can be found, in which θ is the angle between the normal to the surface and the direction of the particle flux emitted from the source.

There are two principle sputtering methods namely:

- Glow-discharge sputtering; a plasma is formed between the target and substrate and the positive gas ions interact with the target material;
- Ion-beam sputtering; here the ion beam is produced in a separate ion gun and directed onto a target.

Because the glow-discharge method is the most important for thin-film media production only this method will be further discussed.

3.1.1. DC glow-discharge sputtering

A glow discharge is formed in a low-pressure gas when a DC voltage is applied across two planar electrodes (cathode − and anode +) at the so-called break-down voltage (Chapman 1980). The glow discharge for sputtering is sustained by the secondary electrons which the ions produce on striking the cathode. Each secondary electron produces 10 to 20 ions to sustain the discharge. The principle of the DC-planar diode-sputtering system is shown in fig. 3.1.

The luminous regions of a DC discharge show a dark space near the cathode (target) and the anode (substrate holder). In order to obtain uniform sputtering of the cathode, the anode should be located at a distance from the cathode of about 2–4 times the thickness of the cathode dark space. This distance is inversely related to the gas pressure. If the pressure is increased to reduce the size of the dark space, the deposition rate is limited because the sputtered atoms experience multiple collisions before reaching the substrate plate (the mean free-path length is a function of the pressure). For a simple laboratory DC-sputtering system, a practical compromise of 10^{-2} to 20×10^{-2} Torr is used for a target substrate distance of 2–5 cm. In addition to the removal of neutral atoms from the surface of the target by the bombardment of the ionized sputtering gas to form the deposited film, there are several other effects that occur at the target surface which influence the film growth. The particle mechanism at the target and substrate during sputtering is shown in fig. 3.2.

With a view to the process of nucleation and growth of the layer, the interaction of particles with the substrate is very important. As can be seen in fig. 3.2 most of these particles are generated after interaction with the target. The effects of the particles are very complicated, for example the secondary electrons produced at the target surface not only generate secondary positive ions but also a heat flux to the substrate.

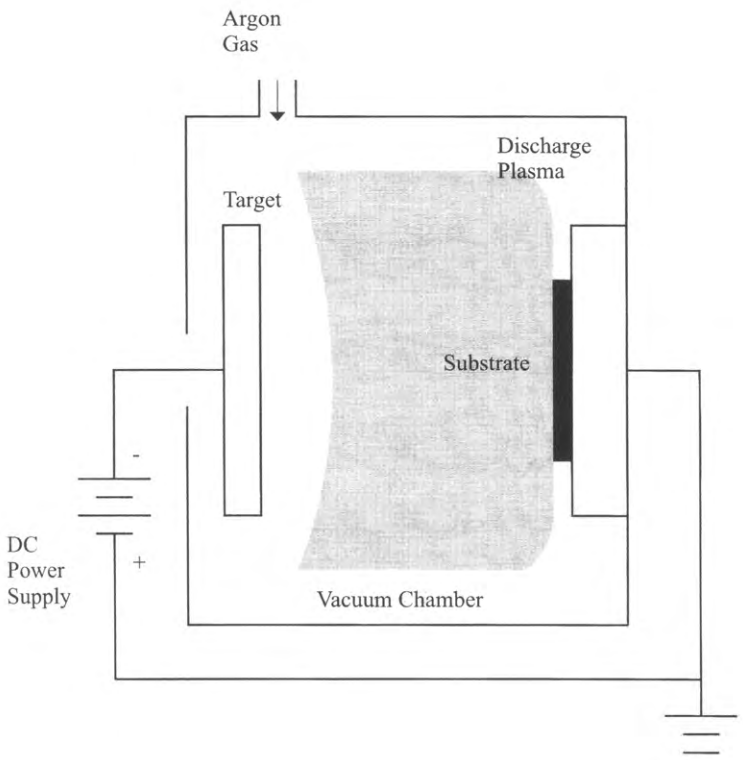

Fig. 3.1. Principle of DC-planar diode sputtering system.

The negative ions of the target material can sputter the already deposited film. The characteristics of the film deposited on the substrate will therefore depend on the relative numbers and energies of the various species as they reach the growth surface and their subsequent behaviour. This will depend on a number of factors such as substrate temperature and substrate potential. In the literature 14 effects have been mentioned which may result from changes in deposition rate, substrate temperature and bombardment of the film by species in the discharge (Vossen 1971).

The effect which different parameters have on the growth of a film may also vary greatly from material to material.

3.1.1.1. Sputter yield. A very important characteristic of the sputtering process is the sputter yields; defined as the number of ejected species per incident ion. This parameter increases with the energy and mass of the bombarding ions as well as with increasing obliqueness of the incident ions. In order to obtain the yield for low bombardment energies the following equation can be used (Sigmund 1974):

$$S = \frac{3\alpha}{4\pi^2} \frac{4m_i m_t}{m_i + m_t} \frac{E}{U_0} \quad \text{[atom/ion]} \tag{3.1}$$

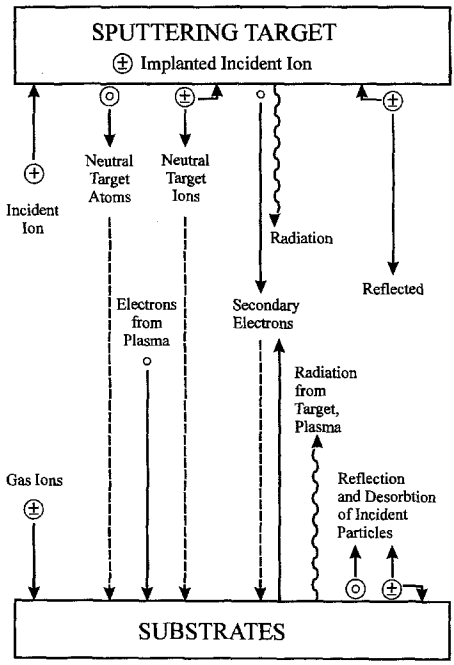

Fig. 3.2. Particle interaction, at the substrate and the target in a glow-discharge sputtering system.

where α is a monotonically increasing function of m_t/m_i which has a value of 0.17 for $m_t/m_i = 0.1$, increasing up to 1.4 for $m_t/m_i = 10$. The values m_i and m_t are the masses of the colliding atoms, E is the energy of the incoming ion and U_0 the surface binding energy. For energies of about 1 keV a modified equation is given by (Chapman 1980).

Another sputter parameter which can be used is the choice of the sputter gas. Ar is mostly used but other gases for instance Kr and Xe can also be applied as alternatives, or in combination with Ar. For instance reflected Kr atoms have less energy than Ar atoms. This can drastically influence the nucleation and growth processes.

The actual values of sputter yields are given in table 3.1 for several materials and different energies for Ar (0.5 keV, 0.6 keV and 1.0 keV), the most commonly used sputtergas (Ar) as well as for two other important gases (Kr, Xe).

With respect to the conditions mentioned in the table the yield varies between 0.4 and 3.8 and increases with the mass and energy of the sputter gas.

3.1.2. RF glow discharge sputtering

The DC configuration cannot be used for sputtering dielectric materials. An RF frequency of 13.56 MHz is used and the generator is coupled through a so-called blocking capacitor to the insulator (target). The target area is small in comparison to the substrate area (the substrate is connected to the system ground and consequently connected to the base plate and walls of the system). The dependence of the ratio of the voltages V on the

TABLE 3.1
Sputtering yield for some metals (Chapman 1980; Ohring 1992).

Energy (keV)	0.5	0.5	0.5	0.6	1.0
Sputter gas	Ar	Kr	Xe	Ar	Ar
Al	1.05	0.96	0.82	1.24	1.0
Ti	0.51	0.48	0.43	0.58	–
Cr	1.18	1.39	1.55	1.30	–
Fe	1.10	1.07	1.00	1.26	1.3
Co	1.22	1.08	1.08	1.36	–
Ni	1.45	1.30	1.22	1.52	2.2
Cu	2.35	2.35	2.05	2.65	2.85
Ag	3.12	3.27	3.32	3.40	3.8
Ta	0.57	0.87	0.88	0.62	–
Pt	1.40	1.82	1.93	1.56	–
Au	2.40	3.06	3.01	2.7	3.6

two electrodes (T – target, S – substrate) and the relative electrode areas A is given by (Chapman 1980) as:

$$\frac{V_T}{V_S} = \left[\frac{A_S}{A_T}\right]^4. \tag{3.2}$$

The exponent can be less than 4. Between the glow discharge and the electrode is a narrow region in which a change from the plasma potential to the electrode potential occurs. This is called a sheath or dark space. A typical RF diode-sputtering system looks the same as the DC unit.

The capacitor allows a net negative DC voltage to be developed at the target. The thickness of the dark space and the flow regions are similar to those of the DC mode and are dependent on the gas pressure. In RF sputtering the operating pressure ranges from 2×10^{-3}–20×10^{-3} Torr and the commonly used spacing between the electrodes is 5 cm. It is, of course, also possible to sputter metals with the RF mode.

3.1.3. Magnetron sputtering

Magnetron sputtering has been widely used for the deposition of the magnetic thin films, especially for magnetic and magneto-optical recording media. It can be realized simply by placing a planar magnet assembly behind the target (see fig. 3.3).

Magnetron sputtering (with DC or RF power) is used to increase the ionizing efficiency. In normal glow-discharge processes only a few percent of the sputter gas atoms are ionized. A magnetic field normal to the electric field is used to increase the path length of the ionizing electrons. There are several configurations for planar magnetron sputtering, of which the principle one is given in fig. 3.3.

The advantage of magnetron sputtering is that the applied magnetic field traps electrons and ions closely to the target surface and increases the number of collisions between electrons and gas atoms. Consequently advantages are, (1) the higher deposition rate and the

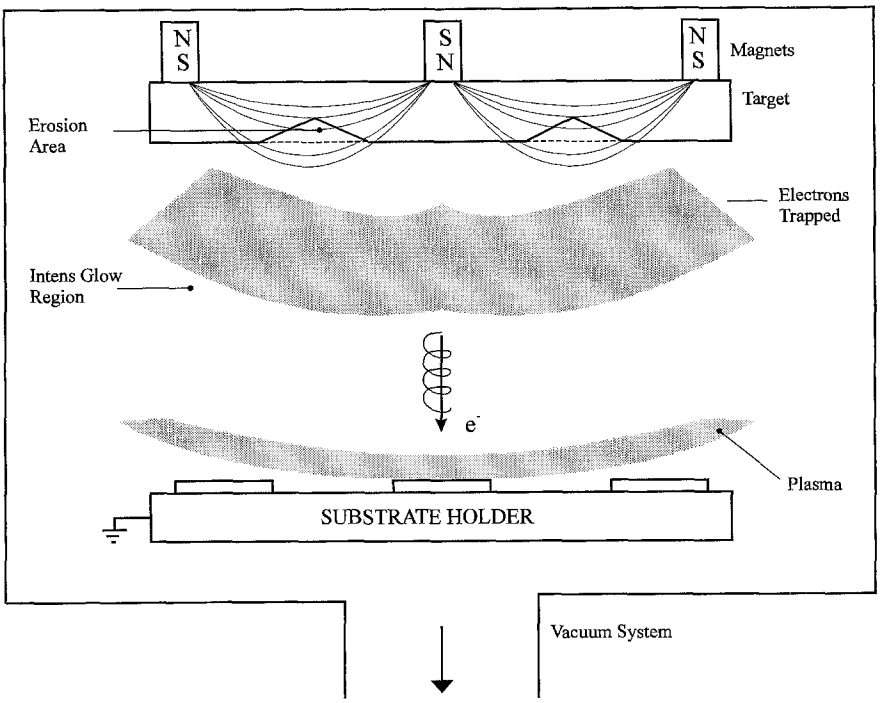

Fig. 3.3. Planar-magnetron sputter system.

more efficient use of the target material by an optimal arrangement of the magnets, (2) the bombardments of electrons and ions on the growing film can be reduced, which results in a low substrate temperature (the secondary electrons are responsible for 80% of the heat flux to the substrate), and (3) a stable glow discharge can be maintained at low sputtering pressures. The properties of the deposited film depend on the magnetic field strength H or magnetic flux density B around the target surface. Actually the component of the field which is parallel to the target surface plays an important role. The field strength can be varied by using different magnets and/or by using different thicknesses of the target (Nakajima et al. 1993). However, by using such a planar magnetron sputtering source, a very locally sputtered erosion on the target surface is formed (see fig. 3.3), which results in a very low utilization of the target. Furthermore, the magnetic field causes a very narrow *dark space* at the glow discharge which is very close to the target and results in making it difficult to shield the target and target supports. A magnetic shield must be used around the magnet assembly.

3.1.4. Bias sputtering

An interesting parameter which depends on the system geometry, sputter conditions, target material and the residual gas pressure is the bias voltage. During sputtering a negative voltage (< 200 eV) is maintained at the substrate holder and this will influence the layer

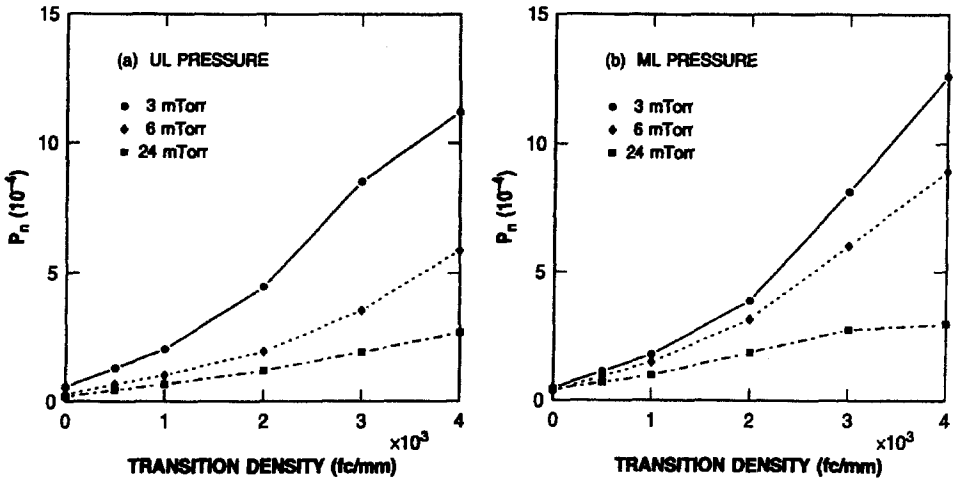

Fig. 3.4. Normalized media-noise power P_n as a function of written transition density, (a) when bias is applied to the underlayer and magnetic layer and (b) when bias power is independently applied to the underlayer and the magnetic layer (Nakajima et al. 1993).

properties by changing the flux and energy of incident (charged) particles. In contrast to normal sputtering, in the case of a bias, some of the positive Ar ions will also reach the substrate surface. Consequently a weak (low-voltage) sputtering effect occurs during film growth. In the case of small bias voltages the cathode sheath is so thin that this area will be collision free. The following phenomena are present at a biased substrate:

- removal of contamination from the substrate surfaces (sputter-cleaning),
- influencing the growing layer by removing loosely bonded particles and consequently modifying the structure.

For instance, the bias voltage can influence the composition of the growing film which is sputtered from an alloyed target (Cuomo and Gambino 1975). It can also influence the structural properties like the crystal size, the morphology and related properties such as stress (Blachman 1973), resistivity (Vossen and O'Neill 1986), hardness (Patten and McClanahan 1972) and dielectric properties (Vossen 1971). All these properties influence, directly or indirectly, the final recording performance of the layer.

It was reported (Yogi et al. 1991) that the layer growth morphology of Co–Pt–Cr longitudinal media deposited on a Cr underlayer was influenced by V-bias and therefore has a great influence on the media-noise performance.

In fig. 3.4(a) the normalized media-noise power (Nakajima et al. 1993) is given as a function of the written transition density when the RF bias voltage was applied to both the magnetic (ML) and underlayer (UL). With increasing bias it was found from measurements that the surface becomes smoother and the H_c squareness increases. The media noise increases substantially. Yogi et al. (1991) also found that by independent biasing of the magnetic and non-magnetic underlayers they could influence the growth and consequently the media noise. Biasing only the underlayer the surface of the Cr becomes very

smooth and the non-biased magnetic layer grows like a continuous film which leads to a significant increase of the medium noise.

3.1.5. Reactive sputtering

This mode is used to grow compounds or alloys by using a reactive gas environment such as reactive evaporation. The target will be a metal (alloy) or a compound. Many different layers such as oxides, nitrides, sulphides, fluorides etc. have been deposited (Vossen and Cuomo 1978). The mechanism of reactive sputtering can be generally explained by a chemical reaction at both electrodes (substrate and target). Using a pure metal target the sputter rate then decreases from the metal value to the compound value as the partial pressure of the reactive gas increase because this gas will be adsorbed on the target. This depends on the reactivity between the gas and target materials. This method was used for perpendicular recording media to prepare thin films consisting of very small ferromagnetic particles. As an example Fe–Co–O films have been prepared in this way, e.g., Nasu et al. (1987). The relatively large perpendicular anisotropy is due to the strong shape anisotropy of the magnetic metal phase (Fe–Co cubic b.c.c.) in the non-ferromagnetic Fe-oxide phase (Fe–O NaCl-structure). The very small metal fibres (10 nm diameter) grow perpendicular to the substrate surface. In the oxidized state the surface properties are mechanically very stable and suitable for recording.

3.2. Sputtering of alloys

As can be seen from the table 3.1 materials can have different yields. In the materials used for hard disks 3 or 4 different materials are used. Although the ion surface reactions are very complex (Cuomo et al. 1978) it can be finally concluded that the composition of the deposited thin film tends to be the same as that of the target used.

In this case it must be assumed that the target is used at the correct temperature which means no bulk diffusion that, no reactions at the surface take place that the, sticking coefficients for the various components on the substrate are the same and finally that the target does not decompose during sputtering. If one of the components (of a binary AB alloy) has a higher yield than the other, than the target surface concentration ratio can be modified to (Ohring 1992):

$$\frac{C'_A}{C'_B} = \frac{C_A(1 - n_g S_A/n)}{C_B(1 - n_g S_B/n)}, \tag{3.3}$$

in which $C_A = n_A/n$ and $C_B = n_B/n$ are the target concentrations, with sputter yields S_A and S_B. The total number of A and B atoms is $n = n_A + n_B$ while n_g is the number of sputtered gas atoms impinging on the target. The numbers of ejected atoms are $C_A n_g S_A$ and $C_B n_g S_B$. If $S_A > S_B$ the surface is enriched in B atoms, which begin to sputter in a relatively larger quantity, namely:

$$\psi'_A/\psi'_B = S_A C'_A/S_B C'_B = \frac{S_A C_A(1 - n_g S_A/n)}{S_B C_B(1 - n_g S_B/n)}. \tag{3.4}$$

The target surface composition will change progressively and will alter the sputtered flux ratio to the level where it is equal to C_A/C_B, which is the same as the original target

composition. Also the target surface concentration ratio will reach the value $C'_A/C'_B = C_A S_B/(C_B S_A)$, which is maintained afterwards. This gives a steady-state transfer of bulk atoms of the target to the plasma, resulting in stoichiometric film deposition. A change in sputter conditions will in general require an adjustment of the altered surface layer. An important conclusion is that target compositions can be transferred very closely to the film composition (Ohring 1992).

3.3. Substrate temperature

The substrate temperature is a very important parameter for determining the final microstructure of the thin film. The energy of the ejected target atoms ranges from several tenths of an electron volt to the full energy of ions impinging on the target, but because of scattering within the discharge the atoms frequently arrive at the substrate with low energies, roughly a few eV's.

The incidence power flux in a glow discharged configuration consists of three important components:

(a) Heat of condensation of atoms;
(b) Average kinetic energy of incident adatoms;
(c) Plasma heating from bombarding by neutral atoms and electrons.

The table 3.2 gives an idea about the involved energies (Thornton 1978) for some of the metals mentioned in table 3.1.

In the case of Co–Cr alloyed films the substrate temperature T_s is determined as a function of the P_{Ar} at a fixed power for an RF sputtering machine. The experimental data obtained by measuring the temperature of a large volume of Al_2O_3 is given in fig. 3.5.

In this case T_s is probably due to the competitive heating caused by the kinetic energy of the condensing atoms and the secondary electrons from the target. At a lower P_{Ar} the heating of the secondary electrons is reduced, but the mean free path in the argon gas is simultaneously enlarged. As a result the sputtered atoms will arrive at the surface with a higher kinetic energy, less decelerated by collisions with argon atoms. The minimum of

TABLE 3.2
Energies during magnetron sputtering at 1 keV (Thornton 1978).

Metal	Heat of condensation (eV/atom)	Kinetic energy of atoms (eV/atom)	Plasma energy (eV/atom)
Al	3.33	6	4
Ti	4.86	8	9
Cr	4.11	8	4
Fe	2.26	9	4
Ni	4.45	11	4
Cu	3.50	6	2
Au	3.92	13	2

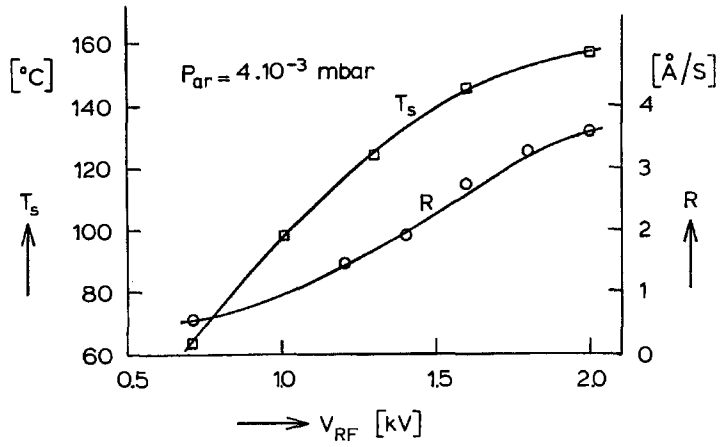

Fig. 3.5. The substrate temperature and the deposition rate as functions of the sputter power V_{RF}.

T_S is not caused by an anomalous minimum in the sputter power because R continuously increases in the entire argon pressure range as can be seen in fig. 3.5.

The complex heating mechanism not only makes it difficult to determine an accurate surface temperature (whatever this may imply) but also means that this temperature will not be stationary during the sputter run. Consequently inhomogeneities can easily be created by this process.

3.4. Contamination in sputtered films

Contaminated gases during sputtering can be dissociated and ionized in the glow discharge, and are therefore more reactive. Also absorbed gases at the chamber wall can be emitted and introduced into the sputtering plasma. This can all lead to contaminated films. If, for instance, the sputter process is carried out with a base pressure of $10^{-7} \sim 10^{-8}$ Torr then the outgasing rate of the chamber will be $10^{-5} \sim 10^{-6}$ Torrl/s. Moreover the Ar sputter gas commonly used contains H_2O and O_2 in a concentration of about $1 \sim 10$ ppm ($10^{-5} \sim 10^{-6}$), which corresponds to $10^{-5} \sim 10^{-6}$ Torrl/s of an impurity gas rate into the chamber. Therefore, not only the use of an UHV-chamber with low out-gassing rate is essential but also the use of highly purified Ar gas is found to be necessary to realize the purified atmosphere during film growth. This technical problem has also prevented the clarification of the relation between the cleanness of the atmosphere during sputtering and the obtained microstructure of the film.

Several studies on various materials have shown the crucial role of cleanliness during the deposition process regarding the properties of the resulting films. As an example, the influences on GMR values have been shown in by Egelhoff Jr. et al. (1996). The influence of cleanness for a CoCrTa hard disk thin film recording medium has been demonstrated in (Shimatsu and Takahashi 1995a, 1995b). These authors clearly demonstrated that the improvement of the microstructural properties are responsible for the improved magnetic properties. By dry etching the substrate before sputtering the Cr underlayer and

magnetic layer (CoCrNi and CoCrTa) an increase of H_c and H_k can be obtained. Moreover in the same laboratory they also found a decrease of the intergranular exchange coupling (Kawakita et al. 1996).

4. Microstructure, and magnetic and structural aspects of Co-alloyed thin film media

As mentioned in section 2.3 the most important properties for thin film recording media are a sufficient magnetization M for reading with an appropriate S/N and an acceptable field strength to create a magnetization reversal which is directly related to the coercivity H_c. The latter should not be too high for successful writing by the head field but it must be large enough to protect the medium against an unwelcome reduction of the stored information by demagnetization. In the case of high density recording a major potential for changing the signal during the required storing time is the self-demagnetizing field originating from the material itself and this field is proportional to the medium magnetization. Consequently, the H_c must be made higher for a more strongly magnetizable medium and this is also the case if the recording density increases.

Although many different configurations have to be discussed for the different types of thin-film media used in the various fields of application (tape, floppy and hard disk), in general the following essential design parts of such thin-film media are those already given in fig. 2.4.

In the next sections a motivation is given for the choice of Co-alloys as well as a short discussion on the growth of the sputtered layers. Moreover, attention is paid to the microstructural aspects such as crystal structure, texture, crystal size, compositional separation, and finally the most important magnetic properties are discussed in relation to the microstructure and the deposition parameters.

4.1. Microstructure of thin films

The process parameters (flux rate, substrate temperature, etc.), the type of material (desorption, dissociation and diffusion-energy terms) and the substrate properties influence the growth process.

Depending on the process, the film materials and the substrate behaviour, all types of layer structures can be grown (amorphous, polycrystalline and single crystal). A thin-film microstructure can be modified by means of substrate temperature, surface diffusion of the atoms, bombardment during film formation, incorporation of impurity atoms and the angle-of-incidence effect of the incoming particle flux. The higher mobility of adatoms makes it possible to create films with deviating stoichiometry. Variations in substrate temperatures make it even possible to deposit metastable structures. Treating the substrate surface or depositing pre-nucleation centres also makes it possible to grow films with a preferential crystallographic orientation (texture) and specific morphology.

In most cases the final properties of the deposited layers differ basically from materials made by standard metallurgical methods. The substrate temperature is the most important process parameter for explaining the morphology of evaporated films (Movchan and Demschishin 1969). This result is modified for the sputtering process (Thornton 1974, 1977)

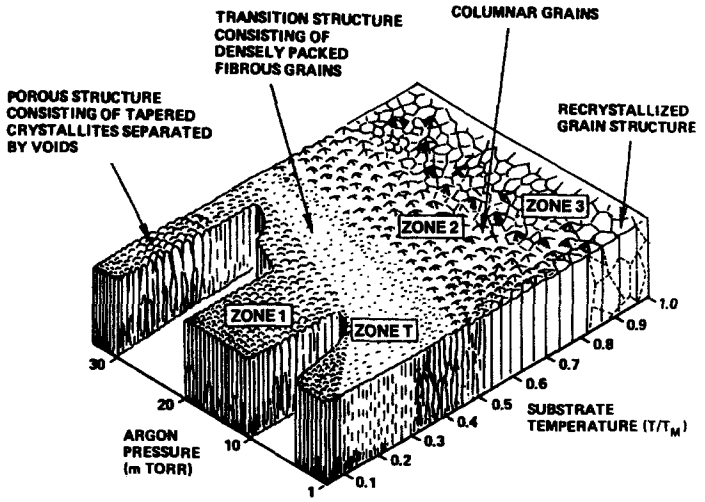

Fig. 4.1. Structural effects as a function of the sputter pressure and substrate temperature (Thornton 1974).

and is extended with a second parameter, namely the argon pressure and also the influence of the surface roughness is considered. An impression of the structural features for sputtered films is given in fig. 4.1 called the "Thornton diagram".

Figure 4.1 shows a schematic representation of the superposition of physical processes with established structural zones. The influences of the substrate (shadowing process), surface diffusion and bulk diffusion can be seen from this. The films discussed here are all made in the area where surface diffusion is the driving force for the nucleation and growth process.

This zone-structure "model" has been revised by (Messier et al. 1984) and accounts for the evolutionary growth stages of structure developments as well as for the separate effects of thermally-and bombardment-induced mobility.

The reported experimental results between the microstructural aspects and deposition parameters should be used very carefully for individual results. Variation of the experimental parameters, using different types of material may result in divergent behaviour.

Generally, deposited thin films have higher defect densities than bulk materials. The defects in polycrystalline thin films are grain boundaries, column boundaries, voids, vacancies, dislocations and gas-bubble inclusions. Defects are mostly responsible for the low-temperature interdiffusion processes. In the case of polycrystalline films the grain boundary is the most important detail.

4.2. Choice of Co-alloyed thin film media

Promising thin-film media for magnetic recording consist of the materials Co–Cr–X (X = Pt, Ta, Ni). It is essential to deposit this alloy on a Cr underlayer in order to obtain the necessary in-plane orientation. The second element combined with Co has important consequences for the Curie temperature T_c of the alloy, at which the spontaneous magnetization disappears. The T_c for Co is very high, namely 1131°C, and provides a reasonable

margin for the amount of an additional element by which T_c usually decreased. It is also true, at least for bulk materials, that adding Cr to Co can finally make the h.c.p. structure unstable and at certain compositions two crystal structures (f.c.c. and h.c.p.) may be present. Furthermore, it has been shown that even two different phases, one with a high Co-rich composition (ferromagnetic) and the other with a high Cr-rich content (paramagnetic) can be formed (Ishida and Nishizawa 1990). Consequently, adding Cr to Co has two important effects, namely reduction of the T_c and M_s. These values should be optimized for recording applications. The T_c must not be too close to room temperature, because then the magnetic behaviour becomes too sensitive to temperature variations. M_s should have a certain value because otherwise the information cannot be read by the head. It is very difficult to understand the physics behind the reduction of M_s and T_c because they are very complicated and not completely known. However, the most useful model when Cr is added to Co is to consider that the magnetic moment of Co atoms is reduced by electron transfer to its 3d band from Cr. It has been shown experimentally that the T_c drastically decreases with the Cr content and becomes paramagnetic just above 22 wt% at room temperature. This is not expected if Cr only acts as a simple diluent (Wielinga 1983). Also the transfer of 4s electrons from Cr to the 3d shell of Co may lower the magnetic moment (Aboaf and Klokholm 1981). Furthermore, pure Cr is antiferromagnetic at room temperature and a ferromagnetic sublattice coupling also seems to be an acceptable explanation of the relatively strong decrease in T_c when compared with the other element X, which forms an h.c.p. phase with Co (Kobayashi and Ishida 1981). Adding Cr to Co also gives an enhanced anisotropy field. Furthermore, with the variation of the Cr content it is possible to adjust H_c.

Another favorable influence of Cr on the film morphology is the reduction of the column dimensions (Smits et al. 1984) and the appearance of the compositional separation. As previously mentioned, the latter has a great influence on the magnetic microstructure because it can lead to more or less magnetically uncoupled columns if the enhancement of Cr at the column boundaries becomes higher than about 27 at%. Smaller grain size has the advantage of lower surface roughness which results in a better head–medium interface. Last but not least, the choice of Cr also improves the corrosion resistance and mechanical hardness of the Co-based medium, although in a few cases other elements have been added to increase these properties.

Sputtered Co–Cr films for perpendicular magnetic recording were first made at the Tohoku University in 1975 (Iwasaki and Yamazaki 1975). An overview of the preparation, microstructure and magnetic properties of Co–Cr thin films is given in (Lodder 1993).

Before Co–Cr was chosen, many different alloys of Co–M materials were investigated (Iwasaki et al. 1980; Kobayashi and Ishida 1981). They include X = Rh, Pd, Mo, W, V, Ti, Cr, Mo, Pt and Mn. All the Co–M films exhibit an h.c.p. crystal structure with the c-axis oriented perpendicular to the film surface deposited on a variety of substrate materials. However, if a Cr layer was used as seed layer (or buffer layer), the Co–Cr started growing with an in-plane c-axis which is a condition for longitudinal recording. For further tailoring longitudinal media ternary and quaternary alloys such as Co–Cr–Pt–X (X = Ta, B, Ni, B) have been prepared and used as high density media (Tsang et al. 1990; Futamoto et al. 1991; Yamashita et al. 1991; Paik et al. 1992).

4.2.1. Phase diagram of Co alloys

Because Co and Cr are always two components of the present hard disk media the phase diagram will be discussed in a little more detail. Much literature has been published on the Co–Cr binary phase diagram; the most important diagrams so far being those of (Elsea et al. 1949; Grgor'ev et al. 1961; Allibert et al. 1978). The most complete overview and new data were published in (Ishida and Nishizawa 1990).

With respect to the application of Co–Cr as thin-film medium for magnetic recording the most interesting area of the phase diagram is around the temperature range from room temperature to 1000°C. Furthermore, the compositional area of interest is < 35 at% Cr. In this part of the diagram two phases, α-f.c.c. and ε-h.c.p., are represented.

It can be seen from the latest published phase diagram (Ishida and Nishizawa 1990) that even at 35 at% Cr a h.c.p. ε-Co may exist (see fig. 4.2). There can be two phases, one with a Co-rich composition (ferromagnetic) and the other with a Cr-rich content (paramagnetic). The phase diagrams are based on an equilibrium process and achieved from thermodynamical calculations. The thin-film materials discussed here are made by deposition which is by definition a non-equilibrium process. In this case a very important fact was assumed in (Ishida and Nishizawa 1990), namely that the phase diagram at a high Co concentration below 800°C is very complicated because sluggish diffusion inhibits the equilibrium. It is known, for instance, that during sputtering the surface temperature of a grown film is quite different from that of the substrate (Chapman 1980). The bombardment exerted by various particles from the plasma on the surface results in a much higher temperature at the surface. This and also the increase in substrate temperatures, ion-assisted deposition and geometrical deposition effects can stimulate the state of compositional inhomogeneity of the thin film.

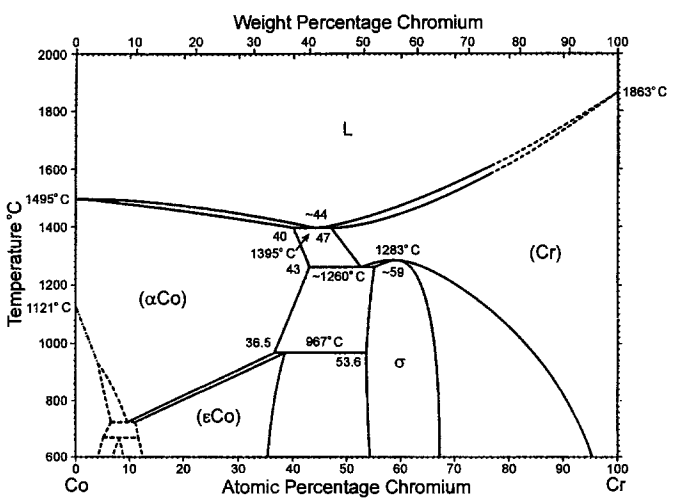

Fig. 4.2. Co–Cr phase diagram with the equilibrium phases: L – liquid; α-Co – f.c.c. solid solution; ε-Co – h.c.p. solid solution; Cr – b.c.c. solid solution and σ – intermetallic phase (Ishida and Nishizawa 1990).

Experimental data for ternary and quaternary Co based alloys made in thin film form are not available. Thermodynamically calculated phase diagrams for Co–Cr–Ta systems are presented in Putland et al. (1980). Experimental data on Co–Cr–Ni and another Co based ternary isothermal phase diagram are given in Zhanpeng (1981). Consequently very little recent information is available about ternary Co based alloys.

4.3. Growth of Co-alloy films

In general the film structure is usually described by its two most important properties: the crystallographic (preferred) orientation (or texture) and the morphology (crystal size and shape). These two features of thin films are often described independently (Bauer 1964; Drift 1967; Sanders 1971; Thornton 1977) but sometimes there is a strong relation between them. Especially in the case of the "survival of the fastest" model (Drift 1967) the morphology is strongly determined by the crystallographic orientation; i.e., the film orientation is finally determined by the crystallographic axis that grows the fastest. In the h.c.p. structure this is the [0 0 0 1] or *c*-axis.

These properties are more or less determined by the process involved, i.e., in sputtering by the process parameters which are: substrate temperature, argon pressure, contamination and sputter rate. In the case of sputtered films the substrate temperature and argon pressure are the most important parameters.

4.3.1. Growth of Co–Cr films having perpendicular anisotropy

Much research was published on the growth of Co–Cr sputtered films having the *c*-axis orientation perpendicular to the substrate surface. These films can be used as a medium for perpendicular recording. In general they can be deposited directly on the substrate (without seed layer) because h.c.p. Co–Cr growth in principle has its axis perpendicular to the substrate. Consequently such films have perpendicular magnetic anisotropy.

The *c*-axis orientation will be disturbed at higher Ar pressures (Wielinga and Lodder 1981). It has been shown that a perpendicular *c*-axis orientation is obtained at a large variety of rates (0.2–600 nm s^{-1}) (Iwasaki and Ouchi 1978; Coughlin et al. 1981; Kadokura et al. 1981; Sugita et al. 1981; Wielinga and Lodder 1981). The most important, but unfortunately also the most elusive parameter in the case of sputtering is the temperature. The complex heat mechanism during sputtering not only makes it difficult to determine an accurate surface temperature (whatever this may imply) but also means that this temperature will not be stationary during the sputter run. The surface temperature in r.f. sputtering was determined by measuring the h.c.p.–f.c.c. transition temperature and comparing it with bulk data for Co–Cr. This temperature was found to be 550°C higher than the measured substrate temperature (Iwasaki et al. 1980). However, surface formation should not be compared directly with bulk formation. First, the *c*-axis orientation is suitable, being independent of the film thickness from very thin films up to film thickness of a few microns. Secondly, the grain size increases continuously with the film thickness as measured for films in the range of 25–2000 nm. After 1 hour a constant substrate temperature of 150°C is reached with a sputter rate of 0.2 nm s^{-1}. The thickness range examined far exceeds the value measured when the temperature becomes stationary. Therefore, it is assumed that during film growth the surface temperature can be considered as constant, i.e., at least temperature variations are too small to cause different growth characteristics. The relative

surface temperature (relative to the melting point) was evaluated to be about 0.3–0.5, which means that the layers are growing within the transition zone of the Thornton diagram (see also fig. 4.1).

The *c*-axis orientation of the nuclei originates from the tendency to condense with the most densely populated crystal planes, the {0 0 0 2} planes, parallel to the substrate. This is supported by the orientation ($\Delta\Theta_{50} = 5°$) of a 25 nm thick Co–Cr film, sputtered on a silicon substrate which was placed at an angle of 45° to the substrate holder.

The preferred orientation is maintained as the film thickness is increased. This could be caused by a mechanism of self-epitaxy. In this case, however, the orientation would deteriorate with increasing film thickness (Drift 1967). This normal *c*-axis orientation is more likely to be maintained because it is also the fastest growing crystallographic orientation. It has been shown (Drift 1967) that a certain crystallographic orientation may arise from a mechanism described as "the survival of the fastest", i.e., the crystallites with the fastest growing axis (perpendicular to the substrate) survive, suppressing crystallites with other orientations. This type of layer is therefore recognizable by a poorly oriented initial layer, as is the case when glass substrates are used for Co–Cr. However, when silicon or carbon/mica substrates are used the first nuclei are better oriented which means that the film grows along its fastest direction from the very beginning.

Now the question remains: Why does the crystal diameter increase with the film thickness? In the case of the "survival of the fastest" there is a simple mechanism which explains this feature. In our case there has to be a different cause. A formal reason could be the crystal boundary energy, i.e., by increasing the crystal diameter the energy density is decreased. This, however, does not explain how some crystals grow at the expense of others. A simple explanation could therefore be that the average increase in the crystal diameter is only governed by statistical rules. The relative surface temperature, in the order of 0.4, is in the range where surface diffusion is believed to be the dominant factor (Thornton 1977). Therefore, a statistical variation in the local flux at the individual crystallites may result in the increase in the "highest" at the expense of the "lowest" crystals which is made possible by the surface diffusion, i.e., the crystallites are capable of growing sideways not hindered by intermediate crystallite layers. Clearly this effect is self-enhancing.

In the layers studied there is still a statistical variation in crystal diameter. Using TEM studies, a physical separation between the columns has not been observed, but from NMR and the selective etching process it is known that there is at least a chemical inhomogeneity in the lateral direction (see also section 4.7).

So far Co–Cr layers having a perpendicular *c*-axis have been discussed but for longitudinal recording the magnetization should be in-plane and consequently the crystallographic anisotropy must have its *c*-axis in plane. As discussed above, this is for many substrate materials not automatically the case. In order to create an in plane anisotropy the *c*-axis should be in the plane of the film. A so-called seed layer (mostly Cr) this used for is purpose.

4.3.2. Growth of Co-alloyed media with in-plane anisotropy

The hard disk media used at present have their magnetization in plane and consequently it is necessary that these media have a magnetic anisotropy in-plane. Besides the choice of the magnetic alloy, the magnetic properties can be controlled by choosing the right substrate, substrate texture and underlayer materials but also by the deposition process parameters.

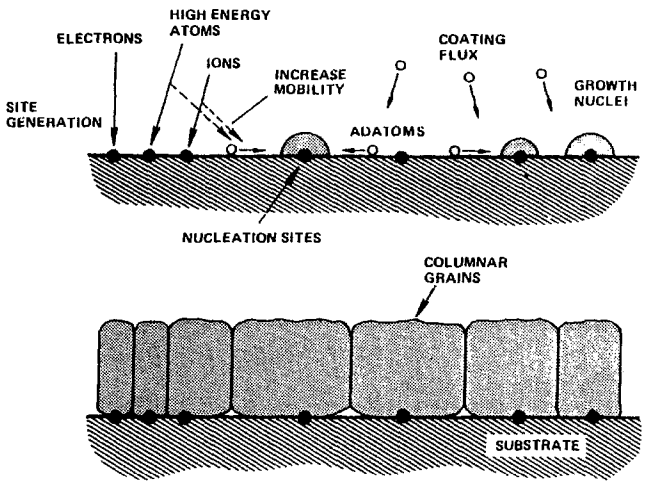

Fig. 4.3. Schematic illustration of the nucleation process during sputtering (a) and the morphology (b) of the grown film (cross-section) (Thornton 1988).

The nucleation and growth processes of a thin film are dependent on the method of deposition and the process parameters used. On the other hand the type of substrate, the use of underlayers (seed layers) and the type of magnetic material also play very important roles. Various papers about magnetic and magneto-optic materials have been published during an MRS symposium held in 1991 (Suzuki 1991). Special attention has been paid to the correlation of the microstructure with the recording performance. In particular the magnetic coupling between grains and/or columns has been discussed in relation with deposition parameters.

A schematic illustration of the nucleation and growth process of sputtered films is given in fig. 4.3 (Thornton 1988).

The incoming flux energies have an important effect on the processes of nucleation and growth and consequently on the interface formation. If it is assumed that there is no chemical reaction between the growing layer and the substrate and both are insoluble, the interface which is formed is of the type that has an abrupt discontinuity in composition. After an interaction of the vapor stream with the substrate an adatom can be formed if the kinetic energy of the "atom" is small. An adatom is a physically absorbed atom with the probability of re-evaporation. Adsorption occurs if the binding energy between the atom and surface is large. If the binding energy is small, nucleation never occurs, since it is also dependent on the temperature and the vibrational energy of the atoms at the surface. Formation of critical nuclei is essential for thin-film growth. A critical nucleus is determined by the interfacial free energy and the free energy per unit volume of the growing nuclei. During the growth of the nuclei two energies are in competition with each other, namely the surface free energy, which increases as the surface area increases and another energy which is the difference between the free energy of the solid and that of the vapor phases.

The thin-film formation process (as given in fig. 4.3) can be classified by the following stages:

- condensation of an atom (adatoms) and forming nuclei by the surface diffusion process;
- further growth of critical nuclei which leads to clustering and island forming. Islands grow in size rather than in number;
- a coalescence stage arising from large touching islands;
- proceeding the coalescence process the film reaches continuity;
- finally the film starts growing in the thickness direction and forms columnar grains.

The nucleation theory (forming nuclei from adatoms) can be explained by two theoretical models (Neugebauer 1970), based on condensation of the vapor phase, namely the atomistic model (few atoms) and the capillary or droplet model (valid from approximately 100 atoms). For the sake of simplicity it can be assumed that the first model is based on the physical (thermodynamic) theory and the second on chemical principles. With respect to the capillary model the size of the nuclei (clusters) varies continuously as a function of the free Gibbs' energy while the atomistic model is based on a discontinuous variation of the size as a function of the dissociation energy.

The process parameters (flux rate, substrate temperature etc.), type of material (desorption, dissociation and diffusion energy terms) and the substrate properties influence the growth process.

The thin-film microstructure can be modified by means of substrate temperature, surface diffusion of the atoms on bombardment during film formation, incorporation of impurity atoms and the angle-of-incidence effect of the incoming particle flux.

In most cases the final properties of the deposited layers differ from materials made by standard metallurgical methods.

As already mentioned, the zone-structure "model" introduced by (Thornton 1974, 1977) presented in fig. 4.1, has been revised by (Messier et al. 1984) and accounts for the evolutionary growth stages of structure developments as well as for the separate effects of thermally-and bombardment-induced mobility. In fact, it was pointed out by Messier that the pressure axis should be considered as the energy axis. In this case increasing pressure means a decrease of kinetic energy of the sputtered atoms. It is clear from this that application of a bias voltage will influence the energy-axis as well.

Usually deposited thin films have a higher defect density than bulk materials. The defects in polycrystalline thin films are grain boundaries, column boundaries, voids, vacancies, dislocations and interior gas bubbles. Defects are mostly responsible for the low temperature interdiffusion processes. In the case of polycrystalline films the grain boundary is the most important property.

Epitaxial growth is a very special form of nucleation and growth and has unique orientation relation with the substrate. This phenomena can be used to increase a certain texture in the magnetic film.

4.4. Crystallographic texture

Many of the Co–X(=Cr, P)–Y(=Ta, Pt, Ni) thin film media do have an h.c.p. structure with the texture axis (c-axis) parallel or perpendicular to the substrate surface depending on the properties of the Cr underlayer. It is also possible for the films to have f.c.c. phases.

The texture of a polycrystalline material can be simply defined as the crystallographic preferential orientation. In the case of a ferromagnetic thin film the orientation distribution

of the column is of great importance because it determines the quality of the direction of the magnetic anisotropy. The texture axis should be perpendicular or in-plane oriented depending on the recording mode.

Another influence on the orientation is caused by the pressure of the sputter gas and a worsening background pressure. It has been shown that a small amount of residual N_2 gas in the process chamber causes the formation of the f.c.c. phase which also destroys the well-oriented h.c.p. structure. A higher Ar pressure usually means that the atoms are more scattered during their movement from target to substrate and, consequently, their kinetic energy is reduced. Therefore, for producing well-oriented ($\Delta\Theta_{50} < 5$) films, every sputter equipment has to be optimized for certain process parameters. Much data has been published on the deposition of non-magnetic underlayers or seed layers to improve the nucleation and growth of the Co–X–Y layers and to increase the c-axis orientation.

4.4.1. Random in-plane texture

The c-axis orientation is very important for the magnetic anisotropy. The Co-based alloys used, mostly have an h.c.p. structure with the c-axis randomly in-plane, but it is also possible to create a tilted c-axis depending on the underlayer structure, see, for example, Johnson (1990). On the Cr (1 1 0) lattice an (1 0 $\bar{1}$ 1) Co–Cr–Ta orientation growth will be found and finally lead to a tilted Co alloy h.c.p. c-axis of 28° with respect to the substrate plane. But, for instance, the (1 1 $\bar{2}$ 0) of Co–Cr–Pt layers grow epitaxially on the Cr (0 0 2) resulting in a c-axis orientation of the magnetic layer in-plane. An optimized Cr thickness is found for this type of epitaxial growth. Much research will have to be carried out before this type of growth is completely understood.

4.4.2. Oriented in-plane texture

In this kind of film the properties (H_c and M_r) in the various in-plane directions (texture and non-texture directions) are different. The texture of the film can be supported by the texture of the substrate and the crystals may be smaller in the texture direction than in the transverse direction. This may be the source of strain-induced magnetic anisotropy (magnetostriction). It is also found that the crystals are aligned in the texture direction (Simpson et al. 1987).

4.5. Morphology and "grain" size

Most of the deposited films reported in the literature have a so-called columnar structure (see also fig. 4.1). Depending on the substrate materials the columnar diameter may increase with the layer thickness or it may be constant throughout the layer thickness.

The columnar diameter depends on the argon gas pressure during sputtering, the substrate temperature and the bias voltage on the substrate. The method of deposition also has a large influence on the development of the columnar growth. In the case of Co-alloys deposited on polymer substrates, extraordinary column or nodular growth is found. It can be seen from TEM observations that the average crystal has a 10–50 nm diameter. Depending on the preparation conditions the crystals can be mechanically separated (spacing about 4 nm) at the grain boundaries. Another magnetic separation mechanism between the crystals/columns is by segregated crystal boundaries with a non-ferromagnetic material. This

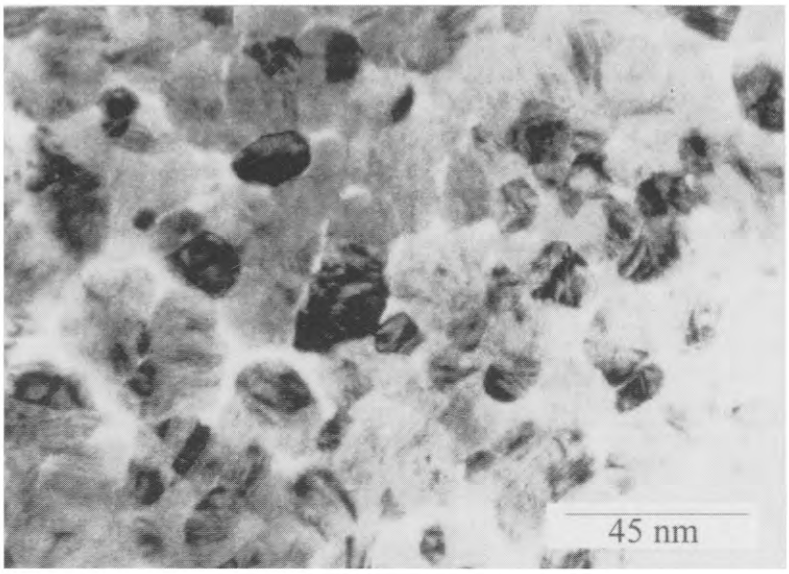

(a)

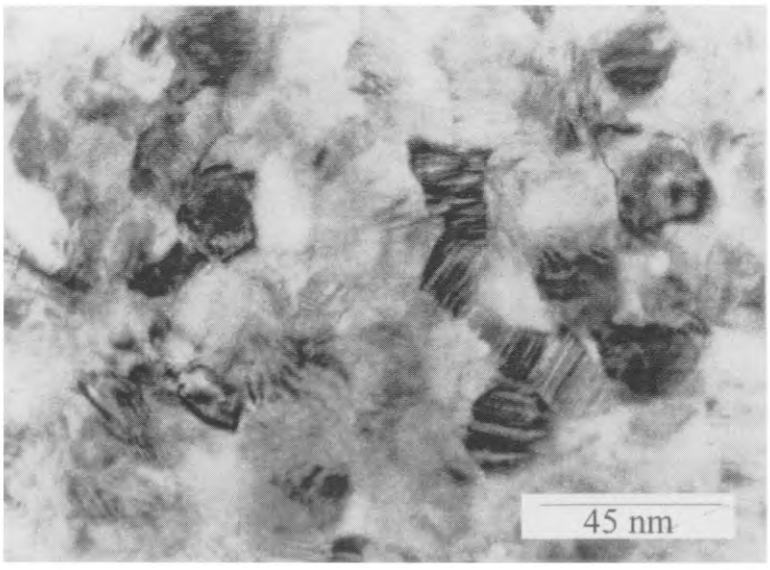

(b)

Fig. 4.4. TEM planar view of sputtered Co–Cr–Pt films prepared at room temperature (a) and 150°C (b).

has been shown by Aspland et al. (1969) in CoP plated disks. The grain size or columnar size is strongly influenced by the microstructure of the underlayer/substrate.

As discussed previously, thin films should magnetically operate as individual particles. The exchange between the crystals should be broken or at least minimized. This can be realized by mechanical separation or by segregated crystal boundaries with non-ferromagnetic compositions. The Cr underlayer is responsible for the physical separation. Cr grows with a columnar morphology and has a rough surface structure (Agarwal 1986). It was reported that the dome-like surface roughness of in the order of tens of nm's depending on the thickness of the Cr layer. TEM observations (Yamashita et al. 1991) indicate that in combination with a high Ar sputter-gas pressure the Co–Cr–Pt layer shows physically separated crystal boundaries.

Figure 4.4 shows a planar TEM observation of a Co–Cr–Pt film prepared at room temperature and at 150°C. The sample made at a low surface diffusion shows a more uncoupled grain structure than the one deposited at a higher temperature. This is also reflected in the magnetic properties.

4.6. Surface structure

In the case of very high density recording the surface becomes increasingly important. On the one hand, the surface smoothness and wearability are important because the head/medium distance is very close and, on the other hand, the magnetic behaviour is a key factor for writing as well as reading (Lopez and Klark 1985a, 1985b; Nakamura 1989; Geerts et al. 1992). Therefore, analyzes of the chemical and structural properties (e.g., surface topology) in relation to the magnetic properties are necessary. One conclusion is obvious, namely that for films with different surface and bulk hysteresis, the magnetization cannot be homogeneous throughout the film thickness during all stages of the hysteresis curve. Therefore this aspect should be studied in more detail because, as film media are becoming even thinner, the surface volume ratio will be more important. The surface roughness strongly depends on the sputter conditions, the thickness of the layer and of course the substrate roughness.

4.7. Compositional separation

Polycrystalline h.c.p. Co–Cr thin films grown on heated substrates have shown an inhomogeneous chemical composition at the grain boundaries as well as within the grains themselves. This phenomenon is called compositional separation (CS).

CS at the grain boundaries influences the magnetic interactions of the individual grains. In principle, different origins for obtaining the compositional separation can be mentioned such as the deposition temperature, the geometry of the deposition process or magnetic inducement.

Most of the experimental results on CS have been published about Co–Cr media for perpendicular recording.

A model of Co–Cr sputtered films in which the morphology is determined by CS is given in fig. 4.5. The microstructure with equal columnar size and shape and a columnar boundary (crystal boundary) is shown in fig. 4.5(a). In this case, the interaction between the columns occurs by exchange and magnetostatic interactions. The (crystal) boundary

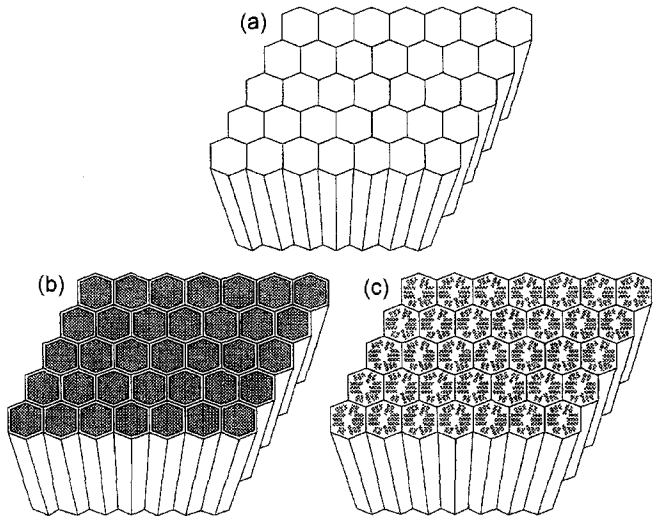

Fig. 4.5. Model of Co–Cr sputtered films in which the morphology is determined by the type of compositional separation (CS). Part (a) shows the ideal microstructure without CS, (b) -- the morphology if CS is only at the columnar boundaries, and (c) – CS at the columnar boundaries as well as CP-like structures in the columns (Lodder 1996).

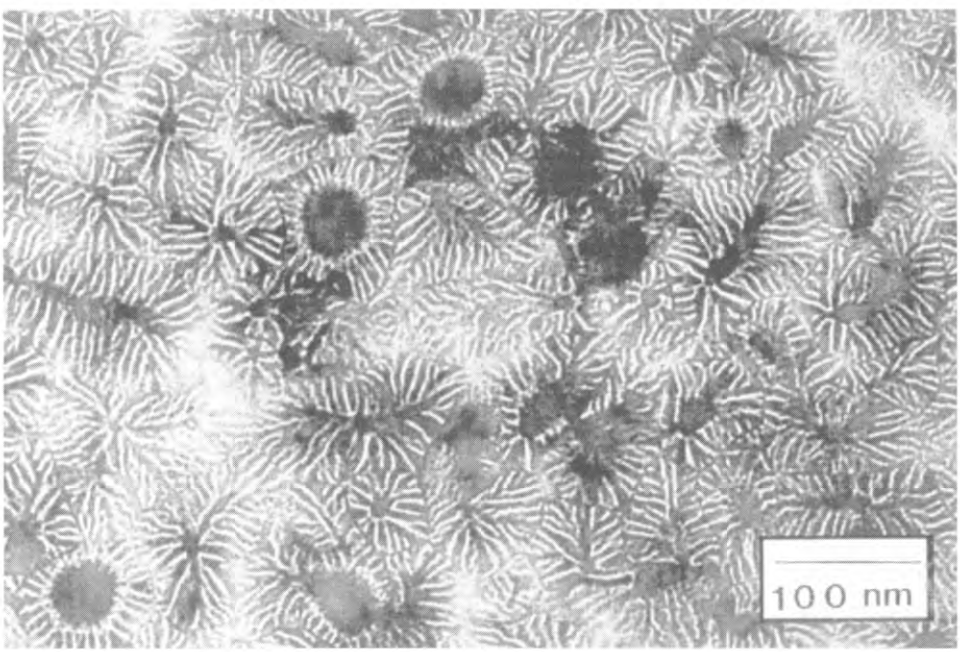

Fig. 4.6. TEM observation of a selectively etched Co–Cr sample (Courtesy Dr. Maeda, NTT Basic Research Laboratory, Japan).

can only hinder the movement of the domain wall which means an increase in H_c. In order to increase the H_c a break of the exchange forces between the crystals is necessary. This can be realized by mechanical separation of the crystals, which has also been shown in the case of longitudinal hard disks (see also fig. 4.4). The compositional separation may result in a non-ferromagnetic composition of Co–Cr between the columns (fig. 4.5(b)). Here, a Cr-rich columnar boundary is present. Moreover, a more complicated CS structure may occur (chrysanthemum-pattern, CP) which could create a composition difference in one column in combination with a Cr-enriched columnar boundary (see fig. 4.5(c)). In this case, Co-rich (ferromagnetic) and Cr-rich (non-ferromagnetic) are distributed over the whole sample.

Complicated microstructures with Cr-rich and Co-rich areas occur and have many consequences for the switching behaviour of the magnetization and, moreover, for the coercivity.

Compositional separation has also been shown (Maeda and Takei 1992) in Co–Cr–X materials used for longitudinal recording and in Rogers et al. (1994) it was confirmed that the CS is suppressed by increasing Ta content.

Most data from in-plane media is derived from macroscopic magnetic measurements, which on Co–Cr–Ta showed that an increase in Ta content also increases the magnetization. This suggests that this effect is due to increasing Cr segregation at the boundaries. Another effect of applying Ta is the increase in the lattice constant which leads to or reduces strain in the lattice. It was suggested that this influences the H_c. In Co–Cr–Pt it was found that the increase in the lattice constant can be correlated with the increase in H_c. The Pt in these types of ternary alloys may also play a role in the formation of the very hard $Co_{50}Pt_{50}$ composites which have a large influence on the reversal behaviour.

The CP structures are observed by TEM but also in the case of very thick samples by SEM (Maeda et al. 1991). These kinds of observations are only possible in combination with selective etching techniques (Maeda and Asahi 1987).

Figure 4.6 shows a TEM observation of a typical CS microstructure, a so-called CP structure revealed by chemical etching. The white stripes within each crystal are thought to correspond to dissolved Co-rich regions and the dark areas correspond to passivated Cr-enriched regions. Consequently, this TEM observation shows Co-rich and Cr-rich regions in one crystal which means that a Co–Cr crystal consists of ferromagnetic regions smaller than one grain (see also fig. 4.7).

The main features of the CP structure are Co-rich stripes that tend to be perpendicular to the column boundaries. The CP structure also developed as a function of the thickness of the layer. The substrate temperature plays an important role in the formation of this particular nanostructure. The Co-rich and the Cr-rich components strongly influence the magnetic properties. The spatial periodicity of compositional separation in sputtered Co–Cr layers on top of soft magnetic Ni–Fe layers is in the range of 3–7 nm (Maeda et al. 1991).

The possible explanations of such a CS structure (which has never been observed in Co–Cr bulk alloys) vary in the literature.

The boundary enrichment with Cr is also described as oxygen gettering (Smits et al. 1984) which means that during growth the Cr mainly reacts with oxygen. Consequently, the M_s of the magnetic composition increases. Another explanation is that there is a recombination of atoms, molecules or clusters before they interact with the substrate (Jinghan

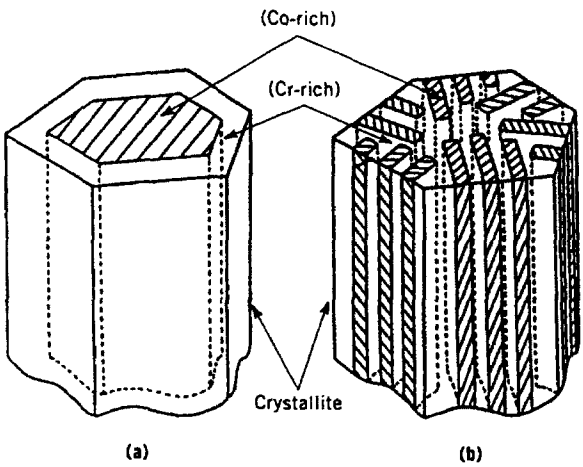

Fig. 4.7. The two possible CS structures in an Co–Cr–(X) alloy sputtered film showing Cr-enriched boundaries (a) and the so-called CP structure in (b).

1986). The formation of Cr–Cr and/or Co–Co clusters produces a compositional change. The same result can be obtained by using non-homogeneous targets (in the case of sputtering). Cr concentration fluctuations on the lattice faults present in the column have also been used for explaining CS (Hwang et al. 1987). Other explanations, where the Cr migrates to the boundary for thermodynamic reasons, can be found in (Abraham and Bundle 1981; Chapman et al. 1986; Sagoi et al. 1986). These explanations are based on the fact that the Co–Cr system strives to attain the lowest possible surface energy by enrichment of the boundaries with Cr atoms, because these have a larger surface than Co and also the binding energy is lower. The Cr atoms are exchanged with Co atoms at the surface and also at the column boundaries. The grain boundaries are also assumed to be fast diffusion paths at which diffusion takes place by vacancies (Petersen 1986).

Very often the phase diagrams of bulk Co–Cr systems have been used to explain the chemical composition although such a diagram is only valid at thermodynamic balance. A complete overview and new data were published (Ishida and Nishizawa 1990). With respect to the application of Co–Cr the most interesting area of the phase diagram (see fig. 4.2) is around the temperature range from room temperature to 1000°C. It can be seen from this phase diagram that at 35 at% Cr and lower, two h.c.p. phases, one with a high Co-rich composition (ferromagnetic) and the other with a high Cr-rich content (paramagnetic) may exist. The thin-film materials discussed here are made by deposition which is by definition a non-equilibrium process. In studying these materials, a very important fact was assumed, namely that the phase diagram at high Co concentration below 800°C is very complicated because sluggish diffusion inhibits the attainment of equilibrium.

It is known, for instance, that during sputtering the surface temperature of a grown film is quite different from that of the substrate (Chapman 1980). The bombardment exerted by various plasma particles on the surface results in a much higher temperature at the surface.

Most of the literature, when explaining the magnetic behaviour of Co–Cr thin films, have suggested that there is Cr segregation at the columnar boundaries which could explain the

higher coercivity and the magnetic reversal behaviour of the layers. However, only a few research groups have experimentally shown the existence of such a compositional separation. The most consistent work in this field has been carried out by Maeda et al. (1994). He considered two origins of CS namely precipitation of the Co–Cr σ-phase intermetallic compound as suggested by (Sagoi and Nashikawa 1989). These authors based their phase diagram on the assumption that the Cr solubility limit in the h.c.p. solid solution is 13 at% Cr. The second mechanism is the magnetically induced-phase separation predicted by (Hasabe et al. 1982) from thermodynamic calculations.

NMR studies of 5–22 at% Cr films were carried out and it was shown that CS occurs in all compositions sputtered at 200°C (Films prepared at RT do show homogeneity over the whole composition range). This result suggests that CS is not due to precipitation of the σ-phase. The next experiment was to study the CS in materials such as Co–Ru and Co–Mn, of which both alloys exhibit a sharp decrease in T_c with the composition.

According to (Takayama et al. 1981) who have developed a theory about magnetically induced phase separation (MIPS), CS should occur. In Maeda et al. (1993) a strong CS was found in h.c.p. Co–Ru films sputtered at elevated temperature. Moreover, no intermetallic compounds precipitate for any composition. Similar effects are also found for f.c.c. $Co_{75}Mn_{25}$ magnetic thin films. Rogers et al. (1995) deposited at a substrate temperature of 300°C. In this system the T_c decreases to 270 K for Mn of about 30 at%. The results have shown that for a deposited Co_{76} Mn_{24} film a very strong CS occurs (with about 95 at% of Co). It is interesting to realize that both Co–Cr and Co–Mn alloy systems have been predicted to exhibit a phase separation by using thermodynamic calculations which consider the magnetic ordering effect (Hasabe et al. 1982).

Although further study is necessary, so far these results strongly support the idea that the CS in Co–X sputtered films deposited at higher substrate temperature lies in magnetically induced phase separation due to the enhanced surface diffusion during thin film growth.

Consistent results from experimental studies of TEM in combination with etching techniques such as: NMR, APFIM (Hono et al. 1993a) and SANS (Takei et al. 1994) are presented in the literature.

The results recently obtained by APFIM studies have shown how the concentration fluctuations in the grains (columns) are distributed (Hono et al. 1993a, 1993b; Hono 1994). Such measurements can only be made after a special preparation technology of the Co–Cr film and substrate. The results show the atom-probe concentration depth in the planar direction of a Co–Cr column with an average composition of 22 at% Cr. Over a depth of about 40 nm compositional differences of 30 at% Cr and 7 at% Cr have been measured. The latter composition is ferromagnetic while the composition above 26 at% Cr is paramagnetic. The fluctuations extend to regions of less than 10 nm, in diameter.

The results obtained by CS studies in Co–Cr thin films having a perpendicular anisotropy support the experimental results obtained by anomalous Hall effect (AHE) measurements (Lodder et al. 1994; Haan and Lodder 1997). Here, we have measured about 4 times more jumps in the hysteresis loop than the number of columns, which means that a Co–Cr column switches non-uniformly due to the variation of the magnetization in one column. A very preliminary conclusion is that this effect is related to the CS structures in the Co–Cr. In micromagnetic simulation the CS is incorporated and with this addition the AHE results can be calculated and are qualitatively in agreement with the measured results (Kooten et al. 1994).

4.8. Magnetic properties and microstructure

The ideal magnetic structure for a magnetic recording medium consisting of a polycrystalline microstructure is that of a crystallite which reverses its magnetization by rotation and not by domain-wall motion. In other words, for high density recording the crystallites should act as independent single-domain particles, consequently, without exchange coupling but depending on the particle distance and still with magneto-static coupling. In practice thin films possess a wide distribution of grain size and not all crystallites are completely separated from each other. This influences the reversal behaviour. As mentioned in section 2.5.2 there are two main models from the microstructural point of view, namely the particulate and the continuous microstructural model. In the first one the crystals that are formed during film deposition are believed to interact only through magnetostatic interaction. No exchange force acts over the column boundaries due to physical separation. In the continuous model the reversal mechanism is thought to take place by Bloch walls as in stripe domains, hindered by the column boundaries which may increase the coercivity of the medium.

In this section the relation is given between the microstructural aspects such as crystal structure, texture, crystal size, compositional separation and some of the magnetic properties such as magnetization, coercivity, anisotropy and magnetic structure.

4.8.1. Magnetization of deposited alloys

The relation between the magnetization and composition is frequently presented by the Slater–Pauling curve shown in fig. 1.10b which gives the relation between the saturation magnetization M_S and homogeneous bulk Co–X (Pauling 1938; Slater 1938; Bozorth 1951). In general, most papers reported that the M_S of sputtered and evaporated films, deposited at higher substrate temperatures, is found to be larger than that for bulk alloys having the same average chemical composition. Although in the literature various origins have been proposed, the most likely explanation is phase separation. Two h.c.p. phases, which hardly occur in bulk Co–Cr material at low temperatures, cause compositional fluctuations along the grain boundaries as the film growth proceeds.

In fig. 4.8 Haines' calculations (Haines 1984) is used to compare our experimental data (Kranenburg 1992). In the random Co–Cr alloy the Cr atoms are not distributed in the most suitable way for reducing the M_S of the alloy. Therefore, the maximum local content of Cr for this distribution is much higher than in the case where Cr–Cr bonds are not present. The lower curve in fig. 3.5 shows the behaviour when the latter are present and it can be seen that the M_S becomes zero at 25 at% Cr, because for bulk material the measured M_S for this composition is zero. Consequently, 4 Cr NN (Nearest Neighbor) in an h.c.p. lattice makes the final M_S zero.

4.8.2. Coercivity of thin-film media

The coercivity in a magnetic material is a very important parameter for applications but it is very difficult to understand its physical background. It can be varied from almost zero to more than 2000 kA/m in a variety of materials. Values of more than 250 kA/m have been reported for thin-film recording media. First of all, the coercivity is an extrinsic parameter and is strongly influenced by the microstructural properties of the layer such as crystal size and shape, composition and texture. These properties are directly related to

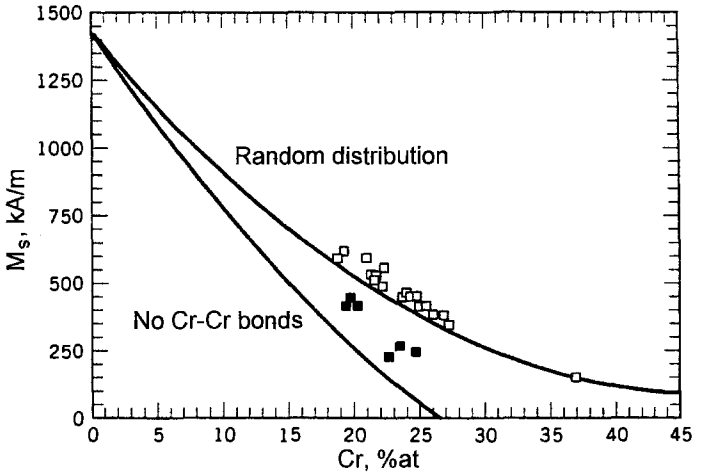

Fig. 4.8. The magnetization as a function of Cr concentration. Experimental data (□ – co-evaporated samples at low temperature, ■ – sputtered samples) compared with calculated distribution lines (Haines 1984).

the preparation conditions. Material choice and chemical inhomogeneities are responsible for the M_S of a material and this is also an influencing parameter of the final H_c. If only crystalline material is considered, then the crystalline anisotropy field plays an important role. It is difficult to discriminate between all these parameters and to understand the origin of the coercivity in the different thin-film materials in detail.

As has been seen in an ideal single-domain particle which switches coherently, the H_c is equal to the H_k if a field is applied in the easy-axis direction. Depending on various factors, incoherent switching occurs and the H_c decreases. Even in a matrix of particles, with magnetostatic interaction, the coercivity will be influenced. Multidomain particles and thin films will switch by domain-wall motion and again the coercivity decreases in comparison with the H_k. Although we have to deal with many different morphologies it would seem that the H_c is satisfactorily described by a general relation introduced by Kronmüller (1987):

$$H_c = \alpha \frac{2K_1}{\mu_0 M_S} - N_{eff} M_S. \tag{4.1}$$

It can be seen that this relation takes account of the magnetocrystalline anisotropy as well as of demagnetizing fields. The parameters α and N_{eff} relate to the microstructural aspects and the dimensions of the magnetic units. The influences of α and N_{eff} on the H_c for polycrystalline thin films were extensively discussed by (Kronmüller 1993). In addition, for thin films, surface and interface properties also influence the H_c. The above leads to the assumption that the coercivity (an extrinsic property) can only be determined by means of the macroscopic hysteresis loop in combination with the theory of micromagnetism (Brown 1963). Knowledge of the microstructural properties of the material is indispensable. In the first place the size and shape of the magnetic unit (crystal, column) material

play an important role. In SDP the coercivity increases to a maximum at a critical particle-size diameter. Future increase in the diameter results in a multidomain-state particle. When the SDP diameter is decreased, it finally becomes superparamagnetic. At this stage the reversal takes place by thermal activation which again leads to a lower H_c. In the case of an MDP the H_c is either nucleation-controlled or determined by pinning mechanisms of the domain wall. These mechanisms are determined by the magnetically inhomogeneous regions such as columnar boundaries, chemical inhomogeneities, stacking faults etc.

4.8.3. Magnetic structure

An important characteristic of a medium is its magnetic structure, the magnetic unit (intrinsic domain structure or written bit) in the magnetizable layer which has, in principle, two opposite stable directions parallel to the anisotropy axis. The switching of the magnetic units can be achieved by a sufficiently large applied field.

Study of the magnetic structures and their switching behaviour can be carried out by several techniques. The study of the M–H loop gives information about the macroscopic behaviour of the media. More knowledge about the micromagnetic behaviour is needed for increasing the density. More insight can be obtained by computer simulations. New experimental methods are available and are being developed for collecting more information about the meso-magnetic (an area between macro and micro) properties of the media like the methods used for observing the magnetic domains, domain walls, written bits and stray fields using the Bitter-colloid SEM method, MO Kerr observations, Lorentz TEM observations, Electron Holography, SEMPA, AHE (Anomalous Hall Effect) measurements (only applicable for media with perpendicular anisotropy) and MFM.

The microstructure of the thin-film medium has a great influence on the magnetic behaviour of the film. Is the magnetic behaviour of the layer continuous or particulate? Both qualifications refer to the degree to which exchange forces are able to extend throughout the medium. In a continuous medium the exchange forces are hardly disturbed by structural discontinuities such as crystal boundaries. As a consequence, the magnetic-domain boundaries usually consist of Bloch walls. The typification "particulate" refers in the first instance to the method of preparation, whereby particles, usually single-domain particles, are compounded together with non-magnetic materials. In these media, the exchange forces are restricted to the volume of the particles, which therefore show only magnetostatic interactions. Within this definition, from the magnetic point of view, even thin films may be considered as particulate, showing distinct structural ferromagnetic units like crystals, columns, or clusters of crystals or columns separated by non-ferromagnetic materials or voids. Such kinds of microstructures may be influenced by the deposition methods and the nucleation and growth process of the layers as noted previously. If the thin film has a continuous microstructure in which there is an exchange between the magnetic units, then in the remanent magnetic state the layer consists of magnetic domains having their direction of magnetization anti-parallel and separated by a domain wall. The wall is a transition region in which the spins are rotated from one direction into the other direction. The thickness of such a 180° wall is determined by minimizing the various energies and is, of course, dependent on the type of material (Co = 8.4 nm; Fe = 30 nm; Ni = 72 nm).

In conclusion, the magnetization reversal in a thin-film medium is very strongly dependent on the microstructural properties. Depending on the morphology and chemical inhomogeneities of thin-film media the reversal take place as follows:

- The reversal in one grain is strongly dependent on the CS structure in one grain.
- Exchange coupled grains show a magnetic-domain structure which covers many grains and gives a reversal originating from domain-wall motion. The wall energy, influenced by crystalline anisotropy, magnetostatic energy at the wall, strain, chemical inhomogeneities and film surface properties, dominates the coercivity H_c.
- Uncoupled grains when reversed are, of course, independently influenced by magnetostatic interactions. Here, the H_c is determined by the crystalline anisotropy of the grain, shape and strain anisotropy.
- Clusters of grains which are locally magnetically coupled can reverse in unison. These reversals are independent of other clusters, but again magnetostatic coupling may influence their behaviour.

The shape of a magnetic material (sample geometry) is the most obvious feature which may influence the anisotropy. Depending on the geometry there will be a "magnetic charge" at the surface of the uniformly magnetized sheet, cylinder, ball or sphere. This magnetic-pole density produces an internal uniform demagnetizing field H_d ($= -N_d M$) which is, in fact, proportional to M and directed opposite to it. Here, N_d is the linear demagnetizing factor. The sum of the three orthogonal vectors is equal to one ($N = N_x + N_y + N_z = 1$). The values for these demagnetizing vectors depend on the shape of the magnetic unit. An important factor is that the magnitude of the internal field H_{int} is less than that of the applied field H_{appl} by the amount of the H_d. Consequently, the H_{appl} must overcome the H_d in order to saturate the material (see also chapter 1).

4.8.4. Deposition parameters, microstructure and magnetic properties

It has been discussed in section 4.3.2 that the substrate temperature is the most important sputter parameter. In fact, this is only an indication of the real temperature at the growing surface. The difference in growth mechanism is understood considering the activation energies for surface, grain boundary and bulk diffusion. The ratio of these energies is 1:2:4, respectively. This means that at low temperatures the surface diffusion rates can be orders of magnitude larger than the bulk diffusion rates. It was found that binary and ternary Co-alloys during sputtering are deposited within a temperature range by which bulk diffusion can be neglected (Lodder et al. 1983). But nevertheless it is very hard to understand all the relationships between sputter parameters, microstructural features, and magnetic parameters. In fig. 4.9 the relations between the many parameters and events are given.

It can be seen from fig. 4.9 that the "substrate temperature" is finally determined by the substrate holder temperature, the sputter power, deposition rate and sputtergas pressure. The substrate temperature affects all structural features such as their CS, grain size, texture, d-spacing and HCP formation. The sputter power and the residual gases have an influence on the grain size, while the argon pressure influences the texture and crystal structure. The bias voltage also has an influence on the crystallographic properties and moreover also on the CS. As we have already seen the microstructural properties influence the magnetic properties. Grain size is important for the noise and bit density, while the crystallographic texture and crystal structure are important for the H_k and indirectly for the H_c and the compositional separation has an influence on the M_s and H_c. Finally the residual gases can influence the anisotropy and M_s.

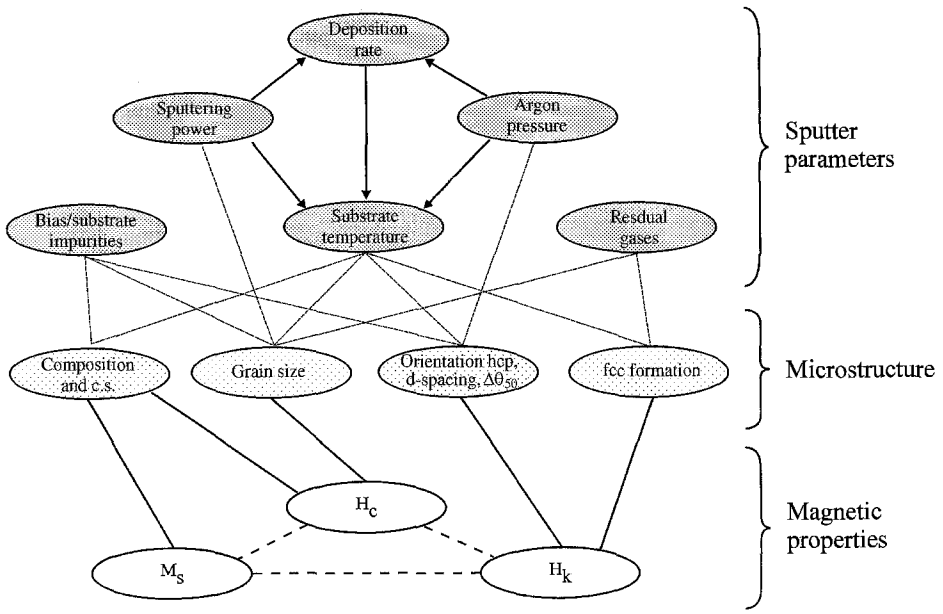

Fig. 4.9. The relation between the sputter parameters, the structural features and the magnetic properties.

5. Thin film hard disk media

Disk manufacturers are using sputtering technologies for thin film medium production. New substrate materials such as glass and ceramics now promise to replace aluminum. Substrate surfaces have to be prepared to create the right properties, so firstly, the surface roughness has to be controlled by texturing in order to roughen it in a controlled pattern. The final surface topology should then be smooth but not too smooth in order to avoid stiction of the head.

In order to develop the right microstructure and mechanical properties of the magnetic media a complicated disk structure with various types of layers have been proposed. As can be seen in fig. 5.1, a possible hard disk medium can consist of a substrate, a transition layer (intermediate, under and seed layer) between the substrate and the magnetic (recording) layer(s) and a top layer for protection and/or lubrication. This layout is more complicated than for the medium given in fig. 2.4. The presentation in fig. 5.1 is a very special one because it proposes the design of a so-called multilayered media consisting of a magnetic bilayer medium and all possible types of layers which can be used (Laughlin et al. 1996). It should be pointed out that this configuration does not belong to any realistic medium commercially made. In this schematic representation the two magnetic layers are separated by an interlayer. All the different layers in fig. 5.1 have their own specific properties and need special process parameters for the realization. The names used are defined in relation to their positions with respect to the magnetic layer(s) the underlayer is positioned under the magnetic layer(s), the intermediate layer lies between the underlayer and magnetic layer and the interlayer separates the two magnetic layers.

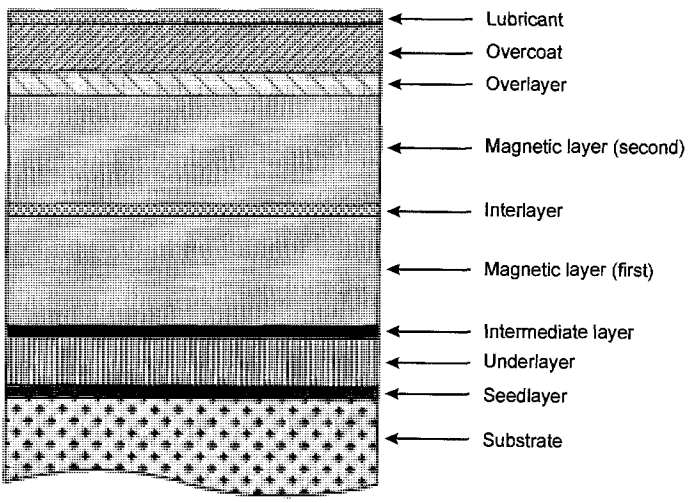

Fig. 5.1. An advanced multilayer medium for high density magnetic recording (Laughlin et al. 1996).

In order to improve the disk media for future high densities (> 10 Gbit/in^2) two directions are proposed by (Howard 1994) namely the evolutionary and the revolutionary approach. The first focused on the gradual improvement of the h.c.p. Co alloy media. The revolutionary development of new media is focused on materials with higher anisotropies than the present hexagonal Co alloys. In the literature sputtered BaF thin films, granular media and amorphous CoSm alloyed films on Cr underlayers are mentioned. The main reason for this is to provide more stable particles with smaller diameters. Several examples of both approaches will be given in more detail.

5.1. Substrate materials

The substrate choice for hard disk application is very important not only from the sputtering point of view but also because of the important role of the substrate in fly-ability and reliability. The performance of the substrate is one of the key factors to improving the hard disk performance (Bhushan 1993). One of the most critical factors, for obtaining gigabit recording is the near contact recording technology. Therefore a continuous decrease in flying height over the years appears. For instance, to obtain the 10 Gbit/in^2 in 2 areal recording density in 2000 it was estimated in 1990 that a 10 $\times$ decrease in spacing will be necessary. In fact the decrease in physical spacing from about 200 nm to 20 nm.

The wear life of the head disk interface as well as the friction force between the two surfaces are strongly dependent on the disk surface texture and lubrication condition. The surface texture has been characterized mostly by the amplitude parameters of surface roughness. From the point of view of areal density the disk should be quite flat, but to avoid head stiction the surface of the medium should not be totally flat. Texturing of the disk is the solution to overcome stiction.

Another new aspect for hard disk substrates is that the disk is spinning faster and faster. Some of the today's high-end drives already have a velocity of 7200 rpm while for the

TABLE 5.1
Some physical properties of substrate materials (Miller and Bhushan 1996).

Substrate property	NiP	Alumino silicate glass	Soda lime glass	Carbon	Glass ceramic	SiC
Density (g/cm^2)	2.7	2.5	2.5	1.8	2.7	3.2
Young's modulus (GPa)	27	85	75	35	83	460
Hardness (kg/mm^2)	500	590	540	650	650	2500

near future 14 000 rpm is being discussed. Application in laptops also requires thinner substrates.

Extremely rigid disks (high specific module) seem to be the most ideal substrates.

The standard hard disk was made from a 10 μm amorphous NiP layer coated on top of an Al–Mg alloy substrate. The NiP layer is used to improve the polishing properties and surface hardness of the Al–Mg substrate. In order to alleviate slider-disk stiction the NiP layer is roughened or textured. Here a compromise must be made between the typical requirements for stiction, durability and magnetic performances. New texturing methods are discussed in the literature such as sputter texturing which has been demonstrated on super smooth glass and metal substrates. Other methods to create texture surfaces are to use pulsed infrared laser radiation (Ranjan et al. 1991) and laser melting (Baumgart et al. 1995) on Ni–P disks. Each pulse of the laser creates a small single bump with diameters between 10–20 μm having a height from several to 100 nm. This laser technique is clean, precise and economical. It satisfies all tribological requirements.

At present new materials for substrates are also being sought in order to satisfy the mentioned requirements. At present glass substrates (amorphous and crystalline) are already commercially available as well as, glass/ceramic and ceramic/metal composites. A discussion on all relevant properties and a comparison between the different substrate materials is given in (Miller and Bhushan 1996).

A comparison of the physical properties of various substrate materials is given in table 5.1.

The most important properties for a substrate are a high hardness and a low density for shock resistance as well as a high modulus for reduced vibration and a good thermal stability. The mass and dimensions are important for the miniaturization of the hard disk drive.

Besides the properties necessary for the (mechanical) recording performance the substrate largely determines the magnetic properties of the magnetic films. Smoothness, chemical composition and thermal conductivity, for instance, are important parameters for determining the nucleation and growth of the sputtered films. Nucleation and growth process of the underlayer can vary for different types of substrates, and consequently this will change the grain size and texture of the magnetic layer.

In fig. 5.2 the surface roughnesses of various substrates are given as measured by AFM (Miller and Bhushan 1996). Here, R_a is the arithmetic average, R_q represents the root mean

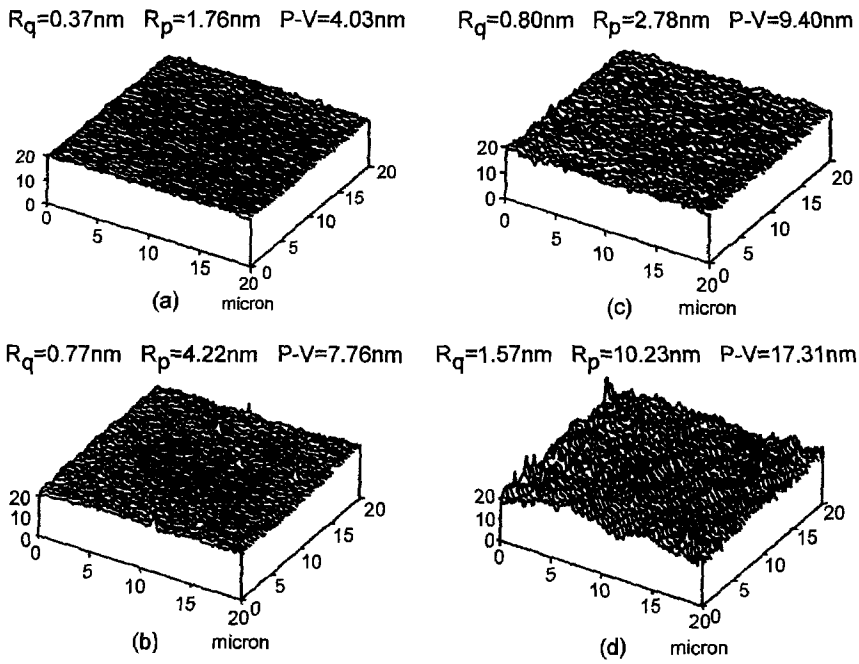

Fig. 5.2. Surface structures (topology) of substrate materials for a hard disk, determined with an AFM 20 μm ×20 μm. In (a) a very smooth NiP/Al, (b) corning code 0313 glass, (c) corning code 9647 glass-ceramic, and (d) Ohara TS-10A glass-ceramic substrates (Miller and Bhushan 1996).

square roughness and R_p the maximum peak-to-valley distance. On one hand we need a very smooth substrate surface to create a minimum head–medium distance but the on the other hand we must minimize the stiction (static friction) between the slider and the disk during rest.

In order to obtain a low flying height of the heads above the disk we need a low roughness which in turn is limited by the stiction. The trend is to use R_a's of the order of 1 nm and a glide height of about 20 nm for future applications.

Therefore the substrate surface has to be textured or roughened. This can be carried out by "polishing" the surface to make a circumferential scratch pattern which is called mechanical texturing. As a result this type of texturing is also related to texture noise in the recorded signal (Wui et al. 1994) and of course the roughness of the substrate can introduce defects in the magnetic layer as well as changing the head–medium spacing. Laser texturing was introduced which gives a more precise control by creating the location of small holes in the substrate (Ranjan et al. 1991; Baumgart et al. 1995).

Another texturing method is to create an island structure on the substrate by depositing a small amount of low melting point metal layer such as Ga or In before the Cr underlayer is deposited (Allegranza and Wui 1995). A small amount of deposited material gives a collection of spherical features on the substrate surface. On top of this island structure the underlayer (i.e., Cr) and the magnetic layer more or less confirm the island structure of the

TM seed layer and maintain morphology and the rough surface structure, which is very good for avoiding stiction (Mirzamaani et al. 1992).

The advantage of non-metallic substrates for future high density, small form factor disk drives is distinct, while the challenges to realize it in practice are not trivial, was written in 1993 (Tsai 1993) and in 1996 (Miller and Bhushan 1996) the authors concluded their paper with a feeling, based on experimental data, that glass or glass-ceramics will replace NiP/Al as the substrate of the future.

5.2. Role of the underlayer

The underlayer is very important for adjusting the magnetic and recording properties of the hard disk. The function of the underlayer is to create the right crystallographic orientation, adjusting the crystal size and to stimulate the intergranular separation.

Besides influencing the magnetic behaviour the underlayer also protects the substrate from corrosion and increases the adhesion of the media.

For the recording layer use is made of the uniaxial anisotropy of the Co alloy which is in the same direction as the h.c.p. *c*-axis. When preparing an h.c.p. Co alloy film with its *c*-axis [0 0 0 1] parallel or about parallel to the film plane an epitaxial growth is necessary. Usually h.c.p. Co grows with its *c*-axis perpendicular to the substrate surface (Wielinga and Lodder 1981; Lodder et al. 1983) because the closely packed planes (for h.c.p. (0 0 0 1) planes, for b.c.c. {1 1 0}, for f.c.c. {1 1 1} planes and B2 structures {1 1 0}) will grow parallel to the film plane. The B2 structure is closely related to b.c.c.

The epitaxial relationship is evident and therefore we must choose an underlayer material with lattice parameters close to the magnetic Co alloy. A Cr underlayer is mostly used and very successful because of the epitaxial fit. Recently other new materials such as NiAl, FeAl, MgO, GaAs, Ti, CrV, CrTi have also been introduced. For tailoring the magnetic and recording properties a so-called intermediate layer is sometimes necessary between the underlayer and magnetic layer as well as a seed layer between the underlayer and substrate (see fig. 5.1).

The general idea is that the underlayer adjusts the in-plane coercivity by supporting the right crystallographic orientation of the Co alloy layer. It should have a sharp in-plane *c*-axis orientation. Another function of the underlayer is to control the crystal size of the magnetic layer. In the case of high density recording the grain size should be between 5 and 100 nm. The intergranular separation is to stimulate the single domain behaviour of the magnetic grain. These are all needed to create sharp transitions, low media noise and high linear density.

5.2.1. Cr underlayer

One of the methods to overcome the problem of low coercivity in vacuum evaporated films is an intermediate layer between the substrate and the ferromagnetic layer, which was already proposed in 1967 (Lazarri et al. 1967). Here it was reported that by very slow deposition (0.1 nm/s) of a Co layer (thickness less than 100 nm) on a Cr underlayer with b.c.c. structure the coercivity increases at a level suitable for magnetic recording. The H_c was strongly dependent on the rate of deposition, the thickness of the Co, as well as the Cr layers and the substrate temperature. The Cr underlayer induces the growth of the Co layer with an exclusive hexagonal crystalline structure and a very narrow crystallite-size

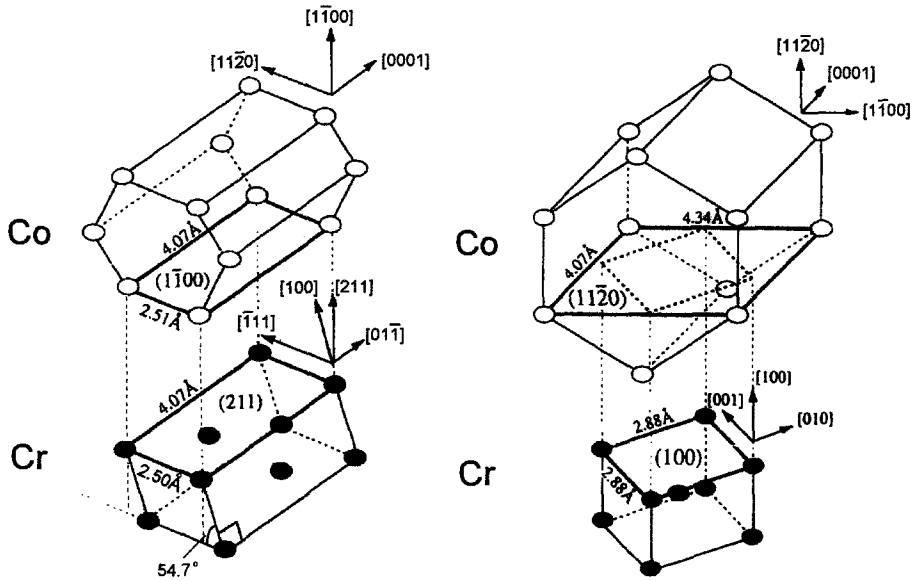

Fig. 5.3. The relationship between the Co (1 $\bar{1}$ 0 0) planes and Cr (2 1 1) planes (left) and Co (1 1 $\bar{2}$ 0) planes and Cr (1 0 0) planes (right) and the related lattice distances (Huang et al. 1996).

distribution. If the Cr layer increases, its crystal size also increases and the Co grows more quasi-epitaxial. The *c*-axis orientation of the Co becomes more in-plane if the substrate temperature increases. An important fact is that this effect is strongest if the deposition of the Co occurs immediately after the deposition of the Cr underlayer (no oxidation). The role of the Cr underlayer is thus the creation of the right conditions for epitaxial growth of the polycrystalline layer having the h.c.p. texture with the *c*-axis in the plane of the medium.

In the case of sputtered Co alloys it is also important to use an underlayer of Cr. Without an underlayer it was shown that the H_c decreases drastically if the Co alloyed layer were sputtered directly on the NiP substrate (Nolan et al. 1993a).

Optimizing the Cr layer also controls the crystal size and morphology. It was already reported in 1986 (Chen 1986; Ischikawa 1986) that the Cr underlayer thickness has a great influence on the coercivity of the Co–Ni–Cr layer. In most of the literature it can be found that with increasing Cr thickness the H_c increases. Under ideal conditions and the right material combinations coercivities above 240 kA/m have been achieved.

In fig. 5.3 the schematic diagrams of the geometry and the unit cells of the h.c.p. Co (1 $\bar{1}$ 0 0) and b.c.c. Cr (2 1 1) are presented in the left figure and the epitaxial relationship between Co(1 1 $\bar{2}$ 0)/Cr(1 0 0) is given at the right. The plane (indicated in bold) of Co (1 $\bar{1}$ 0 0), 4.07 Å × 2.51 Å fits perfectly with that of Cr (2 1 1), 4.07 Å × 2.50 Å. In the case of the Co (1 1 $\bar{2}$ 0) and Cr (1 0 0), the parameters for the Co (1 1 $\bar{2}$ 0) plane which are 4.07 Å × 4.34 Å match poorly with the rotated cell of Cr (1 0 0), having diagonal lengths of $\sqrt{2} \times 2.88 = 4.07$ Å. The Cr (1 0 0) has a fourfold and the Co (1 1 $\bar{2}$ 0) a twofold crystal

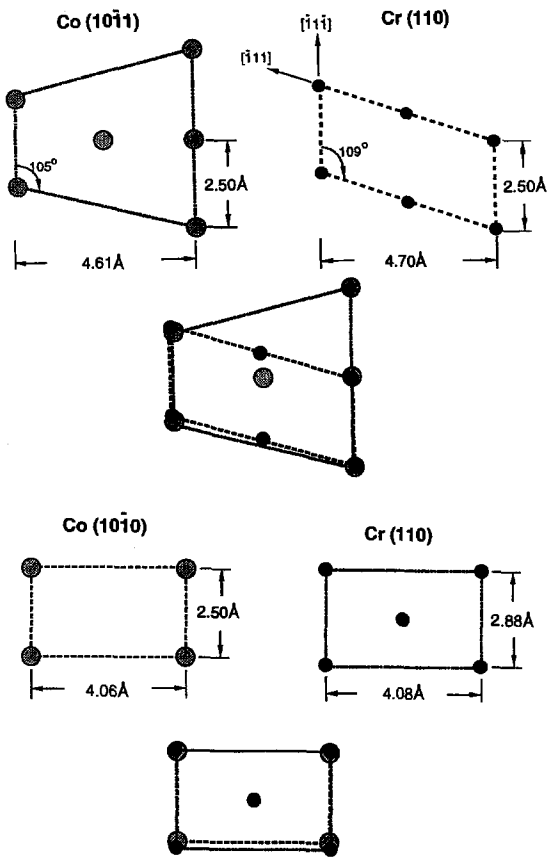

Fig. 5.4. Other crystallographic relations between h.c.p. Co and b.c.c. Cr lattices. Both (a) and (b) give the atomic positions in the (1 0 $\bar{1}$ 0) Co planes and in the (1 1 0) planes of Cr (Laughlin et al. 1996).

symmetry. As will be shown later this symmetry will result in a bicrystalline structure of the Co (1 1 $\bar{2}$ 0) layers which means that the Co c-axis [1 0 0 0] can be parallel either to the Cr [0 1 1] or [0 0 $\bar{1}$] direction.

In conclusion, for h.c.p. Co with the (1 0 $\bar{1}$ 0) or (1 1 $\bar{2}$ 0) planes parallel to the plane of the substrate, the c-axis will be directed in the film plane.

Other crystallographic relations between Co and Cr are given in fig. 5.4.

If the (1 0 $\bar{1}$ 1) Co planes are parallel to the substrate the c-axis will be 28 degrees out of the film plane (see fig. 5.4(a)) (Laughlin and Wong 1991). In fig. 5.4(b) a very good match can be seen between the two planes. But because the Cr (1 1 0) plane has twice the number of atoms as the Co (1 0 $\bar{1}$ 0), the interfacial energy will be large and consequently this epitaxial relationship is not preferable.

The matching of the magnetic layer lattice with the Cr underlayer lattice is strongly dependent on the type of Co-alloy. In ternary alloys of Co–Cr with X (=Pt, Ta, B) the lattice parameter expands and if this mismatch becomes too large then the hetero-epitaxial

growth decreases. Also Cr–Ti and Cr–Si underlayers have been proposed (Choe 1996) as an underlayer for Co–Cr–Pt magnetic media. The Cr–Ti underlayer showed changes in the crystallography with increasing Ti content and consequently has a great effect on the growth texture of the Co grains.

The Cr–Si underlayer showed uniformly grown Co grains without large clusters or grouped fine crystals in comparison with the same magnetic layer on Cr, while $Ti_{90}Cr_{10}$ underlayers are also proposed for Co–Cr–Pt perpendicular recording media to improve the perpendicular anisotropy (Nolan et al. 1996)

5.2.1.1. Deposition of the Cr underlayer. Various deposition parameters are important for determining the properties of the underlayer and consequently the magnetic recording layer. The most important parameters are the substrate temperature, argon pressure and layer thickness.

Increase of the substrate temperature gives higher coercivities and better squareness due to the reduction of the intergranular exchange coupling (Shen et al. 1994). This also results in better SNR. The sputtering parameters such as Ar pressure, power and biasing have an influence on the orientation of the Cr layer. Figure 5.5 shows the XRD spectra as a function of the various parameters.

It can be concluded from fig. 5.5 that the Cr layer can have either the (0 0 2) or the (1 1 0) texture depending on the sputtering parameters. The (0 0 2) texture can be initiated directly on the substrate surface, while the (1 1 0) texture does not appear to form directly but rather as a result of film growth.

In fig. 5.6 the grain size of the Cr underlayer is given as a function of the layer thickness (Tang and Thomas 1993) greater thickness the roughness of the Cr underlayer in combination with thin magnetic layers can also determine the H_c, due to the fact that intergranular exchange coupling is reduced by open crystal boundaries. The S as function of the Cr

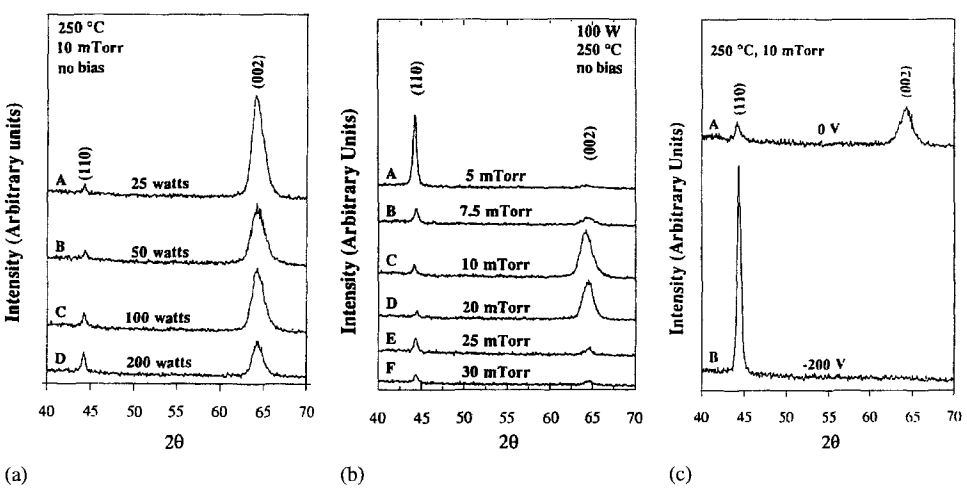

Fig. 5.5. XRD spectrum of a thin Cr underlayer measured at various sputter parameters. Sputtering powers (a), argon pressures (b), and substrate bias (c) (Feng et al. 1994).

underlayer thickness is studied by (Lal et al. 1994). A sharp optimum is found at a Cr thickness of 25 nm. This layer was prepared by using a bias voltage $V_{bias} = -250$ V. Biasing in general gives a clean deposition and a better crystallinity followed by a higher H_c of the medium.

The texture of the Cr layer is normally (1 1 0). It can be concluded from XRD experiments that the (0 0 2) texture is developed during the nucleation process and that the (1 1 0) texture is developed during the growth of the layer (Laughlin et al. 1995a, 1996).

TABLE 5.2
Dependence of the nucleation and growth parameters on sputter conditions (Feng et al. 1994).

Nucleation and growth parameters	Preheating	Par.	Sputtering conditions	
			V_{bias}	power
Substrate temperature	1st	3rd	2nd	2nd
Deposition rate	no	2nd	2nd	1st
Kinetic energy Ar	no	2nd	1st	3rd
Kinetic energy Cr	no	1st	2nd	2nd

The relation is given by 1st: very strong; 2nd: less strong; 3rd: weak; no: no effect.

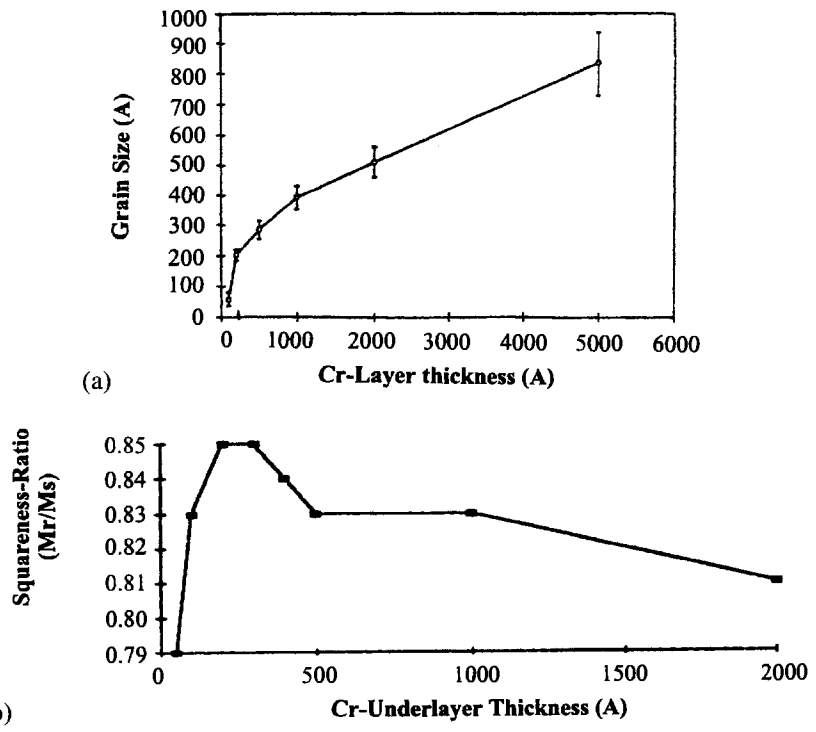

Fig. 5.6. The grain size vs. thickness (a) of the Cr underlayer (Tang and Thomas 1993) and (b) the S (squareness ratio) of a Co–Cr–Ta as a function of the Cr thickness (Lal et al. 1994).

A model for the formation of the texture of Cr is given in (Feng et al. 1994; Laughlin et al. 1995a, 1995b, 1996) and on the minimization of the surface and interfacial energies during the growth process.

It was clearly shown in (Tang and Thomas 1993) that each nucleation and growth parameter depends on several sputter parameters. A qualitative order between the nucleation and growth parameters (substrate temperature, deposition rate and the kinetic energies for Cr and Ar) and the sputter conditions (preheating, argon pressure PAr, substrate bias V_{bias} and sputter power) is given in table 5.2.

5.2.2. NiAl underlayer

In fig. 5.7 a comparison is made between the Cr b.c.c. and the NiAl B2 crystal structure.

It has been shown that b.c.c. Cr underlayers promote the epitaxial growth of the h.c.p. Co alloy thin films. In Lee et al. (1994) an ordered structural derivative (B2) of the b.c.c. structure of the NiAl ordered alloy is discussed. It can be seen from fig. 5.7 that (b.c.c.) Cr has a structure similar to NiAl (B2) and the lattice constant is more or less equal. Experimental results have shown that the grain size of NiAl is smaller than that of Cr (Lee et al. 1994). This is due to the strong binding between the Ni and Al. Moreover this strong

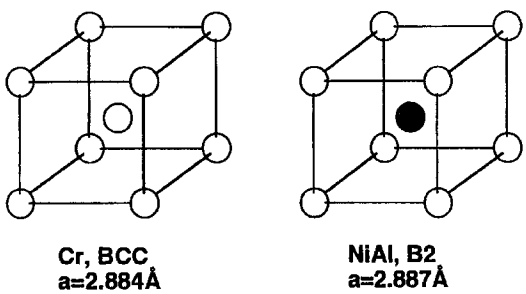

Fig. 5.7. Crystal structures of Cr b.c.c. and the NiAl B2 structure.

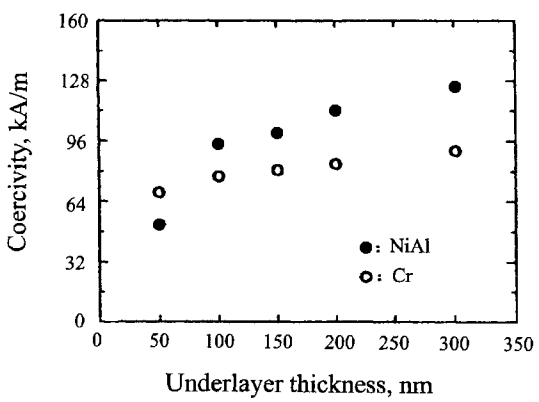

Fig. 5.8. The coercivity as function of the Cr and NiAl underlayer thickness for a 40 nm thick CoCrTa magnetic layer (Lee et al. 1994).

binding also gives a low atom mobility and consequently a low growth rate of the nuclei. The NiAl enhances the Co alloy [1 0 $\bar{1}$ 0] texture and increases the in-plane H_c (see also fig. 5.8). Figure 5.8 shows the relation of the H_c of a 40 nm thick CoCrTa magnetic film on various thickness of NiAl and Cr underlayers. In both cases the H_c increases with increasing thickness of the underlayers and finally reaches a plateau. In the case of CoCrTa/NiAl the H_c becomes larger at a thickness of about 100 nm. The smaller grain growth can lead to a lower noise rate.

5.3. Seed layers and precoated layers

Because it is more difficult to obtain a strong (1 0 0) Cr texture on glass or glass-ceramic substrates in comparison with NiP covered with an Al–Mg new seed layer materials such as Ta (Kanabe et al. 1995), MgO (Lee et al. 1995a) and NiAl (Lee et al. 1995b) have been proposed.

From the lattice constant point of view NiAl looks like Cr. It is an intermetallic alloy with a B2 structure. Its lattice parameter is $a = 2.887$ Å which is very close to the b.c.c. Cr ($a = 2.884$ Å).

A seed layer is necessary to improve the texture in the underlayer and finally to increase the size of the magnetic anisotropy and to control its direction.

It was found that magnetic layers deposited on glass substrates tend to have higher noise compared with the same media on NiP/AlMg disks. Large output signals and low noise were obtained from Co–Cr–Pt media deposited on a Cr–Ti underlayer deposited on Ta precoated glass (Kataoka et al. 1995). The reason for this is that the Co–Cr–Pt layer has a large anisotropy due to the strong (1 0 0) CrTi orientation on the Ta layer.

Using 20 nm Ta the coercivity was zero kA/m with S^* as defined in section 2.4 becoming equal to 0.85. For a Ta thickness of 100 nm these values were respectively 257 kA/m and 0.77. In the same paper Cr, W and Zr have also been used as precoated materials but the Ta layer shows the best data.

5.4. Intermediate layer

The intermediate layer is situated between the magnetic layer and the underlayer. For instance the Cr intermediate layer between the NiAl underlayer and the magnetic layer. Another example of an intermediate layer is given in (Fang and Lambeth 1994). Here a CoCrTa layer was sputtered between the Cr underlayer and the CoCrPt magnetic layer. The result was a very good lattice matching between the two CoCr compositions resulting in better in plane magnetic properties (Laughlin et al. 1996).

5.5. Interlayers

An interlayer is a non-magnetic layer situated between two magnetic layers in order to isolate the magnetic layers from each other. This multilayered structure will be discussed in section 5.6.3.

5.6. Evolutionary improvement of Co-alloy media

One of the most important parameters for a high density medium is to realize an optimal value for H_c. Such a value can be created by the texture of the layer (which influences the

magnetic crystalline anisotropy), and the morphology of the layer and more precisely the exchange coupling between the grains. The keyword here is the reduction of intergranular exchange. Exchange coupling between the grains can be influenced by voids or open areas between the grains or by another composition at the grain boundaries which magnetically isolates more or less one grain from the other.

5.6.1. Ternary and quaternary Co–Cr–X–Y layers

Sputtered hard disks of Co–Cr–X (X=Ni, Ta, Pt, C) for very high density longitudinal recording have been prepared and tested by many industrial and university groups. The first disks with a density larger than 1 Gbit/in^2 have been reported by (Yogi et al. 1990) and (Futamoto et al. 1991). The recording layers are deposited on a Cr underlayer which is deposited on the hard disk substrate. Sputtering is the most favorable deposition technology for preparing these disks. The substrate can consist of Ni:P plated on Al, glass or canasite.

The most important process parameters for depositing a suitable magnetic layer are the composition, thickness and structure of the layer. The latter also depends on the structure of the type of underlayer. The deposition parameters for both the magnetic and non-magnetic layers, such as substrate temperature, bias voltage and surface texture are very important for optimizing the recording behaviour.

Recently quaternary Co–Cr–Pt–X (X=Si, B, P, Ni, Ta) alloys have been proposed as suitable media for longitudinal high-density thin-film media. Underlayers (mostly Cr) are necessary for controlling the magnetic properties. Higher density in longitudinal recording requires thinner layers and smaller crystallites.

In combination with a spin-valve read head, read/write experiments have been carried out by (Kanai et al. 1996) on a low noise $Co_{74}Cr_{17}Pt_5Ta_4$ having a $H_c = 200$ kA/m. The results show that 5 Gbit/in^2 density recording with a linear density of 217 kBPI and a track density of 23 kTPI is achievable.

A trend is that the layer thickness for hard-disk application must decrease to about 10–15 nm in order to obtain 10 Gbit/in^2 density recording. The addition of Pt, Ta, Ni and Si to Co–Cr in combination with a higher substrate temperature favors the enhancement of M_s and H_c. An example is given in (Gao et al. 1996) with CoCrPtTa sputtered on glass ceramic substrates using a Cr/CrV underlayer combination to obtain the right growth process.

5.6.2. Laminated (double layer) hard disk media

Many studies have been published on thin film media consisting of several magnetic layers separated by a non-ferromagnetic interlayer (Hata et al. 1990; Murdock et al. 1990; Lambert et al. 1990, 1993; Palmer et al. 1991; Zhang et al. 1996). The main aim of studying the laminated medium structures for high density recording is to improve the-signal-to noise ratio by reducing the medium noise. The linear density is determined by the macroscopic magnetic properties H_c and the remanence thickness product $M_r\delta$ while the medium noise is related to the individual grain structure and the exchange coupling between the grains.

Individual control of the parameters H_c and the $M_r\delta$ in thin films was already announced by (Maloney 1979) proposing stacked Co-films. The increase in H_c and $M_r\delta$ in a four-layer system consisting of a Cr underlayer (300 nm)/CoNiCr (35 nm)/Cr interlayer (12.5 nm)/CoNiCr (35 nm) have shown better read/write characteristics (Katayama et al. 1988).

It has also been reported that the noise contribution in such a system can be reduced because the combined noise of the individual layers is lower than that of a thicker single layer (Murdock et al. 1990). The authors found that the total noise is the sum of the noise of the two individual layers plus a cross term. The key is now to design individual layers with low-noise behaviour. One of the advantages of the laminated technology is that the growth of the magnetic layer is interrupted at a very early stage which provides a better opportunity to obtain uncoupled (exchange) crystals. This research is in progress using a variety of materials and deposition parameters. An important aspect is that the interlayer thickness should be thick enough to interrupt the exchange between the magnetic layers but thin enough to retain magnetostatic coupling.

In comparison with common technologies the manufacturing control of macromagnetic and micromagnetic properties will be more difficult when employing the laminated process (Johnson et al. 1993).

The medium structure given in fig. 2.4 has been modified to a more complicated one as given in fig. 5.1. Promising media for high density recording are all multilayered structures consisting of a substrate (special glass, ceramics); seed layer, underlayer, intermediate layer, first magnetic layer, interlayer(s), second magnetic layer, overlayer, overcoat and lubricant. Although more research has to be carried out it is clear that the underlayer determines the orientation and grain size of the first magnetic layer. At present NiAl, MgO and GaAs are mentioned in the literature. Like Cr these materials also improve the epitaxial growth of the Co-based magnetic layer. The interlayer materials between the two magnetic layers can consist of Al, Ag, Cr and Cu. The function is to change the texture of the second magnetic layer which influences the interaction between the grains and the noise performance.

5.6.3. Keepered medium

A keepered longitudinal recording medium was reintroduced and consists of a standard in plane magnetic layer with and overlaying high permeability soft magnetic "keeper" layer (it is called a keepered layer because the role of the soft magnetic layer is the same as that of a permanent magnet's keeper). It was shown (Gooch et al. 1991) that about a 12% smaller transition length can be obtained in a disk covered with a Ni–Fe keeper layer. The keeper layer reduces the demagnetization of the magnetic transition in the hard magnetic medium layer. In Coughlin et al. (1996) and Reed et al. (1996) a model has shown that a keepered medium, after a small optimization, can improve the areal density with 35% at very low flying heights and proximity recording heads. The keepered media seems to be very important when media will be used at higher densities ($> 10\,\mathrm{Gb/in^2}$). In that area the recorded transitions may become unstable causing magnetically recorded information to degrade over time (Coughlin et al. 1996). It has also been shown experimentally (Chen et al. 1997) that the thermal decay rates for keepered media is better than for standard media. A review about the various concepts is given by Wood et al. (1997).

5.6.4. Ultraclean sputtering process

The ultraclean sputtering (UC) process was introduced by (Imakawa et al. 1994). Co–Cr–Ta films for LMR are sputtered at a pressure of less than 3×10^{-9} Torr, which is about an order of two lower than in a standard production machine. The impurity level used in

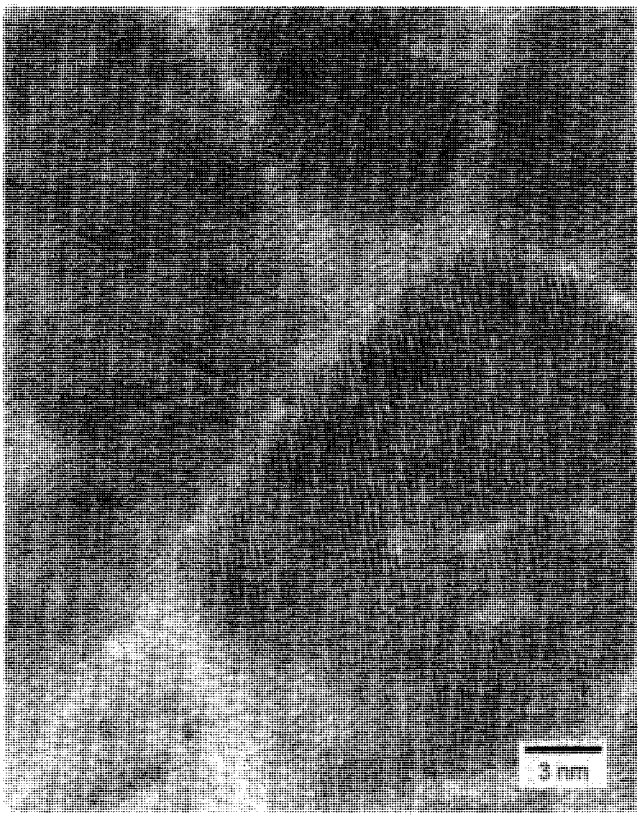

Fig. 5.9. TEM microstructure of an ultra clean sputtered Co–Cr–Ta film (Courtesy of Dr. M. Kuwabara, Kobe Steel Inc., USA, and Prof. Dr. M. Takahashi, Tohoku University, Sendai, Japan).

the process chamber is about 1 ppb (H_2O level), which is about a factor three lower than in the present systems. Ultraclean sputtering has been applied for preparing Co–Ni–Cr and Co–Cr–Ta thin film media for longitudinal recording. A typical thickness of the Co–Cr–Ta layer is 40 nm. The substrate material is NiP/Al together with an intermediate layer of Cr (50 nm).

Figure 5.9 shows a plane view high resolution TEM observation of such a layer having a $H_c = 188$ kA/m. In this picture only a few crystals can be seen together with the very clear crystal boundaries.

The crystal structure is almost perfect and at the boundaries another structure can be observed. It is suggested that Cr from the underlayer diffuses homogeneously into the grain boundary by the presence of the clean top surface of the Cr underlayer metal during sputtering. In comparison with media fabricated by a standard process, an anisotropy field higher by a factor of two has been determined, which means that the intergranular coupling is less. This was evaluated via rotational hysteresis loss analysis by determination of the magnetocrystalline anisotropy field of an individual crystal (H_k^{grain}). The intergranular

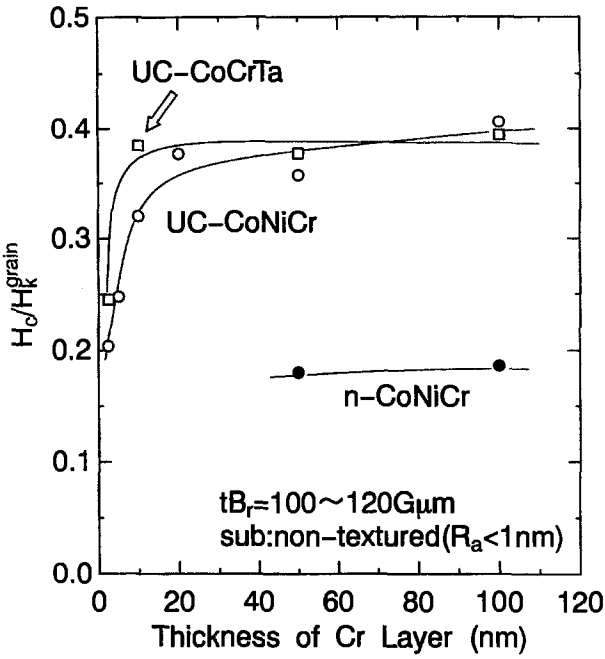

Fig. 5.10. H_c/H_k^{grain} as a function of the Cr underlayer thickness for media (CoCrTa and CoNiCr) deposited by the UC process as well as for the CoNiCr media processed in a standard sputtering system (Kikuchi et al. 1996).

coupling between the grains are found to play a dominant role in the appearance of high H_c (Takahashi et al. 1992; Shimatsu et al. 1993). In this kind of study the H_c/H_k^{grain} is used as the parameter for determining the intergranular magnetic coupling and reaches a maximum value of about 0.5 in the case of isotropic media without intergranular magnetic coupling (Takahashi et al. 1992). It can be concluded from all experimental data that the values of H_c/H_k^{grain} in UC films are much higher than those sputtered in standard systems.

In fig. 5.10 the H_c/H_k^{grain} is plotted vs. the thickness of the Cr underlayer. It can be seen from this figure that the values for the media sputtered with UC process are much higher than for the medium prepared in the standard process. In the case of CoCrTa for the UC process the H_c/H_k^{grain} value remains high for more than 0.35 to 10 nm Cr thickness. With further reduction of the thickness H_c/H_k^{grain} remains at about 0.35 even at 2.5 nm Cr thickness. This result implies that with the UC process an extremely low intergranular coupling is realized even in media prepared on extremely thin underlayers. It can be seen for UC–CoNiCr that the H_c/H_k^{grain} values also remain high right down to thin Cr layers. However below about 40 nm Cr these values are lower than in the case of CoCrTa. It has been shown for both materials that the UC process strongly enhanced the segregation of Cr at the grain boundaries. The normalized medium noise for the media deposited with the UC process was much higher than for the media prepared with the normal sputtering process (Kikuchi et al. 1996). More studies about the UC process and the relation with structural

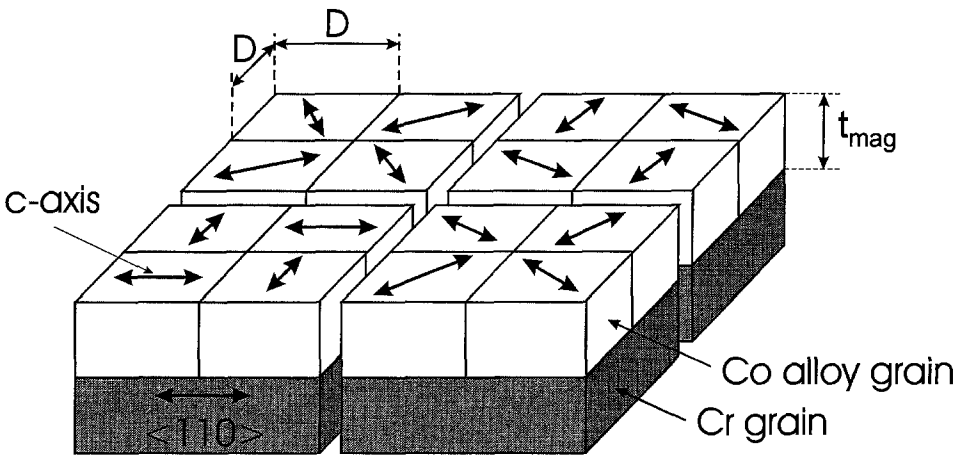

Fig. 5.11. Bicrystalline cluster structure (Hosoe et al. 1995).

and magnetic parameters are given in Kawakita et al. (1996), Nakai et al. (1996) and Sato et al. (1996). Takahashi et al. (1997) discussed the media noise properties in relation with the magnetic microstructures of thin film media prepared by the UC sputtering process.

5.6.5. Bicrystalline thin film media

In the case of certain crystallographic orientation relationship between the underlayer and the magnetic Co alloy, so-called bicrystal clusters of magnetic material can be grown on the Cr underlayer (Mirzamaani et al. 1991; Nolan et al. 1993a, 1993b; Wong et al. 1993).

A model (Hosoe et al. 1995) of such a bicrystal structure is given in fig. 5.11, where four Co-alloy grains are grown on a Cr grain from a bicrystal cluster.

As mentioned above (section 5.2.1.1) the Cr (1 0 0) has a fourfold and the Co (1 1 $\bar{2}$ 0) a twofold crystal symmetry. This symmetry will result in a bicrystalline structure of the Co (1 1 $\bar{2}$ 0) layers which means that the Co *c*-axis [1 0 0 0] can be either parallel to the Cr [0 1 1] or [0 1 $\bar{1}$] direction. This results in two areas having their *c*-axis perpendicular to each other (Nolan et al. 1993a, 1993b).

Bicrystal disks have been prepared by using a Co–Cr–Ta magnetic layer applying Cr as an underlayer which was deposited on a {0 0 1} GaAs crystalline wafer. The epitaxial relationship of Cr on GaAs is {0 0 1}⟨0 0 1⟩Cr/{0 0 1}⟨1 1 0⟩GaAs (Ding and Zhu 1994). The GaAs substrate wafer was used to give the correct orientation to the Cr layer with a very small lattice mismatch (about 1.5%) and consequently the magnetic layer has the (1 1 $\bar{2}$ 0) planes parallel with the Cr {0 0 1}. Another example is the growth of Co–Cr–Pt medium on an MgO (1 0 0) single crystal disk substrate (Futamoto et al. 1994).

In this case the magnetic layer was sputtered on a 50 nm thick Cr layer which was deposited on the MgO substrate. Using XRD analysis two kinds of Co–Cr–Pt with the (1 1 $\bar{2}$ 0) planes parallel to the MgO (1 0 0) having their *c*-axis perpendicular to each other.

By depositing a Co–Cr–Pt layer on a Cr–V underlayer it has been shown (Peng et al. 1995) that the bicrystal structure can be obtained also here (see fig. 5.12).

Fig. 5.12. TEM image of a bicrystal of $Co_{75}Pt_{12}Cr_{13}$ on an underlayer of C_rV_{20} (Peng et al. 1995).

TEM observations revealed a distinct orientation relationship with the [0 0 1] direction of the Cr underlayer matching the Co alloy [2 $\bar{1}$ $\bar{1}$] in the growth direction. The grains in the magnetic layer exist in a bicrystal cluster (see area in fig. 5.11) in which a group of CoPtCr grains grow on a single Cr grain such that the *c*-axis of the Co alloy grains line up perpendicularly (see arrows in fig. 5.12) to one another along the (1 1 0) or (1 $\bar{1}$ 0) directions of the Cr underlayer grains (Mirzamaani et al. 1991; Nolan et al. 1993b; Peng et al. 1995). Using Cr as underlayer directly on the substrate (NiP-plated Al-alloy), bicrystal structures of Co–Cr–Ta layers can also be prepared (Hosoe et al. 1995).

The main aim for preparing the bicrystalline structures is to obtain very high density recording materials with low noise levels (Klik and Chang 1995).

Bicrystal materials have been modeled to look further into the relationship between structural and recording parameters. In Peng et al. (1996) transitions have been calculated in a model based on an ensemble of clusters of four particles which interact by means of short-range exchange coupling. It was found that the bicrystalline properties lead to sharp transitions.

The effects of medium inhomogeneities in the microstructure and exchange configuration have been studied with a micromagnetic model (Peng et al. 1996). Introducing partial random non-bicrystal sites reduces the medium noise in the case of a with homogeneous intergranular exchange.

Using 2–3 grains in a single cluster, micromagnetic simulations have been performed in Co–Cr–Ta/Cr media (Hosoe et al. 1995). With this structure coercivity decreases as the grain size decreases even when the intergranular exchange coupling is strong and a high S of the hysteresis loop can be obtained. It was also found that coercivity for small grains can be increased by reducing the exchange coupling. This is a very important conclusion concerning very high densities and the noise.

Micromagnetic calculations have been performed using data obtained by VSM and torque measurements in Peng et al. (1995). The cross-talk correlation length was evaluated from the noise calculation and compared well with experimental data.

5.7. "Revolutionary" development of media

In this section the most important new type of thin film materials for application as a high density recording media are discussed.

5.7.1. Barium ferrite media

$BaFe_{12}O_{19}$ h.c.p. particles have already been used as longitudinal media on tape, floppy and hard disk for a long time. The large anisotropy (easy axis parallel to the h.c.p. c-axis) is one of the main features but moreover the magnetic decoupling of the particles plays an important role (Speliotis 1990). Ba ferrite thin films have already been prepared for the last 15 years. Preparations with the easy axis perpendicular as well as in the longitudinal direction has been reported. Relatively large H_c's and crystalline anisotropy have been mentioned. In the case of longitudinal recording experiments it was also announced that Ba ferrite thin films have shown mechanical hardness, chemical stability, good durability and corrosion resistance. One of the biggest problems was to control the grain size. It has been shown (Hylton et al. 1994) that an addition of Cr_2O_3 (0.1–1 vol%) to $BaFe_{12}O_{19}$ and an annealing process can result in a reduction of the crystal size by a factor of 5–10 compared with pure Ba ferrite. In Sui and Kryder (1994) similar effects have been published on CoTi doping followed by an annealing process. Moreover they also reported that with a multilayer structure consisting of pure Ba ferrite and CoTi doped Ba ferrite, media with a variety of coercivities (80–320 kA/m) can be prepared without degradation of the other magnetic properties.

The most important point in this kind of research is to find a way to reduce the annealing temperature. This is, in fact, the question of how the crystallization temperature of the Ba ferrite can be reduced and/or of how the grain growth can be restricted to achieve

the 8–10 nm decoupled grains needed for 10 Gbit/in^2. The thermal activation process and the magnetic switching were studied in c-axis aligned Ba-ferrite films (Chen et al. 1996) and evidence was found that the switching of the magnetization is linked to the incoherent rotation. The "deadlayer" caused by the interdiffusion of substrate atoms into the Ba ferrite layer deteriorates the magnetic properties. To overcome this Chen et al. (1998) have first deposit a low Ba-content layer on the substrate as an underlayer for the high-Ba content film. Higher H_c, S^* and narrow SFD are obtained in these layers. Besides sputtered Ba-ferrite thin films also laser ablation deposition films have been produced (Lisfi and Lodder 1998).

5.7.2. *Granular films*

Granular films consist of clusters of ferromagnetic materials in an non ferromagnetic matrix. This can be prepared by thin film technology and are know as "granular films". Examples of such thin films for potential hard disk application are for instance Fe, Co, FeCo, CoNiPt, CoCrPt mixed with oxides or nitrides such as SiO_2.

In Murayama et al. (1994) a $Co_{81}Ni_7Pt_{12}$ alloy target was used with pure SiO_2 chips placed on the target and from this thin films were sputtered on a hard disk substrate. The SiO_2 composition was controlled by changing the number of chips. A schematic drawing of changes in magnetic and structural properties as a function of the SiO_2 content is presented in fig. 5.13.

The in-plane H_c remarkably increases from 1400 Oe to 2400 Oe and S^* slightly decreases by increasing SiO_2 up to 4%. The increase of the grain separation is mainly responsible for this. Media noise is also reduced as a function of the grain separation (Chen and Yamashita 1988; Zhu and Bertram 1988). The grain separation which is determined by TEM and grows from about 1 nm (2% SiO_2) to very clear separations at 4% oxide.

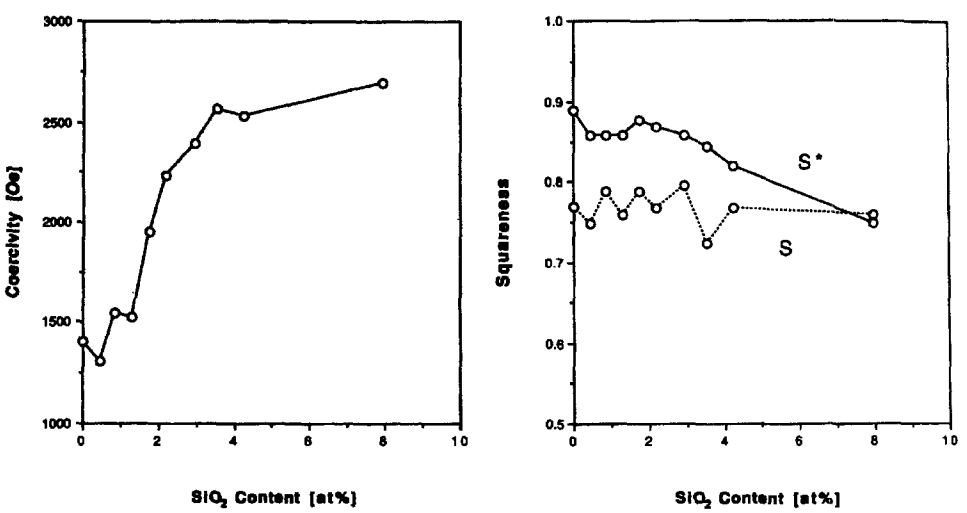

Fig. 5.13. In-plane coercivity (left) and the squarenesses S and S^* (right) as a function of the SiO_2 content in CoNiPt(SiO_2) sputtered films (Murayama et al. 1994).

TABLE 5.3
Recording characteristics in CoNiPt(SiO_2) films measured with a thin film head with PW_{50} as a measure for the signal, the integrated media noise (Integr. MN) and the signal to media noise ratio (STMR) (Murayama et al. 1994).

Alloy	H_c (kA/m)	Signal ampl. (mV)	PW_{50} (ns)	Integr. MN (mV^2)	STMNR (db)
CoNiPt	134	0.330	103.90	21.35	23.28
CoNiPt(SiO_2)$_2$	161	0.350	96.96	15.67	27.26
CoNiPt(SiO_2)$_4$	193	0.322	95.61	12.31	29.37

The phase segregation at the grain boundary was studied with HRTEM EDS techniques. In a boundary with a width of 1–3 nm in a CoNiPt(SiO_2)$_4$ film Si atoms have been clearly detected while they are absent in the grain it self and the oxygen content in the peaks are at the boundary much higher than those inside the grain. These results indicate that that SiO_x is located in the grain-boundary region. The CoNiPt shows an HCP structure from which the lattice expands as a function of the increasing SiO_2 content. The effect of this expansion originated from the interfacial stress at the grain boundary and can also make a possible contribution to the increased H_c. The crystal size decreases as a function of the oxide content. Pure CoNiPt films do not show very clear grains with sizes of 20–50 nm while very clear outline and shape of the grains are observed in films having an SiO_2 content. In the case of 4% SiO_2 the grain size is 5–20 nm.

Finally the recording characteristics are given in table 5.3 for three different films pure CoNiPt and films added with 2% and 4% SiO_2.

The signal (PW_{50}) slightly decrease when SiO_2 is added but the integrated media noise decreases and consequently the signal-to-media-noise ratio (STMNR) increases. A large value means lower noise because in this series of media the intensity of read-back signal (which is proportional to δM_r) is almost constant. Consequently, the addition of SiO_2 is very effective for the reduction of media noise.

Co–Cr, Co–Pt and Co–Ru granular films in a SiO_2 matrix have been made by DC sputtering. In the case of Co–Pt granular films the H_c was about 128 kA/m.

In Kaitsu et al. (1996) it is suggested, from the results of the resistance measurements, that the H_c increases by grain separations. The crystal size has to be reduced in order to improve the magnetic properties

5.8. Overcoats and lubrication layer

Thin film disk media have a smoother surface compared to the disks prepared with particulate media but they are relatively soft. In order to obtain higher densities the head must be very close to the medium surface. From the point of view of tribology there is a principle difference between contact and non-contact recording (air film between head and medium). Due to the high speed between the head and the medium in a hard disk system a high pressure is locally present. The head flies above the disk and the air operates as a lubricant film. To obtain the maximum storage density the head must be in contact with the medium (contact recording).

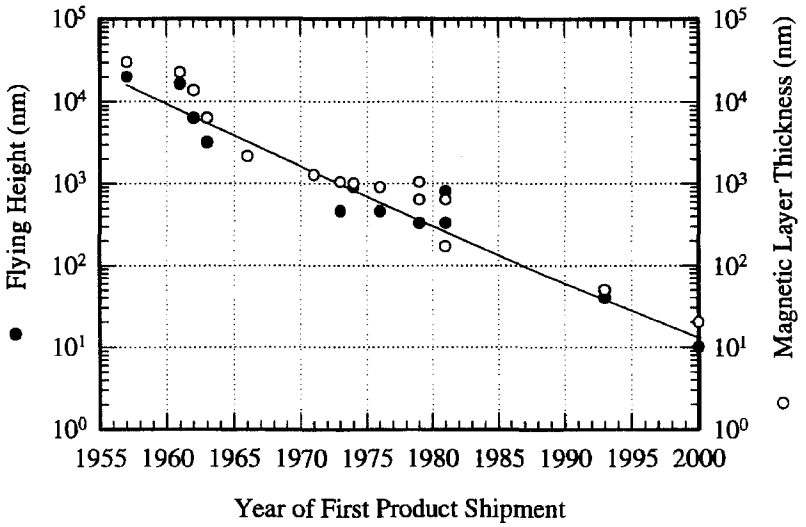

Fig. 5.14. The flying height (black dots) and magnetic layer thickness (open circles) as a function of the year of product shipment. For the year 2000 predictions from the literature are used (Visser 1997).

In fig. 5.14 the flying height between head and the medium as well as the magnetic layer thickness are given as a function of the year of product shipment (Li and Menon 1996). It can than be seen that based on the predictions of year 2000 they are both approaching 10 nm.

Experimental contact recording systems have been used and it is expected that it will also be used in commercial systems within 5 years. In the case of thin film media it is possible to fly already very close to the disk surface, but it results in higher friction and, consequently, more head-to-disk interactions. Therefore thin film hard disks require an overcoat for providing wear resistance and low friction. The type of overcoat used are plasma polymerized films, sputtered carbon, SiO_2 or ZrO_2–Y_2O_3 thin films. The wear resistance of thin film disks in a continuous sliding test is one or two orders in magnitude lower than that of particulate disks (Bhushan 1990).

An increase in effective hardness and Young's modulus of the disk structure improves its wear resistance.

Rigid disk drives run almost continuously for several years, with temperatures at about 60°C. Consequently, the lubricant used can then be evaporated. The volatility of perfluoropolyether lubricant (which is very frequently used: such as Fomblin Z-15, Z-25 or Z-dol) has been analyzed by (Dillman et al. 1988). The measured and predicted weight losses are given in the fig. 5.15.

Experimental data are obtained with thermogravimetric analysis (TGA) and the predicted curves have been calculated with a so-called volatilization model based on mass transfer and thermodynamics (Dillman et al. 1988). It can be estimated from this work that at a temperature of 60°C and a realistic volume-to-surface area that the loss of the lubricant is only about 7% during 10 years, which is in fact the lifetime of a disk.

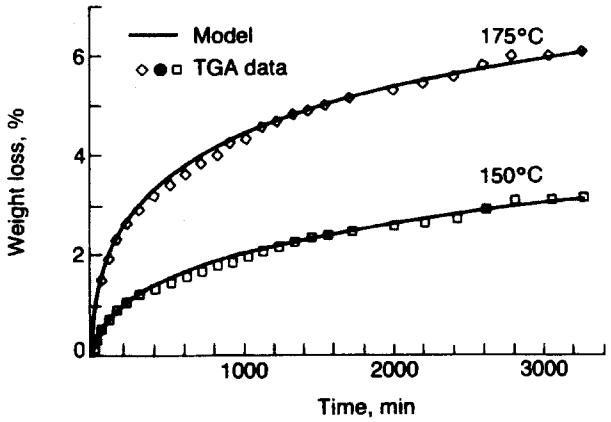

Fig. 5.15. Measured and predicted weight loss data of perfluoropolyether as a function of time at various temperatures (Dillman et al. 1988).

5.8.1. DLC coatings

Flatter and smoother thin film disks which permit lower flying heights and even contact recording are necessary. Therefore a protective layer is needed on the magnetic coating to avoid corrosion as well as wear due to the contact-start-stop sliding of the slider against the disk. The protective coating must be as thin as possible. In current products the thickness is about 15–20 nm. On top of the protective coating a very thin lubricant layer is added (thickness about 2 nm).

Carbon-based overcoats are preferable in the disk industry because of their hardness. The diamond phase of carbon (f.c.c. lattice) has a very high density of atom arrangement resulting in the highest hardness known at present. The DLC films ("diamond-like carbon") are amorphous (a-C). The density, elastic stiffness and hardness of the layer are of course also very important for the tribological performance.

The a-C layer can be deposited by plasma CVD and has been known to be useful as a protective layer against mechanical wear for a long time (Holland and Ojha 1976; Nayiesh and Holland 1984). DLC coating properties, application and deposition methods have been reviewed in (Agnus 1991).

An important development for the hard disk applications is the sputtering of carbon during the introduction of hydrocarbon dopants (CH_4, C_2H_2 and C_4H_{10}). Recently, carbon nitride coatings have also been prepared by reactive sputtering and the durability was tested of layers consisting of various amount of incorporated nitrogen (Zou et al. 1995). The overcoats having the highest level of nitrogen showed the most resistance against wear.

The DLC coatings can be also deposited also with a hydrogen dopant (a-C:H) which means that layers with a very wide range of properties (hardness) can be prepared based on the hydrogen content. Depending on the hydrogen the carbon atoms are bonded with four neighboring atoms (sp^3 hybridization) or a threefold co-ordination (sp^2 hybridization). The general idea is that the hydrogen increases the presence of sp^3 bonds.

As the hydrogen content of the carbon films increased from 16% to 53%, the carbon bonding character changed from sp^2 to sp^3 (Lee et al. 1993). Structural and tribology per-

formance of sputtered a-C and a-C:H overcoats have been investigated systematically by (Agarwal et al. 1993). It is also reported that a-C films having a wide range of properties can be easily sputtered depending on the sputter conditions such as energy and argon pressure (White et al. 1990).

It was shown (Kokaku et al. 1993) that DLC films can be prepared with the RF plasma deposition in-line system together with the magnetic coating (CoCrTa) and an underlayer of Cr on a NiP plated Al substrate. The thickness of the DLC layer was 30 nm. Improvement of the wear durability has been shown.

The performance of the DLC film was strongly dependent on the hardness. Besides the disk coating sliders have also been coated with DLC films. Commercial 90 mm thin film disk have been tested with Al_2O_3–TiC sliders coated with 20–30 nm of DLC coatings covered by 2 nm of lubricant (Bogy et al. 1994). Also two sliders have been coated with 7 and 12 nm thick DLC films. Drag and CSS tests were conducted and in both cases the friction build-up occurred much more rapidly for the uncoated sliders than for the coated sliders. This was also true for the very thin (7 nm) coating.

Comparison of the tribological performance of pure carbon and the carbon–nitrogen coated head sliders is given in (Wang et al. 1996) and it was found that the during CDT test the head may fail before the disk does.

Hydrogenation of the surface of the disk is also very important for the durability. It has been shown that overcoats of a-CH have much better properties than those of a-C (Marchon et al. 1990).

Carbon coatings and SiC coatings have been prepared by various deposition methods and tested by nanoindentation and microscratch studies (Cupta and Bushnan 1995). From this study It can be concluded from this study that cathodic arc carbon coatings exhibit the highest hardness, elastic modulus, scratch resistance and wear resistance.

5.8.2. Lubrication layer

In order to reduce the wear and friction in hard disk recording a thin layer of a liquid lubricant on top of the carbon overcoat is used. Such perfluoropolyether (PFPE) layers have a thickness of 1–2 nm and are very stable lubricants (Bhushan 1990).

Many different polymer structures (in which the hydrogen atoms are replaced by fluorine atoms) are used for such lubrication coatings. In general they should have the properties of a lubricant,viz. low vapor pressure and high thermal stability. The disks are covered with several monolayers of the lubricant and to increase the bonding a baking procedure can be applied. The thickness of the lubricant is very critical and depends on the surface roughness. In general, if the thickness is above the optimum this can increase the stiction and below it the wear will increase. Bonding of the lubricant to the disk surface can also be realized by electrostatic interaction between the functional end group of the lubricant and the surface of the carbon coating (Sano et al. 1994).

An alternative coating mechanism of liquid perfluoropolyether lubricants has been shown by (Coffey et al. 1994). It is a solvent-free process whereby hysteretic surface adsorption is used to provide a very thin uniform coating of about 1 nm thick. The contact stop/start performance of the disks is equivalent to those coated by dipping. An alternative for hard disk lubricant is phosphazene because it has a very low vapor pressure (Nader et al. 1992; Yang et al. 1994). Recently an overview about lubrication issues in magnetic storage devices has been given by (Homola 1996) and a state of the art review about tribology by (Bhushan 1996).

6. Trends, expectations and future

Looking back over the past 30 years the recording density has increased by a factor of 4000 (1966: IBM-2314 having 0.22 Mb/in^2 and in 1995: IBM Travelstar 2LP having 923 Mb/in^2) as can be seen in table 6.1.

Based on this trend extremely high density will be available in the 21st century as predicted in (Nakamura 1991) for the perpendicular recording mode. This work was based on computer simulation studies reported in (Tagawa and Nakamura 1989). Since the Intermag Conference of 1992, the 10 Gbit/in^2 longitudinal recording, having bit areas less than 0.1 μm^2, has been discussed (Murdock et al. 1992). From the design point of view many improvements can be made to achieve a system for very high density recording (several gigabit per square inch). Developments over the years have shown a drastic scale-down of the track pitch, bit-cell length, head gap, medium thickness and head-medium spacing.

Nowadays complete integration of technologies, based on electrical and electronic engineering, mechanical engineering, physics, magnetic thin film and microsystem technologies such as etching, masking is available. This development will show the unlimited possibilities for the magnetic recording technologies during the coming years.

6.1. Bit cell length and track pitch

Progress in track pitch and bit length for commercially available (solid lines) hard disk systems over the last years is shown in fig. 6.1 (Yogi et al. 1990).

The dotted lines including the shaded areas show the respective contributions from track pitch and bit cell length to realize a 1 Gbit/in^2 system. They have been demonstrated since 1990 (Tsang et al. 1990; Yogi et al. 1990; Futamoto et al. 1991; Murdock et al. 1992).

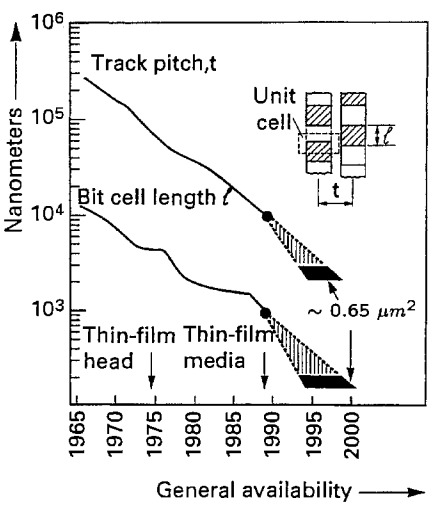

Fig. 6.1. Progress in track pitch and bit cell length implemented in disk files and the expected changes in dimensions to obtain commercial 1 Gbit/in^2 (0.65 μm^2) recording (Yogi et al. 1990).

TABLE 6.1
Thirty-eight years of progress in disk drive technology (Asher 1997).

Year	Model	Bit density Kb/in	Track density T/in	Areal density Mb/in^2	Flying height nm	Gap nm	Media thickness nm	Head	Slider
1957	350	0.1	20	0.002	20000	25000	30000	Mu-metal	Aluminum
1962	1301	0.52	50	0.026	6250	12500	13575	Laminated mu-metal	Stainless steel
1966	2314	2.2	100	0.220	2125	2625	2125	Epoxy bonded ferrite	Alumina
1971	3330	4.04	192	0.776	1250	2500	1250	Glass bonded ferrite	Barium titanate
1973	3340	5.64	300	1.69	450	1500	1025	Integrated ferrite	Taper flat ferrite
1980	3380	15.2	800	7.68	320	600	550	8 turn thin film	Ceramic
1984	3380E	16.1	1386	22.3	254	600	500	18 turn thin film	Ferrite
1987	3380K	15.2	2088	32.8	216	550	432	31 turn thin film	Ceramic
1989	3390	27.5	2241	61.6	160	550	230	31 turn thin film	Ceramic
1992	0663-E12	59	2685	158	–	–	Thin film	Magneto-resistive	Ceramic
1995	travelstar 2LP	127.2	7257	923	–	–	Thin film	Magneto-resistive	Ceramic

As an illustration three key developments have led to increased density. In 1970 a ferrite head was used together with a particulate medium having a coercivity of 28 kA/m with a head/medium spacing of 430 nm followed 10 years later by a configuration of a plated medium ($H_c = 56$ kA/m), a thin film head and a spacing of 200 nm. In 1990 a magnetoresistive read head combined with an inductive write head were introduced together with a sputtered medium having a $H_c = 120$ kA/m and a head/medium distance of 100 nm. As can be seen not only media are being developed with thin-film technologies but also film heads. The small spacing for high densities has introduced an additional field of research on protective layers and tribology. As has been shown sputtered thin-film media are already commercially available for data recording. It can safely be stated that the next generation of magnetic recording products will all be dependent on the advances in the volume packing density of recorded information. Consequently, there is not only a future for thin-film media but also for thin-film magnetic recording heads (smaller gap width and track width) based on inductive reading and writing as well as magnetoresistive sensors for the read process.

Developments in multilayer deposition technologies have been the basis for the so-called Giant Magneto Resistance (GMR) layers for integration in the read head.

It has been demonstrated by (Tsang et al. 1990; Yogi et al. 1990; Murdock et al. 1992) that for a longitudinal hard disk system, with 1.18 Gbit/in^2, the bit area ba = 0.76 μm^2. Here, the bit cell length (bl) is 0.19 μm and the track width (tw) 4 μm. In a publication one year later (Futamoto et al. 1991) reported an areal bit density of 2 Gbit/in^2 with (bl = 0.21 μm) × (tw = 1.5 μm). Mutoh et al. (1996) reported about 5 Gbit/in^2 with (bl = 0.11 μm) × (tw = 1.2 μm) using a spin valve head and a Co–Cr–Pt–Ta medium.

With respect to the recording system, modern developments and knowledge of electronics, mechanics, control engineering etc. have also led to an increase in the densities in actual commercial systems.

6.2. Head and media interface

Continuous improvements in head design, air bearing design and disk surfaces have narrowed head-to-disk spacing from over 10 μm thirty years ago to less than 100 nm today (in an IBM hard disk application for 1.5 Mbit/mm^2 it is 50 nm). The reduction in flying height requires further development in the areas of micro-tribology and hard coatings.

Integrated head flexure structures with small mass have also been proposed. These structures do not crash and have the potential for very low wear of both head and media when operating in continuous sliding contact with rigid media. The microcontact head not only contributes to the downsizing trend, but it is also promising for very high linear and high track densities.

Fujitsu achieved an areal density of 2 Gbit/in^2 (linear density of 4700 bits/mm and a track density of 670 tracks/mm) with an inductive head used as a monopole design that has a 33 turn coil, ferrite return yoke and a magnetic pole of amorphous CoZr which is deposited on a planarized surface. The headpole thickness is 0.4 μm and the track width 1 μm. The monopole is attached to the end of a metal cantilever sized 8 mm long, 0.4 mm wide and 40 μm thick, the contact force being 50 mg.

A Magneto-Resistive (MR) element can be used as an integrated element in the inductive write head. The inductive head part writes a wide track but the MR head only reads in the

middle of the track. Consequently, the head will not jump to or pick up information from another track. The sensitivity of the MR head is about four times as high as other types which is an advantage when reading the inner tracks of the smaller disks (lower velocity).

As higher recording densities lead automatically to a weaker magnetic flux above the medium, more sensitive head materials are required. A new issue at present is the study of the so-called Giant Magneto-Resistive effect (GMR). GMR materials are metallic multilayers prepared by deposition technologies consisting of alternating ferromagnetic and non-ferromagnetic layers. GMR-based heads (spin valve heads) are expected to increase the recording density in hard disks by a factor of 4 to 6 in the next five years.

In magnetic disk drives the spacing between the head and the disk is reduced as much as possible to increase recording density. Contact recording is the final goal which various technologies are trying to reach. For example, when using a microslider head; a small head slider has a low weight and inertia, and therefore the loading force can be reduced while maintaining stable flight. Consequently, a negative pressure-head slider "Guppy" has been developed, for ultra low flying at 50 nm above the disk with a new shape of air-bearing surface to provide sufficient suction force.

An integrated head flexure structure with an effective mass of about 300 mg has also been proposed. These structures do not crash and have the potential for very low wear of both head and media when operating in continuous sliding contact with rigid media. The microcontact head not only contributes to the downsizing trend, but is also promising for very high linear and high track densities.

6.2.1. Contact recording

A slider normally moves on a thin layer of air that circulates above the disk surface. In order to increase the density the flying height should become smaller and smaller because of the spacing loss factor $dB = 54.6\,d/\lambda$. Here λ is the written wavelength on the disk and d is the head–medium spacing. At present in hard disk systems λ is 0.5 μm which means that $d = 50$ nm is already critical to avoid significant signal loss. A spacing of 50 nm has been reported for 5 Gbit/in^2 recording (Mutoh et al. 1996). For ultra high densities λ must be less than 100 nm to keep the d below 10 nm.

It is forecast to be 25 nm in 1998 and 15 nm by 2000 (Simonds 1995). At these low distances a 1 μm particle can easily cause a head crash. If the disk rotates continuously during one year it travels more than 150 000 km at a speed of 10 m/s. During that time dust can very easily be accumulated on the slider and can cause serious head bumps and failure of the drive. It can be easily understood that contaminations are a major problem in the case of high densities, therefore disk drives should have a very high contamination control. Besides the particle control, also in the case of near contact recording, more attention should be paid to the electrostatic discharge between the head and the medium, shock and vibration (more stiff suspension), the capillary forces between the head and the lubricant, and localized heating (of the head and the medium) (Cooper 1996).

Head–disk spacings of less than 25 nm have been reported using a so-called continuously lubricated interface (French and Lemke 1990). A stiction-free slider has been developed coated with hydrogenated carbon and using a ultrasmooth disk surface (Katsamatsu et al. 1995) and with this configuration flying heights of 20 nm have been obtained. A contact recording head for perpendicular recording has been designed and tested (Hamilton 1991,

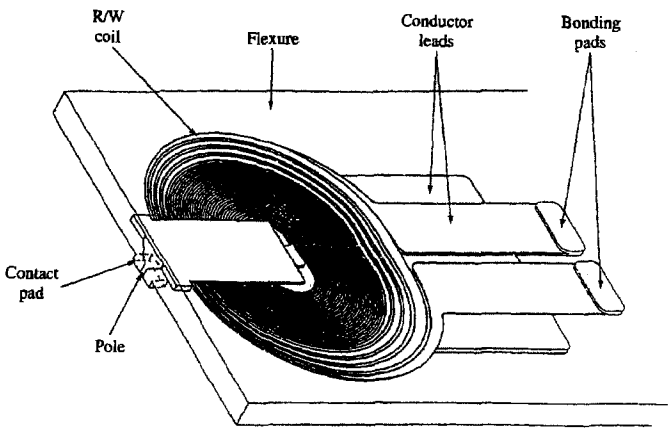

Fig. 6.2. Flexhead for perpendicular "contact" recording (Hamilton 1991).

1994). The so-called "flex head" integrates head, suspension, and flexure in one structure and has a very low mass.

This results in wear of the head of less than 12.5 nm per week if used in the contact mode in a hard disk application. The construction used for the pole head can tolerate a maximum of 5 μm erosion which means that the head has a lifetime of 7 years (Hamilton 1991).

6.3. Downsizing hard disk drives

Most of the improvements in magnetic recording involve the reduction in mechanical dimensions such as flying height, gap length, track spacing and medium thickness. The history of magnetic-disk drives has also seen several other important technological innovations. Head and medium technology, signal processing and precision mechatronics such as spindle motor and head positioner have been improved. Head-to-medium interfacing has always been hard to control. Reduction in the flying height compromises between read and write performance and reliability. Through downsizing, the integration of interface electronics and packaging technology became inevitable. The uppermost track density is limited by the misalignment between the servo head and the data head. Smaller drives benefit not only from reduced power consumption but also from storage capacity normalized by drive size (form factor). The developments in downsizing (Miura 1991) can be seen in table 6.2.

High density recording accelerates disk drive downsizing both in computer systems and in integrated high performance subsystems such as disk arrays. The access time for magnetic disk drives is, nevertheless, very long compared to that of solid-state memories. Combining cache memory with disk drive could greatly improve disk-access performance. Instead of replacing a magnetic disk, solid state memory will combine with disk drives to improve performance. If the small disk drives were used in arrays much higher data rates and shorter access times could be achieved. Moreover, the hard disk drive, originally a computer peripheral, becomes more a component.

TABLE 6.2
Downsizing hard disk drives (Miura 1991).

Disk size [inch]	10.5	8.25	5.25	3.5	2.5
Drive volume [l]	30	12	2.5	0.6	0.12
Weight [kg]	36	17	5	1	0.2
Power consumption [W]	180	100	40	10	2

Looking ahead, downsizing of the disk diameter will lead to new forms of drive, such as removable disk cartridges and chip modules that are mounted directly onto a printed circuit board. The magnetic disk drive will be widely used as an on-line file in information network systems. The dimensions of magnetic disk drives are decreasing rapidly. The common 5.25 inch disk drive is being superseded by 3.5, 2.5, 1.8 and even 1.3 inch drives. The long-term trend is towards smaller drives which will gradually take over the market. Production of 2.5 inch drives is increasing rapidly due to their use in notebook computers. The technology for even smaller disk drives is being pushed by the development of sub-notebook computers and personal digital assistants. Heads and medium, prepared by thin film technologies, are the components most responsible for higher density and decreasing sizes.

It is expected (Grochowski and Hoyt 1996) that 3.5 inch form factor drives, originally developed for PC applications, will have a sufficient gigabit capacity to be used in large system storage such as RAID. In this system over 60 drives per box are used and consequently the storage capacity is in the hundreds of gigabyte. The smaller form factor of 2.5 inch will have a capacity larger than 10 GB by the year 2000.

Smaller disk diameter allows lower linear velocities and, as a result, a weaker signal for the inductive heads (sensing the change in the magnetic field with respect to time). Also, with a smaller track size, the signal will be weaker. Consequently, the signal level decreases as the density increases. The magnetoresistive head offers a way around both problems since they are not velocity-dependent and, in any case, provide larger signals.

Increasing the track density also needs extreme requirements also on the precision of the actuator servo system. The servo bandwidth must increase from 1.5 to 2.5 kHz when the track density increases from 20 to 25 ktpi. At present research is carried out on the design and fabrication of mm sized micro fabricated actuators by Si technology (Fan 1996).

Fully integrated mm sized wobble micromotor and wobble actuators with potential applications for chip sized data storage, such as tip-based high density recording, are also made possible by this process (Fan and Woodman 1995).

6.4. Heads and nanosliders

Thin film heads hold the future for many reasons. For instance, the ferrite head technology has supposedly reached its limits with respect to machining processes and high frequency magnetic characteristics; although the more recently developed metal-iron-garnet head offers performances similar to thin film heads.

Producing an inductive thin film head is a complex process since masking techniques (photolithography), selective etching processes (ion milling) and deposition technologies (electrodeposition, sputtering) are needed to make a wafer consisting of hundreds of such

elements. Such a head consists of various different layers (roughly 10–20) prepared on a ceramic substrate. After slicing the wafers the heads are mounted on aerodynamic sliders and subsequently finished to fly over the surface of a rotating disk. Then a precision polishing step is performed to realize the correct air bearing surfaces and the desired electromagnetic characteristics. After assembly of the finished slider suspensions and wires the complete heads are tested for their writing and reading functions.

Because of the vertical head dimension limit the number of platters that can be added to a disk drive, the size of heads has also been decreasing. Here, the throat height is the distance from the head tip to the coil region, which has to be as small as possible because it is an area of constant reluctance. This can be controlled by very accurate polishing.

A very important development is the magnetoresistive read head. The MR head is based on the principle that the electric resistivity of a magnetic material changes slightly when it is placed in a magnetic field. At a steady current through the MR strip the change in resistance produces a change of voltage. For reading increased densities, the MR element can be used as an integrated element in the inductive write head. The inductive head part writes a wide track and the MR head reads only in the middle of the track. Consequently, the head will not jump to or pick up information from another track. The sensitivity of the MR head is multiplied about four times which is an advantage when reading the inner tracks of the smaller disks (lower velocity). Not all problems around the MR head have been solved. Besides magnetic and material problems careful design also has to be completed.

As higher recording densities lead automatically to a weaker magnetic flux above the medium, more sensitive head materials are required. A new issue at present is the study of the so-called Giant Magneto-Resistive effect (GMR). GMR materials are metallic multilayers prepared by deposition technologies consisting of alternating ferromagnetic and non-ferromagnetic layers, e.g., Co–Cu. It is expected that GMR-based heads can increase the recording density in hard disks by a factor of 4 to 6 within the next five years.

A 3 Gbit/in^2 has been demonstrated (Tsang et al. 1996) by using a narrow track inductive-write MR-read dual element head on a low noise Co-alloy thin film disk.

A new MR head design using the Current Perpendicular to the Plane (CPP-mode) has been proposed (Rottmayer and Zhu 1995). In this case the GMR multilayer is placed in between two softmagnetic shields with conductors connected to the two sides of the GMR film surfaces and also function as writing poles. It was concluded from micromagnetic analysis that with this type of head recording, densities as high as 25 Gbits/in^2 can be obtained.

The slider head technology allows the required disk-to-disk spacing to fit within the 10 mm height ceiling and provides an exceptional reliability of head and disk. HP has developed a proprietary technology that acts much like an airbag sensor of a motor car. It detects impending impact and causes the drive to revert to a protective mode instantly to ensure no loss of data. This technology increases the impact force the HP Kittyhawk can exert while in operations to a 3-millisecond shock of $100g$. A force large enough to break a liquid crystal display screen.

6.5. Perpendicular magnetic recording media

Based on the trend of increasing densities an area density of more than 300 Gbit/in^2 will be available in the 21st century as predicted in (Nakamura 1991). This statement was based

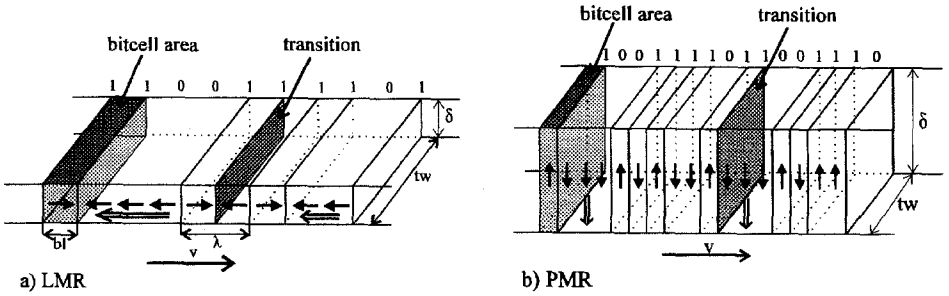

Fig. 6.3. An isolated recorded track with written bits for LMR (a) and PMR (b), PMR in a medium having a thickness δ and a track width tw, recorded wavelength λ, linear bit length bl, recorded transition and bitcell area (Lodder 1996).

on computer simulation (Tagawa and Nakamura 1989) using the perpendicular recording mode (PMR) instead of the current LMR.

In fig. 6.3 one track with written bits is given for the PMR mode of magnetic recording. As for the LMR, the area density is given by the product of the linear bit density and the track density. Higher density means creating narrower tracks and more compact bits. Transition shape and length are extremely important for the recording performance. In the case of LMR the magnetization vector forms a head-on state of transition which results, for thin film media, in a saw-tooth shaped transition. Medium noise, mainly originating from the transition becomes larger at higher densities (Belk et al. 1985). In the case of PMR the anti-parallel magnetization in the adjacent bits are responsible for a significant reduction of the demagnetizing field especially at higher densities. The medium noise mechanism is very low in the case of high densities (Belk et al. 1985). After searching the published results in the literature one can find that the ratio bitlength/medium thickness (bl/δ) for Co–Cr–(X) thin film media in LMR is about 10–20 and for PMR about 1/3–1/5. It can be concluded from this data that media having a perpendicular anisotropy can be made with larger layer thickness which are favorable for higher densities (higher signal, easier preparation conditions and smaller crystal size in relation to the critical volume for superparamagnetic behaviour). In the case of LMR densities around 10 Gbit/in^2 one of the problems will be the thermal stability of the recorded bits (Lu and Charap 1990). In the case of PMR the ratio kT/KV is much larger ($\sim$ 800) than for LMR media. This means that PMR is very stable in thermal fluctuation (Yoshida et al. 1996). The SNR of PMR with weak exchange interaction are much higher than those of LMR, despite the larger grain size of the PMR media. Also in the case of PMR the H_c is not a very important parameter for high densities because there is no strong relation between this parameter and the linear density as there is in the case of LMR. The amount of PMR research and the published results (PMRC 1989, 1991, 1994, 1997; Intermag 1996) shows that it is still a serious candidate for super high density recording. In Futamoto et al. (1996), read/write experiments are given from the combination single-layered perpendicular media (Co–Cr–Pt; Co–Cr–Pt–Ta) and ring-type heads. In the case of contact recording using a narrow gap head with gap length smaller than 0.2 μm and a linear recording resolution (D_{50}) of 300 kFCI is confirmed. This correspond with a linear bit length of 63 nm. Track density can be 25 kTPI. It is concluded

from Futamoto et al. (1996) that taking into account medium noise and overwrite characteristics, signal processing, and bit stability, this single layered/ring head system indicates a possibility of 10 Gbit/in^2. This density is also claimed by (Iwasaki et al. 1996) using a MIG ring head in combination with a double layered medium (hard Co–Cr layer with a soft magnetic back layer).

High output and high linear density recording of over 300 kFRPI was obtained by using Co–Cr–(Nb, Ta, Pt) media in combination with a Single Pole Tip (SPT) head with pole thickness of 0.2 μm (Honda et al. 1996). Also it is demonstrated that a high linear density of 1040 kFRPI (bit length 24 nm) can be obtained and an areal density of 29.6 Gbit/in^2 has been verified. Before this can be used commercially better write and read performances of the head must be realized as well as further reduction of the medium noise. The role of perpendicular recording in the future of hard disk storage has been discussed by Thompson (1997). He concludes that there is a little reason for optimism about the commercial availability of PMR considering the today's densities of LMR.

6.6. Data storage and nanotechnology

State of the art in hard disk recording is a bit density of 5 Gbit/in^2. The general opinion is that 10 Gbit/in^2 will be available around 2000. In order to exceed this number for longitudinal recording many technical problems must be solved. With the potential of the nanotechnology new challenges for ultrahigh density recording are possible either by using magnetic detection or not. From that point of view we only want to discuss a few different possibilities namely:

(a) Memories with atomically resolving techniques,
(b) Magnetic memories with nanometer size bits,
(c) Preparation of an ordered face centred tetragonal structure.

The first option is a non magnetic memory and in this case the ultimate density of course will be obtained if we can use one single atom per bit. The bit-area would be in the order of 0.1 × 0.1 nm^2, thus bit-densities of 6×10^{16} bits/in^2, 250 000 times as high as the limit for magnetic recording (50 × 50 nm^2). The bottle-neck for such a memory, based on Scanning Probe Microscopic techniques (SPM), is of course the data-transfer rates. At present a scanning speed of about 1000 samples/s is possible. If every sample is a bit, than we get a transfer rate of 1 kBit/s. In hard disk memories 10 MByte/s is used, but new computer systems will require 100 MByte/s and more. This is a principle obstacle for SPM recording which might be solved by using parallel read-out techniques. Assuming that a transfer rate of one channel can be made for 10 Mbit/s, then 800 channels would be needed in parallel to achieve 100 MByte/s. This does not seem impossible. If we can construct one active cantilever with a Scanning Tunneling Microscope (STM) tip each μm, the read/write head would be about 1 mm wide. Of course a tremendous effort has to be made to achieve this.

Much attention has to be paid to access times. Assuming a bit cell size of 1 nm, a 1 Mbit/s data rate per channel will result in a linear velocity of only 1 mm/s. A disk diameter of 1 cm would only make one revolution every 30 s. This will result in an average access time as high as 15 s. One solution might be to use scanning probe microscopy piezo scanners for media displacement.

Perhaps it is not necessary to aim for memories which are 250 000 times better than the magnetic memories we can expect 10 years from now. If the current rate of a doubling of the density per year is continued, this density will only be needed in about 30 years.

During the coming 10 years, however, the recording industry will be looking for new techniques capable of bit areas in the order 10×10 nm^2 (6 Tbit/in^2). There is an option for this type of magnetic memory, but this would require patterned media with isolated dots of magnetic material (magnetic memories with nanometer size bits). They could also be realized in a kind of magneto-optical system using a nano-magneto-optical disks, using Scanning Near-field Optical Microscopy (SNOM) and a nano MO-disk. Of course also pure optical recording and AFM techniques can be used in the case. Also for these applications there will be the need for parallel write and read heads, with the same demands as above (Terris et al. 1997).

It has been showed (Wiesendanger 1993) to image the magnetic structure of magnetite (0 0 1) surface on an atomic scale by a ferromagnetic Fe tip. It was possible to get contrast between Fe(3+) and Fe(2+) on the atomic level and local modifications in the surface spin configuration have been observed which are localized on a scale of 1 nm. It is suggested that such localized changes are induced by the exchange interaction between tip and sample at very close tip–surface distances. Potentially this mechanism can be used for the very future magnetic data storage applications.

6.6.1. Creation of small CoPt spheres with high coercivity

The coercivity in certain alloys, such as CoPt, FeNd, FeAg, can be very high. Together with other favorable properties (high magnetization, chemical stability), this makes the CoPt alloy an interesting medium for ultrahigh ($>$ 10 Gbit/in^2) recording densities. In CoPt alloys a crystal phase transition that the alloys undergo upon annealing, increases the magnetocrystalline anisotropy and with that the coercivity. The crystal transforms from the disordered f.c.c. (face centred cubic) structure (see fig. 6.4) to the ordered f.c.t. (face centred tetragonal) structure ($L1_0$-phase). $L1_0$-phase In the latter all Co and Pt atoms are arranged in rows which means that the anisotropy shows a significant higher values. Coercivities as high as 85 kA/m have been reported for annealed thin films of $Co_{50}Pt_{50}$ (Tsoukatos et al. 1993). It seems to be very difficult to obtain a thin film in which all grains have the ordered phase.

When the CoPt films are made thinner the grain-size decreases and the coercivity increases. The theoretical value of the coercivity from the single domain particle theory is $H_c = H_k$ (see section 1.3.3). For $Co_{50}Pt_{50}$ ($K = 4 \times 10^6$ J/m^3 and $M_s = 800$ kA/m) this gives 600 kA/m. The reason for the difference between the theoretical value and the observed coercivity is thought to be due to interactions between the grains.

The film tends to orientate with the [1 1 1] fibre texture, as is the normal case for metallic f.c.c. films. After annealing the ordered $L1_0$ thin film has the same orientation with the axis of easy magnetization inclined by 36° above the thin film, providing primarily longitudinal magnetization. In order to prevent excessive grain growth can be reduced by co-sputtering CoPt with zirconia (ZrO_x) can be applied (about 20% on a 125 Å thick film). The grain size, after annealing at 700°C, is about 50 Å, but the coercivity was reduced from 1040 kA/m (13 kOe) to 200 kA/m (2.5 kOe). The zirconia and CoPt are expected to be immiscible and, as a consequence, different phases can be formed. The samples were grown on Si with

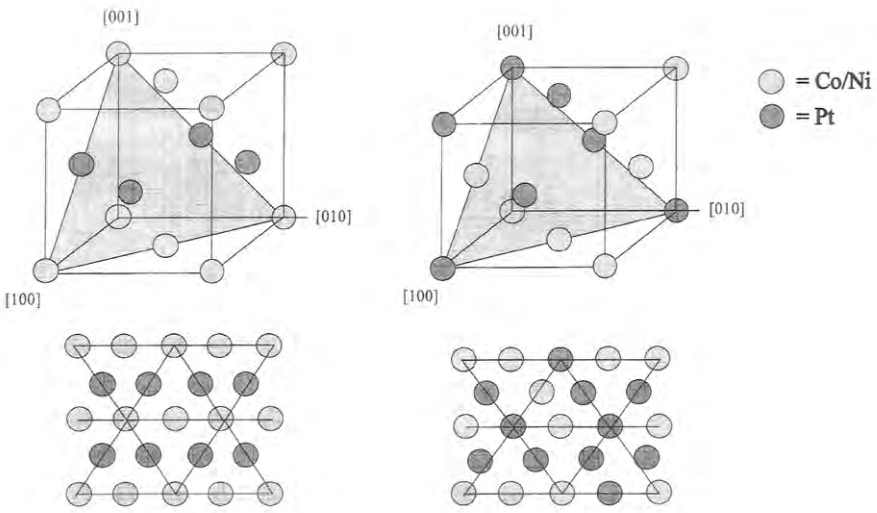

Fig. 6.4. Two possible structures of Co–Pt alloys, namely, the ordered f.c.t. structure (left) and the disordered f.c.c. structure (right).

an thermally grown oxide surface layer, by DC magnetron sputtering in 0.4 Pa argon/4% hydrogen. The films were annealed in a gas mixture of argon and 4% hydrogen (1 atm) for 10 minutes at a fixed temperature. Noise performance of disks of these materials ($L1_0$) is still inferior to conventional CoPtCr disk optimized for noise, but additional improvements to $L1_0$ media can be made (Coffey et al. 1995).

In other cases CoPt films on fused quartz substrates led to coercivities of 2400 kA/m (Liou et al. 1996). The films were made by dc magnetron sputtering and annealed afterwards in one atmosphere Ar/H_2 (optimal temperature 750°C, 10 nm film, 1760 kA/m). After annealing, particles of 50–300 nm are formed on the substrate, while the area near the particles is cleaned. In the large particles there are several crystallites. The growth of crystallites is partly responsible for the high H_c. Increasing the annealing temperature increases the size of the crystallites, which reduces the coercivity due to the formation of multidomains. The particles in this case are almost non-interactive, which explains the high coercivity. The separation of the particles is greater when the film is thinner. The intrinsic coercivity was largest after annealing a 10 nm thick film for 3 hours at 750°C. This H_c of 2400 kA/m is approaching the theoretical value of 3840 kA/m.

6.6.2. Artificial particulate magnetic recording media

As we have seen, the extremely high densities demand special requirements for the magnetic medium. The largest noise factor in high density magnetic recording is the medium noise. In order to reduce this noise it is desirable to choose a medium that consists of magnetically separated particles. These particles must have a high coercivity. It is possible to use several different particles for each bit, but the number of particles per bit has to be at least a hundred.

Another approach is to use one particle per bit. When all particles have the same magnetization and volume, this last solution gives the least noise in the readout signal. However,

this requires the particles to be equidistant. The particles will be so small that it is likely that they are single domain, which is another advantage from the point of view of the noise.

There are several approaches to the realization of a magnetic medium that supports high areal information densities. The objective is to make the particles in a parallel manner, that is it should be possible to produce a large area of particles at the same time by this method.

It has been shown previously that it is possible to create a medium by writing dots serially across a substrate. Possible methods make use of electron beams (Chou and Krauss 1996) or scanning probe microscope nanofabrication (Kent et al. 1994; Bessho et al. 1996a).

In New et al. (1994) the patterning of thin magnetic films has been described by multistep masking, e-beam lithography and ion milling processes. Small dots of magnetic material have been made, e.g., $0.1 \times 0.25\ \mu m^2$.

Using an SPM probe local transfer of magnetic material was realized onto a substrate by applying voltage pulses between the probe and the substrates (Bessho et al. 1996b). Using this method Fe, Co and CoCr dots of several tens of manometers were fabricated on insulator and metal substrates. The height of the dots was about 60 nm and the shape was assumed to be truncated cone. MFM observations enabled the authors to conclude that the magnetic structure of the Co dots is still multidomain.

There are three key factors for the production of patterned media consisting of arrays of single domain particles, namely: (a) particle size should be smaller than 100 nm to avoid multidomain behaviour; (b) uniform shape and dimensions over a large area; and (c) in principle it must be easy to scale the fabrication method for inexpensive high volume manufacturing. The interference lithography method seems to be one of the possible methods.

6.6.2.1. Laser interference lithography for patterned structures. It is possible to use the interference of two laser-beams to create a pattern on a substrate. Atoms can now be deposited through the laser pattern or a resist-step can be used to create the pattern on the substrate. The FWHM of these dots is 80 nm and they are approximately 13 nm high (Celotta et al. 1996). It is also possible to use metastable rare gases to expose a lithographic resist instead of directly writing the material (such as chromium, aluminum).

Several groups have made the arrays of magnetic dots by interference lithography (Fernandez et al. 1996; Haast et al. 1998). Haast et al. (1998) have used this method with a laser wavelength of 350 nm and a resist thickness of 60 nm. This allows a minimal spacing of 175 nm between the dots of 50 nm height. In practice the minimal distance between the dots of resist appears to be around 200 nm. An array of CoPt dots from which the width of the dots can be varied by varying the exposure time of the resist. The smallest dot diameter prepared by this method is 60 nm (Haast et al. 1998). An example of such a structure is shown in fig. 6.5. In the right upper corner the dotlike structure is shown by an AFM image. The large figure shows an MFM observation in the remanent state of the magnetic dots. Black and white contrast represents magnetization up and down.

6.6.2.2. Quantum magnetic disk. The so-called Quantum Magnetic Disk (QMD) also consists of single domain particles separated from each other by a nonmagnetic matrix. The idea of a QMD is not new. The principle idea was already discussed in 1968 (Barlow 1968). Later the so-called Alumite medium was introduced by (Kawai and Ueda 1975) and the

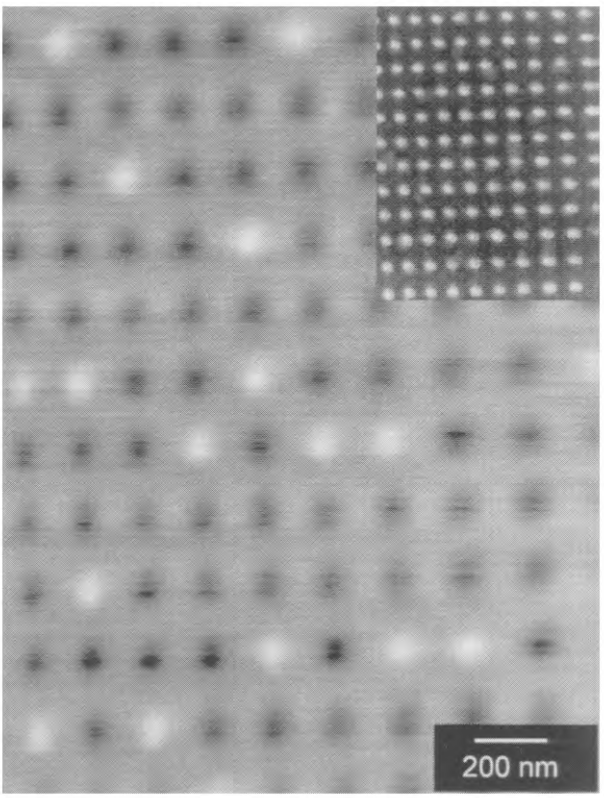

Fig. 6.5. Arrays of small ferromagnetic dots made by a laser interference pattern of Co alloy, photolithography and ionmilling. The dot size is about 70 nm and the spacing between the dots about 200 nm (Haast et al. 1998).

first recording experiments were carried out. At that time Alumite consisted of well defined needle like particles placed perpendicular to the film plane in a regular array, separated by the nonmagnetic Al_2O_3 matrix. The ferromagnetic material grows by electrodeposition in the pores of the matrix. In 1984 (Tsuya et al. 1986) a method was developed for widening the pore diameters to increase the packing density. The needle diameter was varied from 30–60 nm and the spacing from between 60–120 nm. The disks have shown a perpendicular anisotropy which in the case of Fe was based on shape anisotropy. In Huysmans et al. (1988) it has been shown from the radius dependence of the H_c, that the reversal mechanism in the case of the single domain Fe needles is the curling reversal mode.

The proposed QMD (Chou et al. 1994) having a density of 65 GBit/in^2 (Chou and Krauss 1996) is based on the same principles as the Alumite media but the preparation technology here is based on IC technology processes. Also a low cost method has been proposed and is called nanoimprinting and with this method mass production of sub-25 nm structures can be carried out (Chou 1995). Simple writing and reading experiments were obtained up to 7.5 Gbits/in^2 in longitudinal QMDs using MFM tips (Kong et al. 1997).

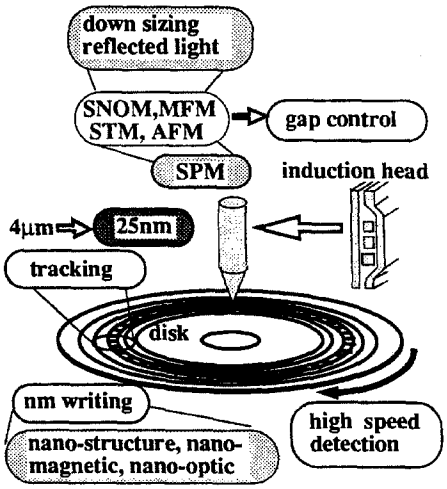

Fig. 6.6. Some techniques used for the development of an advanced data storage system (Hosaka 1996).

6.6.3. SPM based storage

When replacing the inductive head with a Scanning Probe Microscope (SPM) head in principle superhigh densities can be stored. The SPM methods are not only proposed for magnetic data storage but are more in general applied atomic manipulation and nano surface modification for writing and atomic or nanometer sized probe detection and for the reading process. In literature many proposals can be found about such storage systems based on Atomic Force Microscopy (AFM) (Hosaka et al. 1993), Scanning Tunneling Microscopy (STM) (e.g., Mamin et al. 1990), Magnetic Force Microscopy (MFM) (e.g., Ohkubo et al. 1991), Scanning Near-field Optical Microscopy (SNOM) (e.g., Betzig et al. 1992). An overview about SPM based storage systems is given in Hosaka (1996). A schematic for the development of an advanced high density data storage system is given in fig. 6.6.

In this figure a possible approached is given for writing and reading information with bit size smaller than 100 nm, a readout speed of 0.1 Mbyte/s using a medium surface roughness smaller than 1 nm and a grain size in the order of 10 nm. In fig. 6.7 the positions of the various SPM methods are given in an areal density and readout speed map.

AFM (1 Tb/in^2) and SNOM (170 Gb/in^2) based storage systems have the potential to reach ultra high densities and can achieve a high speed readout of more than 1 Mhz. However many problems have to be solved before SPM systems can become a commercial product.

6.7. Final remarks and trends

Magnetic hard disk recording technologies are good examples of microsystem technologies, the dimensions of the various essential parts being within the definition. There is a complete integration of technologies based on electrical and electronic engineering, mechanical engineering, physics, thin film technologies and microsystem technologies such

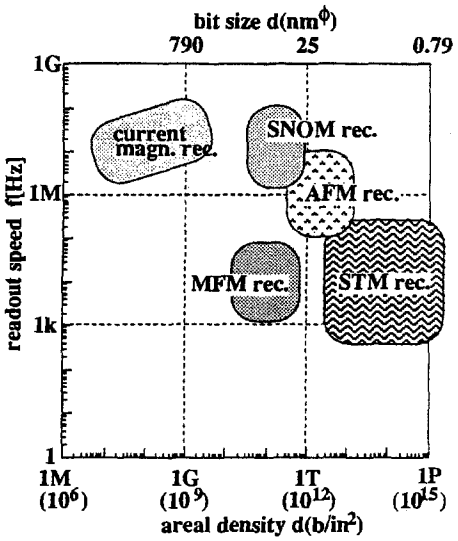

Fig. 6.7. Positions of SPM based storage in an areal density readout speed map (Hosaka 1996).

as etching, masking and magnetism. The evolution to higher densities is not only valid for hard disk applications but also other consumer applications based on magnetic and other recording technologies.

The future directions for hard disk high density recording is illustrated in fig. 6.8 (Grochowski (1997)). In this figure the most important current recording technologies are given in relation with the year of introduction and the effect on the density for IBM hard disk drives in Gbit/in^2 (left) and Gbit/cm^2 (right). Moreover the corresponding bit area (in nm^2) is given also. The principle limit for magnetic recording media is the transition from a ferromagnetic material (particle) into superparamagnetic behaviour. The dotted line given in the figure at about 100 nm^2 is the superparamagnetic limit for the LMR mode. Because the medium thickness is less critical in the case of the PMR mode the limit for superparamagnetism will be above this line which means in principle at a higher density. At the top of the figure a dotted line is given for the atom surface area limit and in the dotted line in the middle is the reference for application of AFM like storage. It is expected these two type of storage technologies will start in 2005 (AFM like storage) and around 2010 (Atom level storage).

Continuous improvements in head design, airbearing design and disk surfaces have narrowed head-to-disk spacing from over 10 μm thirty years ago to less than 100 nm today (in an IBM hard disk application for 1 Gbit/in^2 it is 50 nm). It is predicted that for the year 2000 the spacing between head will be smaller than 20 nm. For future technologies with bitlength of 50 nm this distance should be smaller and around 10 nm.

For very high densities new medium materials (such as multilayers) can give another factor of 3, so that in the coming twenty to thirty years 65 Gbit/in^2 can be obtained. However, this will require technological breakthroughs in the fields of micromechanics, micromotors and microactuators. Furthermore, from other recording modes such as perpendicular

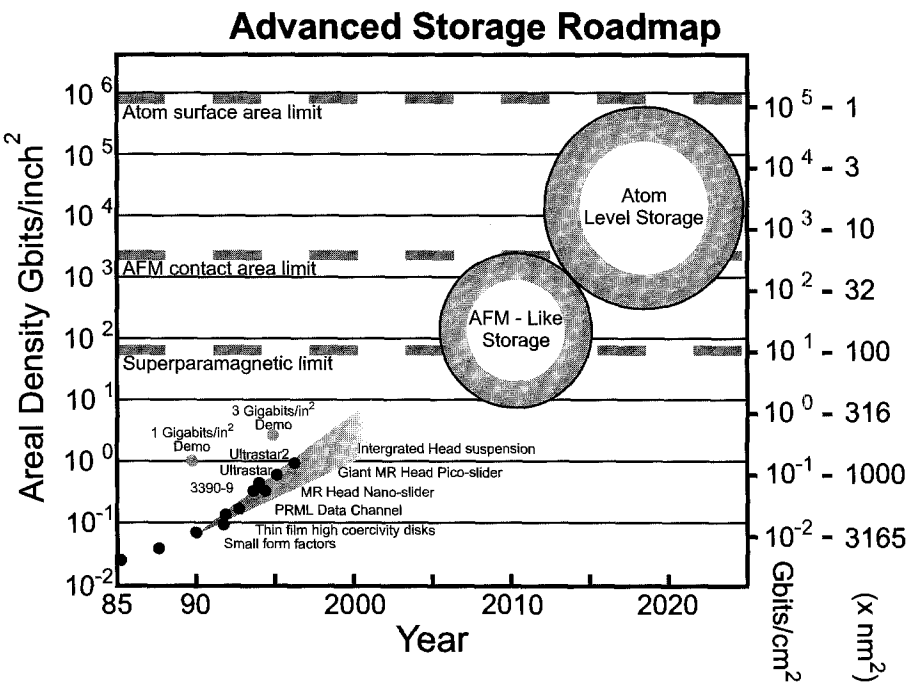

Fig. 6.8. The storage density road map (based on Grochowski (1997)).

recording and (magneto-)optic recording we can expect an increase in density. Laboratory demonstrations have already shown a density of 5 Gbits/in^2 in the case of submicron trackwidth perpendicular recording.

Head design is at present concentrated on constant flying height and the reduction of flight height aiming at a result in contact recording. This requires more development in the areas of microtribology and hard coatings.

In the case of microsystems, many changes are needed concerning the construction and manufacture of the slider. Firstly, the size of the slider (1 × 1 mm^2) has to be reduced. Furthermore, a reduction of the flexure and automatic bonding is needed. Finally, for faster positioning a lower mass is essential. The future probe head will have a needle shape.

Acknowledgements

I wish to thank MESA Research Institute and the University of Twente for their financial and technical support. Special thanks are due to Leon Abelman for critical reading the manuscript and his useful remarks. Many thanks to all postdocs, PhD and MSc students involved in the various projects of the Information Storage Technology Group. The results obtained from their work have been used as the basis for this paper. Last but not least I would like to acknowledge the helpful advise of Professor Buschow before finalizing the manuscript.

References

Abraham, F.F. and C.R. Bundle, 1981, J. Vac. Sci. Technol. **18**(2), 506.

Aboaf, J.A. and E. Klokholm, 1981, IEEE Trans. Magn. **17**(6), 3160.

Agarwal, S., 1986, IEEE Trans. Magn. **21**, 1527.

Agarwal, S., E. Li and N. Heilman, 1993, IEEE Trans. Magn. **29**(1), 264.

Agnus, J.C., W. Wang and M. Sunkara, 1991, Ann. Rev. Mater. Sci. **21**, 221.

Aharoni, A., 1986, IEEE Trans. Magn. **22**, 478.

Allegranza, O.C. and T. Wui, 1995, IEEE Trans. Magn. **31**, 2797.

Allibert, C.A, C. Allibert, C. Bernard, N. Valignat and M. Dombre, 1978, J. Less-Common Met. **59**, 211.

Asher, K.G., 1997, Magnetic disk drive technology (IEEE Press, Piscateway, NJ, USA).

Aspland, M., G.A. Jones and B.K. Middleton, 1969, IEEE Trans. Magn. **5**, 314.

Barlow, J.M., 1968, IBM Techn. Disc. Bulletin **II**, 238.

Bauer, E., 1964, in: Single-Crystal Films, eds M.H. Francombe and H. Sato (Pergamon Press, Oxford) pp. 43–67.

Baumgart, P., D. Krajnovich, T. Nguyen and A. Tam, 1995, IEEE Trans. Magn. **31**, 2946.

Bean, C.P., 1955, J. Appl. Phys. **26**(11), 1381.

Belk, N.R., P.K. George and G.S. Mowry, 1985, IEEE Trans. Magn. **23**, 1350.

Bertram, H.N., 1994, Theory of Magnetic Recording (Cambridge University Press, Cambridge).

Bertram, H.N. and R. Arias, 1992, J. Appl. Phys. **71**, 3439.

Bessho, K., Y. Iwasaki, and S. Hashimoto, 1996a, J. Appl. Phys. **79**(8), 5057–5059.

Bessho, K., Y. Iwasaki and S. Hashimoto, 1996b, IEEE Trans. Magn. **32**(5), 4443–4447.

Betzig, E., J.K. Trautman, R. Wolfe, E.M. Gyorgy, P.L. Finn, M.H. Kryder and C.-H. Chang, 1992, Appl. Phys. Lett. **61**, 142–144.

Bhushan, B., 1990, Tribology and Mechanics of Magnetic Storage Devices (Springer-Verlag, New York).

Bhushan, B., 1993, Adv. Inform. Storage Syst. **5**, 175–209.

Bhushan, B., 1996, J. Magn. Magn. Mater. **155**, 318–322.

Blachman, A.G., 1973, J. Vac. Sci. Technol. **10**, 299.

Bogy, D.B., X. Yun and B.J. Knapp, 1994, IEEE Trans. Magn. **30**(2), 369.

Bozorth, R.M., 1951, Ferromagnetism (Van Nostrand, New York) p. 441.

Brown, W.F., 1963, Micromagnetics (Wiley/Interscience, New York) p. 75.

Bunshah, R.F., ed., 1994, Handbook of Deposition Technologies for Films and Coatings (Science, Technology and Application, 2nd edn (Noyes Publications, New Jersey, USA).

Buschow, K.H.J. et al., eds, 1993, High Density Digital Recording, NATO ASI Series E, Vol. 229 (Kluwer, Dordrecht, The Netherlands).

Celotta, R.J., R. Gupta, R.E. Scholten and J.J. McClelland, 1996, J. Appl. Phys. **79**(8).

Chapman, B., 1980, Glow Discharge Processes (Wiley, New York).

Chapman, J.N., I.R. McFadden and J.P.C. Bernards, 1986, J. Magn. Magn. Mater. **62**, 358.

Chen, G., 1986, IEEE Trans. Magn. **22**, 334.

Chen, T. and T. Yamashita, 1988, IEEE Trans. Magn. **24**, 2700.

Chen, Y., L. Tang, D.E. Laughlin and M.H. Kryder, 1996, IEEE Trans. Magn. **32**(5), 3608–3610.

Chen, J., X. Lin, J.-G. Zhu and J.H. Judy, 1997, IEEE Trans. Magn. **33**(5), 3040–3042.

Chen, Y., M. Rao, D.E. Laughlin and M.H. Kryder, 1998, paper presented at the Intermag/MMM conference, January 1998, San Francisco, USA, and will be published in IEEE Trans. Magn. (1998).

Choe, G., 1996, J. Appl. Phys. **79**(8), 4923.

Chopra, K.L., 1969, Thin Film Phenomena (McGraw-Hill, New York).

Chou, S., 1995, Data Storage **2**(5), 35–40.

Chou, S.Y. and P.R. Krauss, 1996, J. Magn. Magn. Mater. **155**, 151–153.

Chou, S.Y., M. Wei, P.R. Krauss and P.B. Fischer, 1994, J. Vac. Sci. Technol. B **12**, 3695.

Coffey, K.R., V. Raman, N. Staud and D.J. Pocker, 1994, IEEE Trans. Magn. **30**, 4146.

Coffey, K.R., M.A. Parker and J.K. Howerd, 1995, IEEE Trans. Magn. **31**, 2737–2739.

Cooper, D., 1996, Data Storage **3**(8), 65–69.

Coughlin, T.M., J.H. Judy and E. Wuori, 1981, IEEE Trans. Magn. **17**(6), 3169–3171.

Coughlin, T., B. Gooch and B. Lairson, 1996, Data Storage **3**(8), 33–38.

Cox, A., G.B. Dalrymple and R.R. Doell, 1967, Reversals of the Earth's magnetic fields, Scientific American **216**, 44.

Cullity, S.D., 1972, Introduction to Magnetic Materials (Addison-Wesley, Reading, MA) pp. 399–418.

Cuomo, J.C. and R.J. Gambino, 1975, J. Vac. Sci. Technol. **12**, 79.

Cuomo, J.J., R.J. Gambino, J.M.E Harper, J.D. Kuptsis and J.C. Webber, 1978, J. Vac. Sci. Technol. **15**, 281.

Cupta, B.K. and B. Bushnan, 1995, IEEE Trans. Magn. **31**(6), 3012.

Daveport W.B. Jr., and W.L. Root, 1958, An Introduction on the Theory of Random Signals and Noise (McGraw-Hill, New York).

Dillman, S.H., R.B. Prime and R.B. Hannon, 1988, Presented at the Symp. on Polymers in Information Storage Technology, ACS National Meeting, Los Angeles, California, September 25–30.

Ding, J. and J.-G. Zhu, 1994, IEEE Trans. Magn. **30**(6), 3978.

Drift, A.V., 1967, Philips Res. Rep. **22**, 267–288.

Egelhoff W.F. Jr., P.J. Chen, C.J. Powell, M.D. Stiles, R.D. McMichael, C.-L. Lin, J.M. Sivertsen, J.H. Judy, K. Takano, A.E. Berkowitz, T.C. Anthony, and J.A. Brug, 1996, J. Appl. Phys. **79**(8), 5277–5281.

Elsea, A.R., A.B. Westerman and G.K. Manning, 1949, Trans. AIME **180**, 579.

Fan, L.-S., 1996, IEEE Trans. Magn. **32**(3), 1855–1861.

Fan, L.-S. and S.J. Woodman, 1995, in: Proc. Int. Conf. on Solid State Sensors and Actuators, June 1995, pp. 434–437.

Fang, L. and D.N. Lambeth, 1994, Appl. Phys. Lett. **65**, 3137.

Feng, Y.C., D.E. Laughlin and D.E. Lambeth, 1994, J. Appl. Phys. **76**, 7311.

Fernandez, A., P.J. Bedrrossian, S.L. Baker, S.P. Vernon and D.R. Kania, 1996, IEEE Trans. Magn. **32**(5), 4472–4474.

French, W.W. and J.U. Lemke, 1990, US Patent 5 193 046, September.

Futamoto, M., F. Kugiya, M. Suzuki, H. Takano, Y. Matsuda, N. Inabe, Y. Miyamura, K. Akagi, T. Nakano, and H. Sawaguchi, 1991, IEEE Trans. Magn. **27**, 5280.

Futamoto, M., M. Suzuki, N. Inaba, A. Nakamura and Y. Honda, 1994, IEEE Trans. Magn. **30**(6), 3975.

Futamoto, M., Y. Honda, Y. Hirayama, K. Itoh, H. Ide and Y. Maruyama, 1996, IEEE Trans. Magn. **32**(5), 3789–3794.

Gao, C., S.Y. Lee, R. Malmhall and G.C. Rauch, 1996, IEEE Trans. Magn. **32**(5), 3569–3571.

Geerts, W.J.M.A., J.C. Lodder and Th.J.A. Popma, 1992, J. Magn. Magn. Mater. **104–107**, 971.

Gooch, B., R. Niedermeyer, R. Wood and R. Pisharody, 1991, IEEE Trans. Magn. **27**(6), 4549–4554.

Grgor'ev, A.T., E. Yu-p'u and E.M. Sokolovskaya, 1961, Russ. J. Inorg. Chem. **6**, 827.

Grochowski, E., 1997, picture taken from: http://www.storage.ibm.com/storage/technolo/grochows/grocgo17.htm.

Grochowski, E. and R.F. Hoyt, 1996, IEEE Trans. Magn. **32**(3), 1850–1854.

Haan, S. de, J.C. Lodder and Th.J.A. Popma, 1991, J. Magn. Soc. Japan **15**(S2), 349–354.

Haan, S. de and J.C. Lodder, 1997, J. Magn. Magn. Mater. **168**, 321–335.

Haast, M.A.M., J.R. Schuurhuis, L. Abelmann, J.C. Lodder and Th.J.A. Popma, 1998, accepted for publication in IEEE Trans. Magn.

Haines, W. G., 1984, J. Appl. Phys. **55**(6), 2263.

Hamilton, H., 1991, J. Magn. Soc. Japan **15**(S2), 483–490.

Hamilton, H., 1994, J. Magn. Soc. Japan **18**(S), 425–430.

Hamilton, H., R. Anderson and R. Goodson, 1991, IEEE Trans. Magn. **27**, 5301.

Hasabe, M., K. Oikawa and T. Nishikawa, 1982, J. Jpn. Inst. Met. **46**, 577.

Hata, H.T., K. Fukuichi, K. Yabushita, M. Umesaki and H. Shibata, 1990, J. Appl. Phys. **67**, 642.

Herring, C., 1966, in: Magnetism, Vol. IIB, eds G.T. Rado and H. Suhl (Academic Press, New York) p. 2.

Hoagland, A.S. and J.E. Monson, 1991, Digital Magnetic Recording, 2nd edn (Willey, New York).

Holland, L. and S.M. Ojha, 1976, Thin Solid Films **38**, L17.

Homola, A.M., 1996, IEEE Trans. Magn. **32**(3), 1812.

Honda, N., K. Ouchi and S. Iwasaki, 1996, IEEE Trans. Magn. **32**(5), 3804–3806.

Hono, K., 1994, Presentation during PMRC'94 Extended workshop on Co–Cr system alloy films, October 17–18, Akita, Japan.

Hono, K., Y. Maeda, S. Babu, J. Li and T. Sakurai, 1993a, IEEE Trans. Magn. **29**, 3745.

Hono, K., S.S. Babu, Y. Maeda, N. Hasagawa and T. Sakurai, 1993b, Appl. Phys. Lett. **62**, 2504.

Hosaka, S., 1996, IEEE Trans. Magn. **32**(3), 1873–1877.

Hosaka, S., H. Koyanagi and A. Kikuwa, 1993, Jpn. J. Appl. Phys. **32B**, L464–L467.

Hosoe, Y., Y. Yahisa, R. Tsuchiyama, A. Ishikawa, K. Yoshida, M. Igarashi and Y. Shirois, 1995, IEEE Trans. Magn. **31**(6), 2824.

Howard, J.K., 1994, J. Magn. Soc. Japan **18**(S1), 59–61.

Huang, J.C.A., F.C. Tang, W.W. Fang, R.L. Liu, Y.M. Hu, C.K. Lo, Y. Liou, Y.D. Yao, W.T. Yang, C.P. Chang and S.Y. Liao, 1996, J. Appl. Phys. **79**(8), 4790–4792.

Huysmans, G.T.A., J.C. Lodder, and J. Wakui, 1988, J. Appl. Phys. **64**(4), 2016–2021.

Hwang, U., Y. Uchiyama, K. Ishibashi and T. Suzuki, 1987, Thin Solid Films **147**, 231.

Hylton, T.L., M.A. Parker, M. Ullah, K.R. Coffey, R. Umphress and J.K. Howard, 1994, J. Appl. Phys. **75**(10), 5960–5965.

Imakawa, M., S. Ishibashi, A. Hatashita, T. Shimatsu and M. Takahashi, 1994, in: Proc. 14th ICMFS and E-MRS Joint Colloqium, Dusseldorf, Germany, p. 247.

Intermag, 1996, Proc. Intermag 1996, Session Magnetic recording: Perpendicular Media, IEEE Trans. Magn. **32**(5), 3789–3857.

Ishida, K. and T. Nishizawa, 1990, Bull. Alloy Phase Diag. **11**, 357.

Ischikawa, M., 1986, IEEE Trans. Magn. **22**(5), 573–575.

Iwasaki, S. and K. Ouchi, 1978, IEEE Trans. Magn. **14**(5), 849–851.

Iwasaki, S. and K. Ouchi, 1980, in: Dig. 4th Annual Conf. on Magnetism, November 1980, Japan, Paper 6aA-4.

Iwasaki, S. and H. Yamazaki, 1975, Proc. 7th Conf. of Magn. Soc. Japan, Paper 4pA-7, in Japanese.

Iwasaki, S., K. Ouchi and N. Honda, 1980, IEEE Trans. Magn. **16**(5).

Iwasaki, S., K. Ouchi and N. Honda, 1996, IEEE Trans. Magn. **32**(5), 3795–3800.

Jacobs, I.S. and C.P. Bean, 1955, Phys. Rev. **100**, 1060.

Jinghan, A.K., 1986, J. Magn. Magn. Mater. **54–57**, 1685.

Johnson, J. et al., 1990, J. Appl. Phys. **67**, 4686.

Johnson, K.E., J.B. Mahlke, K.J. Schulz and A.C. Wall, 1993, IEEE Trans. Magn. **29**(1), 215.

Judy, J.H., 1997, Thermal decay brickwall in storage of magnetic recording densities beyond 10 Gbit/in^2, Invited talk at the 4th Perpendicular Magnetic Recording Conf., October 20–23, 1997, Akita, Japan.

Kadokura, S., T. Tomie and M. Naoe, 1981, IEEE Trans. Magn. **17**(6), 3175–3177.

Kaitsu, I., A. Inomata, I. Okamoto and M. Shinohara, 1996, IEEE Trans. Magn. **32**(5), 3813–3815.

Kanabe, T., H. Kishiwase, E. Fujita, Y. Yahisa and K. Furasawa, 1995, IEEE Trans. Magn. **31**, 2734.

Kanai, H., K. Yamada, K. Aoshima, Y. Ohtsuka, J. Kane, M. Kanamine, J. Toda and Y. Mizoshita, 1996, IEEE Trans. Magn. **32**(5), 3368–3373.

Karlqvist, O., 1954, Trans. R. Inst. Technol. (Stockholm) **86**, 3.

Kataoka, H., T. Kanbe, H. Kashiwase, E. Fujita, Y. Yahisa and K. Furusawa, 1995, IEEE Trans. Magn. **31**(6), 2734.

Katayama, S., T. Tsuno, K. Enjoji, N. Ishii and K. Sono, 1988, IEEE Trans. Magn. **24**(6), 2982–2984.

Katsamatsu, Y., T. Yamamoto, S. Yoneoka and Y. Mizoshita, 1995, IEEE Trans. Magn. **31**, 2961–2963.

Kawai, S. and R. Ueda, 1975, J. Electrochem. Soc. **122**, 32.

Kawakita, S., T. Sakurai, A. Kikuchi, T. Shimatsu and M. Takahashi, 1996, J. Magn. Magn. Mater. **155**, 172–175.

Kent, A.D., T.M. Shaw, S. von Molnar and D.D. Awschalom, 1994, Science **262**, 1249.

Kikuchi, A., I. Okamoto, J. Nakai, S. Kawakita, T. Shimatsu and M. Takahashi, 1996, J. Magn. Magn. Mater. **155**, 238–241.

Klik, I. and C.R. Chang, 1995, Phys. Rev. B **52**, 3540.

Kobayashi, K. and G. Ishida, 1981, J. Appl. Phys. **52**(3), 2453.

Kokaku, Y., H. Matsumoto, H. Inabe, S. Fujimaki, M. Kitoh and K. Abe, 1993, IEEE Trans. Magn. **29**(6), 3942.

Kong, L., L. Zhuang and S.Y. Chou, 1997, IEEE Trans. Magn. **33**(5), 3019–3021.

Kooten, M. van, S. de Haan, J.C. Lodder and Th.J.A. Popma, 1994, J. Appl. Phys. **75**(10), 5508.

Koster, E., H. Jakusch and U. Kullmann, 1981, IEEE Trans. Magn. **17**(6), 2550.

Kranenburg, H. van, 1992, Obliquely co-evaporated thin films for magnetic recording, PhD thesis (University of Twente, Enschede, The Netherlands) pp. 110–112.

Kronmüller, H., 1987, Phys. Status Solidi (b) **144**, 385.

Kronmüller, H., 1991, in: Supermagnets, Hard Magnetic Materials, eds G.J. Longand and F. Grandjean (Kluwer, The Netherlands) Ch. 19, pp. 461–498.

Kronmüller, H., 1993, J. Magn. Soc. Japan **17**(S1), 260.

Kübler, J. and V. Eyert, 1991, in: Materials Science and Technology, Vol. 3A, eds R.W. Cahn et al. (VCH Verlag, Weinheim) p. 3.

Lal, B.B., M. Tobise and T. Shinohara, 1994, IEEE Trans. Magn. **30**(6), 3954.

Lambert, S.E., J.K. Howard and I.L. Sander, 1990, IEEE Trans. Magn. **26**(5), 2706–2708.

Lambert, S.E., J.K. Howard, I.L. Sanders and O.C. Allegranza, 1993, IEEE Trans. Magn. **29**(1), 223–229.

Laughlin, D.E. and B.Y. Wong, 1991, IEEE Trans. Magn. **27**, 4713.

Laughlin, D.E., B. Cheong, Y.C. Feng, D.N. Lambeth, L.-L. Lee and B. Wong, 1995a, Scripta Metall. Mater. **33**(10/11), 1525–1536.

Laughlin, D.E., Y.C. Feng, L.-L. Lee and B. Wong, 1995b, Mater. Res. Soc. Symp. Proc. **343**, 327.

Laughlin, D.E., Y.C. Feng, D.N. Lambeth, L.-L. Lee and L. Tang, 1996, J. Magn. Magn. Mater. **155**, 146–150.

Lazarri, J.P., I. Melnick and D. Randet, 1967, IEEE Trans. Magn. **3**(3), 205.

Lee, J.K., M. Smallen, J. Enguero, H.J. Lee and A. Chao, 1993, IEEE Trans. Magn. **29**(1), 276.

Lee, L.-L., D.E. Laughlin and D.N. Lambeth, 1994, IEEE Trans. Magn. **30**(6), 3951–3953.

Lee, L.L., B.K. Cheong, D.E. Laughlin and D.N. Lambeth, 1995a, Appl. Phys. Lett. **67**, 3638.

Lee, L.L., D.E. Laughlin, L. Fang and D.N. Lambeth, 1995b, IEEE Trans. Magn. **31**, 1728.

Li, Y. and A. Menon, 1996, IEEE Trans. Magn. **32**(1), 129–134.

Liou, S.H., Y. Liu, S.S. Malhotra, M. Yu and D.J. Sellmeyer, 1996, J. Appl. Phys. **79**, 5060–5062.

Lisfi, A. and J.C. Lodder, 1998, paper accepted for publication in IEEE Trans. Magn.

Lodder, J.C., 1993, in: High Density Recording, NATO ASI Series E, Vol. 229, eds K.H.J. Buschow et al. (Kluwer, Dordrecht) Ch. 6, pp. 161–195.

Lodder, J.C., 1996, J. Magn. Magn. Mater. **159**, 238–248.

Lodder, J.C., T. Wielinga and J. Worst, 1983, Thin Solid Films **101**, 61.

Lodder, J.C., S. de Haan, M. van Kooten, H. te Lintelo and S. Porthun, 1994, J. Magn. Soc. Japan **18**(S1), 493–499.

Lopez, O. and D.A. Clark, 1985a, J. Appl. Phys. **57**(1), 3943.

Lopez, O. and D.A. Clark, 1985b, IEEE Trans. Magn. **21**(5), 1401.

Lu, P.-L. and S.H. Charap, 1990, IEEE Trans. Magn. **30**, 4230.

Lu, P.-L. and S.H. Charap, 1994a, J. Appl. Phys. **75**(10), 5768–5770.

Lu, P.-L. and S.H. Charap, 1994b, IEEE Trans. Magn. **30**(6), 4230–4232.

Maeda, Y. and M. Asahi, 1987, J. Appl. Phys. **61**(5), 1972.

Maeda, Y. and K. Takei, 1992, J. Magn. Soc. Japan **16**(2).

Maeda, Y., K. Takei, S. Yamamoto and Y. Nakamura, 1991, J. Magn. Soc. Japan **15**(S2), 457.

Maeda, Y., K. Takei and D.J. Rogers, 1993, Jpn. J. Appl. Phys. **32**, 4540.

Maeda, Y., D.J. Rogers and K. Takei, 1994, J. Magn. Soc. Japan **18**(S1), 27–30.

Maisel, L.I. and R. Glang, eds, 1970, Handbook of Thin Film Technology (McGraw-Hill, New York).

Mallinson, J.C., 1993, The Foundations of Magnetic Recording, 2nd edn (Academic Press, London).

Maloney, W.T., 1979, IEEE Trans. Magn. **15**(3), 1135.

Mamin, J., P.H. Guenther and D. Rugar, 1990, Phys. Rev. Lett. **65**, 2418–2421.

Marchon, B., N. Heiman and M.R. Khan, 1990, IEEE Trans. Magn. **26**, 168.

Mee, C.D. and E.D. Daniel, 1990, Magnetic Recording Handbook, Technology and Application, updated edition of Mee and Daniel (1987–1988).

Mee, C.D. and E.D. Daniel, 1996, Magnetic Recording Technology, revised edition of Mee and Daniel (1990).

Mee, C.D. and E.D. Daniel, 1987–1988, Magnetic Recording, Vols I, II and III (McGraw-Hill, New York).

Messier, R. et al., 1984, J. Vac. Sci. Technol. A **2**(2), 500.

Middleton, B.K., 1996, Recording and reproducing processes, in: Magnetic Recording Technology, 2nd edn, eds C.D. Mee and E.D. Daniel (McGraw-Hill, New York) Ch. 2, p. 2.5.

Miller, R.A. and B. Bhushan, 1996, IEEE Trans. Magn. **32**(3), 1805–1811.

Mirzamaani, M., C.V. Jahnes and M.A. Russak, 1991, J. Appl. Phys. **69**(8), 5169.

Mirzamaani, M., C.V. Jahnes and M.A. Russak, 1992, IEEE Trans. Magn. **28**, 3090.

Miura, Y., 1991, J. Magn. Soc. Japan **15**(S1), 133–138.

Movchan, B.A. and A.V. Demschishin, 1969, Phys. Met. Metallogr. **28**, 83.

Murayama, A., M. Miyamyra and S. Kondoh, 1994, J. Appl. Phys. **76**(9), 5361–5370.

Murdock, E.S., B.R. Natarajan and R.G. Walmsley, 1990, IEEE Trans. Magn. **26**(5), 2700.

Murdock, E.S., R.F. Simmons and R. Davidson, 1992, IEEE Trans. Magn. **28**(5), 3078–3083.

Mutoh, H., H. Kanai, I. Okamoto, Y. Ohtsuka, T. Sugawara, J. Koshikawa, J. Toda, Y. Uematsu, M. Sinohara and Y. Mizoshita, 1996, IEEE Trans. Magn. **32**(5), 3914–3916.

Nader, B.S., K.K. Kar, T.A. Morgan, C.E. Pawloski and W.L. Dilling, 1992, STLE Tribol. Trans., J. Tribology **35**(1), 37.

Nakai, J., A. Kikuchi, N. Nakatani, M. Hirasaka, T. Shimatsu and M. Takahashi, 1996, J. Magn. Magn. Mater. **155**, 234–237.

Nakajima, J., A. Takahashi, K. Ohta and T. Ischikawa, 1993, J. Appl. Phys. **73**, 7612.

Nakamura, Y., 1989, J. Magn. Soc. Japan **13**(S1), 33.

Nakamura, Y., 1991, J. Magn. Soc. Japan **15**(S2).

Nasu, S., K. Matsumoto, K. Hashimimoto and K. Saiki, 1987, Jpn. J. Appl. Phys. **11**(2), 61.

Nayiesh, A.R. and L. Holland, 1984, Vacuum **34**(5), 523.

Neugebauer, C.A., 1970, in: Handbook of Thin Film Technology, eds L.I. Maisel and R. Glang (McGraw-Hill, New York) Ch. 8.

New, R.M.H., R.F.W. Pease and R.L. White, 1994, J. Vac. Sci. Technol. B **12**, 3196.

Nolan, T.P., R. Sinclair, R. Ranjan and T. Yamashita, 1993a, IEEE Trans. Magn. **29**, 292.

Nolan, T.P., R. Sinclair and T. Yamashita, 1993b, J. Appl. Phys. **73**(10), 5566.

Nolan, T.P., Y. Hirayama and M. Futamoto, 1996, J. Appl. Phys. **79**(8), 5359.

Ohkubo, T., J. Kishigami, K. Yanagisawa and R. Kaneko, 1991, IEEE Trans. Magn. **27**, 5286–5288.

Ohring, M., 1992, The Materials Science of Thin Films (Academic Press, San Diego).

Paik, C.R., I. Suzuki, N. Tani, M. Ischikawa, Y. Ota and K. Nakamura, 1992, IEEE Trans. Magn. **28**(5), 3084.

Palmer, D.C., K.E. Johnson, E.Y. Wu and J.V. Peske, 1991, IEEE Trans. Magn. **27**, 307.

Patten, J.W. and E.D. McClanahan, 1972, J. Appl. Phys. **43**, 4811.

Pauling, L., 1938, Phys. Rev. **54**, 899.

Peng, Q., H.N. Bertram, N. Fussing, M. Doerner, M. Mirzamaani, D. Margulies, R. Sinclair and S. Lambert, 1995, IEEE Trans. Magn. **31**(6), 2821.

Peng, Q., H.N. Bertram and M. Doerner, 1996, J. Appl. Phys. **79**(8), 4916.

Petersen, N.L., 1986, J. Vac. Sci. Technol. A **4**(6), 3066.

PMRC, 1989, Proceedings of the PMRC'89, J. Magn. Soc. Japan **13**(S1).

PMRC, 1991, Proceedings of the PMRC'91, J. Magn. Soc. Japan **15**(S2).

PMRC, 1994, Proceedings of the PMRC'94, J. Magn. Soc. Japan **18**(S1).

PMRC, 1997, Proceedings of the PMRC'97, J. Magn. Soc. Japan **21**(S2).

Poulsen,V., 1890, Das Telegraphon, Annalen der Physik **3**, 754.

Putland, F., T. Chart and A. Dinedale, 1980, CALPHAD (Comput. Coupling Phase Diagrams and Termochem.) **4**(2), 133–141.

Ranjan, R.Y., D.N. Lambeth, M. Tromel, P. Goglia and Y. Li, 1991, J. Appl. Phys. **69**, 5745–5747.

Reed, W., U. Cohen, D. Hollars, R. Zubeck, B. Gooch, J. Loven and J.H. Judy, 1996, IEEE Trans. Magn. **32**(5), 3581–3583.

Richards, D.B. and T.J. Szczech, 1978, J. Appl. Phys. **49**(3), 1819.

Rogers, D.J., Y. Maeda and K. Takei, 1994, J. Magn. Soc. Japan **8**(S1), 79–82.

Rogers, D.J., Y. Maeda and K. Takei, 1995, J. Appl. Phys. **78**(9), 5842–5844.

Rottmayer, R. and J.-G. Zhu, 1995, IEEE Trans. Magn. **31**(6), 2597–2599.

Sagoi, M. and T. Nashikawa, 1989, J. Appl. Phys. **66**, 3173.

Sagoi, M., R. Nishikawa and T. Suzuki, 1986, IEEE Trans. Magn. **22**(5), 1335.

Sanders, V., 1971, in: Chemisorption and Reaction on Metallic Films, ed. J.R. Anderson (Academic Press, London) pp. 1–38.

Sano, K., H. Murayama and F. Yokoyama, 1994, IEEE Trans. Magn. **30**(6), 4140.

Sato, H., A. Kikuchi, J. Nakai, M. Mitsuya, T. Shimatsu and M. Takahashi, 1996, IEEE Trans. Magn. **32**(5), 3596–3598.

Shen, Y., D.E. Laughlin and D.N. Lambeth, 1994, J. Appl. Phys. **76**, 8167.

Shimatsu, T. and M. Takahashi, 1995a, Mat. Chem. Phys. **41**, 134–140.

Shimatsu, T. and M. Takahashi, 1995b, IEICE Trans. Electron. **E78-C**(11), 1550–1556.

Shimatsu, T., M. Takahashi, M. Suekane, M. Miyamura, K. Yamaguchi and H. Yamasaki, 1993, in: Advanced Materials'93, II/B: Information Storage Materials, eds M. Abe et al., Trans. Mat. Res. Soc. Japan **15B**, 777–782.

Simonds, J.L., 1995, Physics Today **48**(4), 26–32.

Sigmund, P., 1974, Phys. Rev. **184**, 383.

Simpson, J.M. et al., 1987, IEEE Trans. Magn. **23**, 3405.

Slater, J.C., 1938, J. Appl. Phys. **8**, 385.

Smith, O., 1888, Some possible forms of phonograph, The Electric World **161**.

Smits, J., S.B. Luitjens and F.J.A. den Broeder, 1984, J. Appl. Phys. **55**(6), 2260.

Speliotis, D.E., 1990, IEEE Trans. Magn. **26**, 141.

Stoner, E. and E.P. Wohlfarth, 1948, Philos. Trans. R. Soc. London Ser. A **240**, 74.

Sugita, R., T. Kunieda and F. Kobayashi, 1981, IEEE Trans. Magn. **17**(6), 3172–3174.

Sui, X. and M. Kryder, 1994, IEEE Trans. Magn. **30**(6), 4044–4046.

Suzuki, T., 1984, IEEE Trans. Magn. **20**(5), 675.

Suzuki, T., 1991, in: Magnetic Materials: Microstructure and Properties, MRS, Vol. 232, eds T. Suzuki, Y. Sugita, B. Clemens, K. Ouchi and D.E. Laughlin (MRS, Pittsburgh, PA).

Tagawa, I. and Y. Nakamura, 1989, J. Magn. Soc. Japan **13**(S1), 97.

Takahashi, M., T. Shimatsu, M. Suekane, M. Miyamura, K. Yamaguchi and H. Yamasaki, 1992, IEEE Trans. Magn. **28**, 3285.

Takahashi, M., H. Shoji and A. Kikuchi, 1997, J. Magn. Soc. Japan **21**(S2), 499–504.

Takayama, T., M.Y. Wei and T. Nishizawa, 1981, J. Jpn. Inst. Met. **45**, 341.

Takei, K., J. Suzuki, Y. Maeda and Y. Morii, 1994, IEEE Trans. Magn. **30**(6), 4029–4031.

Tang, L. and G. Thomas, 1993, J. Appl. Phys. **74**, 5025.
Terris, B.D., S.A. Rishton, R. Read, H.J. Mamin and D. Rugar, 1997, presentation Th9.1M04 at the 9th Int. Conf. on Scanning Tunneling Microscopy/Spectroscopy and Related Techniques, Hamburg, Germany, July 20–25.
Thompson, D.A., 1997, J. Magn. Soc. Japan **21**(S2), 9–15.
Thornton, J.A., 1974, J. Vac. Sci. Technol. **11**, 666.
Thornton, J.A., 1977, Am. Rev. Mater. Sci. **7**, 239–260.
Thornton, J.A., 1978, Thin Solid Films **54**, 23.
Thornton, J.A., 1988, in: Semiconductor Materials and Process Technology Handbook, ed. G.E. McGuire (Noyes Publications) p. 414.
Thurlings, L., 1983, IEEE Trans. Magn. **19**(2), 84–109.
Tsai, H.-C., 1993, IEEE Trans. Magn. **29**(1), 241.
Tsang, C., M.M. Chen, T. Yogi and K. Ju, 1990, IEEE Trans. Magn. **26**, 1689.
Tsang, C., H. Santini, D. McCown, J. Lo and R. Lee, 1996, IEEE Trans. Magn. **32**(1), 7–12.
Tsoukatos, A., H. Wan, G.C. Hajipanayis, Y.J. Zhang, M. Waite and S.I. Shah, 1993, J. Magn. Magn. Mater. **118**, 387–393.
Tsuya, N., T. Tokushima, M. Shiraki, Y. Wakui, Y. Saito, H. Nakamura and Y. Katsumata, 1986, J. Magn. Magn. Mater. **54–57**, 1681.
Visser, H., 1997, On the friction of thin film disks, PhD thesis (University of Twente Enschede, The Netherlands).
Vossen, J.L., 1971, J. Vac. Sci. Technol. **8**, 512.
Vossen, J.L. and J.J. Cuomo, 1978, in: Thin Film Processes, eds J.L. Vossen and W. Kern (Academic Press, New York) p. 11.
Vossen, J.J. and J.J. O'Neill, 1986, RCA Review **29**, 566.
Wang, G., J.M. Silversten, J.H. Judy and G.-L. Chen, 1996, J. Appl. Phys. **79**(8), 5782.
Wehner, G.K., 1957, Phys. Rev. **108**, 35.
White, R.L., M.F. Doerner and G.G. Walker, 1990, in: Thin Films: Stresses and Mechanical Properties II, eds M. Doerner, W.C. Oliver, G.M. Pharr and F.R. Brotzen, Mater. Res. Soc. Symp. Proc. **188**, 213.
Wielinga, T., 1983, Investigations on perpendicular recording, PhD thesis (University of Twente, Enschede, The Netherlands).
Wielinga, T. and J.C. Lodder, 1981, IEEE Trans. Magn. **17**(3), 3178–3180.
Wiesendanger, R., 1993, in: Atomic and Nanometer-Scale Modification of Materials: Fundamentals and Applications, NATO ASI Series E, Vol. 239, ed. P. Avouris (Kluwer, Dordrecht) pp. 65–73.
Williams, M.L. and R.L. Comstock, 1971, AIP Conf. Proc. **5**, 378.
Wong, B.Y., Y. Shen and D.E. Laughlin, 1993, J. Appl. Phys. **73**, 418.
Wood, R., T. Coughlin and J. Monson, 1997, J. Magn. Soc. Japan **21**(S2), 197–204.
Wui, E.Y., J.F. Peske and D. Palmer, 1994, IEEE Trans. Magn. **30**, 3996.
Yamashita, T., L.H. Chan, T. Fujiwara and T. Chen, 1991, IEEE Trans. Magn. **27**, 4727.
Yang, M., F.E. Talke, D.J. Peretti, T.A. Morgan and K.K. Kar, 1994, IEEE Trans. Magn. **30**(6), 4143.
Yogi, T., C. Tsang, T.A. Nguyan, K. Ju, G.L. Gorman and G. Castillo, 1990, IEEE Trans. Magn. **26**(5), 2271.
Yogi, T., T.A. Nguyen, S.E. Lambert, G.L. Gorman, and G. Castillo, 1991, Mater. Res. Soc. Symp. Proc. **232**, 3–13.
Yoshida, K., M. Hara, Y. Hirayama and Y. Sugita, 1996, J. Appl. Phys. **79**(8), 5664–5666.
Zhang, B., W.R. Bennett, C. Gao, G.C. Rauch and J.R. Blanchere, 1996, IEEE Trans. Magn. **32**(5), 3590–3592.
Zhanpeng, J., 1981, Scand. J. Metall. **10**, 279–287.
Zhu, J.G. and H.N. Bertram, 1988, J. Appl. Phys. **63**, 3248.
Zou, P., M. Scherge and D.N. Lambeth, 1995, IEEE Trans. Magn. **1**(6), 2985.

chapter 3

MAGNETISM OF PERMANENT MAGNET MATERIALS AND RELATED COMPOUNDS AS STUDIED BY NMR

CZ. KAPUSTA*, P.C. RIEDI and G.J. TOMKA

Department of Physics and Astronomy
University of St. Andrews
St. Andrews, Fife, KY16 9SS
U.K.

** Permanent address:*
Department of Solid State Physics
University of Mining and Metallurgy
30-059 Cracow, Poland

Handbook of Magnetic Materials, Vol. 11
Edited by K.H.J. Buschow

CONTENTS

1. Permanent magnet materials

Modern magnetoelectric devices and systems such as stepper motors in computer and office equipment, and loudspeakers need small, lightweight and stable permanent magnets to produce the utilized fields. The properties of such permanent magnet materials are of considerable scientific and technological interest, and so have been the subject of a great deal of research and development. This has ranged from the study of the fundamental theoretical aspects, to the development of new materials based on rare earth (RE) and transition metal (TM) compounds, with high magnetocrystalline anisotropies and large remanent magnetizations. Important advances have been made in the understanding and developing of these RE–TM systems by employing the nuclear magnetic resonance (NMR) techniques discussed in section 2.

The maximum value of the product of the flux density B and field H as a magnet is swept through its hysteresis loop is a physical parameter useful in determining the suitability of a permanent magnet for static applications. Samples with a large maximum energy product exhibit large remanent magnetizations, high coercivities and square hysteresis curves. Although $(BH)_{\max}$ is an important figure of merit, other significant criteria include Curie temperature, mechanical strength, resistance to corrosion and, of course, manufacturing and processing costs. Figure 1.1, updated after Rahman and Slemon (1985), illustrates some of the remarkable advances made in permanent magnet technology this century.

At the turn of the century, the available steels had coercivities of less than a few tens of mT. In the early 1930s it was discovered that the coercivity of alloys of Al, Ni and Co with Cu and Ti dopants had significantly higher coercivities than the best Co steels. The next major technological advance came with the development of hexagonal ferrimagnetic oxides, known as ferrites, from 1933 to 1944 at the Philips research laboratory in Holland. These were marketed from 1952 under the tradename Ferroxdure. Their low cost and diverse magnetic and dielectric properties give rise to a number of widely used devices operating at micro and millimeterwave frequencies, as well as their use in many everyday appliances. NMR studies have provided useful information in characterizing the hexagonal ferrites. For example, in a study by Stepankova et al. (1995), the overlapping ^{57}Fe NMR lines from the seven Fe^{3+} sites of barium hexaferrite were resolved by the application of a 3 T field.

It can be seen from fig. 1.1, that the most significant steps have been made in the last three decades, with the advent of new permanent magnets based on rare earth and transition metal intermetallics. In these systems, the TM sublattice principally provides the magnetization, whereas the RE component provides most of the magnetocrystalline anisotropy. This anisotropy originates physically from the aspherical 4f charge distribution of the RE

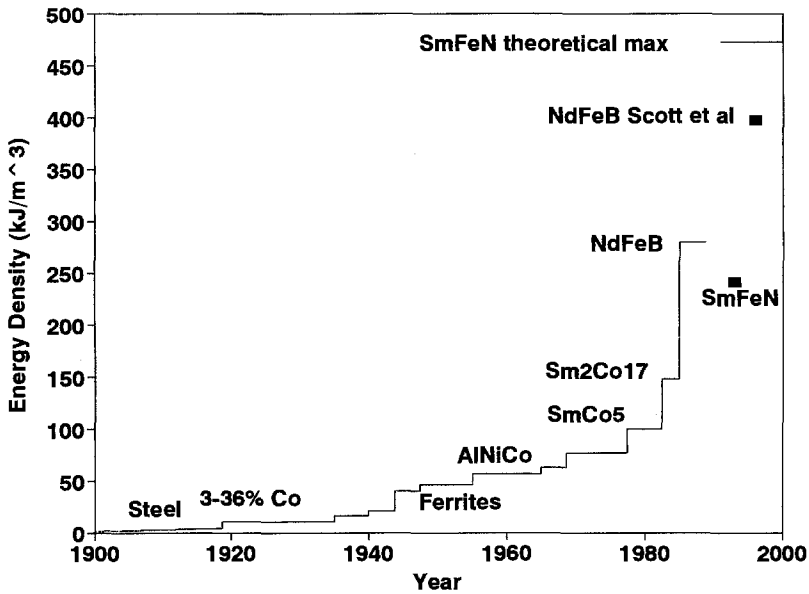

Fig. 1.1. Increase in $(BH)_{max}$ this century. A point corresponding to a consistently attainable $(BH)_{max}$ in a Nd–Fe–B based system (Scott et al. 1996) is shown. A record $(BH)_{max}$ for $Sm_2Fe_{17}N_x$ (Suzuki et al. 1993), is also shown together with the theoretical maximum value. The figure is updated after Rahman and Slemon (1985).

ion ($L \neq 0$) interacting with the crystal electric field (CEF). Directional preferences of the RE from the 4f spin–orbit coupling affect the anisotropy of the whole system via the RE–TM exchange coupling. A uniaxial magnetocrystalline anisotropy gives rise to an easy axis, along which the magnetic moment will tend lie. The anisotropy field associated with this, is an upper limit to the coercivity of the system.

The coercivity of magnetic systems also depends upon the reversal mechanism, and has been the subject of a great deal of study. Magnetic materials either consist of fine, single domain grains or larger multidomain grains, but it is the strong interactions between grains which often dictate the magnetic behaviour. Magnetic reversal in single domain particle systems can occur by coherent rotation, or by an incoherent process, such as curling, fanning or buckling. Magnetic reversal in multidomain particle systems is controlled by domain wall nucleation and pinning.

The presence of soft magnetic phases such as α-Fe can reduce the coercivity of magnetic systems, by providing easy nucleation sites. NMR provides an ideal technique for identifying the presence of unwanted phases such as α-Fe. This is discussed in sections 3.1.1, 3.2 and also in section 5, where the removal of the Fe by Nb doping in Sm_2Fe_{17} is discussed. NMR techniques can also provide important clues which help to identify pinning sites, Kapusta et al. (1992a) and section 4, since NMR signals from nuclei in domain walls are enhanced as compared to those from domain interiors.

In the 1960s it was recognized that $RECo_5$, with a hexagonal $CaCu_5$ structure, possessed a large uniaxial anisotropy. The NMR studies on materials of this form are detailed

in section 11. In the late 1970s and early 1980s, much of the research was directed towards the development of RE_2Co_{17} materials with a rhombohedral Th_2Zn_{17} structure. Materials of this form have a larger saturation magnetization than the $RECo_5$, but have a lower magnetocrystalline anisotropy, tending to lead to an inherently low coercivity. Nevertheless, multiphase permanent magnets have been successfully developed. A rhombohedral cellular structure of the softer 2:17 phase, typically 150 nm in size is precipitation hardened by 4 nm thick platelets of the 1:5 phase forming cell boundaries. Energy products as large as 262 kJ/m^3 have been reported in a magnet with composition $Sm(Co_{0.65}Cu_{0.5}Fe_{0.28}Zr_{0.02})_{7.67}$ (Mishra et al. 1981). It is believed that the coercivity mechanism is principally one of strong pinning of domain walls at the cell boundaries, though the magnetic behaviour as a function of orientation is more like that expected for coherent reversal (Kronmüller et al. 1984; Tomka et al. 1995). Further information on the $RECo_5$ and RE_2Co_{17} may be found in the review by Kumar (1988). Some results of the NMR characterization of the RE_2Co_{17} materials are summarized in section 3.6.

The widespread use of these Sm–Co based permanent magnets was limited by the high expense of Sm and Co. In 1984, Croat et al. reported the discovery of an energy product of over 110 kJ/m^3 in an Nd–Fe–B-based melt-spun ribbon, which has since been commercially developed into the family of MAGNEQUENCH Nd–Fe–B-based magnetic powders (Croat et al. 1984a, 1984b). These are used to make epoxy bonded isotropic magnets. They derive their coercivity from grains, showing a single domain like character, of the highly anisotropic $Nd_2Fe_{14}B$ phase, with grain sizes typically around 30 nm. These grains are partially isolated from each other by grain boundaries consisting of a Nd-rich, B-deficient amorphous phase. There is however a strong exchange interaction between neighboring grains. Correlation domains, frustrated by the random orientations of the easy axes of the grains, have been observed across several grains in ribbons with a fine grain structure. Domain walls are apparently pinned at the grain boundaries, Hadjipanayis and Kim (1988).

A $Nd_2Fe_{14}B$, magnet made by powder metallurgy and liquid phase sintering, with a $(BH)_{max}$ of over 280 kJ/m^3 was announced by Sagawa et al. (1984). The larger energy product in the sintered material arose because of the crystallite texturing allowed by the powder metallurgy process. Unlike in the melt-spun material, the grains are clearly multidomain in the virgin state. Grains are largely defect free $Nd_2Fe_{14}B$ and are around 1000 nm in size. There remains some controversy over the exact nature of the coercivity mechanism, but it seems clear that nucleation or pinning processes take place in the Nd-rich grain boundary phase. It can be seen that the careful control and monitoring of the metallurgy of the magnetic system is essential in optimizing the performance of the permanent magnet. This is exemplified by fig. 1.1 in the publication by Scott et al. (1996), in which it has been demonstrated that a $(BH)_{max}$ as high as 397 kJ/m^3 (i.e., about 80% of the theoretical maximum energy product) can be consistently attained by careful control of alloying and annealing processes in an Nd–Fe–B-based magnet. The study of $Nd_2Fe_{14}B$ and related systems by NMR form a large part of this review and are discussed in depth in sections 7–9.

The discovery of $Nd_2Fe_{14}B$ has prompted the investigation of many related compounds in the 2:14 family, though none has been discovered to rival $Nd_2Fe_{14}B$. The substitution of Fe by a small amount of Co, for example, does increase the Curie temperature and is reflected in the changes of hyperfine parameters. Upon such a substitution the hyperfine field

(HFF) of Nd initially decreases and then recovers, whereas the substitution by Ni causes a dramatic reduction of HFF (section 7.5). This trend also is clearly seen for RE = Y (section 7.4). Furthermore, across the range of RE compounds, Co systems have a strong tendency to prefer basal, rather than uniaxial anisotropy. For both TM = Fe and Co, when the RE ions have a positive second order Stevens coefficient α_J, such as RE = Sm, then a basal plane anisotropy is preferred (section 7.3). For RE = Nd, with a negative α_J, a low temperature canted magnetic structure can be observed from NMR measurements of ^{10}B resonances, as shown in section 7.3. The $Nd_2Fe_{14}C$ system does show promising permanent magnet properties, however, there are significant difficulties involved in its preparation, as discussed in section 8. The Curie temperature of $Nd_2Fe_{14}B$ can be enhanced by the introduction of interstitial H, though NMR studies have shown (section 9) that this has a detrimental affect on the lattice electric field gradient (EFG), reflecting an associated drop in magnetocrystalline anisotropy and coercivity.

Some other important modifications to $Nd_2Fe_{14}B$ include the partial substitution of Nd by Dy, which can enhance the Curie temperature and increase the coercivity, and the addition of Al, which despite its detrimental effect on the intrinsic properties such as the reduction in anisotropy field, has a beneficial microstructural effect, significantly enhancing the coercivity. A detailed review of the major developments leading to the development of Nd–Fe–B as a commercial magnet, and of the properties of related magnetic systems has been given by Herbst (1991).

Despite these remarkable technological advances, the simplest magnetic system, α-Fe, continues to receive attention, because of the potential impact of the large magnetic moment provided by Fe on the future development of permanent magnets. Controversy has surrounded an apparent 25% enhancement in the Fe moment when the α-Fe lattice was expanded by the introduction of N, because of the multiphase nature of samples produced to date. However in a NMR investigation of specific sites in $Fe_{16}N_2$, in conjunction with magnetization measurements, it was conclusively demonstrated that an Fe atom in Fe metallics can possess a spin of greater than 3.0 μ_B (Zhang et al. 1996b). These fundamental studies have been paralleled by an interest in the development of practical expanded lattice permanent magnets, of the form $RE_2TM_{17}A_x$ and $RETM_{12-y}M_yA_x$ (M = Mo, Ti). The properties of these magnetic system can be enhanced by the introduction of interstitials A such as N, C or H. The NMR studies of $RE_2TM_{17}A_x$ and $RETM_{12-y}M_yA_x$ are detailed in sections 3–6 and 10, respectively.

The widespread interest in these systems was heralded by the publication of the discovery of the promising new interstitially modified compound $Sm_2Fe_{17}N_x$ (Coey and Sun 1990). Indeed the nitrogenation of Sm_2Fe_{17} had a tremendous effect on its magnetic properties, increasing the Curie temperature considerably, from below 440 K to above 700 K. Furthermore, the effect of nitrogen on the CEF at the Sm site was found to cause the easy magnetization direction (EMD) to switch to the c-axis from the c-plane (perpendicular to the c-axis) leading to an enormous increase in the magnetocrystalline anisotropy, with a consequent increase in coercivity and $(BH)_{max}$. The current record value of $(BH)_{max}$ = 240.5 kJ/m^3 by Suzuki et al. (1993), for $Sm_2Fe_{17}N_x$ is illustrated in fig. 1.1. The theoretical maximum value of $(BH)_{max}$ is also indicated. The main reason that it has proved difficult to approach this theoretical maximum value is the poor thermal stability of the systems. This has hindered the development of the high density

anisotropic sintered systems required for magnets with a large saturation magnetization M_s and a hysteresis curve with a high squareness. The powders produced by processes such as mechanical grinding and alloying or hydrogen disproportionation, desorption and recombination (HDDR) however can be used for making epoxy or metal bonded isotropic magnets. The effects of hydrogen combination and desorption are discussed in terms of NMR data in section 3.1.4. Anisotropic magnets can be made by crushing Sm–Fe ingots into homogenized powders of about 10 μm diameter followed by interstitial modification by N_2, NH_3, and H_2 gases at around 450°C, though the gasification and diffusion processes can lead to a non-uniform distribution of interstitials through grains of the host lattice, as discussed in section 3.1.2 and section 4. The use of C as an interstitial is limited by its solubility, $x < 1.5$ (see sections 3.1.5 and 3.3.2), however it has been reported that carbonitrides prepared by nitrogenation followed by a C_2H_2 gasification have a better thermal stability than pure nitrides (Altounian et al. 1993).

NMR is the superlative technique for the study of the diffusion processes and can provide a quantitative evolution of phases containing light interstitials, since for a series of samples distinct spectral lines can clearly be identified for RE nuclei with different numbers of interstitial neighbors. The influence of these on the individual site magnetic properties (as determined by NMR) of the systems with nonmagnetic RE = Y, Lu are discussed in sections 3.1 and 3.2, and for RE = Sm, Nd, Tb are discussed in sections 3.3, 3.4 and 3.5, respectively.

For further general information on 2:17 and 1:12 interstitially modified intermetallics of rare earth and 3d elements, the reader is directed towards the review by Fujii and Sun (1995), in this series. General information on the properties of the 2:14 systems can be found, for example, in the review by Herbst (1991) and in Interstitial Intermetallic Alloys (Grandjean et al. 1995).

2. NMR techniques for magnetic material investigation

2.1. The effective field at the nucleus

The characteristic features of NMR in strongly magnetic materials are related to the presence of internal fields resulting from magnetic order. Thus, the resonant condition for a nucleus with spin I can be fulfilled at zero applied magnetic field making use of the effective internal field at the nucleus with its magnetic induction denoted as B_e. Where the quadrupole interaction is much smaller than the magnetic interaction, the resonant frequencies to a first order approximation are given by the relation:

$$\nu_{m,m-1} = |\gamma_n B_e/2\pi + P_q(2m - 1)|, \tag{2.1}$$

where m runs in integer steps from $1 - I$ to I and γ_n is the gyromagnetic constant relating the resonance frequency to the field at the nucleus. P_q is the quadrupole parameter. For ease of reference, the gyromagnetic constants of the isotopes of the elements most commonly used in permanent magnet systems are listed in table 1.1. The abundance, sensitivity at constant field for a given number of nuclei, and the values of I are also tabulated.

TABLE 1.1
Gyromagnetic constants, abundance, nuclear spin and sensitivity at constant field (^{1}H=1) for the materials discussed in this review.

Isotope	$\gamma_n/2\pi$ (MHz/T)	Abundance %	Nuclear spin I	Sensitivity of nuclei at constant field
^{1}H	42.5759	99.9844	1/2	1
^{10}B	4.575	18.83	6/2	1.99×10^{-2}
^{11}B	13.660	81.17	3/2	1.65×10^{-1}
^{13}C	10.705	1.108	1/2	1.59×10^{-2}
^{14}N	3.076	99.655	2/2	1.01×10^{-3}
^{15}N	4.315	0.365	1/2	1.04×10^{-3}
^{57}Fe	1.38	2.245	1/2	3.38×10^{-5}
^{59}Co	1.005	100	7/2	2.81×10^{-1}
^{89}Y	2.086	100	1/2	1.18×10^{-4}
^{93}Nb	10.407	100	9/2	4.82×10^{-1}
^{139}La	6.014	99.911	7/2	5.92×10^{-2}
^{141}Pr	11.95	100	3/2	2.99×10^{-2}
^{143}Nd	2.72	12.20	7/2	5.49×10^{-3}
^{145}Nd	1.7	8.30	7/2	1.33×10^{-3}
^{147}Sm	1.5	15.07	7/2	7.30×10^{-1}
^{149}Sm	1.2	13.84	7/2	5.91×10^{-1}
^{155}Gd	1.2	14.68	3/2	1.33×10^{-4}
^{157}Gd	1.7	15.64	3/2	3.34×10^{-4}
^{159}Tb	7.72	100	3/2	2.99×10^{-2}
^{167}Er	1.04	22.82	7/2	3.11×10^{-4}
^{175}Lu	4.86	97.4	7/2	3.12×10^{-2}

In a NMR experiment at zero applied field the internal magnetic field B_e at a nucleus can be expressed as follows:

$$B_e = B_{loc} + B_{hf}, \tag{2.2}$$

B_{loc} is the local field consisting of the Lorentz field and the dipolar field B_{dip}, which is usually the dominant contribution, to B_{loc}. B_{dip}, however, rarely exceeds 1 T. The hyperfine field B_{hf} is usually the dominant contribution and B_e is sometimes called synonymously "hyperfine field" and abbreviated as HFF. B_{hf} can be expressed as a sum:

$$B_{hf} = B_s + B_{orb} + B_n, \tag{2.3}$$

B_s is the self polarization term originating from core and conduction electron polarization by the spin moment of the parent atom. B_{orb} is the orbital field produced by nonvanishing orbital moments of the 4f electrons at the rare earth nuclei and of the 3d electrons at the 3d transition metals nuclei. B_{orb} is dominant for the non S-state rare earths and can be comparable with B_s for the 3d metals. B_n is the polarization contribution from neighboring magnetic atoms often called the "transferred" HFF. The contributions to HFF are related

to the partial moments through the hyperfine coupling and can be written as $B_i = A_i\mu_i$, where 'i' stands for 's' and 'orb' indexes.

The quadrupole parameter can be expressed as:

$$P_q = \frac{-3eQ_nV_{zz}}{4hI(2I-1)}, \tag{2.4}$$

where Q_n is the nuclear quadrupole moment and V_{zz} is the electric field gradient component with maximum absolute value. For a nucleus with $I > 1/2$ and a "small" quadrupole interaction, i.e., with $2mP_q \ll \gamma_n B_e$, the spectrum has the form of $2I$ equidistant lines. From the quadrupole splittings $\Delta\nu_q$ derived from the line separations of the quadrupole spectra the corresponding values of the EFG component along the hyperfine field V_{ii} can be derived using the formula:

$$|V_{ii}| = \frac{2I(2I-1)h\Delta\nu_q}{3e|Q_n|}. \tag{2.5}$$

The EFG at the nucleus of a non-S state rare earth originates mainly from a nonspherical distribution of the 4f electron density of the parent ion as well as from the asphericity of the 6p and 5d electron density of the parent ion due to the presence of neighboring atoms in the lattice (Coehoorn and Buschow 1991). Thus, the diagonal EFG component along the hyperfine field direction may be written as:

$$V_{ii} = V_{ii}(4f) + V_{ii}(\text{latt}). \tag{2.6}$$

In the compounds where the RE–TM exchange interaction is much stronger than the crystal electric field, e.g., in $RE_2TM_{17}A_x$, where TM = Fe, Co and A = N, C, H, the rare earth usually preserves its fully polarized ground state with $J_z = J$ irrespectively of the direction of magnetization. Thus, $V_{ii}(4f)$ is independent of the magnetic moment direction and has its maximum value denoted as $V_{zz}(4f)$, which is proportional to the quantum number J_z. Also B_{orb} preserves its maximum value.

2.2. *NMR of ferromagnets*

The NMR frequency of a given atom is sensitive to its local environment and is often dominated by nearest neighbor (NN) interactions. Changes in the local environment can result in changes in both the quadrupolar interaction and the hyperfine field. The NMR spectra can also depend on the direction of the easy axis of the material, as in $Sm_2Fe_{17}N_x$, for example. The whole spectrum of a nucleus, such as ^{147}Sm, very often covers a range corresponding to a few hundred MHz, so the most useful technique is frequency swept spin-echo NMR at zero applied field. A standard two-pulse sequence of radiofrequency (rf) pulses is usually applied and the amplitude of the nuclear spin-echo appearing after the second pulse after a time equal to the pulse separation is measured. An external magnetic field can be applied for saturation of the sample or determination of the origin of an unknown signal. Progress in broadband rf electronics has allowed the construction of an untuned, 10–1000 MHz,

computer controlled frequency swept spectrometer (Lord and Riedi 1995), and made the NMR research in magnetic materials much more effective.

The presence of magnetic domain structure in ordered materials leads to enhancement of the rf field and lowers the pulse power required to form a spin echo. However, NMR signals corresponding to different magnetic regions appear and very often overlap, which brings about some difficulties in the interpretation of the spectra. For studying anisotropic properties such as orbital contributions to magnetic moments and EFGs it is essential to be able to obtain a signal corresponding to a well defined direction of local magnetization with respect to the crystallographic axes. In the subsequent paragraphs we will briefly outline the way of solving this problem.

The enhancement effect is caused by oscillations of the electronic magnetization excited by the rf pulses. A rf field enhanced through the hyperfine coupling appears at the nucleus. The effect is much larger at the centre of the domain walls than in domains so the signals from domain walls are usually observed. The rf enhancement varies across the domain wall and is larger at the domain wall centre (DWC) than at the domain wall edge (DWE). Thus, the DWC signals can be distinguished from the DWE signals on the basis of their dependence on the rf pulse power. The maximum of the former corresponds usually to a much lower pulse power than for the latter. Thus, by increasing pulse power we can scan through the domain wall. For large enough power we can study DWE regions adjacent to domain interiors, where the directions of magnetic moments are nearly parallel and are representative of moments direction in the domain interior.

Another possible way of distinguishing between the DWC and DWE signals is to make use of the differences between the nuclear relaxation rates. Since the relaxation of the DWC signal is much faster than the DWE signal, measurement at large pulse separation removes the DWC signal but leaves the DWE signal, e.g., the La resonance in $La_2Fe_{14}B$, section 7.9.

A feature of zero applied field NMR worth noting is that the spectrum depends on the mutual directions of B_e, which usually follows the local magnetization, and the principal axes of the EFG tensor, which are rigidly coupled to the crystal lattice. The spectra of polycrystalline samples are therefore equivalent to those of single crystals.

2.3. Measurement of NMR spectra

If a rf pulse of the correct power (a $\pi/2$ pulse) is applied to a magnetic system, the nuclear spins will precess about B_e. Slight differences between fields at each nucleus result in different precession rates and a rapid decay in the resonant signal. However, the application of a second rf pulse (a π pulse) can effectively flip the precessing moments through 180° and reverse the sense of the precession, causing the appearance of a spin-echo. If the first pulse is at time $t = 0$ and the second pulse is at time $t = \tau$, then an echo with an integrated signal amplitude A will appear at a time $t = 2\tau$, with A given by the expression

$$A(2\tau) = A(0)e^{-2\tau/T_2}, \tag{2.7}$$

where T_2 is the transverse relaxation time. The receiver of the spectrometer will have a dead time (T_d) that is typically around 5 μs. The maximum NMR signal available is therefore

$\sim A(2T_d)$ and may be below the level of detection against thermal noise if $A(0)$ is too small or $2T_d/T_2$ is large.

The importance of the two terms depends upon the particular nucleus under investigation and the temperature range of interest. The ^{57}Fe isotope for example has a large T_2, but it is present in only 2.2% abundance in natural Fe (see table 1.1), so $A(0)$ is small, whereas for Sm, the signal is strong at 4.2 K, but T_2 becomes too short above about 10 K for $A(2T_d)$ to be detected.

The value of $A(0)$ for a given nucleus is proportional to B_e^2/T, where T is the absolute temperature, though the measured value of $A(0)$ may also depend on enhancement effects, as discussed above. T_2 may change according to $T_2T \approx$ constant, as is found in Fe for example, or it may decrease exponentially with temperature as in Sm. Most of the NMR measurements discussed here have been carried out at or below 4.2 K.

A rf pulse of angular frequency ω_0 and width $\sim \tau_\omega$ will excite nuclei with resonant frequency within $\sim 1/\tau_\omega$ about ω_0. In most of the spectra discussed here, the spread of NMR frequencies, even within a single quadrupole split line, is greater than $1/\tau_\omega$. The spectrum is therefore constructed point by point by sweeping the frequency. The spin-echo signal is usually measured with "quadrature detection". At each point, the spin echo signal is split and measured with respect to a reference signal and with respect to the reference signal phase-shifted by $\pi/2$. Although the spin echo signal is at an unknown phase ϕ to the reference signal, the integrated amplitudes S_ϕ and $S_{(\phi+\pi/2)}$ can be combined to form a phase insensitive quantity

$$S = (S_\phi^2 + S_{(\phi+\pi/2)}^2)^{1/2}, \tag{2.8}$$

which is then plotted as a function of frequency. A good discussion of the relation between the driving pulses and the NMR spectrum has been given by Walstedt (1992).

3. $RE_2TM_{17}A_x$

The host compounds of the form $RE_2TM_{17}A_x$ crystallize in the rhombohedral structure for the light rare earths and in the hexagonal structure for Y and the heavy rare earths. The compounds of primary interest here are with RE = Nd, Sm, Y, Gd, Er and Tb, with TM = Fe and Co, and with A = N, C and H.

The reaction of RE_2TM_{17} with N_2, NH_3 or H_2 gases to form interstitial nitrides and hydrides, preserves the structure of parent materials. The interstitial carbides of hexagonal host compounds prepared by melting, however, show a preference for the rhombohedral structure, if the concentration of interstitial carbon is high enough (Coene et al. 1990; Sun et al. 1990). A schematic diagram of unit cells of both structures is presented in fig. 3.1. Both structures contain four inequivalent TM sites denoted as 12k, 12j, 6g, 4f in the hexagonal form, which correspond to 18h, 18f, 9d, 6c, respectively, in the rhombohedral compound. RE elements occupy a single site 6c in the rhombohedral and two sites: 2b and 2d in the hexagonal structure. Neutron diffraction experiments have shown that in the interstitial carbides prepared from melt the C atoms randomly occupy the interstitial positions 9e (6h) (Helmholdt and Buschow 1989). The hydrogen atoms locate at 9e and 18g (6h and 12i)

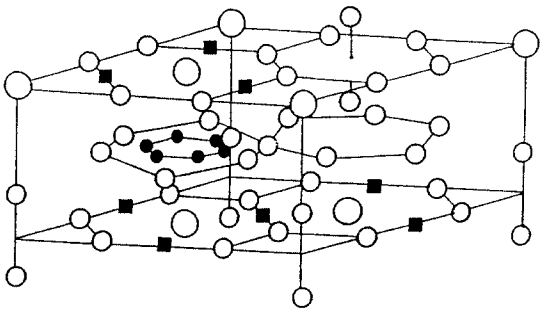

Fig. 3.1. A building block of rhombohedral or hexagonal $RE_2TM_{17}A_x$. Large empty circles = RE. Small empty circles = TM. Filled squares = A 9e(6h) sites. Filled circles = A 18g(12i) sites.

sites (Isnard et al. 1992a). The 9e (6h) sites can be completely filled, whereas the maximum of 1/3 of the total number of the 18g (12i) sites can be occupied only, which leads to the maximum content of the interstitial hydrogen, $x = 5$ (Isnard et al. 1992b).

There is some controversy concerning the location of nitrogen atoms at the interstitial positions in the material. According to Isnard et al. (1992c), nitrogen locates entirely at 9e (6h) interstitial positions to a maximum content of $x = 3$ in the formula $RE_2TM_{17}N_x$ when prepared in N_2 gas atmosphere. For the hydrogen pre-treated samples nitrided in ammonia, Brennan et al. (1994), reported the nitrogen content of 4 and concluded that some 18g or 3b sites are occupied in addition to the 9e sites. Some authors reported the nitrogen contents x as large as 5 (Uchida et al. 1993), 8 (Wei et al. 1993), or even 10 (Uchida et al. 1992). Most of the interstitial sites, e.g., 3a or 3b, are too small to contain the relatively large N atoms (Christodoulou and Takeshita 1993), however, the location of some N atoms at the 18g (12i) sites (as concluded by Wei et al. (1993) and Yan et al. (1993) from neutron diffraction measurements) in addition to the 9e (6h) site occupation seems to be feasible. The number of 9e (6h) and 18g (12i) NN positions to RE sites is 3 and 6, respectively.

Further work on $RE_2TM_{17}A_x$ is also discussed in sections 4, 5 and 6. In section 4, effects on the properties of Sm_2Fe_{17} based magnets prepared by different processing routes is reviewed. Section 5 contains a discussion of the effects of the addition of Nb, used to reduce the content of unwanted α-Fe and in section 6, the results of some important measurements on the influence of pressure on $RE_2TM_{17}N_x$ systems are reviewed.

Structural and magnetic properties of interstitial nitrides, carbides and hydrides have been surveyed by Fujii and Sun (1995). A summary reviewing important data on HFF and CEF parameters of $Sm_2Fe_{17}N_x$ and related compounds is given in table 3.1.

3.1. ^{89}Y resonance

3.1.1. $Y_2Fe_{17}C_x$

The NMR spectra measured on the samples prepared by co-melting appropriate amounts of the constituents have been reported by Kapusta et al. (1990, 1991). The spectra, shown in fig. 3.2, consist of three well resolved satellite lines, in addition to the ^{89}Y ($I = 1/2$ – no quadrupole splitting) line of the host compound. The lines at 42, 37, 29 and 17 MHz

TABLE 3.1

Hyperfine and crystal electric field parameters of $Sm_2Fe_{17}N_x$ and related compounds.

Sample	x	ν (MHz)	$\lvert B_e \rvert$ (T)	Parameters for EFGs[a,b,c,d]	Notes	Source
					^{89}Y NMR, $T = 4.2$ K,	
$Y_2Fe_{17}C_x$	0	42.5	20.4		interstitial neighbors $n = 0$	Kapusta et al. (1991)
	0.4	42.4	20.3		in the 6h sites	
		36.8	17.6		$n = 1$	
		29.0	13.9		$n = 2$	
	1	41.9	20.1		$n = 0$	
		36.5	17.5		$n = 1$	
		28.3	13.6		$n = 2$	
		17.0	8.1		$n = 3$	
	1.5	41.9	20.1		$n = 0$	
		36.0	17.3		$n = 1$	
		27.6	13.2		$n = 2$	
		16.7	8.0		$n = 3$	
			6.1		Theory, 2b	Beuerle and Fahnle (1992)
			8.0		2d	
$Y_2Fe_{17}N_x$	1.5, 2.8	42.7			$n = 0$, vanishes for $x = 2.8$ annealed at 460°C 6 h	Zhang et al. (1995d)
		36.5			$n = 1$	
		29.3			$n = 2$	
		26.5			$n = 3$	
	~2.5	42.4	20.3			Kapusta et al. (1991)
		36.4	17.4			
		29.6	14.2			
		26.2	12.6			
			13.2		Theory, 2b	Beuerle and Fahnle (1992)
			14.7		2d	
$Y_2Fe_{17}CN_x$	~1.5	41.9	20.1			Kapusta et al. (1991)
		36.5	17.5			
		29.4	14.1			

TABLE 3.1 (Continued)

Sample	x	ν (MHz)	$\lvert B_e \rvert$ (T)	Parameters for EFGs[a,b,c,d]	Notes	Source
		24.7	11.8			
		20.0	9.6			
		15.4	7.4			
$Y_2Fe_{17}H_x$	1.6	41.5	19.9			
	5.5	40.9	19.6			
	4.7	63.5			^{1}H NMR, 1.3 K	Zhang et al. (1995c)
		47.1			weak for $x < 3.0$	
			24.4		Theory, 2b	Beuerle and Fahnle
			21.4		2d	(1992)
					At Fe sites, $T = 4.2$ K	
Y_2Fe_{17}			31.1		– from Fe Mössbauer	Kapusta et al. (1992a)
			21.02		^{89}Y NMR hexagonal 2b	Shen et al. (1996a)
			20.16		hexagonal 2d	
			20.40		rhombohedral 6c	
					$[\delta \ln \mathrm{Be}/\delta P(10^{-4}\ \mathrm{kbar}^{-1})]$	Armitage et al. (1989)
		42.60	20.4		rhomb/hex, $[17.4 \pm 1.0]$	(range 0–5 kbar)
		42.59	20.4		rhomb, $[13.8 \pm 0.2]$	
			24.4		Theory, 2b	Beuerle and Fahnle
			21.4		2d	(1992)
		42.5	20.4		^{89}Y NMR	Kapusta et al. (1990)
$Y_2Fe_{17}N_x$		45–55			^{57}Fe NMR	Zhang et al. (1995d)
		46.7			attributed to α-Fe	
	~2.5		35.0		– from Fe Mössbauer	Kapusta et al. (1992a)
	2.6	8.5			^{14}N NMR 1.3 K – both	Zhang et al. (1995c)
		11.7			hexagonal and	and (1995a)
					rhombohedral	
	0–2.8				As x: $0 \rightarrow 2.8$, $n = 0$	
					weakens, and $n = 1, 2, 3$	
					strengthen	
		42.9(42.7)			^{89}Y 4.2 K, $n = 0$	

TABLE 3.1 (Continued)

Sample	x	ν (MHz)	$\lvert B_e \rvert$ (T)	Parameters for EFGs[a,b,c,d]	Notes	Source
		36.5			weaker in rhomb. $n = 1$	
		29.3			$n = 2$	
		26.5			weaker in rhomb. $n = 3$	
Sm_2Fe_{17}			30.5		– from Fe Mössbauer 4.2 K	Kapusta et al. (1992a)
$Sm_2Fe_{17}N_x$	~2.5		35.5		4.2 K	
			35.5		77 K	
			33.5		Room temperature	
Sm_2Fe_{17}		568.30	323.28	12.017^a, -262.58^b	^{147}Sm NMR, 4.2 K	
		468.50	323.28	3.467^a, -262.14^b	^{149}Sm	
		568.0	323.1	12^a, -262^b, -13^c, -66^d(0N)	^{147}Sm	Kapusta et al. (1994)
		567.64	322.93	11.99^a		(1996d)
$Sm_{10.2}Fe_{85.8}Nb_4$		567.25	322.71	11.78^a	Induction/arc melt, cast 1.	
$Sm_{10.2}Fe_{85.8}Nb_4$		567.21	322.69	11.78^a	Induction and arc melting, cast 2.	
$Sm_{10.2}Fe_{85.8}Nb_4$		567.18	322.67	11.88^a	By HDDR + N_2	
$Sm_{9.5}Fe_{80.5}Nb_{10}$		567.46	322.83	11.95^a		
					For the nitrided systems below: -205^d(2N), -309^d(3N).	Kapusta et al. (1994) and Kapusta et al. (1996a)
$Sm_2Fe_{17}N_x$	0.4	565.8	321.9	10.4^a, -227^b, 22^c	main septet	
	1.2	566.0	322.0	10.2^a, -223^b, 26^c		
		575.0	327.1	7.7^a, -168^b, 81^c	weak septet	
	2	566.3	322.1	10.2^a, -223^b, 26^c	main septet*	
	2.5	582.2	331.2	5.875^a, -127.21^b, $+122^c$		

TABLE 3.1 (Continued)

Sample	x	ν (MHz)	$\lvert B_e \rvert$ (T)	Parameters for EFGs[a,b,c,d]	Notes	Source
	~2.5	582.20	331.19	5.875[a], −128.37[b]		Kapusta et al. (1992a)
		480.00	331.19	1.667[a], −126.04[b]	^{149}Sm	
	1.5	466.5		2.9[a]	NH_3 at 425°C, 72 h (0N)	Kapusta et al. (1996c)
		480–500			Unresolved line. (3N)	
	1.5	466.5		2.88[a](0N)	Sample in He	
				2.41[a](1N)	250°C for 3 weeks.	
				1.99[a](2N)		
$Sm_2Fe_{17}H_x$	2.9	569.1	323.7	11.9[a], −260[b]	^{147}Sm	Kapusta et al. (1996b)
	4.6	568.2	323.2	11.0[a], −240[b]	main septet	
		564.7	321.2	11.2[a], −245[b]	weak septet	
Nd_2Fe_{17}		508.5	353.4	4.01[a], −94.1[b]	^{145}Nd	Kapusta et al. (1995a)
$Nd_2Fe_{17}N_x$	3	555.0	385.7	1.64[a], −38.5[b]		
$Gd_2Fe_{17}N_x$	2.5	10.7			^{14}N, 1.3 K	Zhang et al. (1995c)
$Lu_2Fe_{17}N_x$		10.2				Kapusta et al. (1992e)
		9			Shoulder.	
					^{57}Fe-close lines, 4.2 K:	
		50			13 Fe NN (4f, 4e, 12j sites)	
		43			10 Fe NN (12j, 12k, 6g)	
		38.5 & 40			9 FeNN (dipolar split 12k)	
		34			8 Fe NN (6g, 12k).	
			31.04		Centre of gravity of spectrum ⟨|HFF|⟩.	
$Lu_2Fe_{17}C_x$	0.6		31.61			
$Lu_2Fe_{17}N_x$			32.04			
$Lu_2Fe_{17}H_x$			30.11			

TABLE 3.1 (Continued)

Sample	x	ν (MHz)	$\lvert B_e \rvert$ (T)	Parameters for EFGs[a,b,c,d]	Notes	Source
$Y_2Co_{17}C_x$	0.8	15.7	7.53		^{89}Y	Kapusta et al. (1992c)
		18.4	8.82			
		21.0	10.07			
		102	10.1		^{59}Co	
		152	15			
		158	15.6			
		178	17.6			
		192	19.0			
		202	20.0			
$Y_2Co_{17}H_x$	3.3	18.4	8.82		^{89}Y	
		21.0	10.07			
		101	10.0		^{59}Co	
		158	15.6			
		179	17.7			
$Y_2Co_{17}N_x$	1.4	10.5	5.03		^{89}Y	
		11.9	5.70			
		13.7	6.57			
		15.4	7.38			
		18.3	8.77			
		18.9	9.06			
		21.0	10.07			
		102	10.1		^{59}Co	
		148	14.7			
		173	17.1			
		180	17.8			
		191	18.9			
		201	19.1			
		219	21.7			

TABLE 3.1 (Continued)

Sample	x	ν (MHz)	$\lvert B_e \rvert$ (T)	Parameters for EFGs[a,b,c,d]	Notes	Source
	High	10.5	5.03		^{89}Y, (x corresponds to	
		11.9	5.70		a 5% lattice expansion).	
		13.4	6.42			
		16.7	8.01			
		18.2	8.72			
		103	10.2		^{59}Co	
		149	14.8			
		174	17.2			
		180	17.8			
		190	18.8			
Nd_2Co_{17}		563	391		^{145}Nd	Streever (1977)
		905		7[a], -700 (ergs/cm^{-2})[d]	^{143}Nd	
		563.7	391.7	3.88[a]	^{145}Nd (6c)	Kapusta et al. (1997a)
		160–200			^{59}Co structured signal.	
$Nd_2Co_{17}H_x$	3.6	560.0	389.3	3.8[a]	^{145}Nd 3H(9e), 1H(18g).	
		563.7	391.7		3H(9e).	
		160–200			^{59}Co structured signal.	
		210–230			Spurious phase.	
$Nd_2Co_{17}N_x$	3	556	386.4	0.37[a]	^{145}Nd	
		894.5	386.4	0.71[a], 8.7[b]	^{143}Nd	
		100			^{59}Co – large τ.	
		130				
		150				
		175				
Sm_2Co_{17}		602	342.5	9.3[a]	^{147}Sm – strong	Figiel et al. (1991)

TABLE 3.1 (Continued)

Sample	x	ν (MHz)	$\lvert B_e \rvert$ (T)	Parameters for EFGs[a,b,c,d]	Notes	Source
$Sm_xY_{2-x}Co_{17}$	0.1	597.6	339.95	11.82[a], −91[d](6c)	strong	Kapusta et al. (1993a)
		601.0	341.89	9.38[a]	weak	
	0.2	601.2	342.00	9.37[a]	strong	
		597.6	339.95	11.82[a]	weak 1	
		603.1	343.08	9.30[a]	weak 2	
		606.6	345.07	8.97[a]	weak 3	
	0.4	601.5	342.17	9.33[a]	strong	
		603.4	343.25	9.27[a]	weak 1	
		606.8	345.19	9.00[a]	weak 2	
	1	601.8	342.34	9.28[a]	strong	
$Nd_xY_{2-x}Co_{17}$	0.1	560.85	389.74	4.02[a], −94.3[b],	^{145}Nd	Kapusta et al. (1996f)
	0.2	560.25	389.32	4.04[a], −94.7[b]		
	0.4	560.98	389.83	4.06[a], −95.2[b],		
	0.8	561.31	390.06	4.06[a], −95.2[b]		
	1.2	561.78	390.39	4.03[a], −95.4[b]		
	1.6	562.67	391.01	3.97[a], −93.1[b]		
	1.8	563.16	391.35	3.95[a], −92.6[b]		
	2	563.70	391.72	3.88[a], −91.0[b]		
$Y_2(Co_{1-x}M_x)_{17}$					^{59}Co NMR, 77 K M = Cu, Al	Inomata (1981)
	0–0.15	152			Cu: $x \geqslant 0.15$. Al: $x \geqslant 0.05$	
		166			Cu: All x. Al: All x.	
		174			Cu: All x. Al: $x \geqslant 0.05$	
		191–196			Cu: $x \geqslant 0.05$. Al: $x = 0.05$	
		203			Cu: All x. Al: $x = 0$.	
		216–220			Cu: $x \leqslant 0.1$. Al: $x \geqslant 1.5$	

Comments and values apply to lines on and below the note. The symbol * terminates validity where required for clarity.
a = $\Delta\nu_q$ [MHz], b = V_{ii} [10^{20} V m^{-2}], c = V_{ii}(latt) [10^{20} V m^{-2}], d = A_0^2 [Ka$_0^{-2}$] – units (unless otherwise specified).

were assigned to the Y sites with 0, 1, 2 and 3 C atoms respectively. A comparison of the corresponding B_e values shows that for the 1C configuration B_e is reduced by 12% with respect to the value in Y_2Fe_{17}. For the 2C and 3C environments it is reduced by 31% and 60%, respectively. As B_e on yttrium largely originates from transferred hyperfine fields, there must be a large C NN influence on the valence electron distribution and polarisation at the RE site. Note that the inelastic neutron scattering measurements of Loewenhaupt et al. (1995, 1996) have shown similar reductions of the molecular field coefficient n_{Gd-Fe} caused by one or two carbon atoms neighbouring to a Gd atom. The reduction was found to be 12% and 29% for the Gd sites with 1C and 2C neighbours, respectively. The main contribution to the molecular field coefficient n_{RE-Fe} in these materials has been associated with the RE-5d electrons and with polarisation via 3d–5d hybridisation (Brooks et al. 1989). The transferred HFF on the RE nucleus has been found to arise from the 6s and 5d valence electrons (Y-5s and 4d, respectively) (Coehoorn and Buschow 1993). The almost identical changes in the transferred hyperfine field and in the molecular field coefficient showed the same reduction ratio for the 6s and 5d (Y-5s and 4d) electron polarisation. This reflects the reduction of n_{RE-Fe}, caused by the presence of carbon neighbours.

In fig. 3.2 the line at 46 MHz, appearing in the spectra of the carbides, has the broad echo shape characteristic of an ^{57}Fe signal from a spurious α-Fe phase. The ^{57}Fe signals from

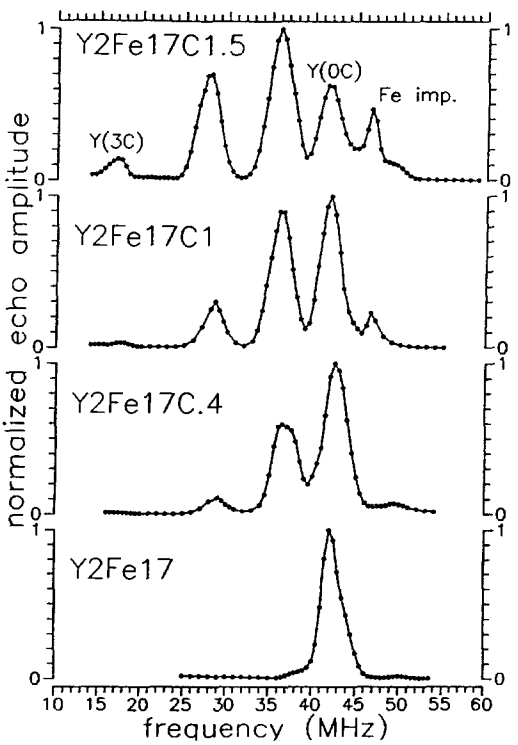

Fig. 3.2. ^{89}Y spin-echo NMR spectra of $Y_2Fe_{17}C_x$ at 4.2 K. After Kapusta et al. (1991).

the Fe sites in the structure are overlapped by the much stronger signal of ^{89}Y. However, the Fe resonance line at about 50 MHz has been detected in all the samples.

3.1.2. $Y_2Fe_{17}N_x$

The ^{89}Y NMR measurements have been reported by Kapusta et al. (1991) and Zhang et al. (1995a). The ^{57}Fe and ^{14}N study has been carried out by Zhang et al. (1995b, 1995c). Kapusta et al. (1991) measured ^{89}Y spectra of four samples prepared by heating the Y_2Fe_{17} powder in an atmosphere of N_2. The amount of absorbed nitrogen x was estimated from the pressure difference before and after the reaction for the first three samples. With increasing reaction time between subsequent samples, approximate values of $x = 0.5$, 1.2 and 2.5 were obtained. However, the distribution of nitrogen was found to be non-uniform, as discussed below.

The ^{89}Y spectra, shown in fig. 3.3, consist of four resonance lines; the main line at 42 MHz and the lines at 36, 30 and 26 MHz, respectively. As with the carbon containing compounds, the 36, 30 and 26 MHz lines have been assigned to Y atoms with 1N, 2N and 3N atoms as NNs, respectively. The set including 1N, 2N and 3N lines has been found to increase in intensity with x with respect to the 0N line. The intensity ratio within the set,

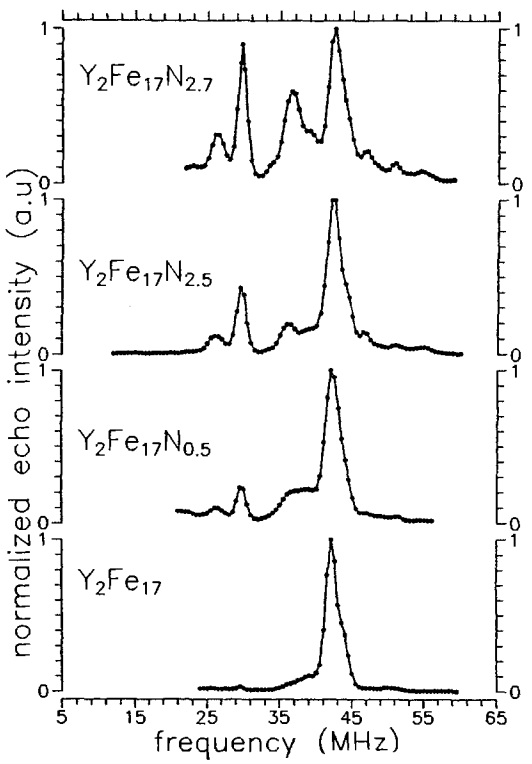

Fig. 3.3. ^{89}Y spin-echo NMR spectra of $Y_2Fe_{17}N_x$ at 4.2 K. After Kapusta et al. (1991).

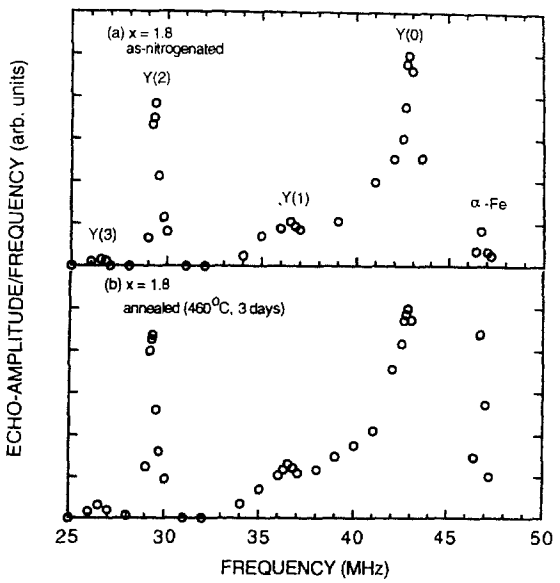

Fig. 3.4. ^{89}Y spin-echo NMR spectra of $Y_2Fe_{17}N_{1.8}$ at 4.2 K, (a) as nitrogenated and (b) annealed at 460°C in a vacuum for 3 days. The annealing leaves the N atom distribution unchanged but precipitates some α-Fe. After Zhang et al. (1995a).

however, remained unchanged, reflecting the growth of the nitrided outer shells of grains. As X-ray diffraction has shown, the samples contained both the expanded nitride phase and the unnitrided phase. Most of the 0N intensity can therefore be attributed to the unnitrided cores of the grains. The intensity of the 2N line is the largest and the relative intensities within the set of 1N, 2N and 3N lines are approximately constant with x. This indicates that, during the growth of the nitrided outer shell, the nitrogen concentration in it was approximately constant, with $2 < x < 2.5$. The ^{89}Y spin-echo spectra of a set of the samples of different nitrogen content, treated by regrinding and subsequently vacuum annealing, have been studied by Zhang et al. (1995a). The measurements did not show any noticeable changes of the spectrum on annealing, except for an increase in the amount of α-Fe. As an example, the spectra of the sample with $x = 1.8$ are shown in fig. 3.4. A similar pattern to that found by Kapusta et al. (1991), with a pronounced 0N line for the samples with low x, was also found by Zhang et al. (1995b). Zhang et al. (1996a) proposed a model of nitrogen diffusion which involves two states of nitrogen atoms in the lattice; a free type and a trapped type. In this model the free nitrogen atoms diffuse towards the interface between the nitrided shell and the unnitrided core where they become trapped. The diffusion can proceed only in nitrogen atmosphere and at appropriately high temperatures. Once the nitrogen atmosphere is removed, the interface stops its advance towards the centre of the grain and the nitriding is stopped. The nitrided region is characterised by an x value which is slightly larger than 2, neither x nor nitrogen distribution normally change on annealing. Some of 5% of the total amount of nitrogen absorbed in the material can, however, desorb

on vacuum annealing. The amount of interstitial nitrogen was found to be smaller than the total value of x deduced from the mass enhancement or from the change of nitrogen pressure. The applicability of the above model seems to be limited. Some authors have reported existence of Sm_2Fe_{17} nitrides with intermediate nitrogen content $0 < x < x_{max}$ based on results of X-ray diffraction (Brennan et al. 1994), AC susceptibility (Katter et al. 1992), and electron microscopy studies (Edgley et al. 1994). The results of the samarium NMR study of Sm_2Fe_{17} nitrides (Kapusta et al. 1994), confirm this finding, as will be discussed in more detail in the section 3.3.

In the carbon containing compounds the reduction of the Y HFF per NN atom decreases with the increasing number of neighbours, while in the nitrides an opposite tendency is observed. For the environments with three N neighbours the reduction compared to the 2N and 1N environments is especially small. This finding and a double peak structure of the ^{14}N resonance line reported by Zhang et al. (1995c), led the authors to conclude that, in the yttrium environments with three nitrogen neighbours, two of the nitrogen atoms occupy the octahedral sites 6h and one occupies the rhombohedral site 12i. This is in contrast to the carbides, in which carbon exclusively occupies the rhombohedral sites. The evaluation of dipolar fields, produced by neighbouring Fe moments on the 6h and 12i sites, shows that they vary by more than 2.5 T (11 MHz), with the magnetisation direction in the basal plane. This causes a large splitting or broadening of the ^{14}N resonance line, and can lead to difficulties in the interpretation of the nitrogen resonance (Zhang et al. 1995c). In view of these difficulties and problems in the interpretation of the neutron diffraction results for the hexagonal structure, because of the disorder of the RE and the Fe dumb-bell sites, the conclusion that the tetragonal sites are partially occupied by nitrogen (Jaswal et al. 1991; Zhang et al. 1995c), must be treated with some caution.

3.1.3. $Y_2Fe_{17}CN_x$

The ^{89}Y NMR spectrum presented in fig. 3.5 has been reported by Kapusta et al. (1991). It consists of 6 lines at 42, 36, 30, 25, 20 and 15 MHz, respectively. The results are consistent with those for carbides and nitrides. Thus, the 36 MHz line is assigned to Y atoms either with 1C or with 1N as NN, the 30 MHz line to either 2C or 2N as NN and 25 MHz line to either 3N or 2N + 1C as NN. The 20 MHz line is thought to arise from 2C + 1N NN and the 15 MHz line from a 3C configuration. The environments with 2C and 1N + 1C contribute to the shoulder at about 27 MHz. The lowering of the Y HFF in 2C + 1N and 1C + 2N environments, calculated by summation of the contributions per one atom in 3N and 3C configurations of $Y_2Fe_{17}C$ and $Y_2Fe_{17}N_x$, provides the expected resonance lines at 19.5 MHz and 22 MHz respectively, very close to that observed experimentally. From this it may be concluded that C and N independently influence the Y HFF in mixed environments, resulting in an additive contribution from nitrogen and carbon neighbours.

3.1.4. $Y_2Fe_{17}H_x$

The ^{89}Y spectra have been reported by Kapusta et al. (1991), fig. 3.6, and Shen et al. (1996b), fig. 3.7. The spectra of the hydrides reported in both papers do not show the satellite pattern observed for the nitrides or carbides. Only one Y resonance line has been detected, see fig. 3.6 after Kapusta et al. (1991). The line was found to broaden from a

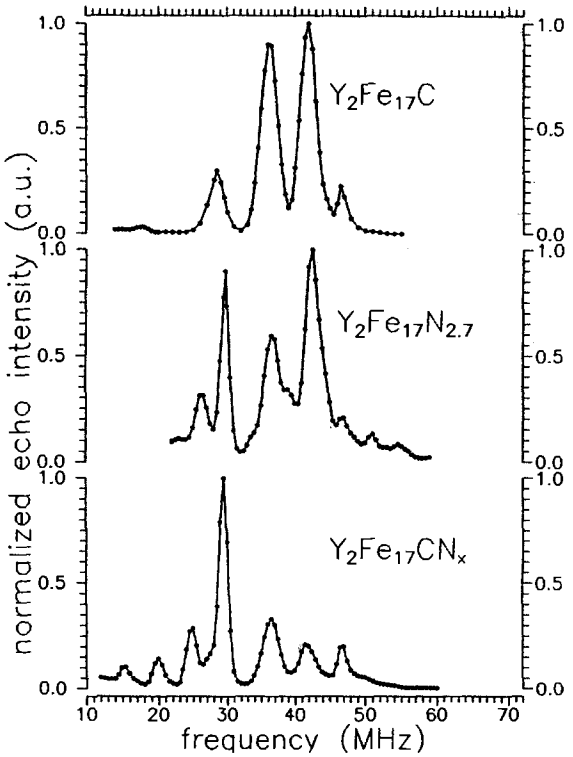

Fig. 3.5. ^{89}Y spin-echo NMR spectra of $Y_2Fe_{17}CN_x$ at 4.2 K. After Kapusta et al. (1991).

2.7 MHz linewidth for $x = 0$ to 4.0 MHz and 4.2 MHz for $x = 1.6$ and 5.5, respectively. The resonant frequency shifted from 42.5 to 41.5 and 40.9 MHz for $x = 0$, 1.6 and 5.5, respectively. A larger shift was observed by Shen et al. for the fully hydrided sample, see fig. 3.7. After removal of hydrogen from the sample the resonance line was found to return to the position observed for the host compound. It can be concluded that hydrogen only has a slight global influence on the Y HFF. The Y–H distance is 2.5 Å for the hydrogen 6h sites and 2.35 Å for the 12i sites. As found by Isnard et al. (1992b), the 6h sites are filled for $x < 3$ and up to two of the 12i sites can be occupied, leading to a maximum $x = 5$. The excess over $x = 5$ in the values of x equal to 5.5 given by Kapusta et al. (1991), and 5.8 given for the hydride of Gd_2Fe_{17} by Shen et al. (1996b), is possibly related to the formation of a spurious rare earth hydride phase.

The ^1H spectra reported by Zhang et al. (1995c), and Shen et al. (1996b), as shown in fig. 3.8, contained two distinct peaks. The authors discussed possible line assignments and they attributed the upper line corresponding to a HFF of 1.5 T to hydrogen in the octahedral sites and the lower line with a HFF of 1.1 T to hydrogen in the tetrahedral sites. The results indicated that the tetrahedral sites may already begin to be occupied for hydrogen contents of $x < 3$. As discussed in the preceding paragraph (section 3.1.2), when the easy magnetisation direction is in the basal plane, there is a splitting of the octahedral

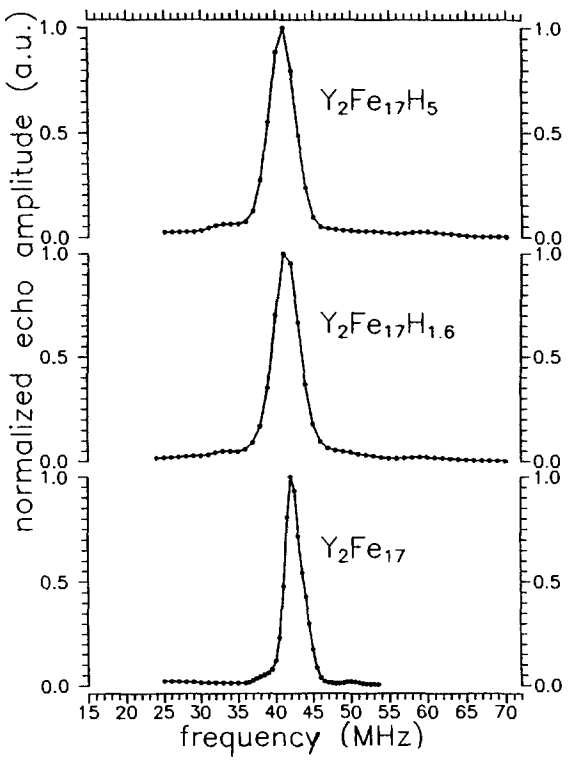

Fig. 3.6. ^{89}Y spin-echo NMR spectra of $Y_2Fe_{17}H_x$ at 4.2 K. After Kapusta et al. (1991).

sites into magnetically inequivalent sites. The difference in the values of the largely dipolar B_e at these inequivalent hydrogen sites is 2.5 T. This difference may provide an alternative explanation for the presence of the two peaks, observed by Zhang et al. (1995c) and Shen et al. (1996b). Further studies are needed to clarify the nature of the ^1H spectra.

3.1.5. $Y_2Fe_{17-y}Co_yC_x$

The ^{89}Y NMR measurements of the samples prepared by co-melting with $x = 0$ and 0.8 have been reported by Kapusta et al. (1991). The main line at 18.5 MHz ($B_e = 8.9$ T) as well as a weaker line at 21 MHz ($B_e = 10.1$ T) appearing in Y_2Co_{17} sample according to Figiel et al. (1976), were assigned to Y resonance in rhombohedral and hexagonal structures, respectively. The additional weak line observed in $Y_2Co_{17}C_{0.8}$ at 15.7 MHz ($B_e = 7.5$ T) has been attributed to Y environments with one carbon NN, as shown in fig. 3.9. The corresponding relative decrease of HFF equals 14.5% and is very close to that observed in the Fe based compound (13%) which indicates that the relative influence of carbon on the polarisation of the yttrium valence electrons is similar in both systems. The difference in magnitude of the HFF decrease between compounds containing different 3d elements must have its origin in the 3d moment interaction rather than in the Y valence electron distribution alone.

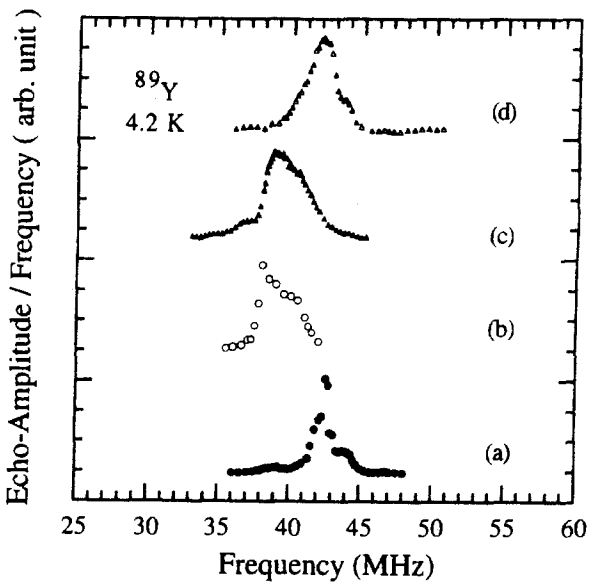

Fig. 3.7. ^{89}Y spin-echo NMR spectra of $Y_2Fe_{17}H_x$ at 4.2 K, for (a) $x = 0$, (b) $x = 3$, (c) $x = 4.7$ and (d) $x = 3$ (annealed). After Shen et al. (1996b).

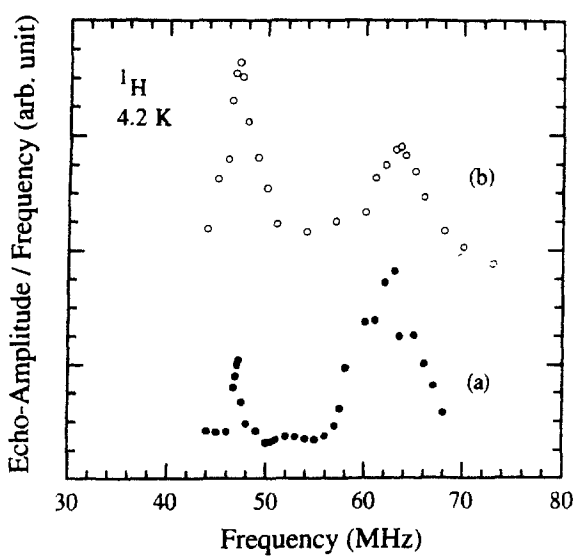

Fig. 3.8. ^1H spin-echo NMR spectra of $Y_2Fe_{17}H_x$ at 4.2 K, for (a) $x = 3$ and (b) $x = 4.7$. After Shen et al. (1996b).

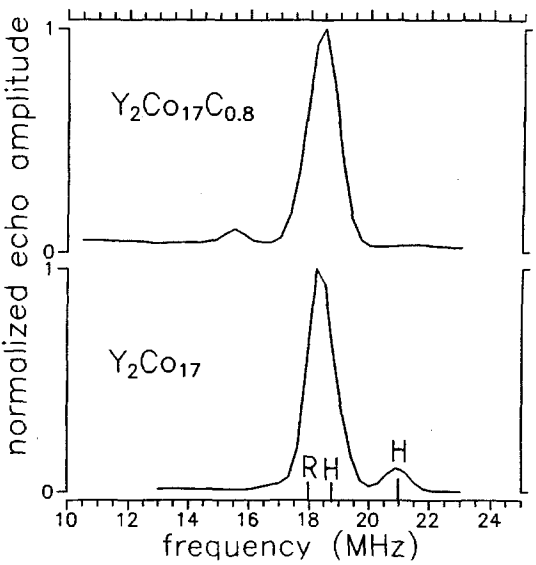

Fig. 3.9. ^{89}Y spin-echo NMR spectra of $Y_2Co_{17}C_x$ at 4.2 K. After Kapusta et al. (1991).

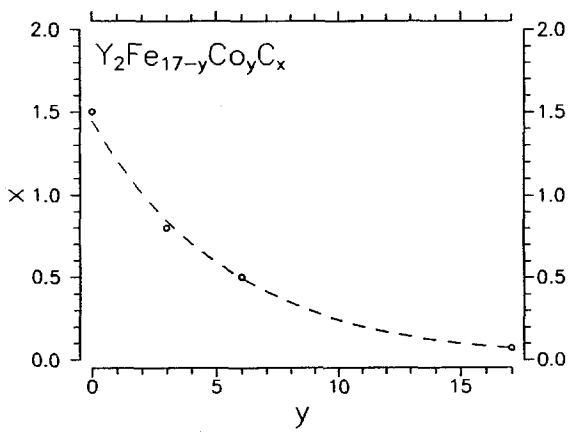

Fig. 3.10. Concentration of interstitial C in $Y_2Fe_{17-y}Co_yC_x$ at 4.2 K. After Kapusta et al. (1991).

The relative intensity of the 15.7 MHz line to the main line is 7%. Assuming a random distribution of C atoms over the 6h sites and using the binomial distribution function, the authors arrive at a true concentration of interstitial carbon of $x = 0.07$. This is an order of magnitude smaller than the nominal value of $x = 0.8$, deduced from weight measurements. This shows that only a slight amount of carbon can be introduced into the Y_2Co_{17} lattice by co-melting. It is worth mentioning here that the accuracy of determination of interstitial carbon content is of order of $x = 0.01$, which is far beyond the accuracy that can be achieved with the neutron diffraction technique.

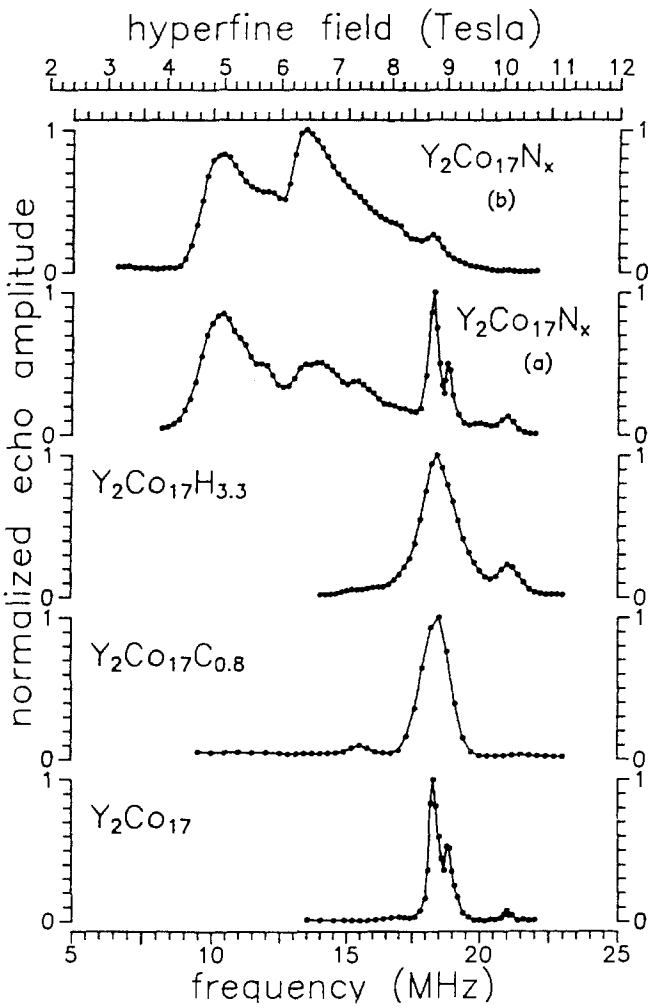

Fig. 3.11. ^{89}Y spin-echo NMR spectra of $Y_2Co_{17}A_x$ at 4.2 K, with concentrations determined by NMR in (a) of $x = 1.6$ and in (b) of $x = 2.0$. After Kapusta et al. (1992c).

From NMR, samples with nominal compositions $Y_2Fe_6Co_{11}C_x$ ($x = 0.8$) and $Y_2Fe_3Co_{14}C_x$ ($x = 0.8$), were estimated to have true compositions with $x = 0.8$ and $x = 0.5$, respectively (Kapusta and Riedi 1995). These values can be treated as solubility limits for the compounds prepared from the melt. With increasing Co concentration the solubility of carbon decreases from $x = 1.5$ for Y_2Fe_{17} down to $x = 0.07$ for Y_2Co_{17}, fig. 3.10.

3.1.6. $Y_2Co_{17}N_x$, $Y_2Co_{17}H_x$

A similar evolution of the ^{89}Y spectra with x to that in the iron based compound is reported by Kapusta et al. (1992c), fig. 3.11. However, the effect of broadening of the lines

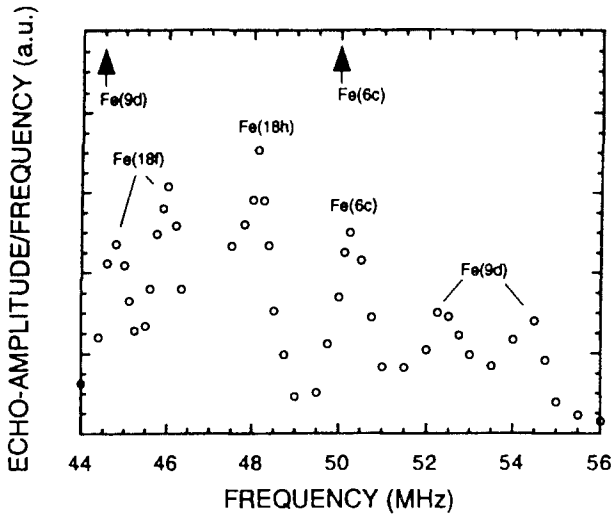

Fig. 3.12. ^{57}Fe spin-echo NMR spectra of $Y_2Fe_{17}N_{2.8}$ at 1.3 K. Arrows indicate ^{57}Fe resonances for Fe(6i) and Fe(9d) from the parent Y_2Fe_{17}. After Zhang et al. (1995b).

is stronger, especially for the nitride. The real concentration of the interstitial nitrogen evaluated on the basis of satellite line intensities in the NMR spectrum is close to $x = 2$. For the measured sample of $Y_2Co_{17}H_{3.3}$, as in $Y_2Fe_{17}H_x$, no local influence of hydrogen on the yttrium hyperfine field is observed. The resonance line broadens, but remains at the same position as in Y_2Co_{17}.

3.2. *^{57}Fe resonance*

The ^{57}Fe signal in $Y_2Fe_{17}A_x$, where it does not overlap with the much stronger Y signal or with the ^{57}Fe signal from α-Fe impurities, has been observed at 50 MHz ($B_e = 36.2$ T) by Kapusta et al. (1991), fig. 3.5. The position of this line in carbides was found to be independent of x and no other Fe signals appeared at higher frequencies. This line was assigned to the 4f (6c) dumb-bell site.

In the nitrogen containing compound an additional Fe resonance line at 55 MHz ($B_e = 40.0$ T) appeared, in good agreement with Mössbauer results of Zhou et al. (1993), whereas the 50 MHz line still remained at the same frequency. A significant decrease of the NMR enhancement factor indicated a considerable influence of nitrogen on local magnetic anisotropies of Fe sites. Such changes are not observed in the carbon and hydrogen containing interstitial compounds.

A better resolved ^{57}Fe spectrum has been reported for $Y_2Fe_{17}N_{2.8}$ by Zhang et al. (1995b), fig. 3.12. The authors proposed assignments of the six ^{57}Fe lines observed in the 44–55 MHz range from $Y_2Fe_{17}N_{2.8}$ to specific Fe sites in the compound. Single lines corresponding to the 6c (4f in the hexagonal structure) and 18h (12k) sites were suggested, whereas two pairs of lines were attributed to the 9e (6g) and 18f (12i) sites respectively. The unchanged position of the 6c (4f) dumb-bell site has been related by the

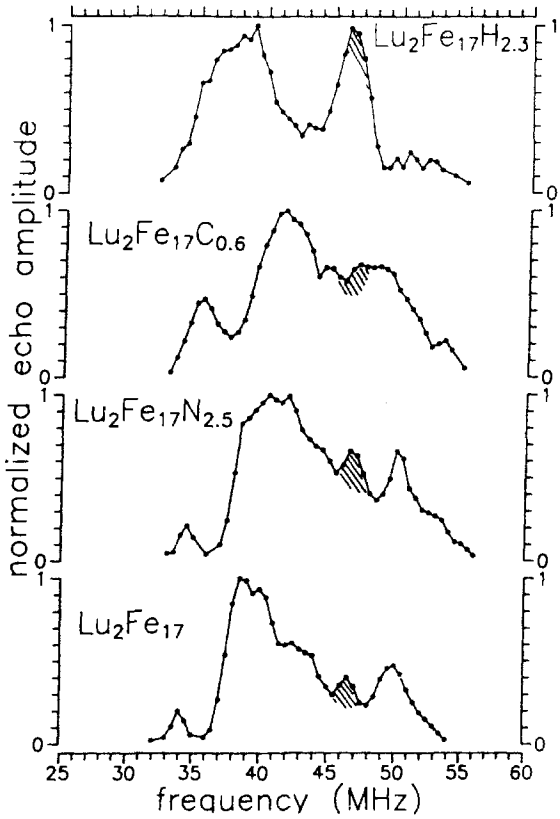

Fig. 3.13. ^{57}Fe spin-echo NMR spectra of $Lu_2Fe_{17}A_x$ at 4.2 K. After Kapusta et al. (1992e).

authors with unchanged distances of Fe atoms neighbouring the 6c site. These assignments were confirmed by the neutron diffraction study by Kajitani et al. (1993). The assignments correspond to the following order of the absolute values of the hyperfine fields: $B_e(g) < B_e(f) < B_e(k) < B_e(i)$. This, however, is not consistent with that obtained from a Mössbauer study by Hu et al. (1991), where $B_e(f) < B_e(g) < B_e(i) < B_e(k)$ was reported. Also the values of HFF given by Zhang et al. (1995b) are much higher than those obtained from Mössbauer measurements. Thus, the question arises whether the ^{57}Fe spectrum shown contains all the Fe resonance lines, or whether it is possible that some of the lines overlap with the strong yttrium signal.

The ^{57}Fe spectra of $Lu_2Fe_{17}A_x$ have been reported by Kapusta et al. (1992e), fig. 3.13. Polycrystalline samples prepared in the same way as yttrium containing compounds were measured. In the real structure of Lu_2Fe_{17} a statistical distribution of the Lu atoms and the Fe dumb-bells (4f) has been found, Givord et al. (1972). This leads to a splitting of the HFF values at the Fe sites making the comparison of results with those for the Y-containing compounds difficult. The average HFF has been found to increase more in the nitride than the carbide, but to decrease for the hydride.

Two competing mechanisms have to be taken into account in analysing the Fe HFF changes; the magnetovolume effect and the local influence of the interstitial atom via bonding effects. The former mechanism leads to an increase of magnetic moments (and HFFs) as the lattice expands, whereas the latter causes a decrease. Thus, in the hydride, where the lattice expansion per one interstitial atom has been found to be about three times smaller than in the nitride, the local influence appears to be dominant, in contrast to the carbide and nitride. It is worth noting here, that a similar decrease of the average hyperfine field upon hydriding was found in Mössbauer measurements for $Y_2Fe_{17}H_{2.7}$ by Qi et al. (1992).

3.3. *^{147}Sm and ^{149}Sm resonance*

3.3.1. *$Sm_2Fe_{17}N_x$*

The host compound Sm_2Fe_{17} possesses a planar anisotropy due to the anisotropy of the Fe sublattice which overcomes the preference of the Sm sublattice to align along the c-axis. The introduction of nitrogen gives rise to a dramatic increase of the CEF potential at the Sm site, leading to a strong enhancement of the anisotropy of the samarium sublattice. This results in the large uniaxial magnetic anisotropy of $Sm_2Fe_{17}N_x$ making it suitable for permanent magnet application. NMR measurements on two groups of finely powdered samples, prepared as described by Katter et al. (1991, 1992) (A) and Buschow et al. (1990) (B) were reported by Kapusta et al. (1994) and (1992b), respectively. The samples (A) were prepared with concentrations of nitrogen in the range $0 < x < 3$. Sample (B) was fully nitrided with $x = 2.5$. The ^{147}Sm spectra of $Sm_2Fe_{17}N_x$, $x = 0, 0.4, 1.2, 2.0$, samples (A), and $x = 2.5$, sample (B), are shown in fig. 3.14. The ^{149}Sm and ^{147}Sm spectra were found to be consistent with each other. The observed sets of quadrupole septets (the nuclear spin, I, for both Sm isotopes is $7/2$) have been assigned to Sm 6c sites with different numbers of nitrogen neighbours. The samples (A) have linewidths 5 times larger than those of (B). This difference was attributed to much larger local inhomogeneities as a result of a fine pulverisation of samples (A).

Measurements on the aligned samples and as a function of applied field have shown that the observed signal in $Sm_2Fe_{17}N_x$ originates from the DWE. The directions of the Sm moments were found to depend on x. It was found that they were perpendicular to the c-axis for Sm_2Fe_{17}, parallel to the c-axis for $x > 1.2$ and tilted from the c-axis for $x = 0.4$. The main septet for $x = 0.4$ was ascribed to Sm with 0N, the change of its quadrupole splitting with respect to Sm_2Fe_{17} could be ascribed to the change of easy magnetisation direction (EMD). A septet with a lower signal intensity was attributed to Sm with 2N neighbours and the septet in the fully nitrided sample (B) to Sm with 3N neighbours. A deviation of the intensities of the septets from those expected for a random distribution of nitrogen may have arisen from large differences in the individual site anisotropies and a consequent smearing of the signal of the low symmetry Sm sites, with 1 and 2 N atoms as nearest neighbours.

The slight change of HFF with magnetic moment direction for the 0N site indicates that Sm preserves its fully polarised state with $J_z = J = 5/2$. As the lattice EFG (eq. (2.6)) at the 0N site is axially symmetric with its V_{zz} along the c-axis, Laplace's equation can be applied, i.e.:

$$V_{cc}(\text{latt}) = -2V_{pp}(\text{latt}), \tag{3.1}$$

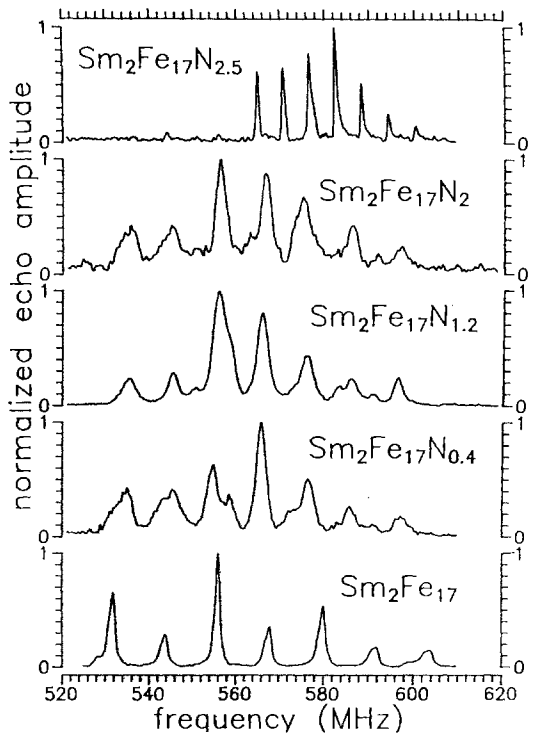

Fig. 3.14. ^{147}Sm spin-echo NMR spectra of $Sm_2Fe_{17}N_x$ at 4.2 K. After Kapusta et al. (1994?).

where 'c' and 'p' stand for c-axis and c-plane (i.e., perpendicular to the c-axis) components. V_{zz}(4f) and V_{cc}(latt) were obtained using eq. (2.6) and from the measured quadrupole splitting for Sm_2Fe_{17} and for the 0N septet in the nitrided samples. The slightly smaller quadrupole splitting of the 0N septet observed for $x = 0.4$ than for $x = 1.2$ indicated a deviation of EMD from the c-axis. The angle between the c-axis and EMD for $x = 0.4$ was estimated to be 26°.

For 0N sites the V_{cc}(latt) value of 26×10^{20} V/m^2 was obtained, and for the 3N environments V_{cc}(latt) as large as 122×10^{20} V/m^2 is measured. The latter value agrees, within experimental error, with Gd Mössbauer measurements for $Gd_2Fe_{17}N_x$, V_{cc}(latt) = 126×10^{20} V/m^2 (Dirken et al. 1991).

For V_{zz}(4f) a value of -249×10^{20} V/m^2 was obtained, about 20% larger than the absolute value of 211×10^{20} V/m^2 derived from an atomic beam experiment (Bleaney 1972), indicating a contraction of the 4f shell in the compound as compared with that of a free atom.

The lowest order term of the CEF interaction corresponds to the interaction of the quadrupole moment of the 4f electron shell with the EFG produced mainly by the asphericity of the 6p and 5d shells of the parent atom. This asphericity arises from the presence of neighbours in the lattice (Coehoorn and Buschow 1991). The CEF coefficient A_2^0 used

in the CEF formalism is proportional to this EFG. The lack of a strict relation between the EFG at the nucleus and the EFG exerted by the 4f shell, necessitates the use of the approximation:

$$A_2^0 = -\frac{D}{4} e V_{cc}(\text{latt}). \tag{3.2}$$

Taking the value of 1/320 for the coefficient D, as obtained from a comparison of a Mössbauer spectroscopy study with bulk magnetic data for Gd_2Fe_{17} and other RE-3d intermetallics (Gubbens et al. 1989), the CEF coefficients A_2^0 for the Sm sites with different numbers of nitrogen neighbours in the compound can be determined. They change from $-66\ \text{K}\,a_0^{-2}$ for 0N to $-309\ \text{K}\,a_0^{-2}$ for 3N atoms as nearest neighbours to the Sm site, where a_0 is the Bohr radius. The value of $-242\ \text{K}\,a_0^{-2}$ reported for A_2^0 in $Sm_2Fe_{17}N_3$ from extrapolation of bulk anisotropy data by Li and Coey (1992), is about 20% smaller than the value of A_2^0 for Sm with 3N derived from the nuclear magnetic resonance spectra.

The A_2^0 value derived from ^{166}Er Mössbauer measurements on $Er_2Fe_{17}N_{2.7}$ by Gubbens et al. (1991a) and Moolenaar et al. (1991), amounts to $-400\ \text{K}\,a_0^{-2}$, 30% larger than the above value derived from NMR for $Sm_2Fe_{17}N_3$. However, the value obtained by Gubbens et al. (1991b), from ^{169}Tm Mössbauer measurements for $Tm_2Fe_{17}N_{2.7}$ amounts to $-300\ \text{K}\,a_0^{-2}$. Thus, there is an agreement within experimental limits between the values obtained from Mössbauer and NMR experiments.

3.3.2. $Sm_2Fe_{17}C_x$

The ^{147}Sm and ^{149}Sm NMR spin echo spectra and the spin echo decays of the samples with $x = 0$, 0.5, 1 and 3 have been reported by Kapusta et al. (1996a), fig. 3.15. Carbides $Sm_2Fe_{17}C_x$ with $x = 0.5$ and 1 were prepared by arc melting and the carbide with $x = 3$ was prepared by heating a fine powder of Sm_2Fe_{17} in acetylene. These samples, together with a Sm_2Fe_{17} sample were measured. Similar changes in the Sm spectra to those for the nitrides have been observed upon carbon uptake. A change of quadrupole splitting of the 0C septet between Sm_2Fe_{17} and $Sm_2Fe_{17}C_{0.5}$ has been attributed to the change of EMD between the compounds. A conical magnetic structure was found for $Sm_2Fe_{17}C_{0.5}$ at 4.2 K, with the EMD slightly tilted from the c-axis. This was similar to the magnetic structure of $Sm_2Fe_{17}N_{0.4}$ (Kapusta et al. 1994). The quadrupole splittings of the septets have been attributed to the Sm environments with 1C and 3C NN, corresponding to the EFG values V_{cc}(latt) of $64 \times 10^{20}\ \text{V m}^{-2}$ and $137 \times 10^{20}\ \text{V m}^{-2}$, respectively.

Relating V_{cc}(latt) and A_2^0 as above, the values of $-162\ \text{K}\,a_0^{-2}$ for the 1C site and $-350\ \text{K}\,a_0^{-2}$ for the 3C site were obtained. The change of A_2^0 caused by 1C neighbour was determined to be $-96\ \text{K}\,a_0^{-2}$, whereas 3C neighbours changed A_2^0 by $-284\ \text{K}\,a_0^{-2}$, which corresponds to $-95\ \text{K}\,a_0^{-2}$ per one C neighbour. Therefore it can be concluded that the contributions to A_2^0 from the individual carbon neighbours are additive. For the Sm_2Fe_{17} nitrides the contribution to A_2^0 expressed per one N neighbour was found to increase with increasing number of N neighbours. Gubbens et al. (1991a) have derived from ^{166}Er Mössbauer measurements for $Er_2Fe_{17}C_1$ the A_2^0 value of $-290\ \text{K}\,a_0^{-2}$, which, as with the nitrides, is much larger than the $-162\ \text{K}\,a_0^{-2}$ of $Sm_2Fe_{17}C_1$.

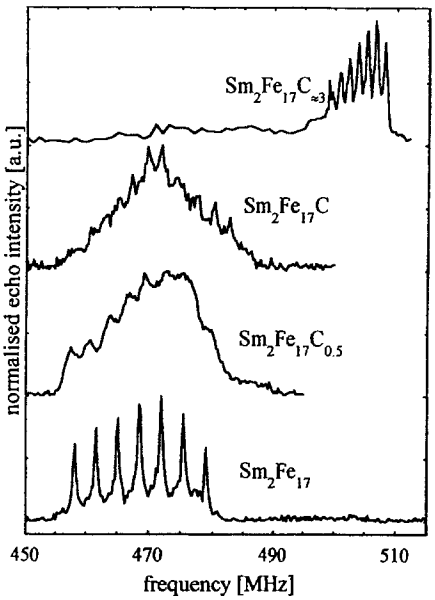

Fig. 3.15. ^{149}Sm spin-echo NMR spectra of $Sm_2Fe_{17}C_x$ at 4.2 K. After Kapusta et al. (1996a).

From a value of $V_{cc}(\text{latt}) = 122 \times 10^{20}$ Vm^{-2}, a corresponding value for A_2^0 of -309 K a_0^{-2} was derived for the 3N sites in the Sm_2Fe_{17}. This is smaller in magnitude than for the 3C sites in the carbides, implying that a hypothetical $Sm_2Fe_{17}C_3$ would have a larger magnetocrystalline anisotropy than $Sm_2Fe_{17}N_3$. Unfortunately, however, as with $Y_2Fe_{17}C_x$ (see sections 3.1.1 and 3.1.5), the solubility limit for $Sm_2Fe_{17}C_x$ prepared from the melt is $x \leqslant 1.5$.

The difference in HFF between 1C and 0C sites is 7.7 T. For the 3C sites the change in HFF of 23.9 T, which when expressed per one carbon neighbour corresponds to a change in HFF by 8 T. This is slightly larger than for the 1C sites. The result is consistent with that for the Y_2Fe_{17} carbides (Kapusta et al. 1990), where the magnitude of carbon influence on the yttrium HFF, per one C neighbour, was also found to increase with increasing number of nearest neighbour C atoms.

3.3.3. $Sm_2Fe_{17}H_x$

The ^{147}Sm NMR spectra of the $Sm_2Fe_{17}H_x$ ($x = 0$, 2.9, 4.6) series at 4.2 K are reported by Kapusta et al. (1996b). Powder samples prepared in the same way as for the Y_2Fe_{17} hydrides were measured. Hydrogen enters the octahedral 9e and the tetrahedral 18g sites, as shown in the neutron diffraction study on the isostructural rhombohedral $Nd_2Fe_{17}H_x$ (Isnard et al. 1992b). Hydrogen atoms were found to fill the 9e sites first, up to their full occupation corresponding to the formula $Sm_2Fe_{17}H_3$, and subsequently to enter the 18g sites. The maximum concentration of hydrogen in the compound corresponds to the formula $Sm_2Fe_{17}H_5$, i.e., the maximum number of H atoms occupying the 18g sites is two per formula unit.

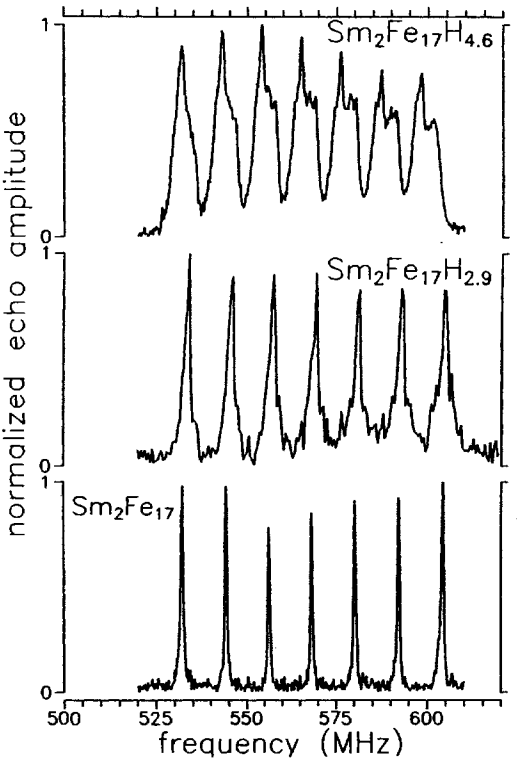

Fig. 3.16. ^{147}Sm spin-echo NMR spectra of $Sm_2Fe_{17}H_x$ at 4.2 K. After Kapusta et al. (1996b).

The ^{147}Sm spectra of Sm_2Fe_{17} and $Sm_2Fe_{17}H_{2.9}$, fig. 3.16 after Kapusta et al. (1996b), consist of a single septet with very similar central line positions and line separations for both samples. The quadrupole splitting and the HFF, which were obtained from the spectra in the same way as for $Sm_2Fe_{17}N_x$, are 11.9 MHz and 323.7 T (central frequency 569.1 MHz) for $Sm_2Fe_{17}H_{2.9}$, which is very close to the values of 12.0 MHz and 323.1 T (central frequency 568.8 MHz) for the host Sm_2Fe_{17}. For the $Sm_2Fe_{17}H_{4.6}$, two overlapping septets with different quadrupole splittings and HFFs have been found to appear. This feature can be explained in terms of a partial occupation of the 18g sites. At such a concentration, all (3 per formula unit (f.u.)) 9e sites are filled, and the remaining hydrogen atoms (1.6 H per f.u.) are distributed over the 18g sites (2 per f.u. available to hydrogen). Using the formula of binomial distribution for 1.6 H atoms randomly distributed over these two available 18g sites, the probabilities of finding 0, 1 or 2 hydrogen at 18g sites as nearest neighbours to a Sm atom are 4%, 32% and 64%, respectively. The last two values are close to the relative intensities of the two septets in the NMR spectrum of $Sm_2Fe_{17}H_{4.6}$. Thus, the septet with larger intensity can be attributed to the Sm sites with 3H atoms at the 9e and 2H atoms at the 18g NN sites. The septet with the smaller intensity can consequently be assigned to the Sm sites with 3H atoms at the 9e sites and 1H atom at the 18g sites. As

the Sm sites with 3H atoms at the 9e sites and 0H atoms at the 18g sites have an order of magnitude smaller population, the corresponding septet in the spectrum is not resolved.

A significant influence of H 18g and a slight influence of H 9e on the lattice EFG can be explained in terms of the strength of the bonding effects being strongly distance dependant. According to the above results the influence of H on the RE 5d and 6p electron population becomes apparent for the Sm–H(18g) distance of 2.35 Å but is negligible for the Sm–H(9e) separation of 2.5 Å.

3.3.4. $Sm_xY_{2-x}Co_{17}$

The spin echo spectra of ^{147}Sm and ^{149}Sm of $Sm_xY_{2-x}Co_{17}$ at zero applied field have been reported by Kapusta et al. (1993a). The spectra show a step-like change of quadrupole splitting and hyperfine field between the samples with $x = 0.1$ and 0.2. The effect is attributed to change of EMD from the c-plane (perpendicular to the c-axis) for $x = 0.1$ to the c-axis for $x = 0.2$. From the difference in the quadrupole splittings between the samples, the 4f electron contribution to the EFG was evaluated. It was found that $V_{zz}(4f) = -240 \times 10^{20}$ V/m^2. This was very close to that for the Fe based samples, as discussed in section 3.3.1. The V_{cc}(latt) of 35.7×10^{20} V/m^2 and the corresponding A_2^0 of -91 Ka_0^{-2} were derived. The A_2^0 value was found to be 40% larger than the corresponding value deduced from NMR for Sm_2Fe_{17}.

3.4. ^{143}Nd and ^{145}Nd resonance

3.4.1. $Nd_2Fe_{17}N_x$

The rhombohedral Nd_2Fe_{17} sample and its nitride, with x close to 3 prepared as described by Buschow et al. (1990), were measured by Kapusta et al. (1995a). The ^{145}Nd spectra are presented in fig. 3.17. The spectrum of Nd_2Fe_{17} consists of a quadrupole septet (nuclear spin of ^{145}Nd $I = 7/2$) corresponding to the single Nd crystallographic site in the structure. A single septet with a shoulder at the low frequency side is also obtained for the nitride and assigned to the Nd sites with three nitrogen NN.

As with to the Sm based series (Kapusta et al. 1994), the value of B_e for the Nd sites with nitrogen neighbours was found to be higher than that of the non-nitrided sample. Since for Sm and Nd, B_{orb} is dominant and antiparallel to the transferred HFF, the effect is consistent with that for the Y-based compounds.

The planar anisotropy of the Nd and other rare earths with the second order Stevens factor $\alpha_J < 0$, strengthens with nitriding. Thus, from the difference between quadrupole splittings between Nd_2Fe_{17} and the nitride the EFG change caused by the three nitrogen neighbours ΔV_{pp}^{3N}(latt) can be obtained. The value of ΔV_{cc}^{3N}(latt) was found to be 111.2×10^{20} V/m^2, close to that of 96×10^{20} V/m^2 obtained in the Sm based nitride (Kapusta et al. 1994). This indicates that the change of A_2^0 caused by 3N neighbours is only weakly dependent on the RE type in these compounds.

3.4.2. $Nd_2Co_{17}A_x$

The ^{145}Nd and ^{143}Nd NMR spin-echo spectra have been reported by Streever (1977). The central frequencies of 563 MHz and 905 MHz were obtained, respectively. The

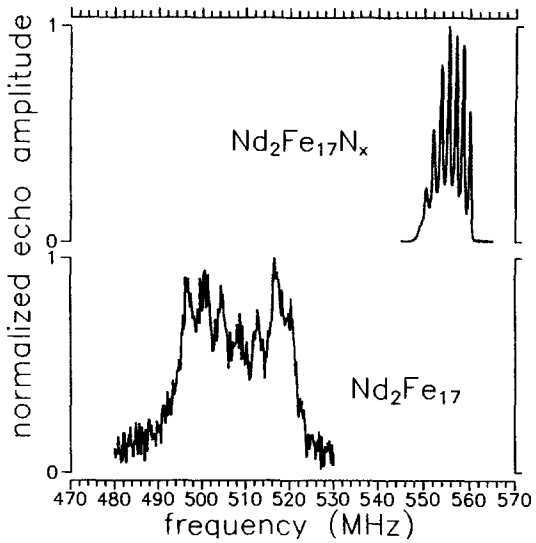

Fig. 3.17. ^{145}Nd spin-echo NMR spectra of $Nd_2Fe_{17}N_x$ at 4.2 K. After Kapusta et al. (1995b).

quadrupole splitting of ^{143}Nd of 7 MHz was derived. The ^{145}Nd and ^{143}Nd NMR spin-echo spectra and echo decays for Nd_2Co_{17} and its interstitial nitride $Nd_2Co_{17}N_3$ and hydride $Nd_2Co_{17}H_{3.6}$ have been measured by Kapusta et al. (1997a). The ^{145}Nd spectrum of Nd_2Co_{17}, fig. 3.18 shows a well resolved septet corresponding to a single Nd site 6c of the compound. The quadrupole splitting and the HFF for this material was found to be 3.88 MHz and 391.7 T (central frequency 563.7 MHz), respectively. In the spectrum of the hydride the linewidths were much larger than in the host Nd_2Co_{17} and two septets could be distinguished. The overall quadrupole splitting determined from the line spacing was 3.8 MHz and B_e values of 391.7 T and 389.3 T (central frequencies 563.7 MHz and 560.0 MHz, respectively) were obtained. The ^{145}Nd spin echo decays show characteristic oscillations, fig. 3.19, caused by quadrupole interactions (Abe et al. 1966). The oscillation period τ_q was related to the quadrupole splitting ν_q by the equation $\nu_q\tau_q = 1$, giving $\nu_q = 3.66$ MHz for the hydride. The value is close to that obtained from the line spacing. A non-monotonic decay of the oscillations indicates presence of two quadrupole frequencies of very close values, corresponding to the presence of two septets in the spectrum. Assuming that 3 H atoms per f.u. occupy 9e sites and 0.6 H enters the two 18g sites, as with $Nd_2Fe_{17}H_x$, and using binomial distribution function the probabilities of 0.49, 0.42 and 0.09 for 0, 1 and 2 H 18g atoms as the NN to a Nd site were obtained. Thus, the upper septet has been assigned to the Nd sites with 3 H 9e neighbours and the lower septet has been assigned to the Nd sites with 3 H 9e and 1 H 18g sites. Hydrogen has only a slight influence on the Nd hyperfine parameters. When H occupies the 18g NN site, a decrease of quadrupole splitting of 0.1–0.2 MHz and a decrease of B_e by 2.4 T has been observed.

A single unresolved line has been obtained for both Nd isotopes in $Nd_2Co_{17}N_3$, corresponding to B_e of 386.4 T. The spectra of an aligned powder show a shift of the line to

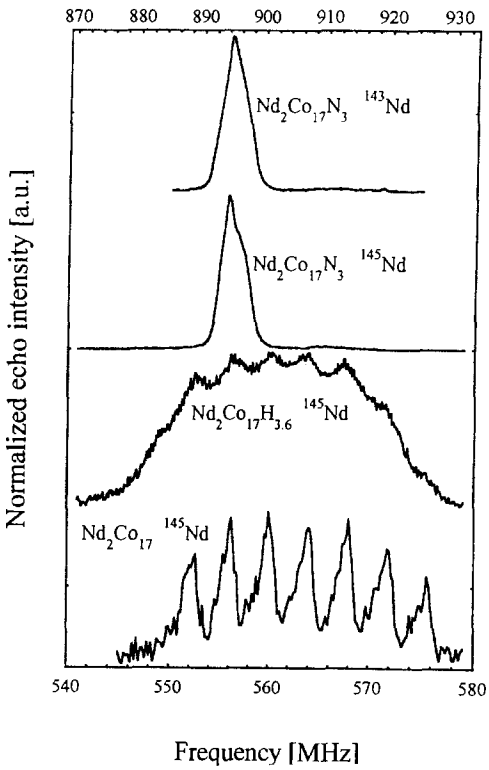

Fig. 3.18. ^{145}Nd and ^{143}Nd spin-echo NMR spectra of $Nd_2Co_{17}A_x$ at 4.2 K. The top frequency scale corresponds to the 143 isotope. After Kapusta et al. (1997a).

higher frequencies in an applied field. This shows that the hyperfine field of Nd is positive with respect to the magnetisation direction as expected from a parallel coupling of Nd and Co moments and a dominant positive orbital contribution of the 4f electron shell to the hyperfine field of Nd. The NMR signal is found to originate from Nd atoms in domain wall edges, where moments are nearly parallel to the applied field.

The values of ν_q determined from the quadrupole oscillations of spin echo decays were 0.37 MHz and 0.71 MHz for ^{145}Nd and ^{143}Nd, respectively, which corresponds to the EFG component along the hyperfine field direction, $V_{ii} = 8.7 \times 10^{20}\ V\,m^{-2}$. The easy magnetisation directions in the host compound, the hydride and the nitride, as with the Fe based compounds, were found to lie in the plane perpendicular to the crystallographic c-axis. The HFF, which arises predominantly from the 4f electron shell of the parent atom, is only slightly changed upon nitriding, again as in the Fe based compounds. Thus, it can be concluded that the spectroscopic state of the 4f shell is practically unchanged upon nitriding or hydriding and the contribution of the 4f shell to the EFG remains unchanged too. The difference of EFG between the nitride and the host Nd_2Co_{17} of $-82 \times 10^{20}\ V\,m^{-2}$ could then be attributed mainly to the influence of the nitrogen NN atoms. An analysis similar to that cited above for the Fe based compound has led to a value of the increase

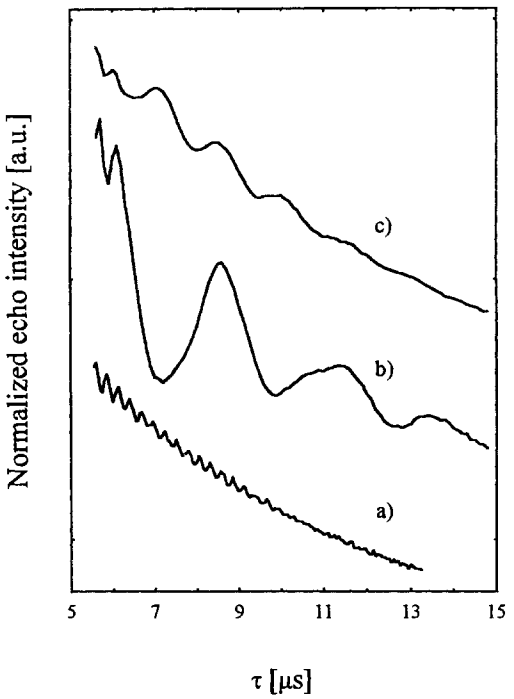

Fig. 3.19. ^{145}Nd spin-echo decay at 4.2 K showing characteristic quadrupole oscillations, (a) ^{145}Nd in $Nd_2Co_{17}H_{3.6}$ at 560 MHz, (b) ^{145}Nd in $Nd_2Co_{17}N_3$ at 554.5 MHz, and (c) ^{143}Nd in $Nd_2Co_{17}N_3$ at 892 MHz. After Kapusta et al. (1997a).

of the EFG component along the c-axis, ΔV_{cc}^{3N}(latt) of $164 \times 10^{20}\,V\,m^{-2}$. Mulder et al. (1992) derived the corresponding value of $149 \times 10^{20}\,V\,m^{-2}$ from a Mössbauer study of $Gd_2Fe_{17}N_x$. Relating the above V_{cc}^{3N}(latt) to A_2^0 gives a value as large as $-416\,K\,a_0^{-2}$ for Nd sites with three nitrogen atoms as NN. This is about 50% greater in magnitude than for the isostructural Fe based compound, $Nd_2Fe_{17}N_x$ (Kapusta et al. 1995a). The decrease of A_2^0 related to the hydrogen uptake in $Nd_2Co_{17}H_{3.6}$ was found to be 12–24 $K\,a_0^{-2}$, which is similar in magnitude to the effect of hydrogen in $Sm_2Fe_{17}H_{2.9}$, but of opposite sign (Kapusta et al. 1996b). In $Nd_2Co_{17}H_{3.6}$ the change of the EFG is related to the influence of hydrogen atoms at 18g sites (in the amount 0.6 H atom per f.u.) located along the c-axis direction. This is unlike in $Sm_2Fe_{17}H_{2.9}$ where only the 9e sites located in the plane perpendicular to the c-axis are occupied. Hydrogen atoms at the 9e site are expected to have a slight effect with the signs of the EFG and of A_2^0 opposite to those of the 18g sites.

3.5. ^{159}Tb resonance

The zero field NMR spectrum of ^{159}Tb in a mixed phase Tb_2Fe_{17} has been measured by Li et al. (1995), fig. 3.20. The spectra arising from the unique RE site in the rhombohedral phase and from the two inequivalent sites in the hexagonal phase have been distinguished.

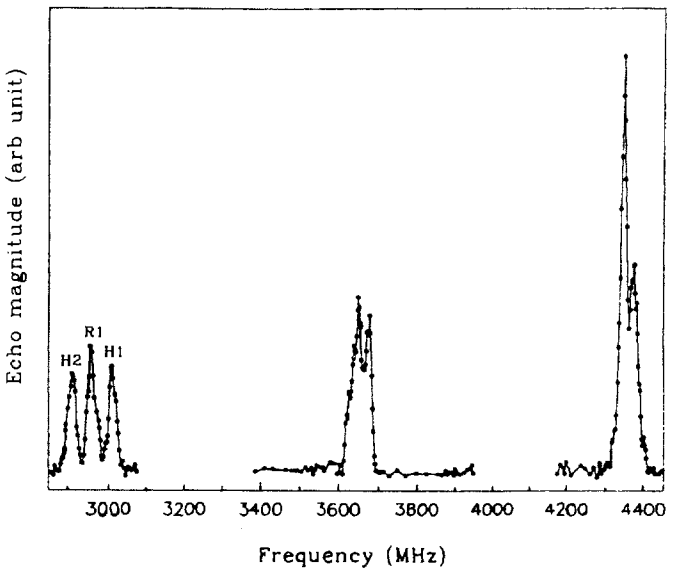

Fig. 3.20. ^{159}Tb spin-echo NMR spectra of Tb_2Fe_{17} at 4.2 K. After Li et al. (1995).

Different hyperfine magnetic and quadrupole parameters were found for these sites and the corresponding B_2^0 parameters were evaluated at 1.9 K and −0.6 K for the hexagonal sites and 0.9 for the rhombohedral site. Note that the values of the parameter for the hexagonal sites are of opposite sign. The error margin of the evaluation, however, exceeds 100%.

3.6. ^{59}Co resonance

The ^{59}Co spectrum of Nd_2Co_{17}, fig. 3.21, reported by Kapusta et al. (1997a), was found to consist of a structured signal at 160–200 MHz. A similar spectrum, with some additional weak resonances at lower frequencies and the signal of a spurious cobalt phase at 210–230 MHz was obtained for the hydride. The nitride showed a different spectrum, consisting of much narrower lines with different relaxation times T_2. Since the local symmetry of the Co sites is low, the anisotropy of HFF related to the anisotropic orbital contribution to the Co moment affects the ^{59}Co spectra (Streever 1979). It can give rise to separate resonance lines, corresponding to the local easy direction and local hard direction of the site. This was found to be the case for Y_2Co_{17} by Machowska (1993). At a large pulse separation, faster relaxing hard direction signals vanished, and the spectrum was found to consist of four peaks at 100 MHz, 130 MHz, 150 MHz and 175 MHz. A similar spectrum was obtained in an applied magnetic field for the aligned sample, but the lines were found to shift to lower frequencies with increasing field. The antiparallel alignment of HFF with respect to the magnetisation, dominated by Co moments, indicates a major core polarisation contribution to the Co HFF in the compound. The Co hyperfine fields in the nitride are different from those in the host compound. Furthermore, "hard direction signals" can be observed. This indicates that nitrogen has a significant influence on the Co HFF and on

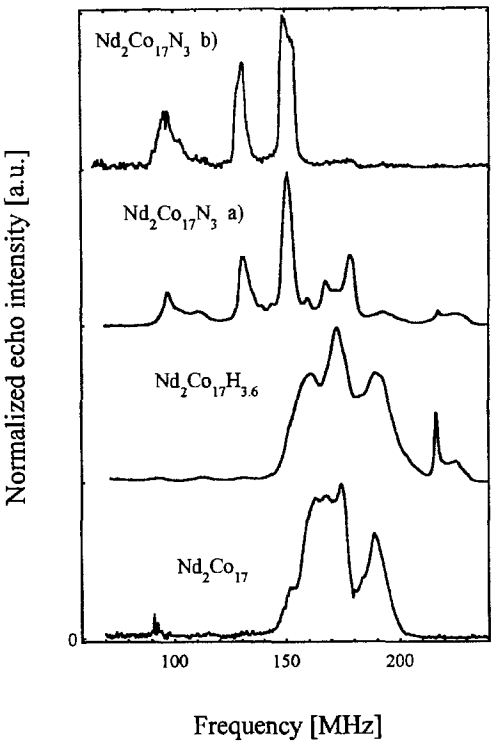

Fig. 3.21. ^{59}Co NMR spin-echo NMR spectra at 4.2 K of Nd_2Co_{17}, $Nd_2Co_{17}H_{3.6}$ and $Nd_2Co_{17}N_3$ with (a) pulses (0.2 and 0.4 μs) separated by $\tau = 10$ μs and (b) pulses (1.0 and 2.0 μs), $\tau = 300$ μs eliminates hard direction signals. After Kapusta et al. (1997a).

the magnetocrystalline anisotropy energy (MCAE) at the Co sites. This in turn affects the orbital contribution to the Co magnetic moments.

A similar behaviour of the ^{59}Co spectra in $Y_2Co_{17}A_x$ (A = N, C, H) was reported by Kapusta et al. (1992c). Nitrogen was found to cause much stronger changes of the spectrum of the host Y_2Co_{17}, than hydrogen. Since a tiny amount of carbon ($x = 0.07$) was found to enter the octahedral sites, a slight change observed in the spectrum of the carbide could be attributed to the change of crystallographic structure from hexagonal, for the host Y_2Co_{17}, to rhombohedral for the carbide, rather than to the influence of interstitial carbon atoms. Different spectra for the rhombohedral and hexagonal Y_2Co_{17} compounds have been reported by Figiel et al. (1977), Figiel and Jaszczewski (1980).

4. Sm_2Fe_{17} nitrides prepared under different conditions

As has been pointed out above, the nitrogenation of Sm_2Fe_{17} can result in a reorientation of the easy direction of from the c-plane (perpendicular to the c-axis) to the c-axis, with a consequent enhancement of permanent magnet properties. The nitrogenation process is

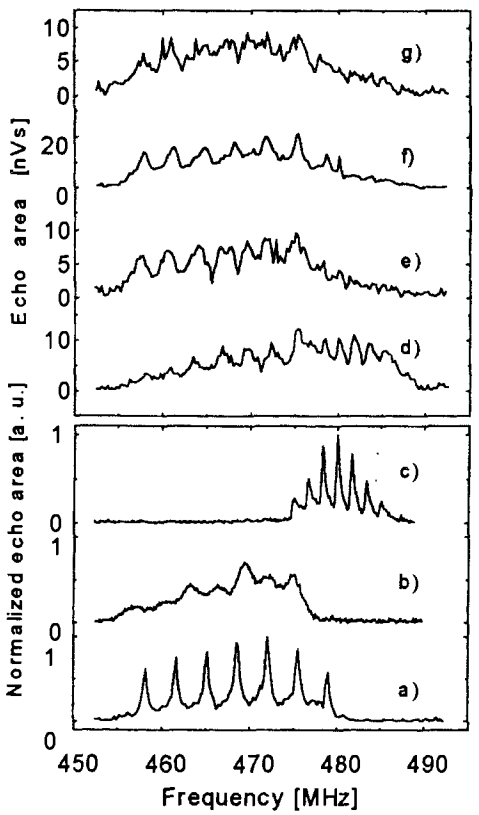

Fig. 4.1. ^{149}Sm spin-echo NMR spectra of $Sm_2Fe_{17}C_x$ at 4.2 K. Samples prepared under different conditions have differing amounts of unnitrided phase: (a) Sm_2Fe_{17}, (b) $x = 0.4$, (c) $x = 3$ in N_2 at 500°C, (d) in N_2 at 450°C, (e) and (f) in NH_3/H_2, (g) quasistatic in NH_3. After Kapusta et al. (1996c).

usually conducted in a N_2 or NH_3 atmosphere. The reaction with ammonia is much more vigorous than with nitrogen, which can lead to strains and microcracks in the $Sm_2Fe_{17}N_x$ grains. The nitriding process is a nonequilibrium phenomenon, with the equilibrium state corresponding to a decomposition into Sm nitrides and Fe. In order to inhibit the formation of the magnetically soft α-Fe phase, minimise decomposition, and avoid an inhomogeneous nitrogen distribution in the grains, nitriding times, temperature and pressure must be adjusted to a compromise. NMR can be used to study the diffusion processes and can provide information on the presence of spurious phases.

A study of the NMR spectra of ^{147}Sm and ^{149}Sm in Sm_2Fe_{17} powders nitrided under different conditions in NH_3 and N_2 has been reported by Kapusta et al. (1996c). The power dependence of the signal and the echo decays of the spin echo spectra in zero applied field, were measured to obtain information on the distribution of the nitrogen interstitials adjacent to Sm sites. The spectra, fig. 4.1, were found to correspond to the domain wall edges in the materials. The contributions to the overall spectrum from each of the sites

with 0 and 3 nitrogen neighbours were found to have the form of quadrupole split septets with their intensities depending on the nitriding conditions. Different conditions resulted in different nitrogen distributions and thus, in differences in the domain wall structure. For the samples nitrided in ammonia the septets corresponding to Sm sites with N neighbours were found to be smeared out, which led to the conclusion that these samples have many more defects in the atomic environments than those nitrided in nitrogen. It was also found that annealing in helium changed the distribution of nitrogen and the structure of domain walls in the material.

From the variations in the intensity of the septets on annealing, the changes of nitrogen distribution and the domain wall structure have been deduced. The 0N septet which appear in some samples nitrided for a short time revealed the presence of unnitrided material. In the samples nitrided for a short time, the unnitrided phase has its EMD in the basal plane. In the samples nitrided for a long time, the unnitrided phase has its EMD along the crystallographic c-axis. As little as 1% unnitrided material can be detected using NMR. Thus, the sensitivity of the NMR technique to the amount of the unnitrided phase is an order of magnitude higher than X-ray or TMA techniques. The application of a 7 T field had no effect on the zero field ^{149}Sm NMR signal of fine milled nitrided powders. This result means that the domain walls at the interface with unnitrided regions were not removed, even in such high fields.

5. Nb containing Sm_2Fe_{17} powders and their nitrides

The preparation process of Sm_2Fe_{17} has generally been accompanied by the formation of α-Fe. The presence of magnetically soft α-Fe grains results in a reduction of coercivity. One method of removing these nucleation sites is by the process of extended annealing, however, work of Platts et al. (1992), has led to an effective process of preparing α-Fe free as-cast material. The addition of $\sim$ 4% Nb suppresses the formation of α-Fe, resulting in the pure 2:17 phase, with traces of $NbFe_2$. For Nb contents of $\sim$ 10%, α-Fe cannot be detected by SEM or Mössbauer measurements. A small amount of Nb does enter the Sm_2Fe_{17}, but this results in a lattice expansion and a consequent enhancement of the magnetic properties (Sinan et al. 1995).

A ^{57}Fe, ^{93}Nb, ^{147}Sm and ^{149}Sm nuclear magnetic resonance study of powders for permanent magnet applications based on Sm_2Fe_{17} with 0%, 4%, and 10% Nb additions, and their nitrides has been reported by Kapusta et al. (1996d). Spin echo NMR spectra at zero applied field and the echo decays were measured in order to determine the sites of the elements in various phases of the materials. Two ^{93}Nb resonances observed were identified, corresponding to Nb in α-Fe and Nb in the 2:17 phase. The presence of Nb in the majority 2:17 phase was also found to be reflected in the linewidths and quadrupole splittings of the samarium spectra. The quantity of niobium entering the 2:17 phase was dependent on the amount of Nb added. This confirmed the results of the magnetic and metallographic studies (Platts et al. 1992; Sinan et al. 1995). On the basis of the Nb and Sm NMR signals a study was made (Kapusta et al. 1996d) of the difference between Nb distribution in the samples prepared using conventional and HDDR routes. The smallest Nb content in the 2:17 phase was found for the sample prepared using a HDDR route, which is consistent with the study of Gutfleisch et al. (1996).

From the intensities of the corresponding ^{57}Fe and ^{93}Nb lines the amount of α-Fe was estimated at 0.5% to 0.7%. A strong decrease of the signal of Nb in α-Fe, together with a shift of the corresponding ^{57}Fe line to lower frequencies observed upon nitriding was attributed to the occupation by nitrogen of the sites adjacent to Nb atoms. The NMR of ^{149}Sm spectra provided a sensitive probe used to monitor the degree of nitrogenation of the majority 2:17 phase. For a sample in which the nitrogenation was incomplete, it was presumed that the 5% unnitrided material was located in grain interiors. The results were found to be consistent with those obtained for the Nb free Sm_2Fe_{17} material and with the metallographic and magnetic data (Platts et al. 1992; Sinan et al. 1995).

6. NMR measurements at high pressure

Considering the importance of lattice expansion in the enhancement of the properties of Sm_2Fe_{17} and related RE–TM systems, surprisingly little significant NMR research has been undertaken as a function of pressure. It seems clear that the reduction in overlap between the Fe 3d states, caused by a lattice expansion enhances interatomic exchange interactions between Fe atoms, leading to an increase in the Fe moment and an increase in the Curie temperatures. However, the presence of N atoms close to Fe atoms causes a drop in the magnetic moment of the Fe atom, because of strong hybridisation between N 2p states and Fe 3d states. Similarly, interstitial neighbours are likely to influence the distribution and polarisation of RE valence electrons. Therefore it is of fundamental value to perform measurements as a function of applied pressure in order to disentangle the effects of "chemical" and "real" pressure.

NMR measurements of ^{89}Y and ^{147}Sm spin-echo spectra at 4.2 K and pressures to 10 kbar for samples of Y_2Fe_{17}, $Y_2Fe_{17}C_x$, $Y_2Fe_{17}N_x$, $Y_2Fe_{17}H_x$, $Y_2Fe_{17}CN_x$ and Sm_2Fe_{17} have been reported by Armitage et al. (1989), and Kapusta et al. (1996e). Pressure derivatives of Y HFF were determined for different numbers of interstitial C, N and H neighbours, fig. 6.1. From quadrupole split Sm spectra of Sm_2Fe_{17} changes of EFG with pressure have been derived. Changes of HFF with pressure correspond to a decrease of transferred hyperfine field, arising from the polarisation of valence electrons at the rare earth sites by neighbouring Fe moments.

The effect of pressure on Y resonance lines with the same number of N (C) neighbours depends on the crystal structure (rhombohedral or hexagonal) of the material. Resonance lines corresponding to the sites with no interstitial neighbours have been shown to have the same pressure dependence as in the hexagonal host Y_2Fe_{17}. In the rhombohedral carbide and carbonitride, the pressure sensitivity has been observed to be about 40% lower than for the hexagonal compounds. In the hexagonal carbide, the sensitivity of resonance lines to pressure decreased slightly with increasing numbers of C neighbours, whereas an increase is observed in the rhombohedral compound.

For the Y HFF in the hydride, in which the local influence of interstitial H neighbours is not significant, a slightly larger dependence of HFF on pressure was observed than in Y_2Fe_{17}, whereas N neighbours dramatically reduce the pressure dependence of the Y HFF. A reduction as large as 90% for two N neighbours in the nitride and carbonitride has been observed. The effects may be considered in terms of the influence which interstitial neighbours have on the distribution and polarisation of Y (Sm) valence electrons. The LMTO

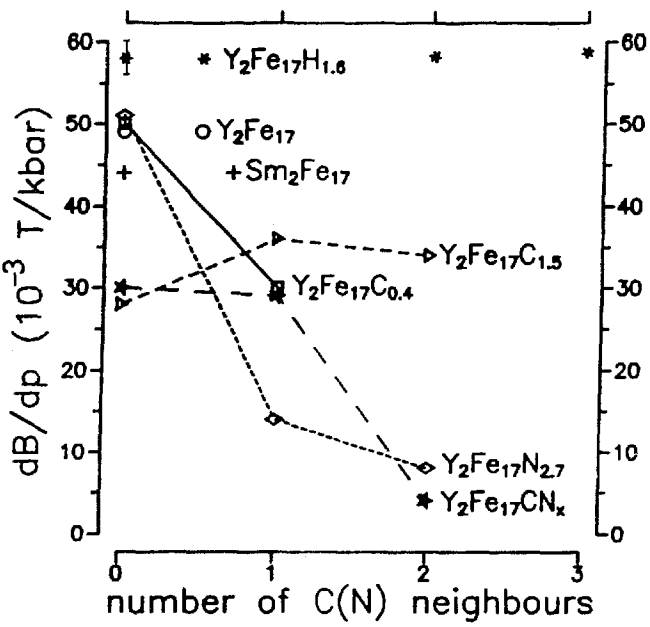

Fig. 6.1. Pressure derivatives of HFF at RE nuclei as a function of number of nearest neighbours. After Kapusta et al. (1996e).

ASA calculations for Y_2Fe_{17} and its interstitial nitrides, carbides and hydrides carried out by Beuerle and Fähnle (1992), have shown that there exists a difference in the influence of interstitial elements on the magnetic moments of yttrium 5s and 4d electrons and thus that there are different contributions from these electrons to the HFF. The similar pressure derivative of Y and Sm HFF in Y_2Fe_{17} and Sm_2Fe_{17} indicates that the 4f electron shell remained unchanged for the range of pressures used in the experiment. The effect of pressure must therefore be largely related to the behaviour of valence electrons. The pressure change of the ^{147}Sm quadrupole splitting measured for Sm_2Fe_{17} can thus be attributed to a change of the EFG related to non-4f electrons. On this basis it is deduced that the crystal electric field coefficient A_2^0 decreases by 0.7% per kbar. For an isotropic compressibility an increase of A_2^0 is expected, therefore the results indicate that there exists a large anisotropy in the compressibility of the material.

7. $RE_2TM_{14}B$

In $RE_2TM_{14}B$ compounds a strong exchange interaction of the 3d metal sublattice gives rise to the high Curie temperature and saturation magnetisation. Whereas it is the rare earth element which is responsible for the magnetocrystalline anisotropy, through the interaction of its aspherical 4f electron shell with the CEF, and the strong RE–TM exchange interaction. The crystal structure of $RE_2TM_{14}B$, shown in fig. 7.1, was first determined by Herbst

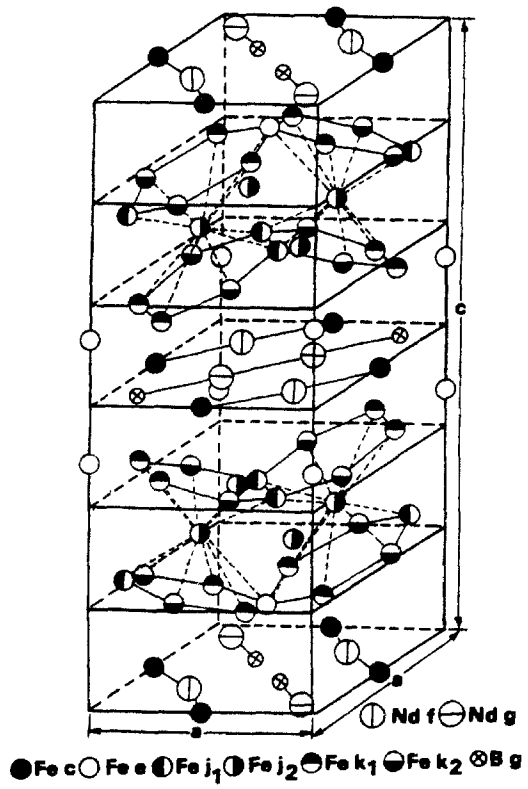

Fig. 7.1. Unit cell of $Nd_2Fe_{14}B$. The c/a ratio is exaggerated to show the puckering of the hexagonal Fe nets. After Herbst (1991).

et al. (1984, 1985), by neutron powder-diffraction analysis, and by Givord et al. (1984) and Shoemaker et al. (1984), from single crystal X-ray investigations. All the materials described in this section of the review are isomorphic, with a tetragonal structure (space group $P4_2/mnm$). There is some variation in the notation used by authors to denote the location of the different atomic sites in this structure, as detailed by Herbst (1991), but the structure is now well established. As shown in the figure, the unit cell consists of a stack of eight atomic layers in the c-direction, with all B, Nd and 4 out of 56 Fe atoms located at $z = 0$ and $z = 1/2$. There are two inequivalent rare earth sites (4f and 4g in the notation after Herbst). The 4f site has two B atoms at a distance of 3.30 Å, whereas the 4g site has a much closer single boron neighbour at 2.87 Å. Both sites have the same number of 3d neighbours. These are at a distance of 3.06 Å–3.27 Å for the 4f sites and 3.09 Å–3.40 Å for the 4g sites. The number and distances of the rare earths are 2 at 3.76 Å and 3 at 3.49 Å–3.76 Å for the 4f and 4g sites, respectively. The coordination of the B is straightforward, with every B atom in centre of a trigonal prism of Fe atoms at around 2.11 Å with 3 Fe above and 3 below the plane containing the B and neighbouring Nd atoms. There are 6 inequivalent Fe sites, denoted by c, e, j_1, j_2, k_1 and k_2 as detailed by Herbst (1984),

and shown in fig. 7.1. The compound $RE_2Fe_{14}C$ is isostructural to $RE_2Fe_{14}B$ and exhibits extremely similar magnetic properties. Some results of an NMR study of the RE = Gd compound are given in section 8. Section 9 discusses the effect of hydriding $Nd_2Fe_{14}B$.

The reader is directed towards a detailed review of the crystallography, and the material and magnetic properties of $RE_2TM_{14}B$ and related compounds by Herbst (1991). A summary reviewing important data on HFF and CEF parameters of $RE_2Fe_{14}B$ and related compounds is given in table 7.1.

7.1. ^{57}Fe resonance

Combined NMR–Mössbauer studies of the $RE_2Fe_{14}B$ and $RE_2Co_{14}B$ compounds have been reported by Rosenberg et al. (1985, 1986a, 1986b, 1989), Erdmann et al. (1987, 1988a, 1988b) and Ge et al. (1992). For $Nd_2Fe_{14}B$ NMR studies have also been carried out by Zhang et al. (1987, 1988a, 1988b, 1989). The authors take the advantage of using both ^{57}Fe Mössbauer and NMR techniques in order to obtain the values of hyperfine parameters and assign them more reliably to the six Fe sites in the compounds. A particularly good agreement between the data has been obtained by Ge et al. (1992), table 7.1. The authors have used a sample prepared from boron enriched in ^{10}B isotope, similar to that of Zhang et al. It allowed them to obtain an ^{57}Fe NMR signal not overlapped with the strong ^{11}B signal of natural abundance boron.

Most of the authors, including Rosenberg et al., Erdmann et al. and Ge et al. have attributed the largest ^{57}Fe resonance frequency (the largest hyperfine field) to the j_2 site, which has the largest number of Fe nearest neighbours. Also in Mössbauer work of Fruchart et al. (1987), the largest HFF in $RE_2Fe_{14}B$ (RE = Nd, Gd, Tb, Dy, Ho, Er) has been assigned to this site. Theoretical calculations of magnetic contact hyperfine fields with LMTO-ASA (Hummler et al. 1992) and FLMTO (Hummler and Fähnle 1996), however, have predicted that the largest field should appear at the k_2 site. The discrepancy may be due to the HFF contribution from the unquenched orbital moment, omitted from the theory. This contribution is likely to be quite significant at the j_2 site, since its symmetry is very low, i.e., the highest symmetry axis is only twofold.

Rosenberg et al., Erdmann et al., Ge et al., as cited above, and other authors have related the values of hyperfine fields to the Fe magnetic moments using a conversion factor of 15 T/μ_B. This gave a large value of magnetic moment at the j_2 site of 2.4–2.7 μ_B depending on the rare earth. From a neutron diffraction study, Givord et al. (1985), obtained a larger value of 2.85 μ_B for the j_2 site in $Nd_2Fe_{14}B$. The discrepancy between the values obtained from NMR (Mössbauer) and neutron diffraction can be as large as 0.7–1 μ_B at the 4c site in $Nd_2Fe_{14}B$ (Ge et al. 1992; Fruchart et al. 1987; Givord et al. 1985). The discrepancies arise from difficulty in deriving the values of magnetic moments from the hyperfine fields. The core polarisation is proportional to the 3d spin moment, but other significant contributions, including the valence electron polarisation term, are not (Hummler and Fähnle 1996). Therefore the use of a single conversion factor between HFF and magnetic moment is often too crude an approximation. This may explain the discrepancy of up to 0.7 μ_B between magnetic moments obtained from the NMR HFF and the theoretical moments, table 7.1.

TABLE 7.1

Hyperfine and crystal electric field paramaters of $Nd_2Fe_{14}B$ and related compounds.

Sample	x	ν (MHz)	$\lvert B_e \rvert$ (T)	Parameters for EFGs[a,b,c,d]	Notes	Source
$Nd_2Fe_{14}B$					^{143}Nd, NMR, 4.2 K	Kapusta et al. (1993b)
				10.2[a], 26.2[c], 170[d]	4g	
				7.6[a], 82.9[c], 63[d]	4f	
		800	345.6	6.67[a]		Figiel et al. (1992)
		834	360.2	3.13[a]		
					^{57}Fe NMR (Mössbauer)	Ge et al. (1992)
		52.0 & 53	37.8 [37.8]		j_2 (dipole split)	
		48.5	35.2 [34.6]		k_2	
		46.0	33.4 [33.4]		j_1	
		44.7	32.5 [32.5]		k_1	
		44.0	32.0 [32.2]		c	
		41.5	30.2 [30.6]		e	
		14.1			^{10}B	
		42.4			^{11}B	
			3.1			Rosenberg et al. (1986a)
		14.1	3.10		^{10}B, g,	Zhang et al. (1989)
		42.4	3.10		^{11}B, g,	
		53.0	38.5		^{57}Fe, j_2 (DWC)	
		52.0	37.8		j_2 (DWE)	
		48.5	35.2		k_2	
		46.0	33.4		j_1	
		44.7	32.5		k_1	
		44.0	32.0		c	
		41.5	30.2		e	
		46.7			α-Fe	
		801	348		^{143}Nd 4f	Potenziani (1985)
		820	356		4g	
		498.6	348		^{145}Nd, 4f	

TABLE 7.1 (Continued)

Sample	x	ν (MHz)	$\lvert B_e \rvert$ (T)	Parameters for EFGs[a,b,c,d]	Notes	Source
		510.5	356		4g	
			37.2		^{57}Fe-Mössbauer, c	Rosenberg et al. (1985)
			36.6		e	
			34.2		k	
			33.5		k	
			32.0		j	
			30.7		j	
		14.3	3.125		^{11}B, NMR	
		45–47	33.0		^{57}Fe	
		47.5	35.0			
		52	37.5			
		41.5	30.0			
		44	32.0			
		345			^{143}Nd	Berthier et al. (1986)
		360				
				1.5[a]	^{145}Nd 4f	Nadolski et al. (1989a)
				3.3[a] & 2.2[a]	4g	
		498		1.5[a]	4f	Nadolski et al. (1989b)
		512		3.1[a] & 2.2[a]	4g	
$Nd_{15}Fe_{77}B_8H_x$		440				
		455		1[a] & 2–3[a]	main peak	
		485				
$Y_2Fe_{14}B$		48.4			^{89}Y	Erdmann et al. (1987)
		36.7				
		42			^{11}B	
$Y_2Co_{14}B$		14.6			^{89}Y, 4g	
		21.2			4f	
		19.2			^{11}B	

TABLE 7.1 (Continued)

Sample	x	ν (MHz)	$\lvert B_e \rvert$ (T)	Parameters for EFGs[a,b,c,d]	Notes	Source
$Pr_2Fe_{14}B$					^{141}Pr, 1.4 K	Shimizu and Ichinose (1995b)
		3356.5	257.4 ± 0.4		4f	
		3656	280.3 ± 0.4		4g	
$Pr_{1,8}Lu_{0.2}Fe_{14}B$			256.0 ± 0.4		4f	
			280.4 ± 0.4		4g	
$Sm_2Fe_{14}B$					^{147}Sm	Kapusta et al. (1993b)
				3.5^a, -34.2^c	4g	
				7.6^a, 82.9^c	4f	
			4.03		^{11}B	Erdmann et al. 1988b
$La_2Fe_{14}B$		218.2	36.1	4.05^a, -38^c, 96^d		Kapusta (1996)
		267.0	44.1	1.93^a, -79^c, 200^d		
					^{57}Fe-Mössbauer, 295 K	Rosenberg et al. (1986b)
			30.8		k_1, k_2	
			28.7			
			29.8		j_1	
			33.9		j_2	
			27.6		c, e	
			26.1			
			35.5		20 K	
			33.6			
			34.6			
			38.7			
			32.1			
			30.3			
			34.3		^{57}Fe NMR, 4.2 K, ⟨HFF⟩	Erdmann et al. (1988b)
			2.81		^{11}B	

TABLE 7.1 (Continued)

Sample	x	ν (MHz)	$\lvert B_e \rvert$ (T)	Parameters for EFGs[a,b,c,d]	Notes	Source
$La_2Fe_{14}B$		38.4				Erdmann et al. (1987)
$Ce_2Fe_{14}B$			2.71		^{11}B NMR, 4.2 K	Rosenberg et al. (1986a)
			2.70			Erdmann et al. (1988b)
			32.3		^{57}Fe NMR, ⟨HFF⟩	
		36.9			^{11}B NMR, 4.2 K	Erdmann et al. (1987)
$Nd_2Co_{14}B$			19.60		Co HFF 4.2 K, c	Wójcik et al. (1989)
			18.21		j_1	
			16.63		k_2	
			12.95		k_1	
			12.57		j_2	
			5.48		e	
					– HFF increases with Fe substitution of Co.	
		544.1	378.1	2.69[a]	^{145}Nd	Figiel et al. (1992)
		545.7	379.2	0.47[a]		
		565.79	393.18	0.35[a]		
					^{59}Co	Panissod et al. (1989)
			19.60		c	
			18.21		j_1	
			16.63		k_2	
			12.95		k_1	
			12.57		j_2	
			5.48		e	
		217			f.c.c. precipitate	
					^{143}Nd NMR 4.2 K	Shimizu et al.
		798.5			4f	(1995)
		830.5			4g	

TABLE 7.1 (Continued)

Sample	x	ν (MHz)	$\lvert B_e \rvert$ (T)	Parameters for EFGs[a,b,c,d]	Notes	Source
Nd_2–$(Fe_xCo_{1-x})_{14}B$	0	217			f.c.c. Co, ^{59}Co	Jedryka et al. (1988)
	$\geqslant 0.634$	220–240			Co–Fe alloy	
		285			Co–Fe alloy	
		290–295			Co–Fe alloy	
	$\leqslant 0.634$	130				
	$\geqslant 0.146$	150			increase in ^{59}Co HFF with x	
Nd_2–$(Fe_xCo_yNi_z)_{14}B$	(x, y, z)				Data taken from figures, ^{143}Nd	
	1, 0, 0	798			4f	
		831			4g	
	0.9, 0, 0.1	787			4f	
		821			4g	
	0.7, 0.2, 0.1	791			4f	
		828			4g	
	0.7, 0.3, 0	795			4f	
		831			4g	
	0.5, 0.5, 0	799			4f	
		836			4g	
$Lu_2Fe_{14}B$					^{57}Fe	Erdmann et al. (1988a)
			29.4		$8j_1$	
			33.0		$16k_2$	
			37.1		$8j_2$	
			3.16		^{11}B (signal range 1.3 T*)	
$Er_2Fe_{14}B$			4.98		^{11}B NMR	Erdmann et al. (1988b)
			804.2 ± 8	400[d]	^{167}Er, 4f	Shimizu (1993)
			797.7 ± 8	350[d]	4g	

TABLE 7.1 (Continued)

Sample	x	ν (MHz)	$\lvert B_e \rvert$ (T)	Parameters for EFGs[a,b,c,d]	Notes	Source
$Gd_2Fe_{14}B$						Erdmann et al. (1988a)
					NMR (Mössbauer)	
			33.3 [34.1]		^{57}Fe, $16k_1$	
			35.9 [35.9]		$16k_2$	
			– [32.9]		$8j_1$	
			40.1 [40.1]		8j2	
			– [32.1]		4e	
			– [29.7]		4c	
			2.40		^{11}B, 4g, signal range 2.6 T	
			2.43			Rosenberg et al. (1986a)
		75	44.0		^{157}Gd	
		65	38.3			
		57.7	44.0		^{155}Gd	
		49.6	38.3			
			27.6 ± 0.2	310[d]	^{155}Gd Mössbauer 4f	Bogé et al. (1986)
			15.3 ± 0.2	320[d]	4g	
$(Er_{1-x}Gd_x)_2Fe_{14}B$	0.1		804.2 ± 1.6	400[d]	^{167}Er, NMR 4f	Shimizu (1993)
			797.7 ± 1.6	350[d]	4g	
$Tb_2Fe_{14}B$			367.4 ± 0.4	430[d]	^{159}Tb, 4f	
			336.5 ± 0.4	420[d]	4g	
$Sm_2Co_{14}B$			1.16		^{11}B (signal range 0.2 T)	Erdmann et al. (1988a)
$Gd_2Co_{14}B$			1.49		^{11}B (signal range 0.5 T)	
$Sm_2(Co_{1-x}T_x)_{14}B$					^{59}Co NMR-approximate values from graphs:	Maruyama et al. (1990)
T = Fe	0		15.5		$16k_1$	
			14		$16k_2$	
			10		$8j_1$	
			8.5		$8j_2$	

TABLE 7.1 (Continued)

Sample	x	ν (MHz)	$\lvert B_e \rvert$ (T)	Parameters for EFGs[a,b,c,d]	Notes	Source
	0.3				approx. monotonic increase with x to:	
			17		$16k_1$	
			15		$16k_2$	
			11.5		$8j_1$	
			10.5		$8j_2$	
					independent of x to $x = 0.6$	
T = Ni	0				$x = 0$ as above	
	0.1				approx. monotonic decrease with x to $x = 0.1$:	
			14.5		$16k_1$	
			13		$16k_2$	
			10		$8j_1$	
			8		$8j_2$	
T = Mn					Shift to lower frequency with x.	
$La_2Co_{14}B$		18.4				
					^{59}Co c-axis:	Wójcik et al. (1988)
		158	15.65		$16k_1$	
		160	16.12		$16k_2$	
		156	16.03		$8j_1$	
		168	17.05		$8j_2$	
		165	15.20		c	
		154	15.62		e	
					c-plane:	
		100	9.90		$16k_1$	
		112	10.81		$16k_2$	
		86	8.91		$8j_1$	

TABLE 7.1 (Continued)

Sample	x	ν (MHz)	$\lvert B_e \rvert$ (T)	Parameters for EFGs[a,b,c,d]	Notes	Source
		133	12.95		$8j_2$	
		125	12.12		c	
		122	12.77		e	
$Th_2Fe_{14}B$		35.6			^{11}B NMR	Erdmann et al. (1987)
					^{57}Fe	
		50.2			j_2	
		45.5			k_2	
		42.5	36.3		k_1	
		40.4	29.3		j1	
		39.1			e	
		37.2			c	
					NMR (Mössbauer)	Erdmann et al. (1987)
$Gd_2Fe_{14}C$			32.3 [32.4]		^{57}Fe, 16k1	
			34.9 [35.3]		$16k_2$	
			31.4 [32.3]		$8j_1$	
			39.0 [39.3]		$8j_2$	
			– [30.8]		4e	
			– [27.9]		4c	
			2.38		^{13}C, 4g	
			33.76		⟨Fe HFF⟩	
					^{145}Nd	Kapusta et al. (1996f)
$Nd_xY_{2-x}Co_{14}B$	0.1	560.6		4.00^a, 12.7^c	4g	
		533.5		5.80^a, 56.0^c	4f	
	0.2	562.1		1.80^a, -38.9^c	4g	
		537.3		3.60^a, 4.5^c	4f	
	0.4	563.8		1.50^a, -46.0^c	4g	
		541.5		3.50^a, 2.1^c	4f	

TABLE 7.1 (Continued)

Sample	x	ν (MHz)	$\lvert B_e \rvert$ (T)	Parameters for EFGs[a,b,c,d]	Notes	Source
	0.6	564.2		1.60[a], −43.6[c]	4g	
		542.1		3.18[a], −3.1[c]	4f	
	1	564.6		0.80[a], −62.4[c]	4g	
		543.0		3.00[a], −9.6[c]	4f	
	1.4	565.4		0.70[a], −64.0[c]	4g	
		543.6		2.83[a], −18.3[c]	4f	
	2	566.5		0.36[a], −71.8[c]	4g	
		544.2		2.66[a], −19.0[c]	4f	
				192[d]	4g	
				57[d]	4f	

Comments and values apply to lines on and below the note. The symbol * terminates validity where required for clarity.
$a = \Delta\nu_q$ [MHz], $b = V_{ii}$ [10^{20} V m^{-2}], $c = V_{ii}$(latt) [10^{20} V m^{-2}], $d = A_0^2$ [K a_0^{-2}] – units (unless otherwise specified).

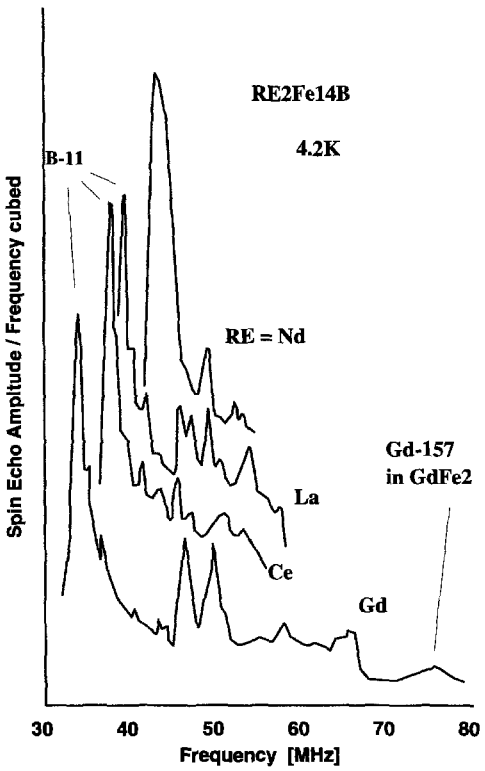

Fig. 7.2. Frequency corrected spin-echo spectrs of $RE_2Fe_{14}B$ at 4.2 K. After Rosenberg et al. (1986b).

7.2. *^{10}B and ^{11}B resonances*

The NMR spectra of ^{11}B and ^{10}B in the $RE_2Fe_{14}B$ and $RE_2Co_{14}B$ compounds have been reported by Rosenberg et al. (1985, 1986a, 1986b), Erdmann et al. (1987, 1988a, 1988b), Zhang et al. (1987) and Ge et al. (1992). The hyperfine field at the boron site was found to vary from 2.43 T for $Gd_2Fe_{14}B$ to 3.1 T for $Nd_2Fe_{14}B$ (Rosenberg et al. 1986a, 1986b). The spectra are shown in fig. 7.2. Erdmann et al. (1987) applied different pulse separations in order to separate ^{57}Fe and ^{89}Y signals overlapping with the ^{11}B signal, which had a shorter relaxation time, fig. 7.3. The HFF at boron nuclei originates mainly from the polarisation of the valence electrons of boron by nearest magnetic neighbours. The FLMTO calculations by Hummler and Fähnle (1996) showed that for $Nd_2Fe_{14}B$ the HFF at the boron site should be 3.9 T. A discrepancy between theory and experiment is possibly caused by a large dipolar field from magnetic RE (Gd, Nd) neighbours. This accounts for a 0.7 T difference between the experimental HFF values in Gd and Nd compounds. The HFF values at the boron site in $Y_2Co_{14}B$ and $La_2Co_{14}B$ reported by Erdmann et al. (1987), were found to be 0.92 T and 0.88 T, respectively. Note that the HFF in the Y based compound is larger than in the La based compound, in spite of a slightly smaller magnetisation of $Y_2Co_{14}B$. This discrepancy is possibly related to the strong dependence of the boron HFF on the magnetic

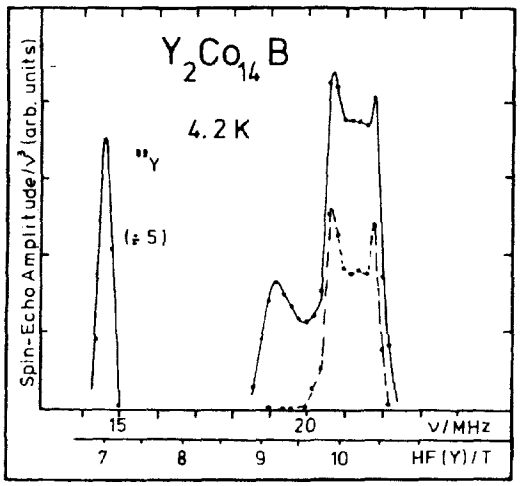

Fig. 7.3. NMR spectra of $Nd_2Fe_{14}B$ at 4.2 K. Full line is for pulse separation $\tau = 200$ μs. Dashed line, $\tau = 500$ μs removes ^{11}B signal. After Erdmann et al. (1987).

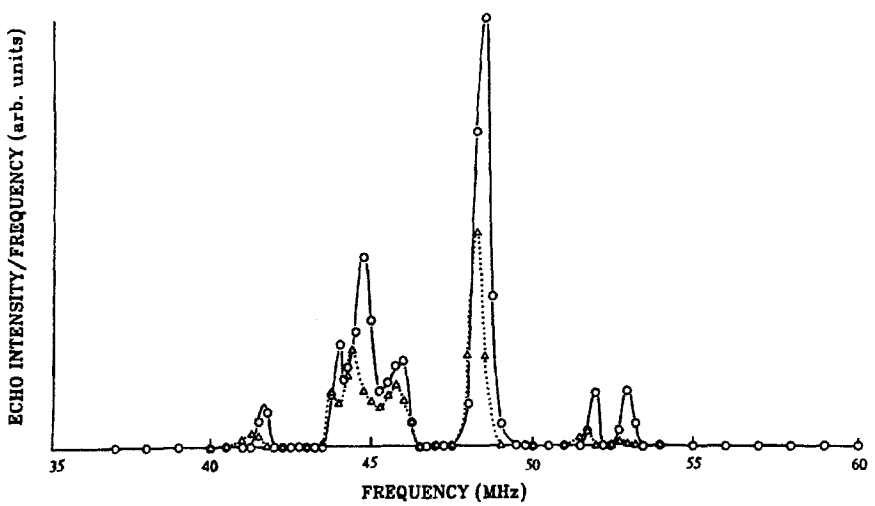

Fig. 7.4. ^{57}Fe frequency normalised spin-echo spectrum at 1.3 K for ^{10}B enriched $Nd_2Fe_{14}B$. Solid line is zero field. Dotted line is at 6 kOe. After Zhang et al. (1988b).

neighbour separation. The average distance between B and its Co nearest neighbours is smaller in the yttrium based compound than in the lanthanum based compound.

Measurements of ^{57}Fe and ^{11}B spectra of $Nd_2Fe_{14}B$ and $Y_2Fe_{14}B$ under applied field by Zhang et al. (1988b), have shown that the Fe and B hyperfine fields have a negligible anisotropy, i.e., they have the same values at the domain wall centres as at the domain wall edges. In the spectrum shown in fig. 7.4, only one line was found to disappear under applied

field and, thus, it was assigned to a domain wall centre signal of a site with a possible large anisotropy of the field related with anisotropic dipolar field contribution. A non-collinear magnetic structure of $Nd_2Fe_{14}B$ at 4.2 K and 77 K was concluded from a deviation of the slope of the resonant frequency vs. applied field dependence from the ^{11}B gyromagnetic ratio. For $Y_2Fe_{14}B$, which shows a collinear structure no deviation was found. A shift of Fe and B resonance lines in the applied field to lower frequencies revealed an antiparallel orientation of the Fe and B HFF with respect to the magnetisation.

7.3. ^{59}Co resonance

The spin echo spectra of the $RE_2Co_{14}B$ compounds with RE = Nd, Y, Pr, La are reported by Kapusta et al. (1986), Berthier et al. (1988), Wójcik et al. (1988, 1990) and Panissod et al. (1989). The study of the compounds with substituted rare earths has been carried out by Kapusta and Figiel (1988), Ichinose et al. (1990, 1992; Ichinose and Nagai 1993); Jedryka et al. (1991) and Myojin et al. (1993). The most pronounced differences in the spectra of the compounds are related to their different easy magnetisation directions. The cobalt sublattice prefers an easy plane anisotropy, but compounds containing rare earths with a negative second order Stevens factor, α_J, prefer a uniaxial anisotropy (for Nd a canted structure appears below 30 K). The substitution of the rare earth with negative α_J by a RE with a positive α_J (or Gd, Lu, Y) can lead to a change of the EMD with the RE concentration. The dramatic changes in the spectra upon crossing the boundary concentration for this change are illustrative of the huge anisotropy of the Co HFF.

Kapusta and Figiel (1988), studied the $(Nd_xY_{1-x})_2Co_{14}B$ system and found that a change between EMD in the basal plane and EMD along the c-axis (canted) takes place between $x = 0$ and 0.2. A similar transition region $0 < x < 0.15$ was found by Ichinose et al. (1990), fig. 7.5. Jedryka et al. (1991) have studied the $(Nd_xY_{1-x})_2Co_{14}B$ system with smaller steps in x in the transition region and found that a sudden change in the character of the spectra measured at 4.2 K occurs at $x = 0.08$, where the anisotropy of the Nd sublattice overcomes the planar anisotropy of the Co sublattice, so that the compound with this Nd content is no longer planar. Measurements of the $(Nd_{0.1}Y_{0.9})_2Co_{14}B$ spectra as a function of temperature showed that the resonance lines corresponding to both axial and planar anisotropies coexist around the spin reorientation temperature T_{sr2}. From this, the conclusion has been drawn that the transition between the uniaxial and planar state is first order, with the transition temperature probably varying from grain to grain.

The substitution of Pr, Sm, Gd and Tb for Nd was studied by Ichinose et al. (1992), and Ichinose and Nagai (1993). They observed that the transition from planar to uniaxial anisotropy on the substitution of gadolinium occurred at $x = 0.1$, close to that of the yttrium. For samarium, the boundary concentration was found to be at $x = 0.55$. For Pr no significant changes in the spectrum were observed, other than the appearance of a doublet structure of the lines at $x = 0.8$. This was attributed to the presence of a canted magnetic structure, using a similar interpretation of the spectra to that used for Nd rich compounds by Jedryka et al. (1991). Additional magnetic measurements led to the construction of spin phase diagrams of the systems, figs 7.6 and 7.7.

A study of $(RE_xY_{1-x})_2Co_{14}B$ compounds with RE = Gd and Tb by Myojin et al. (1993), led to the conclusion that the change of the EMD for the Tb containing compound occurs at $0.02 < x < 0.04$. For the series of Gd containing compounds no significant

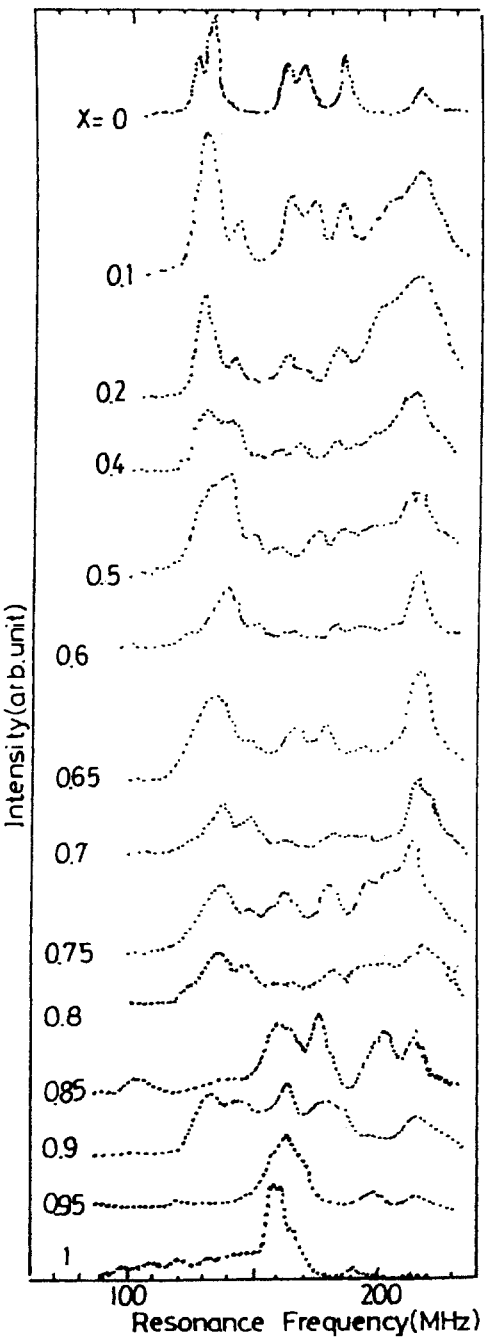

Fig. 7.5. ^{59}Co spin-echo NMR spectra of $(Nd_{1-x}Y_x)_2Co_{14}B$ at 4.2 K. After Ichinose et al. (1990).

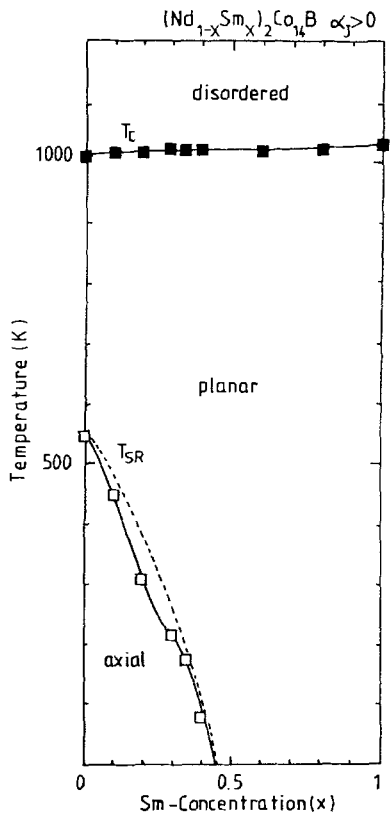

Fig. 7.6. Spin phase diagram of $(Nd_{1-x}Sm_x)_2Co_{14}B$ compounds (Sm $\alpha_J > 0$). The solid curve is a guide to the eye. The dashed curve is a theoretical calculation. After Ichinose et al. (1992).

changes have been observed in the spectra and thus it can be concluded that there is no change of the EMD. Since Gd is an S-state ion, there is no CEF induced contribution to the magnetocrystalline anisotropy from the Gd site. The contribution to the MCAE from the dipolar interaction can, however, be quite significant. This was found to be the case for Gd_2Fe_{17} (Kakol et al. 1987), and for $GdCo_4B$ (Kapusta et al. 1992d). A planar anisotropy of $Gd_2Co_{14}B$ indicates, that the contribution to the MCAE from the cobalt sublattice is dominant, as in $Y_2Co_{14}B$.

Temperature measurements of the NMR spectra of $Nd_2Co_{14}B$ have been reported by Panissod et al. (1989), fig. 7.8. They have shown that the spectrum changes smoothly with increasing temperature between 20 and 32 K. From their measurements they have concluded that a second order transition occurred at 32 K. They showed that this transition involved a spin reorientation from a conical to the axial state. Furthermore, it was found that the canting angle changed smoothly between 20 and 32 K from 12° below 20 K to 0° above 32 K. A multiplet structure which appeared in the canted state was attributed to the HFF anisotropies of the individual sites and to the presence of conical domain walls.

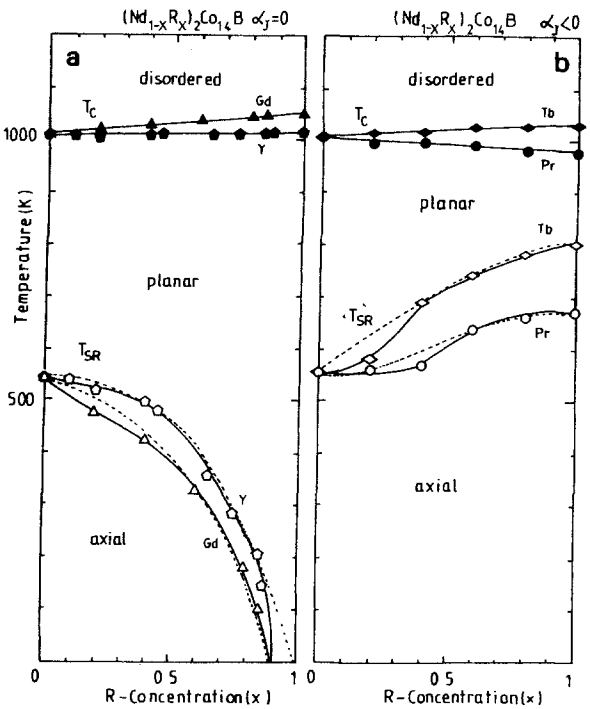

Fig. 7.7. Spin phase diagram of $(Nd_{1-x}RE_x)_2Co_{14}B$ compounds. (a) RE = Y, Gd ($\alpha_J = 0$); (b) RE = Pr, Tb ($\alpha_J < 0$). The solid curve is a guide to the eye. The dashed curve is a theoretical calculation. After Ichinose et al. (1992).

The directions of the corresponding Co moments in the domain walls with respect to the crystallographic axes were established from an analysis of the power dependence of the resonance lines by Wójcik et al. 1990. The analysis allowed the resonance lines to be reliably assigned to the six crystallographic cobalt sites in the compound, fig. 7.9.

The spectra for samples in which the Co was partially substituted by Fe have been reported by Zhang et al. (1988a), Jedryka et al. (1988) and Wójcik et al. (1989). Zhang et al. found that for a very low Co content the Fe occupied the k_2 sites preferentially, whereas Deppe et al. (1987) concluded from Mössbauer experiments that there was a preferential substitution at the j_2 sites in the low Fe concentration range. Jedryka observed an increase of the HFF of the k_2 site with increasing iron content in the range above 50% Fe. This was much stronger than for the other sites and it was concluded that an enhancement of the Co moment at this site was a result of preferential substitution. NMR signals from b.c.c. Fe–Co alloys with 25% Fe, 50% Fe and 75% Fe have been detected, corresponding to almost the whole range of possible substitution. Fe substitution was found to cause a strong decrease in the large anisotropy of the hyperfine field originating from an orbital contribution to the cobalt magnetic moment at this site (Wójcik et al. 1989).

The substitution of TM = Mn, Fe and Ni for Co in $Sm_2(Co_{1-x}TM_x)_{14}B$ has been studied by Maruyama et al. (1990). The hyperfine fields at the Co sites were found to increase

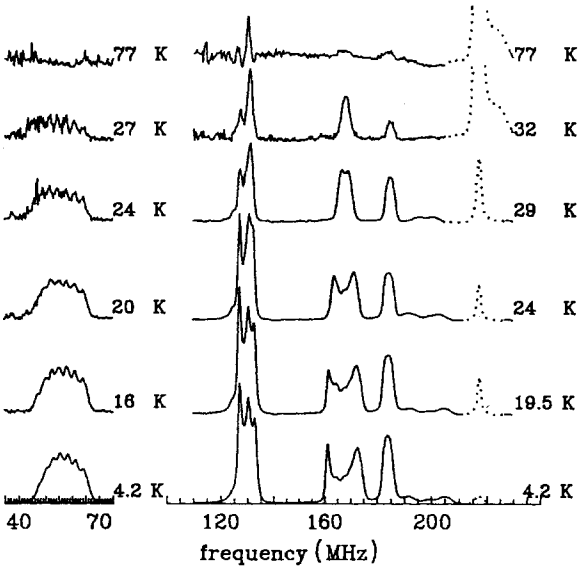

Fig. 7.8. ^{59}Co spin-echo NMR spectra of $Nd_2Co_{14}B$ around the spin reorientation temperture. Dotted lines are from f.c.c. Co. After Panissod et al. (1989).

rapidly for the j sites and gradually for the k sites with Fe substitution, whereas Ni or Mn substitution caused a decrease in the HFF. The results indicate that the Co HFF is very sensitive to the type of 3d metal atoms substituted at the neighbouring sites.

7.4. ^{89}Y resonance

Erdmann et al. (1987) have reported on the ^{89}Y spectra in $Y_2Fe_{14}B$, fig. 7.10, and $Y_2Co_{14}B$, fig. 7.3. Berthier et al. (1986) have reported only one Y resonance line in $Y_2Fe_{14}B$ corresponding to a HFF of 23 T. For the Fe containing compound Erdmann obtained HFF values of 17.6 T and 23.2 T and assigned them to the yttrium 4g and 4f sites, respectively. It was assumed that the larger HFF corresponded to the site where magnetic neighbours were closer, i.e., to the 4f site. For the Co based compound the HFF values were 7.0 T and 10.2 T, respectively. Note that the ratio of HFF at the 4f site in the Fe containing compound to that in the Co containing compound is 2.5. This is very close to the value of 2.3, obtained for the 4g sites.

7.5. ^{143}Nd and ^{145}Nd resonances

^{143}Nd and ^{145}Nd NMR measurements in $Nd_2Fe_{14}B$ have been reported by Potenziani (1985). Identical spectra have been obtained for the alloy $Nd_{15}Fe_{77}B_8$ indicating that its Nd signal arises from the $Nd_2Fe_{14}B$ phase. A broad double peak structure was attributed to two Nd crystallographic sites with unresolved quadrupole splitting (nuclear spin of both isotopes, $I = 7/2$). Potenziani attributed the hyperfine field values of 348 T and 356 T to the 4f and 4g sites, respectively (the notation is after Givord et al. (1985)). A polarised

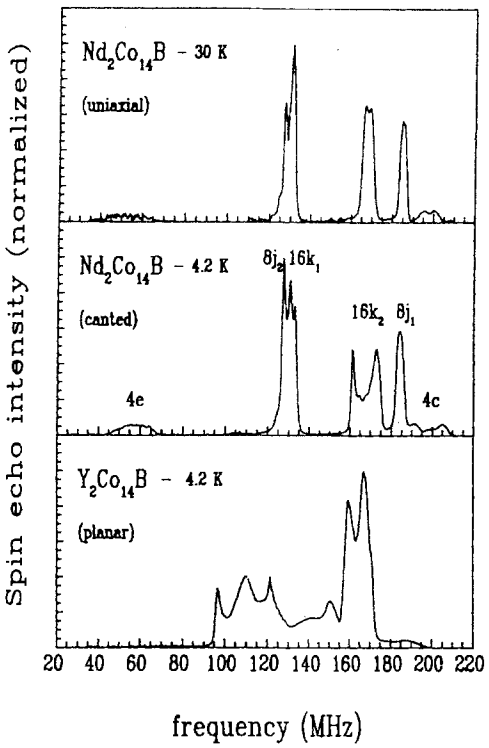

Fig. 7.9. ^{59}Co spin-echo NMR spectra of $Nd_2Co_{14}B$ and $Y_2Co_{14}B$. After Wójcik et al. (1990).

neutron diffraction study gave the values of magnetic moments at the Nd sites of 2.25–2.3 μ_B (Givord 1985). These are much smaller than that of 3.27 μ_B for the free ion. This may be because the polarised neutrons measure the projection of the Nd moment along the direction of magnetisation. Indeed the HFF values obtained from NMR measurements do indicate that the Nd moments in the compound have their values close to that of the free Nd^{3+} ion.

A better resolved ^{143}Nd spectrum has been reported by Berthier et al. (1986) and the authors gave HFF values for the two Nd sites of 345 T and 360 T, respectively. The authors attribute the difference between the free ion HFF and the values obtained for the two sites to different transferred HFF contributions. These contributions mainly arise from the polarisation of the RE s-like valence electrons by neighbouring Fe moments. Berthier et al. have attributed the larger transferred HFF to a RE site to which Fe neighbours are closer (4f in the notation of Herbst). They have obtained the same ratio of the transferred HFF for the two RE sites in the compounds with Y and Lu. For the rare earths with large magnetic moments a significant contribution of the RE neighbours to the transferred HFF has been found.

Double resonance of ^{145}Nd has been used by Nadolski et al. (1989a), in order to determine quadrupole splittings of the unresolved ^{145}Nd spectrum. The method is very useful

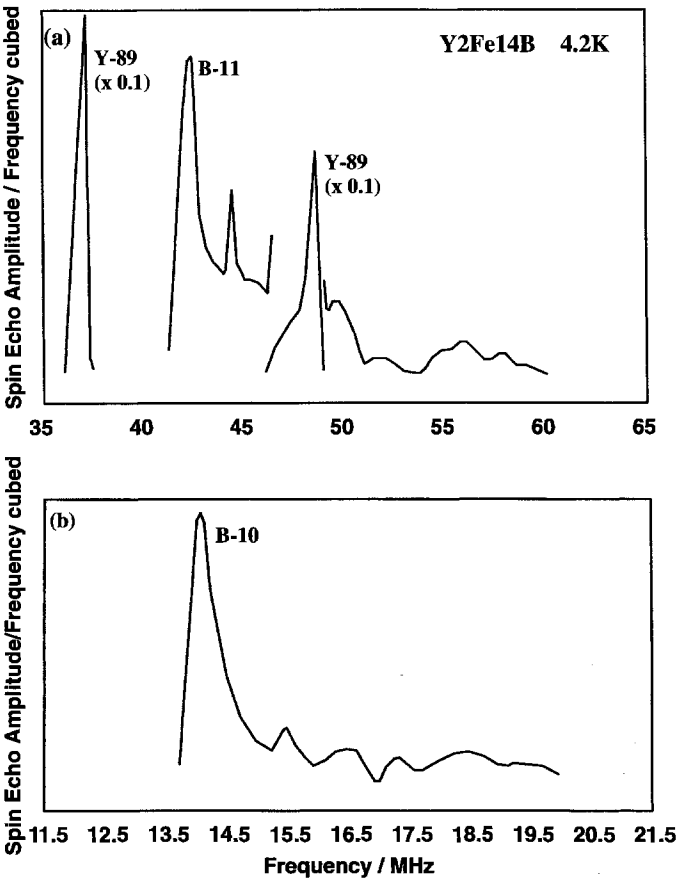

Fig. 7.10. NMR spectrum of $Y_2Fe_{14}B$ at 4.2 K with $\tau = 300$ μs, showing pure ^{10}B (lower part) and signals from ^{89}Y, ^{57}Fe and ^{11}B (upper part). After Erdmann et al. (1987).

in the study of unresolved quadrupole spectra. It relies on the application of a third pulse of a frequency slightly different from that of the main two pulses (Pieper et al. 1986). By varying the frequency of the third pulse the amplitude of the spin-echo signal undergoes modulation caused by the quadrupole interaction. The difference in the frequency between subsequent maxima (minima) corresponds to the quadrupole splitting. Nadolski et al. (1989a) obtained two values for the quadrupole splitting of 3.3 MHz and 2.2 MHz for the low frequency line, but with a single value of 1.5 MHz for the high frequency line, fig. 7.11. They assigned the two quadrupole splittings at the low frequencies to overlapping resonances from two magnetically inequivalent 4f sites, whereas the high frequency line was attributed to the 4g site. A noncolinear magnetic structure of Nd leads to a splitting of the 4f site into two magnetically inequivalent sites, and thus, two values of the quadrupole splitting appear. ^{143}Nd and ^{145}Nd spectra of $Nd_2Fe_{14}B$ have also been reported by Kapusta et al. (1993b) as discussed in section 7.6.

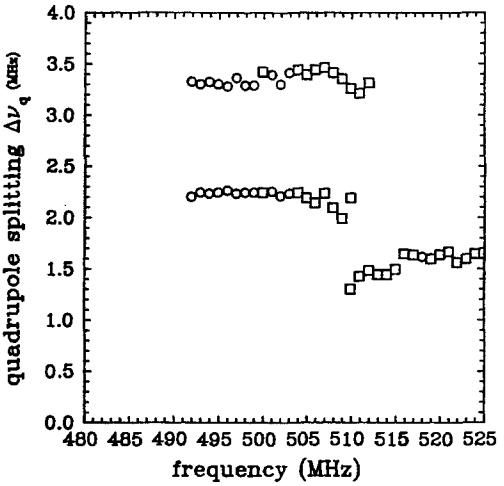

Fig. 7.11. ^{145}Nd NMR quadrupole splitting vs. frequency across the spin echo spectrum of $Nd_2Fe_{14}B$ at 4.2 K. Squares – perturbing mode. Circles – pumping mode. After Nadolski et al. (1989a).

A ^{145}Nd study of $Nd_2Co_{14}B$ has been carried out by Figiel et al. (1987). A single line at 566 MHz with two quadrupole splittings was observed. The overlooked 544 MHz line was found by Nadolski et al. (1989a), fig. 7.12. The quadrupole splittings have values of 2.58 MHz and 0.3 MHz for the low frequency and the high frequency lines, respectively. The evolution of both resonances observed in a later study of the $(Nd_{1-x}Y_x)_2Co_{14}B$ system by Kapusta et al. (1997b), has shown that the 544 MHz and the 566 MHz lines can be attributed to the Nd 4f and 4g sites, respectively.

A NMR study of ^{145}Nd in $Nd_2(Fe_{1-x}Co_x)_{14}B$ by Jedryka et al. (1992) revealed the presence of an additional Nd signal at lower frequencies in the intermediate concentration range, assigned to the appearance of Nd ions in a different spectroscopic state from that in the $Nd_2Fe_{14}B$ and the $Nd_2Co_{14}B$ compounds.

A ^{143}Nd study of the $Nd_2(Fe_{1-x}Co_x)_{14}B$ and $Nd_2(Fe_{1-x}Ni_x)_{14}B$ systems has been reported by Shimizu et al. (1995). A significant reduction of the HFF with substitution of Ni for Fe has been observed. Cobalt substitution was found to cause a smaller reduction of HFF and, after an initial decrease, the HFF was found to recover at high Co concentrations. The authors concluded that the amount of nickel corresponding to $x = 0.1$ caused a reduction of Nd moment averaged over the two sites, from 3 μ_B to 2.9 μ_B.

7.6. ^{147}Sm and ^{149}Sm resonances

^{147}Sm, ^{149}Sm, ^{143}Nd and ^{145}Nd spectra of $Sm_2Fe_{14}B$ and $Nd_2Fe_{14}B$ have been measured by Kapusta et al. (1993b). The Nd spectra, fig. 7.13 had a better resolution than those of Potenziani described above, therefore allowing the determination of the quadrupole splitting for the ^{143}Nd. The Sm spectra were relatively well resolved septets, especially ^{147}Sm with its much larger nuclear quadrupole moment, fig. 7.14. Since the highest symmetry

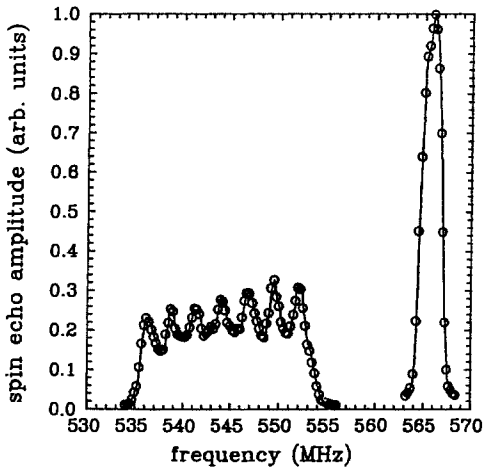

Fig. 7.12. ^{145}Nd spin-echo NMR spectra of $Nd_2Co_{14}B$ at 4.2 K. After Nadolski et al. (1989a).

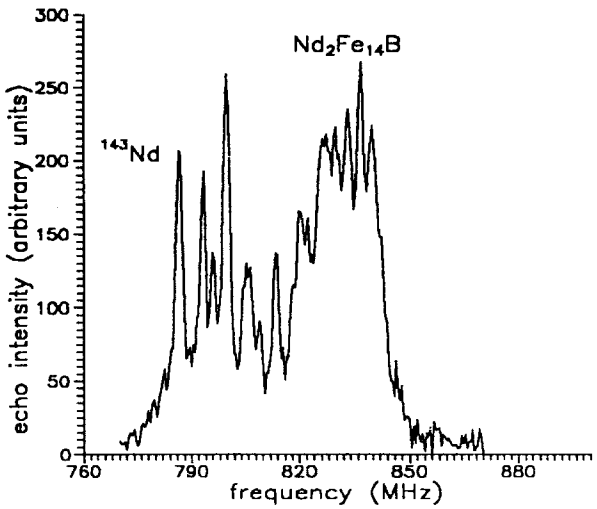

Fig. 7.13. ^{143}Nd spin-echo NMR spectra of $Nd_2Fe_{14}B$ at 4.2 K. After Kapusta et al. (1993b).

axis for both RE sites, 4f and 4g, is only two-fold, the lattice EFG is not axially symmetric and V_{ii}(latt) can be expressed as:

$$V_{ii}(\text{latt}) = -0.5\, V_{zz}(\text{latt})\left(1 - 3\cos^2\theta - \eta \sin^2\theta\, \cos 2\varphi\right), \tag{7.1}$$

where η is the asymmetry parameter, θ is the polar and φ is the azimuthal angle between the direction of the principal EFG component of the maximum absolute value, V_{zz} and V_{ii}. From the quadrupole splittings the EFG values in the c-plane (perpendicular to the

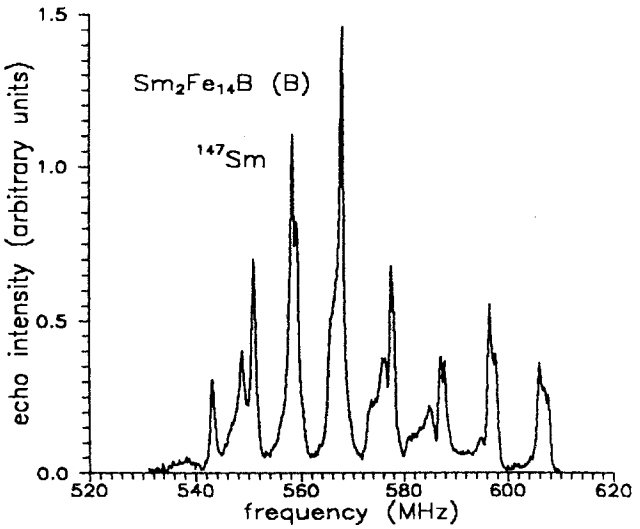

Fig. 7.14. ^{147}Sm spin-echo NMR spectra of $Sm_2Fe_{14}B$ at 4.2 K. After Kapusta et al. (1993b).

c-axis, from $Sm_2Fe_{14}B$) and at 30° to the c-axis (from $Nd_2Fe_{14}B$) were obtained. By subtracting the 4f electron contributions to the EFG, the "lattice EFG" values were derived. The corresponding V_{cc}(latt) values were found to be -67×10^{20} V m^{-2} for the 4g site and -25×10^{20} V m^{-2} for the 4f site. The lattice EFG components V_{zz}(latt) were, -67×10^{20} V m^{-2} and 82.9×10^{20} V m^{-2}, and the asymmetry parameters η were 0.22 and 0.40 for the 4g and 4f sites, respectively. Assuming proportionality between V_{cc}(latt) and A_2^0, as in the preceding paragraphs, A_2^0 values of 170 K a_0^{-2} for the 4g site and 63 K a_0^{-2} for the 4f site were derived. The V_{zz}(latt) values are taken with respect to the c-axis for the 4g site and to the c-plane for the 4f site, as with the Gd Mössbauer results of Bogé et al. (1986). The values of V_{zz}(latt) given by Bogé et al. were -75.9×10^{20} V m^{-2} and 114.1×10^{20} V m^{-2}. These are larger than those obtained from the NMR. The asymmetry parameter η was found to be 0.66 for the 4g and 0.35 for the 4f site. Unlike the results of the NMR study, the V_{cc}(latt) values were nearly the same for both sites, i.e., -75.9×10^{20} V m^{-2} and -77.0×10^{20} V m^{-2} for the 4g and 4f sites, respectively.

7.7. ^{159}Tb and ^{167}Er resonances

Spectra of $Tb_2Fe_{14}B$, $Er_2Fe_{14}B$ and $(Er_{0.1}Gd_{0.9})_2Fe_{14}B$ have been reported by Shimizu (1993), fig. 7.15, and of $(Er_{1-x}Tb_x)_2Fe_{14}B$ by Shimizu and Ichinose (1995a), fig. 7.16. In the former cited work, HFF values of 367.4 T and 356.5 T for the 4f and 4g sites, respectively, were derived. Using the values of the asymmetry parameters after Bogé et al. (1986), and combining the NMR and Mössbauer data for the Tb, Er, Dy and Gd containing compounds Shimizu obtained the lattice EFG values V_{zz} of 15.6×10^{20} V m^{-2} for the 4f site and -10.3×10^{20} V m^{-2} for the 4g site. The corresponding A_2^0 coefficient of 430 K a_0^{-2} for the 4f site and 420 K a_0^{-2} for the 4g site in $Tb_2Fe_{14}B$ were given, table 7.1. From

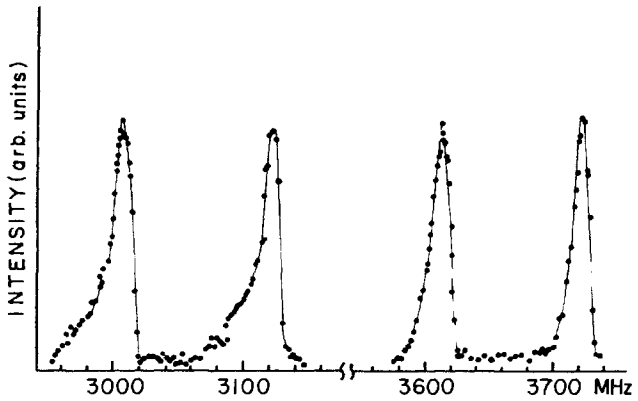

Fig. 7.15. ^{159}Tb spin-echo NMR spectra of $Tb_2Fe_{14}B$ at 1.4 K, corresponding to $-3/2 \leftrightarrow -1/2$ and $-1/2 \leftrightarrow 1/2$ transitions. After Shimizu (1993).

the Er resonance in $Er_2Fe_{14}B$ an A_2^0 coefficient of 400 K a_0^{-2} for the 4f site and 350 K a_0^{-2} for the 4g site was derived. Within error, the same values of the Er hyperfine field and EFG as in $Er_2Fe_{14}B$ have been found in $(Er_{0.1}Gd_{0.9})_2Fe_{14}B$, and thus, the same values of A_2^0 have been deduced for this compound. This result indicates, that the compound has its EMD at 4.2 K in the basal plane, as in $Er_2Fe_{14}B$ and the spectroscopic state of Er ion remains the same upon such doping. It also indicates, that the difference in the lattice EFG (A_2^0) values between the two compounds is less than 5%. The Tb spectra in $(Er_{1-x}Tb_x)_2Fe_{14}B$ show a large difference in HFF and quadrupole splitting between the axial $Tb_2Fe_{14}B$ and planar compounds with $x < 0.1$. The hyperfine fields at the 4f and 4g sites decrease from 367.4 T and 356.5 T in $Tb_2Fe_{14}B$, respectively, to 360 T and 352 T in $(Er_{0.98}Tb_{0.02})_2Fe_{14}B$, respectively (Shimizu and Ichinose 1995a). The observed shift of the resonance lines to lower frequencies when a magnetic field is applied is consistent with an antiparallel coupling of Tb and Fe moments. The dominant orbital contribution to the Tb HFF is parallel to the Tb moment. A conical structure has been deduced for $0.15 < x < 0.4$ region, where broad resonances with unresolved quadrupole splittings have been found.

7.8. *^{141}Pr resonance*

A study of $Pr_2Fe_{14}B$ and $(Pr_{0.9}Lu_{0.1})_2Fe_{14}B$ has been reported by Shimizu and Ichinose (1995b). The HFF values of 257.4 T for the 4f site and 280.3 T for the 4g site are obtained for $Pr_2Fe_{14}B$. Similar values of 256 T and 280.4 T for the respective sites, have been derived for $(Pr_{0.9}Lu_{0.1})_2Fe_{14}B$. The authors used the Y transferred hyperfine field data of Erdmann et al. (1989a), to relate a decrease of HFF from the Pr^{3+} free ion value to a decrease of Pr magnetic moment. The values of 2.9 μ_B for the 4f site and 3.0 μ_B for the 4g site have been derived, compared with the value of 3.2 μ_B for the free ion. There is no quadrupole splitting of the resonance lines and quadrupole oscillations of the spin echo decays do not appear. This has been attributed to the very small nuclear quadrupole moment of ^{141}Pr and the presence of large inhomogeneous magnetic hyperfine broadening.

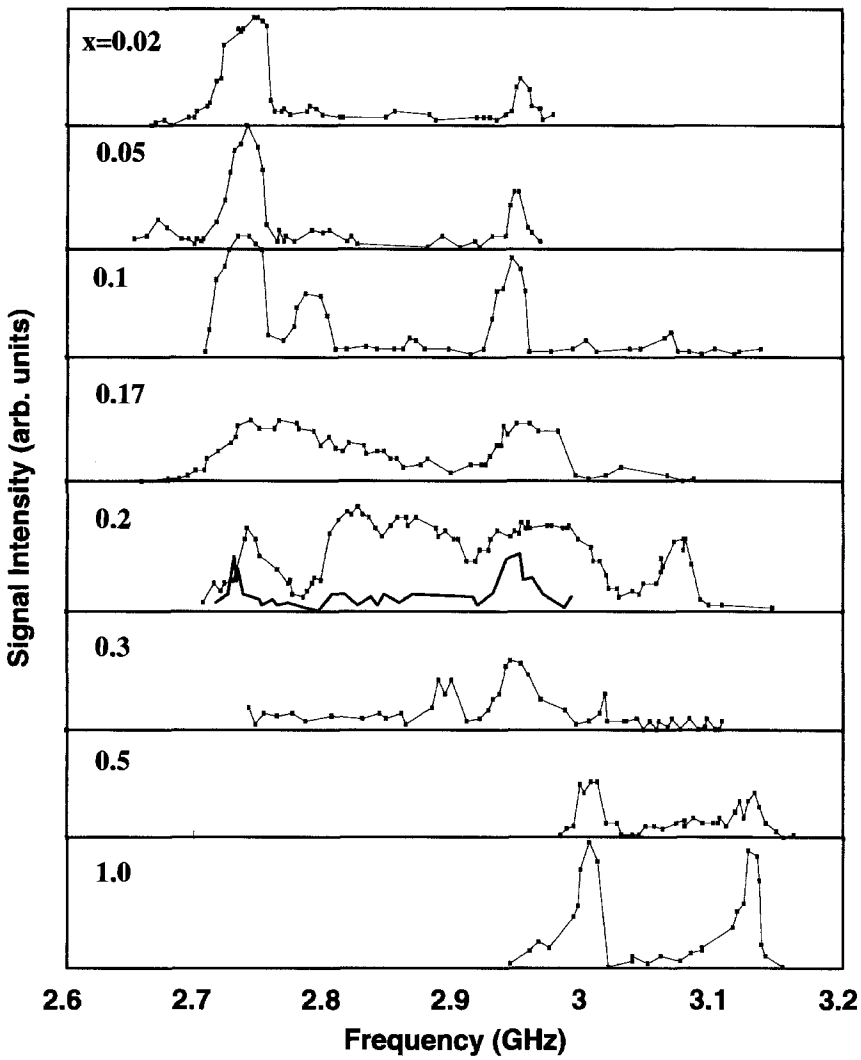

Fig. 7.16. ^{159}Tb spin-echo NMR spectra of $(Er_{1-x}Tb_x)_2Fe_{14}B$ at 1.4 K in zero field, corresponding to $-3/2 \leftrightarrow -1/2$ transitions. The solid line is in 20 kOe. After Shimizu and Ichinose (1995a).

7.9. *^{139}La resonance*

The spin echo spectra of $La_2Fe_{14}B$ have been reported by Kapusta and Riedi (1995). As lanthanum has the $4f^0$ configuration, the 4f electron contributions to the HFF and EFG vanish, giving the opportunity for an accurate determination of the lattice EFG and transferred HFF at the 4f and 4g crystallographic sites. Similar V_{cc}(latt) and A_2^0 values for both sites were found from the Gd Mössbauer measurements of Bogé et al. (1986), as from the theoretical calculations for $Gd_2Fe_{14}B$ of Coehoorn and Buschow (1991). However, both

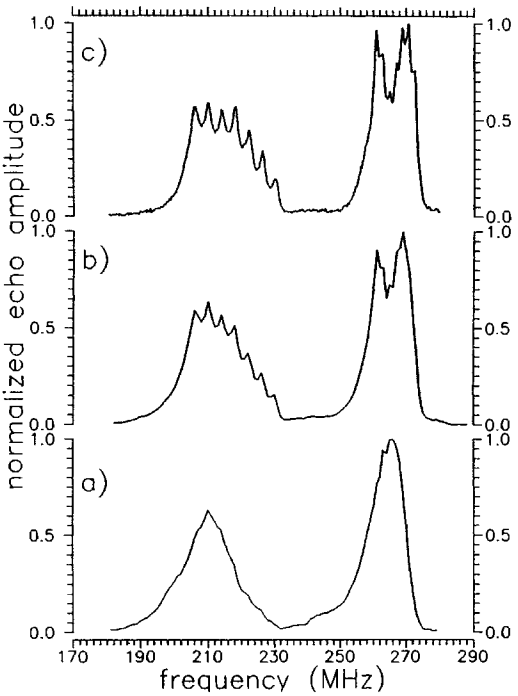

Fig. 7.17. ^{139}La spin-echo NMR spectra of $La_2Fe_{14}B$ at 4.2 K, for (a) $\tau = 15$ μs, (b) $\tau = 200$ μs, (c) $\tau = 500$ μs. After Kapusta et al. (1995a).

values differed by a factor of more than two for the Sm and Nd NMR in $Sm_2Fe_{14}B$ and $Nd_2Fe_{14}B$ (Kapusta et al. 1993b).

The spectra obtained for different pulse separations are presented in fig. 7.17. No quadrupole pattern could be resolved from the two broad resonance lines of the spectrum obtained for the pulse separation of $\tau = 15$ μs. As indicated in section 2, in order to remove DWC signals large pulse separations were used. For $\tau = 200$ μs, two resolved quadrupole septets were obtained. The resolution further improved for $\tau = 500$ μs. As the EMD for $La_2Fe_{14}B$ is the c-axis, the quadrupole splitting corresponds directly to V_{cc}(latt). Following the theoretical calculations of the "transferred" HFF by Coehoorn and Buschow (1993), the upper septet is assigned to the 4f site and the lower septet to the 4g site. The corresponding B_e are 36.1 T for the 4g and 44.1 T for the 4f site.

The values of the quadrupole splittings are 4.05 MHz for the 4g and 1.93 MHz for the 4f site indicating that V_{cc}(latt) and thus A_2^0 of the 4g site is more than two times larger than that of the 4f site. Different values of A_2^0 parameters of 136 $K a_0^{-2}$ for the 4f site and 190 $K a_0^{-2}$ for the 4g site have been derived from the analysis of the spin structure of the compounds by Yamada et al. (1985). However, the theoretical FLMTO calculations by Hummler and Fähnle (1996), have given similar V_{cc}(latt) values for both sites. Thus, a question arises concerning errors in the calculation of EFG with this newest computational method.

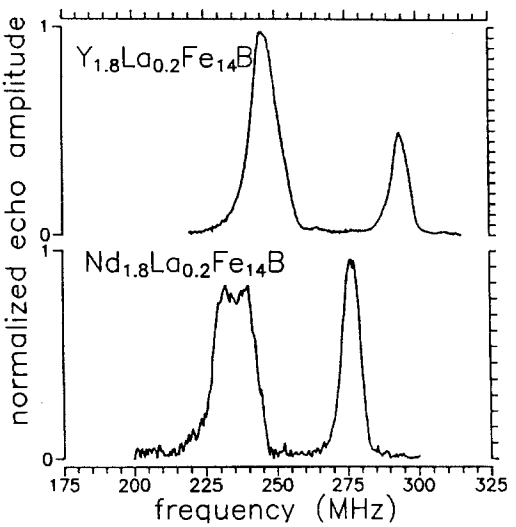

Fig. 7.18. ^{139}La spin-echo NMR spectra of $La_{0.2}Nd_{1.8}Fe_{14}B$ and $La_{0.2}Y_{1.8}Fe_{14}B$ at 4.2 K, for $\tau = 15$ μs. After Kapusta (1996).

On the basis of the EFG values obtained from NMR it was concluded that the lowest order contribution to the CEF at the 4g site is about two times larger than from the 4f site. The FLMTO calculations by Hummler and Fähnle (1996) led to the A_2^0 values of 476 K a_0^{-2} for the 4g and 284 K a_0^{-2} for the 4f site with their ratio of 1.7, which is close to that derived from NMR.

A strong line intensity corresponding to the 4g site was observed in the spectra of ^{139}La for samples $La_{0.2}Nd_{1.8}Fe_{14}B$ and $La_{0.2}Y_{1.8}Fe_{14}B$ (10% La substitution), fig. 7.18 after Kapusta (1996). The ratio of the area under the 4g and the 4f peak was found to be 1.8 for the Nd and was found to be 3.7 for the Y sample. These values are a measure of the ratio of lanthanum occupancy at the 4g and the 4f sites. The larger ratio for the Y sample is in agreement with a prediction based on the difference of the atomic radii. This difference is larger for La and Y than for La and Nd.

The measurement on $La_{0.1}Y_{1.9}Fe_{14}B$ (corresponding to 5% La substituted for Y) gives the ratio of 3.9. This is larger than for the sample with 10% La, i.e., at a low content of the substituent, the deviation from a random distribution is larger than for the more substituted sample.

8. $RE_2Fe_{14}C$

The magnet properties of the 2:14 carbides are extremely similar to the 2:14 borides, but have not been developed into commercial magnetic systems, because of the difficulties in the material preparation. Crystallites of $R_2Fe_{14}C$ will not form from the melt, but can be prepared via a solid-solid transformation. It may be due to these difficulties that contradictory reports on the effects on Curie temperature of replacing B by C have been published

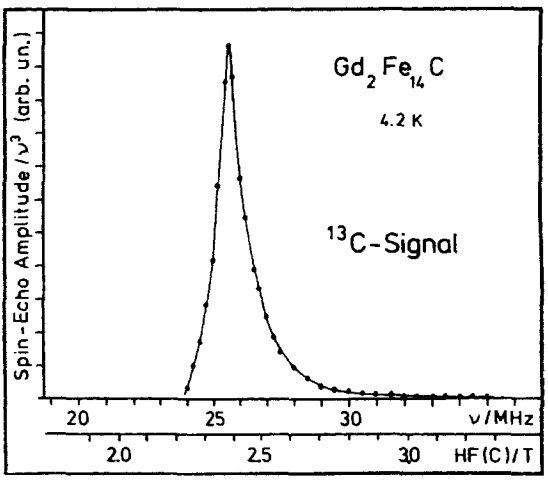

Fig. 8.1. ^{11}C frequency corrected spin-echo NMR spectra of $Gd_2Fe_{14}C$ at 4.2 K. After Erdmann (1989b).

(see Herbst (1991) for a detailed review). The only notable NMR study of HFF at iron and carbon nuclei in $Gd_2Fe_{14}C$ was reported by Erdmann et al. (1989b). The HFF at carbon nuclei found from the resonance frequency of the ^{13}C line, fig. 8.1, was found to be 2.38 T, the same as at the boron nuclei in $Gd_2Fe_{14}B$. The hyperfine fields at the Fe sites were found to be smaller than in $Gd_2Fe_{14}B$. This was attributed to a stronger electron transfer from the carbon to the iron than that from the boron to the iron.

9. $RE_2Fe_{14}BH_x$

As with Sm_2Fe_{17}, section 3.3.3, the $RE_2Fe_{14}B$ materials are able to absorb ~ 5 hydrogen atoms per formula unit, in agreement with a model by Fruchart et al. (1985), based on hydrogen occupying tetrahedral RE_3Fe and RE_2Fe_2 coordination sites. The introduction of interstitial hydrogen can lead to up to a 6% increase in the unit cell volume, slightly enhances the Fe moments and increases T_c, but strongly decreases the anisotropy field (Herbst 1991). This observed decrease in anisotropy field is in agreement with the marked drop in A_2^0 found from NMR measurements, discussed below.

A ^{145}Nd NMR study of $Nd_{15}Fe_{77}B_8H_x$ has been reported by Nadolski et al. (1989b). The hydride had a 1% larger $Nd_2Fe_{14}B$ unit cell volume than the unhydrided material. As for the unhydrided material, fig. 9.1, the spectrum of the hydrided material consisted of broad lines with an unresolved quadrupole splitting. The resonant frequencies of these lines were found to decrease on hydriding, with the spectrum of $Nd_{15}Fe_{77}B_8H_x$ extending from 430 MHz to 500 MHz and exhibiting a peak at 455 MHz and two smaller peaks at 440 and 485 MHz. Using the double resonance technique of Pieper et al. (1986), the authors measured the quadrupole splitting of the unresolved spectrum and found a decrease of quadrupole splitting on hydriding from that shown in fig. 9.1. There were found to be two values of the quadrupole splitting; one increasing monotonically from a value of 2

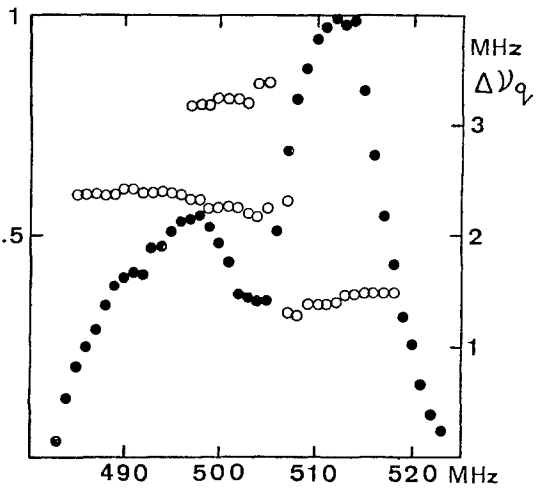

Fig. 9.1. Solid circles – ^{145}Nd spin-echo NMR spectra of $Nd_{15}Fe_{77}B_8$ at 4.2 K. Open circles – ^{145}Nd quadrupole splitting of $Nd_{15}Fe_{77}B_8$ at 1.8 K vs. frequency. After Nadolski et al. (1989b).

to 3 MHz in the range 440 and 480 MHz, and the second with a value of 1 MHz in the range 445 to 475 MHz. The authors have suggested that these changes may be the result of a reduction, by the hydrogen, of the Nd–Fe magnetic coupling. This is reflected in the influence of hydrogen on the spin reorientation, as observed by Pourarian et al. (1986) and Zhang et al. (1988). A ^{139}La study of $La_2Fe_{14}B$ and its hydrides by Kapusta et al. (1996f), showed that hydrogen strongly decreases the magnitude of the lattice EFG. Hence the uptake of hydrogen results in a reduction of A_2^0. Therefore the presence of hydrogen does appear to influence the RE contribution to the magnetocrystalline anisotropy in $RE_2Fe_{14}B$ compounds.

10. $RE\,Fe_{12-y}M_yN_x$

A promising RE–TM magnetic phase with a high Fe content, and thus a potentially very high saturation magnetisation and theoretical maximum energy product is the $RE\,Fe_{12-y}M_yN_x$ series. To date, however, the best interstitially unmodified candidate, $SmFe_{11}Ti$, has a lower $(BH)_{max}$ and saturation magnetisation than the Nd–Fe–B based magnets described in the previous sections. Binary compounds RFe_{12}, are not stable, but a 1:12 phase may be formed with addition of M = Mo, Ti, V or with a number of other additives. The $RE\,Fe_{12-y}M_yN_x$ family of compounds have the body centred tetragonal $ThMn_{12}$ structure (space group I4/mmm). The structure is shown in fig. 10.1, after Fujii and Sun (1995), which illustrates there are three inequivalent sites occupied by the Fe and M atoms denoted 8f, 8i and 8j. The RE and N atoms each occupy only one kind of crystallographic site. The 2b sites occupied by the N interstitials are equivalent to the 9e and 6h sites in the 2:17 compounds, the RE site potentially having two N nearest neighbours. The maximum site occupancy is $x = 1$, at which concentration the lattice expands by $\sim 3\%$.

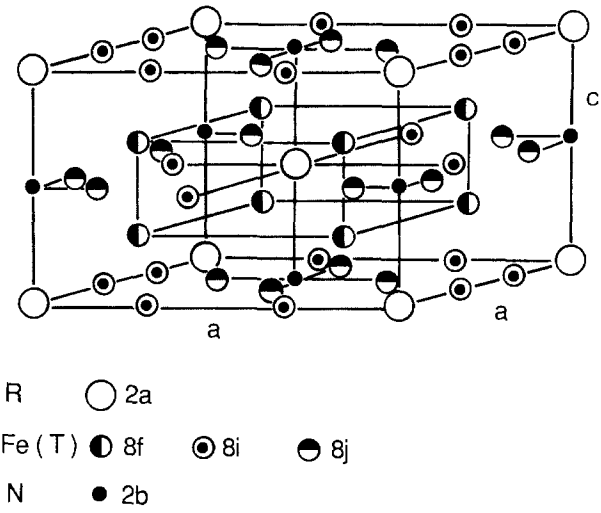

Fig. 10.1. Crystal structure of RE $Fe_{12-y}M_y$ (ThM_{12} structure – I4/mmm). After Fujii and Sun (1995).

Nitrogenation can significantly enhance the magnetic properties of these systems, as shown by NMR for example in $NdFe_{11}TiN_x$, as discussed below.

Structural and magnetic properties of RE $Fe_{12-y}M_y$ and the interstitial nitrides have been reviewed in detail by Fujii and Sun (1995).

The ^{57}Fe, ^{95}Mo and ^{97}Mo resonances of $YFe_{10}V_2$ and of $GdFe_{10}Mo_2$ have been studied by Sinnemann et al. (1989). The broad spectrum of $GdFe_{10}Mo_2$ below 50 MHz with pronounced peaks was attributed to the ^{57}Fe signal, whereas the resonances in the range 54–71.3 MHz were assigned to ^{95}Mo and ^{97}Mo resonances. Some α-Fe with dissolved Mo has also been identified in the ^{57}Fe signals at 40.8 and 47.7 MHz, whereas the 43.5 MHz signal has been attributed to Mo resonances in the $GdFe_{10}Mo_2$ phase. The low frequency spectrum was found to have distinct peaks. These reflect the presence of well defined HFF values at the Fe nuclei, related to the influence of Mo NN atoms on the Fe magnetic moment. The authors also reported on a Mössbauer study of $GdFe_{10}Mo_2$ and other materials. They found that the HFF obtained from the NMR and from the Mössbauer measurements were only in partial agreement. They attributed the discrepancies to the influence of the dipolar field distribution in the domain walls. Such a field distribution can give rise to a shifting and a broadening of the NMR resonances when compared to the HFF obtained from Mössbauer measurements which correspond to domain interiors. Possible discrepancies may also arise where proper account is not taken of contributions from ^{155}Gd and ^{157}Gd resonances, which have similar intensities to those of the Mo resonances.

The spin echo spectra on ^{147}Sm nuclei in $SmFe_{12-x}M_x$ (M = Ti, Mo) and $SmCo_{11}Ti$ have been reported by Kapusta et al. (1996g), fig. 10.2. The spectra have the form of septets of broad lines and are assigned to the single (2a) crystallographic site of Sm. The broadening of the lines is attributed to the influence of M elements distributed over the 8i sites. The structure visible on each line of the septet in the spectrum of $SmFe_{10.5}Mo_{1.5}$

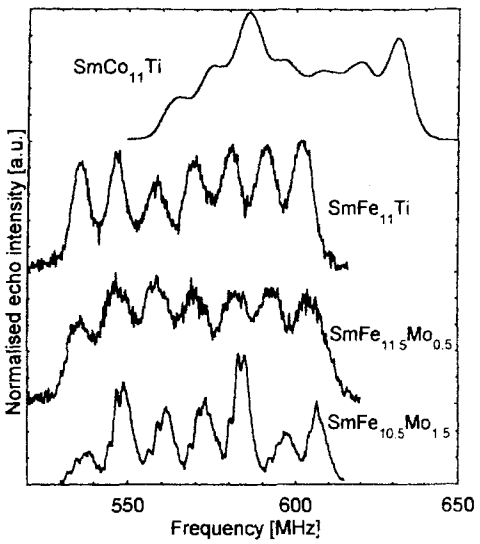

Fig. 10.2. ^{147}Sm spin-echo NMR spectra of $SmTM_{12-y}M_y$ at 4.2 K. After Kapusta et al. (1996g).

indicates a superposition of at least four septets. This spectrum has been interpreted in terms of the presence of different numbers of Mo atoms at the four 8i nearest neighbour M sites. The authors suggested that the narrower linewidths in the compounds with a larger x ($SmFe_{10.5}Mo_{1.5}$) than in the samples with smaller x, was related to tendency of M to stabilise the $ThMn_{12}$ type structure. Samples with x close to the boundary composition for the formation of the structure have a higher local disorder and are thus expected to have broader spectral lines.

An increase of HFF with increasing Mo content was observed and attributed to an associated decrease of the transferred HFF. The presence of one extra Mo nearest neighbour resulted in a decrease of the transferred HFF at the RE of 1.2 T. This decrease of the transferred HFF with x is in accord with the reduction of the Fe sublattice moment with x in the $REFe_{12-x}Mo_x$ reported by Agnostou et al. (1994) and Middleton et al. (1995).

From the quadrupole splittings, the lattice contribution to the electric field gradient and the crystal electric field coefficient A_2^0 were obtained. The magnitude of A_2^0 is larger for $SmFe_{11}Ti$ and $SmCo_{11}Ti$ than for Mo containing compounds and it decreases with increasing Mo content.

The ^{145}Nd spectra of $NdFe_{11}Ti$ and its interstitial nitride have been reported by Kapusta et al. (1995b), fig. 10.3. A single line with an unresolved quadrupole splitting was observed for the host material. This line was assigned to the single Nd site 2a in the structure of the compound. A narrow line at high frequency, appearing in the spectrum of the nitride, was attributed to the Nd sites with two nitrogen at the nearest neighbour 2b sites. The very small linewidth was related to a large reduction of the quadrupole splitting caused by a huge increase in magnitude of the lattice EFG produced at the Nd site by the neighbouring nitrogen atoms. The larger HFF at the Nd sites with nitrogen neighbours was consistent with the effects observed for the related RE_2Fe_{17} nitrides.

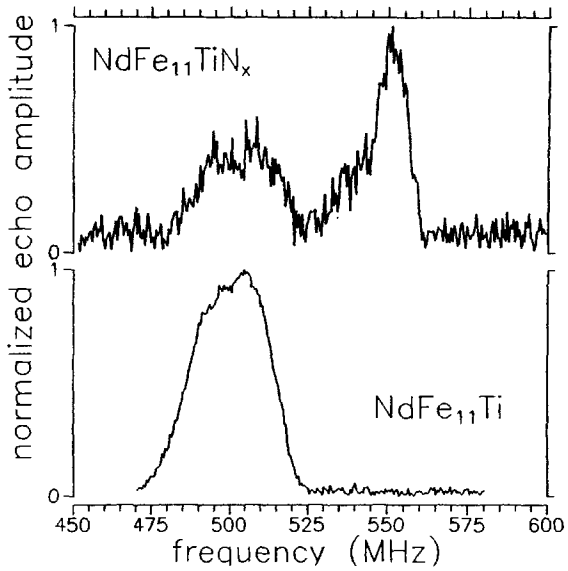

Fig. 10.3. ^{145}Nd spin-echo NMR spectra of $NdFe_{11}TiN_x$ at 4.2 K. After Kapusta et al. (1995b).

Fitting the lines with septets of equidistant lines (nuclear spin of ^{145}Nd is 7/2) allowed a determination of the change of Nd quadrupole splitting caused by the introduction of nitrogen neighbours. The change of the lattice EFG, V_{cc}(latt), caused by two nitrogen neighbours was found to be -73×10^{20} V m^{-2}, corresponding to a change of A_2^0 by 185 K a_0^{-2}. The change calculated per one N neighbour was 92.5 K a_0^{-2}, whereas for $Nd_2Fe_{17}N_x$ a value of -94 K a_0^{-2} was obtained. The difference in sign reflects the opposite contributions of the nitrogen atoms located along the c-axis in the RE $Fe_{11}TiN_x$ structure and in the basal plane in the $RE_2Fe_{17}N_x$ structure. The effect is consistent with bulk anisotropy measurements on the RE_2Fe_{17} nitrides, for which a strong uniaxial anisotropy appeared for the rare earths with the second order Stevens factor $\alpha_J > 0$, whereas for the RE $Fe_{12-y}M_y$ nitrides, uniaxial anisotropy was obtained for rare earths with $\alpha_J < 0$.

11. RE Co_5

Magnetic materials of the form RE Co_5 were the first RE–TM compounds to be identified as important candidates for permanent magnet applications. The results of an investigation of $SmCo_5$ by NMR were reported by Streever in 1975. These materials crystallise in the hexagonal $CaCu_5$ structure (space group P6/mmm) as shown in fig. 11.1. The crystal structure is similar to that of $Nd_2Fe_{14}B$, see fig. 7.1, which also consists of stacks of hexagonal and triangular layers with hexagonal TM prisms enclosing RE atoms. Although $SmCo_5$ was superseded by the rhombohedral Sm–Co 2:17 system in the early 1980s, it is important to note that it is the uniaxial grain boundary 1:5 phase, with its large magnetocrystalline anisotropy, which is thought to give the 2:17 materials their high coercivity.

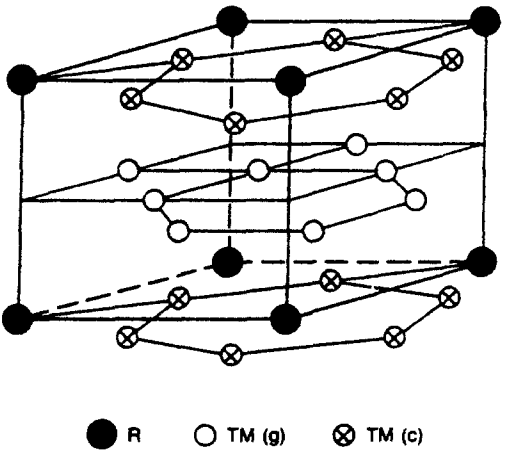

Fig. 11.1. Crystal structure of $RECo_5$ ($CaCu_5$ structure – P6/mmm). After Herbst (1991).

The intrinsic properties of the 1:5 systems are therefore of continuing interest and may still play a role in future developments of permanent magnet technologies.

^{59}Co spectra of YCo_5 have been reported by Inomata (1976), Streever (1978, 1979), Figiel et al. (1977) and Laforest et al. (1983). The spectra and the site assignments differed between the authors. The discrepancies were caused by the presence of signals originating from the Y_2Co_{17} impurity phase in some of the samples studied, as well as from the coexistence of the domain and domain wall signals. The ambiguity has been removed by Yoshie et al. (1987, 1988, 1991, 1993; Yoshie and Nakamura 1989), who have reported the spectra of $RECo_5$ (RE = Y, Ce, Pr, Nd, Sm, Gd, Tb, Dy, Ho) under applied magnetic fields of up to 5.5 T. From the study they determined the values and the signs of hyperfine fields at the Co sites in magnetic domains of the compounds. In particular, for YCo_5 they found a positive hyperfine field of +1.5 T at the 2c site and a negative field of −9.2 T at the 3g site, fig. 11.2. They attributed the effect to a huge positive HFF arising from a large orbital contribution to the Co magnetic moment, dominating the negative core polarisation term at the 2c site. Theoretical calculations of the Co magnetocrystalline anisotropy and HFF in YCo_5 and $GdCo_5$ (Daalderop et al. 1996), have shown that the contributions from the valence electrons differ much more between the sites than the orbital contributions do. The authors evaluated the valence electron contribution at +5.0 T for the 2c site and −5.2 T for the 3g site, whereas the orbital contributions were +16.4 T and +18.3 T, respectively. The orbital contributions to the magnetic moment were 0.23 μ_B at both Co sites.

The huge magnetocrystalline anisotropy of YCo_5 has been attributed by Streever (1978, 1979) to the anisotropy of the cobalt orbital moment, and the corresponding anisotropy of the spin–orbit interaction. The author related the anisotropy of HFF of a cobalt site (i.e., the difference in the HFF between the easy and the hard magnetisation directions) with the anisotropy of the orbital moment. This was related to the individual site contribution to the magnetocrystalline anisotropy. The largest contribution to the magnetocrystalline anisotropy energy was found to arise from the 2c site. This result was supported by the

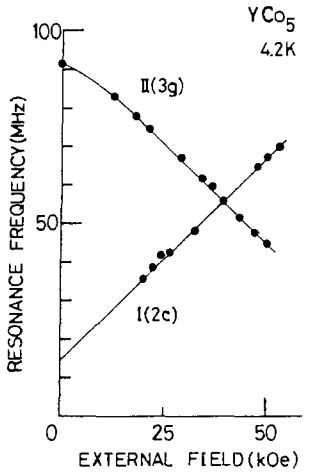

Fig. 11.2. Magnetic field dependence of ^{59}Co resonance frequency of YCo_5 at 4.2 K. After Yoshie et al. (1987).

LMTO ASA calculations by Nordström et al. (1992) and Daalderop et al. (1996). In these calculations the magnetocrystalline anisotropy energy was found to follow the anisotropy of the Co orbital moment.

The ^{89}Y resonance in YCo_5 at zero applied field has been reported by Figiel et al. (1976) and by Kapusta et al. (1992d). A single resonance line corresponding to the HFF of 10.2 T was attributed to the single crystallographic yttrium site 1a in the compound.

^{147}Sm and ^{149}Sm spin echo spectra of $SmCo_5$ have been reported by Streever (1975). A resolved quadrupole spectrum of ^{147}Sm was obtained and the HFF of 342 T and the quadrupole splitting of 9.4 MHz was derived. The values are nearly identical with those in the Sm_2Co_{17} system of 342.1 T and 9.3 MHz reported by Figiel et al. (1991). Thus, the signal attributed to the $SmCo_5$ phase possibly originated from a small amount of the Sm_2Co_{17} impurity phase which produces a relatively strong signal. This interpretation has been confirmed by the unsuccessful attempts of Kapusta et al. (1996h), to obtain a measurable Sm NMR signal from a good single phase $SmCo_5$ sample. The lack of a signal in the 10–1000 MHz range is possibly caused by a huge magnetocrystalline anisotropy of the compound and the same uniaxial anisotropy preference of both Sm and Co sublattices.

^{141}Pr and ^{159}Tb spectra of $PrCo_5$ and $TbCo_{5.1}$ are reported by Shimizu et al. (1994). At zero applied field a double hump resonance of ^{141}Pr and a double line structure of the two quadrupole satellites of ^{159}Tb is obtained, as shown in figs 11.3 and 11.4. An unresolved quadrupole splitting of Pr was attributed to the small nuclear quadrupole moment of the isotope. Under an applied magnetic field of 4 T, single line resonances were obtained, which in both cases originated from magnetic domain interiors. In zero field, the broad structure for Pr and the additional line observed for both Tb quadrupole satellites were attributed to the signals from domain walls. The HFF values of 293.5 T and 394.3 T were obtained for domain signals of Pr and Tb, respectively. The measured hyperfine fields and quadrupole

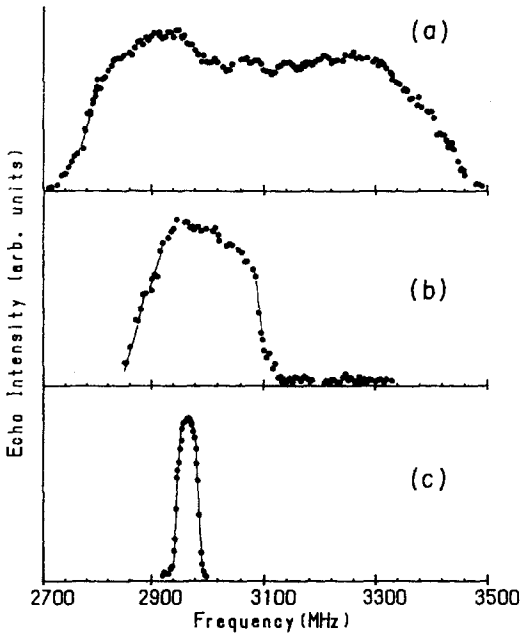

Fig. 11.3. ^{141}Pr spin-echo NMR spectra of $PrCo_5$ at 4.2 K in (a) zero external field, (b) 40 kOe, (c) 50 kOe. After Shimizu et al. (1994).

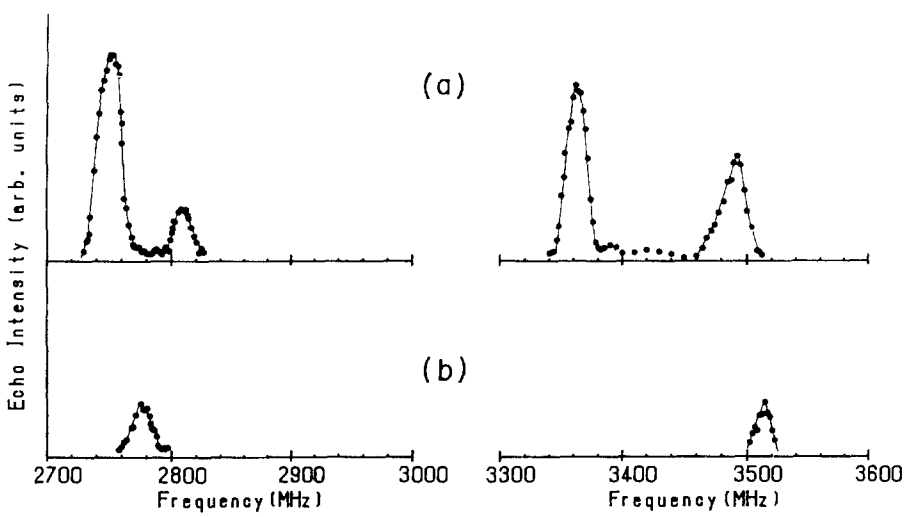

Fig. 11.4. ^{159}Tb spin-echo NMR spectra of $TbCo_{5.1}$ at 4.2 K in (a) zero external field at 1.4 K, (b) 40 kOe at 2 K. After Shimizu et al. (1994).

parameters were compared to the theoretical values obtained from an analysis of the exchange and CEF Hamiltonian. It was shown that the true Pr HFF is much lower than the theoretical and the free Pr^{3+} ion HFFs. For Tb, however, a good agreement between the experimental and the theoretical values was found. Similar discrepancies have also been observed by Han-Min et al. (1992), in a Pr NMR study of $Pr_xRE_{1-x}Co_5$ (RE = Y, Sm). The anomalously low Pr HFF was attributed to valence fluctuations in the compounds.

12. Conclusions

Frequency swept spin echo NMR provides a technique which allows the accurate determination of hyperfine fields and electric field gradients at individual sites. NMR may be performed on the nuclei of most of the constituent elements of modern materials used for permanent magnet applications. The resolution which can be obtained from NMR is generally higher than in Mössbauer measurements. The development in construction of untuned, computer controlled NMR spectrometers has made the experiments much more effective.

The local influence of the neighbouring atoms on HFF and EFG can be studied with a high accuracy. Note that the technique is highly sensitive to the presence of light interstitial elements which influence the valence electrons of neighbouring atoms of the host material. These features enable the determination of the content and distribution of interstitial elements at the various atomic sites. They allow the phases present in the material to be distinguished and provide an ideal tool to study the effects of substitution or doping with a sensitivity, which is often impossible to achieve by other experimental techniques.

The measurement of nuclear relaxation times, power dependence and the changes in behaviour under applied magnetic fields are helpful in the determination of the origin of the NMR signal. These measurements make it possible to distinguish between the domain wall centre and domain wall edge signals, enabling a reliable and comprehensive interpretation of the NMR results to be made.

The accurate determination of the spectroscopic state of the rare earth sites is a source of information on the EFGs at individual sites which can be used to ascertain the origin of the magnetocrystalline anisotropy. This, together with the information on the distribution of elements over atomic sites, is vital for a correct description of magnetic and anisotropic properties of materials such as $Nd_2Fe_{14}B$ with rare earth substitution.

The study of the 3d metal sites is a method of monitoring the distribution of the 3d elements and changes of easy magnetisation direction upon substitution. The anisotropy of the cobalt HFF arising from orbital contributions to the magnetic moment can be related with the individual contributions to the magnetocrystalline anisotropy from the Co sites.

Some information on the crystallographic and magnetic structure can also be obtained from NMR signal of "nonmagnetic" light elements such as boron, nitrogen or hydrogen.

There is a significant enhancement of the NMR signal in magnetic materials. This is especially large for the low anisotropy materials, enabling a very accurate comparative determination of the amounts of spurious soft magnetic phases such as α-Fe or unnitrided Sm_2Fe_{17}. Such information, as well as the information which NMR can yield on the distribution of the small quantities of dopant elements such as Nb or Ga, used to tailor the properties of commercial permanent magnetic materials, can be applied to optimise the technological routes of magnet processing for specific end products.

Acknowledgements

The financial support of the Engineering and Physical Sciences Research Council is greatfully acknowledged. One of us (Cz. K.) acknowledges the support of the Leverhulme Trust.

References

Abe, H., H. Yasuoka and A. Hirai, 1966, J. Phys. Soc. Japan **21**, 77.

Agnostou, M., E. Devlin, V. Psycharis, A. Kostikas and D. Niarchos, 1994, J. Magn. Magn. Mater. **131**, 157.

Altounian, Z., X. Chen, L.X. Liao, D.H. Ryan and J.O. Ström-Olsen, 1993, J. Appl. Phys. **73**, 6107.

Armitage, J.G.M., T. Dumelow, P.C. Riedi and J.S. Abell, 1989, J. Phys. Condens. Matter **1**, 3987.

Berthier, Y., M. Bogé, G. Czjzek, D. Givord, C. Jeandey, H.S. Li and J.L. Oddou, 1986, J. Magn. Magn. Mater. **54–57**, 589.

Berthier, Y., N. Nassar and T. Viadieu, 1988, J. Physique **49**(C8), 585.

Beuerle, T. and M. Fähnle, 1992, Phys. Status Solidi **174**, 257.

Bleaney, B., 1972, in: Magnetic Properties of Rare Earth Metals, ed. J.R. Elliot (Plenum, New York) Ch. 8.

Bogé, M., G. Czjzek, D. Givord, C. Jeandey, H.S. Li and J.L. Oddou, 1986, J. Phys. F: Metal Phys. **16**, L67.

Brennan, S., R. Skomski and J.M.D. Coey, 1994, IEEE Trans. Magn. **30**, 571.

Brooks, M.S.S., O. Eriksson and B. Johansson, 1989, J. Phys. Condens. Matter **1**, 5861.

Buschow, K.H.J., R. Coehoorn, D.B. de Mooij, K. DeWaard and T.H. Jacobs, 1990, J. Magn. Magn. Mater. **92**, L35.

Christodoulou, C.N. and T. Takeshita, 1993, J. Alloys Comp. **198**, 1.

Coehoorn, R. and K.H.J. Buschow, 1991, J. Appl. Phys. **69**, 5590.

Coehoorn, R. and K.H.J. Buschow, 1993, J. Magn. Magn. Mater. **118**, 175.

Coene, W., F. Hakkens, T.H. Jacobs, D.B. de Mooij and K.H.J. Buschow, 1990, J. Less-Common Met. **57**, 255.

Coey, J.M.D. and H. Sun, 1990, J. Magn. Magn. Mater. **87**, L251.

Croat, J.J., J.F. Herbst, R.W. Lee and F.E. Pinkerton, 1984a, J. Appl. Phys. **55**, 2078.

Croat, J.J., J.F. Herbst, R.W. Lee and F.E. Pinkerton, 1984b, Appl. Phys. Lett. **44**, 148.

Daalderop, G.H.O., P.J. Kelly and M.F.H. Schuurmans, 1996, Phys. Rev. B **53**, 14415.

Deppe, P., M. Rosenberg, S. Hirosawa and M. Sagawa, 1987, J. Appl. Phys. **61**, 4337.

Dirken, M.W., R.C. Thiel, R. Coehoorn, T.H. Jacobs and K.H.J. Buschow, 1991, J. Magn. Magn. Mater. **94**, 415.

Edgley, D.S., B. Saje, A.E. Platts and I.R. Harris, 1994, J. Magn. Magn. Mater. **138**, 6.

Erdmann, K., P. Deppe, M. Rosenberg and K.H.J. Buschow, 1987, J. Appl. Phys. **61**, 4340.

Erdmann, K., M. Rosenberg and K.H.J. Buschow, 1988a, J. Appl. Phys. **63**, 4116.

Erdmann, K., M. Rosenberg and K.H.J. Buschow, 1988b, J. Physique **12**(C8), 583.

Erdmann, K. and M. Rosenberg, 1989a, J. Magn. Magn. Mater. **82**, 273.

Erdmann, K., T. Sinnemann, M. Rosenberg and K.H.J. Buschow, 1989b, J. Less-Common Met. **146**, 59.

Figiel, H. and M. Jaszczewski, 1980, J. Magn. Magn. Mater. **15–18**, 673.

Figiel, H., E. Dormann, A. Oppelt and K.H.J. Buschow, 1976, Phys. Status Solidi (b) **82**, 275.

Figiel, H., A. Oppelt, E. Dormann and K.H.J. Buschow, 1977, Physica B **86–88**, 77.

Figiel, H., D. Fowler, T. Dumelow, P.C. Riedi and Cz. Kapusta, 1987, J. Magn. Magn. Mater. **65**, 83.

Figiel, H., N. Spiridis, P.C. Riedi and R. Graham, 1991, J. Magn. Magn. Mater. **101**, 401.

Figiel, H., Cz. Kapusta, N. Spiridis, G. Stoch, P.C. Riedi and M. Rosenberg, 1992, J. Magn. Magn. Mater. **104–107**, 1198.

Fruchart, D., P. Wolfers, P. Vulliet, A. Yaouanc, R. Fruchart and P. L'Heritier, 1985, in: Nd–Fe Permanent Magnets: Their Present and Future Applications, ed. I.V. Mitchell (Elsevier, London/NewYork) p. 173.

Fruchart, R., P. L'Heritier, P.D. DeReotier, D. Fruchart, P. Wolfers, J.M.D. Coey, L.P. Ferriera, R. Guillen, P. Vulliet and A. Yaouanc, 1987, J. Phys. F: Metal Phys. **17**, 483.

Fujii, H. and H. Sun, 1995, in: Handbook of Magnetic Materials, Vol. 9, ed. K.H.J. Buschow (Elsevier) p. 303.

Ge, S.H., Y.D. Zhang, F.S. Li, J.I. Budnick and P. Panissod, 1992, J. Magn. Magn. Mater. **116**, 211.

Givord, D., R. Lemaire, J.M. Moreau and E. Roudaut, 1972, J. Less-Common Met. **29**, 361.

Givord, D., H.S. Li and J.M. Moreau, 1984, Solid State Commun. **50**, 497.

Givord, D., H.S. Li and F. Tasset, 1985, J. Appl. Phys. **57**, 4100.

Grandjean, F., G.J. Long and K.H.J. Buschow, eds, 1995, Interstitial Intermetallic Alloys, NATO ASI Series, Vol. 281 (Kluwer, Dordrecht).

Gubbens, P.C.M., A.M. van der Kraan and K.H.J. Buschow, 1989, Hyperfine Interact. **53**, 37.

Gubbens, P.C.M., A.A. Moolenaar, G.J. Boender, A.M. van der Kraan, T.H. Jacobs and K.H.J. Buschow, 1991a, J. Magn. Magn. Mater. **97**, 69.

Gubbens, P.C.M., A.A. Moolenaar, T.H. Jacobs and K.H.J. Buschow, 1991b, J. Alloys Comp. **176**, 115.

Gutfleisch, O., J.C. Clarke, A.C. Neiva, S.A. Sinan and I.R. Harris, 1996, J. Alloys Comp. **233**, 139.

Hadjipanayis, G.C. and A. Kim, 1988, J. Appl. Phys. **63**, 3310.

Han-Min, J., K. Shimizu, H. Xiu-Feng, Y. Yu and Z. Tie-Song, 1992, J. Phys. Condens. Matter **4**, 8609.

Helmholdt, R.B. and K.H.J. Buschow, 1989, J. Less-Common Met. **155**, 15.

Herbst, J.F., 1991, Rev. Mod. Phys. **63**, 819.

Herbst, J.F., J.J. Croat, F.E. Pinkerton and W.B. Yelon, 1984, Phys. Rev. B **29**, 4176.

Herbst, J.F., J.J. Croat and W.B. Yelon, 1985, J. Appl. Phys. **57**, 4086.

Hu, B.P., H.S. Li, H. Sun and J.M.D. Coey, 1991a, J. Phys. Condens. Matter **3**, 3983.

Hummler, K. and M. Fähnle, 1996, Phys. Rev. B **53**, 3290.

Hummler, K., T. Beuerle and M. Fähnle, 1992, J. Magn. Magn. Mater. **115**, 207.

Ichinose, K. and H. Nagai, 1993, J. Appl. Phys. **32**, 329.

Ichinose, K., K. Fujiwara, F. Maruyama, M. Misawa, M. Oyasato, H. Nagai and A. Tsujimura, 1990, J. Magn. Magn. Mater. **90–91**, 549.

Ichinose, K., F. Maruyama, M. Misawa, A. Tsujimura, H. Nagai and K. Adachi, 1992, J. Magn. Magn. Mater. **104–107**, 1159.

Inomata, K., 1976, Jpn. J. Appl. Phys. **15**, 821.

Inomata, K., 1981, Phys. Rev. B **23**, 2076.

Iriyama, T., K. Kobayashi, N. Imaoka, T. Fukuda, H. Kato and Y. Nakagawa, 1992, IEEE Trans. Magn. **28**, 2326.

Isnard, O., S. Miraglia, J.L. Soubeyroux and D. Fruchart, 1992a, Solid State Commun. **81**, 13.

Isnard, O., J.L. Soubeyroux, S. Miraglia, D. Fruchart, L.M. Garcia and J. Bartolome, 1992b, Physica B **180**, 629.

Isnard, O., S. Miraglia, J.L. Soubeyroux, D. Fruchart and L. Pannetier, 1992c, Phys. Rev. B **45**, 2920.

Jaswal, S.S., W.B. Yelon, G.C. Hadjipanayis, Y.Z. Wang and D.J. Sellmyer, 1991, Phys. Rev. Lett. **67**, 644.

Jedryka, E., M. Wojcik, P. Panissod, M. Rosenberg, S. Hirosawa and M. Sagawa, 1988, J. Physique **49**(C8), 587.

Jedryka, E., M. Wojcik, P. Panissod and K.H.J. Buschow, 1990, J. Appl. Phys. **67**, 4586.

Jedryka, E., M. Wojcik, P. Panissod, A.T. Pedziwiatr and M. Slepowronski, 1991, J. Appl. Phys. **69**, 6043.

Jedryka, E., M. Wojcik and P. Panissod, 1992, J. Magn. Magn. Mater. **104**, 1405.

Kajitani, T., Y. Morii, S. Funahashi, T. Iriyama, K. Kobayashi, H. Kato, Y. Nakagawa and K. Hiraya, 1993, J. Appl. Phys. **73**, 6032.

Kakol, Z., H. Figiel and Cz. Kapusta, 1987, Phys. Status Solidi (b) **143**, 255.

Kapusta, Cz., 1996, J. Magn. Magn. Mater. **157–158**, 71.

Kapusta, Cz. and H. Figiel, 1988, J. Physique **49**(C8), 559.

Kapusta, Cz. and P.C. Riedi, 1995, in: NATO ASI Series, Vol. 281, eds F. Grandjean, G.J. Long and K.H.J. Buschow (Kluwer, Dordrecht) p. 497.

Kapusta, Cz., Z. Kakol, H. Figiel and R. Radwanski, 1986, J. Magn. Magn. Mater. **59**, 169.

Kapusta, Cz., M. Rosenberg, K. Erdmann and K.H.J. Buschow, 1990, Solid State Commun. **76**, 121.

Kapusta, Cz., M. Rosenberg, J. Zukrowski, H. Figiel, T.H. Jacobs and K.H.J. Buschow, 1991, J. Less-Common Met. **171**, 101.

Kapusta, Cz., R.J. Zhou, M. Rosenberg, P.C. Riedi and K.H.J. Buschow, 1992a, J. Alloys Comp. **178**, 139.

Kapusta, Cz., M. Rosenberg, R.G. Graham, P.C. Riedi, T.H. Jacobs and K.H.J. Buschow, 1992b, J. Magn. Magn. Mater. **104**, 1333.

Kapusta, Cz., M. Rosenberg, P.C. Riedi, J. Zukrowski, G. Stoch, H. Figiel and K.H.J. Buschow, 1992c, J. Alloys Comp. **182**, 331.

Kapusta, Cz., M. Rosenberg and K.H.J. Buschow, 1992d, J. Alloys Comp. **187**, 409.

Kapusta, Cz., M. Rosenberg, H. Figiel, T.H. Jacobs and K.H.J. Buschow, 1992e, J. Magn. Magn. Mater. **104**, 1331.

Kapusta, Cz., P.C. Riedi and K.H.J. Buschow, 1993a, J. Alloys Comp. **198**, 59.

Kapusta, Cz., H. Figiel, G. Stoch, J.S. Lord and P.C. Riedi, 1993b, IEEE Trans. Magn. **29**, 2893.

Kapusta, Cz., M. Rosenberg, P.C. Riedi, M. Katter and L. Schultz, 1994, J. Magn. Magn. Mater. **134**, 106.

Kapusta, Cz., J.S. Lord, P.C. Riedi and K.H.J. Buschow, 1995a, J. Alloys Comp. **221**, 105.

Kapusta, Cz., H. Figiel, X.C. Kou, G. Wiesinger, J.S. Lord, P.C. Riedi and K.H.J. Buschow, 1995b, J. Alloys Comp. **221**, 102.

Kapusta, Cz., P.C. Riedi, J.S. Lord, R. Mycielski and K.H.J. Buschow, 1996a, J. Alloys Comp. **235**, 66.

Kapusta, Cz., J.S. Lord and P.C. Riedi, 1996b, J. Magn. Magn. Mater. **159**, 207.

Kapusta, Cz., P.C. Riedi, G.J. Tomka, W. Kocemba, S. Brennan and J.M.D. Coey, 1996c, in: Proc. IX Int. Symp. on Magnetic Anisotropy and Coercivity in Rare Earth Transition Metal Alloys, Sao Paulo, eds F.P. Missell, V. Villas-Boas, H.R. Rechenberg and F.J.G. Landgraf (World Scientific, Singapore) p. 217.

Kapusta, Cz., P.C. Riedi, G.J. Tomka, R. Mycielski, B. Saje, S.A. Sinan and I.R. Harris, 1996d, in: Proc. IX Int. Symp. on Magnetic Anisotropy and Coercivity in Rare Earth Transition Metal Alloys, Sao Paulo, eds F.P. Missell, V. Villas-Boas, H.R. Rechenberg and F.J.G. Landgraf (World Scientific, Singapore) p. 327.

Kapusta, Cz., J.S. Lord, G.J. Tomka, P.C. Riedi and K.H.J. Buschow, 1996e, J. Appl. Phys. **79**, 4599.

Kapusta, Cz. et al., 1996f, unpublished.

Kapusta, Cz., H. Figiel, J.S. Lord, G.J. Tomka, P.C. Riedi, K.H.J. Buschow, X.C. Kou and G. Wiesinger, 1996g, J. Magn. Magn. Mater. **157–158**, 109.

Kapusta, Cz. et al., 1996h, unpublished.

Kapusta, Cz., P.C. Riedi, G.J. Tomka and R. Mycielski, 1997a, J. Appl. Phys. **81**, 4563.

Kapusta, Cz., P.C. Riedi, W. Kocemba, G. Stoch, G.J. Tomka, H. Figiel and K.H.J. Buschow, 1997b, J. Alloys Comp. **261**, 42.

Katter, M., J. Wecker and L. Schultz, 1991, J. Appl. Phys. **70**, 3188.

Katter, M., J. Wecker, C. Kuhrt, L. Schultz and R. Grössinger, 1992, J. Magn. Magn. Mater. **117**, 419.

Kronmüller, H., K. Durst, W. Ervens and W. Fernengel, 1984, IEEE Trans. Magn. **20**, 1569.

Kumar, K., 1988, J. Appl. Phys. **63**, R13.

Laforest, J., R. Lemaire, H. Nagai and A. Tsujimura, 1983, Solid State Commun. **48**, 941.

Li, H. and J.M.D. Coey, 1992, J. Magn. Magn. Mater. **152–154**, 153.

Li, Y., R.G. Graham, D.St.P. Bunbury, P.W. Mitchell and M.A.H. McCausland, 1995, J. Magn. Magn. Mater. **140–144**, 1007.

Loewenhaupt, M., P. Tils, K.H.J. Buschow and R.S. Eccleston, 1995, J. Alloys Comp. **222**, 39.

Loewenhaupt, M., P. Tils, K.H.J. Buschow and R.S. Eccleston, 1996, J. Magn. Magn. Mater. **152**, 10.

Lord, J.S. and P.C. Riedi, 1995, Meas. Sci. Technol. **6**, 149.

Machowska, E., 1993, PhD thesis, Institute of Physics, Polish Academy of Sciences, Warsaw.

Maruyama, F., K. Ichinose, K. Fujiwara, M. Misawa, M. Oyasato, H. Nagai and A. Tsujimura, 1990, J. Magn. Magn. Mater. **90–91**, 552.

Middleton, D.P., F.M. Mulder, R.C. Thiel and K.H.J. Buschow, 1995, J. Magn. Magn. Mater. **146**, 123.

Mishra, R.K., G. Thomas, T. Yoneyma, A. Fukuno and T. Ojima, 1981, J. Appl. Phys. **52**, 2519.

Moolenaar, A.A., P.C.M. Gubbens, G.J. Boender, T.H. Jacobs and K.H.J. Buschow, 1991, J. Magn. Magn. Mater. **101**, 395.

Mulder, F.M., R.C. Thiel, R. Coehoorn, T.H. Jacobs and K.H.J. Buschow, 1992, J. Magn. Magn. Mater. **117**, 413.

Myojin, T., M. Hayashi, T. Ohno, Y. Imaeda, T. Ushida, A. Tsujimura and T. Hilhara, 1993, J. Alloys Comp. **193**, 252.

Nadolski, S., E. Machowska and E. Burzo, 1989a, Solid State Commun. **71**, 97.

Nadolski, S., E. Machowska, P. Byszewski, E. Dynowska and S. Filipek, 1989b, Hyperfine Interact. **59**, 342.

Nordström, L., M.S.S. Brooks and B. Johansson, 1992, J. Phys. Condens. Matter **4**, 3261.

Panissod, P., E. Jedryka, M. Wojcik and J.I. Budnick, 1989, Phys. Rev. B **40**, 2606.

Pieper, M.W., H. Lütgemeier and W. Zinn, 1986, Z. Phys. B **63**, 369.

Platts, A.E., I.R. Harris and J.M.D. Coey, 1992, J. Alloys Comp. **185**, 251.

Potenziani, E., 1985, J. Appl. Phys. **58**, 2764.

Pourarian, F., M.Q. Huang and W.E. Wallace, 1986, J. Less-Common Met. **120**, 63.

Qi, Q.N., H. Sun, R. Skomski and J.M.D. Coey, 1992, Phys. Rev. B **45**, 12278.

Rahman, M.A. and G.R. Slemon, 1985, IEEE Trans. Magn. **21**, 1712.

Rosenberg, M., P. Deppe and M. Wojcik, 1985, J. Appl. Phys. **57**, 4124.

Rosenberg, M., P. Deppe and H. Stadelmaier, 1986a, Hyperfine Interact. **28**, 503.

Rosenberg, M., P. Deppe, K. Erdmann, M. Sostarich and H. Stadelmaier, 1986b, J. Magn. Magn. Mater. **54**, 599.

Rosenberg, M., P. Deppe and T. Sinnemann, 1989, Hyperfine Interact. **45**, 3.

Sagawa, M., S. Fujimara, N. Togawa, H. Yamamoto and T. Matsuura, 1984, J. Appl. Phys. **55**, 2083.

Scott, D.W., B.M. Ma, Y.L. Liang and C.O. Bounds, 1996, J. Appl. Phys. **79**, 4830.

Shen, N.X., Y.D. Zhang, J.I. Budnick, W.A. Hines and R. Lyver, 1996a, Appl. Phys. Lett. **69**, 3194.

Shen, N.X., Y.D. Zhang, J.I. Budnick, W.A. Hines and U. Binninger, 1996b, J. Appl. Phys. **79**, 5530.

Shimizu, K., 1993, J. Magn. Magn. Mater. **123**, L9.

Shimizu, K. and K. Ichinose, 1995a, J. Magn. Magn. Mater. **140–144**, 953.

Shimizu, K. and K. Ichinose, 1995b, Solid State Commun. **94**, 619.

Shimizu, K., K. Ichinose and H.M. Jin, 1994, J. Magn. Magn. Mater. **134**, 41.

Shimizu, K., K. Ichinose, Y. Fukuda and M. Shimotomai, 1995, Solid State Commun. **96**, 671.

Shoemaker, C.B., D.P. Shoemaker and R. Fruchart, 1984, Acta Crystallogr. C **40**, 1665.

Sinan, S.A., D.S. Edgley and I.R. Harris, 1995, J. Alloys Comp. **226**, 170.

Sinnemann, Th., K. Erdmann, M. Rosenberg and K.H.J. Buschow, 1989, Hyperfine Interact. **50**, 675.

Stepankova, H., J. Englich, J. Kohout and H. Lütgemeier, 1995, J. Magn. Magn. Mater. **140–144**, 2099.

Streever, R.L., 1975, Phys. Rev. B **12**, 4653.

Streever, R.L., 1977, Phys. Rev. B **16**, 1796.

Streever, R.L., 1978, Phys. Lett. A **65**, 360.

Streever, R.L., 1979, Phys. Rev. B **19**, 2704.

Sun, H., B.P. Hu, H.S. Li and J.M.D. Coey, 1990, Solid State Commun. **74**, 727.

Suzuki, S., T. Miura and M. Kawasaki, 1993, IEEE Trans. Magn. **29**, 2815.

Tomka, G.J., P.R. Bissell, R.W. Chantrell and K. O'Grady, 1995, J. Magn. Magn. Mater. **140–144**, 1097.

Uchida, H.H., H. Uchida, T. Yanagisawa, S. Kise, V. Koeninger, Y. Matsumura, U. Koike, K. Kamada, T. Kurino and H. Kaneko, 1992, in: Proc. Int. Workshop on Rare-Earth Magnets, July 12–15, The University of Western Australia, Nedlands, p. 342.

Uchida, H.H., H. Uchida, T. Yanagisawa, S. Kise, T. Suzuki, Y. Matsumura, U. Koike, K. Kamada, T. Kurino and H. Kaneko, 1993, J. Alloys Comp. **196**, 71.

Walstedt, R.E., 1992, in: Pulsed Magnetic Resonance, ed. D.M.S. Bagguley (Oxford University Press).

Wei, Y.N., K. Sun, Y.B. Fen, Y.X. Zhang, B.P. Hu, Y.Z. Wang, X.L. Rao and G.C. Liu, 1993, J. Alloys Comp. **194**, 9.

Wójcik, M., E. Jedryka, G. Jasiolek, W. Paszkowicz and M. Slepowronski, 1988, J. Magn. Magn. Mater. **72**, 330.

Wójcik, W., E. Jedryka, P. Panissod, S. Hirosawa and M. Sagawa, 1989, J. Magn. Magn. Mater. **80**, 19.

Wójcik, W., E. Jedryka, P. Panissod and K.H.J. Buschow, 1990, J. Magn. Magn. Mater. **83**, 243.

Yamada, M., Y. Yamaguchi, H. Kato, H. Yamamoto, Y. Nakagawa, S. Hirosawa and M. Sagawa, 1985, Solid State Commun. **56**, 663.

Yan, Q.W., P.L. Zhang, Y.N. Wei, K. Sun, B.P. Hu, Y.Z. Wang, G.C. Lui, C. Gau and Y.F. Cheng, 1993, Phys. Rev. B **48**, 2878.

Yoshie, H., K. Ogino, H. Nagai, A. Tsujimura and Y. Nakamura, 1987, J. Magn. Magn. Mater. **70**, 303.

Yoshie, H., K. Ogino, H. Nagai, A. Tsujimura and Y. Nakamura, 1988, J. Phys. Soc. Japan **57**, 1063.

Yoshie, H. and Y. Nakamura, 1989, J. Phys. Soc. Japan **58**, 2603.

Yoshie, H., S. Ozasa, M. Shiga and Y. Nakamura, 1991, J. Phys. Soc. Japan **60**, 2761.

Yoshie, H., T. Kojima, Y. Amako, H. Nagai, K. Ichinose, K. Adachi, M. Shiga and Y. Nakamura, 1993, J. Phys. Soc. Japan **62**, 3353.

Zhang, L.Y., F. Pourarian and W.E. Wallace, 1988, J. Magn. Magn. Mater. **71**, 203.

Zhang, Y.D., J.I. Budnick, M. Wójcik, E. Potenziani, A.T. Pedziwiatr and W.E. Wallace, 1987, Phys. Rev. B **36**, 8213.

Zhang, Y.D., J.I. Budnick, E. Potenziani, A.T. Pedziwiatr, W.E. Wallace and P. Panissod, 1988a, J. Appl. Phys. **63**, 3719.

Zhang, Y.D., J.I. Budnick, D.P. Yang, E. Potenziani, A.T. Pedziwiatr, W.E. Wallace and M. Sagawa, 1988b, J. Appl. Phys. **64**, 5586.

Zhang, Y.D., J.I. Budnick, D.P. Yang, E. Potenziani, A.T. Pedziwiatr, W.E. Wallace and M. Sagawa, 1989, J. Magn. Magn. Mater. **79**, 136.

Zhang, Y.D., J.I. Budnick, D.P. Yang, G.W. Fernando, W.A. Hines, T.D. Xiao and T. Manzur, 1995a, Phys. Rev. B **51**, 12091.

Zhang, Y.D., J.I. Budnick, N.X. Shen, W.A. Hines, G.W. Fernando and T. Manzur, 1995b, J. Magn. Magn. Mater. **144**, 987.

Zhang, Y.D., J.I. Budnick, W.A. Hines, N.X. Shen, T.D. Xiao and T. Manzur, 1995c, J. Magn. Magn. Mater. **145**, L11.

Zhang, Y.D., D.P. Yang, J.I. Budnick, W.A. Hines, W.Q. Xu, N.X. Shen, D.M. Pease, G.W. Fernando and T.D. Xiao, 1995d, Scripta Metall. Mater. **33**, 1817.

Zhang, Y.D., J.I. Budnick, W.A. Hines and D.P. Yang, 1996a, J. Appl. Phys. **79**, 4596.

Zhang, Y.D., J.I. Budnick, W.A. Hines, M.Q. Huang and W.E. Wallace, 1996b, Phys. Rev. B **54**, 51.

Zhou, R.J., M. Rosenberg, M. Katter and L. Schultz, 1993, J. Magn. Magn. Mater. **118**, 110.

chapter 4

CRYSTAL FIELD EFFECTS IN INTERMETALLIC COMPOUNDS STUDIED BY INELASTIC NEUTRON SCATTERING

O. MOZE

Istituto Nazionale per la Fisica della Materia
Dipartimento di Fisica
Università di Parma
43100 Parma
Italy

now at:
Istituto Nazionale per la Fisica della Materia
Dipartimento di Fisica
Università di Modena
41100 Modena
Italy

Handbook of Magnetic Materials, Vol. 11
Edited by K.H.J. Buschow

CONTENTS

1. Introduction

The crystal field interaction in rare-earth intermetallic compounds is responsible for an enormous variety of magnetic phenomena. In such compounds, magnetism is partially due to the incompletely filled 4f shells. The wavefunctions of these electrons are known to be reasonably well localized. This implies that, to a good approximation, the rare-earth ions have a characteristic free ion behaviour, with the ground state obeying the Hund rules. The LS (spin–orbit coupling) therefore characterizes the ground state in terms of the total angular momentum $J = L \pm S$. The large spin–orbit coupling gives rise to separations between multiplets of more than 200 meV, with the notable exceptions of Sm^{3+} and Eu^{3+} ions (table 1). At temperatures of interest for most magnetic materials only the lowest multiplets will thus be populated. The electrostatic interaction experienced by these ions, arising from the presence of near neighbor ions and outer valence electrons is much smaller than the spin–orbit coupling, because of the minute spatial extent of the 4f electron wavefunctions. This CF (crystal field) interaction gives rise to splittings of the ground state multiplet of the order of 1–100 meV for lanthanide intermetallics. The consequences of such an interaction for the electronic structure and magnetism are well established and documented. The crystal field Hamiltonian is an important source of magneto-crystalline anisotropy, and can govern the existence of magnetic order. The 4f shells interact with the rest of the electrons in the system and consequently stabilize the magnetization and anisotropy. Given that the electronic properties of 4f ions are rather well understood, good estimates of the rare-earth ion contribution to the anisotropy depend crucially on the crystalline environment around the appropriate rare-earth ion.

An intimate knowledge of the CF parameters is a necessary prequisite for a detailed analysis of physical properties such as susceptibility, specific heat, and complex magnetization processes and transitions. The CF interaction reflects the crystallographic point symmetry of the lanthanide ion and splits the $(2J + 1)$ fold degeneracy of the ground state according to rules dictated by group theory, first elegantly formulated by Bethe (1929). Another pertinent interaction is that which arises from magnetic interactions between ions. In many instances both these interactions compete with each other, resulting in a truly phenomenal variety of magnetic properties. The three important limiting cases of (i) a dominant CF interaction, (ii) a dominant exchange interaction, and (iii) CF and exchange interactions of comparable size are found to exist in virtually all lanthanide intermetallics in various stages of structural complexity.

The situation pertaining to compounds with an unstable or delocalized 4f shell leads to complications due to the manner in which conduction electrons can couple to 4f electrons. Compounds of Ce, for example, are a notable example and give rise to valence fluctuating

TABLE 1

Spin, orbital and total angular momentum quantum numbers for lanthanide R^{3+} ions. Other terms are: n, the number of 4f electrons, g_J, the Landé factor, Δ, the energy separation between the ground and first excited state multiplets (in meV).

Ion	n	S	L	J	g_J	Ground state	Δ
Ce^{3+}	1	1/2	3	5/2	16/7	$^2F_{5/2}$	275.7
Pr^{3+}	2	1	5	4	4/5	$^3H_4$	267.1
Nd^{3+}	3	3/2	6	9/2	8/11	$^4I_{9/2}$	232.7
Sm^{3+}	5	5/2	5	5/2	2/7	$^6H_{5/2}$	120.6
Gd^{3+}	7	7/2	0	7/2	2	$^8S_{7/2}$	–
Tb^{3+}	8	3	3	6	3/2	$^7F_6$	249.9
Dy^{3+}	9	5/2	5	15/2	4/3	$^6H_{15/2}$	405.0
Ho^{3+}	10	2	6	8	5/4	$^5I_8$	646.3
Er^{3+}	11	3/2	6	15/2	6/5	$^4I_{15/2}$	810.0
Tm^{3+}	12	1	5	6	7/6	$^3H_6$	732.4
Yb^{3+}	13	1/2	3	7/2	8/7	$^2F_{7/2}$	129.5

or Kondo systems. Rare-earth mixed valence or Kondo systems have 4f spin-fluctuation energies which are comparable or even larger than the CF splitting. This gives rise to a characteristic extremely broad excitation neutron scattering spectrum and henceforth there are no sharp and distinct lines which can be interpreted as arising only from a CF splitting (Murani 1997). Similar circumstances appear to be pertinent for 5f heavy-fermion intermetallics (Krimmel et al. 1996).

The experimental determination of the parameters that control both CF and exchange interactions is now extremely well established with an enormous literature. Both spectroscopic and thermal techniques are widely used. Optical spectroscopy is, however, obviously limited to transparent materials, virtually precluding all lanthanide intermetallics from any systematic study with this technique. Other spectroscopic techniques such as ESR and hyperfine interaction techniques (NMR and the Mössbauer effect) are important but indirect ways of determining unique CF interaction parameters that can sufficiently account for magnetic properties observed by other different experimental methods. Traditional thermal methods are an excellent way for investigation of the magnetic interactions present in these materials. Combined interpretation of specific heat, magnetic susceptibility, thermal expansion, magnetostriction and high field magnetization measurements can provide a consistent description of the CF interaction. Transport measurements such as electrical conductivity and resistivity are important for determining coupling of rare-earth ions to conduction electrons and phonons, but provide no direct way of determining the CF eigenvalues and eigenfunctions.

By far the most unique and perhaps direct experimental method for the determination of both CEF and exchange interactions in rare-earth intermetallics is provided by neutron scattering. The reasons are extremely simple. Neutron scattering is still the most fundamental investigative probe of the microscopic magnetization (Hirst 1997). Neutron inelastic scattering yields the *spatial and time dependence* of the dynamical susceptibility, a most

fundamental quantity for magnetic species. Past experience in investigations of the CF interaction in tetragonal, hexagonal and orthorhombic symmetries has clearly demonstrated that a combined effort using both INS and traditional techniques is necessary for a realistic determination of the CF parameters.

The purpose of this chapter is to provide a comprehensive review of crystal field effects in stable lanthanide intermetallic compounds, as determined by inelastic neutron scattering over the past 30 years, and to compare the results obtained with more traditional techniques such as those cited above. Much new work has appeared since the appearance of previous review chapters, principally driven by vastly improved methods in neutron instrumentation and a corresponding large emphasis on systems with rather low CF point symmetries. The contents of this review are based essentially only on systems with stable 4f electrons, principally for reasons of lack of space, but also because extremely comprehensive reviews on neutron scattering studies of valence fluctuating and anomalous lanthanides already exist (Loewenhaupt and Fischer 1993a, 1993b; Aeppli and Broholm 1994; Holland-Moritz and Lander 1994). Higher order, and generally weaker, magneto-elastic and quadrupolar interactions are also of some importance in rare-earth intermetallics, and thorough reviews of these types of interactions have been performed by Morin and Schmitt (1990) and Thalmeier and Lüthi (1991). This chapter is outlined in the following manner. A total of approximately 250 rare-earth intermetallics which have been investigated by INS have been classified according to their respective crystal structures, commencing with the simplest, and by far most numerous systems, those with a cubic crystal field and then progressively proceeding down to CF of a lower point symmetry. Material concerning INS studies of the magnetic excitations in the rare-earth elements has been excluded, as it does not form a part of the scope of this review and has been in any case reviewed elsewhere (Sinha 1978; Jensen 1982; Moon and Nicklow 1991) as well as in what has now become a classic text by Jensen and MacIntosh (1991). Brief mention is also made of some limited work on the CF interaction in dilute R alloys. A discussion of CF effects in hydride, carbide, icosahedral and amorphous systems then follows, terminating in a brief resume of the current theoretical and computational efforts which have been devoted to obtain a microscopic description of the CF interaction in metallic systems. Much of the contents of this chapter are complementary to the reviews of Loewenhaupt and Fischer (1993a) and Gignoux and Schmitt (1997). The latter review, in particular, is an up-to-date compilation of the magnetic properties and magnetic structures of a large part of the compounds discussed in the present chapter. A much earlier review, compiled by Wallace et al. (1977), summarizes in some detail crystal field effects in rare-earth aluminum, nickel, cobalt and iron compounds.

2. Neutron scattering from rare-earth intermetallics

The notion that neutron scattering could be used as a direct probe of the crystal field interaction in solids was first demonstrated in studies of CF excitations for the oxides Ho_2O_3 (Cribier and Jacrot 1960) and Er_2O_3 (Brockhouse et al. 1962) and since then the CF excitations for an enormous number of important systems such as the high T_c superconducting cuprates have been studied in detail by INS techniques (e.g., Henggeler et al. 1996) and

other non-metallic rare-earth compounds (e.g., Schmid et al. 1987; Loong et al. 1993; Furrer and Güdel 1997). Reviews of such investigations have been compiled by Loong and Soderholm (1994) and, in particular, by Mesot and Furrer (1997), and Henggeler and Furrer (1998) for rare earth based high temperature superconductors. The first observation of CF transitions in metallic systems by inelastic neutron scattering was reported as far back as 1967 (Furrer et al. 1967) followed by measurements of Ce monopnictides by Rainford et al. (1968). Inelastic neutron scattering studies of intermetallics up till this date have been briefly reviewed by Furrer (1974). The existence of a neutron magnetic moment has enormous consequences for magnetic materials and other specific advantages of thermal neutrons should also be recalled, such as, rather low absorption coefficients compared with X-rays and electrons. The details of neutron sources and production can be found in the appropriate monographs and reviews (e.g., Windsor 1981; White and Windsor 1984). The topic is very extensive and so this chapter can attempt to emphasis only the study by neutron inelastic scattering of *well defined* crystal field excitations and spin dynamics in stable intermetallic compounds.

The de Broglie relationship between the neutron energy and wavevector is of the simple form:

$$E = \frac{\hbar}{2m_{\mathrm{N}}}k^2, \tag{2.1}$$

where m_{N} is the neutron mass, 1.67495×10^{-27} kg. Convenient conversion factors for neutrons of energy E (in units of meV) and wavevector k (in units of Å^{-1}) or wavelength λ (in Å) are:

$$E = 2.072\,k^2 \quad \text{and} \quad E = \frac{81.799}{\lambda^2}. \tag{2.2}$$

The above expressions thus clearly show that neutrons, with wavelengths which are of the same order of magnitude as typical interatomic distances in solids, also have energies of the order of the low lying elementary excitations. This means that changes in the neutron energy after an interaction with an elementary excitation are quite significant and hence easy to measure. The radii of typical nuclei and the short range of the strong nucleon-neutron interaction, of the order of 10^{-15} cm, implies a point-like isotropic nuclear scattering and a scattering amplitude totally independent of scattering angle. This interaction of the neutron with the nucleus is most suitably parameterized by the Fermi pseudo-potential

$$V(\boldsymbol{r}, \boldsymbol{R}) = \frac{2\pi\hbar^2}{m_{\mathrm{N}}}[b + B\boldsymbol{I}\cdot\boldsymbol{\sigma}]\delta(\boldsymbol{r} - \boldsymbol{R}), \tag{2.3}$$

where the neutron and nucleus are located at $\boldsymbol{r}$ and $\boldsymbol{R}$, respectively (Squires 1978; Hicks 1996). The short range nuclear interaction has an amplitude given by the Fermi scattering length b and the remaining term in eq. (2.3), $B\boldsymbol{I}\cdot\boldsymbol{\sigma}$, represents the interaction of the neutron with the magnetic moments of the nuclei, $\boldsymbol{I}$, with B the spin-dependent nuclear scattering length and $\boldsymbol{\sigma}$ the Pauli spin matrices. Values of b and the spin dependent nuclear scattering cross sections for the elements are tabulated in most monographs on neutron scattering, in particular by Marshall and Lovesey (1971), Lovesey (1984) and Sears (1992).

2.1. *Magnetic neutron scattering cross section*

A full treatment of inelastic magnetic neutron scattering is not within the scope of this review. Only the basic results most frequently used for investigations of magnetic interactions in rare-earth intermetallics will be quoted. The details of the theory of magnetic neutron scattering can be found in the classic monographs of Marshall and Lovesey (1971), Squires (1978), Lovesey (1984), Jensen and Mackintosh (1991), Izyumov and Chernoplekov (1994) and in a less detailed manner by Bacon (1975). A historical perspective on the impact of neutron scattering techniques in magnetism is discussed by Brockhouse (1995) and Shull (1995). The earliest computations of the cross section of neutrons scattered from the electrons of a magnetic crystal was reported by Bloch (1936) and Halpern and Johnson (1939). A theoretical treatment of the magnetic cross section for paramagnetic rare-earth ions in the Hund ground state and with RS (Russell–Saunders) coupling was then reported by Trammell (1953). De Gennes (1963) presented a calculation of the expected inelastic cross section for transitions within a purely crystal field split multiplet. More specialized reviews on magnetic excitations in rare-earth intermetallics already exist (Sinha 1978; Fulde and Loewenhaupt 1985; Stirling and McEwen 1987). The latter review is totally dedicated to magnetic excitations in crystal-field split 4f metallics. A truly outstanding review of the experimental and theoretical techniques of neutron diffraction used in the determination of magnetic structures was written by Rossat-Mignod (1987). Other relevant monographs, with both theoretical and experimental aspects, are those by Izyumov and Chernoplekov (1994) on neutron spectroscopy, and Izyumov et al. (1991) on magnetic neutron diffraction, respectively. The theory and experimental methods required for the use of polarized neutron scattering is detailed in the monograph by Williams (1988). The use of polarization analysis of neutron scattering in order to separate in an unambiguous manner magnetic from non-magnetic neutron elastic and inelastic scattering, first experimentally demonstrated by Moon et al. (1969), is reviewed by Hicks (1996). The aspects of this technique relevant to magnetic systems are summarized by Stirling and McEwen (1987).

The obvious power of neutron scattering for magnetic species lies in the fact that the measured neutron cross section is most easily expressed in terms of the *generalized susceptibility*, a quantity which describes the dynamics of magnetic moments and can be calculated theoretically. The rule of energy conservation implies that the sample energy difference must be transferred in its entirety to the neutron:

$$\omega = \frac{\hbar^2}{2m_{\mathrm{N}}}\left(k_{\mathrm{i}}^2 - k_{\mathrm{f}}^2\right), \tag{2.4}$$

whilst the conservation of linear momentum implies the momentum transferred to the sample is $\hbar\boldsymbol{Q} = \hbar\boldsymbol{k}_{\mathrm{i}} - \hbar\boldsymbol{k}_{\mathrm{f}}$, where the scattering vector is defined by

$$\boldsymbol{Q} = \boldsymbol{k}_{\mathrm{i}} - \boldsymbol{k}_{\mathrm{f}}. \tag{2.5}$$

In its entirety, a neutron scattering experiment is all about measuring the scattered intensity neutron as a function of these two fundamental variables, the neutron energy transfer ω and

momentum transfer $\hbar\boldsymbol{Q}$. The operator for the neutron magnetic dipole moment is defined by

$$\boldsymbol{\mu}_{\mathrm{N}} = -1.913\,\mu_{\mathrm{N}}\boldsymbol{\sigma} \tag{2.6}$$

where μ_{N} is the nuclear magneton and $\boldsymbol{\sigma}$ the Pauli neutron spin operator.

The total magnetic field $\boldsymbol{B}$ generated by an electron at a point $\boldsymbol{R}$ is given by the sum of the spin and orbital contributions

$$\boldsymbol{B}(\boldsymbol{R}) = -\left[\nabla \times \frac{\boldsymbol{s}\times\widehat{\boldsymbol{R}}}{R^2} + \frac{1}{\hbar}\frac{\boldsymbol{p}\times\widehat{\boldsymbol{R}}}{R^2}\right], \tag{2.7}$$

where $\boldsymbol{s}$ is the electron spin operator and $\boldsymbol{p}$ is the electron momentum operator. The magnetic interaction operator for a neutron with a dipole moment in this field thus becomes

$$V(\boldsymbol{R}) = -\boldsymbol{\mu}_{\mathrm{N}} \cdot \boldsymbol{B}(\boldsymbol{R}). \tag{2.8}$$

In the Born approximation and using time dependent perturbation theory, valid for thermal neutrons since the interaction is very weak, the experimentally determined differential magnetic scattering cross section, for neutrons scattered into an element of solid angle $\mathrm{d}\Omega$ and with a corresponding energy transfer, $\omega = E_{\mathrm{f}} - E_{\mathrm{i}}$, is given by

$$\left(\frac{\mathrm{d}^2\sigma}{\mathrm{d}\Omega\,\mathrm{d}E}\right)_{q_{\mathrm{i}},q_{\mathrm{f}}} = \frac{k_{\mathrm{f}}}{k_{\mathrm{i}}}\left(\frac{m_{\mathrm{N}}}{2\pi\hbar^2}\right)^2 \sum_{q_{\mathrm{i}}}\sum_{q_{\mathrm{f}}} p_{\mathrm{i}}p_{\sigma_{\mathrm{i}}}\langle\sigma_{\mathrm{f}}q_{\mathrm{f}}|V(\boldsymbol{R})|\sigma_{\mathrm{i}}q_{\mathrm{i}}\rangle\langle\sigma_{\mathrm{i}}q_{\mathrm{i}}|V^*(\boldsymbol{R})|\sigma_{\mathrm{f}}q_{\mathrm{f}}\rangle \times \delta(\omega + E_{\mathrm{i}} - E_{\mathrm{f}}) \tag{2.9}$$

where $\sigma_{\mathrm{i,f}}$ and $q_{\mathrm{i,f}}$ are initial and final states for the neutron spin and sample, respectively. The associated thermal occupation factors for sample and neutron spin states are denoted by p_{i} and $p_{\sigma_{\mathrm{i}}}$. Evaluation of the matrix elements requires an integration over the spatial neutron co-ordinates and results in the standard expression for the magnetic scattering cross-section

$$\left(\frac{\mathrm{d}^2\sigma}{\mathrm{d}\Omega\,\mathrm{d}E}\right)_{q_{\mathrm{i}},q_{\mathrm{f}}} = \frac{k_{\mathrm{f}}}{k_{\mathrm{i}}}(\gamma r_{\mathrm{e}})^2 \sum_{q_{\mathrm{f}},q_{\mathrm{i}}} p_{\mathrm{i}}p_{\sigma_{\mathrm{i}}}\langle\sigma_{\mathrm{f}}q_{\mathrm{f}}|\boldsymbol{\sigma}\cdot\boldsymbol{M}_{\perp}|\sigma_{\mathrm{i}}q_{\mathrm{i}}\rangle\langle\sigma_{\mathrm{i}}q_{\mathrm{i}}|\boldsymbol{\sigma}\cdot\boldsymbol{M}_{\perp}^*|\sigma_{\mathrm{f}}q_{\mathrm{f}}\rangle \times \delta(\omega + E_{\mathrm{i}} - E_{\mathrm{f}}), \tag{2.10}$$

where the magnetic interaction operator $M_{\perp}(\boldsymbol{Q})$ is defined by:

$$M_{\perp}(\boldsymbol{Q}) = \sum_j \left[\widehat{\boldsymbol{Q}}\times(\boldsymbol{s}_j\times\widehat{\boldsymbol{Q}}) + \frac{\mathrm{i}}{\hbar Q}(\boldsymbol{p}_j\times\widehat{\boldsymbol{Q}})\right]\exp\mathrm{i}(\boldsymbol{Q}\cdot\boldsymbol{r}_j) \tag{2.11}$$

with $\boldsymbol{r}_j$ the electron co-ordinate. Other terms are: γ, the neutron gyromagnetic ratio, equal to 1.913, and $r_{\mathrm{e}} = \mathrm{e}^2/(m_{\mathrm{e}}c^2)$, the classical electron radius (2.818×10^{-15} m). The term

$(\gamma r_e)^2$ corresponds to a magnetic cross section of 0.29058 barns (1 barn $= 10^{-28}$ m^2). This is the general expression for the partial differential neutron magnetic scattering cross section. The approximation for dipolar transitions is always generally used in investigations of the unpaired 4f electrons in rare-earth intermetallics. Estimates of the cross sections for magnetic quadrupolar or octupolar excitations have been calculated (Chiu-Tsao and Levy 1976; Levy and Trammell 1977; Sablik 1985) for circumstances where quadrupolar or similar higher terms are larger than dipolar interactions.

The matrix element which needs to be evaluated in the case of nuclear scattering is less complicated, not depending on the value of $\boldsymbol{Q}$, since the interaction is extremely short-ranged. Its magnetic counterpart is more complex, being of a longer range and non-central. In the context of rare-earth intermetallics, where J is the appropriate quantum number for the rare earth ion, manipulation of eqs (2.10) and (2.11) gives the following general result for the unpolarized magnetic neutron scattering cross section, in the dipole approximation, for localized electrons (the dipolar scattering is dominant for $\boldsymbol{Q} \cdot \boldsymbol{r} \ll 1$, an approximation particularly valid for rare-earth ions where the mean radius of unpaired electrons, r, is typically about 0.6 Å)

$$\left(\frac{\mathrm{d}^2\sigma}{\mathrm{d}\Omega \mathrm{d}E}\right) = \frac{k_\mathrm{f}}{k_\mathrm{i}}(\gamma r_\mathrm{e})^2\left[\frac{1}{2}g_J f(\boldsymbol{Q})\right]^2 \sum_{\alpha,\beta}\left(\delta_{\alpha\beta} - \hat{Q}_\alpha \hat{Q}\beta\right) \sum_{\mathrm{i,f}} p_\mathrm{i} \sum_{i,j} \langle \mathrm{i}|J_{j\alpha}|\mathrm{f}\rangle\langle \mathrm{f}|J^*_{j\beta}|\mathrm{i}\rangle \times \exp \mathrm{i}\boldsymbol{Q} \cdot (\boldsymbol{r}_i - \boldsymbol{r}_j)\, \delta(\omega + E_\mathrm{i} - E_\mathrm{f}) \tag{2.12}$$

with g_J the Landé g-factor. In arriving at this general result, the important vector identity:

$$\begin{aligned} M_\perp(\boldsymbol{Q}) \cdot M^*_\perp(\boldsymbol{Q}) &= \left(\boldsymbol{Q} \times M(\boldsymbol{Q}) \times \boldsymbol{Q}\right) \cdot \left(\boldsymbol{Q} \times M^*(\boldsymbol{Q}) \times \boldsymbol{Q}\right) \\ &= \left[M(\boldsymbol{Q}) - \left[\hat{\boldsymbol{Q}} \cdot M(\boldsymbol{Q})\right]\hat{\boldsymbol{Q}}\right] \cdot \left[M^*(\boldsymbol{Q}) - \left[\hat{\boldsymbol{Q}} \cdot M^*(\boldsymbol{Q})\right]\hat{\boldsymbol{Q}}\right] \\ &= \sum_{\alpha,\beta}\left(\delta_{\alpha\beta} - \hat{Q}_\alpha \hat{Q}_\beta\right) M_\alpha(\boldsymbol{Q}) \cdot M^*_\beta(\boldsymbol{Q}) \end{aligned} \tag{2.13}$$

has been utilized (α, β are Cartesian components of the scattering and magnetization vectors). In table 2 are listed the nuclear and paramagnetic scattering cross sections relevant for lanthanide ions. The magnetic form factor $f(\boldsymbol{Q})$ is defined as the Fourier transform of the magnetization density of unpaired electrons and comprises both spin and orbital magnetization terms. An accurate measurement of the form factor will allow, in principle, a determination of the ground state electron wavefunction and hence the appropriate CF and exchange parameters. In such cases, the eigenstates are described in terms of linear combinations of states $|J, M_J\rangle$ of the total angular momentum J,

$$|\psi\rangle \sum_{M_J} \lambda_M |J, M_J\rangle. \tag{2.14}$$

The magnetic form factor can be expressed in terms of tensor operators and calculated by conventional Racah algebra (Johnston 1966; Lovesey and Rimmer 1969; Stassis and

TABLE 2

Thermal neutron scattering and absorption cross sections for the most commonly studied lanthanide ions. σ_{coh}, σ_{inc} and σ_{abs} are the bound coherent, incoherent scattering and absorption cross sections, respectively (in units of barns, 1 barn = 10^{-28} m^2). The para-magnetic scattering cross section σ_{mag} (also in units of 10^{-28} m^2) is calculated for the forward direction, where $f(0) = 1$ (Trammell 1953; Squires 1978). All the parameters listed here refer to neutrons with a thermal energy of 25.30 meV (293 K), wavelength = 1.798 Å and velocity of 2200 m/sec (adapted from Sears (1992)).

Ion	σ_{coh}	σ_{inc}	σ_{abs}	σ_{mag}
Ce	2.93	2.93	0.63	3.9
Pr	2.64	0.02	11.5	7.8
Nd	7.43	16.6	50.5	7.9
Sm	0.42	39.0	5922	0.43
Gd	29.3	151.2	49700	38.3
Tb	6.84	0.004	23.4	57.5
Dy	35.9	54.4	994	68.9
Ho	8.06	0.36	64.7	68.5
Er	7.63	1.1	159	55.9
Tm	6.28	0.10	100	34.8
Yb	19.4	4.0	34.8	12.5

Paramagnetic cross sections are calculated from the expression:

$$\sigma_{mag} = \frac{8\pi}{3}(\gamma r_e)^2\left[\frac{1}{2}g_J f(\boldsymbol{Q})\right]^2 J(J+1).$$

Deckman 1975). The magnetic scattering length is then defined as a vector $\boldsymbol{E}$, with components $\boldsymbol{E}_q(\boldsymbol{Q})$ given by

$$E_q(\boldsymbol{Q}) = -2\sqrt{4\pi}\sum_{K'q'}\sum_{K''q''} Y_{q''}^{K''}(\boldsymbol{Q})\left[A(K'', K') + B(K'', K')\right] \times \sum_{MM'} \lambda_M \lambda_{M'} \langle K'q'J'M'|JM\rangle\langle K''q''K'q'|1q\rangle. \tag{2.15}$$

The coefficients $A(K, K')$ and $B(K, K')$ are the orbital and spin contributions to the form factor, which are appropriate linear combinations of radial integrals

$$\langle j_K(Q)\rangle = \int_0^\infty r^2 |f(r)|^2 j_K(Qr)\,\mathrm{d}r \tag{2.16}$$

for $K = 0, 2, 4, 6$, where $|f(r)|^2$ is the probability distribution of the radial component of the 4f electron wavefunction and $j_K(Qr)$ are spherical Bessel functions. These linear combinations are tabulated for the rare-earths (Lander and Brun 1970) and radial integrals have also been calculated within a relativistic approximation (Freeman and Watson 1962;

Freeman and Desclaux 1979). In most experimental configurations, with a magnetic field applied in order to saturate the moment in a direction perpendicular to the scattering vector, only the component E_0 is actually measured, and this is simply related to the R moment;

$$E_0(\boldsymbol{Q}) = -\mu_R f_R(\boldsymbol{Q}), \tag{2.17}$$

where

$$f(\boldsymbol{Q}) = \langle j_0 \rangle + C_2\langle j_2 \rangle + C_4\langle j_4 \rangle + C_6\langle j_6 \rangle, \tag{2.18}$$

with the coefficients, importantly, independent of the scattering vector. Thus, the form factor is separated into angular and radial components. In this manner, the coefficients λ_M and the magnetic moment are determined with a good precision.

Experimental and theoretical techniques of this highly specialized aspect of *elastic* magnetic neutron scattering are discussed in detail for rare-earth intermetallics by Sinha (1978) and in the chapter on neutron determination of magnetic structures by Rossat-Mignod (1987), as well as by Lander (1993). These measurements are generally performed using single crystals and polarized neutrons. Form factor measurements have been performed on numerous rare-earth intermetallics in order to obtain the relevant coefficients of the eigenstates. In certain circumstances, it is not possible to assign unambiguously a CF ground state from INS data alone. An example is the case of Ce ($J = 5/2$), in a cubic CF, for which the ground state multiplet splits into two levels, a Γ_7 doublet and a Γ_8 quadruplet, INS observes only the splitting between these two levels. The ground state assignment can be obtained by an accurate determination of the magnetic moment in the ordered state. Magnetic form factor investigations are ideal for this purpose. The Q-dependence of the form factor implies that magnetic scattering tends to fall off rapidly with increasing Q, with the exception of Sm (Boucherle et al. 1982), where the orbital magnetization density almost cancels the spin density and due to the more localized nature of the spin density, the magnetic form factor exhibits a maximum at a non-zero value of Q. It is one of the means by which magnetic scattering can be simply isolated from the nuclear scattering. The temperature dependence of the magnetic scattering, via the population term p_i, also provides a means of isolating the magnetic scattering, as CF excitations obey Boltzmann statistics, whilst phonons obey Bose–Einstein statistics.

The phonon cross section increases with increasing Q, in contrast to the magnetic scattering, which generally decreases with decreasing Q. This is the simplest way to isolate the inelastic magnetic scattering from the phonon contribution. The definitive way to separate the two contributions is to perform experiments with polarized neutrons (Williams 1988). In the simplest case, analysis of the scattering is performed with the direction of the neutron polarization along the z axis. The Cartesian components of the Pauli spin matrices are given by

$$\sigma_x = \begin{bmatrix} 0 & 1 \\ 1 & 0 \end{bmatrix}, \qquad \sigma_y = \begin{bmatrix} 0 & -\mathrm{i} \\ \mathrm{i} & 0 \end{bmatrix}, \qquad \sigma_z = \begin{bmatrix} 1 & 0 \\ 1 & -1 \end{bmatrix}. \tag{2.19}$$

In this formalism, the matrix element, $\langle\sigma_f|\boldsymbol{\sigma}\cdot\boldsymbol{M}_\perp|\sigma_i\rangle$, of the neutron spin-magnetization operator can be decomposed into the appropriate spin-state matrix elements

$$\begin{aligned}
&\langle +|\boldsymbol{\sigma}\cdot\boldsymbol{M}_\perp|+\rangle = M_{\perp z}, && \langle -|\boldsymbol{\sigma}\cdot\boldsymbol{M}_\perp|-\rangle = -M_{\perp z},\\
&\langle +|\boldsymbol{\sigma}\cdot\boldsymbol{M}_\perp|-\rangle = M_{\perp x}+\mathrm{i}M_{\perp y}, && \langle -|\boldsymbol{\sigma}\cdot\boldsymbol{M}_\perp|+\rangle = M_{\perp x}-\mathrm{i}M_{\perp y},
\end{aligned} \tag{2.20}$$

where terms of the type $\langle\pm|\boldsymbol{\sigma}\cdot\boldsymbol{M}_\perp|\pm\rangle$ imply a scattering process which does not reverse the polarization of the incident neutron spin (non spin-flip), whilst the terms $\langle\pm|\boldsymbol{\sigma}\cdot\boldsymbol{M}_\perp|\mp\rangle$ involve scattering with neutron spin-flip. The corresponding spin dependent matrix elements for nuclear scattering are obtained from an identical manipulation of eq. (2.3)

$$\begin{aligned}
&\langle +|b'(\boldsymbol{k})|+\rangle = b+\frac{B}{2}I_z, && \langle -|b'(\boldsymbol{k})|-\rangle = b-\frac{B}{2}I_z,\\
&\langle +|b'(\boldsymbol{k})|-\rangle = \frac{B}{2}(I_x+I_y), && \langle -|b'(\boldsymbol{k})|+\rangle = \frac{B}{2}(I_x-I_y).
\end{aligned} \tag{2.21}$$

Thus the spin-flip scattering is entirely magnetic with an additional contribution from the interaction with the nuclear spin. The non-spin-flip scattering amplitudes have both nuclear and scattering contributions, unless the scattering vector is along the neutron polarization direction and, therefore, $M_{\perp z} = 0$. A full three dimensional polarization analysis of the scattered intensity, where analysis of the neutron polarization after scattering is performed along the x, y and z directions, allows isolation of the magnetic from the nuclear scattering as well as between longitudinal and transverse components of the magnetization (Moon et al. 1969; Hicks 1996). The technique of polarization analysis, however, can only generally be done at a prohibitive cost in available incident neutron intensity, and is rarely used to identify CF transitions in rare-earth intermetallics.

Use of the integral representation of the δ-function

$$\delta(\omega - E_f + E_i) = \frac{1}{2\pi\hbar}\int_{-\infty}^{\infty}\exp\left[\mathrm{i}(\omega - E_f + E_i)t/\hbar\right]\mathrm{d}t, \tag{2.22}$$

with the integration carried over time, simplifies eq. (2.12) to the compact and well known form:

$$\frac{\mathrm{d}^2\sigma}{\mathrm{d}\Omega\,\mathrm{d}E} = \frac{k_f}{k_i}(\gamma r_0)^2\left[\frac{1}{2}g_J f(\boldsymbol{Q})\right]^2 \mathrm{e}^{-2W(\boldsymbol{Q})}\sum_{\alpha,\beta}\left(\delta_{\alpha\beta}-\widehat{Q}_\alpha\widehat{Q}_\beta\right)S_{\alpha\beta}(\boldsymbol{Q},\omega), \tag{2.23}$$

where the scattering function $S(\boldsymbol{Q},\omega)$ (Van Hove 1954) is defined by the spatial and temporal Fourier transform of the magnetic correlation function $\langle \boldsymbol{J}_\alpha(t)\boldsymbol{J}^*_\beta(0)\rangle$:

$$S_{\alpha\beta}(\boldsymbol{Q},\omega) = \frac{1}{2\pi}\int\left\langle \boldsymbol{J}_\alpha(\boldsymbol{Q},t)\boldsymbol{J}^*_\beta(\boldsymbol{Q},t)\right\rangle\exp(-\mathrm{i}\omega t)\,\mathrm{d}t. \tag{2.24}$$

The term $\exp[-2W(\boldsymbol{Q})]$ is the Debye–Waller factor, representing the thermal vibrational motion of atoms (Willis and Pryor 1975).

2.2. Generalized dynamical susceptibility

There is now a further and more powerful connection between the scattering function and the generalized susceptibility of the magnetic system under consideration. This connection has its origins in the fluctuation-dissipation theorem of statistical mechanics. Within the approximation of linear response theory, the neutron generates a frequency and wave-vector dependent magnetic field in the sample and detects the linear response which, for magnetic systems, is the susceptibility. This response is described by the dynamical susceptibility tensor $\chi_{\alpha\beta}(\boldsymbol{Q}, \omega)$, defined as

$$M_{\alpha\beta}(\boldsymbol{Q}, \omega) = \sum_{\beta} \chi_{\alpha\beta}(\boldsymbol{Q}, \omega) H_{\beta}(\boldsymbol{Q}, \omega), \tag{2.25}$$

where the magnetization M responds linearly to a spatially and temporally varying magnetic field applied in the β direction, $H_{\beta}(\boldsymbol{Q}, \omega)$. The fluctuation dissipation theorem then simply connects the scattering law $S_{\alpha\beta}(\boldsymbol{Q}, \omega)$ to the imaginary part of the dynamical susceptibility $\chi''_{\alpha\beta}(\boldsymbol{Q}, \omega)$, at any temperature:

$$S_{\alpha\beta}(\boldsymbol{Q}, \omega) = \frac{1}{\pi} \frac{1}{1 - \exp(-\omega/k_{\mathrm{B}}T)} \chi''_{\alpha\beta}(\boldsymbol{Q}, \omega). \tag{2.26}$$

The magnetic cross section, for unpolarized neutrons, is now finally reduced to a quantity which can be calculated on a theoretical basis, for N magnetic ions, the *imaginary* part of the *dynamical susceptibility*

$$\begin{aligned} \frac{\mathrm{d}^2\sigma}{\mathrm{d}\Omega \mathrm{d}E} &= N \frac{k_{\mathrm{f}}}{k_{\mathrm{i}}} (\gamma r_{\mathrm{e}})^2 \left[\frac{1}{2} g_J f(\boldsymbol{Q}) \right]^2 \mathrm{e}^{-2W(\boldsymbol{Q})} \frac{1}{\pi} \frac{1}{1 - \exp(-\hbar\omega/k_{\mathrm{B}}T)} \\ &\quad \times \sum_{\alpha,\beta} \left(\delta_{\alpha\beta} - Q_{\alpha} Q_{\beta} \right) \chi''_{\alpha\beta}(\boldsymbol{Q}, \omega). \end{aligned} \tag{2.27}$$

The neutron scattering cross section is therefore related to the dissipative response of the magnetization. A further important connection is that between the real and imaginary parts of the dynamical susceptibility, which via the Kramers–Kronig relationship are related by

$$\chi'_{\alpha\beta}(\boldsymbol{Q}, 0) = \frac{1}{\pi} \int_{-\infty}^{\infty} \frac{\chi''_{\alpha\beta}(\boldsymbol{Q}, \omega)}{\omega} \, \mathrm{d}\omega. \tag{2.28}$$

In the classical limit, when $\omega \ll k_{\mathrm{B}}T$, the following sum rule also holds

$$\int_{-\infty}^{\infty} S_{\alpha\beta}(\boldsymbol{Q}, \omega) \, \mathrm{d}\omega = \frac{N}{g_J^2 \mu_{\mathrm{B}}^2} k_{\mathrm{B}} T \chi'_{\alpha\beta}(\boldsymbol{Q}). \tag{2.29}$$

The power and beauty of eq. (2.27) for magnetic species scan now be appreciated. Firstly, the measured neutron scattering cross section can be compared to model calculations of the dynamic susceptibility. Secondly, only components of the magnetization perpendicular to the scattering vector are effective in scattering neutrons. In addition, if the

total z-component of the angular momentum J_z^{tot} is a constant of motion and hence commutes with the Hamiltonian, then in eq. (2.27) only terms with $\alpha = \beta$ contribute. The cross section is then expressed in terms of the longitudinal and transverse components of the generalized susceptibility if a unique axis, such as the z direction, is chosen as the axis of quantization:

$$\frac{\mathrm{d}^2\sigma}{\mathrm{d}\Omega \mathrm{d}E} = N\frac{k_\mathrm{f}}{k_\mathrm{i}}(\gamma r_\mathrm{e})^2\left[\frac{1}{2}g_J f(\boldsymbol{Q})\right]^2 \mathrm{e}^{-2W(\boldsymbol{Q})}\frac{1}{\pi}\frac{1}{1-\exp(-\omega/k_\mathrm{B}T)} \times \left\{(1-\widehat{Q}_z^2)\chi''_{zz}(\boldsymbol{Q},\omega) + (1+\widehat{Q}_z^2)\chi''_{xx}(\boldsymbol{Q},\omega)\right\}. \tag{2.30}$$

It is thus possible to discriminate between longitudinal and transverse magnetic excitations by a suitable manipulation of the direction of the neutron scattering vector with respect to the magnetization direction. This can, of course, only be performed for a single crystal specimen. A more richer expression for the cross section is obtained if one considers the experimental possibility of analyzing the components of neutron polarization after scattering (Stirling and McEwen 1987; Hicks 1996).

2.3. Magnetic excitations and inelastic neutron scattering

2.3.1. Crystal field interaction

The most commonly expressed formalism for the crystal field Hamiltonian, for rare-earth intermetallics, is given by the series expansion (Fulde 1978; Fulde and Loewenhaupt 1985)

$$H_{\mathrm{CF}} = \sum_{m,n} B_n^m O_n^m \tag{2.31}$$

where B_n^m and O_n^m are, respectively, CF parameters and Stevens operator equivalents (Stevens 1951). This expression is valid when considering a CF splitting of only the ground state multiplet. The matrix elements of the CF Hamiltonian between states belonging to different multiplets can be calculated utilizing the Racah tensor operator technique (de Wijn et al. 1976; Wallace et al. 1977). The Stevens operators have been compiled by Hutchings (1964) and the required number of CF parameters corresponding to the appropriate point symmetry of the rare-earth ion are tabulated in table 3, whilst in table 4 the ground state multiplet splittings for J integral and J half integral values are classified according to the designated point symmetry of the crystal field. The CF parameters are naturally intimately related to the corresponding 4f charge distribution in the presence of a crystal field (Sievers 1982; Walter 1986). An alternative is to express the Hamiltonian in terms of CF coefficients A_n^m:

$$H_{\mathrm{CF}} = \sum_{m,n} A_n^m \langle r^n \rangle \theta_n O_n^m \tag{2.32}$$

where $\langle r^n \rangle$ are radial averages over the 4f electron wavefunctions (calculated by Freeman and Watson 1962; Freeman and Desclaux 1979) and θ_n are the Steven's coefficients α_J,

TABLE 3

Crystal field coefficients relevant for the 32 point groups (adapted from Walter (1984) and Loewenhaupt (1990)). Complex values are indicated by $\underline{A}_n^m$ and N denotes number of CF coefficients.

CF symmetry	Point group (Schoenflies)	Point group (International)	CF coefficients	N
Triclinic	$C_1\,C_i$	$1\,\bar{1}$	$A_2^0\ A_2^1\ \underline{A}_2^2\ A_4^0\ \underline{A}_4^1\ \underline{A}_4^2\ \underline{A}_4^3\ \underline{A}_4^4\ A_6^0\ \underline{A}_6^1\ \underline{A}_6^2\ \underline{A}_6^3\ \underline{A}_6^4\ \underline{A}_6^5\ \underline{A}_6^6$	26
Monoclinic	$C_2\ C_{2h}$	2 2/m	$A_2^0\ A_2^2\ A_4^0\ \underline{A}_4^2\ A_4^4\ A_6^0\ \underline{A}_6^2\ \underline{A}_6^4\ \underline{A}_6^6$	14
Orthorhombic	$D_2\ C_{2v}\ D_{2h}$	222 2mm mmm	$A_2^0\ A_2^2\ A_4^0\ A_4^2\ A_4^4\ A_6^0\ A_6^2\ A_6^4\ A_6^6$	9
Trigonal	$C_3\ S_6$	$3\,\bar{3}$	$A_2^0\ A_4^0\ A_4^3\ A_6^0\ \underline{A}_6^3\ \underline{A}_6^6$	8
Trigonal	$C_{3v}\ D_{3d}\ D_3$	$3m\ \bar{3}m\ 32$	$A_2^0\ A_4^0\ A_4^3\ A_6^0\ A_6^3\ A_6^6$	6
Hexagonal	$C_{3h}\ D_{3h}\ C_{6v}\ D_6\ C_6\ D_{6h}\ C_{6h}$	$\bar{6}\ \bar{6}m2\ 6mm\ 622\ 6/mmm\ 6/m$	$A_2^0\ A_4^0\ A_6^0\ A_6^6$	4
Tetragonal	$D_{4h}\ D_{2d}\ C_{4v}\ D_4$	$4/mmm\ \bar{4}2m\ 4mm\ 422$	$A_2^0\ A_4^0\ A_4^4\ A_6^4\ A_6^6$	5
Tetragonal	$C_4\ S_4\ C_{4h}$	$4\,\bar{4}\,4/m$	$A_2^0\ A_4^0\ A_4^4\ A_6^4\ \underline{A}_6^0$	6
Cubic	$T\ T_d\ T_h\ O\ O_h$	$23\ \bar{4}3m\ m3\ 432\ m3m$	$A_4^0\ A_6^0$	2

For cubic symmetry, $A_4^4 = \frac{5}{2}A_4^0$ and $A_6^4 = -\frac{21}{2}A_6^0$.

TABLE 4

Ground state multiplet splitting classified according to the CF point group symmetry for Kramers (J half-integral) and non-Kramers (J integral) ions (adapted from Walter (1984)).

	J integral								
Point group symmetry	1	2	3	4	5	6	7	8	
Cubic	0	0	1	1	0	2	1	1	s
	0	1	0	1	1	1	1	2	d
	1	1	2	2	3	3	4	4	t
Tetragonal	1	3	3	5	5	7	7	9	s
	1	1	2	2	3	3	4	4	d
Hexagonal	1	1	3	3	3	5	5	5	s
	1	2	2	3	4	4	5	6	d
Lower	$2J+1$ singlets								

	J half-integral								
Point group symmetry	3/2	5/2	7/2	9/2	11/2	13/2	15/2	17/2	
Cubic	0	1	2	1	2	3	2	3	d
	1	1	1	2	2	2	3	3	q
Tetragonal	$J+1/2$ doublets								
Hexagonal	$J+1/2$ doublets								
Lower	$J+1/2$ doublets								

s – singlet, d – doublet, t – triplet, q – quartet.

TABLE 5

Radial averages $\langle r^l \rangle$ over 4f wavefunctions and Stevens factors α_J, β_J, γ_J for lanthanide R^+ ions (after Freeman and Watson 1962; Freeman and Desclaux 1979). The conversion factor from atomic units to units in Å is $r_0 = 0.52918$ Å.

Ion	$\langle r^2 \rangle$ [r_0^2 (Å^2)]	$\langle r^4 \rangle$ [(r_0^4 (Å^4)]	$\langle r^6 \rangle$ [r_0^6 (Å^6)]	$\alpha_J \times 10^2$	$\beta_J \times 10^4$	$\gamma_J \times 10^6$
Ce^{3+}	1.309 (0.367)	3.964 (0.311)	23.31 (0.512)	−5.71	63.5	0.00
Pr^{3+}	1.208 (0.335)	3.396 (0.261)	18.72 (0.403)	−2.10	−7.35	61.0
Nd^{3+}	1.114 (0.312)	2.910 (0.228)	15.03 (0.330)	−0.643	−2.91	−38.0
Sm^{3+}	0.974 (0.273)	2.260 (0.177)	10.55 (0.232)	4.13	25.0	0.00
Gd^{3+}	0.867 (0.243)	1.820 (0.143)	7.831 (0.172)	0.00	0.00	0.00
Tb^{3+}	0.822 (0.230)	1.651 (0.129)	6.852 (0.151)	−1.01	1.22	−1.12
Dy^{3+}	0.781 (0.219)	1.505 (0.118)	6.048 (0.133)	−0.635	−0.592	1.03
Ho^{3+}	0.745 (0.209)	1.379 (0.108)	5.379 (0.118)	−0.222	−0.333	−1.30
Er^{3+}	0.711 (0.199)	1.270 (0.099)	4.816 (0.106)	0.254	0.444	2.07
Tm^{3+}	0.680 (0.191)	1.174 (0.092)	4.340 (0.095)	1.01	1.63	−5.60
Yb^{3+}	0.652 (0.183)	1.089 (0.085)	3.932 (0.086)	3.17	−17.3	148.0

TABLE 6

Table for conversion from crystal field parameters B_n^m (in K) to crystal field coefficients A_n^m (in K r_0^{-n}). To obtain the appropriate value of A_n^m, the corresponding parameter B_n^m is multiplied by the relevant entry in the table.

Ion	B_2^0	B_4^0	B_6^0
Ce	−13	40	0
Pr	−39	−400	876
Nd	−140	−1180	−1750
Tb	−120	4948	−130000
Sm	25	177	0
Dy	−200	−11223	159744
Ho	−597	−21786	−143699
Er	546	17730	100311
Tm	143	5220	−41100
Yb	48	−530	1718

β_J, γ_J for $n = 2, 4, 6$, respectively. These parameters, for lanthanide ions, are collected in table 5. This representation is particularly convenient since the CF coefficients should display a smooth variation in a given series of intermetallics with the same structure. Due to a very confusing labeling of either CF parameters, B_n^m or coefficients A_n^m, often quoted in the literature, useful conversion factors from B_n^m to A_n^m (in degrees K) are contained in table 6.

The CF parameters invariably need to be determined by a variety of experimental techniques, of which INS is undoubtedly the most powerful, since it is extremely sensitive to the details of the CF interaction. This can be readily seen when the INS cross section for CF excitations is derived. If there are no magnetic correlations between moments at dif-

ferent sites, as for example is the case for a pure CF system, the dynamic susceptibility is simply related to the CF eigenstates $|\Gamma_i^1\rangle$ and the cross section in eq. (2.12) reduces to the compact form, in the dipole approximation:

$$\frac{\mathrm{d}^2\sigma}{\mathrm{d}\Omega\,\mathrm{d}E} = N\frac{k_\mathrm{f}}{k_\mathrm{i}}(\gamma r_\mathrm{e})^2 \mathrm{e}^{-2W(\boldsymbol{Q})}\left[\frac{1}{2}g_J f(\boldsymbol{Q})\right]^2 \times \sum_{i,j} p_i \langle i|\boldsymbol{J}_\perp|j\rangle\langle j|\boldsymbol{J}_\perp^*|i\rangle \delta(\omega - E_i + E_j), \tag{2.33}$$

where the subscripts i and j now refer to different CF eigenfunctions. The delta function, $\delta(\omega - E_i + E_j)$, is appropriate only for vanishing CF linewidths, but the linewidth in practice always has an intrinsic temperature dependent CF component, with a distribution characterized by a Lorentzian component $P(\omega, T)$. The delta function is thus replaced by a spectral weight function

$$P(\omega, T) = \frac{1}{\pi}\frac{\Gamma}{\Gamma^2 + \omega^2}. \tag{2.34}$$

This spectral weight function has the obvious normalization condition:

$$\int_{-\infty}^{+\infty} P(\omega, T)\,\mathrm{d}\omega = 1. \tag{2.35}$$

In more general terms, the spectral weight function can be further divided into quasi-elastic and inelastic components:

$$P(\omega, T) = P_\mathrm{quasi}(\omega, T) + P_\mathrm{inel}(\omega, T), \tag{2.36}$$

where

$$P_\mathrm{inel}(\omega, T) = \sum_{i,j} a_{ij} P_{ij}(\omega \pm \omega_{ij}), \tag{2.37}$$

with a_{ij} the matrix elements for CF transitions. The Lorentzian full width at half height maximum 2Γ is inversely proportional to the relaxation rate of the magnetization fluctuation energy. The intrinsic CF linewidths are connected to magnetic interactions by (Becker et al. 1977; Sugawara 1977, 1979):

$$\Gamma_{ij} = 2\{(g_J - 1)\sigma(E_\mathrm{F})J_\mathrm{ex}\}^2\left[a_{ij}^2 \coth\left(\frac{\beta\omega_{ij}}{2}\right)\chi''(\omega_{ij}) + \sum_{n\neq i} a_{in}^2 \frac{\chi''(\omega_{in})}{(\mathrm{e}^{\beta\omega_{in}} - 1)} + \sum_{n\neq j} a_{ij}^2 \frac{\chi''(\omega_{nj})}{(\mathrm{e}^{\beta\omega_{nj}} - 1)}\right], \tag{2.38}$$

where a_{ij} is the matrix element for CF transitions from state i to j, $\sigma(E_\mathrm{F})$ the conduction electron density of states at the Fermi energy, J_ex is the exchange integral between 4f and

conduction electrons and $\chi''(\omega)$ is the imaginary part of the susceptibility, appropriately summed over the Brillouin zone. At high temperatures the linewidths vary linearly with temperature, giving a Korringa relaxation behaviour.

The CF excitations are non-dispersive or weakly so, and are most conveniently studied with polycrystalline material. For transitions between J-multiplets, which can only be observed by high energy transfer INS, the magnetic cross sections have been calculated exactly (Balcar and Lovesey 1986). The relevant experimental and theoretical details are reviewed by Osborn et al. (1991). Via the orientation factor expressed in eq. (2.13), the relative intensities between CF levels are given, for polycrystalline material, by the squared matrix elements:

$$\langle \Gamma_i | J_\perp | \Gamma_j \rangle^2 = \frac{1}{3}\big(\langle \Gamma_i | J_+ | \Gamma_j \rangle^2 + \langle \Gamma_i | J_- | \Gamma_j \rangle^2 + 2\langle \Gamma_i | J_z | \Gamma_j \rangle^2\big), \tag{2.39}$$

where the CF states are now further labeled in terms of their irreducible representations Γ_i. Clearly, the specific advantages of INS are that both the eigenvalues and eigenvectors of the CF interaction are simultaneously probed. The composition of these irreducible representations for all J are easily constructed from available compiled tabulations of the characters of the relevant space groups (Koster et al. 1963; Joshua 1991; Görller-Walrand and Binnemans 1996). For a cubic crystal field Lea et al. (1962) (nominated LLW) introduced an ingenious method of representing the eigenfunctions and eigenvalues of the CF Hamiltonian for represented by:

$$H_{\mathrm{CF}} = B_4^0\big[O_4^0 + 5O_4^4\big] + B_6^0\big[O_6^0 - 21O_6^4\big], \tag{2.40}$$

by setting the two parameters required for description of the CF in terms of parameters x and W defined by:

$$B_4^0 = \frac{Wx}{F(4)}, \qquad B_6^0 = \frac{W(1-|x|)}{F(6)}, \tag{2.41}$$

where $-1 \leqslant x \leqslant 1$, and listing all the eigenvalues and eigenfunctions as functions of *only one* parameter x (the factors $F(4)$ and $F(6)$ are functions only of J, and are tabulated by Lea et al. (1962)). For systems with a lower symmetry, their exists no similar method of the same ingenuity and simplicity for parameterizing the CF interaction. Extensions of the LLW technique have been carried further by, for example, Walter (1984) in the general case and by Segal and Wallace (1970, 1973, 1974, 1975) for systems of hexagonal point symmetry and for tetragonal groups (Amoretti et al. 1986). Walter introduced a parameterization in such a way as to limit the range in the variation of the reduced parameters. For very small deformations from cubic point symmetry, the number of CF parameters can be suitably reduced (Lévy 1969). In the context of the INS scattering cross section for CF excitations, Birgeneau (1972) has tabulated all the matrix elements for magnetic dipole transitions for cubic symmetry in terms of the LLW parameter x. In this case, as $\langle \Gamma_i | J_x | \Gamma_j \rangle = \langle \Gamma_i | J_y | \Gamma_j \rangle = \langle \Gamma_i | J_z | \Gamma_j \rangle$, eq. (2.39) reduces to

$$\langle \Gamma_i | J_\perp | \Gamma_j \rangle^2 = 2\langle \Gamma_i | J_z | \Gamma_j \rangle^2. \tag{2.42}$$

TABLE 7

Crystal field states $|\Gamma_i\rangle$, in the representation $|J, M_J\rangle$, and associated dipolar matrix elements $|\langle\Gamma_i|J_z|\Gamma_j\rangle|^2$ for cubic CF symmetry tabulated for $J = 9/2$ (Kramers) and $J = 6$ (non-Kramers) ions (adapted from Birgeneau (1972)). CF states are calculated for $x = -1$ in the LLW notation.

$J = 9/2$				
	CF state	Γ_6	$\Gamma_8^{(1)}$	$\Gamma_8^{(2)}$
Γ_6	$0.612 \mid \pm 9/2\rangle + 0.764 \mid \pm 1/2\rangle + 0.204 \mid \mp 7/2\rangle$	6.722	8.944	0.833
$\Gamma_8^{(1)}$	$-0.789 \mid \pm 9/2\rangle + 0.573 \mid \pm 1/2\rangle + 0.224 \mid \mp 7/2\rangle$		16.134	7.922
	$0.489 \mid \pm 5/2\rangle + 0.872 \mid \mp 3/2\rangle$			
$\Gamma_8^{(2)}$	$0.054 \mid \pm 9/2\rangle - 0.298 \mid \pm 1/2\rangle + 0.953 \mid \mp 7/2\rangle$			24.244
	$0.872 \mid \pm 5/2\rangle + 0.489 \mid \mp 3/2\rangle$			

$J = 6$							
	CF state	Γ_1	Γ_2	Γ_3	Γ_4	$\Gamma_5^{(1)}$	$\Gamma_5^{(2)}$
Γ_1	$-0.661 \mid 4\rangle + 0.354 \mid 0\rangle - 0.661 \mid -4\rangle$	0	0	0	14.00	0	0
Γ_2	$-0.395 \mid 6\rangle + 0.586 \mid 2\rangle + 0.586 \mid -2\rangle - 0.395 \mid -6\rangle$		0			9.58	
Γ_3	$0.586 \mid 6\rangle - 0.395 \mid 2\rangle + 0.395 \mid -2\rangle + 0.586 \mid -6\rangle$				2.00		0
	$0.250 \mid 4\rangle + 0.935 \mid 0\rangle + 0.250 \mid -4\rangle$						
Γ_4	$0.685 \mid \pm 3\rangle - 0.433 \mid \mp 1\rangle - 0.586 \mid \mp 5\rangle$				0.50	0.58	24.92
	$-0.707 \mid 4\rangle + 0.000 \mid 0\rangle + 0.707 \mid -4\rangle$						
$\Gamma_5^{(1)}$	$-0.382 \mid \pm 3\rangle - 0.898 \mid \mp 1\rangle - 0.217 \mid \mp 5\rangle$			25.82			0.73
	$-0.701 \mid 6\rangle - 0.097 \mid -2\rangle - 0.701 \mid -6\rangle$						
$\Gamma_5^{(2)}$	$-0.621 \mid \pm 3\rangle - 0.075 \mid \mp 1\rangle - 0.781 \mid \mp 5\rangle$		4.42	0.18		5.29	7.19
	$-0.097 \mid 6\rangle - 0.700 \mid -2\rangle - 0.097 \mid -6\rangle$						

Examples of the required matrix elements, which determine the allowed transitions, are tabulated in table 7 and displayed in fig. 1 for $J = 5/2$ (Kramers ion) and for $J = 6$ (non-Kramers ion), in a cubic CF, as a function of the parameter x. For systems of a lower point symmetry, there are no pure J_+, J_+ and J_z transitions and the corresponding powder average is:

$$\langle\Gamma_i|J_\perp|\Gamma_j\rangle^2 = \frac{2}{3}\left[\langle\Gamma_i|J_x|\Gamma_j\rangle^2 + \langle\Gamma_i|J_y|\Gamma_j\rangle^2 + \langle\Gamma_i|J_z|\Gamma_j\rangle^2\right]. \tag{2.43}$$

Clearly, for INS measurements on a polycrystalline sample with a very low R point symmetry, the CF parameters are undetermined. Recourse must be made to INS investigations on large single crystals.

A further useful relationship is the sum rule, which follows from the conservation of the total angular momentum J for each crystal field state:

$$\sum_{i,j}\sum_{k=x,y,z}\left|\langle\Gamma_i|J_k|\Gamma_j\rangle\right|^2 = N_i J(J+1), \tag{2.44}$$

with N_i the degeneracy of the state $|\Gamma_i\rangle$. This is easily verified, by example, for all the cubic CF states in table 7. For non-cubic CF symmetries and Kramers ions (double degeneracy) a

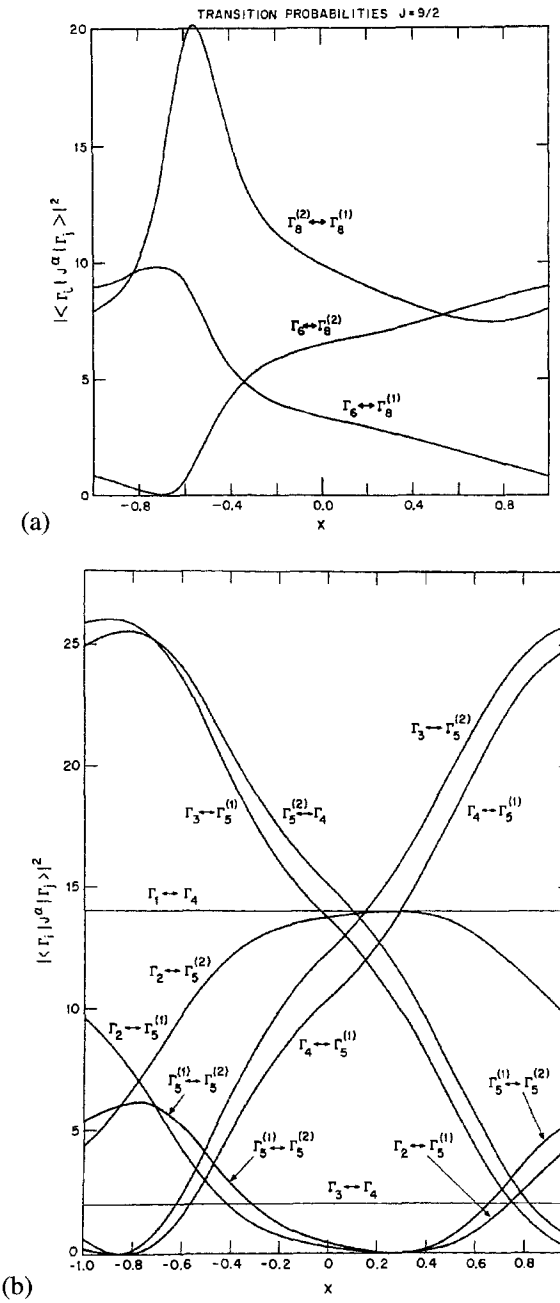

Fig. 1. (a) Dipolar transition probability matrix elements $|\langle\Gamma_i|J_z|\Gamma_j\rangle|^2$ for $J = 5/2$, as a function of the LLW parameter x, in a cubic CF (from Birgeneau 1972). (b) Dipolar transition probability matrix elements $|\langle\Gamma_i|J_z|\Gamma_j\rangle|^2$ for $J = 6$, as a function of the LLW parameter x, in a cubic CF (from Birgeneau 1972).

further very useful relationship is the connection between quasi-elastic and inelastic matrix elements

$$\left|\langle\Gamma_i|J_\perp|\Gamma_j\rangle\right|^2 = \frac{4}{3}J(J+1) - \sum_{i\neq j}\left|\langle\Gamma_i|J_\perp|\Gamma_j\rangle\right|^2. \tag{2.45}$$

This term can be sometimes utilized for polycrystalline systems of a low CF symmetry to identify at least a reasonable energy level scheme, after an accurate background subtraction of non-magnetic scattering around the quasi-elastic line.

As no LLW analogue exists for non-cubic crystal fields, the CF Hamiltonian can be alternatively expanded in terms which consist of successive cubic, axial and rhombic contributions. However, in circumstances were the point symmetry of the rare-earth ion is far from cubic, as is the case in numerous non-cubic rare-earth intermetallics, such an approximation must be used with some caution. It has, however, been utilized with some success for CF interactions in high T_c superconducting oxides (Mesot and Furrer 1997). A superposition model for the CF, developed by Newman (1971), is often used to analyze contributions to the CF, in metallic systems. The relative simplicity of the model lies in the fact that the CF potential is expressed solely in terms of three 2nd, 4th and 6th order parameters, $\overline{A}_2$, $\overline{A}_4$, $\overline{A}_6$. These represent only the cylindrically symmetric part of the potential generated by the ligands of the R ion and are related to the actual CF parameters which need to be determined, via a factor which is determined solely by the specific geometry of the local environment around the R ion. In this way, approximate values of the CF parameters can be calculated, even by experimentalists. This is of utmost importance for systems with a low CF point symmetry. The CF superposition model appears to be valid in a large number of metallic systems (Newman 1983).

The linewidths of the CF excitations naturally increase with increasing temperature, due to interactions with the lattice vibrations (spin–lattice interactions) and conduction electrons. At high enough temperatures, the inelastic CF excitations collapse into a broad quasi-elastic Lorentzian distribution. A theoretical treatment of the dynamics of 4f moments coupled to the conduction electrons, in the context of INS, has been formulated by Becker et al. (1977) (BKF) and Peregudov et al. (1982). Dynamical exchange interactions arising from large fluctuations in $\boldsymbol{J}$, present near a magnetic phase transition and in the paramagnetic regime, also need to be taken into account in addition to the normal CF term. The effects of such interactions on CF excitations, as observed by INS, have been treated by Furrer and Heer (1973), Furrer (1977) and Sugawara (1977, 1979). Typically, the CF excitations are broadened, undergo a further splitting or are even shifted, in the presence of magnetic interactions. Many rare-earth intermetallics, in particular the RAl_2 series, are superconductors at low temperatures, and measurements of the CF relaxation rate by INS have been used with great effect for investigations of the electronic mechanisms responsible for the superconducting state in metals (Fulde and Loewenhaupt 1985; Boothroyd 1997). The linewidths in such cases largely obey the predictions of the BFK theory. The interaction of 4f moments with conduction electrons is reviewed by Fulde and Loewenhaupt (1988).

In summary, a typical INS investigation of CF interactions should first aim to establish a rather definitive CF energy level scheme, together with the appropriate transition

probabilities between levels, by time-of-flight techniques, on polycrystalline material. If the magnetic excitations are non-dispersive or weakly so, the tremendous advantage of the time-of-flight technique is that the solid angle of the detector can be very large. Consequently, the scattering law can be measured for a large number of wavevector transfers simultaneously. This is done by an extensive set of temperature dependent scans, in order to identify the ground and excited states, via the CF population term. The total CF splitting is obtained by measurements with different energies of incident neutrons, since the total spread in CF levels is necessarily comparable to the magnitude of the incident neutron energy. The actual CF parameters can only then be obtained by combining INS investigations with complementary techniques which are also sensitive to the CF interaction. Use of single crystals is clearly always an advantage and is encouraged, particularly if the CF symmetry is very low. Investigation of an isostructural series is also strongly advised, since the CF *coefficients* should not generally display any large variations in sign and magnitude across a series.

2.3.2. Exchange interactions

Inclusion of an exchange interaction means that the transitions arise from a magnetic coupling between neighboring ions and an analysis is subsequently more complicated. The simplest and most widely used approximation for the exchange interaction is the localized Heisenberg isotropic three dimensional Hamiltonian:

$$H_{\mathrm{ex}} = -\sum_{i,j} J(\boldsymbol{r}_i - \boldsymbol{r}_j)\boldsymbol{J}_i \cdot \boldsymbol{J}_j, \tag{2.46}$$

where J is the exchange interaction between two neighboring ions located at $\boldsymbol{r}_i$ and $\boldsymbol{r}_j$. For intermetallics, when only exchange between rare-earth ions is significant, the long range RKKY-exchange interaction is a good approximation (Sinha 1978; Jensen 1982; Jensen and MacIntosh 1991). The Mean Field-Random Phase Approximation (MF-RPA) is then used to express the generalized dynamical susceptibility tensor in the following form (Buyers et al. 1975; Henggeler and Furrer 1998):

$$\chi^{\alpha\beta}(\boldsymbol{q}, \omega) = \frac{\chi_0^{\alpha\beta}(\omega)}{1 - 2J(\boldsymbol{q})\chi_0^{\alpha\beta}(\omega)} \tag{2.47}$$

where $J(\boldsymbol{q})$ is the Fourier transform of the exchange coupling, with $\boldsymbol{q}$ now the wavevector of the propagating magnetic excitation and $\chi_0(\omega)$ the single-ion CF non-interacting dynamic susceptibility:

$$\chi_0^{\alpha\beta} = g_J^2 \mu_{\mathrm{B}}^2 \sum_{n,m} \frac{\langle n|J_\alpha|m\rangle\langle m|J_\beta|n\rangle}{E_n - E_m + \hbar\omega}(p_n - p_m). \tag{2.48}$$

The dispersion observed by INS is determined by the poles of the dynamical susceptibility, i.e., when $2J(\boldsymbol{q})\chi_0^{\alpha\beta}(\omega) = 1$. This formalism in terms of the MF-RPA allows a determination of the Fourier transform of the exchange interactions to be made. For this purpose,

the dispersion of the magnetic excitations must be measured inside the Brillouin zone. The radial dependence of the exchange interactions is then obtained by an inverse Fourier transformation of $J(\boldsymbol{q})$. The simplest case is that of a CF ground state singlet Γ_s and an excited Γ_e state separated by a CF splitting of Δ. The dispersion relation is of the form:

$$\omega^2(\boldsymbol{q}) = \Delta\big[\Delta - 2\langle\Gamma_s|J_\alpha|\Gamma_e\rangle\langle\Gamma_e|J_\beta|\Gamma_s\rangle\big]J(\boldsymbol{q})(p_{\Gamma_s} - p_{\Gamma_e}). \tag{2.49}$$

In rare-earth intermetallics, under circumstances when there is a significant R–T (rare-earth transition metal) exchange interaction such as that occurring in Fe and Co rich compounds, the transition metal sublattice causes the rare-earth moments to order. The low lying moderately dispersive excitations are then essentially single ion excitations of the rare-earth moment, arising from interactions with the crystal field and transition metal exchange field. This means that these systems can be particularly well described by the mean field approximation. In multi-sublattice intermetallics such as RFe_2 and R_2Co_{17}, R_2Fe_{17}, closed expressions for the dispersion of the low lying magnetic excitations in terms of CF and exchange parameters have been obtained (Clausen and Lebech 1982; Colpa et al. 1989a, 1989b). Examples of more generalized treatments of the dispersion of magnetic excitations, in multi-sublattice rare-earth intermetallic ferromagnets and ferrimagnets which undergo spin re-orientation transitions, are those reported by del Moral (1992a, 1992b); Zhi-dong (1996) and Zhi-dong and Tong (1997).

The excitations of the transition metal sublattice are observed to be generally highly dispersive and this dispersion is reminescent of the spin-wave dispersion observed, for example, in elemental Fe and Co (Stirling and McEwen 1987)

$$\omega(\boldsymbol{q}) = Dq^2 + Eq^4 + Fq^6, \tag{2.50}$$

where D, E and F are the dispersion constants. The magnetic excitations in intermetallics can also couple with the phonons when there are strong magneto-elastic effects present (Fulde and Loewenhaupt 1985; Morin and Schmitt 1990; Thalmeier and Lüthi 1991).

3. Complementary techniques for determination of the crystal field interaction

Crystal field parameters deduced from INS measurements must always be verified by complementary spectroscopic and bulk macroscopic investigations. In particular, when there is a progressive lowering of the point group symmetry, where more than two CF parameters need to be determined, INS techniques alone may not suffice to give a unique set of parameters. Alternative spectroscopic techniques exist and are briefly mentioned in the following sections. For rare-earth 3d-transition metal intermetallics, most of these techniques have been discussed in more detail by Franse and Radwanski (1993).

3.1. Light scattering

Methods using Raman spectroscopy are hardly an useful alternative for investigation of CF levels in intermetallic systems. The CF interaction has been studied with this technique

in mixed valence systems such as CeB_6 (Zirngiebl et al. 1984), $CeAl_2$ (Güntherodt et al. 1983), $CePd_3$ (Zirngiebl et al. 1984). The intermetallics PrB_6 and NdB_6 (Pofahl et al. 1987) are stable lanthanide intermetallic which have been studied in detail. The technique offers a higher resolution than that attainable by neutron spectroscopy but single crystals are generally required and there is no simple relationship between the observed intensity and the CF eigenstates. Light scattering in intermetallic compounds has been reviewed by Zirngiebl and Güntherodt (1991).

3.2. Photoemission

High resolution photoemission spectroscopy is extremely sensitive to details of the electronic structure near the Fermi level, E_F. The method suffers from a poorer energy resolution and only information at high energies can be extracted. Takahashi et al. (1995) have demonstrated that the method can, in principle, be also used to deduce the eigenvalues of the CF interaction in rare-earth intermetallics. This was performed on a heavy fermion compound, CeB_6, and the Γ_7–Γ_8 transition at 70 meV was tentatively identified. The drawbacks are that extreme experimental conditions (high vacuum, of the order of 10^{-11} Torr) are required, the instrumental resolution is rather poor (of the order of 20 meV) and single crystals need to be utilized. There is no simple correlation between the observed signal intensity and CF matrix elements, which is the principle advantage of the INS technique. The technique does not appear to offer complementary information about the low lying CF levels in rare-earth intermetallics, but is of importance for mixed valence and heavy fermion compounds (Lynch and Weaver 1988). Herbst and Wilkins (1988) have reviewed computational techniques and calculations of high energy 4f electron excitations in metallic compounds.

3.3. X-ray absorption spectroscopy

Sacchi et al. (1991a, 1991b, 1992a, 1992b) have pointed out the possibility of investigating CF splittings in rare-earth intermetallics by using X-ray absorption spectroscopy with linearly polarized light at $M_{4,5}$ edges of rare-earths. The idea follows on from calculations by Thole et al. (1985) for the expected linear dichroism of the rare-earths. The calculated linear dichroism is subject to the following dipole selection rules; $\Delta M_J = 0$ for $\boldsymbol{E}$ parallel to $\boldsymbol{q}$ and $\Delta M_J = \pm 1$ for $\boldsymbol{E}$ perpendicular to $\boldsymbol{q}$, where $\boldsymbol{E}$ is the light polarization vector and $\boldsymbol{q}$ the photon wavevector and the intensity is proportional to $\langle M_J^2 \rangle$, with M_J the component of J along the quantization axis. The technique is less direct than INS but is very sensitive to the type of rare-earth and minute quantities of material can be investigated. With incident energies of 1 keV and a 1 eV energy resolution, the details of splittings of a few meV can be obtained. The technique has promising prospects for investigation of crystal field effects in surfaces, interfaces, magnetic multilayers and thin films which cannot, at present, be investigated by INS. The theory and techniques of high energy X-ray absorption spectroscopy are reviewed by Röhler (1988). The scattering and absorption of X-rays by magnetic materials are discussed in immense detail by Lovesey (1995) and Lovesey and Collins (1996).

3.4. *Magnetic resonance*

Magnetic resonance methods measure the hyperfine splitting at rare-earth nuclei in rare-earth intermetallics. As has been previously stressed by Franse and Radwanski (1993), Mössbauer spectroscopy of Gd compounds provides rather crucial information about the CF, since the measured electric field gradient is generated by the surrounding charges and is hence directly related to the second order coefficient A_0^2. The technique is very much less sensitive to the higher order CF parameters since the intensity is orders of magnitude smaller for the higher order multipolar interactions. Additionally, 5d and 6s electrons contribute to the hyperfine splitting and, consequently, the electric field gradient is not necessarily directly related to the 4f CF coefficients (Coehoorn 1991). Dormann (1991) has presented an extensive theoretical and experimental review of NMR methods in intermetallics. Results pertaining to compounds related to permanent magnet materials have been reviewed by Kapusta et al. (1998) in chapter 3 of this volume.

3.5. *Point-contact spectroscopy*

Electrical point-contact spectroscopy is a method which can be used for a *direct microscopic* study of CF levels in metallic systems. In this sense, it is a highly complementary alternative to INS investigations. The energy levels of the Pr^{3+} ion in $PrNi_5$ were first investigated by Akimenko et al. (1984) and this technique was subsequently used for the first time to measure directly the Zeeman splitting of the CF levels in applied magnetic fields, up to 20 Tesla, for the same compound (Reiffers et al. 1989). The anisotropic magnetic field dependence of CF levels is directly observed and in addition, CF transitions which are forbidden in zero magnetic field, can be stimulated (fig. 2). The intensities of the CF levels are given by the transition probability between initial $|\Gamma_i\rangle$ and final $|\Gamma_f\rangle$ states (Fulde and Loewenhaupt 1985),

$$\left|\langle\Gamma_f|\boldsymbol{J}\cdot\boldsymbol{s}|\Gamma_i\rangle\right|^2, \tag{3.1}$$

where $\boldsymbol{J}$ and $\boldsymbol{s}$ are the total angular momentum and conduction electron spin operators, respectively. In spite of the obvious usefulness of this method, it has been rarely used for investigation of CF states in rare-earth intermetallics. It should become a much more widely utilized technique for a complementary determination of CF levels and states in *single crystal* rare-earth intermetallic compounds.

Bulk techniques provide a useful way to verify the CF parameters determined by spectroscopic methods for rare-earth intermetallic compounds. The most significant of these are described below.

3.6. *Magnetic susceptibility*

A distinct quantity of information about the CF interaction can be obtained from the anisotropy of the temperature dependent magnetic susceptibility in the non-interacting regime via the paramagnetic susceptibility,

$$\chi_{\alpha\alpha}(T) = \frac{\partial M_\alpha}{\partial H_\alpha}$$

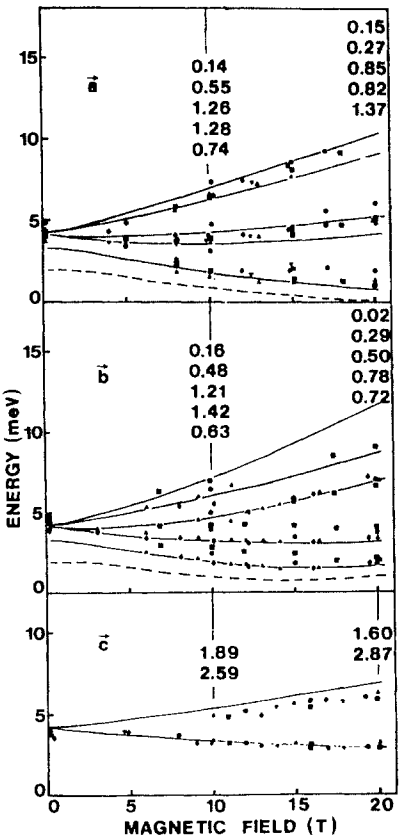

Fig. 2. Magnetic field dependence of the CF energies obtained for $PrNi_5$–Cu point contacts for fields along the a, b and c axes (different symbols for different contacts). The solid curves are calculated by a diagonalization of the Hamiltonian consisting of CF and Zeeman terms. The calculated numbers are proportional to the transition probabilities at 10 and 20 T and are given in the same order as the calculated energy levels. The dashed curves show the calculated energy of the Γ_1 level with CF parameters obtained from INS and magnetization data (after Reiffers et al. 1989).

$$= g_J^2\mu_B^2\left\{\sum_{m=n} p_n\frac{\langle\Gamma_m|J_\alpha|\Gamma_n\rangle^2}{k_BT} + 2\sum_{n\neq m} p_n\frac{\langle\Gamma_m|J_\alpha|\Gamma_n\rangle^2}{E_m - E_n}\right\}$$
$$- \frac{g_J^2\mu_B^2}{k_BT}\left(\sum_n p_n\langle\Gamma_n|J_\alpha|J_n\rangle\right)^2 \tag{3.2}$$

where summations over terms with $m = n$ are the Curie-like components of the susceptibility and those with $m \neq n$ are the Van Vleck contributions, with M and H the magnetization and applied magnetic field, respectively. The terms E_n and $|\Gamma_n\rangle$ are the eigenvalues and eigenfunctions of the Hamiltonian and $p_n = \exp(-\beta E_n)/Z$, with Z the partition function

$Z = \sum_n \exp(-\beta E_n)$. There is an explicit dependence on the energy of the CF levels and the matrix elements connecting the eigenstates, but the sum is over all levels at a particular temperature and any information about a level or set of levels is lost. It obviously serves as a fundamental test of CF parameters obtained by other techniques. From determination of the three paramagnetic Curie temperatures (measured along the three principal axes of a *single* crystal), θ_a, θ_b and θ_c, the CF parameters B_2^0 and B_2^2 are directly obtained from the high temperature susceptibility (Bowden et al. 1971; Wang 1971; Boutron 1973; Shohata 1977)

$$\begin{aligned} k_B\theta_a &= k_B\theta_p + \frac{1}{10}\left(B_2^0 + B_2^2\right)(2J-1)(2J+3), \\ k_B\theta_b &= k_B\theta_p - \frac{1}{5}B_2^0(2J-1)(2J+3), \\ k_B\theta_c &= k_B\theta_p + \frac{1}{10}\left(B_2^0 - B_2^2\right)(2J-1)(2J+3), \end{aligned} \tag{3.3}$$

where the CF parameters are in degrees Kelvin and θ_p is the paramagnetic Curie temperature. Clearly, for tetragonal and hexagonal crystal fields, the parameter B_2^0 can be determined whilst for orthorhombic and lower symmetries, B_2^0 and B_2^2 are similarly determined.

3.7. Magnetization

In the presence of combined CF, exchange and applied magnetic fields, the expectation value of the magnetization can be calculated in the mean field approximation. The magneto-crystalline anisotropy energy at any particular temperature is determined by calculation of the variation of the magnetic moment as a function of the direction of the applied magnetic field. The thermal variation of the component α ($\alpha = x, y, z$) of the magnetic moment is given by:

$$\langle\mu_\alpha\rangle = \beta\frac{\partial \ln Z}{\partial H_\alpha} = g_J\mu_B\sum_n p_n\langle\Gamma_n'|J_\alpha|\Gamma_n'\rangle, \tag{3.4}$$

with $|\Gamma_n'\rangle$ now eigenstates of the Hamiltonian with inclusion of exchange and applied fields. In the paramagnetic regime, high magnetic fields are required to mix the different CF eigenstates. In the ordered regime, when an exchange field is present, the ordered moment as a function of temperature is calculated, in standard fashion, by obtaining self-consistent solutions which simultaneously satisfy the above equation and the molecular field condition

$$h = \lambda N_A g_J \mu_B^2 \langle\mu_\alpha\rangle. \tag{3.5}$$

The molecular field constant, λ, is determined by measurement of the ordering temperature. If this self-consistent solution is not unique, the minimum in the free energy

$$F(T) = -k_B T \ln Z + \frac{1}{2}\lambda\langle\mu_\alpha\rangle^2 \tag{3.6}$$

is calculated for various orientations of the molecular or applied field, for a given set of CF and exchange parameters. Quadrupolar terms can also be included in the free energy calculation, if this interaction is of significance (Morin and Schmitt 1990). Ideally, the ordered magnetic moment is measured by neutron diffraction on powder or single crystal samples. The calculated temperature variation of the ordered moment with a given set of CF and exchange parameters can be compared with the neutron data. For single crystal samples, the high field magnetization, measured along specific crystallographic directions, provides a further important cross-check for CF and exchange field parameters obtained via INS or other techniques. In a more simplified approach, the magneto-crystalline anisotropy energy is modeled in terms of phenomenological anisotropy constants or coefficients (Asti 1990; Zvezdin 1995). By way of example, for tetragonal symmetry, the free energy expansion for the anisotropy energy is simply expressed as:

$$\begin{aligned} E_A(T) = K_1(T)\sin^2\theta &+ \left[K_2(T) + K_2'(T)\cos 4\varphi\right]\sin^4\theta \\ &+ \left[K_3(T) + K_3'(T)\cos 4\varphi\right]\sin^6\theta \end{aligned} \tag{3.7}$$

where $K_i(T)$ are temperature dependent anisotropy constants and θ, φ are polar angles which describe the direction of the rare-earth moment with, respect to orthogonal crystallographic axes. The anisotropy constants are determined from the applied magnetic field dependence and temperature dependence of the magnetization. When the CF can be considered as a small perturbation of a dominant rare-earth transition metal exchange interaction, simple relationships exist between the anisotropy constants $K_i(T)$ and CF parameters (Rudowicz 1987). For tetragonal symmetry,

$$\begin{aligned} K_1(T) &= -\left[\frac{3}{2}B_2^0\langle O_2^0\rangle + 5B_4^0\langle O_4^0\rangle + \frac{21}{2}B_6^0\langle O_6^0\rangle\right], \\ K_2(T) &= \frac{7}{8}\left[5B_4^0\langle O_4^0\rangle + 27B_6^0\langle O_6^0\rangle\right], \\ K_2'(T) &= \frac{1}{8}\left[B_4^4\langle O_4^4\rangle + 5B_6^4\langle O_6^4\rangle\right], \\ K_3(T) &= -\frac{231}{16}B_6^0\langle O_6^0\rangle, \\ K_3'(T) &= -\frac{11}{16}B_6^4\langle O_6^4\rangle, \end{aligned} \tag{3.8}$$

where the terms $\langle O_m^n\rangle$ are thermal averages of the Stevens operators. The transferability of CF parameters obtained from investigation of systems where the CF is the dominant interaction to those where the exchange dominates must, however, always be treated with some caution.

3.8. Specific heat

The magnetic specific heat is sensitive only to the eigenvalues of the magnetic system. In the paramagnetic phase, where CF effects are important, the levels are evidenced via a Schottky type contribution. The level degeneracy can also be deduced and the technique is

routinely used in analysis of systems with a significant CF interaction. For a sequence of CF field only eigenstates E_n, at a temperature T, the magnetic part of the specific heat is given by the standard expression:

$$C(T) = \left(\frac{\partial U}{\partial T}\right)_V = k_B \left\{ \sum_n p_n \left(\frac{E_n}{k_B T}\right)^2 - \sum_n \left(\frac{E_n}{k_B T} p_n\right)^2 \right\} \tag{3.9}$$

where U is the internal energy. The non-magnetic background contribution to the specific heat is usually obtained by measurements on isomorphous La or Y compounds (except when these themselves become superconducting at low temperatures). Limitations in the accuracy of the technique arise from spin–phonon contributions and experience has shown that several sets of CF parameters can equally well fit the specific heat data.

3.9. Magnetostriction

Magneto-elastic interactions can be significant if the magnetic moment is strongly coupled to the lattice. Such a coupling has been observed in many rare-earth intermetallics where magnetoelastic energies can be considered as a weak perturbation of the CF and exchange interactions. The measured magneto-strictive strains for cubic and non-cubic crystals can be successfully modeled in terms of the irreducible deformation modes appropriate for the crystal point symmetry. An a priori knowledge of the CF and exchange interactions is usually required for a detailed analysis of the magnetoelastic coefficients. The magneto-elastic Hamiltonian is quite a complex function of the magnetoelastic parameters. For example, a suitable magneto-elastic Hamiltonian developed for cubic symmetry (del Moral and Brooks 1974) is given by

$$\begin{aligned} H_{\mathrm{me}} = & -M_0^\alpha \varepsilon^\alpha - M_2^\gamma \left[\varepsilon_1^\gamma O_2^0 + \sqrt{2}\,\varepsilon_2^\gamma \overline{O}_2^2\right] \\ & - M_2^\varepsilon \left(\varepsilon_1^\varepsilon \left[\overline{O}_2^1\right] + \varepsilon_2^\varepsilon \left[-\mathrm{i}\widehat{O}_2^1\right] + \varepsilon_3^\varepsilon \left[\widehat{O}_2^2\right]\right) \\ & - \left[M_4^\alpha \left(O_4^0 + 5O_4^4\right) - M_6^\alpha \left(O_6^0 - 21O_6^4\right) - D^\alpha \langle J_x\rangle^2 + \langle J_z\rangle^2\right]\varepsilon^\alpha \end{aligned} \tag{3.10}$$

where M_1^α and $\varepsilon_1^\varepsilon$ are magnetoelastic CF and elastic energy parameters, respectively whilst D^α is the magnetoelastic exchange parameter. The terms $\overline{O}_1^m$ and $\widehat{O}_1^m$ are linear combinations of Stevens operators, $\overline{O}_1^m = (O_1^m + O_1^{-m})/2$, $\widehat{O}_1^m = (O_1^m - O_1^{-m})/2\mathrm{i}$. The CF and exchange parameters can be verified by fitting appropriate magnetostriction data performed at various temperatures. Magnetostriction in rare-earth intermetallics is reviewed by Clark (1980), Ibarra and del Moral (1990) and Andreev (1995).

3.10. Electrical resistivity

This is the best known method amongst transport property measurements (thermopower, electrical resistivity and conductivity) for detecting CF effects. An approximation, with inclusion of the CF interaction, for the spin-disorder resistivity in rare-earth intermetallics was obtained by Rao and Wallace (1970). In the first order Born approximation for scattering from conduction electrons and rare-earth moments, the single ion CF contribution to

the electrical resistivity is expressed as (Hessel-Andersen et al. 1974; Purwins and Leson 1990):

$$\rho(T) = \frac{3\pi N s}{\hbar e^2 E_F} J_{sJ}^2 (g_J - 1)^2 \times \sum_{i,j} p_i f_{ij} \left[\langle i, s_i | s_z \cdot J_z | j, s_j \rangle^2 + \langle i, s_i | s_+ \cdot J_+ | j, s_j \rangle^2 + \langle i, s_i | s_- \cdot J_- | j, s_j \rangle^2 \right] \tag{3.11}$$

with

$$f_{ij} = \frac{2}{1 + \exp[\beta(E_i - E_j)]} \tag{3.12}$$

and where i and s_i refer to initial 4f and conduction electron states, respectively, with energy E_i, N the total number of rare-earth ions, J_{sJ} the exchange integral between conduction electron and rare earth spins and E_F the Fermi energy. The effect is important at temperatures lower then the overall CF splitting and, in practical terms, is of limited use for a precise determination of CF parameters, since other interactions, in particular those arising from quadrupolar scattering, need to be included in order to obtain even a correct theoretical description. More details can be found in the chapters by Fulde (1978) and Fulde and Peschel (1972). Transport properties of rare-earth and actinide intermetallics are reviewed by Fournier and Gratz (1993).

4. Inelastic neutron scattering experiments on stable cubic lanthanide intermetallics

The most systematic and numerous INS studies have been carried out on systems where the point symmetry of the rare earth ion site is cubic. This is because the details of the CF interaction for cubic point symmetry requires the determination of only two CF parameters, and usually INS studies are sufficient for this purpose. Correspondingly, a large number of intermetallic systems, polycrystalline and single crystal, have been investigated. These include those of the type RX with the CsCl structure, cubic Laves phase RX_2, RX_3 (Cu_3Au structure type), RBe_{13} ($NaZn_{13}$ structure) and some Heusler intermetallics. The work on the CsCl systems was preceded by the INS investigations of the CF interaction in pnictides and chalcogenides which crystallize in the cubic rocksalt NaCl structure. These were the first examples of rare earth intermetallics studied by INS where the magnetic properties are determined by CF splittings, magnetic exchange coupling and (to a lesser extent) magneto-elastic interactions. The magnetism of these systems, and in particular their magnetic structures, has been reviewed by Gignoux and Schmitt (1997).

4.1. RX (X = Bi, P, As, Sb)

The first INS studies of the CF and exchange interactions in metallic systems were performed on these compounds. This early work has already been reviewed in the past (Fulde

1978; Sinha 1978; Fulde and Loewenhaupt 1985, 1988). The magnetic properties have been reviewed by Kirchmayer and Poldy (1971) and Buschow (1980).

These compounds form a very rich field for the study of the interplay between comparable crystal field and exchange interactions as well as interactions with lattice phonons. The RN series are anomalous in that they appear to be semiconductors. The results obtained from INS investigations for the pnictides indicate that the CF parameters in these intermetallics are reasonably well parameterized within a simple nearest-neighbor point-charge model, except for the heavy rare-earth lanthanides where there is a deviation. Das and Ray (1969) had already pointed out that conduction electrons would have a considerable part to play in influencing the CF potential, giving rise to a point-charge enhancement. Herbst et al. (1977) also noted the important role of the 5d band electrons in generating a 4f–5d interaction having the appropriate cubic symmetry for the R pnictides. The intermetallic TmSb, in particular, is the ideal exchange free singlet ground state paramagnet, as proposed by single crystal high field magnetization measurements performed by Cooper and Vogt (1970). Birgeneau et al. (1971, 1973) were able to verify this conjecture since no appreciable exchange broadening of the CF transitions was observed, even at low temperatures. In detailed INS studies on single crystals, anisotropic two-ion exchange interactions were confirmed for the systems PrSb (McWhan et al. 1978, 1979), TbP (Kötzler et al. 1979; Loidl et al. 1979, 1982; Knorr et al. 1980, 1981), ErSb (Knorr et al. 1983) and HoP (Furrer et al. 1977a; Furrer and Kaldis 1980; Fischer et al. 1985). The magnetic Γ_1–Γ_4 CF exciton of the singlet ground state system TbP in the *paramagnetic* phase was observed to contain a considerable dispersion as well as a large splitting in the [1 0 0] and [1 1 0] directions (fig. 3). This implies a long ranged anisotropic exchange coupling. In the *antiferromagnetic* phase, however, the anisotropic nature of the exchange interaction could not be confirmed, probably because of domain formation which ruled out a detailed analysis of the polarization of the observed modes.

The antimonides have also been studied in detail by INS on single crystal materials. The earlier polycrystalline INS measurements which characterized the CF interaction served as very useful starting parameters for fitting the data to complex models for the magnetic excitation spectrum in the presence of exchange interactions. The lattice dynamics for these types of materials had already been well characterized, as for example in NdSb (Wakabayashi and Furrer 1976), by INS. No phonon anomalies were observed at points near or at those of interest for the observed magnetic excitations. In the case of NdSb, a large quadrupolar exchange interaction was also observed, in addition to cubic CF and isotropic Heisenberg exchange interactions (Furrer et al. 1972, 1976, 1977c). The magnetic excitations in the singlet-ground state antiferromagnet TbSb were investigated by Holden et al. (1972, 1974). The exchange interaction in this system induces a ground state moment by mixing excited states in to the ground state, where a critical ratio between exchange and CF interactions is necessary to ensure a net magnetic moment. In this particular case, the CF Hamiltonian also contained an additional B_2^0 term which takes into account the effects of the observed rhombohedral distortion of the cubic cell below the ordering temperature of 15 K (Lévy 1969). An excellent description of the observed frequencies and intensities was obtained within the framework of an CF-exchange model specifically developed for these types of systems (Pink 1968; Cooper 1969; Wang and Cooper 1969; Hsieh and Blume 1972). With only the ground state populated, as measurements were performed at 4 K, a

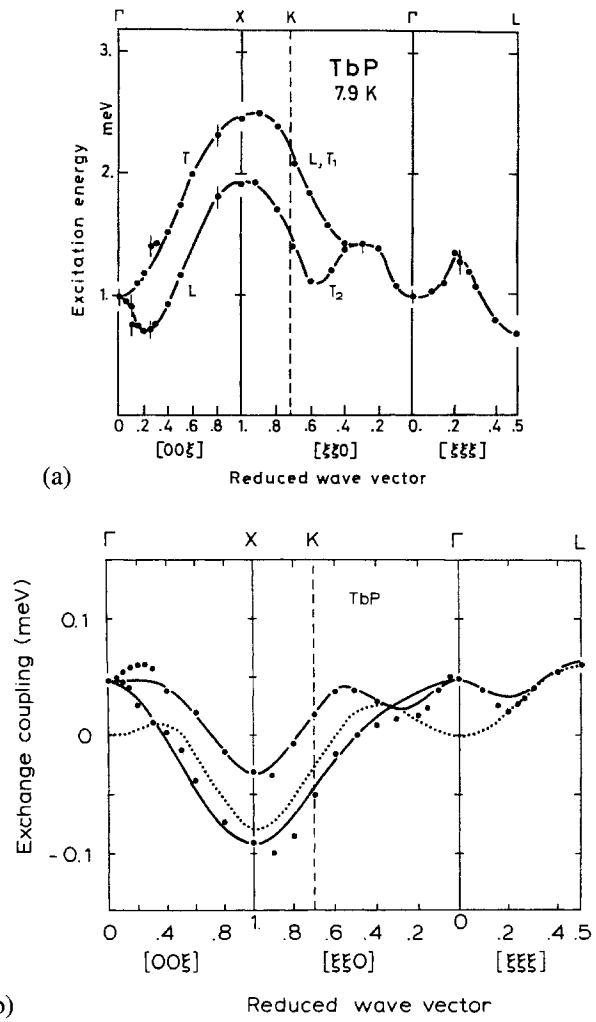

Fig. 3. (a) Dispersion of the $\Gamma_1-\Gamma_4$ magnetic excitation, at 7.9 K, for cubic TbP, measured along the principal high symmetry directions. Lines are fits using an RPA approximation with coupling to fourth nearest Tb neighbors. (b) The wavevector dependence of the anisotropic exchange coupling for cubic TbP. The solid line is the best fit of a phenomenological anisotropic exchange model to the experimental data which are given by dots. The dotted line illustrates the fit with an isotropic exchange model (from Loidl et al. 1982).

pseudoboson method (Grover 1965; Buyers et al. 1971) was used to treat the wave-vector dependence of the magnetic excitations.

For the compound DySb, a theoretical treatment of the expected magnetic excitation spectrum has been published (Sablik and Wang 1979), but no corroborative neutron spectroscopy measurements appear to have been performed as of yet. The motivation here is the fact that this system is an excellent example of a type-II antiferromagnet with isotropic

TABLE 8

Crystal field coefficients for rare-earth RX intermetallics (cubic NaCl structure) determined by INS experiments. Units for A_n^m are in $K r_0^{-n}$.

Compound	x	W (K)	A_4^0	A_6^0	Ground state	Ref.
PrBi	−0.94	3.59	22.64	0.14	Γ_1	[1,2,4]
NdBi	0.77	−2.92	24.28	0.39	$\Gamma_8^{(2)}$	[6]
TmBi	−0.74	−1.46	94.44	2.06	Γ_1	[6]
PrP	−0.95	7.10	44.93	0.27	Γ_1	[2,4,6]
NdP	0.77	−2.92	43.70	0.48	$\Gamma_8^{(2)}$	[5,6]
TbP	−0.79	−0.68	43.26	0	Γ_1	[6,15,16,17]
HoP	0.75	−0.29	76.88	0.71	Γ_1	[6,18]
ErP	0.82	0.41	99.29	0.81	$\Gamma_8^{(1)}$	[6]
TmP	−0.75	−1.07	88.96	1.36	Γ_1	[6]
$YbP_{0.84}$			135.3	1.34	Γ_6	[26]
PrSb	−0.97	4.47	28.21	0.10	Γ_1	[2,4,13,14]
NdSb	0.78	−1.81	27.61	0.28	$\Gamma_8^{(2)}$	[5,6]
NdSb	0.76	−1.82	26.36	0.29	$\Gamma_8^{(2)}$	[10,11]
TbSb	−0.81	−0.77	51.23	0	Γ_1	[6]
TbSb	−0.80	−0.53	35.20	0	Γ_1	[7,8]
ErSb	0.78	0.37	83.50	0.60	$\Gamma_8^{(1)}$	[12,19]
TmSb	−0.79	−0.99	64.74	1.13	Γ_1	[3,6]
YbSb			135.0	0.19	Γ_6	[27]
PrAs	−0.95	6.55	41.33	0.24	Γ_1	[2,4]
NdAs	0.78	−2.71	40.65	0.44	$\Gamma_8^{(2)}$	[5]
TmAs	−0.75	−1.49	97.34	2.01	Γ_1	[6]
YbAs			116.0	1.39	Γ_6	[28,29]
PrS	−0.92	7.17	47.16	0.45	Γ_1	[2,4]
NdS	0.69	−3.91	53.00	0.84	$\Gamma_8^{(2)}$	[9]
PrSe	−0.95	6.88	43.40	0.26	Γ_1	[2,4]
NdSe	0.69	−3.57	48.46	0.77	$\Gamma_8^{(2)}$	[9]
$Tm_{0.87}Se$	−0.10	0.69	−6.06	−3.34	$\Gamma_5^{(4)}$	[20]
PrTe	−0.95	5.09	32.12	0.09	Γ_1	[2,4]
NdTe	0.66	−2.55	33.10	0.60	$\Gamma_8^{(2)}$	[21]
PrN	−0.91	20.7	125.61	1.26	Γ_1	[22,23]
NdN	0.78	−8.35	128.1	1.28	$\Gamma_8^{(2)}$	[24,25]
HoN	0.80	−0.69	202.2	1.44	Γ_1	[25]
TmN	−0.38	−3.85	127.4	1.28	Γ_1	[22,23]
YbN			262.0	1.19	Γ_6	[30]

References:

[1] Birgeneau et al. (1970)
[2] Turberfield et al. (1970)
[3] Birgeneau et al. (1971)
[4] Turberfield et al. (1971)
[5] Furrer et al. (1972)
[6] Birgeneau et al. (1973)
[7] Holden et al. (1972)
[8] Holden et al. (1974)
[9] Furrer and Warming (1974)
[10] Furrer et al. (1976)
[11] Furrer et al. (1977c)
[12] Shapiro et al. (1975)
[13] Vettier et al. (1977)
[14] McWhan et al. (1979)
[15] Kötzler et al. (1979)

Heisenberg exchange interactions, with quadrupolar couplings in a cubic CF. For PrSb, another singlet ground state model system, the evolution of induced moment magnetism with pressure has also been investigated (Vettier et al. 1977; McWhan et al. 1978). The observed decrease in the energies of the Γ_1–Γ_4 and Γ_4–Γ_5 CF transitions were suggested as a possible indication of a pressure-induced soft-mode magnetic transition to an antiferromagnetic structure.

The CF level scheme in an induced moment spin glass, $PrP_{0.9}$, where vacancies created in random fashion on the P sublattice change the CF field considerably in comparison with stoichiometric PrP, decreases the Γ_1–Γ_4 splitting by approximately 10% (Yoshizawa et al. 1983). Also, in contrast to the stoichiometric compound, additional excitations were observed at low temperature. These authors modeled the CF structures for a vacancy distribution of one and two on the six nearest neighbor sites of the Pr ion, the nonstoichiometry lifting the degeneracies of the cubic CF. On this basis, the positions and relative intensities of these extra transitions were found to be in approximate agreement with the data. The magnetic quasi-elastic scattering exhibited a peak at 8 K, as also observed by bulk susceptibility measurements, giving rise to a typical spin-glass behaviour, induced by the random vacancy distribution (Sherrington 1979; Hasanain et al. 1981).

Crystal field coefficients for the series are tabulated in table 8. Also included are the results of INS studies for YbP (Dönni et al. 1990a; Kohgi et al. 1990), YbN (Dönni et al. 1990b), YbSb (Dönni et al. 1991) and YbAs (Dönni et al. 1992; Keller et al. 1994) which display a characteristic Kondo or heavy fermion behaviour. The CF coefficients for these compounds are, however, also in approximate accord with the variation shown for each isostructural series, having the same signs and approximate orders of magnitude. The fourth order term is the dominant one, as it is for the whole series.

4.2. RB_6

The rare earth hexaborides can be visualized to crystallize in the CsCl type structure, characterized by two interpenetrating simple cubic lattices, one with boron octahedra and the other consisting of R atoms. Rare-earths in this structure are found to exhibit Kondo lattice behaviour in CeB_6 (Komatsubara et al. 1983) and valence fluctuations in SmB_6 (Wachter and Travaglini 1985) whilst PrB_6 and NdB_6 display a much more conventional magnetic behaviour. Inelastic neutron scattering measurements have been reported for PrB_6 and NdB_6 (Lowenhaupt and Prager 1986; Erkelens et al. 1988). The measurements for polycrystalline PrB_6 (Loewenhaupt and Prager 1986), performed above the antiferromagnetic ordering temperature of 6.9 K (McCarthy et al. 1980), indicate a Γ_5 triplet as the ground state whilst those reported for polycrystalline NdB_6 propose a Γ_8 quartet ground state,

References (continued):

[16] Loidl et al. (1979)
[17] Knorr et al. (1981)
[18] Fischer et al. (1985)
[19] Knorr et al. (1983)
[20] Furrer et al. (1981)
[21] Furrer and Tellenbach (1975)
[22] Davis and Mook (1973)
[23] Davis and Mook (1975)
[24] Warming and Bak (1975)
[25] Furrer and Hälg (1976)
[26] Dönni et al. (1990a)
[27] Dönni et al. (1991)
[28] Dönni et al. (1992)
[29] Keller et al. (1994)
[30] Dönni et al. (1990b)

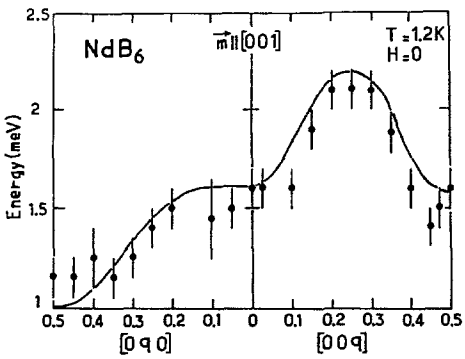

Fig. 4. Dispersion of the magnetic excitations, measured along the high symmetry directions [0 0 1] and [1 0 1] at 1.2 K, for cubic NdB_6. Lines are fits to a CF and exchange model with interactions up to third nearest neighbors and a CF splitting from the ground to first excited state of 16 K (from Erkelens et al. 1988).

TABLE 9

Crystal field coefficients for a few representative cubic REB_6 (CsCl structure) and $REBe_{13}$ ($NaZn_{13}$ structure) intermetallics determined by INS experiments. Units for A_n^m are in $K\,r_0^{-n}$.

Compound	x	W (K)	A_4^0	A_6^0	Ground state	Ref.
PrB_6	0.95	9.50	−60.17	0.33	Γ_5	[1]
NdB_6	−0.84	−3.85	−63.60	0.43	$\Gamma_8^{(2)}$	[1]
ErB_{13}	−0.28	0.09	−7.55	0.49	Γ_7	[2]

References:

[1] Loewenhaupt and Prager (1986)
[2] Vigneron et al. (1980)

also in agreement with Raman scattering measurements (Pofahl et al. 1987). The magnetic ordering in PrB_6 was also found to be rather complex, with a further transition from an incommensurate to a commensurate double-k structure at 3.9 K (Burlet et al. 1988). This is consistent with a strong quadrupolar interaction which is extremely weak in NdB_6. Negative fourth order CF parameters and small positive sixth order parameters obtained from these studies were in agreement with susceptibility and resistivity data for PrB_6 (Fisk and Johnston 1977) but in disagreement with the level scheme deduced from specific heat and resistivity measurements available for NdB_6 where a positive fourth order parameter was deduced (Luft et al. 1983). A detailed study of the magnetic excitations within the Γ_8 quartet in a single crystal of NdB_6 (Erkelens et al. 1988) which orders antiferromagnetically at 8.6 K (McCarthy and Thompson 1980) was interpreted in terms of up to 3rd nearest neighbor isotropic exchange interactions. A negligible quadrupolar interaction was inferred, and this study confirmed the values of the CF parameters obtained on powder material (fig. 4). The Newman superposition model has also been tested for this series of intermetallics (Newman 1983). The CF coefficients, as determined by INS, are tabulated in table 9.

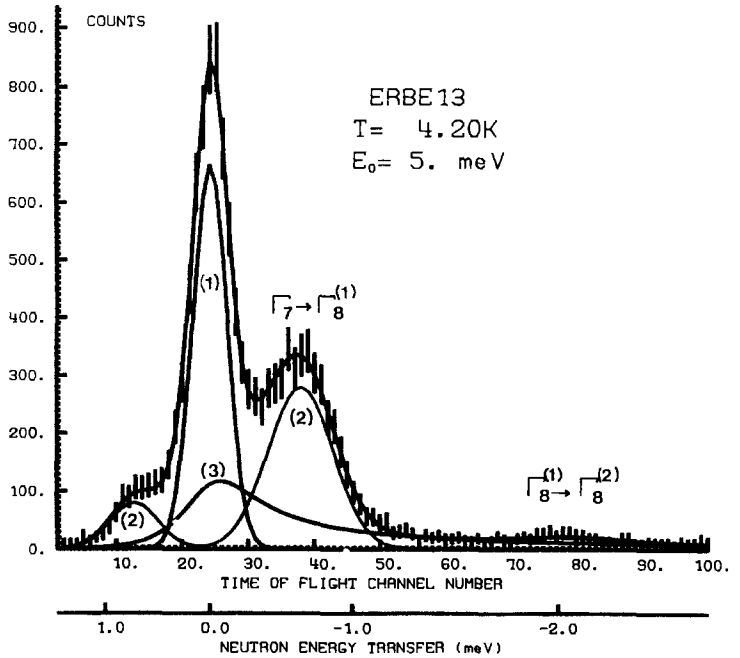

Fig. 5. Crystal field transitions observed for polycrystalline cubic $ErBe_{13}$ by INS at 4.2 K, which is above the AF ordering temperature for this compound. The curves refer to fits of: (1) the elastic nuclear incoherent scattering; (2) inelastic CF excitations and (3) quasielastic paramagnetic scattering (from Vigneron et al. 1980).

4.3. RBe_{13}

A competition between CF and exchange interactions is a characteristic of R beryllides RBe_{13}, which crystallize in the cubic $NaZn_{13}$ structure, with a CF generated by 24 Be nearest neighbor atoms. Neutron diffraction studies have revealed incommensurate and/or commensurate structures for $DyBe_{13}$ (Vigneron et al. 1982) and $TbBe_{13}$ (Bouton et al. 1980; Vigneron et al. 1985a) whilst $HoBe_{13}$ undergoes a series of incommensurate helical and commensurate magnetic structures (Vigneron et al. 1985b). The largest overall CF splitting in the series, on the basis of specific heat measurements (Bucher et al. 1975; Van der Linden et al. 1980), is estimated at approximately 40 K for $ErBe_{13}$, going down to a low value of about 10 K for $TbBe_{13}$. INS measurements have been carried on $ErBe_{13}$ in order to determine the CF parameters (Vigneron et al. 1980). This system is the most appropriate for an INS investigation, as it has the lowest ordering temperature at 3.0 K and largest overall CF splitting, of the series. The ground state is deduced as a Γ_7 doublet (fig. 5). A point charge calculation failed to explain the observed signs of the CF parameters. Different parameters (Van der Linden et al. 1980), deduced from specific heat measurements, fail to reproduce all the observed INS transitions. The magnetic phase diagram of the series, incorporating reasonable values of the experimentally determined CF and exchange energies, has been deduced from a free energy calculation (Vigneron et al. 1985a, 1985b).

The CF parameters, obtained from various bulk magnetic measurements for the series, are comprehensively summarized by Besnus et al. (1983) and those determined by INS for $ErBe_{13}$ are tabulated in table 9. There is a peculiar and unexplained sign reversal of the fourth order parameter in the series.

4.4. RX (X = Ag, Zn, Cu)

The measurements of the magnetic excitations by INS in equiatomic R intermetallics with Ag, Cu and Zn, which crystallize in the cubic CsCl structure, has played a large part in the determination of fundamental interactions which are responsible for a particularly rich variety of magnetic properties exhibited by the series. These include the single-ion anisotropy determined principally by CF effects, a long range Heisenberg exchange interaction, anisotropic exchange and higher order pair interactions which are particularly prevalent in RZn compounds. The quadrupolar interactions and magneto-elastic effects present in these systems have been summarized by Morin and Schmitt (1990) and Thalmeier and Lüthi (1991). The magnetic properties of the entire series have been reviewed by Gignoux and Schmitt (1997).

4.4.1. RAg

The CF interaction in this series has been investigated by powder INS spectroscopy on compounds with Pr, Er and Ho. The magnetic structure of PrAg is of the so called antiferromagnetic (π π 0) type (Brun et al. 1974) with an ordering temperature of 14 K. The cubic CF parameters have been determined in two separate INS investigations. The LLW CF parameters $W = -5.4$ K, $x = -0.79$ determined by Morin and Schmitt (1982) and $W = -3.66$, $x = -1.00$ proposed by Brun et al. (1974) give an overall CF splitting of about 20 meV and the Γ_5 triplet as the ground state. The observed parameters are fortuitously in agreement with a point charge calculation with assignment of a zero Ag charge and tri-positive Pr ions. Morin and Schmitt (1982) also observed an additional weak ferromagnetic component of the magnetic structure below 6.9 K and proposed strong quadrupolar interactions as being responsible for the non collinear structure. The CF parameters in the HoAg compounds, determined by INS, are reported by Tellenbach et al. (1975) and Schmitt et al. (1977a, 1977b). In order to isolate the CF interaction, systems diluted with Y were studied in the first instance, since the ordering temperature of HoAg is rather high at 33 K. Tellenbach et al. (1975) also investigated the pure compound HoAg at 78 K. Both results propose the $\Gamma_5^{(1)}$ triplet for the ground state. Within a mean field model, the temperature dependence of the Ho moment is perfectly reproduced using the determined CF parameters, lending additional credence to their reliability. The ErAg system has been investigated in two separate INS studies (Morin et al. 1974; Furrer 1975). Both report $W = -0.48$ K and $x = 0.42$ with a $\Gamma_8^{(3)}$ ground state quartet and a large CF splitting of about 200 K. These results are in total contradiction with susceptibility (Williams and Hirst 1969) and EPR measurements (Rettori et al. 1973) on dilute compounds with 0.28 at.% and 1.1 at.% Er which propose a Γ_7 ground state doublet and $W = 0.55$ K, $x = -0.35$. The magnetic structure, as reported in the neutron diffraction measurements of Nereson (1973), presents two AF transitions at 18 K and 9.5 K. Below 9.5 K, the structure is commensurate, and intermediate between 9.5 K and 18 K, it is reported as sinusoidally modulated.

This complex behaviour was modeled by Furrer (1975) in a particularly elegant manner using CF and exchange parameters determined by INS. Total agreement is obtained with the susceptibility results for ErAg (Walline and Wallace 1964; Pierre and Pauthenet 1965) and the temperature dependence of the zero field magnetization as determined by neutron diffraction.

4.4.2. RZn

The CF parameters for compounds with Pr, Nd, Tb, Ho, Er and Tm have been determined by INS studies. In addition, a large effort was devoted to studying the magnetic excitations in these systems displaying strong quadrupolar interactions, especially by use of single crystals. Inelastic neutron scattering for Pr and Nd compounds is reported by Morin et al. (1978a, 1978b) and for NdZn by Amara and Morin (1996) for diluted compounds, in order to suppress the strong exchange interactions between R ions. The compound TbZn orders ferromagnetically above 204 K (Morin and Pierre 1973) with a temperature variation in the easy axis directions, with ⟨1 1 0⟩ being the axis easy until 65 K above which the ⟨1 0 0⟩ axis becomes the easy magnetization direction. The rather high ordering temperature precludes an investigation of CF effects only by INS and no experiments have been reported with compounds diluted by Y. The dispersion of the magnetic excitations in a single crystal of TbZn was studied by Hamaguchi et al. (1980). Above the spin rotation temperature of 65 K, the dispersion of the excitations displayed a long range oscillatory exchange interaction and single-ion anisotropy. In this case, CF parameters with $W = 1.0$ K and $x = -0.3$ determined by bulk means were implemented into the model CF and exchange Hamiltonian as hardly any non-dispersive excitations were observed. Data below the spin re-orientation temperature were also taken but it was not possible to adequately fit it in terms of just CF and exchange interactions, invoking the presence of a possible quadrupolar interaction.

In the case of HoZn, which also presents a spin re-orientation at 23 K (Morin and Pierre 1973), numerous INS studies exist. The CF interaction in a Y diluted polycrystalline compound, $Ho_{0.15}Y_{0.85}Zn$ was determined by Schmitt et al. (1977a, 1977b). They obtain a $\Gamma_5^{(1)}$ triplet ground state with an overall CF splitting of 275 K. A reasonable but not totally satisfactory agreement for the field dependence of the magnetization along the three high symmetry directions [1 1 0], [1 1 1] and [1 0 0] was obtained with these CF parameters inserted into a MF model. More substantive measurements on a single crystal of HoZn report the magnetic excitations at 4.2 K (Hennion et al. 1977; Pierre et al. 1977) as well as near the spin re-orientation temperature (Hennion and Pierre 1979). At all temperatures a consistent fit to the intensity and dispersion of the modes using the previously determined CF parameters could only be obtained by also invoking quadrupolar interactions. The exchange interaction shows a dominant ferromagnetic coupling at first and third nearest neighbors with significant interactions even up to sixth nearest neighbors (fig. 6).

Powder measurements on $Er_{0.2}Y_{0.8}Zn$ also assign a Γ_8 quartet to the ground state (Morin et al. 1974, 1976) and account for the bulk magnetic properties in good fashion when used as inputs in a CF and mean field exchange calculation of the magnetic anisotropy (Morin and Pierre 1973). Single crystal magnetization and magnetostriction measurements carried out on ErZn are well accounted for when CF parameters determined by INS are used for their interpretation (del Moral et al. 1974).

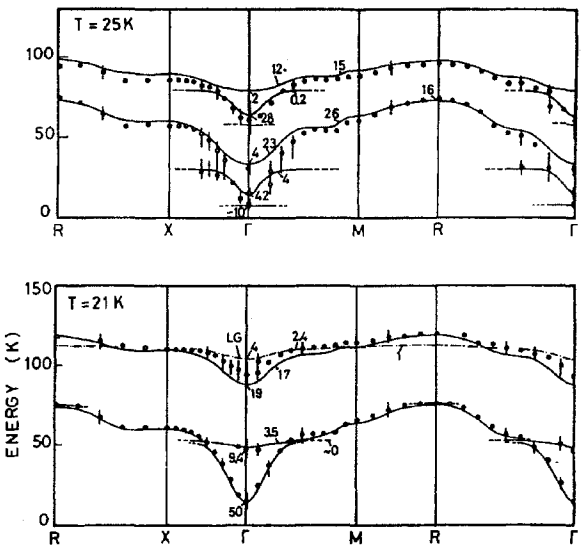

Fig. 6. Dispersion of magnetic excitations measured for a cubic single crystal of HoZn at 21 and 25 K. Crystal field parameters $x = 0.08$ and $W = 0.36$ K were used, as well as quadrupolar interactions. Continuous lines refer to transverse excitations whilst dashed lines refer to longitudinal excitations. Numbers are the imaginary part of the dynamic susceptibility (from Hennion and Pierre 1979).

Neutron spectroscopy measurements are also reported for the quadrupolar compound TmZn. Powder measurements slightly above both the magnetic ordering at 8.1 K and the structural transition induced by quadrupolar ordering at 8.6 K, lead to the $\Gamma_5^{(1)}$ triplet ground state in the paramagnetic phase (Morin et al. 1978b). Measurements of the dispersion of magnetic excitations in a single crystal of TmZn however failed to show any appreciable effect on the excitations, which could be modeled adequately by just cubic CF and isotropic exchange terms (Morin et al. 1980). This was also the case in a similar study of the magnetic excitations in $Tm_{0.9}Lu_{0.1}Zn$ (Morin et al. 1981). The only possibility is to couple the dipole susceptibilities, which are very sensitive to neutrons, to the quadrupolar ones via an external perturbation such as a magnetic field (Fulde and Loewenhaupt 1985). Magnetic form factor measurements are reported for TmZn in the ordered phase (Givord et al. 1982, 1983) with CF parameters determined, but not in agreement with INS investigations.

4.4.3. RCu

The intermetallic HoCu orders antiferromagnetically below 28 K (Wintenberger and Chamard-Bois 1972) but the magnetic structure remains ambiguous. INS measurements on $Ho_{0.25}Y_{0.75}Cu$ (Schmitt et al. 1977a, 1977b) report a CF Γ_5 triplet ground state which accounts for the observed high field magnetization measurements reported in the previous reference. Measurements on ErCu (Morin et al. 1974; Pierre et al. 1978) assign a Γ_8 quartet to the ground state, similar to ErZn and ErAg. The CF parameters account for the observed [1 0 0] easy axis direction of magnetization. The magnetic excitations in a single crystal of

ErCu were investigated by Pierre et al. (1978). Also in this case, higher order interactions beyond CF and isotropic exchange were required to account for details of the observed modes. The dispersion of the modes could only adequately be described by interactions extending out to fourth nearest neighbors. A similar dispersion of the magnetic excitations is reported for TmCu (Morin et al. 1984) with an even longer ranged bilinear exchange interaction.

4.4.4. RMg, RRh

Neutron spectroscopy investigations of the CF interaction are reported for ErMg, ErPd (Morin et al. 1976; Schmitt et al. 1977b), HoMg (Schmitt et al. 1977a, 1977b), RRh, R = Tb, Ho, Er and Tm (Rossat-Mignod et al. 1974) and for HoRh (Chamard-Bois et al. 1973). The principal motivation for studying these compounds was to test the dependence of CF parameters as a function of the valence of the ligand atoms and electronic structure. As is usual in neutron investigations of CF transitions, non-magnetic reference compounds like YZn (Morin et al. 1974) and YRh (Chamard-Bois et al. 1973) were also measured in order to isolate the CF excitations form phonon scattering. For ErMg, parameters $W = -0.32$ K and $x = -0.03$ give a $\Gamma_8^{(3)}$ ground state quartet. These give a fourth order CF parameter which is opposite in sign to corresponding ErAg, ErCu and ErZn materials. For ErPd a definitive solution for W and x was not deemed possible due to the presence of an additional FeB type orthorhombic phase. Both proposed solutions, however, lead to similar and negative values of the sixth order CF parameter. The INS data for ErMg, which orders AF below 5.5 K, reproduced the measured high field magnetization data for the high symmetry directions (Morin et al. 1976). The INS data for HoRh, which orders antiferromagnetically at 5.5 K with a moment of 5.2 μ_B (Chamard-Bois et al. 1973), assign a $\Gamma_5^{(1)}$ triplet for the ground state with $W = 6.0$ K and $x = 0.43$. The composition of this state with the fitted INS parameters is in good agreement with the observed magnetic moment at 1.2 K. For HoMg, the ordering temperature is much higher, at 21 K and because of this, a compound diluted with Y, $Ho_{0.2}Y_{0.8}Mg$, was investigated.

The CF coefficients for the series of CsCl type compounds, as determined by INS, are collected together in table 10. There is clearly a very satisfying consistency in the signs and magnitudes of the determined coefficients. The Newman superposition model has also been satisfactorily tested for the series (Newman 1983) and ab initio electronic structure calculations of the CF parameters now exist (Divis and Kuriplach 1993, Divis et al. 1995).

4.5. RX_3 (X = Sn, Pb, In, Pd, Tl, Al, Ga)

Intermetallics which crystallize in the cubic Cu_3Au structure have been extensively investigated by INS. These include systems with Pd, Sn, In, Pb, Tl, Al and Ga. They are ideal as the series present a high coordination and a large number of valence electrons, which range from 12 in In and Tl compounds up to 15 for Sn and Pb compounds, and hence the magnetic properties are dominated by CF effects. The magnetic properties have been summarized and reviewed by Buschow (1980). The magnetic structures of the systems with In and Sn have been investigated in the past (Arnold and Nereson 1969; Nereson and Arnold 1970; Lethuillier et al. 1973) whilst later neutron diffraction data for RPd_3 compounds are reported by Elsenhans et al. (1988, 1991). Crystal field effects for some members of the series have already been discussed by Lüthi (1980). The magnetic properties of the entire series have been reviewed by Gignoux and Schmitt (1997).

TABLE 10

Crystal field coefficients for rare-earth intermetallics REX (X = Ag, Zn, Cu, Rh, Pd) which crystallize in the cubic CsCl structure determined by INS experiments. Units for coefficients A_n^m are in Kr_0^{-n}.

Compound	x	W (K)	A_4^0	A_6^0	Ground state	Ref.
PrAg	−0.97	−3.66	−23.69	−0.80	$\Gamma_5^{(3)}$	[1]
PrAg	−0.79	−5.40	−28.56	−0.80	$\Gamma_5^{(3)}$	[2]
HoAg	0.43	0.312	−48.71	−1.84	$\Gamma_5^{(1)}$	[3]
$Ho_{0.2}Y_{0.8}Ag$	0.40	0.335	−48.66	−1.83	$\Gamma_5^{(1)}$	[3,4]
ErAg	0.43	−0.435	−55.40	−1.85	$\Gamma_8^{(3)}$	[5]
$Er_{0.2}Y_{0.8}Ag$	0.43	−0.493	−61.90	−2.06	$\Gamma_8^{(3)}$	[6]
$Tb_xLa_{1-x}Ag$			Not reported			[7]
$Pr_{0.25}La_{0.75}Zn$	−0.57	−3.6	−13.68	−1.08	Γ_3	[8]
$Nd_{0.1}La_{0.9}Zn$	0.18	2.5	−7.56	−1.79	Γ_6	[9]
$Nd_{0.2}La_{0.8}Zn$	0.05	2.0	−1.96	−1.32	Γ_6	[8]
TbZn	−0.30	1.0	−24.74	−1.20		[10]
HoZn	0.08	0.36	−10.46	−3.35	$\Gamma_5^{(1)}$	[11,12,13]
$Ho_{0.15}Y_{0.85}Zn$	0.08	0.36	−10.46	−3.35	$\Gamma_5^{(1)}$	[4]
$Er_{0.2}Y_{0.8}Zn$	0.16	−0.58	−27.33	−3.57	$\Gamma_8^{(3)}$	[5]
TmZn	−0.31	1.25	−32.37	−4.52	$\Gamma_5^{(1)}$	[14,15]
$Tm_{0.9}Lu_{0.1}Zn$	−0.29	1.30	−33.25	−4.99	$\Gamma_5^{(1)}$	[16]
$Ho_{0.25}Y_{0.75}Cu$	0.34	0.40	−49.31	−2.79	$\Gamma_5^{(1)}$	[4]
ErCu	0.34	0.40	−49.31	−2.79	$\Gamma_8^{(3)}$	[13]
ErCu	0.34	−0.63	−63.71	−2.70	$\Gamma_8^{(3)}$	[17]
$Er_{0.2}Y_{0.8}Cu$	0.34	−0.63	−63.71	−2.70	$\Gamma_8^{(3)}$	[5]
TmCu	−0.42	1.4	−51.16	−4.41	$\Gamma_5^{(1)}$	[18,19]
$Pr_{0.15}La_{0.85}Mg$	0.68	−5.8	26.29	−1.29	Γ_3	[8]
$Nd_{0.25}La_{0.75}Mg$	−0.47	3.5	32.01	−1.30	Γ_6	[8]
$Ho_{0.20}Y_{0.80}Mg$	−0.26	−0.32	30.46	−2.42	$\Gamma_5^{(1)}$	[4]
ErMg	−0.03	−0.32	2.83	−2.24	$\Gamma_8^{(3)}$	[20]
ErPd	−0.22	−0.58	37.40	−3.26	$\Gamma_8^{(3)}$	[20]
HoRh	0.43	0.56	−88.86	−3.29	$\Gamma_5^{(1)}$	[21,22]
$Tb_{0.6}Y_{0.4}Rh$			−51.0	−4.15	$\Gamma_5^{(1)}$	[22]
TmRh	0.43	0.56	−88.9	−3.56	Γ_3	[22]
ErRh			−106.9	−3.95	$\Gamma_8^{(3)}$	[23]

References:

[1] Brun et al. (1974)
[2] Morin and Schmitt (1982)
[3] Tellenbach et al. (1975)
[4] Schmitt et al. (1977a, 1977b)
[5] Furrer (1975)
[6] Morin et al. (1974)
[7] Loewenhaupt and Hoenig (1978)
[8] Morin et al. (1978a)
[9] Amara and Morin (1996)
[10] Hamaguchi et al. (1980)
[11] Pierre et al. (1977)
[12] Pierre et al. (1978)
[13] Hennion and Pierre (1979)
[14] Morin et al. (1980)

4.5.1. RSn_3

Murasik et al. (1976) and Furrer et al. (1977b) performed INS measurements at high temperatures on $PrSn_3$ and obtained CF parameters $x = 0.80$ and $W = 0.158$, giving a Γ_5 ground state. The good consistency of this solution was checked with the available experimental bulk data, such as susceptibility (Tsuchida and Wallace 1965; Czopnik et al. 1970) and neutron diffraction (Lethuillier et al. 1973). The available resistivity data at low temperatures (Czopnik et al. 1970) is also in reasonable agreement with a calculation of CF effects on the spin-disorder resistivity. In this particular investigation, the importance of including the effects of exchange fluctuations in the dynamic effective field approximation (Furrer and Heer 1973; Furrer 1975) was amply demonstrated where calculated CF transition probabilities in the limit of non-interacting ions gave a less satisfactory fit. The CF level scheme in $La_xPr_{1-x}Sn_3$ with $x = 0.98$ and $x = 0.92$, is reported by Hoenig and Loewenhaupt (1979a). These measurements were carried out on the dilute compounds as these present ideal model systems for investigation of CF effects in the superconducting state (Lethuillier 1975). Unfortunately, only one CF transition was identified and thus a definitive CF assignment was not possible, but in this instance a Γ_1 groundstate is in agreement with specific heat data for the dilute series (McCallum et al. 1975). Measurements using INS at a temperature just above the ordering point for $PrSn_3$ are also reported by Groß et al. (1977, 1980) but revealed only a quasielastic line. These authors attribute the excitation observed by Murasik et al. (1976) to scattering from phonons. More extensive investigations of the magnetic excitations in a single crystal of $PrSn_3$ are reported by Knorr et al. (1988). The quasielastic distribution reported in the previous work was confirmed and implies a small CF splitting, which is in contrast to the overall CF splitting of 74 K deduced by Murasik et al. (1976). These measurements are in agreement with the INS data on the $La_xPr_{1-x}Sn_3$ series, where the Γ_1 state is also alternatively proposed as the ground state (Hoenig and Loewenhaupt 1979a, 1979b). This ground state is compatible with the experimentally determined ordered moment lying along the (0 0 1) direction, albeit however with a moment magnitude larger ($2.9\,\mu_B$) than the experimental value of $2.65\,\mu_B$. The nature of the magnetic excitations reveals a strongly anisotropic coupling between first nearest neighbor Pr ions. The reduction of the moment from its free ion value is postulated as being due to k–f scattering (Becker et al. 1977).

The CF level scheme in $NdSn_3$ is reported by Lethuiller et al. (1975) who used the INS and neutron diffraction technique to obtain two alternative solutions for the CF parameters. The Γ_6 ground state is the correct one since it reproduces in a precise way the temperature dependence of the susceptibility and the observed magnitude of the ground state moment, $1.6\,\mu_B$. The calculated contribution of the CF splitting to the measured spin-disorder resistivity, using the CF parameters determined by INS, gives a good qualitative agreement with

References (continued):

[15] Morin et al. (1978b)
[16] Morin et al. (1981)
[17] Pierre et al. (1978)
[18] Morin et al. (1984)
[19] Jaussaud et al. (1980)
[20] Morin et al. (1976)
[21] Chamard-Bois et al. (1973)
[22] Rossat-Mignod et al. (1974)
[23] Schmitt et al. (1977b)

the reported low temperature resistivity for $NdSn_3$ (Kletowski et al. 1980). The CF interaction in a dilute compound, $La_{0.92}Nd_{0.08}Sn_3$, also studied by INS, confirmed the ground state determined for the pure compound (Umlauf et al. 1979). The calculated specific heat was in excellent agreement with the INS result. Furthermore, in this dilute system, which is a superconductor at low temperatures, the concentration dependence of the superconducting transition temperature could be fitted, for low Nd concentrations, by the theory of Keller and Fulde (1971), using the above mentioned CF level scheme. The CF coefficients determined for RSn_3 compounds are collected together in table 11.

4.5.2. RPb_3

In this series, intermetallics with Pr, Nd, Er and Ho have been studied by INS techniques for the purpose of determining the CF interaction. Measurements on polycrystalline $PrPb_3$ established two CF transitions from the ground state, Γ_3–Γ_4 (19 K) and Γ_3–Γ_5 (29 K) (Groß et al. 1980). Subsequent INS data performed on a single crystal demonstrated a substantial dispersion of these two CF excitations (Niksch et al. 1982, fig. 7). These data

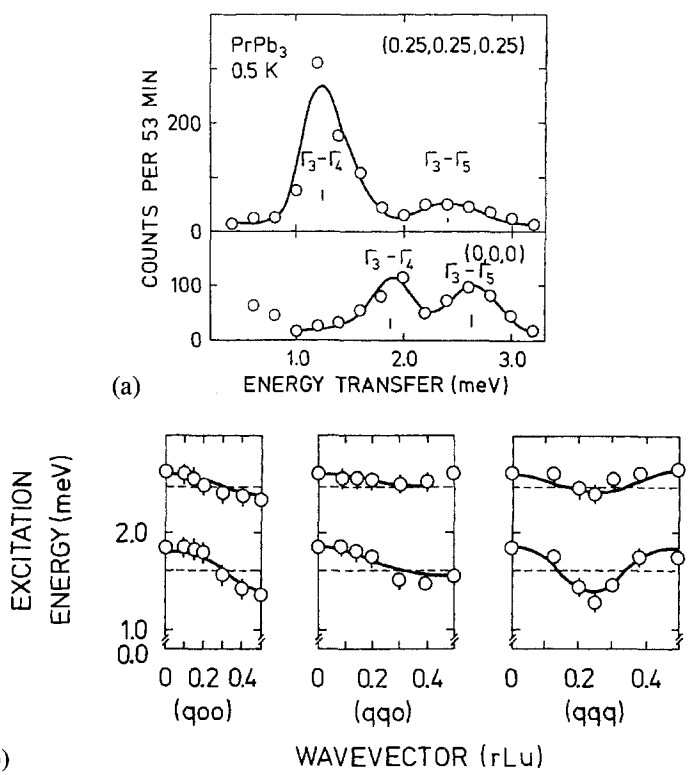

Fig. 7. (a) Dispersion of the Γ_3–Γ_4 and Γ_3–Γ_5 CF excitations for a single crystal of cubic $PrPb_3$ displayed for two values of the reduced momentum transfer q (from Niksch et al. 1982). (b) Dispersion of the Γ_3–Γ_4 and Γ_3–Γ_5 CF excitations for a single crystal of cubic $PrPb_3$ along the three principal symmetry directions. Continuous lines are fits of a mean field RPA model with a dominant second nearest neighbor anti-ferromagnetic exchange interaction (from Niksch et al. 1982).

TABLE 11

Crystal field coefficients for cubic RX_3 intermetallics determined by INS experiments. Coefficients are in units of $K r_0^{-n}$.

Compound	x	W (K)	A_4^0	A_6^0	Ground state	Ref.
$PrSn_3$	–	$\leqslant 0.15$	–	–	Γ_5	[1]
$PrSn_3$	−1	0.45	2.97	0	Γ_5	[2]
$PrSn_3$	0.8	1.76	−9.39	0.24	Γ_5	[3]
$PrSn_3$					Γ_1	[4]
$Pr_{0.02}La_{0.98}Sn_3$		Not reported			Γ_1	[5]
$Pr_{0.08}La_{0.92}Sn_3$		Not reported			Γ_3	[6]
$NdSn_3$	0.24	1.37	−6.74	−0.75	Γ_6	[7]
$Nd_{0.08}La_{0.92}Sn_3$	0.24	1.37	−6.74	−0.75	Γ_6	[8]
$Tb_xLa_{1-x}Sn_3$ $x = 0.02, 0.08, 0.15$		Not reported				[5]
$NdPb_3$	0.13	1.22	−3.35	−0.99	Γ_6	[7]
$PrPb_3$	0.11	−0.37	0.27	−0.25	Γ_3	[1,9,10]
$Pr_{0.02}La_{0.98}Pb_3$	0.39	−0.35	1.00	−0.15	Γ_3	[5]
$Pr_{0.08}La_{0.92}Pb_3$		Not reported				[6]
$ErPb_3$	0.33	−0.32	−31.24	−1.55	$\Gamma_8^{(3)}$	[1,9]
$HoPb_3$	0.08	0.13	−3.73	−1.35	$\Gamma_5^{(1)}$	[1]
$PrIn_3$	−0.66	2.68	11.79	0.63	Γ_1	[1]
$NdIn_3$	0.45	−1.19	10.48	0.45	Γ_6	[11]
$ErIn_3$		$\leqslant 0.02$				[1]
$HoIn_3$	0.40	0.18	−26.14	−1.12	$\Gamma_5^{(1)}$	[1]
$PrPd_3$	0.85	4.24	−23.29	0.44	Γ_5	[12]
$Pr_{0.05}Y_{0.95}Pd_3$	0.87	3.57	−20.14	0.29	Γ_5	[15]
$NdPd_3$	−0.91	−1.46	−19.65	0.27	$\Gamma_8^{(2)}$	[12]
$Nd_{0.05}Y_{0.95}Pd_3$	−0.91	−1.38	−23.17	0.27	$\Gamma_8^{(2)}$	[15]
$TbPd_3$		Not resolved				[13]
$TbPd_3$		Not resolved				[16,17]
$Tb_{0.05}Y_{0.95}Pd_3$	0.97	−0.38	−21.73	0.33	Γ_3	[14,15]
$DyPd_3$	0.87	0.18	−24.00	0.15	$\Gamma_8^{(1)}$	[16,17]
$Dy_{0.07}Y_{0.93}Pd_3$	0.88	0.19	−23.44	0.26	$\Gamma_8^{(1)}$	[15]
$Ho_{0.06}Y_{0.94}Pd_3$	−0.94	−0.09	−23.14	0.55		[13]
$ErPd_3$	−0.83	0.09	−23.90	0.12	Γ_6	[17,18]
$Er_{0.05}Y_{0.95}Pd_3$	−0.84	0.10	−23.90	0.12	Γ_6	[15]
$TmPd_3$	−0.69	0.42	−26.33	−0.26	Γ_3	[17]
$Tm_{0.05}Y_{0.95}Pd_3$	−0.85	0.34	−24.85	−0.28	Γ_3	[15]
$YbPd_3$	0.87	4.28	−30.28	1.12	Γ_7	[17]
$PrTl_3$	−0.61	0.88	3.58	0.24	Γ_1	[1]
$Pr_{0.5}La_{0.5}Tl_3$		Not resolved				[1]
$Pr_{0.17}La_{0.83}Tl_3$		Not resolved				[1]
$HoTl_3$		Quasi-elastic line. Not resolved				[1]
$ErTl_3$	0.10	−0.17	−5.02	−1.11	$\Gamma_8^{(3)}$	[1]

TABLE 11 (Continued)

Compound	x	W (K)	A_4^0	A_6^0	Ground state	Ref.
$TmAl_3$	−0.58	−0.43	21.69	0.98	Γ_3	[19]
$TmGa_3$	−0.32	1.03	−28.68	3.81	$\Gamma_5^{(1)}$	[20]
$PrMg_3$	0.64	−3.71	15.83	−0.93	Γ_3	[21]
$NdMg_3$	−0.25	2.51	12.34	−1.31	Γ_6	[21,22]

References:

[1] Groß et al. (1980)
[2] Knorr et al. (1988)
[3] Murasik et al. (1976)
[4] Knorr et al. (1985)
[5] Hoenig and Loewenhaupt (1979a)
[6] Hoenig and Loewenhaupt (1979b)
[7] Lethuillier et al. (1975)
[8] Umlauf et al. (1979)
[9] Knopp et al. (1985)
[10] Niksch et al. (1982)
[11] Amara et al. (1994a, 1994b)
[12] Furrer and Purwins (1976)
[13] Loewenhaupt and Holland-Moritz (1979)
[14] Ludwigs et al. (1980)
[15] Walter and Holland-Moritz (1981)
[16] Elsenhans et al. (1988)
[17] Elsenhans et al. (1990a)
[18] Holland-Moritz et al. (1979)
[19] Davis et al. (1974)
[20] Morin et al. (1987)
[21] Galera et al. (1981)
[22] Galera et al. (1985)

are nicely reproduced by a simple RPA model assuming an isotropic anti-ferromagnetic exchange coupling for the two CF transitions. A linear variation of the CF parameters was observed in INS studies performed on the diluted series $Pr(Pb_cTl_{1-c})_3$ (Knopp et al. 1985). In a further INS investigation, Lethuillier et al. (1975) measured the CF transitions in $NdPb_3$. They initially found that five sets of parameters could reproduce the observed splitting. On the basis of the transition probabilities, however, the probable CF parameters were reduced to two solutions. Neutron diffraction measurements of the ordered moment below the Néel point gives a value of $1.4\,\mu_B$ (Lethuillier et al. 1973). The solution with $x = 0.24$ and $W = 1.43$ K gives such a moment and a Γ_6 ground state. The overall CF splitting is of the order of 120 K, similar to that observed for $NdSn_3$. For both compounds, $NdSn_3$ and $NdPb_3$ the magnetization in high fields of up to 26 T does not saturate and has values well below the free ion value of $3.3\,\mu_B$. This is further proof of a Γ_6 ground state.

In the INS study of Groß et al. (1980), the CF parameters for compounds with Pr, Ho and Er were determined. These all order anti-ferromagnetically between 3 and 5 K with the exception of Pr, which probably orders at much lower temperatures. The INS measurements for these compounds were also extended to temperatures below their respective ordering points. Due to the fact that powder material was employed, only a general broadening of the transitions could be observed. A linear variation of the CF parameters, akin to that previously discussed for $Pr(Pb_cTl_{1-c})_3$, was similarly observed in INS studies performed on the diluted series $Er(Pb_cTl_{1-c})_3$ (Knopp et al. 1985). The CF coefficients for RPb_3 compounds, as determined by INS, are collected in table 11.

4.5.3. RPd_3

This series has been particularly well characterized by the INS technique. Crystal field transitions in $PrPd_3$ and $NdPd_3$ were analyzed by Furrer and Purwins (1976). Elsenhans

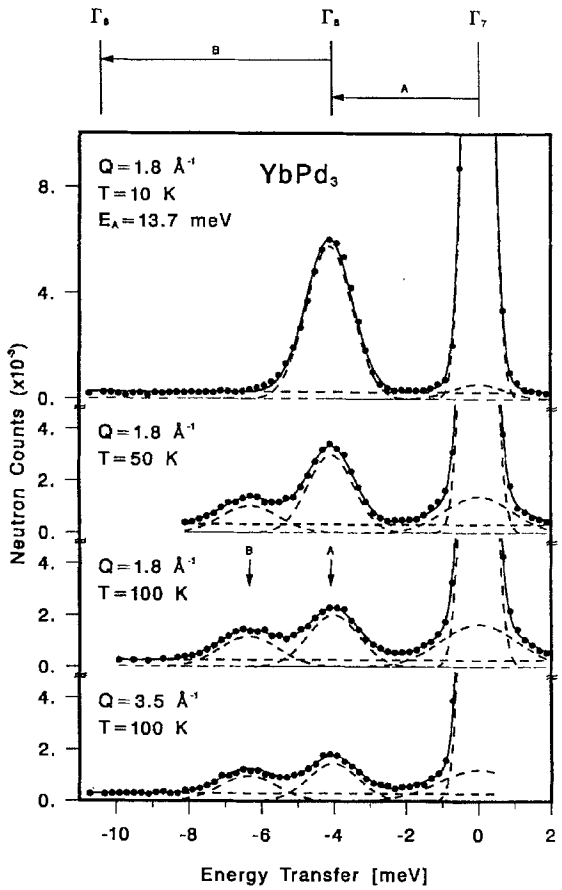

Fig. 8. Crystal field transitions measured and calculated (dashed lines) for polycrystalline cubic $YbPd_3$, as a function of temperature and scattering vector Q, together with the CF energy levels and compositions (from Elsenhans et al. 1990a).

et al. (1990a) have studied the series with Dy, Er, Tm and Yb whilst the whole series of dilute compounds $(R_xY_{1-x})Pd_3$ has been measured by Walter and Holland-Moritz (1981). Holland-Moritz et al. (1979) have also studied the dilute series $(Er_xY_{1-x})Pd_3$ as well as the full compound $ErPd_3$. Ludwigs et al. (1980) have observed CF transitions in $(Tb_{0.05}Y_{0.95})Pd_3$. The CF level scheme in $TbPd_3$ and $DyPd_3$ has also been studied by Elsenhans et al. (1988). These parameters reproduce consistently the observed magnetization and specific heat data reported for $PrPd_3$ (Drewes et al. 1988). For Nd, the corresponding CF parameters are $x = -0.90$ and $W = -0.131$ meV which yield a $\Gamma_8^{(2)}$ quartet ground state. The calculated susceptibility for both compounds is in total agreement with magnetization and specific heat measurements reported by Drewes et al. (1988).

The result obtained for Tb compounds (Walter and Holland-Moritz 1981) reproduce the observed susceptibility (Ludwigs et al. 1980) and the low temperature specific heat

(Drewes et al. 1988). Furthermore, for this particular system, the magnetic excitations measured on a single crystal, agreed well with the CF deduced from powder material (Elsenhans et al. 1990a). For Dy, the measurements on the dilute compound $(Dy_{0.07}Y_{0.93})Pd_3$ (Walter and Holland-Moritz 1981) and the full compound (Elsenhans et al. 1990a), showing a $\Gamma_8^{(1)}$ ground state, agree with the parameter set finally chosen by Drewes et al. (1988) from magnetization and specific heat data. The CF parameters reported for $(Ho_{0.06}Y_{0.94})Pd_3$ by Walter and Holland-Moritz (1981) are not in agreement with those obtained for the full compound (Drewes at al. 1988). The three separate investigations by INS for $ErPd_3$ all give CF parameters with $x = -0.8$ and $W = 0.10$ K and a Γ_6 ground state. These corroborate in a complete way the magnetization and specific heat data for this compound as presented by Drewes et al. (1988). Likewise for $TmPd_3$, the Γ_3 ground state determined by Walter and Holland-Moritz (1981) and Elsenhans et al. (1990a, 1990b) is in reasonable accord with the bulk data. A Γ_7 ground state for $YbPd_3$ is even reported by these authors, who observed well defined CF transitions (fig. 8).

A neutron diffraction study of the magnetic ordering in this series (Elsenhans et al. 1991) reveals the existence of very low ordering temperatures, ferromagnetic, ferrimagnetic and commensurate–incommensurate antiferromagnetic ordering. The ordering temperatures scale very well with the de Gennes factor, with the exception of Er. The CF parameters determined by INS were used by these authors to calculate the temperature dependence of the zero-field magnetization in the MF approximation. With the exceptions of Er and Tm, a good agreement between the two was obtained. In addition to the CF and RKKY interactions, the easy magnetic polarizability of Pd (a Pd magnetic moment observed in $TbPd_3$) and hybridization effects are pointed out as being important in the RPd_3 system. The CF coefficients, as determined for the RPd_3 series, are collected together in table 11.

4.5.4. RIn_3

In this series, all compounds order at low temperatures with the exception of $PrIn_3$ (Lethuiller et al. 1973). The magnetic susceptibilities are reported by Buschow et al. (1969). The magnetic structures for Tb, Dy and Ho, investigated using powder material, showed that the structure is characterized by a $(1/2, 1/2, 0)$ propagation vector (Arnold and Nereson 1969; Nereson and Arnold 1970) whilst the magnetic structures of the series with Nd, Tb, Dy, Ho and Er have been investigated by Galera and Morin (1992), again using neutron powder diffraction. The various energies which act to stabilize multi-axis spin structures in this particular class of compounds were pointed out. The magnetic structure of a single crystal of $NdIn_3$, determined by neutron diffraction (Amara et al. 1994b), is of particular interest in this series, and some effort has been devoted to obtain an understanding of the occurrence of three successive magnetic phase transitions. The CF interaction has been investigated for $NdIn_3$ by INS (Amara et al. 1994b) with LLW CF parameters, $x = 0.45$ and $W = -1.19$ K which corresponds to a $\Gamma_8^{(2)}$ ground state. This gives the ground state quartet separated by about 7 K from the first excited Γ_6 doublet. This level scheme leads to one or two possible changes of spin direction among the possible 4-fold (0 0 1), 2-fold (1 1 0) and 3-fold (1 1 1) axes possible for these cubic systems (Galera and Morin 1992). Magnetization, specific heat and longitudinal magnetoresistance data for $TbIn_3$ is reported

by Czopnik et al. (1990). Extrapolated values of the CF parameters obtained from the INS measurements reported for $NdIn_3$ were used in calculating the magnetic phase diagram. Neutron spectroscopy measurements have also been reported by Groß et al. (1980) for $PrIn_3$, $HoIn_3$ and $ErIn_3$. The nonmagnetic ground Γ_1 state is confirmed for Pr whilst for Ho the determined ground state is assigned to the $\Gamma_5^{(1)}$ representation. The LLW CF parameters are similar to those obtained by Lethuillier et al. (1977). For Er, only a quasielastic component with a linewidth of 0.39 meV was observed and no definitive CF parameters could be quoted for this compound. The large magneto-crystalline anisotropy with several totally equivalent directions in the cubic structure, which has its origins in the CF interaction, antiferromagnetic interactions and a non-negligible antiferroquadrupolar coupling all contribute to stabilize the magnetic structure (Gignoux and Schmitt 1995).

4.5.5. RTl_3

In the RTl_3 system, Groß et al. (1980) have reported on CF parameters determined by INS. The full compounds with Pr, Er and Ho as well as the dilute compounds $La_{0.83}Pr_{0.17}Tl_3$, $La_{0.5}Pr_{0.5}Tl_3$ and $Pr(In_{0.5}Tl_{0.5})_3$ were studied. The Γ_1 nonmagnetic ground state is observed for $PrTl_3$ whilst for Er, the $\Gamma_8^{(3)}$ quartet is assigned to the ground state. In circumstances similar to those observed for $ErIn_3$, for $HoTl_3$ only a quasi-elastic linewidth of 0.8 meV was observed and no definitive CF parameters could be quoted for this compound. For the La substituted $PrTl_3$ compounds, CF transitions similar to those observed in the pure compound were observed. Only a rather broad group of transitions at 5.0 meV were observed for $Pr(In_{0.5}Tl_{0.5})_3$ and no CF assignment was possible.

4.5.6. RX_3 ($X = Al$, Ga)

An INS study of $TmAl_3$ is reported by Davis et al. (1974). This compound presents a nonmagnetic CF ground state and the available susceptibility (de Wijn et al. 1970), magnetization and specific heat data (Deutz et al. 1989) can all be satisfactorily fitted with three sets of CF parameters but none of these can be reconciled with a totally different set obtained from the INS data. The total CF splitting is similar for all sets of parameters. Only one INS study for the corresponding Ga compounds of the series has been reported, that of $TmGa_3$ (Morin et al. 1987). In this case, antiferromagnetic and antiferroquadrupolar orderings are certainly present (Gignoux and Schmitt 1995, 1997). In circumstances similar to those found in the case of $TmAl_3$, the CF parameters derived from neutron spectroscopy cannot consistently explain the specific heat data of Deutz et al. (1989). It must however be remarked that two different values of the antiferromagnetic ordering temperature for $TmGa_3$ are reported (3.3 K, Deutz et al. (1989) and 4.3 K, Morin et al. (1987)).

The INS technique has provided a reasonably consistent view of the contribution of the CF interaction to the overall magnetic properties for the RX_3 series. However, as can be expected, calculations based on the PCM (point charge model) do not predict in any consistent manner the magnitudes and signs of the crystal field parameters in this particular series of rare-earth intermetallics. Lethuillier et al. (1977) pointed out the positive exchange contributions from the d-like and f-like conduction electrons to the fourth order parameter. Band calculations are still needed in order to characterize the size of the Coulomb and exchange contributions to the cubic CF field. The CF coefficients for the series, as determined by INS, are tabulated in table 11.

4.6. RMg_3

RMg_3 compounds crystallize in the cubic Fe_3Al structure (Iandelli and Palenzona 1979). Interatomic R–R distances are larger than in corresponding compounds which crystallize in the Cu_3Au structure, with resulting smaller magnetic interactions. The magnetic properties were first investigated by Buschow (1976), and low ordering temperatures were reported. The CF interaction in $PrMg_3$ and $NdMg_3$, as characterized by the INS technique, has been investigated by Galera et al. (1981, 1985). The CF ground states are Γ_3 for Pr and a Γ_6 doublet for Nd. These authors also reported electrical resistivity and susceptibility data for the two compounds which are adequately reproduced from the CF parameters deduced from the INS investigation. The CF coefficients, as determined by INS, are also tabulated in table 11.

4.7. RPd_2X (X = Sn, In)

Rare-earth intermetallics which crystallize in the cubic Heusler structure, Cu_2MnAl type, display a co-existence of antiferromagnetic order and superconductivity. Low ordering temperatures indicate that the CF interaction would play a fundamental role at low temperatures. Various INS measurements have been carried out to determine the effects of the CF interaction on the low temperature magnetic properties. The compound $ErPd_2Sn$ was studied by Stanley et al. (1987) who identified two distinct CF levels at 7.4 and 11 meV. They also observed an antiferromagnetic transition at approximately 1.0 K, just below the superconducting transition. More detailed INS measurements on $ErPd_2Sn$ as well as $HoPd_2Sn$ (Li et al. 1988, 1989), allowed the CF parameters to be determined. For $ErPd_2Sn$, LLW values of $x = 0.302$ and $W = -0.045$ meV were those which gave best agreement with the observed transition levels and intensities. This corresponds to a magnetic $\Gamma_8^{(3)}$ quartet ground state, in agreement with neutron diffraction data for the magnitude of the Er moment reported by the same authors. For $HoPd_2Sn$, values of $x = 0.324$ and $W = 0.0287$ meV give the magnetic $\Gamma_5^{(1)}$ triplet as the ground state (fig. 9), which ties in nicely with the observed moment of $5.49\,\mu_B$ obtained by neutron diffraction (Li et al. 1989). Extrapolated values for other members of the series were scaled up from the values determined for $HoPd_2Sn$. The predicted ground states indicated that compounds with Dy and Yb would also have magnetic CF ground states, in agreement with bulk data (Kierstead et al. 1985; Malik et al. 1985).

Some attention has also been focused on Heusler alloys of the type RPd_2In, where replacement of Sn by In increases the number of conduction electrons by one. In an INS investigation of $HoPd_2In$, LLW parameters, $x = 0.3543$ and $W = 0.0267$ were obtained. Scaling of these values to the compound $YbPd_2In$ yielded good agreement with the observed INS spectra (Babateen et al. 1995a). Employing these values in a standard MFA calculation, sufficient agreement was obtained with the experimental magnetization curves. In this study, the compound $YbPd_2Sn$ was also investigated. A transition at a lower energy was observed, a sign that the W parameter is slightly reduced and x remains invariant. The scaling behaviour of the CF parameters in passing from Sn to In, as discussed by Babateen et al. (1995b), is taken into account by a phenomenological argument based on a variant of the simple charge model. The R atom in this structure is surrounded by the eight first nearest neighbor Pd atoms which give rise to the overall CF splitting of the R ion. The In

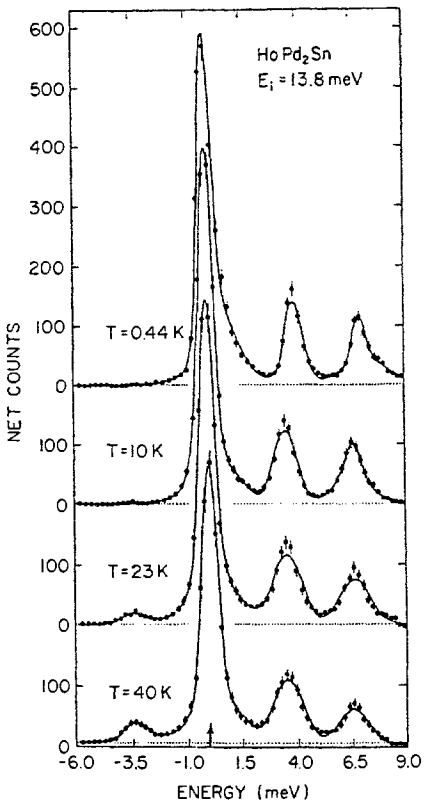

Fig. 9. Temperature dependence of elastic and inelastic CF excitations observed for polycrystalline cubic $HoPd_2Sn$. The data at $T = 23$ and 40 K clearly demonstrate the CF transitions from high energy to low energy levels. These are evident at 40 K for neutron energy gain ($E < 0$) (from Li et al. 1989).

and Sn atoms are located at the centre of a cube containing Pd atoms. This cube is adjacent to the one containing the R ion. Substitution of In by Sn increases the number of conduction electrons and these participate in screening of the Pd charge, resulting in a net charge reduction. Crystal field coefficients, as determined by INS, are collected in table 12.

4.8. $RInAg_2$

Compounds of the type $RInAg_2$ also crystallize in the Heusler structure. The magnetic and electrical properties have been investigated by Galera et al. (1984). They all order antiferromagnetically at low cryogenic temperatures and the heavy rare-earth series obey the de Gennes scaling law. The CF interaction for the light rare-earth series with Ce, Pr and Nd was also investigated by the same authors using INS techniques. The CF parameters and CF ground states for compounds with R = Ce, Pr and Nd are tabulated in table 12. The fit of the high temperature susceptibility is in good agreement with CF parameters obtained from the INS investigation. A negligible 4th order parameter is obtained for Pr

TABLE 12

Crystal field coefficients for cubic RPd_2X, RAg_2In (Cu_2MnAl-type structure) and $RXCu_4$ ($AuBe_5$-type structure) intermetallics determined by INS experiments. Units for A_n^m are in $K r_0^{-n}$.

Compound	x	W (K)	A_4^0	A_6^0	Ground state	Ref.
$HoPd_2Sn$	0.325	0.333	−39.29	−2.33	$\Gamma_5^{(1)}$	[1,2]
$ErPd_2Sn$	0.302	−0.522	−46.58	−1.14	$\Gamma_8^{(3)}$	[1,2,3]
$HoPd_2In$	0.354	0.310	−39.84	−2.07	$\Gamma_5^{(1)}$	[4]
$YbPd_2Sn$	−0.790	−2.430	−16.95	−0.69	Γ_7	[4]
$YbPd_2In$	−0.748	−6.03	−39.82	−2.07	Γ_7	[4]
$PrAg_2In$	0	−1.20	0	−0.84	Γ_3	[5]
$NdAg_2In$	0	1.20	0	−0.84	Γ_6	[5]
$ErAuCu_4$	0.731	0.101	21.79	0.19	$\Gamma_8^{(1)}$	[6]
$ErPdCu_4$			Not resolved			[6]
$ErAgCu_4$			Not resolved			[6]
$YbAuCu_4$	−0.945	−2.611	21.79	0.02	Γ_7	[6]
$YbPdCu_4$			Not resolved			
$YbAgCu_4$	−0.945	−6.266	52.29	0.04	Γ_7	[6]

References:

[1] Li et al. (1989)
[2] Stanley et al. (1987)
[3] Li et al. (1988)
[4] Babateen et al. (1995a, 1995b)
[5] Galera et al. (1984)
[6] Severing et al. (1990)

and Nd compounds, whilst for $CeInAg_2$, the 4th order parameter dominates. The reasons for this behaviour are not clear but in contrast to most Ce intermetallics, $CeInAg_2$ does not appear to display a distinctive Kondo or intermediate valence behaviour.

4.9. $RXCu_4$ ($X = Au, Pd, Ag$)

Intermetallics of the $RXCu_4$ series crystallize in the cubic $AuBe_5$ structure. Compounds with Yb display a heavy fermion behaviour (Rossel et al. 1987) and in order to determine crystal field effects on the magnetic properties, two relevant series were investigated by the INS technique, $ErXCu_4$ and $YbXCu_4$, with X = Au, Pd and Ag (Severing et al. 1990). The stable 4f compound with Er was chosen as a reference point since it is close to Yb in the periodic table. For $ErAuCu_4$, the ground state is the $\Gamma_8^{(1)}$ quartet, whilst no CF determination for the corresponding Ag and Pd compounds was possible (table 12). In similar fashion, the magnetic response for $YbAuCu_4$ was interpreted in the framework of a CF model, with the Γ_7 doublet as the ground state, whilst the magnetic response for Ag and Pd consisted of a broad inelastic line superimposed on a similarly broad quasi-elastic response. The integrated magnetic response function (which is proportional to the bulk susceptibility) for $YbAgCu_4$ is in good agreement with bulk susceptibility data. For the Pd compound, this was interpreted as possibly arising from the presence of impurity phases. An interpretation of the INS data for $YbAgCu_4$, in terms of the Anderson impurity model, is reported by Polatsek and Bonville (1992). A hybridization of the 4f Yb electron states with band electrons, in conjunction with a non-vanishing CF interaction, formed the basis

TABLE 13
Crystal field coefficients determined by INS for Chevrel phase RMo_6Se_8 intermetallics. Units for A_m^n are in $K r_0^{-n}$.

Compound	x	W (K)	A_4^0	A_6^0	Ground state	Ref.
$TbMo_6Se_8$	0.42	1.28	44.2	−12.7	$\Gamma_5^{(1)}$	[1,2]
$ErMo_6Se_8$	0.41	−0.24	29.4	−1.04	$\Gamma_8^{(3)}$	[1,2]
$HoMo_6Se_8$	Unique values could not be determined				Γ_5	[1,2]

References:

[1] Lynn and Shelton (1979)
[2] Lynn and Shelton (1980)

of this model calculation. The CF parameters employed in the calculation were similar to those determined by INS for the compound $YbAuCu_4$. The model gave good a rather good agreement with the observed neutron spectra, as well as the bulk susceptibility.

4.10. RMo_6X_8 (X = Se, S)

Ternary Chevrel-phase intermetallics RMo_6X_8 display a co-existence between superconducting and magnetic order, and the relevant structural and magnetic properties have been reviewed by Fischer (1990). The crystal structure is of the rhombohedral Chevrel phase (Chevrel et al. 1971; Marezio et al. 1973) and magnetic transition temperatures are typically less than 1 K (Fischer 1978). Since the R ions occupy a simple primitive lattice, with rhombohedral angles close to 90°, and an eight-fold cubic co-ordination, the CF point symmetry is approximately cubic. Inelastic neutron scattering investigations of the CF interaction have been reported for $Tb_{1.2}Mo_6Se_8$, $HoMo_6Se_8$, $ErMo_6Se_8$ and $HoMo_6S_8$ (Lynn and Shelton 1979, 1980). Overall CF splittings are observed to be about 25 K for the selenides, but for $HoMo_6S_8$, no sharp CF transitions were observed, but the free ion moment is induced with a field of 20 kOe (Lynn et al. 1978a). The CF coefficients, as determined by these INS studies, are collected together in table 13. Magnetic CF ground states are observed for the selenide compounds, with a reduced moment. The INS data is in good accord with specific heat (McCallum et al. 1977), susceptibility (Johnston and Shelton 1977) and neutron diffraction data (Lynn et al. 1978b).

4.11. RX_2 (X = Al, Ni, Fe, Co)

There is a massive abundance of INS measurements on rare-earth intermetallics which crystallize in the cubic Laves phase $MgCu_2$ structure. The CF experienced by the R ion is generated by the presence of 12 first nearest neighbor T atoms, located at a distance of $\sqrt{11}a/8$, where a is the cubic lattice parameter. This lattice parameter is found to decrease practically in linear fashion with an increasing number of 4f electrons for the series. The availability of large single crystals, most particularly for the series RAl_2, makes them immensely attractive model systems for investigating CF, exchange and quadrupolar interactions. The magnetic interactions are dominated by the R ion in systems of the type RAl_2

and RNi_2, whilst in compounds with Fe and Co, the strong exchange coupling between 3d electrons also influences in a marked way the overall magnetic properties. Inelastic neutron scattering has made an immense contribution to the understanding of the CF interaction in this particular series of intermetallics.

4.11.1. RAl_2

The magnetic excitations in RAl_2 compounds have been determined for almost the whole series. These range from measurements on compounds diluted with non-magnetic Lu, Y and Sc to those of the full compound. In the first case, CF interactions can be determined rather accurately, whilst in the latter case, propagating magnetic excitations in the ordered magnetic phase are characterized. Comprehensive reviews of the magnetic properties of RAl_2 intermetallic compounds are reported by Purwins and Leson (1990) and Gignoux and Schmitt (1997).

The CF parameters, as studied by INS, in dilute $Pr_{0.05}Y_{0.95}Al_2$, are reported by Walter and Holland-Moritz (1981). Inelastic neutron scattering measurements on polycrystalline $PrAl_2$ are reported by Happel et al. (1977), Henning et al. (1977) and Frauenheim et al. (1979) and similar LLW parameters were obtained. Investigations of compounds with smaller concentrations of Pr in $Pr_cX_{1-c}Al_2$ with X = La and Sc are reported by Frick and Loewenhaupt (1986a). The LLW parameters are found to progressively increase in passing from Sc to Y thru to La. These all give the Γ_3 doublet as the CF ground state. The magnetic excitation spectrum for a single crystal of $PrAl_2$ has also been investigated (Purwins et al. 1976a, 1976b; Holden et al. 1977). The CF and exchange parameters extracted from these studies are compatible with those obtained from bulk measurements. Other interactions besides CF and exchange appear to be present in this system. Magneto-elastic couplings are observed to be significant in $PrAl_2$ (Godet and Purwins 1976; Abell et al. 1983). Aksenov et al. (1981) have calculated the magneto-vibrational excitation spectrum for $PrAl_2$ and obtained an apparently reasonable fit with experimentally determined INS spectra.

Magnetic excitations for a single crystal of $NdAl_2$ are reported by Houmann et al. (1974) and Furrer and Purwins (1977a, 1977b) whilst Walter and Holland-Moritz (1981), Barbara et al. (1982) and Frick and Loewenhaupt (1986a) obtained CF parameters from INS studies on dilute $Nd_cSc_{1-c}Al_2$, $Nd_cY_{1-c}Al_2$ and $Nd_cLa_{1-c}Al_2$ compounds, respectively. The Γ_6 magnetic doublet is determined as the ground state. In all cases, the signs and magnitudes of the LLW CF parameters are fairly consistent with heat capacity (Deenadas et al. 1971), magnetization (Eyers et al. 1982) and NMR measurements (Berthier and Belorizky 1984). The interatomic exchange interaction is found to qualitatively agree with a prediction based on the RKKY mechanism. A fit of the ground state wavefunction to the magnetic form factor, as obtained from single crystal polarized neutron scattering investigations (Boucherle and Schweizer 1981), agrees with the INS determinations. The influence of the observed magneto-elastic interactions (Abell et al. 1979; Pourarian et al. 1981) on the magnon dispersion was found to be negligible (Purwins and Leson 1990).

The high neutron absorption cross section for natural Sm precludes the compound $SmAl_2$ from a detailed INS study as does the small magnetic moment. Magnetic form factor measurements, however exist, and CF parameters were obtained (Boucherle et al. 1979). The agreement with single crystal magnetization (Leson et al. 1986) and NMR

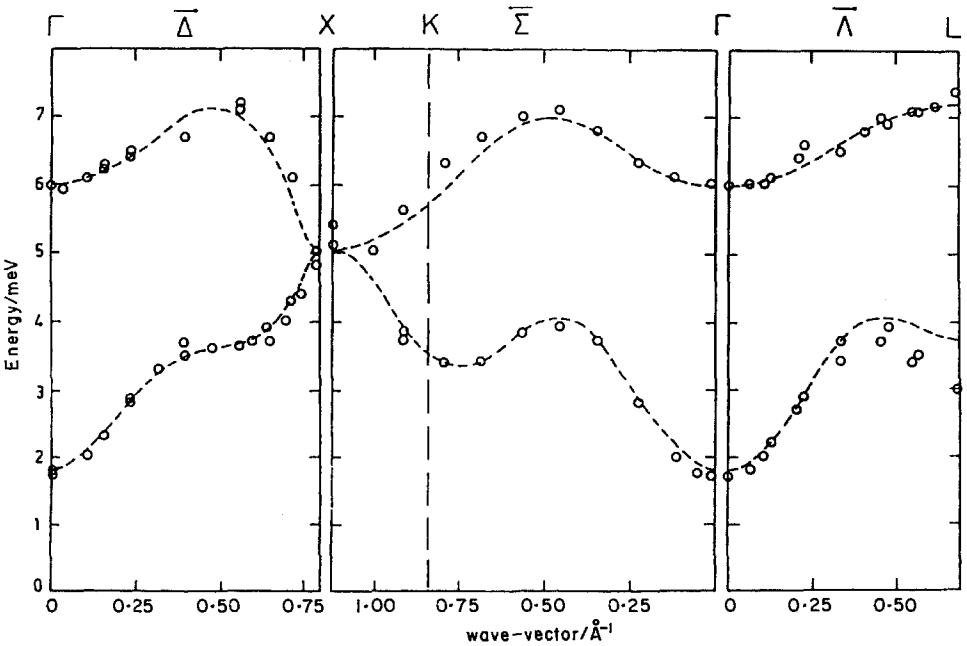

Fig. 10. Dispersion curves for a single crystal of cubic $TbAl_2$ measured at 4.2 K along the three high symmetry directions. Dashed lines are fits to a CF–isotropic exchange model (from Bührer et al. 1973).

(Buschow et al. 1973) measurements is only qualitative. Inelastic neutron scattering studies using compounds of $Sm_cY_{1-c}Al_2$ diluted with non-absorbing Sm isotopes have failed to determine the CF level scheme (Holland-Moritz 1985, unpublished).

The compound $TbAl_2$ has a higher ordering temperature than the corresponding $PrAl_2$ and $NdAl_2$ compounds, and thus it can be expected that the exchange interaction is large in comparison with the overall CF splitting. The CF interaction, as determined by INS investigations, is well documented. Due to the large exchange, it is necessary to study dilute systems. Such investigations are reported by Loewenhaupt and Hoenig (1978), Hoenig and Loewenhaupt (1979a, 1979b), Loewenhaupt (1980), Feile et al. (1981), Walter and Holland-Moritz (1981), Barbara et al. (1982) and later by Frick and Loewenhaupt (1985a). The Γ_1 singlet is the ground state and the LLW parameters display an increase in x when passing from Sc to La substitution. These are in good agreement with the published magnetization curves. The specific heat data of Schelp et al. (1986) can be fitted with CF parameters which are not too far distant from the INS interpretation. Single crystal INS measurements have also been reported (Bührer et al. 1973; Purwins et al. 1973, 1974). Due to the large exchange energy, the CF interaction gives rise to an energy gap for acoustic magnons at the Brillouin zone centre (fig. 10). The theoretically calculated value for this anisotropy energy gap is in good agreement with the neutron data. As in the case of $NdAl_2$, the interatomic Tb–Tb exchange parameters were obtained from the single crystal INS data. Interactions up to sixth nearest neighbors could be fitted and these have the

characteristic long-range, oscillatory nature of the RKKY interaction. The magneto-elastic coupling is small and modeling of the observed magnetostriction gives CF parameters which are totally compatible with INS data (del Moral et al. 1986). The anisotropy in the paramagnetic phase for a single crystal of $TbAl_2$ as well as for $DyAl_2$ and $ErAl_2$, has been measured and modeled by del Moral et al. (1987), using CF parameters determined by INS. These authors also investigated the strength of quadrupolar couplings in these systems, via the higher rank susceptibility tensor components.

Parameters for the CF interaction have been obtained in a series of INS studies on dilute $DyAl_2$ non-magnetic compounds (Walter and Holland-Moritz 1981; Barbara et al. 1982; Frick and Loewenhaupt 1986a). A large variation in the x and W parameters is observed in the series with Sc, Y and La substitutions. Nevertheless, the investigations performed on the dilute compounds all attribute the ground state to the $\Gamma_8^{(3)}$ doublet, which is in marked disagreement with ESR measurements (Levin et al. 1979) which report a Γ_7 doublet ground state. The specific heat data (Schelp et al. 1986) can be comfortably reproduced with the CF parameters obtained from the INS measurements as can the single crystal magnetization curves. The magnetic excitation spectrum for a single crystal of $DyAl_2$ is reported by Holden et al. (1984), but interpretation in terms of a simple CF and exchange model was marred by a strong magnon–phonon coupling. Similarly to $TbAl_2$, the principal effect of the CF interaction was to create an energy gap in the zone centre acoustic magnon branch.

A magnetic phase transition in which Ho moments rotate from the $\langle 1\,1\,0\rangle$ easy direction at low temperature to a $\langle 1\,0\,0\rangle$ easy direction has been of principal interest in $HoAl_2$. Heat capacity (Schelp et al. 1983), magnetization (Barbara et al. 1975), torque (Williams et al. 1979), magneto-elastic (Ibarra et al. 1988) measurements have been devoted to obtain an understanding of the low temperature part of the magnetic phase diagram for this system. A key to the understanding of the influence of the CF interaction on these properties has been played by the INS technique. Again, dilute compounds of $Ho_cX_{1-c}La_2$, X = Y (Walter and Holland-Moritz 1981), La (Barbara et al. 1982) and Sc (Frick and Loewenhaupt 1985a, 1985b, 1986a, 1986b) were investigated. In this case, a level crossing of the ground state from the Γ_1 singlet for compounds diluted with La to the $\Gamma_5^{(1)}$ triplet for Y and Sc dilution appears to occur. The magnetic excitations in single crystal $HoAl_2$ have been investigated in zero magnetic field (Rhyne and Koon 1982; Schelp et al. 1984) along the three principal symmetry directions at 4.2 K. A standard RPA pseudo-boson analysis was applied to the magnetic modes. The CF parameters are consistent with those reported in the investigations of the diluted compounds by INS. An oscillatory RKKY type variation of the exchange interaction was observed. The dispersion of the low magnon branch has also been investigated in an applied magnetic field (Schelp et al. 1985). The magnetic field shifts the mode energies up by about 1 meV and this field dependence of the excitations can be well accounted for in a model CF and exchange calculation. The CF parameters derived from the INS studies on $HoAl_2$ appear to be quite reliable. They are able to consistently reproduce magnetization (Schelp et al. 1983), specific heat (Schelp et al. 1984) and neutron diffraction data (Millhouse et al. 1972). The anomalous thermal expansion and magnetostriction observed at the spin re-orientation transition (Ibarra et al. 1988) are satisfactorily modeled using CF parameters obtained from INS investigations. Measurements of the magnetic form factor (Boucherle and Schweizer 1982) have also been utilized to determine the ground state. These, however, imply larger CF values than those deduced from

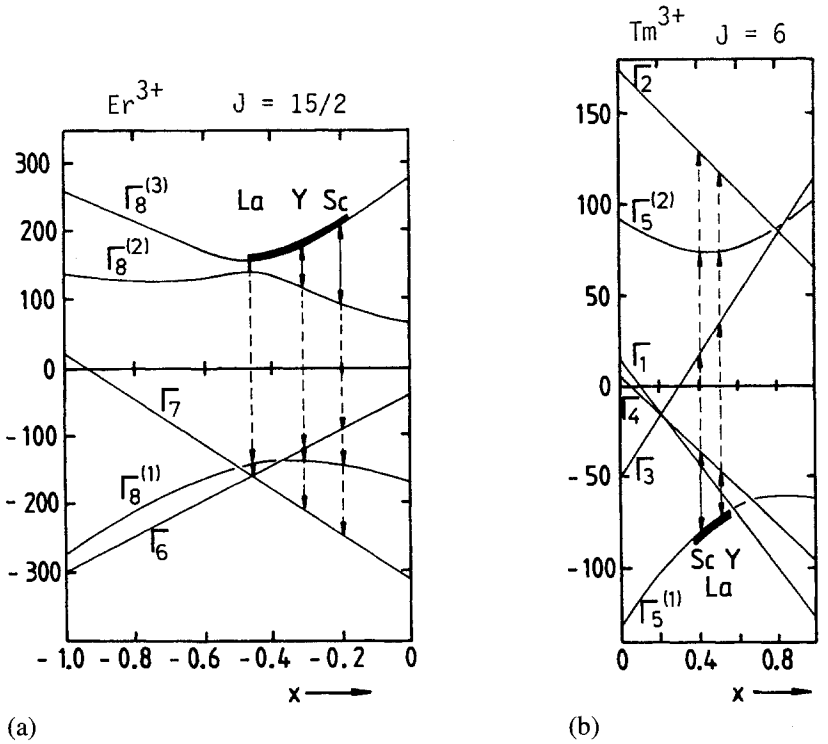

Fig. 11. LLW diagrams and CF level schemes determined for dilute cubic (Er, X)Al_2 and (Tm, X)Al_2 intermetallics, X = La, Y, Sc. The ground state is marked by a solid line. Arrows indicate CF transitions observed by INS (from Frick and Loewenhaupt 1986a).

INS work. Boucherle et al. (1982) suggested the importance of higher order quadrupolar pair interactions. The polarized neutron diffraction study appears to overestimate the conduction electron contribution to the total moment. Indeed, NMR measurements for $HoAl_2$ (Prakash et al. 1984) give a value for the conduction electron contribution which is three times less than that obtained from the neutron study. These NMR results also give a CF ground state which is in better agreement with INS determinations.

Determinations of the CF parameters for $ErAl_2$ by INS are also abundant. Heer et al. (1974) investigated the diluted compound $Er_cY_{1-c}Al_2$ with $c = 0.15$. Measurements on even more dilute systems with Y and La were subsequently performed by Knorr et al. (1978a), Blanckenhagen et al. (1978), Loewenhaupt et al. (1980), Walter and Holland-Moritz (1981), Barbara et al. (1982), Frick and Loewenhaupt (1986a, 1986b). A summary of the various INS determinations for Y diluted compounds suggests that the best set of LLW parameters is $x = -0.30$ and $W = -0.025$ K (Loewenhaupt et al. 1983). These give the $\Gamma_8^{(3)}$ quartet as the ground state. The same ground state is observed for compounds diluted with Sc and La with, however, a variation of the CF parameters when passing from Y to Sc, La (fig. 11). A single crystal study of the dispersion of magnetic excitations in $ErAl_2$ (Stanley et al. 1985) shows only a weak dispersion of the excitations. Thus it was

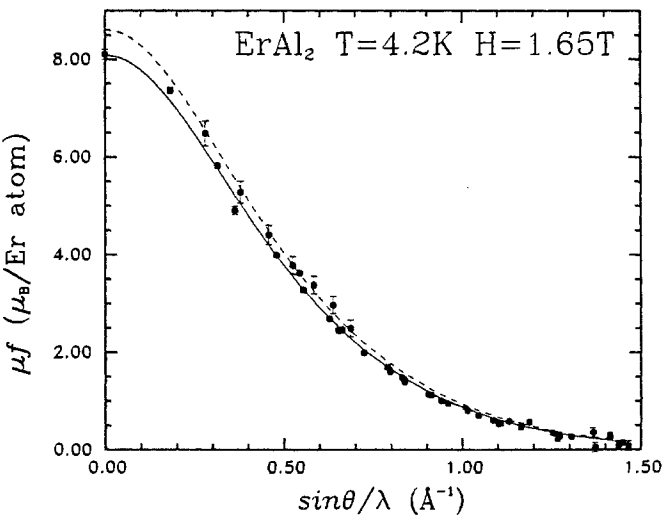

Fig. 12. Observed (dark circles) and calculated magnetic form factor for cubic $ErAl_2$ (dashed line: calculation with $\theta_p = 15.8$ K; continuous line: calculation with $\theta_p = 7.9$ K) (from Boucherle et al. 1989).

not possible to determine with a sufficient precision the distance dependence of the exchange interactions. The CF parameters determined from this study are in close agreement with INS measurements on polycrystalline material as well as single crystal magnetization measurements. Electron spin resonance measurements report a large variation in the CF parameters (Döbler et al. 1983). Specific heat measurements on a single crystal (Schelp et al. 1986) are in better agreement with INS studies than those reported for polycrystalline $ErAl_2$ (Inoue et al. 1977). Magnetic form factor measurements for $ErAl_2$ (Boucherle et al. 1989) give a good confirmation of the CF parameters but a different molecular field value is obtained, if compared with magnetization data (fig. 12).

Amongst the series, $TmAl_2$ presents unusual magnetic behaviour. The ferromagnetic ordering temperature is rather low, at 4.2 K (Horn et al. 1979). Below the Curie point, the neutron and specific heat data on polycrystalline $TmAl_2$ indicate a second phase transition which is, however, not observed in a single crystal of $TmAl_2$ (Chattopadhyay et al. 1995). Inelastic neutron scattering studies reported for $Tm_cLa_{1-c}Al_2$ (Walter and Holland-Moritz 1981; Feile et al. 1983; Frick et al. 1985) give a Γ_1 non-magnetic singlet ground state whilst INS work on diluted Sc and Y compounds report instead a $\Gamma_5^{(1)}$ triplet ground state (Walter and Holland-Moritz 1981; Frick and Loewenhaupt 1986a, 1986b). The reported variation of the CF ground state Sc, Y and Lu compounds is displayed in fig. 11. The general set of CF parameters, $x = 0.50$ and $W = 0.44$ K (Purwins and Leson 1990) can consistently describe the specific heat (Heininger et al. 1974; Schelp et al. 1986), elastic constant (Lingner and Lüthi 1983) and Mössbauer data (Gubbens et al. 1982). The magnetic excitations in this system are almost dispersionless (Chattopadhyay et al. 1995). An observed excitation of about 5.7 meV can be attributed to CF excitations, most likely from a $\Gamma_5^{(1)}$ ground state to successive Γ_3, $\Gamma_5^{(2)}$ states (Wentworth and Deutz 1989). The last

two are separated by about only 0.5 meV, and are difficult to resolve. The weak dispersion is of course reflected in the low ordering temperature.

The CF parameters for the series RAl_2 determined by INS measurements are summarized in table 14. It is clear that a rather consistent set of parameters that are applicable for the series have been obtained. Particularly relevant have been the measurements of the CF parameters in RAl_2 compounds diluted with Y, Sc and La. The magnitudes of the reduced CF parameters $A_4^0 a^{-5}$ and $A_6^0 a^{-7}$ have the same sign and order of magnitude. The influence of conduction electrons is clearly reflected in the unrealistic values of the effective R and Al charges calculated on the basis of a PC model (Purwins and Leson 1990).

4.11.2. RNi_2

The bulk magnetic properties of these intermetallics, which also crystallize in the cubic $MgCu_2$ Laves phase, have been summarized by Buschow (1977), Franse and Radwanski (1993) and Gignoux and Schmitt (1997). They order ferromagnetically at low temperatures. There is no evidence that Ni is magnetically polarized in these systems and therefore the exchange interaction between R ions occurs via the RKKY interaction. The low temperature magnetic properties are dominated by the CF interaction. This interaction has been investigated in the series with R = Pr, Nd, Tb, Er, Ho and Tm by the INS technique (Goremychkin et al. 1989). A particular emphasis has been placed on compounds with Pr for which additional INS data exist for PrX_2 with X = Pt, Rh, Ir, Ru (Greidanus et al. 1982, 1983a) and for $PrMg_2$ (Loidl et al. 1981). Compounds of $PrNi_2$ diluted with La and Y are reported by Mühle et al. (1989). Other INS measurements for $PrNi_2$ are reported by Andreeff et al. (1982), Matz et al. (1982) and Aksenov et al. (1983). The magnetic excitations, as determined by the INS technique, in single crystal material have been investigated only for the compound $HoNi_2$ (Castets et al. 1982b). The parameters of the CF interaction determined by INS measurements for the series are displayed in table 15.

The compound $PrNi_2$ is regarded as an exchange enhanced Van Vleck paramagnet and displays strong magneto-elastic interactions (Ibarra et al. 1984a, 1984b; del Moral and Ibarra 1985). Evidence to support this hypothesis is found in the strong coupling of the $\Gamma_1 \rightarrow \Gamma_5$ CF excitation to a low energy phonon excitation (Mühle et al. 1989). Measurements in the paramagnetic state for the series PrX_2 with X = (Pt, Rh, Ir and Ru) yield values of the CF parameters which contain a level-crossing point of the LLW diagram, where the ground state can pass from either a non-magnetic Γ_1 singlet or the non-magnetic Γ_3 doublet (Greidanus et al. 1983a). The CF parameters determined by INS for this series give a satisfactory agreement, after a mean field calculation, of the specific heat, magnetization, neutron diffraction (Greidanus et al. 1983b) and resistivity and AC susceptibility data (Greidanus et al. 1983c). There still remain problems with the true ground state. Later specific heat and susceptibility studies for $PrNi_2$ indicate either the Γ_1 (Javorsky et al. 1994) or the Γ_3 ground state (Melero et al. 1995). The situation appears clearer if one takes into account the INS studies on Y and L diluted $PrNi_2$ (Mühle et al. 1989). In both compounds, the Γ_3 doublet is determined as the ground state. This result has also been obtained by Andreeff et al. (1982) and Aksenov et al. (1983) in previous INS studies of $PrNi_2$.

For $NdNi_2$, ESR measurements give a g-factor which would indicate a Γ_6 ground state (Donosco et al. 1981). The INS results of Goremychkin et al. (1989) confirm this doublet

TABLE 14

Crystal field coefficients for RAl_2 intermetallics (cubic $MgCu_2$ structure) determined by INS experiments. Crystal field coefficients are in units of $K r_0^{-n}$.

Compound	x	W (K)	A_4^0	A_6^0	Ground state	Ref.
$PrAl_2$	0.70	−4.19	19.53	−0.873	Γ_3	[1]
$PrAl_2$	0.77	−2.92	15.99	−0.548	Γ_3	[2]
$PrAl_2$	−0.58	5.36	20.72	−1.565	Γ_3	[3]
$PrAl_2$	0.75	−3.52	17.60	−0.611	Γ_3	[4]
$Pr_{0.05}Y_{0.95}Al_2$	0.73	−3.62	17.62	−0.775	Γ_3	[5]
$Pr_{0.02}Sc_{0.98}Al_2$	0.59	−3.00	11.82	−0.833	Γ_3	[6,7]
$Pr_{0.02}La_{0.98}Al_2$	0.85	−5.70	32.39	−0.588	Γ_1	[6,7]
$Pr_{0.01}La_{0.99}Al_2$	0.85	−2.40	16.19	−0.293	Γ_1	[7,8]
$NdAl_2$	−0.37	1.78	13.17	−0.778	Γ_6	[9]
$NdAl_2$	−0.37	1.78	13.17	−0.778	Γ_6	[10]
$NdAl_2$	−0.37	1.78	13.17	−0.778	Γ_6	[11]
$Nd_{0.05}Y_{0.95}Al_2$	−0.40	2.29	15.84	−0.918	Γ_6	[5]
$Nd_{0.02}Sc_{0.98}Al_2$	−0.28	2.27	12.51	−1.118	Γ_6	[6]
$Nd_{0.10}La_{0.90}Al_2$	−0.58	1.76	20.09	−0.512	Γ_6	[12]
$SmAl_2$*			44.4 ± 14.8			[13]
$TbAl_2$	0.90	0.223	16.55	−0.383	Γ_1	[14]
$TbAl_2$	0.90	0.223	16.55	−0.383	Γ_1	[15]
$Tb_{0.02}La_{0.98}Al_2$	0.75	0.524	32.41	2.253	Γ_1	[16]
$Tb_{0.04}Y_{0.96}Al_2$	0.82	0.26	17.44	−0.798	Γ_1	[5]
$Tb_{0.03}Y_{0.97}La_2$	0.90	0.30	22.27	−0.52	Γ_1	[6,7,8]
$Tb_{0.10}Y_{0.90}La_2$	0.95	0.30	25.07	−0.28	Γ_1	[12]
$Tb_{0.003}Y_{0.997}La_2$	0.90	0.30	22.27	−0.52	Γ_1	[17,18]
$Tb_{0.01}Sc_{0.99}La_2$	0.58	0.22	10.52	−1.58	Γ_1	[6,7,8]
$DyAl_2$	0.49	−0.11	10.17	−0.65	$\Gamma_8^{(3)}$	[19]
$Dy_{0.05}Y_{0.95}La_2$	0.43	−0.16	12.70	−1.06	$\Gamma_8^{(3)}$	[5]
$Dy_{0.10}Y_{0.90}La_2$	0.68	−0.11	17.58	−0.41	$\Gamma_8^{(3)}$	[6,7,12]
$Dy_{0.02}Y_{0.98}La_2$	0.27	−0.17	8.43	−1.38	$\Gamma_8^{(3)}$	[6,7]
$HoAl_2$	−0.34	0.17	20.62	−1.14	$\Gamma_5^{(1)}$	[20,21]
$HoAl_2$	−0.24	0.21	18.48	−1.67	$\Gamma_5^{(1)}$	[22]
$HoAl_2$	−0.34	0.17	20.62	−1.14	$\Gamma_5^{(1)}$	[23,24]
$Ho_{0.05}Y_{0.95}La_2$	−0.31	0.16	17.67	−1.12	$\Gamma_5^{(1)}$	[5]
$Ho_{0.02}La_{0.98}La_2$	−0.49	0.11	19.23	−0.56	Γ_1	[6,7,8]
$Ho_{0.01}Sc_{0.99}La_2$	−0.18	0.16	10.60	−1.39	$\Gamma_5^{(1)}$	[6,25]
$ErAl_2$	−0.16	−0.33	15.80	−2.04	$\Gamma_8^{(3)}$	[26,27]
$ErAl_2$	−0.30	−0.25	22.16	−1.27	$\Gamma_8^{(3)}$	[28,29,31]
$Er_xY_{1-x}La_2$ $x = 0.02, 0.05, 0.2, 0.4$	−0.30	−0.25	22.16	−1.27	$\Gamma_8^{(3)}$	[8,29]
$Er_{0.003}Y_{0.997}La_2$	−0.31	−0.26	23.68	−1.27	$\Gamma_8^{(3)}$	[6,7]
$Er_{0.05}Y_{0.95}La_2$	−0.30	−0.23	20.74	−1.19	$\Gamma_8^{(3)}$	[5]
$Er_{0.08}Y_{0.92}La_2$	−0.36	−0.52	54.57	−2.38	$\Gamma_8^{(3)}$	[26,30]

TABLE 14 (Continued)

Compound	x	W (K)	A_4^0	A_6^0	Ground state	Ref.
$Er_{0.15}Y_{0.85}La_2$	−0.54	−0.21	33.51	−0.69	$\Gamma_8^{(3)}$	[27]
$Er_{0.90}Y_{0.10}La_2$	−0.58	−0.27	46.28	−0.82	$\Gamma_8^{(3)}$	[32]
$Er_{0.10}Y_{0.90}La_2$	−0.59	−0.26	44.56	−0.77	$\Gamma_8^{(3)}$	[26,28,32]
$Er_{0.003}La_{0.997}La_2$	−0.51	−0.19	28.63	−0.67	$\Gamma_8^{(3)}$	[6]
$Er_{0.003}Sc_{0.997}La_2$	−0.19	−0.25	14.11	−1.43	$\Gamma_8^{(3)}$	[6,7,8,25]
$Tm_xY_{1-x}Al_2$ $x = 1, 0.02, 0.07, 0.15$			Not reported			[33,36]
$Tm_{0.25}Y_{0.75}La_2$	0.50	0.45	24.44	−1.21	$\Gamma_5^{(1)}$	[34]
$Tm_{0.003}La_{0.997}La_2$	0.72	0.44	26.44	−1.35	Γ_1	[35,37]
$Tm_{0.02}Y_{0.98}La_2$	0.52	0.40	19.19	−1.05	$\Gamma_5^{(1)}$	[5]
$Tm_{0.003}Sc_{0.997}La_2$	0.42	0.48	17.54	−1.51	$\Gamma_5^{(1)}$	[7]
$TmAl_2$			Not reported			[38]

* From magnetic form factor measurements.

References:

[1] Purwins et al. (1976a)
[2] Holden et al. (1977)
[3] Henning et al. (1977)
[4] Frauenheim et al. (1979)
[5] Walter and Holland-Moritz (1981)
[6] Frick and Loewenhaupt (1985a)
[7] Frick and Loewenhaupt (1986a)
[8] Frick and Loewenhaupt (1986b)
[9] Houmann et al. (1974)
[10] Furrer and Purwins (1977a)
[11] Furrer and Purwins (1977b)
[12] Barbara et al. (1982)
[13] Boucherle et al. (1979)
[14] Bührer et al. (1973)
[15] Purwins et al. (1974)
[16] Loewenhaupt and Hoenig (1978)
[17] Feile et al. (1981)
[18] Loewenhaupt (1980)
[19] Holden et al. (1984)
[20] Rhyne and Koon (1982)
[21] Rhyne and Koon (1983)
[22] Schelp et al. (1984)
[23] Schelp et al. (1983)
[24] Schelp et al. (1985)
[25] Loewenhaupt et al. (1982)
[26] Blanckenhagen et al. (1978)
[27] Heer et al. (1974)
[28] Knorr et al. (1978a)
[29] Loewenhaupt (1980)
[30] Loewenhaupt et al. (1980)
[31] Stanley et al. (1985)
[32] Barbara et al. (1980)
[33] Horn et al. (1979)
[34] Purwins et al. (1973)
[35] Feile et al. (1983)
[36] Frick and Loewenhaupt (1985b)
[37] Frick et al. (1985)
[38] Chattopadhyay et al. (1995)

ground state, also in agreement with magnetization data (Ibarra et al. 1984a, 1984b). The calculated heat capacity using the INS parameters is in good agreement with heat capacity data (Melero and Burriel 1996). The Γ_6 ground state is also obtained from INS studies performed on $NdMg_2$ (Loidl et al. 1981). This result is in accord with the observed ground state magnetic moment for Nd in $NdMg_2$

The INS studies performed on $TbNi_2$ result in a Γ_1 ground state (Goremychkin et al. 1989). This compound has a Curie point of 33 K. The INS measurements were performed at 10 and 80 K. At the higher temperature, CF transitions can be almost washed out, i.e., significantly broadened, whilst at the lower temperature, well into the ordered phase, single crystal measurements appear desirable. The calculated heat capacity, using the INS parameters, is too low above 40 K, whilst magnetization measurements (Ibarra et al. 1984a, 1984b) are in better agreement with specific heat data for $TbNi_2$ (Melero and Burriel 1996).

TABLE 15

Crystal field coefficients for RX_2 intermetallics (cubic $MgCu_2$ structure) for X = Ni, Rh, Ir, Pt, Ru and Mg determined by INS experiments. Units for A_n^m are in $K\,r_0^{-n}$.

Compound	x	W (K)	A_4^0	A_6^0	Ground state	Ref.
$PrNi_2$	0.62	−2.21	9.11	−0.58	Γ_3	[1]
$PrNi_2$	−0.64	−2.67	11.37	−0.67	Γ_3	[2]
$PrNi_2$	−0.63	−2.70	11.51	−0.63	Γ_3	[3]
$PrNi_2$	0.58	−2.09	8.08	−0.61	Γ_3	[4]
$Pr_{0.05}Y_{0.95}Ni_2$	0.05	−0.81	0.28	−0.53	Γ_3	[5]
$Pr_{0.1}La_{0.9}Ni_2$	0.56	−1.78	6.59	−0.55	Γ_3	[5]
$PrRh_2$	0.93	−4.06	25.17	−0.19	Γ_1	[1]
	0.75	−3.83	19.15	−0.67	Γ_3	[1]
$PrIr_2$	0.86	−6.62	37.90	−0.64	Γ_1, Γ_3, Γ_4	[1]
$PrPt_2$	0.93	−4.40	27.28	−0.19	Γ_1	[1]
$PrRu_2$	0.68	−3.83	17.36	−0.85	Γ_3	[1]
$PrMg_2$	0.67	−4.00	17.89	−0.91	Γ_3	[1,6]
$NdNi_2$	−0.89	3.25	56.89	−0.25	Γ_6	[4]
$NdMg_2$	−0.37	1.89	13.70	−0.81	Γ_6	[6]
$TbNi_2$	−0.73	−0.77	46.11	−3.56	Γ_1	[4]
$HoNi_2$	−0.44	0.24	38.98	−1.42	$\Gamma_5^{(1)}$	[4]
$HoNi_2$	−0.50	0.27	49.00	1.40	$\Gamma_5^{(1)}$	[7]
$ErNi_2$	−0.54	−0.39	53.56	−1.31	$\Gamma_8^{(3)}$	[4]
$TmNi_2$	0.62	0.71	38.29	−1.46	Γ_1	[4]

References:

[1] Greidanus et al. (1983a)
[2] Andreeff et al. (1982)
[3] Aksenov et al. (1983)
[4] Goremychkin et al. (1989)
[5] Mühle et al. (1989)
[6] Loidl et al. (1981)
[7] Castets et al. (1982b)

Two separate INS results are reported for $HoNi_2$. In the first instance, Castets et al. (1982b) reported an investigation of the magnetic excitations propagating in the [0 0 1] direction. The observed excitations cannot be accounted for by using the CF and exchange parameters deduced from magnetization data (Gignoux et al. 1975). In this first neutron study, CF parameters of $x = -0.5$ and $W = 0.27$ K are in better agreement with a second INS investigation reported for polycrystalline $HoNi_2$ (Goremychkin et al. 1989). Both INS studies assign the $\Gamma_5^{(1)}$ triplet to the ground state. The magnetization data (Ibarra et al. 1984a, 1984b) also give the same ground state but with a larger overall CF splitting.

Inelastic neutron studies for $ErNi_2$ are reported by Goremychkin et al. (1989) with the ground state deduced to be the $\Gamma_8^{(3)}$ quartet. This compound orders at 6.5 K. This ground state is also deduced from the specific heat data (Melero et al. 1995) but with a slightly different CF parameter set, as do magnetization measurements (Gignoux and Givord 1983; Ibarra et al. 1984a, 1984b). In their analysis of INS data for the series, Goremychkin et al. (1989) invoked quadrupolar interactions but a more detailed analysis of the magnetic excitations determined by INS studies on single crystals are necessary.

A Γ_1 singlet is the proposed ground state for Tm in $TmNi_2$, as investigated by Goremychkin et al. (1989), in accordance with specific heat data (Deutz et al. 1989). The INS data were plagued by a very broad distribution of the CF excitations as well as the large absorption cross section of the Tm ion. The INS measurements were performed well above the ordering temperature of approximately 14 K. An introduction of a tetragonal distortion and a supposed large quadrupolar ordering (Gubbens et al. 1984; Deutz et al. 1986) did not lead to any significant improvement in the data analysis of the INS spectra.

As can be expected, neither the PCM or the modified PCM (Zolnierek et al. 1984) nor models which include electronic structure effects are able to explain the generally observed behaviour of the CF parameters in this series, i.e., a positive fourth order CF coefficient and a negative sixth order coefficient. Unfortunately, no detailed INS study of diluted compounds, analogous to the very detailed data which exists for the RAl_2 series, has been performed to date. The parameters determined by INS are, however, generally capable of giving a reasonable account of the observed bulk magnetic properties throughout the series.

4.11.3. RX_2 (X = Fe, Co)

In contrast to Ni compounds of the series, the presence of a significant Fe–Fe and Co–Co exchange interaction in these compounds, changes dramatically the interpretation of INS spectra determined for these compounds. The magnetic properties of these intermetallics are reviewed by Kirchmayr and Poldy (1979), Buschow (1977, 1980) and later by Franse and Radwanski (1993). The important magnetostrictive effects observed in the series are summarized by Clark (1980), Koon et al. (1991) and Andreev (1995). A detailed investigation of the magnetic excitation spectrum for these compounds requires preparation of large single crystals. These have been synthesized for both series, principally with R = Er and Ho. In the RFe_2 series, compounds with Pr and Nd have only been synthesized in small quantities in polycrystalline form (Meyer et al. 1981). The magnetic excitations in these compounds have previously been reviewed by Sinha (1978), Koon and Rhyne (1980a, 1980b), Rhyne (1980), Jensen (1982), Stirling and McEwen (1987), Rhyne (1987) and Moon and Nicklow (1991). There are no distinct crystal field transitions, as the level splitting of the R ion is established by the presence of a large Fe or Co exchange field. A schematic diagram of the dispersion of magnetic excitations arising from Fe–Fe, Fe–R and R–R interactions is displayed in fig. 13. The magnetic behaviour in the RFe_2 series is different from RCo_2 compounds in that for the former, the Curie points are of the order of 600 K, whilst for the latter, Curie points are a factor of three or four times smaller (Buschow 1977). Thus for the RFe_2 series, CF effects are an order of magnitude smaller than the corresponding exchange effects. The highly dispersive Fe–Fe spin wave excitations are very similar to those observed for elemental Fe. An INS investigation of the magnetic excitations in UFe_2 has even demonstrated a strong hybridization between 5f and 3d electrons, resulting in an enhancement of the spin wave stiffness constant, even though the Curie point is much lower than in the corresponding RFe_2 intermetallics (Paolasini et al. 1996). Thus, in RFe_2 intermetallics, the R wave functions are thus almost pure J_z states and only spin wave type excitations are expected. There is however, a CF induced reduction of the R moment, as evidenced for example in the polarized neutron diffraction studies of the magnetic form factor in $HoFe_2$, where the Ho moment is shown to be reduced from its free ion value (Collins et al. 1993).

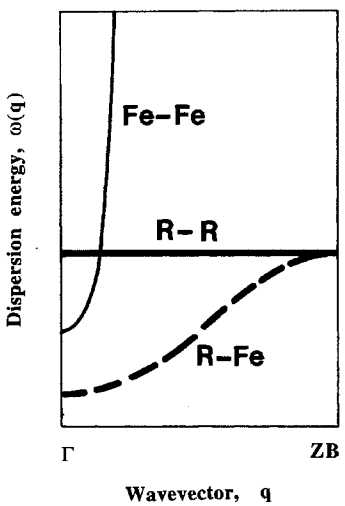

Fig. 13. Schematic diagram displaying the general energy dependence of the dispersion of magnetic excitations in systems governed by predominant Fe–Fe exchange interactions and weaker R–Fe and R–R exchange interactions.

The localized modes which are dominated by the CF interaction, and which crossover with the modes dominated by the Fe exchange interaction, have been investigated by Clausen et al. (1982) for $ErFe_2$. In corresponding RCo_2 compounds, CF effects are extremely important and affect the magnetic excitation spectrum in a more marked manner. The much weaker R–Co exchange allows significant transitions from the ground state to states which are above the first excited state. In fig. 14, the temperature dependence of such modes for $ErCo_2$ is displayed, together with a model fit based on a linear spin wave calculation incorporating a bilinear exchange and cubic CF interaction. The localized mode is a function of the CF parameters and the parameters employed in the fit are in good agreement with those obtained from bulk measurements. In contrast to the Fe compounds, the Co sublattice moment displays metamagnetic behaviour and the Co moment in RCo_2 intermetallics is induced only by the 3d–4f exchange interaction. The eigenstates of the R ion are no longer pure and equally spaced J_z states. In both cases, a suitable Hamiltonian is one consisting of CF and exchange terms. The magnetic excitations in this instance consist of localized transitions between single ion levels which propagate through the lattice via the rare-earth transition metal exchange with a weak dispersion. In RCo_2 compounds, the relative strengths of CF and exchange obtained from magnetization (Gignoux et al. 1975, 1977), spin reorientation phenomena (Aubert et al. 1978), specific heat (Imai et al. 1995) as well as magnetic form factor measurements (Gignoux et al. 1977, 1979a, 1979b) clearly show that these compounds have CF and exchange interactions which are comparable in size.

Intermetallics of the series RFe_2 and RCo_2, as investigated by INS, are tabulated in table 16 together with deduced CF parameters. The R–R exchange interaction is small for both RFe_2 and RCo_2 compounds. Model calculations incorporating localized R moments and itinerant d-electrons have been performed by Yamada and Shimizu (1982, 1983). The

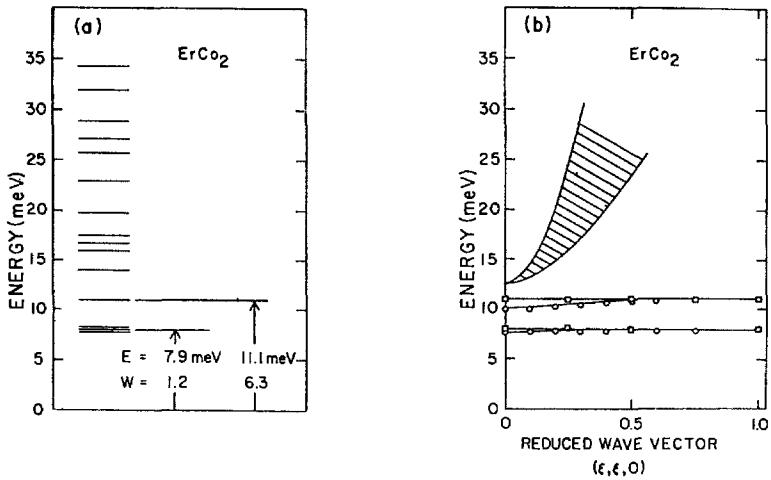

Fig. 14. Observed low lying magnetic excitations for a single crystal of cubic $ErCo_2$ as a function of wavevector, measured in the [1 1 0] symmetry direction, together with energy levels calculated in a CF – isotropic exchange mean field–RPA approximation. CF parameters used are as tabulated in table 16. The exchange parameters used were $J_{Er-Er} = 0$ and $J_{Er-Co} = -1.78$ K. The hatched region shows the range of energies expected for the highly dispersive Co–Co modes, where J_{Co-Co} varies from 60 to 230 K (from Koon and Rhyne 1981).

TABLE 16

Crystal field coefficients for RFe_2 and RCo_2 intermetallics (cubic $MgCu_2$ structure) determined by INS experiments. Units for A_n^m are in K r_0^{-n}.

Compound	x	W (K)	A_4^0	A_6^0	Ref.
$ErFe_2$	−0.40	−0.277	37.4	−1.45	[1–5]
$HoFe_2$	−0.44	0.127	23.2	−0.81	[5,6,12]
$Ho_{0.88}Tb_{0.12}Fe_2$	−0.49	0.109	22.0	−1.01	[7]
$ErCo_2$	−0.43	−0.40	49.9	−1.74	[5,8,13]
$HoCo_2$			49.9	−2.32	[5,9,10]
$HoCo_2$	−0.48	0.30	52.4	−1.59	[11,12]

References:

[1] Rhyne et al. (1977)
[2] Koon and Rhyne (1978)
[3] Clausen et al. (1982)
[4] Koon and Rhyne (1980a, 1980b)
[5] Rhyne (1980)
[6] Rhyne and Koon (1979)
[7] Nicklow et al. (1976)
[8] Koon and Rhyne (1980a, 1980b)
[9] Koon and Rhyne (1981)
[10] Rhyne et al. (1979)
[11] Castets et al. (1980)
[12] Castets et al. (1982a)
[13] Rhyne (1987).

CF parameters for RCo_2 intermetallics are generally found to be larger than the corresponding Fe series, a fact which can be attributed to a smaller d-band density of states for Co in this structure. Point charge estimates of the CF parameters for the Co series predict smaller parameters than those determined experimentally (Gignoux et al. 1975). For the

Fe series, the CF parameters determined by INS are in rather favorable agreement with Mössbauer effect studies (Atzomy et al. 1973).

4.12. Crystal fields of rare-earths in dilute alloys

First measurements of the CF levels in R ions in noble metals by INS were reported by Murani et al. (1975), who investigated 5% Er in Pd. This investigation followed on from earlier ESR results for dilute alloys of R ions in Ag (Griffith and Coles 1966). A negative value of the sixth order parameter was observed, in contrast to the positive values observed in other face centered cubic alloys of Er such as Au and Ag (Davidov et al. 1972). This difference was attributed to differences in the electronic band structures between Pd and Ag. In further studies devoted to the origins of the CF in metallic systems, attention was later focused on R ions dissolved in Au and Ag (Hahn et al. 1992). Noble metals were chosen because of the fairly simple electronic band structures adopted by these metals. In this study, the CF interaction of concentrations as small as 0.08 at% of Er and Dy dissolved in cubic alloys of Au and Ag. Other information about the CF states previously available for these systems is from susceptibility data (Williams and Hirst 1969; Chelkomski and Orbach 1975; Oseroff et al. 1981), Mössbauer data (Kikkert and Niesen 1981a, 1981b) and EPR measurements (Davidov et al. 1971, 1972).

The cubic crystal structure again allows a description of the CF in terms of just two parameters. Due to the low concentration of dissolved R ions, these measurements were performed using neutron spectrometers with an extremely high incident neutron flux. In this instance, it can be inferred that the CF states were determined with sufficient accuracy (see table 17) to compare them with those available from theoretical calculations (Dixon and Dupree 1973; Christodoulos and Dixon 1987a, 1987b; Albanesi et al. 1989). The parameters determined by the INS studies are at some variance with the calculations, which also considered the conduction electron contribution. The sign difference in the sixth order parameters observed between Ag and Pd alloys is verified. All these experimental studies of CF interactions in dilute alloys have obviously pointed out the necessity for *ab initio* calculations of the CF in metallic systems as well as follow-up INS studies on an extensive series of similar systems.

TABLE 17

Crystal field coefficients determined by INS for dilute face centered cubic R alloys. Units for A_n^m are in $\mathrm{K}\,r_0^{-n}$.

Compound	x	W (K)	A_4^0	A_6^0	Ground state	Ref.
ErPd	0.47	−0.170	−23.8	−0.64	$\Gamma_8^{(3)}$	[1]
ErAu	−0.26	0.190	−14.6	1.02	Γ_7	[2]
DyAu	0.85	0.125	−19.9	0.21	Γ_8	[2]
ErAg	−0.15	0.215	−9.5	1.32	Γ_7	[2]
DyAg	0.37	0.147	−10.2	1.07	Γ_7	[2]

References:

[1] Murani et al. (1975)
[2] Hahn et al. (1992)

5. Inelastic neutron scattering experiments on stable hexagonal lanthanide intermetallics

In systems of hexagonal symmetry, where the number of CF parameters increases to four, the INS technique has been used to investigate the CF interaction in a large variety of different structural types. These include dilute R alloys, RNi_5 and RCu_5, R_2Co_{17}, R_2Fe_{17}, RAl_3 and RGa_2. The increased number of CF parameters makes a combined analysis of data obtained by INS and other techniques, such as magnetization and specific heat, imperative.

5.1. R_cX_{1-c} (X = Y, Lu, Sc, Mg)

Due mention must be made of INS studies of Rare-Earth CF states in dilute hexagonal alloys. This is the most appropriate way to separate out the crystal field interaction from the indirect exchange interaction. Even though such systems cannot be classed as true intermetallics, it is again instructive to examine the level and type of information obtained about the CF interaction in the pure rare-earth elements. (The subject of magnetic excitations in the rare-earth metals themselves is dealt with in detail in the monograph of Jensen and MacIntosh (1991).) The results themselves have a considerable impact on our understanding of the origins of crystal fields in metals. The first measurements of CF levels in a dilute alloy were reported by Rathmann et al. (1974). An alloy of Er–Y containing 2% Er, which crystallizes in a hexagonal close packed structure, was studied by triple-axis spectrometry in order to test in a critical manner the reliability of CF parameters for this system previously obtained by bulk magnetization techniques. A low Er concentration was chosen in order to study the CF interaction in isolation from the strong Er–Er exchange interaction. The CF parameters obtained in this way were rather accurate because it was possible to probe different states by measuring along high symmetry directions of the hexagonal lattice. With the scattering vector oriented along the high symmetry ΓA direction (c-axis), the scattering cross section arises only from the transverse components of the angular momentum operator, J_x and J_y. For the scattering vector along the ΓM (b-axis) symmetry direction, only matrix elements containing J_z are probed. In this way, the problem of obtaining reliable values of the four parameters necessary for a description of the hexagonal CF Hamiltonian is completely resolved.

A further measurement on this system with an improved energy resolution (Kjems et al. 1979) showed the effects of transitions arising even from nearest neighbor Er pairs and in this instance a CF model incorporating cluster effects was invoked (Furrer and Güdel 1977) in order to explain an additional transition observed over and above those expected from single ion CF excitations. These studies were then followed by a systematic investigation of a series of Sc, Y and Lu rare-earth alloys (Rathman and Touborg 1977; Touborg 1977). Again, the necessity arose to check in an independent manner, CF parameters deduced from bulk magnetization investigations for these alloy systems. A check for a more universal behaviour of the CF interaction was carried out in a study of CF interactions in dilute MgR (R = Dy, Ho, Er and Tm) single crystal alloys by de Jong and Kjems (1983). Magnesium was chosen because of the ease with which it was possible to grow relatively large single crystals (of the order of a few cm^3 in volume) and the markedly different properties such as valence, ionic volume, c/a ratio and d-electron contribution of the Mg ion, in contrast to R like hosts such as Y and Lu. Using greatly improved instrumentation, single crystals

TABLE 18

Crystal field coefficients for R ions in dilute hexagonal close packed alloys as determined by INS experiments on single crystals. Units for A_n^m are in $\mathrm{K}r_0^{-n}$.

Compound	A_2^0	A_4^0	A_6^0	$A_6^6(*)$	Ref.
YEr	−156.0	10.6	2.5		
YTb	−114.0	2.9	1.9	$c/a = 1.573$	[1–3]
YDy	−67.8	29.2	5.3		
LuEr	−78.3	7.6	3.3		
LuTb	−76.6	3.2	1.8	$c/a = 1.584$	[1–3]
LuDy	−28.2	32.0	5.5		
LuHo	−48.4	0.6	2.4		
ScTb	−37.7	8.1	3.6		
ScDy	−38.4	9.8	3.5	$c/a = 1.594$	[1–3]
ScEr	−40.8	6.5	3.8		
MgTb	−17.0	10.9	3.5	-	
MgDy	−7.2	2.6	2.7	22.7	
MgHo	−6.0	2.0	2.4	22.0	[4,5]
MgEr	−18.3	10.2	2.1	23.6	
MgTm	−1.5	1.5	2.9	24.8	

* For the ideal hexagonal close packed structure, $c/a = 1.573$ and $A_6^6 = \frac{77}{8} A_6^0$ (Segal and Wallace 1970). For MgR alloys, $c/a = 1.624$.

References:

[1] Rathmann et al. (1974)
[2] Rathmann and Touborg (1977)
[3] Touborg (1977)
[4] Kjems et al. (1979)
[5] de Jong and Kjems (1983)

containing about 0.1 at% of R ions were studied in an extremely demanding experiment. A knowledge of the non-magnetic contribution from the phonon spectrum of Mg (Mishra and Kushwaha, 1978) enabled a good discrimination between CF excitations and non-magnetic scattering to be carried out. The CF coefficients determined for the series of alloys with Y, Lu, Sc and Mg are collected in table 18. There is a broad and satisfying internal consistency of the determined coefficients.

5.2. RNi_5

Intermetallics of the type RNi_5 crystallize in the hexagonal $CaCu_5$ structure (Wernik and Geller 1959). The magnetic properties have been reviewed by Franse and Radwanski (1993) and Gignoux and Schmitt (1997) and a comprehensive investigation of the magnetic properties of the series (susceptibility, specific heat, magnetization and INS) has been completed by Kayzel (1997). There are a significant number of INS studies of the series and these are summarized in the following sections.

Early INS investigations by Alekseev et al. (1980) and later work by Alekseev et al. (1991) on polycrystalline material assign the Γ_4 singlet ground state to the Van Vleck paramagnet $PrNi_5$. In a more precise single crystal INS study, Amato et al. (1992) have

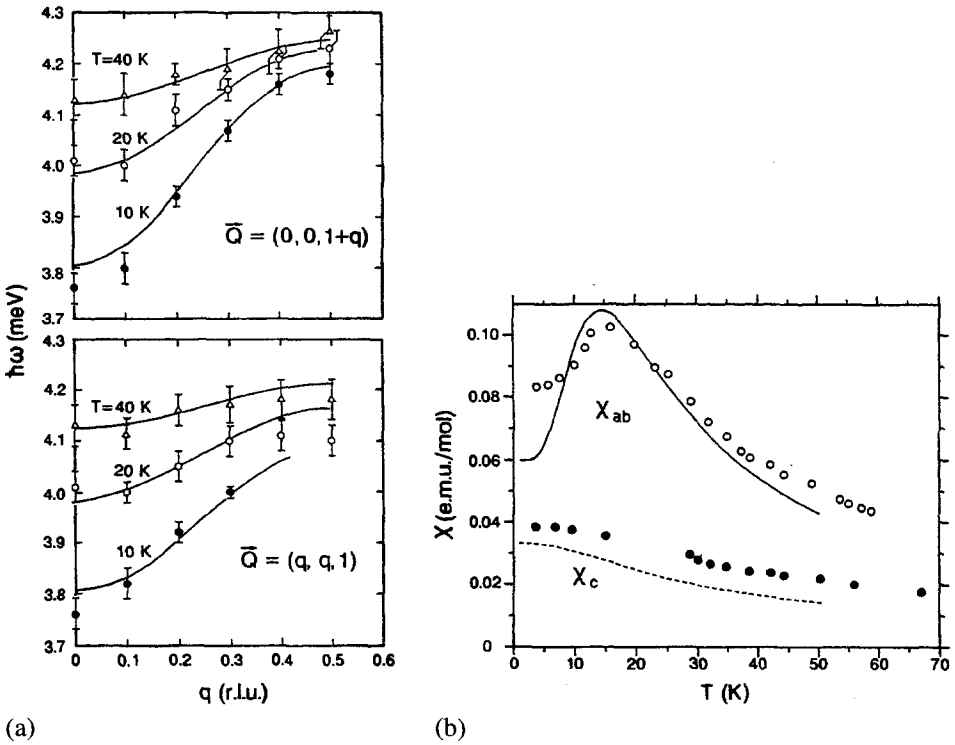

Fig. 15. Dispersion of the Γ_4–$\Gamma_5^{(1)}$ CF excitation for a single crystal of hexagonal $PrNi_5$ measured for wavevectors parallel and perpendicular to the hexagonal axis. The thermal variation of the low temperature susceptibility, measured parallel and perpendicular to the c-axis is displayed in the right hand part of the figure. Solid and dashed lines are the calculated susceptibilities using the CF parameters obtained from the INS data (from Amato et al. 1992).

determined the CF parameters as well as a dispersion of the Γ_4–$\Gamma_5^{(1)}$ doublet excitation. This they attributed to the existence of a Pr–Pr exchange interaction. The nearest and next nearest neighbor exchange interactions are respectively the isotropic interactions along the c-axis and in the (ab) plane. The coupling was found to be ferromagnetic and reminiscent of a RKKY behaviour (fig. 15). The value of the exchange susceptibility is not sufficient to induce long range magnetic order. In contrast with bulk measurements, no appreciable susceptibility is attributed to the Ni sublattice below 50 K. The CF parameters determined in these studies are fairly consistent with detailed specific heat (Kim-Ngan et al. 1995) as well as single crystal magnetization measurements (Barthem et al. 1988a, 1988b). Point contact spectroscopy in zero (Akimenko et al. 1984) and applied magnetic field (Reiffers et al. 1989) has also been used to determine the CF parameters. The applied field measurements in particular make the Γ_4–Γ_1 transition visible, and the behaviour of the Γ_1 level in a magnetic field allowed the CF parameters to be obtained. They are in overall accord with the INS results. Muon spin resonance studies had previously proposed a significant Ni susceptibility below 50 K (Kaplan et al. 1989) but following the suggestion by Amato et

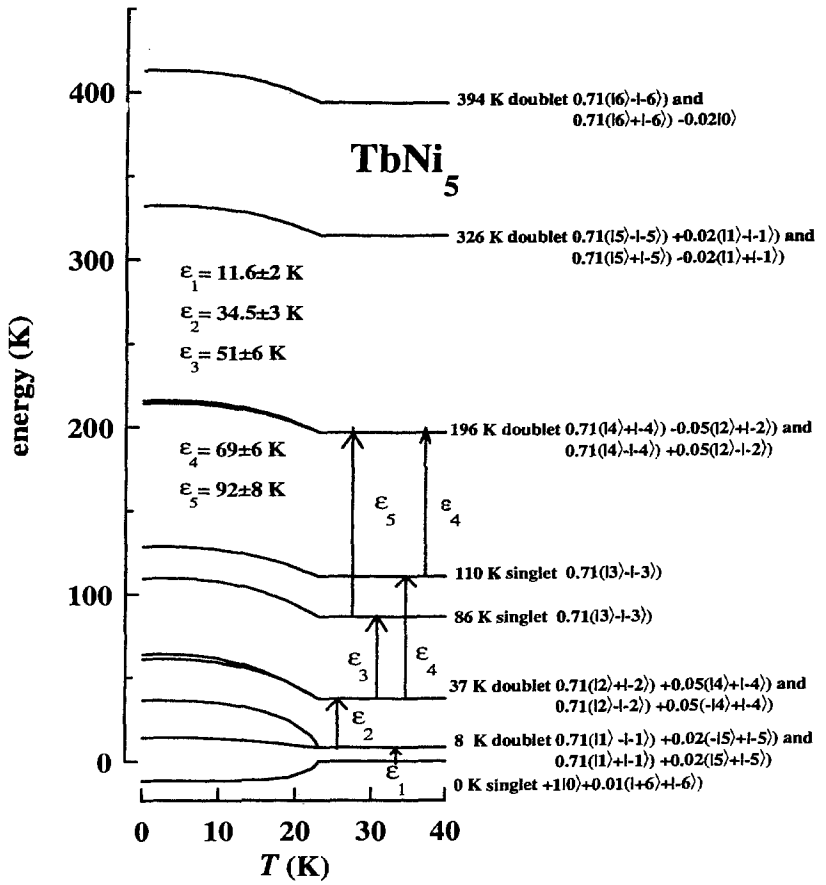

Fig. 16. Temperature dependence of the energy level diagram and level composition for hexagonal $TbNi_5$, deduced from a combined analysis of specific heat, magnetization and INS data. Arrows indicate the dipolar transitions observed by INS, with energies denoted by ε_i (from Kayzel 1997).

al. (1992) that a modification of the hexagonal CF field could be induced by the presence of interstitial μ^+, a more detailed single crystal muon study found that the interstitial 6i (1/2, 0, 0.21) site occupied by the muon in fact lowers the energy of the Γ_4 level and splits the Γ_6 doublet by 14 K (Feyerherm et al. 1995).

Goremychkin et al. (1985a) found a Γ_8 doublet ground state for $NdNi_5$. The CF parameters from this study are able to reproduce the CF contribution to the paramagnetic anisotropy determined by Morellon et al. (1996) in an exposition of the fourth and sixth rank susceptibility tensor for the RNi_5 series.

Three INS investigations exist for $TbNi_5$. Goremychkin et al. (1984) obtained CF parameters for polycrystalline material, whilst a single crystal study of the magnetic excitations is reported by Gignoux and Rhyne (1986). The ground state is the $\Gamma_1^{(2)}$ singlet. The powder CF parameters are sufficient for explaining hyperfine field splitting data (Carboni

et al. 1996) as well as single crystal high field magnetization data (Gignoux et al. 1979a). Gignoux and Rhyne could not obtain a particularly good agreement with bulk data and suggested the possibility of higher order quadrupolar and magneto-elastic interactions, a conjecture supported by the results of paramagnetic anisotropy studies of $TbNi_5$ (Morellon et al. 1996). The energy level diagram for $TbNi_5$ is displayed in fig. 16, together with transitions observed by INS.

Goremychkin et al. (1984, 1985b) report an INS powder study of $HoNi_5$. The second order CF parameter is in agreement with bulk single crystal high field magnetization measurements (Gignoux et al. 1979a). Morellon et al. (1996) used the high field magnetization results for the CF parameters in their study of the paramagnetic anisotropy, but the INS set can equally well account for the anisotropy in the paramagnetic phase.

Four separate INS studies of $ErNi_5$ are reported. Escudier et al. (1977) propose a Γ_7 CF ground state, whilst Goremychkin et al. (1984, 1985b) obtain a $\Gamma_8^{(3)}$ doublet CF ground state as do Radwanski et al. (1992) in analysis of specific heat data. A very consistent set of CF parameters for this compound is obtained by Zhang et al. (1994) in a combined analysis of single crystal high field magnetization data and previous INS data (Goremychkin et al. 1984).

The compound $TmNi_5$ has a low ordering point and presents extremely anisotropic magnetic properties (Barthem et al. 1988b). Inelastic neutron scattering studies of the CF interaction confirm a pseudo-doublet CF ground state which is composed of two very close lying Γ_1 singlets (Gignoux et al. 1982). The CF parameters determined by INS work are in general accord with bulk results with only the A_2^0 coefficient being about 15% larger in the case of the INS determinations. Both the magnetization and INS investigations report a negative value of the A_6^0 coefficient, which is the only exception in the series.

The high sensitivity of CF splittings to the presence of local disorder has been investigated by the INS technique in amorphous $PrNi_5$. Interpretation of this data is discussed in the section on amorphous lanthanide intermetallics. The CF parameters determined for the RNi_5 series by INS are collected in table 19. It can be seen that throughout the series, a fairly consistent set of parameters is available. Electronic band structure calculations have been performed for the series (Novák and Kuriplach 1994). The final calculation is difficult, but the signs and orders of magnitude of the CF parameters are in agreement with INS data. The Newman superposition model also is valid for this series (Newman 1983).

5.3. RCu_5

Inelastic neutron scattering data exist only for the light rare-earth intermetallics $PrCu_5$ and $NdCu_5$. INS measurements have determined the CF level scheme in the Van Vleck paramagnet $PrCu_5$ (Andreeff et al. 1981; Matz et al. 1982; Goremychkin et al. 1988). The Van Vleck susceptibility is reported by Andres et al. (1975) who proposed a Γ_4 singlet CF ground state with the first excited state at 30 K composed of the Γ_3 singlet. The INS results are at variance with this result, as they propose a Γ_1 singlet ground state. The CF parameters obtained from the bulk susceptibility cannot reproduce the observed INS transitions and intensities. The electrical resistivity has been measured by Takayanagi (1984) who used level schemes obtained from the susceptibility and INS investigations. The Γ_4 singlet is favored also in this case.

TABLE 19

Crystal field coefficients for RNi_5 and RCu_5 (hexagonal $CaCu_5$ structure) intermetallics determined by INS experiments. Units for A_n^m are in $K r_0^{-n}$.

Compound	A_2^0	A_4^0	A_6^0	A_6^6	Ground state	Ref.
$PrNi_5$	−210	−16.2	0.79	25.6	Γ_4	[1,2]
$PrNi_5$	−222	−17.8	0.76	25.4	Γ_3	[3,4,5]
$NdNi_5$	−342	−7.1	0.64	23.4	$\Gamma_8^{(1)}$	[5]
$TbNi_5$	−430	−8.6	1.44	46.4	Γ_1	[6,7,8]
$HoNi_5$	−692	−15.6	1.27	36.9	Γ_3	[6,9]
$ErNi_5$	−337	−38.7	2.23	12.7	$\Gamma_9^{(3)}$	[6,7]
$ErNi_5$	−464	−18.9	1.44	34.1	$\Gamma_9^{(3)}$	[10,11]
$ErNi_5$	−481	−18.9	1.44	33.0	$\Gamma_9^{(3)}$	[16]
$TmNi_5$	−543	−63.1	−7.23	30.0	Γ_1	[12]
$PrCu_5$	−209	3.8	0.48	13.6	Γ_1	[13]
$PrCu_5$	−200	4.8	0.53	10.6	Γ_1	[14]
$NdCu_5$	−14	18.4	1.06	36.1	$\Gamma_9^{(1)}$	[15]

References:

[1] Alekseev et al. (1980)
[2] Alekseev et al. (1991)
[3] Amato et al. (1992)
[4] Alekseev et al. (1992b)
[5] Goremychkin et al. (1985a)
[6] Goremychkin and Mühle (1984)
[7] Goremychkin et al. (1984)
[8] Gignoux and Rhyne (1986)
[9] Goremychkin et al. (1985b)
[10] Escudier et al. (1977)
[11] Zhang et al. (1994)
[12] Gignoux et al. (1982)
[13] Andreeff et al. (1981)
[14] Goremychkin et al. (1988)
[15] Divis et al. (1991)
[16] Kayzel (1997)

Inelastic neutron scattering data also exist for $NdCu_5$, which orders ferromagnetically below 15 K (Barthem et al. 1989). Divis et al. (1991) obtain a set of CF parameters which consistently account for the specific heat, high field magnetization, susceptibility and spin re-orientation transition reported by the same authors at 5.6 K. The CF ground state is the $\Gamma_9^{(1)}$ doublet. The sixth order CF coefficients are similar to those obtained for $PrCu_5$, but the second and fourth order coefficients are much smaller than for the corresponding Pr compound. A negative fourth order coefficient which is as large as the second order one, accounts for the observed spin re-orientation transition from axis to plane. The CF coefficients, as determined by INS, are also tabulated in table 19.

The CF parameters for these intermetallics have also been discussed in terms of the superposition model (Newman 1983; Newman and Ng 1989). A fair agreement is obtained for $PrCu_5$.

5.4. *RPd_2X_3 ($X = Al$, Ga)*

Inelastic neutron scattering measurements are reported for the light rare-earth compounds $PrPd_2X_3$ and $NdPd_2X_3$ for X = Al and Ga (Dönni et al. 1997a, 1997b). In this case, Pd atoms reside at the 2c site with Al distributed over the 3g site of the modified $CaCu_5$ structure. The compound $PrPd_2Al_3$ is paramagnetic down to low temperatures (Ghosh et al. 1993) whilst $NdPd_2Al_3$ displays antiferromagnetic order below 7.7 K (Dönni et al. 1997a). The corresponding Ga compounds have a similar be-

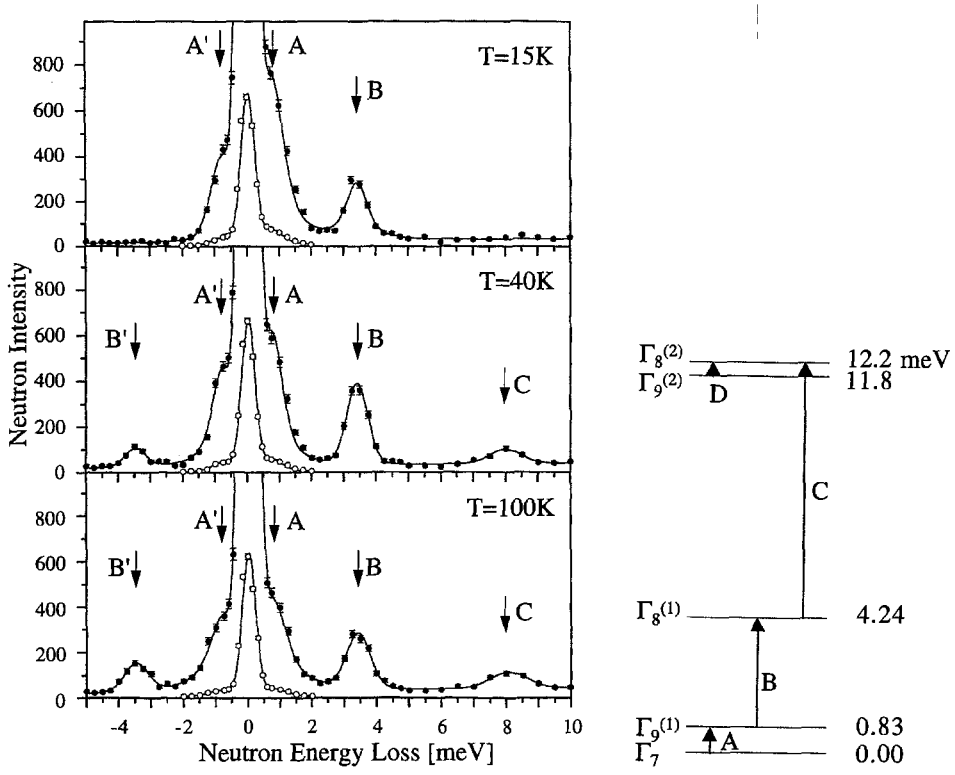

(a)

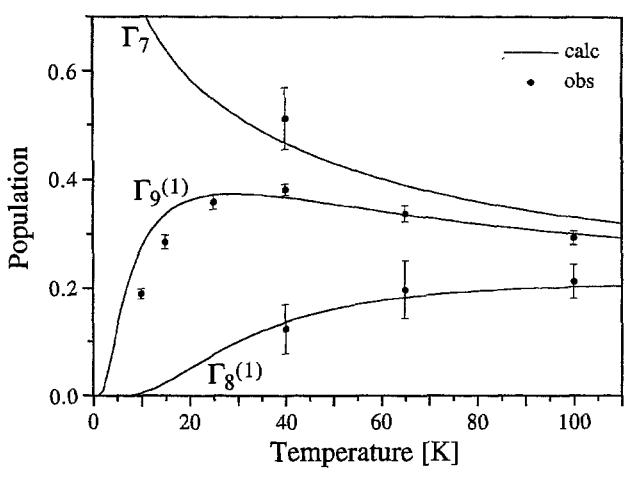

(b)

Fig. 17. (a) Inelastic neutron scattering spectra and energy level scheme deduced for polycrystalline hexagonal $NdPd_2Al_3$. Arrows indicate the dipolar transitions observed by INS (from Dönni et al. 1997a). (b) Calculated and observed temperature dependence of the CF levels deduced for polycrystalline hexagonal $NdPd_2Al_3$ from INS data (from Dönni et al. 1997a).

TABLE 20

Crystal field coefficients for RPd_2Al_3 and RPd_2Ga_3 hexagonal intermetallics as determined by INS experiments. Units for A_n^m are in Kr_0^{-n}.

Compound	A_2^0	A_4^0	A_6^0	A_6^6	Ground state	Ref.
$CePd_2Al_3$ *	−354.0	15.2			Γ_7	[1]
$PrPd_2Al_3$	−343.0	14.4	0.45	−9.1	Γ_1	[1]
$NdPd_2Al_3$	−347.0	14.4	0.45	−8.9	Γ_7	[1]
$CePd_2Ga_3$ *	−387.2	16.6			Γ_7	[2]
$PrPd_2Ga_3$	−374.7	13.8	0.31	−6.3	Γ_1	[2]
$NdPd_2Ga_3$	−380.2	13.7	0.30	−6.2	Γ_7	[2]

* Extrapolated from Pr and Nd compounds.

References:

[1] Dönni et al. (1997a)
[2] Dönni et al. (1997b)

haviour with $PrPd_2Ga_3$ paramagnetic down to 0.3 K and $NdPd_2Ga_3$ antiferromagnetic below 6.5 K (Bauer et al. 1997). Compounds with Ce display a heavy fermion behaviour and the ordered magnetic moments are all perpendicular to the hexagonal c-axis. Clearly such magnetic properties are strongly influenced by the CF interaction. The INS data were supplemented with single crystal susceptibility data and a good agreement was obtained between these two different sets of measurements. The temperature dependence of the inelastic spectra and level scheme for $NdPd_2Al_3$ are displayed in fig. 17, together with the calculated and observed temperature dependence of the level populations. The CF ground state Γ_7 doublet correctly fixes the ordered Nd moments in the basal plane, for both Al and Ga compounds, as observed experimentally by neutron diffraction. The changes in the CF coefficients (table 20) between Al and Ga compounds is attributed to differences in the electronic structure, since an expected change in the coefficients due only to a difference in the crystal structure was not observed.

5.5. R_2X_{17} (X = Fe, Co)

5.5.1. R_2Fe_{17}

The magnetic properties of R_2Fe_{17} compounds, which crystallize in the hexagonal Th_2Ni_{17} structure are summarized by Franse and Radwanski (1993). Structural and magnetic data are tabulated by Buschow (1977, 1980). Inelastic neutron scattering measurements have been reported only for a single crystal of Ho_2Fe_{17} (Clausen and Lebech 1982). The low energy part of the ground state excitation spectrum was found to consist of three modes; a highly dispersive Fe–Fe mode, one weakly dispersive mode as well as a non-dispersive mode (fig. 18). The crystal structure places Ho ions at two distinct crystallographic sites, 2b and 2d. Given the tendency for a certain amount of local disorder to exist in this type of intermetallic (Christensen and Hazell 1980; Moze et al. 1994) the two sites can be considered to be magnetically equivalent (the disorder inhibits an averaging of the

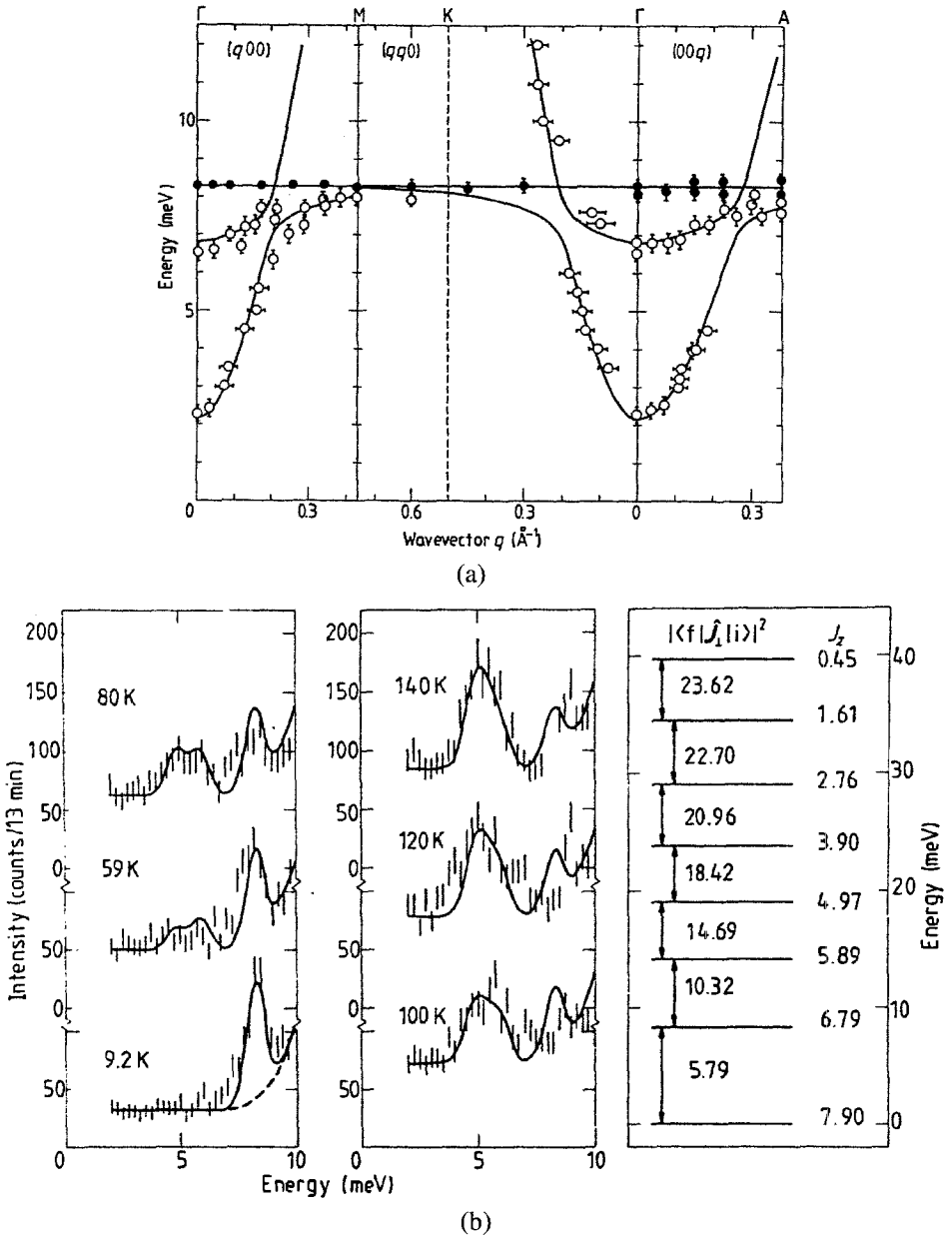

Fig. 18. (a) Dispersion of the low lying magnetic excitations for a single crystal of hexagonal Ho_2Fe_{17}, measured along the high symmetry directions, at 4.2 K. Lines are results of a fit to the q-dependence of the modes using a spin wave approximation. (b) Temperature dependence of the scattering from the non-dispersive (localized) mode. Lines are results of a mean-field calculation. The calculated energy levels, the value of the z component of J and the dipolar matrix elements for adjacent state transitions, within the mean field approximation, are also shown in the right hand part of the figure (from Clausen and Lebech 1982).

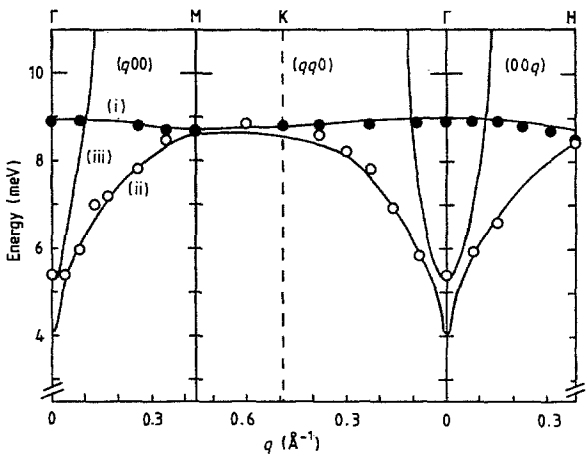

Fig. 19. Dispersion of the low lying magnetic excitations for a single crystal of hexagonal Dy_2Co_{17}, measured along three high symmetry directions, at 4.2 K. Lines are results of a fit to the q-dependence of the modes using a linear spin wave approximation (from Colpa et al. 1989b).

close surroundings of the two sites). This structural detail is crucial for analysis of the magnetic excitations. A linear spin wave approximation was used to model the dynamic susceptibility as well as the bulk anisotropy behaviour. A negligible Ho–Ho exchange interaction was assumed as only one non-dispersive mode was observed. This non-dispersive mode is in particular an intimate function of the four CF parameters and the Ho–Fe exchange interaction. The CF parameters determined in this way are substantially larger than those obtained from specific heat, high field magnetization and Mössbauer measurements (Franse and Radwanski 1993). The CF parameters for the series with Y, Dy, Ho and Er have been obtained from a detailed and comprehensive high field magnetization investigation (García-Landa et al. 1997). The parameters for Ho_2Fe_{17} are a factor of 10 less than those obtained from the INS investigation, but the signs are in agreement on both counts. This demonstrates the tremendous difficulty in obtaining a consistent set of parameters for a particular isostructural series with a CF of low symmetry.

5.5.2. R_2Co_{17} (R = Ho, Dy)

A similar analysis was performed by Clausen and Lebech (1980, 1982) for INS data obtained on a single crystal of Ho_2Co_{17}. Colpa et al. (1989a, 1989b) also report INS data for a single crystal of Dy_2Co_{17}. In contrast to Ho_2Fe_{17} and Ho_2Co_{17}, the analysis for Dy_2Co_{17} was generalized to include an exchange interaction between Dy ions and closed expressions for the dispersion relations were obtained (these are listed in detail by Colpa et al. 1989b). This gave a better agreement between INS and bulk studies for Dy_2Co_{17}. The results are displayed in fig. 19. The CF coefficients determined by INS for the intermetallics Ho_2Fe_{17}, Ho_2Co_{17} and Dy_2Co_{17} are tabulated in table 21. Clearly, there are discrepancies in the variations of the coefficients between Ho and Dy and further INS single crystal measurements for other members of the series are needed.

TABLE 21

Crystal field coefficients for hexagonal and rhombohedral R_2X_{17} (X = Fe, Co, Zn) intermetallics determined by INS experiments. Units for A_n^m are in Kr_0^{-n}.

Hexagonal (Th_2Ni_{17} structure)

Compound	A_2^0	A_4^0	A_6^0	A_6^6	Ref.
Ho_2Fe_{17}	−900	−30	−3.4	−1.7	[1]
Ho_2Co_{17}	−66	19.4	−1.4	−3.9	[1,2]
Dy_2Co_{17}	−71	−3.1	0	−45.4	[3,4]

Rhombohedral (Th_2Zn_{17} structure)

	A_2^0	A_4^0	A_4^3	A_6^0	A_6^3	A_6^6	Ref.
Nd_2Co_{17} *	−169	−14.2	−4.7	0.35	−5.25	0.14	[5]
Sm_2Fe_{17}		1.5		2.9			[6]
$Sm_2Fe_{17}N$	−160	8		−2.5			[6]
Pr_2Zn_{17}	55.5	10.3	333.9	−0.10	−4.75	8.26	[7,8]
Tb_2Zn_{17}	208.2	6.2	138	−0.95	−7.16	−68.1	[7,8]
Dy_2Zn_{17}							[7,8]
Ho_2Zn_{17}							[7,8]
Er_2Zn_{17}	208.5	7.9	150	−0.75	−3.74	−29.9	[7,8]

* These values were taken from high field magnetization studies and then used to calculate dipole transitions.

References:

[1] Clausen and Lebech (1982)
[2] Clausen and Lebech (1980)
[3] Colpa et al. (1989a)
[4] Colpa et al. (1989b)
[5] Colpa et al. (1994)
[6] Moze et al. (1992a)
[7] Ibarra et al. (1992)
[8] García-Landa et al. (1995)

5.6. RAl_3

Compounds of this type with the light rare-earths crystallize in the hexagonal Ni_3Sn structure (Van Vucht and Buschow 1966). Compounds with the heavy rare-earths crystallize in the rhombohedral $HoAl_3$ structure, with the exception of $ErAl_3$ which crystallizes in the cubic Cu_3Au structure (Buschow 1980). INS data exist for the light rare-earths with Pr and Nd.

Inelastic neutron scattering data for $PrAl_3$ are reported by Alekseev et al. (1976) and Andreeff et al. (1978) for this Van Vleck paramagnet. Compounds diluted with La and Y have also been investigated (Alekseev et al. 1979, 1982). The ground state is the Γ_1 singlet, with the first excited state composed of the Γ_4 singlet. The agreement with specific heat (Mahoney et al. 1973) and susceptibility data (Mader et al. 1969) is reasonable. Goossens et al. (1996, 1998) have also observed CF excitations in $PrAl_3$ by using the technique of neutron polarization analysis. Transitions were observed at 3.5 and 4.5 meV, the same as observed in previous determinations, but unequivocally identified as CF transitions due to the ability of polarized neutrons to separate magnetic from non-magnetic

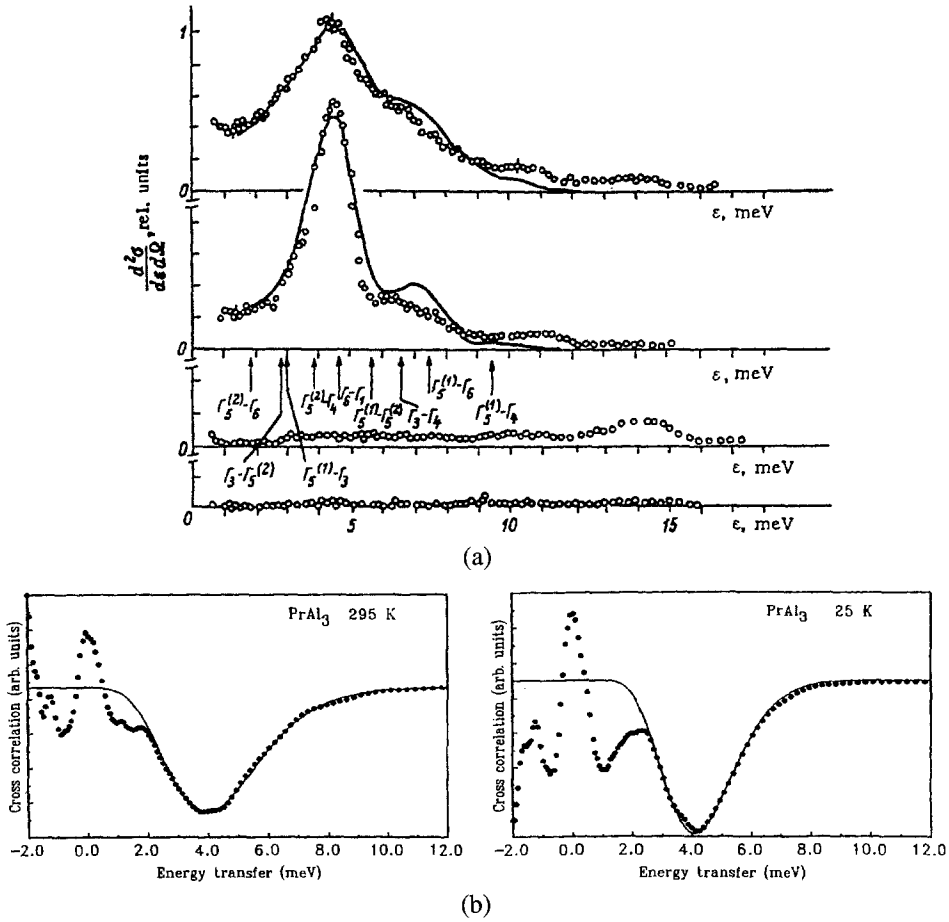

Fig. 20. (a) Inelastic neutron scattering spectra measured for polycrystalline hexagonal $PrAl_3$ at 295 K and 100 K. These are shown as the first two spectra at the top of the figure. The scattering from a non-magnetic reference compound $LaAl_3$, is also displayed, for 295 and 10 K respectively, in last two spectra in the bottom part of the figure. Solid lines are a least squares fit to the INS cross-section for a hexagonal CF and the calculated dipolar transitions are marked by arrows (from Alekseev et al. 1982). (b) Clear separation of crystal field excitations from non-magnetic scattering displayed for polycrystalline hexagonal $PrAl_3$, at 295 K and 25 K, using neutron polarization analysis. The CF scattering appears as negative dips whilst non-magnetic scattering appears as positive dips. Lines through the points have been obtained by fitting two CF transitions with a simple Gaussian lineshape. These correspond to the Γ_4–$\Gamma_5^{(2)}$ and Γ_1–Γ_6 transitions observed at 3.5 and 4.5 meV displayed in (a) (from Goossens et al. 1996, 1998).

scattering (fig. 20). No CF parameters are reported are reported in these later investigations.

Alekseev et al. (1983) determined the CF ground state in $NdAl_3$ and assigned it the $\Gamma_8^{(2)}$ doublet. A Γ_7 doublet ground state was rejected because this failed to reproduce the specific heat data even though the CF contribution to the susceptibility at low temperatures can be accounted for by both sets of CF parameters. Four alternative sets of CF parameters

TABLE 22

Crystal field coefficients for RAl_3 hexagonal (Ni_3Sn structure) intermetallics determined by INS experiments. Units for A_n^m are in $K r_0^{-n}$.

Compound	A_2^0	A_4^0	A_6^0	A_6^6	Ground state	Ref.
$PrAl_3$	−32	+6.5	1.32	7.0	Γ_1	[1]
$PrAl_3$	−95	+6.3	1.17	7.8	Γ_1	[2]
$PrAl_3$	−92	+8.8	1.10	15.9	Γ_1	[3,4]
$Pr_{0.25}La_{0.75}Al_3$	−60	+6.5	0.91	14.1	Γ_1	[4]
$Pr_{0.50}La_{0.50}Al_3$	−75	+8.0	0.91	15.0	Γ_1	[4]
$Pr_{0.75}La_{0.25}Al_3$	−79	+8.6	1.01	15.6	Γ_1	[4]
$Pr_{0.25}Y_{0.75}Al_3$	−102	+8.6	1.23	16.7	Γ_1	[4]
$Pr_{0.50}Y_{0.50}Al_3$	−123	+8.6	1.31	18.3	Γ_1	[4]
$PrAl_3$						[5]
$NdAl_3$	−124	+3.1	1.21	17.6	$\Gamma_8^{(2)}$	[6]

References:

[1] Alekseev et al. (1976)
[2] Andreeff et al. (1978)
[3] Alekseev et al. (1979)
[4] Alekseev et al. (1982)
[5] Goossens et al. (1996, 1998)
[6] Alekseev et al. (1983)

were proposed in a series of specific heat, susceptibility and resistivity data (Mahoney et al. 1975), none of which can reproduce the observed CF transitions and intensities. The anomaly in the specific heat at approximately 5 K is attributed to magnetic ordering of the Nd ions. The INS determinations of the CF parameters for this series are collected in table 22. There is a rather satisfying and consistent variation for the parameters, at least for the light rare-earths which have been investigated.

5.7. RGa_2

This series of intermetallics are an example of a frustrated magnetic structure that occurs on a simple hexagonal lattice. The strong uniaxial anisotropy coupled with a long range oscillatory exchange interaction leads to either an Ising or X–Y behaviour. They crystallize in the AlB_2 type with a space group P_6/mmm (Haszko et al. 1961). The magnetic properties were investigated by Tsai et al. (1978) and are summarized by Buschow (1980) and Gignoux and Schmitt (1997). The intriguing variety of magnetic phase diagrams presented by these systems are reviewed by Gignoux and Schmitt (1995). In the series, compounds with Nd, Pr and Ho have been studied by INS techniques in order to determine the CF interaction.

Ball et al. (1993a) have determined the CF level scheme for $PrGa_2$, using INS. A Γ_1 ground state with a Γ_6 first excited state lying very close to each other explains the existence of the collinear long range periodic-antiphase magnetic structure at low temperatures, as has been observed by neutron diffraction (Ball et al. 1993b). The derived CF parameters account well also for the variation of the specific heat with temperature and the field and temperature dependence of the magnetization (Ball et al. 1993c; Garnier et al. 1997). This material is a particularly beautiful example of a system displaying multi-step magnetiza-

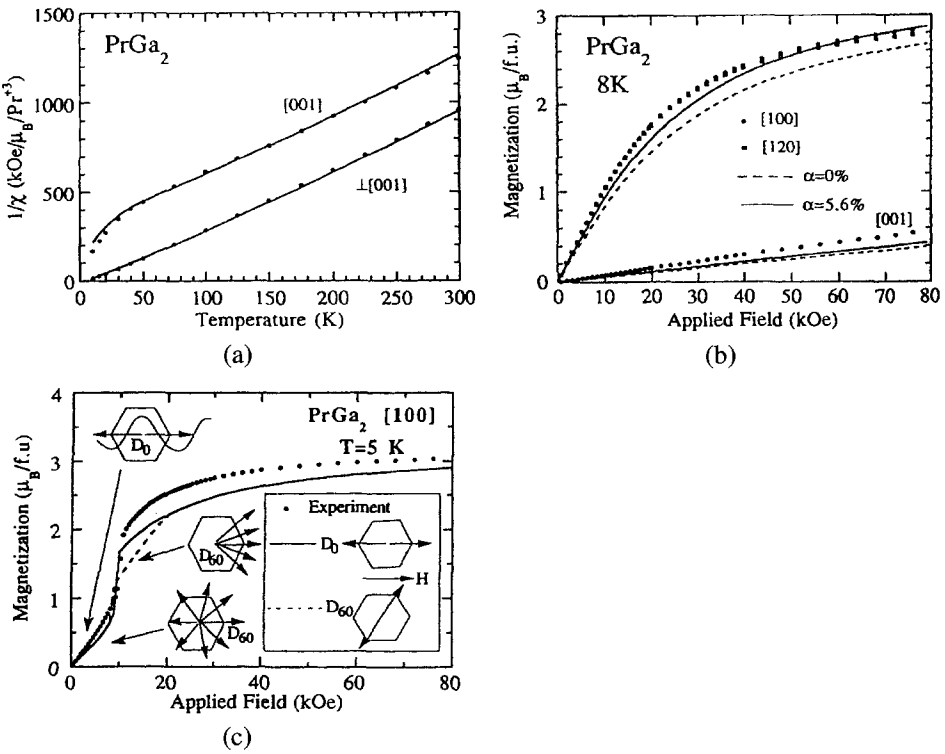

Fig. 21. Reciprocal susceptibility, magnetization at 8 K and field dependence of the magnetization at 5 K (along [1 0 0]) for single crystal hexagonal $PrGa_2$. Lines through the reciprocal susceptibility and magnetization at 8 K have been calculated by inclusion of CF parameters determined from INS data for polycrystalline $PrGa_2$. Model calculations for the magnetization at 5 K have been performed using a CF and periodic exchange field model. Configurations are shown for D_0 domains (magnetic propagation vector parallel to the applied magnetic field) and for D_{60} domains (magnetic propagation vector at 60° to the applied magnetic field) (from Ball et al. 1993a, 1993b, 1993c).

tion processes which result from the competition between a strong planar CF anisotropy and long-ranged oscillatory exchange interactions (fig. 21).

Anti-ferromagnetic order was found to exist in the series of hexagonal $NdAl_xGa_{2-x}$ compounds (Martin et al. 1983). In particular, the easy axis of magnetization is parallel to the c-axis for $x = 1.25$ and perpendicular to the c-axis for $x < 1$. The c/a ratio changes in a drastic fashion for the series and this determines the CF interaction. Furrer and Martin (1986) used INS to determine the CF parameters in this series and found the CF parameters to be strongly correlated to the geometrical co-ordination of the Nd ion. A radial RKKY type dependence of the exchange parameters determined from the neutron diffraction data for NdAlGa is displayed in fig. 22. The sign of the parameter B_2^0 is consistent with the observed easy axis directions whilst a rapid decrease in the overall CF splitting by almost one order of magnitude when passing from $NdAl_{1.25}Ga_{0.75}$ to NdAlGa was observed. The sign reversal in B_2^0 in passing between these two compositions was correctly predicted by

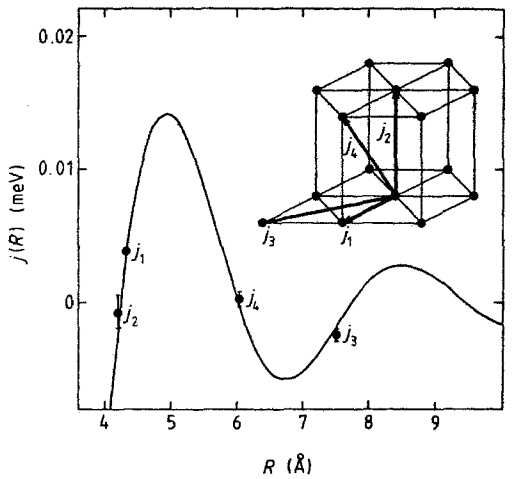

Fig. 22. Radial dependence of the Nd–Nd exchange interaction parameters $j(R)$ for NdAlGa obtained from analysis of magnetic structural data. The resultant magnetic structure is stabilized by the CF interaction (from Furrer and Martin 1986).

considerations of the geometrical co-ordination factor. For the series, the calculated ground state magnetic moments are in agreement with the bulk studies (Martin et al. 1983). Further INS studies were subsequently carried out on a single crystal of $NdAl_{0.8}Ga_{1.2}$ (Elsenhans et al. 1990b). In this instance, the polarization factor for magnetic scattering allows for a total suppression of the longitudinal CF excitations for measurements performed with the scattering vector parallel to the c-axis. The fitted CF parameters were in overall good agreement with previous determinations. The INS measurements were also extended to below the ordering temperature. The CF excitations displayed little or no dispersion and could be analyzed in the mean field approximation. The observed splitting of the ground state Γ_7 doublet into two low lying transverse excitations was in good agreement with the expected CF level scheme. In a later INS investigation, Ball et al. (1994) deduced an overall CF splitting of 50 K for $Nd_{0.5}Y_{0.5}Ga_2$. This is twice that proposed by Furrer and Martin (1986) for $NdGa_2$. The parameters obtained in this study could account for the anisotropy in the paramagnetic susceptibility, the temperature dependence of the magnetic entropy and the complex multi-step magnetization processes observed.

The compound $HoGa_2$ also exhibits an extremely complicated H–T magnetic phase diagram along the (0 0 1) axis (Gignoux et al. 1991). An INS investigation on diluted HoY-AlGa is reported by Ball et al. (1993c). A $\Gamma_6^{(1)}$ ground state doublet with a first excited $\Gamma_1^{(2)}$ singlet was deduced after an exhaustive trial search combining the INS data with the available data for the anisotropic paramagnetic susceptibility. From the obtained CF and exchange field parameters, the authors were able to give a surprisingly accurate description of (a) the multi-step magnetization process, (b) magnetization curves along the hard axis of magnetization, (c) moment magnitude and direction, and (d) reduced value of the specific heat discontinuity in the λ anomaly below T_N.

TABLE 23

Crystal field coefficients for hexagonal RGa_2 (AlB_2 structure) intermetallics determined by INS experiments. Units for A_n^m are in $K r_0^{-n}$.

Compound	A_2^0	A_4^0	A_6^0	A_6^6	Ground state	Ref.
$PrGa_2$	−149	−3.95	−0.18	−2.6	Γ_1	[1]
$Nd_{0.5}Y_{0.5}Ga_2$	−100	−3.48	−0.24	−2.6	Γ_7	[2]
$NdGa_2$	−11.7	2.73	−0.02	−2.4	Γ_7	[3]
$NdAl_{0.5}Ga_{1.5}$	−18.7	4.2	0.12	−5.5	Γ_7	[3]
NdAlGa	−20.8	4.7	−0.3	−7.8	Γ_7	[3]
$NdAl_{1.25}Ga_{0.75}$	11.0	9.8	3.12	−9.2	$\Gamma_8^{(1)}$	[3]
$NdAl_{0.8}Ga_{1.2}$ *	−14.1	8.6	−0.3	−4.5	Γ_7	[4]
$Ho_{0.25}Al_{0.75}Ga_2$	162	14.9	−6.2	−2.1	$\Gamma_6^{(1)}$	[5]

* Single crystal.

References:

[1] Ball et al. (1993a)
[2] Ball et al. (1994)
[3] Furrer and Martin (1986)
[4] Elsenhans et al. (1990b)
[5] Ball et al. (1993b)

The CF coefficients determined for this series by INS are collected in table 23. There are glaring contrasts between the INS results reported by Furrer and Martin (1986) and Ball et al. (1994) for the Nd compounds. In only one instance have INS measurements been carried out on single crystal material and these are reported for $NdAl_{0.8}Ga_{1.2}$ (Elsenhans et al. 1990b). The origins of the sign change in A_2^0, reported for the compound HoAlGa, are most likely similar to those reported for the Nd series. These INS studies are surely a harbinger of the large number of rare earth intermetallic compounds with intricate magnetic phase diagrams which still await investigation by combined INS and bulk studies.

6. Inelastic neutron scattering experiments on stable rhombohedral lanthanide intermetallics

Rare-earth intermetallics which crystallize in a rhombohedral lattice present a total of six CF parameters which need to be determined. Inelastic neutron scattering investigations of these systems are scarce, with only Nd_2Co_{17} and the series R_2Zn_{17} (R = Pr, Tb, Dy, Ho and Er) having been studied in any detail. In the former compound, the R–Co and Co–Co exchange interactions dominate whilst in the later, CF effects are important at low temperatures. High energy INS has also been employed to study intermultiplet transitions in Sm_2Fe_{17} and nitrogenated Sm_2Fe_{17} as well as the details of the rare-earth transition metal exchange interaction in Gd_2Fe_{17} and Gd_2Co_{17} together with their corresponding nitrides and carbides.

6.1. R_2Co_{17}

Colpa et al. (1994) have used INS to observe the non dispersive excitations in Nd_2Co_{17} which arise from the excitations of the Nd ion. In this case, a set of CF parameters which

were derived from high field magnetization measurements (Sinnema et al. 1986, 1987) were used to model these limited number of modes. In this way, the molecular field experienced by the Nd ion, approximately 320 Tesla, was deduced. Such information is difficult to arrive at for the light rare-earths from just magnetization measurements alone, in contrast to the heavy rare-earths, where the coupling is ferrimagnetic. The accuracy of the determined molecular field is very sensitive to the set of CF parameters chosen.

6.2. R_2Zn_{17}

The difficulty of deriving, even from INS experiments, six reliable CF parameters is highlighted by INS measurements performed on this series, which crystallize in the rhombohedral Th_2Zn_{17} structure (Iandelli and Palenzona (1979), space group $R\bar{3}m$). A paramagnetic behaviour is observed over a large temperature range (Stewart and Coles 1974). The highest Néel points are observed for Gd_2Zn_{17} (10 K), Tb_2Zn_{17} (23 K) and Dy_2Zn_{17} (9 K). Specific heat and susceptibility data are reported by Marquina et al. (1993) and Gignoux et al. (1994). Low temperature neutron diffraction investigations of Tb and Dy compounds clearly reveal that these systems order magnetically in a complex helical magnetic structure (Moze et al. 1996). For the series, INS measurements are reported by Ibarra et al. (1992) and García-Landa et al. (1995).

The large number of observed transitions observed for Pr_2Zn_{17} allowed imposition of severe restrictions on the number of possible CF parameter sets. Nevertheless, it proved difficult to obtain a consistent set. This was due to a lack of information about transitions from levels lying below 1 meV to higher energies. The CF parameters reported in table 21 give a reasonable fit to the INS spectra but should be treated with some care.

The high ordering point for Tb_2Zn_{17} makes analysis particularly difficult for this system. The CF parameters give a qualitative fit to the INS spectra and the specific heat data. Additionally, a scaling of the parameters to the Er_2Zn_{17} system gives a good account of the transition energies and intensities observed for this latter material.

A first set of CF parameters was obtained from fits of the specific heat and paramagnetic susceptibility data for Dy_2Zn_{17}. These do not give an adequate description of the INS data and, conversely, a good fit to the INS spectra does not adequately describe the bulk data. A scaling of these parameters from those obtained from Er_2Zn_{17} did, however, yield a parameter set which reproduced the observed INS spectra.

The large number of possible transitions possible for the non-Kramers Ho ion in Ho_2Zn_{17} entirely precluded an analysis in this case. A combined interpretation of INS and specific heat data could not produce a unique set of parameters. All the trial solutions obtained from INS, specific heat and susceptibility data indicated a CF splitting of greater than 30 meV, a range not accessible with the particular type of TOF spectrometer employed.

Of the entire series investigated, Er_2Zn_{17} was the one for which a reliable CF parameter set was obtained. This is displayed in figs 23 and 24 where the INS and paramagnetic susceptibility data are displayed together with predictions based on the parameter set reported in table 21.

For this series, INS measurements with single crystal material would most likely allow a more definitive set of CF parameters to be obtained, since the longitudinal and transverse CF excitations are more easily distinguished. Additionally, suppression of the exchange

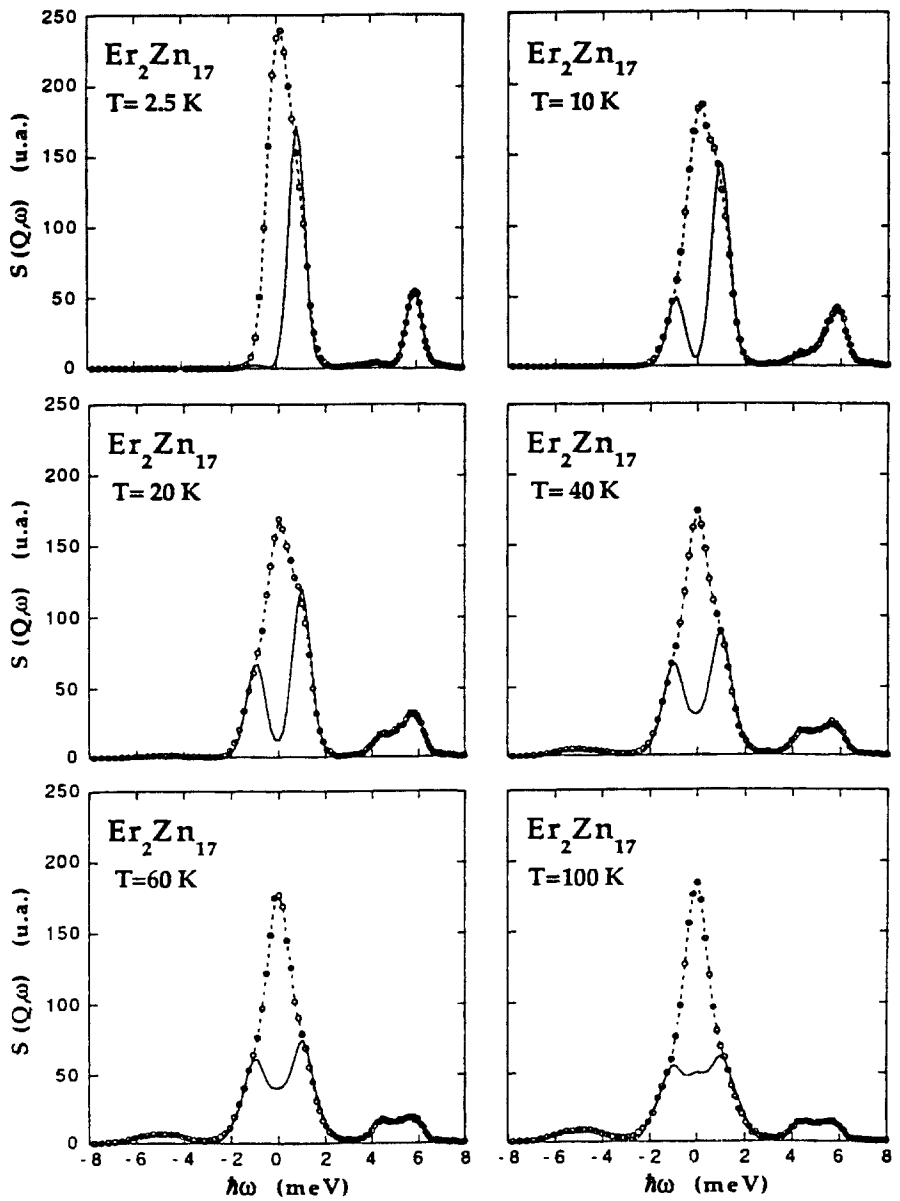

Fig. 23. Temperature dependence of CF transitions observed for polycrystalline rhombohedral Er_2Zn_{17}. Solid lines are results of Gaussian fits used to obtain the positions, intensities and linewidths of the inelastic transitions (from García-Landa 1995).

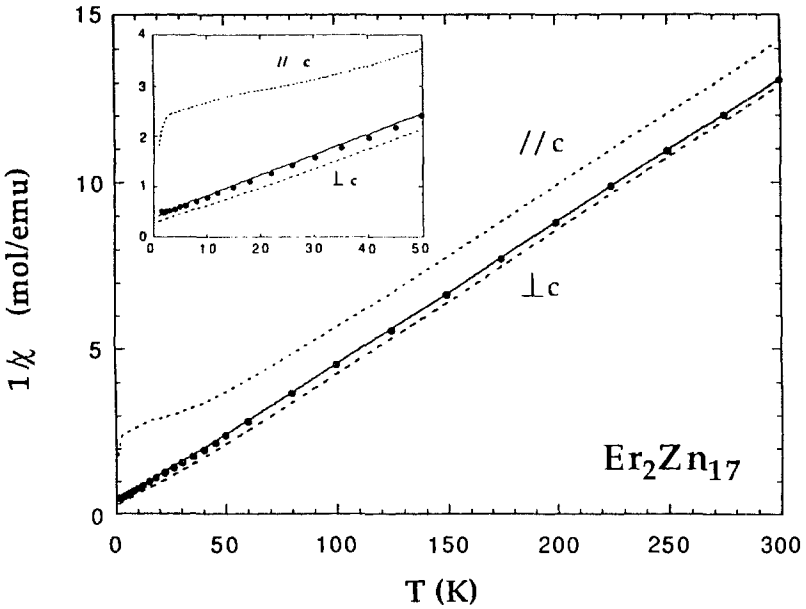

Fig. 24. Fits of the reciprocal parallel and perpendicular susceptibility for Er_2Zn_{17}, using CF parameters obtained from combined analysis of specific heat, susceptibility and INS data (from García-Landa 1995).

interaction for Tb_2Zn_{17} by dilution with non-magnetic lanthanide ions, would surely allow a more consistent set of parameters to be obtained.

6.3. R_2Fe_{17}

The magnetic properties of these compounds and their modification by interstitial solid solutions have been reviewed by Fujii and Sun (1995). Moze et al. (1992a) employed high energy INS to explore the mixing of the $J = 5/2$ state with the $J = 7/2$ and $9/2$ excited states of the Sm^{3+} ion in Sm_2Fe_{17} and the corresponding nitride $Sm_2Fe_{17}N_{2.7}$, where the location of the N atom in the 9e site of the rhombohedral structure induces a large enhancement of the Curie point (Ibberson et al. 1991). The mixing of the states is induced by CF, exchange and spin–orbit interactions. The only observed transition was a dispersionless excitation of 174 meV at 5 K. The limited observation of just one intense peak appears to make a detailed analysis of the CF interaction precarious. However, the intensity and energy of this excitation was adequately modeled by a Hamiltonian incorporating a predominant exchange term and a much smaller CF interaction, as well as the known spin–orbit splitting of 129 meV for Sm^{3+}. The CF parameters used were those obtained from magnetization measurements (Zhao et al. 1991). These parameters, together with the exchange coefficient, derived from the Curie temperature, were used to obtain eigenvalues, eigenfunctions and transition probabilities. These yielded three levels in the range from 0 to 250 meV which are coupled to the ground state in the dipole approximation. The most intense of these was at 170 meV, based on estimates of the intensities of transitions.

The associated energy level scheme and composition of the eigenfunctions reproduce the macroscopic magnetic properties, in particular the observed spin reorientation from plane to axis at 165 K. For the nitrogenated compound, $Sm_2Fe_{17}N_{2.7}$, a broad inelastic intensity was observed in the energy range from 140 to 170 meV. In order to obtain a strong transition at these energies, an enhanced exchange constant as well as a large second order CF coefficient A_2^0 are necessary. However, the presence, in approximately the same energy range, of a non-magnetic signal arising from localized N vibrational modes precluded a more detailed analysis. Nevertheless, the confirmation by INS of the proposed transition energy levels and their associated intensities does imply that the proposed CF and exchange parameters obtained from other methods can then be pinpointed more accurately.

The absence of the transitions between CF states in Gd compounds, where the level splitting arises from the Zeeman splitting due to the presence of the molecular field, makes INS an attractive technique for investigating the exchange interaction between the Gd and transition metal sublattices. This exchange interaction can be determined from INS measurements by use of the well known SW (spin wave) model. The alternative is to establish the coupling by use of the high field free powder method. The very weakly dispersionless spin wave mode corresponds to the out-of-phase precession of the Gd spins which experience the molecular field B_{mol} of near neighbor Fe or Co spins. The relationship between the neutron energy transfer Δ (in meV) and the molecular field B_{mol} (in T) is given by (Loewenhaupt et al. 1994a):

$$\Delta = 2\,\mu_B B_{mol}. \tag{6.1}$$

In the mean field approximation, and for Gd–Fe compounds, this reduces to:

$$\Delta = 2Z_{RT}J_{GdFe}S_{Fe}, \tag{6.2}$$

where J_{GdFe} is the Gd–Fe exchange interaction (in meV), S_{Fe} the mean Fe moment and Z_{RT} the R nearest neighbor co-ordination. The values of the molecular field can then be obtained directly from the observed energy transfers. The use of a rather high incident neutron energy (above 250 meV) means that compounds containing the naturally occurring Gd isotope can be investigated. The measurements performed on Gd_2Fe_{17} and the associated nitrogenated compounds (Loewenhaupt et al. 1994a, 1996a) have been compared with those available from HFFP measurements (Liu et al. 1994) and band structure calculations (Beuerle et al. 1994; Liu et al. 1994). Similar measurements are reported by Loewenhaupt et al. (1994b) for Gd_2Co_{17}. The molecular field determined by this method is 10% higher (219 T) than that determined for the same compound by the HFFP technique. Amongst a large series of Gd–Co intermetallics, this is the lowest value observed.

7. Inelastic neutron scattering experiments on stable tetragonal lanthanide intermetallics

The general considerations about the CF point group symmetry interaction points to a total of five CF parameters which need to be determined for tetragonal symmetry. Inelastic

neutron scattering studies have been performed on a rather wide class of materials where the R ion possesses tetragonal point symmetry. These consist of intermetallics which crystallize in the $ThMn_{12}$, $ThCr_2Si_2$ and $MoSi_2$ structures for which the relevant space group is I_4/mmm, and where the point group symmetry of the R ion is 4/mmm. The magnetic properties of compounds which crystallize in the $ThMn_{12}$ structure have been reviewed by Suski (1996). Gignoux and Schmitt (1997) have reviewed the magnetic structures of compounds which crystallize in the $ThCr_2Si_2$ and $MoSi_2$ structures.

7.1. RT_4Al_8 (T = Cu, Mn, Fe)

Ternary rare-earth intermetallic compounds which crystallize in the body-centered tetragonal $ThMn_{12}$ structure (Florio et al. 1952) display an extremely rich variety of magnetic phenomena (H.-S. Li and Coey 1991; Suski 1996). The magnetic behaviour, in particular of the R sublattice, are reported for Al rich compounds of the type RT_4Al_8 (Felner and Nowik 1978, 1979) using bulk magnetization and Mössbauer techniques with antiferromagnetic ordering at low temperatures (< 15 K) reported for all the rare-earths of the series RM_4Al_8 (M = Cr, Mn and Cu), where the transition metal sublattice is non-magnetic or only very weakly magnetic. Neutron powder diffraction measurements on RCu_4Al_8 have shown the existence of collinear and helical magnetic order at low temperatures, respectively for R = Er, Dy and Ho and R = Tb (Dèportes et al. 1979; Baio et al. 1997), whilst for members of

TABLE 24

Crystal field coefficients for tetragonal RT_4Al_8 (T = Mn, Cu, Fe) and $RNi_{10}Si_2$ intermetallics determined by INS experiments. Units for A_n^m are in $K r_0^{-n}$.

Compound	A_2^0	A_4^0	A_6^0	A_4^4	A_6^4	Ground state	Ref.
$TbMn_4Al_8$	−102.7	26.8	−3.5	123.0	−23.4	Γ_1	[1,2,4]
$HoMn_4Al_8$	−189.7	17.9	−3.8	26.8	−5.5	Γ_1	[1,2,4,9]
$ErMn_4Al_8$	−212.0	26.8	−3.0	18.9	−7.1	Γ_7	[1,4]
$ErCu_4Al_8$	122.8	44.6	−7.7	−55.8	−49.1	Γ_6	[3,4]
$ErFe_4Al_8$	245.5	412.9	−3.0	44.6	−6.7	Γ_7	[3,4]
$HoFe_4Al_8$	Not reported					Γ_7	[9]
$SmMn_4Al_8$	Observed spin–orbit coupling of 1439 K for $J = 5/2$–$7/2$ multiplets						[5]
$SmFe_{11}Ti$*	−126	3.8		6.7			[5]
$ErFe_{11}Ti$			3.9		−0.37		[6]
$ErFe_{11}TiN$			−25.8		2.21		[6]
$TbNi_{10}Si_2$	Not reported. Estimated overall CF splitting of 60 K						[7]
$ErNi_{10}Si_2$	Not reported. Estimated overall CF splitting of 70 K						[7,10]
$HoNi_{10}Si_2$	Not reported. Estimated overall CF splitting of 80 K						[7]
$TmNi_{10}Si_2$	−77.2	−4.2	−2.54	−1.98	2.10	$\Gamma_5^{(2)}$	[8*,10]

* From susceptibility measurements.

References:

[1] Moze et al. (1989)
[2] Moze et al. (1990c)
[3] Paci et al. (1995)
[4] Caciuffo et al. (1995)
[5] Moze et al. (1990d)
[6] Hurley et al. (1995)
[7] Moze et al. (1992b)
[8] Stefanski et al. (1995)
[9] Tils et al. (1997)
[10] Moze et al. (1997)

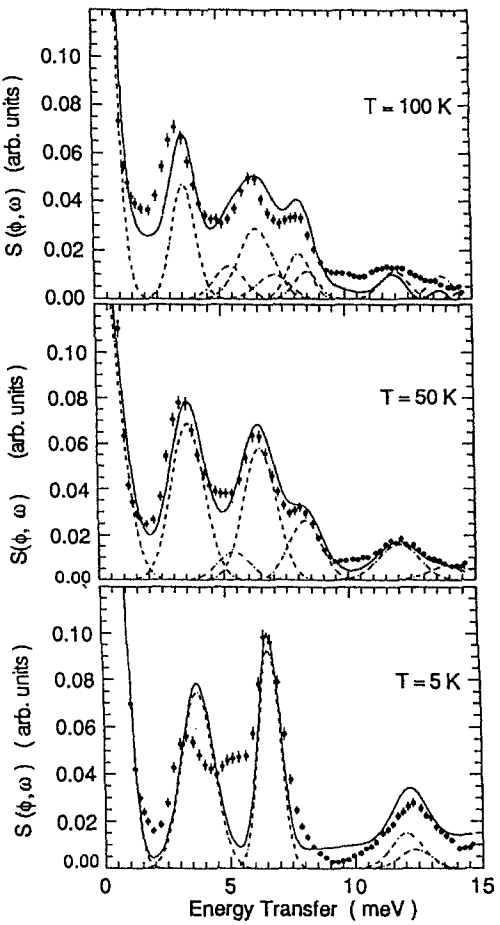

Fig. 25. Temperature dependence of INS spectra for polycrystalline tetragonal $ErCu_4Al_8$. Lines are results of a least squares fit of the data to the CF cross section for a tetragonal CF (from Caciuffo et al. 1995).

the series RMn_4Al_8, neutron diffraction studies report no long range magnetic order above 1.6 K (Schobinger-Papamantellos et al. 1996; Baio et al. 1997). This is in contrast with the bulk magnetization measurements. The preferential site occupation in the series for T = Mn (Moze et al. 1990a) and T = Fe (Moze et al. 1990b) has been investigated by neutron diffraction. Aluminum atoms are found to reside at sites 8i and 8j with a small residual disorder of T–Al atoms on all three sites.

Inelastic neutron scattering studies of the CF interaction are reported by Moze et al. (1989) for $ErMn_4Al_8$, $TbMn_4Al_8$ and $HoMn_4Al_8$ (Moze et al. 1990c), $ErCu_4Al_8$ and $ErFe_4Al_8$ (Paci et al. 1995) and by Tils et al. (1997) for HoT_4Al_8, T = Mn, Fe. A comprehensive analysis of the INS data has been performed for most of the above series (Caciuffo et al. 1995). The CF parameters obtained from INS investigations are collected in table 24. A crucial element in the analysis is the value of the CF coefficient A_2^0 which has been

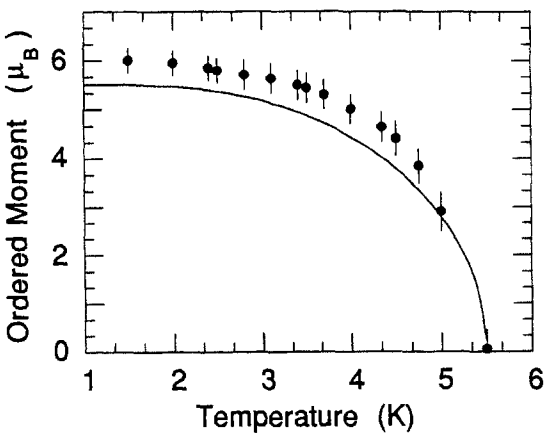

Fig. 26. Temperature dependence of ordered Er magnetic moment for $ErCu_4Al_8$, as measured by neutron diffraction (full circles). The full line is the result of a mean field–CF model fit, using CF parameters determined by INS and a molecular field parameter determined by neutron diffraction (from Baio et al. 1997; Paci et al. 1997).

obtained from ^{155}Gd Mössbauer spectroscopy for GdT_4Al_8 (T = Cu, Fe) compounds (Felner and Nowik 1979) via the quadrupole coupling constant. This served as a basic starting point, even though having unphysical origins, for the least squares fitting of the parameters in the CF Hamiltonian (fig. 25). As can be seen from table 24, the resulting parameters are rather consistent throughout the series. The RMn_4Al_8 compounds with R = Tb, Ho and Er are found to have Γ_1, Γ_1 singlet and Γ_6 doublet CF ground states, respectively. For $ErFe_4Al_8$, where the Er and Fe sublattices order at 25 and 110 K, respectively, further INS measurements on the expected dispersion of the excitations would be necessary, due to the presence of the molecular field up to high temperatures.

The validity of the CF parameters, as determined by INS, has been tested by a neutron diffraction study of the magnetic structure of $ErCu_4Al_8$ (Baio et al. 1997; Paci et al. 1997). The refined magnetic moment is clearly reduced from the free ion value, definitive proof of a strong crystal field interaction. The Er ions are found to order in a type 1 AF structure and the temperature dependence of the moment has been modeled using a standard CF and exchange Hamiltonian. The CF parameters point to a Γ_6 ground state doublet and this reproduces the strong reduction of the reduced moment with respect to the free ion value of 9 μ_B (fig. 26) and lends further credence to the general validity of the CF parameters determined by the INS technique.

7.2. *$RFe_{11}Ti$*

Compounds of the type $RFe_{11}Ti$ are interesting candidates for permanent magnet applications. The magnetic properties of these compounds and their interstitial modifications have been reviewed by Fujii and Sun (1995). The high Curie temperature and moderate Fe moment give rise to a sequence of equally spaced levels (Abadia et al. 1998). Under such circumstances, only INS studies performed on large single crystals are able to furnish any information on the details of the CF and exchange interactions. These are very difficult to

synthesize and very limited INS results have been reported. The crystal structure has been established by neutron diffraction and shows that Ti atoms substitute preferentially into the 8i sites (Moze et al. 1988). High energy neutron spectroscopy has been used to investigate the excitations in $SmFe_{11}Ti$ (Moze et al. 1990d; Moze 1991), $ErFe_{11}Ti$ (Hurley et al. 1995). The dispersionless electronic excitation observed in $SmFe_{11}Ti$ at 176 meV corresponds to transitions between mostly exchange split ground ($J = 5/2$) and first excited state ($J = 7/2$) multiplets of the Sm^{3+} ion. This excitation, observed for the first time in a rare-earth intermetallic, was modeled in the framework of an exchange and CF model by assuming a bare spin–orbit coupling of 129 meV for the $J = 5/2$ and $J = 7/2$ multiplets (this coupling was confirmed directly by high energy INS for the isomorphous intermetallic $SmMn_4Al_8$). The intermultiplet J-mixing of the eigenfunctions by the CF and exchange interactions observed in the INS data were explained with the same parameters used to fit the experimental magnetization curves for a single crystal of $SmFe_{11}Ti$.

Hurley et al. (1995) have measured the level scheme of low lying states within the ground state multiplet for the compounds $ErFe_{11}Ti$ and $ErFeTi_{11}N$, where the interstitial N atoms occupy vacant octahedral sites close to the R ion. This occupation results in a unit cell expansion, increasing the Fe–Fe interatomic distances and enhancing the Fe–Fe exchange. The CF interaction is also strongly modified by the presence of the interstitial N atom. The transition energies and intensities were fitted with, respect to the CF and exchange parameters in order to determine the effects of the interstitial occupation on the main terms in the CF Hamiltonian. The sixth order term $B_6^0\langle O_6^0\rangle$ was found to be dominant. This confirmed the existence of the spin reorientation transition (Hurley 1993) for both compounds, which is dominated by this term. Loewenhaupt et al. (1996a) have also used high energy INS to determine the intersublattice interactions in $GdFe_{10}Si_2$ and $GdFe_{10.6}V_{1.4}$. The Gd–Fe exchange constants were obtained from the position of the dominant transition at low values of the momentum transfer. Similar studies are reported for $GdCo_{10}V_2$ (Loewenhaupt et al. 1994a, 1994b). Hurley et al. (1994), by INS techniques, obtained the Gd–Fe exchange constants for $GdFe_{11}Ti$ and $GdFe_{11}TiN$ intermetallics. In the latter case, the exchange field acting at the Gd sites was found to be reduced by 35 T in comparison with the parent $GdFe_{11}Ti$ compound (255 T). For all the Gd compounds investigated by INS, the values deduced *directly* by the INS method are in accord with those obtained from the Curie temperature using the mean field approximation.

7.3. $RNi_{10}Si_2$

A class of compounds which are ideal model candidates for an investigation of the CF interaction on the ground state properties of R ions in the $ThMn_{12}$ structure are those of the type $RNi_{10}Si_2$. The Ni sublattice exhibits practically zero magnetization and the magnetic properties appear to be dominated by the CF interaction. The crystal structure has been determined by neutron powder diffraction (Moze et al. 1991) with Si atoms found to preferentially occupy the 8f site. Paramagnetic susceptibility and magnetization measurements are reported only for $TmNi_{10}Si_2$ (Stefanski et al. 1995). The Ni paramagnetic susceptibility displays a Pauli paramagnetic behaviour. A fit of the paramagnetic susceptibility proposes a Γ_5 doublet ground state, separated by 15 K from a first excited Γ_4 singlet. The magnetic moment associated with the ground state doublet reproduces the magnetization at 4.2 K. The overall CF splitting of 70 K (determined by the CF parameters as obtained from a fit

of the paramagnetic susceptibility and displayed in table 24) is in approximate agreement with the INS data reported for the compounds $TbNi_{10}Si_2$, $ErNi_{10}Si_2$ and $HoNi_{10}Si_2$ (Moze et al. 1992b). Later INS data for $TmNi_{10}Si_2$ and $ErNi_{10}Si_2$ display even the presence of a molecular field at low temperatures (Moze et al. 1997).

The transferability of CF parameters to isomorphous compounds must be treated with extreme caution for metallic systems. This is exemplified in the example of $RCo_{10}Mo_2$ systems. A neutron powder diffraction investigation of the magnetic structure of $TbCo_{10}Mo_2$ and $ErCo_{10}Mo_2$ (Moze and Bushow 1996) has shown that Tb displays an axial anisotropy at low temperatures whilst Er exhibits a low temperature planar anisotropy. The Co sublattice displays an axial anisotropy at room temperature (Moze et al. 1995). This confirms the positive nature of the first order CF terms, in contrast to Fe compounds, where it is negative. There are obvious underlying fundamental differences in the electronic band structure between these systems. In this case, even the sign of A_2^0 is different. The CF parameters determined for the RMn_4Al_8 system are able to give a reasonable account of the low temperature easy directions but are much less suited for describing the room temperature behaviour.

7.4. RNi_2B_2C

Quaternary intermetallics of the type RNi_2B_2C display a co-existence of superconductivity with magnetic ordering of the rare-earth moments (Cava et al. 1994; Nagarajan et al. 1994). Superconductivity above 4 K has been reported for compounds with R = Y, Lu, Tm, Er and Ho. The AF ordering temperatures and superconducting critical temperatures are found to be of the same order of magnitude. They crystallize in a structural variant of the $ThCr_2Si_2$ structure, with R–C planes alternating with two dimensional Ni_2B_2 layers stacked along the *c*-axis (Rainford and Cywinski 1994; Siegrist et al. 1994). The magnetic ordering temperatures and the decrease of the superconducting transition point are

TABLE 25

Crystal field coefficients for tetragonal RNi_2B_2C quaternary intermetallics determined by INS experiments. Units for A_n^m are in $K r_0^{-n}$.

Compound	A_2^0	A_4^0	A_6^0	A_4^4	A_6^4	Ground state	Ref.
EPCM*	−876	32.2	−0.11	−966	43.1		[1,5]
$HoNi_2B_2C$	−161.8	25.7	−4.7	−796.8	130.6	Γ_4	[1,5]
$HoNi_2B_2C$							[2]
$ErNi_2B_2C$	−70.3	36.8	−6.8	−824.7	112.7	Γ_6	[1,5]
$ErNi_2B_2C$	−390	−6.7	−0.9	−28.6	−31.4	Γ_6	[3]
$TmNi_2B_2C$	−145	24.1	−14.7	−704	174.1	Γ_5	[1,5]
$TmNi_2B_2C$	106.9	−52.4	13.8	137	32.4	Γ_5	[4]

* Extended point charge model calculation.

References:

[1] Gasser et al. (1996)
[2] Grigereit et al. (1995)
[3] Gardner et al. (1995)
[4] Lappas et al. (1995)
[5] Mesot et al. (1997)

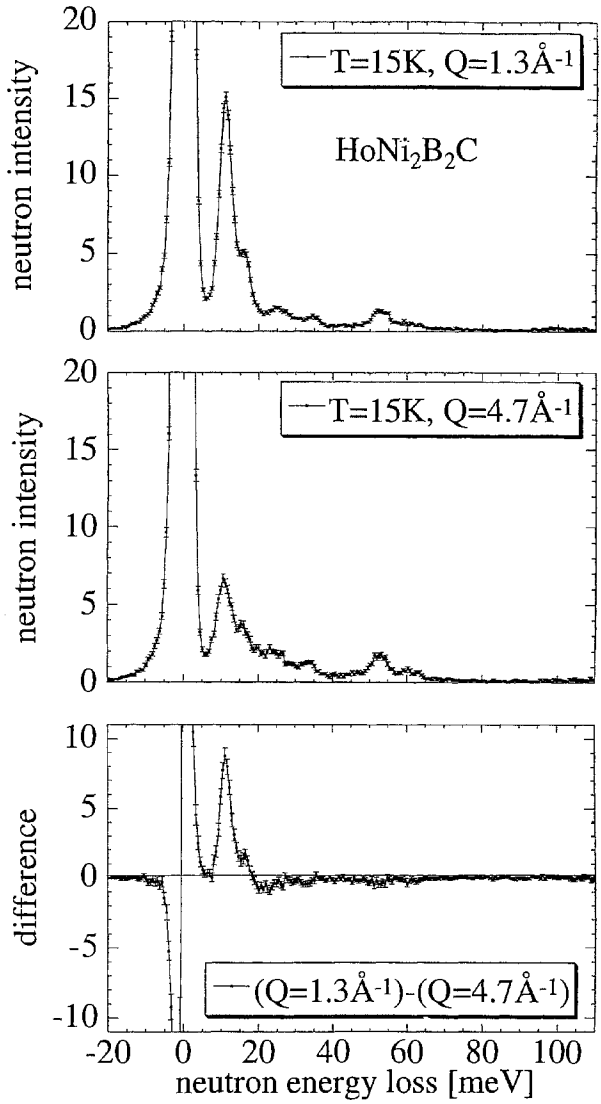

Fig. 27. Inelastic neutron spectra measured for $HoNi_2B_2C$ at 15 K. The difference curve is the subtracted data at low and high scattering vectors and yields the intensity due to CF excitations (from Gasser et al. 1996).

found to scale approximately with the de Gennes factor (Cho et al. 1995a). A reentrant behaviour into the normal state is observed for compounds with Er, Ho and Tm (Eisaki et al. 1994; Lai et al. 1995). The high anisotropies observed in single crystal susceptibility measurements (Cranfield et al. 1994; Cho et al. 1995b, 1995c) have been confirmed by neutron diffraction measurements which clearly show that for Ho and Er, the ground state moments lie in the basal plane whilst for Tm, the moments are aligned along the tetragonal c-axis

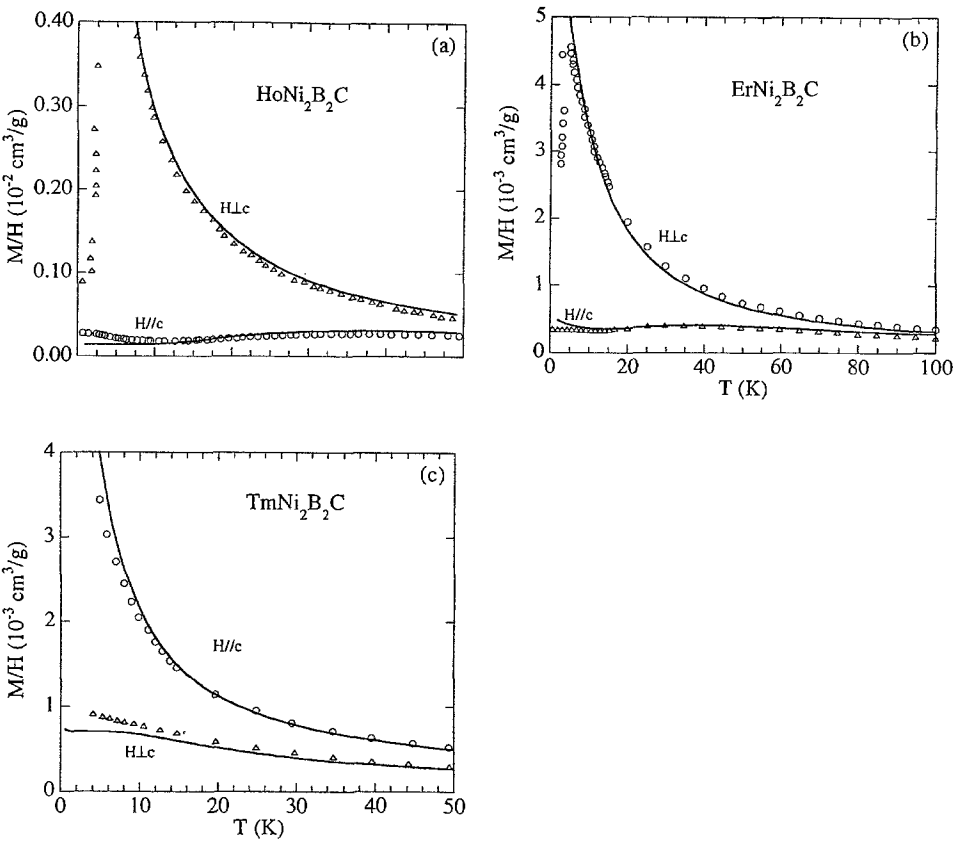

Fig. 28. Temperature dependence of the magnetic susceptibility, measured parallel and perpendicular to the c-axis for RNi_2B_2C (R = Ho, Er, Tm) intermetallics. Full lines are fits using CF parameters obtained from INS data (Gasser et al. 1996).

(Grigereit et al. 1995; Sinha et al. 1995; Zaretsky et al. 1995). The magnetic structures also exhibit incommensurate spirals which reaches a maximum near the reentrant superconducting transition. Clearly such magnetic behaviour must have its origins in the crystal field interaction. This interaction, in compounds with Er, Ho and Tm, has been investigated by the INS technique. These results are discussed below and reported in table 25.

Crystal field excitations are reported for $HoNi_2B_2C$ by Grigereit et al. (1995), Gasser et al. (1996) and Mesot et al. (1997). Grigereit et al. (1995) report two transitions out of the ground state, at 11.3 and 16.0 meV, with a further transition between these two levels of 4.7 meV at higher temperatures. Magnetic doublet Γ_5 states were assigned to these levels as well as to the ground state. Experiments performed with a higher energy resolution and over a larger energy range, assigned a Γ_4 singlet to the ground state, with a very close lying first excited Γ_5 doublet at 0.15 meV (fig. 27). This CF level scheme reproduces the available magnetic specific heat and single crystal magnetization measurements. An extended point charge approximation was used in order to obtain a sufficiently reasonable

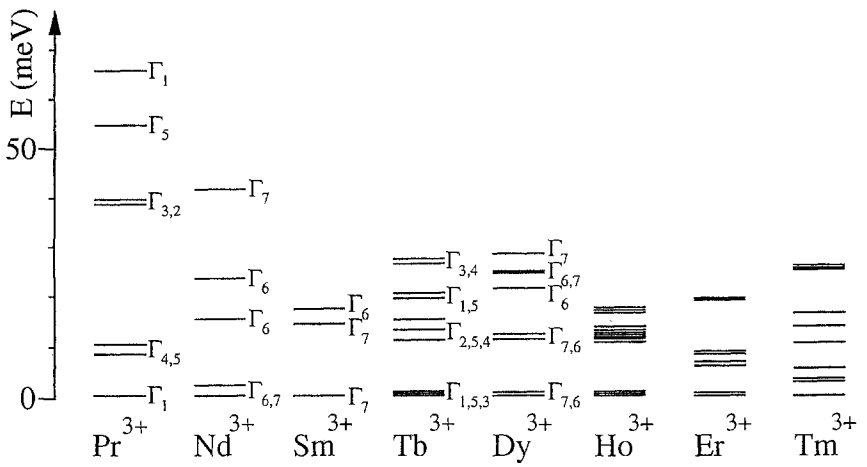

Fig. 29. Ground state multiplet energy levels and compositions for RNi_2B_2C intermetallics as determined from INS studies (Gasser et al. 1996). The levels for Pr, Nd, Sm, Tb and Dy have been interpolated from the CF parameters determined for Ho, Er and Tm by INS. The ground state representation for Ho, Er and Tm compounds is given in table 25 (from Gasser et al. 1996).

starting set of CF parameters. An important element in this approximation is the effect of screening of the charge carriers. The two-dimensional nature of the charge carriers (the surroundings of the R ion are square planar in this structure) enhances the screening, which is taken into account by introducing a correction having a Yukawa-type potential into the expression for the CF potential. All ions within a sphere of radius 5 Å around the R were included in the calculation. In this manner, starting parameters (also displayed in table 25) rapidly converged to a set of parameters consistent with the INS data. This procedure was also followed for the Er and Tm compounds. The enormous value of A_4^4 is also verified in the single crystal magnetization data (Cho et al. 1996).

Inelastic neutron studies are reported for $ErNi_2B_2C$ by Gardner et al. (1995), Gasser et al. (1996) and Mesot et al. (1997). The preliminary CF parameters by Gardner et al. are based on observation of one transition at approximately 6 K and are markedly different from those of Gasser et al., who reported a further ground state transition at 18 meV, with further observation of the excited transition of 12 meV between these two states at higher temperatures. The parameters reported by Gasser et al. (Γ_6 ground state doublet and a Γ_7 first excited doublet at 5.78 meV) give a very impressive reproduction of the single crystal magnetization data (fig. 28). The CF level scheme reproduces the generally observed maximum at 20 K in the magnetic specific heat above the magnetic ordering temperature (Movshovich et al. 1994; Süllow et al. 1995; Bonville et al. 1996).

Preliminary INS data for $TmNi_2B_2C$ were firstly reported by Lappas et al. (1995) followed by a more extensive data set and analysis (Gasser et al. 1996; Mesot et al. 1997). Both give a Γ_5 doublet ground state and a first excited state composed of two closely spaced (0.4 meV) Γ_1 and Γ_3 singlets. The CF parameters reported by Gasser et al. give an excellent agreement with the observed single crystal magnetization data (Cho et al. 1995c)

and a reasonable reproduction of the broad maximum between 5 and 20 K observed in the magnetic specific heat (Movshovich et al. 1994). Neutron diffraction measurements have also been reported for Co and Cu doped isotopically enriched $ErNi_2^{11}B_2C$ and $HoNi_2^{11}B_2C$ compounds (Gasser et al. 1997).

The set of CF coefficients display the same order of magnitude and sign variation when passing from Ho to Tm, indicating that such a qualitative determination by INS can be taken to be rather reliable. In fig. 29 are displayed the CF level schemes extrapolated to other R ions in the series. The INS measurements for the three compounds with Ho, Er and Tm were also extended by Gasser et al. (1996) to below their respective ordering temperatures. These revealed, as can be expected, a splitting in the CF levels by the molecular field. This inevitably leads to a dispersion of the CF energy levels. Future investigation of these dispersive magnetic excitations by INS are surely warranted, since this will provide crucial information on the co-existence of magnetic order and superconductivity in these systems.

7.5. RT_2X_2 (T = Fe, Cu, Ni)

Ternary RT_2X_2 intermetallics exhibit an extraordinary range of magnetic as well as superconducting and heavy fermion behaviour. They crystallize mostly in the $ThCr_2Si_2$-type tetragonal structure. The crystallographic and magnetic properties of a truly enormous number of these intermetallics are reviewed by Parthè and Chabot (1984), Rogl (1984), Szytula and Leciejewicz (1989), Szytula (1991) and Gignoux and Schmitt (1997). With the general exception of the RMn_2X_2 series, the ordering points are rather low, so that the CF interaction can be studied in isolation, by the INS technique, for most of the series. The CF is generated by the presence of a square prism of eight X atoms as well as eight almost equidistant T atoms, both of which have a large variation in their electronic structures, implying an equally large variety in the magnetic properties. Inelastic neutron scattering investigations of the CF interaction have been reported for $PrFe_2Si_2$, $PrFe_2Ge_2$, and for almost the whole of the series RCu_2Si_2 and RNi_2Si_2. These are collected in table 26, together with the determined CF coefficients.

7.5.1. RFe_2X_2 (X = Si, Ge)

Blaise et al. (1995) have determined the CF parameters for $PrFe_2Si_2$ and $PrFe_2Ge_2$ in a combined INS and specific heat investigation. Neutron diffraction measurements (Malaman et al. 1992, 1993) reveal low temperature type II AF structures with quite different ordered Pr moments between the Si (1.41 μ_B) and Ge (2.75 μ_B) compounds, with $PrFe_2Ge_2$ displaying an additional incommensurate–commensurate transition below the Néel point. The anisotropy is axial for both compounds. The ground states are two close lying Γ_1 and Γ_2 singlets and similar level schemes, with the Si compound displaying an overall CF splitting of 550 K and that of Ge approximately half this value. The CF parameters tabulated in table 26 also give a good description of the magnetic specific heat, entropy and ordered values of the Pr^{3+} ion in both structures. The method of Santini et al. (1993), who treat the $J = 4$ multiplet for tetragonal symmetry by parameterizing the CF Hamiltonian such that selected sets of CF parameters can be chosen, enabled best solutions to all the available INS and bulk data to be quickly located. These parameter sets are self-consistent solutions of the CF and molecular field Hamiltonian with fixed values of both the ordered moment

TABLE 26

Crystal field coefficients for tetragonal RT_2X_2 (T = Fe, Cu, Si; X = Si, Ge) ternary intermetallics determined by INS experiments. Units for A_n^m are in $K r_0^{-n}$.

Compound	A_2^0	A_4^0	A_6^0	A_4^4	A_6^4	Ground state	Ref.
$PrFe_2Si_2$	343	17.8	−0.48	−351	−2.53	$\Gamma_1^{(2)}$	[1]
$PrFe_2Ge_2$	117	28.1	−0.05	−122	−1.09	$\Gamma_1^{(1)}$	[1]
$NdFe_2Si_2$	452	−0.38	1.88	69.0	−20.1	$\Gamma_6^{(1)}$	[2]
$PrCu_2Si_2$	43.7	8.0	0.48	85.6	5.63	$\Gamma_5^{(2)}$	[3,4,5]
$NdCu_2Si_2$	48.4	−16.4	0.61	20.1	12.96	$\Gamma_7^{(1)}$	[5,6]
$HoCu_2Si_2$	−149	−17.2	0.35	37.5	18.4	$\Gamma_3^{(1)}$	[5]
$ErCu_2Si_2$	−90.5	−23.6	0.66	62.0	31.7	Γ_7	[5,7]
$PrNi_2Si_2$	140	−4.2	0.68	108	−8.7	$\Gamma_1^{(1)}$	[8]
$PrNi_2Si_2$	140	11.0	3.40	93.4	−4.85	$\Gamma_1^{(1)}$	[9,10,13]
$NdNi_2Si_2$	117	−2.6	0.81	115	−3.6	$\Gamma_6^{(1)}$	[2]
$TbNi_2Si_2$	117	14.3	9.21	280	−137	$\Gamma_4^{(1)}$	[9,11]
$DyNi_2Si_2$	58	−16	1.93	119	32	Γ_7	[12]

References:

[1] Blaise et al. (1995)
[2] Osborn et al. (1993)
[3] Osborn and Goremychkin (1994)
[4] Goremychkin et al. (1994)
[5] Goremychkin et al. (1996)
[6] Goremychkin et al. (1992)
[7] Gubbens et al. (1995)
[8] Blanco et al. (1992a)
[9] Blanco et al. (1992b)
[10] Blanco et al. (1995)
[11] Blanco et al. (1992c)
[12] Fåk et al. (1997)
[13] Blanco et al. (1997a, 1997b)

and ordering temperature. Osborn et al. (1993) also obtained CF parameters for $PrFe_2Si_2$ and $NdFe_2Si_2$ via the INS technique, but these were not verified with any observed bulk behaviour. The parameters for $PrFe_2Si_2$ are different from those of Blaise et al. (1995), particularly in the signs and magnitudes of A_4^4 and A_6^0. The parameters obtained for $NdFe_2Si_2$ scale well with those obtained by the same authors for $PrFe_2Si_2$ but there are differences in sign for the CF coefficients.

7.5.2. RCu_2Si_2

The CF coefficients for this series, as determined by INS, are reported by Osborn and Goremychkin (1994), and Goremychkin et al. (1992, 1996). The signs and magnitudes are in approximate agreement when passing from $PrCu_2Si_2$ to $NdCu_2Si_2$ and in a much more consistent fashion between $HoCu_2Si_2$ and $ErCu_2Si_2$. As an example, the INS spectra and energy level scheme for $ErCu_2Si_2$ is displayed in fig. 30. These authors have also analyzed the CF parameters in terms of the Newman superposition model. For $NdCu_2Si_2$ the conclusion is that the CF is dominated by the Cu sublattice, the same applying to other members of the series, with the exception of $CeCu_2Si_2$, where hybridization between the Ce f-electrons and 3p electrons of Si is proposed (Goremychkin and Osborn 1993). A ^{141}Pr Mössbauer investigation of $PrCu_2Si_2$ (Moolenaar et al. 1995) also confirms the positive value of A_2^0. The anomalously large specific heat coefficient (Sampathkumaran and Das

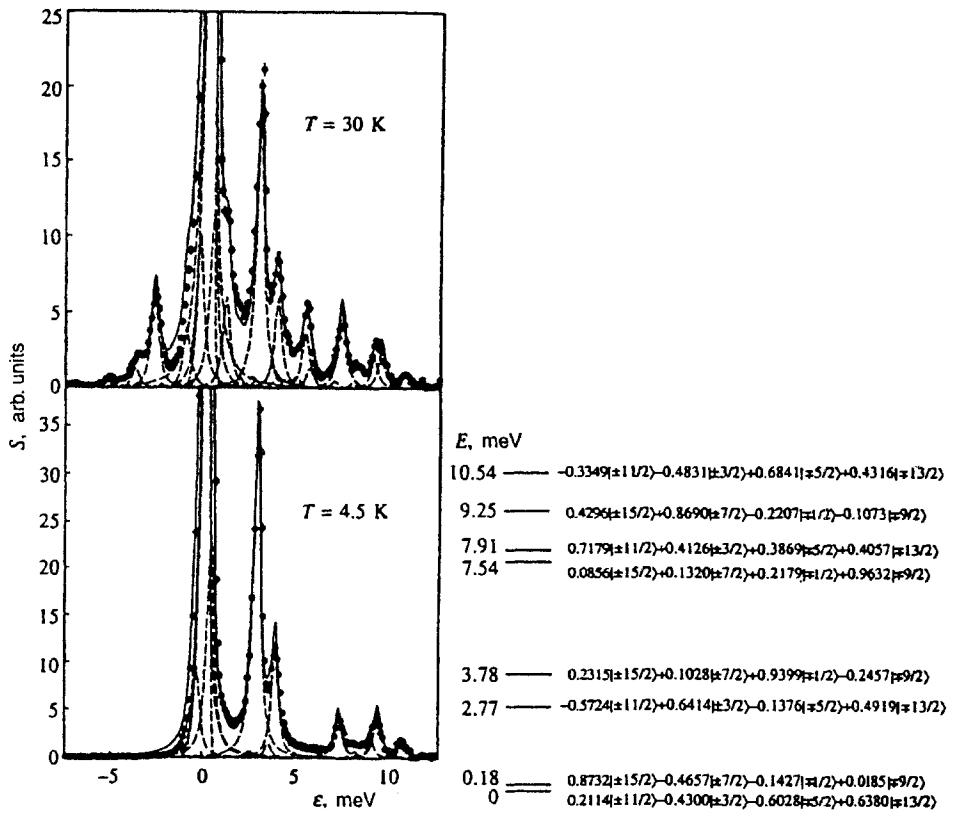

Fig. 30. INS spectra for polycrystalline tetragonal $ErCu_2Si_2$ at 4.5 and 30 K, together with the determined energy levels and level eigenfunction composition. Dashed lines are least squares fits to the spectra (from Goremychkin et al. 1996).

1992) of $\gamma = 225$ mJ/mol indicates a possible hybridization effect here also. From the determined CF parameters, Goremychkin et al. (1994) were able to account for the specific heat, and concluded that $PrCu_2Si_2$ is a normal stable rare-earth intermetallic. The overall behaviour of the CF parameters determined by Goremychkin et al. (1996) for $ErCu_2Si_2$ concord with a ^{166}Er Mössbauer and INS investigation reported by Gubbens et al. (1995).

7.5.3. RNi_2Si_2

These are yet another example of systems which present a large range of magnetic structures due to competing isotropic exchange and a large magnetocrystalline anisotropy which confines the moments either along the c-axis or in the basal plane. The resulting structures are invariably simple antiferromagnets or incommensurate modulated phases, with sometimes a remarkable transition of phases between these two states in the ordered regime. The CF interaction in such systems, which plays a crucial role in determining the free energy minimum, has been investigated in some detail by INS for the compounds $PrNi_2Si_2$ (Blanco et al. 1992a, 1992b), $NdNi_2Si_2$ (Osborn et al. 1993), $TbNi_2Si_2$ (Blanco et al.

1992b, 1992c) and $DyNi_2Si_2$ (Fåk et al. 1997). The magnetic excitations in single crystal $PrNi_2Si_2$ (Blanco et al. 1995, 1997a, 1997b), studied in both disordered and ordered phases, display a moderate dispersion for one of the longitudinal modes (fig. 31). The inter-ionic coupling constants were fitted up to 8th nearest neighbors along the c-axis and 5th nearest neighbors in the basal plane direction. A long ranged feature of the axial coupling constants was observed. These beautiful and rather conclusive results support the idea that the amplitude modulated structure observed in this compound below the Néel point of 20 K is a direct consequence of such long ranged exchange interactions in the presence of a large uniaxial anisotropy driven by the CF. A strong enhancement of the Fourier transform of the exchange interaction $J(\boldsymbol{q})$ (fig. 31) close to the propagation vector of the magnetic structure is likely associated with details of the shape of the Fermi surface.

As can clearly be noted from table 26, for the RCu_2Si_2 and $NdNi_2Si_2$ series, there is no overall internal consistency between signs and magnitudes of the CF coefficients, even though the determined values, when obtained from a combined analysis of the susceptibility, specific heat and magnetization, are able to account in large part for the magnetic properties. Further INS investigations on La and Y diluted compounds appear to be highly desirable.

7.6. RAg_2

Tetragonal RAg_2 compounds crystallize in the $MoSi_2$ structure (I_4/mmm, Dwight et al. (1967)) and the magnetic structures have been determined sometime ago (Atoji 1969a, 1969b, 1972). Two compounds have been investigated by INS, as well as by magnetic susceptibility techniques, particularly in the paramagnetic regime. The main characteristics of the magnetic structure of $HoAg_2$ are the existence of an incommensurate longitudinal mode just below the Néel point of 6.4 K with a subsequent transverse mode below 4.5 K. The second order CF parameter (which turns out to be very weak) could be determined with sufficient precision from the high temperature behaviour of the parallel and perpendicular susceptibility, whilst the origins of the change of easy magnetization direction in the paramagnetic regime at about 75 K lie in the relative strengths of the higher order CF parameters. The ground state is a $\Gamma_5^{(1)}$ doublet and the small value of the second order CF parameter appears to be responsible for the resultant change in sign of anisotropy of the high temperature susceptibility (Morin and Blanco 1993).

The weak value of this second order parameter probably arises from the almost cubic point symmetry of the R ions in this structure, akin to the cubic symmetry present in intermetallics of the type RBe_{13}. Gignoux and Schmitt (1995) have pointed out that in this particular case the susceptibility and INS data appear to be sufficient for determination of the five CF parameters. The INS measurements were particularly useful, with five very well defined transitions observed above the ordering temperature. Such a large number of transitions is to be expected from an ion such as Ho^{3+}, with $J = 8$.

The compound $TmAg_2$ presents a tetragonal to orthorhombic transition at 5 K, with a ferroquadrupolar ordering and a $\Gamma_5^{(1)}$ ground state doublet, as determined from INS and susceptibility measurements (Morin and Rouchy 1993). A thorough determination of the CF parameters, governing the stronger first order magnetic interactions, allowed the weaker higher order magneto-elastic coupling and quadrupolar pair interactions to be determined from third-order susceptibility, parastriction and ultrasonic data. The CF parameters determined by INS for these two compounds are collected in table 27.

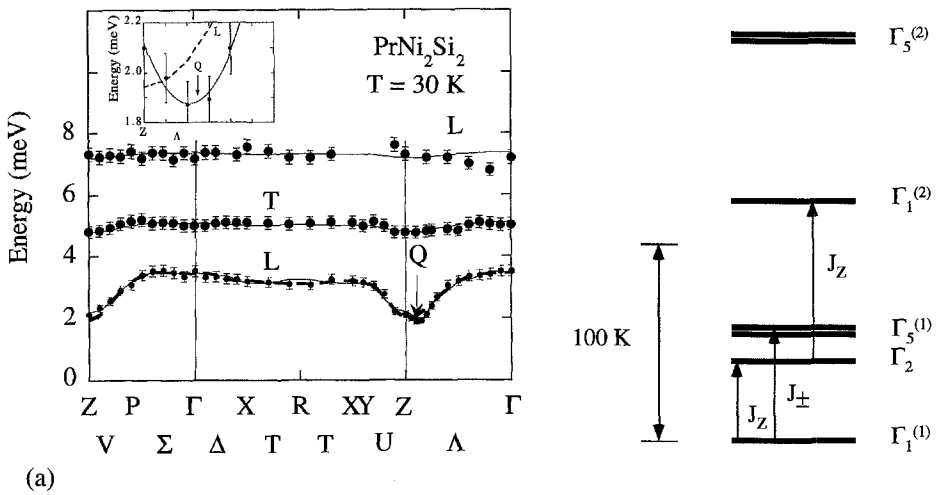

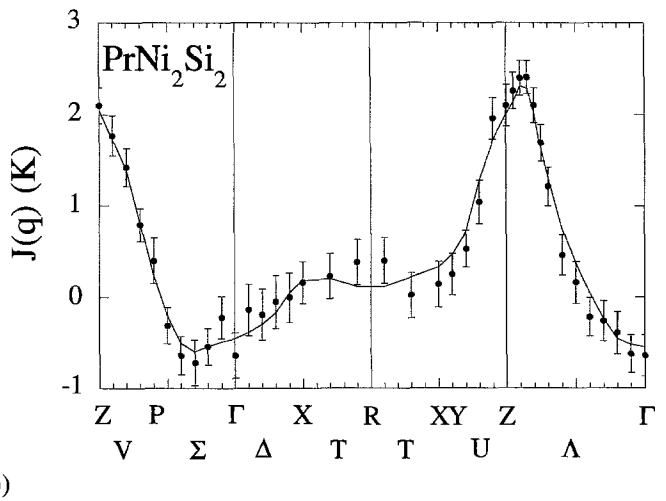

Fig. 31. (a) Dispersion of the magnetic excitations for a single crystal of tetragonal $PrNi_2Si_2$ at 30 K. Continuous lines are results of fits for the longitudinal (L) and transverse modes (T) in a single ion CF and isotropic exchange modelism. The localized (non-dispersive) mode at approximately 5 meV (55 K) corresponds to excitations from the ground state $\Gamma_1^{(1)}$ singlet to the $\Gamma_5^{(1)}$ doublet (T mode) whilst the highly dispersive L mode corresponds to coupled excitations from the ground state $\Gamma_1^{(1)}$ singlet to the Γ_2 singlet. The propagation vector of the magnetic structure is labeled by $\boldsymbol{Q}$. The q dependence of the longitudinal modes in the vicinity of $\boldsymbol{Q}$ are shown in the inset. The overall paramagnetic CF level scheme for $PrNi_2Si_2$, labeled with the observed longitudinal and transverse excitations, is displayed in the right hand part of the figure. (b) The Fourier transform $J(\boldsymbol{q})$ of the exchange coupling constants for $PrNi_2Si_2$ along the principal directions of the Brillouin zone. The solid line corresponds to a fit incorporating exchange parameters with 8 nearest neighbors along the c-axis and 5 nearest neighbors in the basal plane (from Blanco et al. 1997b).

TABLE 27

Crystal field coefficients for tetragonal $REAg_2$ ($MoSi_2$ structure) intermetallics determined by INS experiments. Units for A_n^m are in $K r_0^{-n}$.

Compound	A_2^0	A_4^0	A_4^4	A_6^0	A_4^6	Ground state	Ref.
$HoAg_2$	62.3	4.4	−282.9	−2.8	36.3	$\Gamma_5^{(1)}$	[1]
$TmAg_2$	13.0	1.7	−336.0	−3.7	52.9	$\Gamma_5^{(1)}$	[2]

References:

[1] Morin and Blanco (1993)
[2] Morin and Rouchy (1993)

7.7. $R_2Fe_{14}B$

The magnetism of high magnetic energy product $R_2Fe_{14}B$ supermagnets is dominated by large exchange interactions and smaller CF effects. The intrinsic magnetic properties of these highly important materials have been reviewed by Herbst (1991), Buschow (1991) and Franse and Radwanski (1993). All compounds of the series are known to crystallize in the tetragonal ($P4_2/mnm$) $Nd_2Fe_{14}B$ structure (Herbst et al. 1984; Herbst and Yelon 1985). Investigation of the microscopic magnetic properties by INS techniques is compounded by the complex crystal structure (68 atoms per unit cell). This alone leads to a total of 64 spin wave modes. The R ions are situated at two distinct crystallographic sites, 4f and 4g, and the symmetry of the CF is *orthorhombic* (each R ion has mm orthorhombic point symmetry). As a consequence, a total of 18 CF parameters need to be determined. A relevant discussion of CF effects in $R_2Fe_{14}B$ compounds is that presented by Cadogan and Coey (1984).

It is not possible to suppress the molecular field at Fe sites, since no isomorphous and weakly magnetic compounds are known to exist. Hence, for exchange dominated systems such as these, the energy level splitting is Zeeman like, with virtually pure J_z eigenfunctions. Inelastic neutron scattering studies of the magnetic excitations have been performed by Loewenhaupt et al. (1988, 1990, 1995a), Loewenhaupt and Sosnowska (1991) for practically the whole series of $R_2Fe_{14}B$ intermetallics and by Mayer et al. (1991, 1992) for single crystal $Nd_2Fe_{14}B$ and $Y_2Fe_{14}B$. The analysis is tremendously complicated for the reasons cited above. In general terms, the excitations from the ground state to the first excited state are located in an energy range between 5 and 40 meV (fig. 32). For $Y_2Fe_{14}B$, where the scattering is due to spin wave excitations of the four Fe sublattices, a similar distribution of the scattering is observed. A more detailed fine structure is present for the compounds with Pr, Nd, Tb, Er, Ho and Tm. Modeling of the INS spectra was performed by calculating the dynamic susceptibility from CF and exchange parameters obtained from single crystal high field magnetization measurements (Cadogan et al. 1988; Yamada et al. 1988). Due to the large number of required CF parameters, the magnetization measurements were analyzed with a reduced set of six CF parameters, as the CF interaction at 4f and 4g sites was assumed to be the same, with the additional constraint that $A_6^{-2} = A_6^6 = 0$. On this basis, the measured and calculated splittings are in good accord, but the observed fine structure could not be reproduced.

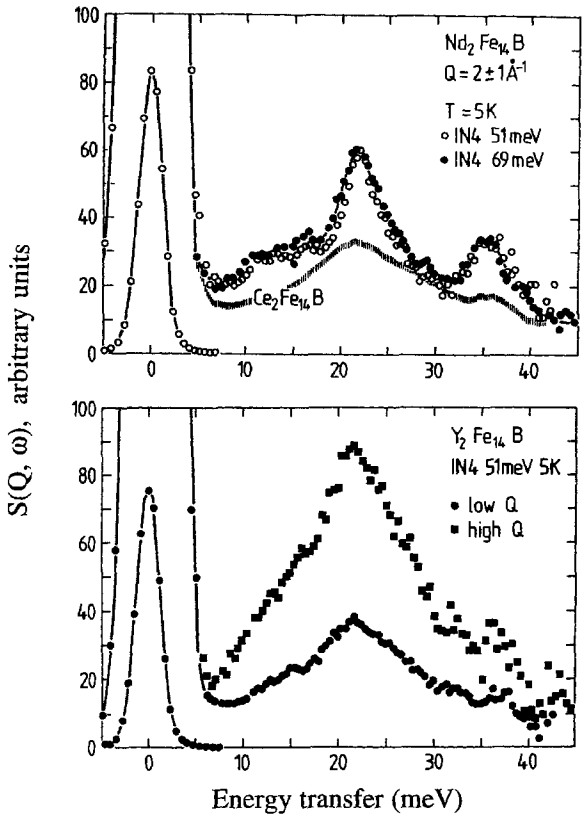

Fig. 32. INS spectra for polycrystalline $Nd_2Fe_{14}B$, $Ce_2Fe_{14}B$ and $Y_2Fe_{14}B$ intermetallics measured at 5 K with incident neutron energies ranging from 50 to 70 meV. The data for Nd and Ce are displayed at small Q values, where magnetic scattering is dominant. The data for $Y_2Fe_{14}B$ are displayed for both low and high values of Q. Peaks at approximately 22 and 35 meV correspond to transitions between the ground and first and second excited states calculated using CF and exchange parameters adapted from magnetization data (from Loewenhaupt et al. 1990).

High resolution INS studies of polycrystalline $Dy_2Fe_{14}B$ (Loewenhaupt et al. 1995a) reveal a detailed fine structure at low temperatures with a dominant excitation at 12 meV, a small shoulder to this line at 11 meV and two further weak transitions at 3.8 and 5.5 meV (fig. 33). The dominant mode corresponds to the Fe molecular field, since the temperature dependence of this mode (followed up to the Curie point) is practically identical to the spontaneous magnetization observed for $Y_2Fe_{14}B$, but small deviations at 200 K (a small increase in energy) were proposed as arising from CF effects, which indicates that the level scheme of Dy is not purely Zeeman like. A spin wave model of the magnetic excitation spectrum for $Dy_2Fe_{14}B$, within the framework of a two sublattice model incorporating a single ion anisotropy (Ried et al. 1994), predicts only one sharp peak at 12 meV.

The single crystal data reported by Mayer et al. (1991, 1992) clearly highlights the general problem encountered in INS studies of these difficult systems. For $Y_2Fe_{14}B$, a low ly-

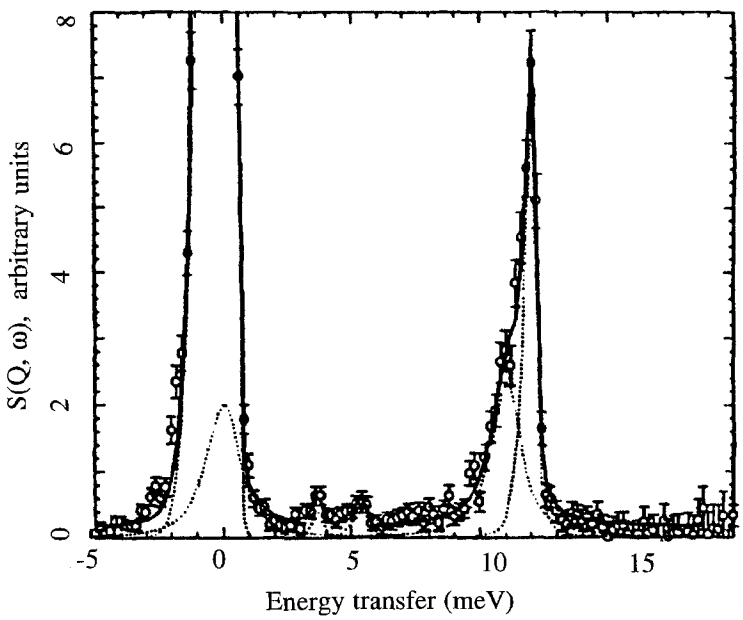

Fig. 33. INS spectra for polycrystalline $Dy_2Fe_{14}B$ measured at 12 K with an incident neutron energy of 25 meV (from Loewenhaupt et al. 1995a). Magnetic excitations are shown as dashed lines.

ing and highly dispersive acoustic excitation, arising from the Fe–Fe exchange, is observed. A small gap observed at the zone center of approximately 0.25 meV corresponds to the Fe sublattice anisotropy (Bolzoni et al. 1987). Similar measurements reported for $Nd_2Fe_{14}B$ reveal only one highly dispersive magnon mode which has a temperature dependent spin wave energy gap, highly reminiscent of the temperature dependence of the observed spin re-orientation transition. Mayer et al. (1991) analyzed the dispersive mode observed for $Nd_2Fe_{14}B$ with a highly approximative classical spin wave model incorporating a nearest neighbor Heisenberg exchange with uniaxial anisotropy (fig. 34). The agreement with the measured energy gaps and dispersion was extremely poor, as should be expected from such a model which neglects the expected strong itinerant effects and longer range exchange interactions.

The intersublattice coupling has also been directly determined by INS studies for $Gd_2Fe_{14}B$ (Loewenhaupt et al. 1996a) and $Gd_2Co_{14}B$ (Loewenhaupt et al. 1994b). The results for $Gd_2Fe_{14}B$ are in good agreement with band structure calculations (Liebs et al. 1993) and for both Fe and Co compounds, the coupling strengths are also in agreement with experimental determinations using HFFP (High Field Free Powder) magnetization measurements (Liu et al. 1994).

Interpretation of INS data for this series, even if performed on single crystals, is rendered difficult by the crystal structure. New methods and techniques of investigation, perhaps using magnetic X-ray elastic and inelastic scattering, are clearly urgently needed.

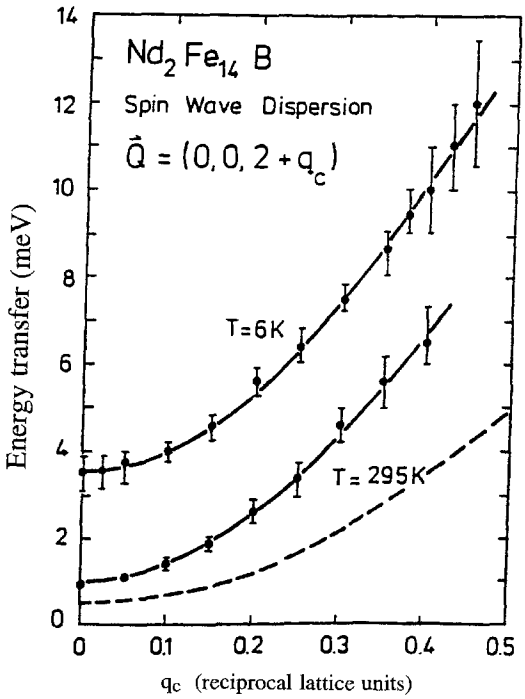

Fig. 34. Measured dispersion curves for magnetic excitations in a single crystal of $Nd_2Fe_{14}B$ at 6 K and 295 K. Solid lines are results of a least squares fit to $E = a + b[1 - \cos(\pi q_c)]$ around the reciprocal lattice vector $Q = (0\,0\,2)$. Numerical calculations of the dispersion, using a classical linear spin wave model with nearest neighbor interactions and an uniaxial anisotropy, are shown as dashed lines (from Mayer et al. 1992).

8. Inelastic neutron scattering experiments on orthorhombic lanthanides

The crystal field Hamiltonian for rare-earth ions residing in a site which possesses orthorhombic point symmetry is described by a total of nine parameters. Needless to say, in such a case, it is of utmost importance to use the largest number of experimental techniques for a complete and unambiguous determination of the level scheme and eigenfunction composition. To date, only a limited number of such systems have been investigated by INS. Compounds investigated are those which crystallize in the $CeCu_2$ structure whilst some limited INS data exists only for $PrCu_6$ and $NdCu_6$ (orthorhombic $CeCu_6$ structure, but with a monoclinic R point symmetry).

8.1. RCu_2

The magnetic and structural properties of this series have been reviewed by Luong and Franse (1995) and by Gignoux and Schmitt (1997). These compounds crystallize in the orthorhombic structure $CeCu_2$ (Larson and Cromer 1961). There exists a phenomenal series of different types of magnetic structures as well as a possible ferroquadrupolar ordering (in $PrCu_2$), the stability of which both appear to be determined in large part, if not totally,

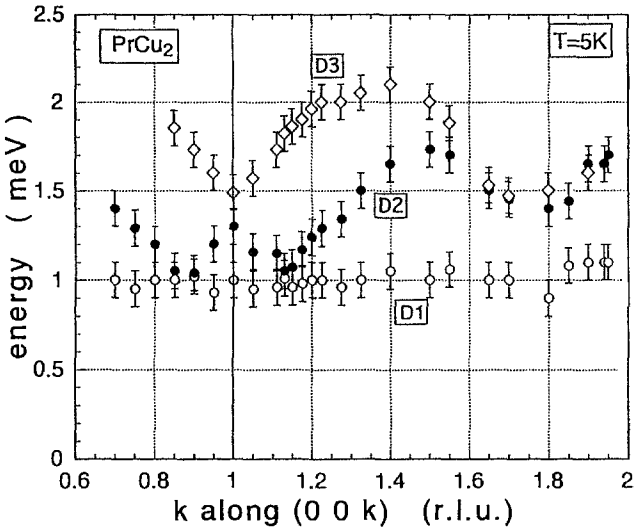

Fig. 35. Anisotropic dispersion of magnetic excitations for $PrCu_2$, measured at 5 K in the [0 0 1] direction. Open circles refer to J_y transitions and the other two sets of data refer to peaks for remaining two branches of J_x transitions (from Kawarazaki et al. 1995).

by the CF interaction. The intermetallic $PrCu_2$ has been investigated by INS for the past twenty years or so. It is a Van Vleck paramagnet, with a Jahn–Teller transition at 7.5 K. This structural distortion has been investigated by neutron diffraction and INS (Kjems et al. 1978). Later, the CF transitions (singlet-singlet) in the paramagnetic state have been investigated by INS on single crystal material (Kawarazaki et al. 1995). The J_x transitions are found to be strongly dispersive (fig. 35) whilst J_y transitions are weakly dispersive, a clear signature of an anisotropic RKKY interaction. Below the structural transition, metamagnetic transitions are observed (Settai et al. 1995). The highly anisotropic CF is confirmed by anisotropic thermal expansion and magnetostriction data (Takeuchi et al. 1996). A ferroquadrupolar ordering has been suggested as a possible origin of the structural distortion (Morin and Schmitt 1990). A combined analysis of INS, magnetic susceptibility, thermal expansion, magnetostriction and high field magnetization data have allowed a rather consistent set of CF parameters to be determined for $PrCu_2$ (Ahmet et al. 1996). In fig. 36 are displayed the susceptibility and high field magnetization data together with model calculations using the CF parameters contained in table 28. The data is adequately reproduced for the a and b directions, but the observed metamagnetic transition observed along c cannot be reproduced, even with inclusion of quadrupolar interactions.

In a similar fashion, the CF parameters for $NdCu_2$ have been determined (Gratz et al. 1991) in a combined analysis of INS, magnetization, specific heat, thermal expansion, and electrical resistivity data. The nine CF parameters were obtained using the Newman superposition model, from the energy level scheme comprising five doublets, clearly observed by INS (fig. 37). The specific heat measured below 1 K and in magnetic fields of up to 6 T has allowed for a rather definitive (B, T) phase diagram to be determined for $NdCu_2$

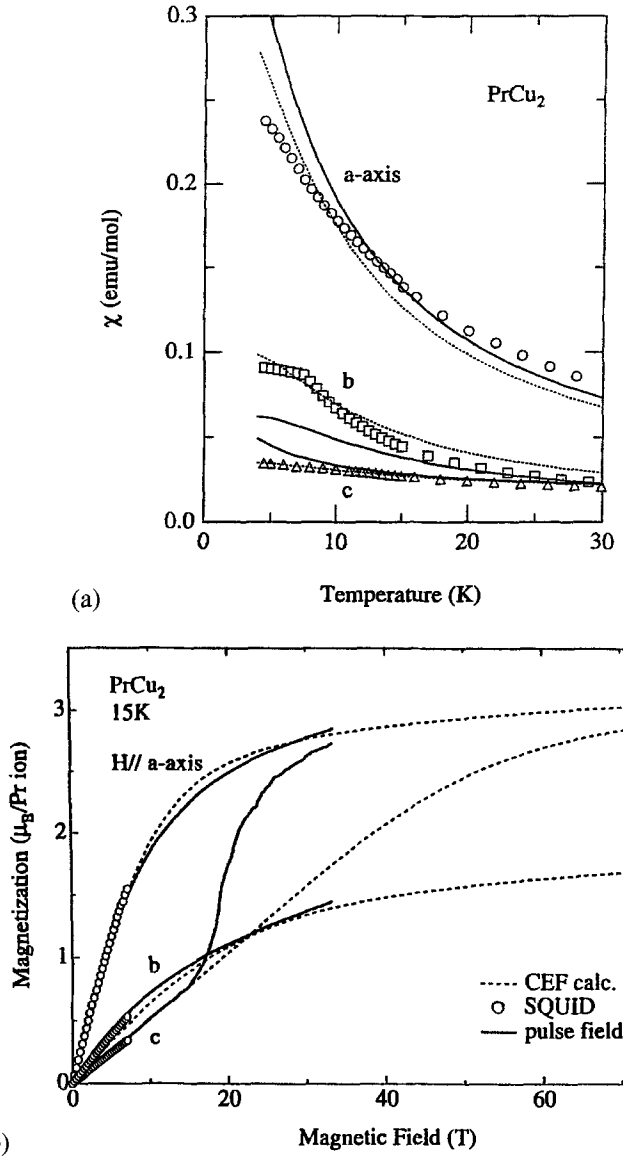

Fig. 36. (a) Temperature dependence of the magnetic susceptibility for $PrCu_2$, measured along the three crystallographic directions *a*, *b* and *c*. Dashed lines are calculated using CF level schemes determined by INS below 8 K. (b) Magnetization curves for $PrCu_2$ at 15 K measured along the *a*, *b* and *c* axes. Circles and solid lines are experimental data, whilst broken lines are calculated from CF parameters contained in table 28 (from Ahmet et al. 1996).

TABLE 28

Crystal field coefficients for orthorhombic $RECu_2$ ($CeCu_2$ structure) intermetallics determined by INS experiments. Units for A_n^m are in Kr_0^{-n}.

	Compound			
	$PrCu_2$	$NdCu_2$	$ErCu_2$	$TmCu_2$
A_2^0	−203.6	−189.0	−152.9	−134.4
A_2^2	−181.3	−218.4	−120.1	−175.9
A_4^0	−23.7	−26.3	−53.2	−46.9
A_4^2	−58.9	−11.9	−24.8	20.4
A_4^4	199.6	−23.1	53.2	−18.8
A_6^0	−0.96	−0.97	−2.0	−2.4
A_6^2	−15.2	−0.24	−4.7	−10.2
A_6^4	−31.1	−0.86	−9.7	1.97
A_6^6	−40.7	−7.44	−29.7	−25.9
Ground state	$\Gamma_5^{(1)}$			
Ref.	[1–4*]	[5]	[6,7]	[8,9]

* Single crystal magnetization measurements, using INS data from references [1–3].

References:

[1] Kjems (1977)
[2] Kjems et al. (1978)
[3] Kawarazaki et al. (1995)
[4] Ahmet et al. (1996)
[5] Gratz et al. (1991)
[6] Gubbens et al. (1991)
[7] Lange (1992)
[8] Gubbens et al. (1992)
[9] Heidelmann (1992)

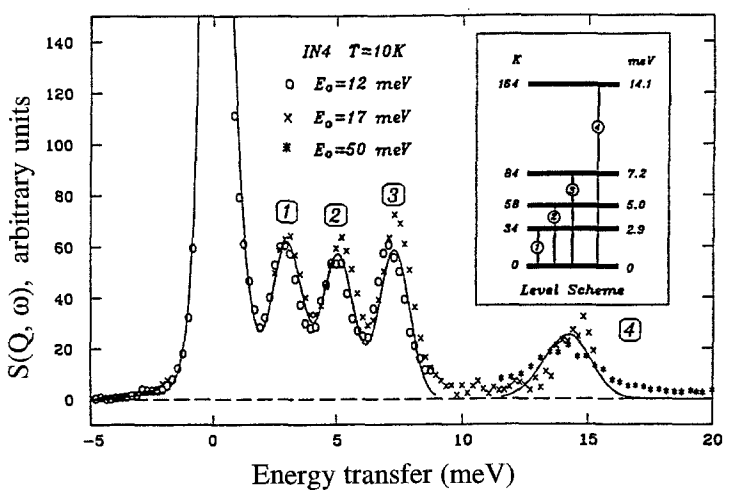

Fig. 37. Inelastic neutron scattering spectra for $NdCu_2$, measured in the paramagnetic state ($T = 10$ K). These measurements have been obtained for different incident neutron energies. The numbered levels correspond to successive CF excitations from the ground state doublet to the four excited doublet levels, giving an overall CF splitting of 14 meV (from Gratz et al. 1991).

(Sieck et al. 1995). The magnetic structure, as determined by neutron diffraction (Arons et al. 1994; Loewenhaupt et al. 1995b, 1996b; Kawarazaki et al. 1996) exhibits a rather amazing sequence of incommensurate amplitude (at the Néel point) and long period commensurate modulations. These appear to be stabilized by CF and anisotropic exchange interactions.

The CF interaction for two compounds in this series, $ErCu_2$ and $TmCu_2$, have also been investigated by INS. Again, a myriad of magnetic structures are present. For $ErCu_2$, two single crystal neutron diffraction investigations (Lebech et al. 1987; Hashimoto et al. 1995) indicate up to two distinct incommensurate phases below the Néel point (11.5 K). Metamagnetic transitions in the magnetization curves are strongly reminescent of dominant CF effects, with a large CF associated anisotropy in the *b*-direction (Hashimoto et al. 1979). Mössbauer ^{155}Er spectroscopy also confirm the strong anisotropy along the *b*-axis (Gubbens et al. 1991) and a good agreement is observed between these and INS data (Lange 1992). A similar situation pertains to $TmCu_2$, where three different ordered magnetic phases exist below the Néel point (Heidelmann et al. 1992). The temperature dependence of the electric quadrupole splitting, as measured by Mössbauer ^{169}Tm spectroscopy, combined with the usual INS, magnetization, specific heat and thermal expansion data (Sima et al. 1989; Gubbens et al. 1992; Heidelmann 1992) yield a set of CF parameters which are broadly consistent with those determined for the Pr, Nd and Er compounds. As already discussed by Gignoux and Schmitt (1995, 1997), inclusion of higher order coupling interactions could lead to an improvement in the modeling of the magnetic structures adopted by these systems. This is exemplified by the results for $PrCu_2$.

The CF coefficients for this series, as determined by combined INS and other techniques are displayed in table 28. Throughout the series, there is a reasonable consistency in the signs and magnitudes of the determined coefficients, with the particular exception of A_4^4, where a change in sign is apparent. This must reflect the global difficulty in determining a large set of consistent CF parameters in systems with such a low CF symmetry.

8.2. RCu_6

For this series, INS data exists for $CeCu_6$, $PrCu_6$ and $NdCu_6$. These compounds crystallize in the $CeCu_6$ structure (Cromer et al. 1960). The magnetic properties and incipient structural instabilities for the series are reviewed by Gignoux and Schmitt (1997). The compound $CeCu_6$ is a very thoroughly investigated (by INS) heavy fermion system (Walter et al. 1986a; Loewenhaupt and Fischer 1993a, 1993b), whilst INS studies have also been performed for the compounds $PrCu_6$ and $NdCu_6$. The R ion resides in a site with a monoclinic point symmetry and consequently the CF is described by a total of 14 parameters. Needless to say, a complete determination of these is an almost impossible task. The level scheme and dipole matrix elements between levels were obtained by a careful profile analysis of the inelastic transitions, including a modeling of non-magnetic scattering from multi-phonon processes (Walter et al. 1986a, 1986b). A total of nine transitions at low temperatures were clearly identified for $PrCu_6$ and one should expect nine non-magnetic singlets (Walter et al. 1986c). The level scheme with associated transition matrix elements is displayed in fig. 38. The ground state is composed of two extremely close lying singlets (separated by approximately 0.23 K). This quasi-doublet ground state displays no

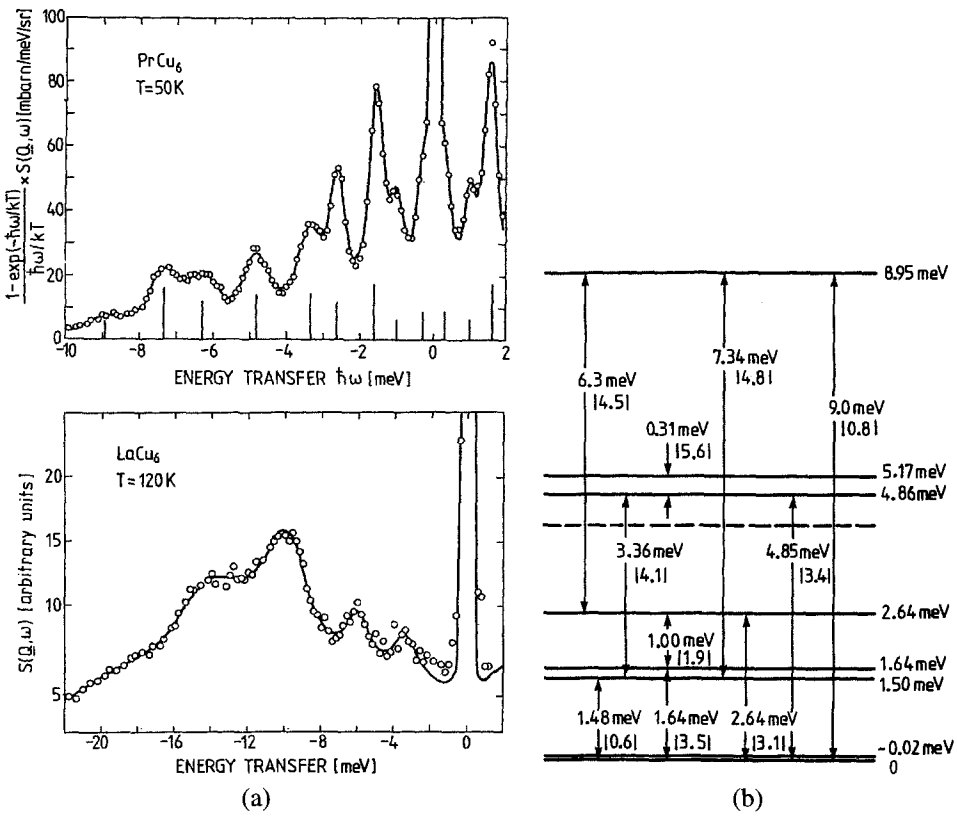

Fig. 38. Measured INS spectra for $PrCu_6$ at 50 K, and non-magnetic $LaCu_6$ at 120 K, together with the determined CF level scheme for the nine singlets and associated dipolar transition probabilities (from Walter et al. 1986c).

quasi-elastic scattering and the effective moment obtained from this analysis is in broad agreement with static magnetic susceptibility data (Andres and Bucher 1972).

A similar result was obtained for $NdCu_6$ (Walter et al. 1988), where a much simpler CF level scheme is expected for a Kramers ion with $J = 9/2$, i.e., only five doubly degenerate levels. The level scheme was obtained from a line profile analysis, again after a careful subtraction of the one-phonon and multi-phonon contributions. The proposed CF level scheme was used to calculate the CF contribution to the specific heat and the static susceptibility resulting in a satisfying agreement with measured data for these (Onuki et al. 1986). Higher order CF terms appear to govern the CF splitting for this compound. Point contact spectroscopy revealed three CF transitions at the same energies as observed by INS, thus adding further confirmation for the proposed level scheme (Yonemitsu et al. 1991).

The overall CF splitting for these compounds is rather small (about 100 K). There exist at present no qualitative theoretical calculations of the CF splitting in these systems, but the uniqueness of the INS technique for probing CF eigenstates in materials with such a

low CF point symmetry, clearly demonstrates that it can be usefully extended to similarly complex systems.

9. Inelastic neutron scattering experiments on hydrides and carbides of lanthanide intermetallics

Rare earth metal hydrides form phases which are stable over large composition ranges. The dihydrides RH_2 crystallize in the CaF_2-type structure, with hydrogen atoms occupying tetrahedral sites. Trihydrides, RH_3, crystallize in the RH_3-type structure, with octahedral sites also occupied. In both structures, the rare earth nearest neighbor environment consists of eight H atoms located on tetrahedral sites. The magnetic properties of rare earth metal hydrides are naturally enhanced, due to an observed lattice expansion associated with hydrogen absorption. The magnetism of hydrides has been reviewed by Wiesinger and Hilscher (1991). Structural and electronic properties of hydrogen in rare-earth metals have been reviewed by Vajda (1995). Hydrogen absorption in intermetallic compounds is reviewed by Buschow (1984).

Inelastic neutron scattering studies of the CF splitting in rare earth metal hydrides are not very numerous. The most detailed studies exist for the Pr deuterides. Knorr and Fender (1977) and Knorr et al. (1978b) determined the CF splitting in Pr deuterides, PrD_2 and $PrD_{2.5}$. For the former compound, the CF is cubic, but for the latter, a determination of the CF parameters is rendered difficult. This is due to a non statistical occupation of the octahedral sites which generates a CF of orthorhombic symmetry. Successive investigations on $PrD_{1.95}$ assign a Γ_5 state to the ground state, with an overall CF splitting of 41 meV (Arons et al. 1986, 1987). This magnetic ground state is confirmed in an analysis of the spin-disorder resistivity for PrH_{2+x}, $x = 0, 0.08$ (Burger et al. 1990).

Inelastic neutron scattering measurements have also been carried out on light rare earth carbides, RC_2, which crystallize in the CaC_2-type structure (Atoji 1961) and order antiferromagnetically, with moments aligned along the c-axis (Atoji 1967). The R site in this structure has a tetragonal point symmetry. Wegener et al. (1981) report INS data for CeC_2 whilst Wegener et al. (1982) report measurements for the other light rare earth carbides, PrC_2 and NdC_2. The low temperature ordered moments are considerably smaller than their free ion values. Crystal field parameters obtained from an analysis of the INS data reproduce the values of the ordered moments, but due to the difficulty in determining five CF parameters uniquely from weakly resolved CF transitions, the global reliability of these parameters for the whole RC_2 series must be treated with caution.

10. Icosahedral crystal fields in lanthanide intermetallics

The crystal field splitting of rare-earth ions in icosahedral symmetry has been treated in detail by group theoretical and numerical calculations (Walter 1987a, 1987b) which followed earlier theoretical treatments (Judd 1957; Golding et al. 1985). The calculation is based on assumption of an R ion surrounded by 12 next nearest neighbors with a simple and highly

TABLE 29

Crystal field states $|\Gamma_i\rangle$, in the representation $|J, M_J\rangle$, and associated dipolar matrix elements $|\langle\Gamma_i|J_z|\Gamma_j\rangle|^2$ for the icosahedral CF operator O_6^5 tabulated for $J = 9/2$ and $J = 4$ (adapted from Walter 1987b).

$J = 9/2$

	CF state	Γ_8	Γ_9
Γ_8	$0.529\,\|\pm 9/2\rangle - 0.849\,\|\mp 1/2\rangle$ $0.917\,\|\pm 7/2\rangle - 0.400\,\|\mp 3/2\rangle$	16.2	16.8
Γ_9	$0.849\,\|\pm 9/2\rangle + 0.529\,\|\mp 1/2\rangle$ $0.917\,\|\pm 3/2\rangle + 0.400\,\|\mp 7/2\rangle$ $1.000\,\|\pm 5/2\rangle$		32.7

$J = 4$

	CF state	Γ_5	Γ_4
Γ_5	$0.683\,\|\pm 4\rangle - 0.730\,\|\mp 1\rangle$ $0.966\,\|\pm 3\rangle - 0.258\,\|\mp 2\rangle$ $1.000\,\|0\rangle$	18.9	14.4
Γ_4	$0.730\,\|\pm 4\rangle + 0.683\,\|\mp 1\rangle$ $0.258\,\|\pm 3\rangle + 0.966\,\|\mp 2\rangle$		24.55

spherically symmetrical icosahedral co-ordination. Due to the high symmetry of the icosahedron, the CF Hamiltonian is simple, being of the form (with the z-axis parallel to the five-fold axis and the threefold axis parallel to the x–z plane):

$$H_{\mathrm{CF}} = B_6\left(O_6^0 - 42O_6^5\right) \tag{10.1}$$

with

$$O_6^5 = \frac{1}{4}\left[J_z\left(J_+^5 + J_-^5\right) + \left(J_+^5 + J_-^5\right)J_z\right]. \tag{10.2}$$

(O_6^0 is tabulated in Hutchings, 1964.) The CF Hamiltonian is governed by only one parameter. The CF level schemes derived here are expected to be applicable to *metallic glasses* as well as to quasicrystals. The irreducible representations of the icosahedral group I_h for all the rare-earths have been tabulated in detail by Walter (1987b). In addition, numerical calculations of the CF eigenstates, dipole transition matrix elements $\langle\Gamma_i|J_z|\Gamma_j\rangle^2$, static susceptibility and specific heat for R ions in icosahedral symmetry are presented in the same article. These are tabulated for ions with $J = 4$ and $J = 9/2$ in table 29. It is obviously a classic reference work for experimental studies of the magnetic properties of R ions in systems displaying an icosahedral symmetry. Further tabulations can be found in Görller-Walrand and Binnemans (1996).

Neutron diffraction and magnetization measurements confirm the existence of antiferromagnetic interactions in icosahedral $R_8Mg_{42}Zn_{50}$ (R = Tb, Dy, Ho and Er) intermetallics,

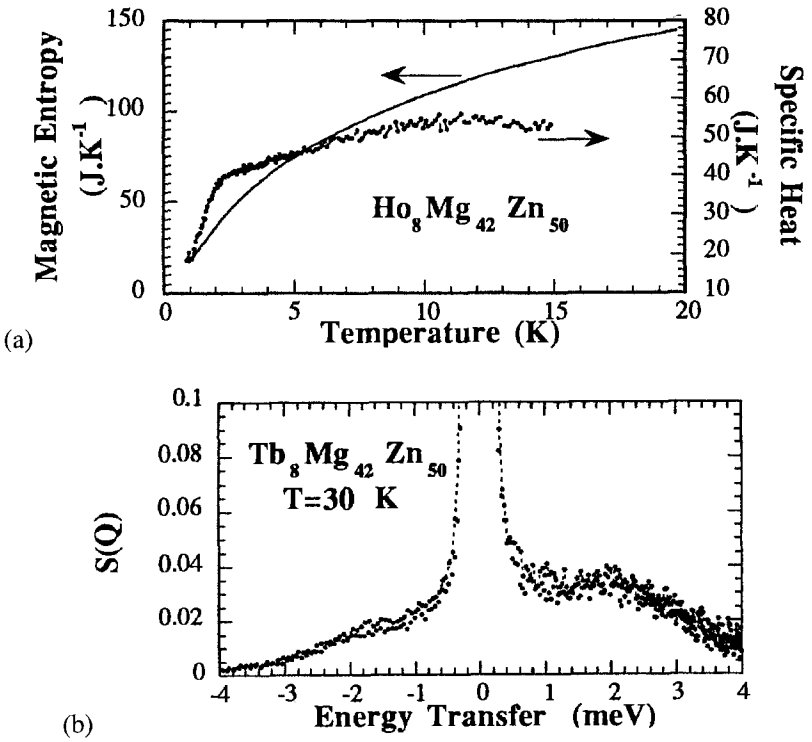

Fig. 39. (a) Temperature dependence of the magnetic entropy and magnetic specific heat for icosahedral quasicrystalline $Ho_8Mg_{42}Zn_{50}$. The magnetic entropy at 20 K has almost reached its maximum value of $R\ln(2J+1) =$ 188 Joules per degree K. (b) Magnetic excitation spectrum, measured at 30 K, for icosahedral quasicrystalline $Tb_8Mg_{42}Zn_{50}$ (after Charrier and Schmitt 1997b).

which are the only known rare-earth based icosahedral quasicrystals (Charrier et al. 1997; Charrier and Schmitt 1997a). The low ordering temperatures are comparable to those observed in crystalline intermetallics which have similar compositions, such as R_2Zn_{17} and RZn_{12}. Preliminary INS measurements of the magnetic excitations in $R_8Mg_{42}Zn_{50}$ icosahedral quasicrystals, together with specific heat and magnetic entropy data indicate a broad distribution of CF excitations, in the range 0.5 to 4 meV (Charrier and Schmitt 1997b). The INS, magnetic entropy and specific heat data (fig. 39) imply that, due to the very high symmetry of the icosahedron, crystal field effects in these systems are much weaker than in crystalline intermetallics. The degeneracy of the multiplets are raised only very weakly, confirming the high symmetry of the icosahedron. Walter (1987a, 1987b) has pointed out that not all icosahedra are compatible with a long range translational order. In the special case of quasicrystals, a long range orientational order as well as a "quasitype" of translational order most likely exist. Unfortunately, details of the local environment around the rare earth and the occupancy at different crystallographic sites, are at present almost unknown. In this context, a continuous distribution of 4f levels has been proposed.

11. Crystal fields in amorphous lanthanide alloys

Crystal field splittings are obviously extremely sensitive to the local structure comprising the environment around the R ion, particularly the distribution of bond angles, which is difficult to obtain even from diffraction techniques for structurally amorphous systems. This sensitivity should allow the local topology such as that present in amorphous rare-earth alloys to be investigated and modeled. The proposed random nature of the CF in such amorphous systems is based on model calculations and some bulk magnetic measurements, with a simple distribution of quadratic uniaxial crystal fields (Harris et al. 1973; Fert and Campbell 1978; Bieri et al. 1982).

Experimental investigations concerning INS of CF states in metallic glasses are extremely scarce. Amorphous Y–Cu alloys, where 5% of the Y was diluted by Ce, Pr and Er were investigated by INS (Rainford et al. 1982) and a well defined inelastic CF transition at 2 meV was observed only for Er alloys. More detailed INS investigations and modeling of CF states in amorphous $PrNi_5$ have, however, been carried out in the last few years. The motivation for studying $PrNi_5$ is that in the crystalline state, the hexagonal CF has been abundantly characterized by INS, and the degree of crystallization (or amorphization) can be reliably controlled by a simple heat treatment. The three pronounced low temperature CF transitions from the Γ_4 ground state observed in polycrystalline $PrNi_5$, are absent in

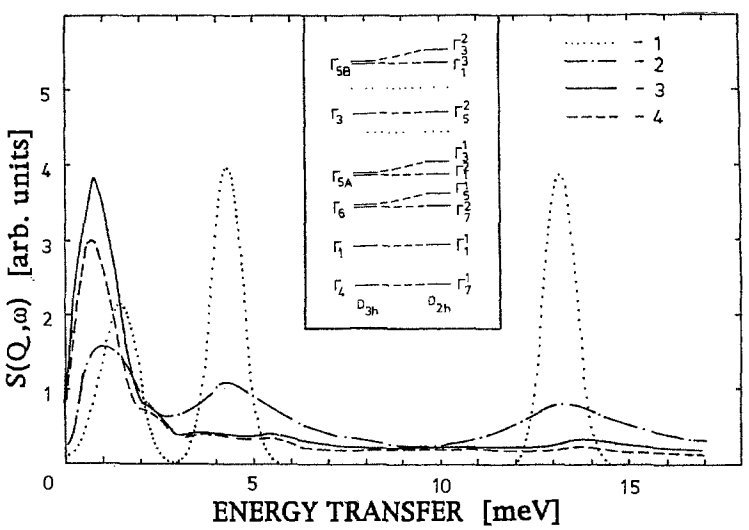

Fig. 40. Calculated scattering law $S(\theta, \omega)$ for the crystalline and amorphous phases of $PrNi_5$. Curve 1 – model spectrum for polycrystalline material at $T = 15$ K, calculated from CF parameters determined for the hexagonal phase. Curve 2 – the result of averaging over only the lattice parameters of the model spectrum corresponding to the hexagonal CF Hamiltonian, at $T = 15$ K. Curve 3 – result of averaging the model spectrum calculated taking into account an orthorhombic distortion of the hexagonal symmetry, at 15 K. Curve 4 – same as curve 3, but calculated for $T = 50$ K. The inset shows the CF level schemes for hexagonal and orthorhombic symmetries (corresponding point groups are D_{3h} and D_{2h}, respectively) (from Alekseev et al. 1996).

amorphous $PrNi_5$ (Alekseev et al. 1991, 1992a, 1992b). Rather a broad and strong magnetic signal located near the elastic peak, and extending approximately 10 meV into the inelastic part of the spectrum, is observed. The nonlinearities observed in the magnetization curves of amorphous $PrNi_5$ (Alekseev et al. 1995) is also strong evidence for the existence of ferromagnetic correlations. A way to model the disorder is to progressively lower the symmetry of the CF, by introduction of an orthorhombic distortion. In this case, the degeneracy of the ground state multiplet in crystalline $PrNi_5$ is removed and the associated distortion allows for transitions between the ground and low lying levels, transitions which are otherwise forbidden for a hexagonal CF. This gives rise to a characteristic broad structure in the low energy part of the INS spectrum, a feature observed experimentally (fig. 40). The magnetic contribution to the specific heat, the magnetization as well as the INS data, are reasonably accounted for on the basis of this "deformed crystal" model for amorphous $PrNi_5$ (Alekseev et al. 1996).

12. Theoretical aspects of crystal fields in lanthanide intermetallics

An abundant quantity of experimentally determined CF coefficients for a large number of rare-earth intermetallics now exists. Within a given series, there are consistent trends in the signs and variations of these coefficients. There appear to be three principal contributions to the CF in rare-earth intermetallics (Das and Ray 1970): (a) a point charge like contribution, (b) the contribution from conduction electrons, and (c) overlap and covalency contributions from the ligand ions. The APW (Augmented Plane Wave) method had already been suggested as a suitable approach for attempting realistic band calculations of CF parameters in metals (Lethuillier et al. 1977). The predictive powers of the PC (Point Charge) approximation are noticeably lacking in metallic systems due to charge screening and 5d VBS (Virtual Bound States), features which are caused by the conduction electrons. Improvements to the PC model proposed a splitting of the d-charge distribution by the electric field of nearest neighbor ions (quasi bound 5d states). This splitting is subsequently experienced by the 4f-electron states (Williams and Hirst 1969).

Given the obvious general inadequacies of the PC approximation for metallic systems, a large effort has been devoted to numerical *ab initio* computation of the CF interaction, computations which are based on more firmer realistic microscopic physical principles for metals (Coehoorn 1991; Coehoorn and Daalderop 1992). This is exemplified in the RX system, R = Er, X= Rh, Cu, Ag, Zn and Mg (cubic CsCl structure) where the CF parameters were determined some 20 years ago. Schmitt performed calculations for this series (Schmitt 1977, 1979), using APW techniques and partially accounted for the variation in the fourth order CF parameters, obtaining a good order of magnitude for A_4^0. Disagreement in the calculation with the observed parameters included, however, much smaller sixth order A_6^0 parameters as well as rather large differences between RCu and RAg intermetallics. Inclusion of exchange contributions as well as the Coulomb part did not lead to any significant improvement. Later computations for the RX series, using the LAPW method (Linear Augmented Plane Wave) by Novák and Kuriplach (1992) and within the LSDA (Local Spin Density Approximation, Fähnle (1995)) are in encouraging overall agreement with experimentally observed trends (Divis and Kuriplach 1995). Similar results are obtained for R impurities in noble metals (Steinbeck et al. 1994) as well as for RNi_5 compounds

(Novák and Kuriplach 1994). This is also the situation obtained for the RAl_2 series (Divis et al. 1995). Problems remain, however, in obtaining a total microscopic description of the CF potential. For example, first principles density functional computations of CF parameters in RCo_5 intermetallics lead to a correct sign for all the parameters but nevertheless considerably overestimate A_2^0 (Richter et al. 1992, 1993a, 1993b). Later and more successful first principles calculations, within the LSDA approximation, applied to cubic PrSb and TmSb intermetallics, now propose that crystal field excitations should be more properly considered as "quasi-particle" excitations which now consist of a 4f excitation *together* with the associated cloud of conduction electrons (Brooks et al. 1997). A review of density functional theory of the ground state magnetic properties of rare-earth and actinide intermetallics is reported by Brooks and Johansson (1993).

A generalized phenomenological model, the Newman superposition model of crystal fields (Newman 1971; Newman and Ng 1989), employed widely even by experimentalists because of its simplicity, appears to be valid in a very general way for rare-earth intermetallics. In this approach, the total CF experienced by the R ion is a sum of axially symmetric contributions from nearest neighbors only. Calculations on this basis have been performed for the following systems; RX (CsCl structure, Newman (1983)), cubic RAl_2, RPd_3, RB_6, RNi_2, hexagonal RNi_5 (Divis 1991), tetragonal RCu_2Si_2 (Goremychkin et al. 1992; Goremychkin et al. 1996) and orthorhombic RCu_2 intermetallics (Gratz et al. 1991). The "superposed" CF parameters are found to be in remarkable agreement with those determined by INS or other techniques. The model clearly represents a reasonable basis for more advanced, sophisticated ab-initio electronic band structure calculations.

Much simplified analytical approximations have also been utilized in accounting for the CF parameters. The screening of the point charges by the conduction electrons, using Thomas–Fermi and Hartree type screening functions, were calculated by Duthie and Heine (1979). Friedel like oscillations in the effective electrostatic interaction between R ions were considered by Orlov and Jensen (1988) in analytical calculations of the CF parameters for dilute R alloys. Another phenomenological approach is the *analytical* screened charge model which treats the conduction electron contribution as a weakly disturbed linearized Thomas–Fermi gas (Skomski 1994; Skomski and Coey 1995). In this approximation, the predicted zero-temperature anisotropy constants for $R_2Fe_{17}N_3$ and $RFe_{11}N$ compounds are even of the correct sign and order of magnitude (Hurley 1993).

It can be expected that, on the basis of CF parameters determined in particular by INS techniques, similar numerical and analytical computations can now be safely attempted on more extensive series of rare-earth intermetallics.

13. Conclusion

The technique of neutron inelastic scattering is a unique and powerful spectroscopic technique which has been used with large effect for the determination of CF levels and level composition in an enormous number of rare-earth intermetallics. An intimate knowledge of the CF interaction allows us to model, and understand in a more profound way, the principle mechanisms responsible for what are truly beautiful and complex magnetic structures and phase transitions in systems composed of stable lanthanide intermetallics. There still remains much to be done, as there exist many systems which have not yet been investigated

in any way by INS, including cubic compounds. Measurements on single crystal materials, when they can be synthesized, are always highly desirable, since the transverse and longitudinal components of non-dispersive CF transitions (and transitions which are highly dispersive in the presence of magnetic order) can be identified clearly. For systems where the R ion resides in a site of low symmetry, which makes a determination of the large number of CF parameters an almost impossible task, the energy level scheme and intensity of transitions can, in principle, be determined. With such information at hand, the temperature dependence of the specific heat and the low temperature magnetic moment can, for example, be suitably modeled within the CF formalism. It is hoped that this chapter will strongly encourage even those who are only vaguely familiar with neutron scattering to contemplate use of INS techniques in the determination of magnetic excitations, and more particularly CF transitions, in rare-earth intermetallic compounds.

Symbols and abbreviations

A_m^n	crystal field coefficients
B_m^n	crystal field parameters
APW	augmented plane wave
barn	unit of scattering cross-section ($= 10^{-28}$ m^2)
β	$1/(k_B T)$
c	velocity of light
CF	crystalline electric field
D	dispersion stiffness constant
e	electron charge
E_F	Fermi energy level
E_i	incident neutron energy
E_f	final neutron energy
EPR	electron paramagnetic resonance
$f(\boldsymbol{Q})$	magnetic form factor
Γ_i	irreducible representation of a symmetry group
g_J	Landé g-factor
g_N	neutron gyromagnetic ratio $= 1.91$
$\hbar$	Planck's constant$/2\pi$
$\omega(\boldsymbol{q})$	energy for magnetic excitations with a wavevector $\boldsymbol{q}$
INS	inelastic neutron scattering
$\boldsymbol{J}$	angular momentum operator
$\boldsymbol{J}_\pm$	raising and lowering operators of the angular momentum
J_z	z-component of the angular momentum operator
$J(\boldsymbol{q})$	Fourier transform of the bilinear exchange interaction
$\boldsymbol{k}$	propagation vector of magnetic structure
$\boldsymbol{k}_i$	initial neutron wavevector
$\boldsymbol{k}_f$	final neutron wavevector
k_B	Boltzmann's constant
LAPW	linear augmented plane wave
LCAO	linear combination of atomic orbitals

LLW	Lea, Leask and Wolf formalism for cubic crystal fields
LSDF	local spin density functional
m_e	electron mass
m_N	neutron mass
meV	milli-electron Volts
N_A	Avogadro's constant
N	number of rare-earth ions per unit cell
NMR	nuclear magnetic resonance
O_m^n	Stevens operator equivalents
$\boldsymbol{q}$	wavevector of a magnetic excitation
$\boldsymbol{Q}$	momentum transfer or scattering vector ($= \boldsymbol{k}_i - \boldsymbol{k}_f$)
R	rare-earth
$\boldsymbol{R}_i$	atomic position
r_e	electron radius
r_0	atomic radius
RKKY	Rudermann–Kittel–Kasuya–Yosida interaction
$S(\boldsymbol{Q}, \omega)$	scattering law
T	temperature (Kelvin degrees)
T_c	Curie temperature (Kelvin degrees)
T_N	Néel temperature (Kelvin degrees)
θ_p	paramagnetic Curie temperature
μ_B	magnetic moment, in Bohr magnetons
$\chi(\boldsymbol{Q}, \omega, T)$	dynamic magnetic susceptibility
χ	bulk magnetic susceptibility

References

Abadia, C., P.A. Algarabel, B. García-Landa, M.R. Ibarra, A. del Moral, N.V. Kudrevatykh and P.E. Markin, 1998, J. Phys. Condens. Matter **10**, 349.

Abell, J.S., P. Hendy, E.W. Lee and K. Al-Rawi, 1979, J. Phys. C **12**, 3551.

Abell, J.S., A. del Moral, M.R. Ibarra and E.W. Lee, 1983, J. Phys. C **16**, 769.

Aeppli, G. and C. Broholm, 1994, in: Handbook on the Physics and Chemistry of Rare Earths, Vol. 19, eds K.A. Gschneidner Jr., L. Eyring, G.H. Lander and G.R. Choppin (Elsevier, Amsterdam) ch. 131, p. 123.

Ahmet, P., M. Abliz, R. Settai, K. Sugiyama, Y. Onuki, T. Takeuchi, K. Kindo and S. Takayanagi, 1996, J. Phys. Soc. Japan **65**, 1077.

Akimenko, A.I., N.M. Ponomarenko, I.K. Yanson, S. Janos and M. Reiffers, 1984, Sov. Phys. Solid State **26**(8), 1374.

Aksenov, V.L., Th. Frauenheim, N.M. Plakida and J. Schreiber, 1981, J. Phys. F: Metal Phys. **11**, 905.

Aksenov, V.L., E.A. Goremychkin and Th. Frauenheim, 1983, Physica B **120**, 176.

Albanesi, E.A., H.M. Passawski and M.C.G. Passeggi, 1989, Physica B **154**, 397.

Alekseev, P.A., I.P. Sadikov, I.A. Markova, E.M. Savitskii, V.F. Terekhova and O.D. Chistyakov, 1976, Sov. Phys. Solid State **18**, 389.

Alekseev, P.A., I.P. Sadikov, A.A. Filipov, E.M. Savitskii, V.F. Terekhova, I.A. Markova and O.D. Chistyakov, 1979, J. Physique **40**(C5), 147.

Alekseev, P.A., A. Andreef, H. Greissmann, L.P. Kaun, B. Lippold, W. Matz, I.P. Sadikov, O.D. Chistyakov, I.A. Markova and E.M. Savitskii, 1980, Phys. Status Solidi B: **97**, 87.

Alekseev, P.A., I.P. Shadikov, Yu.L. Shitikov, I.A. Markova, O.D. Chistyalov, E.M. Savistkii and J. Kjems, 1982, Phys. Status Solidi **114**, 161.

Alekseev, P.A., E.A. Goremychkin, B. Lippold, E. Mühle and I.P. Sadikov, 1983, Phys. Status Solidi B: **119**, 651.

Alekseev, P.A., V.N. Lazukov, V.G. Orlov, I.P. Sadikov, J.-B. Suck and V.V. Kotunov, 1991, Europhys. Lett. **15**, 29.

Alekseev, P.A., E.S. Klementjev, V.N. Lazukov, V.G. Orlov, I.P. Sadikov and J.B. Suck, 1992a, Europhys. Lett. **18**, 505.

Alekseev, P.A., V.N. Lazukov, V.G. Orlov, I.P. Sadikov and J.-B. Suck, 1992b, Physica B **180–181**, 167.

Alekseev, P.A., V.N. Lazukov, V.G. Orlov, I.P. Sadikov, V.I. Nizhankovskii, J.-B. Suck and H. Schmidt, 1995, J. Magn. Magn. Mater. **140–144**, 861.

Alekseev, P.A., M.N. Kchlopkin, V.N. Lazukov, V.G. Orlov, I.P. Sadikov, J.-B. Suck and H. Schmidt, 1996, Phys. Rev. B **54**, 3884.

Amara, M. and P. Morin, 1996, Physica B **222**, 61.

Amara, M., P. Morin and J. Rouchy, 1994a, J. Magn. Magn. Mater. **130**, 115.

Amara, M., R.M. Galéra, P. Morin, T. Veres and P. Burlet, 1994b, J. Magn. Magn. Mater. **130**, 127.

Amato, A., W. Bührer, A. Grayevsky, F.N. Gygax, A. Furrer, N. Kaplan and A. Schenck, 1992, Solid State Commun. **82**, 767.

Amoretti, G., O. Ori and A. Blaise, 1986, J. Less-Common Met. **121**, 199.

Andreeff, A., L.P. Kaun, B. Lippold, W. Matz, N.I. Moreva, K. Walther, 1978, Phys. Status Solidi B: **87**, 535.

Andreeff, A., H. Gresimann, L.P. Kaun, W. Matz, P.A. Alekseev, I.P. Sadikov, O.D. Chistyakov, I.A. Markova and E.M. Savitskii, 1980, in: Crystalline Electric Field and Structural Effects in f-Electron Systems, eds J. Crow, R.P. Guertin and T.W. Mihalisin (Plenum Press, New York) p. 205.

Andreeff, A., E.A. Goremychkin, H. Griessmann, L.P. Kaun, B. Lippold, W. Matz, O.D. Chistyakov, E.M. Savitskii and P.G. Ivanitskii, 1981, Phys. Status Solidi B: **108**, 261.

Andreeff, A., Th. Frauenheim, E.A. Goremychkin, H. Greissmann, B. Lippold, W. Matz, O.D. Chistyakov and E.M. Savitskii, 1982, Phys. Status Solidi B: **111**, 507.

Andreev, A.V., 1995, in: Handbook of Magnetic Materials, Vol. 8, ed. K.H.J. Buschow (Elsevier, Amsterdam) ch. 2, p. 59.

Andres, K. and E. Bucher, 1972, J. Low. Temp. Phys. **9**, 267

Andres, K., E. Bucher, P.H. Schmidt, J.P. Maita and S. Darack, 1975, Phys. Rev. B **13**, 4364.

Arnold, G. and N. Nereson, 1969, J. Chem. Phys. **51**, 1495.

Arons, R.R., J.W. Cable and R.M. Nicklow, 1986, Physica B **136**, 407.

Arons, R.R., J.W. Cable and R.M. Nicklow, 1987, J. Appl. Phys. **61**, 3423.

Arons, R.R., M. Loewenhaupt, Th. Reif and E. Gratz, 1994, J. Phys. Condens. Matter **6**, 6789.

Asti, G., 1990, in: Handbook of Magnetic Materials, Vol. 5, ed. K.H.J. Buschow (Elsevier, Amsterdam) p. 397.

Atoji, M., 1961, J. Chem. Phys. **35**, 1950.

Atoji, M., 1967, J. Chem. Phys. **46**, 1891.

Atoji, M., 1969a, J. Chem. Phys. **51**, 3877.

Atoji, M., 1969b, J. Chem. Phys. **51**, 3882.

Atoji, M., 1972, J. Chem. Phys. **57**, 851.

Atzomy, U., M.P. Dariel, E.R. Bauminger, D. Lebenbaum, I. Nowik and S. Ofer, 1973, Phys. Rev. B **7**, 4220.

Aubert, G., D. Gignoux, F. Givord, R. Lemaire and B. Micheletti, 1978, Solid State Commun. **25**, 85.

Babateen, K., K.-U. Neumann and K.R.A. Ziebeck, 1995a, J. Magn. Magn. Mater. **140–144**, 921.

Babateen, M., J. Crangle, F. Fauth, A. Furrer, K.-U. Neumann and K.R.A. Ziebeck, 1995b, Physica B **213–214**, 300.

Bacon, G.E., 1975, Neutron Diffraction (Clarendon Press, Oxford).

Baio, G., O. Moze, G. Amoretti, R. Sonntag, N. Stüßer and K.H.J. Buschow, 1997, Z. Phys. B **102**, 449.

Balcar, E. and S.W. Lovesey, 1986, J. Phys. C: Solid State Physics **19**, 4605.

Balcar, E. and S.W. Lovesey, 1989, Theory of Magnetic Neutron and Photon Scattering (Clarendon Press, Oxford).

Ball, A.R., D. Gignoux, A.P. Murani and D. Schmitt, 1993a, Physica B **190**, 214.

Ball, A.R., D. Gignoux, D. Schmitt and F.Y. Zhang, 1993b, Phys. Rev. B **47**, 11887.

Ball, A.R., D. Gignoux and D. Schmitt, 1993c, J. Magn. Magn. Mater. **119**, 96.

Ball, A.R., D. Gignoux, J. Rodriguez Fernandez and D. Schmitt, 1994, J. Magn. Magn. Mater. **137**, 281.

Barbara, B., M.F. Rossignol and J.X. Boucherle, 1975, Phys. Lett. A **55**, 321.

Barbara, B., M.F. Rossignol, R.A.B. Devine, Y. Berthier and A.P. Murani, 1980, in: Crystalline Electric Field and Structural Effects in f-Electron Systems, eds J. Crow, R.P. Guertin and T.W. Mihalisin (Plenum Press, New York) p. 481.

Barbara, B., Y. Berthier, R.A.B. Devine and M.F. Rossignol, 1982, J. Phys. F: Metal Phys. **12**, 2625.

Barthem, V.M.T.S., D. Gignoux, A. Naït-Saada, D. Schmitt and G. Creuzet, 1988a, Phys. Rev. B **37**, 1733.

Barthem, V.M.T.S., G. Creuzet, D. Gignoux and D. Schmitt, 1988b, J. Physique **12**(C8), 527.

Barthem, V.M.T.S., D. Gignoux, A. Nait-Saada, D. Schmitt and A.Y. Takeuchi, 1989, J. Magn. Magn. Mater. **80**, 142.

Bauer, E., M. Liendl, L. Naber, D. Werner, H. Michor, G. Hilscher, A. Dönni, P. Fischer, F. Fauth and M. Zolliker, 1997, Z. Phys. B **102**, 291.

Becker, K.W., P. Fulde and J. Keller, 1977, Z. Phys. B **28**, 9.

Berthier, Y. and E. Belorizky, 1984, Solid State Commun. **49**, 1099.

Besnus, M.J., P. Panissod, J.P. Kappler, G. Heinrich and A. Meyer, 1983, **31–34**, 227.

Bethe, H., 1929, Ann. Physik **3**, 133.

Beuerle, T., M. Liebs, K. Hummler and F. Fähnle, 1994, J. Magn. Magn. Mater. **132**, L1.

Bieri, J.B., J. Sanchez, A. Fert, D. Bertrand and A.R. Fert, 1982, J. Appl. Phys. **53**, 2347.

Birgeneau, R.J., 1972, J. Phys. Chem. Solids **33**, 59.

Birgeneau, R.J., E. Bucher, L. Passell, D.L. Price and K.C. Turberfield, 1970, J. Appl. Phys. **41**, 900.

Birgeneau, R.J., E. Bucher, L. Passell and K.C. Turberfield, 1971, Phys. Rev. B **4**, 718.

Birgeneau, R.J., E. Bucher, J.P. Maita, L. Passell and K.C. Turberfield, 1973, Phys. Rev. B **8**, 5345.

Blaise, A., B. Fåk, J.P. Sanchez, G. Amoretti, P. Santini, R. Caciuffo, D. Schmitt, B. Malaman and G. Venturini, 1995, J. Phys. Cond. Matter **7**, 8317.

Blanckenhagen, P.V., H. Happel and K. Knorr, 1978, Solid State Commun. **9**, 20.

Blanco, J.A., D. Gignoux, P. Morin and D. Schmitt, 1991a, Europhys. Lett. **15**, 671.

Blanco, J.A., D. Gignoux, D. Schmitt and C. Vettier, 1991b, J. Magn. Magn. Mater. **97**, 4.

Blanco, J.A., D. Gignoux and D. Schmitt, 1992a, Phys. Rev. B **45**, 2529.

Blanco, J.A., D. Gignoux and D. Schmitt, 1992b, Z. Phys. B **89**, 343.

Blanco, J.A., D. Gignoux, J.C. Gomez Sal and D. Schmitt, 1992c, J. Magn. Magn. Mater. **104–107**, 1273.

Blanco, J.A., D. Schmitt and J.C. Gomez Sal, 1992d, J. Magn. Magn. Mater. **116**, 128.

Blanco, J.A., R.M. Nicklow and D. Schmitt, 1995, Physica B **213–214**, 327.

Blanco, J.A., B. Fåk, R.M. Nicklow, B. Roessli and D. Schmitt, 1997a, Physica B **234–236**, 756.

Blanco, J.A., R.M. Nicklow and D. Schmitt, 1997b, Phys. Rev. B **56**, 11666.

Bloch, F., 1936, Phys. Rev. **50**, 259.

Blume, M., 1963, Phys. Rev. B **130**, 1670.

Blume, M., A.J. Freeman and R.E. Watson, 1962, J. Chem. Phys. **37**, 1245.

Bolzoni, F., O. Moze and L. Pareti, 1987, J. Appl. Phys. **62**, 615.

Bonville, P., J.A. Hodges, C. Vaast, E. Alleno, C. Godart, L.C. Gupta, Z. Hossain, R. Nagarajan, G. Hilscher and H. Michor, 1996, Z. Phys. B **101**, 511.

Boothroyd, A.T., 1997, Neutron News **8**(2), 28.

Boucherle, J.X. and J. Schweizer, 1981, J. Magn. Magn. Mater. **24**, 308.

Boucherle, J.X. and J. Schweizer, 1982, J. Appl. Phys. **53**, 1947.

Boucherle, J.X., D. Givord, J. Laforest, J. Schweizer and F. Tasset, 1979, J. Physique **40**(C5), 180.

Boucherle, J.X., D. Givord, D. Gregory and J. Schweizer, 1982, J. Appl. Phys. **53**, 1947, 1950.

Boucherle, J.X., A. Gregory, J. Schweizer and G. Will, 1989, Physica B **156–157**, 734.

Bouton, J.M., R. Clad, A. Herr, P. Mériel, A. Meyer and F. Vigneron, 1980, J. Magn. Magn. Mater. **15–18**, 49.

Boutron, P., 1973, Phys. Rev. B **7**, 3226.

Bowden, G.J., D.St.P. Banbury and M.A.H. McCausland, 1971, J. Phys. C: Solid State Phys. **4**, 1840.

Brockhouse, B.N., 1995, Rev. Mod. Phys. **67**, 735.

Brockhouse, B.N., L.N. Beka, L.R. Rao and A.D.B. Woods, 1962, J. Phys. Soc. Japan **17**(Suppl. B-111), 63.

Brooks, M.S.S. and B. Johansson, 1993, in: Handbook of Magnetic Materials, Vol. 7, ed. K.H.J. Buschow (Elsevier, Amsterdam) ch. 3, p. 139.

Brooks, M.S.S., O. Eriksson, J.M. Wills and B. Johansson, 1997, Phys. Rev. Lett. **79**, 2546.

Brun, T.O., G. Lander, D.L. Price, G.P. Felcher and J.F. Reddy, 1974, Phys. Rev. B **9**, 248.

Bucher, F., J.P. Maita, G.W. Hull, R.C. Fulton and A.S. Cooper, 1975, Phys. Rev. B **11**, 440.

Bührer, W., M. Godet, H.-G. Purwins and E. Walker, 1973, Solid State Commun. **13**, 881.

Burger, J.P., J.N. Daou and P. Vajda, 1990, Z. Phys. B **80**, 233.

Burlet, P., J.M. Effantin, J. Rossat-Mignod, S. Kunii and T. Kasuya, 1988, J. Physique **49**(C8) 459.

Buschow, K.H.J., 1976, J. Less-Common Met. **44**, 301.

Buschow, K.H.J., 1977, Rep. Prog. Phys. **40**, 1179.

Buschow, K.H.J., 1980, in: Ferromagnetic Materials, Vol. 1, ed. E.P. Wohlfarth (North-Holland, Amsterdam) p. 297.

Buschow, K.H.J., 1984, in: Handbook on the Physics and Chemistry of Rare Earths, Vol. 6, eds K.A. Gschneidner Jr. and L. Eyring (North-Holland, Amsterdam) p. 1.

Buschow, K.H.J., 1991, Rep. Prog. Phys. **54**, 1123.

Buschow, K.H.J. and A.M. van der Kraan, 1978, J. Phys. F: Metal Phys. **8**, 92.

Buschow, K.H.J., H.W. de Wijn and A.M. van Diepen, 1969, J. Chem. Phys. **50**, 137.

Buschow, K.H.J., A.M. van Diepen and H.W. de Wijn, 1973, Phys. Rev. B **8**, 5134.

Buschow, K.H.J., J.H.N. van Vucht and W.W. van den Hoogenhof, 1976, J. Less-Common Met. **50**, 145.

Buyers, W.J.L., T.M. Holden, E.C. Svenson, R.A. Cowley and M.T. Hutchings, 1971, J. Phys. C: Solid State Phys. **4**, 2139.

Buyers, W.J.L., T.M. Holden and A. Perreault, 1975, Phys. Rev. B **11**, 266.

Caciuffo, R., G. Amoretti, K.H.J. Buschow, O. Moze, A.P. Murani and B. Paci, 1995, J. Phys. Condens. Matter **7**, 7981.

Cadogan, J.M. and J.M.D. Coey, 1984, Phys. Rev. B **30**, 7326.

Cadogan, J.M., J.P. Gavigan, D. Givord and H.S. Li, 1988, J. Phys. F: Metal Phys. **18**, 779.

Canfield, P.C., B.K. Cho, D.C. Johnston and D.K. Finnemore, 1994, Physica C **230**, 397.

Carboni, C., D. Gignoux, Y. Li, J.W. Ross and A. Tari, 1996, J. Phys. Condens. Matter **8**, 1763.

Castets, A., D. Gignoux and B. Hennion, 1980, J. Magn. Magn. Mater. **15–18**, 375.

Castets, A., D. Gignoux and B. Hennion, 1982a, Phys. Rev. B **25**, 337.

Castets, A., D. Gignoux, B. Hennion and R.M. Nicklow, 1982b, J. Appl. Phys. **53**, 1979.

Cava, R.J., H. Takagi, B. Battlog, H.W. Zandbergen, J.J. Krajewsji, W.F. Peck Jr., R.B. van Dover, R.J. Felder, T. Siegrist, K. Miuhashi, J.O. Lee, H. Eisaki, S.A. Carter and S. Uchida, 1994, Nature **367**, 146.

Charrier, B. and D. Schmitt, 1997a, J. Magn. Magn. Mater. **171**, 106.

Charrier, B. and D. Schmitt, 1997b, in: Proc. Int. Conf. on Aperiodic Crystals, Alpe d'Huez, France (World Scientific, Singapore).

Chamard-Bois, R., J. Rossat-Mignod, K. Knorr and W. Drexel, 1973, Solid State Commun. **13**, 1549.

Charrier, B., B. Ouladdiaf and D. Schmitt, 1997, Phys. Rev. Lett. **78**, 4637.

Chattopadhyay, T., P. Vorderwisch and U. Stuhr, 1995, Hahn Meitner Institute, BENSC experimental reports, HMI-B 525, p. 30.

Chelkowski, A. and R. Orbach, 1975, Phys. Rev. B **12**, 208.

Chevrel, R., M. Sergent and J. Prigent, 1971, Solid State Commun. **3**, 515.

Chiu-Tsao, S.T. and P.M. Levy, 1976, Phys. Rev. B **13**, 3046.

Cho, B.K., Ming Xu, P.C. Canfield, L.L. Miller and D.C. Johnston, 1995a, Phys. Rev. B **52**, 3676.

Cho, B.K., P.C. Canfield and D.C. Johnston, 1995b, Phys. Rev. B **52**, 3844.

Cho, B.K., P.C. Canfield, L.L. Miller, D.C. Johnston, W.P. Beyermann and A. Yatskar, 1995c, Phys. Rev. B **52**, 3684.

Cho, B.K., B.N. Harmon, D.C. Johnston and P.C. Canfield, 1996, Phys. Rev. B **53**, 2217.

Chow, H.C., 1973, Phys. Rev. B **7**, 3404.

Christensen, A.N. and R.G. Hazell, 1980, Acta Chem. Scand. Ser. A **34**, 455.

Christodoulos, F. and J.M. Dixon, 1987a, Phys. Lett. A **124**, 437

Christodoulos, F. and J.M. Dixon, 1987b, J. Phys. C: Solid State Phys. **20**, 5537.

Clark, A.E., 1980, in: Handbook of Ferro-Magnetic Materials, Vol. 1, ed. E.P. Wohlfarth (Elsevier, Amsterdam) ch. 7, p. 531.

Clausen, K.N. and B. Lebech, 1980, J. Magn. Magn. Mater. **15–18**, 347.

Clausen, K. and B. Lebech, 1982, J. Phys. C: Solid State Phys. **15**, 5095.

Clausen, K.N., J.J. Rhyne, B. Lebech and N.C. Koon, 1982, J. Phys. C: Solid State Phys. **15**, 3587.

Coehoorn, R., 1989, Phys. Rev. B **39**, 13072.

Coehoorn, R., 1991, in: Supermagnets, Hard Magnetic Materials, NATO-ASI Series C: Mathematical and Physical Sciences, Vol. 331, eds G.J. Long and F. Grandjean (Kluwer) ch. 20, p. 499.

Coehoorn, R. and G.H.O. Daalderop, 1992, J. Magn. Magn. Mater. **104–107**, 1081.

Collins, S.P., D. Laundy and G.Y. Guo, 1993, J. Phys. Condens. Matter **5**, L637.

Colpa, J.H.P., S. Sinnema, J.J.M. Franse, R.J. Radwanski and P.H. Frings, 1989a, Physica B **156–157**, 731.

Colpa, J.H.P., S. Sinnema, P.H. Frings, J.J.M. Franse and R.J. Radwanski, 1989b, J. Phys. Condens. Matter **1**, 2047.

Colpa, J.H.P., P.H. Frings, R.J. Radwanski, J.J.M. Franse and M. Alba, 1994, J. Magn. Magn. Mater. **131**, 167.

Cooper, B.R., 1969, J. Appl. Phys. **40**, 1344.

Cooper, B.R. and O. Vogt, 1970, Phys. Rev. B **1**, 1218.

Cribier, D. and B. Jacrot, 1960, C. R. Acad. Sci. (Paris) **250**, 2871.

Cromer, D.T., A.C. Larson and R.B. Root, 1960, Acta Crystallogr. **13**, 913.

Czopnik, A., Z. Kletowski and B. Stalinski, 1970, Phys. Status Solidi A: **3**, K263.

Czopnik, A., F.R. de Boer, P.A. Veenhuizen, B. Gren and B. Stalinski, 1990, Physica B **167**, 49.

Das, K.C. and D.K. Ray, 1969, Phys. Rev. **7**, 777.

Das, K.C. and D.K. Ray, 1970, Solid State Commun. **8**, 2025.

Davidov D., R. Orbach, L.J. Tao and C.P. Chock, 1971, Phys. Lett. A **34**, 490.

Davidov, D., R. Orbach, C. Rettori, L.J. Tao and C.P. Chock, 1972, Phys. Rev. Lett. **28**, 490.

Davis, H.L. and H.A. Mook, 1973, AIP Conf. Proc. **10**, 1548.

Davis, H.L. and H.A. Mook, 1975, AIP Conf. Proc. **24**, 229.

Davis, H.L., H.A. Mook and E. Bucher, 1974, Bull. Am. Phys. Soc. **19**.

de Wijn, H.W., A.M. van Diepen and K.H.J. Buschow, 1970, Phys. Rev. B **1**, 4203.

de Wijn, H.W., A.M. van Diepen and K.H.J. Buschow, 1976, Phys. Status Solidi B: **76**, 11.

de Gennes, P.G., 1963, in: Magnetism, Vol. 3, eds G.T. Rado and H. Suhl (Academic Press) p. 115.

de Jong, M.H. and J.K. Kjems, 1983, J. Phys. F: Metal Phys. **13**, 1187.

Decrop, B., J. Deportes, D. Givord, R. Lemaire and J. Chapert, 1982, J. Appl. Phys. **53**, 1953.

Deenadas, C., A.W. Thompson, R.S. Craig and W.E. Wallace, 1971, J. Phys. Chem. Solids **32**, 1853.

del Moral, A., 1992a, J. Phys. Condens. Matter **4**, 4687.

del Moral, A., 1992b, J. Phys. Condens. Matter **4**, 4703.

del Moral, A. and M.S.S. Brooks, 1974, J. Phys. C: Solid State Phys. **7**, 2540.

del Moral, A. and M.R. Ibarra, 1985, J. Phys. Chem. Solids **46**, 127.

del Moral, A., J.I. Arnaudas, M.R. Ibarra, J.S. Abell and E.W. Lee, 1986, J. Phys. C: Solid State Phys. **19**, 579.

del Moral, A., M.R. Ibarra, J.S. Abell and J.F.D. Montenegro, 1987, Phys. Rev. B **35**, 6800.

Dèportes, J., D. Givord and B. Kebe, 1979, J. Physique **40**(C5), 154.

Deutz, A.F., H.B. Brom, H. Deelen, L.J. de Jongh and W.J. Huiskamp, 1986, Solid State Commun. **60**, 917.

Deutz, A.F., H.B. Brom, W.J. Huiskamp, L.J. de Jongh and K.H.J. Buschow, 1989, Physica B **160**, 83.

Devine, R.A.B., 1973, Solid State Commun. **13**, 1495.

Devine, R.A.B. and Y. Berthier, 1978, Solid State Commun. **26**, 315.

Divis, M., 1991, Phys. Status Solidi B: **164**, 227.

Divis, M. and J. Kuriplach, 1993, Physica B **183**, 25.

Divis, M. and J. Kuriplach, 1995, Physica B **205**, 353.

Divis, M., E.A. Goremychkin, P. Svoboda, V. Nekvasil, J. Bishof and R. Osborn, 1991, Physica B **168**, 251.

Divis, M., J. Kuriplach and P. Novak, 1995, J. Magn. Magn. Mater. **140–144**, 1117.

Dixon, J.M. and R. Dupree, 1973, J. Phys. F: Metal Phys. **3**, 118.

Döbler, U., K. Baberschke and S.E. Barnes, 1983, Phys. Rev. B **27**, 6593.

Dönni, A., P. Fischer, A. Furrer and F. Hulliger, 1989, Solid State Commun. **71**, 365.

Dönni, A., P. Fischer, A. Furrer, P. Bonville, F. Hulliger and H.R. Ott, 1990a, Z. Phys. B – Condens. Matter **81**, 83.

Dönni, A., P. Fischer, A. Furrer, W. Bacsa and P. Wachter, 1990b, Z. Phys. B – Condens. Matter **80**, 269.

Dönni, A., A. Furrer, P. Fischer, F. Hulliger and P. Wachter, 1991, Physica B **171**, 353.

Dönni, A., A. Furrer, P. Fischer, F. Hulliger and S.M. Hayden, 1992, J. Phys. Condens. Matter **4**, 4283.

Dönni, A., H. Kitazawa, P. Fischer, T. Vogt, A. Matushita and T. Matsumoto, 1993, Physica B **186–188**, 661.

Dönni, A., A. Furrer, H. Kitazawa and M. Zolliker, 1997a, J. Phys. Condens. Matter **9**, 5921.

Dönni, A., A. Furrer, E. Bauer, H. Kitazawa and M. Zolliker, 1997b, Z. Phys. B **104**, 403.

Donosco, J.P., C. Rettori, G.E. Barberis and D. Davidov, 1981, Solid State Commun. **39**, 203.

Dormann, E., 1991, in: Handbook on the Physics and Chemistry of Rare Earths, Vol. 14, eds K.A. Gschneidner Jr. and L. Eyring (Elsevier, Amsterdam) p. 63.

Drewes, W., A. Leson, W. Schelp and H.G. Purwins, 1988, J. Phys. F: Metal Phys. **18**, 137.

Dunlap, B.D. and D. Niarchos, 1982, Solid State Commun. **44**, 1577.

Duthie, J.C. and V. Heine, 1979, J. Phys. F: Metal Phys. **9**, 1349.

Dwight, A.E., J.W. Downey and R.A. Conner, 1967, Acta Crystallogr. **22**, 745.

Eisaki, H., H. Takagi, R.J. Cava, K. Mizuhashi, J.O. Lee, B. Bartlogg, J.J. Krajewski, W.F. Peck Jr. and S. Uchida, 1994, Phys. Rev. B **50**, 647.

Elsenhans, O., P. Fischer, A. Furrer, K.N. Clausen, H.-G. Purwins and F. Hulliger, 1988, J. Physique **49**(C8), 415.

Elsenhans, O., A. Furrer, H.G. Purwins and F. Hulliger, 1990a, Z. Phys. B **80**, 281.

Elsenhans, O., A. Furrer, K.N. Clausen and E. Walker, 1990b, J. Phys. Condens. Matter **2**, 4737.

Elsenhans, O., P. Fischer, A. Furrer, K.N. Clausen, H.G. Purwins and F. Hulliger, 1991, Z. Phys. B **82**, 61.

Erkelens, W.A.C., L.P. Regnault, J. Rossat-Mignod, M. Gordon, S. Kunii, T. Kasuya and C. Vettier, 1988, J. Physique **C8**, 457.

Escudier, P., D. Gignoux, D. Givord, R. Lemaire and A.P. Murani, 1977, Physica B **86–88**, 197.

Eyers, A., A. Alke, A. Leson, D. Kohake and H.-G. Purwins, 1982, J. Phys. C: Solid State Phys. **15**, 2459.

Fähnle, M., 1995, J. Magn. Magn. Mater. **151**, L5.

Fåk, B., R.A. Garnier, D. Gignoux, R. Kahn and D. Schmitt, 1997, Physica B **233**, 17.

Feile, R., M. Loewenhaupt, J.K. Kjems and H.E. Hoenig, 1981, Phys. Rev. Lett. **47**, 610.

Feile, R., K. Knorr, J.K. Kjems, B. Frick and M. Loewenhaupt, 1983, J. Phys. C: Solid State Phys. **16**, L465.

Felner, I. and I. Nowik, 1978, J. Phys. Chem. Solids **39**, 951.

Felner, I. and I. Nowik, 1979, J. Phys. Chem. Solids **40**, 1035.

Fert, A. and I.A. Campbell, 1978, J. Phys. F: Metal Phys. **8**, L57.

Feyerherm, R., A. Amato, A. Grayevsky, F.N. Gygax, N. Kaplan and A. Schenck, 1995, Z. Phys. B **99**, 3.

Fischer, O., 1978, Appl. Phys. **16**, 1.

Fischer, O., 1990, in: Handbook of Magnetic Materials, Vol. 5, ed. K.H.J. Buschow (Elsevier, Amsterdam) p. 465.

Fischer, P., A. Furrer, E. Kaldis, D. Kim, J.K. Kjems and P.M. Levy, 1985, Phys. Rev. B **31**, 456.

Fisk, Z. and D.C. Johnston, 1977, Solid State Commun. **22**, 359.

Florio, J.V., R.E. Rundle and A.I. Snow, 1952, Acta Crystallogr. **5**, 449.

Fournier, J.M. and E. Gratz, 1993, in: Handbook on the Physics and Chemistry of Rare Earths, Vol. 17, eds K.A. Gschneidner Jr. and L. Eyring (Elsevier, Amsterdam) ch. 115, p. 409.

Franse, J.J.M. and R.J. Radwanski, 1993, in: Handbook of Magnetic Materials, Vol. 7, ed. K.H.J. Buschow (Elsevier, Amsterdam) ch. 5, p. 307.

Frauenheim, Th., W. Matz and G. Feller, 1979, Solid State Commun. **29**, 805.

Freeman, A.J. and J.P. Desclaux, 1979, J. Magn. Magn. Mater. **12**, 11.

Freeman, A.J. and R.E. Watson, 1962, Phys. Rev. B **127**, 2058.

Frick, B. and M. Loewenhaupt, 1985a, J. Magn. Magn. Mater. **52**, 195.

Frick, B. and M. Loewenhaupt, 1985b, Physica B **130**, 372.

Frick, B. and M. Loewenhaupt, 1986a, Z. Phys. B – Condens. Matter **63**, 213.

Frick, B. and M. Loewenhaupt, 1986b, Z. Phys. B – Condens. Matter **63**, 231.

Frick, B., M. Loewenhaupt, A. Murani and R. Feile, 1985, Solid State Commun. **54**, 563.

Fujii, H. and H. Sun, 1995, in: Handbook of Magnetic Materials, Vol. 9, ed. K.H.J. Buschow (Elsevier, Amsterdam) ch. 3, p. 303.

Fulde, P., 1978, in: Handbook on the Physics and Chemistry of Rare Earths, Vol. 2, eds K.A. Gschneidner Jr. and L. Eyring (North-Holland, Amsterdam) ch. 17, p. 295.

Fulde, P. and M. Loewenhaupt, 1985, Adv. Phys. **34**, 589.

Fulde, P. and M. Loewenhaupt, 1988, in: Spin Waves and Magnetic Excitations, Vol. 1, eds A.S. Borovik-Romanov and S.K. Sinha (North-Holland, Amsterdam) ch. 6, p. 367.

Fulde, P. and I. Peschel, 1972, Adv. Phys. **21**, 1.

Furrer, A., 1974, Proc. 11th Rare Earth Research Conference, Traverse City, MI, USA, p. 308.

Furrer, A., 1975, J. Phys. C: Solid State Phys. **8**, 824.

Furrer, A., 1977, Solid State Commun. **16**, 839.

Furrer, A. and H.-U. Güdel, 1977, Phys. Rev. Lett. **39**, 657.

Furrer, A. and H.-U. Güdel, 1997, Phys. Rev. B **56**, 15062.

Furrer, A. and W. Hälg, 1976, J. Phys. C: Solid State Phys. **9**, 3499.

Furrer, A. and H. Heer, 1973, Phys. Rev. Lett. **31**, 1350.

Furrer, A. and E. Kaldis, 1980, in: Crystalline Electric Field and Structural Effects in f-Electron Systems, eds J. Crow, R.P. Guertin and T.W. Mihalisin (Plenum, New York) p. 497.

Furrer, A. and O.E. Martin, 1986, J. Phys. C: Solid State Phys. **19**, 3863.

Furrer, A. and H.-G. Purwins, 1976, J. Phys. C: Solid State Phys. **9**, 1491.

Furrer, A. and H.-G. Purwins, 1977a, Physica B **86–88**, 189.

Furrer, A. and H.-G. Purwins, 1977b, Phys. Rev. B **16**, 2131.

Furrer, A. and U. Tellenbach, 1975, Phys. Status Solidi B: **71**, K31.

Furrer, A. and E. Warming, 1974, J. Phys. C: Solid State Phys. **7**, 3365.

Furrer, A., W. Hälg and T. Schneider, 1967, Helv. Phys. Acta **40**, 821.

Furrer, A., J. Kjems and O. Vogt, 1972, J. Phys. C: Solid State Phys. **5**, 2246.

Furrer, A., W.J.L. Buyers, R.M. Nicklow and O. Vogt, 1976, Phys. Rev. B **14**, 179.

Furrer, A., P.M. Lévy and E. Kaldis, 1977a, in: CEF Effects in Metals and Alloys, ed. A. Furrer (Plenum, New York) p. 24.

Furrer, A., A. Murasik and Z. Kletowski, 1977b, in: CEF effects in Metals and Alloys, ed. A. Furrer (Plenum, New York) p. 31.

Furrer, A., W.J.L. Buyers, R.M. Nicklow and O. Vogt, 1977c, Physica B **86–88**, 105.

Furrer, A., W. Bührer and P. Wachter, 1981, Solid State Commun. **40**, 1011.

Galera, R.M. and P. Morin, 1992, J. Magn. Magn. Mater. **116**, 159.

Galera, R.M., A.P. Murani and J. Pierre, 1981, J. Magn. Magn. Mater. **23**, 317.

Galera, R.M., J. Pierre, E. Siaud and A.P. Murani, 1984, J. Less-Common Met. **97**, 151.

Galera, R.M., A.P. Murani and J. Pierre, 1985, J. Physique **46**, 303.

García-Landa, B., M.R. Ibarra, P.A. Algarabel and O. Moze, 1995, Phys. Rev. B **51**, 15132.

García-Landa, B., P.A. Algarabel, M.R. Ibarra, F.E. Kayzel and J.J.M. Franse, 1997, Phys. Rev. B **55**, 8313.

Gardner, J.S., C.V. Tomy, L. Afalfiz, G. Balakrishnan, D. McKPaul, B.D. Rainford, R. Cywinski, R.S. Eccleston and E.A. Goremychkin, 1995, Physica B **213–214**, 136.

Garnier, A., D. Gignoux, J.L. de la Peña and D. Schmitt, 1997, J. Magn. Magn. Mater. **167**, 52.

Gasser, U., P. Allenspach, F. Fauth, W. Henggeler, J. Mesot, A. Furrer, S. Rosenkranz, P. Vorderwisch and M. Buchgeister, 1996, Z. Phys. B **101**, 345.

Gasser, U., P. Allenspach and A. Furrer, 1997, Physica B **234–236**, 846.

Ghosh, K., S. Ramakrishnan, S.K. Malik and G. Chandra, 1993, Phys. Rev. B **48**, 6249.

Gignoux, D. and F. Givord, 1977, Solid State Commun. **21**, 499.

Gignoux, D. and D. Givord, 1979, J. Phys. F: Metal Phys. **9**, 1409.

Gignoux, D. and F. Givord, 1983, J. Magn. Magn. Mater. **31–34**, 217.

Gignoux, D. and J.J. Rhyne, 1986, J. Magn. Magn. Mater. **54–57**, 1179.

Gignoux, D. and D. Schmitt, 1995, in: Handbook on the Physics and Chemistry of Rare Earths, Vol. 20, eds K.A. Gschneidner Jr. and L. Eyring (North-Holland, Amsterdam) ch. 138, p. 293.

Gignoux, D. and D. Schmitt, 1997, in: Handbook of Magnetic Materials, Vol. 10, ed. K.H.J. Buschow (North-Holland, Amsterdam) ch. 2, p. 239.

Gignoux, D., F. Givord and R. Lemaire, 1975, Phys. Rev. B **12**, 3878.

Gignoux, G., D. Givord, F. Givord, W.C. Koehler and R.M. Moon, 1976, Phys. Rev. B **14**, 162.

Gignoux, G., F. Givord and J. Schweizer, 1977, J. Phys. F: Metal Phys. **9**, 1823.

Gignoux, D., A. Nait-Saada and R. Perrier de la Bathie, 1979a, J. Physique Colloq. **40**(C5), 188.

Gignoux, D., F. Givord, R. Perrier de la Bathie and F. Sayetat, 1979b, J. Phys. F: Metal Phys. **9**, 763.

Gignoux, D., B. Hennion and A. Naït-Saada, 1982, in: CEF Effects in f-Electron Magnetism, eds R.P. Guertin, W. Suski and Z. Zolnierek (Plenum, New York) p. 485.

Gignoux, D., D. Schmitt, A. Takeuchi, F.Y. Zhang, C. Rouchon and E. Roudaut, 1991, J. Magn. Magn. Mater. **98**, 333.

Gignoux, D., D. Schmitt, M.R. Ibarra, B. García-Landa and C. Marquina, 1994, J. Alloys Comp. **210**, 91.

Givord, D., P. Morin and D. Schmitt, 1982, J. Appl. Phys. **53**, 2445.

Givord, D., P. Morin and D. Schmitt, 1983, J. Magn. Magn. Mater. **40**, 121.

Godet, M. and H.-G. Purwins, 1976, Helv. Phys. Acta **49**, 821.

Golding, R.M., R.O. Pascual and I.C. Hoare, 1985, Theor. Chim. Acta (Berlin) **67**, 157.

Goossens, D.J., S.J. Kennedy and T.J. Hicks, 1996, Nucl. Instr. Methods Phys. Res. A **380**, 572.

Goossens, D.J., S.J. Kennedy and T.J. Hicks, 1998, Physica B, to appear.

Goremychkin, E.A. and E. Mühle, 1984, Sov. Phys. JETP Lett. **39**(7), 571.

Goremychkin, E.A. and R. Osborn, 1993, Phys. Rev. B **47**, 14280.

Goremychkin, E.A., E. Mühle, P.G. Ivanitskii, V.T. Krotenko, M.V. Pasechnik, V.V. Slisenko, A.A. Vasilkevich, B. Lippold, O.D. Chistyakov and E.M. Savitskii, 1984, Phys. Status Solidi B: **121**, 623.

Goremychkin, E.A., E. Mühle, I. Natkaniec, M. Popescu and O.D. Chistyakov, 1985a, Sov. Phys. Solid State **27**, 1195.

Goremychkin, E.A., E. Mühle, B. Lippold, O.D. Chistyakov and E.M. Savitskii, 1985b, Phys. Status Solidi **127**, 371.

Goremychkin, E.A., E. Mühle and I. Natkaniec, 1988, Phys. Status Solidi B: **145**, K15.

Goremychkin, E.A., I. Natkaniec, E. Mühle and O.D. Chistyakov, 1989, J. Magn. Magn. Mater. **81**, 63.

Goremychkin, E.A., R. Osborn and A.Yu. Muzychka, 1992, Physica B **179**, 184.

Goremychkin, E.A., R. Osborn and A.Yu. Muzychka, 1994, Phys. Rev. B **50**, 13863.

Goremychkin, E.A., A.Yu. Muzychka and R. Osborn, 1996, Sov. Phys. JETP **83**, 738.

Görller-Walrand, C. and K. Binnemans, 1996, in: Handbook on the Physics and Chemistry of Rare-Earths, Vol. 23, eds K.A. Gschneidner Jr. and L. Eyring (Elsevier, Amsterdam) ch. 155, p. 121.

Gratz, E., M. Loewenhaupt, M. Divis, W. Steiner, E. Bauer, N. Pillmayr, H. Muller, H. Nowotny and B. Frick, 1991, J. Phys. Condens. Matter **3**, 9297.

Greidanus, F.J.A.M., L.J. de Jongh, W.J. Huiskamp, A. Furrer and K.H.J. Buschow, 1982, in: CEF Effects in f-Electron Magnetism, eds R.P. Guertin, W. Suski and Z. Zolnierek (Plenum, New York) p. 13.

Greidanus, F.J.A.M., G.J. Nieuwenhuys, L.J. de Jongh, W.J. Huiskamp, H.W. Capel and K.H.J. Buschow, 1983a, Physica B **119**, 228.

Greidanus, F.J.A.M., L.J. de Jongh, W.J. Huiskamp, A. Furrer and K.H.J. Buschow, 1983b, Physica B **115**, 137.

Greidanus, F.J.A.M., L.J. de Jongh, W.J. Huiskamp, P. Fischer, A. Furrer and K.H.J. Buschow, 1983c, Physica B **115**, 215.

Griffiths, D. and B.R. Coles, 1966, Phys. Rev. Lett. **16**, 1093.

Grigereit, T.E., J.W. Lynn, R.J. Cava, J.J. Krajevski and W.F. Peck Jr., 1995, Physica C **248**, 382.

Groß, W., K. Knorr, A.P. Murani and K.H.J. Buschow, 1977, in: CEF Effects in Metals and Alloys, ed. A. Furrer (Plenum, New York) p. 37.

Groß, W., K. Knorr, A.P. Murani and K.H.J. Buschow, 1980, Z. Phys. B **37**, 123.

Grover, B., 1965, Phys. Rev. A **140**, 1944.

Gubbens, P.C.M., A.M. van der Kraan and K.H.J. Buschow, 1982, J. Magn. Magn. Mater. **29**, 155.

Gubbens, P.C.M., A.M. van der Kraan and K.H.J. Buschow, 1984, J. Phys. F: Metal Phys. **14**, 2195.

Gubbens, P.C.M., K.H.J. Buschow, M. Divis, J. Lange and M. Loewenhaupt, 1991, J. Magn. Magn. Mater. **98**, 141.

Gubbens, P.C.M., K.H.J. Buschow, M. Divis, M. Heidelmann and M. Loewenhaupt, 1992, J. Magn. Magn. Mater. **104–107**, 1283.

Gubbens, P.C.M., C.F. de Vroege, M. Divis, K. Prokes, F.M. Mulder, R.C. Thiel and K.H.J. Buschow, 1995, J. Magn. Magn. Mater. **140–144**, 909.

Güntherodt, G., A. Jayaraman, B. Batlogg and M. Croft, 1983, Phys. Rev. Lett. **51**, 2330.

Güntherodt, G., E. Zirngiebl, S. Blumenröder and H. Woike, 1985, J. Magn. Magn. Mater. **52**, 147.

Hahn, W., M. Loewenhaupt and B. Frick, 1992, Physica B **180–181**, 176.

Halpern, O. and M.H. Johnson, 1939, Phys. Rev. **55**, 895.

Hamaguchi, Y., H. Betsuyaku and S. Funahashi, 1980, J. Magn. Magn. Mater. **15–18**, 377.

Happel, H., P.V. Blankenhagen, K. Knorr and A.P. Murani, 1977, in: CEF Effects in Metals and Alloys, ed. A. Furrer (Plenum, New York) p. 273.

Harris, R., M. Plischke and M.J. Zuckermann, 1973, Phys. Rev. Lett. **31**, 160.

Hasanain, S.K., R.P. Guertin, K. Westerholt, M. Guyot and S. Foner, 1981, Phys. Rev. B **24**, 5165.

Hashimoto, Y., H. Fujii, H. Fujiwara and T. Okamoto, 1979, J. Phys. Soc. Japan **47**, 67.

Hashimoto, Y., H. Kawano, H. Yoshizawa, S. Kawano and T. Shigeoka, 1995, J. Magn. Magn. Mater. **140–144**, 1131.

Haszko, S.E., 1961, Trans. Metal. Soc. AIME **221**, 201.

Heer, H., A. Furrer, E. Walker, A. Treyvaud, H.-G. Purwins and J. Kjems, 1974, J. Phys. C: Solid State Phys. **7**, 1207.

Heidelmann, M., 1992, Thesis, University of Cologne.

Heidelmann, M., B. Lebech, Z. Smetana and M. Loewenhaupt, 1992, J. Phys. Condens. Matter **4**, 8773.

Heininger, F., H.-G. Purwins and E. Walker, 1974, Phys. Lett. A **47**, 53.

Henggeler, W., T. Chattopadhyay, P. Thalmeier, P. Vorderwisch and A. Furrer, 1996, Europhys. Lett. **34**, 537.

Henggeler, W. and A. Furrer, 1998, J. Phys. Condens. Matter **10**, 2579–2596.

Henning, K., L.P. Kaun, B. Lippold, S. Matthies, W. Matz, W. Drexel, P. Seifert and N.I. Moreva, 1977, Solid State Commun. **21**, 297.

Hennion, B. and J. Pierre, 1979, J. Physique **40**(C5), 141.

Hennion, B., J. Pierre, D. Schmitt and P. Morin, 1977, in: CEF Effects in Metals and Alloys, ed. A. Furrer (Plenum, New York) p. 19.

Herbst, J.F., 1991, Rev. Mod. Phys. **63**, 819.

Herbst, J.F. and J.W. Wilkins, 1988, in: Handbook on the Physics and Chemistry of Rare Earths, Vol. 10, eds K.A. Gschneidner Jr. and L. Eyring (Elsevier, Amsterdam) ch. 68, p. 321.

Herbst, J.F. and W.B. Yelon, 1985, J. Appl. Phys. **57**, 2342.

Herbst, J.F., P. Bak and R.E. Watson, 1977, Physica B **123–124**, 123.

Herbst, J.F., J.J. Croat, F.E. Pinkerton and W.B. Yelon, 1984, Phys. Rev. B **29**, 4176.

Hessel-Andersen, N., P.E. Gregers-Hansen, E. Holm, H. Smith and O. Vogt, 1974, Phys. Rev. Lett. **32**, 1321.

Hicks, T.J., 1996, Adv. Phys. **45**, 243.

Hirst, L.L., 1997, Rev. Mod. Phys. **6**, 607.

Hoenig, H.E. and M. Loewenhaupt, 1979a, J. Physique **C5**, 136.

Hoenig, H.E. and M. Loewenhaupt, 1979b, J. Magn. Magn. Mater. **13**, 125.

Høg, J. and P. Touborg, 1974, Phys. Rev. B **9**, 2920.

Høg, J. and P. Touborg, 1975, Phys. Rev. B **11**, 520.
Holden, T.M., E.C. Svensson, W.J.L. Buyers and O. Vogt, 1972, Neutron Inelastic Scattering (IAEA, Vienna) p. 553.
Holden, T.M., E.C. Svensson, W.J.L. Buyers and O. Vogt, 1974, Phys. Rev. B **10**, 3864.
Holden, T.M., W.J.L. Buyers, E.C. Svenson and H.-G. Purwins, 1977, in: CEF Effects in Metals and Alloys, ed. A. Furrer (Plenum, New York) p. 189.
Holden, T.M., W.J.L. Buyers and H.-G. Purwins, 1984, J. Phys. F: Metal Phys. **14**, 2701.
Holland-Moritz, E. and G.H. Lander, 1994, in: Handbook on the Physics and Chemistry of Rare Earths, Vol. 19, Lanthanides/Actinides: Physics – II, eds K.A. Gschneidner Jr., L. Eyring, G.H. Lander and G.R. Choppin (Elsevier, Amsterdam), ch. 130, p. 1.
Holland-Moritz, E., D. Wohlleben, H. Scheuer and M. Loewenhaupt, 1979, J. Magn. Magn. Mater. **14**, 234.
Horn, S., M. Loewenhaupt, H. Scheuer and F. Steglich, 1979, J. Magn. Magn. Mater. **14**, 239.
Houmann, J.G., P. Bak, H.-G. Purwins and E. Walker, 1974, J. Phys. C: Solid State Phys. **7**, 2691.
Hsieh, Y.Y. and M. Blume, 1972, Phys. Rev. B **6**, 2684.
Hu, B.P., H.-S. Li, J.P. Gavigan and J.M.D. Coey, 1989, J. Phys. Condens. Matter **1**, 755.
Hurley, D.P.F., 1993, PhD Thesis, Trinity College, Dublin.
Hurley, D.P., J.M.D. Coey, T. Osakabe, Y. Kuroiwa and M. Kohgi, 1994, J. Phys. Soc. Japan **63**, 3048.
Hurley, D.P.F., M. Kuz'min, J.M.D. Coey and M. Kohgi, 1995, J. Magn. Magn. Mater. **140–144**, 1053.
Hutchings, M.T., 1964, Solid State Phys. **16**, 227.
Iandelli, A. and A. Palenzona, 1979, in: Handbook on the Physics and Chemistry of Rare Earths, Vol. 2, eds K.A. Gschneidner Jr. and L. Eyring (Elsevier, Amsterdam) ch. 13, p. 1.
Ibarra, M.R. and A. del Moral, 1990, J. Magn. Magn. Mater. **83**, 121.
Ibarra, M.R., A. del Moral and J.S. Abell, 1984a, J. Phys. Chem. Solids **45**, 789.
Ibarra, M.R., J.J. Arnaudas, P.A. Algarabel and A. del Moral, 1984b, J. Magn. Magn. Mater. **46**, 167.
Ibarra, M.R., E.W. Lee, A. del Moral and J.S. Abell, 1986, J. Magn. Magn. Mater. **54–57**, 882.
Ibarra, M.R., O. Moze, P.A. Algarabel, J.I. Arnaudas, J.S. Abell and A. del Moral, 1988, J. Phys. C: Solid State Phys. **21**, 2735.
Ibarra, M.R., B. García-Landa, C. Marquina, O. Moze, K.H.J. Buschow, T.H. Jacobs and A. Murani, 1992, J. Magn. Magn. Mater. **104–107**, 1375.
Ibberson, R.M., O. Moze, T.H. Jacobs and K.H.J. Buschow, 1991, J. Phys. C: Condens. Matter **3**, 1219.
Ikeda, M., Y. Aoki and T. Kasuya, 1985, J. Magn. Magn. Mater. **52**, 264.
Imai, H., H. Wada and M. Shiga, 1995, J. Magn. Magn. Mater. **140–144**, 835.
Inoue, T., S.G. Sankar, R.S. Craig, W.E. Wallace and K.A. Gschneidner, 1977, J. Phys. Chem. Solids **38**, 487.
Izyumov, Yu.A. and N.A. Chernoplekov, 1994, Neutron Spectroscopy (Plenum, New York).
Izyumov, Yu.A., V.E. Naish and R.P. Ozerov, 1991, Neutron Diffraction of Magnetic Materials (Plenum, New York).
Jaussaud, C., P. Morin and D. Schmitt, 1980, J. Magn. Magn. Mater. **22**, 98.
Javorsky, P., G. Schaudy, T. Holubar and G. Hilscher, 1994, Solid State Commun. **91**, 259.
Jensen, J., 1974, J. Phys. F: Metal Phys. **4**, 1065.
Jensen, J., 1982, J. Magn. Magn. Mater. **29**, 47.
Jensen, J. and A.R. Mackintosh, 1991, Rare Earth Magnetism – Structure and Excitations (Clarendon Press, Oxford).
Johnston, D.F., 1966, Proc. Phys. Soc. London **88**, 37.
Johnston, D.C. and R.N. Shelton, 1977, J. Low Temp. Phys. **26**, 561.
Joshua, S.J., 1991, Symmetry Principles and Magnetic Symmetry In Solid State Physics, ed. D.F. Brewer (Adam Hilger, Bristol).
Judd, B.R., 1957, Proc. R. Soc. London Ser. A **241**, 122.
Kaplan, N., A. Grayevsky, P. Birrer, F.N. Gygax, B. Hitti, E. Lippelt and A. Schenk, 1989, Phys. Rev. Lett. **62**, 2732.
Kapusta, Cz., P.C. Riedi and G.J. Tomka, 1998, in: Handbook of Magnetic Materials, Vol. 11, ed. K.H.J. Buschow (Elsevier, Amsterdam).
Kawarazaki, S., Y. Kobashi, M. Sato and Y. Miyako, 1995, J. Phys. Condens. Matter **7**, 4051.
Kawarazaki, S., M. Soto and Y. Miyako, 1996, J. Magn. Magn. Mater. **153**, 202.
Kayzel, F.E., 1997, PhD Thesis, University of Amsterdam.
Keller, J. and P. Fulde, 1971, J. Low Temp. Phys. **4**, 289.
Keller, L., W. Henggeler and A. Furrer, 1994, Europhys. Lett. **26**, 353.
Kierstead, H.A., B.D. Dunlap, S.K. Malik, A.M. Umarji and G.K. Shenoy, 1985, Phys. Rev. B **32**, 135.
Kikkert, P.J. and L. Nielsen, 1981a, Phys. Rev. B **23**, 2126.
Kikkert, P.J. and L. Nielsen, 1981b, J. Phys. F: Metal Phys. **11**, 547.

Kim-Ngan, N.H., R.J. Radwanski, F.E. Kayzel and J.J.M. Franse, 1995, J. Magn. Magn. Mater. **140–144**, 863.

Kirchmayr, H.R. and C.A. Poldy, 1979, in: Handbook on the Physics and Chemistry of Rare Earths, Vol. 2, eds K.A. Gschneidner Jr. and L. Eyring (Elsevier, Amsterdam) ch. 14, p. 1.

Kjems, J.K., 1977, Electron Phonon Interaction and Phase Transitions (Plenum, New York) p. 302.

Kjems, J.K., H.R. Ott, S.M. Shapiro and K. Andres, 1978, J. Physique **C6**, 1010.

Kjems, J.K., P. Touborg and M. de Jong, 1979, J. Magn. Magn. Mater. **14**, 277.

Kletowski, Z., B. Stalinski and J. Mulak, 1980, J. Magn. Magn. Mater. **15–18**, 53.

Knopp, G., K. Knorr, H. Wehr and A.P. Murani, 1985, J. Magn. Magn. Mater. **52**, 326.

Knorr, J. and B.E.F. Fender, 1977, in: Crystalline Electric Field and Structural Effects in f-Electron Systems, ed. A. Furrer (Plenum Press, New York) p. 42.

Knorr, K., P.V. Blanckenhagen and W. Happel, 1978a, Solid State Commun. **26**, 613.

Knorr, K., B.E.F. Fender and W. Drexel, 1978b, Z. Physik B **30**, 265.

Knorr, J., A. Loidl and J.K. Kjems, 1980, in: Crystalline Electric Field and Structural Effects in f-Electron Systems, eds J. Crow, R.P. Guertin and T.W. Mihalisin (Plenum, New York) p. 141.

Knorr, K., A. Loidl and J.K. Kjems, 1981, Z. Physik B **40**, 287.

Knorr, K., A. Loidl and C. Vettier, 1983, Phys. Rev. B **27**, 1769.

Knorr, K., R. Feile, J.K. Kjems and W. Assmus, 1985, J. Magn. Magn. Mater. **52**, 323.

Knorr, K., R. Feile, J.K. Kjems and W. Assmus, 1988, Z. Phys. B – Condens. Matter **73**, 81.

Kohgi, M., K. Ohoyama, A. Oyamada, T. Suzuki and M. Arai, 1990, Physica B **163**, 625.

Komatsubara, T., N. Sato, S. Kunii, I. Oguro, Y. Furakawa, Y. Onuki and T. Kasuya, 1983, J. Magn. Magn. Mater. **31–34**, 368.

Koon, N.C. and J.J. Rhyne, 1978, Solid State Commun. **26**, 537.

Koon, N.C. and J.J. Rhyne, 1980a, in: Crystalline Electric Field and Structural Effects in f-Electron Systems, eds J. Crow, R.P. Guertin and T.W. Mihalisin (Plenum, New York) p. 125.

Koon, N.C. and J.J. Rhyne, 1980b, J. Magn. Magn. Mater. **15–18**, 349.

Koon, N.C. and J.J. Rhyne, 1981, Phys. Rev. B **23**, 207.

Koon, N.C., C.M. Williams and B.N. Das, 1991, J. Magn. Magn. Mater. **100**, 173–185.

Koster, G.F., J.O. Dimmock, R.G. Wheeler and H. Statz, 1963, Properties of the Thirty Two Point Groups (MIT Press, Cambridge, MA).

Kötzler, J., G. Raffius, A. Loidl and C.M.E. Zeyen, 1979, Z. Physik B **35**, 125.

Krimmel, A., A. Loidl, R. Eccleston, C. Geibel and F. Steglich, 1996, J. Phys. Condens. Matter **8**, 1677.

Lai, C.C., M.S. Lin, Y.B. You and H.C. Ku, 1995, Phys. Rev. B **51**, 420.

Lander, G.H., 1993, in: Handbook on the Physics and Chemistry of Rare Earths, Vol. 17, Lanthanides/Actinides: Physics – I, eds K.A. Gschneidner Jr., L. Eyring, G.H. Lander and G.R. Choppin (Elsevier, Amsterdam) ch. 117, p. 635.

Lander, G.H. and T.O. Brun, 1970, J. Chem. Phys. **53**, 1387.

Lange, J., 1992, Diploma thesis, University of Cologne.

Lappas, A., K. Prassides and P. Fabi, 1995, Annual Report, ISIS Facility, Rutherford Appleton Laboratory, RAL-95-050, p. 56.

Larson, A.C. and D.C. Cromer, 1961, Acta Crystallogr. **14**, 73.

Lea, K.R., J.M. Leask and W.P. Wolf, 1962, J. Phys. Chem. Solids **23**, 1381.

Lebech, B., Z. Smetana and V. Sima, 1987, J. Magn. Magn. Mater. **70**, 97.

Leson, A., W. Schelp, W. Drewes and H.-G. Purwins, 1986, J. Magn. Magn. Mater. **54–57**, 473.

Lethuillier, P., 1975, Phys. Rev. B **12**, 4836.

Lethuillier, P., J. Pierre, G. Fillion and B. Barbara, 1973, Phys. Status Solidi A: **15**, 613.

Lethuillier, P., J. Pierre, K. Knorr and W. Drexel, 1975, J. Physique **36**, 329.

Lethuillier, P., J. Pierre and D.K. Ray, 1977, J. Phys. F: Metal Phys. **7**, 175.

Levin, R., A. Grayevsky, D. Shaltiel and V. Zevin, 1979, J. Physique **40**(C5), 48.

Lévy, F., 1969, Physik Kondens. Materie **10**, 85.

Levy, P.M. and G.T. Trammell, 1977, J. Phys. C: Solid State Phys. **10**, 1303.

Li, H.-S. and J.M.D. Coey, 1991, in: Handbook of Magnetic Materials, Vol. 6, ed. K.H.J. Buschow (Elsevier, Amsterdam) p. 1.

Li, W.-H., J.W. Lynn, H.B. Stanley, T.J. Udovic, R.N. Shelton and P. Klavins, 1988, J. Physique **C8**, 373.

Li, W.-H., J.W. Lynn, H.B. Stanley, T.J. Udovic, R.N. Shelton and P. Klavins, 1989, Phys. Rev. B **39**, 4119.

Liebs, M., K. Hummler and M. Fähnle, 1993, J. Magn. Magn. Mater. **124**, 1993.

Lingner, C. and B. Lüthi, 1983, J. Magn. Magn. Mater. **36**, 86.

Liu, J.P., F.R. de Boer, P.F. de Châtel, R. Coehoorn and K.H.J. Buschow, 1994, J. Magn. Magn. Mater. **132**, 159.

Loewenhaupt, M., 1980, in: Crystalline Electric Field and Structural Effects in f-Electron Systems, eds J. Crow, R.P. Guertin and T.W. Mihalisin (Plenum, New York) p. 589.

Loewenhaupt, M., 1990, Physica B **163**, 479.

Loewenhaupt, M. and K.H. Fischer, 1993a, in: Handbook of Magnetic Materials, Vol. 7, ed. K.H.J. Buschow (Elsevier, Amsterdam) ch. 6, p. 503.

Loewenhaupt, M. and K.H. Fischer, 1993b, in: Handbook of the Physics and Chemistry of Rare-Earths, Vol. 16, eds K.A. Gschneidner Jr. and L. Eyring (Elsevier, Amsterdam) ch. 105, p. 1.

Loewenhaupt, M. and H.E. Hoenig, 1978, Solid State Commun. **25**, 197.

Loewenhaupt, M. and E. Holland-Moritz, 1979, J. Appl. Phys. **50**, 7456.

Loewenhaupt, M. and M. Prager, 1986, Z. Phys. B **62**, 195.

Loewenhaupt, M. and I. Sosnowska, 1991, J. Appl. Phys. **70**, 5967.

Loewenhaupt, M., K. Baberschke and H. Scheuer, 1980, Solid State Commun. **33**, 175.

Loewenhaupt, M., S. Horn and B. Frick, 1982, in: Crystalline Electric Field and Structural Effects in f-Electron Systems, eds P. Guertin, W. Suski and Z. Zolnierek (Plenum, New York) p. 125.

Loewenhaupt, M., B. Frick, U. Walter, E. Holland-Moritz and S. Horn, 1983, J. Magn. Magn. Mater. **31–34**, 187.

Loewenhaupt, M., M. Prager, A.P. Murani and H.E. Hoenig, 1988, J. Magn. Magn. Mater. **76–77**, 408.

Loewenhaupt, M., I. Sosnowska and B. Frick, 1990, Phys. Rev. B **42**, 3866.

Loewenhaupt, M., I. Sosnowska, A. Taylor and R. Osborn, 1991, J. Appl. Phys. **69**, 5593.

Loewenhaupt, M., P. Tils, D.P. Middleton, K.H.J. Buschow and R.S. Eccleston, 1994a, J. Magn. Magn. Mater. **129**, L151.

Loewenhaupt, M., P. Tils, K.H.J. Buschow and R. Eccleston, 1994b, J. Magn. Magn. Mater. **138**, 52.

Loewenhaupt, M., P. Fabi, I. Sosnowska, B. Frick and R. Eccleston, 1995a, J. Magn. Magn. Mater. **140–144**, 1053.

Loewenhaupt, M., Th. Reif, R.R. Arons, E. Gratz, M. Rotter and B. Lebech, 1995b, Z. Phys. B **96**, 491.

Loewenhaupt, M., P. Tils, K.H.J. Buschow and R. Eccleston, 1996a, J. Magn. Magn. Mater. **152**, 10.

Loewenhaupt, M., Th. Reif, P. Svoboda, S. Wagner, M. Waffenschmitt, H. v. Löhneysen, E. Gratz, M. Rotter, B. Lebech and Th. Hauß, 1996b, Z. Phys. B **101**, 499.

Loidl, A., K. Knorr, J.K. Kjems and B. Lüthi, 1979, Z. Physik B **35**, 253.

Loidl, A., K. Knorr, M. Müllner and K.H.J. Buschow, 1981, J. Appl. Phys. **52**, 1433.

Loidl, A., K. Knorr and C. Vettier, 1982, in: CEF Effects in f-Electron Magnetism, eds R.P. Guertin, W. Suski and Z. Zolnierek (Plenum, New York) p. 83.

Loong, C.-K. and L. Soderholm, 1994, J. Alloys Comp. **207–208**, 153.

Loong, C.-K., L. Soderholm, G.L. Goodman, M.M. Abraham and L.A. Boatner, 1993, Phys. Rev. B **48**, 6124.

Lovesey, S.W., 1984, Theory of Neutron Scattering from Condensed Matter (Oxford Univ. Press).

Lovesey, S.W., 1995, in: Handbook of Magnetic Materials, Vol. 9, ed. K.H.J. Buschow (Elsevier, Amsterdam) ch. 5, p. 545.

Lovesey, S.W. and S.P. Collins, 1996, X-Ray Scattering and Absorption by Magnetic Materials (Clarendon Press, Oxford).

Lovesey, S.W. and D.E. Rimmer, 1969, Rep. Prog. Phys. **32**, 333.

Ludwigs, H.-W., U. Häfner, E. Holland-Moritz, W. Zell, B. Roden and D. Wohlleben, 1980, J. Magn. Magn. Mater. **15–18**, 607.

Luft, H., K. Baberschke and K. Winzer, 1983, Phys. Lett. A **95**, 186.

Luong, N.H. and J.J.M. Franse, 1995, in: Handbook of Magnetic Materials, Vol. 8, ed. K.H.J. Buschow (Elsevier, Amsterdam.) ch. 5, p. 415.

Lüthi, B., 1980, J. Magn. Magn. Mater. **15–18**, 1.

Lynch, D.W. and J.H. Weaver, 1988, in: Handbook on the Physics and Chemistry of Rare Earths, Vol. 10, eds K.A. Gschneidner Jr. and L. Eyring (Elsevier, Amsterdam) ch. 66, p. 231.

Lynn, J.W. and R.N. Shelton, 1979, J. Appl. Phys. **50**, 1984.

Lynn, J.W. and R.N. Shelton, 1980, J. Magn. Magn. Mater. **15–18**, 1577.

Lynn, J., D.E. Moncton, G. Shirane, W. Thomlinson, J. Eckert and R.N. Shelton, 1978a, J. Appl. Phys. **49**, 1389.

Lynn, J., D.E. Moncton, W. Thomlinson, G. Shirane and R.N. Shelton, 1978b, Solid State Commun. **26**, 493.

Mader, K.H., E. Segal and W.E. Wallace, 1969, J. Phys. Chem. Solids **30**, 1.

Mahoney, J.V., W.E. Wallace and R.S. Craig, 1973, J. Appl. Phys. **45**, 2733.

Mahoney, J.V., W.E. Wallace, R.S. Craig and S.G. Sankar, 1975, Inorg. Chem. **14**, 2918.

Malaman, B., G. Venturini, A. Blaise, G. Amoretti and J.P. Sanchez, 1992, J. Magn. Magn. Mater. **104–107**, 1359.

Malaman, B., G. Venturini, A. Blaise, J.P. Sanchez and G. Amoretti, 1993, Phys. Rev. B **47**, 8681.

Malik, S.K., A.M. Umarji and G.K. Shenoy, 1985, Phys. Rev. B **32**, 4426.

Marezio, M., P.D. Dernier, J.P. Remeika, E. Corenzwit and B.T. Matthias, 1973, Mat. Res. Bull. **8**, 657.

Marquina, C., N.H. Kum-Ngan, K. Bakker, R.J. Radwanski, T.H. Jacobs, K.H.J. Buschow, J.J.M. Franse and M.R. Ibarra, 1993, J. Phys. Condens. Matter **5**, 2009.

Marshall, W. and S.W. Lovesey, 1971, Theory of Thermal Neutron Scattering (Clarendon, Oxford).

Martin, O.E., K. Girgis and P. Fischer, 1983, J. Magn. Magn. Mater. **37**, 231.

Matz, W., B. Lippold, E.A. Goremychkin, A. Andreef, H. Greissman and T. Frauenheim, 1982, in: CEF Effects in f-Electron Magnetism, eds R.P. Guertin, W. Suski and Z. Zolnierek (Plenum, New York) p. 69.

Mayer, H.M., M. Steiner, N. Stüsser, H. Weinfurter, K. Kakurai, B. Dorner, P.A. Lindgård, K.N. Clausen, S. Hock and W. Rodewald, 1991, J. Magn. Magn. Mater. **97**, 210.

Mayer, H.M., M. Steiner, N. Stüßer, H. Weinfurter, B. Dorner, P.A. Lindgard, K.N. Clausen, S. Hock and R. Verhoef, 1992, J. Magn. Magn. Mater. **140–144**, 1295.

McCallum, R.W., W.A. Fertig, C.A. Luengo, M.B. Maple, E. Bucher, J.P. Maita, A.R. Sweedler, L. Mattix, P. Fulde and J. Keller, 1975, Phys. Rev. Lett. **34**, 1620.

McCallum, R.W., D.C. Johnston, R.N. Shelton, W. Fertig and M.B. Maple, 1977, Solid State Commun. **24**, 501.

McCarthy, C.M. and C.W. Thompson, 1980, J. Phys. Chem. Solids **41**, 1319.

McCarthy, C.M., C.W. Thompson, R.J. Graves, H.W. White, Z. Fisk and H.R. Ott, 1980, Solid State Commun. **36**, 861.

McWhan, D.B. and C. Vettier, 1979, J. Physique **C5**, 107.

McWhan, D.B., S.M. Shapiro, J. Eckert, H.A. Mook and R.J. Birgeneau, 1978, Phys. Rev. B **18**, 3623.

McWhan, D.B., C. Vettier, R. Youngblood and G. Shirane, 1979, Phys. Rev. B **20**, 4612.

Melero, J.J. and R. Burriel, 1996, J. Magn. Magn. Mater. **157–158**, 651.

Melero, J.J., R. Burriel and M.R. Ibarra, 1995, J. Magn. Magn. Mater. **140–144**, 841.

Mesot, J. and A. Furrer, 1997, J. Supercond. **10**, 623–643.

Mesot, J., P. Allenspach, U. Gasser and A. Furrer, 1997, J. Alloys Comp. **250**, 559.

Meyer, C., F. Hartmann-Boutron, Y. Gros and Y. Berthier, 1981, J. Physique **42**, 605.

Millhouse, A.H., H.-G. Purwins and E. Walker, 1972, Solid State Commun. **11**, 707.

Mishra, S.K. and S.S. Kushwaha, 1978, Phys. Rev. B **18**, 6719.

Moolenaar, A.A., P.C.M. Gubbens, J.J. van Loef and K.H.J. Buschow, 1995, J. Magn. Magn. Mater. **140–144**, 895.

Moon, R.M. and R.M. Nicklow, 1991, J. Magn. Magn. Mater. **100**, 139.

Moon, R.M., T. Riste and W.C. Koehler, 1969, Phys. Rev. **181**, 920.

Morellon, L., P.A. Algarabel, M.R. Ibarra, A. del Moral, D. Gignoux and D. Schmitt, 1996, J. Magn. Magn. Mater. **153**, 17.

Morin, P. and J.A. Blanco, 1993, J. Magn. Magn. Mater. **119**, 59.

Morin, P. and A. de Combarieu, 1975, Solid State Commun. **17**, 975.

Morin, P. and J. Pierre, 1973, Solid State Commun. **13**, 537.

Morin, P. and J. Rouchy, 1993, Phys. Rev. B **48**, 256.

Morin, P. and D. Schmitt, 1982, Phys. Rev. B **26**, 3891.

Morin, P. and D. Schmitt, 1990, in: Handbook of Magnetic Materials, Vol. 5, ed. K.H.J. Buschow (Elsevier, Amsterdam) ch. 1, p. 1.

Morin, P. and D. Schmitt, 1995, J. Magn. Magn. Mater. **140–144**, 1135.

Morin, P., J. Pierre, J. Rossat-Mignod, K. Knorr and W. Drexel, 1974, Phys. Rev. B **9**, 4932.

Morin, P., J. Pierre, D. Schmitt and W. Drexel, 1976, J. Physique **37**, 611.

Morin, P., J. Rouchy and E. du Tremolet de Lachaisserie, 1977, Phys. Rev. B **16**, 3182.

Morin, P., J. Pierre, D. Schmitt and A. Murani, 1978a, Solid State Commun. **25**, 265.

Morin, P., J. Rouchy and D. Schmitt, 1978b, Phys. Rev. B **17**, 3684.

Morin, P., D. Schmitt, C. Vettier and J. Rossat-Mignod, 1980, J. Phys. F: Metal Phys. **10**, 1575.

Morin, P., D. Schmitt and C. Vettier, 1981, J. Phys. F: Metal Phys. **11**, 1487.

Morin, P., D. Schmitt and C. Vettier, 1984, J. Magn. Magn. Mater. **40**, 287.

Morin, P., M. Giraud, P.L. Regnault, E. Roudaut and A. Czopnik, 1987, J. Magn. Magn. Mater. **66**, 345.

Movshovich, R., M.F. Hundley, J.D. Thompson, P.C. Canfield, B.K. Cho and A.V. Chubukov, 1994, Physica C **227**, 381.

Moze, O., 1991, in: Supermagnets, Hard Magnetic Materials, NATO-ASI Series C: Mathematical and Physical Sciences, Vol. 331, eds G.J. Long and F. Grandjean (Kluwer, Dordrecht) ch. 20, p. 499.

Moze, O. and K.H.J. Buschow, 1996, Z. Phys. B **101**, 521.

Moze, O., L. Pareti, M. Solzi and W.I.F. David, 1988, Solid State Commun. **66**, 465.

Moze, O., K.H.J. Buschow, R. Osborn, Z. Bowden and A.D. Taylor, 1989, Solid State Commun. **72**, 248.

Moze, O., R. Caciuffo, R.M.I. Ibberson and K.H.J. Buschow, 1990a, J. Less-Common Met. **166**, 329.

Moze, O., R.M. Ibberson and K.H.J. Buschow, 1990b, J. Phys. Condens. Matter **2**, 1677.

Moze, O., R. Caciuffo and K.H.J. Buschow, 1990c, Solid State Commun. **76**, 331.

Moze, O., R. Caciuffo, H.S. Li, B.P. Hu, J.M.D. Coey, R. Osborn and A.D. Taylor, 1990d, Phys. Rev. B **42**, 1940.

Moze, O., R.M. Ibberson and K.H.J. Buschow, 1991, Solid State Commun. **78**, 473.

Moze, O., R. Caciuffo, G. Amoretti, J.M.D. Coey, H.S. Li and B.P. Hu, 1992a, in: Proc. 7th Int. Symp. on Magnetic Anisotropy and Coercivity in RE–TM Alloys, Hi-Perm Laboratory, University of Western Australia, p. 1.

Moze, O., R. Caciuffo, K.H.J. Buschow and G. Amoretti, 1992b, J. Magn. Magn. Mater. **104–107**, 1391.

Moze, O., R. Caciuffo, B. Gillon, G. Calestani, F.E. Kayzel and J.J.M. Franse, 1994, Phys. Rev. B **50**, 9293.

Moze, O., L. Pareti and K.H.J. Buschow, 1995, J. Phys. Condens. Matter **7**, 9255.

Moze, O., R. Sonntag and K.H.J. Buschow, 1996, Hahn Meitner Institute, BENSC Experimental Report, HMI-B536, p. 145.

Moze, O., S. Rosenkranz, R. Osborn and K.H.J. Buschow, 1997, unpublished.

Mühle, E., E.A. Goremychkin and I. Natkaniec, 1989, J. Magn. Magn. Mater. **81**, 72.

Murani, A.P., 1997, Neutron News **8**(2), 28.

Murani, A.P., D. Gignoux and D. Givord, 1975, in: Proc. 14th Low Temperature Physics Conference, Vol. 3, p. 302.

Murasik, A., A. Furrer and Z. Kletowski, 1976, Solid State Commun. **19**, 65.

Nagarajan, R., C. Mazumdar, Z. Houssain, S.K. Dhar, K.V. Gopalakrishnan, L.C. Gupta, C. Godart, B.D. Padalia and R. Vijaaraghavan, 1994, Phys. Rev. Lett. **72**, 274.

Nereson, N., 1973, J. Appl. Phys. **44**, 4727.

Nereson, N. and G. Arnold, 1970, J. Chem. Phys. **53**, 2818.

Newman, D.J., 1971, Adv. Phys. **20**, 197.

Newman, D.J., 1983, J. Phys. F: Metal Phys. **13**, 1511.

Newman, D.J. and B. Ng, 1989, Rep. Prog. Phys. **52**, 699.

Nicklow, R.M., N. Wakabayashi, M.K. Wilkinson and R.F. Reed, 1974, Phys. Rev. Lett. **27**, 334.

Nicklow, R.M., N.C. Koon, C.M. Williams and J.B. Milstein, 1976, Phys. Rev. Lett. **36**, 532.

Niksch, M., W. Assmus, B. Lüthi and H.R. Ott, 1982, Helv. Phys. Acta **55**, 688.

Novák, P. and J. Kuriplach, 1992, J. Magn. Magn. Mater. **104–107**, 1499.

Novák, P. and J. Kuriplach, 1994, Phys. Rev. B **50**, 2958.

Onuki, Y., K. Ina, M. Nishihara, T. Komatsubara, S. Takayanagi, K. Kameda and N. Wada, 1986, J. Phys. Soc. Japan **55**, 1818.

Orlov, V.G. and J. Jensen, 1988, J. Magn. Magn. Mater. **71**, 279.

Osborn, R. and E.A. Goremychkin, 1994, J. Appl. Phys. **76**, 6124.

Osborn, R., S.W. Lovesey, A.D. Taylor and E. Balcar, 1991, in: Handbook on the Physics and Chemistry of Rare Earths, Vol. 14, eds K.A. Gschneidner Jr. and L. Eyring (Elsevier, Amsterdam) ch. 93, p. 1.

Osborn, R., E.A. Goremychkin and A. Muzychka, 1993, Rutherford Appleton Laboratory, Experimental Report RB 4243.

Oseroff, S., M. Passeggi, D. Wohlleben and S. Schultz, 1981, Phys. Rev. B **15**, 1283.

Paci, B., R. Caciuffo, G. Amoretti, O. Moze, K.H.J. Buschow and A.P. Murani, 1995, Solid State Commun. **94**, 489.

Paci, B., G. Baio, G. Amoretti, O. Moze, R. Caciuffo and K.H.J. Buschow, 1997, Physica B **234–236**, 741.

Paolasini, L., G.H. Lander, S.M. Shapiro, R. Caciuffo, B. Lebech, L.-P. Ragnault, B. Roessli and J.-M. Fournier, 1996, Phys. Rev. B **54**, 7222.

Parthé, E. and B. Chabot, 1984, in: Handbook of the Physics and Chemistry of Rare Earths, Vol. 6, eds K.A. Gschneidner Jr. and L. Eyring (North-Holland, Amsterdam) p. 113.

Peregudov, V.N., A.M. Afanas'ev and V.D. Gorobchenko, 1982, Sov. Phys. JETP **56**, 1059.

Pierre, J. and R. Pauthenet, 1965, C. R. Acad. Sci. Paris **260**, 2739.

Pierre, J., D. Schmitt, P. Morin and B. Hennion, 1977, J. Phys. F: Metal Phys. **7**, 1965.

Pierre, J., P. Morin, D. Schmitt and B. Hennion, 1978, J. Physique **39**, 793.

Pink, D., 1968, J. Phys. C: Solid State Phys. **1**, 1246.

Pofahl, G., E. Zirngiebl, S. Blumenröder, H. Brenten, G. Güntherodt and K. Winzer, 1987, Z. Phys. B – Condens. Matter **66**, 339.

Polatsek, G. and P. Bonville, 1992, Z. Phys. B **88**, 189.

Potzel, W., G.M. Kalvius and J. Gal, 1993, in: Handbook on the Physics and Chemistry of Rare Earths, Vol. 17, eds K.A. Gschneidner Jr. and L. Eyring (Elsevier, Amsterdam) ch. 116, p. 539.

Pourarian, F., S.K. Malik, W.E. Wallace and R.S. Craig, 1981, J. Magn. Magn. Mater. **24**, 43.

Prakash, O., D.S.P. Bunburry and M.A.H. McCausland, 1984, Z. Phys. B **58**, 39.

Purwins, H.-G. and A. Leson, 1990, Adv. Phys. **39**, 309.

Purwins, H.-G., E. Walker, P. Donzé, A. Treyvaud, A. Furrer, W. Bührer and H. Heer, 1973, Solid State Commun. **12**, 117.

Purwins, H.-G., J.G. Houman, P. Bak and E. Walker, 1974, Phys. Rev. Lett. **31**, 1585.

Purwins, H.-G., W.J.L. Buyers, T.M. Holden and E.C. Svenson, 1976a, AIP Conf. Proc. **29**, 259.

Purwins, H.-G., E. Walker, B. Barbara, M.F. Rossignol and A. Furrer, 1976b, J. Phys. C: Solid State Phys. **9**, 1025.

Radwanski, R.J., N.H. Kim-Ngan, F.E. Kayzel, J.J.M. Franse, D. Gignoux, D. Schmitt and F.Y. Zhang, 1992, J. Phys. Condens. Matter **4**, 8853.

Rainford, B.D. and R. Cywinski, 1994, Annual Report, ISIS Facility, Rutherford Appleton Laboratory, RAL-94-050, p. 113.

Rainford, B., K.C. Turberfield, G. Busch and O. Vogt, 1968, J. Phys. C (Proc. Phys. Soc.) **1**, 679.

Rainford, B.D., V. Samadian, R.J. Begum, E.W. Lee and S.K. Burke, 1982, J. Appl. Phys. **53**, 7725.

Rao, V.U.S. and W.E. Wallace, 1970, Phys. Rev. B **2**, 4613.

Rathmann, P. and P. Touborg, 1977, Phys. Rev. B **16**, 1212.

Rathmann, O., J. Als-Nielsen, P. Bak, J. Høg and P. Touborg, 1974, Phys. Rev. **10**, 3983.

Reiffers, M., Yu.G. Naidyuk, A.G.M. Jansen, P. Wyder, I.K. Yanson, D. Gignoux and D. Schmitt, 1989, Phys. Rev. Lett. **62**, 1560.

Rettori, C., D. Davidov and H.M. Kim, 1973, Phys. Rev. B **8**, 5335.

Rhyne, J.J., 1980, in: Science and Technology of Rare-Earth Materials (Academic Press, New York) p. 261.

Rhyne, J.J., 1987, J. Magn. Magn. Mater. **70**, 88.

Rhyne, J.J. and N.C. Koon, 1979, J. Appl. Phys. **49**, 2133.

Rhyne, J.J. and N.C. Koon, 1982, J. Appl. Phys. **53**, 8354.

Rhyne, J.J. and N.C. Koon, 1983, J. Magn. Magn. Mater. **31–34**, 608.

Rhyne, J.J., N.C. Koon, J.B. Milstein and H.A. Alperin, 1977, Physica B **86–88**, 149.

Rhyne, J.J., N.C. Koon and B.N. Das, 1979, J. Magn. Magn. Mater. **14**, 273.

Richter, M., P.M. Oppeneer, H. Eschrig and B. Johansson, 1992, Phys. Rev. B **46**, 13919.

Richter, M., P.M. Oppeneer, H. Eschrig and B. Johansson, 1993a, Physica B **186–188**, 918.

Richter, M., P.M. Oppeneer, H. Eschrig and B. Johansson, 1993b, Int. J. Mod. Phys. B **7**, 737.

Ried, K., V. Ötzpamir and H. Kronmuller, 1994, Phys. Rev. B **50**, 10027.

Rogl, P., 1984, in: Handbook of the Physics and Chemistry of Rare Earths, Vol. 7, eds K.A. Gschneidner Jr. and L. Eyring (North-Holland, Amsterdam) p. 1.

Röhler, J., 1988, in: Handbook on the Physics and Chemistry of the Rare Earths, Vol. 10, eds K.A. Gschneidner Jr. and L. Eyring (Elsevier, Amsterdam) ch. 70, p. 425.

Rossat-Mignod, J., 1987, in: Methods of Experimental Physics, Vol. 23, eds K. Sköld and D.L. Price (Academic, New York) part C, ch. 19, p. 69.

Rossat-Mignod, J., R. Chamard-Bois, K. Knorr and W. Drexel, 1974, in: Proc. Rare Earth Research Conference (US Atomic Energy Commission Technical Information Center, Oak Ridge, TN).

Rossel, C., K.N. Yang, M.B. Maple, Z. Fisk, E. Zirngiebl and J.D. Thompson, 1987, Phys. Rev. B **35**, 1914.

Rudowicz, C., 1987, J. Phys. C: Solid State Phys. **20**, 6033.

Sablik, M.J., 1985, Phys. Rev. B **32**, 5880.

Sablik, M.J. and Y.L. Wang, 1979, Phys. Rev. B **19**, 2729.

Sacchi, M., O. Sakho and G. Rossi, 1991a, Phys. Rev. B **43**, 1276.

Sacchi, M., O. Sakho, F. Sirotti, X. Jin and G. Rossi, 1991b, Surf. Sci. **251–252**, 346.

Sacchi, M., F. Sirotti and G. Rossi, 1992a, Solid State Commun. **81**, 977.

Sacchi, M., O. Sakho, F. Sirotti and G. Rossi, 1992b, Appl. Surf. Sci. **56–58**, 1.

Sampathkumaran, E.V. and I. Das, 1992, J. Phys. Condens. Matter **4**, L475.

Santini, P., G. Amoretti, A. Blaise and R. Caciuffo, 1993, J. Appl. Phys. **73**, 6560.

Schelp, W., A. Leson, W. Drewes, H.-G. Purwins and H. Grimm, 1983, Z. Phys. B **51**, 41.

Schelp, W., W. Drewes, H.-G. Purwins and G. Eckold, 1984, Solid State Commun. **52**, 825.

Schelp, W., W. Drewes, A. Leson, H.-G. Purwins and G. Eckold, 1985, J. Magn. Magn. Mater. **50**, 147.
Schelp, W., W. Drewes, A. Leson and H.-G. Purwins, 1986, J. Phys. Chem. Solids **47**, 855.
Schmid, B., B. Hälg, A. Furrer, W. Urland and R. Kremer, 1987, J. Appl. Phys. **61**, 3426.
Schmitt, D., 1977, J. Phys. F: Metal Phys. **7**, 1521.
Schmitt, D., 1979, J. Phys. F: Metal Phys. **9**, 1559.
Schmitt, D., P. Morin and J. Pierre, 1977a, Phys. Rev. B **15**, 1698.
Schmitt, D., P. Morin and J. Pierre, 1977b, in: CEF Effects in Metals and Alloys, ed. A. Furrer (Plenum, New York) p. 203.
Schobinger-Papamantellos, P., P. Fischer, C.H. de Groot, F.R. de Boer and K.H.J. Buschow, 1996, J. Alloys Comp. **232**, 154.
Sears, V.F., 1992, Neutron News **3**, 26.
Segal, E. and W.E. Wallace, 1970, J. Solid State Chem. **2**, 347.
Segal, E. and W.E. Wallace, 1973, J. Solid State Chem. **6**, 99.
Segal, E. and W.E. Wallace, 1974, J. Solid State Chem. **11**, 203.
Segal, E. and W.E. Wallace, 1975, J. Solid State Chem. **13**, 201.
Settai, R., M. Abliz, P. Ahmet, K. Motoki, N. Kimura, H. Ikezawa, T. Ebihara, H. Sugawara, K. Sugiyama and Y. Onuki, 1995, J. Phys. Soc. Japan **64**, 383.
Severing, A., A.P. Murani, J.D. Thompson, Z. Fisk and C.-K. Loong, 1990, Phys. Rev. B **41**, 1739.
Shapiro, S.M. and P. Bak, 1975, J. Phys. Chem. Solids **36**, 579.
Shapiro, S.M., Birgeneau, R.J. and E. Bucher, 1975, Phys. Rev. Lett. **34**, 470.
Shelton, R.N., L.S. Hausermann-Berg, M.J. Johnson, P. Klavins and H.D. Yang, Phys. Rev. B **34**, 199.
Sherrington, D., 1979, J. Phys. C: Solid State Phys. **12**, L929.
Shohata, N., 1977, J. Phys. Soc. Japan **42**, 1873.
Shull, C.G., 1995, Rev. Mod. Phys. **67**, 753.
Sieck, M., O. Stockert, S. Wagner, M. Loewenhaupt and H. v. Löhneysen, 1995, J. Magn. Magn. Mater. **140–144**, 1125.
Siegrist, T., H.W. Zandbergen, R.J. Cava, J.J. Krajewski and W.F. Peck Jr., 1994, Nature **367**, 759.
Sievers, J., 1982, Z. Phys. B **45**, 289.
Sima, V., M. Divis, P. Svoboda, Z. Smetana, S. Zajac and J. Bischof, 1989, J. Phys. Condens. Matter **1**, 10153.
Sinha, S.K., 1978, in: Handbook on the Physics and Chemistry of Rare Earths, Vol. 1, eds K.A. Gschneidner Jr. and L. Eyring (Elsevier, Amsterdam) ch. 7, p. 489.
Sinha, S.K., J.W. Lynn, T.E. Grigereit, Z. Houssain, L.C. Gupta, R. Nagarajan and C. Godart, 1995, Phys. Rev. B **51**, 681.
Sinnema, S., J.J.M. Franse, A. Menovsky and R.J. Radwanski, 1986, J. Magn. Magn. Mater. **54–57**, 1639.
Sinnema, S., J.J.M. Franse, R.J. Radwanski, A. Menovsky and F.R. de Boer, 1987, J. Phys. F: Metal Phys. **17**, 233.
Skomski, R., 1994, Philos. Mag. B **70**, 175.
Skomski, R. and J.M.D. Coey, 1995, J. Magn. Magn. Mater. **140–144**, 965.
Squires, G., 1978, Thermal Neutron Scattering (Cambridge Univ. Press, London).
Stanley, H.B., B.D. Rainford, W.G. Stirling and J.S. Abell, 1985, Physica B **130**, 355.
Stanley, H.B., J.W. Lynn, R.N. Shelton and P. Klavins, 1987, J. Appl. Phys. **61**, 3371.
Stassis, C. and H.W. Deckman, 1975, Phys. Rev. B **12**, 1885.
Stefanski, P., W. Suski, K. Wochowski and T. Mydlarz, 1995, Solid State Commun. **97**, 465.
Steinbeck, L., M. Richter, H. Eschrig and U. Nitzsche, 1994, Phys. Rev. B **49**, 16289.
Steinbeck, L., M. Richter, H. Eschrig and U. Nitzsche, 1995, J. Magn. Magn. Mater. **140–144**, 739.
Stevens, K.W.H., 1951, Proc. Phys. Soc. London **LXV**(3-A), 14.
Stewart, M. and B.R. Coles, 1974, J. Phys. F: Metal Phys. **4**, 458.
Stirling, W. and K.A. McEwen, 1987, in: Methods of Experimental Physics, Vol. 23, part C (Academic Press, New York) p. 159.
Sugawara, K., 1977, Phys. Status Solidi B: **81**, 313.
Sugawara, K., 1979, Phys. Status Solidi B: **92**, 317.
Süllow, S., B. Ludolph, C.E. Snel, F.E. Kayzel, E. Brück, G.J. Nieuwenhuys, A.A. Menovsky and J.A. Mydosh, 1995, Z. Phys. B **98**, 17.
Suski, W., 1996, in: Handbook on the Physics and Chemistry of Rare-Earths and Actinides, Vol. 22, eds K.A. Gschneidner Jr. and L. Eyring (North-Holland, Amsterdam) ch. 149, p. 144.
Svoboda, P., M. Divis, A.V. Andreev, N.V. Baranov, M.I. Bartashevich and P.E. Markin, 1992, J. Magn. Magn. Mater. **104–107**, 1329.
Szytula, A., 1991, in: Handbook of Magnetic Materials, Vol. 6, ed. K.H.J. Buschow (Elsevier, Amsterdam) ch. 2, p. 85.
Szytula, A. and J. Leciejewicz, 1989, in: Handbook of the Physics and Chemistry of Rare Earths, Vol. 12, eds K.A. Gschneidner Jr. and L. Eyring (North-Holland, Amsterdam) p. 133.

Takahashi, T., T. Morimoto, T. Yokoya, S. Kunii, T. Komatsubara and O. Sakai, 1995, Phys. Rev. B **52**, 9140.

Takayanagi, S., 1984, J. Phys. Soc. Japan **53**, 676.

Takeuchi, T., P. Ahmet, M. Abliz, R. Settai and Y. Onuki, 1996, J. Phys. Soc. Japan **65**, 1404.

Tellenbach, U., A. Furrer and A.H. Milhouse, 1975, J. Phys. C: Solid State Phys. **8**, 3833.

Thalmeier, P. and B. Lüthi, 1991, in: Handbook on the Physics and Chemistry of Rare Earths, Vol. 14, eds K.A. Gschneidner Jr. and L. Eyring (Elsevier, Amsterdam) ch. 96, p. 225.

Tils, P., M. Loewenhaupt, C.-K. Loong and H. Schober, 1997, Physica B **234–236**, 739.

Thole, B.T., G. van der Laan and G.A. Sawatzky, 1985, Phys. Rev. Lett. **55**, 2086.

Touborg, P., 1977, Phys. Rev. B **16**, 1201.

Touborg, P., R. Nevald and T. Johansson, 1978, Phys. Rev. B **17**, 4454.

Trammell, G.T., 1953, Phys. Rev. **92**, 1387.

Tsai, T.H., J.A. Gerber, J.W. Weymouth and D.J. Sellmyer, 1978, J. Appl. Phys. **49**, 1507.

Tsuchida, T. and W.E. Wallace, 1965, J. Chem. Phys. **43**, 3811.

Turberfield, K.C., L. Passell, R.J. Birgeneau and E. Bucher, 1970, J. Appl. Phys. **42**, 1746.

Turberfield, K.C., L. Passell, R.J. Birgeneau and E. Bucher, 1971, Phys. Rev. Lett. **25**, 752.

Umlauf, E., W. Schmid, C.D. Bredl, F. Steglich and M. Loewenhaupt, 1979, Z. Physik B **34**, 65.

Vajda, P., 1995, in: Handbook on the Physics and Chemistry of Rare Earths, Vol. 20, eds K.A. Gschneidner Jr. and L. Eyring (Elsevier, Amsterdam) ch. 137, p. 207.

Van der Linden, H.W.M., G.J. Nieuwenhuys, H.D. Dokter, D. Davidov and I. Felner, 1980, J. Magn. Magn. Mater. **15–18**, 42.

Van Hove, L., 1954, Phys. Rev. **95**, 249.

Van Vucht, J.H.N. and K.H.J. Buschow, 1966, J. Less-Common Met. **50**, 1.

Vettier, C., D.B. McWhan, E.I. Blout and G. Shirane, 1977, Phys. Rev. Lett. **39**, 1028.

Vigneron, F., M. Bonnet and R. Kahn, 1980, in: Crystalline Electric Field and Structural Effects in f-Electron Systems, eds J.E. Crow, R.P. Guertin and T.W. Mihalisin (Plenum, New York) p. 513.

Vigneron, F., M. Bonnet, A. Herr and J. Schweizer, 1982, J. Phys. F: Metal Phys. **12**, 223.

Vigneron, F., M. Bonnet and P. Becker, 1985a, Physica B **130**, 366.

Vigneron, F., M. Bonnet and J. Chappert, 1985b, J. Phys. F: Metal Phys. **15**, 181.

Vogt, O. and K. Mattenberger, 1993, in: Handbook on the Physics and Chemistry of Rare Earths, Vol. 17, eds K.A. Gschneidner Jr. and L. Eyring (Elsevier, Amsterdam) ch. 114, p. 301.

Wachter, P. and G. Travaglini, 1985, J. Magn. Magn. Mater. **47–48**, 423.

Wakabayashi, N. and A. Furrer, 1976, Phys. Rev. B **13**, 4343.

Wallace, W.E., S.G. Sankar and V.U.S. Rao, 1977, in: Structure and Bonding, Vol. 33, eds J.D. Dunitz, P. Hemmerich, J. Ibers, C.K. Jørgensen, J.B. Neilands, D. Reinen and R.J.P. Williams (Springer-Verlag, Berlin) p. 1.

Walline, R.E. and W.E. Wallace, 1964, J. Chem. Phys. **41**, 3285.

Walter, U., 1984, J. Phys. Chem. Solids **45**, 401.

Walter, U., 1986, Z. Phys. B **62**, 299.

Walter, U., 1987a, Europhys. Lett. **4**, 1285.

Walter, U., 1987b, Phys. Rev. B **36**, 2504.

Walter, U. and E. Holland-Moritz, 1981, Z. Phys. B **45**, 107.

Walter, U., D. Wohlleben and Z. Fisk, 1986a, Z. Phys. B **62**, 325.

Walter, U., C.-K. Loong, M. Loewenhaupt and W. Schlabitz, 1986b, Phys. Rev. B **33**, 7875.

Walter, U., A. Slebarski and U. Steigenberger, 1986c, J. Phys. Soc. Japan **55**, 650.

Walter, U., Y. Onuki and T. Komatsubara, 1988, J. Phys. Soc. Japan **57**, 2518.

Wang, Y.-L., 1971, Phys. Lett. A **35**, 383.

Wang, Y.L. and B.R. Cooper, 1969, Phys. Rev. **185**, 696.

Warming, E. and P. Bak, 1975, J. Phys. C: Solid State Phys. **8**, 1054.

Wegener, W., A. Furrer, W. Buhrer and S. Hautecler, 1981, J. Phys. C **14**, 2387.

Wegener, W., A. Furrer, W. Buhrer and S. Hautecler, 1982, in: Crystalline Electric Field and Structural Effects in f-Electron Systems, eds R.P. Guertin, W. Suski and T.W. Mihalisin (Plenum, New York) p. 185.

Wentworth, C.D. and A.F. Deutz, 1989, Solid State Commun. **79**, 179.

Wernik, J.H. and S. Geller, 1959, Acta Crystallogr. **12**, 662.

White, J.W. and C.G. Windsor, 1984, Rep. Prog. Phys. **47**, 707.

Wiesinger, G. and G. Hilscher, 1991, in: Handbook of Magnetic Materials, Vol. 6, ed. K.H.J. Buschow (Elsevier, Amsterdam) ch. 6, p. 511.

Williams, G.W., 1988, Polarized Neutrons (Clarendon Press, Oxford, UK).

Williams, G. and G.L. Hirst, 1969, Phys. Rev. B **185**, 402.

Williams, C.M., N.C. Koon and B.N. Das, 1979, J. Appl. Phys. **50**, 1669.

Willis, B.T.M. and A.W. Pryor, 1975, Thermal Vibrations in Crystallography (Cambridge Univ. Press, Cambridge, UK).

Windsor, C.G., 1981, Pulsed Neutron Scattering (Taylor and Francis, London).

Wintenberger, M. and R. Chamard-Bois, 1972, Acta Crystallogr. A **28**, 341.

Yamada, H. and M. Shimizu, 1982, J. Phys. F: Metal Phys. **12**, 2413.

Yamada, H. and M. Shimizu, 1983, J. Magn. Magn. Mater. **31–34**, 211.

Yamada, M., H. Kato, H. Yamamoto and Y. Nakagawa, 1988, Phys. Rev. B **38**, 620.

Yeh, C.T., W. Reichardt, B. Renker, N. Nücker and M. Loewenhaupt, 1981, J. Physique **C6**, 371.

Yonemitsu, K., T. Takenobu, H. Sato and Y. Onuki, 1991, J. Phys. Soc. Japan **60**, 1672.

Yoshizawa, H., S.M. Shapiro, S.K. Hasanain and R.P. Guertin, 1983, Phys. Rev. B **27**, 448.

Zaretsky, J., C. Stassis, A.I. Goldman, P. C. Canfield, P. Dervengas, B.J. Cho and D.C. Johnston, 1995, Phys. Rev. B **51**, 678.

Zhang, F.Y., D. Gignoux, D. Schmitt, J.J.M. Franse, F.E. Kayzel, N.H. Kim-Ngan and R.J. Radwanski, 1994, J. Magn. Magn. Mater. **130**, 108.

Zhao, T.S., X.C. Kou, R. Grössinger and H.R. Kirchmayr, 1991, Phys. Rev. B **44**, 2846.

Zhi-dong, Z., 1996, Phys. Rev. B **53**, 2569.

Zhi-dong, Z. and Z. Tong, 1997, J. Phys. Condens. Matter **9**, 8101.

Zirngiebl, E. and G. Güntherodt, 1991, in: Handbook on the Physics and Chemistry of Rare Earths, Vol. 10, eds K.A. Gschneidner Jr. and L. Eyring (Elsevier, Amsterdam) ch. 95, p. 163.

Zirngiebl, E., B. Hillebrands, S. Blumenröder, G. Güntherodt, M. Loewenhaupt, J.M. Carpenter, K. Winzer and Z. Fisk, 1984, Phys. Rev. B **30**, 4052.

Zolnierek, Z., 1984, J. Phys. Chem. Solids **44**, 523.

Zvezdin, A.K., 1995, in: Handbook of Magnetic Materials, Vol. 9, ed. K.H.J. Buschow (Elsevier, Amsterdam) ch. 4, p. 405.

Subject Index

Materials Index